

The structural and temporal constraints on regional propylitic alteration: a study of the Quellaveco Cu-Mo porphyry, Peru

Rebecca Strachan

A thesis submitted in partial fulfilment of the requirements for the degree of

Doctor of Philosophy

University of London

Department of Earth Sciences

29th May 2021



I, Rebecca Strachan, confirm that the work presented in this thesis is my own.
Where information has been derived from other sources, I confirm that this has
been indicated in the work.

Primary Supervisor

Prof Pieter Vermeesch

Secondary Supervisor

Prof Jamie Wilkinson

Abstract

The propylitic halo is one of the least studied parts of the porphyry system, however advancements in geochemical vectoring and fertility studies have highlighted the importance of propylitic alteration for the future of porphyry exploration. This study furthers our understanding of the development of district-scale propylitic alteration by applying an innovative approach which considers the potential spatial, structural and temporal controls on district-scale propylitic alteration, generating a 4-dimensional model of the evolution of propylitic alteration in a specific region: the giant Quellaveco Cu-Mo porphyry in southern Peru.

Over 20,000 structural data points and 107 samples were collected from two ~25 km transects in the Quellaveco region. SEM analysis of 82 samples yielded grain-scale petrographic and textural information of veining and alteration assemblages. This enabled the classification of 18 wall rock and vein alteration assemblages 10 of which represented propylitic-related assemblages. Specifically identified sites were selected from the propylitic minerals for geochronological (apatite, titanite, epidote and zircon) and geochemical trace element analysis (epidote and chlorite) using the LA-ICP-MS.

Dating revealed an extensive period of propylitic alteration between 72-60 Ma with an alteration maximum concentrating at 65-69 Ma. This peak in propylitic alteration occurred ~8-12 My prior to the onset of mineralisation at the known porphyry regional centers: Quellaveco (58.4-54.3 Ma); Toquepala (57.0-54.0 Ma) and Cuajone (56.5-53.0 Ma). Fluctuations of propylitic alteration continued throughout this period, with geothermic and geochemical vectors indicating a period of high temperature fluids between 72-68 Ma, consistent with early Yarabamba Batholith emplacement. The principal NW-SE faults act as major fluid conduits during this period, with specifically the NNW-SSE Puca-Porquene splay-fault. Where the NW-SE fault intersect the major NE-SW faults there are apparent areas of fluid localization.

In summary, this project's multi-disciplinary approach elucidates the temporal and spatial complexity of the development of propylitic alteration in porphyry regions.

Impact Statement

The increase in global demand for copper is inversely impacting the availability of copper resources, thereby emphasizing the necessity for the development of new, efficient techniques for the detection of obscure and complex copper systems. Previous and current studies on the propylitic halo of a porphyry deposit have identified geochemical characteristics that highlight the importance of the propylitic zone as an indicator for the economic potential of an area. Despite this, propylitic alteration is one of the least studied and least understood parts of the porphyry system. However, because of the potential and significant implications of the findings, these studies are often closely partnered with the mining and exploration industry, therefore highlighting the importance of this area research.

This study, which is sponsored by the international mining corporation Anglo American, significantly develops our understanding of the distribution and genetic evolution of district-wide propylitic alteration in the economically-important Quellaveco region in southern Peru. Applying an innovative approach, this study considers the potential spatial, geochemical, structural and temporal controls on propylitic alteration, but crucially, the evolution of district-scale (10's km), porphyry-related alteration. This innovative, multidimensional approach applied to district scale sampling provides analysis of propylitic alteration that would not conventionally be used in porphyry-propylitic studies and yields a 4-dimensional idea of the genetic development of precursor propylitic alteration. To date, this revolutionary concept has been absent from the literature.

The impact of this novel study is wide-reaching with several key primary and secondary beneficiaries. These are as follows:

- Anglo American: The Quellaveco Cu-Mo porphyry is one of the world's largest, currently unexploited copper deposits, and with the first copper production expected for 2022, the deposit and wider license area is a particularly valuable asset to Anglo American. On a fundamental level, the extensive geochemical, structural and geochronological dataset accumulated from fieldwork and lab work in this study provides a geographically comprehensive database for areas of the license area

previously deficient in temporal and geochemical information. All findings are directly shared with Anglo American, for use at their discretion.

- Academia: The successful dating of propylitic minerals which have been attributed to specific events achieved in this study, is a considerable advancement in the academic understanding of early-stage alteration. Subsequent detailed geochemical analysis of the dated events provides even further insight to the evolution of a porphyry system. By the nature of new research, it has generated new questions which will give direction for the advancement of the field of study. Additionally, the comprehensive database provided will act as a useful tool for comparative work on similar or contrasting areas in future.
- Exploration industry – the refinement of geochemical and geochronological techniques developed in this study forms an integral part of the increasing accuracy in using propylitic vectoring. As with academia, the successful application of innovative field techniques, such as UAV aided 3D structural modelling, provides additional confidence in using these techniques to aid future work.

Acknowledgements

Firstly, I would like to thank my primary supervisor, Pieter Vermeesch, for taking on this project with great enthusiasm and contributing his extensive, world-leading geochronological knowledge – in doing so providing an exciting and crucial dimension to the project. Equally importantly, I'm extremely thankful for his significant time, patience and understanding of the challenges a PhD poses. I am exceptionally grateful to my secondary supervisor, Jamie Wilkinson, who was able to take my vague ideas for a project and turn it into reality, from generating the initial concept of the project to procuring the funding required to make it achievable. I am indebted to both supervisors for their belief in the project from start to finish and support throughout.

This project is primarily funded by the Natural Environment Research Council, to whom I am very grateful. However, the dynamic nature and extensive scope of this study has only been made possible by the very generous financial and technical support provided by Anglo American. This collaboration enabled the essential physical and informatic access to the giant economic Quellaveco Cu-Mo porphyry district. I would like to give my special thanks to Victor Valdivia and Thomas Mitchell for providing their expertise in the field, and to Victor Ramos for facilitating a smooth and efficient field season enabling me to maximize my time in the field. Financial contributions from the McKinstry Fund for geochronological work are also gratefully acknowledged.

This project has been very fortunate to be able to conduct lab work in the Natural History Museum's state-of-the-art Image Analysis Centre, with the professional support from all the team in IAC. My sincere thanks go to Yannick Buret for his extensive technical knowledge and geochronological expertise. I would also like to give a special thank you to Lauren Tuffield for giving me her time throughout the project and for providing understandable explanations for even the most complex of equipment.

I am hugely appreciative to have had the support of everyone in the LODE group at the Natural History Museum, and a special thank you to Lisa Hart-Madigan for her words of wisdom and encouragement for the project and PhD process. I feel very lucky to have had the moral support of the friends I have made during

the last five years, in particular the hot chocolate team, Claire and Thomas, for their great friendship and fun even through tough times. I must also express my immense gratitude for Thomas' emergency tech support no matter the challenge or the time zone.

Last, but certainly not least, I am eternally thankful to my amazing family: my parents, Amanda and Dave, and sister, Beth, for their unconditional love and support through every turn, loop and dip on my PhD rollercoaster, and without whom the completion of this journey simply would not have been possible. I am forever grateful to Toby and Tilly, for their unparalleled ability to brighten my day, no matter the weather, and for sticking with me even in the latest work shift. Finally, thank you to my partner, John, to whom I am indebted, for his unwavering love, support, patience, and belief in me despite all the additional challenges of writing-up a PhD in a global pandemic. Thank you will never be enough.

Table of Contents

1	Introduction.....	29
1.1	Research motivation.....	29
1.2	Aims and objectives	30
1.3	Overview of Porphyry Copper Deposits	32
1.3.1	<i>Formation of Porphyry Copper Deposits</i>	<i>32</i>
1.3.2	<i>Porphyry-related alteration</i>	<i>35</i>
1.3.3	<i>Early-Stage Alteration.....</i>	<i>37</i>
1.3.4	<i>Late-Stage Alteration.....</i>	<i>40</i>
1.3.5	<i>Lithocap.....</i>	<i>42</i>
1.4	Geochemical Vectoring on the Propylitic Zone.....	42
1.4.1	<i>Porphyry Indicator Minerals.....</i>	<i>44</i>
1.4.2	<i>Porphyry Fertility and Vectoring Tools.....</i>	<i>46</i>
1.4.3	<i>Vertical Zonation.....</i>	<i>52</i>
1.5	Summary.....	53
2	Structural Controls on Fluid Flow and Ore Deposit Formation.....	54
2.1	Controlling Factors on Fluid Flow	54
2.2	Syn-Tectonic Fluid Transport	56
2.2.1	<i>Magma and Fluid Transportation.....</i>	<i>56</i>
2.2.2	<i>Permeability.....</i>	<i>57</i>
2.2.3	<i>Seismicity</i>	<i>59</i>
2.2.4	<i>Key Transtensional Structural Features</i>	<i>60</i>
2.3	Porphyry Copper in South America	62
2.3.1	<i>Metallogeny of South America.....</i>	<i>62</i>
2.3.2	<i>Volcanism.....</i>	<i>63</i>
3	Methodology and background	65
3.1	Structural data acquisition.....	65
3.1.1	<i>Structural transects and sampling</i>	<i>65</i>

3.1.2	<i>Field mapping</i>	66
3.1.3	<i>Drone Mapping for 3D modelling</i>	67
3.2	Basic principles of radiometric dating	70
3.2.1	<i>Radioactivity</i>	70
3.2.2	<i>Age Equations</i>	72
3.2.3	<i>The U-Pb-Th decay system</i>	74
3.2.4	<i>Data visualisation</i>	78
3.2.5	<i>Mean squared weighted deviations (MSWD)</i>	86
3.2.6	<i>A brief overview of K-Ar and Ar-Ar</i>	87
3.3	Geochronological and geochemical analytical procedure	88
3.3.1	<i>Whole rock geochemistry</i>	88
3.3.2	<i>Scanning electron microscope</i>	91
3.3.3	<i>The LA-ICP-MS system</i>	91
3.3.4	<i>LA-ICP-MS geochronological analysis</i>	95
3.3.5	<i>Epidote and chlorite trace element geochemistry</i>	96
4	The Geology of the Quellaveco Region	101
4.1	Introduction	101
4.2	Regional Geology of the Central Andes	103
4.2.1	<i>South America's Porphyry Belts</i>	103
4.2.2	<i>Brief tectonic history</i>	103
4.3	Geology of the Quellaveco District	111
4.3.1	<i>Lithologies</i>	111
4.3.2	<i>Structural Geology</i>	115
4.3.3	<i>Mineralisation</i>	118
4.3.4	<i>Alteration</i>	120
4.3.5	<i>Neighbouring Deposits</i>	122
4.4	Summary	124
5	Alteration in the Quellaveco District	125

5.1	Aims	125
5.2	Introduction	125
5.3	Recognition of primary igneous and secondary alteration minerals	126
5.3.1	<i>Primary igneous minerals.....</i>	128
5.3.2	<i>Overprinted igneous minerals.....</i>	128
5.4	Pervasive hydrothermal alteration	129
5.4.1	<i>Potassic (A1)</i>	129
5.4.2	<i>Actinolite propylitic (A2).....</i>	131
5.4.3	<i>Epidote-actinolite propylitic (A3).....</i>	131
5.4.4	<i>Epidote-chlorite-albite propylitic (A4).....</i>	133
5.4.5	<i>Epidote-titanite propylitic (A5).....</i>	134
5.4.6	<i>Chlorite-calcite propylitic (A6).....</i>	135
5.4.7	<i>Sericitic (A7)</i>	135
5.4.8	<i>Advanced argillic (A8).....</i>	136
5.5	Veins and vein-related alteration.....	139
5.5.1	<i>K-feldspar-Quartz (V1)</i>	139
5.5.2	<i>Epidote-actinolite (V2)</i>	139
5.5.3	<i>Epidote-quartz (V3)</i>	140
5.5.4	<i>Albite-epidote (V4).....</i>	141
5.5.5	<i>Quartz (V5).....</i>	141
5.5.6	<i>Quartz-albite-epidote (V6)</i>	141
5.5.7	<i>Calcite-epidote-chlorite (V7)</i>	142
5.5.8	<i>Sericite-dickite (V8)</i>	143
5.5.9	<i>Quartz-pyrite (V9).....</i>	143
5.5.10	<i>Breccia (BX)</i>	144
5.6	Spatial occurrence of vein and alteration assemblages.....	147
5.6.1	<i>Alteration assemblages</i>	147

5.6.2	<i>Veins</i>	151
5.7	Relative chronology of vein and alteration assemblages	154
5.8	Discussion	160
5.8.1	<i>Area 1 and Area 2</i>	160
5.8.2	<i>Area 3</i>	162
5.8.3	<i>Area 4</i>	163
5.8.4	<i>Area 5</i>	163
5.9	Conclusions	166
6	Structural analysis of the Quellaveco region	167
6.1	Aims	167
6.2	Introduction	167
6.2.1	<i>Structural Definitions</i>	167
6.2.2	<i>Data collection</i>	168
6.3	Structural analysis of regional dataset	169
6.3.1	<i>Digital orientation analysis</i>	169
6.3.2	<i>Fracture density and intensity modelling</i>	170
6.3.3	<i>Spatial distribution of fracture intensity and density with respect to key structural trends</i>	173
6.3.4	<i>Fracture connectivity</i>	173
6.4	Fracture mapping from field data	176
6.4.1	<i>Principal orientation domains</i>	176
6.4.2	<i>High-resolution modelling using outcrop-scale drone imagery</i> ..	179
6.5	Veining and fault- fill	185
6.5.1	<i>Groupings and spatial significance</i>	185
6.5.2	<i>Fault Kinematics</i>	188
6.6	Discussion	189
6.6.1	<i>Area 1</i>	192
6.6.2	<i>Area 2</i>	192

6.6.3	Area 3.....	192
6.7	Conclusions	193
7	Geochronology	195
7.1	Aims and questions	195
7.2	Introduction	196
7.3	Raw data, date calculations	198
7.3.1	<i>IsoplotR</i>	198
7.3.2	<i>Visual assessment and unconstrained isochron regression on Tera-Wasserburg concordia diagrams</i>	199
7.4	Investigating the spatial variability of the common Pb	203
7.4.1	<i>Assessment of common Pb homogeneity</i>	204
7.4.2	<i>Visual representation of common Pb using radial plots</i>	204
7.4.3	<i>Pooled model-3 regressions</i>	207
7.5	Anchoring of the $^{207}\text{Pb}/^{206}\text{Pb}$, y-intercept	209
7.6	Comparing dates – raw vs anchored.....	211
7.7	Discussion.....	217
7.7.1	<i>Spatial distribution of dates in the region</i>	217
7.7.2	<i>A comparison of the published dates – possible limitations</i>	220
7.8	Conclusions	223
8	Regional variations in mineral chemistry of propylitic chlorite and epidote at Quellaveco	225
8.1	Aims and questions	225
8.2	An introduction to chlorite and epidote chemistry and structure	225
8.2.1	<i>Chlorite</i>	225
8.2.2	<i>Epidote</i>	227
8.3	Results.....	229
8.3.1	<i>Chlorite</i>	229

8.3.2	<i>Epidote</i>	233
8.3.3	<i>Exploratory data analysis</i>	234
8.4	Discussion of chlorite chemistry	238
8.4.1	<i>Potential igneous protolith control on chlorite chemistry</i>	238
8.4.2	<i>Comparison with chlorite from metamorphic terranes</i>	241
8.4.3	<i>Comparison with chlorite from porphyry systems</i>	244
8.4.4	<i>Chlorite geochemical variation between alteration assemblages</i>	
	247
8.4.5	<i>Spatial variations in chlorite chemistry</i>	248
8.4.6	<i>Temporal constraints on chlorite-bearing assemblages and geochemistry</i>	256
8.4.7	<i>Identification of potential propylitic chlorite formation environments using linear discriminant projection analysis</i>	258
8.5	Discussion of epidote chemistry	264
8.5.1	<i>Potential protolith control</i>	264
8.5.2	<i>Comparison with epidote from metamorphic terranes</i>	264
8.5.3	<i>Comparison with epidote from porphyry systems</i>	267
8.5.4	<i>Comparison of the chemistry of the different epidote-bearing assemblages</i>	268
8.5.5	<i>Spatial variations in epidote chemistry</i>	270
8.5.6	<i>Temporal variations in epidote chemistry</i>	273
8.5.7	<i>Interpretation of epidote chemistry using discriminant projection analysis</i>	280
8.6	Comparative summary of chlorite and epidote	284
8.7	Conclusions	284
9	Timing and Origins of Propylitic Alteration in the Quellaveco District	
	286
9.1	Regional metamorphic or metasomatic propylitic alteration	286
9.2	Model 1 (72- 67 Ma)	287

9.2.1	<i>The onset of plutonism</i>	287
9.2.2	<i>Early high temperature fluids and alteration</i>	287
9.2.3	<i>Porphyry-like signals (area g-h)</i>	289
9.3	Model 2 (66 – 64 Ma)	292
9.3.1	<i>Pacay high-sulphidation epithermal system</i>	292
9.4	Model 3 (62 – 57 Ma)	293
9.4.1	<i>A change in far-field stress axis</i>	293
9.4.2	<i>Evidence of transpression and thrusting</i>	295
9.4.3	<i>Magmatism and associated porphyry formation</i>	295
9.4.4	<i>Post mineralisation fault activity and alteration</i>	298
10	Conclusions	300
11	References	302

List of Figures

Figure 1.1. A conceptual model which considers the role of faults in the facilitation of regional fluids. Key questions are indicated in blue....	31
Figure 1.2. A schematic diagram depicting the ideal conditions for giant porphyry deposit formation. See text for 1-4 explanation (Wilkinson, 2013) .	34
Figure 1.3. A schematic section (after Pacey, 2017), depicting the alteration assemblages of the porphyry system with convectively circulating meteoric waters, causing the late-stage alteration of the sericitic and advanced argillic zones.....	35
Figure 1.4. Schematic figure showing the chronology of the main vein types: A, B, D, and M in, a) Cu-Mo porphyry deposit, and b) Cu-Au porphyry deposit, both associated with calc-alkaline intrusions. From Sillitoe (2010).....	36
Figure 1.5. a) schematic diagram of alteration zonation at Cu porphyry systems; b) generalised alteration-mineralisation sequence with paleodepth with respect to life span of the Cu porphyry deposit (after Sillitoe, 2010).....	38
Figure 1.6. Schematic diagram compiled from Cooke et al. (2017); Wilkinson et al. (2017a), Halley (2015), and Cooke et al. (2014b), of the porphyry system with main alteration zones, depicting the minor and trace elements used as porphyry vectoring tools.	45
Figure 1.7. Schematic diagram from Cooke et al. (2014a); showing the lateral enrichment of trace elements in chlorite.....	48
Figure 1.8. Expected pathfinder element concentrations in a porphyry system with a) showing vertical zonation of pathfinder elements; and b) horizontal zonation of pathfinder elements (Halley, 2016)	52
Figure 2.1 The South American metallogenic belts highlighting the location of Cu-rich and Au-rich porphyry deposits with respect to the major and transverse fault systems (figure after: Camus & Dilles, 2001; Elderry et al., 1996; Masterman, 2003; Ramos & Folguera, 2009; Spencer et al., 2015).....	55
Figure 2.2 diagram from Richards (2003) depicting the progression of magma through the crust.	56

Figure 2.3. **a)** major and minor faulting with associated fault damage zone – the damage zone has a higher percentage fracture density than surrounding rock Faulkner et al. (2003); **b)** a diagram adapted from Caine et al. (1996) showing the resultant fault and therefore fluid flow pathways associated with the increase and decrease of the percentage damage zone and core..... 58

Figure 2.4. diagrams adapted from Fossen (2016) and Sibson (2001). **a)** block model of expected faulting and dilation in the Andersonian stress regime; **b-c)** simplified fault-fracture meshes in an extensional regime: **b)** areas of dilation and strike-slip faulting in relation to the orientation of σ_1 and σ_3 ; **c)** displaying the same stress orientation as **(b)**, but with the presence of an unfavorably aligned pre-existing fault structure. 61

Figure 2.5. Common structures that form as a result of transtensional and transpressional tectonics. Adapted from Cunningham and Mann (2007)..... 62

Figure 2.6. major deposits of South America in relation the five metallogenic belts. Diagram adapted from (Camus & Dilles, 2001; Sillitoe & Perello, 2005; Cembrano et al., 2005; Quang et al., 2005) 64

Figure 3.1. Sampling map of the study area showing the two transect lines (section 1 and 2) orientated perpendicular to the major NW-SE structures. 65

Figure 3.2. Screenshots from the iPad Pro showing the layout of the MOVE application. Individual structural measurements, observations and photos are shown down the left-hand side, and geographic positioning displayed on the map. 66

Figure 3.3. Screenshots showing: **a)** the creation of a 3D model of a structurally complex area using drone imagery in Agisoft Photoscan (the positioning of the drone images are shown in blue); **b)** the Dem and orthomosaic exported into MOVE for structural analysis (the red circular planes indication 3D fault planes),..... 69

Figure 3.4. A diagram from Schoene (2014) depicting the decay chains of U and Th, to their intermediate daughter isotopes (only shown those with a half-life greater than 10 years). The parent and stable daughter

isotopes are highlighted in red. The decay series are colour-coded: ^{238}U in green; ^{235}U in yellow; and ^{232}Th in orange. 76

Figure 3.5. **a)** A Wetherill concordia diagram after Dickin (2018) showing data affected by variable Pb loss, with discordant plots coloured grey and concordant plots in yellow. T_1 and T_2 are the higher and lower concordia incepts. **b)** A 2D Tera-Wasserburg concordia diagram after White (2015). The y-incept indicates the composition of Pb_0 . **c)** Figure from Ludwig (1998): 3D Tera-Wasserburg plot showing the Total-Pb/U isochron (represented here as the oblique solid line). The left end of the isochron is anchored to common-Pb along the $^{207}\text{Pb}/^{206}\text{Pb}$ - $^{204}\text{Pb}/^{206}\text{Pb}$ plane, with a crustal Pb growth curve (with ticks labelled in Ma). The right end of the isochron intersects the concordia curve, which is labelled in Ma. The ellipsoids along the isochron mark individual samples, yielding their age..... 79

Figure 3.6. **a)** Cathodoluminescence (CL) image of a zircon from Kielman et al., (2018). **b)** Schematic of the zircon showing a homogenous core with oscillatory zone progressively younging outward. The circles represent potential sites for LA-ICPMS analysis: green spots are completely within one zone; red overlaps multiple zones and therefore would lead to discordance. However, it is worth noting that there is likely to be an age difference between the two green spots. 80

Figure 3.7. Diagram from Albarède (2009)) - T_c represents the closure temperature of the system, above which the system is considered 'open' and diffusion can result in the loss of the daughter isotope. The curve trajectory representing the evolution of radiogenic daughter isotope equals the decay rate by the amount of radioactive parent ($= \lambda P$). 81

Figure 3.8. a semitotal-Pb/U isochron on a Tera-Wasserburg using apatite data from this study. The isochron regression highlights an age of 60.45 Ma and a $(^{207}\text{Pb}/^{206}\text{Pb})_0$ value of 0.8221. This plot uses ISOPLOT software (Vermeesch, 2018). 85

Figure 3.9. a graph showing the distributions of MSWD frequency with varying degrees of freedom (f), edited from Wendt and Carl, 1991 89

Figure 3.10. an annotated schematic diagram of a mass spectrometer, highlighting a magnetic sector mass analyser (adapted from Vermeesch, 2017; and Arevalo et al., 2020).....	92
Figure 3.11. From Reiners et al., 2018 demonstrating precision and accuracy using data clusters of 250 points.....	94
Figure 4.1 Quellaveco location map, situated on the major fault system extending from northern Chile to southern Peru.....	101
Figure 4.2 the five metallogenic belts of South America with major porphyry deposits. Quellaveco is situated in the Palaeocene-Eocene belt in southern Peru.....	102
Figure 4.3 Convergence rate of the South American and Nazca plate are 3.1 cm/yr and 4.8 cm/yr respectively (Sdrolias & Müller, 2006 and Horton, 2018).....	109
Figure 4.4. A timeline compiling data of major tectonic events in the central Andes, and locally to Quellaveco	112
Figure 4.5. A lithology map of the Quellaveco region with major NW-SE trending faults mapped and labelled.	115
Figure 4.6. Satellite imagery highlighting major faults in the Moquegua region. The crust-scaled Incapuquio Fault System (IFS). A splay of the IFS Purgatorio Fault (Audin et al., 2008; Audin et al., 2006).....	116
Figure 5.1 Geological map of the Quellaveco region with sample localities from transect 1 and 2 marked.	127
Figure 5.2. SEM-BSE images showing igneous and metasomatic examples of dated minerals.....	129
Figure 5.3. SEM-BSE images showing wallrock alteration textures.....	137
Figure 5.4. Field images with examples of three propylitic vein types in the field.	142
Figure 5.5. Examples of type 2, quartz-pyrite 'D' veins.	144
Figure 5.6. SEM-BSE images showing vein types	145
Figure 5.7. A series of lithology-based maps highlighting the distribution of each alteration category A1-A8 in the Yarabamba Batholith (left column) and Toquepala Group (right).....	149

Figure 5.8 A series of lithology-based maps highlighting the distribution of each alteration category A1-A8 in the Yarabamba batholith (left column) and Toquepala Group (right).....	150
Figure 5.9. A series of lithology-based maps highlighting the distribution of each alteration category A1-A8 in the Yarabamba batholith (left column) and Toquepala Group (right).....	151
Figure 5.10. Sample location map of vein occurrences	153
Figure 5.11. Cross-cutting relationships observed within the three vein samples are displayed in a grid format. V1-V9 are shown on both axes, the horizontal axis indicates a vein is cross-cut by a later stage vein, and vertical indicates the vein type which cuts across an older vein type.	156
Figure 5.12. A map view sketch of the sample distribution around the Capulline Fault (CF) and Pacay Fault (PF) in Area 4 (left); and a schematic block model of the possible cause for the distribution of sericitic and propylitic alteration observed in Area 4 (right).....	162
Figure 5.13. A map view sketch of the sample distribution around the Incapuquio Fault System (IFS), Puca-Porquene Fault (PPF) and Capulline Fault (CF) from Areas 1 and 5	164
Figure 5.14. A summary alteration map for the study area with the locations of the propylitic alteration (A2-A6) represented as colour-coded strips. Areas 1-5 are highlighted and referenced in the discussion.....	165
Figure 6.1. A lithological map highlighting the two transect lines followed for structural data collection. Locations of the samples collected are also indicated.....	168
Figure 6.2. a) Fault map of the region, colour-coded by strike, with deposits and major faults highlighted; b) Rose plot of mapped structures in the region, colour-coded by strike, with two clear structural trends: WNW-ESE and NE-SW.....	171
Figure 6.3. Fracture intensity (left) and density (right) mapping: a-b) pixelated grid of all fracture orientations; c-d) mapping of fractures trending NW-SE only; e-f) mapping of fractures trending NE-SW only.....	172
Figure 6.4. Cross-sections illustrating variations in fracture density and intensity. a) Section perpendicular to major WNW-ESE fault sets, intersecting	

Quellaveco and the IFS; b) Quellaveco Fault-parallel section; and c) IFS-parallel section	174
Figure 6.5. a) A map showing nodes detected as I-Y-X : nl- 4508, ny 3, nx = 519, b) IXY ternary diagram of the fracture set (Barton and Hsieh, 1989; and Manzocchi 2002) c) fracture density connectivity map; d) intensity connectivity map with fault and deposit locations highlighted	175
Figure 6.6. Structural domains mapped along two transects, coloured based on dominant structural trend in each: NE-SW – purple; N-S – blue; NW- SE – pink; and WNW-ESE – yellow.	176
Figure 6.7. Fracture sketch map of the two transects. Four insets are shown, A, B, C and D; these are expanded in Figure 6.8.	177
Figure 6.8. Fracture sketch map insets from Figure 6.7. Fracture lines: green indicates moderately- to shallowly-dipping fractures (<70°); grey indicates steeply-dipping fractures (>70°).	178
Figure 6.9. Drone model location map of 7 sites.	179
Figure 6.10. Interpretation of conjugate faulting at Site 6.	181
Figure 6.11. Structural data for the different generations of veining and fault-infill observed. a-b) stereonet and contour plot of veins containing only epidote; c-d) stereonet and contour plot of fractures containing only clay.....	186
Figure 6.12. Structural domains, colour-coded based on the occurrence of vein and fault-fill types.	187
Figure 6.13. a) slicken lines along an E-W fault showing left-lateral movement, b) NE-trending fracture plane with two directions of slicken line visible, 215.27 and 189.68.	188
Figure 6.14. a) NW-SE-trending fault with white mineral infill within bends, b) Steeply-dipping, NE-SW shear zone with fabrics indicating dextral movement.	189
Figure 6.15. Sinistral strike-slip model adapted from Fossen (2016) to incorporate the observations made: a) Riedel shear model; b) other indicative large- and small-scale structures.	190
Figure 6.16. Sample transect map with areas of structural significance highlighted.....	191

Figure 6.17. A summary model of the key structural interpretations in the district.	194
Figure 7.1. Collection of raw age estimates produced using IsoplotR. For dates that comprise all isotopic data from that sample, the classifications are coloured-coded. The specific examples are referenced in-text.	200
Figure 7.2. The spatial distribution of precise epidote common Pb estimates.	204
Figure 7.3. A radial plot plotting two datasets: U/Pb zircon dates from this study in green, and SIMS based U-Pb zircon dates from Simmons (2013) in red. The age of each aliquot can be determined from the projection of a line from the origin through the aliquot on the circular scale (represented by the white dashed line).The confidence intervals are obtained from the projection of 2-sigma error bar on to the selected aliquot: 55.5 +2.5/ -2.5 and 73 +0.5/ -0.5.	205
Figure 7.4 Radial plots showing the uncertainty distribution of the common Pb intercept of all the raw dates. Each value is coloured based on the source of the value (igneous, altered igneous, altered, veins, and 'all' indicating dates per sample that have been combined).	206
Figure 7.5. Pooled Tera-Wasserburg model-3 regressions of all U-Pb data for each mineral: a) apatite, b) epidote, c) titanite, and d) zircon.....	208
Figure 7.6. Example of the successful anchoring of the y-axis on a zircon Tera- Wasserburg concordia plot. Here, the aliquots contain high radiogenic with no inherited common Pb causing a degree of dispersion in the raw data (a) . Anchoring the y-intercept (b) constrains the regression line and nearly doubles precision, with date uncertainty decreasing from 10.01 Ma to 6.83 Ma.	209
Figure 7.7. Radial plots of all the anchored dates for each dated mineral: a) epidote, b) apatite, c) titanite, d) zircon. The points are coloured based on the classification of the date: igneous, altered igneous, altered, veining, and all (for combined dates for each sample).	210
Figure 7.8. Scatter plots comparing the difference between the raw date and anchored dates: a) depicts precise and imprecise dates with uncertainties <1.5, b) only showing dates <30 % uncertainty.	211

Figure 7.9. Scatter plots contrasting the anchored and raw ages between 30-130 Ma. Those data plotting closest to the 1:1 displayed minimal change in age from the anchoring process. 212

Figure 7.10. Kernel density estimates (KDE) and histograms for precise dates with uncertainty of <10%: **a)** raw unanchored dates; **b)** anchored dates. Adding the isochrons reduces the dispersion of the dates. 213

Figure 7.11. Example concordia date diagram of **a)** raw and **b)** anchored apatite data. Here, the aliquots are rich in common Pb with a raw plot (a) 10% precision for the common Pb value. 214

Figure 7.12. Selected reliable dates, combination of raw and anchored. Errors are reported as 95% confidence intervals including any possible overdispersion. 219

Figure 7.13. **a)** radial plot showing the contrast in precision of the zircon ages in this study (green) and zircon ages from Simmons (2013) in red; **b)** a KDE and histogram representation of Simmons (2013)'s zircon data; **c)** a KDE and histogram of the zircon dates from this study 220

Figure 8.1. The 3D simplified structure of a chlorite with the chemical composition $(Mg,Al)_6(Si,Al)_4O_{10}(OH)_8$. The 2:1 structure is shown with the talc-like layers $[Mg_3(AlSi_3O_{10}(OH)_2)]^-$ and brucite-like interlayer of $[Mg_2Al(OH)_6]^+$ (Klein and Philpotts, 2017). 226

Figure 8.2. **a)** polyhedral structure of epidote showing M, A and T sites (Pacey, 2017 after Franz and Liebscher; and Dollase, 1968); **b)** the structure of the octahedral chains with numbered oxygens (modified from Franz and Liebscher after Dollase 1968). 228

Figure 8.3. Major element compositional data for Si, Fe, Mg and Al, determined by analytical SEM. The box represents the 25th and 75th percentiles; white dot = mean value; white horizontal line = median; vertical whiskers = maximum and minimum values (excluding outliers). 230

Figure 8.4. Summary of compositional ranges for trace elements in chlorite. The box represents the 25th and 75th percentiles; white dot = mean value; white horizontal line = median; vertical whiskers = maximum and minimum values (excluding outliers). 231

Figure 8.5. Chlorite species boundaries after Hey (1954). Samples are attributed on sample number. 232

Figure 8.6. Major element compositional data for Si, Ca, Al and Fe in epidote, determined by analytical SEM. The box represents the 25 th and 75 th percentiles; white dot = mean value; white horizontal line = median; vertical whiskers = maximum and minimum values (excluding outliers).....	233
Figure 8.7 Summary of compositional ranges for trace elements in epidote presented by decreasing median values. The box represents the 25 th and 75 th percentiles; white dot = mean value; white horizontal line = median; vertical whiskers = maximum and minimum values (excluding outliers).....	234
Figure 8.8. PCA plots for chlorite LA-ICP-MS trace element chemistry. Data are attributed by: a) sample number and b) alteration assemblage	236
Figure 8.9. PCA plots for epidote LA-ICP-MS trace element chemistry. Data are attributed by: a) sample number and b) sample assemblage	238
Figure 8.10. An assessment of protolith control on chlorite geochemistry: a) MgO % vs SiO ₂ % b) sample location map for chlorite-bearing samples; c) MgO % (whole rock) vs Cr ppm (chlorite); d) Cr ppm (whole rock) vs Cr ppm (chlorite); e) MgO % (whole rock) vs Li ppm (chlorite); f) Li ppm (whole rock) vs Li ppm (chlorite). The horizontal lines represent the median value for each sample.	240
Figure 8.11. Trace element chemistry bivariate plots showing: Ba vs Pb; Li vs Fe; Mg vs Sn; Mn vs Zn; Sr vs Ca; and Ti vs V. Clusters of data analysed in Figure 8.16 are highlighted in green.	243
Figure 8.12. Bivariate plots of Ba vs Pb, Li vs Fe, Mg vs Sn, Mn vs Zn, Sr vs Ca and Ti vs V. Comparative data from porphyry deposits: Bambu, Batu Hijau, El Teniente and Sekongkang (Wilkinson et al., 2015; AMIRA P1153 database), with a reference metamorphic data cloud shown (from Figure 8.11).	246
Figure 8.13. Tukey plots of each sample separated based on assemblage, and plotted against certain chlorite trace elements: As, Ba, La, Li, Mg, Pb, Sb, Sr, Ti and U.	249
Figure 8.14. Variable maps of chlorite trace element chemistry with As ppm, Mn ppm and Ti ppm, values ranked based on groups of 6 equal tails. Maps are broken down into assemblage.....	250

Figure 8.15. Variable maps of chlorite trace element chemistry with Sb ppm, Zn ppm and Pb ppm, values ranked based on groups of 6 equal tails. Maps are broken down into assemblage.....	251
Figure 8.16. Bivariate plots a) Ti vs V and b) Sr vs Ca, from Figure 8.11 highlighting the location of samples within the clusters of interest.	252
Figure 8.17. Chlorite trace element variations with distance from the Quellaveco Fault. Sample sections 1 and 2 are separated, and locations of the major transverse faults are noted on the sections	255
Figure 8.18. Trace element chemistry specifically for temporally constrained chlorite samples (RCS003, RCS033, RCS047, RCS061, RCS074, RCS075 and RCS104). Samples are attributed based on chlorite assemblage.....	257
Figure 8.19. Mn vs Zn bivariate plot for chlorites at Quellaveco. Specific clusters of samples are labelled. Hypothetical regions devised from constraints discussed in Wilkinson et al. (2017) and Wilkinson et al. (2020)...	263
Figure 8.20. Discriminant plots for chlorite trace element data: a) all data plotted with geochemical fields highlighted; b-k) geographically grouped samples, the alteration assemblage is attributed by shape. Discriminant plot parameters formulated by J.J Wilkinson (PersComm, 2021).....	265
Figure 8.21. Trace element chemistry bivariate plots of As vs Sb, La vs Yb, Mn vs Zn, Pb vs Sn, U vs Ti, Y and Ce. Comparative, metamorphic data from Baker et al. (2017); AMIRA P1153. An area of interest is highlighted in yellow which will be spatially analysed in Section 8.5.5.	266
Figure 8.22. Bivariate plots of As vs Sb, La vs Yb, Mn vs Zn, Pb vs Sn, U vs Ti, Y and Ce. Comparative data from porphyry deposits: Batu Hijau and El Teniente (Wilkinson et al., 2015), with a reference metamorphic data cloud shown.	267
Figure 8.23. Tukey plots of epidote concentration data for As, Co, Ga, Ge, Mg, Mn, Pb, Sb, Ti and U in individual samples, separated based on assemblage.....	269
Figure 8.24. The spatial location of the high As and Sb (>100 ppm) area previously isolated (Figure 8.22) is shown. Compositions of the data	

of certain elements (Cu, Mo, Mn, Zn, Pb and Sn ppm) are contrasted with the deposit dataset and remaining Quellaveco data.....	270
Figure 8.25. A Spatial assessment of As and Sb variations within the A3 assemblage. Samples of interest in the high concentration population are highlighted and grouped based on location, which is indicated on the map.....	271
Figure 8.26. Epidote trace element composition as a function of distance from the Quellaveco Fault. Sample traverses 1 and 2 are shown separately, and locations of the major transverse faults are noted on the sections.....	275
Figure 8.27. Epidote trace element chemistry for temporally constrained samples applying the dates acquired in Chapter 7	278
Figure 8.28. A continuation of epidote trace element chemistry for temporally constrained samples. Data are attributed on epidote alteration assemblage. Sample information and location are shown on Figure 8.28.....	279
Figure 8.29. Discriminant plots for epidote trace element data: a) all data plotted with geochemical fields highlighted; b-k) geographically grouped samples, the alteration assemblage is attributed by shape.....	283
Figure 9.1. Model 1 (72-67 Ma) – a summary model of the findings and interpretations from this study	291
Figure 9.2. Model 2 (66-64 Ma) – a summary model of the findings and interpretations from this study	294
Figure 9.3. Model 3 (62-57 Ma) – a summary model of the findings and interpretations from this study	299

List of Tables

Table 3.1. The U-Th-Pb system parameters; after White (2015).....	75
Table 3.2. Detection limits for whole rock major, minor and trace element analysis	90
Table 3.3. Metadata of the LA-ICP-MS conditions for apatite, titanite, epidote and zircon U-Pb geochronology.....	97
Table 3.4. Metadata of the LA-ICP-MS conditions for apatite, titanite, epidote and zircon U-Pb geochronology continued.....	98
Table 3.5. Metadata of the LA-ICP-MS conditions for epidote and chlorite trace element acquisition.....	99
Table 3.6. Metadata of the LA-ICP-MS conditions for epidote and chlorite trace element acquisition.....	100
Table 5.1. a summary table of the propylitic alteration assemblages with textural descriptions of the five key minerals (used for later analysis) present in each assemblage: zircon, apatite, titanite, epidote and chlorite. The 'suffix' column refers to the suffix that will be applied to minerals within those categories throughout this study.....	138
Table 5.2. A summary table of the propylitic fracture-fill V1-V8 with textural descriptions of the five key minerals present in each assemblage: zircon, apatite, titanite, epidote and chlorite.	146
Table 5.3. Summary of alteration and vein occurrence. Shaded squares highlight where an alteration type is present in a lithological unit. Where veins are present in a particular alteration assemblage and lithological unit, their abbreviation (V1-V9) is written in the appropriate grid. The lithological units are listed chronologically from oldest (bottom) to youngest (top).	155
Table 5.4. Plutonic sample groupings based on lithological unit in the Yarabamba batholith, with alteration types present in each lithology, and vein types seen in each alteration type.	158
Table 5.5. Volcanic sample groupings based on lithological unit in the Toquepala Group, with alteration types present in each lithology, and vein types seen in each alteration type.	159
Table 6.1. Drone data from sites 1 and 2. The rose plots are coloured based on the fracture dip: red = 70 - 90, light green = 52 - 70, light blue = 52 -	

33, and dark blue = 33 - 14. The fractures are plotted on the stereonet as planes, and the poles to planes have been contoured.	182
Table 6.2. Drone data from sites 3 and 4. The rose plots are coloured based on the fracture dip: red = 70 - 90, light green = 52 - 70, light blue = 52 - 33, and dark blue = 33 - 14. The fractures are plotted on the stereonet as planes, and the poles to planes have been contoured.	183
Table 6.3. Drone data from sites 5 and 6. The rose plots are coloured based on the fracture dip: red = 70 - 90, light green = 52 - 70, light blue = 52 - 33, and dark blue = 33 - 14.	184
Table 6.4. Drone data from sites 7. The rose plots are coloured based on the fracture dip: red = 70 - 90, light green = 52 - 70, light blue = 52 - 33, and dark blue = 33 - 14. The fractures are plotted on the stereonet as planes, and the poles to planes have been contoured.	185
Table 7.1. selected reliable dates, combination of raw and anchored. Errors are reported as 95% confidence intervals including any possible overdispersion.....	216
Table 8.1. Precise dates from Chapter 7 which are associated with epidote-bearing assemblages.	274

Abbreviations

Units of measurement

µm/mm/ cm/m/km	Micrometre/millimeter/ centimeter/metre/kilometer
°C	Degrees Celsius
Ma	Millions of years/mega-annum
ppm/ppb	Part per million/billion
apfu	Atoms per formula unit
Wt. %	Weight percent

Analytical

SEM	Scanning electron microscope
LA-ICP-MS	Laser ablation-inductively-coupled mass spectrometry
BSE	Back scatter electron
EDS	Energy dispersive spectrum

Lithology

GRD	Granodiorite
MZT	Monzonite
PDRTM	Monzodiorite
DRT	Diorite
Q-YAR	Yarito Member
Q-SAM	Samanape Member
Q-CAR	Carpanito Member
Q-ASA	Asana Member
PARAL	Paralaque Formation
HUARA	Huaracane Formation
YB	Yarabamba Batholith
TG	Toquepala Group

Exploration

PIMS	Porphyry indicator minerals
PVFT	Porphyry vectoring and fertility tools

Faults

IFS	Incapuquio Fault System
QF	Quellaveco Fault
MF	Micalaco Fault
CF	Capulline Fault
PPF	Puca-Porquene Fault
PF	Pacay Fault

Minerals

Ab	Albite
Ap	Apatite
Act	Actinolite
And	Andalusite
Anh	Anhydrite
Brt	Barite
Bt	Biotite
Cal	Calcite
Chl	Chlorite
Dck	Dickite
Ep	Epidote
Hem	Hematite
Ill	Illite
Kfs	K-feldspar
Mag	Magnetite
Prh	Prehnite
Pmp	Pumpellyite
Py	Pyrite
Qtz	Quartz
Rt	Rutile
Ser	Sericite
Thr	Thorite
Ttn	Titanite
Tur	Tourmaline
Zrn	Zircon

1 Introduction

1.1 Research motivation

Porphyry ore deposits are defined as large, magmatic-hydrothermal systems of typically low-grade metal content. Multiple factors contribute to the principal metallogeny of the deposit type such as tectonic setting and magmatic source composition. The most economically significant type is are porphyry Cu-Mo deposits; these supply 60% to 70% of the world's copper and 99% of the world's molybdenum, often with economic by-products such as gold, rhenium, tellurium and silver (Berger *et al.*, 2008; Robb, 2009; John *et al.*, 2010; Sillitoe, 2010). Global demand for copper is increasing, requiring improved discovery rates of economically viable porphyry deposits. With only one in a thousand exploration prospects successfully reaching mine status, this increase in demand has emphasised the importance of efficient exploration of porphyry systems (Wilkinson, 2013).

The lifespan of a porphyry system ranges from as little as ~100,000 years for an individual centre, to in excess of 10 My for regional clusters of deposits. In these systems, multiple phases of magmatism release hydrothermal fluids that extensively alter up to 100 km³ of the surrounding rock. Such alteration is characteristically zoned, both laterally and vertically (Lowell & Guilbert, 1970; Sillitoe, 2010; Cooke *et al.*, 2014b; Halley *et al.*, 2015). The propylitic zone is the most laterally extensive (up to ~5 km radius) portion of this characteristic halo and therefore should provide a large target for exploration.

However, the propylitic halo is one of the least studied, and least understood, parts of the porphyry system. This has driven recent research to the possibility that this alteration zone may contain subtle indicators that could be used for geochemical vectoring and prospect assessment (e.g. Wilkinson *et al.*, 2015a, 2017, 2020; Baker *et al.*, 2020; Cooke *et al.*, 2020; Pacey *et al.*, 2020). Trace element analysis has successfully identified specific trends and characteristics in the mineral chemistry of propylitic minerals that can be used for exploration purposes. These studies have primarily focused on proximal to distal (~5 km) propylitic alteration directly associated with known porphyry deposits. However,

there is little knowledge of how such intrusion-centered alteration systems relate to the wider propylitic alteration that is frequently observed on a district scale. Thus, this study aims to better understand the controls of the development of district-scale alteration, whether this can be distinguished from porphyry-proximal haloes and regional metamorphic background, and if there are trends in mineral compositions that may assist with targeting porphyry centres from greater distances than currently possible. It also differs from previous work in its scope. It represents an innovative approach which considers the potential spatial, structural and temporal controls on district-scale propylitic alteration. This 4-dimensional approach should enhance our understanding of the evolution of a porphyry district in time and space.

1.2 Aims and objectives

Despite the implicit acknowledgement of the importance of faults in porphyry systems, the structural geology of deposits is relatively under-reported, and especially the potential influence structures may have on the dispersion of fluids and wider regional alteration. This multi-faceted study focuses on district-scale propylitic alteration, and in particular the role that structures play in the facilitation and dispersion of porphyry-related propylitic fluids. With the use of U-Pb geochronology and trace element mineral chemistry of propylitic minerals, this project examines whether specific alteration events can be temporally and geochemically constrained to particular controlling structures, and ultimately to individual porphyry centres (Figure. 1.1). The Quellaveco Cu-Mo porphyry district in southern Peru, which contains three known economic porphyry deposits, exhibits widespread propylitic alteration and has an extensive fault network that has been previously mapped via fieldwork and remote sensing. The district is therefore an ideal study area for such an investigation.

Fundamental questions are: what are the controls of district-scale (10 km+) propylitic alteration in areas known to contain economic porphyry deposits? Is the alteration structurally focused? Is the alteration multi-phase? Can it be linked to mineralised porphyry deposits themselves, for example: a more dispersed or extensive halo than previously recognised, or is it completely unrelated, or part of a much longer time-scale process still loosely linked to the generation of fertile porphyries?

To answer these questions and test the principal hypothesis, several principal objectives were defined which form the basis of the subsequent individual chapters. These objectives were to:

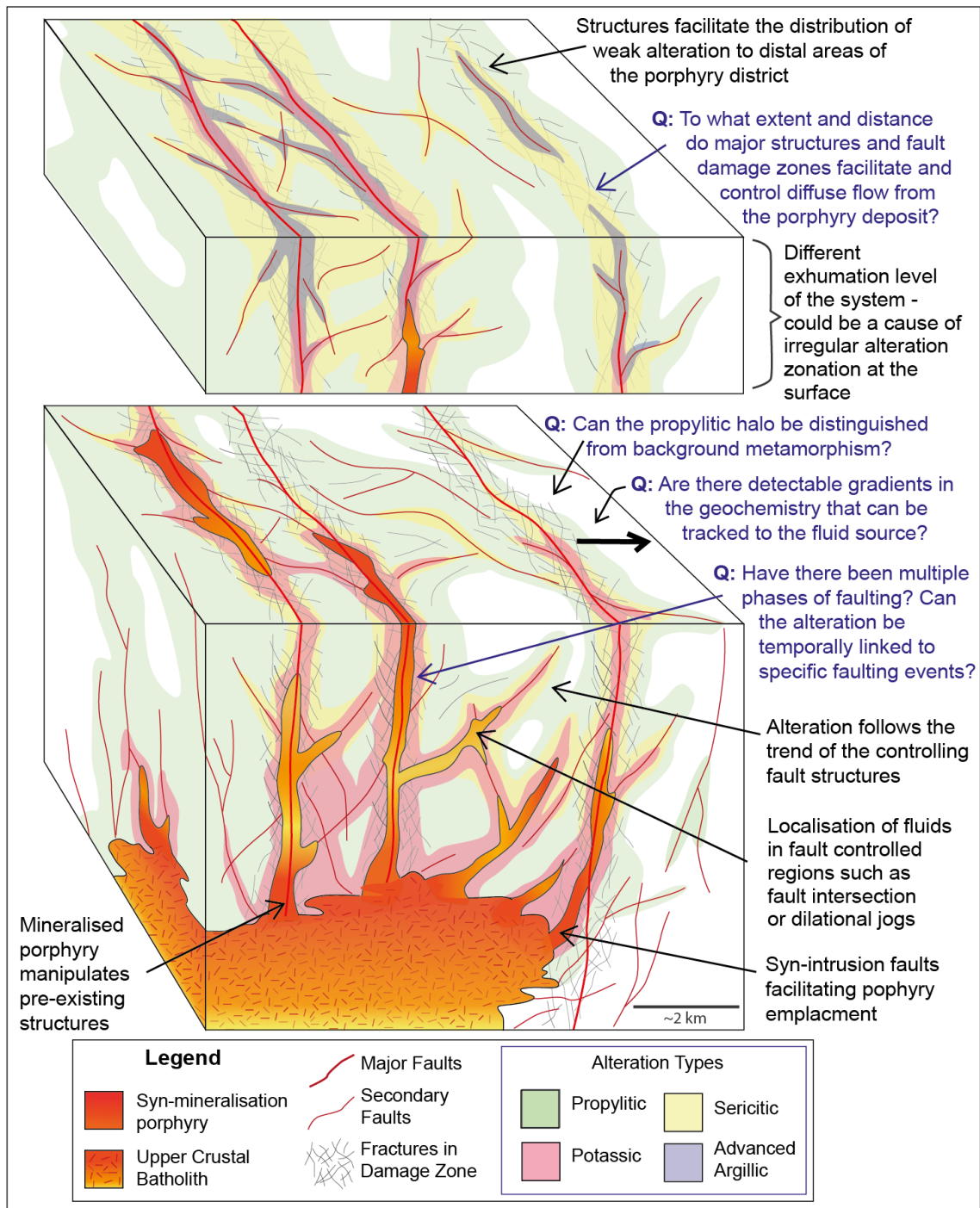


Figure 1.1 A conceptual model which considers the role of faults in the facilitation of regional fluids. Key questions are indicated in blue.

- Characterise the regional alteration and vein occurrences based on systematically collected samples and field observations. Define the propylitic alteration into petrographically compatible assemblages and assess whether there is any spatial significance in the regional setting. (Chapter 5)
- Conduct a multiscale analysis of the structural network using structural data collected from regional mapping, 3-D modelling of drone footage and statistical analysis of regional fault trends. (Chapter 6)
- Follow a clear and methodical workflow to yield precise (<0.1 se) U-Pb dates from four minerals of igneous and hydrothermal origin: zircon, apatite, titanite and epidote. The dated grains of alteration minerals will be individually attributed to a particular assemblage to constrain specific alteration events. (Chapter 7)
- Quantitatively assess major and trace element geochemistry of both propylitic chlorite and epidote in terms of location, age and assemblage type, and highlight any disparity between the two minerals. Determine if any geochemical trends may be related to the structural framework. (Chapter 8)
- Produce a genetic model for the evolution of district-scale propylitic alteration in the Quellaveco region, combining the structural, temporal, geochemical and spatial factors influencing alteration. (Chapter 9)

1.3 Overview of Porphyry Copper Deposits

1.3.1 Formation of Porphyry Copper Deposits

Porphyry copper deposits predominantly form in subduction arc settings within clusters of margin-parallel, temporally contemporaneous, metallogenic belts (Richards, 2003). Within these belts, on a district scale, there are clusters of Cu systems which are often approximately 5 to 30 km in length with 100s – 1000s of metres between each cluster (Sillitoe & Gappe, 1984; Sillitoe, 2015). The deposits optimally form at depths of 1 to 6 km, but often as shallow as 1-2 km (Cooke *et al.*, 1998b; Seedorff *et al.*, 2005). Copper grades are often between 0.5 to 1.5 percent, with secondary products of Mo or Au at grades of 0.01 to 0.04 % and <1.5 g/t, respectively (Sillitoe, 2010).

Globally, porphyry deposits are closely associated with subduction-arc magmatic and tectonic settings, with a minority related to post-collisional settings, and therefore the majority are located around the circum-pacific (Richards, 2003; Sillitoe, 1997, 2010). Dehydration at the blueschist-eclogite transition of the subducting plate, and the overlying marine sediments, triggers the initial melt generation which infiltrates the over-riding plate melt (Richards, 2003; Wilkinson, 2013). It is thought that the metal content of the melt is derived from a couple of principal sources: mass transfer of the subducting plate; partial melting of the overlying lithosphere; and potentially a minor amount of Cu and Au from the recycling of subduction seafloor hydrothermal mineralisation (Hedenquist & Lowenstern, 1994; Mungall, 2002; Sillitoe, 2010). An additional metal source is acquired by assimilation of the surrounding rock as the highly oxidised magma is transported through the crust (Hedenquist & Lowenstern, 1994).

Wilkinson (2013) describes four fundamental stages required to form large prolific porphyry deposits (shown on Figure 1.2): (1) hot zone differentiation; (2) sulphide melt saturation; (3) enhanced partitioning; and (4) efficient precipitation. The initial enrichment of the oxidising magmas occurs with the pooling of magma in the lower crust (1). The magmatic plutons that are more likely to source fertile porphyry deposits are thought to rise and initially pool at 4-10 km depth (Wilkinson, 2013). These I-type magmas are known to vary from calc-alkaline diorite to granodiorite and quartz monzonite compositions (Sillitoe, 2010). These chambers have a lifespan between 100 Kyr and 5 Myr, therefore implying a sustained heat source and multiple magma injection. The constant replenishment of mafic subduction-related magmas undergoes fractional crystallisation simultaneously triggering the sulphide saturation of the more felsic magmas (2). If the condensed saturated sulphides are later remelted, the volatile content would increase and generate highly fertile magmas. Episodically, the magma rises to crustal levels of 1-4 km. In order for the melts to deposit large quantities of sulphide ore, the melt must be sulphur-rich to precipitate the minerals that the magmas need to be reduced (3). The two most likely methods are: magnetite crystallisation, which sequesters Fe^{3+} ; or the assimilation of

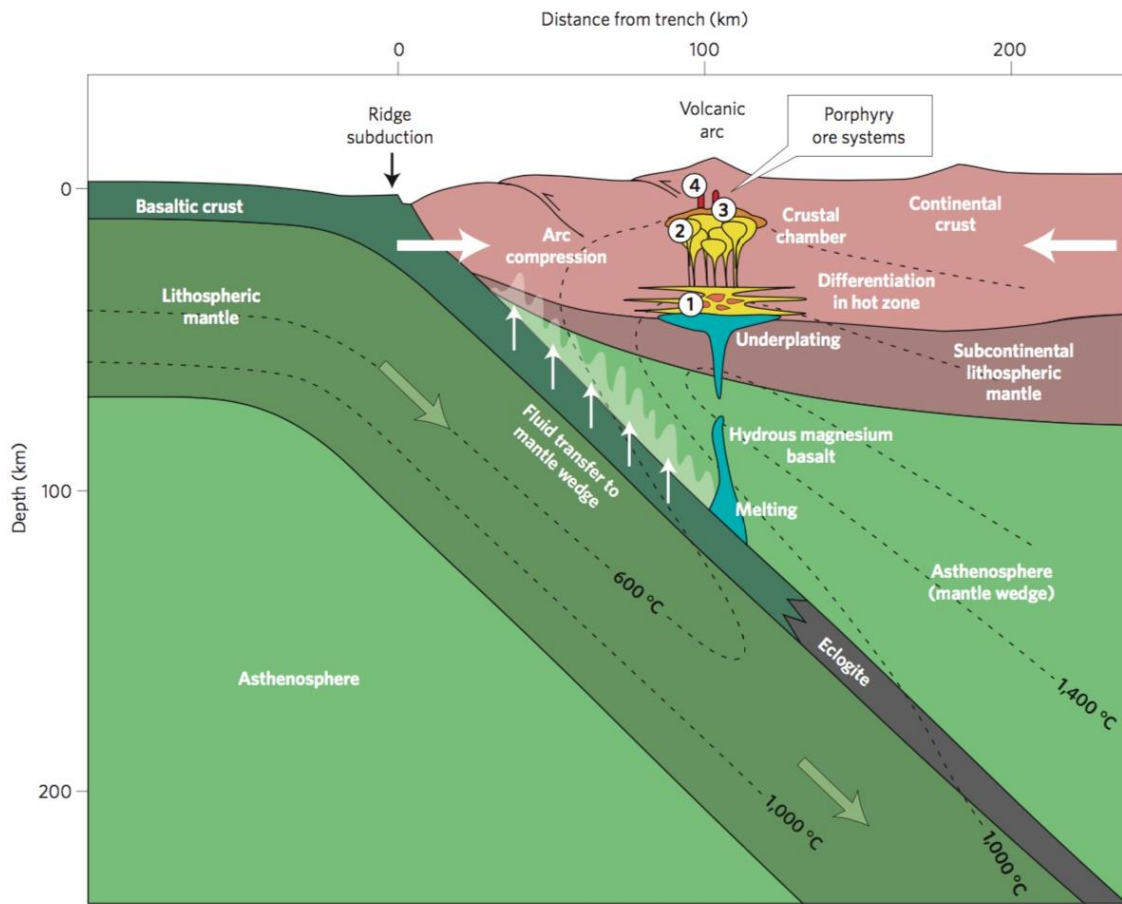


Figure 1.2. A schematic diagram depicting the ideal conditions for giant porphyry deposit formation. See text for 1-4 explanation (Wilkinson, 2013).

reduced host rocks such as limestones or organic-rich sediments. Finally, (4) the effective concentration of the fluids and forced mineral precipitation is a crucial part of economic deposits (Wilkinson, 2013). The composition of the porphyry-related intrusion is also thought to impact the mineralisation present, for example the intrusions in Cu-rich/Au-poor deposits are generally mafic and Mo-rich deposits are more felsic (Sillitoe, 2010). Some documented Au-rich porphyry deposits are associated with extremely felsic, quartz monzonite intrusions (Sillitoe, 2010). In some systems, but not all, magma explosively erupts volcanic material at the surface, although this explosive period normally occurs 0.5 to 3 Ma prior to the mineralising, high-temperature phase (Sillitoe, 1973, 2010). Circulating meteoric water plays a vital role in enhancement of the Cu mineralisation during the final cooling stages of the porphyry system (Hedenquist & Lowenstern, 1994). However, in early studies this has led to some confusion over the source of the volatiles, whether magmatic or meteoric. Due to late-stage overprinting of

minerals (up to >95% of original minerals), the magmatic trace was often obliterated, wrongly implying meteoric water had a greater influence with the original fluid source (Hedenquist & Lowenstern, 1994).

1.3.2 Porphyry-related alteration

An essential characteristic feature of porphyry deposits is the distinctive alteration halo that surrounds the deposit (Sillitoe, 1973; Wilkinson *et al.*, 2015). This alteration halo can reach radial extents of 10 km from the deposit, with volumes of 4 km³ of altered rock, and can therefore provide a much wider search area for porphyry exploration targets (Seedorff *et al.*, 2005; Wilkinson *et al.*, 2015b). The main alteration assemblages (Figure 1.3) typical of porphyry deposits are: potassic; propylitic; phyllic (also referred to as sericitic); argillic and advanced argillic (Cooke, *et al.*, 2014; Wilkinson, *et al.*, 2014). These zones are defined by the chemical change in mineral assemblages which can be observed in field outcrop, or more definitively by geochemical analysis. The alteration zones have been

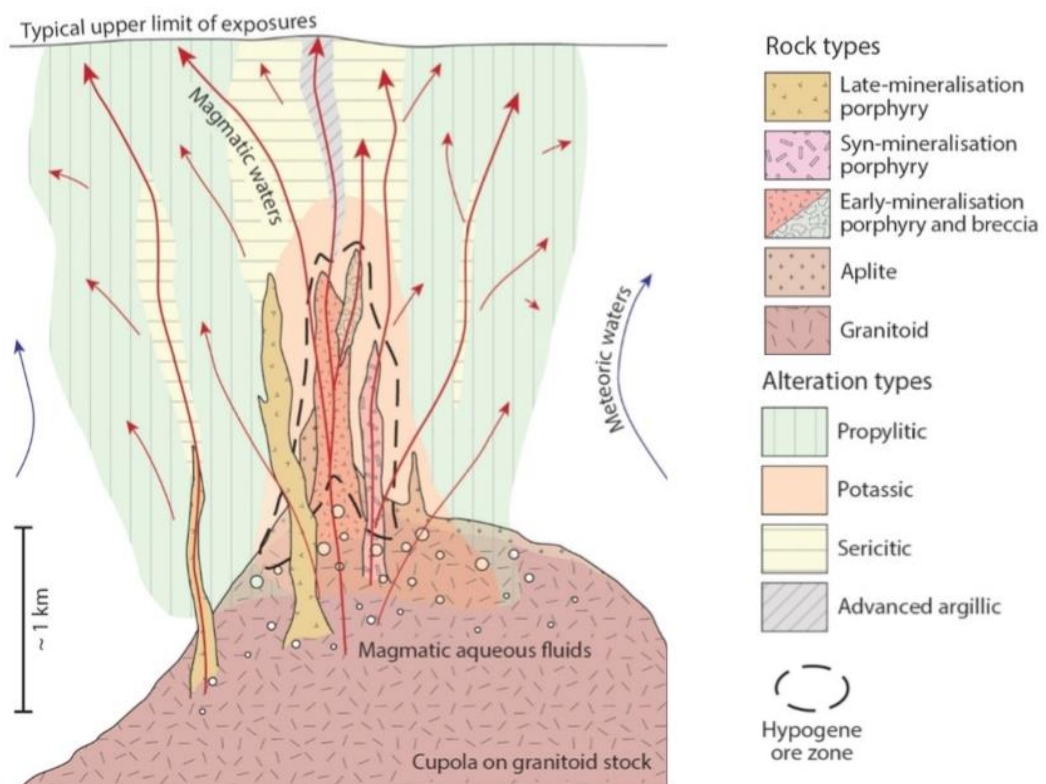


Figure 1.3. A schematic section (after Pacey, 2017), depicting the alteration assemblages of the porphyry system with convectively circulating meteoric waters, causing the late-stage alteration of the sericitic and advanced argillic zones.

described by authors (e.g Lowell & Guilbert, 1970), as coaxial zones that form concentric shells surrounding the ore body. However, parameters such as regional or local structures, the heterogeneity of surrounding rocks, and post-ore intrusive bodies are known to affect the size and geometry of the alteration halos. Determining the extent to which these factors affect porphyry-related alteration, and whether they can be used to work out fertility of a deposit, has been the subject of detailed study for the past couple of decades.

Hydrothermal alteration in the porphyry environment is directly linked to small veinlets approximately 0.1 to 10 cm thick. Temporally classifying veinlets for different alteration stages was first explored in-depth by Gustafson & Hunt (1975) on the El Salvador Cu deposit in Chile. Subsequent studies have since categorised these into five indicative vein types: 'A type' early stage, irregular veins associated with high temperatures; 'B veins' seen to cross-cut 'A veins' but with a thin potassic halo and central pyritic seam; 'D veins' containing massive sulphides which are likely to be a product of late stage phyllic alteration; and the less

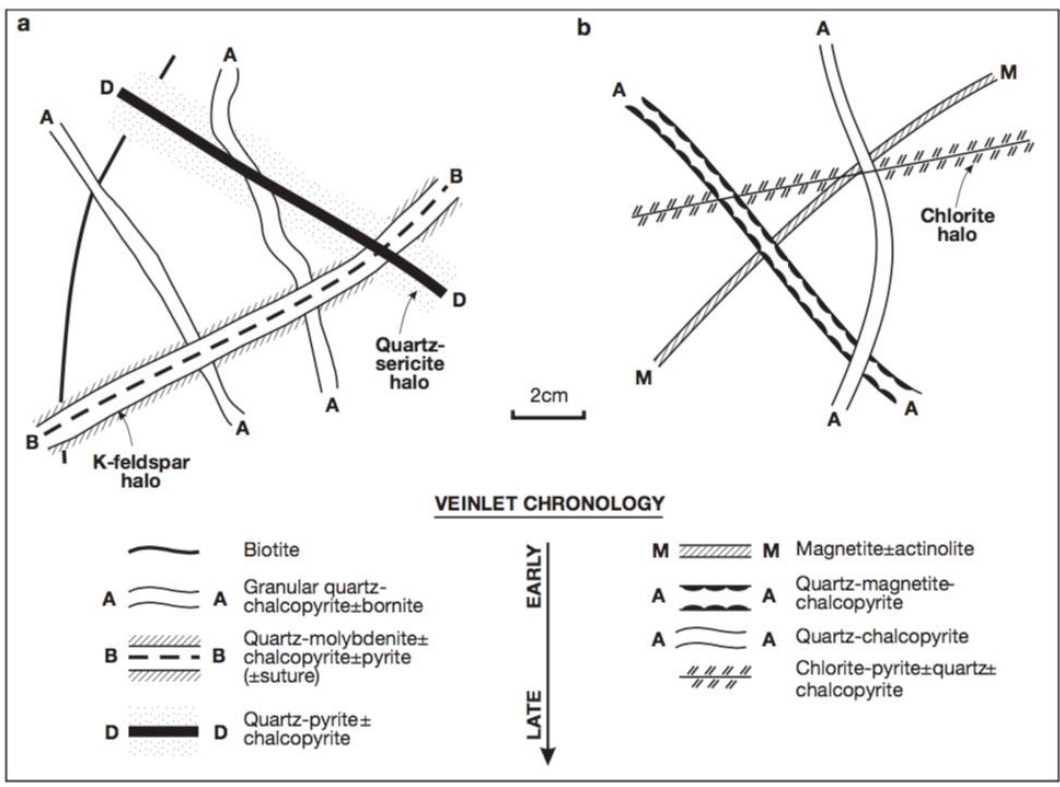


Figure 1.4. Schematic figure showing the chronology of the main vein types: A, B, D, and M in, **a)** Cu-Mo porphyry deposit, and **b)** Cu-Au porphyry deposit, both associated with calc-alkaline intrusions. From Sillitoe (2010).

important 'P veins' and 'M veins' which are primitive, early stage veins, with the 'P veins' providing some indication of the original melt (Cooke *et al.*, 2014b). The early stage veins have a wavy, irregular form, while the late stage veins generally follow a linear, straight-cut line (Berger *et al.*, 2008). This is attributed to the temperature of fluid emplacement: as the early stage veins occur at high temperatures the host rock is relatively ductile; as the temperature drops for the late stage alteration, brittle processes form in response to the local stress applied thereby allowing fluids to flow along new or pre-existing structures. Sillitoe (2010) depicts the cross-cutting vein generations observed at a porphyry Cu-Mo deposit and Cu-Au deposit (Figure 1.4).

It is widely noted that there is a significant relationship between the host rock lithology and the location/size of a porphyry copper deposit and the extent of the associated alteration (John *et al.*, 2010). Certain lithologies appear to positively support the enrichment deposits, such as fine-grained, unfractured rocks near intrusive contacts as there is an impermeable seal for ore development (Sillitoe, 2010; Wilkinson, 2013). The ability of Fe-rich rock types to precipitate Cu from the transport of oxidised magmatic fluids concentrates mineralisation in ferrous lithologies (Sillitoe, 2010). In general, rock types containing plagioclase, K-feldspar, quartz, micas and amphiboles are proven to host a large number of porphyry copper deposits (John *et al.*, 2010).

1.3.3 Early-Stage Alteration

The potassic core and surrounding propylitic alteration zone are synchronously the first alteration halos to form in the system (Cooke *et al.*, 2014a). Both of these early phase alteration phases form under lithostatic loads, as opposed to hydrostatic, and therefore the change from potassic to propylitic occurs as a result of lateral increase in rock water interaction, and wall rock buffering from the centre of the system (Sillitoe, 1993; Cooke *et al.*, 2014a). The hypersaline fluid responsible for the early stages of porphyry formation reaches temperatures of greater than 500°C and salinities of >30 wt% NaCl (Cooke *et al.*, 1998).

Potassic Zone

The potassic domain is the primary alteration zone to form proximal to the porphyry-related magmatic intrusion at high temperatures of up to 550°C, and alongside the sericitic domain, hosting the majority of the economic mineralisation in porphyry copper deposits (John *et al.*, 2010; Halley *et al.*, 2015). This potassic zone is so named due to the high abundance of key pervasive secondary K-feldspar, biotite and magnetite replacement minerals with the common occurrence of additional lesser minerals such as quartz, actinolite, sericite, epidote, andalusite, albite, carbonate, and tourmaline (Lowell & Guilbert, 1970; Berger *et al.*, 2008; Sillitoe, 2010). Generally, the potassic zone contains the majority of the mineralisation in the form of concentric and radial veins around the associated porphyry intrusion of the regional and local stress field surrounding the potassic core; the mineralised veins can show a distinct preferred orientation with respect to the principal stress orientation, sometimes in the form of dyke swarms and sheeted veins (Cooke *et al.*, 2014a). However, commonly present are the irregular and discontinuous quartz veins that are described as the high temperature ‘A-veins’ of the potassic zone (Cooke *et al.*, 2014a).

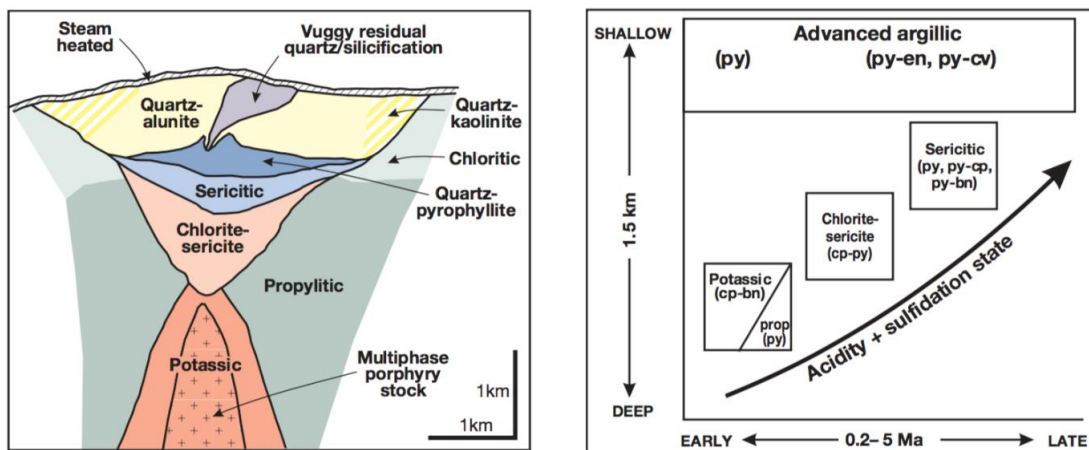


Figure 1.5. **a)** schematic diagram of alteration zonation at Cu porphyry systems; **b)** generalised alteration-mineralisation sequence with paleodepth with respect to life span of the Cu porphyry deposit (after Sillitoe, 2010)

Propylitic Zone

Forming during the early stages of the porphyry system, the low temperature propylitic alteration zone signifies the alteration of the surrounding rocks by hydration, carbonation, oxidation and local sulphidation reactions (John *et al.*, 2010). Thought to form cogenetically with the potassic alteration, the propylitic alteration can extend up to 10 km from the centre of the system and is therefore the most widely dispersed of the porphyry-related alteration zones (Sillitoe, 1973). Particularly in the most distal limits, the propylitic alteration is the weakest imprint associated with the porphyry deposit, but is still a vital part of porphyry exploration (Wilkinson *et al.*, 2015b).

Due to the lateral extent of the propylitic zone, which is generally much greater than the other alteration domains, it has necessarily been divided into three temperature controlled subzones each with a slight change in expected mineral assemblage: (1) the high temperature actinolite subfacies, most proximal to the potassic core, has mineral assemblages of actinolite-epidote-chlorite-calcite±pyrite±hematite±chalcopyrite; (2) the moderate temperature epidote subfacies with epidote-chlorite-calcite±pyrite±hematite±chalcopyrite; (3) the low temperature, and most distal, chlorite subfacies displays chlorite-calcite±pyrite±prehnite±zeolite (Sillitoe, 2010; Cooke *et al.*, 2014b; Wilkinson *et al.*, 2017). The mineral assemblage change from the actinolite subfacies to chlorite subzone is primarily due to the change in temperature and K^+/Ca^{2+} ratios. As the magmatic-hydrothermal fluids migrate laterally away from the potassic zone the progressively cooler temperatures allow Ca aluminosilicates, such as epidote and actinolite to stabilise (Cooke *et al.*, 2014a). Due to the relative abundance of H_2S in the propylitic zone proximal to the potassic-propylitic boundary, pyrite and epidote are found in coexistence as the H_2S causes an extension of the pyrite zone into the propylitic alteration.

1.3.4 Late-Stage Alteration

The lithostatic loads experienced to trigger the early-stage alteration, transitions into hydrostatic load later in the system, to form late-stage alteration assemblages. These late stage alteration zones have been acknowledged to have a greater structural control on the distribution of the alteration, thereby suggesting that these late stage processes are directly controlled by the regional stress regime (Cooke *et al.*, 2013). Given the relative abundance of H₂S in the propylitic zone proximal to the potassic-propylitic boundary, pyrite and epidote are found in coexistence as the H₂S causes an extension of the pyrite zone into the propylitic alteration.

Sericitic Zone

The quartz-sericite zone, commonly known as the phyllic zone, is abundant in quartz, sericite, muscovite and frequently pyrite and chalcopyrite (Lowell & Guilbert, 1970a; Berger *et al.*, 2008; Sillitoe, 2010).

The sericitic alteration is highly controlled by the late-stage 'D veins'. The alteration halos associated with these veins are typically in the region of 1 mm to >1 m, and therefore depending on the extent of the halo, and the abundance of veins, the interconnected boundaries provide pervasive sericitic alteration, sometimes affecting a region of up to 1 km³ (John *et al.*, 2010). The 'D veins' are often pyrite-rich with variable amounts of sphalerite, tetrahedrite, manganese and galena, and due to the nature of their formation, are often structurally controlled (Cooke *et al.*, 2014b; John *et al.*, 2010). The pyrite and sericite generally abundant in the quartz-sericite zone (phyllic) are the product of a chemical interaction that occurs above the ore zone, between 350°C and 450°C (Lowell & Guilbert, 1970; Halley *et al.*, 2015; Halley, 2016). In the shallower parts of the system, meteoric non-magmatic waters play a key role in the alteration and replacement of minerals. The magma-exsolved SO₂ reacts with the circulating meteoric waters to produce acidic fluids, hydrogen sulphide and sulphuric acid. The chemical equation for this reaction is $4\text{SO}_2 + 4\text{H}_2\text{O} = \text{H}_2\text{S} + 3\text{H}_2\text{SO}_4$

(Halley, 2016). In systems where there are ample Cu±Mo sulphide minerals in the porphyry host rocks, sericite replaces the feldspar and mafic phenocrysts with relict albite maintaining the original porphyritic texture (John *et al.*, 2010).

Advanced and Intermediate Argillic Zone

Advanced argillic alteration is a late-stage alteration phase that is associated with primary minerals such as: quartz; alunite; pyrophyllite; dickite and kaolinite, with some possible occurrences of covellite, enargite, pyrite and andalusite (Lowell & Guilbert, 1970; Cooke *et al.*, 1998; Sillitoe, 2010; Cooke *et al.*, 2014b). This high-sulphidation mineral assemblage associated with this alteration zone is the result of extremely low-pH, acidic, low temperature fluids (Sillitoe, 2010). In the overlying lithocap environment (see 1.3.4) the advanced argillic alteration is continually replenished by these low temperature, low-salinity fluids; so even though it is predominantly a late-stage alteration some advanced argillic alteration occurs in the early-stages of the deposit formation, as seen in Figure 1.5 (Hedenquist *et al.*, 1998; Sillitoe, 2010). The advanced argillic alteration phase is thought in some cases to be over 2 My younger than the potassic alteration and therefore is commonly recorded to overprint the early-stage potassic alteration, occasionally to depths greater than 1 km (Sillitoe, 2010). It has been noted that advanced argillic alteration is more prominent in Cu deposits associated with calc-alkaline intrusions, as opposed to alkaline, and preferentially favours alteration of the plagioclase feldspars in more felsic lithologies (Lang *et al.*, 1995; Sillitoe, 2010).

Intermediate argillic alteration is a low-temperature (typically less than 200°C) phase that occurs in relatively acidic conditions, but with a higher pH than advanced argillic alteration (John *et al.*, 2010). Sericite, chlorite, and kaolinite are the predominantly resulting clay minerals, with additional illite, pyrite, and calcite (Cooke *et al.*, 1998b). Like the advanced argillic phase, this late-stage alteration phase overprints the top of the potassic and

sericitic zones (*John et al.*, 2010). However, pyrite and sulphide-rich minerals are much less abundant in the intermediate argillic zone compared with the advanced argillic zone.

1.3.5 Lithocap

A lithocap is a common area of intense advanced argillic and clay alteration in the shallowest part of the porphyry system, and can exceed lateral extents of 10 km² and depths of up to 1 km (Sillitoe *et al.*, 1998b; Wilkinson JJ. & Brugge, 2017). In this shallow subsurface environment, between the subvolcanic intrusive setting and the surface, acidic fluids flow laterally causing the spread of advanced argillic, silicic and argillic alteration assemblages (Sillitoe *et al.*, 1998b; Chang *et al.*, 2011). These zones are quartz-rich and aluminium deficient due to the residual silica alteration from extremely low-pH, high sulphur fluids (*John et al.*, 2010). The interaction of these fluids results in the precipitation of massive sulphides, such as pyrite, in the structural roots of the lithocap, with covellite, digenite, enargite, tennantite, and bornite (Sillitoe *et al.*, 1998; Sillitoe, 2010; *John et al.*, 2010).

Due to their clay composition and presence at, or close to, the surface, lithocaps are not always present at porphyry deposits as they are easily subjected to weathering and denudation (Sillitoe *et al.*, 1998). In low sulphidation environments, the paleosurface is similarly altered, however the steam-heated alteration present at these systems are usually easily identified from porphyry and high-sulphidation lithocaps by the presence of powdery alunite and opaline silica, with distinctive textures (Sillitoe & McKee, 1996; Sillitoe, 2015).

1.4 Geochemical Vectoring on the Propylitic Zone

Detecting the presence of a porphyry system from its hydrothermally altered footprint is vital to exploration. Three important questions are asked. Is there a deposit? If so, how big is the deposit? And, what is the proximity of the deposit? Recent studies have focused on expanding our understanding of mineral

chemistry in porphyry systems in order to answer these questions, and therefore aid future exploration of more obscure deposits (Djouka-Fonkwé *et al.*, 2012b; Cooke *et al.*, 2014b, 2014a; Loader *et al.*, 2017a) and others. By expanding the distance that a deposit can be detected from, this critical aspect of porphyry research aims to utilise mineral alteration chemistry to detect the proximity to a deposit, and its possible fertility, thereby commercialising this process to aid exploration (Cooke *et al.*, 2014b).

Several minerals found in the alteration halos of porphyry systems have been proven to be useful as a porphyry indicator mineral (PIMS) and porphyry vectoring and fertility tools (PVFTs), such as: apatite; chlorite; epidote; zircon; magnetite and titanite (Cooke *et al.*, 2017). Figure 1.6 summaries the key PVFTs discussed in this chapter. Each have particular strengths as a vectoring tool, and some, such as magnetite, zircon and apatite, are useful when determining the fertility of a deposit (Wilkinson *et al.*, 2017). These minerals appear in different abundance reflecting such factors as: alteration zone, proximity to the porphyry-related intrusion; host rock lithology; and formation temperature. Original host rock composition contributes to the nature of the altering magmatic-hydrothermal fluids, for example: Mn, Co, Ni, Zn, Cu, V, Cr, As and Sb, are added to the fluid from the alteration of amphibole; and Na, Ca, K, Sr, Ba, Rb and Pb are contributed upon the alteration of feldspars (Halley *et al.*, 2015).

In order to effectively use these minerals as an exploration tool, it is vital to be able to distinguish between propylitic alteration caused by porphyry-related hydrothermal fluids, and the background regional metamorphic terranes (Djouka-Fonkwé *et al.*, 2012a; Wilkinson *et al.*, 2015b). In the field, outcrop hand sample analysis is generally a useful method for the initial identification of mineral assemblages, and therefore an alteration zone classification. However, in areas of low metamorphic grade, this method can be limited (Djouka-Fonkwé *et al.*, 2012a). The initial grouping of chlorite and epidote minerals into background metamorphism and propylitically altered rocks can be achieved by using plane-polarised light (Djouka-Fonkwé *et al.*, 2012a). Nevertheless, using detailed chemical LA-ICPMS analysis of chlorite, the background metamorphic, porphyry-related propylitic boundary can be accurately determined. Wilkinson *et al.* (2015) demonstrated, using the case study of Batu Hijau in Indonesia, how

elevations of Li and Fe content are more representative in metamorphic chlorites than distal propylitic chlorites, which instead show enrichment of Ca.

1.4.1 *Porphyry Indicator Minerals*

Apatite

Apatite, $\text{Ca}_5(\text{PO}_4)_3(\text{OH},\text{F},\text{Cl})$, is found within some metamorphic and sedimentary rocks, but more helpfully for porphyry fertility studies, it is the most common phosphate mineral of igneous rocks (Deer *et al.*, 2013). Although still in the early stages of development, it has been proven to be a useful indicator mineral for porphyry deposits (Deer *et al.*, 1992; Wilkinson *et al.*, 2017). Using trace elements such as Mg, V, Mn, Sr, Y, La, Ce, Eu, Dy, Yb, Pb, Th and U, Mao *et al.* (2016) showed that apatite in mineralised areas generally have higher Ca, and lower rare earth element content than apatite originating from non-mineralised or carbonatite terranes. This study also highlighted the possibility of using apatite to differentiate between different types of mineral deposit by using the rare element content. For example, porphyry Cu-Au contains high V; whereas high Mn contents were recorded for apatite from calc-alkaline porphyry Cu-Au and Cu-Mo deposits (Mao *et al.*, 2016). Rukhlov *et al.* (2016) further developed the application of apatite by differentiating between apatite in alkalic and calc-alkalic porphyry systems. Due to limited published work, and the variety of geochemical compositions of apatite, even in one deposit alone, apatite is not currently able to give an accurate indication of porphyry fertility (Wilkinson *et al.*, 2017). As a relatively novel technique, however, the application of apatite has developed significantly in little time, and with further work this is likely to be a valuable PIM.

Zircon

Zircon is commonly found as an accessory mineral for Na-rich and acidic igneous rocks, including granite, granodiorite and rhyolites (Bernet & Garver, 2005). The high abundance of zircon in many porphyry-related intrusions and host rocks makes it particularly

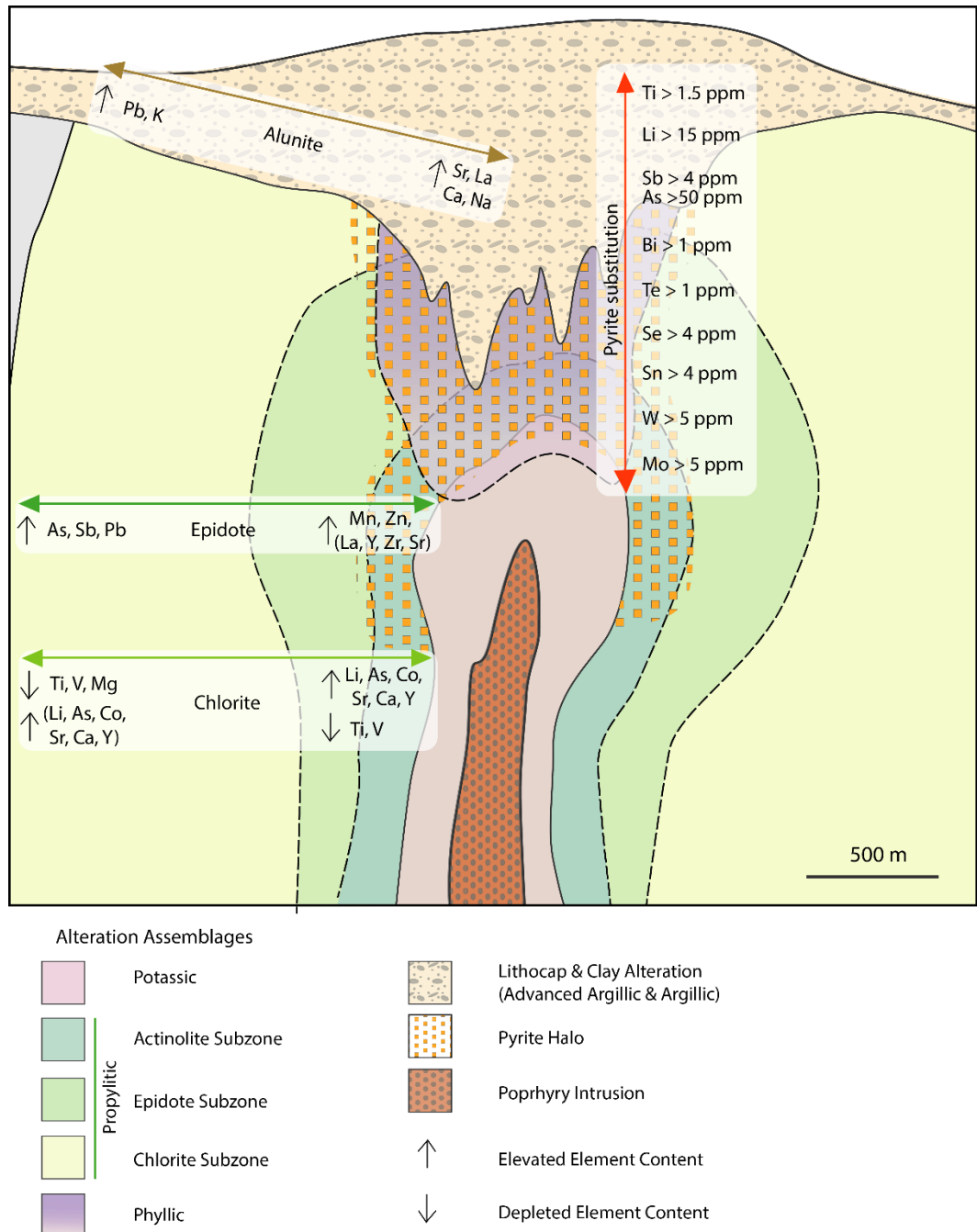


Figure 1.6. Schematic diagram compiled from Cooke et al. (2017); Wilkinson et al. (2017), Halley (2015), and Cooke et al. (2014b), of the porphyry system with main alteration zones, depicting the minor and trace elements used as porphyry vectoring tools. Chlorite, epidote, and alunite show the lateral variation in elevated and depleted elements. Pyrite substitutions highlight a vertical change in anomalous recordings of certain metal trace elements, elevated from background levels (Halley, 2015).

suitable for its use as a porphyry indicator mineral. Other useful properties are that it is: extremely robust and therefore much less likely to be affected by later weathering; highly resistant to diffusive re-equilibrium at high temperatures, thus allowing original magma petrogenesis to be determined; a sensitive temperature geochronometer (Cooke *et al.*, 2017; Wilkinson *et al.*, 2017).

Cu-porphyry deposits are derived from oxidised magmas, so understanding the redox state of magmatic, potentially porphyry-related intrusive rocks could be a crucial indicator of economic deposits (Sillitoe, 2010; Richards, 2015). For example, in magmatic systems of high oxidation, elevated Ce and depleted Eu anomalies have been recorded (Burnham & Berry, 2012; Dilles *et al.*, 2015; Wilkinson *et al.*, 2017).

Magnetite

Magnetite is predominantly found within the potassic zone, but also arises from hydrothermal over-printing in the propylitic zones (Siewwright, 2017; Wilkinson *et al.*, 2017). For many years, particularly before modern techniques were developed, magnetite's high resistivity and easy separation from other minerals meant that it was a very useful mineral for porphyry prospectors (Cooke *et al.*, 2017; Wilkinson *et al.*, 2017). From work carried out by Siewwright (2017), magnetite's utility has been heightened as it was shown how hydrothermal magnetite from the different domains (e.g. potassic or propylitic) can be determined. This has significant implications for using magnetite as an exploration tool.

1.4.2 *Porphyry Fertility and Vectoring Tools*

Epidote

'Epidote' refers to a specific mineral, but also to the mineral supergroup of which it is a part - the epidote-supergroup with the generalised chemical formula $\text{Ca}_2\text{Al}_2\text{O}(\text{Al},\text{Fe}^{3+})\text{OH}[\text{Si}_2\text{O}_7][\text{SiO}_4]$ (Deer *et al.*, 2013). Although epidote occurs as a product of hydrothermal alteration, particularly in the epidote subzone of the

propylitic alteration zone, it also commonly occurs in regional metamorphic terranes, geothermal systems and other hydrothermal deposits (Cooke *et al.*, 2014b). Therefore, to use epidote as a porphyry proximator, it is fundamental to distinguish between metamorphic and porphyry-related epidote. Such traits as: Al substitution occurring within higher temperature metamorphic terranes and Fe³⁺ at lower temperatures can help indicate whether the epidote is metamorphic or porphyry-related (Deer *et al.*, 2013). Another potentially problematic attribute of epidote for porphyry vectoring is that its formation is predominantly confined within intermediate and mafic volcanics, therefore much less common in host rocks of a felsic nature (Wilkinson *et al.*, 2017). As a consequence of the fractionation of the I-type magmas associated with porphyry deposits, felsic igneous rocks are the predominant host of these deposit types, therefore epidote occurrence is more limited.

In a study by Ballantyne (1981) on the North Silver Bell deposits in Arizona, Mn was shown to increase with proximity to the deposit, peaking at around the boundary of the propylitic actinolite subzone of the propylitic alteration and the potassic zone. More recent work detected further trace element changes in epidote with respect to distance from deposits such as Cu, Mo, Au, Sn proximal to the potassic alteration, and increased As, Sb, Pb, Zn, approximately 1.5 km from the deposit (Cooke *et al.*, 2014a). Beyond the pyrite zone, but proximal to it, hydrothermal epidote is enriched in certain elements: Mn and Zn in particular, though La, Y, Zr and Sr are also enriched (Wilkinson *et al.*, 2017). This presence of systematic trace element enrichments has been attributed to the concentration gradient of H₂S with lateral distance from the potassic core (see Figure 1.7). Lateral migration of fluids from the potassic zone into the cooler outer zones causes the stabilisation of Ca in epidote, and the depletion of Cu. The available H₂S in the fluid precipitates pyrite, which scavenges trace elements of As, Pb, Sb into its lattice. Therefore, epidotes presence in the pyrite halo of the system are

usually depleted in these elements due to their preferential substitution into pyrite. However, with distance from the magmatic centre in the propylitic zone, the As, Pb, Sb concentration increases with the depletion of H₂S, thereby forcing the substitution of the trace elements into the epidote lattice (Cooke *et al.*, 2014a).

Some porphyry deposits, particularly those with complex tectonic histories, have multiple phases of porphyry and non-porphyry related, magmatism and hydrothermal activity. This can be responsible for post-mineralisation alteration, and subsequent multifaceted overprinting, which can be problematic for porphyry vectoring. Hart-Madigan (2019) used K-means cluster analysis on epidote to statistically distinguish between the mineralisation porphyry signature from the overprinting alteration events at the Oyu Tolgoi Cu-Au porphyry in Southern Mongolia.

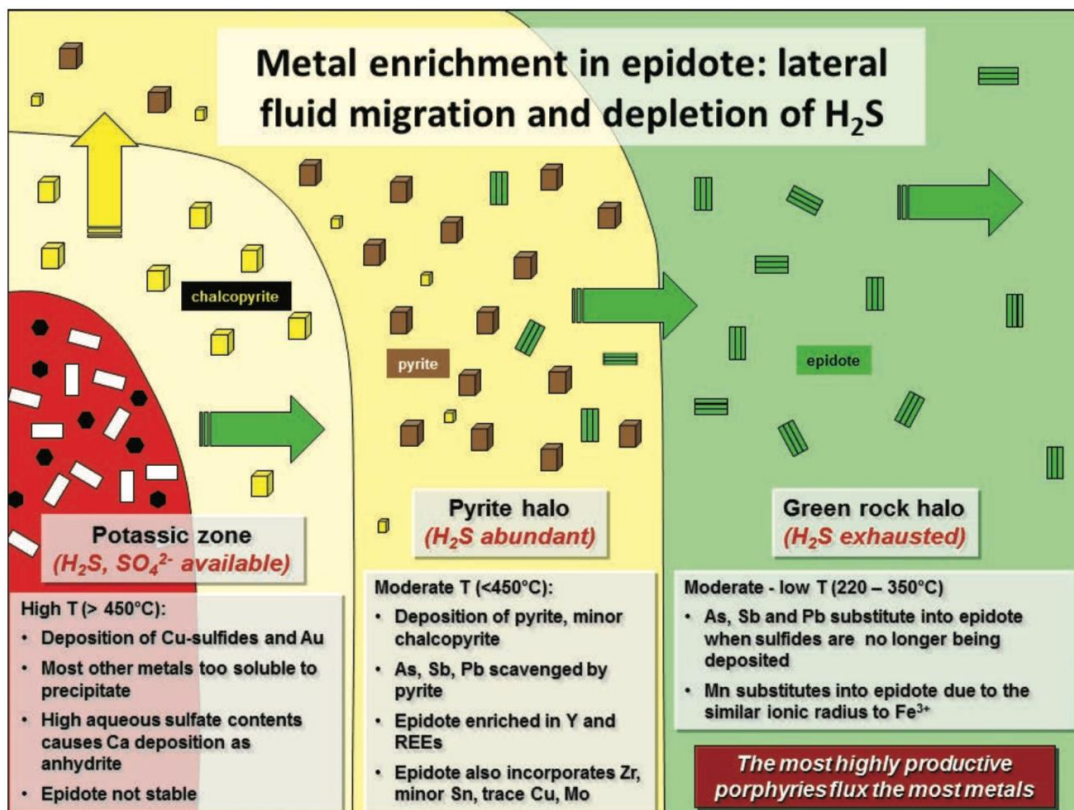


Figure 1.7. Schematic diagram from Cooke *et al.* (2014a); showing the lateral enrichment of trace elements in chlorite, with the depletion of H₂S further from the porphyry centre.

Additionally, epidote acts as a fertility indicator by its presence in fertile deposits, but low abundance in the propylitic zone of weakly mineralised/barren deposits (Cooke *et al.*, 2014a, 2014b).

Chlorite

Chlorite has a composition of $(\text{Mg,Fe}^{2+},\text{Fe}^{3+},\text{Mn,Al})_{12}(\text{SiAl})_8(\text{Si,Al})_8\text{O}_{20}](\text{OH})_{16}$, with common substitutions of cations Mg^{2+} , Al^{3+} , Fe^{2+} , and Fe^{3+} , although it is much less common for chlorite to contain significant amounts of Mn (Murray, 2007; Deer *et al.*, 2013). Forming at low to moderate temperatures of up to 400°C, chlorite is a common mineral in metamorphic rocks of early-stage diagenesis and lithification (Deer *et al.*, 2013). Chlorite is also associated with igneous rocks as the hydrothermal alteration of ferric minerals, pyroxenes, amphiboles, and biotite, and is therefore a common mineral in porphyry-associated hydrothermally altered rocks. The original composition of the altered mineral determines the type of chlorite produced (Deer *et al.*, 2013). Other common chlorite occurrences include: low-temperature hydrothermal veins with adularia and quartz; fissure veins on massive igneous bodies; slickenline lamellar coatings on fault and joint planes; and as inclusions within amygdaloidal lavas (Deer *et al.*, 2013). In porphyry hydrothermal systems, the metal elements within the lattice become more soluble with increasing acid conditions. Therefore Halley, (2016) suggests that there is also a vertical zonation of chlorite with increasing acidity above the deposit, as the disproportionation reactions of the SO_2 in the fluid produces H_2SO_4 and is responsible for some of the pyrite production.

As a porphyry deposit indicator, studies have shown chlorite to be extremely valuable. Changes in chemical composition with distance from the porphyry centre are systematic and predictable, allowing a more precise prediction of the distance of an area to the porphyry-related intrusive host. This distance can be estimated based on systematic increase and decrease in certain major, minor and trace elements that are included in the crystal lattice of chlorite within the

propylitic zone (Wilkinson *et al.*, 2015b). For example, the study carried out by Wilkinson *et al.* (2015) on the Batu-Hijau Cu-Au porphyry deposit in Indonesia significantly developed the use of chlorite as an indicator mineral for economic porphyry deposits, and gauging the proximity to the centre. In the study, a clear decrease in Ti, V, and Mg trace elements was detected with increasing distance from the deposit. Similar results arose from a study conducted on the Northparkes deposit in New South Wales (Pacey, 2017) which showed elevated Ti and Al proximal to the deposit, and an inverse display of Co, Li and Sb. Wilkinson *et al.* (2017) further supported the application of chlorite as a vectoring tool on the El Teniente deposit in Chile where the propylitic footprint was detected up to 5 km from the porphyry source using Ti/Li ratios. The abundance of Mg-rich chlorite proximal to the mineralisation is additionally shown with the use of shortwave infrared reflectance spectrometry in the study by Neal *et al.* (2018).

Complex overprinting of alteration minerals from multiple intrusive events can be problematic when determining relative age of the mineralising ore fluids. By using K-means cluster analysis of specific trace elements (U, As, Sb, Zr and La), Hart *et al.* (2016) distinguished between the original alteration event and two successive overprinting events at the Oyu Tolgoi deposit in Mongolia, using chlorite (and epidote).

Titanite

Titanite $\text{CaTi}(\text{SiO}_4)(\text{O},\text{OH},\text{F})$, also known as sphene, is a common accessory mineral in most igneous rocks, and contains high levels of REE (Deer *et al.*, 2013; Loader *et al.*, 2017b). Common appearances include: the dominant titanium-bearing mineral in many acidic and intermediate plutonic rocks; low-temperature veining associated with epidote, adularia and albite; and ferromagnesian minerals in metamorphic rocks, particularly schists and gneisses (Deer *et al.*, 2013). Titanite also contains significant amounts of the radioactive elements Th and U, thus making titanite

a very useful mineral for dating (Deer *et al.*, 2013; Hart-Madigan, 2019).

The broad study conducted by Celis (2015) looked at the differences between four types of titanite: primary magmatic, metasomatic, secondary, and altered, with the aim of discovering distinguishing features of the different types in order to identify alkalic Cu-Au porphyry related mineralisation. Subtle differences were highlighted in chemical compositions, particularly between: primary magmatic and metasomatic; and the secondary and altered titanite minerals. Primary and metasomatic were shown to have elevated REE and low V and F; while secondary and altered typically show low Fe/Al ratios when influenced by Na-Ca, and high ratios from k-silicate alteration, with overall low REE (Celis, 2015). Titanite has been further developed in the Oyu Tolgoi deposit (Hart-Madigan, 2019; Hart-Madigan *et al.*, 2020) where propylitically altered hydrothermal titanite was successfully dated and multiple growths were constrained to intrusive events in the area. More specifically, for the first time titanite was used to confidently constrain propylitic alteration phases with porphyry-related mineralisation. The study significantly demonstrated titanite's aptitude as a valuable geochemical vector by distinguishing between titanite associated with porphyry-related alteration and background low-grade alteration, and directed exploration to focus on areas with mineralisation coeval propylitic alteration.

Alunite

Alunite, $KAl_3(SO_4)_2$, often occurs from the secondary alteration of minerals such as potassic feldspars, in acidic conditions where the hydrothermal fluid is abundant in sulphate ions, and is therefore a principal alteration mineral of the advanced argillic zone (Celik *et al.*, 1999; Allaby, 2008; Cooke *et al.*, 2014b). Work was carried out by (Chang *et al.*, 2011) on the Mankayan deposit, Philippines, to define any variations in trace elements within the lithocap environment. The trace elements analysed on the LA-ICP-MS

included: Ca, Sr, La, Ce, Nd, Sm, Eu, Gd, Dy, Er, Yb, Le, Zr, Ba, Au, Ag, Pb, Sb, Bi, Mn, Fe, Cu, As and Se. This analysis highlighted the presence of alunite with elevated Na, Ca and depleted K increases with proximity to the porphyry centre. Further analysis by Chang *et al.* (2011) of alunite-bearing samples on the LA-ICP-MS highlighted additional trends such as lower Pb but higher Sr, La, Sr/Pb and Pb/Sr toward the system centre.

1.4.3 Vertical Zonation

The PVFTs previously discussed are mostly studied as lateral proximitors to the porphyry system. However vertically, there is also a zonation of minor/trace elements. Halley (2016) studied several deposits in America and Canada, particularly Yerington in Nevada, and found that there was a pattern of trace element anomalies with vertical extent from the potassic domain up through to the advanced argillic clay alteration. Defined boundaries were detected using SWIR, where certain trace elements had anomalies significantly above their background level (see Figure 1.8). With increasing height from the potassic domain, consistent metal anomalies were detected in order: Mo > 5 ppm; W > 5 ppm; Sn > 4 ppm; Se > 4 ppm;

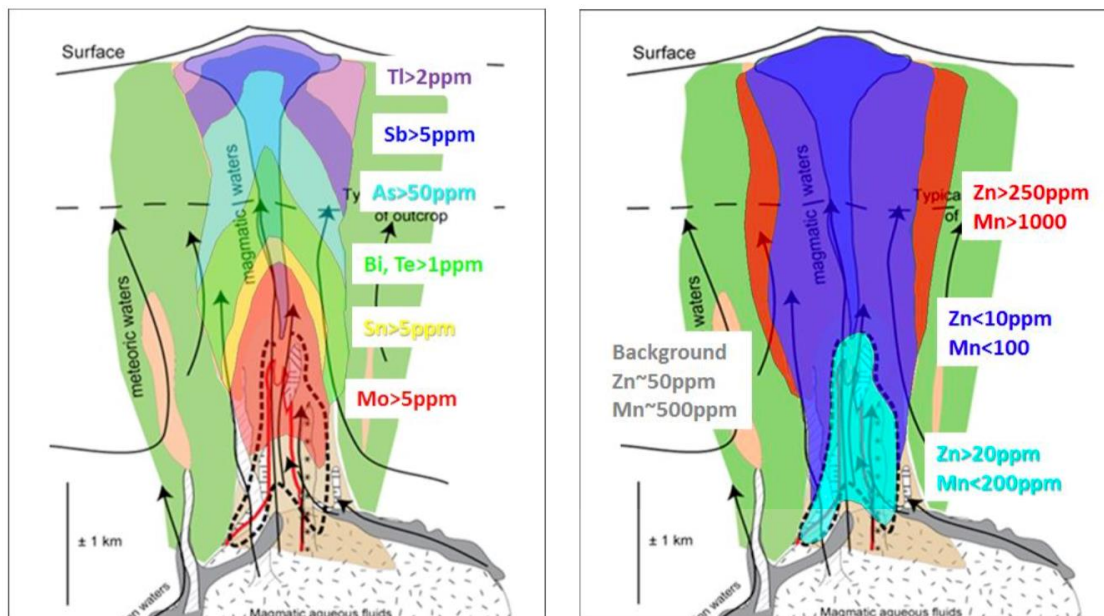


Figure 1.8. Expected pathfinder element concentrations in a porphyry system with **a)** showing vertical zonation of pathfinder elements; and **b)** horizontal zonation of pathfinder elements (Halley, 2016)

Te > 1 ppm; Bi > 1 ppm; Sb > 4 ppm and As > 50 ppm; Li > 15 ppm; and Ti 1.5 ppm (Halley *et al.*, 2015; Halley, 2016). The SWIR results were combined with petrographic, electron microprobe and LA-ICP-MS (laser ablation-inductively coupled plasma-mass spectrometry) analysis to reinforce the vertical zonation model up to 5 km depth.

1.5 Summary

The use of certain minerals as porphyry indicator minerals (PIMS) and porphyry vectors and fertility tools (PVFTS) in recent studies have proven to be highly effective. This has potential significant implications for commercial exploration; detecting porphyry-related propylitic alteration could be increased substantially to a distance of up to 5 km from the porphyry centre (Wilkinson *et al.*, 2017). As this area of using mineral geochemistry as a porphyry proximator is relatively young, the principle application is conducted through academia, and is not yet widely used by industry (Cooke *et al.*, 2017). Continued development and refinement of these methods, however, is likely to lead to the industrial acceptance of the use of this technology, and the investment of companies into commercial equipment to facilitate the application of these valuable techniques.

2 Structural Controls on Fluid Flow and Ore Deposit Formation

2.1 Controlling Factors on Fluid Flow

It is generally well accepted that hydrothermal fluid flow and magma transport are associated with crustal-scaled fracture network and therefore the regional stress field associated with a tectonic setting plays an important role in the facilitation and localisation of porphyry-related magmatism. Cu- and Mo-porphyry deposits are spatially and temporally associated with Mesozoic-Cenozoic orogens, in particular those currently active around the circum-Pacific (Sillitoe, 1972).

Although many studies have documented the intrinsic link between structural setting regionally and locally to economically important porphyry deposits (Berger & Drew, 2002; Berger *et al.*, 2008), some studies, such as Titley (1993) argue that there is not enough evidence to validate a clear correlation for porphyry deposits being structurally controlled. However, a robust piece of evidence for the connection is displayed by the spatial distribution of the porphyry deposits in the Andes (Camus & Dilles, 2001; Cembrano, 2014). The five prolific metallogenic belts of Chile and Peru are aligned along the margin between the obliquely subducting Nazca plate and the South American plate and the subsequent large, predominantly strike-slip fault complexes (Figure 2.1), such as the Domeyko Fault System in Northern Chile (Camus & Dilles, 2001; Masterman, 2003; Piquer *et al.*, 2016). The intersection between crustal first-order N-S trending structures, such as the Domekyo Fault System, and second-order NNW-SSE or third-order ENE-WSW transverse structures, appears to spatially coincide with the positioning of porphyry deposits (Lindsay *et al.*, 1995; Sillitoe, 2010; Cembrano, 2014). There is a direct link with economic deposits and areas of elevated permeability in narrow, structurally constrained areas (Berger *et al.*, 2008). An example of a structural mechanism adequate in concentrating porphyry-related magmatism is in regions of trans-tensional tectonics. In these settings oblique strike-slip displacement triggers the dilation of oblique-normal faults in a stepover fault system (Berger *et al.*, 2008).

Additional to the structural localisation, the occurrence of a porphyry deposit is subject to other crucial factors such as the enrichment and availability of metals in the subducting oceanic crust; a metal endowment of the subducting plate is thought to be a key contributor for the clustering of deposits in Southern Peru and southwestern USA (Sillitoe, 1972). Another factor for the global distribution of porphyries that should be considered is the erosion and uplift rate of the

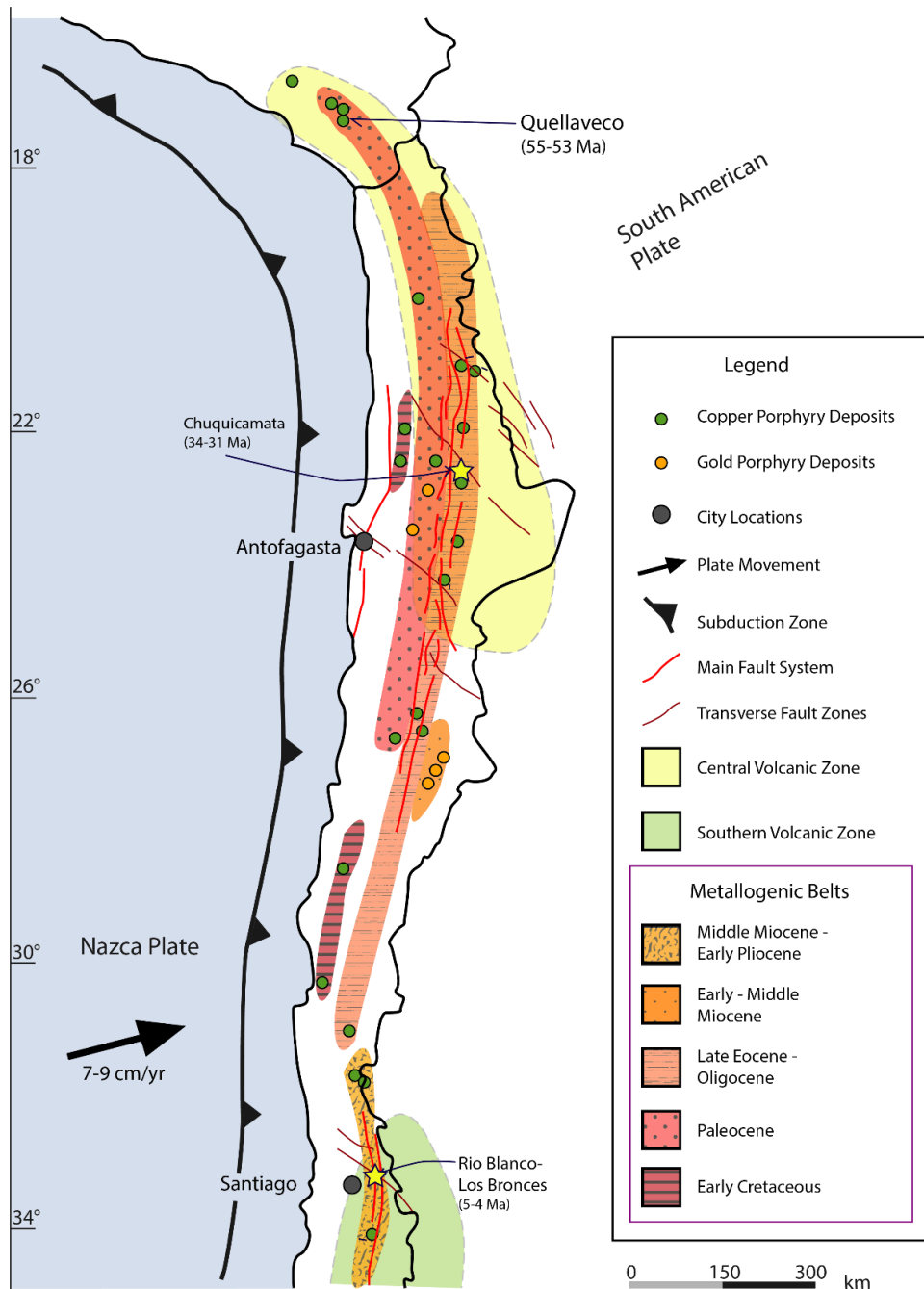


Figure 2.1 The South American metallogenic belts highlighting the location of Cu-rich and Au-rich porphyry deposits with respect to the major and transverse fault systems (figure after: Camus & Dilles, 2001; Elderry et al., 1996; Masterman, 2003; Ramos & Folguera, 2009; Spencer et al., 2015).

deposits. The shallow formation level, 1-3 km depth, along active margins favours younger deposits of Upper Cretaceous - Paleogene age, or younger (Sillitoe, 1972).

2.2 Syn-Tectonic Fluid Transport

2.2.1 Magma and Fluid Transportation

Magma through the brittle-ductile and brittle crust is predominantly thought to be transported via dykes, but in the lower, more ductile crust, it flows through plugs and diapirs. The regional and local stress field throughout the crust controls the amount, and method, of magma flow by means of the differential stress (Richards, 2003). The differential stress is defined by the difference between the maximum and minimum principle stresses (Fossen,

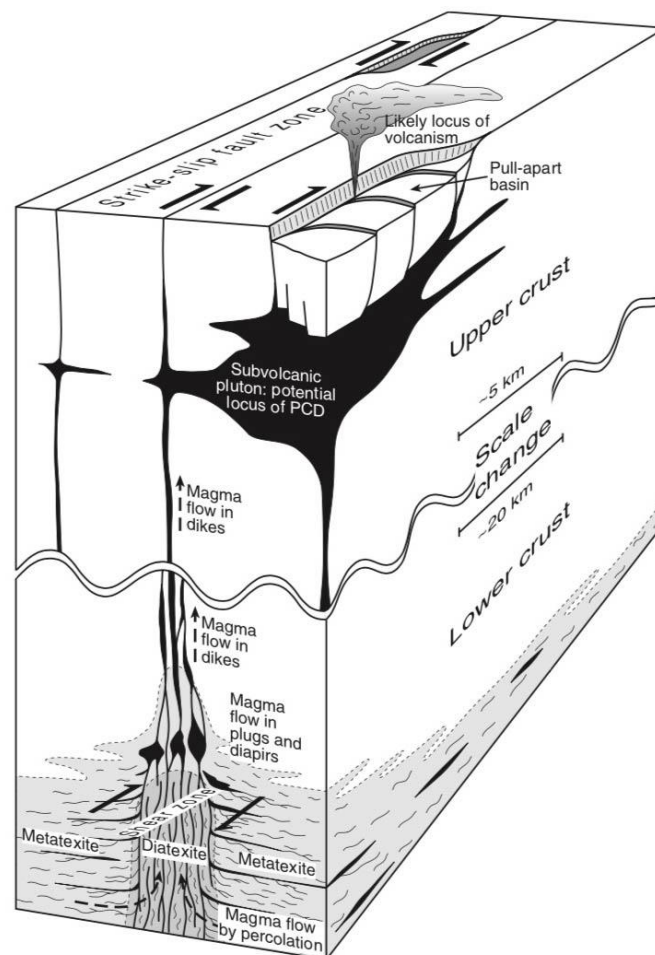


Figure 2.2. Diagram from Richards (2003) depicting the progression of magma through the crust. In the lower crust magma migrates by percolation, pooling in lenses and sills. In the upper crust, magma is facilitated by the formation of jog and step-over faults in a transtensional regime.

2010). At low differential stress, magma exerts a stress on the surrounding host rock leading to extensional fracturing and dyke formation. These 'magma-filled cracks' are normally orientated perpendicular to σ_3 , the minimum principle stress, and therefore in strike-slip settings, the minimum stress is horizontal so opening of the dykes, or veins, is generally vertical (Richards, 2003). On the other hand, at high differential stress, shear failure is induced (Davidson *et al.*, 1994). Fracturing facilitates the movement of fluids, which in turn is important for both the mechanical properties on the fault, and also the transportation and consequently the precipitation of minerals in the final stages of the Cu porphyry formation (Tosdal & Richards, 2001; Faulkner *et al.*, 2003).

Richards (2003) illustrates how magma in the lower region of the crust is transported via percolation under relatively low regional differential stress (Figure 2.2). The diagram shows how transtensional regimes favour magma movement, as the vertically orientated dykes and fracture pathways allow for the buoyant magma to rise more efficiently, pooling in areas of particular dilation, such as jogs, and step-over faults.

2.2.2 Permeability

Permeability in the form of fractures is a key factor in the transportation of fluids through the brittle upper crust, particularly in host rocks of little or no initial permeability (Fossen, 2016). Depending on the lithospheric depth, the brittle upper crust or ductile lower crust, the degree permeability varies of the surrounding host rock. There is, however, a notable decrease in permeability in the fault gouge and an increase in permeability in the fault damage zone (Wibberley & Shimamoto, 2003). In low-permeability zones, the fluid transport is dominantly fracture flow, therefore the flow rate is subject to the aperture of the fracture (Snow, 1968). The presence of hydrothermal alteration around porphyry intrusions is evidence in itself that the permeability through fracturing around these intrusions must be sufficient to allow the distribution of the altering fluids (John *et al.*, 2010).

The architecture of a fault dictates the amount, if any, of fluid flow possible and whether the fault will act as a conduit through the crust. The main fault components are the fault core, which may contain fault gouge, and the fracture damage zone. Factors such as temperature, confining pressure and lithology control which of these constituents of the fault structure are present (Fossen, 2016). The core of a fault is the area of highest strain, and displacement, and depending on the scale and displacement of the fault, sizes can vary from 1 mm – 1 m to over 10 m (Fossen, 2016). Within the core, the fine-grained, foliated, phyllosilicate-rich layer, often present, is termed fault gouge, with significantly low permeability (Faulkner *et al.*, 2003). A damage zone of a fault, shown in (Figure 2.3a), is the transitional zone between the fault and non-fractured rock, where the density of fractures significantly exceeds the host rock (Mitchell & Faulkner, 2009; Fossen, 2010). This zone can range from cm, to 100's m in thickness, but a positive correlation has been noted in the size of fault damage zone with increase in fault displacement (Fossen, 2016). Therefore, fluid flow is blocked by the fault gouge, but facilitated by the damage zone, due to the very low permeability of the fault core, but the high-density fracture network of the fault damage zone, (Faulkner *et al.*, 2003).

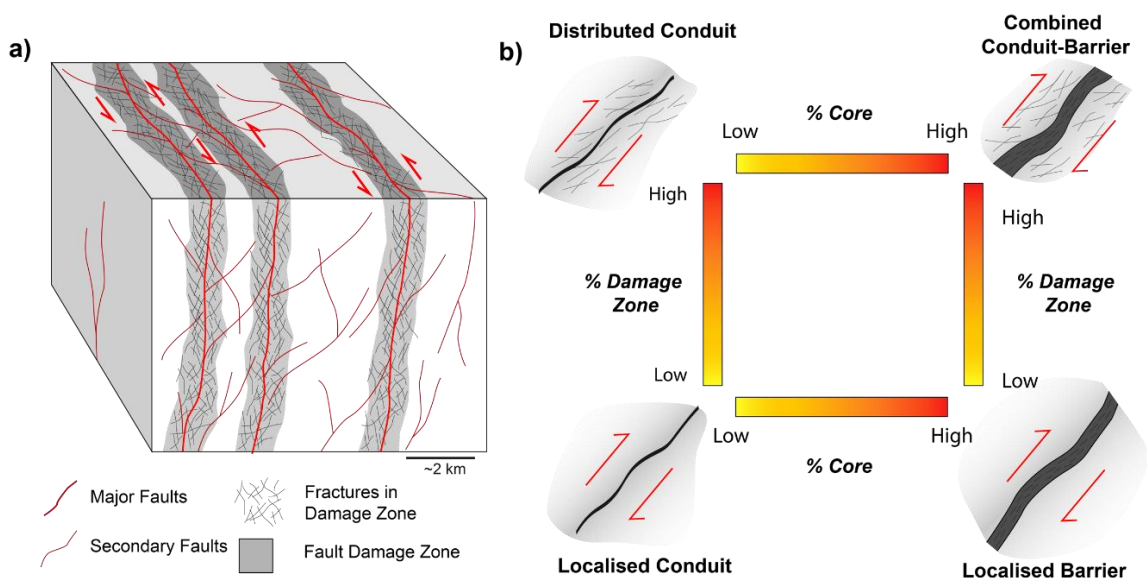


Figure 2.3. **a)** major and minor faulting with associated fault damage zone – the damage zone has a higher percentage fracture density than surrounding rock Faulkner *et al.* (2003); **b)** diagram adapted from Caine *et al.* (1996) showing the resultant fault and therefore fluid flow pathways associated with the increase and decrease of the percentage damage zone and core

Caine et al. (1996) presented four distinct types of fault based on percentage of gouge and damage: distributed conduit; localised conduit; localised barrier; and distributed barrier-conduit. Depending on the varying percentage of each, the fluid flow potential changes. Figure 2.3b demonstrates that the combined barrier-conduit with increased damage zone and fault gouge, and the localised conduit with minimal fault gouge but high damage zone area, create ideal conditions for the channelization of the fluids (Caine *et al.*, 1996). However, fluid can travel along, or pass through the gouge in areas where higher-permeability lenses of the host rock are included within the core (Faulkner *et al.*, 2003).

2.2.3 Seismicity

Strike-slip dilational duplexes act as vertical pipe-like conduits for fluids (discussed further in section 0), as shown in many areas associated with the San Andreas fault system. It is thought that mineral deposition is likely to occur in the top 1-2 km of these systems episodically, related to earthquake rupturing events (Sibson, 1987).

Fracturing of the rock during faulting or a seismic event increases the permeability around the fault, in the damage zone, which allows fluid movement and mineral precipitation as veining (Sibson *et al.*, 1988). Fluid transport in a porphyry system occurs in two principle ways. One way is fluid movement occurring concurrently with earthquake rupture, either instigated by tectonic stresses or fluid pressures along pre-existing fracture, or a combination of both, such as the first stage of mineralisation at the Rosario mine in Collahuasi (Sibson *et al.*, 1988; Masterman, 2003). In areas of particularly low-permeability host rocks, a sudden build-up of fluid pressure, usually following a seismic event, can exert an extreme pressure on the permeable pathways, thereby triggering reactivation of pre-existing faults to accommodate this increased fluid pressure (Sibson, 2001). If there is a build-up in lithostatic fluid pressure, and no alternate pre-existing fractures to manipulate, hydrofracturing can occur. This essentially lowers the pressure by fracturing the rock and creating space to accommodate fluids; this sudden descent in fluid pressure initiates the precipitation of mineralisation (Sibson *et al.*, 1988).

Fluid transport occurs cogenetically with large-scale fault movement, with an emphasis on fluid distribution during aftershock period (Sibson, 2001). The process of brittle failure has two direct, and conflicting, effects on the structural permeability of the system. Synchronously with the earthquake rupture, there is generally an increase in permeability, however this is offset by the hydrothermal cementation of fractures in the low-permeability gouge zones (Sibson, 2001). Following the rupture, the fault undergoes a self-healing phase in which the permeability drops, thereby causing a build-up of pressure and shear stress, and a repeat of the cycle (Sibson *et al.*, 1988).

The orientation of the fault relative to the tectonic regime controls the location of the areas of dilation. If the principle direction of maximum stress is oblique to the fault or fracture, it is termed unfavourable (Piquer *et al.*, 2015). Areas with a predominantly transpressional regime form pull-apart basins, with normal-oblique faulting (Richards *et al.*, 2001; Cembrano *et al.*, 2005).

2.2.4 Key Transtensional Structural Features

Strike-slip movement occurs in a range of tectonic boundary settings in response to collision and extension, and can act as a transfer of energy between two obliquely situated fault systems (Cunningham & Mann, 2007). If the convergence obliquity of the converging plates is high, the internal deformation in the crust is partitioned into domains of varying strain (McCaffrey, 1992). The anisotropic nature of the crust allows for the strain partitioning to be conveyed along ancient and newly formed structures by means of strike-slip and thrust fault deformation (Tikoff & Teyssier, 1994).

Figure 2.5 depicts some of the key structures associated with strike-slip kinematics and the resultant straining and releasing bends. The terms 'bends' and 'stepovers' are often used interchangeably as a bend defines a continuously linked fault which is curved to accommodate the offset, and a stepover delineates the offset-induced rhombic shape between two distinct faults (Cunningham & Mann, 2007).

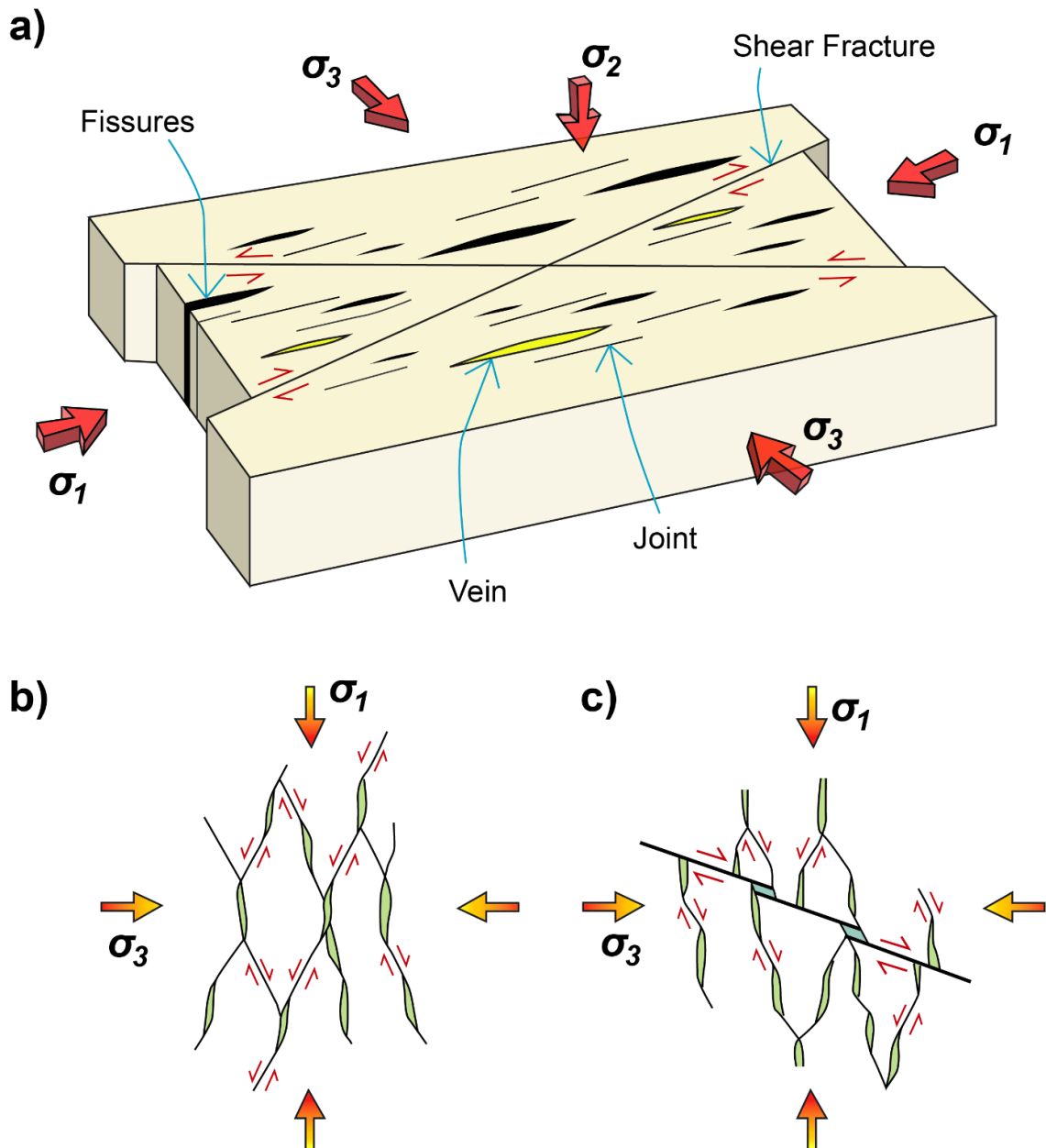


Figure 2.4. Diagrams adapted from Fossen (2016) and Sibson (2001). **a)** block model of expected faulting and dilation in the Andersonian stress regime; **b-c)** simplified fault-fracture meshes in an extensional regime: **b)** areas of dilation and strike-slip faulting in relation to the orientation of σ_1 and σ_3 ; **c)** displaying the same stress orientation as **(b)**, but with the presence of an unfavorably aligned pre-existing fault structure.

2.3 Porphyry Copper in South America

For many decades, South America has been the leading producer of copper from its wealth of porphyry copper deposits. Several factors contribute to the magnitude of deposits, but one of the most significant is South America's complex tectonic history. In the Late Jurassic period, the formation of the current Andean cycle framework began following the early stages super-continental break-up (Coira *et al.*, 1982). Since that time, the Andean Cordillera has experienced periods of transpression and transtension related to the varied obliquity of the subducting Nazca plate beneath the South America plate (Cembrano & Lara, 2009). The variation in angle and rate of the relative movement of the Nazca plate has significantly influenced South America's regional and local tectonics. These differences have here been temporally categorised into five phases: Late Triassic-Late Jurassic; Early-Late Cretaceous; Palaeocene-Late Eocene; Late Eocene-Early Oligocene; and Late-Miocene- Early Pliocene.

2.3.1 Metallogeny of South America

Porphyry ore deposits tend to form in arc-parallel clusters or belts, and in South America these deposits are located from central coastal Peru to central Chile (Figure 2.6). More than half of the world's 25 largest known

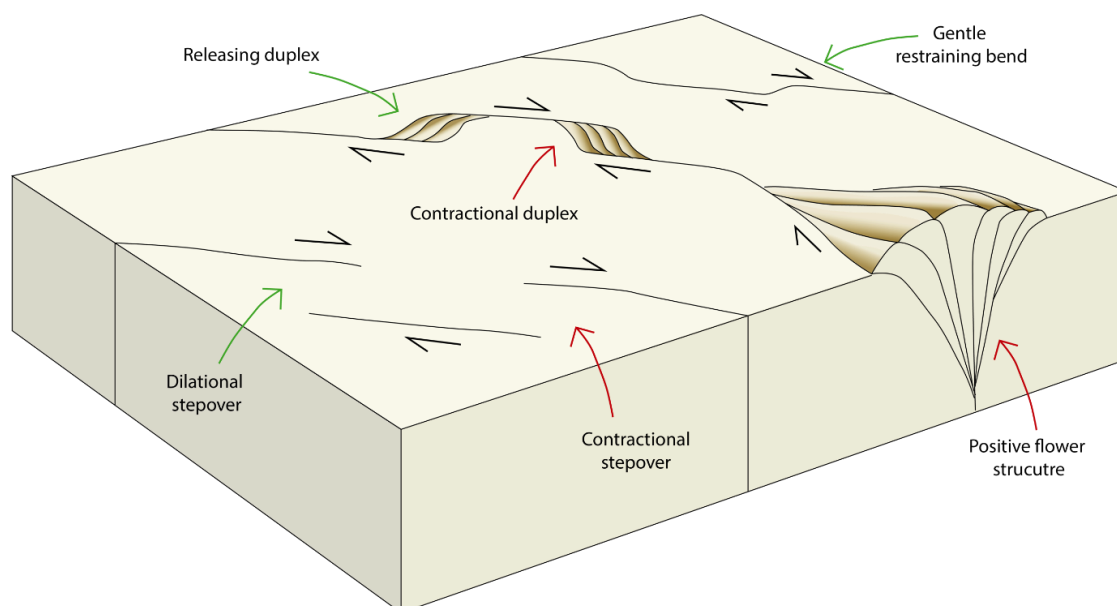
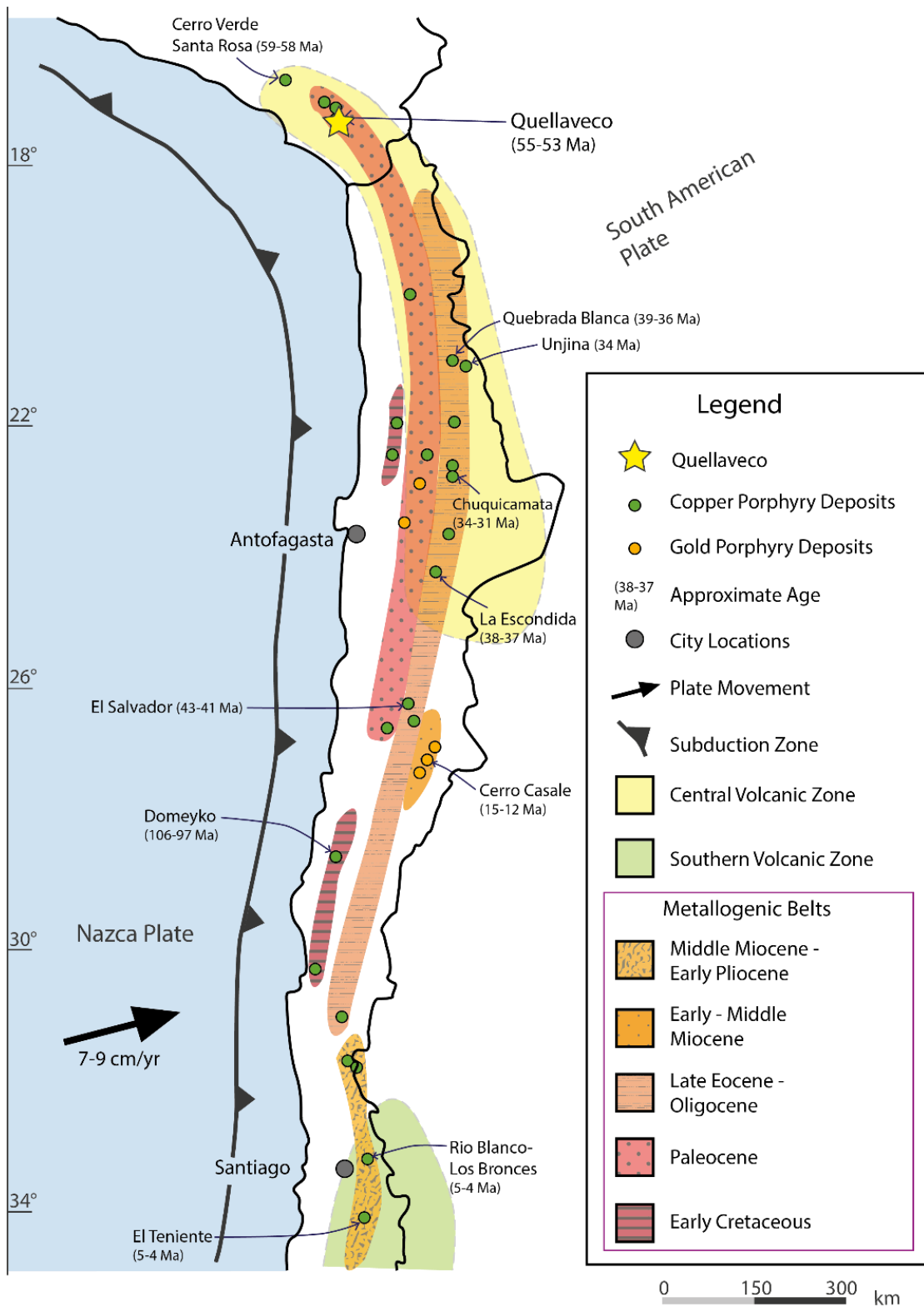


Figure 2.5. Common structures that form as a result of transtensional and transpressional tectonics. Adapted from Cunningham and Mann (2007).

porphyry copper deposits occur in this zone of South America (Cooke *et al.*, 2005). These deposits formed during five, temporally discrete phases of mineralisation: Early Cretaceous; Palaeocene; Late Eocene-Oligocene; Early Miocene-Middle Miocene; and Middle Miocene-Early Pliocene (Camus & Dilles, 2001). One contributing factor to the fertility of these belts is thought to be the angle of the subducting plate at the time of mineralisation (Camus & Dilles, 2001). Deep, slower, typically 'Marianas-type' subduction, produced unfavourable conditions for mineralised porphyry generation, for example from the Triassic to Early Cretaceous. Conversely, shallow, faster, 'Chilean-type' subduction resulted in the formation of the metallogenic belts (Camus & Dilles, 2001). Quellaveco is situated at the northern tip of the prolific Paleocene metallogenic belt (Sillitoe, 2008).

2.3.2 *Volcanism*

Throughout the tectonic framework described above, the Andes has experienced a relatively varied volcanism. Although periods of regional extension and transpression are thought most favourable for magma transport, even in a compressional regime, there are areas of local extension or transpression (Acocella & Funicello, 2010). Work by Tibaldi, (2005) discussed how even in compressional settings, the vertical migration of magma is possible, and when sourced by high production magma chambers, can reach the surface in thicker crustal sections. However, it is important to note that magmas formed under transport through a compressional or transpressional regime are compositionally different to those in extensional or transtensional regimes. The crustal compression and transtension is likely to produce more evolved and differentiated magmas, while less differentiated and evolved magmas are expected in a transtension or extension (Cembrano & Lara, 2009).



3 Methodology and background

In order to cover the scope of the data acquisition in this project, the methodology section is broken down into three key components: structural and field data collection methods and structural processing; the fundamentals of U-Pb geochronology; and the analytical process for the U-Pb geochronology and propylitic whole rock and trace element chemistry.

3.1 Structural data acquisition

3.1.1 Structural transects and sampling

Ensuring the systematic and reliable acquisition of data from the field is one of the most important aspects of the project. As the project primarily focuses on the potential impact that the major NW-SE structures play in the distribution of fluids, two transects (~25 km each) were designed accordingly and orientated perpendicular to the principal faults. The rationale for the NE-SW transects is that, if present, the fault-normal angle will enable detection of any lateral dispersion of fluids away from the

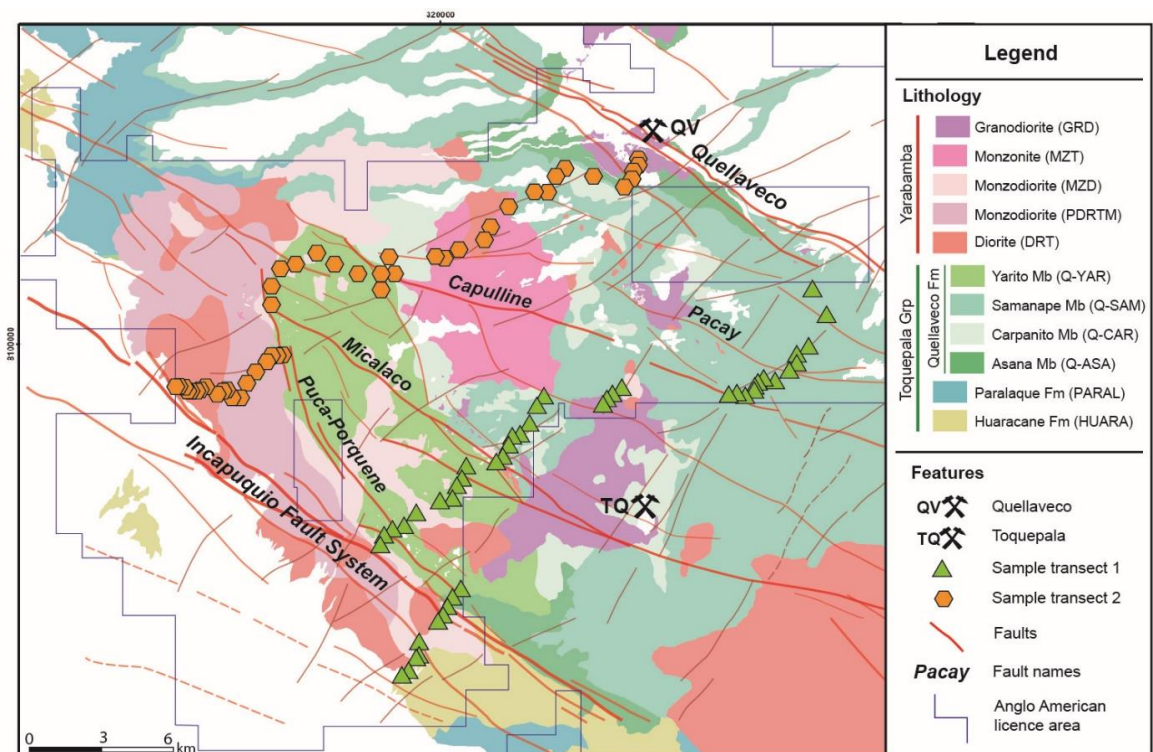


Figure 3.1 Sampling map of the study area showing the two transect lines (section 1 and 2) orientated perpendicular to the major NW-SE structures.

controlling faults. Two modes of data collection were deployed along these transects: structural mapping and systematic sampling.

A total of 107 samples were collected over the two transects, with the samples halved into approximately 1-1.5 kg for whole rock analysis, and a smaller hand specimen used for mineral chemistry and geochronological analysis in the Natural History Museum's LODE laboratory. When relevant, the hand specimens were structurally orientated so any vein data could be structurally analysed at a later time.

3.1.2 Field mapping

A fundamental part of this project is the collection of structural and kinematic data. This includes: orientation; dip and kinematic data from faults; fractures; original bedding; veining; and shear zones including, where necessary, their length, spacing and aperture. These detailed observations and measurements are vital for providing the structural context for the dated and geochemically analysed samples. Alongside the structural and kinematic readings, cross-cutting relationships were recorded in relation to the alteration and mineral assemblages present. On arrival at each outcrop area, the following data was recorded: description of the nature and extent of exposure(s); description of mineral assemblages/lithologies; description of structures present; recording of structural measurements of faults, lineations and any other kinematic indicators, folds and fracture intensity; and observation and recording (sketch, photograph) of relationships between structures, veining, alteration, etc.

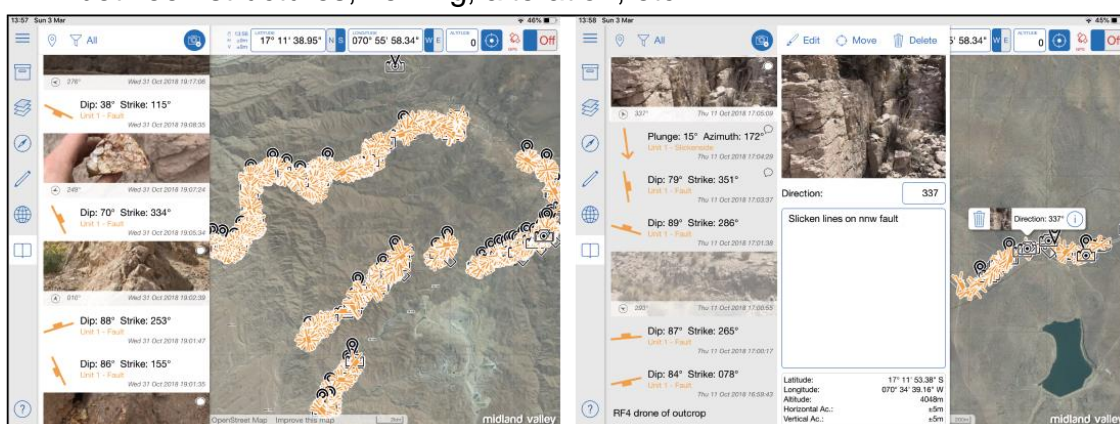


Figure 3.2. Screenshots from the iPad Pro showing the layout of the MOVE application. Individual structural measurements, observations and photos are shown down the left-hand side, and geographic positioning displayed on the map.

Traditionally, field mapping such as this is recorded on a field notebook using a compass-clino and pen. Although this is still a valuable tool for recording data, for this project the data was acquired digitally using an iPad Pro with Midland Valley FieldMove mapping application. This allowed detailed structural mapping, and the accurate recording of the structural measurements and kinematic relationships collected. There are many benefits for employing this approach with the key advantages being: significantly improved accuracy of all readings; clearly represented data which can be easily edited over successive field visits; data that can be easily transferred into different formats and software such as MOVE and Google Earth; and the time saved from computerising the field data.

Using this method, 2345 structural measurements were collected and recorded (Figure 3.2) with corresponding figures and observations.

3.1.3 Drone Mapping for 3D modelling

Rationale for Drone Usage

Unmanned aerial vehicles (UAV), or drones, have become an inexpensive and practical method for geological data collection. Eisenbeiss (2009) first defined this method as UAV photogrammetry implying the remote-controlled, or autonomous technique of acquiring geo-referenced images for geological processing. There are significant benefits for using a drone in geological fieldwork, including: user access to imagery and data from areas that would not otherwise be accessible (i.e. tall mountains, over valleys of rivers); autonomous flights conducted without input from the flyer; and the ability to collect data at different scales, from larger field area to high-resolution outcrop areas. The significant increase of drone technology over the last decade, in conjunction with a decrease in drone price, has resulted in this technology becoming more accessible for research.

Drone technologies can capture imagery on a variety of scales from centimetre resolution to much larger, regional-scale mapping for hyperspectral remote imaging to provide photogeologic evidence of

alteration-structural interactions on a much broader scale (10's km). This project will particularly apply drones to acquire outcrop-scale high-resolution geo-located imagery for the creation of 3D digital elevation models (DEM), before detailed fault and fracture mapping. This will provide a detailed 3D structural map of key (and inaccessible) areas where fault and hydrothermal alteration relationships are particularly prominent. This cutting-edge technique is currently revolutionising fracture/fault orientation analysis in structural geology, and is new to mine/exploration studies.

In the Field

A DJI Mavic Pro drone was used to map several key areas in the field (i.e. areas that with particularly good exposure and clear structural relationships and fault-trend intersections). A 3D structural map will be created from these drone images, thereby allowing high resolution fracture/fault orientation analysis to be done on key representative areas of the Quellaveco region. Each drone flight is approximately 20 mins and allows coverage of ~100 m² in high-resolution.

Data Processing and Analysis

Once the geo-located imagery has been collected in the field, the imagery is processed in Agisoft Photoscan (Figure 3.3). This highly advanced software locates the images in 3D-space to produce a high-resolution dense cloud. From this, a 3D tiled model and digital elevation model (DEM) is generated. To optimise the use of this data, an orthomosaic of the images is created. This is a 2D image that is an amalgamation of the images from the view of maximum extent, therefore often from satellite view.

For the major structural analysis on the selected areas, the DEM is inputted into Midland Valley's MOVE software, and the orthomosaic overlaid, creating a high-resolution 3D model of the desired area. From here, faults and fractures outcropping lineations can be

inferred and their structural measurements approximately measured in 3D. As with the field-collected MOVE data, once the drone-created model has been structurally mapped, stereonet of fault trends can be generated.

Additionally, the DEM that is created by the drone will act as a base layer for a compilation of the structural and geochemical data, and also as an interpretive model of the key faults in the Quellaveco region.

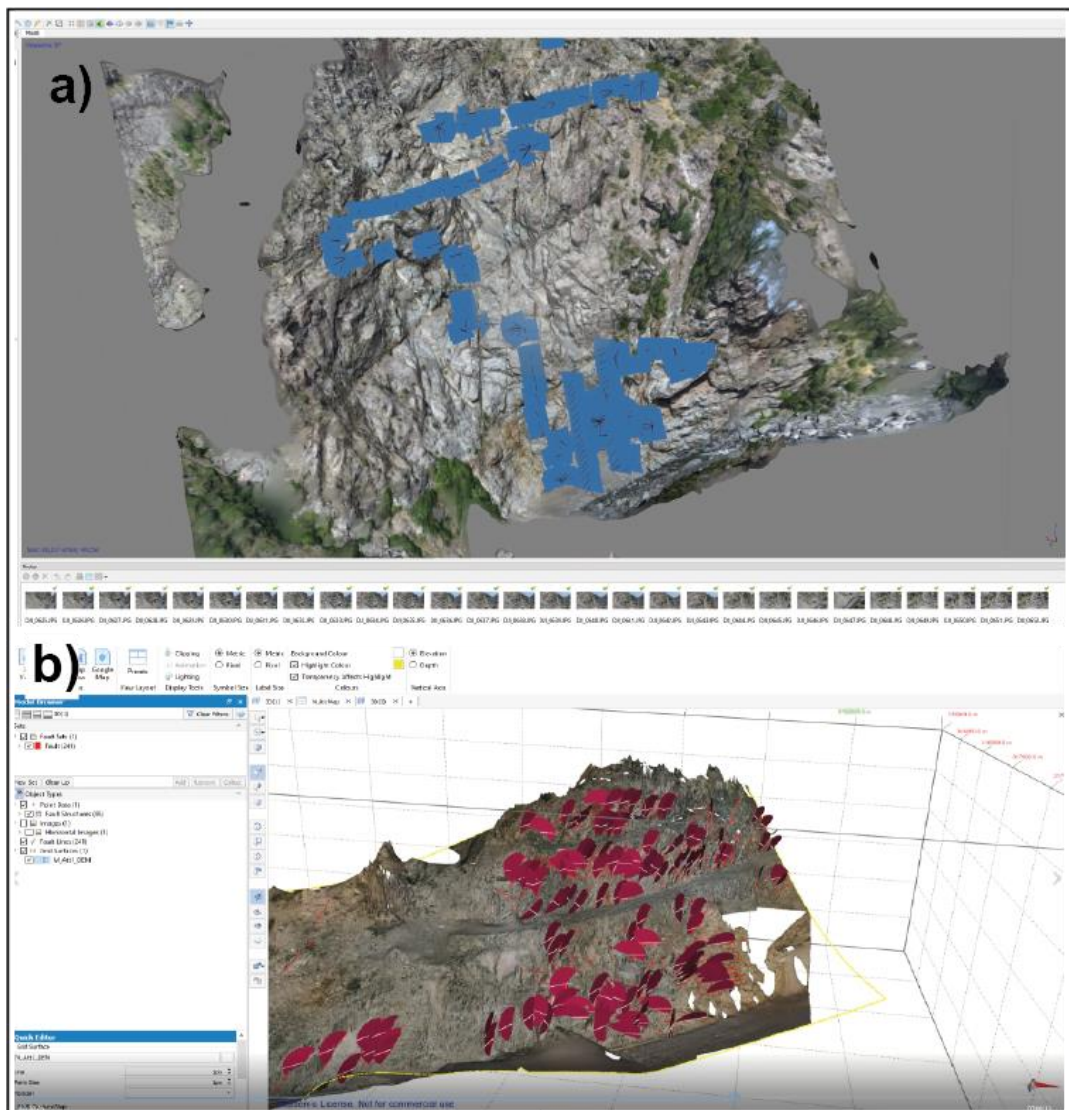


Figure 3.3. Screenshots showing: **a)** the creation of a 3D model of a structurally complex area using drone imagery in Agisoft Photoscan (the positioning of the drone images are shown in blue); **b)** the Dem and orthomosaic exported into MOVE for structural analysis (the red circular planes indication 3D fault planes),

3.2 Basic principles of radiometric dating

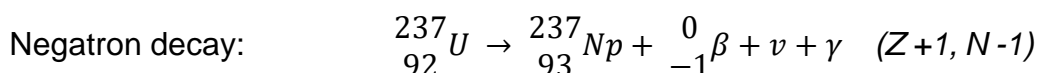
3.2.1 Radioactivity

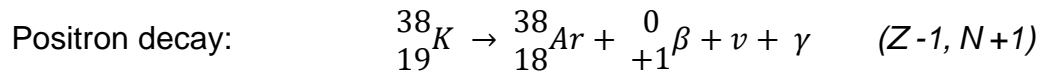
Atoms, which are the building blocks of minerals, contain a nucleus composed of neutrons and protons, surrounded by an electron cloud. A nuclide is a term for an atom, and stable nuclides describes nuclides which do not undergo spontaneous radioactive decay. Radionuclides are unstable and form when there is an imbalance of neutrons to protons (higher or low ratios), causing the nuclide to disintegrate by one of three mechanisms: α decay; β decay, electron capture and nuclear fission.

- α -decay: A process that occurs when the nucleus of an atom is too large, and therefore emits an ' α -particle' which is the equivalent of a helium nucleus (two protons and two neutrons) from the atomic nucleus. In order for the nuclide to emit the α particle, a substantial energy barrier must be reached (White, 2015; Albarède, 2009). The following equation is an example of alpha decay of ^{238}U :



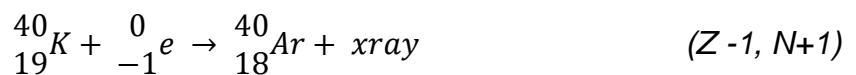
As the α -particle is released, the atomic number of the U decreases by two, thereby yielding the daughter nucleus ^{232}Th . A small amount of mass is converted to kinetic energy of the α -particle and daughter nucleus, which is emitted as γ radiation (White, 2015; Vermeesch, 2018). When the sum of the daughter nuclide and α particle masses are less than that of the parent nuclide, α -decay can occur (Albarède, 2009) β -decay: There are two types of β -decay, negatron (β^-) and positron (β^+). Negatron decay occurs when the nucleus of an unstable atom has a high proton/neutron ratio (Albarède, 2009). Positron decay involves releasing a positron. A positron equals an electron in mass, but is defined by its positive charge. It is uncommon for this decay type to occur naturally (Albarède, 2009). The following are examples of negatron and positron decay:





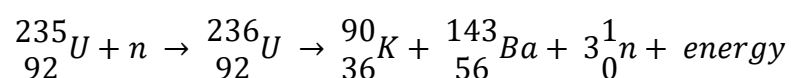
The mass number remains the same from the parent to daughter nuclides as, for negatron a neutron is replaced by a proton and for positron a proton changes to a neutron, thereby the mass change equals 0. γ -radiation is a product of β -decay and is generated by two sources: the excited parent nucleus relaxing; or in β^+ decay, the spontaneous obliteration of an unstable positron (Vermeesch, 2018). β^- is the most common type and is particularly useful for ${}^{87}\text{Rb}$ - ${}^{87}\text{Sr}$, ${}^{40}\text{K}$ - ${}^{40}\text{Ca}$; and β^+ is mostly important in the ${}^{40}\text{K}$ - ${}^{40}\text{Ar}$ system.

- Electron capture: This type of decay often occurs in tandem with positron decay, where an atomic nucleus contains a higher proportion of protons causing instability. An electron is added to the nucleus, thereby causing a mass decrease between the parent and daughter nuclides. This excess mass is removed by a neutrino and dispersed as energy (White, 2015).



As a proton becomes a neutron the atomic mass decreases by 1, but the mass remains the same. Following this, the daughter nucleus is left in an excited state, and rapidly returns to its ground state while emitting γ -radiation. The rearrangement of electrons between the shells also produced electromagnetic energy, and X-rays from electrons in the inner orbits. Electron capture is the dominant decay mechanism for ${}^{40}\text{K}$ - ${}^{40}\text{Ar}$ (White, 2015; Vermeesch, 2018)

- Nuclear fission: This occurs when a heavy, highly unstable nuclei splits into two daughter nuclei of unequal sizes. This process generates vast amounts of energy (~200 MeV), and often the daughter isotopes are as unstable, or more unstable, than the parent isotope. ${}^{235}\text{U}$ is the only naturally occurring nuclide to decay in this way; other nuclides can be fissile, but only in laboratory conditions.



Radioactive decay is independent of time and external factors such as temperature, pressure and chemical bonding of atoms – it is these

characteristics that make radioactive decay such an important chronometer (Albarède, 2009; White, 2015).

3.2.2 Age Equations

The decay rate is dependent on the energy state of the particular nuclide particles and how much of the radioactive parent atom is present (N_P). The transition from a metastable state to the stable radiogenic daughter (D) can take between 10^{-14} seconds to 10^{11} years (Schoene, 2014; White, 2015). The probability that radioactive disintegration will take place per unit time is denoted as the decay constant, λ , with units of time^{-1} . Each radioactive nuclide has a unique decay constant which controls its probability of decay. However, as this is a decay *constant*, the value remains the same irrespective of space and time. Determining the decay constant involves counting the number of energetic particles released over a period of time. This can prove difficult however, as some radioactive isotopes have such extensive half-lives, that the rate of change over the period allocated can be infinitesimal. Therefore 'geologically determined' decay constants are yielded by comparing the ages with the decay constant of a better-known radiometric system (Reiners *et al.*, 2018). The basic equation for radioactive decay is as follows:

$$\frac{dN_P}{dt} = -\lambda N_P \quad (3.1)$$

where t is time, N_P is the number of parent atoms and λ is the decay constant. A half-life is the time taken for half of the radioactive parent nuclide to experience decay to the daughter isotope. Integrating equation (1.1) with time, produces equation (1.2) which shows the number of parent isotopes at a given time as a function of the number of parent isotopes present at crystallisation (Hodges, 2014):

$$N_P = (N_P)_0 e^{-\lambda t} \quad (3.2)$$

where N_P is the number of parent isotopes present and the amount of parent isotopes at $t = 0$ is written as $(N_P)_0$. Therefore, where $(N_P)_0$ is the number of parent atoms at $t = 0$, the half-life can be expressed as: $N_P/(N_P)_0 = 0.5$, or $T_{1/2}$. The half-life and decay constant can be arranged into:

$$T_{\frac{1}{2}} = \frac{\ln(2)}{\lambda} \quad (3.3)$$

Simplified, the amount of daughter isotope produced by radioactive decay can be denoted as:

$$N_D = (N_P)_0 - N_P \quad (3.4)$$

where the number of atoms of daughter isotope (N_D) produced following radioactive decay, is the difference between the number of parent atoms at $t = 0$ by the radioactive parent atom present at a later time (Hodges, 2014; Vermeesch, 2018). When equation (1.2) is rearranged as a function of $(N_P)_0$ and combined with equation (1.4) with respect to each other, it becomes:

$$N_D = N_P(e^{\lambda t} - 1) \quad (3.5)$$

However, some of the daughter isotope may not have been a product of the parent decay, and instead, trapped during crystallisation. Therefore, the total number of daughter isotopes at time t (N_D), must include the sum of the radiogenic isotopes *and* the non-radiogenic daughter isotope $(N_D)_0$ (Hodges, 2014):

$$N_D = (N_D)_0 + N_P(e^{\lambda t} - 1) \quad (3.6)$$

When written as a function of time, it becomes one of the most fundamental equations, which acts as the base for many other geochronological methods (Vermeesch, 2018; Hodges, 2014):

$$t = \frac{1}{\lambda} \ln \left(\frac{N_D - (N_D)_0}{N_P} + 1 \right) \quad (3.7)$$

This age equation can only be used when: the abundance of N_D is a measurable; a reasonable value can be assumed for $(N_D)_0$; and that since the time of crystallisation, the system has remained closed with no loss or gain of the daughter or parent isotopes (Schoene, 2014). In many cases the daughter element has more than one stable isotope which is advantageous as there is much greater precision in measuring isotopic ratios, than the alternative of absolute isotopic abundances. Therefore, the equation (1.6)

can then be normalised to one of the stable daughter isotopes, if present, by dividing through the non-radiogenic (or stable) isotope (Schoene, 2014; Reiners *et al.*, 2018):

$$\frac{N_D}{N_d} = \left(\frac{N_D}{N_d}\right)_0 + \frac{N_P}{N_d}(e^{\lambda t} - 1) \quad (3.8)$$

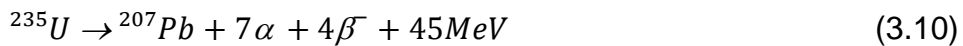
where the normalising stable isotope denoted N_d , and N_P is the radioactive parent.

3.2.3 The U-Pb-Th decay system

U-Pb dating is one of the oldest known methods of radiometric dating; Bertram Boltwood, in 1907, used his understanding of the U decay rate to measure the proportions of U and Pb in minerals. Using U-rich minerals, Boltwood calculated the Earth to be 2.2 billion years, which greatly surpassed any estimate at the time (Davis *et al.*, 2003; White, 2015). In the 1960s, mass spectrometers were first used to record geochronological dates, and since then the amount of mineral required has significantly decreased, whilst the precision has significantly increased (Schoene, 2014).

U-(Th-)Pb Dating

The U-Th-Pb decay system is one of the most powerful and robust geochronological tools because it involves three decay schemes which all produce isotopes of Pb. Pb has four naturally occurring isotopes: ^{204}Pb , ^{206}Pb , ^{207}Pb , and ^{208}Pb . In the U-Pb system, the decay of the two parent nuclides, ^{235}U and ^{238}U to daughter isotopes ^{206}Pb and ^{207}Pb is particularly valuable because both parent and daughters are chemically identical. The combination of these results can be cross-calibrated to ensure the fidelity of the age calculated (White, 2015). The decay occurs through a sequence of α and β decays:



to form various intermediate daughter isotopes but always results in the same stable daughter element, Pb (Table 3.1). The half-lives of ^{238}U and ^{235}U are approximately 4.5 Ga and 0.7 Ga respectively (Elliot, 2014). The string of intermediate daughters have shorter half-lives than their initial parent spanning from 245,000 years to less than a second, each with a shorter half-life than the previous (Figure 3.4). Secular disequilibrium makes it difficult to calculate the U-Pb and Th-Pb's numerous intermediate daughter isotopes and long decay chains (Schoene, 2014).

Secular disequilibrium occurs when the decay rate is equal to the production rate of the intermediate daughter isotope (Reiners *et al.*, 2018). This can be written as:

$$N_1\lambda_1 = N_2\lambda_2 = N_3\lambda_3 \dots \quad (3.12)$$

where the moles of the parent isotope 1 are referred to as N_1 and λ_1 is the decay constant of that isotope. For a system out of secular equilibrium to return to secular equilibrium, time proportional to the longest-lived intermediate daughter half-life must have passed (Reiners *et al.*, 2018; Schoene, 2014).

Parent	Decay Mode	λ	Half-life	Daughter	Ratio
^{235}U	α, β	$9.8571 \times 10^{-11} \text{y}^{-1}$	$7.07 \times 10^8 \text{y}$	$^{207}\text{Pb}, 7 \text{ } ^4\text{He}$	$^{207}\text{Pb}/^{204}\text{Pb}$
^{238}U	α, β	$1.55125 \times 10^{-11} \text{y}^{-1}$	$4.47 \times 10^9 \text{y}$	$^{206}\text{Pb}, 8 \text{ } ^4\text{He}$	$^{206}\text{Pb}/^{204}\text{Pb}$
^{232}Th	α, β	$4.948 \times 10^{-11} \text{y}^{-1}$	$1.4 \times 10^{10} \text{y}$	$^{208}\text{Pb}, 6 \text{ } ^4\text{He}$	$^{208}\text{Pb}/^{204}\text{Pb}$

Table 3.1. The U-Th-Pb system parameters; after White (2015).

Although the intermediate daughters are generally disregarded for dating, in some cases they can be useful. For example: using the intermediate daughters with longer half-lives (of days to hundreds of thousands of years) to provide useful information particularly for measuring recent geological events; if a recrystallisation event causes isotopic disequilibrium, the shorter timescale of the intermediate parent and daughter ratios can be used to date this event (Dickin, 2005; Schoene, 2014; White, 2015; Vermeesch, 2018).

The U-(Th-)Pb and Pb-Pb Methods

U-(Th-)Pb has three decay systems, with separate equations used for each system. For time dependent equations, known as isochron equations, a stable isotope is applied to normalise the equation for common Pb. As ^{204}Pb is the only nonradiogenic, stable isotope of Pb, it is used to normalise the method. To do this, equation 1.8 (section 3.2.2) is written to include the radioactive parents and

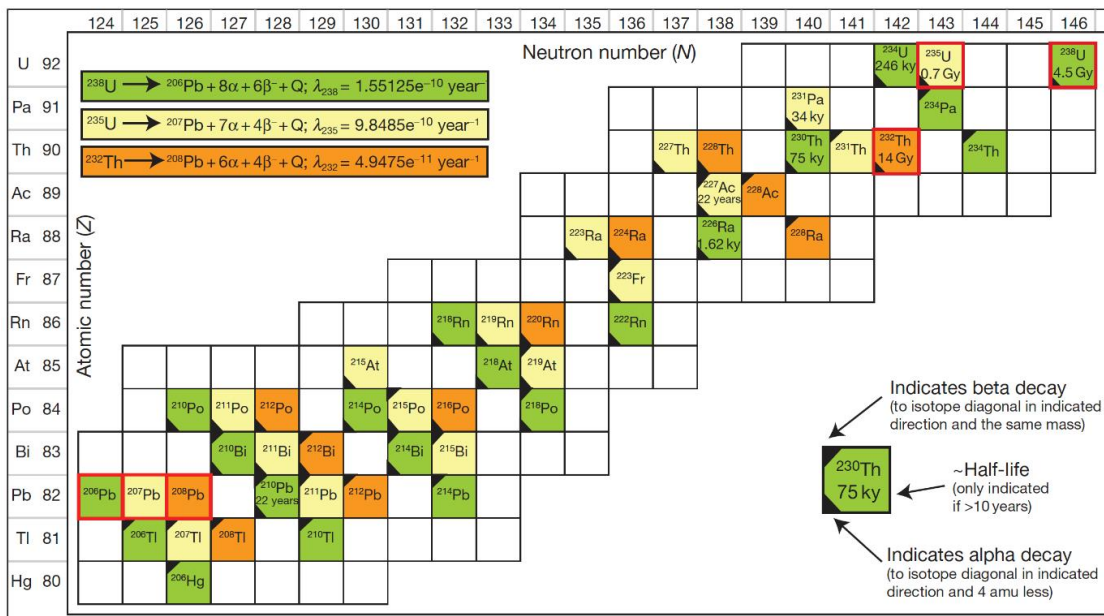


Figure 3.4. A diagram from Schoene (2014) depicting the decay chains of U and Th, to their intermediate daughter isotopes (only shown those with a half-life greater than 10 years). The parent and stable daughter isotopes are highlighted in red. The decay series are colour-coded: ^{238}U in green; ^{235}U in yellow; and ^{232}Th in orange.

radiogenic daughter isotopes of the U-Th-Pb systems, divided by the nonradiogenic ^{204}Pb isotope:

$$\left(\frac{^{206}\text{Pb}}{^{204}\text{Pb}}\right) = \left(\frac{^{206}\text{Pb}}{^{204}\text{Pb}}\right)_0 + \left(\frac{^{238}\text{U}}{^{204}\text{Pb}}\right) (e^{\lambda_{238}t} - 1) \quad (3.13)$$

$$\left(\frac{^{207}\text{Pb}}{^{204}\text{Pb}}\right) = \left(\frac{^{207}\text{Pb}}{^{204}\text{Pb}}\right)_0 + \left(\frac{^{235}\text{U}}{^{204}\text{Pb}}\right) (e^{\lambda_{235}t} - 1) \quad (3.14)$$

$$\left(\frac{^{208}\text{Pb}}{^{204}\text{Pb}}\right) = \left(\frac{^{208}\text{Pb}}{^{204}\text{Pb}}\right)_0 + \left(\frac{^{232}\text{Th}}{^{204}\text{Pb}}\right) (e^{\lambda_{232}t} - 1) \quad (3.15)$$

where $(^x\text{Pb}/^{204}\text{Pb})_0$ represents the component of common Pb at $t = 0$ for isotope 'x', with the assumption that there was secular equilibrium at the system closure (Schoene, 2014; Vermeesch, 2018).

Some minerals, such as zircon, tend not to have assimilated common Pb (Pb_c) at the time of mineral crystallisation (Vermeesch, 2018). When this is the case, and Pb_c is negligible, there is little need to normalise to nonradiogenic ^{204}Pb and equations 1.13, 1.14 and 1.15 and can be simplified to:

$$\left(\frac{^{206}\text{Pb}^*}{^{238}\text{U}}\right) (e^{\lambda_{238}t} - 1) \quad (3.16)$$

$$\left(\frac{^{207}\text{Pb}^*}{^{235}\text{U}}\right) (e^{\lambda_{235}t} - 1) \quad (3.17)$$

$$\left(\frac{^{208}\text{Pb}^*}{^{232}\text{Th}}\right) (e^{\lambda_{232}t} - 1) \quad (3.18)$$

There is a fourth method, known as the $^{207}\text{Pb}/^{206}\text{Pb}$ method, which is based on the same radioactive decay scheme as U-Pb. The equation can be calculated by dividing the two end members from equations 1.14 by 1.13:

$$\frac{\left(\frac{^{207}\text{Pb}}{^{204}\text{Pb}}\right) - \left(\frac{^{207}\text{Pb}}{^{204}\text{Pb}}\right)_0}{\left(\frac{^{206}\text{Pb}}{^{204}\text{Pb}}\right) - \left(\frac{^{206}\text{Pb}}{^{204}\text{Pb}}\right)_0} = \left(\frac{^{235}\text{U}}{^{238}\text{U}}\right) \frac{(e^{\lambda_{235}t} - 1)}{(e^{\lambda_{238}t} - 1)} = \left(\frac{^{207}\text{Pb}}{^{206}\text{Pb}}\right)^* \quad (3.19)$$

where $(^{207}\text{Pb}/^{206}\text{Pb})^*$ denotes the ratio of radiogenic $^{207}\text{Pb}/^{206}\text{Pb}$. The present-day $^{235}\text{U}/^{238}\text{U}$ ratio in terrestrial and meteoric systems

is constant at 137.88 (Steiger & Jäger, 1977). Therefore, the main advantage of using the Pb-Pb method is the ability to gain an age estimate without the need to measure U. The absolute concentration of Pb is also not required, thus eliminating any further systematic uncertainties (Schoene, 2014). Geochronologists prefer to use Pb-Pb method when it is suspected that the U/Pb ratios have changed. This change is likely to be caused by the mobility of U under oxidising conditions, often when the rock reaches the weathering zone, and from magma generation. Magma melting causes the U/Pb ratios in the rock to become identical to those in the magma (White, 2015).

3.2.4 Data visualisation

Wetherill concordia plots

Wetherill (1956) first presented a concordia diagram which was specifically designed to incorporate two simultaneous decay systems: ^{235}U and ^{238}U . This unique dual analysis of the two decay 'clocks', $^{207}\text{Pb}/^{235}\text{U}$ and $^{206}\text{Pb}/^{238}\text{U}$, gives Wetherill plots a particular geochronological value in their ability to visually assess the internal consistency and therefore detect open-system behaviour.

The solutions of equations 12 and 13 form the nonlinear parametric concordia curve of a Wetherill diagram. Data that have been corrected for common Pb, will plot along the concordia line when they have agreeing $^{207}\text{Pb}/^{235}\text{U}$ and $^{206}\text{Pb}/^{238}\text{U}$ ages (Figure 3.5a). This will only occur if Pb or U are lost or gained by no other means than radioactive decay (Schoene, 2014; Reiners *et al.*, 2018).

If the sample has experienced episodic lead loss, the data plots away from concordia, usually forming a linear array (Reiners *et al.*, 2018). The two points where the discordia line intersects the concordia have chronological significance: the upper point (T_1) signifies the true age of the minerals; the lower intercept (T_2) represents a thermal event which caused mineral Pb loss. The lower intercept is only present if the system has closed again

(Schoene, 2014; White, 2015; Dickin, 2018). There are several factors that can cause discordance in the data set which is discussed in part 3.2.4.

Tera-Wasserburg concordia plots

Tera-Wasserburg (T-W) concordia diagrams were developed by Tera and Wasserburg in their 1972 study of lunar soils and are now a complimentary alternative to Wetherill plots. Here, $^{238}\text{U}/^{206}\text{Pb}$ and $^{207}\text{Pb}/^{206}\text{Pb}$ are placed along the x- and y- axes respectively.

If corrected for Pb_c , the concordant and discordant data from T-W plots can be interpreted in the same way as Wetherill plots. When cogenetic samples plot away from the curve a regression line is constructed through the dataset (Figure 3.5b). This straight regression line is termed an 'isochron'. The point at which the regression line intercepts the $^{207}\text{Pb}/^{206}\text{Pb}$ Y-axis indicates the

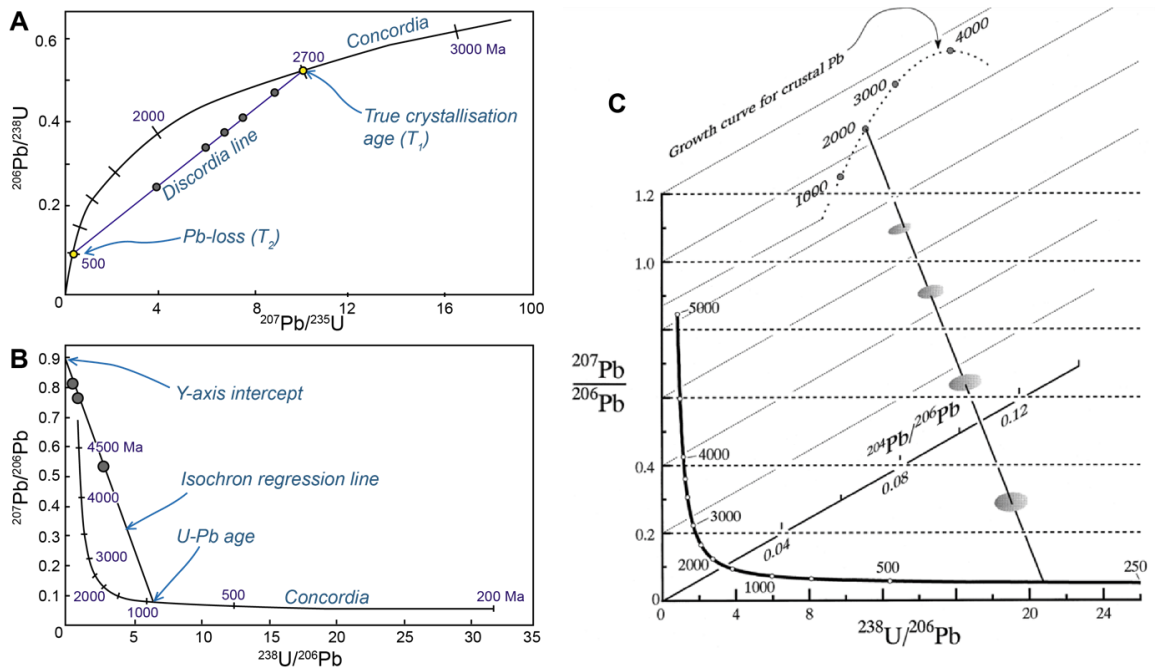


Figure 3.5. **a)** A Wetherill concordia diagram after Dickin (2018) showing data affected by variable Pb loss, with discordant plots coloured grey and concordant plots in yellow. T_1 and T_2 are the higher and lower concordia incepts. **b)** A 2D Tera-Wasserburg concordia diagram after White (2015). The y-incept indicates the composition of Pb_0 . **c)** Figure from Ludwig (1998): 3D Tera-Wasserburg plot showing the Total-Pb/U isochron (represented here as the oblique solid line). The left end of the isochron is anchored to common-Pb along the $^{207}\text{Pb}/^{206}\text{Pb}$ - $^{204}\text{Pb}/^{206}\text{Pb}$ plane, with a crustal Pb growth curve (with ticks labelled in Ma). The right end of the isochron intersects the concordia curve, which is labelled in Ma. The ellipsoids along the isochron mark individual samples, yielding their age.

composition of Pb_0 , and where it intersects the concordia curves it gives the U-Pb age of the sample (Schoene, 2014; Reiners *et al.*, 2018). This ability to determine the initial lead composition is one of the main advantages of using a T-W plot. However, if there is Pb loss in the sample or mixing of multiple age domains, the regression loses the ability to identify Pb_c (Schoene, 2014).

If a sample has experienced Pb loss or mixing of age domains Pb_c cannot be determined by the linear regression. A 3D isochron can provide a more precise Pb_c estimate (Figure 3.5c), by $^{238}U/^{206}Pb$ vs $^{206}Pb/^{204}Pb$ on one plane, and $^{204}Pb/^{206}Pb$ on the z-axis (Ludwig, 1988; Reiners *et al.*, 2018).

2D and 3D isochrons such as T-W concordia plots can be used to obtain the value of the initial daughter product (Pb_0), if the system meets the correct assumptions. Here, if a closed system can be assumed with a well-defined data line, then the y-intercept of the isochron indicates the $^{207}Pb/^{206}Pb$ of Pb_0 (Schoene, 2014; Reiners *et al.*, 2018).

Causes of discordance in the system

The term ‘discordance’ often symbolises ‘open system behaviour’, however there are exceptions to this where a sample may appear

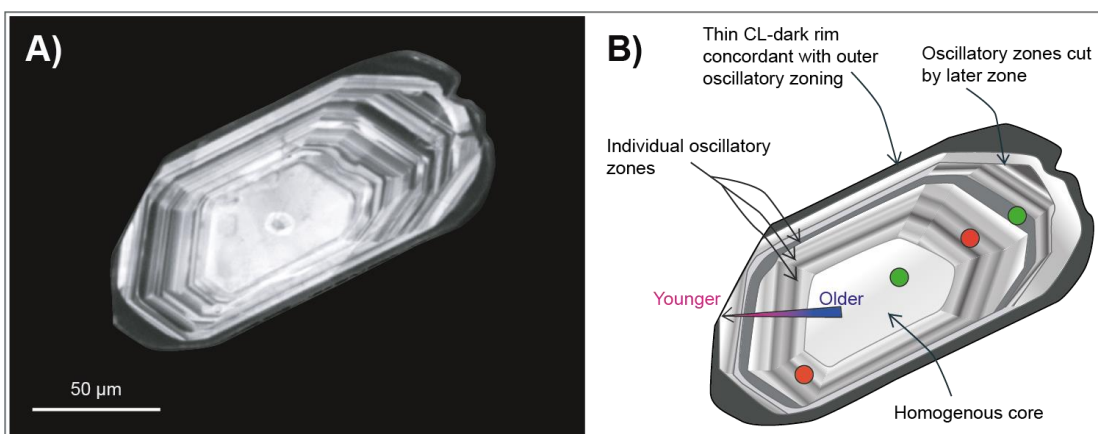


Figure 3.6. **a)** Cathodoluminescence (CL) image of a zircon from Kielman *et al.*, (2018). **b)** Schematic of the zircon showing a homogenous core with oscillatory zone progressively younging outward. The circles represent potential sites for LA-ICPMS analysis: green spots are completely within one zone; red overlaps multiple zones and therefore would lead to discordance. However, it is worth noting that there is likely to be an age difference between the two green spots.

to be concordant, but have experienced an open-system (Schoene, 2014). There are four main reasons for discordance: (i) mixing between samples; (ii) Pb loss; (iii) intermediate daughter disequilibrium; and (iv) initial Pb content (Schoene, 2014; Reiners *et al.*, 2018):

- i) Mixing between growth zones in samples – if a sample containing different temporal phases of a mineral is interpreted synchronously, it can result in the data plotting discordantly if the age difference is significant. Therefore, it is important when interpreting geochronological data to record and track relationships between the dated minerals with the surrounding mineral assemblages. Age domains, such as zoning, within a specific mineral can also be identified through backscatter electron (BSE) and catholuminescence (CL) imaging (Figure 3.6). For example, when attempting to date an oscillatory zoned mineral, even if each zone is too small to date,

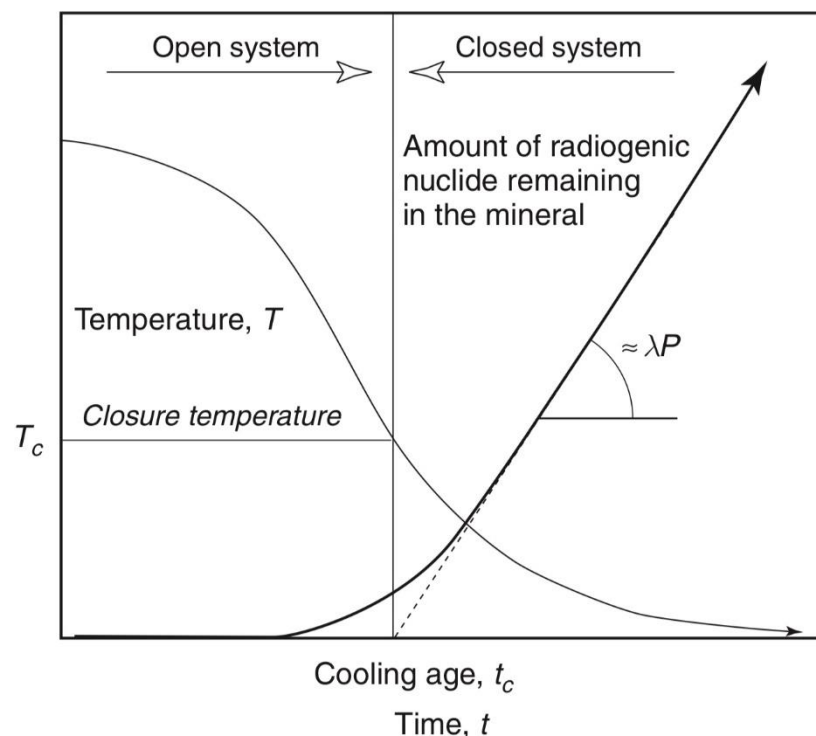


Figure 3.7. Diagram from Albarède (2009)) - T_c represents the closure temperature of the system, above which the system is considered 'open' and diffusion can result in the loss of the daughter isotope. The curve trajectory representing the evolution of radiogenic daughter isotope equals the decay rate by the amount of radioactive parent ($= \lambda P$).

identifying the presence of zoning is important for explaining potentially discordant data (Reiners *et al.*, 2018).

- ii) Pb loss - the loss of radiogenic Pb during igneous and metamorphic activity can cause discordance to the system, and is an area of geochronology that has been thoroughly studied but with elements that remain unclear. Lead can be lost through various mechanisms, and the mineral type is likely to determine the way in which the loss will happen. For example, one of the most studied mechanisms of Pb loss is volume diffusion through the crystal lattice, which is particularly thought to occur in minerals such as titanite, apatite and rutile, but less so for zircon (Figure 3.7). The closure temperature (T_c) is the temperature below which there is no thermally activated volume diffusion (Dodson, 1973). Diffusion in zircons is negligible at temperatures of up to 900-1000°C (Mezger & Krogstad, 1997; Reiners *et al.*, 2018). In low temperatures in U-rich zircons, Pb loss can occur through radiation damage from natural alpha recoil and fission track accumulation (Chew *et al.*, 2011; Schoene, 2014; Reiners *et al.*, 2018). Other methods of Pb loss include fast diffusion pathways generated by plastic crystal deformation and low-temperature dissolution reprecipitation (Geisler *et al.*, 2003, 2007; Reiners *et al.*, 2018). LA-ICPMS data plotted on a Wetherill concordia plot can track any Pb loss along the linear discordia array from the initial formation and closure of the system (T_0). The discordia line is straight as the loss of ^{206}Pb is always directly proportional to the loss of ^{207}Pb . The lower intercept (T_1) represents the percentage loss of radiogenic Pb and the partial resetting of the system (Schoene, 2014; Vermeesch, 2018). In order to plot the discordia line, multiple aliquots are required to determine accurate intercepts.
- iii) Intermediate daughter disequilibrium – as discussed in section 0, secular disequilibrium defines a decay where the decay rate

is equal to the production rate of the intermediate daughter isotope. It is particularly prevalent in systems where the parent nuclide has a long half-life, such as ^{234}U with a half-life of 245 ka (Schoene, 2014; Reiners *et al.*, 2018). For a system in secular equilibrium, certain assumptions are made which are necessarily true and when not acknowledged can lead to discordance. A common example is the fractionation of the intermediate daughter product from the parent isotope during mineral crystallization (Schoene, 2014; Reiners *et al.*, 2018). This can lead to two possible dating errors: if the intermediate daughter product is preferentially partitioned over the parent, excess radiogenic Pb results in an old U-Pb age. However, if the daughter product is excluded from the system during crystallisation, the calculated age will be younger than the true age (Reiners *et al.*, 2018). Nevertheless, within the ^{238}U decay chain, only ^{230}Th and ^{234}U have long enough half-lives (75.4 ka and 245 ka respectively) for fractionation to alter the resulting calculated age (Figure 3.4). As ^{234}U only seems to significantly fractionate at low temperatures, this is generally thought not to cause disequilibrium and discordance (Reiners *et al.*, 2018).

- iv) Initial Pb content – correcting for the initial daughter product (Pb_0) is crucial for accurate dating results, as high levels of inherited non-radiogenic Pb can cause discordance in the system. Correcting for common Pb is discussed in the next section.

Correcting for common Pb

The presence of common Pb in a mineral can cause serious error in U-Pb dating. One way to correct for this is through the isochron method, designed to use the non-radiogenic component of the daughter isotope to normalise the radiogenic daughter and parent isotope (Reiners *et al.*, 2018).

Another method is to normalize the relative abundance of the radiogenic lead isotopes (^{206}Pb , ^{207}Pb and ^{208}Pb) against the non-radiogenic ^{204}Pb . Unlike ^{206}Pb , ^{207}Pb and ^{208}Pb , ^{204}Pb is the only isotope of Pb that cannot naturally be produced from a radioactive parent (Andersen, 2002; Schoene, 2014; Vermeesch, 2018). The ^{204}Pb common-Pb correction is:

$$\left[\frac{^{206|7}\text{Pb}}{^{204}\text{Pb}} \right]_r = \left[\frac{^{206|7}\text{Pb}}{^{204}\text{Pb}} \right]_m - \left[\frac{^{206|7}\text{Pb}}{^{204}\text{Pb}} \right]_0 \quad (3.20)$$

where $[\frac{^{206|7}\text{Pb}}{^{204}\text{Pb}}]_r$ is the radiogenic component of ^{206}Pb or ^{207}Pb , $[\frac{^{206|7}\text{Pb}}{^{204}\text{Pb}}]_m$ represents the measured ratio, and $[\frac{^{206|7}\text{Pb}}{^{204}\text{Pb}}]_0$ is the non-radiogenic component (Vermeesch, 2018).

However, this method assumes the knowledge of ^{204}Pb in a data set, which is not always recorded. This is due to the scarcity of ^{204}Pb , and its isobaric interference with ^{204}Hg ; ^{204}Pb can be hard to detect (Andersen, 2002; Schoene, 2014; Vermeesch, 2018; 2020). Therefore, other common lead corrections can be used that do not involve ^{204}Pb but follow a similar principle, but assuming a concordance between $^{207}\text{Pb}/^{206}\text{Pb}$ or $^{208}\text{Pb}/^{206}\text{Pb}$ and the U-Th systems (Schoene, 2014). This is summarized by the ^{207}Pb -based correction equation (Vermeesch, 2018):

$$\left[\frac{^{207}\text{Pb}}{^{206}\text{Pb}} \right]_m = f \left[\frac{^{207}\text{Pb}}{^{206}\text{Pb}} \right]_0 + (1 - f) \left[\frac{^{207}\text{Pb}}{^{206}\text{Pb}} \right]_r \quad (3.21)$$

where f equals the fraction of common Pb. This semitotal-Pb/U isochron can obtain the radiogenic Pb component, $[\frac{^{207}\text{Pb}}{^{206}\text{Pb}}]_r$ by projecting the data on the concordia line in a Tera-Wasserburg space (Figure 3.8). The initial lead content, $[\frac{^{207}\text{Pb}}{^{206}\text{Pb}}]_0$, is determined by: analysis on a cogenetic mineral; the Stacey and Kramers (1975) model; or by regressing a line through the data from a fixed $^{207}\text{Pb}/^{206}\text{Pb}$ intercept (Schoene, 2014; Vermeesch,

2018). Data visualisation software can correct for common Pb, for example the open-source computer software 'IsoplotR' (Vermeesch, 2018). IsoplotR applies six methods to correct for the initial Pb content, three which rely on ^{204}Pb , and three that do not, such as equation (3.21) (Vermeesch, 2018).

Andersen (2002) applies a different technique that utilises ^{208}Pb by assuming the discordant ratios of $^{206}\text{Pb}/^{238}\text{U}$, $^{207}\text{Pb}/^{235}\text{U}$ and $^{208}\text{Pb}/^{232}\text{Th}$. In this model, the discordance is thought to be caused by Pb-loss at a defined time, and a known amount of present common lead. Andersen (2002) applies a set of equations using: content of radiogenic Pb related to its total lead content; the amount of common lead recorded; initial age of crystallisation; an estimation of the age of Pb-loss; and the amount of lead lost in the process (Andersen, 2002). However, as the timing of Pb loss and the common Pb composition is not often known, there are problems with using this method. Additionally, this method is not effective for

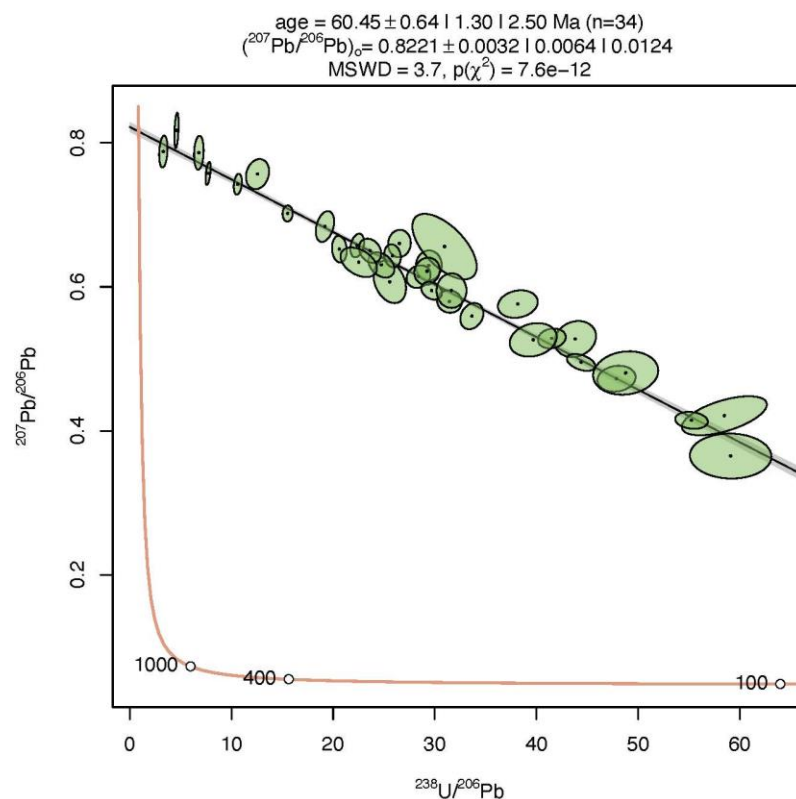


Figure 3.8. A semitotal-Pb/U isochron on a Tera-Wasserburg using apatite data from this study. The isochron regression highlights an age of 60.45 Ma and a $(^{207}\text{Pb}/^{206}\text{Pb})_0$ value of 0.8221. This plot uses ISOPLOT software (Vermeesch, 2018).

minerals with a low crystallisation temperature and those that do not lose Pb diffusively (Vermeesch, 2020).

A new approach from Vermeesch (2020) determines the common Pb component using the least used of the U-Th-Pb decay schemes: the ^{232}Th - ^{208}Pb decay scheme. This is particularly useful for samples, such as carbonates, which are low in Th and therefore ^{208}Pb is more abundant than ^{204}Pb and ^{207}Pb . The algorithm:

$$\frac{{}^{206}\text{Pb}_m}{{}^{208}\text{Pb}_c} = \left[\frac{{}^{206}\text{Pb}}{{}^{208}\text{Pb}} \right]_c + \frac{{}^{238}\text{U}_m}{{}^{208}\text{Pb}_c} (e^{\lambda_{38}t} - 1) \quad (3.22)$$

does not require a known common Pb value, unlike the previous Andersen (2002) method, but assumes no Pb loss has occurred. The isochron slope ($e^{\lambda t} - 1$) is defined when multiple aliquots of the same sample are applied to equation (3.23) (Vermeesch, 2020). When $^{208}\text{Pb}/^{232}\text{Th}$ is plotted against $^{206}\text{Pb}/^{238}\text{U}$ in a Wetherill-styled plot, if the ages fall along the concordia line then there is no common lead present. The presence of common lead is marked by data plotting away from this line (Vermeesch, 2020).

3.2.5 Mean squared weighted deviations (MSWD)

In isotopic dating, the scatter and homogeneity of the data points from the regression line (e.g isochron or discordia line) is quantified using the mean squared weighted deviations (MSWD), or known in statistics as the reduced chi-square statistic (York, 1968; Wendt & Carl, 1991; Vermeesch, 2018). The MSWD value is calculated with the equation:

$$\text{MSWD} = \frac{\sum_i^N \frac{(y_i - bx_i - a)^2}{(b^2\sigma_{x_i}^2 + \sigma_{y_i}^2)}}{N - 2} \quad (3.23)$$

where the deviation from the regression line in the y-direction is represented as $y_i - bx_i - a$, and where σ_{x_i} and σ_{y_i} are the associated errors of x_i and y_i respectively (Wendt & Carl, 1991; White, 2015). Where there is N points, the regression has $(N - 2)$ degrees of freedom (Wendt & Carl, 1991). The data is weighted as an inverse of their variance. This is important as those

values with greater uncertainty are given less weight (Schoene, 2014). This MSWD is used as a validity test for the regression line, so if the value is:

- Equal to 1: it is the 'expected' value for MSWD (Figure 3.9) and any deviations from the regression line are within analytical error (Wendt & Carl, 1991).
- Less than 1: the data is under-dispersed, and the uncertainties are likely to be larger on individual data points than expected from the apparent data scatter. An MSWD value of <0.3 provides a $>99\%$ certainty that the analytical error has been over estimated (Wendt & Carl, 1991; Schoene, 2014).
- Greater than 1: then the measurements are over-dispersed. This could be caused by geological variation from inhomogeneous samples, for instance that the conditions, such as a closed system, were breached between $t = 0$ and time t (McIntyre *et al.*, 1966; White, 2015). Over dispersion can also indicate experimental variation (McIntyre *et al.*, 1966). If the MSWD is greater than 3 the isochron is termed 'errorchron' and any geochronological age should be treated with caution (Wendt & Carl, 1991).

It should be noted that Equation 3.23 only applies in certain cases where the errors are uncorrelated, for example, if the error ellipses are parallel to the plot axes.

3.2.6 A brief overview of K-Ar and Ar-Ar

Although this study uses U-Pb dating for all of the analysis, there are key published ages by Zimmermann & Collado (1983) and Clark *et al.*, (1990) which apply K-Ar and Ar-Ar dating of biotite, feldspar and whole rock to regional samples. Therefore, a brief outline of the K-Ar and Ar-Ar process is given.

Both K-Ar and Ar-Ar dating are based on the natural decay of ^{40}K to ^{40}Ar . This decay is unusual as a chronometer because of its branched decay, where 90% of the parent nuclide, ^{40}K , decays by β - decay to ^{40}Ca and 10% to ^{40}Ar via electron decay (Reiners *et al.*, 2018; Vermeesch, 2018). One of

the fundamental problems with K-Ar dating are the elemental differences between K and Ar: K is highly reactive and decays to Ar which is an inert noble gas. This means that for K-Ar dating, the method in which the isotopic data is measured can be problematic: K uses machines such as flame spectroscopy or isotopic dilution, whilst Ar requires a noble gas spectrometer which is unable to process K (Kelley, 2002; Reiners *et al.*, 2018). This issue in analytical technique is resolved in ^{40}Ar - ^{39}Ar dating, where the measurement of the parent isotopes ^{40}K can be bypassed by using synthetic ^{39}Ar , so that noble gas mass spectrometer can be used for both measurements (Vermeesch, 2018).

Ar is very susceptible to migration because, as a noble gas, it is unable to chemically bond into the k-bearing silicate mineral lattice. Only when the mineral has cooled sufficiently can the Ar be incorporated and the decay 'clock' begin. Any fluctuation in the temperature of a rock can reset the clock (White, 2015; Reiners *et al.*, 2018).

3.3 Geochronological and geochemical analytical procedure

3.3.1 Whole rock geochemistry

Whole rock geochemical analysis was carried out by ACME (Canada). The 87 samples were received on November 08, 2018, and processed by November 26, 2018.

Once recorded by ACME, the samples were dried and crushed with over >70% of the material passing through a 2 mm mesh sieve. 250 g of each sample was pulverised to greater than 85%, passing a 75 μm screen.

Anglo American opts for a whole rock analysis package with ACME that comprises:

- Major element concentrations of SiO_2 , Al_2O_3 , Cr_2O_3 , Fe_2O_3 , K_2O , CaO , MgO , Na_2O , TiO_2 , MnO , P_2O_5 , and MnO . These were obtained using ICP-ES (method code: LF300)

- Trace element concentrations: Ba, Ce, Cr, Cs, Dy, Er, Eu, Ga, Gd, Ge, Hf, Ho, La, Lu, Nb, Nd, Pr, Rb, Sm, Sn, Sr, Ta, Tb, Th, Tm, U, V, W, Y, Yb and Zr), using ICP-MS (method code: LF100).
- Ultratrace element concentrations: Ag, As, Au, B, Bi, Cd, Co, Cr, Cu, Hg, Mn, Mo, Ni, Pb, Sb, Se, Te, Tl, Zn, Ge, In, Re, Be, Li, d and Pt using ICP-MS (method code: AQ252).
- Multi acid, total Ni content (method code: MA370)

The analytical methods and corresponding limits of detection are summarised in Table 3.1.

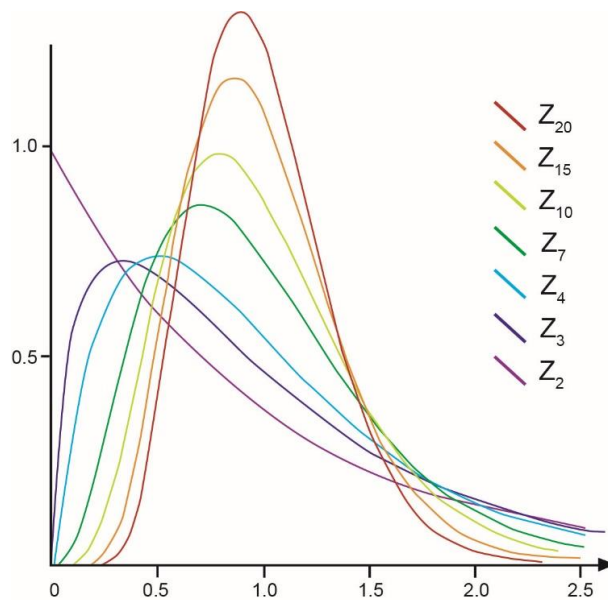


Figure 3.9. a graph showing the distributions of MSWD frequency with varying degrees of freedom (f), edited from Wendt and Carl, 1991

Method Code	Analyte	Unit	Upper detection limit	Lower detection limit	Method Code	Analyte	Unit	Upper detection limit	Lower detection limit
LF300	SiO2	%	100	0.01	MA370	Ag	GM/T	1,500	2
LF300	Al2O3	%	100	0.01	MA370	Cu	%	10	0.001
LF300	Cr2O3	%	100	0.002	MA370	Mo	%	5	0.001
LF300	Fe2O3	%	100	0.04	MA370	Ni	%	10	0.001
LF300	K2O	%	100	0.01	MA370	Pb	%	10	0.02
LF300	MgO	%	100	0.01	MA370	Zn	%	40	0.01
LF300	MnO	%	100	0.01	AQ252	Ag	ppb	100,000	2
LF300	Na2O	%	100	0.01	AQ252	As	ppm	10,000	0.1
LF300	P2O5	%	100	0.01	AQ252	Au	ppb	100,000	0.2
LF300	TiO2	%	100	0.01	AQ252	B*	ppm	2,000	20
LF300	CaO	%	100	0.01	AQ252	Bi	ppm	2,000	0.02
LF300	Sc	ppm	10,000	1	AQ252	Cd	ppm	2,000	0.01
LF300	LOI	%	100	0.1	AQ252	Co	ppm	2,000	0.1
LF300	Sum	%	100	0.01	AQ252	Cr	ppm	10,000	0.5
LF100	Ba	ppm	50,000	1	AQ252	Cu	ppm	10,000	0.01
LF100	Ce	ppm	50,000	0.1	AQ252	Hg	ppb	50,000	5
LF100	Cs*	ppm	1,000	0.1	AQ252	Mn	ppm	10,000	1
LF100	Dy	ppm	10,000	0.05	AQ252	Mo	ppm	2,000	0.01
LF100	Er	ppm	10,000	0.03	AQ252	Ni	ppm	10,000	0.1
LF100	Eu	ppm	10,000	0.02	AQ252	Pb	ppm	10,000	0.01
LF100	Ga	ppm	10,000	0.5	AQ252	Sb	ppm	2,000	0.02
LF100	Gd	ppm	10,000	0.05	AQ252	Se	ppm	100	0.1
LF100	Hf	ppm	10,000	0.1	AQ252	Te	ppm	1,000	0.02
LF100	Ho	ppm	10,000	0.02	AQ252	Tl	ppm	1,000	0.02
LF100	La	ppm	50,000	0.1	AQ252	Zn	ppm	10,000	0.1
LF100	Lu	ppm	10,000	0.01	AQ252	Ge	ppm	100	0.1
LF100	Nb*	ppm	1,000	0.1	AQ252	In	ppm	1,000	0.02
LF100	Nd	ppm	10,000	0.3	AQ252	Re	ppb	1,000	1
LF100	Pr	ppm	10,000	0.02	AQ252	Be	ppm	1,000	0.1
LF100	Rb*	ppm	1,000	0.1	AQ252	Li	ppm	2,000	0.1
LF100	Sm	ppm	10,000	0.05	AQ252	Pd	ppb	100,000	10
LF100	Sn	ppm	10,000	1	AQ252	Pt	ppb	100,000	2
LF100	Sr	ppm	50,000	0.5					
LF100	Ta*	ppm	1,000	0.1					
LF100	Tb	ppm	10,000	0.01					
LF100	Th	ppm	10,000	0.2					
LF100	Tm	ppm	10,000	0.01					
LF100	U	ppm	10,000	0.1					
LF100	V	ppm	10,000	8					
LF100	W	ppm	10,000	0.5					
LF100	Y	ppm	50,000	0.1					
LF100	Yb	ppm	10,000	0.05					
LF100	Zr	ppm	50,000	0.1					

Table 3.2 Detection limits for whole rock major, minor and trace element analysis

3.3.2 *Scanning electron microscope*

The other half of the samples not processed for whole rock concentrations were investigated in the Imaging Analysis Centre at the Natural History Museum in London. Of the 107 samples, 84 were analysed using a Zeiss Evo SEM which operated with a 10 kV accelerating voltage and 3.0 nA beam.

The SEM stage of sample analysis is fundamental for the subsequent geochronological and geochemical analyses by: confirming the presence of minerals used for further analysis (geochronology: apatite, titanite, zircon and epidote; geochemistry: epidote and chlorite); allowing microscale analysis for mineral textures and assemblages for essential alteration classifications; providing approximate identification of mineral types; giving textural information for minerals affected by microstructures or specific textures. For those minerals required for further analysis, grains were only selected if sufficiently sized to accommodate a 35 µm laser ablation spot. The target sum of grains per sample to be analysed for each mineral was 25-30, although in some cases, such as the zircon geochronology, this was not possible.

3.3.3 *The LA-ICP-MS system*

An introduction

There are different ways to obtain U-Pb data from mineral samples, such as TIMS (Thermal Ionization Mass Spectrometry) which involves destruction of the sample for chemical dissolution; or SIMS (Secondary Ion Mass Spectrometry) which is an in-situ analysis method that liberates U and Pb from the sample by oxygen or cesium ion bombardment. However, as this study relies on the textural and petrographic information for each dated mineral, we have used the relatively non-destructive LA-ICP-MS (Laser Ablation Inductively Coupled Plasma Mass Spectrometry) analysis (Storey *et al.*, 2007).

The LA-ICP-MS system was first used for U-Pb zircon geochronological analyses in the early 1990s, where the laser ablator (LA) and ICP-MS was joined for the first time (e.g. Feng *et al.*, 1993; Fryer *et al.*, 1993; Hirata & Nesbitt, 1995; Jackson *et al.*,

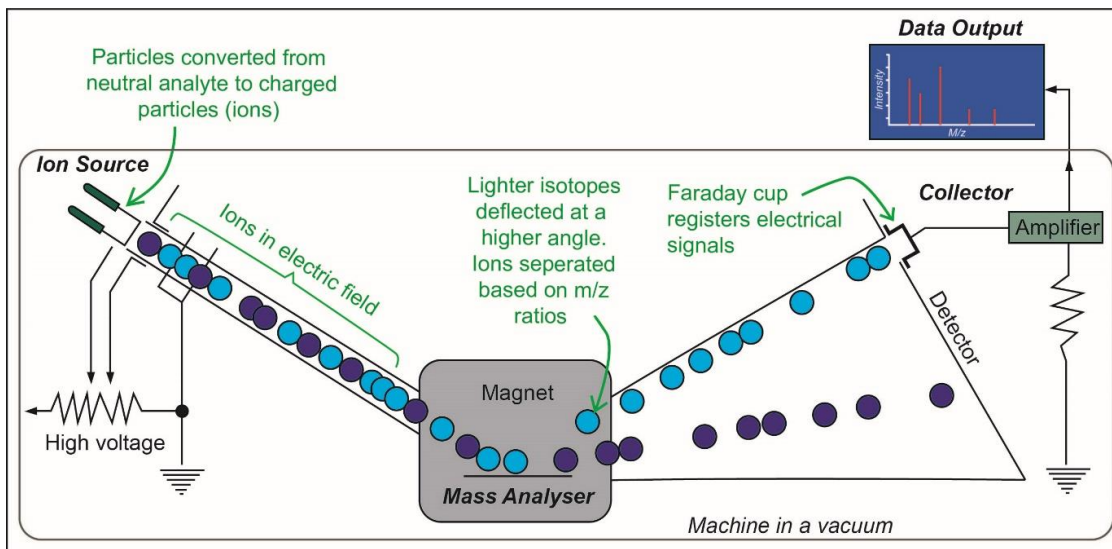


Figure 3.10. An annotated schematic diagram of a mass spectrometer, highlighting a magnetic sector mass analyser (adapted from Vermeesch, 2017; and Arevalo et al., 2020).

1996; Horn *et al.*, 2000; Li *et al.*, 2001; Tiepolo, 2003). In the early 2000s, some of the ultraviolet nanosecond lasers in the LA-ICP-MS were replaced by femtosecond, ultra-short pulse lasers. By decreasing the pulse duration time, photon energy is unable to dissipate to the target lattice to heat and potentially induce melting. However, due to the great expense of the femtosecond lasers there are very few in use. Since the 1990s, crucial developments to the process has allowed for faster analysis time and automated sample analysis with high-spatial resolution (Jenner & Arevalo, 2016). This, combined with its increasing affordability and availability, means the LA-ICP-MS has become the most popular method for in-situ U-Pb dating (Schoene, 2014; Reiners *et al.*, 2018). It is likely that in the next few years, the popularity and usage of the LA-ICP-MS will continue to rapidly increase as their presence in geoanalytical laboratories becomes widespread, and their capabilities continue to develop (Sylvester & Jackson, 2016).

System overview

The LA-ICP-MS is composed of two parts: the air-tight laser ablation system; and the ICPMS. Each of the selected mineral sites are ablated with an ultrashort pulse from the nanosecond laser which converts the target analyte material into fine particulate

aerosol (Schoene, 2014; Lloyd *et al.*, 2018). The aerosol is combined with a gas, often helium, which acts as a carrier for the aerosol to be ionized by an inductively coupled argon plasma. The electrically charged ions that are produced are then accelerated through an electric field to a mass analyzer (Figure 3.10).

There are several types of currently produced mass analyzers for mass spectrometry: quadrupole, time of flight, magnetic sector, electrostatic sector, ion trap and cyclotron. Most of the instruments that are used for geochronology are either quadrupole mass spectrometers (QMS) or sector-field mass spectrometer (SF-MS) which includes the magnetic and electrostatic sector analyzer (White, 2015; Sylvester & Jackson, 2016). The mass spectrometer must be in a vacuum to prevent ion collision at these high velocities. In the magnetic sector mass analyzer, the ions are segregated based on their weight and electric charge as the curvature radius of the deflected ions around the magnet is directly proportional to their mass-to-charge ratio (Sylvester & Jackson, 2016; Reiners *et al.*, 2018; Arevalo *et al.*, 2020). In this study, the LA-ICP-MS incorporates a quadrupole mass analyzer. The quadrupole mass analyzer (QMS) is seen as the 'workhorse' in most commercial and academic laboratories as it is affordable, robust and simple. The QMS consists of four cylindrical rods which function as positive and negative electrodes when ions are projected through them (Kaklamanos *et al.*, 2016). Generally, the QMS achieves lower accuracy than magnetic sector mass spectrometry, however for most U-Pb geochronology, the quadrupole U-Pb uncertainties equal those of SF-MS, but additional sample is required (Schaltegger *et al.*, 2015; White, 2015).

The intensity signal released by the ion is received by a detector, either a Faraday cup or a Secondary Electron Multiplier (SEM), and converted either to its element concentration, or the isotopic ratios (Sylvester & Jackson, 2016).

Data uncertainty, accuracy and precision

There is a tendency for the terms 'error' and 'uncertainty' to be confused. *Error* is the difference between the measured value and the true value whereas the *uncertainty* of a measured quantity is defined as a parameter that characterises the dispersion of the values (Reiners *et al.*, 2018; Schoene *et al.*, 2013). In analytical isotope geochronology, uncertainties are defined as either systematic or random. Random uncertainties are considered 'internal' and occur during the measurement process. Increasing sample analysis can lower the random uncertainty (Reiners *et al.*, 2018). A systematic uncertainty remains constant despite the number of measurements taken. The decay constant is an example of systematic uncertainty (Schoene *et al.*, 2013; Schoene, 2014).

Accuracy and precision are also terms that are often used interchangeably, however distinguishing between these

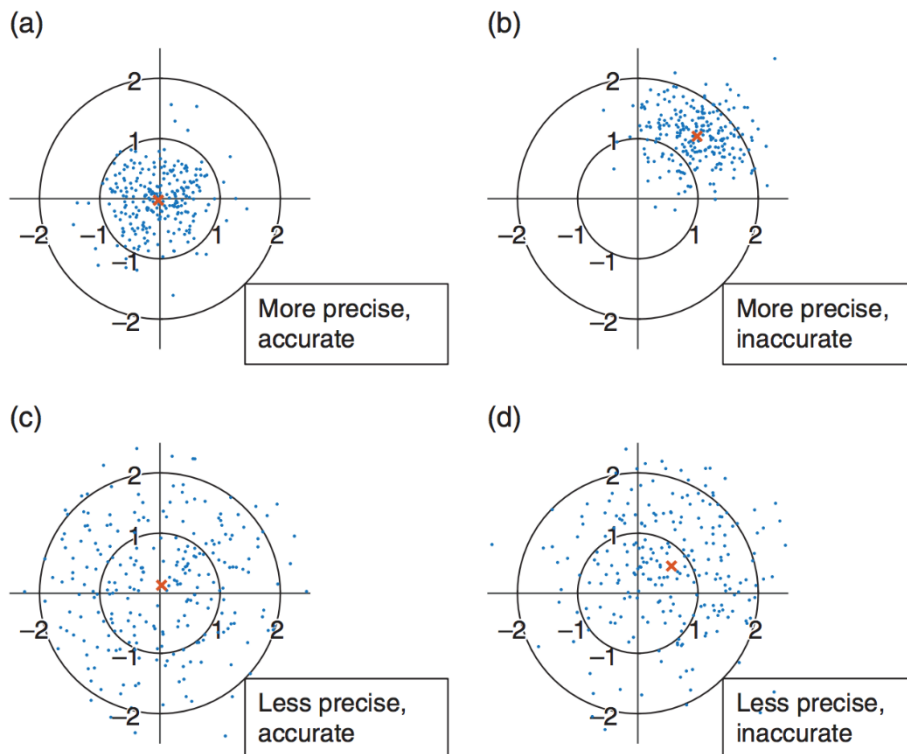


Figure 3.11. From Reiners *et al.*, 2018 demonstrating precision and accuracy using data clusters of 250 points. The population, or 'true', mean of the measured data is at the centre cross hairs, but the sample mean of the data is shown by the red 'x'. Where the data is accurate (a) and (c), the sample mean is closest to the true mean; where the data is precise (a) and (b), the data cluster is more constrained, but the mean is not necessarily close to the true mean.

terminologies is important. Both accuracy and precision are a form of 'uncertainty'.

To appreciate the difference between the two concepts, it is important to distinguish between the population mean and the sample mean. The population mean, also referred as the true mean, is the mean of all the values in the data population, though depending on the dataset, this can often be infinite. The sample mean is the mean of the values analysed as a representative group of the larger population. The difference between high and low precision in a sample is due to the amount of scatter of the data from the sample mean (Figure 3.11): for high precision there is small variability; for low precision there is much larger scatter (Reiners *et al.*, 2018). In geochronological terms, precision describes the reproductivity of the data, for example the consistency of a single analysis to plot on the weighted mean of numerous analyses, and the accuracy of the data depends on its agreeability with the true mean (Schoene, 2014; Horstwood *et al.*, 2016; Reiners *et al.*, 2018).

3.3.4 LA-ICP-MS geochronological analysis

For the geochronology carried out in this study, four minerals were used: apatite, titanite, epidote and zircon. These minerals were dated using an ESR NWR193 laser ablation system coupled to an Agilent 7700x mass spectrometer. Coordinates acquired for each grain on the SEM were compiled and converted to enable static spot analysis. The benefit of using static spot ablation is the preservation of the SEM textural information for each grain. A total of 2584 geochronological isotopic measurements were collected, specifically: apatite 1293, titanite 445, epidote 682 and zircon 164. Primary reference standards used for: apatite = Madagascar apatite (Thomson *et al.*, 2012) with a reference age of 523.5 Ma; titanite = Khan titanite (Heaman, 2009) with an age of 522.2 Ma; and zircon and epidote = GJ-1 (Horstwood *et al.*, 2016) with a reference age of 601.86 Ma. For secondary validation the standards that were used are, for: apatite Durango,(McDowell *et al.*, 2005) 31 Ma, Fish Canyon Tuff (Wotzlav *et al.*,

2013) 28.2 Ma; titanite = also Fish Canyon Tuff (Wotzlaw et al., 2013) with reference age of 28.2 Ma; and zircon and epidote 91500 (Wiedenbeck et al., 1995) with a reference age of 1065 Ma. Because of the paucity and difficulty of epidote dating, the standards used for zircon are applied to epidote. A summary of the analyses and conditions carried out is shown in Table 3.3 and Table 3.4.

3.3.5 *Epidote and chlorite trace element geochemistry*

As with the geochronological data acquisition, the trace element geochemistry was acquired using an ESR NWR193 laser ablation system, with couple Agilent 7700x mass spectrometer. Textural information collected in the SEM processing phases remains fundamental to the contextualisation of the data points in the analysis phase of the trace element data, and therefore the in situ, static spot ablation is crucial. From 42 samples, 1253 epidote grains were analysed: from 33 samples containing chlorite, 956 spots were ablated. The primary standards used for both epidote and chlorite was GSD-1g (Jochum et al., 2011), and a secondary material, NIST612 (National Institute of standards and Technology Standard reference material 612), was used for validation (Jochum et al., 2011). A summary of the analyses and conditions are summarised in Table 3.5 and Table 3.6.

Phase	Apatite	Titanite	Zircon and Epidote
Laser Ablation System			
Make, Model and type	ESI NWR193	ESI NWR193	ESI NWR193
Ablation cell and volume	TwoVol2	TwoVol2	TwoVol2
Laser wavelength (nm)	193 nm	193 nm	193 nm
Pulse width (ns)	~5 ns	~5 ns	~5 ns
Fluence (J cm ⁻²)	~2 J cm ⁻²	~2 J cm ⁻²	~2 J cm ⁻²
Repetition rate (Hz)	5Hz	5Hz	5Hz
Ablation duration (s)	40s	40s	40s
Spot diameter (µm)	30 µm	30 µm	30 µm
Sampling mode/pattern	Static spot ablation	Static spot ablation	Static spot ablation
Carrier gas	100% He in the cell, Ar make-up gas combined using a mixing bulb	100% He in the cell, Ar make-up gas combined using a mixing bulb	100% He in the cell, Ar make-up gas combined using a mixing bulb
Cell carrier gas flow (l min ⁻¹)	~0.7 l min ⁻¹	~0.7 l min ⁻¹	~0.7 l min ⁻¹
Additional gas; flow (l min ⁻¹)	N ₂ ; ~5 ml min ⁻¹	N ₂ ; ~5 ml min ⁻¹	N ₂ ; ~5 ml min ⁻¹
ICP-MS Instrument			
Make, Model and type	Agilent 7700x	Agilent 7700x	Agilent 7700x
Sample introduction	Ablation aerosol	Ablation aerosol	Ablation aerosol
RF power (W)	1350 W	1350 W	1350 W
Make-up gas flow (l min ⁻¹)	~0.8 L min ⁻¹	~0.8 L min ⁻¹	~0.8 L min ⁻¹
Detection system	Electron Multiplier analogue and pulse counting	Electron Multiplier analogue and pulse counting	Electron Multiplier analogue and pulse counting
Typical Oxide Rate (ThO/Th)	<0.18 %	<0.18 %	<0.18 %
Laser Induced elemental fractionation (LIEF; Th/U on NIST612)	>0.95	>0.95	>0.95
Masses measured	⁴³ Ca, ²⁰⁶ Pb, ²⁰⁷ Pb, ²⁰⁸ Pb, ²³² Th, ²³⁸ U	⁴³ Ca, ²⁰⁶ Pb, ²⁰⁷ Pb, ²⁰⁸ Pb, ²³² Th, ²³⁸ U	⁴³ Ca, ²⁰⁶ Pb, ²⁰⁷ Pb, ²⁰⁸ Pb, ²³² Th, ²³⁸ U

Table 3.3 Metadata of the LA-ICP-MS conditions for apatite, titanite, epidote and zircon U-Pb geochronology.

Integration time per peak/dwell times (ms)	0.005 s: ⁴³ Ca 0.01 s: ²⁰⁸ Pb, ²³² U 0.02 s: ²³⁸ U 0.03 s: ²⁰⁶ Pb 0.06 s: ²⁰⁷ Pb	0.005 s: ⁴³ Ca 0.01 s: ²⁰⁸ Pb, ²³² U 0.02 s: ²³⁸ U 0.03 s: ²⁰⁶ Pb 0.06 s: ²⁰⁷ Pb	0.005 s: ⁴³ Ca 0.01 s: ²⁰⁸ Pb, ²³² U 0.02 s: ²³⁸ U 0.03 s: ²⁰⁶ Pb 0.06 s: ²⁰⁷ Pb
Total integration time per mass sweep (s)	0.149 s	0.149 s	0.149 s
Data Processing			
Gas blank	25s on-peak zero subtracted	25s on-peak zero subtracted	25s on-peak zero subtracted
Calibration strategy	Madagascar apatite (Thomson et al., 2012) 523.5 Ma used as primary reference material, Durango, (McDowell et al., 2005) 31 Ma, Fish Canyon Tuff (Wotzlaw et al., 2013) 28.2 Ma, used as secondaries for validation	Khan titanite (Heaman, 2009) 522.2 Ma used as primary reference material, Fish Canyon Tuff (Wotzlaw et al., 2013) 28.2 Ma, used as secondary for validation	GJ-1 (Horstwood et al., 2016) 601.86 Ma used as primary reference material, 91500 (Wiedenbeck et al., 1995) 1065 Ma, used as a secondary for validation
Data processing package used	Iolite v. 3.6, VizualAge_UComPbine for uncertainty propagation and age calculation. LIEF assumes reference material and unknowns behave identically	Iolite v. 3.6, VizualAge_UComPbine for uncertainty propagation and age calculation. LIEF assumes reference material and unknowns behave identically	Iolite v. 3.6, VizualAge_UComPbine for uncertainty propagation and age calculation. LIEF assumes reference material and unknowns behave identically
Mass discrimination	Normalised to reference material	Normalised to reference material	Normalised to reference material
Uncertainty level and propagation	Compositions are quoted at 2s absolute, propagation is by quadratic addition of primary standard reproducibility and measurement counting statistics.	Compositions are quoted at 2s absolute, propagation is by quadratic addition of primary standard reproducibility and measurement counting statistics.	Compositions are quoted at 2s absolute, propagation is by quadratic addition of primary standard reproducibility and measurement counting statistics.
Common Pb correction	Discordia regression	Discordia regression	Discordia regression
Quality Control / Validation	Durango: 42.94 ± 0.21 Ma	Fish canyon: 27.14 ± 1.1 Ma	91500: 1064.16 ± 0.54 Ma

Table 3.4. Metadata of the LA-ICP-MS conditions for apatite, titanite, epidote and zircon U-Pb geochronology continued

Phase	Chlorite	Epidote
Laser Ablation System		
Make, Model and type	ESI NWR193	ESI NWR193
Ablation cell and volume	TwoVol2	TwoVol2
Laser wavelength (nm)	193 nm	193 nm
Pulse width (ns)	~5 ns	~5 ns
Fluence (J cm ⁻²)	~3.5 J cm ⁻²	~3.5 J cm ⁻²
Repetition rate (Hz)	10 Hz	10 Hz
Ablation duration (s)	40s	40s
Spot diameter (µm)	35 µm	35 µm
Sampling mode/pattern	Static spot ablation	Static spot ablation
Carrier gas	100% He in the cell, Ar make-up gas combined using a mixing bulb	100% He in the cell, Ar make-up gas combined using a mixing bulb
Cell carrier gas flow (l min ⁻¹)	~0.7 l min ⁻¹	~0.7 l min ⁻¹
ICP-MS Instrument		
Make, Model and type	Agilent 7700x	Agilent 7700x
Sample introduction	Ablation aerosol	Ablation aerosol
RF power (W)	1350 W	1350 W
Make-up gas flow (l min ⁻¹)	0.8 l min ⁻¹	0.8 l min ⁻¹
Detection system	Electron Multiplier analogue and pulse counting	Electron Multiplier analogue and pulse counting
Typical Oxide Rate (ThO/Th)	<0.18 %	<0.18 %
Laser Induced elemental fractionation (LIEF; Th/U on NIST612)	>0.9	>0.9
Masses measured	⁷ Li, ¹¹ B, ²³ Na, ²⁴ Mg, ²⁷ Al, ²⁹ Si, ³² S, ³⁹ K, ⁴³ Ca, ⁴⁷ Ti, ⁵¹ V, ⁵³ Cr, ⁵⁵ Mn, ⁵⁷ Fe, ⁵⁹ Co, ⁶⁰ Ni, ⁶⁵ Cu, ⁶⁶ Zn, ⁷⁵ As, ⁸⁸ Sr, ⁸⁹ Y, ⁹⁰ Zr, ¹⁰⁷ Ag, ¹¹¹ Cd, ¹¹⁸ Sn, ¹²¹ Sb, ¹³⁷ Ba, ¹³⁹ La, ¹⁴⁰ Ce, ²⁰⁸ Pb, ²⁰⁹ Bi, ²³⁸ U	⁷ Li, ⁹ Be, ¹¹ B, ²³ Na, ²⁴ Mg, ²⁷ Al, ²⁹ Si, ³¹ P, ³⁹ K, ⁴³ Ca, ⁴⁵ Sc, ⁴⁷ Ti, ⁵¹ V, ⁵³ Cr, ⁵⁵ Mn, ⁵⁷ Fe, ⁵⁹ Co, ⁶⁰ Ni, ⁶⁵ Cu, ⁶⁶ Zn, ⁷¹ Ga, ⁷² Ge, ⁷⁵ As, ⁸⁵ Rb, ⁸⁸ Sr, ⁸⁹ Y, ⁹⁰ Zr, ⁹³ Nb, ⁹⁵ Mo, ¹¹¹ Cd, ¹¹⁸ Sn, ¹²¹ Sb, ¹³³ Cs, ¹³⁷ Ba, ¹³⁹ La, ¹⁴⁰ Ce, ¹⁴¹ Pr, ¹⁴⁶ Nd, ¹⁴⁷ Sm, ¹⁵³ Eu, ¹⁵⁷ Gd, ¹⁵⁹ Tb, ¹⁶³ Dy, ¹⁶⁵ Ho, ¹⁶⁶ Er, ¹⁶⁹ Tm, ¹⁷² Yb, ¹⁷⁵ Lu, ¹⁷⁸ Hf, ¹⁸² W, ¹⁹⁷ Au, ²⁰⁸ Pb, ²⁰⁹ Bi, ²³² Th, ²³⁸ U
Integration time per peak/dwell times (ms)	0.005 s: ²³ Na, ²⁴ Mg, ³⁹ K, ⁴³ Ca 0.01 s: ¹¹ B, ²⁷ Al, ²⁹ Si, ⁵¹ V, ⁵⁵ Mn, ⁵⁵ Mn, ⁵⁷ Fe, ⁸⁸ Sr, ²³⁸ U 0.02 s: ⁷ Li, ⁴⁷ Ti, ⁵³ Cr, ⁵⁹ Co, ⁶⁰ Ni, ⁶⁶ Zn, ⁸⁹ Y, ⁹⁰ Zr, ¹³⁷ Ba, ¹³⁹ La, ¹⁴⁰ Ce, ²⁰⁸ Pb 0.03 s: ⁶⁵ Cu, ⁷⁵ As, ¹⁰⁷ Ag, ¹¹¹ Cd, ¹¹⁸ Sn, ¹²¹ Sb, ²⁰⁹ Bi	0.005 s: ²³ Na, ²⁷ Al, ²⁹ Si, ³¹ P 0.01 s: ⁷ Li, ⁹ Be, ¹¹ B, ²⁴ Mg, ³⁹ K, ⁴³ Ca, ⁴⁵ Sc, ⁴⁷ Ti, ⁵¹ V, ⁵³ Cr, ⁵⁵ Mn, ⁵⁷ Fe, ⁵⁹ Co, ⁶⁰ Ni, ⁶⁵ Cu, ⁶⁶ Zn, ⁷¹ Ga, ⁷² Ge, ⁷⁵ As, ⁸⁵ Rb, ⁸⁸ Sr, ⁸⁹ Y, ⁹⁰ Zr, ⁹³ Nb, ¹¹⁸ Sn, ¹²¹ Sb, ¹³³ Cs, ¹³⁷ Ba, ¹³⁹ La, ¹⁴⁰ Ce, ¹⁴¹ Pr, ¹⁴⁶ Nd, ¹⁴⁷ Sm, ¹⁵³ Eu, ¹⁵⁷ Gd, ¹⁵⁹ Tb, ¹⁶³ Dy, ¹⁶⁵ Ho, ¹⁶⁶ Er, ¹⁶⁹ Tm, ¹⁷² Yb, ¹⁷⁵ Lu, ¹⁷⁸ Hf, ¹⁸² W, ²⁰⁸ Pb, ²⁰⁹ Bi, ²³² Th, ²³⁸ U 0.02 s: ⁹⁵ Mo, ¹¹¹ Cd, ¹⁹⁷ Au
Total integration time per mass sweep (s)	0.711 s	0.662 s

Table 3.5. Metadata of the LA-ICP-MS conditions for epidote and chlorite trace element acquisition

Data Processing		
Gas blank	25s on-peak zero subtracted	25s on-peak zero subtracted
Calibration strategy	GSD-1g (Jochum et al., 2011) used as primary reference material, NIST612, (Jochum et al., 2011) used for validation	GSD-1g (Jochum et al., 2011) used as primary reference material, NIST612, (Jochum et al., 2011) used for validation
Data processing package used	In-house Microsoft Excel spreadsheet calculate concentrations from average means background subtracted isotopes. ²⁷ Al concentrations obtained from analytical SEM used for internal standardisation.	In-house Microsoft Excel spreadsheet calculate concentrations from average means background subtracted isotopes. ⁴³ Ca concentrations obtained from analytical SEM used for internal standardisation.
Mass discrimination	Normalised to reference material	Normalised to reference material

Table 3.6. Metadata of the LA-ICP-MS conditions for epidote and chlorite trace element acquisition

4 The Geology of the Quellaveco Region

4.1 Introduction

This study focuses on the Quellaveco Cu-Mo porphyry deposits in the Moquegua region of southern Peru (Figure 4.1). It is situated at approximately 19°S or 17°06'S - 70°37'W on the northern segment of the Palaeocene-Eocene metallogenic belt of South America (Figure 4.2), which includes neighbouring deposits Cuajone and Toquepala. Initially discovered in the 1930's, the deposit has been explored at various periods throughout the mid- and late- 20th century, but the deposits and surrounding area is now held by Anglo American (Lacy, 1991).

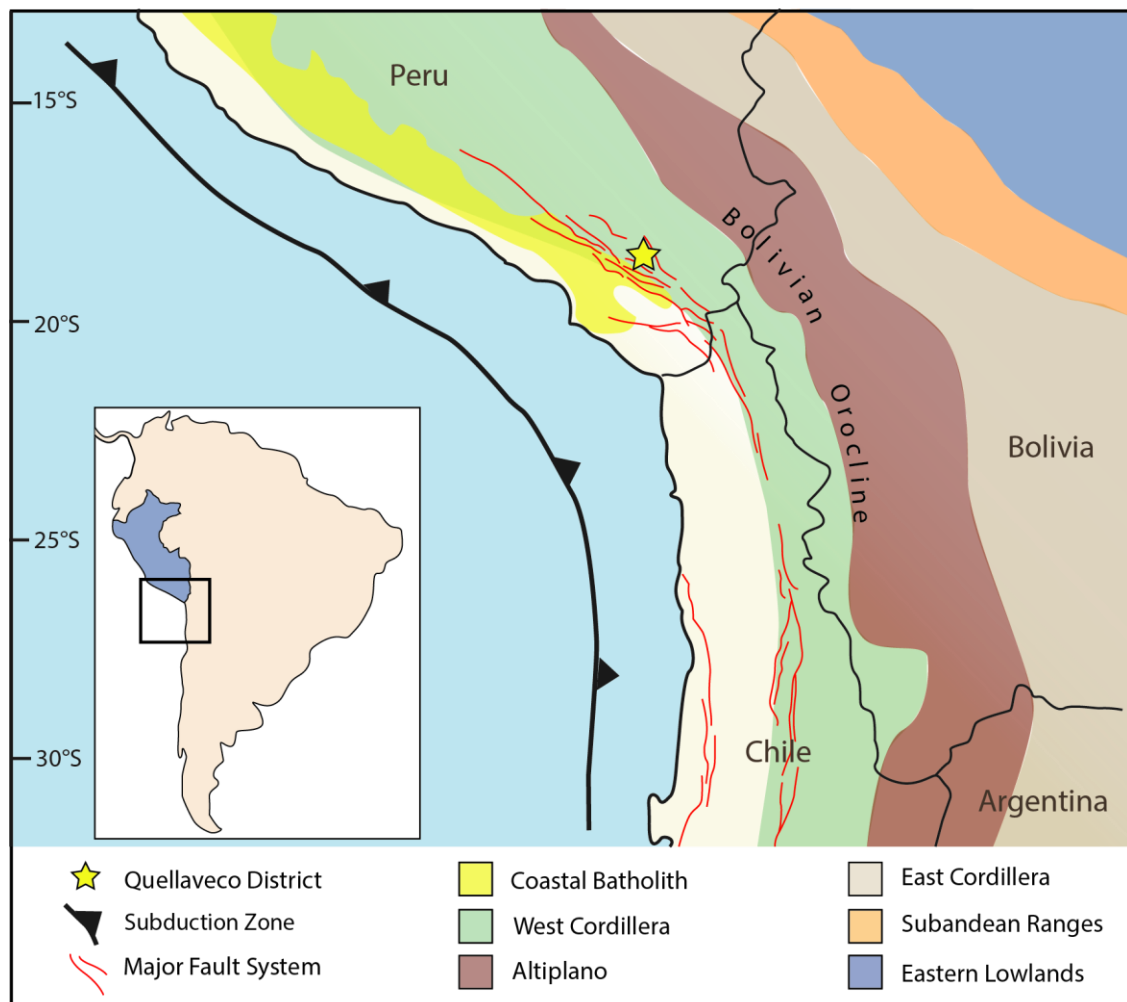


Figure 4.1. Quellaveco location map, situated on the major fault system extending from northern Chile to southern Peru. The Peruvian section of this fault system is named the Incaquio Fault System (after: Jaillard et al., 2010; Jacay et al., 2002; Quang et al., 2005; Di Celma et al., 2016; Sandeman, 1995; Boutelier and Oncken, 2010).

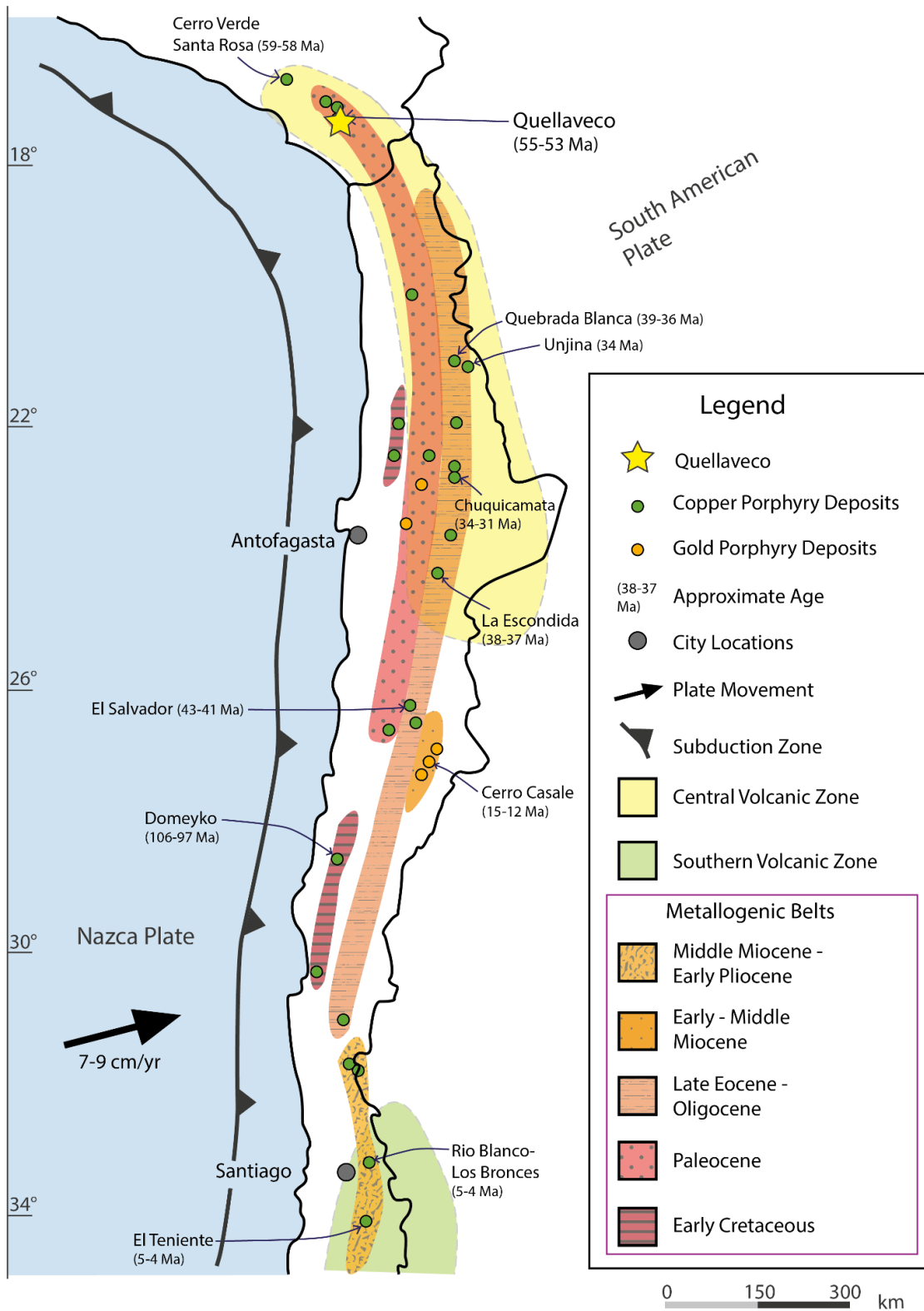


Figure 4.2. the five metallogenetic belts of South America with major porphyry deposits. Quellaveco is situated in the Palaeocene-Eocene belt in southern Peru (Camus & Dilles, 2001a; Sillitoe & Perello, 2005; Cembrano et al., 2005; Quang et al., 2005).

4.2 Regional Geology of the Central Andes

4.2.1 South America's Porphyry Belts

There is a close relationship between porphyry setting and structure, because of the importance of fractures in facilitating magma ascent and localisation (Richards, 2003). Therefore, porphyry deposits tend to form in arc-parallel clusters or belts, and on the west coast of South America these belts are particularly clear, extending from central coastal Peru to central Chile (Figure 4.2). More than half of the world's 25 largest known porphyry copper deposits occur in this zone of South America (Cooke *et al.*, 2005). These deposits formed during five temporally discrete phases of mineralisation: Early Cretaceous; Palaeocene-Eocene; Late Eocene-Oligocene; Early Miocene-Middle Miocene; and Middle Miocene-Early Pliocene (Camus & Dilles, 2001). Quellaveco is situated at the northern tip of the Palaeocene-Eocene metallogenic belt (Sillitoe, 2008).

One contributing factor to the fertility of these belts is thought to be the angle of the subducting plate at the time of mineralisation (Camus & Dilles, 2001). Deep, slower, typically 'Marianas-type' subduction, produced unfavourable conditions for mineralised porphyry generation, for example from the Triassic to Early Cretaceous. Conversely, shallow, faster, 'Chilean-type' subduction resulted in the formation of the metallogenic belts (Camus & Dilles, 2001).

4.2.2 Brief tectonic history

South America has experienced a tectonically active history, in particular since the Cretaceous: the breakup of Gondwana, and the opening of the Atlantic (Coira *et al.*, 1982; Giambiagi *et al.*, 2003; Ramos, 2010). It is important to understand each event that contributed to the development of Quellaveco and surrounding porphyries and recognise any subsequent deformation and uplift.

Cretaceous (145 – 66 Ma)

Throughout the Jurassic to early Cretaceous, multiple deformation phases associated with the breakup of the supercontinent

Gondwana and the beginning of the Andean cycle, were responsible for changes in the regional and local scale stress field. Between 153-143 Ma the western coast of south America experienced sustained calc-alkaline arc magmatism (Coira *et al.*, 1982; Jacay *et al.*, 2002; Giambiagi *et al.*, 2003; Masterman, 2003; Quang *et al.*, 2005). At this time, the boundary between the South American plate and Farallon plate was mostly extensional, with some transtension particularly in the north (Horton, 2018; Chen *et al.*, 2019). This led to the initiation of one of South America's largest structures, the Atacama Fault system (AFS) in northern Chile (Masterman, 2003). The AFS displayed predominantly sinistral strike-slip faulting and minor dip-slip normal faulting from regional subsidence. Towards the end of the Jurassic the obliquity and convergence rate of the subduction Nazca plate increased causing intense coupling between the upper Nazca and lower South American plates (Masterman, 2003; Cembrano *et al.*, 2005).

Following a quasistationary period between 125-100 Ma, rapid sea floor spreading off the eastern coast of South America increased the opening of the Atlantic and coincided with the final stages of the breakup of Gondwana (Ramos, 2010). This increased the gradual westward movement of the South American plate, which resulted in intense compression, increased volcanism, the closure of Jurassic backarc basins, and the initiation of subduction of the Farallon Plate (Coira *et al.*, 1982; Masterman, 2003). Subduction began in the northern latitudes around Ecuador, with the southward propagation of subduction margin through time.

Between approximately 85-75 Ma, the margin of southern Peru shifted from transform, to convergent (Chen *et al.*, 2019). This tectonic shift is marked in southern Peru with the 'Peruvian Orogeny'. Transpression and uplift of this period is noted by the sedimentary change from marine to terrestrial deposits in the western Cordillera of southern Peru (MéGard, 1987; Jaillard *et al.*, 2000; Pfiffner & Gonzalez, 2013). It is during the Peruvian Orogeny

that there is the first documented movement of the major fault system in southern Peru, Incapuquio Fault System (IFS). This also coincided with the inversion of the Domeyko Fault system, in northern Chile between 90-78 Ma (Mpodozis & Ramos, 1989; Jaillard *et al.*, 2000). The IFS appears to be the southern Peru continuation of the northern Chile DFS.

Despite an increase in plate convergence for most of the South American boundary, the end of the Cretaceous in southern Peru coincided with low convergence rate, and the emplacement of the Coastal Batholith between 90-59 Ma (Jaillard *et al.*, 2000; Haederle & Atherton, 2002; Demouy *et al.*, 2012; Pfiffner & Gonzalez, 2013). The Yarabamba Batholith, which is a subsidiary pluton of the Coastal Batholith and part of which is located in the Quellaveco district, spanned between 71-59 Ma (Mukasa, 1986). Continued subduction has contributed to the calculated eastward migration since the Campanian of 1.3 mm/yr of the Coastal Batholith (Mukasa, 1986; Jaillard *et al.*, 2000). The magmatism of the Coastal Batholith was accompanied by the extensive rhyolitic and dacitic volcanism of the Toquepala Group throughout the end of the Cretaceous and into the Palaeocene period, 75-59 Ma (Jaillard *et al.*, 2000; Richards, 2003; Simmons, 2013).

Palaeocene – Eocene (66 – 33 Ma)

At approximately 59 Ma, the absolute relative plate motion of the subducting Nazca plate shifted from approximately north to oblique propagation to the north-east. This plate rotation led to a period of increased plate convergence between 59-52 Ma (Pardo-Casas & Molnar, 1987; Masterman, 2003). The rapid convergence created favorable conditions for a cluster of porphyry deposits to form the associated mineral emplacement in the Quellaveco region (Sandeman H. & Farrar, 1995; Camus & Dilles, 2001). This magmatism was terminated at ~52.5 Ma due to an increase in plate convergence rate (Soler & Bonhomme, 1990; Sandeman H. & Farrar, 1995).

A velocity profile by Horton (2018), denotes a clear split in the plate convergence rate of the South American plate between 50-40 Ma. During this period the lower latitudes, 26°S-49°S, had a convergence between 5-10 mm/yr, whereas at 19°S, the rate was anomalously high at 20 mm/yr. This interesting rapidity of plate convergence coincides with the emplacement of the Palaeocene-Eocene belt porphyries in northern Chile and Southern Peru, including Quellaveco and its neighbouring deposits Cuajone (56-53 Ma) and Toquepala (57-54 Ma) (Jaillard *et al.*, 2000; Simmons, 2013).

At 49.5 Ma, one of the most dramatic changes in plate motion during the Cenozoic occurred and with it, the onset of the fold and thrust belts, and dextral transpression of the Incaic Orogeny (Coira *et al.*, 1982; Pardo-Casas & Molnar, 1987; Masterman, 2003). NNW-SSE orientated fold and thrust belts of the Incaic Orogeny are responsible for the initial formation of the Western cordillera in Southern Peru (Charrier *et al.*, 2013; Pfiffner & Gonzalez, 2013). This tectonic event is thought to have ceased at 40 Ma, however differing reports state the Incaic Orogeny occurred much earlier between 59-55 Ma (Pardo-Casas & Molnar, 1987; Richards, 2003). The north-easterly Nazca plate motion has experienced very little relative change in motion from this time until the present day (Pardo-Casas & Molnar, 1987).

Toward the end of the Incaic Orogeny in the middle Eocene, the lithosphere began to particularly thicken in the central Andes. This was the initial stages of the formation that is now known as the Bolivian Orocline, and whose continual development since this time has defined the iconic bend of the subduction margin in South America (Arriagada *et al.*, 2008; Boutelier & Oncken, 2010; Pfiffner & Gonzalez, 2013). Southern Peru, and therefore the Quellaveco district, is situated on the north-western limb of the orocline, and therefore is subjected to extreme lateral drag from the curvature of the orocline (Boutelier & Oncken, 2010; Roperch *et al.*, 2011). The

Altiplano Plateau, also known as the Altiplano-Puna plateau, is thought to have formed as a result of flat slab subduction of the Nazca plate in the late Eocene. This led to E-W compression and extensive plate shortening of approximately 750,000 km² of the South American plate, and the uplift of the plateau (Arriagada *et al.*, 2008; Ramos & Folguera, 2009; Boutelier & Oncken, 2010). The shallow dip of the flat subducting slab creates the greatest compression in the middle therefore contributing to the seaward-concave nature of the boundary at this time. In its widest section at 19-20°S, the Altiplano is approximately 300 km (Boutelier & Oncken, 2010).

The Abancay Deflection is a 'kink' that has developed on the northern limb of the orocline in the Andes of southern Peru (14°S). The bulk of the deformation started at 42 Ma, where a large structural lineament triggered rotation from NW-SE to E-W by the early Miocene and even rotated to almost NE-SW by the middle Miocene (Roperch *et al.*, 2011).

Following the termination of the Incaic Orogeny, a period of high magmatism between 38-31 Ma resulted in the emplacement of the most economically viable cluster of porphyry deposits in Chile along the Domeyko Fault System (Ossandón C. *et al.*, 2001; Masterman, 2003). This episode was coincident with post-orogenic tectonic relaxation and gravitational collapse, with associated transpression and basin formation (Coira *et al.*, 1982; Richards *et al.*, 2001; Charrier *et al.*, 2002; Masterman, 2003). Flat-slab subduction in northern Chile is also thought to be a contributing factor to the formation and localization of these deposits (Roperch *et al.*, 2011). Increased volcanism led to the extensive rhyolitic and dacitic lavas of the Moquegua Formation until the late Oligocene (Noble *et al.*, 1985).

Oligocene – Miocene (33 – 5 Ma)

Only at the beginning of the Oligocene period did the South American margin become a fully compressive, subducting margin (Chen *et al.*, 2019). At 26-23 Ma, the Fallaron Plate began to break up, leading to the formation of the Nazca and Cocos plates (Jaillard *et al.*, 2000; Martinod *et al.*, 2010). Authors such as Sdrolias and Muller (2006) and Horton (2018) report a period of high convergence of the Nazca plate from the late Oligocene in southern Peru. This contradicts the earlier study from Pardo-Casa and Molnar (1987) which states this initiated a period of a relatively low convergence rate of 50 ± 30 mm/a. Renewed rapid convergence triggered increased alkaline magmatism, reverse faulting and folding, leading to regional uplift in the Precordillera (Pardo-Casas & Molnar, 1987; Sillitoe & McKee, 1996; Masterman, 2003). Further volcanic activity is evident locally from the presence of the Huaylillas Formation ignimbrites 24-15 Ma in southern Peru (Clark *et al.*, 1990; Simmons, 2013).

Uplift on this regional scale had major global climatic implications and resulted in widespread desertification of the Atacama (Masterman, 2003). This process caused large scale exhumation and erosion of approximately 1 mm/yr, leading to supergene enrichment of the late Eocene – early Oligocene metalliferous porphyry belt between 29-9 Ma (Hervé *et al.*, 1993; Camus & Dilles, 2001; Masterman, 2003; Arancibia G; Matthews & de Arce, 2006). It is this supergene enrichment which is thought to have helped enhance the economic viability of the copper-rich deposits in northern Chile (Camus & Dilles, 2001). More recently, since approximately 10 Ma, there has been significantly less deformation in the Altiplano region of southern Peru and northern Chile (Mamani *et al.*, 2008). However, interestingly, the convergence rate since 10 Ma has been significantly greater in Peru than northern Chile (Fig1.1); (Pardo-Casas & Molnar, 1987).

The final named orogenic event in the central Andes is known as the Quechua Orogeny and is divided into three pulses: phase 1

between 17-15 Ma; phase 2 8-9 Ma; and the final phase 3, 7-5 Ma (Pfiffner & Gonzalez, 2013). Throughout the wider Quechua orogeny, there was a NE-SW horizontal maximum stress direction in Southern Peru (MéGard, 1987). This led to the reactivation of pre-existing faults such as the major IFS, and to the formation of the Subandean thrust belt in the Eastern Cordillera (Pfiffner & Gonzalez, 2013). From the end of Quechua 1 at approximately 15 Ma, there was the final uplift of the Altiplano plateau which led to its current average height of 4000 m (Roperch *et al.*, 2011).

On the epoch boundary between the Paleogene and Neogene at 23 Ma, the Farallon plate ruptured and became the Nazca plate (Martinod *et al.*, 2010). Horizontal subduction began at 12 Ma for a 1000 km stretch of the north and central Peru. This flat-slab

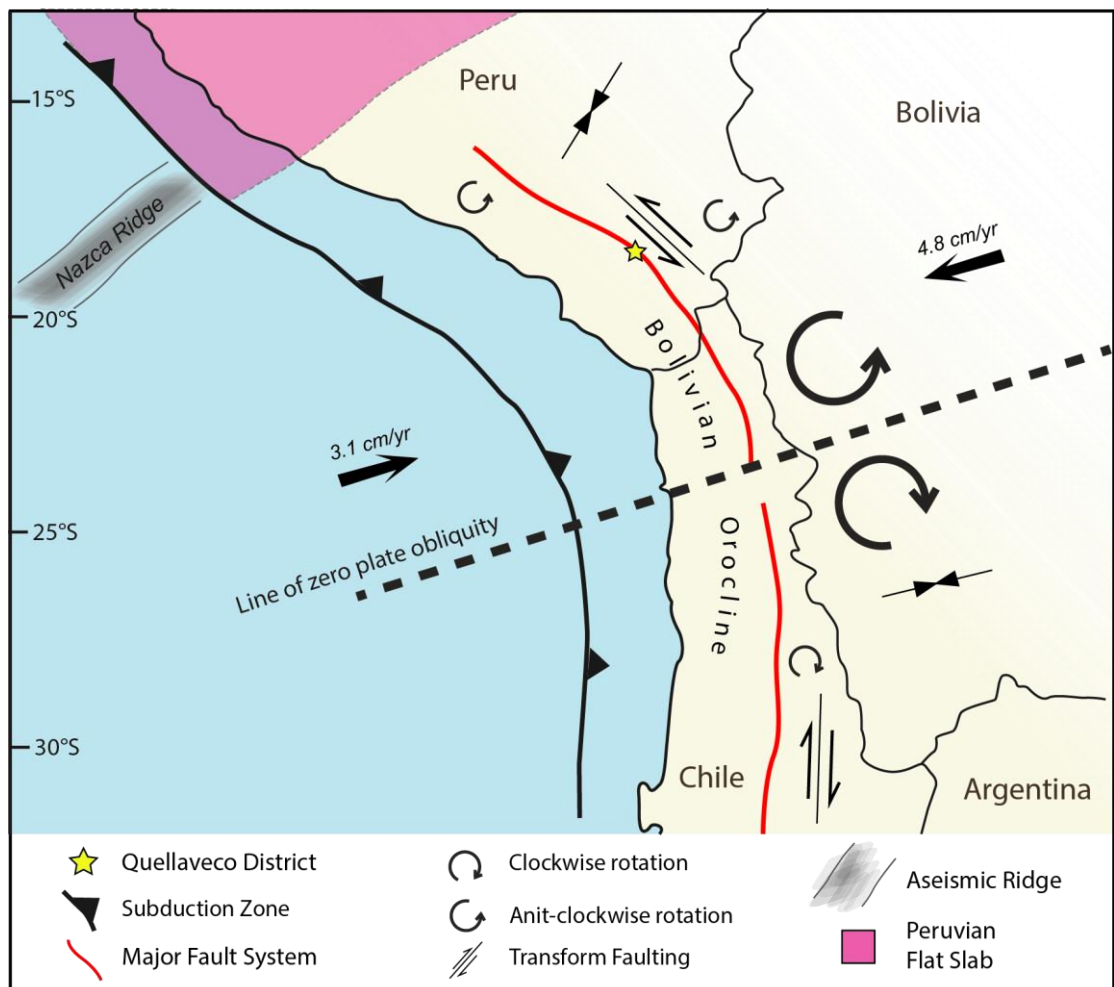


Figure 4.3. (after: Boutelier & Oncken, 2010). Convergence rate of the South American and Nazca plate are 3.1 cm/yr and 4.8 cm/yr respectively (Sdrolias & Müller, 2006 and Horton, 2018)

subduction is deemed to be related to the subduction of two buoyant oceanic ridges: Inca ocean plateau, which is thought to bound the northern edge; and the Nazca Ridge, which coincides with the Southern edge of the flat-slab section (Rosenbaum *et al.*, 2005; Martinod *et al.*, 2010). It is believed that since flat-slab subduction there has been little, or no, rollback of the Nazca plate. This has the potential to accentuate the curvature around the Bolivian Orocline (Schepers *et al.*, 2017). Another horizontal slab, the Pampean slab, developed cogenetically to the Peruvian flat slab in central Chile, which is less geographically extensive than the Peruvian flat slab, but coincides with the current position of the subducting Juan Fernandez ridge (Martinod *et al.*, 2010).

Pliocene – Present (5 – 0 Ma)

Throughout the Pliocene, the architecture of central south America remained recognisable with the present structure. Relative plate motion has been calculated at a constant 7.7 cm/yr, with the subducting plate convergence direction of 79°N (Pardo-Casas & Molnar, 1987; Kley, 1999; Audin *et al.*, 2008). The Bolivian Orocline (17°S-25°S), which is responsible for the identifiable seaward-concave curvature of the ocean trench, formed during the late Eocene and continued to develop the plate boundary during the Pliocene. Its central axis or 'line of zero obliquity' is angled at 79°N, which is the same as the subducting Nazca plate convergence direction.

The use of GPS data on sites north and south of the line of obliquity (e.g Allmendinger *et al.*, 2005) has yielded evidence to the north in Peru and Bolivia of counter clockwise rotation, and clockwise to the south in Argentina and Chile (Figure 4.3). This is due to the interaction of the margin-perpendicular compression in the centre of the orocline with the distribution of these forces on the curvature of the orocline. The plate rotation formed as a result of this trigger's shear traction along the seaward-concave boundary leading to lateral drag (Boutelier & Oncken, 2010). As southern Peru is

situated on the north-western limb of the orocline, the area has experienced significant left-lateral tension along major margin-parallel fault zones, such as the IFS (Kley, 1999; Audin *et al.*, 2006; Boutelier & Oncken, 2010). Therefore, it is a reasonable assumption that the WNW-ESE and NW-SE faults in the Quellaveco region have experienced predominantly sinistral movement since at least the Eocene and the development of the Bolivian Orocline.

4.3 Geology of the Quellaveco District

4.3.1 Lithologies

Toquepala group (90-59 Ma)

The Toquepala Group comprises rhyolitic and dacitic volcanics that began in the late Cretaceous, 75 Ma, and continued into the Palaeocene, 59 Ma (Clark *et al.*, 1990), although some studies (e.g. Demouy *et al.*, 2012; Simmons, 2013) give a much larger scope, 90-45 Ma for this volcanic arc activity. The Toquepala group is a predominantly volcanic group with a progression from basic basalt/trachybasalt, to more evolved, but much less laterally continuous, rhyolitic flows (Simmons, 2013). The group is divided into four formations: Huaracane (oldest); Ingoya; Paralague; and Quellaveco (youngest). Within the Quellaveco formation there are five members (from oldest to youngest): Asana, Carpanito, Samanape, Yarito, Tinajones (Bravo, 1979; Martinez & Zuloaga, 2000; Martinez & Cervantes, 2003).

The primary compositions of these members are: the Asana Mb - light grey, porphyritic layers of rhyolite lavas; Carpanito – dark grey, stratified layers of plagioclase-rich lavas; Samanape – intercalated rhyolites and andesite lava with minor interspersed tuffs and lapilli; Yarito – porphyritic grey/pink lavas; and Tinajones – quartz-rich coherent layers of rhyolite lava (Martinez & Zuloaga, 2000).

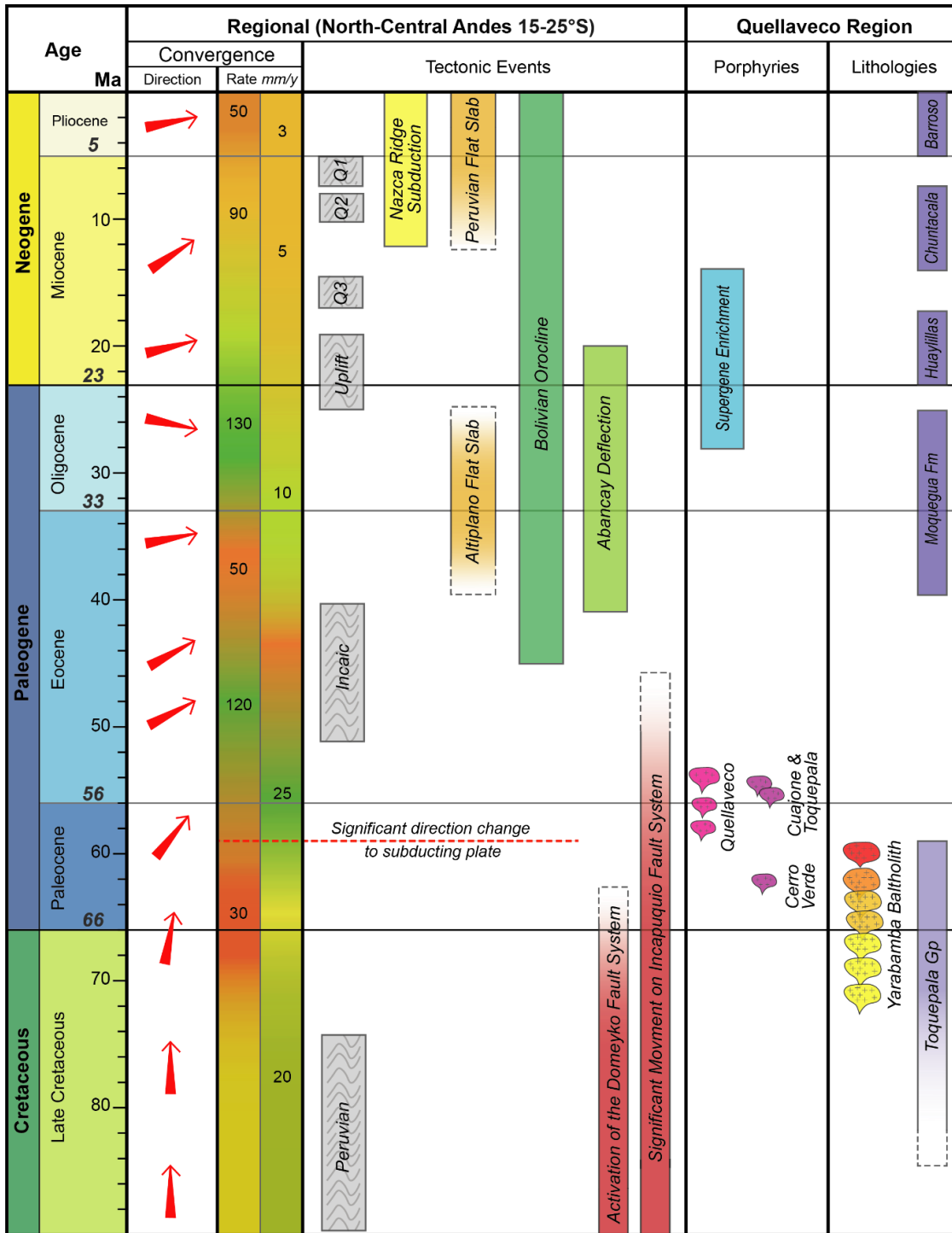


Figure 4.4. Timeline compiling data of major tectonic events in the central Andes. Plate convergence rate is divided in the columns: on the left, represents the Nazca Plate (Sdrolias and Muller, 2006); on the right, represents the motion of the South American Plate (Horton, 2018). The red arrows illustrate the convergence direction of the subducting South America Plate (Pardo-Casas & Molnar, 1987; Chen et al., 2019; Piffner & Gonzalez, 2013; Jaillard et al., 2000; Boutelier & Oncken, 2010; Clark et al., 1990; Horton, 2018; Jacay et al., 2002; Martinod et al., 2010; Quang, 2003; Schepers et al., 2017; Simmons, 2013b; Mpodozis et al., 2005).

Yarabamba Batholith, Coastal Batholith (71-59 Ma)

The Coastal Batholith is a trench-parallel intrusive complex which extends 1600 km through Peru into Ecuador comprising over 1000 plutons (Mukasa, 1986). Gravity profiles suggest an approximate thickness of 2-3.2 km, with the 'root' thickness of 4-10 km wide (Haederle & Atherton, 2002). Plutons locally to Quellaveco are seen to cross-cut, and be hosted by, the Late Cretaceous-Early Paleocene volcanics of the Toquepala Group (Sillitoe & Mortensen, 2010).

It is believed that the Coastal Batholith formed from two major pulses: 200-175 Ma consisting of gabbros and diorites; with a significantly younger, and more notable pulse at 90-60 Ma (Demouy *et al.*, 2012). It is this younger pulse that is dominant in southern Peru, and therefore of interest in this study. The emplacement of this younger pulse occurred in two main magmatic events between 90-76 Ma and 68-60 Ma (Demouy *et al.*, 2012).

Many of the Coastal Batholith plutons have retained their form with very little internal deformation, unlike many batholiths along the western coast of the Americas, many of which are dissected. This has suggested approximately perpendicular subduction of the Nazca plate and little effect of subsequent tectonic events since the time of emplacement (Mukasa, 1986; Pfiffner & Gonzalez, 2013). However, other studies (e.g. Jaillard *et al.*, 2000; Jacay & Sempere, 2005) have suggested that certain suites of the Coastal Batholith have experienced levels of deformation, such as high strike-slip rates between 68-64 Ma. Another indication of structurally influenced emplacement and subsequent deformation is the noted NE-SW alignment of certain plutons and dykes. This would indicate NW-SE extensional forces during the emplacement of some of the Coastal Batholith (Jacay & Sempere, 2005).

The Quellaveco deposit is centered on a multiphase quartz monzonite pluton of the Yarabamba superunit which forms part of

the Toquepala segment of the Coastal Batholith (Mukasa, 1986; Sillitoe & Mortensen, 2010). Hosted by the Toquepala Group volcanics, the Yarabame Batholith emplacement ages range from 71-59 Ma and are sub-divided into four suites: Precursor (66-71 Ma); Parental III (69-64 Ma); Parental II (64-60 Ma); and Parental I (60-59 Ma). Structural features of these largely monzodiorite and granodiorite plutons include steep contact walls and margin-parallel, NW-SE elongation with some intrusions described as 'bell-jar shaped' (Mukasa, 1986; Demouy *et al.*, 2012). Intruded within the Toquepala Formation, and host to the Quellaveco porphyry deposit, is the Regional Granodiorite Batholith. With an approximate size of 2.5 by 5 km, this large batholith is elongated NW – SE (Simmons, 2013).

Moquegua Formation (50-25 Ma)

The Moquegua formation comprises volcano-sedimentary units of fore-arc basin fill during the Eocene and Oligocene (Roperch *et al.*, 2011). The formation is divided into two: the Lower Moquegua formation which represents volcanics from 50-45 Ma; and the Upper Formation units predominantly made of conglomerates with volcanic clasts, and blanketed by a 25 Ma tuff (Noble *et al.*, 1985; Clark *et al.*, 1990). The hiatus in deposition that defines the Upper and Lower Moquegua formations is thought to represent erosion following the Incaic Orogeny (Noble *et al.*, 1985).

Miocene Volcanics (24-Present)

Post-mineralisation Miocene volcanic and sedimentary rocks of the Miocene Huaylillas and Chuntacala Formations cover the northern part of the Quellaveco deposit (Sillitoe & Mortensen, 2010). Particularly prevalent are the ignimbrite deposits Huaylillas Formation, evidence of which can be traced as far as parts of northern Chile (Charrier *et al.*, 2013). Ages of these formations have been dated between 24-15 Ma for the Huaylillas Fm and an approximate age of 14-9 Ma for the Chantacala Fm felsic volcanics and sedimentation (Clark *et al.*, 1990; Simmons, 2013).

Pliocene and Quaternary deposits locally present at Quellaveco include that of the Barroso Group andesitic-dacitic volcanism. These large stratovolcanoes have been present since 5.3 Ma (Clark *et al.*, 1990).

4.3.2 Structural Geology

Quellaveco deposit is part of the Eocene metallogenic belt. Preceding the emplacement of mineralisation, there were two principle orogenic events: the Peruvian Orogeny at 84-79 Ma; and the Incaic Orogeny at 59-55 Ma. Towards the end of the Incaic Orogeny major porphyry cycles occurred between 57-52 Ma at the end of the short-lived tectono-magmatic cycle. This was followed by the shallowing of the subducting plate (Richards, 2003).

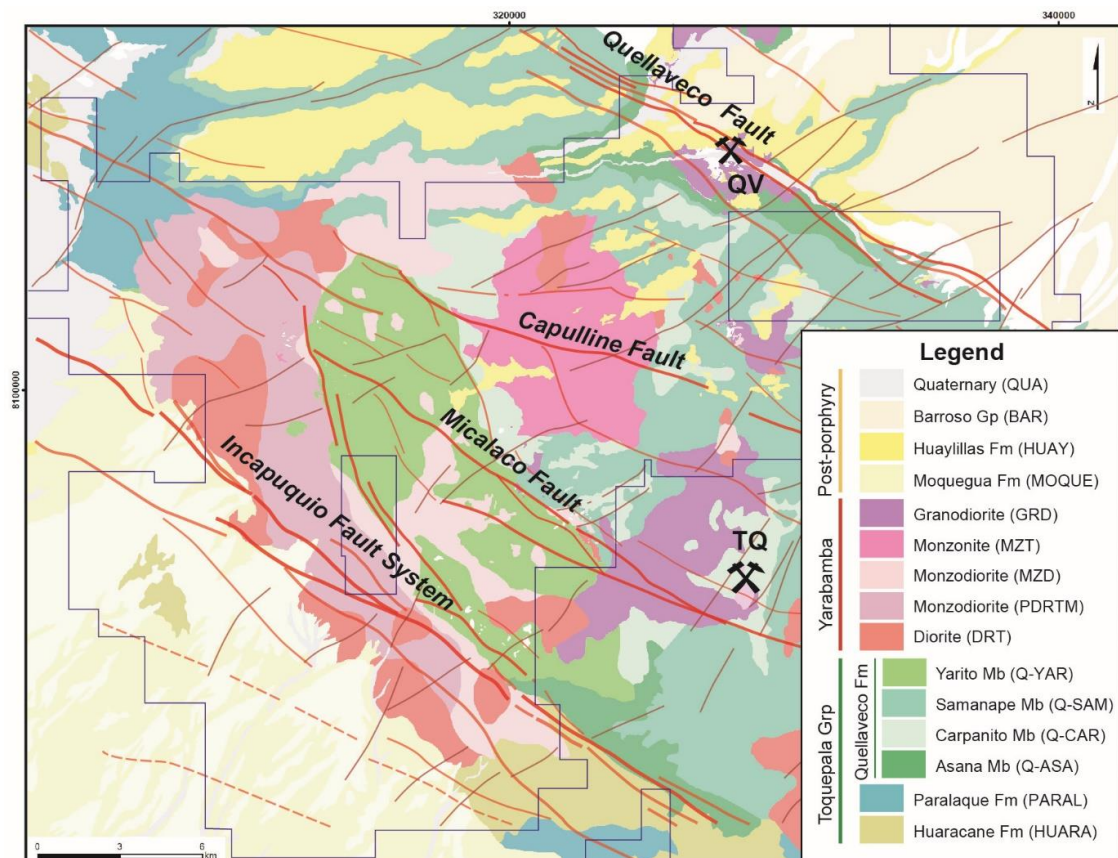


Figure 4.5. Lithology map of the Quellaveco region with major NW-SE trending faults mapped and labelled. The Anglo-American Licence is drawn blue for reference. This data has been provided by Anglo American.

The piedmont of the Western Cordillera in southern Peru, where Quellaveco is situated (Figure 4.1), is controlled by the 400 km-long Incapuquio-Challaviento Fault System, otherwise known as the Incapuquio Fault System (IFS); (Jacay *et al.*, 2002). Reaching widths of >10 km, this N125E-trending transcurrent system has a sinistral sense of movement (Figure 4.6) although the structure can be seen to vary along strike (Jacay *et al.*, 2002). Thought to have initially activated during intense transpression in the late Cretaceous, extensive subsidence during the Jurassic caused the formation of the IFS along the NE inverted edge of the Arequipa Basin in southern Peru (Sempere *et al.*, 2002). Features along the IFS indicate that this fault system has been a part of a transcurrent tectonic regime since then, remaining active throughout the intrusion of the Late Cretaceous-Early Paleogene magmatism. This tectonism is also believed to have facilitated and controlled the abundant magmatism responsible for the mineralization at Quellaveco and the neighbouring deposits (Sandeman *et al.*, 1995; Jacay

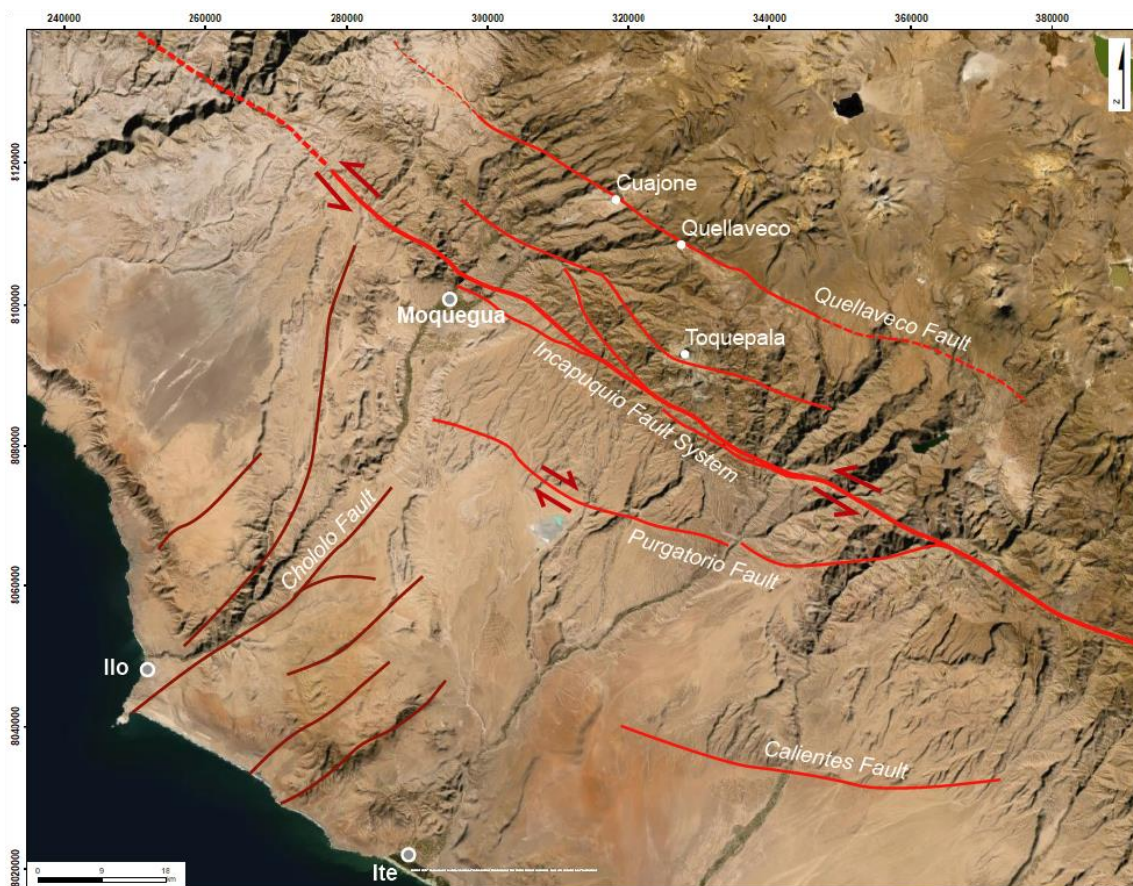


Figure 4.6. Satellite imagery highlighting major faults in the Moquegua region. The crust-scaled Incapuquio Fault System (IFS). A splay of the IFS Purgatorio Fault (Audin *et al.*, 2008; Audin *et al.*, 2006)

et al., 2002). Richards (2003) highlights the significance that Toquepala is situated on the intersection between NNE-trending faults and transverse NE-SW faults. Conversely, some authors (e.g Hoyt, 1965) state that the tectonics only play a minor role in the localisation of deposits, and although the deposits in Southern Peru appear to have some connection to the tectonics, it is only as a facilitator of pathways for fluid and intrusion movement, and not by localising mineralisation. Although the consensus is that structures of the IFS at least facilitated ore-related magmatism in southern Peru, the exact timings of the multiphase movement and reactivation along the IFS are poorly constrained (Jacay *et al.*, 2002).

The Eocene-Present development of the Bolivian Orocline has significantly influenced the tectonics regime in the latitudes north and south of the line of zero obliquity (Boutelier & Oncken, 2010). Regional crustal rotation on a vertical axis has been particularly prominent in the furthest regions of the Altiplano, therefore in southern Peru (Kley, 1999; Allmendinger *et al.*, 2005). The counter-clockwise rotation in southern Peru is accommodated by the sinistral transpression of crustal scale faults, in particular the IFS, and smaller pre-existing fault structures have led to the continued sinistral movement of the IFS (Audin *et al.*, 2006; Roperch *et al.*, 2006; Boutelier & Oncken, 2010).

The IFS system and related parallel and transverse faults are still seismically active (Jacay *et al.*, 2002). A series of coastal- and IFS-perpendicular faults, such as the Cholero in the Moquegua valley (Figure 4.6), have evidence of recent and extensive movement and earthquake rupture (Audin *et al.*, 2008). These NE-SW predominantly sinistral transpressive faults have displaced Quaternary deposits and Coastal Batholith intrusives, thereby indicating high activity during the Holocene. This recent displacement is more noticeable in the NE-SW faults than the margin-parallel faults, NW-SE (Audin *et al.*, 2008). In the last 100 years, the Moquegua region has experienced 6 major earthquakes with magnitudes from 7.7 – 8.4 Mw (Audin *et al.*, 2008).

4.3.3 Mineralisation

The Quellaveco Intrusive Complex (QIC) is formed of 30 to 40 individual magmatic centers that follow a general NW-SE orientation. Porphyry stock emplacement occurred between 58.4 to 54.3 Ma, with the majority of Cu took place during the initial 2.5 ± 0.6 m.y. This is thought to be a longer period of Cu mineralisation than neighbouring deposits Toquepala and Cuajone (Sillitoe & Mortensen, 2010; Simmons *et al.*, 2013). The QIC is comprised of five significant suites which are defined based on chronology and texture (oldest-youngest): Earliest Porphyry; Early Porphyry; Intermineral Porphyry; Monzodiorite; and Late Porphyry: (Simmons, 2013). All the porphyry phases are petrographically similar, so distinguishing between the phases is often based on field observations and genetic relationships (Sillitoe & Mortensen, 2010; Simmons *et al.*, 2013).

Earliest Porphyry

The Earliest Porphyry (or 'Early' in Sillitoe and Mortensen, 2010), is 58.5-57.5 Ma Dated by Simmons (2013) the earliest porphyry ranges in composition from monzodiorite to quartz monzonite. Previous dates for this porphyry suite include those from Sillitoe and Mortensen (2010) at 59.46 ± 0.24 Ma. The xenoliths of the earliest porphyry show type-A and type-B veinlets, despite predominantly occurring as xenoliths within intrusions of the early porphyry, and therefore having a low volumetric presence (Sillitoe & Mortensen, 2010; Simmons, 2013).

Early Porphyry

The Early Porphyry intrusions are dated at 56.6-55.9 Ma, and are volumetrically the most important as the associated NW-SE elongated dykes contribute to nearly half of all the suites (Simmons, 2013). The intrusions are characterised by quartz monzonite to granodiorite compositions, with a large phenocryst of quartz, plagioclase, K-feldspar and minor hornblende (Simmons *et al.*, 2013). A substantial amount of the copper mineralisation is associated with this phase, 0.4 – 0.6 % Cu, and is linked with an

intense potassic alteration. Typical vein associations include A-type chalcopyrite-bearing veins; molybdenum bearing quartz B-type veins; and later stage quartz-pyrite-chalcopyrite veinlets with sericitic halos (Gustafson & Hunt, 1975; Sillitoe & Mortensen, 2010). The quartz-sulphide veinlets with sericitic alteration are much more prominent with increased elevation (Simmons, 2013).

Intermineral Porphyry

The bulk of the Cu and Mo precipitation followed the emplacement of the intermineral and early porphyry phases, ensuring that this is the second most important phase for Cu-mineralisation at Quellaveco, with 0.4-0.6 % Cu content (Simmons, 2013; Simmons *et al.*, 2013). It is thought that the intermineral porphyry was emplaced following the precipitation of three quarters of the copper (Sillitoe & Mortensen, 2010). Veining associated with this suite include minor A-, B- and D- veinlets, but these occurrences are infrequent. The veinlets have weak or no potassic alteration but commonly cross-cut most of the pre-existing potassic and sericitic alteration (Sillitoe & Mortensen, 2010). A vertical segregation of vein types associated with the Intermineral porphyries have been noted indicating a noticeable evolution of vein assemblage and structure from the center of the porphyries. Depth zonation observations include: veins which are predominantly wavy at depth closer to the system, becoming straighter with increased elevation; and vein halo/wall rock alteration changing from potassically altered (K-felspar and biotite) to quartz-sericite with remnant patches of potassic alteration above 3000 m (Simmons, 2013).

Monzodiorite

The monzodiorite suite has been dated at 55.2-57.2 Ma, and contains rocks of monzodiorite-Qtz Monzonite compositions (Simmons, 2013). These intrusions are generally narrow (1-20 m), and therefore not visible on a deposit scale. Volumetrically, this suite is very low, and copper occurrence is minimal, however, copper grade can vary from 0.4 - >1 %, thereby increasing the

importance of this suite (Simmons, 2013). Wavy, non-linear veins are abundant, with biotite- and magnetite-bearing veins seemingly the most important. The alteration of Bt-Kfs \pm Mag with later Qtz-sericite alteration is a distinguishing feature of the rocks in this suite (Simmons, 2013).

Late Porphyry

The Late Porphyry (54.34 Ma) displays weak propylitic alteration, and post-dates all potassic and sericitic alteration, and nearly all the mineralisation. This suite supplies up to 10% of the intrusions, and contains only 0.01 % Cu (Sillitoe & Mortensen, 2010; Simmons, 2013). Distinguishing features of veinlets associated with this suite include the decline of apparent copper, the decrease of intense alteration, with the presence of weak propylitic alteration and pyrite veining (Sillitoe & Mortensen, 2010). The veins associated with this suite are principally linear.

4.3.4 Alteration

Hypogene

First hydrothermal alteration is thought to have occurred following the 'earliest porphyry' (Simmons, 2013). Potassic alteration with K-feldspar, secondary biotite is located in the centre of the deposit with substantial overprinting by pervasive phyllic alteration (Martínez-Valladares *et al.*, 2017). From temporal relationships, significant potassic and sericitic alteration occurred prior to the Intermineral porphyry with only minor alteration occurring during the Intermineral porphyries (Sillitoe & Mortensen, 2010). The fluid responsible for mineralisation and potassic and sericitic alteration occurred at temperatures between 590°C to 340°C.

Two distinct phases of propylitic alteration are identified at Quellaveco: (1) pyrite-bearing alteration attributed to the precursor granodiorite in the wider propylitic halo; and (2) a weak alteration associated with the Late Porphyry phase (Sillitoe & Mortensen, 2010). Potassic alteration within the parent granodiorite grades

outward to wider propylitic alteration, which outlines the limits of the deposit alteration halo (Sillitoe & Mortensen, 2010). The wider propylitic alteration (1) is particularly prevalent in areas of mostly mafic host lithologies, with mafic minerals altering to epidote, chlorite and biotite (Simmons, 2013).

Supergene

The hypogene mineralisation at Quellaveco, and neighbouring deposits, Cuajone and Toquepala, has been recorded to have been significantly enhanced by later supergene alteration (Clark *et al.*, 1990). Following the cessation of the main mineralisation phase at approximately 52 Ma, volcanics of the Toquepala Group, part of a continental volcano-plutonic terrane, dominated the area during the dextral transpression of the Incaic Orogeny (Pardo-Casas & Molnar, 1987; Clark *et al.*, 1990; Quang *et al.*, 2005). Strong transpressional tectonics in the late Eocene – Oligocene caused significant uplift of the Cordillera Occidental and resulted in semiarid climatic conditions (Clark *et al.*, 1990). The combination of the uplift and arid conditions between 29-9 Ma proved optimal for supergene alteration, and this enrichment is seen in many of the porphyry deposits in southern Peru and northern Chile (Clark *et al.*, 1990; Camus & Dilles, 2001; Masterman, 2003). The trough-like, 80 m-thick enrichment blanket produced is divided into two zones: an upper strongly to moderately enriched zone; and a lower zone with minor mineralisation which transitions to unaltered hypogene ores (Clark *et al.*, 1990). This leached blanket consists of sericite, kaolinite, hematite, goethite and jarosite with minor turquoise malachite (Martínez-Valladares *et al.*, 2017). The enrichment blanket is locally displaced by 75 m by an E-W trending fault in the north of the deposit: the Rio Asana-parallel fault, the Quellaveco Fault. This movement is likely to have occurred since 9.5 Ma, where the deposit was blanketed by the Chuntacala tuff and there is no further evidence of massive chalcocite enrichment (Clark *et al.*, 1990).

4.3.5 Neighbouring Deposits

Two known deposits, Cuajone and Toquepala, are proximal to Quellaveco with similar intrusive and mineralisation histories. For both deposits, the youngest porphyry occurs 1-2 Ma after the main mineralisation event and is significantly altered to quartz-sericite-pyrite assemblages. Hydrothermal systems at the three deposits are part of a protracted, but episodic magmatic event (Simmons, 2013). Both deposits are operated and mined by Southern Peru Copper Corporation, and are associated with IFS-parallel subsidiary faults, such as the Quellaveco fault (Tosdal, 2005).

Cuajone

Cuajone is Quellaveco's geographically closest neighbor at 17°02' S - 70°42' W), to the north-east along the Quellaveco Fault. There is a close relationship between Cuajone and Toquepala deposits, with Cuajone having four distinct magmatic events, but which occurred over a longer period than Toquepala, 13 My (Simmons, 2010). Three temporally discrete events have been recognized: 65 Ma pre-mineral event, 56 Ma mineralised porphyry, 53 Ma late-mineral (Clark *et al.*, 1990; Simmons, 2013). In a period terminating at 22.8 Ma, chalcocite supergene enrichment developed at Cuajone although much less enrichment is seen at Cuajone than Quellaveco or Toquepala. This secondary enriched chalcocite zone is approximately 20 m, significantly thinner than at Quellaveco, with a gentle dip of 4° to SW (Clark *et al.*, 1990; Tosdal, 2005; Quang *et al.*, 2005). Supergene alteration is thought to have been protected from erosions at Cuajone in the middle Miocene because of a thick layer of the Chuntacala ignimbrite flows. However, post-13 Ma erosion lead to the removal of part of the Chuntacala cover supergene profile (Quang *et al.*, 2005). Supergene enrichment is likely to have renewed after this period of erosion (Clark *et al.*, 1990).

Toquepala

Situated approximately 23 km southeast of Cuajone (17°15' S - 70°37' W), Toquepala is located on the WNW-ESE Micalaco Fault. Four distinct magmatic events have also been recognised at Toquepala, but these occurred during a shorter magmatic period. Like Cuajone, there are three significant intrusive events: pre-mineral at 62 Ma; the mineralised porphyry at 57 Ma; and the late-mineral event at 54 Ma (Simmons, 2010). The shallow nature of the deposit is likely to have contributed to a clear structural control on the mineralisation particularly localizing in the intersections between NW-SE and NE-SW tensional faults (Zweng and Clark, 1995).

Of the three deposits, Toquepala displays the most extensive record of supergene enrichment with multiple enriched blankets at Toquepala. A number of factors contributed to the prevalence of the deposit's enrichment (especially compared with Cuajone), such as: the open valley nature of the topography in the middle Miocene; and the brief period of volcanic deposition as opposed to protracted volcanism at Cuajone (Clark *et al.*, 1990).

Cerro Verde-Santa Rosa District

The Santa Rosa hydrothermal system is situated 120 km north-west along strike from the Cuajone-Quellaveco-Toquepala systems (16°33' S - 70°34' W), and comprises Cerro Verde, Santa Rosa and Cerro Negro deposits. ⁴⁰Ar-³⁹Ar dates yield mineralisation ages of 62 Ma for the deposits (Quang, 2003). Although this system is not technically directly 'neighbouring' the Cuajone-Quellaveco-Toquepala system, it displays comparable characteristics such as the similarity in age and falls within the Palaeocene-Eocene metallogenic belt of South America. One important characteristic is its location on the northern-most section of the steeply-dipping IFS. A detailed study by Quang (2003) emphasises a strong structural control on the mineralisation, and alteration, of the Cerro Verde and Santa Rosa deposits. The hydrothermal system and associated

alteration is elongated in the NW-SE direction of the IFS with a halo of 5 km along strike and 1.5 km perpendicular. Mineralisation is located in the intersections of NW-SE and tensional NE-SW faults. NW-SE faults are cross-cut by reactivated NE-SW and E-W tensional faults.

4.4 Summary

- Quellaveco Cu-Mo porphyry is located in the Palaeocene-Eocene metallogenic belt of southern Peru. Porphyry emplacement associated with the mineralisation occurred over ~4 My.
- Since the Cretaceous period, South America has experienced a complex tectonic history which has resulted in the wealth of mineralisation along the western boundary. Following the breakup of Gondwana and initiation of subduction of the Farallon plate beneath the South American Plate, there were two major rotations in absolute plate motion of the subducting plate 59.5 Ma and 49.5 Ma. The increase in obliquity appears to have triggered melting, which subsequently formed Palaeocene-Eocene deposits such as Quellaveco, and orogenies such as the Incaic.
- The Eocene development of the Bolivian Orocline in the central Andes has defined the tectonics north and south of the line of zero obliquity. Anti-clockwise rotation to the north has resulted in continued left-lateral transtension on most of the major NW-SE structures, such as the Incapuquio Fault System.
- Quellaveco and its neighbouring deposits (Toquepala, Cuajone and Cerro Verde-Santa Rosa) are located on subsidiary WNW-ESE/NW-SE faults of the crustal-scale sinistral Incapuquio Fault System.
- The emplacement of the Quellaveco Intrusive Complex spanned a 6 m.y period, comprising five chronological and textural suites (oldest-youngest): Earliest Porphyry; Early Porphyry; Intermineral Porphyry; Monzodiorite; and Late Porphyry. The Early and Intermineral Porphyries contain the highest grade of copper.

5 Alteration in the Quellaveco District

5.1 Aims

The purpose of this chapter is to characterise the alteration that is present in the Quellaveco region, with particular focus on the district-wide propylitic alteration and associated veining. The main objectives and guiding questions are:

- Categorise the alteration textures and the alteration mineral assemblages in each lithostratigraphic unit. Do the host lithology and relative ages impact the alteration assemblages seen?
- What are the main vein types and are they restricted to particular lithologies?
- Determine the petrographic characteristics of specific minerals that are used for further analysis in the study: apatite, titanite, chlorite, epidote and zircon. Are these minerals igneous or hydrothermal, or igneous with a hydrothermal overprint?
- Does the initial mapping of alteration infer any potential spatial or temporal relationship with structures or intrusives?

5.2 Introduction

As discussed in the methodology section in Chapter 3, 107 samples were taken along two NE-SW trending transects in the wider district of Quellaveco. A subset of 84 samples, covering a combined distance of 48 km, were analysed in detail. The geographic extent of this sample collection in this study (Figure 5.1) has resulted in a diverse and representative sample of the host lithologies in the area: the Toquepala Group volcanics and Yarabamba Batholith.

The central objective of the study, to develop a model for district-wide propylitic alteration, requires detailed, in situ, isotopic and elemental analysis of key minerals from the sample suite collected. Therefore, to be able to properly interpret the geochronological and geochemical data reported in Chapters 7 and 8 requires the textural context of each mineral grain to be fully understood to discriminate between the multiple possible origins that may exist in altered

igneous rock samples. Consequently, each mineral that has been analysed by SEM-EDS and LA-ICP-MS is categorized into one of the groups described in sections 5.3 and 5.4.

5.3 Recognition of primary igneous and secondary alteration minerals

The range of igneous samples from the Toquepala Group and the Yarabamba Batholith has resulted in a variety of igneous mineral assemblages. These assemblages have experienced different intensities of alteration. Therefore, some samples may contain a mixture of minerals from igneous or hydrothermal stages, or potentially igneous minerals that may have been modified by the interaction with hydrothermal fluids. To differentiate between the mineral assemblages, three classifications have been created: Ig (for igneous minerals); Alt-Ig (for altered igneous minerals); and eight hydrothermal classes from A1-A8.

These classifications are particularly important as this study aims to constrain the timing of propylitic alteration events using four minerals: epidote, titanite, apatite and zircon. Chlorite is also a mineral of particular interest to this study as, along with epidote, it will be used for geochemical mineral analysis in Chapter 8. Each of these minerals needs to be texturally defined into the listed categories. The former two minerals, epidote and titanite, are only observed in propylitic assemblages so are demonstrably of hydrothermal origin. However, in addition to hydrothermal, zircon and apatite occur as primary igneous phases.

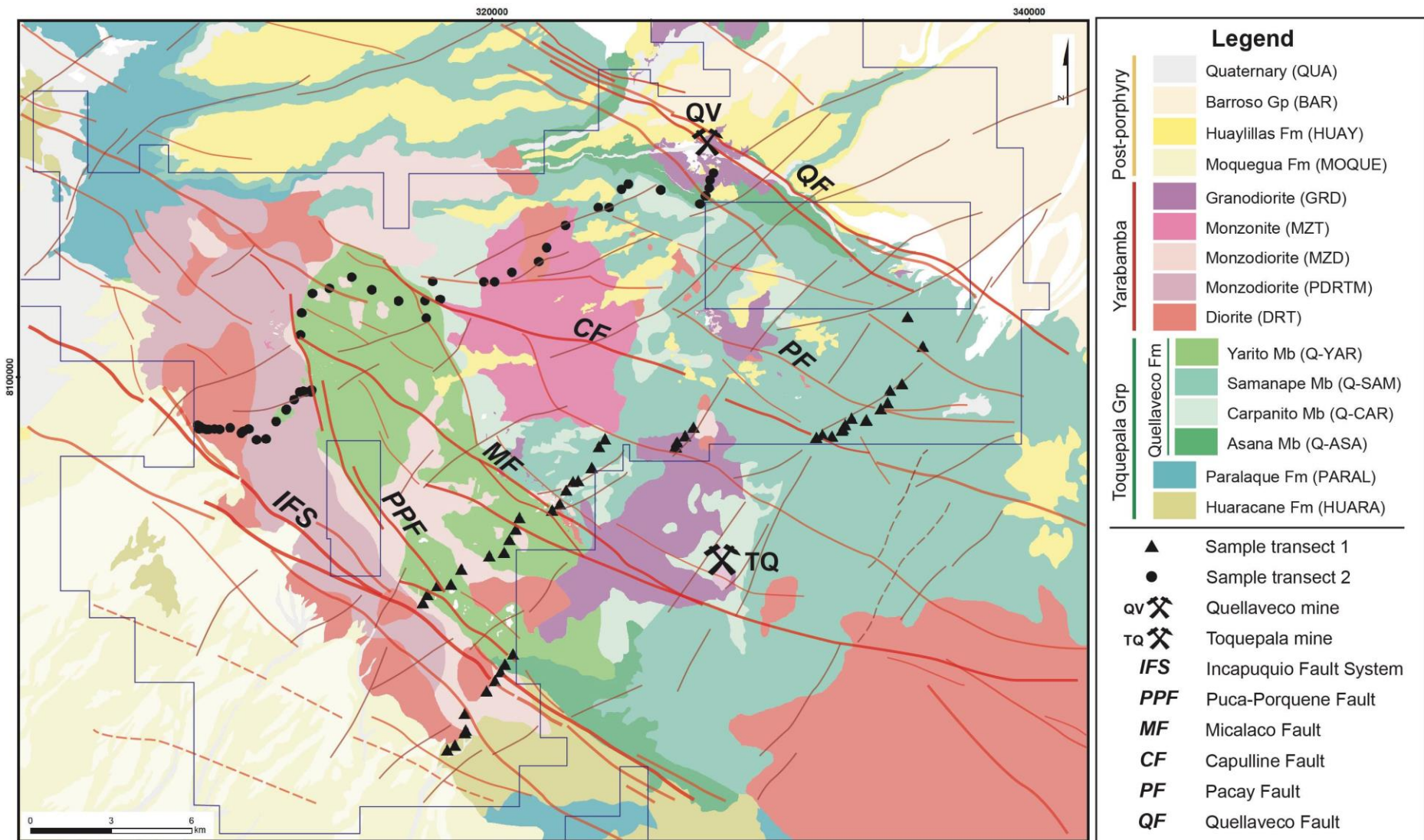


Figure 5.1. Geological map of the Quellaveco region with sample localities from transect 1 and 2 marked.

5.3.1 Primary igneous minerals

Of the five minerals used for further analysis, igneous only examples of apatite and zircon have been texturally identified. These grains have been labelled with the suffix 'lg' for geochronological and geochemical purposes later in the study.

Apatite_{lg}

Igneous apatite (apatite_{lg}) grains can be distinguished by several characteristics. Generally, the grains are smooth, euhedral and clearly display their octagonal crystal habit. These grains are mostly large (150-400 µm but may exceed 500 µm), individual grains, occurring as phenocrysts (Figure 5.2a). Finer-grained microphenocrysts are also observed in the groundmass. Seemingly unaltered grains of this kind are most common in unaltered to weakly propylitically altered samples.

Zircon_{lg}

Primary igneous zircon (zircon_{lg}) is fairly abundant in most of the lithological units, irrespective of the nature and style of alteration. The distribution of these zircons demonstrates no preferential association with specific minerals or alteration assemblages and occur in a variety of sizes from small (<20 µm) angular grains within the groundmass (Figure 5.2b) to larger (400-600 µm) euhedral phenocrysts. A specific form exhibited by zircon should be noted: several grains exhibit a 'skeletal' texture (Figure 5.2c). This could be the result of primary igneous growth or due to the partial destruction of the grain, leaving specific remnants of primary growth zones.

5.3.2 Overprinted igneous minerals

It has been recognized that it is important to distinguish between primary igneous minerals and those that are likely to be igneous but which may have been affected by subsequent hydrothermal alteration events. Zircon is considered to be very resistant to diffusional modification, especially at lower hydrothermal temperatures (Watson & Harrison, 1983; Frost *et al.*, 2000; Watson *et al.*, 2006; Bernini *et al.*, 2013) and so, except in the cases noted above where partial dissolution has occurred, is not included in this category. However, apatite, is known to be relatively easily modified during

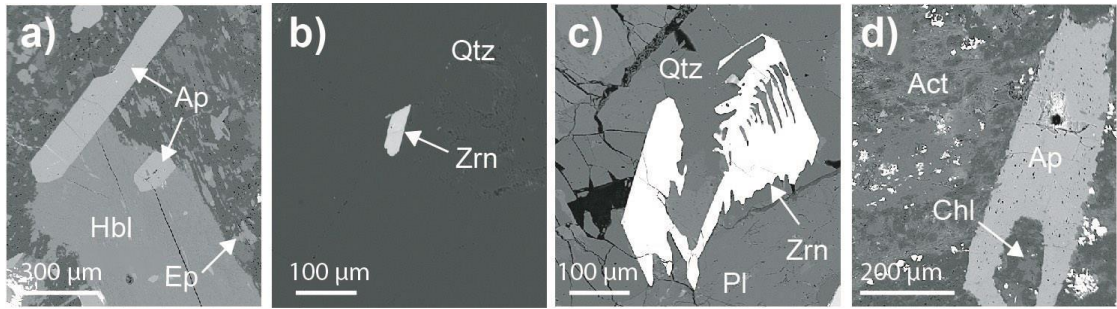


Figure 5.2. SEM-BSE images showing igneous and metasomatic examples of dated minerals: **a**) euhedral, primary apatite_{lg} grain (RCS079); **b**) euhedral zircon grain (RCS028) **c**) a large zircon_{lg} with partial dissolution of original zones resulting in a 'skeletal' texture (RCS046); **d**) a coarse apatite_{lg-alt} grain with pitted texture (RCS017);

hydrothermal events (Belousova *et al.*, 2001; Bouzari *et al.*, 2016; Brugge, 2020) as witnessed by the development of complex cathodoluminescence textures and textural changes, so is considered here.

*Apatite*_{lg-alt}

Altered igneous apatite (apatite_{lg-alt}) demonstrates many of the same characteristics as apatite such as large grain size (sometimes >500 µm) and evidence of a primary igneous habit. However, apatite has a mottled and porous appearance and the grain edges are typically ragged and partially intergrown with surrounding alteration minerals (Figure 5.2d).

5.4 Pervasive hydrothermal alteration

Alteration assemblages have been classified into eight groups (A1-A8) based on textural evidence and mineral assemblage. A condensed summary of the hydrothermal occurrences of epidote, titanite, apatite, zircon and chlorite have been collated in Table 5.1 for later geochronological and geochemical reference.

5.4.1 Potassic (A1)

Two 'phases' of potassic alteration have been identified, however the most common standard phase is the 'early potassic'.

Early potassic

Potassic (A1) alteration is mostly represented by assemblages of Kfs-Qtz-Bt-Mag±Ccp±Cv. Secondary K-feldspar has replaced original plagioclase. Minor secondary, shreddy biotite is present, which has overprinted igneous biotite phenocrysts; however, this

has been widely retrograded to chlorite during later epidote-chlorite alteration assemblages. In some cases, there is evidence of later sericitic alteration.

Remnants of potassic alteration are particularly seen in monzodiorite (DRTM) and granodiorite (GRD) lithologies of the Yarabamba Batholith and the Samanape member (SAM) of the Toquepala volcanics. The potassic assemblage in the GRD includes K-feldspar-quartz-magnetite and, in the porphyry-proximal samples, secondary Cu-rich minerals after chalcopyrite. There are traces of initial potassic alteration in a couple of samples, where K-feldspar and disseminated magnetite are dominant throughout the groundmass. K-feldspar forms a rimmed texture around quartz. Potassic alteration in the Samanape member is characterised by near complete replacement of plagioclase phenocrysts by K-feldspar and quartz blebs. All observed SAM occurrences of potassic alteration have experienced later epidote-titanite-albite (A5) alteration, mostly manifested by the partial overprinting of groundmass and phenocryst K-feldspar by albite, with the production of myrmekitic and micro-myrmekitic textures.

Later potassic

This phase of potassic alteration is distinguished from the 'early potassic' because of its relative timing to the other alteration types listed. There are a couple of samples which exhibit a potassic alteration which is characteristically distinct from the 'early' potassic phase, and there has been separately acknowledged. Similarly to the early potassic alteration, the constituent minerals are K-feldspar-quartz-magnetite. K-feldspar and quartz have partially replaced albite and actinolite in the groundmass from a previous actinolite-facies alteration. In one example, K-feldspar is observed overprinting actinolite-epidote (V3) veining (Figure 5.3a). Discontinuous apatite along a small fracture is partially overprinted by quartz and K-feldspar, which is another indication of a younger

potassic alteration event. The relative temporal relationship of the later potassic alteration is discussed further in section 5.7.

5.4.2 *Actinolite propylitic (A2)*

This alteration facies is principally composed of actinolite-albite-apatite-titanite, sometimes with the presence of chlorite and pyrite. A2 is characterized by partially altered plagioclase laths and phenocrysts with albite. Actinolite, albite and apatite have pervasively altered the groundmass. Where albite has interacted with K-feldspar in the groundmass, a distinct myrmekitic texture resides (Figure 5.3c). In some samples, however, the majority of the alteration minerals are contained within actinolite-altered mafic phenocrysts. Titanite has typically partially replaced igneous titanomagnetite, often leaving remnant linear strips of the original crystal. It is intergrown with actinolite, granular hydrothermal magnetite and sometimes chlorite. Hydrothermal apatite is very abundant in this facies, often occurring as: massive apatite patches incorporating acicular actinolite, magnetite and titanite; ragged grains intergrown with actinolite and magnetite in the groundmass; or an interstitial mass surrounding partially altered plagioclase phenocrysts (Figure 5.3b). Anhedral patches of chlorite are closely associated with actinolite, titanite and magnetite alteration of the groundmass and mafic phases.

5.4.3 *Epidote-actinolite propylitic (A3)*

The main difference between A2 and A3 alteration is the presence of epidote in A3. The strength of alteration is generally stronger in samples containing this assemblage relative to A2, with strong albitization of the groundmass and any plagioclase phenocrysts are fully or partially altered with an albitized rim and unaltered core. In some plagioclase phenocrysts, actinolite with minor apatite and magnetite occur as blebs near the core of the lath. Epidote is abundant in A3 alteration occurring as large, anhedral-subhedral grains often forming aggregates that flood the groundmass, intergrown with albite and actinolite. There are some examples of two phases of epidote (cf. Section 5.5). The earlier, vuggy, Mn-rich and Al-deficient phase of epidote is the least abundant and is only observed in certain samples. Patches of apatite are intergrown with epidote, albite and

hydrothermal magnetite and interstitial apatite is commonly associated with actinolite that has replaced hornblende grains. Titanite is also observed as anhedral patches within massive epidote as elongate grains in chlorite or actinolite, aligned parallel to remnant cleavage; and as patches within igneous magnetite proximal to altered mafic phases. Minor chlorite is present as anhedral grains intergrown with epidote and actinolite that have replaced hornblende and biotite. The hydrothermal zircon appears with a ragged rim over a smooth core, intergrown with massive epidote and is proximal to epidote-actinolite veins (V2).

A3 alteration is the most prevalent alteration type in the different lithological units, with occurrences of A3 in all the Yarabamba Batholith units (granodiorite (GRD), monzodiorite (DRTM), monzodiorite (MZD), monzonite (MZT), diorite (DRT), and in minor amounts in the Carpanito (CAR) and Yarito (YAR) members of the Toquepala Group.

A3 alteration in the DRTM and MZD is characterized by pervasive actinolite and epidote \pm pumpellyite alteration of the groundmass, often with defined needles of actinolite (Figure 5.3d). This alteration is particularly prevalent when proximal to epidote-actinolite (V2) veins. Primary igneous magnetite is partially replaced by an epidote groundmass, with pumpellyite infiltrating the magnetite trellis structure. Pre-existing K-feldspar has developed a myrmekitic texture with albite as part of the hydrothermal alteration process. Hydrothermal zircon is also present within the epidote-actinolite veins, hosted by epidote in the vein selvages. Within the MZT and DRT, quartz and actinolite have pervasively altered most of the groundmass, together with intergrown aggregates of apatite and titanite. Quartz is not a common mineral in the host lithology, but it is abundant in this alteration facies. Quartz, albite and actinolite have overprinted previous epidote-chlorite alteration and small epidote veinlets and produce scalloped edges on earlier hydrothermal apatite, epidote and igneous hornblende. Plagioclase phenocrysts (>1 mm) contain blebs of actinolite and hydrothermal magnetite toward their centres. Albitization of plagioclase is common.

A3 alteration in the CAR and YAR units is characterized by distinct myrmekitic textures of K-feldspar and albite in the groundmass. In the most

intensely altered samples, plagioclase phenocrysts are fully replaced by albite and epidote, but in weaker examples, only the groundmass has experienced alteration with the plagioclase phenocrysts remaining unaltered. Igneous biotite is partially pseudomorphed by actinolite and minor epidote, chlorite and magnetite.

5.4.4 *Epidote-chlorite-albite propylitic (A4)*

Includes epidote-chlorite-albite-apatite-titanite with minor calcite, prehnite and zircon. Ragged, fine to medium-grained epidote is abundant throughout the chlorite-albite-altered groundmass. Anhedral, massive chlorite commonly surrounds altered titanomagnetite and hydrothermal magnetite crystals. Fine, anhedral grains of titanite and apatite are often intergrown with chlorite, in particular occurring around the ragged rims of the chlorite grains or at the contact with hydrothermal magnetite grains. Apatite and titanite is associated with the replacement of igneous titanomagnetite (Figure 5.3e).

This is seen within the Granodiorite (GRD) and diorite (DRT) of the Yarabamba Batholith, and the Yarito (YAR), Carpanito (CAR) and Samanape (SAM) Toquepala units.

This facies is represented in the GRD and DRT by an epidote-chlorite-apatite-albite-titanite assemblage with minor prehnite and K-feldspar. Pitted albite has replaced plagioclase feldspar phenocrysts from the core outward. This pitted texture is suggestive of the volume loss between the two minerals that occurs during this reaction. Albite is also abundant in the groundmass, displaying myrmekitic textures with K-feldspar. Monazite and other REE-rich minerals are associated with the epidote. Diffuse, thin (40-50 μm), epidote-dominant veinlets are partially overprinted by pervasive epidote-albite-apatite.

The level of intensity of A4 alteration within the volcanic members (YAR, CAR, SAM) varies, with some samples exhibiting very minor alteration, for example with epidote limited to plagioclase phenocrysts. In areas of strong A4 alteration, chlorite and epidote are abundant and have replaced both groundmass and phenocrysts with complete albite replacement of

plagioclase phenocrysts. This alteration is associated with epidote-quartz (V3) and fine, parallel, albite-epidote (V4) veinlets. In the samples where epidote-quartz veining is present there is a strong pervasive epidote-albite alteration that extends beyond the immediate vein selvage.

5.4.5 *Epidote-titanite propylitic (A5)*

In the epidote-titanite assemblage, epidote and titanite are the major constituents, with apatite, albite commonly present, and minor magnetite, zircon and rutile. The assemblages in A4 are mostly concentrated in plagioclase and K-feldspar phenocrysts. There is often a pervasive myrmekitic texture between K-feldspar and albite. Where present, epidote occurs as: (1) abundant, disseminated grains in albite-epidote flooded groundmass; (2) clusters of grains in the core of albite-altered plagioclase phenocrysts; and (3) subhedral grains within pseudomorphed plagioclase phenocrysts with other alteration minerals such as magnetite, apatite, zircon and albite. The apatite comprises mostly euhedral to subhedral grains associated with partially pseudomorphed feldspar phenocrysts and altered magnetite phenocrysts (Figure 5.3g). Anhedral patches of titanite are located within epidote after plagioclase. Fine-grained, subhedral to euhedral zircon grains occur within disseminated epidote in groundmass flooded with albite. Zircon occurs proximal to epidote-quartz veins (V3).

Within the MZT and GRD units, patchy, anhedral epidote is the dominant alteration mineral in this subzone, also occurring in very fine (40-50 μm thickness), diffuse, parallel veinlets which are overprinted by later albitization from the aforementioned epidote-actinolite (A3) phase. Thick epidote-quartz veins (<1 cm) with aggregates of epidote, quartz and titanite are present, containing large (~400–500 μm) zircons which are fractured. This is the most common alteration seen in the P-GRD unit.

In the SAM and YAR volcanics, albite mantles K-feldspar phenocrysts, and occurs as a partial replacement of plagioclase feldspar. In some samples, only the K-feldspar phenocrysts are affected, where they are pseudomorphed by epidote, apatite and magnetite.

5.4.6 *Chlorite-calcite propylitic (A6)*

This alteration assemblage primarily comprises chlorite, calcite and apatite with minor albite, titanite and rutile. Massive, fine-grained chlorite forms a corona around epidote after plagioclase and titanomagnetite phenocrysts. Together with calcite, chlorite also occurs as a texturally-destructive groundmass replacement, associated with epidote, apatite, titanite and albite. Apatite occurs primarily as patches within massive and euhedral epidote, but also occurs in disseminated form in a strongly albitized groundmass. Anhedraal titanite grains are intergrown with massive and granular aggregates of epidote. Epidote is not present in all A6 samples, but when visible it is observed as: (1) large aggregates or massive patches with interstitial calcite; or (2) subhedral to euhedral grains that have selectively replaced phenocrysts of plagioclase with an altered albite rim. The interstitial calcite texture is only associated with the epidote in the A6 alteration assemblage. Evidence of sericitic overprinting of chlorite is present in some samples.

A6 chlorite-calcite alteration is found within the Huaracane (HUARA) formation and Yarito (YAR) and Asana (ASA) members of the Toquepala volcanics, with minor amounts in the granodiorite (GRD). Within the volcanics, selective replacement of K-feldspar and plagioclase phenocrysts by epidote, calcite and chlorite is typical. Blades of magnetite and patches of apatite are common in these alteration centres. Albite and minor, patchy chlorite overprint most of the groundmass (Figure 5.3i). Some samples are strongly affected by subsequent sericitic alteration, but in those less affected, secondary apatite exhibits a distinct anhedraal habit, often elongated along the cleavage of the chlorite, making it easy to distinguish from euhedral, primary igneous apatite.

5.4.7 *Sericitic (A7)*

The sericitic alteration observed is typically characterised by quartz-sericite-pyrite-rutile with minor hematite, apatite and chlorite. There is often a strongly pervasive texture, completely destroying primary textures.

Sericitic alteration was observed in the granodiorite (GRD) of the Yarabamba Batholith and in the Samanape (Q-SAM) and Yarito (Q-YAR) members of the Toquepala volcanics. In the GRD, pervasive quartz and sericite have destroyed any pre-existing textures. Minor pyrite is present, although sub-cubic voids are common which are likely to be a result of original pyrite that has been removed. Hematite often coats the inside of these voids. In the porphyritic rhyolites of the SAM member of the Toquepala Group, the pervasive sericite-quartz-rutile alteration is accompanied by minor apatite, pyrite, tourmaline and barite. Strong quartz and sericite replacement has obliterated most of the original textures. Of all the members of the Toquepala volcanics, the Samanape Member is the most notably recorded to show sericitic and silicic alteration (Martinez & Zuloaga, 2000). In the Yarito member, samples displaying sericitic alteration, the sericite is seen outlining the original crystal structure or cleavage of igneous phenocrysts. These trace crystals are often associated with zircon and/or REE-minerals. The pyrite has been partially or fully removed during weathering and, in some cases, vugs have been selectively infilled by hematite and clay. Quartz and sericite alteration of groundmass K-feldspar and albite is particularly strong proximal to the sulphide voids.

5.4.8 *Advanced argillic (A8)*

This alteration type is defined by pervasive sericite-clay alteration of the groundmass, specifically comprising dickite and kaolinite. Cubic voids (100-500 μm in size) indicate the original presence of pyrite which has been subsequently removed. Advanced argillic alteration has resulted in the kaolinization of the plagioclase phenocrysts and clay and quartz alteration of the fine-grained K-feldspar and sericite groundmass. The typical red-orange staining is the result of finely disseminated specular hematite in the groundmass. Advanced argillic alteration has only been observed in the Yarito member of the Toquepala volcanics. Fine stockwork-like veinlets of sericite-clay (V8) are associated with this alteration type.

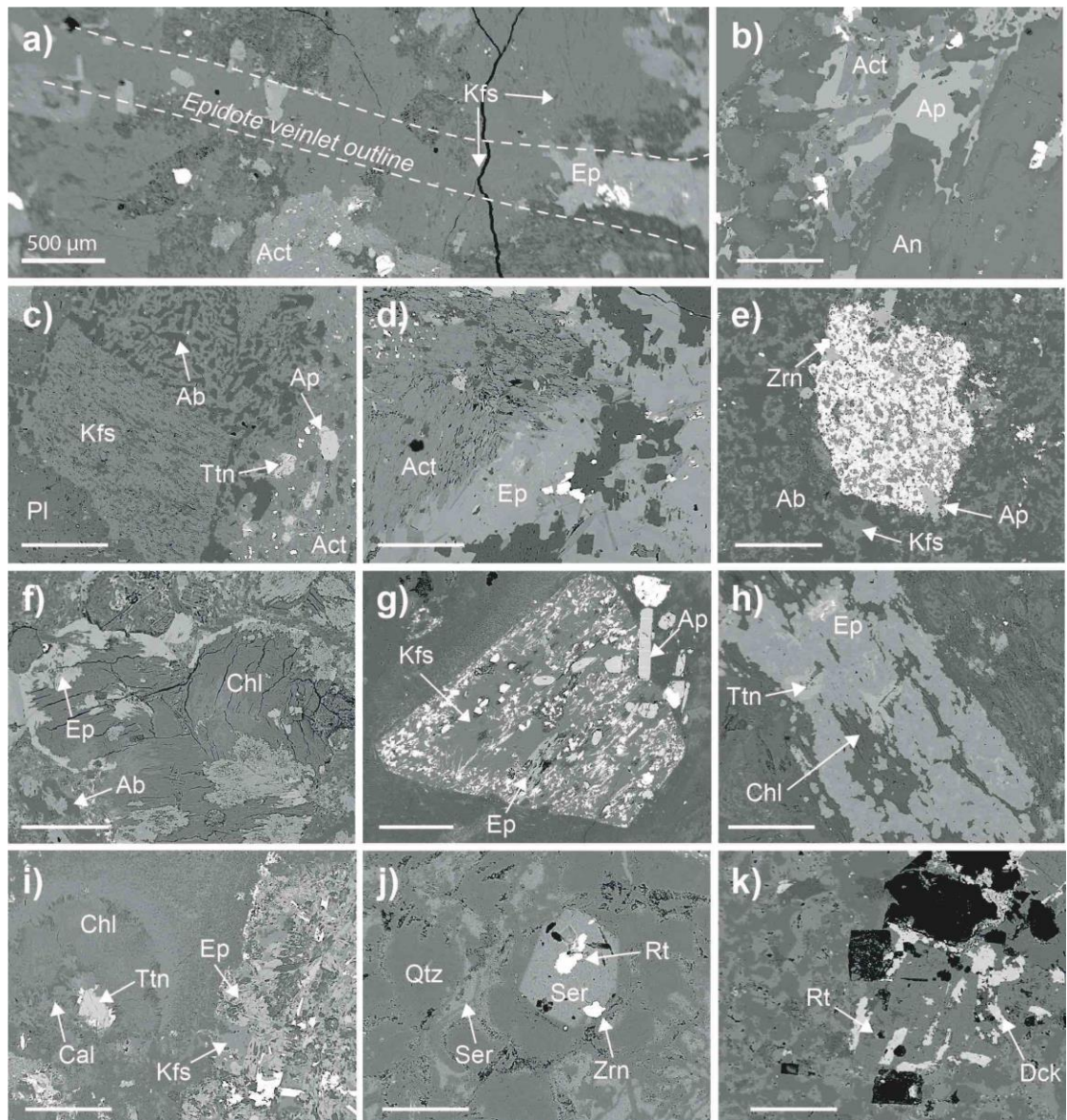


Figure 5.3. SEM-BSE images showing alteration textures. Scale bar indicates 200 μ m unless stated. **a)** epidote-actinolite veinlet (highlighted with dashed line), overprinted by large patches of K-feldspar (RCS052); **b)** epidote-actinolite-albite (A2) flooding groundmass, with well-formed actinolite needles (RCS018); **c)** A2 actinolite alteration actinolite with speckled hydrothermal magnetite, and apatite and titanite grains. There is a strong myrmekitic texture in the groundmass (RCS057); **d)** actinolite-apatite alteration of anorthite crystals (RCS086); **e)** igneous titanomagnetite phenocryst with patchy replacement by apatite and titanite (RCS072); **f)** A4 alteration with chlorite after amphibole phenocryst with a partial halo of epidote (RCS031); **g)** partially pseudomorphed hyalophane K-feldspar phenocryst with anhedral epidote and magnetite grains. Igneous apatite is associated with the phenocryst (RCS030); **h)** epidote-chlorite alteration of a biotite phenocryst; patches of titanite are associated with the epidote (RCS014); **i)** acicular epidote and magnetite replacing a K-feldspar phenocryst, with fine-grained chlorite and calcite fully replacing the groundmass (RCS016); **j)** pervasive quartz-sericite alteration with sericite, rutile and zircon replacing a phenocryst (RCS034); **k)** cubic voids after sulphide mineralisation with a sericite-quartz-rutile (A8) groundmass (RCS063);

Alteration	Alteration assemblage	Mineral	Suffix	Textural comments
A2 Actinolite	Act-Ap-Ttn- Mag±Chl±Ab±Py	Apatite	A2	Ragged grains, intergrown with actinolite
		Titanite	A2	Replacement of primary titanomagnetite, intergrown with actinolite, hydrothermal
		Chlorite	A2	Intergrown with titanite and actinolite
A3 Epidote-actinolite	Ep-Act-Ttn-Ap- Ab±Chl±Prh±Zrn	Epidote	A3	Fine grained patches in the groundmass, intergrown with actinolite and albite
		Apatite	A3	Interstitial grains, intergrown with actinolite and epidote
		Titanite	A3	Elongated along chlorite cleavage and intergrown with apatite and rutile
		Chlorite	A3	Minor chlorite intergrown with epidote and actinolite that have replaced mafic phenocrysts
A4 Albite-epidote	Ep-Chl-Ab-Ap- Ttn±Mag±Cal	Zircon	A3	Occurring as fracture infill around epidote, or intergrown with epidote
		Epidote	A4	Ragged grains occurring throughout the albite-chlorite groundmass
		Chlorite	A4	Grain aggregates surrounding hydrothermal magnetite in an albite groundmass
		Titanite	A4	Anhedral grains within chlorite, associated with hydrothermal magnetite and apatite patches
A5 Epidote-titanite	Ep-Ttn- Ap±Ab±Mag±Anh±Zr n	Apatite	A4	Anhedral grains within massive epidote or chlorite
		Epidote	A5	Occurring as disseminated patches in groundmass or as grains in pseudomorphed plagioclase phenocrysts
		Apatite	A5	Subhedral to anhedral grains associated with pseudomorphed phenocrysts
		Titanite	A5	Occurring in patches within epidote after plagioclase
A6 Chlorite-calcite	Chl-Cal- Ap±Ttn±Ab±Rt	Zircon	A5	Grains within disseminated epidote in albite-flooded groundmass
		Chlorite	A6	Massive aggregates surrounding altered magnetite phenocrysts and intergrown with epidote
		Epidote	A6	Occurring as massive flooding of groundmass with chlorite and interstitial calcite or selective replacement of phenocrysts, with calcite and apatite
		Apatite	A6	Mostly occurring as patches within epidote with minor disseminated grains in the albitized groundmass
		Titanite	A6	Anhedral grains within massive epidote and epidote aggregate

Table 5.1. A summary table of the propylitic alteration assemblages with textural descriptions of the five key minerals (used for later analysis) present in each assemblage: zircon, apatite, titanite, epidote and chlorite. The 'suffix' column refers to the suffix that will be applied to minerals within those categories throughout this study.

5.5 Veins and vein-related alteration

5.5.1 *K-feldspar-Quartz (V1)*

Type 1 veins are sinuous, fine (<0.5 cm width) veinlets with a predominantly K-feldspar-quartz-andalusite composition and accompanied by minor pyrite and magnetite. Sparsely disseminated remnant cubic voids indicate that the original sulphides have been mostly leached out to leave a hematite covering lining the inside of the voids (Figure 5.6a). These potassic veins are similar to veins described in other porphyry systems, such as: 'K-feldspar-sulphide veinlets' at the Northparkes porphyry, Australia; irregular quartz-K-feldspar-anhydrite-sulphide veins in El Salvador, Chile; and 'B-type' sinuous quartz veins described at Quellaveco (Gustafson & Hunt, 1975; Sillitoe, 2010; Sillitoe & Mortensen, 2010; Pacey, 2017). The surrounding vein halo and wallrock has experienced strong sericitic overprinting with sericite cutting feldspar, mostly obliterating the earlier potassic alteration. However, despite this, the K-feldspar-quartz veinlets are relatively well preserved.

5.5.2 *Epidote-actinolite (V2)*

The semi-sinuous V2 veins are epidote-dominant with quartz-actinolite-magnetite±apatite±titanite±prehnite±zircon. The vein-wallrock contact is irregular and indistinct with epidote and actinolite pervading the alteration halo (Figure 5.6b). Actinolite occurs as needles or fibrous grains intergrown with epidote and magnetite. In some samples, two phases of epidote are visible when analysed under SEM-BSE (Figure 5.6c). The distinguishing features of the phases are:

- Type 1: darker BSE response. The epidote of type one is texturally vuggy, and chemically shows elevated Mn and Al. This epidote is intergrown with Al-deficient prehnite and is associated with partially destroyed magnetite crystals.
- Type 2: brighter BSE response. This Fe-rich epidote is most similar in composition to epidote present in all of the V2 veins analysed. The has a similar vuggy texture to type 1. The epidote hosts aggregated patches of

titanite, and minor amounts of hydrothermal zircon and rare earth minerals such as thorite and monazite. Texturally, the hydrothermal zircons have clean cores with ragged overgrowths and appear to be intergrown with this type of epidote.

Based on the textural relationships observed, it would appear that the 'type 1' epidote-prehnite assemblage preceded the abundant 'type 2' epidote-zircon assemblage, although it is possible that the phases are approximately coeval. There is some evidence for a later potassic overprint on the smallest (0.5 mm) epidote veinlets.

In the field, these veins are often accompanied by distinctive, pale pink albite vein halos (Figure 5.4a).

5.5.3 *Epidote-quartz (V3)*

The epidote-quartz veins (V3) are mostly linear (0.2 mm – 2 cm wide) and primarily contain massive epidote with quartz, titanite and apatite (Figure 5.6d). Some of the veins contain large (~400–500 μm), often fractured, zircons and smaller REE-minerals such as monazite and thorite. The fractured zircons are interpreted to be of hydrothermal origin, with fracturing occurring post-vein formation. A couple of these veins show two epidote generations, which are similar to those described in vein type V2.

The V3 veins are almost entirely composed of epidote with minor quartz (5-20% of vein composition). Epidote is mostly vuggy with the grain shape highlighted by internal oscillating zoning. Where there is a higher percentage composition of quartz (~20%), the epidote is less pronounced and appears massive. Epidote grains are mostly massive with vuggy areas of grains. Similarly to V2, in areas of large epidote crystal growth, there is pronounced internal zoning. Apatite are mostly smooth anhedral to subhedral grains desegregated within the massive epidote veining. Fine grained zircon grains are located toward the edge of the vein displaying a mottled texture.

In the field, these veins are the most abundant of the propylitic veins, occurring in more of the regional stratigraphy than the other vein types. They

typically consist of an epidote fracture filling that is exposed as a sheet due to later removal of one of the fractured blocks (Figure 5.4b). The abundance and accessibility of these veins has enabled large amounts of structural data to be collected on them throughout the study area.

5.5.4 *Albite-epidote (V4)*

V4 veins are straight, composed mostly of albite (1 – 1.5 cm width) with minor epidote and actinolite (Figure 5.6e). This vein type is one of the least common in the samples analysed, and is truncated by V6 veins. There is minor epidote and anhedral aggregates intergrown with albite.

5.5.5 *Quartz (V5)*

Quartz is abundant in several of the vein types, either as a key or minor component in the vein or vein selvage. However, from the samples analysed, veins solely comprising quartz (V5) were mostly parallel to quartz-albite-epidote (V6) veins. Interstitial epidote is very minor in this vein type, infilling fractures and inclusions within the quartz vein. However, epidote from the adjacent quartz-albite-epidote (V6) veins infill fractures within the quartz veins (V5). This suggests that V5 precedes V6. It is also possible, therefore, that the interstitial epidote from A5 is temporally similar to epidote originating in V6.

In the field, the outcrop expression of quartz veins is generally very subtle, so their true extent is hard to determine. However, it is likely that quartz veining is extensive throughout the region, particularly in areas of faulting. For example, thick quartz veins (>10 cm width) with dilational vuggy cavities were recovered in several locations proximal to the IFS. The directions of crystal growth and cross-cutting relationships of the vugs suggest multiple phases of quartz precipitation in the vicinity of these fault zones.

5.5.6 *Quartz-albite-epidote (V6)*

This vein type is primarily composed of fine-grained, intergrown quartz-albite-epidote. Compositionally, this vein type is similar to the epidote-quartz veining of V3, but the texture and proportions of the constituents differ. Whereas V3 is epidote-dominant with often massive epidote, in the quartz-

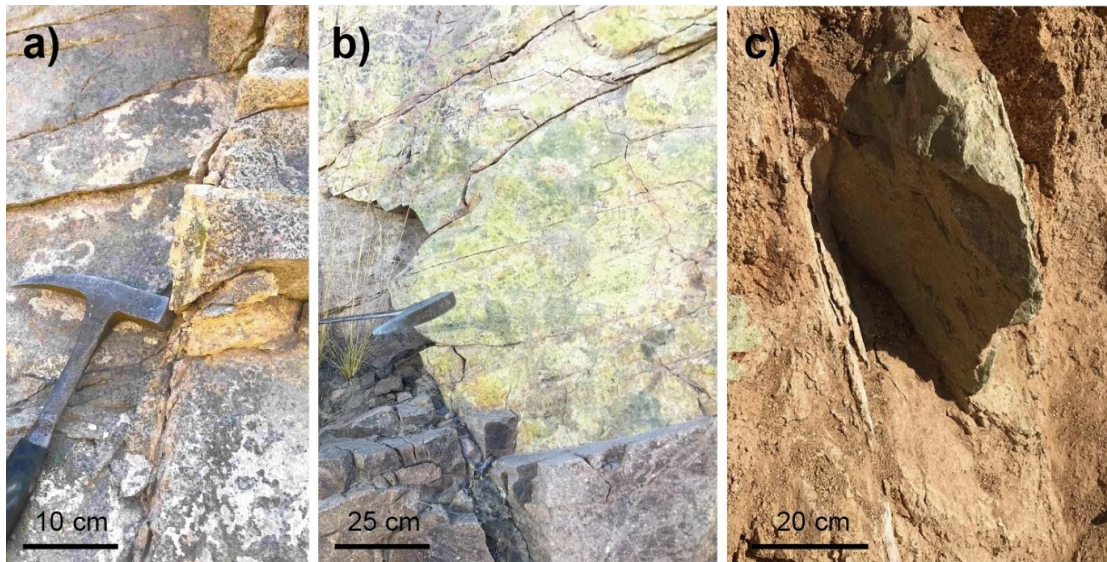


Figure 5.4. Field images with examples of three propylitic vein types: **a)** epidote-actinolite V2 vein (RCS018); **b)** epidote-quartz (V3) vein on exposed fracture plane (RCS031); and **c)** quartz-epidote vein (V6) seen here as a very thick (~40 cm) channel bounded either side by parallel albite-epidote (V4) veining (RCS078).

albite-epidote veins the epidote comprises fine-grained masses (approximately 40-50% abundance) intergrown with albite or quartz (Figure 5.6f). Apatite within the epidote is abundant in two significant forms: mottled aggregated apatite patches randomly distributed appearing coeval within the epidote; and often larger, subhedral to euhedral crystals partially incorporated within the epidote. Anhedral patches of titanite are often intergrown with the epidote, and fractured zircons, possibly of igneous origin, are also present. REE-rich minerals such as thorite (40 μm) and monazite are frequently also intergrown with the epidote matrix. Minor chlorite alters augite and hornblende grains included from the rock's igneous assemblage (Figure 5.6g).

This vein type appears to only occur when accompanied by albite-epidote (V4), epidote-actinolite (V2), or quartz (V5) veining. Of the vein types, this type displays the most variation in thickness from 0.5 to approx. 30 cm, with the thicker veins bounded by albite-epidote veins (Figure 5.4c).

5.5.7 Calcite-epidote-chlorite (V7)

These are sinuous veinlets (0.2 – 1 mm thickness) containing calcite-epidote-chlorite-quartz and minor magnetite, together with patches of apatite. Texturally, the calcite is often interstitial around quartz and epidote

crystals (Figure 5.6h). Vein-proximal alteration assemblages primarily include chlorite, phengite (mica) and epidote, and albitization of plagioclase is observed.

Chlorite intergrown with calcite is particularly present on the vein-wall rock contact and is also common in the thin (0.5 mm) vein halo around several veins. Subhedral grains of apatite are associated with interstitial calcite surrounding large quartz grains within the vein. Epidote, not always present in V7, occurs as subhedral broken grains accompanied by apatite and quartz with interstitial calcite.

5.5.8 *Sericite-dickite (V8)*

V8 veinlets are very fine structures (200-300 μm width) containing sericite-dickite-rutile with disseminated hematite in the vein selvage. Minor pyrite was originally present proximal to the veinlets but has now been leached out to leave cubic voids (Figure 5.6i). Secondary hematite has subsequently precipitated, lining some of the voids. The groundmass of the felsic volcanic host rocks consists of K-feldspar, quartz, sericite and clay minerals.

5.5.9 *Quartz-pyrite (V9)*

These are straight, thin veins (0.5 – 3 cm) that contain a high proportion of pyrite with quartz and possibly minor chalcopyrite. The veins have wide alteration halos that are often double the width of the vein, composed of sericite and quartz. The oxidation of sulphides during weathering has resulted in distinct rusty orange halos. Similar veins are reported in porphyry systems and are commonly referred to as D-type veins (Gustafson & Hunt, 1975; Sillitoe, 2010; Sillitoe & Mortensen, 2010; Simmons, 2013). These veins were observed primarily between 1.5 and 7 km from the Quellaveco deposit system (cf. section 5.6.2) with a clear structural influence, occurring in sheeted arrays oriented NE-SW as well as in multidirectional stockwork (Figure 5.5).

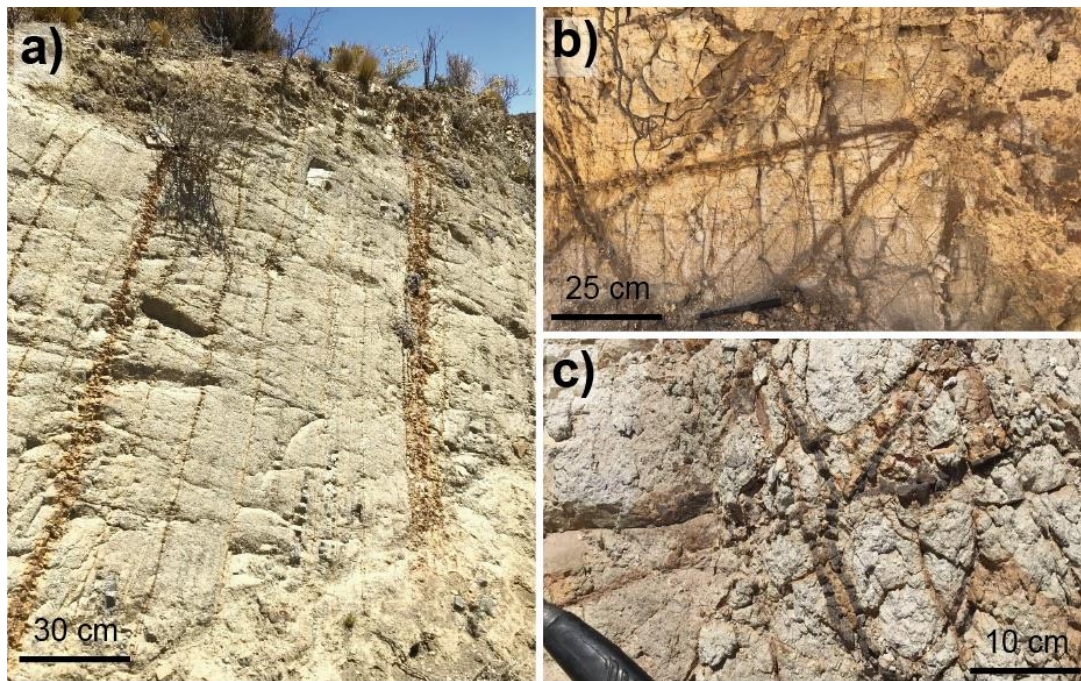


Figure 5.5 Examples of type 2, quartz-pyrite 'D' veins. **a)** Multiple sheeted veins with varying halo thicknesses (1 – 20 cm), orientated NE-SW (GR: 327743, 8106481); **b-c)** multidirectional, stockwork veining with evidence of cross-cutting suggesting a minimum of two phases of veining (GR 333481, 8104449 and 334791, 8103804 respectively).

5.5.10 Breccia (BX)

BX represents brecciated tourmaline-hosted, matrix-supported, breccias that were analyzed to contain three of the minerals of interest: epidote, apatite and zircon. Disseminated grains of epidote form a border between with brecciated fracture and the wall rock. Smooth epidote infill voids between tourmaline laths in the fractures. Minor anhedral patches of apatite are intergrown within the tourmaline-kaolinite-filled groundmass. Individual, rounded grains of zircon occur along the edge of small fractures in the breccia. These zircon grains are only observed within the breccia cement.

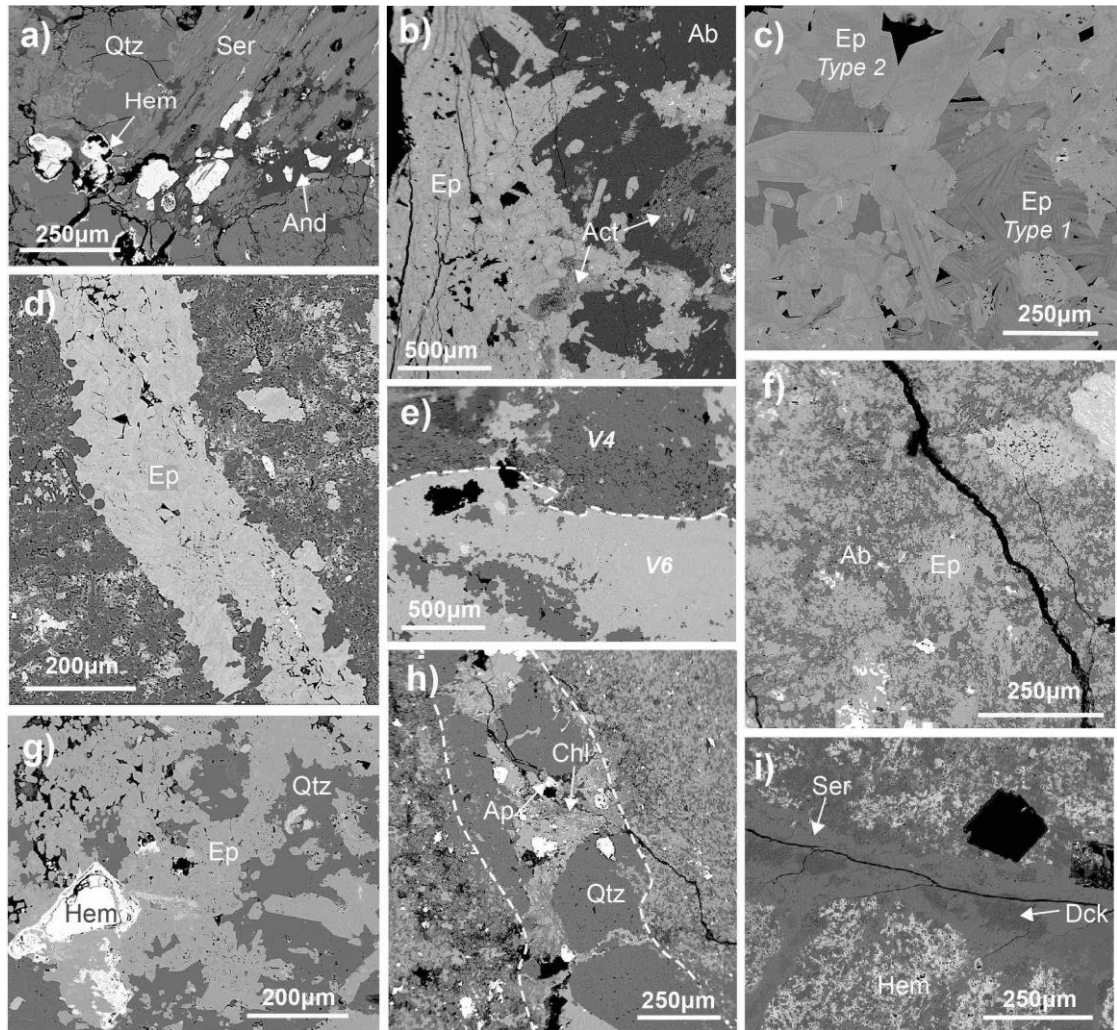


Figure 5.6. SEM-BSE images showing vein types **a)** V1 K-feldspar-quartz vein hematite after sulphides (RCS090); **b)** epidote-actinolite vein (V2) extending down one edge of the sample, comprising clean epidote grains with minor patches of actinolite, and intergrown with apatite and titanite. The vein contact is irregular with epidote crystals incorporated into the albite groundmass (RCS047); **c)** an example from V2 of the two distinct phases of vuggy epidote (type 1 and 2), with pronounced internal zoning (RCS018); **d)** a V3 vein comprising mostly epidote with minor quartz grains flanking the edges of the vein; the epidote crystals exhibit internal zoning (RCS031); **e)** the contact between a V3 epidote-dominant vein and a V5 albite-epidote vein (RCS078); **f)** a very fine-grained V6 epidote-albite vein (RCS074); **g)** epidote-quartz vein showing remnants of a cubic pyrite grain which has undergone subsequent hematization (RCS078); **h)** calcite-epidote-chlorite vein (V7) with minor magnetite and apatite and a fine-grained altered selvage of chlorite and K-feldspar (RCS072); **i)** Vein type V8 sericite-dickite vein with large cubic voids after sulphides, likely pyrite, and a fine-grained pervasive hematitic groundmass (RCS063).

Number & suffix	Name	Assemblage	Dated mineral	Suffix	Textural comments
V2	Epidote-actinolite	Ep-Ttn-Mag-Act±Ab±Prh±Zrn±Thr	Epidote	V2	Massive, often vuggy epidote with two phases: 1. most abundant, intergrown with zircon and titanite; 2. epidote with prehnite and associated with partially destroyed magnetite Anhedral patches of titanite within massive epidote Ragged zircon intergrown with epidote
			Titanite	V2	
			Zircon	V2	
V3	Epidote-quartz	Ep-Qtz	Epidote	V3	Vuggy epidote often with pronounced internal zoning, intergrown with minor quartz Titanite as fine-grained patches within massive epidote Apatite as anhedral to subhedral aggregated patches within the massive epidote Fine grained, mottled zircon commonly within massive epidote on edge of vein
			Titanite	V3	
			Apatite	V3	
			Zircon	V3	
V4	Albite-epidote	Ab-Ep-Rt	Epidote	V4	Minor epidote intergrown with albite
V5	Quartz	Qtz-Ep	Epidote	V5	Minor epidote inclusions within massive quartz vein
V6	Quartz-albite-epidote	Ep-Ap-Ab-Ttn±Qtz±Py±Prh±Kfs±Chl	Epidote	V6	Fine grained ragged epidote intergrown with quartz or albite Subhedral apatite grains within epidote grains, or intergrown with epidote-quartz-albite Titanite with two occurrences: 1. anhedral grains within epidote; 2. subhedral grains intergrown with epidote-quartz Very minor, fine grained occurrence of chlorite in the epidote-quartz groundmass
			Apatite	V6	
			Titanite	V6	
			Chlorite	V6	
V7	Calcite-epidote-chlorite	Cal-Chl-Ep-Qtz-Mag±Ap±Ab	Chlorite	V7	Chlorite intergrown with calcite and hydrothermal magnetite Minor subhedral grains of apatite within interstitial calcite surrounding quartz Diffuse, inconsistent, fine grained epidote intergrown with calcite
			Apatite	V7	
			Epidote	V7	
BX	Tourmaline-quartz breccia	Tur-Qtz±Ep±Ap±Kln±Zrn	Epidote	BX	Disseminated epidote bordering and infilling vugs between tourmaline laths within the fractures Minor anhedral apatite within the tourmaline-filled fractures Rounded, anhedral zircon grains bordering the fractures
			Apatite	BX	
			Zircon	BX	

Table 5.2. A summary table of the propylitic fracture-fill V1-V8 with textural descriptions of the five key minerals present in each assemblage: zircon, apatite, titanite, epidote and chlorite. Veining described in 5.5 is correlated to the V1-V8 system.

5.6 Spatial occurrence of vein and alteration assemblages

5.6.1 Alteration assemblages

Potassic alteration (A1) is present (Figure 5.7a-b) in both the Toquepala volcanics and Yarabamba Batholith along parts of transect 1 and 2. Within the Toquepala Group (TG), the samples are fairly well distributed but are only located within the Samanape (SAM) member. However, potassic occurrences in the Yarabamba Batholith (YB) are interestingly divided geographically and temporally. Spatially, there are two clusters: proximal to Quellaveco within the GRD; and between the IFS and its NNW-SSE splay, the Puca-Porquene Fault (PPF), in the PDTM. The spatial clusters also define the temporal difference. The cluster proximal to Quellaveco exhibits 'early-phase' potassic alteration (discussed in 5.4), whilst the samples within the PDTM are the less common 'late-stage' potassic alteration.

Actinolite propylitic alteration (A2) displays a lithological and spatial bias (Figure 5.7Xc-d): lithologically, all but one sample is part of the Yarabamba Batholith, specifically the DRTM; spatially, all the YB samples are located within the IFS and IFS-splay. The NNW-SSE splay acts as a lithological barrier, but also appears to truncate the clustering of A2 alteration.

With 23 samples exhibiting epidote-actinolite alteration (A3), this is the most abundant alteration category in the samples collected. Despite this, only 2 samples are found within the Toquepala Volcanics (Figure 5.7e-f). There is a strong preference of sample transect 2 with all but 5 samples collected from this transect. This includes the two TG samples which suggests the alteration occurs irrespective of host lithology but with a focus on the location of samples.

Epidote-chlorite propylitic alteration (A4) assemblages are most prominent within the TG but with a relatively even distribution geographically and within the members of the TG (Figure 5.8a-b). As with A4, the distribution of epidote-titanite propylitic alteration (A5) is mostly, but not exclusively, held within the TG with a large spread throughout the area (Figure 5.8c-d). Both A4 and A5 show alteration falling along the Micalaco Fault and Pacay Fault in the north-east.

Within the propylitically altered categories (A2-A6), there is an interesting pattern in the distribution and host lithology. The host rocks for categories A2 and A3 are nearly entirely the Yarabamba Batholith, which shifts to Toquepala Group-hosted in A4-A6. The distribution of those samples in TG units between A4-A6 are sporadic when compared with the distribution of A2 and A3 altered samples in the YB, which are generally clustered. Although in some categories there are less samples in total (i.e. A5 and A6), these can cause an apparent bias when discussing the wider distribution of samples, as they do not necessarily appear clustered.

However, despite this, it is worth noting how the lithology can play a role in the intensity of a propylitically altered sample. For example, the intrusives of the YB mostly comprise granodiorites, monzonite and diorites, and the volcanics of the TG are primarily made up of rhyolites and andesites (Martinez & Cervantes, 2003; Simmons, 2013). Diorite and monzodiorite are silica-poor (<5% Qtz) with 0-35 % alkali feldspar content, compared with rhyolites which have an alkali feldspar content of 35-90% and are silica-rich (20-60% Qtz) (Streckeisen, 1974; Maitre *et al.*, 2002). Where present, minerals such as biotite, plagioclase and mafic minerals are preferentially propylitically altered. The increase of relatively unreactive K-feldspar and lack of ferromagnesian phases in rhyolite could explain why propylitic alteration is less developed in some of the TG volcanics (cf. Pacey, 2017).

Sericitic alteration is widely distributed throughout the study area (Figure 5.9a-b), but only present within the Toquepala volcanics. There are also distinct 'sericitic corridors' where occurrences of sericitic alteration appear to follow certain lineaments. These are particularly distinctive because of the rapid change to epidote zone propylitic alteration on either side. The most prominent example occurs approximately 3 km NW of the Toquepala deposit. Similar observations of quartz-sericite alteration corridors are seen in other deposits, such as the Mitchell porphyry, NW British Columbia (Tombe *et al.*, 2018; Febbo *et al.*, 2019).

The two specimen examples of advanced argillic alteration (Figure 5.9c-d) are found along the faulted contact of the Yarito member from the PPF splay

from the IFS. In the field, several other areas of argillic alteration were observed proximal to major faulting of the IFS and Micalaco Fault.

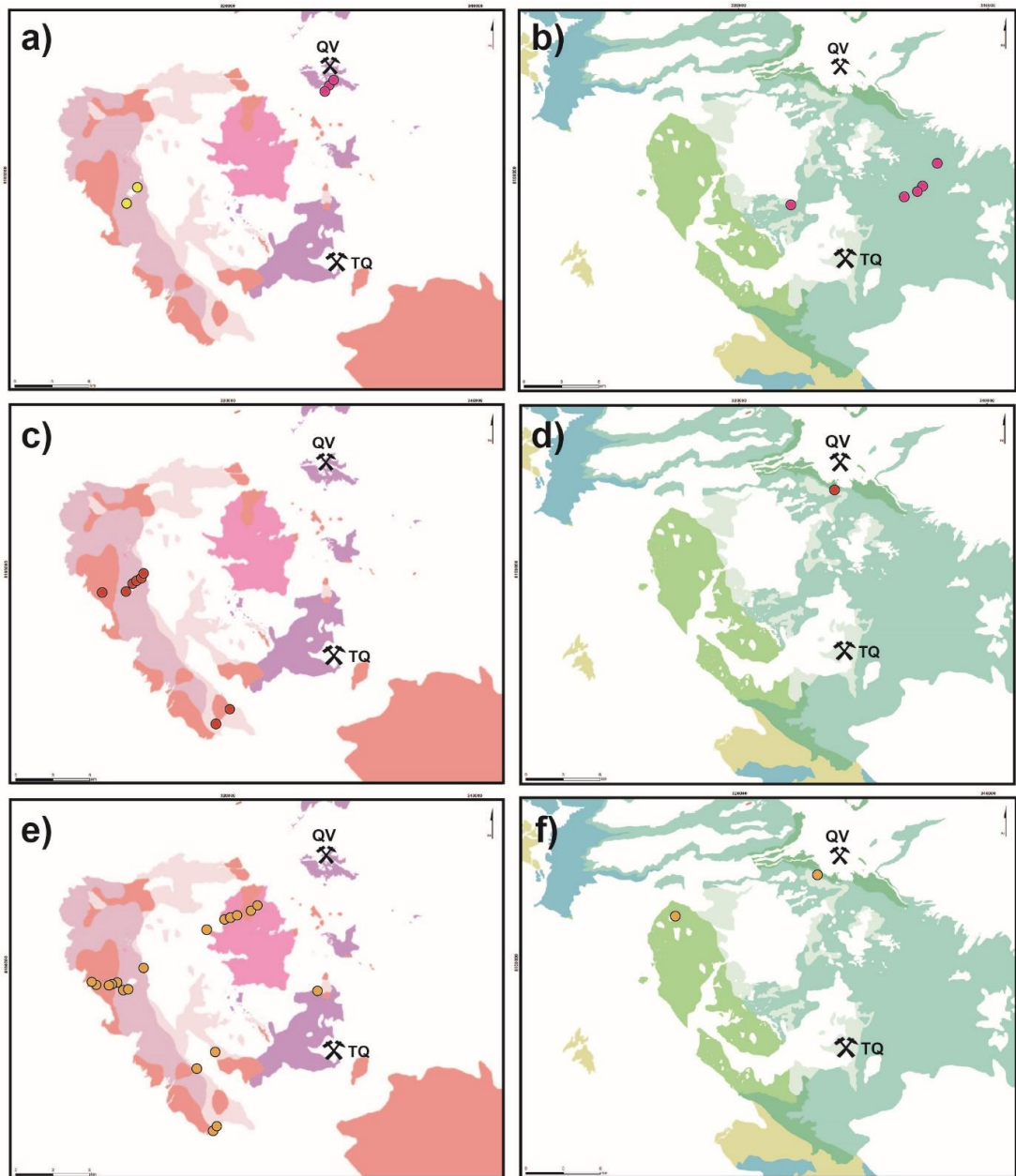


Figure 5.7. A series of lithology-based maps highlighting the distribution of each alteration category A1-A8 in the Yarabamba Batholith (left column) and Toquepala Group (right): **a-b**) A1 potassic, pink dots represent locations of early-stage potassic alteration and the two yellow samples are localities of the later-stage potassic alteration; **c-d**) A2 actinolite propylitic; **e-f**) A3 epidote-actinolite propylitic.

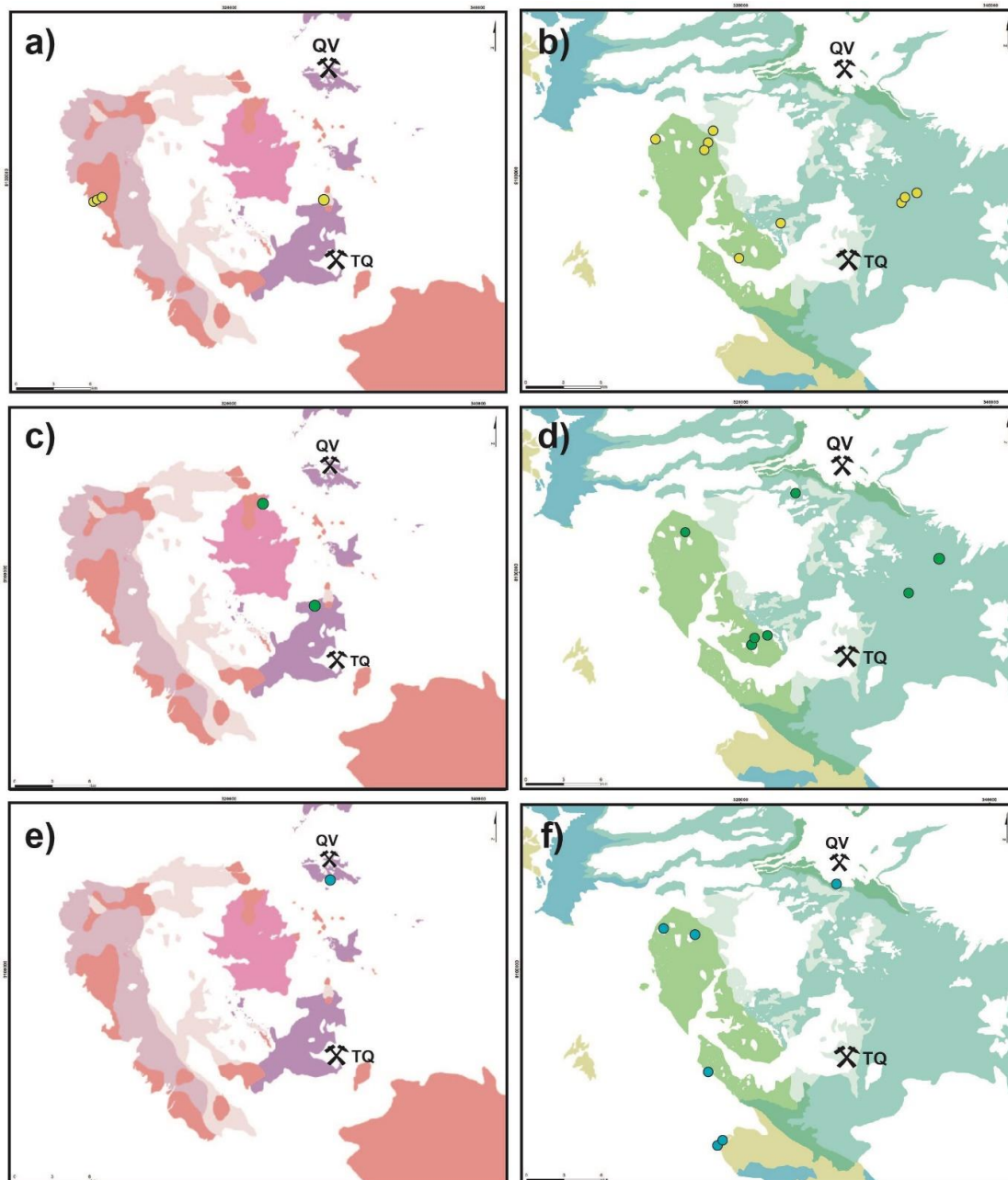


Figure 5.8 A series of lithology-based maps highlighting the distribution of each alteration category A1-A8 in the Yarabamba batholith (left column) and Toquepala Group (right): **a-b)** A4 epidote-chlorite-albite propylitic; **c-d)** A5 epidote-titanite propylitic; **e-f)** A6 chlorite-calcite propylitic.

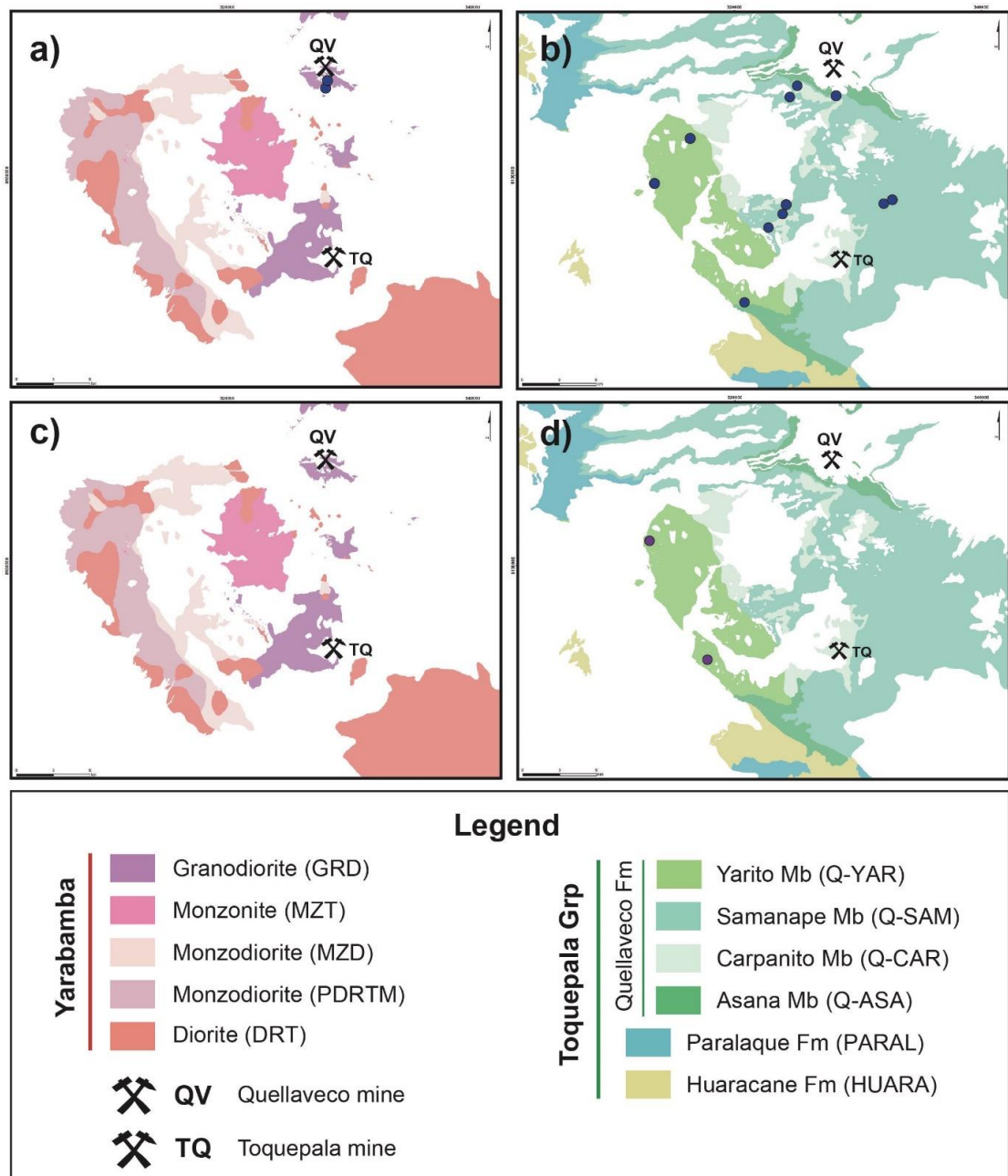


Figure 5.9. A series of lithology-based maps highlighting the distribution of each alteration category A1-A8 in the Yarabamba batholith (left column) and Toquepala Group (right): **a-b**) A7 sericitic; **c-d**) A8 advanced argillic.

5.6.2 Veins

The only example of K-feldspar-quartz veining collected in this study is located within the precursor granodiorite (GRD) proximal to Quellaveco deposit (<500 m). This area is noted for potassic veinlets in the immediate vicinity of quartz-monzonite porphyry stock within the granodiorite (Kihien, 1995; Sillitoe & Mortensen, 2010).

Geographically, the V2 epidote-actinolite veining is only sampled within the DRT and DRTM fault-controlled section between the Incapuquio Fault System (IFS) and the Puca-Porquene (PPF), IFS-fault splay. The epidote-quartz veining (V3), however, is the most evenly distributed of the vein types, along both transects and within the SAM and YAR volcanics, and MZT and GRD plutonics.

Quartz veining (V5) only appears in the MZT and YAR units on the vein map (Figure 5.10), however, as with all the veining occurrences shown, it is only representative of those veins that have been sampled in this study. Quartz veining in the field is much more widespread.

Interestingly, the only sampled occurrences of the calcite-epidote-chlorite (V7) veining are located along the Rio Capuillne Fault which is approximately halfway (~10km) between the IFS and QF/Quellaveco deposit.

Quartz-pyrite (V9) veining, also termed 'D-veins' by other authors (Sillitoe & Mortensen, 2010; Simmons, 2013), are observed in three locations between 1-7.5 km from the Quellaveco deposit within the TG volcanics. The most proximal location is to the south of the deposit in the Asana member volcanics boarding the precursor granodiorite. The veins in this area are sheeted with a unanimous orientation of NE-SW trending and SE dipping. The further localities of V9 occurrence from the Quellaveco deposit (6-7.5 km) display multidirectional, stockwork D-type veining. When viewed geographically, both localities form Quellaveco Fault-parallel lineation and are within 700 m perpendicular distance from this fault. These localities suggest a potential lenticular halo of V9 veining from 1000-700 m around the body of the deposit, which is then elongated to up to 8 km along the Quellaveco Fault.

The tourmaline mineralised samples (BX) are located along the Incapuquio Fault System (IFS) and the NNW-SSE splay from the IFS.

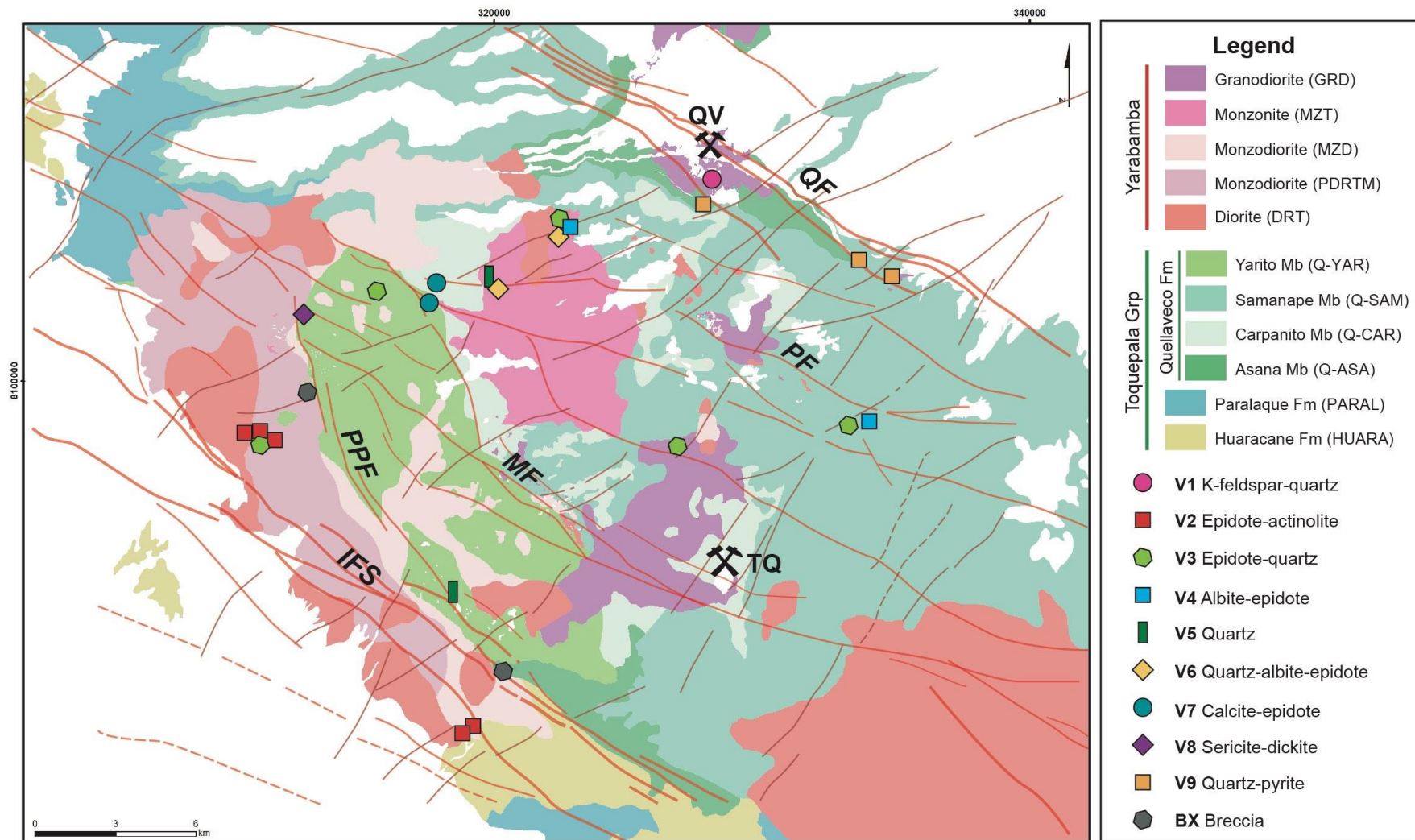


Figure 5.10. Sample location map of vein occurrences.

5.7 Relative chronology of vein and alteration assemblages

Understanding which lithologies visibly host the alteration types described in section 5.6 can help provide a baseline relative chronology for the alteration assemblages. For example, alteration only present in older units may predate the younger units. Although this is only a rough guideline, as proximity to intrusions and structural setting are the major controls on which lithologies alter and which geographic area assemblages may be located. The positioning of the two sample transects was designed to give a representative spread of lithological unit and structural setting, but due to the scope of the study area, there will naturally be areas of alteration that have not been sampled. Therefore, a relative chronology is based on what is seen, without making assumptions of what is not present in the sample spread.

The youngest unit sampled is the Quellaveco granodiorite (GRD) with an approximate age of 60-58 Ma in the Quellaveco portion of the intrusion, and 62-59 Ma in the Toquepala-proximal granodiorite (Nathwani *et al.*, 2021). This provides a lower temporal limit; the alteration present in these areas must at least post-date the age of the host unit. There are two areas of GRD sample collection: proximal to the Quellaveco deposit (<500 m) and <4 km from the Toquepala deposit. All the potassic alteration in the GRD occurs within the Quellaveco granodiorite (Figure 5.7a-b), therefore constraining the ages of the A1 and V1 veining in the GRD samples to the documented potassic alteration associated with the emplacement of the early and intermineral porphyry stock at ~58.5-56 Ma (Sillitoe and Mortenson, 2010). The Huaracane Fm (HUARA), which is recorded to be the oldest unit sampled in this study (Bellido, 1979; Martinez & Zuloaga, 2000), acts as the upper temporal limit for alteration. Although there is not an exact date for the Huaracane Fm specifically, dates from Simmons (2013) range from 90.3 Ma – 68.3 Ma. HUARA samples only exhibit A6 alteration assemblages, although this is likely to be because of the sample size in this unit (Table 5.3).

A1 alteration observed in other areas is less easily constrained temporally, however there are several examples of epidote-actinolite (A3), epidote-titanite (A5) and chlorite-calcite (A6) overprinting. This is an expected observation of propylitic assemblage overprint of high-temperature potassic alteration as fluids

	A1	A2	A3	A4	A5	A6	A7	A8
GRD	V1		V3		V3			
MZT			V5,V6		V3,V4,V6			
MZD			V2					
DRTM			V2,V4,V6					
DRT			V2					
YAR				V7	V3			V8
SAM				V3,V4			V9	
CAR				V7			V9	
ASA							V9	
HUARA								

Table 5.3. Summary of alteration and vein occurrence. Shaded squares highlight where an alteration type is present in a lithological unit. Where veins are present in a particular alteration assemblage and lithological unit, their abbreviation (V1-V9) is written in the appropriate grid. The lithological units are listed chronologically from oldest (bottom) to youngest (top).

cool with a lessening heat source (Seedorff *et al.*, 2005). However, as highlighted previously (Figure 5.7), there are two examples that suggest a later potassic overprint of epidote-actinolite (A3) and epidote-titanite (A5) alteration, and a V2 vein. This unusual sequence is only found within the DRTM and, as noted previously, within the structurally controlled section between the IFS and IFS NNW-SSE splay.

For the vein samples analysed, three display cross-cutting relationships of several vein types. This is a useful way to relatively constrain vein types before or after one another. As the sample area is extensive, the locations of the samples containing temporal relationships are highlighted (Figure 5.11) as it cannot be assumed that the relationships seen in one area are necessarily the same in other parts of the licence area. Albite-quartz veins (V4) are truncated in two of the samples by epidote-actinolite (V2), epidote-quartz (V3) and quartz-albite-epidote (V6) veining. In one sample, RCS051, V2 appears to engulf part of a V6 vein, suggesting a later phase of emplacement. Although V6 predates V2 in RCS051, there is evidence from two of the examples of V6 postdating not only V4 but also V5 quartz veins. V6 epidote is observed following fractures in the quartz vein (V5) therefore indicative of a later phase of emplacement of V6 in this example (RCS074).

More so than with any other vein type, the epidote-actinolite (V2) veins are spatially associated with one alteration type: in this example with samples

displaying pervasive epidote-actinolite alteration (A3). The summary table (Table 5.3) highlights this relationship. Calcite-epidote (V7) only occurs in samples of epidote-titanite (A4) alteration, however epidote-quartz (V3) veining is ubiquitous, occurring in A3, A4 and A5 alteration assemblages.

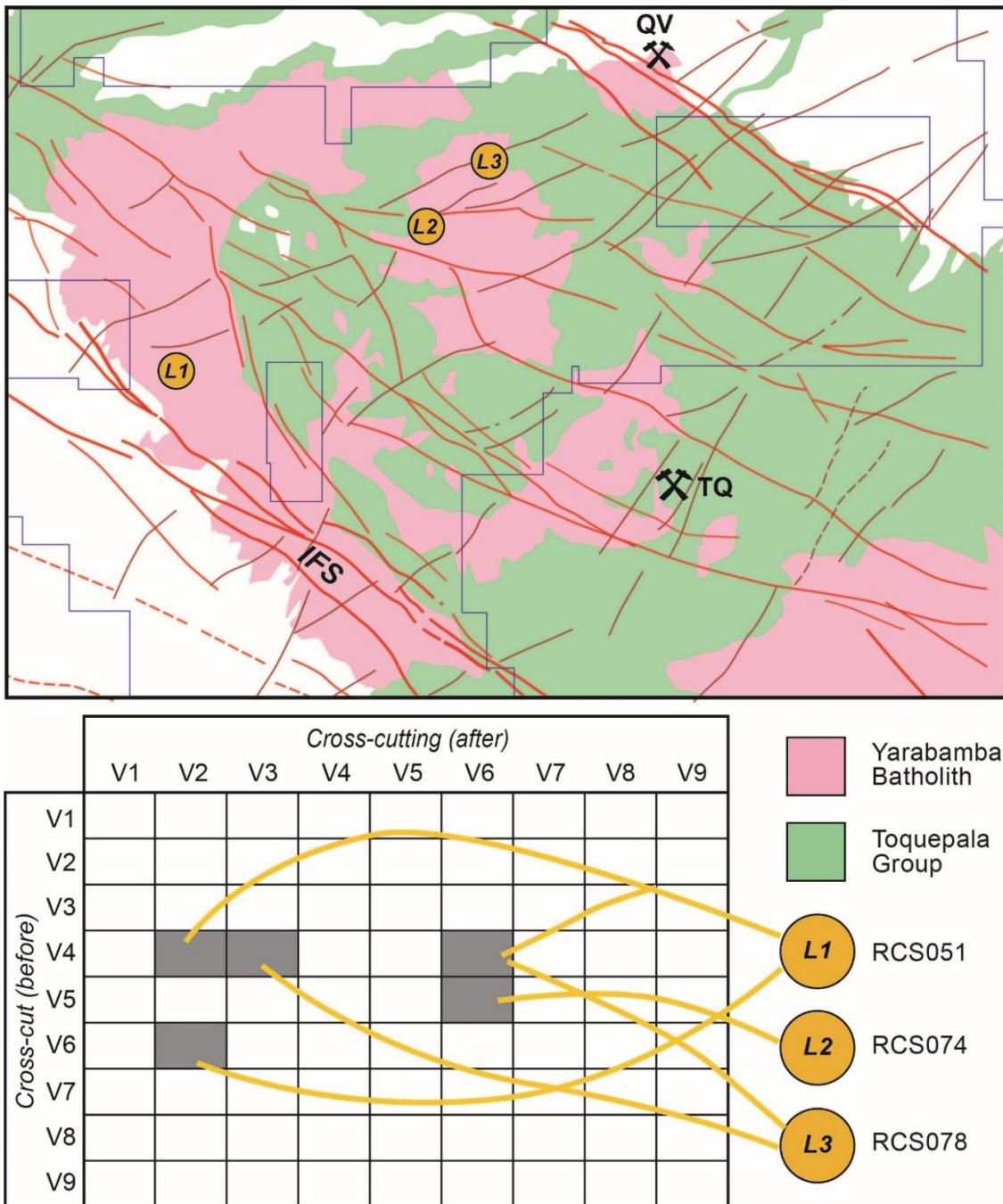


Figure 5.11. Cross-cutting relationships observed within the three vein samples are displayed in a grid format. V1-V9 are shown on both axes, the horizontal axis indicates a vein is cross-cut by a later stage vein, and vertical indicates the vein type which cuts across an older vein type. The locations of these samples are displayed on the simplified map. Location 1 (L1) refers to sample RCS051; location 2 (L2) refers to sample RCS074; and location 3 (L3) refers to sample RCS078.

Quartz-sericite alteration (A7) is seen overprinting epidote-titanite (A5) and chlorite-calcite (A6) propylitic alteration, but in particular potassic (A1) alteration. Where quartz-sericite is present, it is often highly pervasive and frequently with the partial or complete obliteration of any underlying alteration. The overprinting of potassic alteration by quartz-sericite is seen in the precursor granodiorite proximal to the Quellaveco quartz-monzonite porphyry stock. At Quellaveco, this pattern of sericitic overprinting of potassic alteration is thought to have occurred during the emplacement of the Early and Intermineral porphyry phases at temperatures of 590° to 340°C (Sillitoe & Mortensen, 2010). The approximate given ages of the potassic alteration is 58.6-57.2 Ma and 57-56.5 Ma for initial sericitic alteration (Kihien, 1995; Sillitoe & Mortensen, 2010). The sericitic overprinting of the propylitic assemblages A5 and A6 are found within samples in the precursor granodiorite (GRD). The Samanape (SAM) and Asana (ASA) members are also proximal (500 m-2.5 km) from the potassic alteration. Therefore, the sericitic overprinting of these propylitic assemblages is associated with the porphyry-related propylitic halo at Quellaveco.

Another temporal constraint of A7 is the presence of quartz-pyrite (V9) veins, which are associated with sericitic alteration in the porphyry-proximal region. The quartz-pyrite veins (V9) have a clear structural influence, systematically orientated in parallel sheet veining in a NE-SW orientation or as multidirectional stockwork observed between 1.5-7 km from the Quellaveco deposit. Similar veins are recorded at the Quellaveco deposit (Sillitoe & Mortensen, 2010; Simmons, 2013b). As these veins cross-cut the Early and Intermineral porphyries but are truncated by Late-mineral porphyry, the authors classified these veins as late stage, 'D-type' veins (Gustafson & Hunt, 1975; Sillitoe, 2010). No temporal relationships with other vein types were observed for type V9 quartz-pyrite veins in this study but, due to the similarities and spatial proximity, it is assumed that the V9 quartz-pyrite veins are coeval with the D-veins at Quellaveco, constrained by the crosscutting relationships with the porphyry phases to ~54-55 Ma (Nathwani *et al.*, 2021).

Unit	Sample	EAST_X	NORTH_Y	Alteration Types	Assemblage	Vein Type		
Yarabamba	P-GRD	RCS003	327486	8098122	Potassic (A1)	Kfs-Qtz-	V1	
		RCS006	327173	8097815	Epidote-actinolite (A3)	Ep-Act-Ab-Mag-Ap-Ttn±Chl	V3	
		RCS007	326876	8097584				
		RCS008	326826	8097426	Epidote-chlorite-albite (A4)	Ep-Chl-Ttn-Ap±Anh±Zrn		
		RCS009	326840	8097385				
		RCS089	328094	8107074	Epidote-titanite (A5)	Ep-Ttn-Ap±Zrn	V3	
		RCS090	328114	8107383	Sericitic (A7)	Qtz-Ser-Py-Rt		
	RCS091	328253	8107645					
	P-MZT	RCS071	318068	8102904	Potassic (A1)	Kfs-Mag±Bt		
		RCS073	319697	8103557	Epidote-actinolite (A3)	Ep-Act-Qtz-Ab-Ap-Ttn±Mag±Anh	V5, V6	
		RCS074	320100	8103564				
		RCS075	320740	8103917	Epidote-titanite (A5)	Ep-Chl-Rt-Ttn-Ap±Ab	V3, V4, V6	
		RCS078	322734	8105674				
	RCS079	322739	8105681					
	P-MZD	RCS017	318975	8086688	Actinolite (A2)	Act-Ap-Ab±Chl±Mag		
		RCS018	319006	8086784				
		RCS021	319793	8088248				
		RCS022	320101	8088633	Epidote-actinolite (A3)	Ep-Act-Ttn-Ap±Prh±Ab±Mag	V2	
		RCS023	320306	8088971				
		RCS092	317413	8091544				
	RCS096	318853	8092814					
	P-DRTM	RCS051	311239	8097639	Potassic (A1)	Kfs-Qtz-Mag-Cv		
		RCS052	311586	8097667				
		RCS053	311962	8098331				
		RCS054	312332	8098767	Actinolite (A2)	Act-Ap-Ttn±Ep±Ab±Chl		
		RCS056	312635	8099146				
		RCS057	312843	8099427				
		RCS058	312975	8099463	Epidote-actinolite (A3)	Ep-Act-Ap-Ttn-Ab±Chl±Zrn±Rt	V2, V4, V6	
		RCS059	313084	8099435				
		RCS061	313262	8099430				
	P-DRT	RCS019	318978	8087411	Actinolite (A2)	Act-Ap-Ttn-Ab±Chl		
		RCS037	309039	8098201				
		RCS038	309092	8098048				
RCS039		309094	8098144	Epidote-actinolite (A3)	Ep-Act-Ttn±Chl±Ap±Ab	V2		
RCS040		309255	8098068					
RCS041		309255	8098068					
RCS042		309368	8098034					
RCS044		309671	8098052	Epidote-chlorite-albite (A4)	Ep-Chl-Ap-Ab-Ttn±Pmp			
RCS046		310256	8098095					
RCS047		310659	8097900					
RCS049		310936	8098053					
RCS076	321732	8104324						
RCS077	322032	8104843						

Table 5.4. Plutonic sample groupings based on lithological unit in the Yarabamba batholith, with alteration types present in each lithology, and vein types seen in each alteration type.

Grp	Fm	Mb	Sample	EAST_X	NORTH_Y	Alteration Types	Assemblage	Veins		
Toquepala	Quellaveco	Q-YAR	RCS060	313282	8099504	Epidote-actinolite (A3)	Ep-Act-Chl-Ab-Ttn±Brt	V7		
			RCS063	312913	8102391					
			RCS064	313314	8103122					
			RCS065	313946	8103328	Epidote-chlorite-albite (A4)	Ep-Chl-Ab-Ttn-Ap±Cal±Py±Rt			
			RCS066	314786	8103733					
			RCS067	315528	8103261					
			RCS068	316526	8102844	Epidote-titanite (A5)	Ep-Ttn-Ab±Ap±Mag			
			RCS069	317558	8102200					
			RCS070	317511	8102862					
			RCS093	317574	8091857	Chlorite-calcite (A6)	Chl-Ap-Ab-Cal-Ttn±Anh±Hem			
			RCS094	317949	8092193					
			RCS097	322234	8095023	Sericitic (A7)	Qtz-Ser-Hem±Ap±Rt			
			RCS098	321007	8094745					
			RCS099	320874	8094307	Advanced argillic (A8)	Qtz-IlI-Dck-Py			
		RCS100	320637	8093924						
		RCS102	319887	8093304						
		RCS106	320765	8089634	Q-SAM	Potassic (A1)	Kfs-Mag-Qtz-Ap-Rt±Bt	V3, V4		
		RCS001	333933	8098403						
		RCS002	333918	8098392						
		RCS010	324204	8097696						
		RCS011	323967	8097403		Epidote-chlorite-albite (A4)	Ep-Chl-Ap±Cal±Ttn±Ab±Hem			
		RCS012	323711	8096614						
		RCS025	336024	8101160		Epidote-titanite (A5)	Ep-Ttn±Ap±Ab±Rt			
		RCS028	334724	8099048						
		RCS029	334468	8098825		Sericitic (A7)	Ser-Qtz-Rt±Ap±Py±Tur±Brt			
		RCS030	333373	8098457						
		RCS031	333133	8098221						
		RCS032	333020	8098020						
		RCS033	333053	8098079		Q-CAR	Actinolite (A2)		Act-Ab-Mag-Ttn±Ep±Chl±Rt	V7
		RCS034	332652	8097796						
		RCS036	332071	8097749	Epidote-actinolite (A3)		Act-Ep-Chl-Ttn±Ap±Rt			
		RCS081	324357	8106351						
		RCS083	325083	8107222	Epidote-chlorite-albite (A4)		Ep-Chl-Ab-Ap±Cal±Ser±Tur			
		RCS072	317788	8103570						
		RCS084	326283	8106997	Sericitic (A7)	Qtz-Ser-Ap-Ab-Rt				
		RCS086	327743	8106481						
	RCS104	323197	8096126	Chlorite-calcite (A6)	Chl-Cal-Ap-Ab±Brt	V9				
	RCS105	322755	8095774							
	RCS087	327949	8106779	Q-ASA	Qtz-Ser-CuFeSulphate					
	RCS088	327949	8106779							
	Huara	HUARA	RCS014	318331	8086042	Chlorite-calcite (A6)	Ep-Chl-Cal-Ap-Ab±Ttn±Ser±Rt			
		RCS016	318610	8086214						

Table 5.5. Volcanic sample groupings based on lithological unit in the Toquepala Group, with alteration types present in each lithology, and vein types seen in each alteration type.

5.8 Discussion

The discussion is centred around five specific areas of interest which are highlighted on Figure 5.14.

5.8.1 Area 1 and Area 2

Area 1 is a 4-5 km stretch of A2 (Act-Ap-Ttn-Mag \pm Chl \pm Ab \pm Py) and A3 (Ep-Act-Ttn- \pm Chl \pm Ab \pm Ap \pm Prh \pm Zrn \pm Rt) alteration which occurs along transect 2 between the Incapuquio Fault System (IFS) and the NNW-SSE Puca-Porquene Fault (PPF) which is a splay of the IFS.

A2 and A3 are propylitic assemblages both containing actinolite and are therefore believed to represent the higher fluid temperature or $\sim 350^\circ$ compared with low temperature propylitic fluids of 200-250 $^\circ$ (Holliday & Cooke, 2007; Cooke *et al.*, 2014; Lee *et al.*, 2020). As noted in section 5.6.2, Area 1 and 2 host the only sample occurrences of A2 epidote-actinolite veins. Veins such as these are associated with high temperature fluids of 400-450 $^\circ$ C (Battles & Barton, 1995; Dilles *et al.*, 1995; Seedorff *et al.*, 2005).

A possibility for why Area 1 shows an extended section of high temperature alteration is linked to the presence of the IFS and PPF on either side of the actinolite-rich zones. It is possible that the actinolite alteration in Area 1 originated at greater depth than the probably lower temperature assemblages located on the north-eastern side of the PPF. This would imply that the SW block (Area 1) has been uplifted. Sinistral movement during the Incapuquio Fault System's prolonged period of activity (Audin *et al.*, 2006; Roperch *et al.*, 2006; Boutelier & Oncken, 2010) could be responsible for uplift of Area 1. In areas of transtension, transpression will occur, especially in discontinuities in the fault structure (Fossen & Tikoff, 1998; Sibson, 2001; Fossen, 2016). The dominant IFS-splay, the PPF, to the NE of Area 1, is likely to also experience sinistral movement, but because of its obliquity with the IFS, sinistral movement could have triggered transpression and uplift of the south-western throw of the fault. If the alteration on the south-western block of the PPF has been truncated, then there would be temporal implications suggesting that at least this phase of fault activity on the IFS post-dates the propylitic alteration in area 1. As mentioned in Section 5.6.1,

the level of intensity of the propylitic alteration in Area 1 may have been heightened by two factors: the structural setting of Area 1 and the host lithologies. As the area is situated between two major faults (IFS and PPF), it is likely that increased fracture density in the area contributed to higher wall rock permeability and therefore the intensity of alteration experienced (Caine *et al.*, 1996). As previously discussed (section 5.6.1), mineralogy of the sample may have been a factor in the intensity of the alteration displayed (Pacey, 2017).

Area 1 also hosts the 'late-stage' potassic phase which partially overprints propylitic assemblages (A2 and A3). This is considered somewhat anomalous overprinting of a possible 'late-phase' potassic alteration on propylitic assemblages because potassic alteration in the 'normal' model would be the first stage of alteration, followed progressively by lower temperature assemblages and veins (Seedorff *et al.*, 2005). Therefore, this cross-cutting potassic phase contradicts this model and could be the result of several factors. These samples are only found in the DRTM, geographically 1.8 km apart. It is possible that these occurrences were the result of a later intrusive phase, however there was no specific evidence of a proximal intrusion to support this. The most proximal phase of the YB to the samples is the DRT which is known to precede the DRTM and therefore not likely to be responsible for the late stage potassic alteration (Martinez & Zuloaga, 2000). Another possibility, is the structural positioning of the specified samples. Both samples are within the section between the IFS and the PPF (Area 1), which is already noted to have a lithological control, with YB juxtaposed next to the Yarito Mb of the TG, and the truncation of propylitic assemblages from the SW to NE fault block (Figure 5.14). It is possible that if this block has been uplifted, multiple phases of uplift, retrograde metamorphism and further injection of heated fluids could be responsible for a potassic overprinting on propylitic assemblages. There is also the possibility that because Area 1 is in a highly faulted area, the IFS and Puca-Porquene (PPF) faults which act as fluid conduits, readily propagate multiple fluid phases through the fracture network.

On the southwestern side of the IFS (Area 2) propylitic alteration grades laterally from actinolite-bearing alteration (A2/A3) to chlorite-calcite alteration (A6) over a distance of approximately 2.5 km moving away from the IFS. In the centre of Area 2 and just outside of Area 2 to the north-east, there are two areas (of approx. 1 -1.2 km width) where propylitic alteration is absent. These areas correspond with highly deformed fault cores of major strands of the IFS. Fault cores of major structures, such as the IFS, are often accompanied by a surrounding network of complex subsidiary fractures which elevate rock permeability (Faulkner *et al.*, 2003). This, combined with samples showing the lateral gradation of propylitic assemblages from the fault, suggests that the IFS acts as a fluid conduit with the outward lateral dispersion of high temperature fluids from this source.

5.8.2 Area 3

Area 3 is a stretch of consistent high-temperature epidote-actinolite (A3) propylitic alteration. This concentration of A3 alteration mostly coincides with the mapped monzonite body that hosts these samples (Figure 5.14).

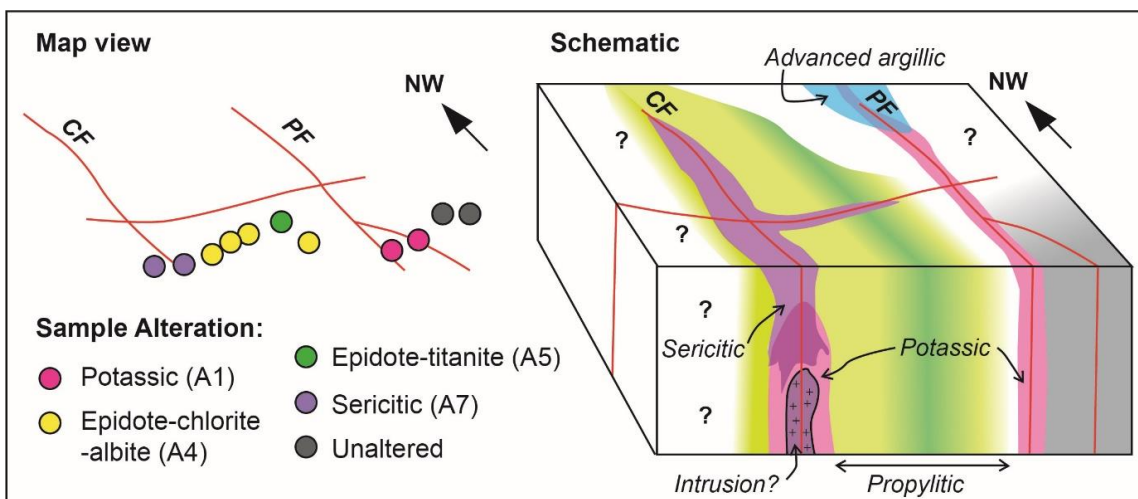


Figure 5.12. A map view sketch of the sample distribution around the Capulline Fault (CF) and Pacay Fault (PF) in Area 4 (left); and a schematic block model of the possible cause for the distribution of sericitic and propylitic alteration observed in Area 4 (right).

5.8.3 Area 4

Area 4 is an anomalous area of highly pervasive propylitic alteration (A4 and A5) within the Samanape Mb of the TG volcanics (Figure 5.12). In the field, this is a ~1.4 km stretch of strongly propylitically altered rock with an abundance of epidote-quartz (V3) veining. It appears to be anomalous because of the lack of any major alteration for 4-5 km along the strike of transect 1.

There are several possibilities for this concentration of propylitic alteration. Immediately to the south-east, samples collected display intense sericitic alteration. These samples coincide with the mapped Rio Capillune Fault (CF) and the intersection of subsidiary NE-SW trending faults. It is known that sericitization often occurs atop a potassic core and heat source, specifically this alteration type which is often controlled by underlying structures (Garwin, 2002; Cooke *et al.*, 2014; Lee *et al.*, 2020). Therefore, the presence of a 600 m zone of sericitic alteration over a named fault structure could indicate the presence of an intrusive body below. This could be an explanation for the north-eastward propagation of pervasive propylitic alteration away from the CF (see Figure 5.13). Although, sericitic alteration is generally regarded to be located <1 km from the surface, the occurrence of sericitic alteration could be representative of a deeper level as the downward collapse and superposition of sericitic alteration over older potassic is relatively common (Gustafson & Hunt, 1975; Halley *et al.*, 2015).

Another interesting feature of Area 4 is 200 m to the north-east of the propylitically altered area are two potassically altered samples of SAM volcanics. Similar to the sericitic samples, both coincide with a major fault, the Pacay Fault (PF). This area lies 5 km down-strike of a GRD outcrop, and is an area where Anglo American has mapped veining and advanced argillic alteration. This may also indicate fault-controlled lateral dispersion of alteration from the source.

5.8.4 Area 5

Area 5 highlights a 6 km area of transect 2 covering the monzodiorite (MZD), Yarito (YAR) and Carpanito (CAR) units. This area displays all five

classifications of propylitic alteration described in this study. Spatially, this area is significant because of its proximity to the Rio Capulline Fault (CF) and the intersection of the Puca-Porquene Fault (PPF). The PPF has already proven important for the lithological and alteration controls on Area 1. Due to access, sampling the NE side of the PPF directly from Area 1 was not possible, therefore Area 5 provides insight to the alteration distribution on the NE throw of the PPF. The direction of this part of transect 2 also parallels the CF, which, as noted in section 0, is potentially responsible for propylitic alteration in Area 4.

Most of the samples taken within Area 5 are from within the CF-parallel fault stepover (see Figure 5.13). In certain conditions, there is the potential for the formation of a local dilational jog leading to an area of increased dilation and locally enhanced permeability (Cox *et al.*, 2001; Sibson, 2001; Febbo *et al.*, 2019). The structural regime and sense of fault movement for this area will be explored further in the next chapter (Chapter 6).

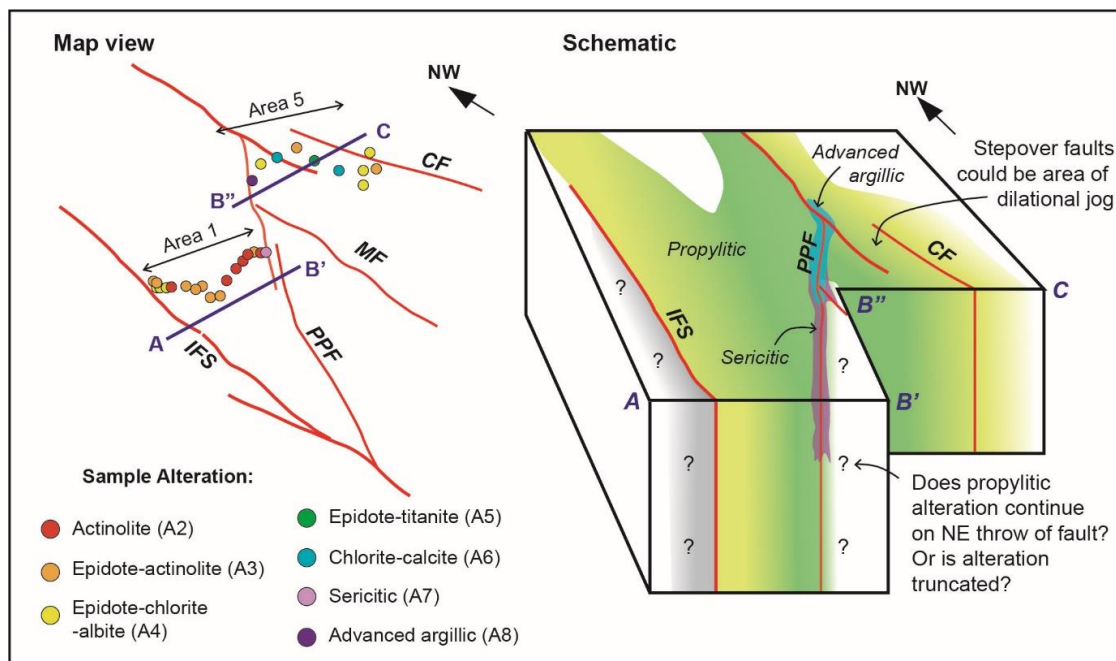


Figure 5.13. A map view sketch of the sample distribution around the Incapuquio Fault System (IFS), Puca-Porquene Fault (PPF) and Capulline Fault (CF) from Areas 1 and 5. The cross-section locations (A-B', B''-C) are shown for the block model (left); and a schematic block model of the possible distribution of propylitic alteration around Areas 1 and 5, with the presence of sericitic and advanced argillic alteration observed along the PPF (right).

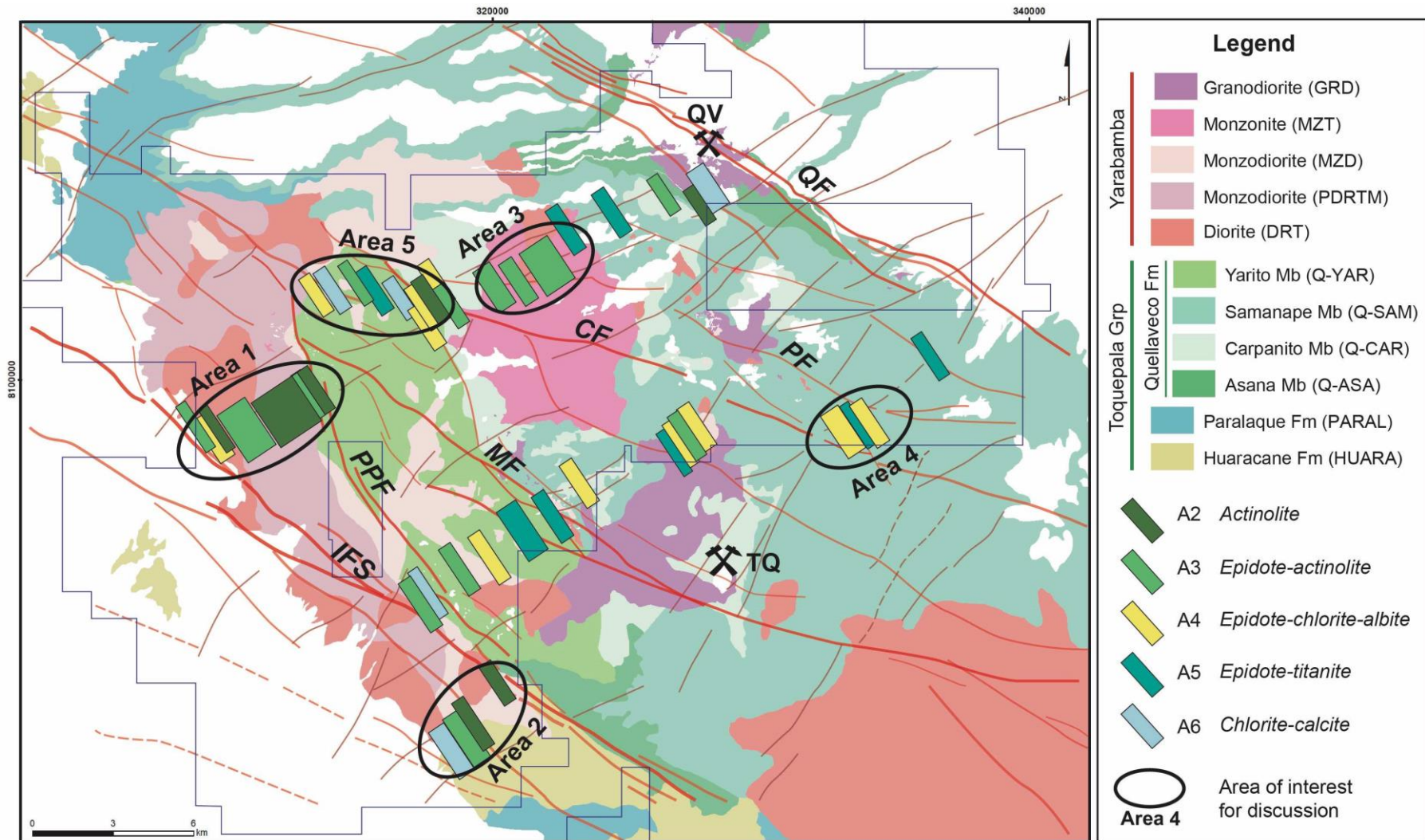


Figure 5.14. A summary alteration map for the study area with the locations of the propylitic alteration (A2-A6) represented as colour-coded strips. Areas 1-5 are highlighted and referenced in the discussion.

5.9 Conclusions

- Primary igneous apatite and zircon, and metasomatized apatite have been acknowledged and classified as $\text{apatite}_{\text{Ig}}$, $\text{zircon}_{\text{Ig}}$ and $\text{apatite}_{\text{Ig-Alt}}$, respectively.
- Eight key alteration assemblages have been identified: potassic (A1), actinolite (A2), epidote-actinolite (A3), epidote-chlorite-albite (A4), epidote-titanite (A5), chlorite-calcite (A6), sericitic (A7) and advanced argillic (A8). From the propylitic assemblages (A2-A6), the descriptions of epidote, titanite, apatite, zircon and chlorite occurrences have been highlighted (for later geochemical and geochronological reference).
- Veining is categorised into ten groups: potassic (V1), epidote-actinolite (V2), epidote-quartz (V3), albite-epidote (V4), quartz (V5), quartz-albite-epidote (V6), calcite-epidote (V7), sericite-dickite (V8), quartz-pyrite (V9) and a tourmaline breccia (BX).
- Between the Incapuquio Fault (IFS) and Puca-Porquene Fault (PPF) actinolite and epidote-actinolite (A3) alteration is consistently present. Epidote-actinolite veining (V2) is only found within the area. The juxtaposition of this block lithologically and in terms of the alteration to the NE side of the PPF, indicates potential fault movement, possibly a post major propylitic alteration event.
- Areas of intense propylitic alteration correlate with proximity to major mapped faulting and in some cases sericitic alteration. An example from the Pacay Fault demonstrates that even in an area of minimal or no wallrock alteration, elevated propylitic alteration is facilitated by the lateral dispersion of propylitic fluids in the surrounding wallrock.

6 Structural analysis of the Quellaveco region

6.1 Aims

This chapter aims to develop the structural model of the Quellaveco region, understand key structures at play during the emplacement of the district porphyries, and subsequent effects on the regional tectonics.

- What does regional network suggest about the fracture intensity and density of the major NW-SE faults and transverse NE-SW faults?
- Can drone footage of specific areas help enhance structural fieldwork in the overall understanding of the fault network?
- What is the importance of the NE-SW structures?
- What are the district-scale distribution fractures? What do the structural domains indicate about the dominant fractures associated with the major NW-SE structures?
- Do the structures act as fluid conduits and can these be kinematically constrained?
- Can a genetic structural model be devised?

6.2 Introduction

6.2.1 Structural Definitions

Discontinuities such as faults, fractures, joints and shear zones can be problematic to identify in the field. Some of the principal terminology are listed here as defined by (Berkowitz, 2002; Fossen, 2016):

- *Fracture* – a sharp planar discontinuity that represents planes of preferential weakness across which there has been separation. The most common types are joints and faults.
- *Fault* – a discontinuity surface across which there has been shear displacement surface or narrow tabular zone with displacement parallel to the surface, and which are usually the result of tectonic scale movement.

- *Joints* – are generally extensional fractures on which any shear displacement is too small to be visible to the unaided eye. Joints are associated with uplift and erosion and chemical action, unlike faults which are the result of tectonic-scale movement.
- *Fault gouge* – an incohesive fault rock with <30% visible fragments surrounded by matrix.
- *Kinematics* – referring to motion; used to describe the phenomena related to the relative movement of an object.
- *Kinematic indicator* – any structure indicating the sense of shear or transport during a deformation event.

6.2.2 Data collection

As discussed in the methodology section in Chapter 4, 107 samples were taken along two NE-SW trending transects in the wider district of Quellaveco (Figure 6.1). Of those 107, 84 were microscopically analysed covering a combined distance of 48 km. The transect orientation was specifically designed to be aligned perpendicular to the major investigated NW-SE structures enabling identification of the fracture trends in the distance

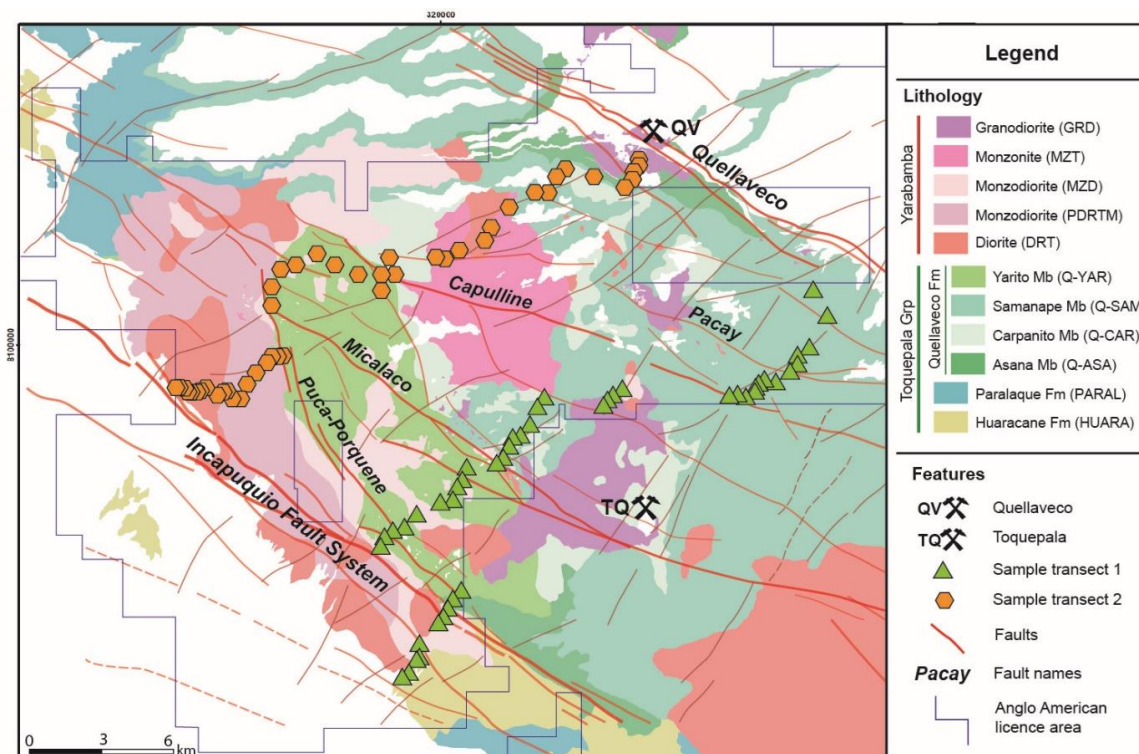


Figure 6.1. A lithological map highlighting the two transect lines followed for structural data collection. Locations of the samples collected are also indicated. The Yarabamba Batholith (YB) intrusions are coloured pink/purple, and Toquepala Group (TG) volcanics are green.

leading away from the faults. Additionally, in the sample collection, any geochemical changes with distance from the fault was to be identified too. One limitation was the absence of an orthogonal data transect (NW-SE) which would allow comparative analysis of the NE-SW structures.

An initial observation of the distribution of the two principal lithological units highlights a potential structural control (Figure 6.1). The intrusive phase of the Yarabamba Batholith (YB) proximal to Toquepala appears to be elongated along a NE-SW lineament. Areas of 'branching' of this body occur at intersection points with the NW-SE structures, in particular the Micalaco Fault (MF). Another apparent structural control on the YB is seen in the southern part of transect 2, where the contact between the YB and Toquepala Group (TG) is very distinct. This boundary follows the Puca-Porquene Fault (PPF), and would therefore imply fault movement leading to this linear juxtaposition of the units.

6.3 Structural analysis of regional dataset

To conduct a regional scale structural analysis of the Quellaveco region, this study has used an extensive fault data set provided by Anglo American. This dataset has been instrumental in providing the location of the major structures. However, there are some limitations to the dataset that should be noted. As the faults were mapped predominantly using satellite imagery and high-resolution DEM's, the existence of the faults is broadly based on topography. This method of mapping may not accurately distinguish between a fracture or fault. Although many of these structures have since been observed and clarified by field observation or remote sensing, there are still many areas that are inaccessible.

6.3.1 Digital orientation analysis

Orientation analysis of all the fractures highlights two very distinctive trends: NW-SE and NE-SW (Figure 6.2). The NW-SE fractures are distributed in narrow zones, the largest zone corresponding to the Incapuquio Fault System. Parallel zones include the Quellaveco Fault, which passes through the Quellaveco and Cuajone deposits, and the Micalaco Fault on which Toquepala is located.

6.3.2 Fracture density and intensity modelling

FracPaQ software was used to extract a graphical representation of fracture intensity and density of the region using this fracture map. In FracPaQ, the density value (m^{-2}) produced corresponds to the number of fractures per unit area and the intensity value (m^{-1}) is the total fracture length per unit area (Healy *et al.*, 2017). Figures 6.3a-f show three density and three intensity plots of the mapped dataset. All densities and intensity values in FracPaQ are calculated using a circular scan window method; the illustrated models have been produced using a 20 pixel diameter circle (Mauldon *et al.*, 2001; Healy *et al.*, 2017). Both figures highlight elevated fracture density and intensity along the NW-SE-trending Incapuquio and Quellaveco Faults. The anomalies associated with the Incapuquio Fault appear to also highlight a NW-SE to NNW-SSE splay from the IFS (Figure 6.3a). On the intensity map (Figure 6.3b) there is a significant drop in fracture intensity on the southwestern side of the IFS. This mirrors changes in the lithology and age of rock units across the IFS, with Toquepala Group volcanics on the north-eastern side, and the diorite and monzonite of the Yarabamba Batholith to the southwest.

By separating the fracture traces into the two structural trends, it is possible to detect any directional-specific density and intensity fracture hotspots (Figure 6.3a-b). Interestingly, the NW-SE models (Figure 6.3c-d) show clear channels (1-2 pixel thickness) that highlight the three major NW-SE faults. Furthermore, there is a marked increase in fracture intensity around, and to the east of, Quellaveco. When the NE-SW structures are separated (Figure 6.3e-f), elevated fracture density still highlights the Quellaveco Fault (QF) and the IFS. Two NE-trending ‘corridors’ of particularly high fracture intensity are evident, coinciding with the Quellaveco and Cuajone deposits.

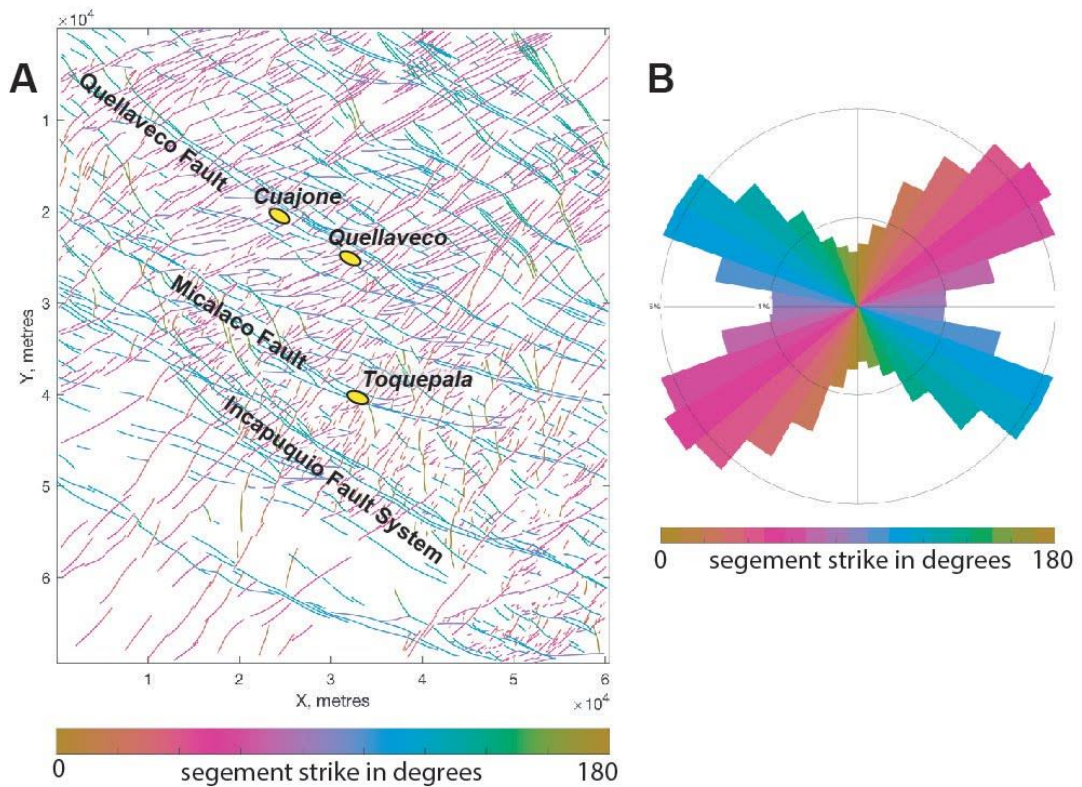


Figure 6.2. a) Fault map of the region, colour-coded by strike, with deposits and major faults highlighted; b) Rose plot of mapped structures in the region, colour-coded by strike, with two clear structural trends: WNW-ESE and NE-SW.

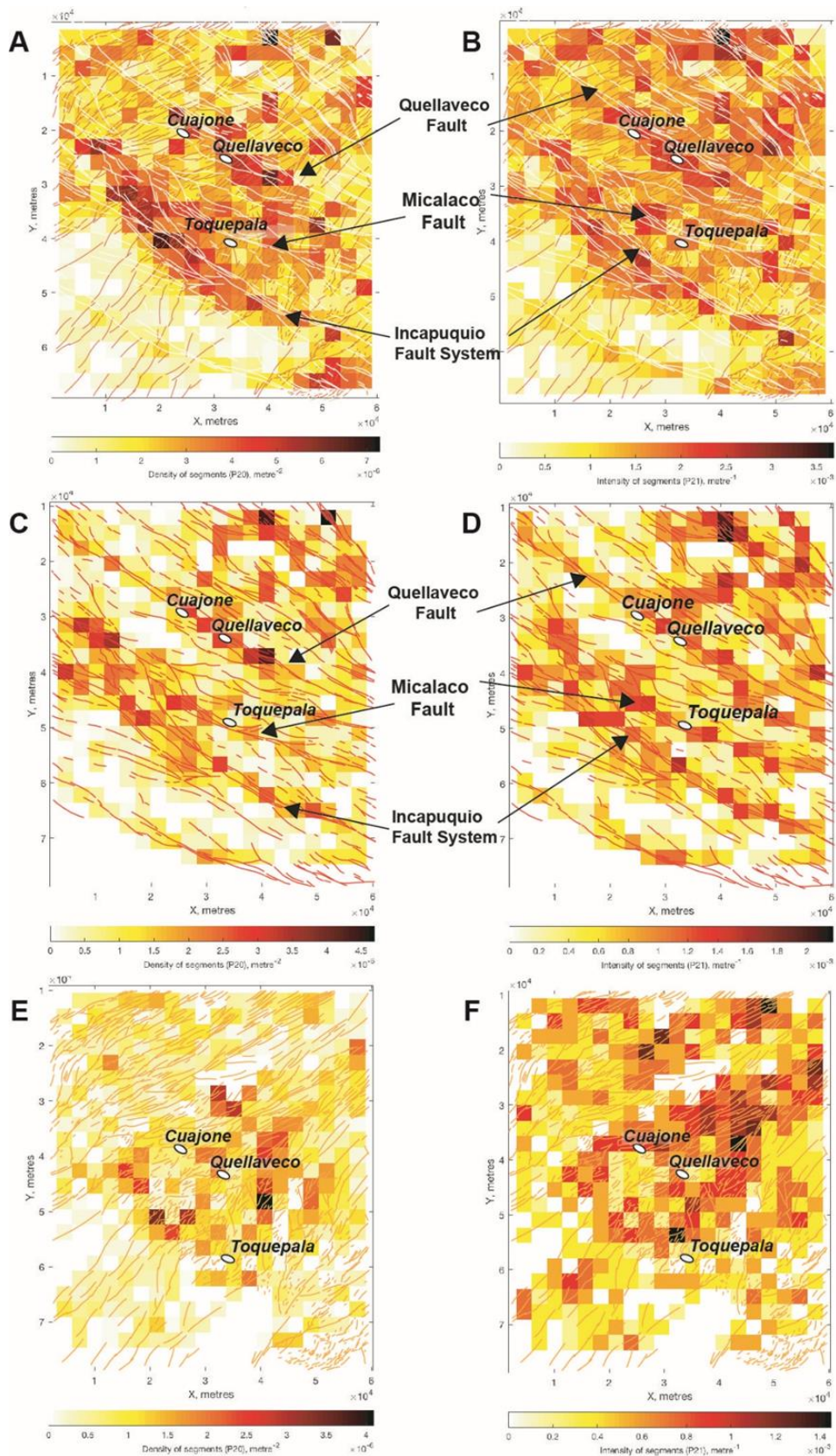


Figure 6.3. Fracture intensity (left) and density (right) mapping: **a-b**) pixelated grid of all fracture orientations; **c-d**) mapping of fractures trending NW-SE only; **e-f**) mapping of fractures trending NE-SW only.

6.3.3 *Spatial distribution of fracture intensity and density with respect to key structural trends*

To further examine links between fracture intensity and density (of all fractures) with major faults and deposit locations, three cross-sections were constructed:

- (1) A section orientated perpendicular to the main WNW-ESE fault trends that crosses the Quellaveco deposit (Figure 6.4a). The highest density value of $9.2 \times 10^{-3} \text{ m}^{-1}$ is found where this section crosses the IFS. The second highest value of 6 m^{-1} coincides with the location of Quellaveco Fault and Quellaveco deposit. The two highest intensity peaks also occur where the section line crosses the IFS and Quellaveco, with the highest value of $3.2 \times 10^{-3} \text{ m}^{-2}$ observed where Quellaveco is located.
- (2) A section line trending WNW-ESE following the strike of the Quellaveco Fault, passing through Cuajone and Quellaveco (Figure 6.4b). Fracture density on this section peaks at $2.6 \times 10^{-3} \text{ m}^{-1}$ between Cuajone and Quellaveco. This section has significantly higher intensity values than observed in Sections 1 and 3, with a peak of 0.012 m^{-2} . A similar pattern of elevated intensity values of $7.2 \times 10^{-3} \text{ m}^{-2}$ occurs between Cuajone and Quellaveco.
- (3) A section parallel to the IFS (Figure 6.4c). This line shows higher fracture density at the WNW end of the section. Intensity along the section is variable.

6.3.4 *Fracture connectivity*

Understanding fracture connectivity of the area is potentially useful, especially when compared with fracture intensity, as it highlights which areas would be more likely to facilitate fluid flow. However, this does not consider that not all fractures were present at a given time in the past. To determine fracture “connectivity” in the area, FracPaQ was used to create an I-Y-X plot of nodes (Figure 6.5a) with ‘I’ representing ‘isolated ends of traces’, ‘Y’ being used for ‘branch points, splays or abutments’, and ‘X’ for ‘cross-cutting intersections’ (Healy et al., 2017). The data processed shows very few ‘Y’ type nodes, with a majority of ‘I’ type nodes. The IYX ternary diagram (Figure 6.5b) is based on work by Barton and Hsieh (1989) and

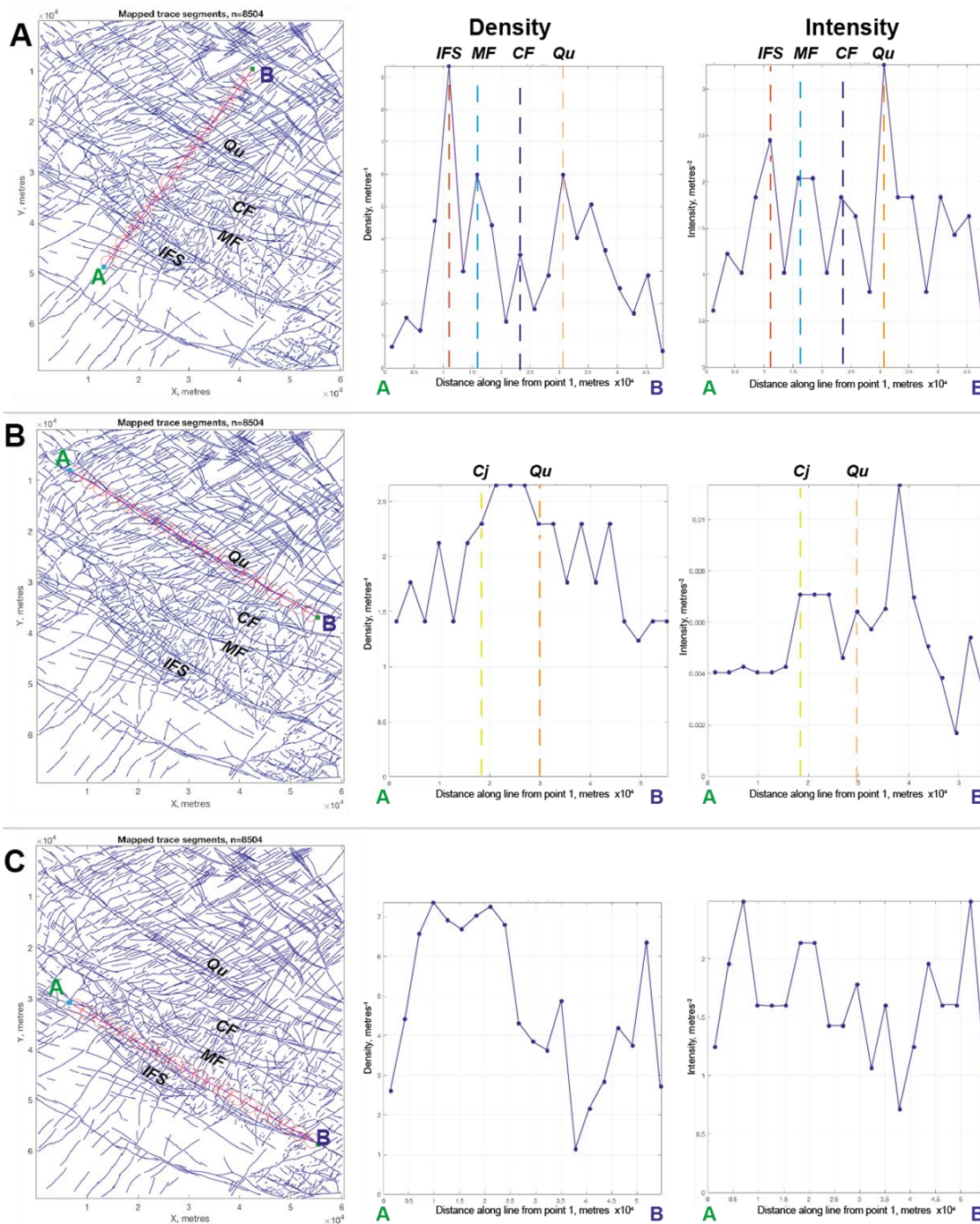


Figure 6.4. Cross-sections illustrating variations in fracture density and intensity. **a)** Section perpendicular to major WNW-ESE fault sets, intersecting Quellaveco and the IFS; **b)** Quellaveco Fault-parallel section; and **c)** IFS-parallel section

Manzocchi (2002) and attempts to represent the connectivity of a system by the relative frequency each of the three nodes: I-Y-X. The contour lines, CL, represent the average number of intersections, with CL = 2.0 indicating the limit above which the system is poorly connected with no clustering and CL = 3.57 being the value modelled by Balberg *et al* (1984) for percolation of a system of random lines of fixed length (Sanderson & Nixon, 2015). The calculated connectivity of traces in the Quellaveco area is Y:X:I =

0.00:0.10:0.90; therefore, the system is seemingly very poorly connected. Fracture connectivity maps, showing the fracture intersection density and intensity respectively, highlight elevated values along the IFS and Quellaveco Fault (Figure 6.5c and 6.5d). Quellaveco and Cuajone are noticeably situated at points of elevated values on the Quellaveco Fault. Interestingly, Toquepala sits within areas of moderate to low connectivity (Figure 6.5c-d).

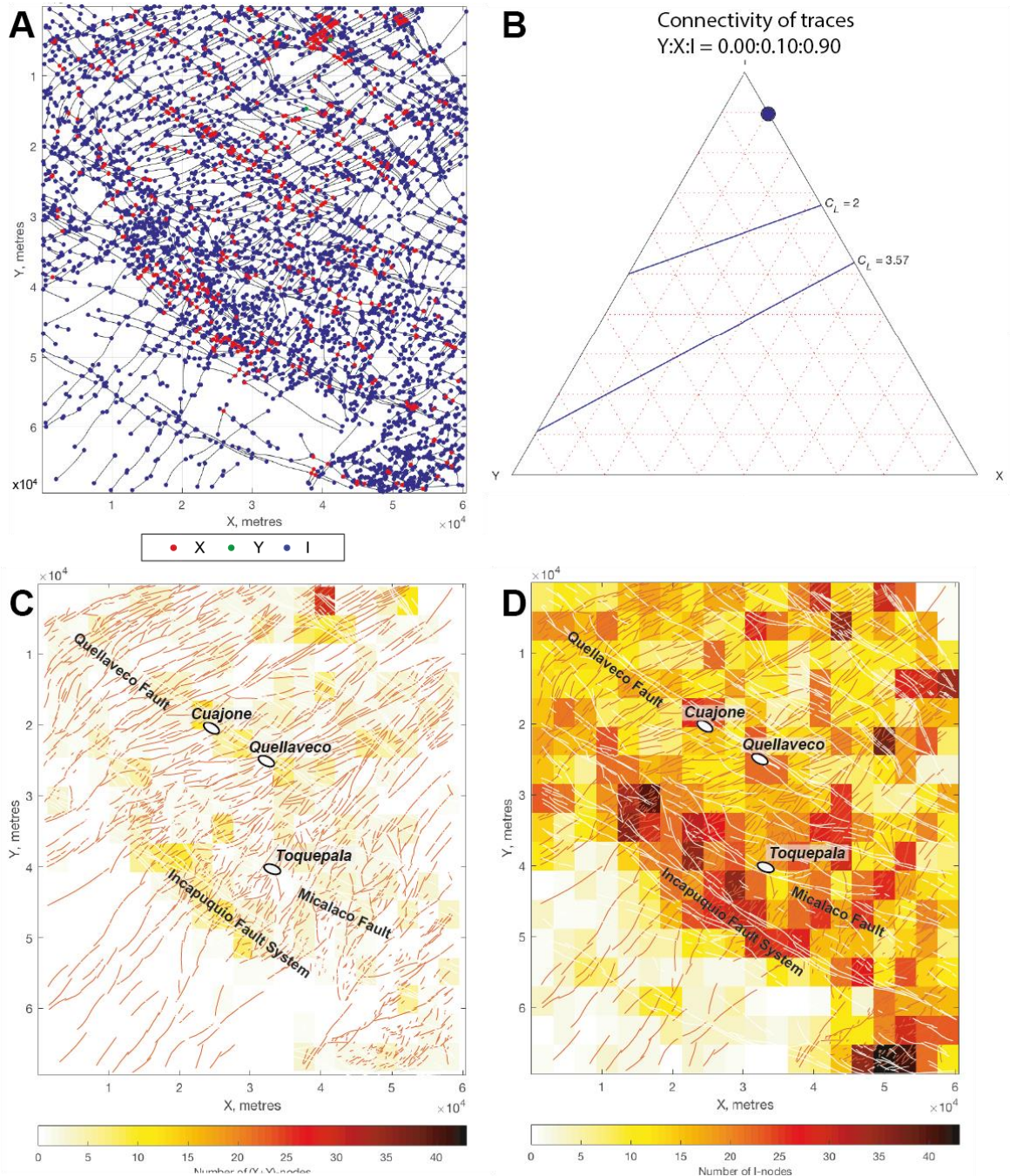


Figure 6.5. **a**) A map showing nodes detected as I-Y-X : $n_I = 4508$, $n_Y = 3$, $n_X = 519$, **b**) IXY ternary diagram of the fracture set (Barton and Hsieh, 1989; and Manzocchi 2002) **c**) fracture density connectivity map; **d**) intensity connectivity map with fault and deposit locations highlighted

For this connectivity modelling, it is important to highlight that the nodes plotted may not be fully indicative of the topology of these structures, as, due to scale and topography, the mapped fracture map will not fully represent the network at depth, thereby changing the CL values (Sanderson & Nixon, 2015).

6.4 Fracture mapping from field data

6.4.1 Principal orientation domains

Fracture orientation data from field mapping of the two transects have been broken down into domains based on the dominant fracture orientation in each. These populations have been numbered and labelled with the predominant orientation direction, and are referred to throughout this chapter (Figure 6.6).

A relationship exists between more intense propylitic alteration and NW-SE dominant domains. WNW-ESE-trending faults and fractures are recorded throughout the area but are subordinate in the majority of the domains. N-S

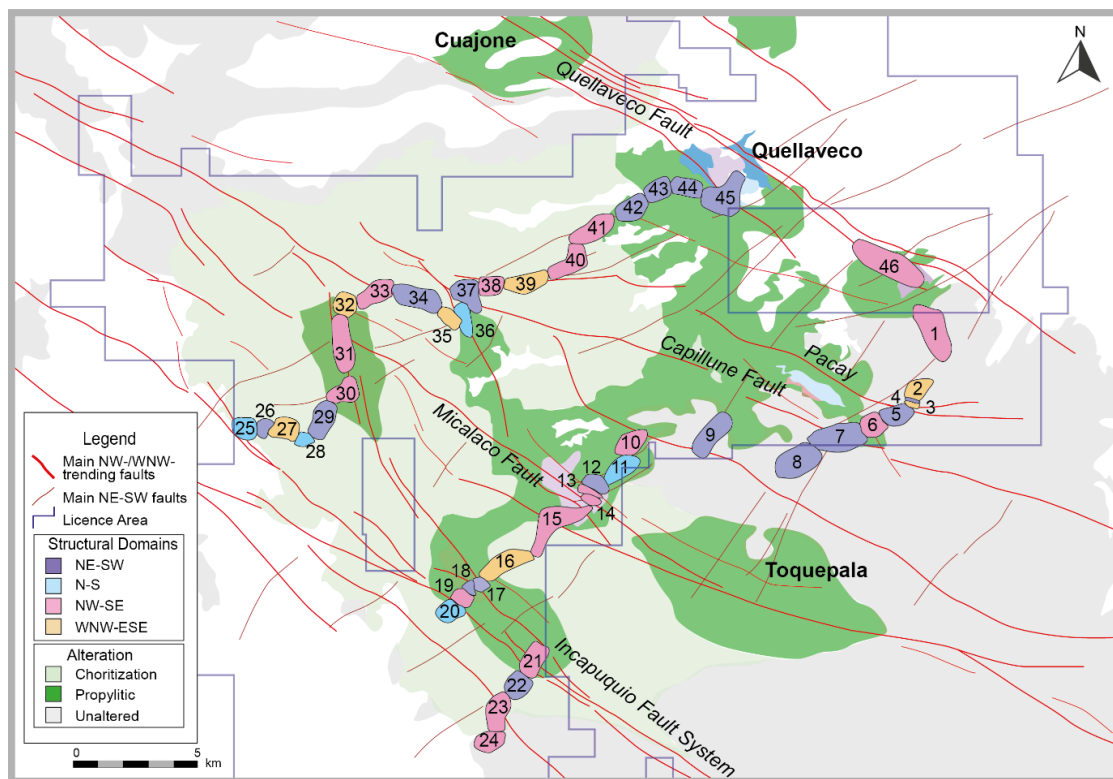


Figure 6.6. Structural domains mapped along two transects, coloured based on dominant structural trend in each: NE-SW – purple; N-S – blue; NW-SE – pink; and WNW-ESE – yellow. Domains are overlaid on Anglo American alteration map – chloritization refers to chlorite-only alteration; propylitic alteration involves the assemblage epidote +/- chlorite +/- calcite.

fractures are also generally present throughout the whole area; however only 5 out of 46 mapped domains have a majority of fractures in this orientation.

To identify areas with a greater population of particular fracture sets, a sketch map of the two transects has been drawn (Figure 6.7) with larger-scale insets shown (Figure 6.8). These are inferred fault lines based on the fracture and domain mapping overlaid on a major fault map of the area. Area A has the least visible propylitic alteration of the areas investigated along the structural transects. Interestingly, a significant decrease in fracture abundance, in particular moderately- to shallowly-dipping fractures, coincides with areas of relatively unaltered wall rock. Area B covers both the Incapuquio Fault System and the Micalaco Fault. Along the IFS and to the SW, there is a high density of moderately- to shallowly-dipping NW-SE fractures which are parallel and at acute angles to the IFS. Over the mapped area of the Micalaco Fault, clusters of steeply-dipping and moderately- to shallowly-dipping NW-SE fractures are observed. In area C, up to ~1 km from the IFS, there is an increase in moderately- to shallowly-dipping NNE-

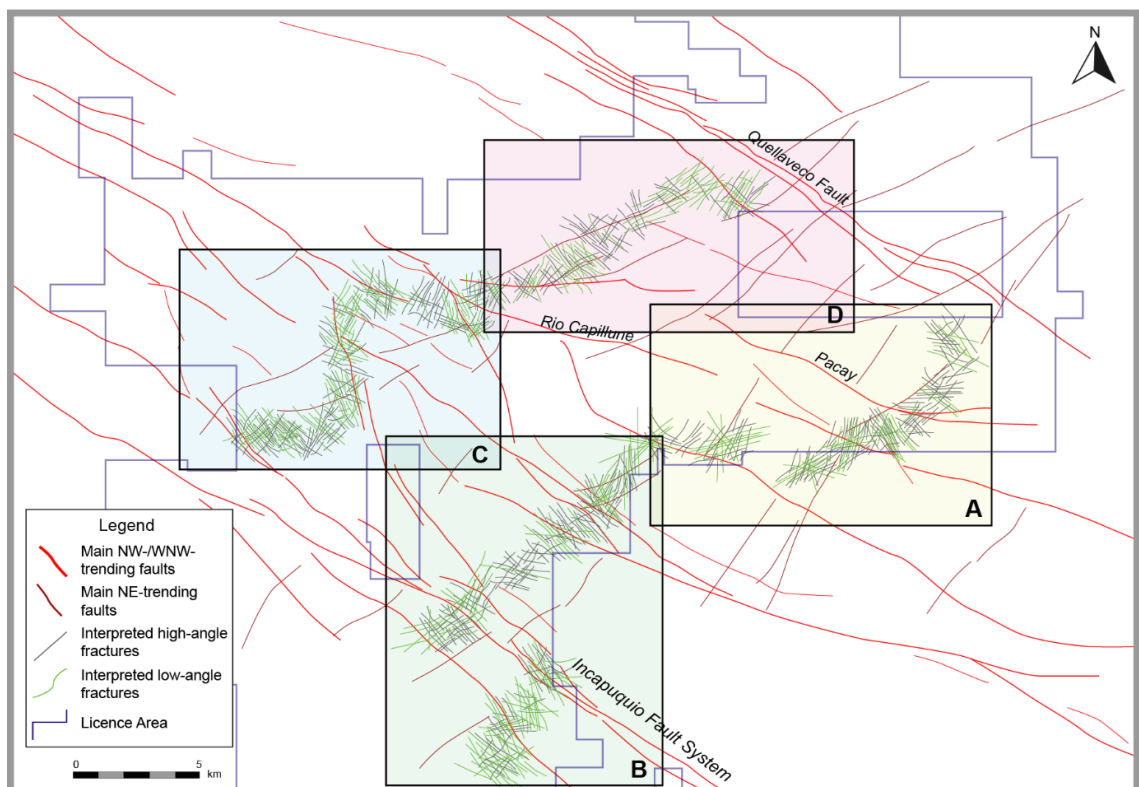


Figure 6.7. Fracture sketch map of the two transects. Four insets are shown, A, B, C and D; these are expanded in Figure 6.8.

SSW fault sets. Parallel to a splay in the IFS, steeply-dipping and moderately- to shallowly-dipping fractures trend NW-SE. In area D, in the vicinity of Quellaveco, there is a cluster of steeply and moderately to shallowly-dipping NW-SE fractures that are replaced by dominantly shallowly-dipping NE-SW fractures proximal to the deposit.

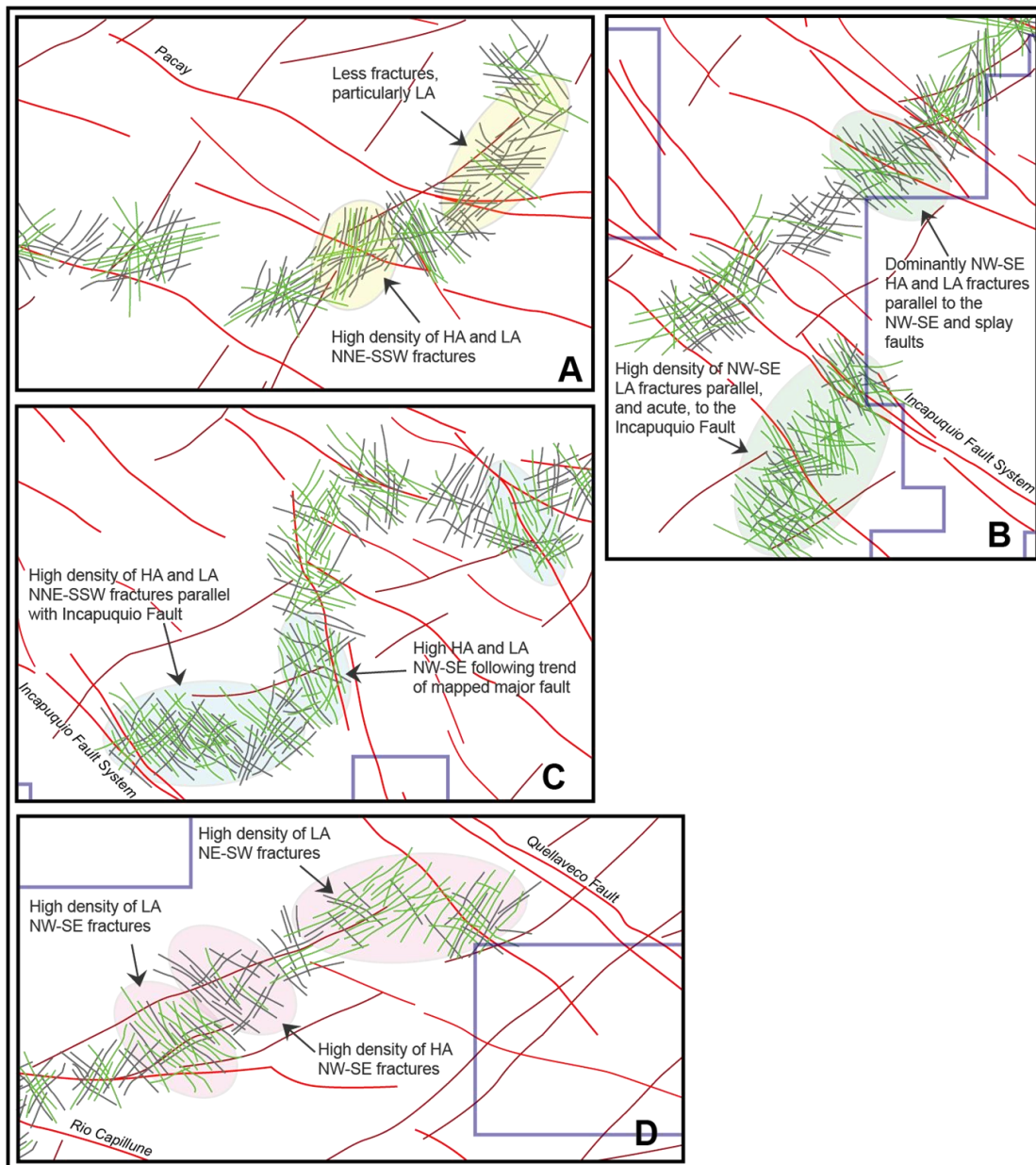


Figure 6.8. Fracture sketch map insets from Figure 6.7. Fracture lines: green indicates moderately- to shallowly-dipping fractures ($<70^\circ$); grey indicates steeply-dipping fractures ($>70^\circ$).

6.4.2 High-resolution modelling using outcrop-scale drone imagery

As a part of this project, drone imagery was used to help build high-resolution models of selected parts of the study area (Figure 6.9). The sites were chosen for their apparent structural significance:

- Site 1 – located along the Pacay Fault, this area interestingly shows no mapped or visible alteration but a high fracture density.
- Site 2 - located on the mapped intersection between the NW-trending Rio Capillune Fault and NE-SW trending fault, this area displayed highly pervasive propylitic alteration (see Chapter 5).
- Site 3 – located approximately 400 m from the major NW-trending Incapuquio Fault core, this area was selected to assess the dominant fracture sets in the damage zone of the IFS.
- Site 4 - located on the uppermost section of the NNW- trending Puca-Porquene Fault (PPF) with proximity to the intersection between the Micalaco Fault (MF) and westernmost part of the CF.
- Sites 5 & 6 – are located on opposing fault branches stemming from the major NW-SE CF.

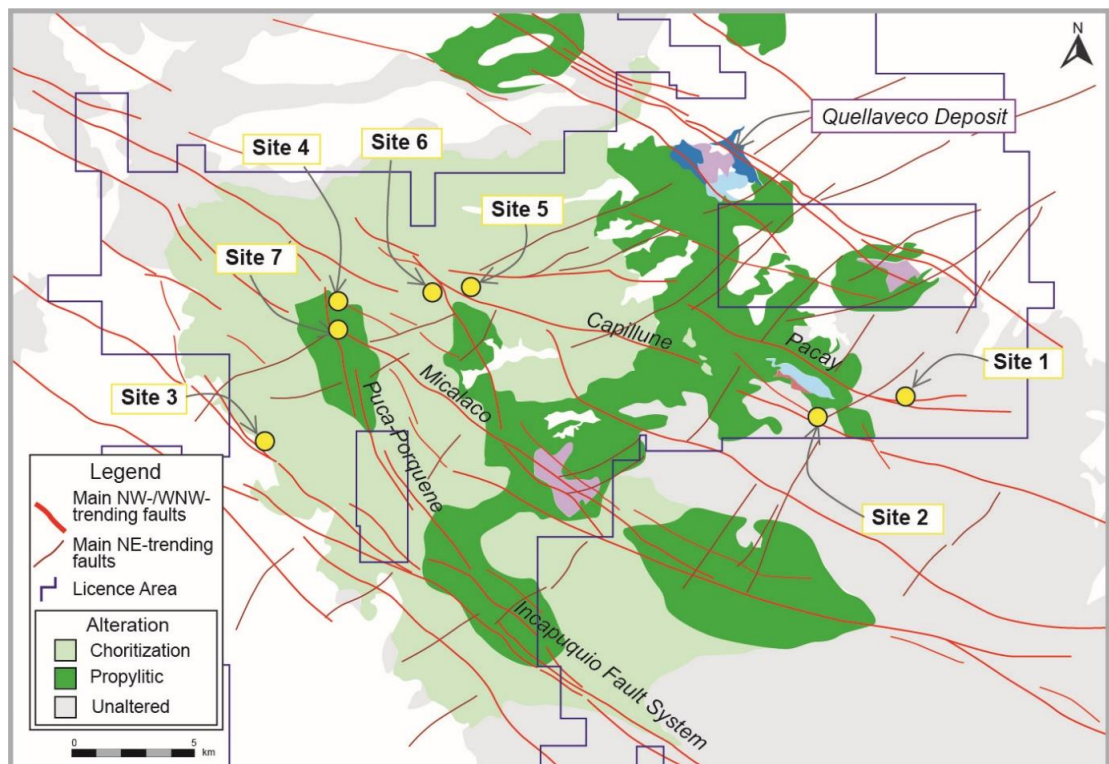


Figure 6.9. Drone model location map of 7 sites.

- Site 7 – located on the intersection between the PPF and MF, this area is highly fractured and situated <500 m from an extensive hydrothermally altered fault damage zone.

For each of these drone sites of interest, the drone data was modelled and mapped and fault/fracture data were extracted. A summary of the data with stereonet and rose plots is presented (Table 6.1-Table 6.4). From the drone mapping, a number of observations can be made.

- Site 1 – relatively small scale (for drone-resolution), E-W and ENE-WSW-trending structures appear to offset the N-S fault valley in a sinistral sense. From cross-cutting relationships there is evidence of simultaneous movement on NW-SE and E-W-trending faults.
- Site 2 – the fractures mapped are steeply dipping, with 13/33 in the ENE-WSW orientation, 7/33 to the WNW-ESE and only 4/33 in the NE-SW orientation. A sub-vertical NE-trending shear (027 NW 86), appears to cut the ENE-WSW and WNW-ESE fractures is, but no relative kinematics were identified.
- Site 3 – approximately 400 m from the major WNW-trending Incapuquio Fault core, this site has two dominant fracture orientations, E-W and NW-SE. Interestingly, all the E-W fractures are steeply-dipping, and the majority of the NW-SE fractures have relatively shallow dips
- Site 4 – the data are much more varied at this locality, with potentially three orientation directions: WNW-ESE high angle; NNW- SSE high angle; and NE-SW moderate to low angle fractures. The fractures are less continuous and therefore it is difficult to find any temporal relationships between the fracture sets.
- Site 5 – this site is situated on the NW-SE Capillune Fault, which extends to Site 2 on transect 1. The clearly dominant fracture orientation is ENE-WSW with approximately 1/3 of the fractures being of low to moderate dip to the NW and SE. NW-trending fractures are high angle/sub-vertical, with most of the WNW-ESE fractures moderately dipping to the NE.
- Site 6 – WNW-ESE fractures are dominant, 65/136, mostly steeply dipping, but with some NW-SE fractures moderately dipping to the SW. Interestingly, all of the NE-SW fractures (25/136) are moderately or

shallowly dipping SE. Many of these fractures appear conjugated with the steeply dipping NW-SE fractures. Figure 6.10a shows a selected conjugate pair in 3D view, with the map view on the right. The two fracture planes have intersecting angles of 60° and 120° . From the stereonet (Figure 6.10b), the resultant plane (shown in black) has a value of 089 S 65 and indicates a possible σ_1 direction parallel to this. It is suggested that there has been sinistral strike-slip movement on the high angle WNW-ESE fault, and dextral strike-slip displacement on the NE-SW fault (Figure 6.10c). Both fracture sets would be likely to have experienced dip-slip normal movement.

- Site 7 – three main fracture orientations are observed: steep E-W; steep, with some moderately dipping NE-SW; and mostly steep N-S fractures. There are several examples of E-W fractures cross-cutting the N-S fractures.

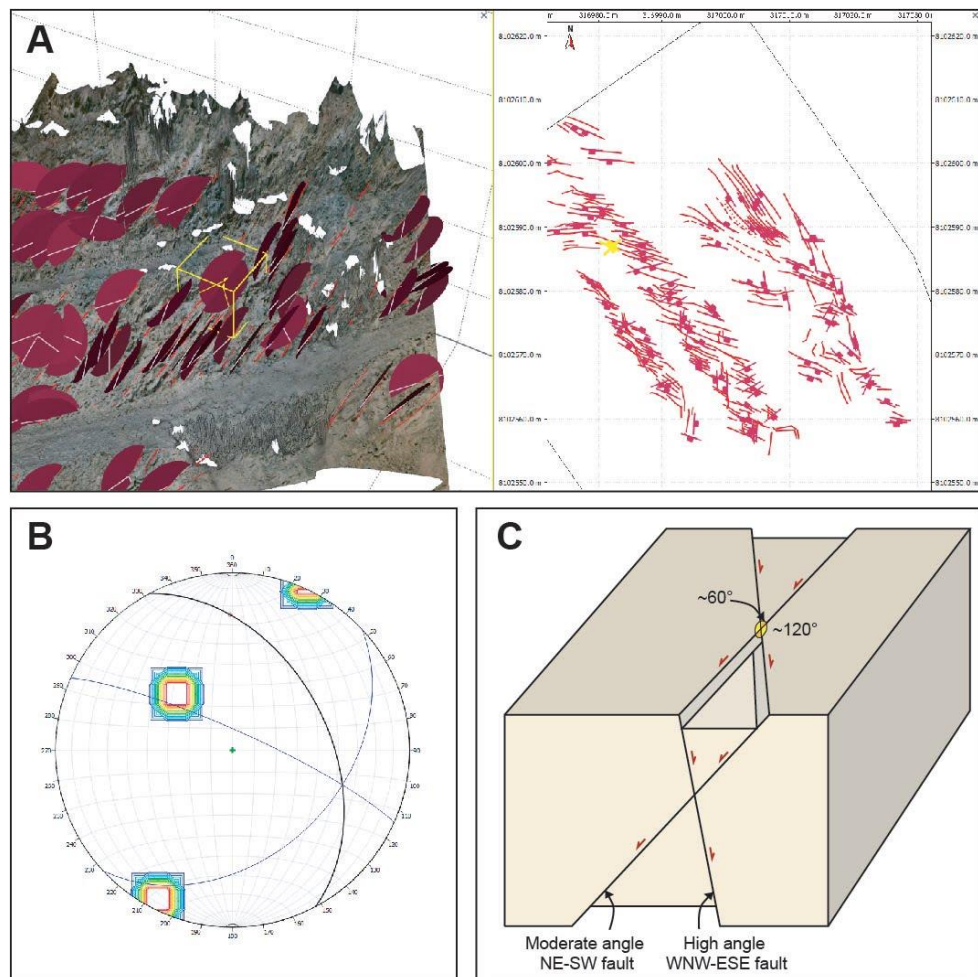


Figure 6.10. Interpretation of conjugate faulting at Site 6.

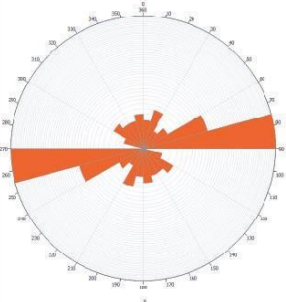
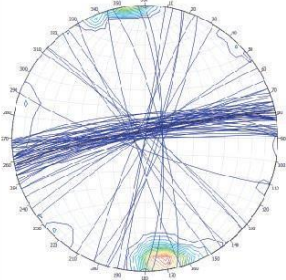
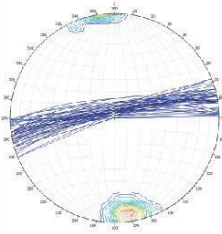
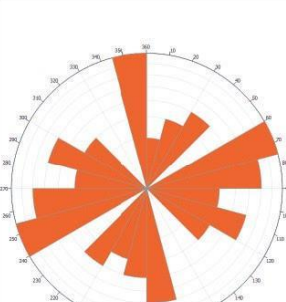
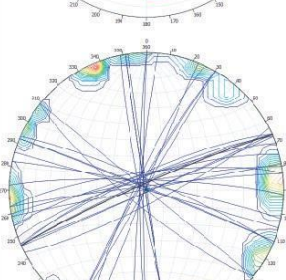
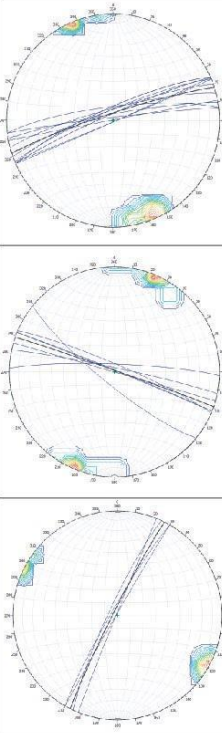
Combined Area Data	Drone Area	Stereonet Breakdown	Plane (strike/dip/sense) No. of Data Points	Breakdown Comments	Overall Comments
  <p>Plane: 259/84 N Point total: 75</p>	1		260/83 N 53	E-W trending high angle faults, dipping to the north	<p>Area is on intersection point between a NE-SW fault and the WNW-ESE Pacay fault</p> <p>All fractures are high angle, >70°</p> <p>Very dominant set of E-W fractures, and no other clear trends</p> <p>Large N-S trending valley, displaying tensional fractures</p>
  <p>Plane: 246/86 NW Point total: 33</p>	2		252/84 N 13 289/89 N 7 3207/86 NW 4	NE-SW trending high angle dip WNW-ESE trending, subvertical NE-SW trending subvertical shear zone	<p>Area in the WNW-ESE trending Rio Capillune Fault, close to the NE-SW Quebrada Honda Fault</p> <p>Most dominant fracture orientation appears to be ENE-trending subvertical fractures</p> <p>Clear NE-SW trending 'shear' channel cutting NW-SE and E-W fractures</p>

Table 6.1. Drone data from sites 1 and 2. The rose plots are coloured based on the fracture dip: red = 70 - 90, light green = 52 - 70, light blue = 52 - 33, and dark blue = 33 - 14. The fractures are plotted on the stereonets as *planes*, and the poles to planes have been contoured.

Combined Area Data	Drone Area	Stereonet Breakdown	Plane (strike/dip/sense) No. of Data Points	Breakdown Comments	Overall Comments
 Plane: 292/76 N Point total: 35	3	(G)	269/90 11	E-W trending high-angle dip to N and S	Area located close to the WNW-trending fault splay (0.4 km) from the Rio Capillune Fault Two distinct fracture orientations in area: NW-SE (dominant) and E-W (secondary)
			322/58 NE 163	NW-SE trending moderate dip to SW	Interesting lack of any NE-SW and N-S trending fractures The only low/moderate dipping faults are NW-SE trending
 Plane: 319/86 NE Point total: 49	4	(H)	230/46 NW 10	NE-SW trending with subvertical, and low-angle NW- and SE-dipping clusters	Area on the intersection point between NNE-SSW and NW-SE section of WNW-ESE Puca-Porquene fault Mostly NE-SW low/moderate angle faults. Opposing dip direction, suggest conjugate faulting
			346/83 E 16	N-S trending subvertical, with some moderate dip	
			112/86 S 21	WNW-ESE trending with high angle dip	

Table 6.2. Drone data from sites 3 and 4. The rose plots are coloured based on the fracture dip: red = 70 - 90, light green = 52 - 70, light blue = 52 - 33, and dark blue = 33 - 14. The fractures are plotted on the stereonets as planes, and the poles to planes have been contoured.

Combined Area Data	Drone Area	Stereonet Breakdown	Plane (strike/dip/sense) No. of Data Points	Breakdown Comments	Overall Comments		
 Plane: 258/83 N Point total: 53	5		247/89 NW 30	EWE-WSW-trending with high/moderate dip to NW & SE	Area situated along major WNW-trending major Rio Capulline fault		
		(l)		318/77 NE 11		WNW-ESE & NW-SE trending with low and high angle dips	
 Plane: 113/79 SW Point total: 136	6		089/71 S 23	E-W trending Subvertical dip	Area close to area 5, near the splay of a NE-SW fault from the WNW-ESE Rio Capulline Fault (0.4 km)		
		(M)		055/43 SE 25		NE-SW trending low/moderate dip to the SE	Dominant fracture orientation is high-angle NW-SE. These appear to be conjugate to NE-SW fractures
				118/87 SW 65		NW-SE-trending high angle to the SW	

Table 6.3. Drone data from sites 5 and 6. The rose plots are coloured based on the fracture dip: red = 70 - 90, light green = 52 - 70, light blue = 52 - 33, and dark blue = 33 - 14. The fractures are plotted on the stereonets as planes, and the poles to planes have been contoured.

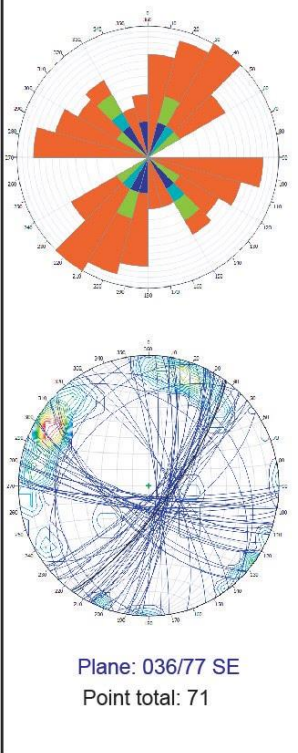
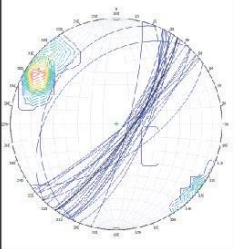
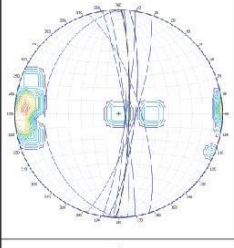
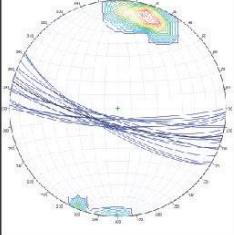
Combined Area Data	Drone Area	Stereonet Breakdown	Plane (strike/dip/sense) No. of Data Points	Breakdown Comments	Overall Comments
 <p>Plane: 036/77 SE Point total: 71</p>	7 (P)		036/79 SE 29	NE-SW trending high-angle dip to the SE	Area in close proximity to the major WNW-trending Incapuquio Fault (0.4 - 0.5 km) NE-fractures are the dominant set in this area.
			001/82 E 10	N-S trending high-angle dip to the east	
			105/78 S 20	NWNW-ESE trending high-angle dip to south	

Table 6.4. Drone data from sites 7. The rose plots are coloured based on the fracture dip: red = 70 - 90, light green = 52 - 70, light blue = 52 - 33, and dark blue = 33 - 14. The fractures are plotted on the stereonets as planes, and the poles to planes have been contoured.

6.5 Veining and fault- fill

6.5.1 Groupings and spatial significance

In Chapter 5, nine vein classifications were defined based on petrological SEM analysis of hand samples. However, in the field it was not possible to distinguish between vein types in such detail. The extensive distance structurally mapped and volume of data recorded meant that a different approach was needed to record the key veins and fault-fill. These were broad groupings based on their observable mineralogy: clay fault-fill, epidote veins and D-veins. Orientation data for these grouping are shown in Figure 6.11.

- Clay fault-fill - a white fibrous mineral was the most abundant mineral filling fractures and fault planes. This hard, platy, inert mineral was found throughout the propylitic alteration domain, even in the most distal parts of the area (>20 km from the Quellaveco deposit). The clay is seen to have a clear preference to NW-SE and NE-SW faults (Figure 6.11c-d)
- Epidote veining – from field observation, these veins primarily contain epidote. From detailed analysis in Chapter 5, it is known that there are multiple epidote vein classifications, however, for the purposes of this broader structural analysis, those propylitic vein types are combined. Interestingly, the dominant orientation direction is in two principal trends: of NE-SW to WSW-ENE (Figure 6.11c-d).

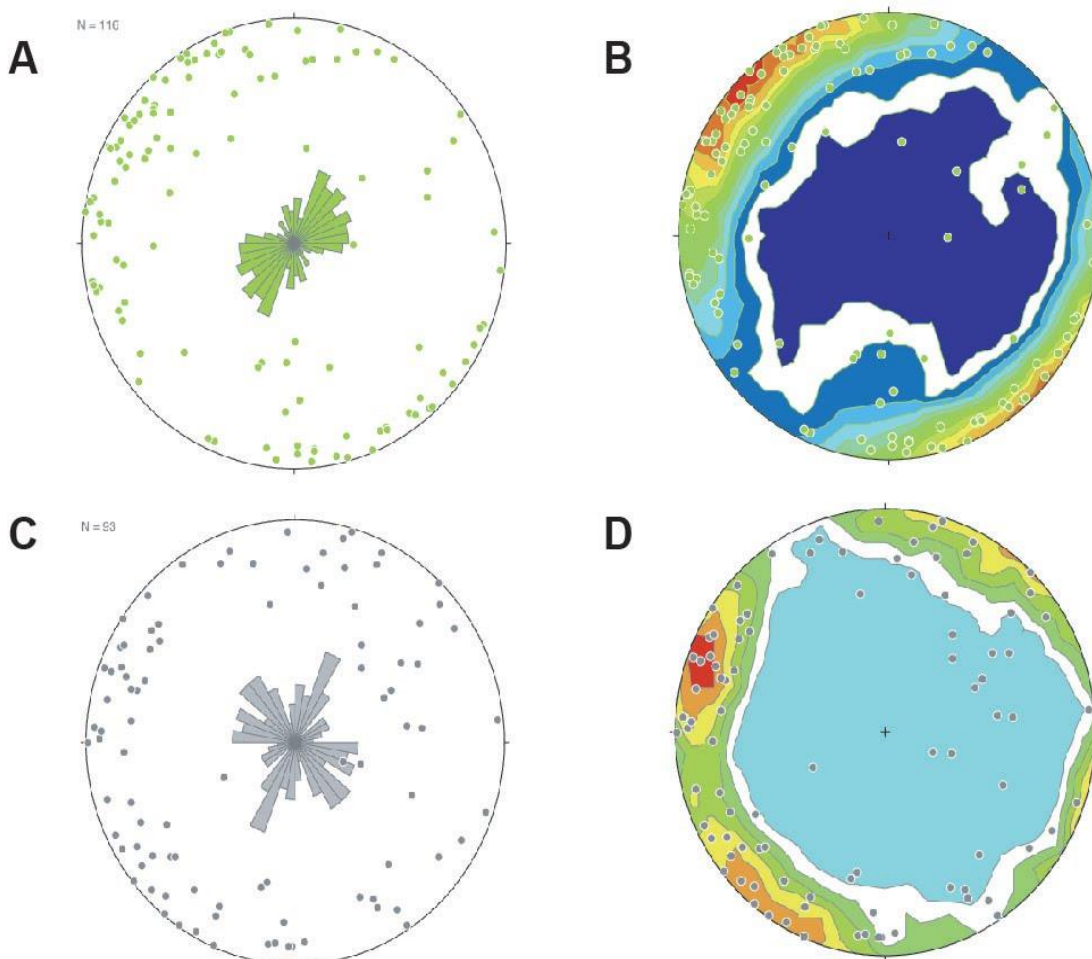


Figure 6.11. Structural data for the different generations of veining and fault-infill observed. **a-b)** stereonet and contour plot of veins containing only epidote; **c-d)** stereonet and contour plot of fractures containing only clay

- D-veins – these are termed ‘V9’ in Chapter 5 and were only recorded in the field, proximal to the deposit itself and the alteration centre at Pacay. These veins occur in sheeted arrays, typically NE-SW trending, and comprise a thin, highly oxidised suture with a 2-4 cm wide Fe-oxide halo. They are characteristically indicative of porphyry-style D-veins that are late-stage, linear veins, which mostly occur in structurally-controlled vein swarms in porphyry districts (Sillitoe, 2010).

When the occurrence of epidote veins or fractures with associated epidote alteration is plotted on the two fieldwork transects (Figure 6.12), it is evident that they predominate in the parts of the study area that are most distal to the known porphyry deposit centres of Quellaveco, Cuacone and Toquepala. Domains where epidote are absent correspond to areas close to the deposits and, in particular, the Quellaveco Fault. These gaps in epidote distribution correlate with areas where D-type veins are developed and where there is sericitization, such as domains 12-15 where there is strong sericitic alteration of the fractures along the Micalaco Fault. Based on the fracture mapping, there do not appear to be epidote-bearing fractures within

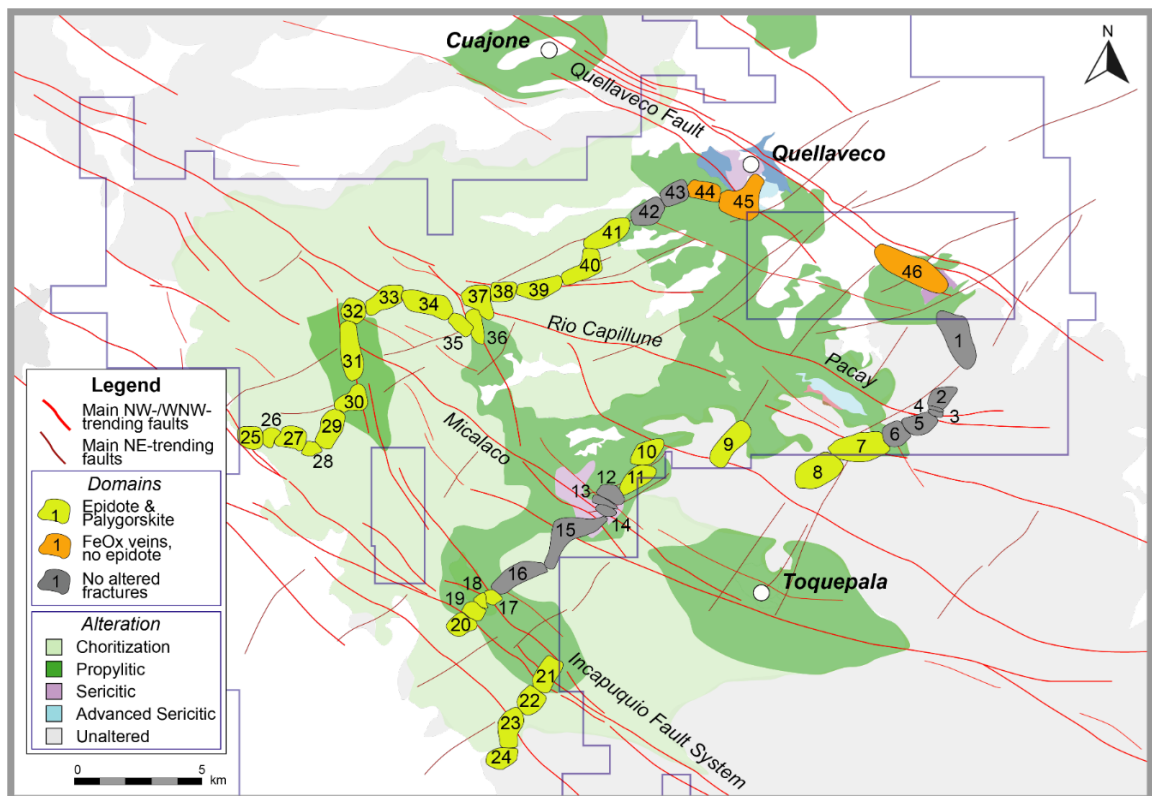


Figure 6.12.. Structural domains, colour-coded based on the occurrence of vein and fault-fill types.

a perpendicular distance of approximately 5 km from the Quellaveco Fault (domains 1-6 and 42-46). An abundance of epidote fractures is recorded on the Section 2 particularly around the IFS.

6.5.2 Fault Kinematics

Understanding fault kinematics is essential for the development of a structural model. In such an extensive field area, kinematic relationships observed in one region do not correlate with structures in another. Therefore, conclusions are not drawn about one-off relationships, and focus is placed on areas of consistent kinematic indicators.

One of the most widespread features is high-angled faulting with slicken lines indicative of sinistral movement. These faults were located primarily in the NE-SW and NW-SE orientation (e.g. Figure 6.13). In some cases, two phases of faulting were recorded on these faults: the sinistral strike-slip, and also reverse. These are particularly observed in NW-SE faults with white clay gouge present.

Between the IFS and PPF there is a dominance of high angled faults with approximately 5–10 cm clay infill. The fabric within the fault bends of these faults indicates sinistral reverse movement (e.g. Figure 6.14a).

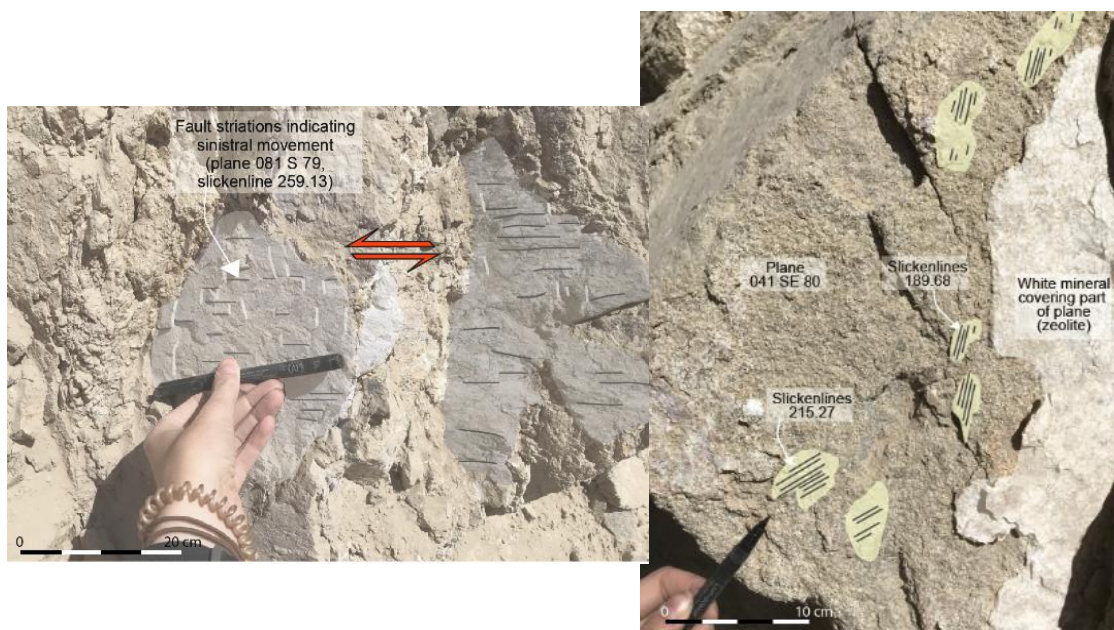


Figure 6.13. **a)** slicken lines along an E-W fault showing left-lateral movement, **b)** NE-trending fracture plane with two directions of slicken line visible, 215.27 and 189.68.



Figure 6.14. **a)** NW-SE-trending fault with white mineral infill within bends, **b)** Steeply-dipping, NE-SW shear zone with fabrics indicating dextral movement.

6.6 Discussion

The regional fracture intensity and density analysis reiterates the known significance of the IFS and also highlights the importance of the parallel Quellaveco Fault. As summarised by Jacay *et al* (2002) and Audin *et al* (2006), the Incapuquio Fault System is thought to be a sinistral transcurrent system that extends for more than 400 km through southern Peru. The location of Quellaveco, Cuajone and Toquepala close to this major system indicates its relevance to the formation of porphyry deposits in the district. The NW-SE-trending Quellaveco and Micalaco Faults that localise the deposits are parallel to the IFS and the fact that parallel, subsidiary structures show evidence for strike-slip sinistral movement (Figure 6.13) implies that regional sinistral transcurrent movement along NW-SE-trending faults was an important control on deposit localisation.

Because of the known prolonged activation history of the IFS (Jacay *et al.*, 2002) and the extent of the area of study, temporally constraining the structure is

problematic. Additional dimensions that will be analysed in Chapters 7 and 8, aim to help constrain this model. However, in order to generate an interpretation for the principal faults at this stage, the known region stress regime is considered.

Towards the end of the Paleocene (~59 Ma), the angle of convergence of the subducting Fallaron plate (subsequently known as the Nazca plate) shifted, from NNE to EWE directed motion (Pardo-Casas & Molnar, 1987; Jaillard & Soler, 1996). Rotation of the plate coincided with an increase in plate velocity of both the overriding (South American plate) and subducting plates (Sdrolias & Müller, 2006; Horton, 2018). Velocity profile by Horton (2018) records trench-normal absolute velocities of 25 mm/yr for 19S. This sudden increase in South American plate subduction is at odds with the middle and southern parts of South America, which experience plate deceleration, for example at 40°S velocity drops from 10 mm/yr to 4 mm/yr (Horton, 2018). The implications of these changes in plate motion were wide-reaching causing a surge of crustal melting and magmatism, and ultimately the initiation and localisation of regional porphyry formation (Camus & Dilles, 2001).

The shift in plate convergence orientation would have triggered orthogonal compression and sinistral transpression because of the orientation of the major NW-SE faults. It is well documented that the IFS has experienced sinistral movement during its activation history (Jacay *et al.*, 2002; Audin *et al.*, 2006), which is confirmed in this study. In transpressional systems such as this it is

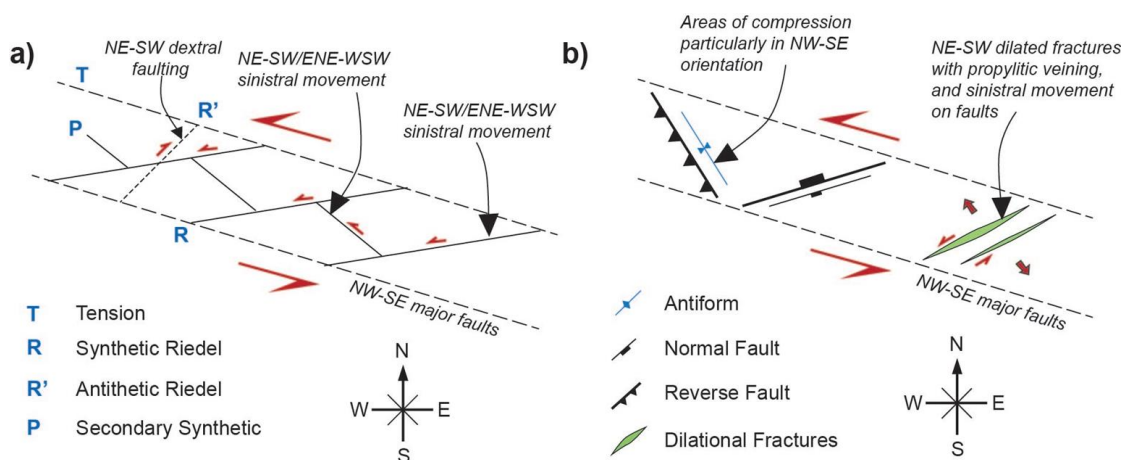


Figure 6.15. Sinistral strike-slip model adapted from Fossen (2016) to incorporate the observations made: **a)** Riedel shear model; **b)** other indicative large- and small-scale structures.

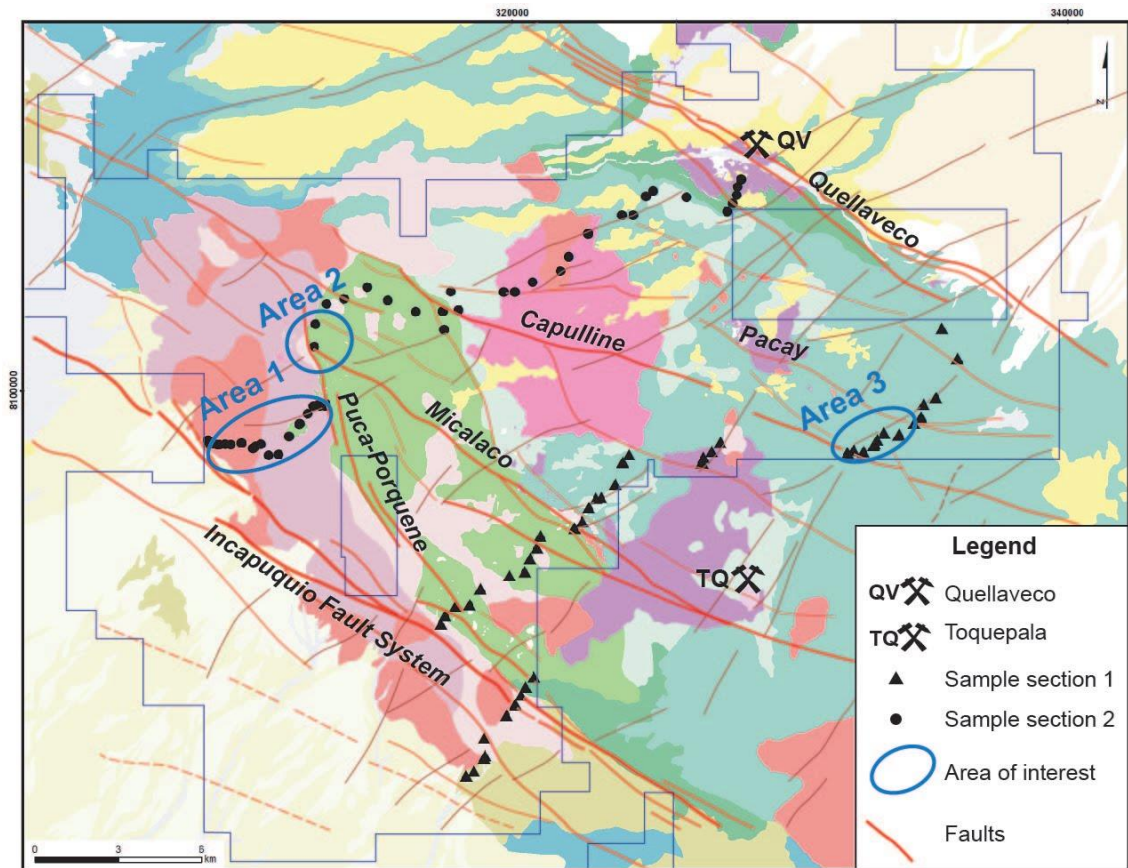


Figure 6.16. Sample transect map with areas of structural significance highlighted.

common to have areas of local transpression and transtension that are characterised by specific structures (Sibson, 1986; Fossen & Tikoff, 1993; Sibson, 2001; Fossen, 2016). The Fossen (2016) Riedel-model has been adapted here to explain how some of the structures observed in this study may have been influenced by the transcurrent regime (Figure 6.15). Between the major NW-SE trending faults (IFS, Quellaveco, and Micalaco), the NE-SW structures act as the Riedel shear fractures (R), where there is sinistral/extensional movement and likely dilation. The Riedel shear orientation gives a good indication of the orientation of σ_1 , as this maximum compressive stress in a strike-slip system cannot be perpendicular to the fault axis (Sibson, 2001). The NW-SE fractures are interpreted to be synthetic Riedel shears, displaying predominantly sinistral strike-slip offsets akin to the main faults, but there can also be a reverse component on structures in this orientation which is sub-parallel to σ_3 .

6.6.1 Area 1

Area 1 (shown on Figure 6.16) was initially noted because of the map-scale lithological outcrop of the Yarabamba Batholith, which appears to be structurally constrained to within the IFS and PPF. Although the Yarabamba Batholith is an intrusive unit and could have therefore been emplaced along this structural corridor, the linear nature of the contact implies it was transected by fault movement. Significant field evidence of high and moderately angled reverse faulting in Area 1 provides further evidence of potential uplift and transpression. Under the regional NE-stress during the Paleocene, the NNW-SSE strike of the northern part of the PPF would have been unfavourably angled to the regional maximum stress direction, and therefore would have resulted in an area of local transpression (Pardo-Casas & Molnar, 1987; Jaillard & Soler, 1996; Fossen, 2016). It is suggested that the uplift here was as a result of a positive flower structure caused by the transpressive regime.

6.6.2 Area 2

This area is located on the intersection of the PPF and MF within ~3 km of the PPF and CF splay, and is therefore structurally significant. In the field this was validated by a clear, highly fractured, fault damage zone from the MF and PPF intersection. It was noted from 3D structural analysis that there is an abundant high angle, of NW-SE/E-W and NE-SW in both drone models from Area 2. An internal structural report (AA internal report, 2018), also flagged this area as one of interest because of the presence of hydrothermal tourmaline breccias proximal to the PPF, and a distinctly low-magnetic anomaly.

6.6.3 Area 3

This Area has been discussed in Chapter 5, because of the noticeable mapped changes between highly pervasive epidote-chlorite-albite (A4) alteration and unaltered surrounding rock. The discontinuity of this alteration appears to coincide with the location of the CF and PF. Structural mapping of this area indicated an abundance of high angled NE-SW epidote-rich veining.

Combining the observations and interpretations of this chapter with known kinematics, a model has been developed to highlight some of the key findings (Figure 6.17).

6.7 Conclusions

- The major regional NW-SE structures (namely Incapuquio Fault System and Quellaveco Fault) have a particularly dense fracture network. This is interpreted as a damage zone.
- Localisation of the younger units of the Yarabamba Batholith favour the intersection points between NE-SW and NW-SE structures. In particular, the major NW-SE structures such as the Capulline Fault.
- The IFS-splay, the Pacay-Porquene Fault, has experienced compression and thrusting. This is validated by the kinematics in clay-filled SW-dipping fractures between the PPF and IFS, and observations by other studies. It also appears to provide the exhumation of the Yarabamba Batholith on its south-west throw. This area has been interpreted to show a period of sinistral transpression and flower structuring most likely to have occurred as a result of dramatic plate rotation at ~59 Ma.
- Epidote veining is favourably oriented in NE-SW indicating NE-directed compression facilitating the localisation of fluids in dilational NE-SW trending fractures. Veining is associated with vein types V2, V3, V6 and V7 discussed in Chapter 5, although categorising each vein recorded in the field was not possible.

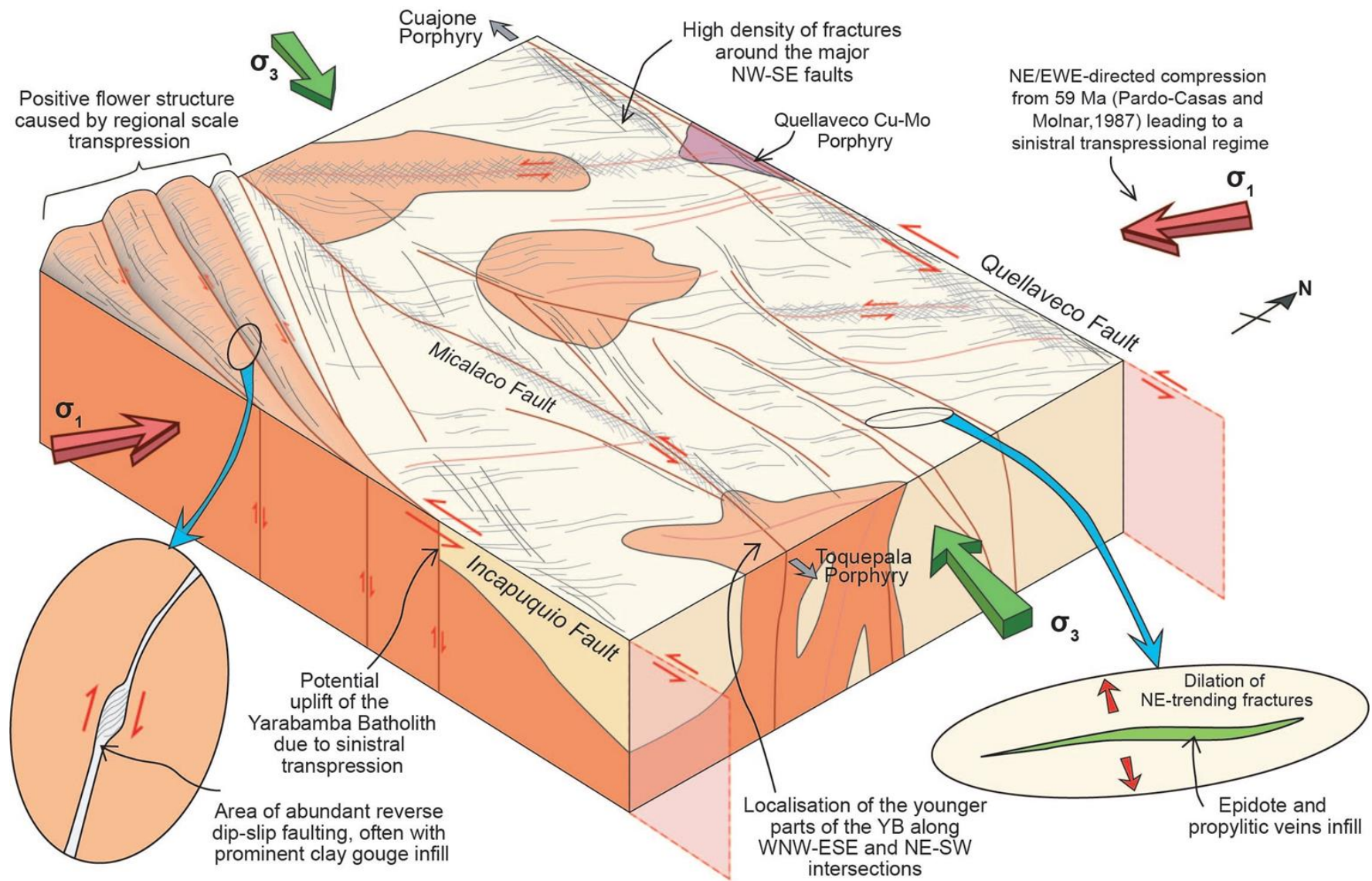


Figure 6.17. A summary model of the key structural interpretations in the district.

7 Geochronology

7.1 Aims and questions

A fundamental aim of this study is to determine whether U-Pb geochronology of propylitic vein-hosted and wallrock alteration can ascertain the temporal evolution of intrusive events and fluid migration pathways developed in the period leading up to porphyry mineralisation. U-Pb in-situ LA-ICP-MS analysis of four minerals: zircon, apatite, titanite and epidote from 82 samples has obtained igneous and alteration dates throughout the region. The novelty of this approach is the combining of U-Pb dating of four minerals over a regional scale, culminating in a large and extensive dataset. Furthermore, each datable grain is divided into the mineral assemblage classification discussed in Chapter 5 (Ig, Ig-Alt, A2-A7 and V2-V6). These classifications are referred to in this chapter.

The acquisition of the precise dates from the extensive U-Pb isotopic data has required a meticulous workflow in order to systematically identify reliable dates. Therefore, the section layout of the questions of this chapter reflects the chronology of the workflow. The process and relevant questions carried out are as follows:

- Visual assessment of the unconstrained regression lines on Tera-Wasserburg concordia diagrams. How many dates are of satisfactory precision and reliability? Is the reliability of the dates particularly prevalent in a specific dated mineral type (for example: zircon, apatite)?
- Investigate the common Pb ($^{207}\text{Pb}/^{206}\text{Pb}$)₀ ratio, in order to identify any spatial heterogeneity between the samples or in relation to lithology/intrusive events. Can precise common Pb intercept values from the Tera-Wasserburg calculations be used to anchor the y-axis of less precise dates to increase the age precision?
- Combine all of the U-Pb data for each mineral using a model-3 regression.
- With the assumption of mapped regional homogeneity of the ($^{207}\text{Pb}/^{206}\text{Pb}$)₀ ratio, refit the discordia line to the raw dates from the first

step by anchoring the concordia y-axis to the approved common Pb value for that mineral.

- Compare the raw and anchored ages obtained. How significant is the increase in precision from anchoring the y-intercept? Are certain minerals more responsive to the anchoring technique?
- Compile a dataset of the most precise raw and anchored ages. When separated into textural classifications, is there a clear difference in the ages between groupings? Are the ages within error of each other? Do the dates vary spatially and lithologically?
- Spatially map precise ages to detect any geochronological trends. Do the dates obtained highlight specific phases of alteration in the region? Can these alteration phases be constrained to specific structures or intrusions?
- Compare the dates from this study with published dates. How do the constrained dates from this study compare with the pre-existing dates from previous authors? Are there any conflicts, and if so, what is the potential cause?

7.2 Introduction

Zircon is one of the most geochronologically important minerals. This is due to a number of factors: it is a common accessory mineral in igneous and metamorphic rocks, especially silica saturated melts; it has a hardness of 7.5 (Mohs Hardness Scale) increasing its resistivity to mechanical processes; it is extremely resistant to metamorphism and chemical changes; it accommodates relatively high concentrations of uranium and low concentrations of Pb during crystallisation, leading to high $^{238}\text{U}/^{204}\text{Pb}$ ratios (Frost *et al.*, 2000; Kirkland *et al.*, 2018). As zircon can only interact with Zr-bearing fluids at high temperatures, it means that it is much harder for the igneous crystal to be metasomatically influenced with the original U-Pb often remaining unaltered (Frost *et al.*, 2000). Therefore, zircon is most regularly relied upon for igneous dates of rocks and is responsible for some of the terrestrial and extra-terrestrial dates in our solar system. However, studies using hydrothermal zircon dates have also been used to constrain alteration dates (e.g Pelletier *et al.*, 2007; Li *et al.*, 2018).

Although apatite is not as frequently used in U-Pb studies as zircon, as a common accessory mineral for igneous and metamorphic rocks it is a useful chronometer. More importantly for this study, however, there is an abundance of apatite in propylitic alteration where there is an increase in $\text{Na} \pm \text{Ca}$ (Battles & Barton, 1995; Frost *et al.*, 2000; Thomson *et al.*, 2012). Unlike zircon and titanite, apatite has a much lower U content which can lead to challengingly high common Pb to radiogenic ratios (Thomson *et al.*, 2012; Kirkland *et al.*, 2018). Despite this, apatite's closure temperature of 500 - 550°C can provide further information of prograde and retrograde processes (Thomson *et al.*, 2012; Schneider *et al.*, 2015; Kirkland *et al.*, 2018). Before the use of LA-ICP-MS dating, fully destructive dilution methods were used for apatite geochronology (Thomson *et al.*, 2012). Following the introduction of in situ dating methods (eg SIMS), U-Pb geochronology of apatite has diversified with studies focusing on specific phases of apatite such as: magmatic apatite (Chew *et al.*, 2014; Schneider *et al.*, 2015), hydrothermal apatite from a range of settings (Corfu & Stone, 1998; Storey *et al.*, 2007), fault and shear zones, and detrital apatite for erosion and landscape studies (Thomson *et al.*, 2012).

The use of titanite (CaTiSiO_5), or sphene, in U-Pb geochronology is a continually developing field. Various forms of titanite can be found naturally, from igneous to metamorphic. For many years, titanite has been used to date igneous phases in rocks, but more recently it has been used to date metamorphic, hydrothermal and deformation events. The occurrence of igneous, metamorphic and hydrothermal titanite provides the opportunity for U-Pb dating of different phases. Titanite's ability to incorporate U in its crystal structure and therefore to contain high $^{238}\text{U}/^{204}\text{Pb}$ ratios is crucial for U-Pb geochronology (Frost *et al.*, 2000; Albarède, 2009). Other important factors include: common accessory mineral to igneous and metamorphic rocks; and a high closure temperature of up to 700°. Examples of studies that have used U-Pb dating of titanite to constrain dates for hydrothermal alteration include Fallourd *et al.* (2014), Storey *et al.* (2007) and Hart-Madigan (2019). Other applications for titanite geochronology include dating orogenic events such as: the U-Pb analysis of metasomatic titanite to date orogenic events during the Western Gneiss Region of Norway (Spencer *et al.*, 2013); and the application of LA-ICPMS titanite analysis to constrain movement of crustal-scaled thrusts in the Himalaya

respective of events such as the south Tibetan Detachment (Kohn & Corrie, 2011).

Epidote is a particularly challenging mineral to radiometrically U-Pb date because of the high levels of common Pb and a low U concentration. Other geochronologically problematic factors include: the unavailability of an epidote reference standard and the common internal and oscillatory crystal zoning (Duncan & Maas, 2014). Despite this, several studies have persevered with dating epidote (e.g. Frei & Kamber, 1995; Buick *et al.*, 1999; Cooke *et al.*, 2014; Duncan & Maas, 2014) because if perfected, it could be a valuable tool to precisely date multiple alteration phases which is particularly helpful due to epidotes abundance in specific metamorphic and hydrothermal terranes. In a similar study, Phillips (2019) uses a zircon standard to substitute for a matrix-matched epidote standard which is noted to cause offset to the date determinations.

7.3 Raw data, date calculations

7.3.1 *IsoplotR*

All dates in this study are calculated by plotting Tera-Wasserburg (T-W) plots in the software package *IsoplotR*.

Unless otherwise stated, all the T-W plots apply $^{207}\text{Pb}/^{235}\text{U}$ and $^{206}\text{Pb}/^{238}\text{U}$ isotopic data to calculate the date and $(^{207}\text{Pb}/^{206}\text{Pb})_0$ calculations and are presented as the discordia 'Model-1'. The presentation and meaning of the output calculations from *IsoplotR* are defined:

$$\begin{aligned} \text{Date} &= t \pm x \mid y \mid z \\ (^{207}\text{Pb}/^{206}\text{Pb})_0 &= t \pm x \mid y \mid z \end{aligned}$$

where: t = the date or common Pb-ratio Maximum Likelihood estimate which applies Ludwig (1998)'s algorithm; x = the analytical uncertainty of t ; y = the confidence interval for t using the appropriate number of degrees of freedom; z = the confidence interval of t with overdispersion included and calculated as $z = y\sqrt{\text{MSWD}}$ (Vermeesch, 2018). In this study, where T-W

plots are included, such as summary tables (e.g. Figure 7.1), this data format is retained for consistency.

In published work, there are often inconsistencies over which uncertainty should be presented. Therefore, as it is the smallest and most favourable value that shows the most precise results, it is the standard error ('x') which is most commonly used. For this study, all of the date and common Pb uncertainties provide 95% confidence intervals. The 'z' value is only present when the p-value of the linear fit is less than 0.05. Therefore, when present, the 'z' uncertainty is used, and for underdispersed data where the 'z' estimate is not calculated, the 'y' error is the most appropriate value. Although these values provide the widest error, they are the most truthful representation of the date and $(^{207}\text{Pb}/^{206}\text{Pb})_0$ estimate uncertainties.

7.3.2 Visual assessment and unconstrained isochron regression on Tera-Wasserburg concordia diagrams

The number of samples analysed, the extent of sample collection area and the dating of four different minerals means there is a very large data set, totalling 234 raw dates. With such an extensive data set, a consistent process to analyse each date calculation is important. This involves: visually inspecting the Tera-Wasserburg (T-W) plot; identifying from the calculated values which samples provide reliable dates and common Pb estimates; identifying and rejecting any outliers; assessing whether the combined plots of the pooled textures show any trends between textural classifications. A summary table (Figure 7.1) shows example T-W plots with specific characteristics which are discussed in the following process description.

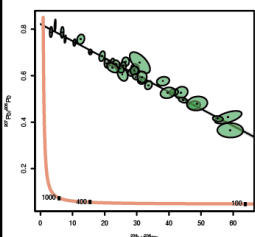
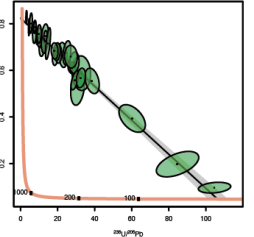
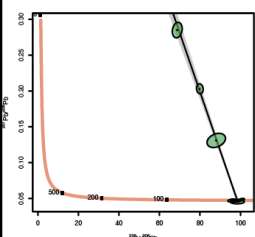
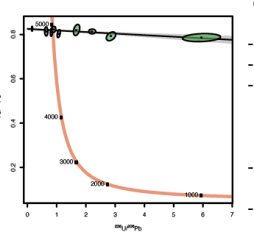
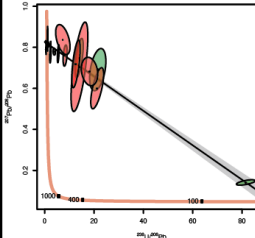
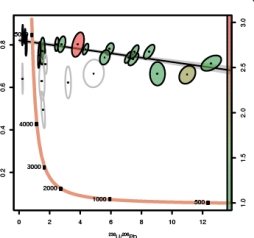
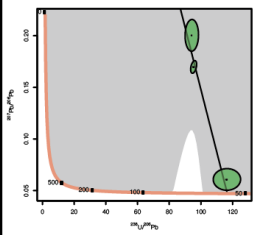
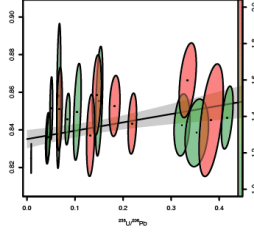
Example: good isochron		Example: good isochron	
<p>RCS056 <i>Titanite A2</i></p> <p>age = 60.45 ± 0.64 1.30 2.50 Ma (n=34) $(^{207}\text{Pb}/^{206}\text{Pb})_0 = 0.8221 \pm 0.0032 0.0064 0.0124$ MSWD = 3.7, $p(\chi^2) = 7.6\text{e-}12$</p>  <ul style="list-style-type: none"> - Large sample size - No major outliers - Good isochron, and data spread, with minor overdispersion - Precise common Pb value and age estimate - Age deemed very reliable 	<p>RCS084 <i>Titanite A3</i></p> <p>age = 60.32 ± 1.45 2.97 4.04 Ma (n=30) $(^{207}\text{Pb}/^{206}\text{Pb})_0 = 0.8237 \pm 0.0049 0.0100 0.0136$ MSWD = 1.9, $p(\chi^2) = 0.0039$</p>  <ul style="list-style-type: none"> - Large sample size - No outliers - Very good isochron and data spread with both intercepts present - Minor overdispersion - Precise common Pb value and age estimate - Age deemed reliable 		
Example: good age constraint		Example: common Pb constraint	
<p>RCS046 <i>Zircon Ig</i></p> <p>age = 65.17 ± 0.17 0.41 1.15 Ma (n=9) $(^{207}\text{Pb}/^{206}\text{Pb})_0 = 0.857 \pm 0.024 0.056 0.158$ MSWD = 7.9, $p(\chi^2) = 1.5\text{e-}09$</p>  <ul style="list-style-type: none"> - Good sample size (for zircon) - MSWD 7.9, sample overdispersed - Six aliquots plot on the lower concordia intercept, therefore there is a good age estimate (1.15 Ma) - Imprecise common Pb estimate - Age deemed reliable 	<p>RCS047 <i>Titanite V2</i></p> <p>age = 58.1 ± 10.5 24.3 27.9 Ma (n=10) $(^{207}\text{Pb}/^{206}\text{Pb})_0 = 0.8254 \pm 0.0025 0.0057 0.0065$ MSWD = 1.3, $p(\chi^2) = 0.23$</p>  <ul style="list-style-type: none"> - Moderate sample size - No outliers - Moderate spread of data, but no plots close to the lower concordia intercept, therefore increasing the age error (27.9 Ma) - Good spread of data, with reliable common Pb estimate - Age deemed unreliable 		
Example: controlling aliquot		Example: multiple outliers	
<p>RCS072 <i>Apatite All A4 V7</i></p> <p>age = 69.09 ± 1.67 3.55 5.23 Ma (n=17) $(^{207}\text{Pb}/^{206}\text{Pb})_0 = 0.8262 \pm 0.0020 0.0044 0.0064$ MSWD = 2.2, $p(\chi^2) = 0.0056$</p>  <ul style="list-style-type: none"> - Small sample size - All but one aliquots cluster in the upper part of the isochron, V7 aliquots appear to show greater uncertainty - Precise common Pb estimate - The one aliquot (A4) with higher radiogenic Pb controls the slope of the discordia line - Age deemed reliable 	<p>RCS041 <i>Apatite All Ig Ig-Alt A3</i></p> <p>age = 84.40 ± 7.28 15.29 26.74 Ma (n=20) $(^{207}\text{Pb}/^{206}\text{Pb})_0 = 0.8210 \pm 0.0054 0.0114 0.0189$ MSWD = 3.1, $p(\chi^2) = 1.3\text{e-}05$</p>  <ul style="list-style-type: none"> - Good sample size - Six outliers (removed) - Mostly Ig texture - No plots close to the lower concordia intercept - Imprecise age estimate (26.74 Ma) - Moderate precision on common Pb age - Age deemed unreliable 		
Example: weakly constrained common Pb		Example: poor isochron	
<p>RCS089 <i>Zircon Ig</i></p> <p>age = 55.02 ± 1.76 22.31 40.96 Ma (n=3) $(^{207}\text{Pb}/^{206}\text{Pb})_0 = 0.75 \pm 0.10 1.33 2.44$ MSWD = 3.4, $p(\chi^2) = 0.066$</p>  <ul style="list-style-type: none"> - Small sample size - Poor isochron, with nearly vertical slope - Very large confidence envelope, covering most of the graph area - Very imprecise common Pb value and age uncertainty - Age deemed very unreliable 	<p>RCS067 <i>Epidote All A5 V2</i></p> <p>age = 5044.3 ± 13.7 29.1 45.2 Ma (n=18) $(^{207}\text{Pb}/^{206}\text{Pb})_0 = 0.8351 \pm 0.0023 0.0048 0.0074$ MSWD = 2.4, $p(\chi^2) = 0.0012$ lower intercept = -370 ± 100 220 340 Ma</p>  <ul style="list-style-type: none"> - Medium sample size - Data plots on the lefthand side of concordia line - Minor overdispersion - Positive isochron, causing very large age uncertainty (45.2 Ma) - Very precise common Pb value - Age deemed very unreliable 		

Figure 7.1. Collection of raw age estimates produced using IsoplotR. For dates that comprise all isotopic data from that sample, the classifications are coloured-coded. The specific examples are referenced in-text.

Visual inspection of Tera-Wasserburg plots

The initial visual assessment looks at the 'goodness-of-fit' of the data along the isochron. The titanite A2 and A3 from RCS056 and RCS084 (Figure 7.1) are examples of very good isochrons. Both have a large sample size (30-34 aliquots) which are well distributed along the negatively-dipping isochron, with no outliers. This ratio of common Pb to radiogenic Pb results in a high precision of the date and the common Pb value. However, if the distribution of the aliquots along the discordia line is inconsistent, clusters of data can occur potentially separating singular aliquots to direct the isochron (e.g. RCS072 'apatite All' in Figure 7.1). In these cases, the deviant aliquot containing higher radiogenic or common Pb than the remaining cluster controls the date or common Pb estimate. Although the precision falls within a reliable realm, an isochron-controlling outlier should be treated with caution.

Sample size is an important consideration for the reliability of the date: for epidote, titanite and apatite, samples with <10 aliquots are considered small, 11-19 moderate, and 20+ large, however the value of the number of aliquots is dependent on the mineral being dated. With zircon being a geochronologically robust mineral, fewer aliquots are required for a reliable date estimate. RCS014 'zircon Ig' (Figure 7.1) is an extreme example of a precise zircon date comprising only two aliquots. This is possible as one aliquot contains high radiogenic Pb and the other common Pb. Contrastingly, RCS089 'zircon Ig' (Figure 7.1) incorporates three radiogenic Pb-rich aliquots, but presents a very imprecise date estimate with 40.96 Ma uncertainty and an extensive confidence envelope.

The size of the error ellipses and regression envelope is an indication of the variance of a sample (Ludwig, 1998). Sample RCS067 'epidote all' date (Figure 7.1) shows all the aliquots with large, elongated error ellipses. This epidote date demonstrates one of the most unreliable dates produced because of the very high

levels of common Pb in the sample. All the aliquots plot on the left-hand side of the concordia line, and the poor distribution of data has resulted in a positive regression line.

Identification of reliable date and common Pb constraints

Naturally, it is important to consider whether the age calculated is plausible for the region. Dates >90 Ma were considered implausible because of the maximum dates for the host lithologies (Yarabamba Batholith 69-59 Ma, Demouy *et al.*, 2012; Simmons, 2013; Nathwani *et al.*, 2020). In some instances, the estimated date exceeded 4 Ga, which clearly indicated a sample with high levels of inherited Pb. All groupings with an implausible and unreliable date were removed.

The uncertainty reported for all dates in this study is the third error which considers dispersion, and 95% confidence intervals. This gives a larger value showing the widest error, but it is the most geologically honest. Any date with an uncertainty greater than 10% is considered imprecise.

Removal of outliers

Data which do not visibly conform with the regression line must be omitted. When the values are recalculated by IsoplotR, the omitted values are not included in the date estimation, however, the trace of these plots remain on the T-W diagram for reference. This is useful as the presence of outliers in the sample should be considered. Mostly, if there are outliers, there are only one or two which clearly differ from the trend of the regression line. However, in some cases multiple data have been rejected, for example, RCS041 (Figure 7.1), resulting in a much cleaner regression line. This new regression line, and resultant date, is unintentionally influenced by human assessment of the most appropriate projection for the isochron. Because of the spread and quantity of the omitted and remaining plots in this example, the integrity of all the data is questioned.

Assessment of any textural classifications trends

As previously mentioned, an additional age calculation has been made for each sample that contains more than one textural date, for example a sample with apatite isotopic data for 'lg' and 'A2' classifications. In these cases, the data that have been combined generate a pooled age (labelled 'all' in the data tables and figure legends). The purpose for this supplementary age estimate is to visually and statistically assess whether the distinct trends can be determined between the different textural classifications.

To visually evaluate this, the Tera-Wasserburg plots for the combined 'all' ages have been colour-coded based on texture so that it is apparent if the aliquots from one texture follow a clear trend when compared with another texture. From this visual analysis of all the combined 'all' dates, no discrete trends are apparent and the aliquots generally fall along the isochron line. For example, with RCS074 'apatite all' (Figure 7.1), it would be very difficult to determine a trend due to the clustering of all the aliquots along the upper section of the isochron. The general increased precision of the 'all' dates, as opposed to the date calculations for the separate groupings, is expected as there is a, sometimes significant, increase in sample size.

7.4 Investigating the spatial variability of the common Pb

The $(^{207}\text{Pb}/^{206}\text{Pb})_0$ value, or common Pb estimate, represents the amount of non-radiogenic Pb in a sample at the time of crystallisation and provides information on mantle or crustal evolution (Stacey & Kramers, 1975; Vermeesch, 2021). The value is derived from the y-intercept of the isochron regression (Schoene, 2014; Reiners *et al.*, 2018). When calculating the common Pb estimate, the balance between the radiogenic and common Pb in the mineral being dated determines the precision: high levels of common Pb increases the precision. Therefore, where the date calculations of the epidote would be imprecise due to the high non-radiogenic Pb content, it provides the most precise and reliable estimate for common Pb y-intercept.

7.4.1 Assessment of common Pb homogeneity

As this study's sample catchment is extensive, there is the possibility that the common Pb isotopic signature may vary between samples, lithology and across a larger distance. Mapping epidote, as the mineral with the most precise (<10% uncertainty) common Pb values, provides a visual indication that there is spatial homogeneity between samples (Figure 7.2). Corresponding common Pb values for such an extensive area suggests that, despite the igneous material crystallising in various phases, the inherited lead component of the samples are the same in the sampled region.

With this knowledge, the decision is made that lithological and intrusive variations have little influence on the common Pb signatures and it is therefore suitable to apply a singular value for the anchored calculations.

7.4.2 Visual representation of common Pb using radial plots

Radial plots, also termed 'Galbraith plots' after Galbraith (1988), are a valuable tool for representing 'heteroscedastic' datasets (heteroscedastic

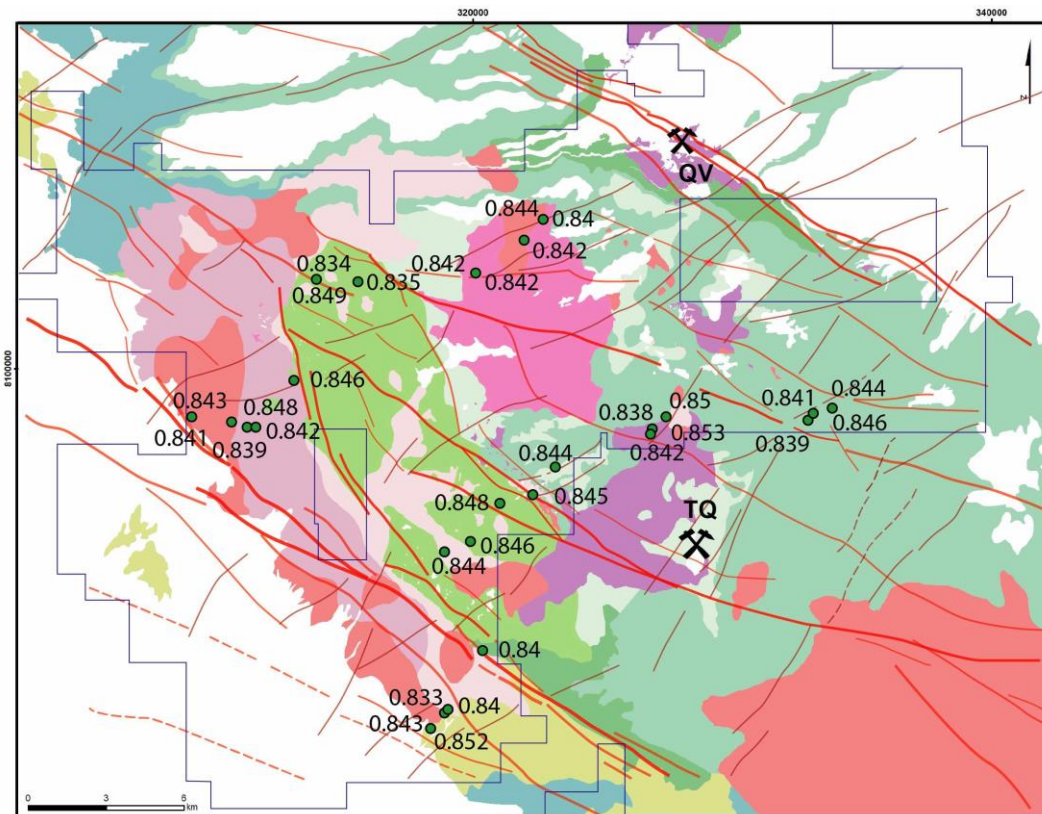


Figure 7.2. The spatial distribution of precise epidote common Pb estimates.

meaning 'data with unequal uncertainties'). This graphical method is unique in its ability to simultaneously visualise: the precision (along the x-axis); the standardised estimate along the y-axis; and the date estimate plotted along the 'z' axis. The z-axis is a circular scale allowing the date estimate to be extrapolated using a line from the origin (0,0) standardised error, through the (x,y) point to the circular scale (Galbraith, 1990; Vermeesch, 2018). A 95% confidence interval is obtained by projecting 2-sigma error bars on the aliquots (Figure 7.3).

Here, it is not the dates that are presented on the radial plots, instead the common Pb intercept values and precision which are separated into minerals (Figure 7.4). Epidote and titanite show clear alignments with a common Pb central value of 0.84295 and 0.8234, respectively. The minimal variance of the epidote data is shown by the particularly narrow corridor of aliquots along the z-axis.

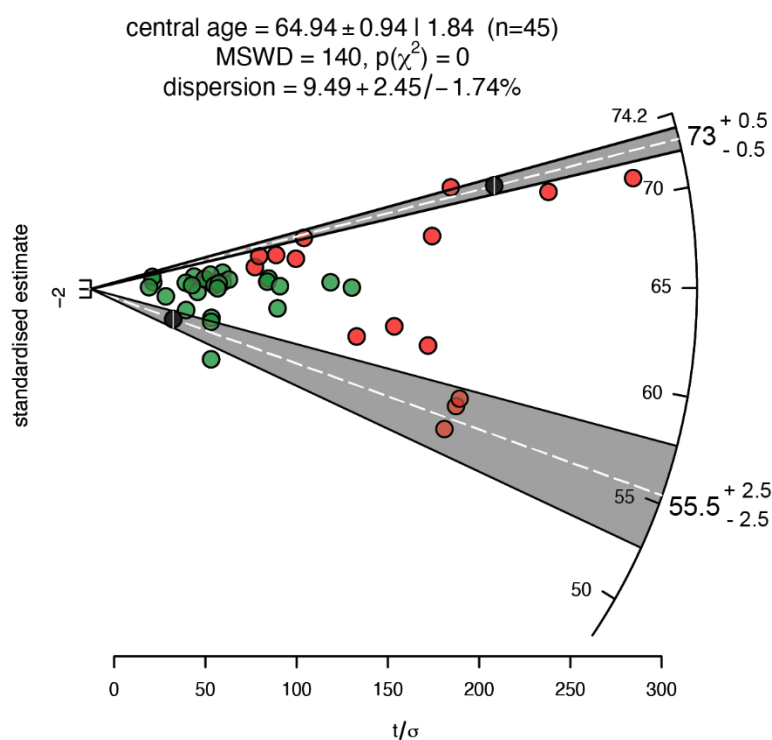


Figure 7.3. A radial plot plotting two datasets: U/Pb zircon dates from this study in green, and SIMS based U-Pb zircon dates from Simmons (2013) in red. The age of each aliquot can be determined from the projection of a line from the origin through the aliquot on the circular scale (represented by the white dashed line). The confidence intervals are obtained from the projection of 2-sigma error bar on to the selected aliquot: 55.5 +2.5/ -2.5 and 73 +0.5/ -0.5.

As noted in the raw date plots, epidote contains very high levels of common Pb, and generally very low levels of radiogenic Pb. While little to no radiogenic Pb proves detrimental for precise date estimates, the elevated levels of common Pb provide highly precise common Pb values, regularly with <1% uncertainty. Apatite and titanite contain varied levels of common Pb. Similarly to epidote, titanite displays a clear, but slightly broader corridor of data.

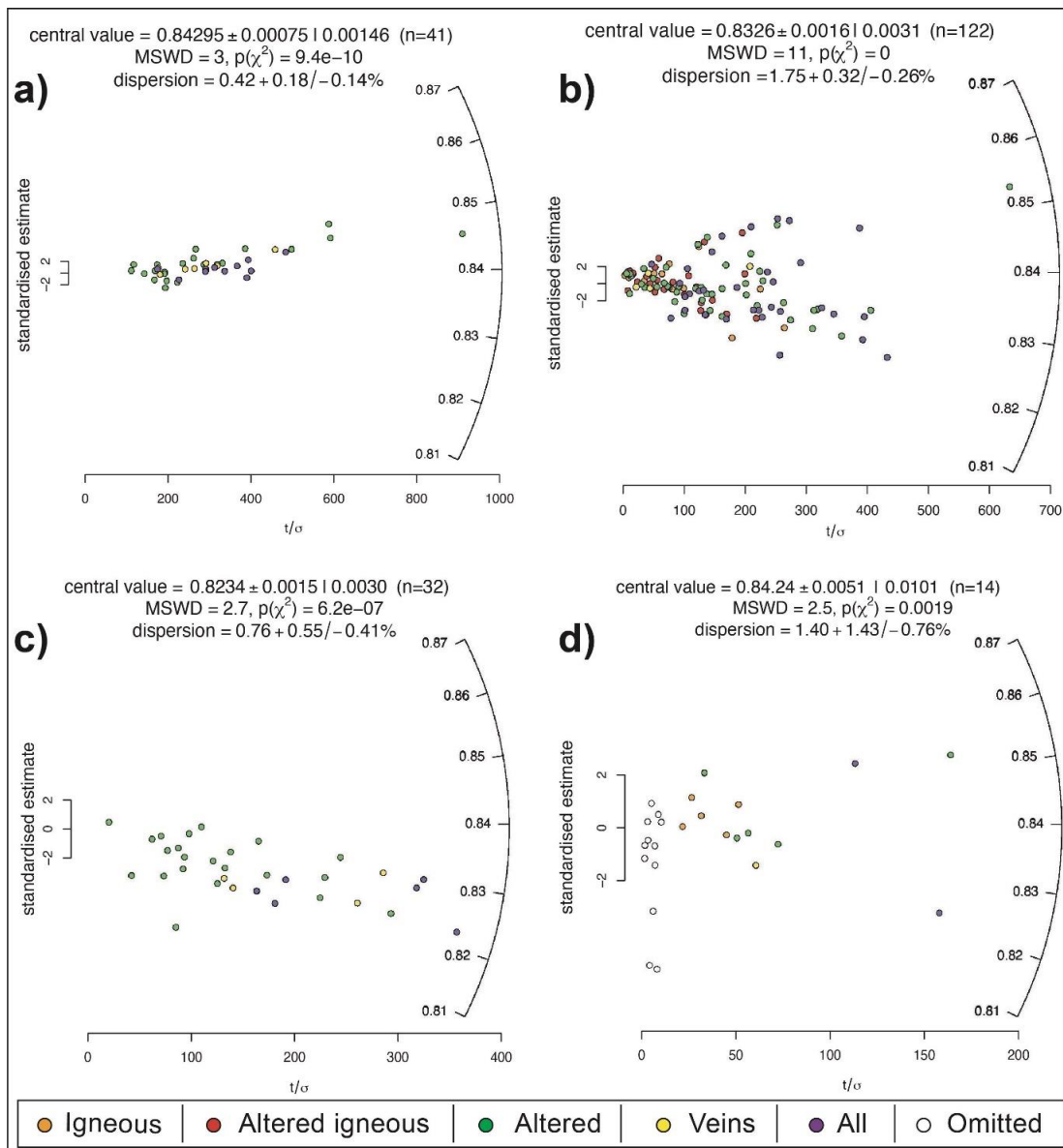


Figure 7.4 Radial plots showing the uncertainty distribution of the common Pb intercept of all the raw dates. Each value is coloured based on the source of the value (igneous, altered igneous, altered, veins, and 'all' indicating dates per sample that have been combined). The radial plots are separated per mineral **a)** epidote, **b)** apatite, **c)** titanite, and **d)** zircon. Due to the uncertainty of the common Pb intercept for zircon, values with an uncertainty >10% were omitted (white circles).

The distribution of apatite aliquots are less focused than that of epidote and titanite, with a noticeably larger spread, although apatite's significantly larger sample size is worth highlighting. Within the broad spread of data, there is the possibility that there are two trends: the first between 0.82-0.83 and the second ~ 0.85 , however the average is 0.8326.

Zircon is less abundant than the other minerals, and generally yields imprecise common Pb compositions because of its high radiogenic Pb content. The amount of imprecise and implausible measurements cause a systematic bias toward implausible values. However, when the least precise are omitted, the central value becomes 0.8424, which is aligned with the other minerals (Figure 7.4).

7.4.3 *Pooled model-3 regressions*

The analysis of the data so far has highlighted a significant spread in dates, and a notable difference between the common Pb composition of the different minerals. Therefore, a model-3 regression is applied to pooled mineral plots of all of the U-Pb isotopic data (Figure 7.5). Although this temporarily disregards the mineral classifications described in Chapter 5 and applied for the dates so far in this chapter, pooling the data points for each mineral significantly increases the sample size and allows the use of a model-3 regression. The benefit of using a model-3 regression is the assumption that the longevity of the magmatic phases in the region follow a 'bell curve' pattern. In other words, the activity started slowly, then intensified (at the peak of the bell curve) and lessened again. Pooling the data in this way constrains the peak date and allows the dispersion parameter to be applied to the duration of igneous activity. A model-1 and model-3 comparison is given in the methodology Chapter 3.

Titanite displays a very good isochron with the most extensive spread of aliquots along the isochron of the four minerals, and no apparent outliers. Zircon, as a naturally robust chronometer and rich in radiogenic Pb, exhibits these values with a precise isochron with intense clustering of values on, and close to, the lower concordia intercept. Despite the particularly large sample size for apatite and epidote (1219 and 631 aliquots respectively),

neither mineral shows precise isochron lines due to a dominance of common Pb values and often large confidence ellipses on aliquots.

The dates for apatite, epidote and titanite are approximately 70 Ma (71.26 Ma, 69.78 Ma, and 70.13 Ma respectively), while zircon has a (precise) average date of 64.03 Ma. Considering that all of the dated epidote and titanite are believed to represent secondary alteration, and a large proportion of the apatite is considered hydrothermal, this average date is older than would be expected. Note that (model-3) isochron regression of strongly dispersed datasets may produce biased results because the isochron equation enforces strict positivity on the isotopic ratios, whereas the uncertainties and dispersion are assumed to follow normal distributions that are free to take on negative values (See: Li & Vermeesch, 2021).

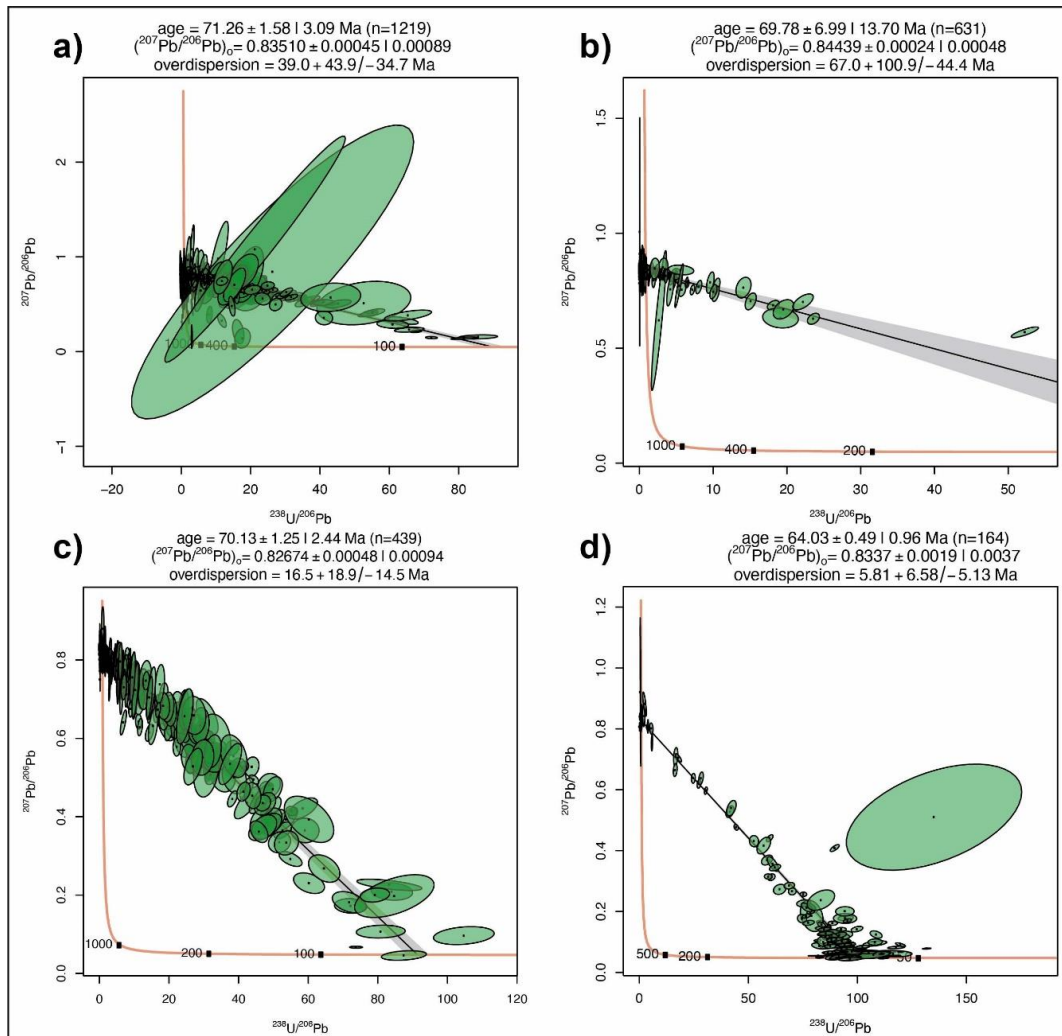


Figure 7.5. Pooled Tera-Wasserburg model-3 regressions of all U-Pb data for each mineral: **a)** apatite, **b)** epidote, **c)** titanite, and **d)** zircon.

Unfortunately, the uncertainties on the dispersion of epidote, titanite and apatite are very large. Zircon, however, has a much narrower overdispersion of 5.81 Ma, providing a plausible date for the length of time for zircon crystallisation. This value is geologically informative as it expresses the coefficient of variability of the true dates (Vermeesch, 2018).

7.5 Anchoring of the $^{207}\text{Pb}/^{206}\text{Pb}$, y-intercept

The precision of the date uncertainties can be increased by anchoring the common Pb value on the Tera-Wasserburg concordia. Anchoring of the y-intercept is particularly effective in small samples that do not plot along a well-defined isochron especially those with elevated radiogenic Pb, but depleted common Pb. If the y-intercept is constrained to a known reliable common Pb value, then principally in those samples with high radiogenic Pb, the upper and lower limit of the isochron are well-defined. When successfully anchored, the confidence envelope is reduced and date uncertainty decreases (Figure 7.6). For the most robust and reliable dates, the disparity between raw and anchored dates is minimal (<3 Ma).

Therefore, all the raw dates previously calculated (in Section 7.3) are recalculated using the central common Pb value devised in the radial plots

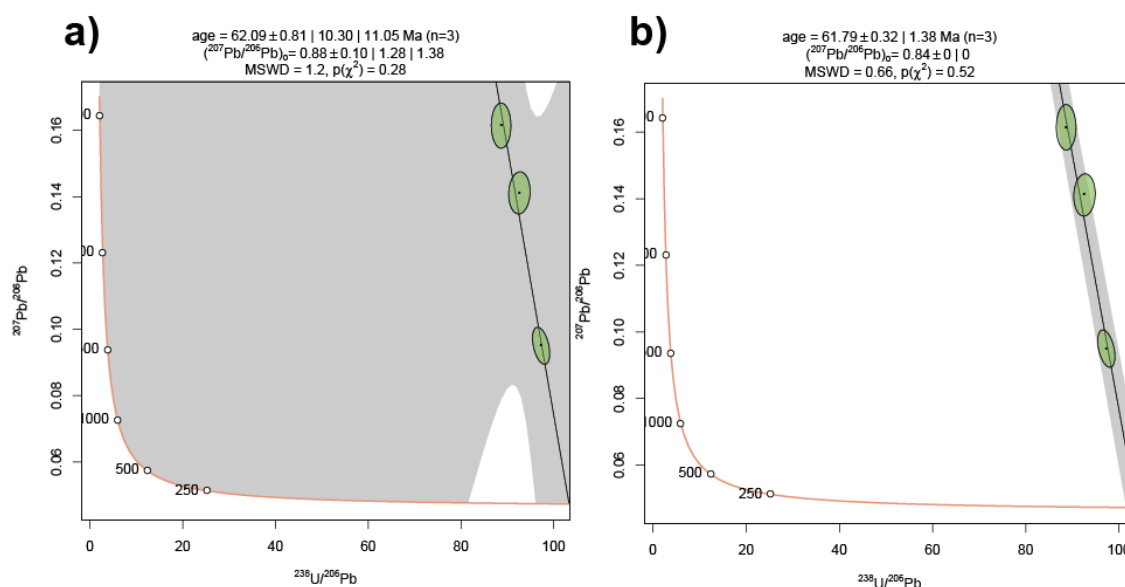


Figure 7.6. Example of the successful anchoring of the y-axis on a zircon Tera-Wasserburg concordia plot. Here, the aliquots contain high radiogenic with no inherited common Pb causing a degree of dispersion in the raw data (a). Anchoring the y-intercept (b) constrains the regression line and dramatically increases the precision, with date uncertainty decreasing from 11.05 Ma to 1.38 Ma.

(Figure 7.4). The values applied to each mineral date calculation are: for epidote 0.84295, for titanite 0.8234, for apatite 0.8326 and for zircon 0.8424.

The anchored date outputs are compiled as radial plots (Figure 7.7) with aliquots coloured based on category type. The imprecision of the epidote date estimates are clearly shown, with the majority of values coalescing at '0' t/σ precision and '0' standardised error. Predictably, the most precise of the epidote dates are all from the compiled 'all' category which have the large sample size. The central age for epidote (81.06 ± 15.06 Ma) is ~ 10 Ma older than the pooled T-W plot

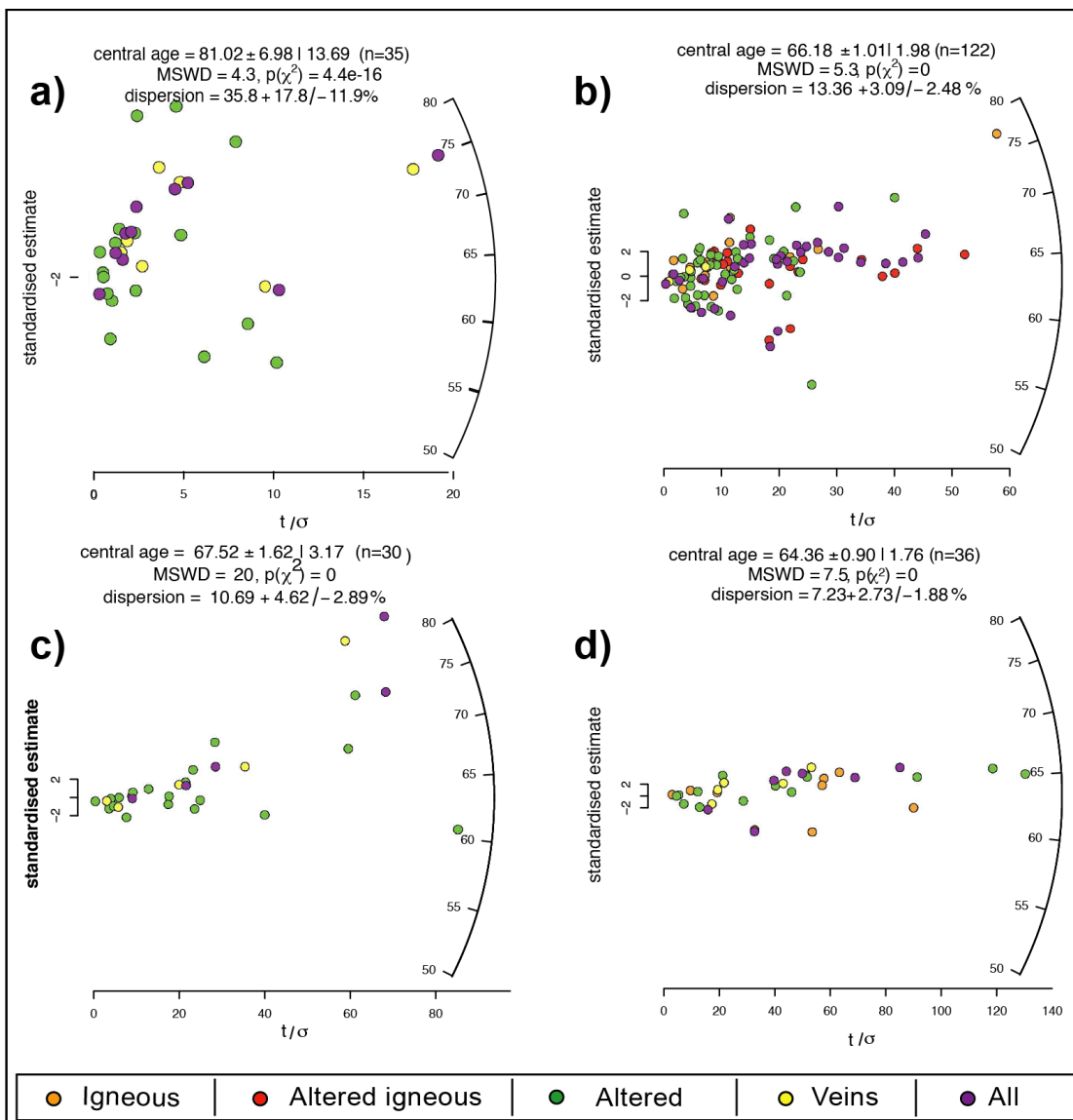


Figure 7.7. Radial plots of all the anchored dates for each dated mineral: **a)** epidote, **b)** apatite, **c)** titanite, **d)** zircon. The points are coloured based on the classification of the date: igneous, altered igneous, altered, veining, and all (for combined dates for each sample).

estimate (Figure 7.5). This disparity also substantiates an unreliability of the raw and anchored epidote ages.

The central ages for titanite and apatite, however, are lowered from the pooled T-W plot from approximately 70 Ma to 66.18 Ma and 67.52 Ma respectively. Zircon had a pooled raw age calculation of 64.03 ± 0.93 , and anchored central age of 64.36 ± 1.76 Ma. Zircon's reliability and precision are shown by the similarity in ages and minor uncertainties. There is no particular classification type that appears to be dominantly more precise, with the exception of the 'all' category which, particularly in epidote and apatite, is located closer to the circular scale. This is expected because of the larger sample size for the combined 'all' dates.

7.6 Comparing dates – raw vs anchored

Directly comparing the raw and anchored dates highlights the date precision for zircon and the general unreliability of the epidote dates (Figure 7.9a). An aliquot's proximity to the $x=y$ line emphasizes the level of change from the raw to anchored dates. Dates plotting close or on the line have experienced little to no change, and therefore this consistency often increases the reliability of both dates. Zircon dates generally have a strong date agreement, forming a close cluster along the $x=y$ line at approximately 65-70 Ma. However, 1:1 date precision can be misleading, for example there is a 1:1 lineament of four implausible epidote dates (Figure 7.9b) with dates between 100-110 Ma. With a

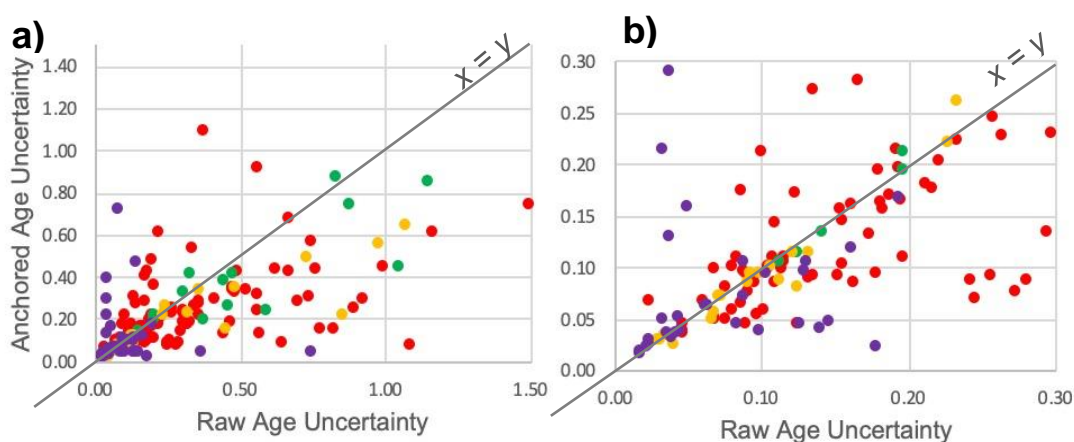


Figure 7.8. Scatter plots comparing the difference between the raw date and anchored dates: **a)** depicts precise and imprecise dates with uncertainties <1.5 , **b)** only showing dates $<30\%$ uncertainty.

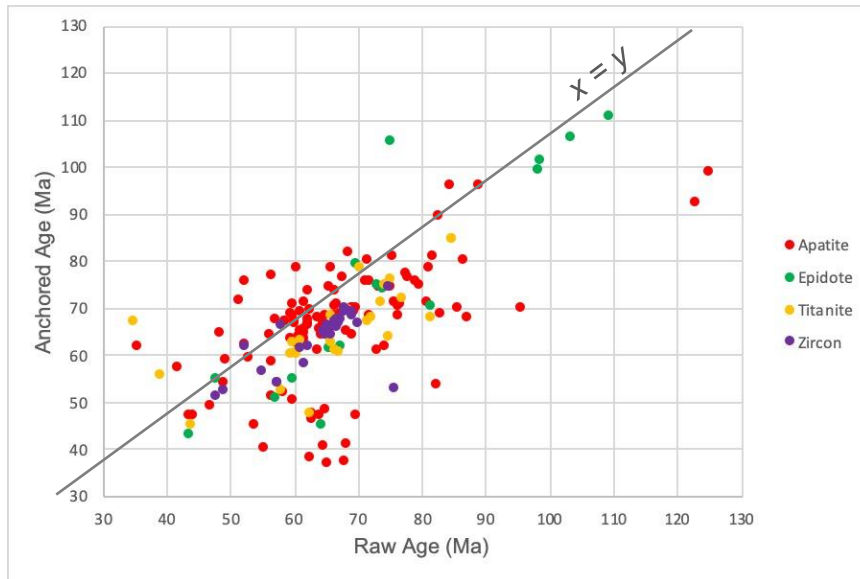


Figure 7.9. Scatter plots contrasting the anchored and raw ages between 30-130 Ma. Those data plotting closest to the 1:1 displayed minimal change in age from the anchoring process.

maximum regional lithological date of 85-90 Ma, it would be impossible for alteration to occur.

The juxtaposition of the raw and anchored date uncertainty demonstrates a general increase in precision from the anchoring of the common Pb intercept (Figure 7.8). The distribution of titanite uncertainties plotting on or below the identity line highlights the particular success of anchoring the titanite as the precision has either remained the same or, in most cases, increased dramatically. Zircon, however, shows three populations of uncertainty: equal with $x=y$; or a vertical or horizontal trend indicating either a steep increase in precision from anchoring or, in several cases, the anchored date significantly losing precision.

A direct comparison between the two data types (raw and anchored) emphasises the concentration of the date estimates for the anchored data by using kernel density estimates (KDE) and histograms (Figure 7.10). A Gaussian kernel is applied to the KDE in order to smooth the data (Vermeesch, 2012). There is a clear contrast between the peak types of the two graphs. For the histograms, data are categorised into 'bins' using Sturges' Rule ($\log_2[n]+1$, where n = number of data points), thereby smoothing the data output (Vermeesch, 2018).

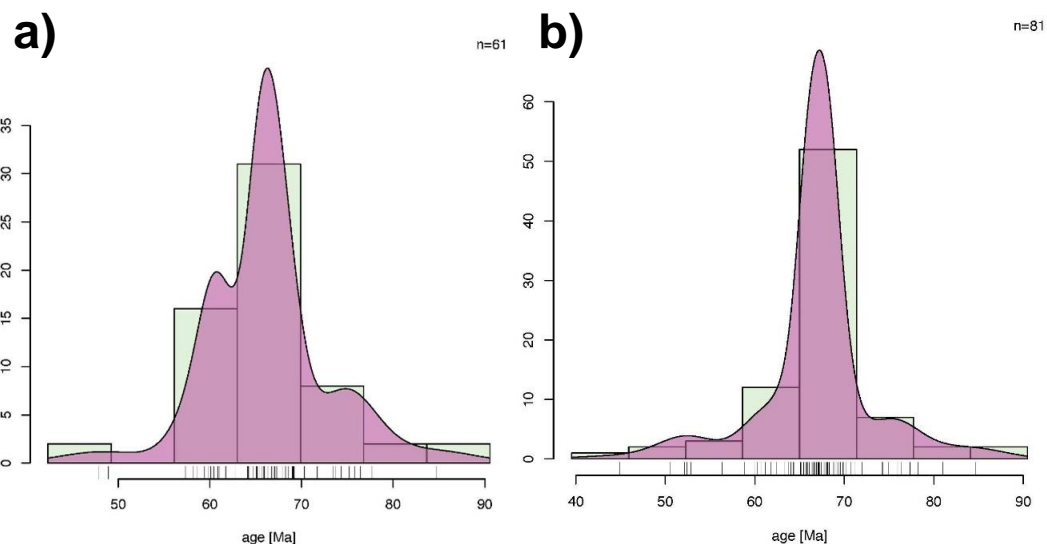


Figure 7.10. Kernel density estimates (KDE) and histograms for precise dates with uncertainty of <10%: **a)** raw unanchored dates; **b)** anchored dates. Adding the isochrons reduces the dispersion of the dates.

For the raw data (Figure 7.10a) there is a broader spread of dates with a major peak between 65-70 Ma and a moderate peak between 56-63 Ma and 71-78 Ma. However, the spurious scatter present in the raw dataset is removed when anchored. The distribution of the anchored dates (Figure 7.10b) exhibits a pronounced, concentrated peak between 65-69 Ma and with a general minor background spread (between 4-8 data plots) from 50-77 Ma. The concentration of the peak in the anchored dataset highlights the increased precision from anchoring.

Although fixing the y-intercept of the T-W concordia plots has proven successful for increasing precision in many of the dates, it is clear that this is not the case for all. Those dates where anchoring has lowered the precision and increased dispersion of the data are due in part to elevated common Pb in the dataset. For samples that are rich in common Pb, even a small amount of change to the common Pb intercept can dramatically negatively alter the date (Figure 7.11).

Therefore, because of the minor inconsistencies between the precision of raw and anchored date calculation, it is important to calibrate and compile the most reliable dates for further interpretation. The raw and anchored dates with the highest precision (<10 % uncertainty) and deemed most reliable were assembled for direct comparison. As shown in this chapter, it is imperative to

make a date reliability judgement based not only on the numerical values, but also on the visual assessment from the Tera-Wasserburg date plots. A summary of the considerations made when visually observing the plots are: the strength and precision of the isochron; sample size; the number of omitted aliquots; the relative frequencies of common Pb or radiogenic Pb-dominated aliquots; and the presence and reliability of outliers.

From this final assessment of the data, 87 dates from 39 samples have been selected as the most reliable (Table 7.1). These include: 29 dates using pooled textures; 39 alteration dates from wallrock and veining; 11 igneous dates (Ig); and 9 dates deemed to be altered igneous (Ig-Alt). For approximately half of the finalised dates there were duplicate dates from both raw and anchored plots which passed the precision threshold. In these cases, a decision on which date to retain was made based on the visual criteria previously stated. In total, 69 of the dates were based on anchored T-W plot calculations and 18 on raw calculations. It is these dates (Table 7.1) which subsequent analysis will focus on.

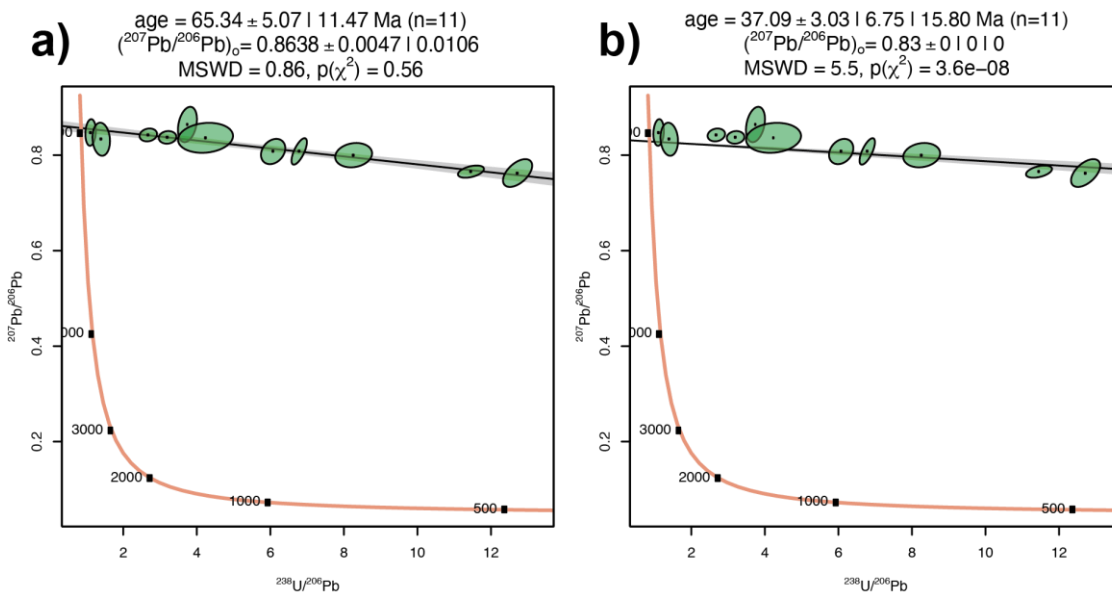


Figure 7.11. Example concordia date diagram of **a)** raw and **b)** anchored apatite data. Here, the aliquots are rich in common Pb with a raw plot (a) 10% precision for the common Pb value. The raw date is 65.34 Ma with a reasonable uncertainty of 11.47 Ma, but shows a good isochron fit of the data (MSWD = 0.86). When the $^{207}\text{Pb}/^{206}\text{Pb}$ y-axis is constrained to 0.83 (b) there is a poor fit of the data (MSWD 5.5) and the date is significantly affected (37.09 Ma) with precision decreasing. In this case, the anchored date would be deemed unreliable.

Sample	Type	EAST	NORTH	Elevation	Dated Mineral	Class	Date (Ma)	Error	% Error
RCS003	RAW	327486	8098122	3617	Zrn		57.32	2.15	3.8
RCS017	ANCH	318975	8086688	2277	Ap		50.52	5.11	10.1
RCS018	ANCH	319006	8086784	2285	Zrn		69.39	3.17	4.6
RCS022	RAW	320101	8088633	2463	Ap		62.73	5.23	8.3
RCS030	RAW	333373	8098457	3958	Ap		77.78	1.94	2.5
RCS033	RAW	333053	8098079	3988	Ap		65.07	5.68	8.7
RCS037	ANCH	309039	8098201	2623	Ap		68.15	4.36	6.4
RCS042	ANCH	309368	8098034	2647	Ap		65.50	2.97	4.5
RCS044	RAW	309671	8098052	2670	Ap		68.28	4.68	6.9
RCS046	ANCH	310256	8098095	2730	Ap		68.90	6.8	9.9
RCS047	RAW	310659	8097900	2749	Ttn		73.75	5.24	7.1
RCS049	ANCH	310936	8098053	2774	Ap		65.06	3.38	5.2
RCS051	ANCH	311239	8097639	2795	Zrn		67.41	3.43	5.1
RCS052	ANCH	311586	8097667	2831	Ap		67.91	4.75	7.0
RCS052	ANCH	311586	8097667	2831	Ttn	All	67.13	6.22	9.3
RCS054	ANCH	312332	8098767	2942	Ap		70.69	6.14	8.7
RCS057	ANCH	312843	8099427	3038	Ap		68.27	3.01	4.4
RCS072	ANCH	317788	8103570	3085	Ap		69.88	5.65	8.1
RCS073	RAW	319697	8103557	3219	Ap		64.72	3.91	6.0
RCS074	ANCH	320100	8103564	3234	Ttn		74.90	2.2	2.9
RCS075	ANCH	320740	8103917	3280	Ap		68.81	5.8	8.4
RCS078	ANCH	322734	8105674	3559	Ap		70.22	5.27	7.5
RCS078	ANCH	322734	8105674	3559	Ttn		84.69	2.5	3.0
RCS078	ANCH	322734	8105674	3559	Zrn		66.86	1.58	2.4
RCS079	RAW	322739	8105681	3560	Ap		58.65	5.27	9.0
RCS081	RAW	324357	8106351	3901	Zrn		66.3	1.58	2.4
RCS089	ANCH	328094	8107074	3992	Zrn		52.41	3.24	6.2
RCS092	ANCH	317413	8091544	2545	Ap		65.47	3.83	5.9
RCS093	ANCH	317574	8091857	2581	Ap		68.05	6.97	10.2
RCS014	RAW	318331	8086042	2296	Zrn		69.23	2.33	3.4
RCS030	ANCH	333373	8098457	3958	Ap		77.36	2.68	3.5
RCS046	ANCH	310256	8098095	2730	Ap		68.11	6.23	9.1
RCS049	ANCH	310936	8098053	2774	Ap		68.96	6.72	9.7
RCS052	RAW	311586	8097667	2831	Zrn		58.15	4.38	7.5
RCS052	ANCH	311586	8097667	2831	Ap	Ig	68.77	5.14	7.5
RCS061	ANCH	313262	8099430	3063	Zrn		61.79	1.38	2.2
RCS073	ANCH	319697	8103557	3219	Zrn		67.28	2.14	3.2
RCS081	ANCH	324357	8106351	3901	Zrn		66.48	2.32	3.5
RCS083	ANCH	325083	8107222	3931	Zrn		65.16	2.3	3.5
RCS089	ANCH	328094	8107074	3992	Zrn		56.31	2.12	3.8
RCS017	ANCH	318975	8086688	2277	Ap		52.15	4.75	9.1
RCS037	ANCH	309039	8098201	2623	Ap		67.05	5.56	8.3
RCS042	ANCH	309368	8098034	2647	Ap	Ig-Alt	65.49	2.51	3.8
RCS044	ANCH	309671	8098052	2670	Ap		63.33	3.34	5.3
RCS049	ANCH	310936	8098053	2774	Ap		63.73	3.18	5.0
RCS054	ANCH	312332	8098767	2942	Ap		65.75	6	9.1

RCS057	ANCH	312843	8099427	3038	Ap		66.65	3.03	4.5
RCS073	ANCH	319697	8103557	3219	Ap		65.89	3.84	5.8
RCS092	ANCH	317413	8091544	2545	Ap		64.36	5.52	8.6
RCS044	ANCH	309671	8098052	2670	Ap	A2	64.30	5.44	8.5
RCS053	RAW	311962	8098331	2931	Ttn		68.99	2.75	4.0
RCS054	ANCH	312332	8098767	2942	Ttn		62.43	5.02	8.0
RCS056	ANCH	312635	8099146	3008	Ttn		60.65	1.43	2.4
RCS056	ANCH	312635	8099146	3008	Zrn		64.02	2.8	4.4
RCS057	ANCH	312843	8099427	3038	Ap		81.03	7.08	8.7
RCS061	RAW	313262	8099430	3063	Ttn		70.28	5.19	7.4
RCS061	ANCH	313262	8099430	3063	Ap		74.28	3.71	5.0
RCS046	ANCH	310256	8098095	2730	Zrn		A3	65.13	1
RCS047	ANCH	310659	8097900	2749	Ttn	71.97		6.2	8.6
RCS049	ANCH	310936	8098053	2774	Zrn	65.82		1.11	1.7
RCS071	ANCH	318068	8102904	3041	Ttn	59.94		5.09	8.5
RCS074	ANCH	320100	8103564	3234	Ttn	75.94		2.49	3.3
RCS075	ANCH	320740	8103917	3280	Ap	68.33		7.16	10.5
RCS084	ANCH	326283	8106997	3913	Ttn	60.27		3.02	5.0
RCS092	RAW	317413	8091544	2545	Ttn	65.85		6.12	9.3
RCS092	ANCH	317413	8091544	2545	Ap	67.00		5.96	8.9
RCS092	ANCH	317413	8091544	2545	Zrn	65.43	1.44	2.2	
RCS003	RAW	327486	8098122	3617	Zrn	A4	57.41	2.91	5.1
RCS033	RAW	333053	8098079	3988	Ap		64.18	6.51	10.1
RCS072	ANCH	317788	8103570	3085	Ap		69.82	6.72	9.6
RCS104	ANCH	323197	8096126	3506	Ap		44.90	3.5	7.8
RCS025	ANCH	336024	8101160	4191	Zrn	A5	74.22	7.09	9.6
RCS030	RAW	333373	8098457	3958	Zrn		66.73	2.24	3.4
RCS081	RAW	324357	8106351	3901	Zrn		65.97	2.4	3.6
RCS089	RAW	328094	8107074	3992	Zrn	A6	47.82	1.8	3.8
RCS034	ANCH	332652	8097796	4011	Zrn	A7	67.19	2.62	3.9
RCS023	ANCH	320306	8088971	2480	Zrn	BX	67.64	2.66	3.9
RCS058	ANCH	312975	8099463	3052	Ap		58.88	5.52	9.4
RCS106	ANCH	320765	8089634	2550	Zrn	Fault	61.16	4.32	7.1
RCS018	ANCH	319006	8086784	2285	Zrn	V2	69.89	6.53	9.3
RCS051	ANCH	311239	8097639	2795	Zrn		66.41	6.94	10.5
RCS052	ANCH	311586	8097667	2831	Ttn		67.76	6.79	10.0
RCS078	ANCH	322734	8105674	3559	Zrn	V3	69.17	2.62	3.8
RCS074	ANCH	320100	8103564	3234	Ttn	V6	69.54	3.94	5.7
RCS074	ANCH	320100	8103564	3234	Zrn		68.13	2.75	4.0
RCS078	ANCH	322734	8105674	3559	Ap		68.25	6.76	9.9
RCS078	ANCH	322734	8105674	3559	Ttn		84.68	2.89	3.4
RCS078	ANCH	322734	8105674	3559	Zrn		66.30	3.11	4.7

Table 7.1 selected reliable dates, combination of raw and anchored. Errors are reported as 95% confidence intervals including any possible overdispersion.

7.7 Discussion

7.7.1 Spatial distribution of dates in the region

A summary map (Figure 7.12) shows the distribution of the 87 precise dates selected through the systematic workflow of this chapter. With such a large data set, it is beneficial to display the dates in this format in order to detect any spatial potential trends of alteration with respect to major fault structures. Many of the samples have multiple dates for different textures which are listed chronologically.

With the exception of a couple of samples, which yielded both igneous and alteration dates, the igneous dates predate the altered or vein date. Naturally, this is expected as the igneous age must be older than any alteration. However, most igneous and alteration ages fall within error of each other. For example, RCS049 in the DRT has an older igneous (I_g) date of 69 ± 6.7 Ma and an (A3) alteration date of 65.8 ± 1.1 Ma. The igneous uncertainty of 6.7 Ma is substantial enough to encompass the A3 age, therefore rendering a definitive distinction between the dates problematic.

As expected close to a porphyry centre, the samples most proximal to Quellaveco show a decrease in age. The closest sample, RCS089, has a granodiorite igneous date of 56.3 ± 2.1 Ma and young alteration age of 47.8 ± 1.8 Ma. Precise sample dates from this study are rare close to the Toquepala porphyry centre with the two nearest samples, RCS003 and RCS104, located ~5 km away. RCS003 is included within the Toquepala granodiorite (GRD), which hosts the Toquepala deposit and has a published emplacement age of 62-59 Ma (Simmons, 2013; Nathwani *et al.*, 2021). Therefore, the A4 propylitic alteration date 57.4 ± 2.9 Ma from RCS003 is likely to correspond with propylitic alteration associated with the Toquepala porphyry emplacement (57-54 Ma). However, because of the age uncertainty of 2.9 Ma, this is not certain. RCS104 provides another A4 alteration age, but within the Carpanito Mb of the Toquepala Group. The date of 44.9 ± 3.5 Ma is surprisingly low considering the porphyry emplacement is thought to have concluded 10 Ma prior to this (Simmons *et al.*, 2013). Interestingly, this sample is located directly along the strike of the

Micalaco Fault from Toquepala, which, as a possible feeder conduit for the Toquepala deposit, could be responsible for later alteration events.

As this study aims to determine whether there is a definable link between the regional propylitic alteration and structures, spatial patterns between the geochronological data and major faults are analysed. Two possible scenarios that might be expected include: migration of the fluid front away from the fault conduit as the fluids are propagated through the wall rock, with the furthest areas being the last to experience alteration; or focused alteration associated with major structures highlighting a dwindling system with later alteration being less extensive from the fault. There is added complexity to the age of the host lithology, which is the difference in alteration assemblage and the potential temporal difference in alteration events. It is apparent from the mapped dates (Figure 7.12), that despite the extensive data set, it is unfeasible to identify robust chronological trends. This is due to the similarity in dates between the different textural groups and their comparatively large analytical uncertainties. It would therefore be questionable to assume patterns in geochronological data at this stage. Potential patterns may become apparent when the trace geochemistry is overlaid.

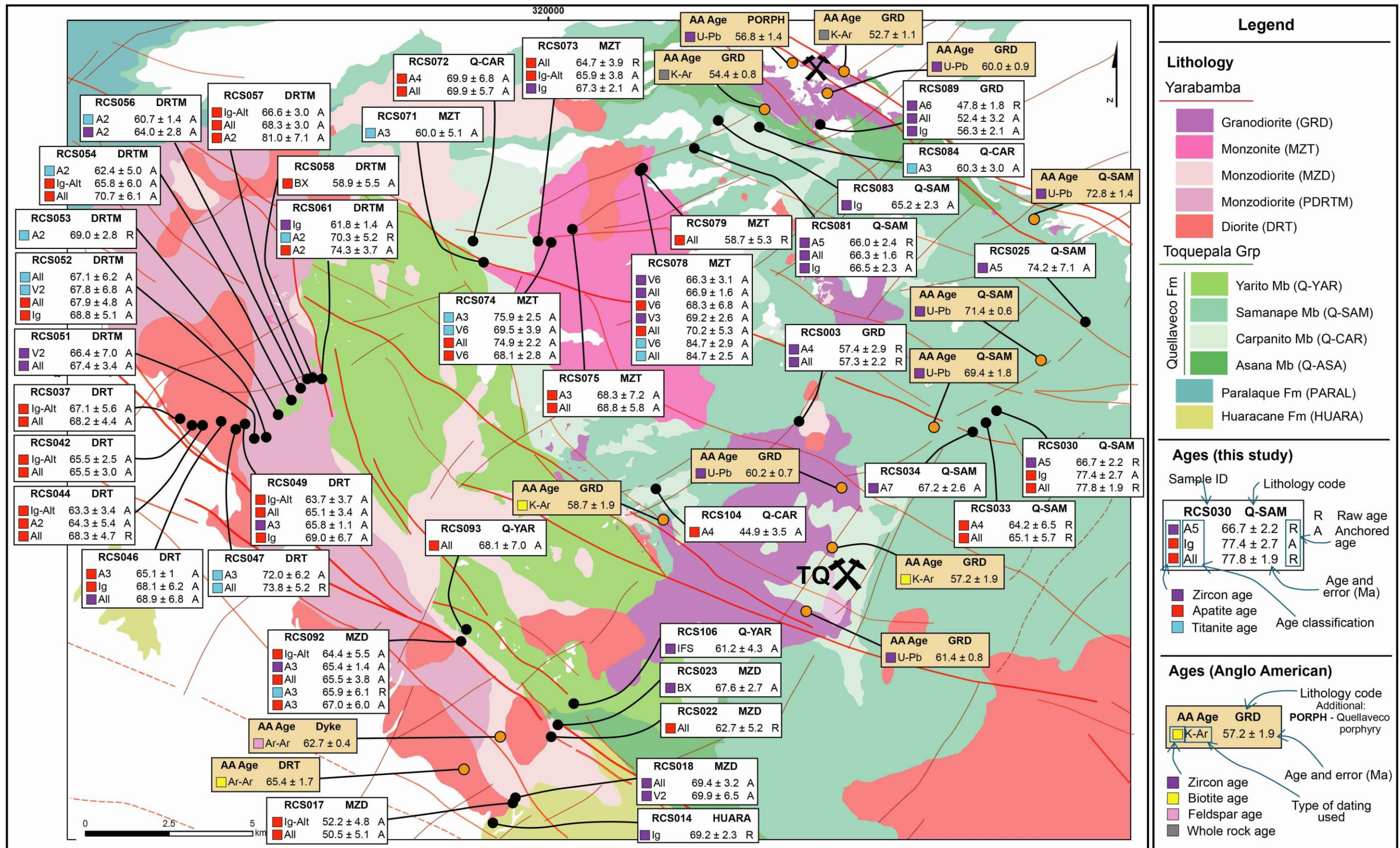


Figure 7.12. Selected reliable dates, combination of raw and anchored. Errors are reported as 95% confidence intervals including any possible overdispersion.

7.7.2 A comparison of the published dates – possible limitations

Compiled by Anglo American, this database comprises dates from: zircon U-Pb dating Simmons (2013) and Sillitoe & Mortensen (2010); biotite, feldspar, and total rock Ar-Ar dating by Clark *et al.* (1990), Martinez and Cervantes (2003) and Zimmermann and Kihien (1983); and total rock K-Ar by Martinez and Cervantes (2003). This dataset has proven useful with dating specifically focused on the porphyry centres (Quellaveco Cu-Mo and Toquepala). Samples in this study are collected in the regional Toquepala Group volcanics and Yarabamba Batholith, therefore the published dates corresponding to these units are also spatially highlighted (Figure 7.12). There is a dearth of published dates in the north-west area of the map.

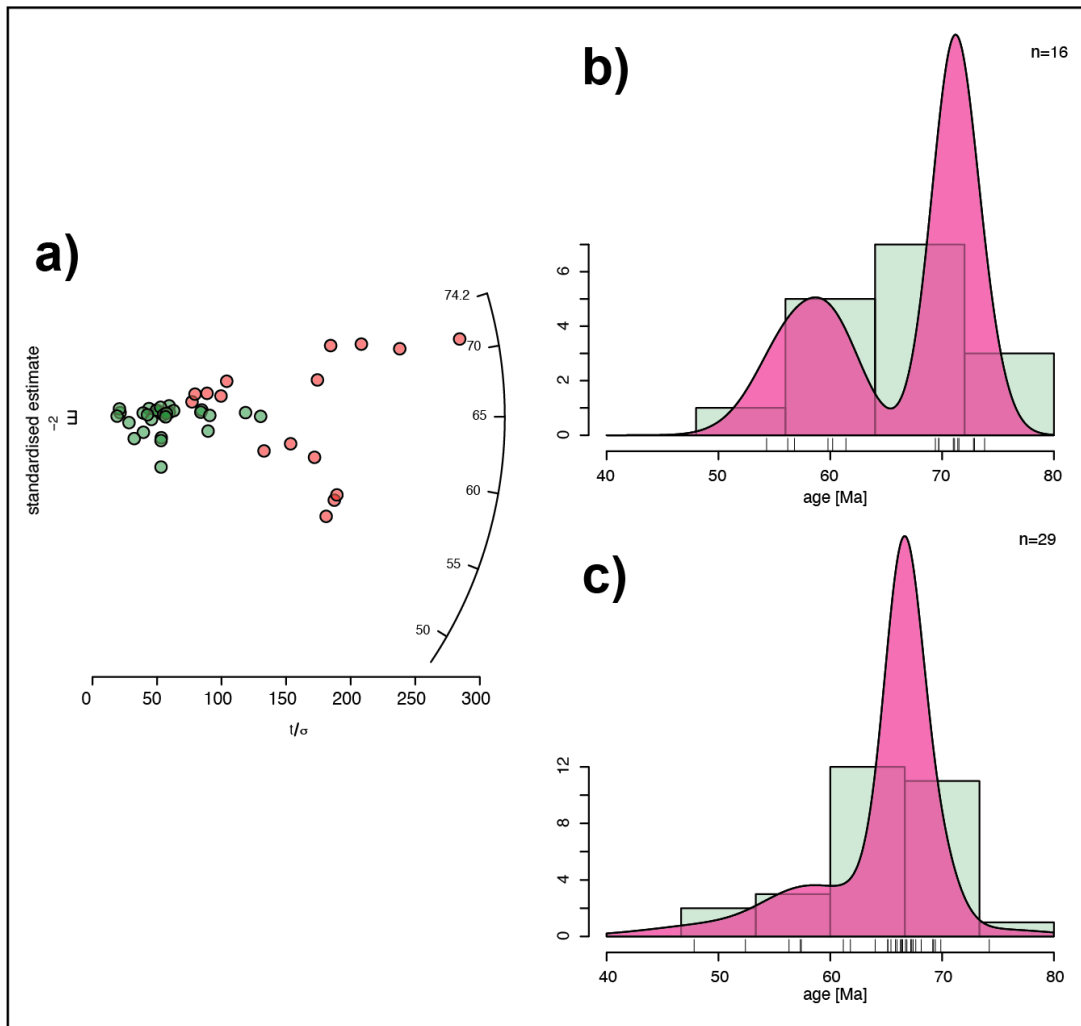


Figure 7.13. **a)** radial plot showing the contrast in precision of the zircon ages in this study (green) and zircon ages from Simmons (2013) in red; **b)** a KDE and histogram representation of Simmons (2013)'s zircon data; **c)** a KDE and histogram of the zircon dates from this study. The kernel bandwidth (which affects curve smoothness) for both KDE plots has been set to 2 Ma in order to keep consistency despite difference in sample size.

Consequently, particularly for section 2, there are very few relevant reference dates.

U-Pb zircon dates

The most reasonably comparable mineral and dating method for dates in this study and the literature are U-Pb zircon dating. The majority of the zircon dates in the area originate from Simmons (2013) and Simmons *et al* (2013) who used Sensitive High-Resolution Ion Microprobe-Reverse Geometry (SHRIMP-RG) to obtain magmatic dates from a variety of the lithological units in the region. In contrast with the aforementioned K-Ar and Ar-Ar data, these zircon U-Pb data can be directly compared with the data in this thesis.

From mapping the relevant dates (Figure 7.12), it is evident that the dates from Simmons (2013) and Simmons *et al.* (2013) are more precise. This is highlighted by a side-by-side comparison of Simmons' SIMS data and our LA-ICP-MS data for the Toquepala Group and Yarabamba Batholith (Figure 7.13a). All the published dates plot close to the circular scale furthest from the origin; increased horizontal distance from the origin represents increased precision. Increased uncertainty of the dates in this study results in the clustering of points closer to the origin. However, the general scatter of the published ages signifies the range of ages from ~54 Ma to ~74 Ma, whereas the focused angular position of the dates from this study highlights an approximate agreement in ages (~62-71 Ma).

This relationship between the two data sets is clearly displayed as a KDE and histogram plot (Figure 7.13b-c). The KDE Gaussian curve of the published data is broad with an undefined peak at ~70 Ma, compared to the extremely well constrained peak of the data in this study at 66 Ma.

K-Ar and Ar-Ar dates

Several studies (Zimmermann & Collado, 1983; Clark *et al.*, 1990; Martinez & Cervantes, 2003) have produced K-Ar and Ar-Ar ages using biotite, feldspar and total rock analysis. These dates are particularly useful for this study as they are the most geographically extensive of the published ages, therefore giving a better comparison for the regional dates in this study. However, there are potential limitations with the use of K-Ar and Ar-Ar dating which should be acknowledged.

A brief outline of the K-Ar and Ar-Ar process is given in Chapter 3. Fundamentally, these methods can have complications because Ar is very susceptible to migration: as a noble gas, it is unable to chemically bond into the K-bearing silicate mineral lattice. Only when the mineral has cooled sufficiently can the Ar be incorporated and the decay 'clock' begin. Any fluctuation in the temperature of a rock can cause the clock to reset (White, 2015; Reiners *et al.*, 2018).

This is especially limiting when K-Ar or Ar-Ar is used to obtain the *formation* age of igneous material. Because of the prolonged cooling of intrusive rocks, any K-Ar or Ar-Ar date is most representative of the cooling age or a younger resetting event and therefore should only be used for rapid-cooling igneous rocks, such as obsidian, that are known to be unaltered. There are further complexities with K-Ar and Ar-Ar dating, with temperature differences depending on the mineral being dated, for example: hornblende retains Ar at higher temperatures than biotite, and biotite at greater temperatures than K-feldspar (Harrison & McDougall, 1980; White, 2015). With this knowledge, it can be assumed that K-feldspar, formed simultaneously with hornblende, would produce a younger date as it is the cooling age that is recorded.

There is a possibility that the ages have been underestimated, and the Ar-Ar and K-Ar ages recorded in the literature are in fact representative of the cooling age rather than formation age, or a period of moderated temperature such as an alteration event (Reiners *et al.*, 2018). This concept is important when comparing dates and highlights why the quantitative comparison between the dates in this study and the literature may not be recommended. For instance, the DRT Ar-Ar biotite date of 65.4 ± 1.7 Ma (original source: Clark *et al.*, 1990) proximal to RCS017, is a particularly crucial date as it provides the only reference for 8 samples along the NW-SE stretch of outcropping DRT along the Incapuquio Fault System (Figure 7.12). If this date represents the igneous formation for the DRT diorite, then it would be assumed that all proximal alteration dates would display a younger age. However, as discussed, there is the possibility that this 65.4 Ma Ar-Ar date represents the cooling age or possibly an alteration event which affected the biotite's Ar content. Samples such as RCS044, RCS042 display alteration (RCS044 64.3 ± 5.4 'A2'; or RCS042 65.5 ± 2.5 Ma 'lg-Alt') dates that are chronologically very close or at least within error of the reference 65.4 Ma date, despite most of the dates representing altered minerals.

7.8 Conclusions

- Widespread district propylitic alteration occurred over an extensive period from 60-72 Ma, with an alteration maximum concentrating at 65-69 Ma. However, as the dates are tightly clustered and generally fall within error of each other, whether igneous or altered, it is difficult to determine a systematic difference between specified textures. Geochronological data interpretation is further complicated by the wide geographic spread of the samples, and therefore there is an expectation that the ages will naturally fluctuate with distance. To assume geochronological patterns would be unreliable.
- Pooled model-3 discordia plots of the four dated minerals show a reasonably tight average age of ~71 - 69 Ma for epidote, titanite and

apatite. Zircon's average age of 64 ± 0.1 Ma is 7 Ma younger and more precise. An overdispersion of ± 5 Ma constrains the crystallisation period for the zircon to 64 ± 5 Ma.

- Epidote does not yield reliable age constraints, but does provide precise common Pb estimates which can be used to improve the accuracy of the dates for the other minerals. Mapping of the precise epidote common Pb values indicated that, despite the crystallising in various phases, the inherited lead component of the samples are the same in the sampled region.
- Anchoring of the common Pb intercept proved to be a useful tool for increasing the precision and accuracy of most of the dates. Of the 87 precise dates selected, 80% were calculated from anchored intercepts highlighting the success of anchoring. For 20% of the precise dates the raw calculations proved more reliable, usually due to higher inherited Pb content in the dated sample.
- Published U-Pb, K-Ar and Ar-Ar dates for the Toquepala and Yarabamba units are often more precise than our LA-ICP-MS-based zircon U-Pb dates. However, directly comparing the published ages with those produced in this study is problematic for two reasons. Firstly, there is no textural information present for the mineral phases dated in other studies which renders comparisons unreliable as the dates presented could be of an alteration phase. Secondly, some of the published ages were acquired using K-Ar and Ar-Ar dating methods which has potential limitations and can affect the reported formation ages for igneous rocks.

8 Regional variations in mineral chemistry of propylitic chlorite and epidote at Quellaveco

8.1 Aims and questions

- Is there a protolith control on certain trace element compositions?
- Does the mineral chemistry highlight populations of samples, assemblages and vein types that are geochemically similar? If so, are these populations spatially associated?
- Can any of the above similarities be linked to a specific alteration event that was constrained by dates acquired in Chapter 6?
- How do regionally collected samples from a district containing several economic porphyry deposits (e.g Quellaveco) compare with data collected in known regional metamorphic terranes?
- How do the chlorite and epidote chemistry data from the Quellaveco region compare with porphyry-proximal (<5 km) data collected from similar regions?

8.2 An introduction to chlorite and epidote chemistry and structure

8.2.1 Chlorite

The chlorite group comprises monoclinic hydrous phyllosilicates with a perfect cleavage. The majority of the chlorite group minerals can be summarised by the formula $[R^{2+}, R^{3+}]_{12}^6 [Si_{8-x}R_x^{3+}]_4 O_{20} (OH)_{16}$ where R^{2+} represents Mg, Fe, Mn, Ni and/or Zn, and R^{3+} represents Al, Fe and/or Cr (Deer *et al.*, 2013).

Chlorite is a 'non-clay' with a distinct layered structure of alternating positively and negatively charged layers (Figure 8.1). The negatively charged, talc-like layers ($Y_6Z_8O_{20}(OH)_4$) follow a tetrahedral-octahedral-tetrahedral (2:1) pattern, and the positive, brucite-like layers ($Y_6(OH)_{12}$) are considered 'interlayers' in the structure, with Y and Z indicating the octahedral and tetrahedral sites respectively (Deer *et al.*, 2013). The

positive charge of this interlayer is often the result of Al^{3+} substitution for Mg^{2+} (Foster, 1962; Klein & Philpotts, 2017).

Clinochlore [end member = $(\text{Mg}_{10}\text{Al}_2)(\text{Si}_6\text{Al}_2\text{O}_{20})(\text{OH})_{16}$] and chamosite [end member = $(\text{Fe}_{10}^{2+}\text{Al}_2)(\text{Si}_6\text{Al}_2\text{O}_{20})(\text{OH})_{16}$] are the end members of the $\text{Mg} \leftrightarrow \text{Fe}$ solid solution series (Deer *et al.*, 2009). Penninite [end member = $(\text{Mn}_5^{2+}\text{Al})(\text{Si}_6\text{Al}_2\text{O}_{20})(\text{OH})_{16}$] is known as the Mn-rich chlorite, where up to 60% of the chlorite structure is made up of manganese. Manganochlorite, and other variations such as Cr-, Ni- and Zn-rich chlorites, are much less common than members of the clinochlore and chamosite series (Bailey, 1980; Deer *et al.*, 2013).

The $\text{Mg} \leftrightarrow \text{Fe}$ substitution between the tri-octahedral chlorite end-members clinochlore and chamosite forms many intermediate chlorite species (Deer *et al.*, 2009). The continual and varied cation substitution that occurs in chlorite has resulted in an abundance of varietal names. Mostly these species cannot be optically differentiated, only distinguished by chemical composition, therefore the species names are often simplified e.g diabantite as ferroan-clinochlore (Bailey, 1980; Deer *et al.*, 2009; Lauf, 2010). With the exception of the Ni-rich chlorite, nimite [end member = $(\text{Ni}_{10}\text{Al}_2)(\text{Si}_6\text{Al}_2\text{O}_{20})(\text{OH})_{16}$], some authors advise that the nomenclature for other potential chlorite species be ignored, and instead adjective modifiers

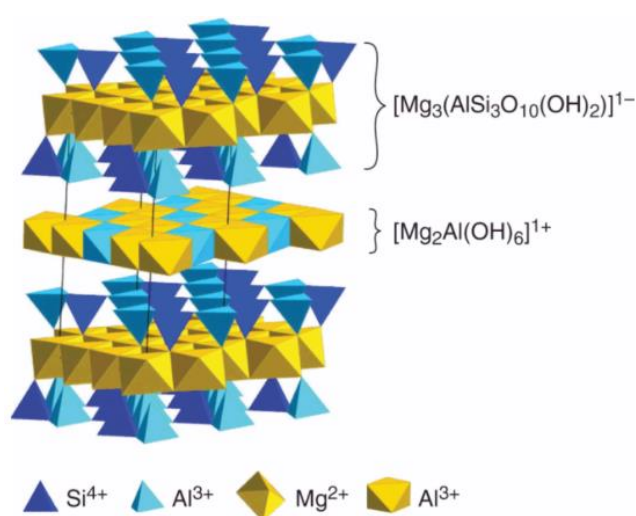


Figure 8.1. The 3D simplified structure of a chlorite with the chemical composition $(\text{Mg},\text{Al})_6(\text{Si},\text{Al})_4\text{O}_{10}(\text{OH})_8$. The 2:1 structure is shown with the talc-like layers $[\text{Mg}_3(\text{AlSi}_3\text{O}_{10}(\text{OH})_2)^-]$ and brucite-like interlayer of $[\text{Mg}_2\text{Al}(\text{OH})_6]^+$ (Klein and Philpotts, 2017).

refer to the chlorite species (Bailey, 1980; Lauf, 2010). For example, brunsvigite could be termed Mg-chamosite (Lauf, 2010).

Chlorite is an index mineral in low- to medium-grade metamorphic terranes, forming at temperatures up to ~400 °C. Clinocllore is often associated with moderate-grade metamorphism, whereas ferroan chlorite (chamosite) is typically formed during diagenesis (Huggett, 2021). Chlorite is also common as a product of hydrothermal alteration, such as in the propylitic haloes of porphyry systems (Sillitoe, 2010; Cooke *et al.*, 2014a) and in epithermal ore deposits, VHMS, and orogenic gold deposits.

8.2.2 Epidote

'Epidote' refers to a group of several monoclinic sorosilicate minerals which are regarded as hydrous Ca-Al-silicates. Each member within the series contains both single silica tetrahedra (SiO₄) and double silica tetrahedra (Si₂O₇). Ito (1950), confirmed by Belov & Rumanova (1953) and Ito *et al.* (1954), proposed the epidote group formula of (A1A2)(M1M2M3)[Si₂O₇][SiO₄]O(OH) where A represents Ca²⁺ and M = Al³⁺ or Fe³⁺. Ca is easily exchanged for REE and Sr, and the M site (usually Al) can accommodate Fe³⁺ and Mn³⁺ (Franz & Liebscher, 2004). These substitutions determine the variation of minerals in the group. The four key constituent minerals in epidote are:

- Clinozoisite $\text{Ca}_2(\text{Al}, \text{Fe}^{3+})\text{Al}_2\text{O}_7 \cdot \text{Si}_2\text{O}_7 \cdot \text{SiO}_4$
- Epidote $\text{Ca}_2(\text{Fe}^{3+}, \text{Al})\text{Al}_2\text{O}_7 \cdot \text{SiO}_7 \cdot \text{SiO}_4$
- Piemontite $\text{Ca}_2(\text{Mn}^{3+}, \text{Fe}^{3+}, \text{Al})_3\text{O}_7 \cdot \text{Si}_2\text{O}_7 \cdot \text{SiO}_4$
- Allanite $(\text{Ca}, \text{Mn}, \text{Ce}, \text{La}, \text{Y})_2(\text{Fe}^{2+}, \text{Fe}^{3+}, \text{Al})_3\text{O}_7 \cdot \text{Si}_2\text{O}_7 \cdot \text{SiO}_4$

Zoisite, a polymorph of clinozoisite, has an orthorhombic crystal structure and is no longer considered part of the epidote group (Frei *et al.*, 2004; Deer *et al.*, 2013) so is not discussed further here. Clinozoisite and true epidote are the most common end members of a series with compositions varying between Ca₂Al₃Si₃O₁₂(OH) and Ca₂Fe³⁺Al₂Si₃O₁₂(OH). Piemontite is structurally similar to other monoclinic minerals in the epidote group, but contains elevated Mn³⁺ (Deer *et al.*, 2013). It can be distinguished optically

from epidote by its brown appearance. Allanite is known as the REE-rich member of the epidote series, and is the only mineral to require Fe^{2+} in its structure (Deer *et al.*, 2009).

The monoclinic structure of the epidote series contains three site-types: A, M and T. The T sites are silica tetrahedra (T1-T3 in Figure 8.2a). The 'M' positions (M1-M3) are non-equivalent sites of different sizes. The M cations form two chain types which are the basis of the monoclinic structure (Figure 8.2b): the first type comprises edge-sharing M1 octahedra with singular M3 octahedra on alternate sides of M1 chains; the second chain exclusively contains edge-sharing M2 octahedra (Franz & Liebscher, 2004). These chains are joined by single SiO_4 tetrahedra (T3) and Si_2O_7 groups (T1T₂O₇) that coincide with large, cavity-like A1 and A2 sites.

The A1 and A2 cavities are important sites for containing trace elements. Alkali and alkaline earth metals are substituted into the A sites via coupled substitution and homovalent substitution respectively. Common substitutions into the Ca^{2+} site include V^{2+} , Mn^{2+} and Fe^{2+} . As A2 is the

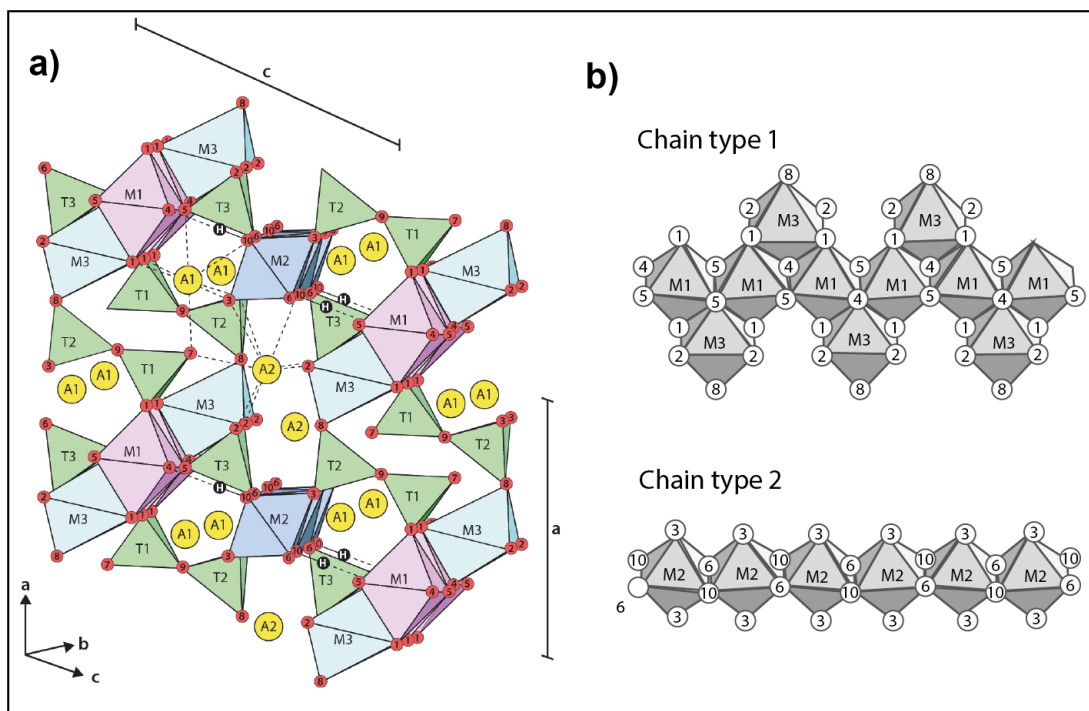


Figure 8.2. **a)** polyhedral structure of epidote showing M, A and T sites (Pacey, 2017 after Franz and Liebscher; and Dollase, 1968); **b)** the structure of the octahedral chains with numbered oxygens (modified from Franz and Liebscher after Dollase 1968).

largest site, divalent cations with a large ionic radius (e.g. Sr, Ba and Pb) preferentially substitute into it (Frei *et al.*, 2004; Duncan & Maas, 2014).

The M sites often contain Al^{3+} and Fe^{3+} , together with small, trivalent transition metals such as V^{3+} , Mn^{3+} , Co^{3+} , Cr^{3+} and Cu^{3+} (Frei *et al.*, 2004). Be^{2+} has a small ionic radius, similar to Al^{3+} , and is therefore incorporated into the M1 and M2 sites. The M sites also allow for the substitution of high field strength elements (HFSE), which are small highly charged ions (e.g. Mo^{4+} and U^{6+}), as the charge balance can be maintained in the octahedral M sites.

The Si^{4+} present in the T sites displays little evidence of significant cation substitution (Bonazzi & Menchetti, 1995; Nozik *et al.*, 1978), although, by analogy with other silicates, it is possible that there may be some substitution by ions such as Al^{3+} , Ge^{4+} , Ti^{4+} and Sn^{4+} .

It is common for epidote to display compositional zoning, in particular related to Fe^{3+} and Al^{3+} incorporated in the M sites. Certain zonation characteristics can be indicative of the formation environment; for example, hydrothermal zonation is often oscillatory, reflecting rapid changes at the growing crystal surface, whereas simple, systematic core-rim zonation is more characteristic of metamorphic growth (Grapes & Hoskin, 2004; Pacey, 2017).

The ability of epidote to incorporate a variety of geochemically important trace elements, such as REE, Mn, Sr and Pb, into its structure (Frei *et al.*, 2004) is the basis by which it has been developed as a porphyry indicator and vectoring mineral (e.g. Wilkinson *et al.*, 2015, 2020; Baker *et al.*, 2020; Cooke *et al.*, 2020; Pacey *et al.*, 2020).

8.3 Results

8.3.1 Chlorite

Major Elements

Major elements were determined using analytical SEM (see chapter 3). The compositional data for chlorite from the Quellaveco district

in terms of the four major elements (Si, Fe, Mg, Al) is summarised in Figure 8.3. It is arranged by decreasing median values, which highlights Si as the most abundant major element and Al the least abundant. Fe has the largest interquartile range, and greatest difference between the maximum and minimum values.

Atomic abundances (atoms per formula unit, or 'apfu') were calculated on the basis of 28 oxygens, and include the partitioning of total Fe between the R2 sites hosting Fe²⁺ and the R3 sites containing Fe³⁺. The calculated apfu values were then used to classify the chlorite types based on the Fe/(Fe+Mg) ratio and Si (after Hey, 1954). This yielded six chlorite types (Figure 8.5): penninite (Mn-chlorite), clinochlore (Mg-chlorite), diabantite (Fe-clinochlore), pycnochlorite (Fe-clinochlore), ripidolite (Fe-Al-clinochlore) and talc-chlorite (after Hey, 1954). The predominant varieties are diabantite (n=560) and pycnochlorite (n=584).

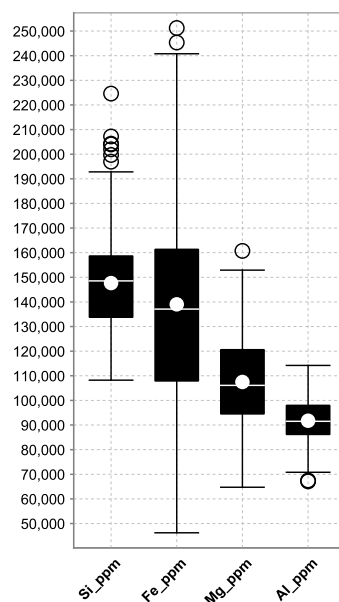


Figure 8.3. Major element compositional data for Si, Fe, Mg and Al, determined by analytical SEM. The box represents the 25th and 75th percentiles; white dot = mean value; white horizontal line = median; vertical whiskers = maximum and minimum values (excluding outliers). Outliers are either shown as circle outlines or triangle outlines. Circles indicate >1.5x interquartile range, and triangles are far outliers with >3x interquartile range from the box.

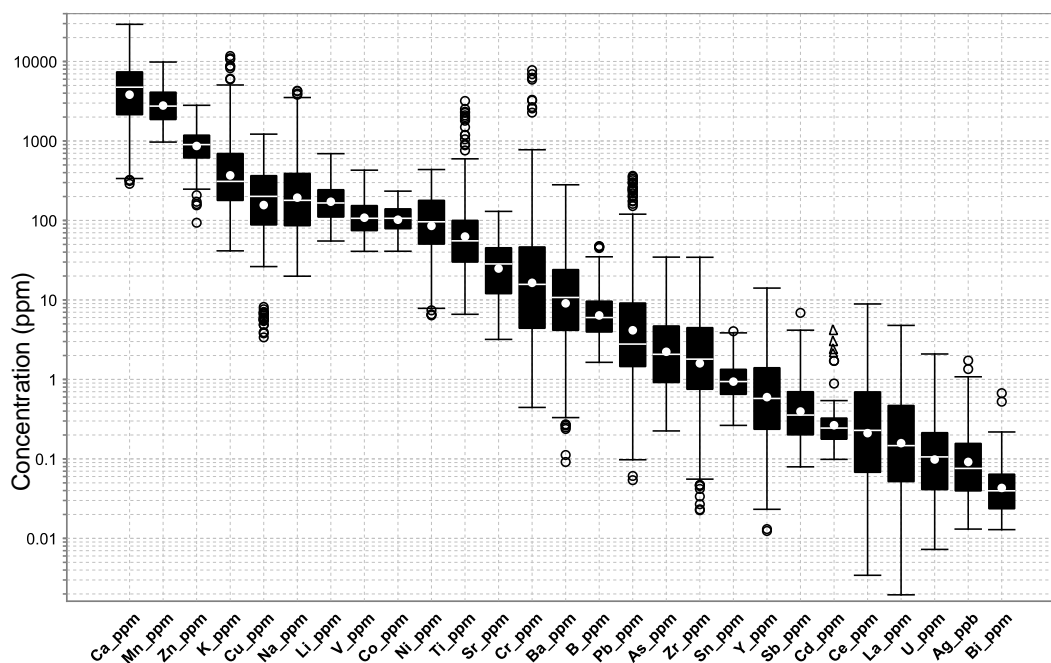


Figure 8.4. Summary of compositional ranges for trace elements in chlorite. The box represents the 25th and 75th percentiles; white dot = mean value; white horizontal line = median; vertical whiskers = maximum and minimum values (excluding outliers). Outliers are either shown as circle outlines or triangle outlines. Circles indicate >1.5x interquartile range, and triangles are far outliers with >3x interquartile range from the box.

There is no clear link between rock type and chlorite species (Figure 8.5). However, the most evolved lithologies, rhyolite, dacite, granodiorite, trachyte and quartz monzonite are mostly categorised as pycnochlorite, although there are some quartz monzonite samples that also contain diabantite-penninite compositions and dacite-hosted chlorite in the penninite field. The more mafic lithologies are more widely spread between the classifications, with perhaps a slight bias towards lower Fe/Fe+Mg and higher Si.

Minor and trace elements

Data were collected for 27 minor and trace elements in chlorite from 33 samples (see Chapter 3 for summary of method and analytical uncertainties). A summary of these results is shown in Figure 8.4, plotted in order of decreasing median concentration. This gives an indication of which elements were most detected, and their variability.

The most common trace elements in the chlorite data with median concentrations of >100 ppm are: Ca, Mn, Zn, K, Cu, Na, Li, V, Co and Ni. Ca is the most abundant element which is somewhat unexpected given that Ca is not typically described as a substituting element (Peacor *et al.*, 1988). Routine detection of Mn, Zn and Ni is expected because of their ability to substitute into the octahedral R^{2+} site (see section 8.2.1). Trivalent vanadium cations are known to substitute into the Al^{3+} octahedral site (Meunier, 1994).

Copper is the 5th most abundant trace element in the chlorite. It is likely that the Cu is incorporated into the chlorite structure and, due to the similarity in ionic radius between Cu^+ and Li^+ , it is suggested that they can both occupy the octahedral site, with charge balancing by Al^{3+} (Černý, 1970; Wilkinson *et al.*, 2020).

Cd, Ce, La, U, Ag and Bi were only detected in <25% of the analyses and are therefore not used in subsequent multivariate plots.

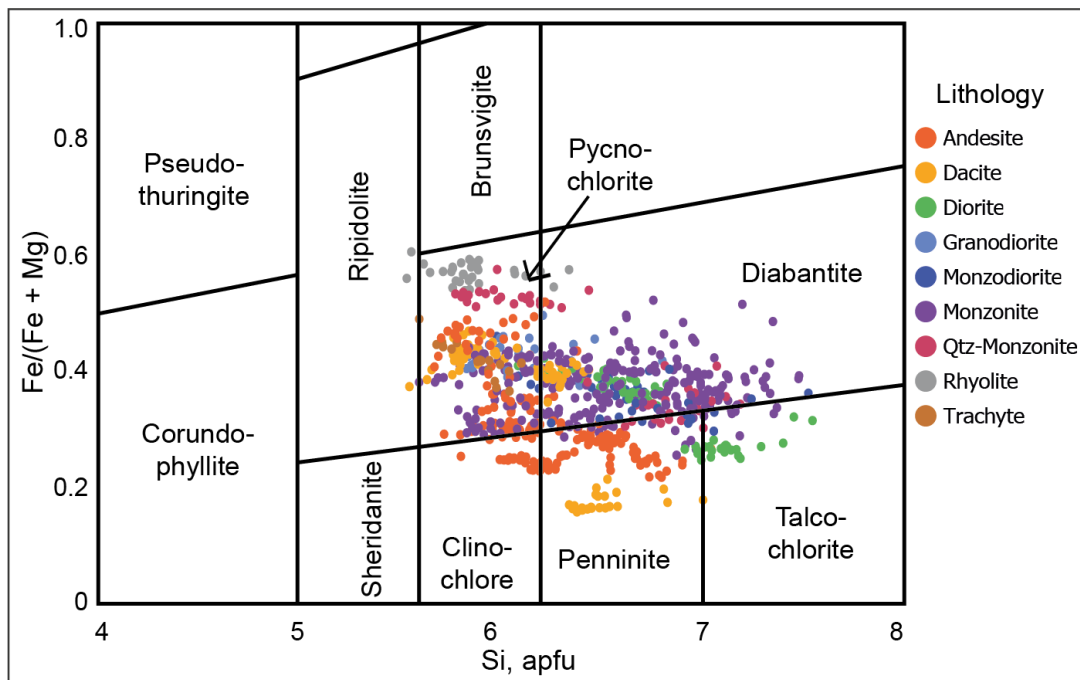


Figure 8.5. Chlorite species boundaries after Hey (1954). Samples are attributed on sample number.

8.3.2 Epidote

Major Elements

The compositional data for epidote from the Quellaveco district for the four major elements (Si, Ca, Al, Fe) is summarised (Figure 8.4) and arranged by decreasing median values, highlighting Si as the most abundant major element and Al the least abundant. Ca has the narrowest interquartile range and smallest difference between the maximum and minimum values.

Minor and Trace Elements.

The most common trace elements detected in epidote with concentrations of >100 ppm are Mn, Sr, Mg, Ti, V, Na and P. The substitution of Mn^{2+} , Mg^{2+} and Sr^{2+} into the Ca^{2+} A-site is likely to account for their abundance. In addition, trivalent Mn substitutes into the M-site in place of Fe^{3+} and Al^{3+} .

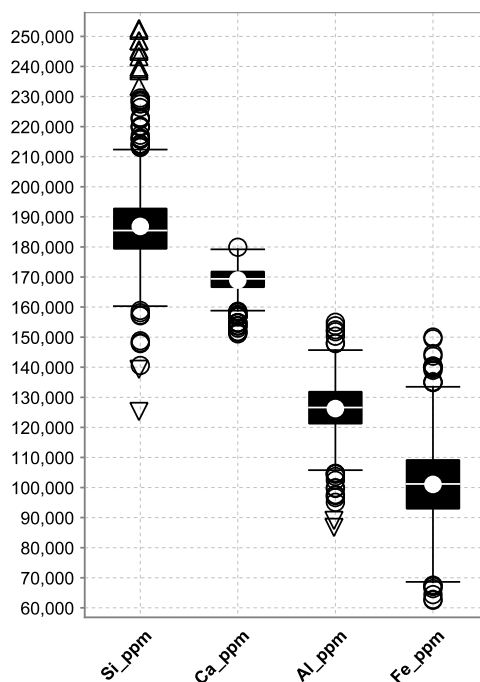


Figure 8.6. Major element compositional data for Si, Ca, Al and Fe in epidote, determined by analytical SEM. The box represents the 25th and 75th percentiles; white dot = mean value; white horizontal line = median; vertical whiskers = maximum and minimum values (excluding outliers). Outliers are either shown as circle outlines or triangle outlines. Circles indicate >1.5x interquartile range, and triangles are far outliers with >3x interquartile range from the box.

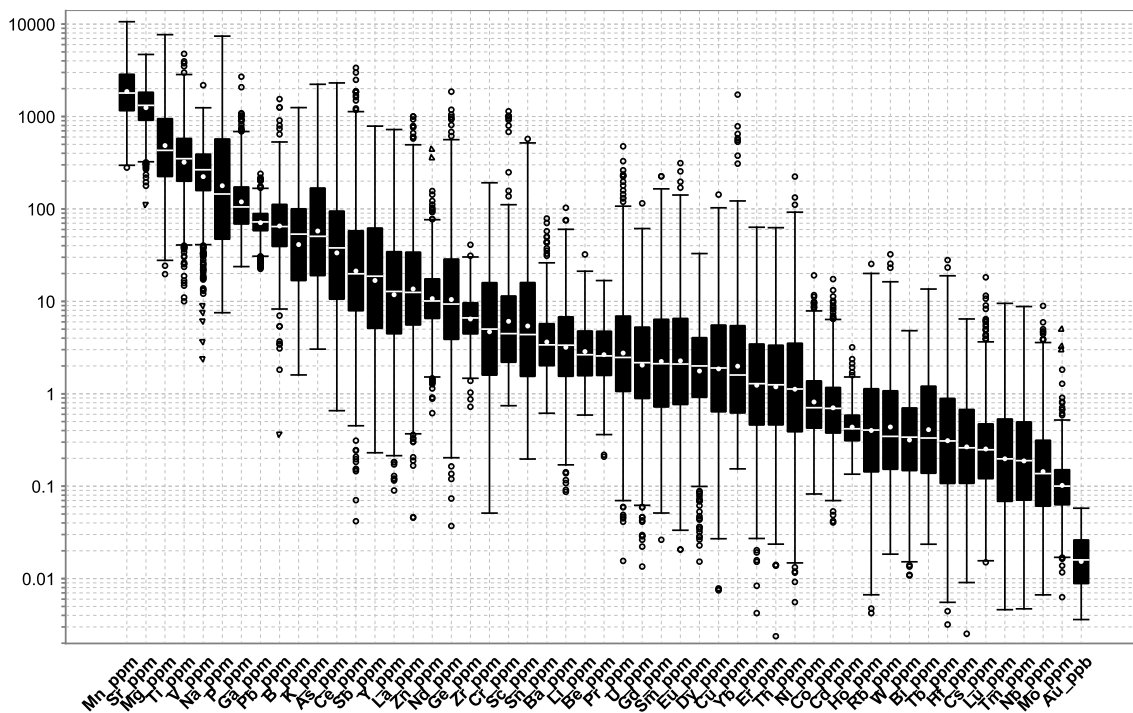


Figure 8.7. Summary of compositional ranges for trace elements in epidote presented by decreasing median values. The box represents the 25th and 75th percentiles; white dot = mean value; white horizontal line = median; vertical whiskers = maximum and minimum values (excluding outliers). Outliers are either shown as circle outlines or triangle outlines. Circles indicate >1.5x interquartile range, and triangles are far outliers with >3x interquartile range from the box.

Ho, Rb, W, Bi, Tb, Hf, Cs, Lu, Tm, Nb, Mo, Au are the least consistently detected trace elements, with concentrations mostly <1 ppm.

8.3.3 Exploratory data analysis

Principal component analysis (PCA) is the most popular statistical method of visualising multidimensional datasets. PCA is a powerful multivariate statistical technique which allows for the dimensionality reduction of a number of variables, in this case the major and trace element compositions of epidote and chlorite. The benefit of using PCA is its ability to identify trends, outliers and relationships within complex datasets (Bonnier & Byrne, 2012).

PCA linearly combines the original variables into new variables, known as the principal components (PC), which account for the highest percentage of the total variance of the dataset (Abdi & Williams, 2010; Bartholomew, 2010). The first principal component (PC1) contains the most variance in

the data. The second principal component (PC2), which is uncorrelated to PC1, is perpendicular to PC1 and explains the second greatest proportion of the variance. Other PCs (e.g PC3, PC4 etc) follow the same trend, each decreasing in representative variability (Korenius *et al.*, 2007; Bonnier & Byrne, 2012). PC1, PC2 and PC3 generally represent up to 99% of the variance in a dataset.

Because PCA strictly requires the data to be free to vary from -infinity to +infinity it cannot be applied directly to concentration data that are subject to closure (i.e. when all components sum to 100 wt%). In order to 'free' the data from those constraints and remove the closure effect, the centred logratio (clr) transformation can be used. Statistically, clr is denoted as:

$$u_i = \ln \left[\frac{x_i}{g_i} \right], v_i = \ln \left[\frac{y_i}{g_i} \right], \text{ and } w_i = \ln \left[\frac{z_i}{g_i} \right]$$

where g_i is the geometric mean of the i^{th} sample (Pawlowsky-Glahn *et al.*, 2007).

Loadings, or eigenvectors, are nonzero 'weights' of each principal component; that provide information about the direction of variance in a component (Smilde *et al.*, 2005). Each eigenvector has an associated coefficient, the eigenvalue, which represents the amount of variance in each PC. The eigenvectors essentially represent the axes where there is the most variance. Therefore, when the eigenvectors are ranked in order, the principal components are ordered by significance.

When interpreting PCA plots, PCs with the highest variance plot furthest away from the origin and have the greatest influence. Data plotting close to the origin indicate average, non-variable data (Pawlowsky-Glahn *et al.*, 2007). Highly correlated data will cluster together, and data on opposing vectors signify an inverse correlation between those data groups.

Using a PCA biplot to visualise such a complex multidimensional dataset like the trace geochemistry, enables preliminary discrimination between samples or clusters of samples and can be done irrespective of the multiple

factors that may be controlling geochemical variability (e.g. age, mineral assemblage, rock type, etc).

PCA of chlorite trace element data

The 20 most significant elements determined by LA-ICP-MS (Mg, Fe, Al, Si, Mn, Zn, Ti, V, Co, Li, Ca, Sr, Pb, Ni, Cu, As, Ag, Sb, Ba, Cr) were selected for the PCA plot (Figure 8.8).

Vectors which plot in the same direction are correlated, such as Cu and Sr, Zn and Mn, and Ti, V and Fe. Opposing vectors suggest an anticorrelation of elements, so chlorites rich in Cu and Sr are low in Ba, and grains rich in Pb are low in Ni (e.g. samples RCS064, RCS079). The fact that these vectors are orthogonal to each other means that there is no correlation between the two relationships. Variables with very short vectors (e.g. Ti, Si, Mg etc) indicate data with the least variance.

The clusters of samples with geochemical similarities of statistical significance for chlorite appear to be:

- RCS064 and RCS079
- RCS031, RCS032, RCS033 and RCS068
- RCS037, RCS042, RCS047

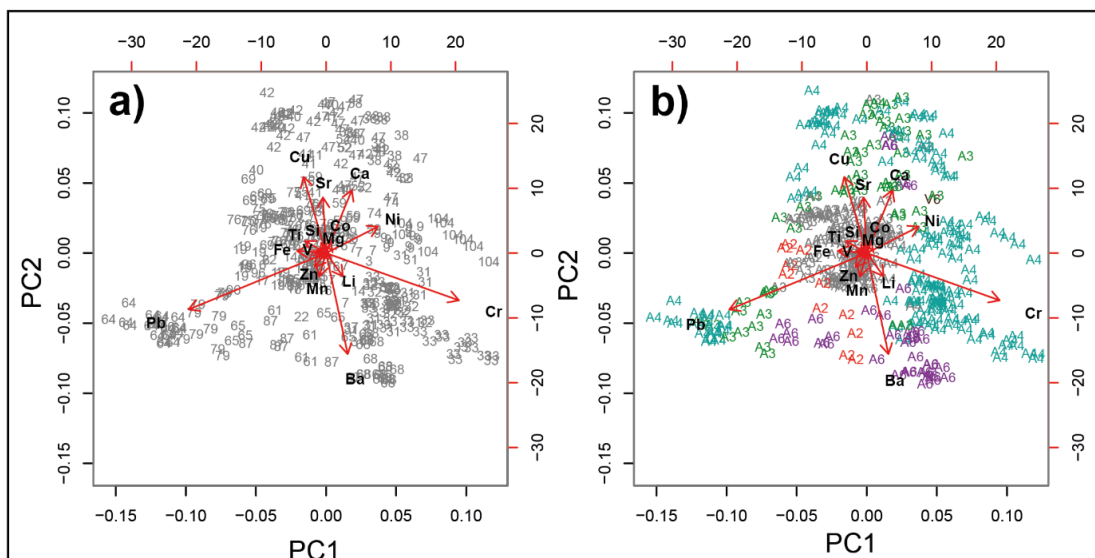


Figure 8.8. PCA plots for chlorite LA-ICP-MS trace element chemistry. Data are attributed by: **a)** sample number and **b)** alteration assemblage

- RCS069, RCS075 and RCS076

However, highlighting these groups of samples does not exclude the possibility of other groups and clusters and does not definitively mean that these groups of samples are connected in some way.

When attributed by assemblage (Figure 8.8b), A4 (see Chapter 5) shows high variance, with data plotting away from the origin loosely along the Pb, Cu, Ca, Ni and Cr vectors. The A2 assemblage displays low to moderate variance, with particular significance attached to Pb, Fe, Ti and Ba.

PCA of epidote trace element data

The 25 most significant major, minor and trace elements in epidote selected from the LA-ICP-MS data for PCA were Mg, Al, Si, Fe, Ti, V, Cr, Mn, Ni, Zn, As, Sb, Pb, Ga, Ge, Sr, Y, Cd, Sn, Yb, Eu, Th, U, W and Bi.

Y, Yb, Mg, As and Sr have the longest eigenvectors showing that, in the epidote dataset, these elements have the most variance. Vectors for Y, Yb, Th, U and Eu are highly correlated. The inverse correlation between Ti+Fe and As+Sb is perpendicular to the inverse correlation between Y (and other elements) and Sr (and other elements) and therefore these two relationships are unrelated.

Two samples are particularly prominent in terms of high geochemical variance of epidote compositions and disparity with other samples (Figure 8.9a). RCS052 has high loadings for PC1 and low for PC2, reflecting a particularly strong inverse correlation between Pb, Sr, V, etc and Y, Yb. RCS042 has a less defined cluster, but has particular significance to Mg, Fe and Ti.

From this analysis, the clusters of samples with geochemical similarities of statistical significance are:

- RCS074, RCS075, RCS076 and RCS059
- RCS047, RCS065, RCS067

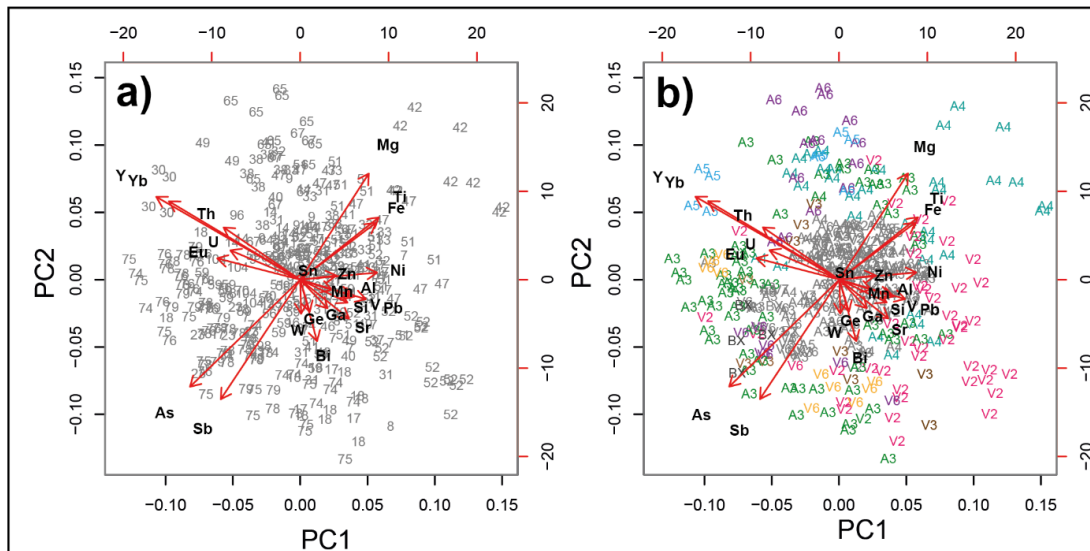


Figure 8.9. PCA plots for epidote LA-ICP-MS trace element chemistry. Data are attributed by: **a)** sample number and **b)** sample assemblage

In terms of epidote, this does not exclude the possibility of other groups and clusters and does not imply that these samples have to be related in some way, but it does have a bearing on later interpretations. Unlike the chlorite data, there appears to be less correlation between samples and within samples. For example, the data from RCS059, RCS074, RCS075 and RCS76 are quite variable spanning the area between the vectors for Eu and Bi.

Attributing the data in the PCA based on epidote assemblage (Figure 8.9b) shows that only two assemblages demonstrate particular cohesion: A6 and BX. The breccia-related epidote (BX) shows a good correlation of data and high variance along the As and Sb vectors. There is a good overlap between epidotes in A4, A5 and A6 assemblages, with a close correlation to Mg. It is worth noting that there are comparatively less data points for both assemblages (BX and A6) which may contribute to the noticeably high correlation within assemblages.

8.4 Discussion of chlorite chemistry

8.4.1 Potential igneous protolith control on chlorite chemistry

It is important to determine if observed inter-sample variability in chlorite chemistry could have been influenced by bulk composition of the host rocks.

In order to assess this, the whole rock composition of the samples is contrasted against the chlorite data for each trace element. Cr ppm and Li ppm are used as examples (Figure 8.10). A positive correlation, such as that seen in the Cr, displays an increase in both the chlorite and the whole rock. In the two examples of Cr and Li, the correlation of median values for Cr is relatively linear, indicating a proportionate increase, however Li shows two dominant clusters of values (~100-300 ppm and ~350-500 ppm), neither displaying proportionality between the axes. There are two fundamental reasons for this: differentiation between the primary protolith; or metasomatic addition of the trace element to the host rock. To determine which is most likely, sample lithology is considered. A scattered distribution with no clustering of more evolved lithologies along the trend suggests a metasomatic control, as the addition of the trace element to the rock is irrespective of host lithology. Predominantly using field-assigned rock types can be problematic for this assessment, particularly in areas where there is little apparent compositional spread of rock type, such as the highly evolved rocks in this study.

Therefore, in this case, geochemical proxies MgO and SiO₂ are used as an indication of how evolved a sample is: high SiO₂ = more evolved; higher MgO = less evolved. When contrasted, the MgO and SiO₂ are distinctly correlated, confirming that increased Mg is coupled with decreasing silica content, thereby validating their use as a differentiation proxy.

When MgO wt% content is compared with the chlorite trace elements, there are two potential trends: incompatible elements will increase with decreasing MgO; and compatible elements will decrease with decreasing MgO. The presence of either of these relationships indicates a primary protolith control on the chlorite chemistry of that element.

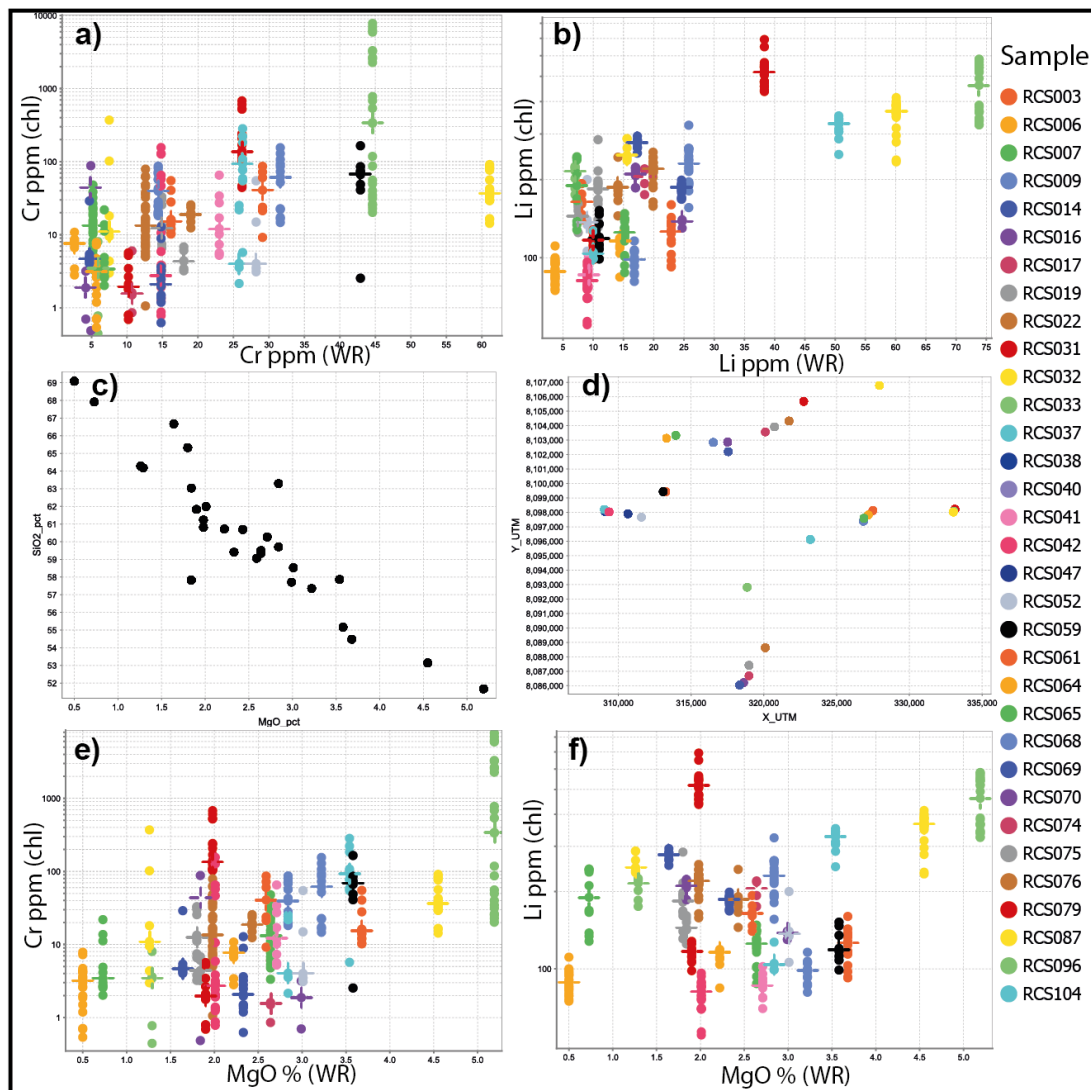


Figure 8.10. An assessment of protolith control on chlorite geochemistry: **a)** MgO % vs SiO₂ % **b)** sample location map for chlorite-bearing samples; **c)** MgO % (whole rock) vs Cr ppm (chlorite); **d)** Cr ppm (whole rock) vs Cr ppm (chlorite); **e)** MgO % (whole rock) vs Li ppm (chlorite); **f)** Li ppm (whole rock) vs Li ppm (chlorite). The horizontal lines represent the median value for each sample.

Chromium, for example, (Figure 8.10c) presents a shallow positive trend, with the median Cr content increasing with increasing MgO. There are nearly two orders of magnitude difference in Cr content between the most mafic sample, RCS033 (at ~400 ppm), and the most felsic sample, RCS064 (at ~3 ppm). This suggests a compatibility of the Cr during differentiation and is therefore strongly indicative of a primary protolith control as opposed to a metasomatic control. With such a significant difference in Cr ppm of two orders of magnitude, from the most felsic to most mafic samples, this protolith control is likely to obscure any other factors that might influence Cr content, such as spatial position within a hydrothermal system.

Lithium is an element that can be susceptible to protolith influence, particularly as elevated concentrations in evolved volcanic rocks. Unlike Cr, lithium does not have a clear relationship with increased host rock differentiation (Figure 8.10e), with the median of the most felsic sample at ~100 ppm, and the most mafic at ~400 ppm Li. Therefore the conclusion is drawn that there is no obvious primary protolith control on Li concentrations in chlorite. However, there is a relationship between the Li content in the chlorite and whole rock (Figure 8.10f). As a protolith control is unlikely, the alternative process of metasomatic addition and/or removal of Li from rocks of initially variable Li content is likely to be at least partially responsible for variations of Li in chlorite.

There are two explanations for this metasomatic enrichment and depletion. Either: net addition or removal of the Li from the rocks was reflected in synchronously forming chlorite; or systematic zonation in the Li content produced by an earlier metasomatic process influenced chlorite Li-content from a subsequent event. In both scenarios however, the chlorite reflects the metasomatic process.

8.4.2 Comparison with chlorite from metamorphic terranes

The chlorite data collected in this study are compared with chlorite reference data from known metamorphic terranes to determine whether district-scale propylitic chlorite in an area containing economic porphyry systems can be distinguished from regional metamorphic chlorite-bearing assemblages. The metamorphic chlorite datasets are derived from Central Chile, the Georgetown Inlier (Australia), Harts Range (Australia), Lers (Pyrenees), Shebandowan Greenstone Belt (Canada), Wasatch Mountains (USA) and West Scotland (UK) (Baker *et al.*, 2010; Wilkinson *et al.*, 2017).

Comparative bivariate plots highlight elements that show a separation between the datasets (Figure 8.11). For example:

- Ba vs Pb: the Quellaveco dataset (QV) plots in the upper section (0.8-300 ppm) of the metamorphic data (MT) cloud (<0.05 – 100 ppm). Although the metamorphic data spread encompasses the majority of the Quellaveco data points, the densest concentration of the data occurs

below 1 ppm, whereas the Quellaveco Pb concentration ranges from 0.8 ppm – 300 ppm.

- Li vs Fe: Although visually it appears that the Quellaveco data set displays higher Li content, the ranges (QV: ~50-900 ppm vs MT: ~30-1000 ppm) are deemed unremarkable. An area of elevated Li data follows a distinct trend in the Quellaveco chlorite towards an anomalously high Li cluster of metamorphic chlorites. For those data, it is possible this elevated Li is lithologically influenced or that there is a spatially localised metasomatic control.
- Mg vs Sn: there is no apparent difference in Mg and Sn concentrations between the datasets. There is more scatter for both elements within the metamorphic data.
- Mn vs Zn: both datasets follow a similar vague positive correlation, but the Quellaveco data is located on the upper side of the correlation due to generally higher Zn contents.
- Sr vs Ca: there is a distinct positive correlation between Ca ppm and Sr ppm in metamorphic and Quellaveco chlorites, with the Quellaveco data exhibiting the highest Sr and Ca concentrations. There are two distinct clusters within the Quellaveco data: the upper cluster defined by Sr 20-150 ppm and Ca 2000-20,000 ppm; the lower cluster between 500-5000 ppm of Ca and between 5-20 ppm Sr. The overlap of the data with the metamorphic dataset primarily occurs with the lower cluster of Quellaveco data. The comparatively high Ca content of the top Quellaveco cluster is indicative of a distal propylitic halo of a porphyry deposit. High Sr is also thought to occur in chlorites from a distal propylitic alteration as opposed to regional metamorphic signals (Cooke *et al.*, 2014a; Wilkinson *et al.*, 2015a; Baker *et al.*, 2020). If this is the case, the lower cluster could represent background metamorphism or proximal propylitic alteration. As the cluster is still in the upper range of the metamorphic dataset, it highlights that whilst the cluster is low relative to the Quellaveco data, it comparatively shows elevation in Ca and Sr relative to the metamorphic data. Any spatial significance of this sample is discussed (Figure 8.16a).

- Ti vs V: As a whole, the Quellaveco dataset displays lower Ti values than the metamorphic dataset (Qv: 15-200 ppm vs MT: 30-1000 ppm). However, an anomalously high group of Quellaveco data (highlighted in blue, Figure 8.11) display exceptionally high Ti values (500-3000 ppm). Ti is thought to act as a geothermometer with elevated values of Ti indicating a high element substitution temperature within the chlorite (Wilkinson et al., 2015; Cooke et al., 2020). Sample and spatial context to this cluster of data is provided in Figure 8.16b. The V concentration of both datasets are similar.

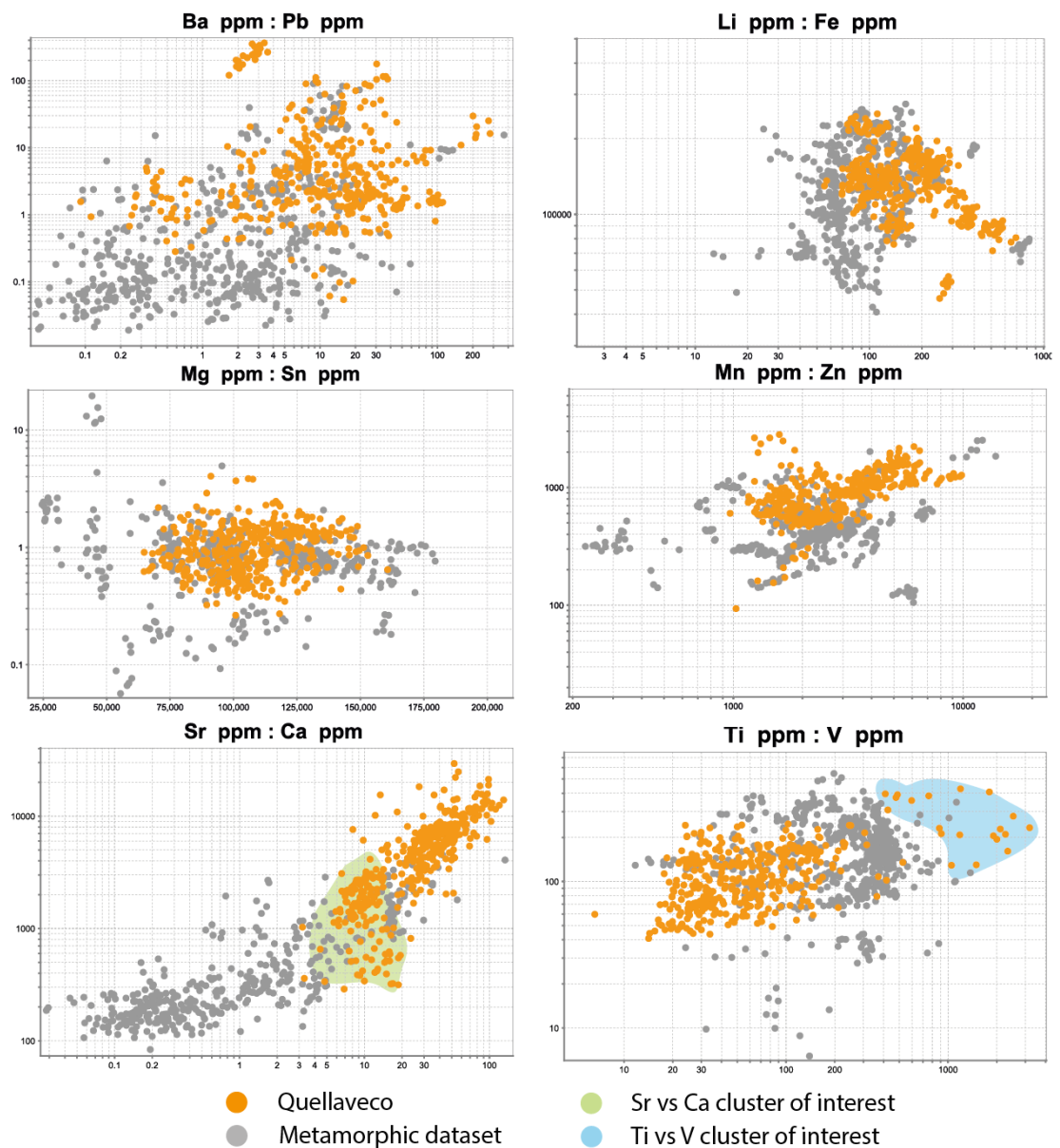


Figure 8.11. Trace element chemistry bivariate plots showing: Ba vs Pb; Li vs Fe; Mg vs Sn; Mn vs Zn; Sr vs Ca; and Ti vs V. Clusters of data analysed in Figure 8.16 are highlighted in green.

Overall, relative to the metamorphic data, the Quellaveco samples from this study show elevated Pb, Sr, Fe, Ca, Si, Zn and Cu with a less substantial elevation of Mn, Ba, Sb, U, K, Ag. The Quellaveco dataset appeared comparatively low in Ti, Al, and Ni. Trace elements, such as, Li, Mg, Sn, V, Mg, Ce, Co, La and Y, showed no apparent differentiation between the datasets. Diagnostic trace elements for distinguishing between background metamorphism and distal porphyry propylitic regions were proposed by Wilkinson et al. (2015). There are some similarities between the findings here, and those at Batu Hijau (Wilkinson et al., 2015), such as the relative depletion of Ca, Sr, Si, Zn, Sb and As and the elevation of Ti and Al in metamorphic chlorites. It is worth noting that the Quellaveco samples from this study are propylitic samples collected at mostly greater distances compared to the 'porphyry-distal' samples from Batu Hijau, and therefore represent district-scale alteration that may not be directly analogous to that investigated in previous studies.

8.4.3 Comparison with chlorite from porphyry systems

The chlorite data from the Quellaveco district were also compared with data from two economic porphyry systems, Batu Hijau and El Teniente, and one sub-economic prospect, Sekongkang in the Batu Hijau district (Wilkinson et al., 2015; 2017; 2020).

So that a comparison can be made back to the metamorphic analysis (Figure 8.11), the deposit data are displayed using the same set of plots with an outline of the metamorphic data cloud for reference.

There is only a minor overlap in Li content between the datasets, with Quellaveco containing significantly higher Li concentrations. There are two potential reasons for this. Increased mobilisation of Li in propylitic rocks could be a district feature, for example, Li can be elevated in evolved lithologies: at Quellaveco the rocks are mostly evolved volcanic from the Toquepala Group, but in other districts, such as El Teniente and Batu Hijau, the base rocks are more mafic. Another possibility for the Li-enriched samples at Quellaveco is the regional spread of the sample collection. Li in propylitic chlorite generally increases rapidly outwards from a deposit,

dropping to background levels at around 5 km distance (Wilkinson *et al.*, 2015). Therefore, the comparatively high Li content could be due to the collection of samples within propylitic halos from multiple areas within the region. Fe concentrations are comparable.

Quellaveco chlorite Sn concentrations are not significantly different from other deposits but Mg tends to be lower. This could be due to a bulk rock control on the comparative deposits.

The Quellaveco data tend to have higher Zn/Mn ratios than the deposit comparisons, with a lower top range. Previous work (e.g. Wilkinson *et al.*, 2017, 2020; Cooke *et al.*, 2020) indicates that general lower concentrations of these elements suggests poor fertility. Therefore, the higher concentrations of Mn and Zn relative to the comparison data could be indicative of an overall increased fertility of proximity to a potential source.

There is a very similar trend in Sr-Ca between the Quellaveco data and deposit chlorite concentrations, however the Quellaveco data fall in the upper half of the comparison data cloud. Based on conclusions in Wilkinson *et al.* (2015) the generally higher concentrations in the Quellaveco data could be indicative of very propylitically distal positions for those samples, or that district-scale alteration is characterised by this kind of signal and sets it apart to some degree from the more localised porphyry-related propylitic haloes. Lower values could indicate true porphyry-halo samples and the locations of samples with this character is explored in Figure 8.15. In the Ca vs Sr bivariate plot, the data range correlates with the middle (Sr 0.3 ppm, Ca 200 ppm) to upper section (Sr 100 ppm, Ca 20,000 ppm) of the metamorphic data range. The spread of the reference porphyry dataset indicates a progression from porphyry-proximal areas (lowest Ca and Sr values), to distal propylitic alteration and background metamorphism (highest Ca and Sr values). A sharp increase in Ca and Sr with distance from a porphyry system has been detected in previous studies, where the values are thought to plateau between 1.5 – 5 km before dropping to background metamorphic levels (e.g. Wilkinson *et al.*, 2015, 2020; Cooke *et al.*, 2020) With the addition of this porphyry deposit dataset, further context is provided for the two distinct clusters discussed previously within the

Quellaveco dataset (Figure 8.11). The higher cluster lies on the upper limit of the porphyry deposit and metamorphic datasets, whilst the lower cluster centres in the middle of the porphyry dataset range. When the spatial distribution of the cluster is also considered (Figure 8.16), there is convincing evidence that these samples (RCS016, RCS017, RCS033, RCS064, RCS065, RCS068, RCS070, RCS079 and RCS104) represent an intermediate position within a propylitic halo. The second, lower, Quellaveco cluster overlaps with more values from the deposit, suggesting that those samples within that cluster are more proximal to a porphyry-like system.

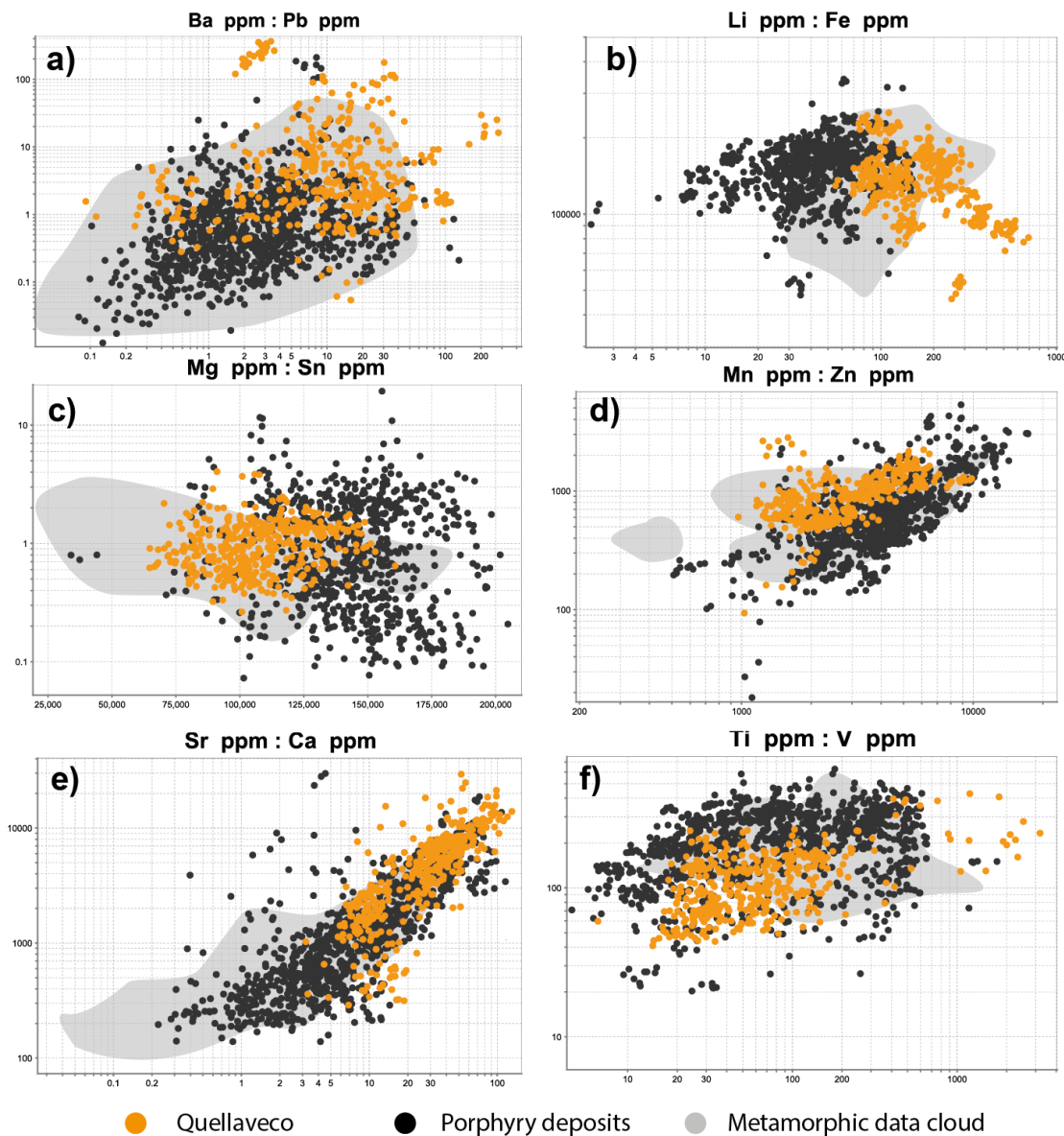


Figure 8.12. Bivariate plots of Ba vs Pb, Li vs Fe, Mg vs Sn, Mn vs Zn, Sr vs Ca and Ti vs V. Comparative data from porphyry deposits: Bambu, Batu Hijau, El Teniente and Sekongkang (Wilkinson et al., 2015; AMIRA P1153 database), with a reference metamorphic data cloud shown (from Figure 8.11).

There is a lot of overlap between QV and the other deposit data in terms of Ti (with the exception of the very high Ti population noted above) but the QV data tend to fall on the low side with respect to V. There is a noticeable overall elevation in the deposit V concentration with a much larger data range than Quellaveco (DP: range ~50-900 ppm; QV: range 50-200 ppm). The comparison with deposit data confirms the significance of the high-Ti cluster discussed (Figure 8.16b), as the data remain anomalously more elevated in chlorite Ti than the other datasets.

Two geochemically distinct clusters were identified as being of interest within the Sr vs Ca and Ti vs V bivariate plots (Figure 8.11). The Quellaveco samples are attributed based on sample in order to spatially locate the components of the two clusters (Figure 8.16).

8.4.4 Chlorite geochemical variation between alteration assemblages

The analysed chlorite can be classified texturally into five of the assemblages previously identified (Chapter 5). These are: A2 - actinolite propylitic; A3 - epidote-actinolite propylitic; A4 - epidote-chlorite-albite propylitic; A6 - chlorite-calcite propylitic; and V6 - quartz-albite-epidote.

Tukey plots are used to gain a comparative overview of the trace element concentrations in the different assemblages (Figure 8.13). This method highlights any preliminary similarities or disparities between the alteration types and possible variation within an assemblage.

In general, there is very little systematic variability between alteration assemblages, with more variability between samples, suggesting that spatial (or other sample-specific) controls are more important in controlling chlorite trace element chemistry than the alteration assemblage itself. This is consistent with previous observations in propylitic haloes where spatial (inter-sample) variability is large, even for samples containing the same alteration assemblage.

However, A2 shows the least in-assemblage variability. The three samples in the A2 assemblage are anomalously high in Ti (700-3000 ppm), an order of magnitude higher than the other samples (~20-100 ppm), and two orders

of magnitude higher than the one V6 sample (~10 ppm). This unambiguous elevation of Ti in the A2 actinolite assemblage provides potential constraints on the formation temperature for the chlorites (see 8.4.5). Spatial analysis of the A2 samples provides context for any potential heat source (see Figure 8.16). The minimal variability in the A2 assemblage could, in part, be because it is composed of three samples.

8.4.5 *Spatial variations in chlorite chemistry*

Variable concentration maps provide a spatial assessment of any major concentrations of trends in the chlorite trace chemistry (Figure 8.14 and Figure 8.15)

Titanium has one of the most clearly defined gradients, which is seen in the cluster of samples furthest south on Section 1. When the assemblages are combined the strong decrease with distance from the IFS is very apparent. This is particularly interesting because titanium is thought to act as a thermal indicator and has been interpreted to reflect crystallisation of high temperature chlorites in the most proximal position in porphyry systems (Wilkinson *et al.*, 2015; 2020). Here, the high temperature chlorites form close to the IFS. This thermal gradient is also reflected in the progression of assemblages, moving from A2 'actinolite' to A6 'chlorite-calcite' propylitic. Actinolite is itself also an indicator of relatively high temperatures of formation (e.g. Cooke *et al.*, 2014b). Both A2 and A3 include actinolite as part of the assemblage, but A3 also contains epidote which is thought to form below 400°C (Dilles, 2010). Consequently, it is suggested that the epidote-free A2 actinolite assemblage formed at temperatures exceeding 400°C. This is supporting evidence of a thermal gradient with distance from the IFS.

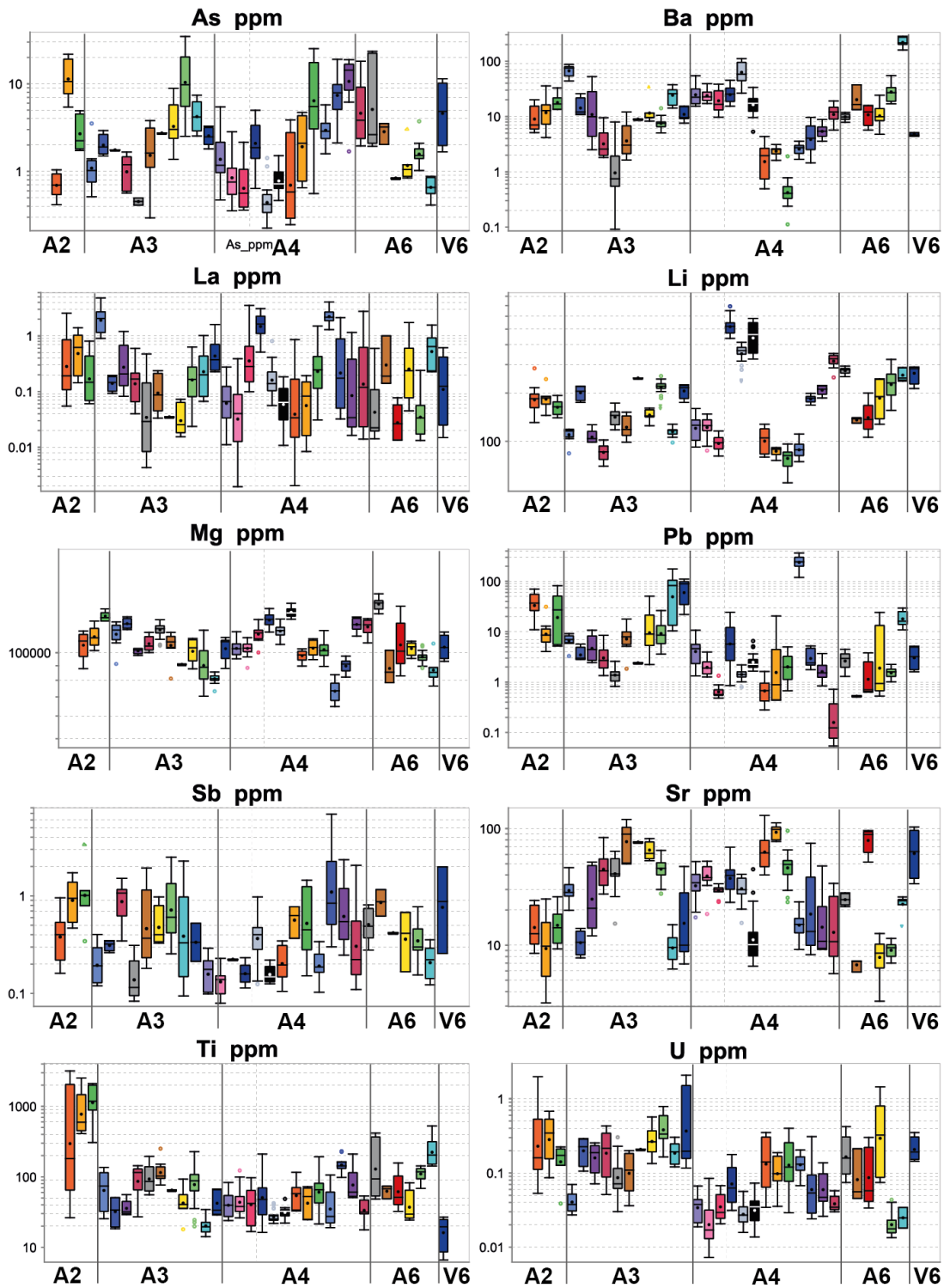


Figure 8.13. Tukey plots of each sample separated based on assemblage, and plotted against certain chlorite trace elements: As, Ba, La, Li, Mg, Pb, Sb, Sr, Ti and U.

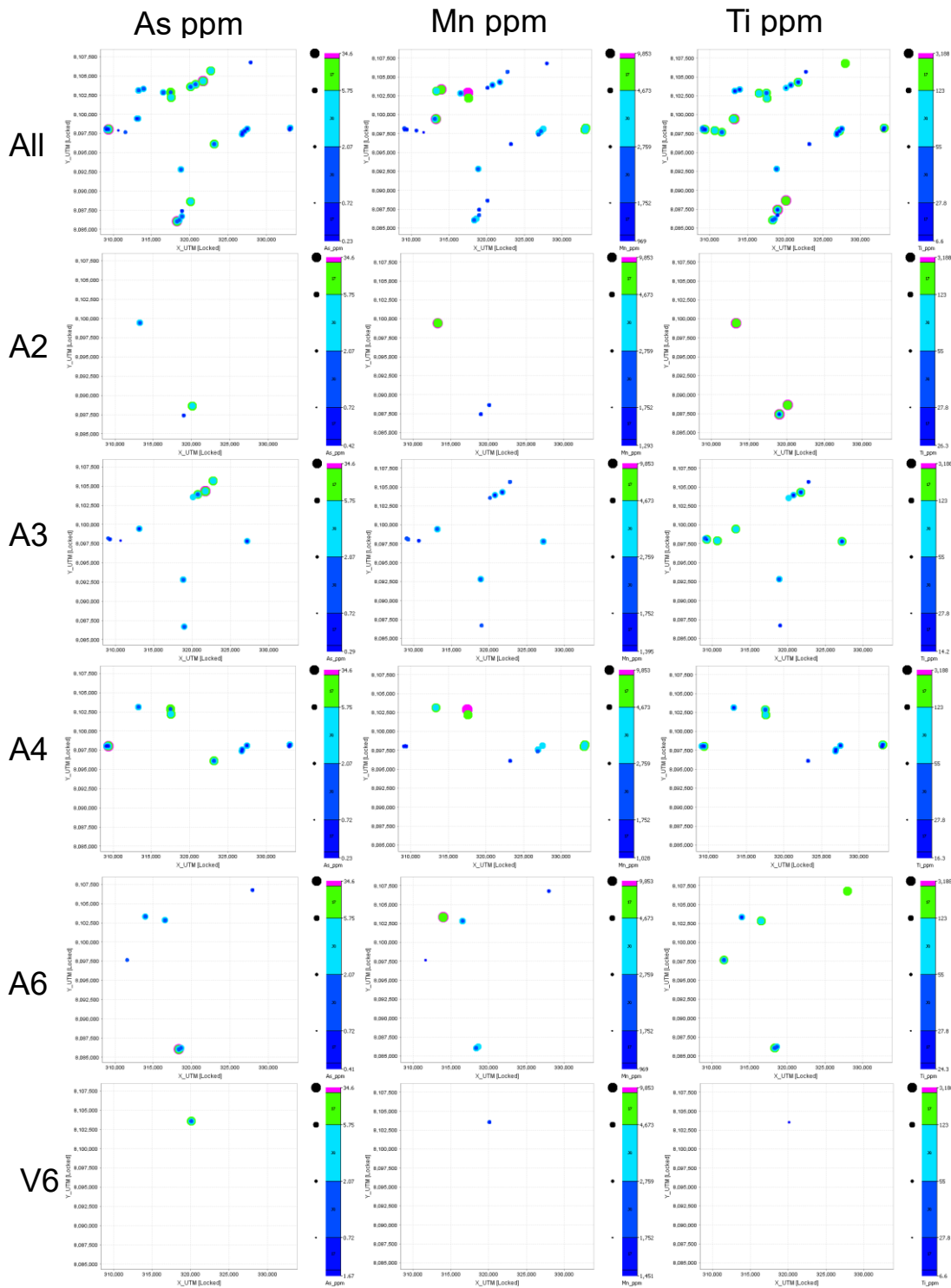


Figure 8.14. Variable maps of chlorite trace element chemistry with As ppm, Mn ppm and Ti ppm, values ranked based on groups of 6 equal tails. Maps are broken down into assemblage.

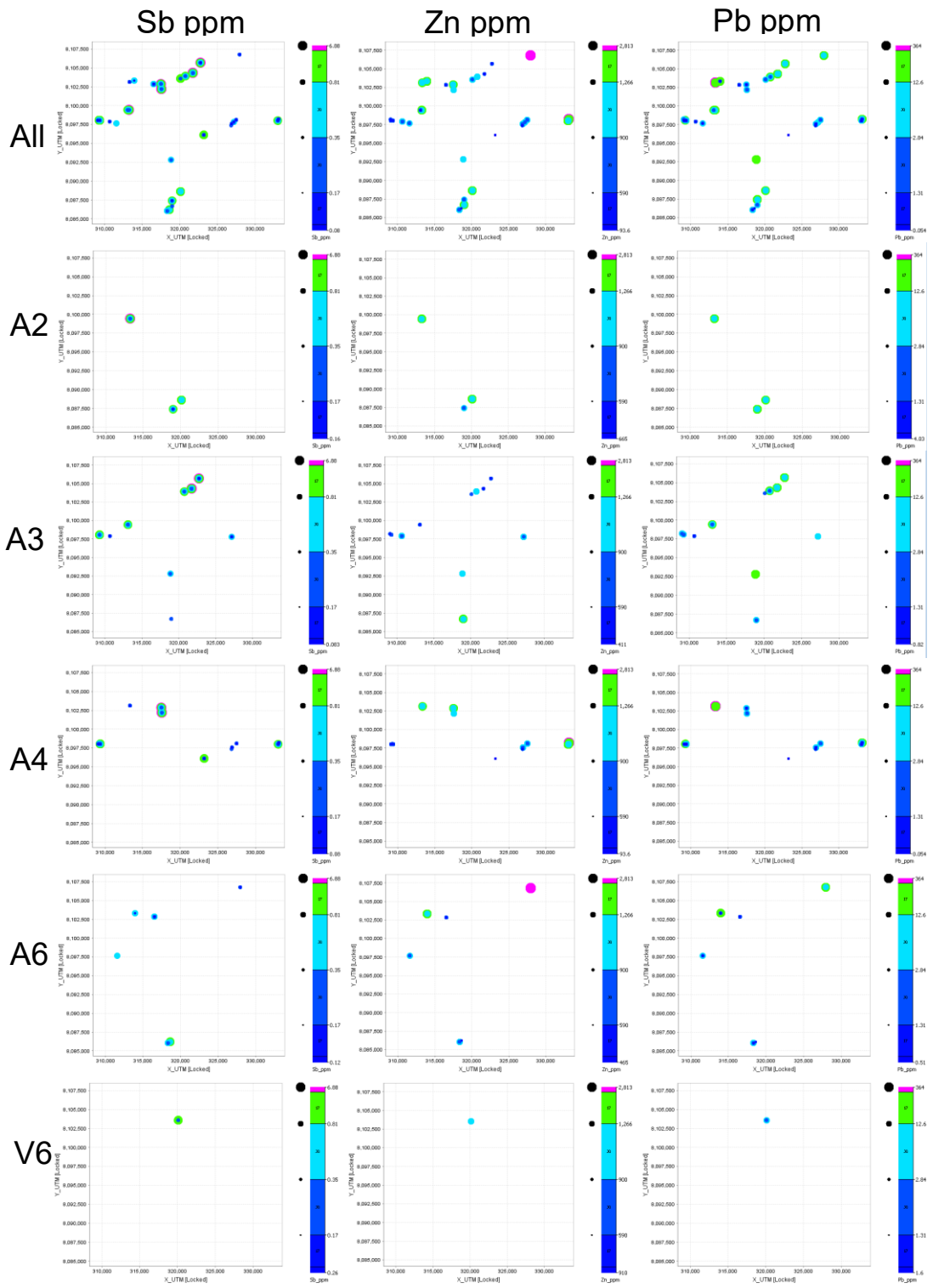


Figure 8.15. Variable maps of chlorite trace element chemistry with Sb ppm, Zn ppm and Pb ppm, values ranked based on groups of 6 equal tails. Maps are broken down into assemblage.

Mapping of the lower cluster of the Sr vs Ca sample highlights a spatial significance, with multiple samples grouping in specific areas (e.g RCS064, RCS065, RCS068 and RCS070). Clustering like this is less likely to indicate a metamorphic signal, as background metamorphism covers regional areas, rather than specific well- constrained areas. This cluster occurs along the Capulline Fault, proximal to its intersection with the Puca-Porquene and Micalaco Faults.

The importance of spatially attributing the anomalous Ti cluster (Figure 8.16b) is the strong geothermic implications that the affected chlorite formed in very high temperature conditions. Two of the three affected samples (RCS019 and RCS022) are adjacent, and are located on the southern part

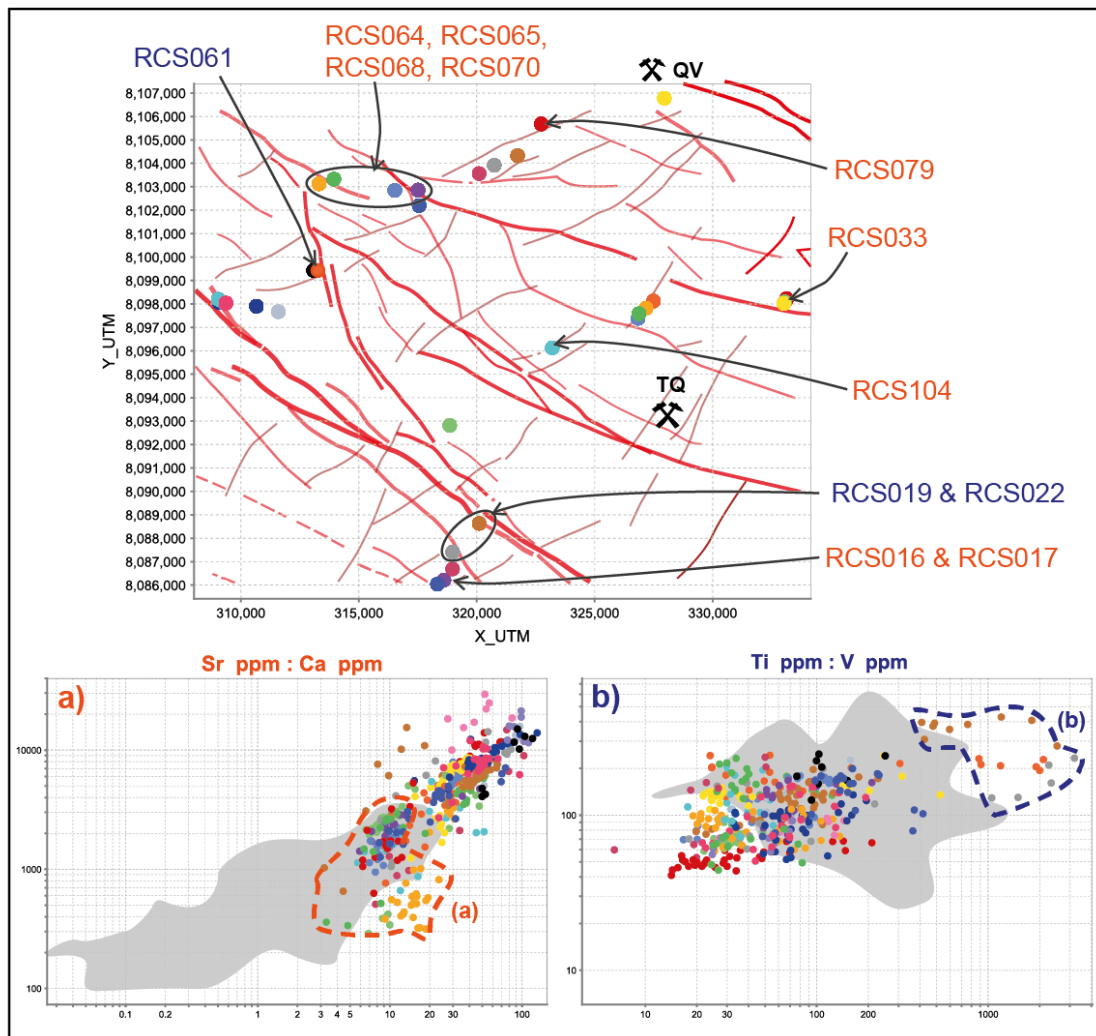


Figure 8.16. Bivariate plots **a)** Ti vs V and **b)** Sr vs Ca, from Figure 8.11 highlighting the location of samples within the clusters of interest.

of section 1 in the most proximal area to the Incapuquio Fault System (IFS) with distances of ~2 km and <500 m, respectively. It is noteworthy that the samples succeeding RCS022 and RCS019 in the lateral transect from the IFS, are highlighted (Figure 8.16a) as the relatively low Sr and Ca cluster of interest. The remaining sample (RCS061) is located within 500 m from the Puca-Porquene Fault (PPF), along section 2. The proximity of RCS061 is potentially very significant because, as discussed previously, the PPF appears to be a substantial splay from the major IFS. Such anomalously high chlorite Ti concentrations in these samples indicate the chlorite formed very close to a high temperature fluid source.

Chlorite compositional variations are assessed as a function of progressive distance from the Quellaveco Fault (Figure 8.17), divided into the sample traverses 1 and 2. The rationale for the choice of NE-SW sample traverses is to capture any gradients that could exist due to the lateral dispersion of fluids from the major NW-SE trending faults. The approximate trace of where the major faults cut each section are labelled for reference (Figure 8.17).

For section 1, there are a few clusters of samples of interest:

Samples RCS031-RCS033, located close to the Capulline Fault (CF), appear to be chemically related showing comparable trends in the trace elements. Relative to the other samples, this cluster contains elevated Ba, Ca, Li, Mn, Sr and Zn, with low values in As, Fe, and Ti.

On the south eastern side of the IFS, samples RCS022, RCS019, RCS017, RCS016 and RCS014 exhibit convincing gradients in several trace elements. For example, concentrations of Fe, Ti and V in the chlorites decrease with distance from the IFS. For V, the maximum concentration (900 ppm) is found in the most proximal sample (RCS022) and there is a progressive decrease of one order of magnitude over ~5 km to the furthest sample (RCS014, 90 ppm). Arsenic is particularly elevated (10-20 ppm) in RCS022, which dramatically decreases to RCS019 (0.5-0.9 ppm), located within ~1.5 km of the IFS. These observations support lateral dispersion of fluids from the IFS. As previously discussed (8.4.5), high Ti concentrations

are indicative of high temperature chlorites (Cooke *et al.*, 2015; Wilkinson *et al.*, 2015, 2020) and therefore the substantial decrease in Ti ppm by a magnitude of 1.5 (from Ti fault-proximal 1000-3000 ppm to 1.5 to 30-50 ppm) indicates very high temperature fluids along the IFS. It is noteworthy, however, that RCS098 (directly on the north east side of the IFS) does not present this unusually high Ti concentration, therefore this gradient does not appear to be reflected on the north-eastern throw of the IFS.

For section 2 there are several features of interest:

RCS087 is unique because of its proximity to the Quellaveco porphyry system. The elevations in trace elements for this samples have been recorded previously. Additionally, the sectional view highlights the geochemical independence of RCS087 with the following samples.

Between RCS087 and the Capulline Fault there is a group of four samples (RCS079, RCS076, RCS075, RCS074) which together define gradients in certain elements toward the Capulline Fault, such as: increasing in Ca (1000 ppm to >10,000 ppm fault-proximal), Li (100 ppm to 300 ppm), Sr (10 ppm to >100 ppm); and decreasing in Ba (40 ppm to 2 ppm fault-proximal). Vanadium also exhibits a decrease towards the Capulline fault, but only from RCS076 to RCS074 (150 ppm to 50 ppm), RCS079 has V values of <30 ppm. This suggests the increase in V away from the Capulline fault peaks at approximately 2.5 km, before dropping to the background levels.

The seven samples closest to the IFS (RCS52-RCS037) appear genetically related based on the similarity in all of the concentrations plotted, except arsenic. As with the Capulline Fault examples, the five most fault proximal samples (RCS037-RCS42) exhibit a less convincing decrease in vanadium with distance from the IFS.

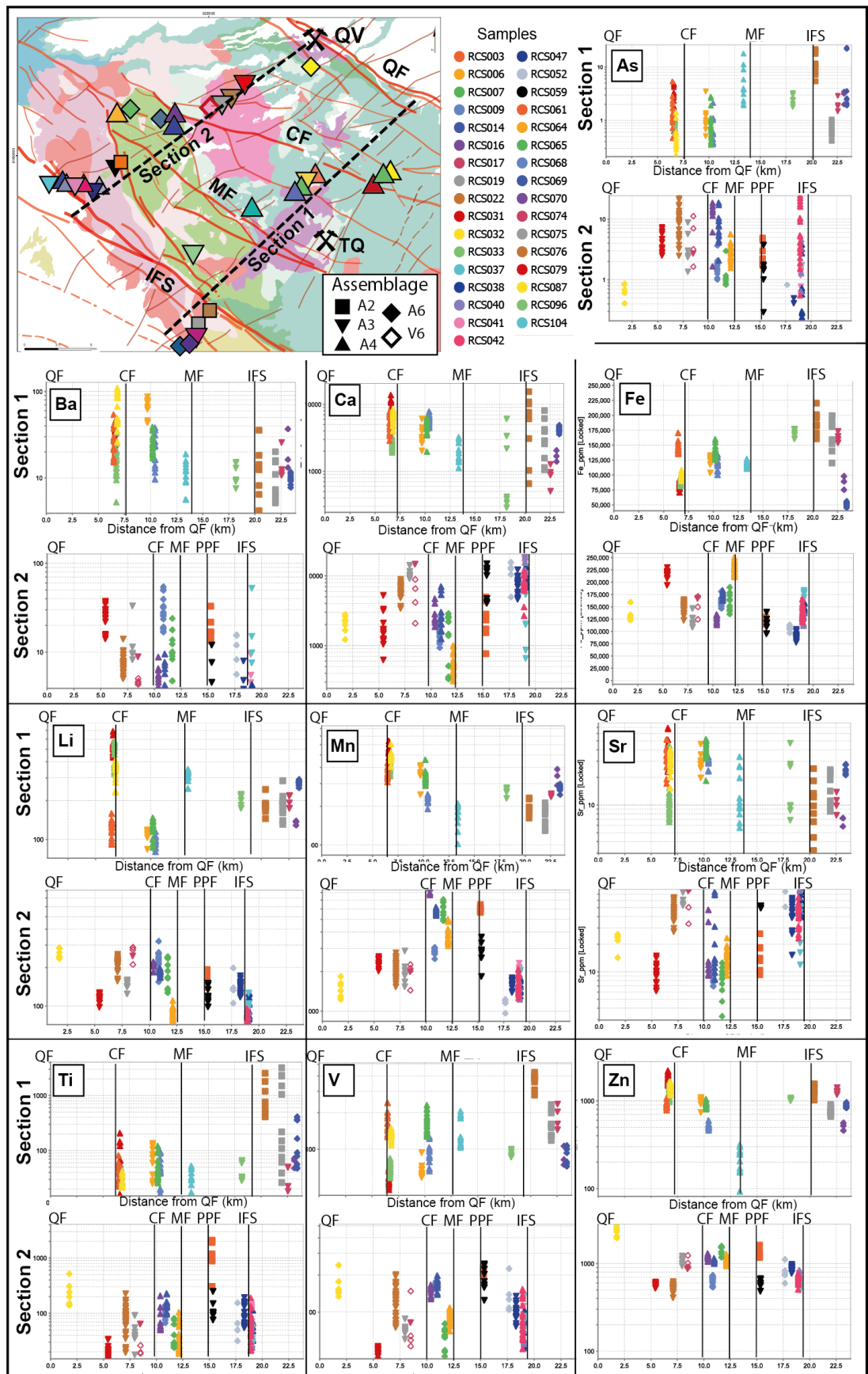


Figure 8.17. Chlorite trace element variations with distance from the Quellaveco Fault. Sample sections 1 and 2 are separated, and locations of the major transverse faults are noted on the sections (QF: Quellaveco Fault; CF: Capulline Fault; MF: Micalaco Fault; PPF: Puca-Porquene Fault; and IFS: Incapuquio Fault System).

8.4.6 Temporal constraints on chlorite-bearing assemblages and geochemistry

Of the 87 precise dates acquired from the geochronology workflow in Chapter 7, only seven are associated with chlorite-bearing assemblages. The seven dates originate from: RCS104 44.9 ± 3.5 Ma (apatite); RCS003 57.4 ± 2.9 Ma (zircon); RCS033 64.2 ± 6.5 Ma (apatite); RCS074 68.1 ± 2.8 Ma (zircon); RCS075 68.3 ± 7.2 (apatite); RCS061 70.3 ± 5.2 Ma (titanite) and RCS047 72 ± 6.2 Ma (titanite). These dated samples are analysed for potential similarities and discrepancies in trace element content of different ages (Figure 8.18).

One clear observation is that the youngest three dates all represent A4 assemblages, and the older samples comprise A2, A3 and V6 assemblages. The sample geochemistry can be viewed by these two clusters: the oldest cluster of dates (~ 68 -72 Ma) originate from the N/NW part of the region along transect two, and the younger dates (~ 45 -64 Ma) are located to the east, from transect 1.

Two samples (RCS074, V6 and RCS075, A3) from the older cluster are particularly interesting when compared because of: their similar dates (RCS074 68.1 Ma and RCS075 68.3 Ma); the proximity between the two samples (<500 m); and the comparable chlorite chemistry (e.g. As, Co, Fe, Mn and Ti, see Figure 8.15). The two samples show corresponding elevations in As, Ca, Fe, Sb, Sr and Zn with lower Ti. The combination of these factors suggests that V6 and A3 in that area are coeval and genetically related, implying that V6 vein forming fluids are responsible for the pervasive A3 alteration assemblage.

The youngest dated chlorite-bearing assemblage is A4 alteration in RCS104 at 44.9 ± 3.5 Ma. Geochemically, chlorite in this sample is distinct, with particular lows in Co, Fe, Mn, Pb and Ti. As it is known that porphyry emplacement at Toquepala and Quellaveco occurred between 58-54 Ma with the cessation of hydrothermal activity at approximately 52 Ma (Clark *et al.*, 1990; Simmons *et al.*, 2013), it is very unlikely that the strong propylitic alteration in RCS104 is porphyry related. Given the age, the A4 alteration in

this sample is likely to represent late stage fluid flow in the area and possibly as a result of late stage reactivation.

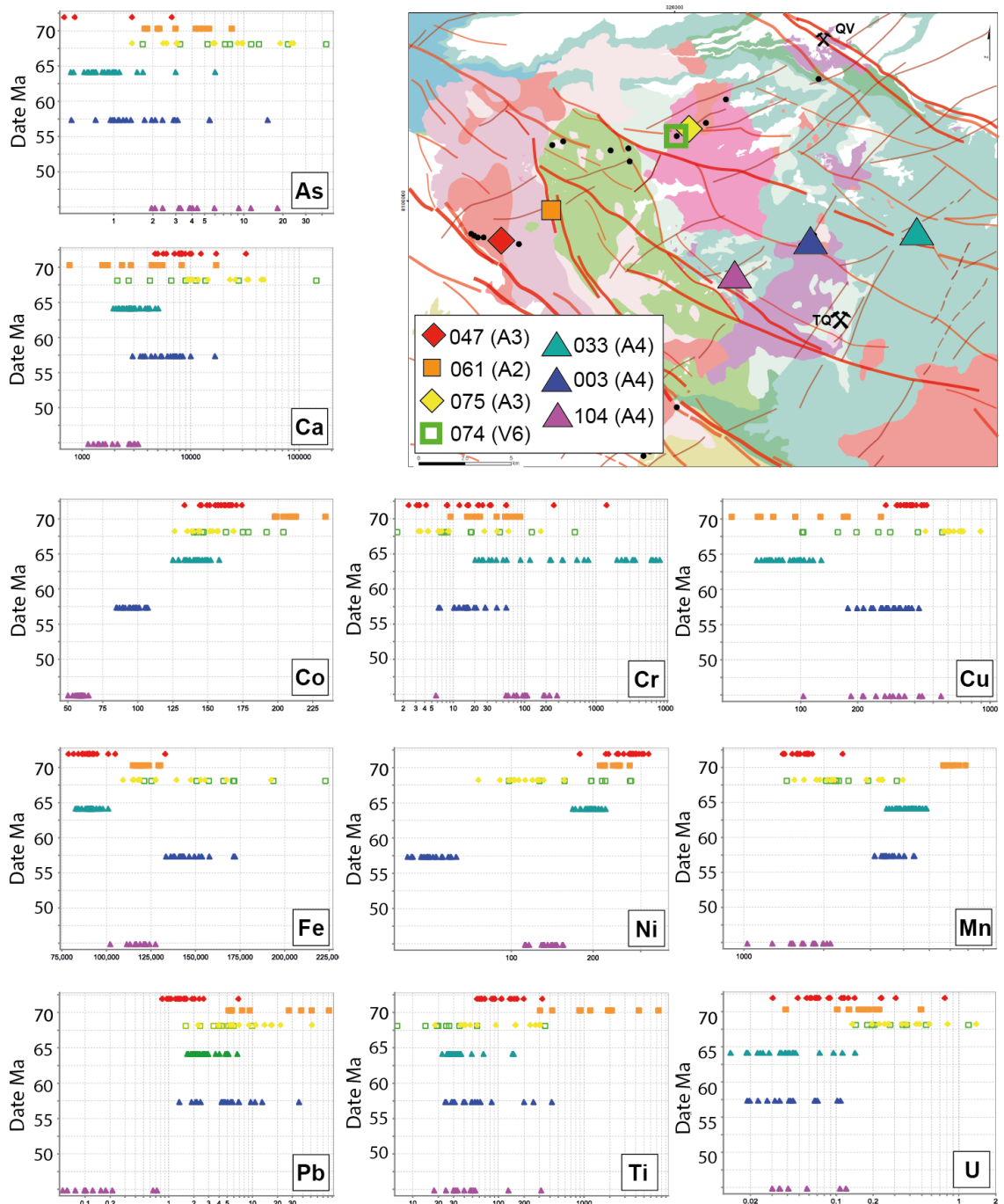


Figure 8.18. Trace element chemistry specifically for temporally constrained chlorite samples (RCS003, RCS033, RCS047, RCS061, RCS074, RCS075 and RCS104). Samples are attributed based on chlorite assemblage.

8.4.7 *Identification of potential propylitic chlorite formation environments using linear discriminant projection analysis*

Geochemical discriminant diagrams are used for varied geological classification problems, e.g. tectonic and geodynamic settings, and mineral deposits (e.g. (Dupuis & Beaudoin, 2011; Condie, 2015; Grebennikov & Khanchuk, 2021)).

Discriminant projection analysis is a form of supervised learning, which shares commonalities with principal component analysis (discussed in Figure 8.8). Like with PCA, discriminant analysis aims to reduce the dimensionality of a dataset. However, where PCA displays the variability of the dataset, discriminant analysis highlights pre-defined clusters within a dataset (Vermeesch, 2017). There are two types of discriminant analysis: quadratic discriminant analysis (QDA) and linear discriminant analysis (LDA). LDA is similar to QDA but without the assumption that the variables share the same covariance matrix. Therefore, QDA is preferentially used for large datasets where the k classes are unlikely to share the same covariance matrix, thereby reducing potential additional bias that can occur with LDA.

Discriminant analyses are an extremely powerful tool which use compositional differences in the mineral chemistry to separate and categorise the data into deposit types. The parameters and fields for the discriminant plot used in this study (Figure 8.20) were generated by J.J. Wilkinson (Pers.Comm. 2021) using the data acquired from numerous porphyry systems and several metamorphic terranes worldwide as part of a series of AMIRA projects, combined with supplementary in-house data from additional metamorphic and epithermal ore systems. The calculation of the axes ($x = DP1$, $y = DP2$) is the linear sum of log concentrations of 11 discriminant trace elements: Cr, Cu, Li, Mn, Ni, Sr, Ti, Zn, Mg, Fe and As. The fields defined by the discriminant plot are: high sulphidation (HS) epithermal, low sulphidation & intermediate sulphidation (LS & IS) epithermal, porphyry Au-Cu,

porphyry Cu-Mo, porphyry Cu-Mo/HS Cu-Mg hybrid and metamorphic.

The discriminant diagram provides a possible classification of unknown samples and it must be borne in mind that analyses concentrating within a certain field (e.g. LS and IS epithermal), are indicative of those conditions, not a definitive classification of those samples in that environment.

A discussion of the discriminant plots are broken down into the areas highlighted in the plot (Figure 8.20a-k):

- a)** A summary discriminant plot combining all the Quellaveco samples with the calculated fields labelled. With the exception of a few analyses, all the data fall within the LS and IS epithermal, porphyry Au- Cu and porphyry Cu-Mo fields. The absence of any data within the metamorphic field is noteworthy, as it reiterates findings from the metamorphic comparison (8.4.2) that the signal displayed by the chlorites in the Quellaveco samples are not those of typical background metamorphism.
- b)** Four samples (RCS003, RCS006, RCS007 and RCS009) showing two alteration assemblages (A3 and A4). On the discriminant plot, the samples form a constrained cluster which straddles the boundary between LS and IS epithermal and porphyry Cu-Mo. This suggests that, despite the difference in alteration assemblage, the geochemical homogeneity of the chlorites in area (b) are the result of conditions similar to a porphyry and LS & IS sulphidation. Spatially, this group of samples are the closest to Toquepala (approx. 4 – 5 km), and therefore within potential range of its associated distal propylitic halo. From the geochronology in this study, the chlorite-bearing assemblage (A4) within RCS003 is thought to have an age of 57.4 Ma. Dating of the Cu-Mo hosting porphyry intrusions at the Toquepala deposit yielded an age span of 54.3 – 58.4 Ma (Simmons *et al.*, 2013; Simmons, 2014). Thus, it is concluded that assemblage A4 in these samples represents the distal propylitic halo of

Toquepala. The A3 assemblage is unlikely to do so because it contains actinolite, which is an inner propylitic indicator that is unlikely to be developed at such a distance from a porphyry centre. One possibility is that there is an underlying intrusive ridge linked to the Toquepala centre, as has been defined in the Batu Hijau district, which allowed for the development of actinolite at greater distances.

- c)** The five samples are widely distributed with: three samples (RCS014, RCS016 and RCS019) located in the LS and IS sulphidation field; one sample (RCS017) in the porphyry Cu-Mo field; and one sample (RCS022) in the porphyry Au-Cu field. These samples are interesting for several reasons: they are structurally significant because of the proximity to the Incapuquio Fault System (IFS), and the systematic transverse collection of the samples from 0-5 km distance; and the spatial plots previously discussed (Figure 8.17) show this cluster of samples to have gradients of trace elements, such as decreasing Ti, V, Zn and Fe with increased distance from the IFS.
- d)** The three samples (RCS031, RCS032 and RCS033) exhibit chlorites from the same A4 assemblage and tightly cluster between the LS and IS epithermal, porphyry Cu-Mo fields and on the boundary of the HS epithermal (Figure 8.20). The concentration of the cluster emphasises the geochemical similarity of the chlorites in the samples. Only RCS032 was noted for being relatively low in Ca and Sr (the lower cluster discussed in Figure 8.16) which can be indicative of proximal propylitic alteration. However, the high Mn and Zn content (Figure 8.19) is characteristic of a propylitic enrichment halo at a distance of approximately 1.5 km (Wilkinson *et al.*, 2017, 2020). Dating of apatite within the A4 assemblage of sample RCS033 (Chapter 7) yielded an age of 64.2 Ma. As the three samples appear genetically and spatially coincident, the assumption is made that the propylitic A4 chlorites are coeval. The combination of all these findings suggests that area (d) may represent a propylitic halo of a

potentially fertile porphyry that is older than any of the known economic porphyry centres in the district.

- e) This area contains seven samples and two alteration assemblages: A3 (RCS037, RCS042 and RCS047); and A4 (RCS038, RCS040, RCS042 and RCS052). The data cluster spans the boundary triple junction between LS and IS epithermal, porphyry Au-Cu, and porphyry Cu-Mo fields. The samples are located approximately 6 km NE of the IFS.

- f) Two samples (RCS059 and RCS061) form a tight cluster within the LS and IS epithermal field on the discriminant plot. This suggests the chlorite in these samples formed under conditions typical of an LS & IS epithermal environment or within the more distal part of a porphyry propylitic halo. Both samples contain chlorites from different assemblages (A2 and A3), which, given the samples' geographical proximity to one another, and the geochemical similarity, would suggest these formed at the same time. RCS061 is part of the anomalously high Ti and V group of A2 samples (discussed in Figure 8.16), which is indicative of very high formation temperatures for the chlorite (Wilkinson *et al.*, 2017). Temperatures above ~400°C contradict an LS or IS origin and are high for a distal propylitic setting, so the exact nature of the event, dated 70.3 ± 5.2 Ma in RCS061, is uncertain, but perhaps could represent contact metamorphism related to the emplacement of the monzodiorite.

- g) From all of the areas highlighted (Figure 8.20), the two samples (RCS064 and RCS065) in area (g) have the strongest porphyry Cu-Mo signature. The chlorites occur within A4 and A6 assemblages. This area has been discussed previously because of its anomalously high Mn and low Ti, and Ca values. The interest in this area is heightened by the geochemical gradation seen in areas (h) and (i) with respect to this area (g). The low Ti content may be slightly unexpected with what would be anticipated of an area with similar signals, however, a low thermal indicator may suggest a deeper target.

- h)** Three samples (RCS068, RCS069 and RCS070) display a porphyry-like signal but spreading into Au-Cu field which could reflect a shallower paleo-level. This is interesting because, as discussed, area (h) appears to show gradation from area (g). If area (g) is formed at depth, but area (h) is indicative of a higher crustal level, then possibly there has been exhumation of area (h).
- i)** Composed of five samples (RCS074, RCS075, RCS076, RCS079 and RCS087) that spread for ~9 km along a series of ENE-trending structures towards QV. One sample, RCS087, geographically and geochemically differs, with the chlorites part of an A6 assemblage. RCS087 is the most proximal chlorite-bearing sample to Quellaveco, and within area (i). The remaining samples contain A3 and V6 (RCS074) assemblages. RCS074, RCS075 and RCS079 form a particularly concentrated group bordering porphyry Au-Cu and porphyry Cu-Mo discriminant fields. The two samples were identified as being temporally similar and displaying similar geochemical signals (such as high As, Cu, Ca, U and low Ti concentrations). Therefore, it is concluded that the samples, possibly including RCS076 but excluding RCS087, are geochemically and spatially related and may all form part of an alteration event at ~68 Ma (see Figure 8.18).
- j)** Only one sample (RCS096) is shown for area (j) because there are no other samples with analysed chlorite nearby. Only a few analyses were acquired for this sample which cluster on the lower boundary of the porphyry Cu-Mo field. Without additional samples and data from this area it is difficult to interpret properly but the signal is permissive of a porphyry system in the general area, but not very proximal to the sample collected.
- k)** Only one sample (RCS104) is in group (k) because it is an isolated, A4-bearing sample to the WNW of Toquepala. In the discriminant diagram, the dispersed data plots predominantly in the lower section of the LS-IS field. This is not suggestive of any porphyry influence in this area. The chlorite trace element data for RCS104 has been

consistently identified for anomalous levels of certain trace elements relative to the other Quellaveco samples, such as: low Zn (80-300 ppm), Mn, Pb, Co and Ca (e.g. Fig. 1.22). Area (k) is also located along the Micalaco Fault-strike from Toquepala. This is worth noting, as one of the major faults in the region, the Micalaco Fault is considered a potential source of fluids for the Toquepala deposit. The longevity of this fault is likely to postdate the Toquepala porphyry; indicating continued activity of the IFS and connected faults (Jacay *et al.*, 2002).

Mn/Zn fertility analysis

The relationship between elevated manganese and zinc in chlorite with increasing proximity to porphyry centres can be further extrapolated to provide a guide on the type of system and the potential fertility. Studies by Wilkinson *et al.* (2015, 2017, 2020) contrasted multiple data from several metamorphic terranes and proximal, distal and background porphyry regions, which highlighted distinct groups of data on the Mn/Zn bivariate plot. When these potential regions are displayed alongside the Mn/Zn chlorite data for the Quellaveco samples (Figure 8.19), there is an

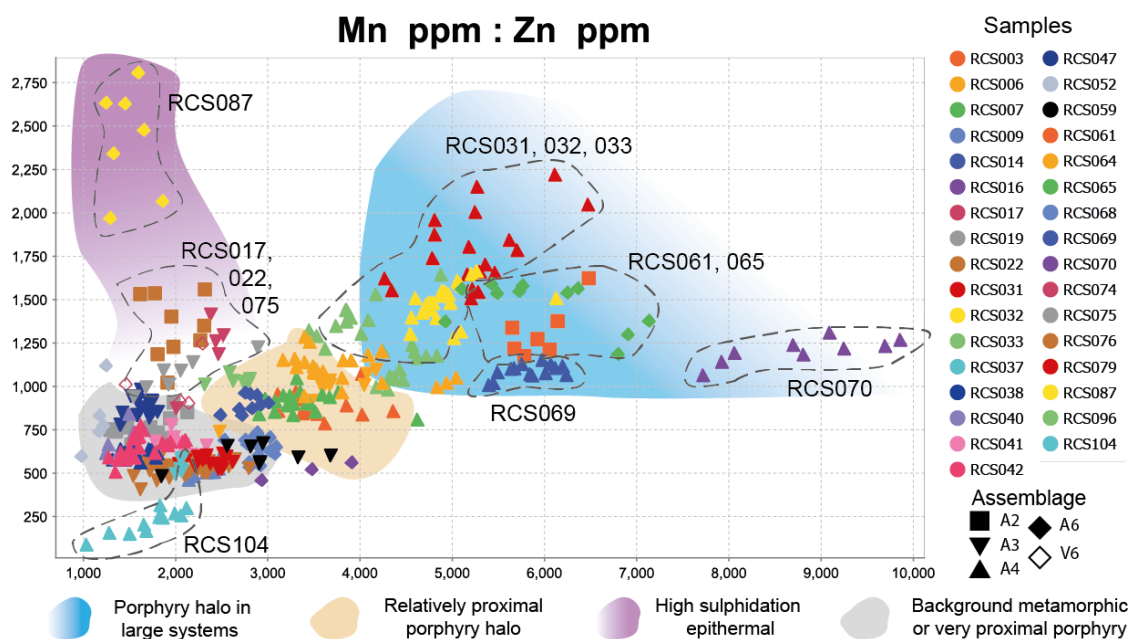


Figure 8.19. Mn vs Zn bivariate plot for chlorites at Quellaveco. Specific clusters of samples are labelled. Hypothetical regions devised from constraints discussed in Wilkinson *et al.* (2017) and Wilkinson *et al.* (2020).

interesting segregation of the samples, seemingly consistent with the discriminant analysis.

8.5 Discussion of epidote chemistry

8.5.1 Potential protolith control

A similar procedure was adopted for the epidote data as was used in the chlorite analysis to assess for potential primary protolith or metasomatic controls on epidote chemistry. However, the lack of any correlation between whole rock composition or differentiation proxy with epidote composition for any samples, suggests that any such effects are minor, so are not considered further here.

8.5.2 Comparison with epidote from metamorphic terranes

The epidote trace element geochemistry from this study is compared with data acquired from reference material from known metamorphic terranes to determine whether district-scale propylitic alteration in an area of economic porphyry systems can be distinguished from regional metamorphic epidote-bearing assemblages. The metamorphic epidote data are derived from studies carried out in several areas: Chalkidiki Peninsula, El Volcan Valley, Georgetown Inlier, Harts Range, Portillo, Rio Blanco, West Scotland, Yeso Valley (Baker et al., 2017; AMIRA P1153)

Potentially diagnostic trace elements for distinguishing between distal porphyry propylitic regions and background metamorphism have been considered by several authors (e.g. (Baker *et al.*, 2017, 2020; Cooke *et al.*, 2020; Pacey *et al.*, 2020; Wilkinson *et al.*, 2020). Distal propylitic alteration from these studies generally yielded elevated As, Sb, Ti, Pb, Zn and Mn relative to metamorphic background.

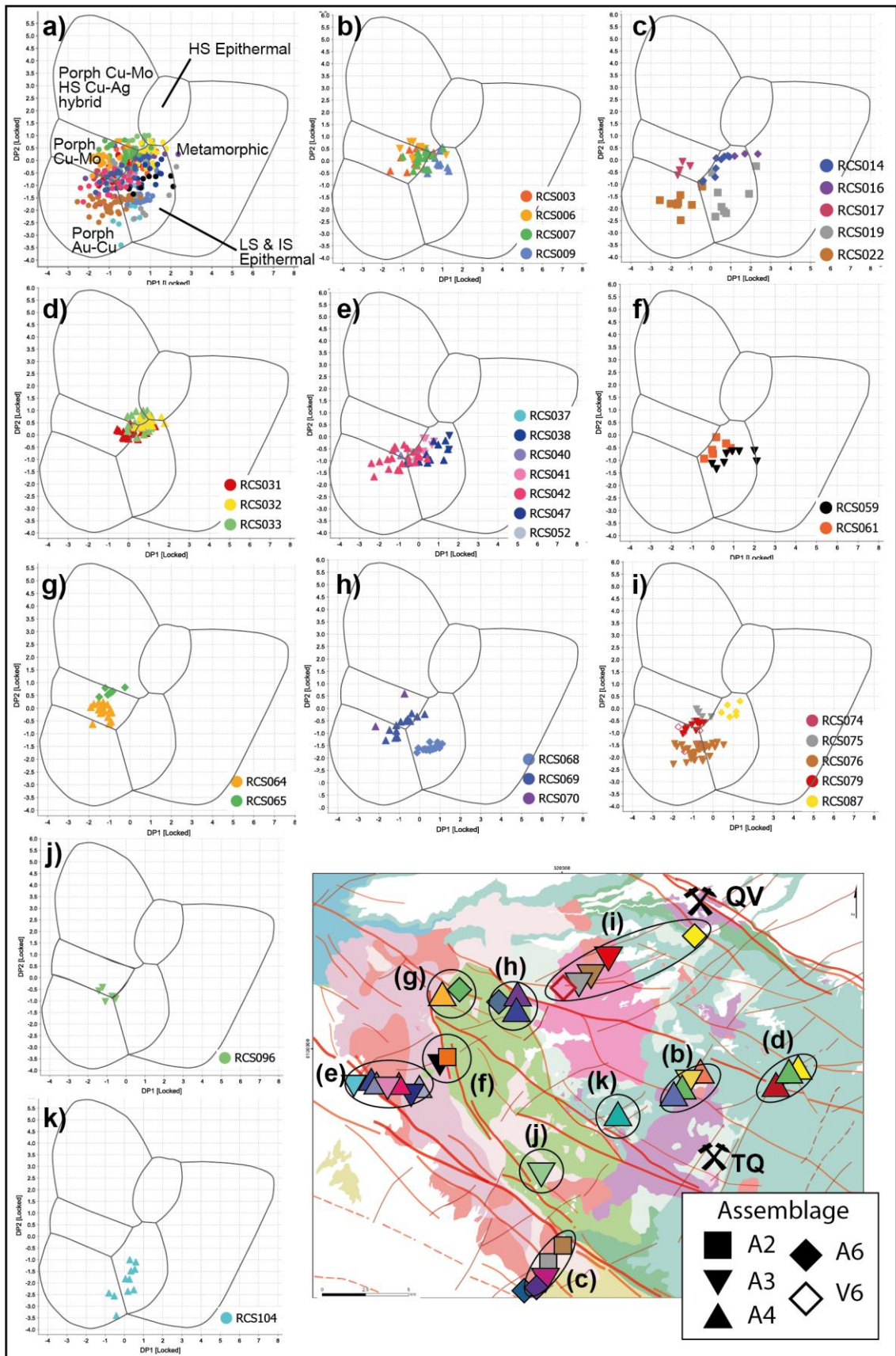


Figure 8.20. Discriminant plots for chlorite trace element data: **a)** all data plotted with geochemical fields highlighted; **b-k)** geographically grouped samples, the alteration assemblage is attributed by shape. Discriminant plot parameters formulated by J.J Wilkinson (PersComm, 2021).

The As vs Sb bivariate plot is particularly useful for discriminating metamorphic epidote data because of the reported consistency of elevated As and Sb in porphyry regions (e.g. Baker *et al.*, 2017;2020; Cooke *et al.*, 2020; Wilkinson *et al.*, 2020). Although there is overlap, the Quellaveco dataset displays a bias towards elevated As and Sb (As: 2 to >1000 ppm, Sb: 0.3 to 800 ppm) compared with the metamorphic dataset (As: 0.2 to 150 ppm, Sb: LOD to 20 ppm). Typically, very high concentrations of these elements, as noted in the upper part of the Quellaveco distribution, are only observed in the more distal parts of porphyry-propylitic haloes (e.g. Cooke *et al.*, 2020) so that samples with As >100 ppm and Sb >10 ppm) are highlighted for further examination in section 8.5.5

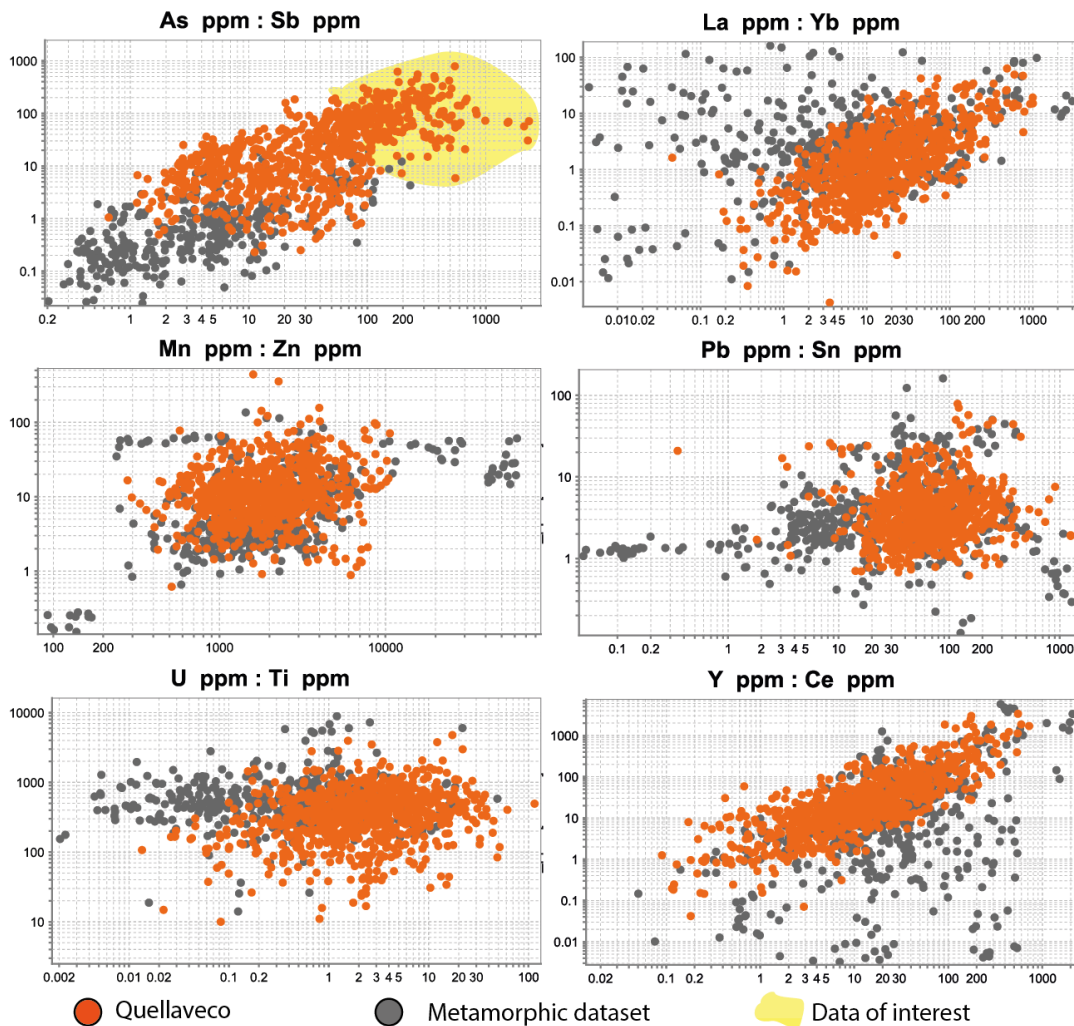


Figure 8.21. Trace element chemistry bivariate plots of As vs Sb, La vs Yb, Mn vs Zn, Pb vs Sn, U vs Ti, Y and Ce. Comparative, metamorphic data from Baker *et al.* (2017); AMIRA P1153. An area of interest is highlighted in yellow which will be spatially analysed in Section 8.5.5.

In the bivariate comparisons between the Quellaveco (QV) and metamorphic (MT) data for the remaining trace elements (Figure 8.21), Quellaveco tends to show higher concentration ranges in U (QV: 0.1 – 60, MT: 0.05 – 20 ppm), and Pb (QV: 10 – 1000 ppm, MT). Other trace elements display limited systematic differences in concentration between the two datasets.

8.5.3 Comparison with epidote from porphyry systems

A comparison was made between the Quellaveco district epidote data and results from the Batu Hijau (AMIRA P1153 database) and El Teniente porphyry deposits (Wilkinson et al., 2020), plus the porphyry prospect of Sekongkang in the Batu Hijau district.

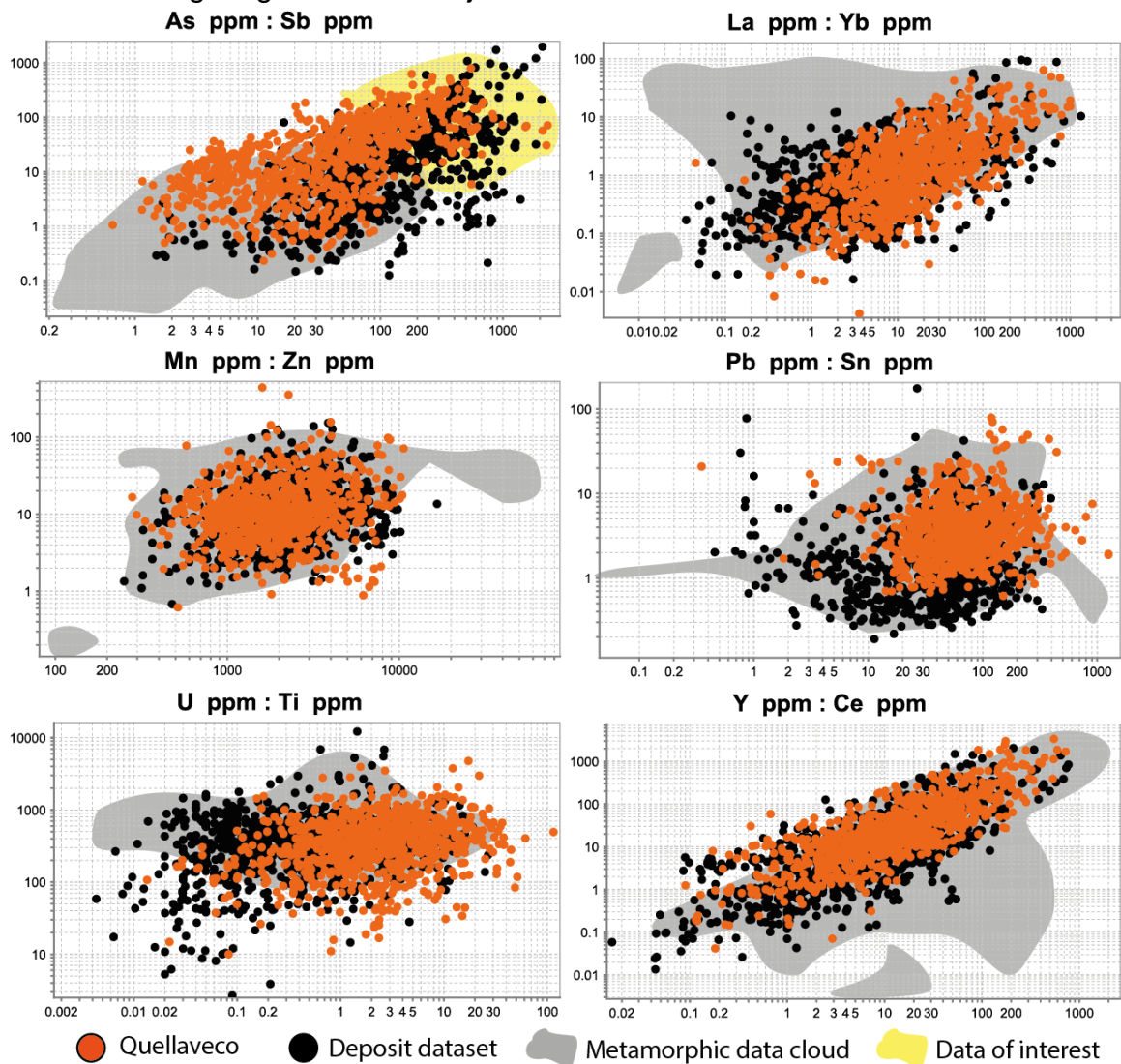


Figure 8.22. Bivariate plots of As vs Sb, La vs Yb, Mn vs Zn, Pb vs Sn, U vs Ti, Y and Ce. Comparative data from porphyry deposits: Batu Hijau and El Teniente (Wilkinson et al., 2015), with a reference metamorphic data cloud shown.

As previously discussed, As and Sb in epidote can also be useful porphyry fertility discriminators (e.g. Baker et al., 2017; 2020; Cooke et al., 2020; Wilkinson et al., 2020). Comparing these data between the Quellaveco district and the other deposits shows significant overlap, with a slight bias in the former data towards higher Sb.

Both datasets demonstrate extensive overlap in terms of Mn, Zn, Y and Ce concentrations, with the Quellaveco data showing slight bias towards higher concentrations of Sn and U.

In both of the comparison deposit studies, sampling extended up to ~6 km from the porphyry centres, focused mainly within the deposit-related propylitic haloes. Therefore, the likeness in the epidote trace elements between Quellaveco and the other deposits suggests that propylitic alteration at Quellaveco bears more resemblance to the propylitic alteration of a porphyry system than to background regional metamorphism.

8.5.4 Comparison of the chemistry of the different epidote-bearing assemblages

The epidote analysed occurs in four replacement-type assemblages: A3 'epidote-actinolite', A4 'epidote-chlorite-albite', A5 'epidote-titanite', A6 'chlorite-calcite'; and five vein-type assemblages: V2 'epidote-actinolite', V3 'epidote-quartz', V6 'quartz-albite-epidote', V7 'calcite-epidote-chlorite', and BX 'breccia'.

Tukey plots are used for a preliminary overview of the disparities within and between the assemblage types in epidote trace element concentrations (Figure 8.23). Initial observations reveal a high level of variation in the data from within individual assemblages, which is in accord with the chlorite data (see 8.4.4). This suggests that the sample-to-sample spatial and temporal controls on epidote chemistry are likely to be more significant than the particular assemblage within which the epidote occurs

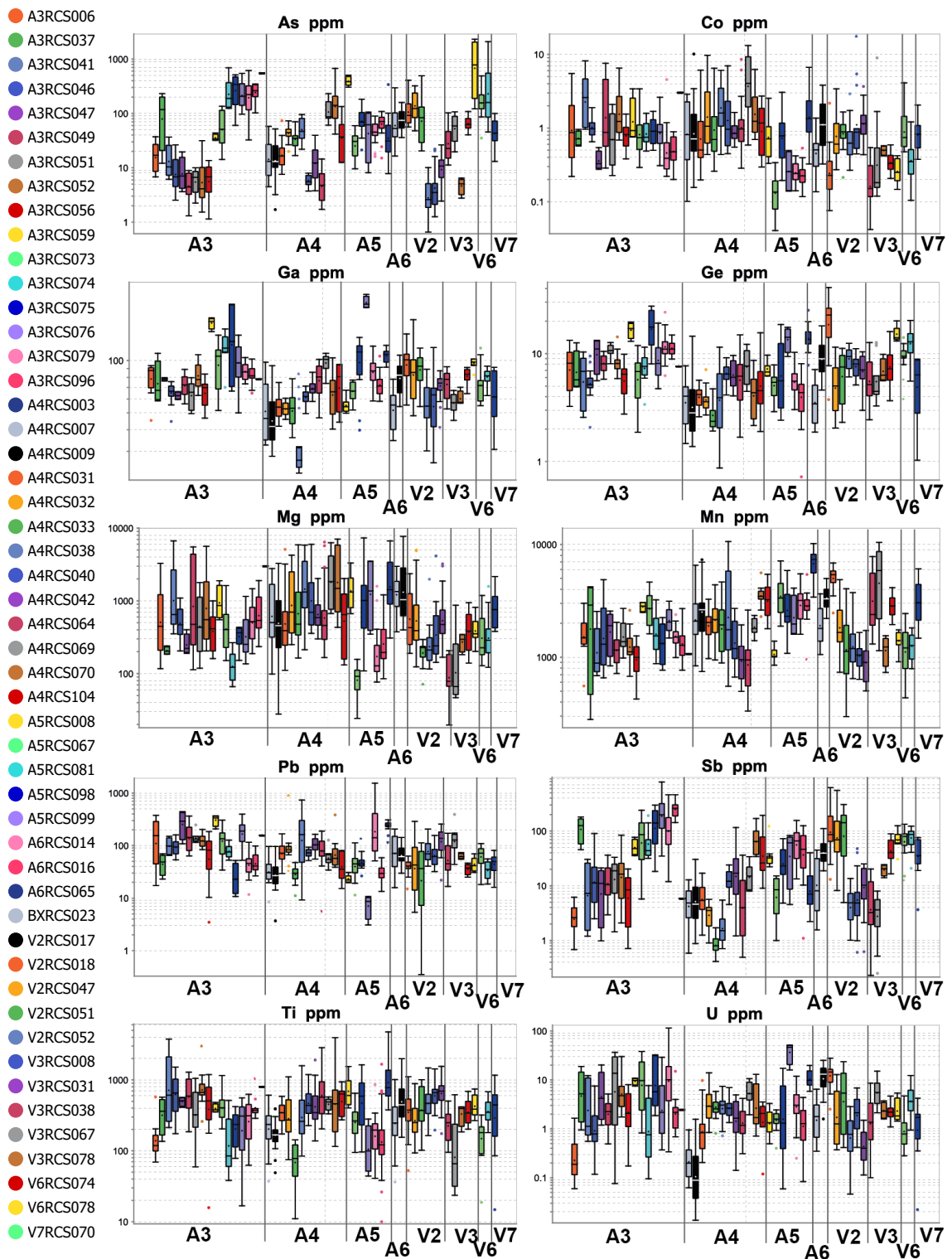


Figure 8.23. Tukey plots of epidote concentration data for As, Co, Ga, Ge, Mg, Mn, Pb, Sb, Ti and U in individual samples, separated based on assemblage.

However, the Tukey plots suggest a link between a vein and replacement type, A3 and V2. Both assemblages appear to have bimodal populations in Sb ppm and As ppm. Arsenic and Sb often show a correlation because of

their simultaneous substitution into the crystal lattice. These distinct populations within A3 and V2 indicate genetic compatibility between the assemblage textures.

8.5.5 Spatial variations in epidote chemistry

Anomalous As-Sb samples.

From the metamorphic dataset comparison (see Figure 8.19), the data with highest As and Sb (>100 ppm) were isolated, and are now presented with spatial context (Figure 8.24). As discussed, this cluster is interesting because of the suggestion that high As and Sr recordings such as these are indicative of distal propylitic of a moderate to large porphyry system (Cooke *et al.*, 2020; Wilkinson *et al.*, 2020).

On the map view (Figure 8.24), samples containing data within the high As – Sb cluster are specifically located: in particular, a long chain on Section 2 between RCS064 to RCS079. The other data

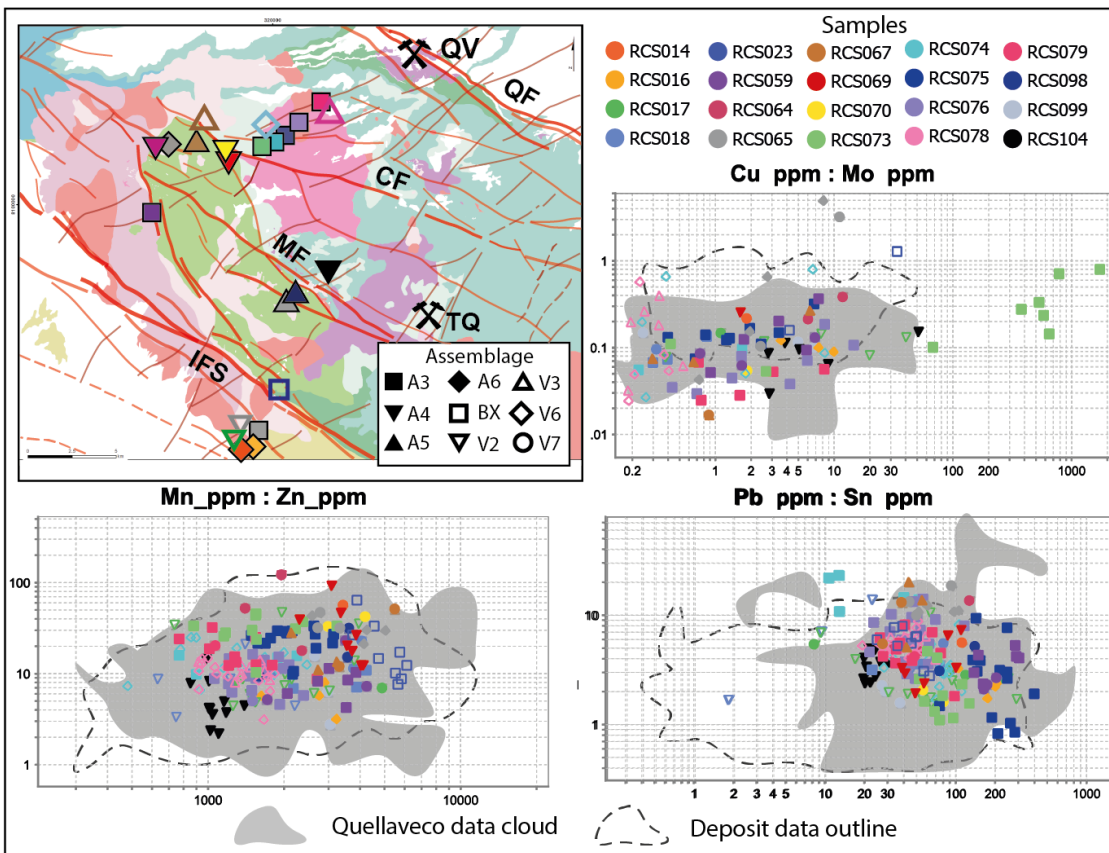


Figure 8.24. The spatial location of the high As and Sb (>100 ppm) area previously isolated (Figure 8.22) is shown. Compositions of the data of certain elements (Cu, Mo, Mn, Zn, Pb and Sn ppm) are contrasted with the deposit dataset and remaining Quellaveco data.

from the cluster are located in samples RCS098, RCS099 and RCS104, which are situated proximally to the Micalaco fault; and in a cluster southeast of the IFS samples RCS023-RCS014. The data size contained within the high As – Sb cluster diminishes from NE to SW (from RCS023 to RCS014), so with distance from the IFS from 11-18, down to 1 data in RCS014. This suggests a gradational decrease of the amount of propylitic epidotes with high As and Sb per sample, with increased distance from the IFS.

Another spatial analysis of the As and Sb data focused purely on the bimodal A3 assemblage identified (Figure 8.23). When isolated and spatially located (Figure 8.25) the elevated samples are

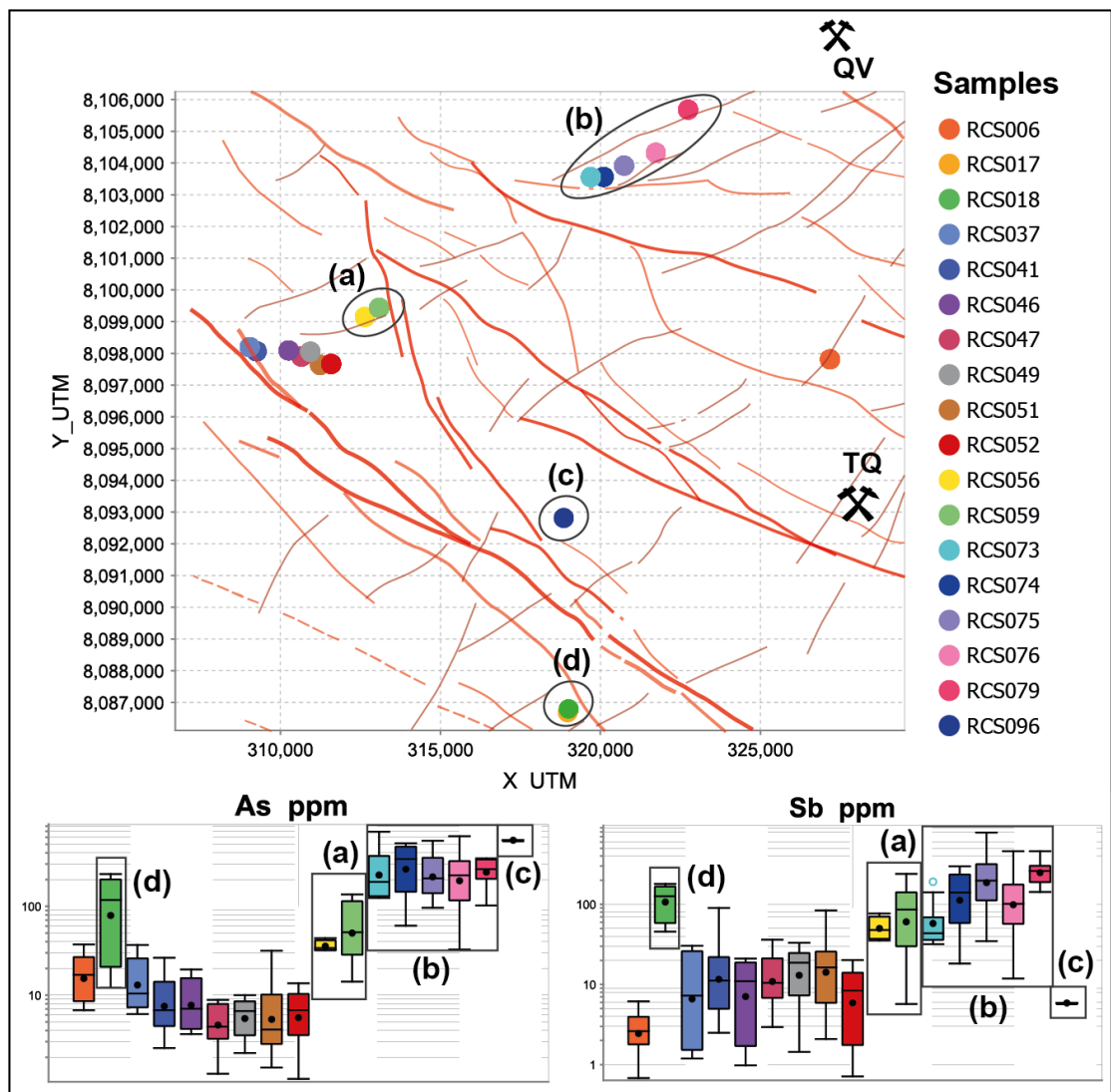


Figure 8.25. A Spatial assessment of As and Sb variations within the A3 assemblage. Samples of interest in the high concentration population are highlighted and grouped based on location, which is indicated on the map.

equivalent in both elements. Cluster (a) comprises RCS056 and RCS059, which are both the most proximal samples (<2 km) to the Puca-Porquene Fault (PPF), which is a splay of the Incapuquio Fault (IFS). With values succeeding those of (a), group (b) is a collection of five samples (RCS073, RCS074, RCS075, RCS076 and RCS079) which are located parallel to the transverse fault leading toward Quellaveco. RCS018 (d) shows elevated As and Sb with similar values to (a) of ~100 ppm As and Sb, and is located on the southwestern part of section 1. The disparity between As and Sb in (c) is high, with As concentration (~500 ppm) and a low Sb concentration of ~7 ppm. This sample (RCS096) is the only example within the A3 assemblage where elevated or depleted values in As do not correspond with Sb.

Spatial variations with distance from the Quellaveco Fault

Analogous to the chlorite analysis, the compositions of epidote are represented as a function of distance from the Quellaveco Fault. These transects are purposely orientated to traverse the main fault orientations (NW-SE) in order to detect, if present, any zonation patterns around the major faults, although this does not acknowledge possible zonation related to the transverse NE-SW faults. For ease of comparison, both sections have fixed vertical (concentration, ppm) and horizontal scales (km).

One of the most striking trends is manifested by As in section 2. There is a significant and seemingly systematic decrease along the whole section from the NE to SE of the transect. This poses some interesting questions because zonation on such a scale (15-20 km) has not been previously reported. At this point, this trend is observed irrespective of any age or assemblage differences between the samples. The significance of this trend is backed up by the parallel variation observed in the Sb data.

Other elements of interest in section 2 are Mn, Zn and Sb which all show a potential trend from samples RCS064-RCS079. This is

quite an extensive distance of 5-6 km, and yet the correlation between the samples and the elements are apparent. Mn and Zn both show a maxima between the CF and MF at RCS069, with a sharp decrease to RCS064, and more gradual decline toward RCS079 in the NE and a possible decreasing gradient towards the QF. Similar to As, Sb follows a consistent rise from RCS064 toward RCS079. These patterns are all suggestive of a transition from proximal to distal propylitic trends in epidote indicating that RCS064 is most proximal.

The trends seen in As and Sb almost mirror the samples for Sb in Section 1, manifested as a low near the CF and increasing to a maximum towards the IFS in the WSW. Viewed as a whole, section 1 shows less significant, systematic variations. There is a possible gradient in the cluster of samples on the southwestern side of the IFS (RCS023-RCS014) in which As exhibits a decrease away from the IFS over ~3.5 km from the breccia sample, RCS023, to the furthest sample (RCS014). A corresponding trend is also seen in Sb concentrations in the same samples. However, it is possible that this apparent gradient is misleading because the samples are from different assemblages (from proximal breccia, intermediate A3 and distal A6). However, the actual assemblages reflect a zonation, with high temperature assemblages (actinolite facies) grading to lower temperature 'chlorite facies' (Cooke *et al.*, 2014).

8.5.6 *Temporal variations in epidote chemistry*

Another complexity when analysing propylitic alteration on a regional scale is that the assemblages recorded may well not have formed synchronously. As concluded in Chapter 7, this is the case in the Quellaveco district, with 87 precise dates obtained for alteration assemblages spanning the period of 40 Ma. Of these results, 17 are from minerals that are thought to form part of the analysed epidote mineral assemblages (see Table 8.1). From the dated sample assemblages, comparisons are made with the epidote trace element chemistry to determine if any of the vein or replacement assemblages are compatible geochemically, temporally and spatially.

Sample	X UTM	Y UTM	Z UTM	Epidote Assemblage	Mineral Dated	Date (Ma)	Error (Ma)
RCS003	327486	8098122	3617	A4	Zircon	57.4	2.9
RCS018	319006	8086784	2285	V2	Zircon	69.9	6.5
RCS023	320306	8088971	2480	BX	Zircon	67.6	2.7
RCS033	333053	8098079	3988	A4	Apatite	64.2	6.5
RCS046	310256	8098095	2730	A3	Zircon	65.1	1.0
RCS047	310659	8097900	2749	A3	Titanite	72.0	6.2
RCS049	310936	8098053	2774	A3	Zircon	65.8	1.1
RCS051	311239	8097639	2795	V2	Zircon	66.4	6.9
RCS052	311586	8097667	2831	V2	Titanite	67.8	6.8
RCS056	312635	8099146	3008	A3	Titanite	66.7	1.4
RCS074	320100	8103564	3234	A3	Titanite	75.9	2.4
RCS074	320100	8103564	3234	V6	Titanite	69.5	3.9
RCS075	320740	8103917	3280	A3	Apatite	68.3	7.2
RCS078	322734	8105674	3559	V3	Zircon	69.1	2.6
RCS078	322734	8105674	3559	V6	Zircon	66.3	3.1
RCS081	324357	8106351	3901	A5	Zircon	66.0	2.4
RCS104	323197	8096126	3506	A4	Apatite	44.9	3.5

Table 8.1. Precise dates from Chapter 7 which are associated with epidote-bearing assemblages.

General observations that can be made from this summary are that the six dated vein samples and one breccia sample all fall between 66-70 Ma (ignoring uncertainty). Replacement assemblage dates are between 65-76 Ma, excluding three younger dates obtained from apatite in A4 assemblages. These data lead to the conclusion that the majority of epidote-bearing alteration sampled in the district was formed in the Maastrichtian (Late Cretaceous), during the earlier phases of construction of the Yarabamba batholith (Simmons, 2013).

From the WSW limit of section 2 there are three precise zircon and titanite dates from A3 assemblages that fall between 65.1 ± 1.0 and 66.7 ± 1.4 Ma. These constrain the formation of A3 assemblages in this area to quite a narrow time window at the tail end of this Late Cretaceous alteration phase.

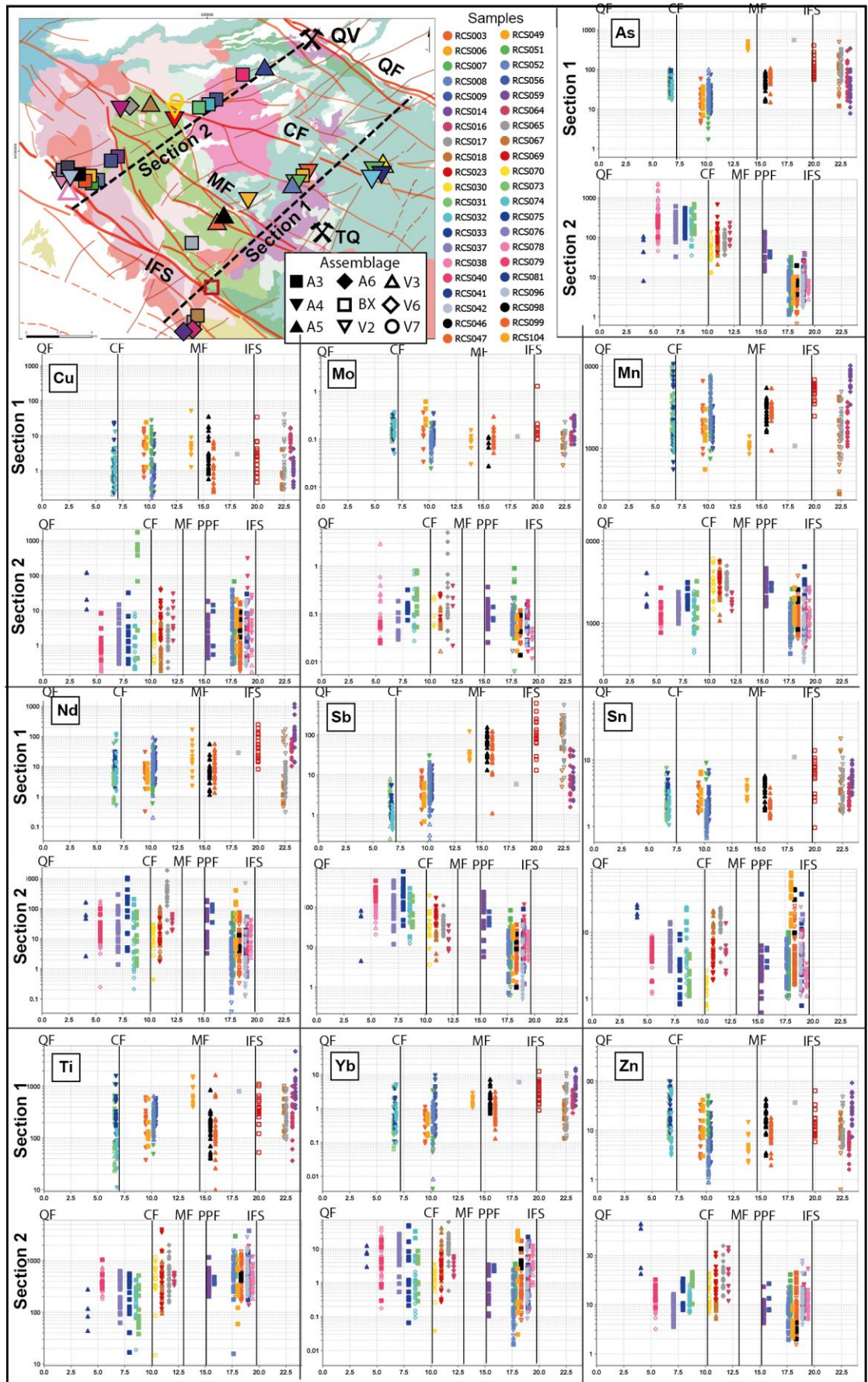


Figure 8.26. Epidote trace element composition as a function of distance from the Quellaveco Fault. Sample traverses 1 and 2 are shown separately, and locations of the major transverse faults are noted on the sections (QF: Quellaveco Fault; CF: Capulline Fault; MF: Micalaco Fault; PPF: Puca-Porquene Fault; and IFS: Incapuquio Fault System).

High As-Sb samples on section 2, RCS073-RCS079 (Figure 8.27) have assemblage dates of 69.5 ± 3.9 to 66.3 ± 3.1 Ma, excluding the older titanite from RCS074 (which is of possible primary igneous origin), indicating that this 'fertile' signature developed in the Late Cretaceous alteration event, despite the general proximity of these samples (~5-10 km) to the Quellaveco porphyry system.

The dates of the V3 and V6 veins that both occur in sample RCS078, located in the middle of section 2, overlap within uncertainty. This, combined with their almost identical epidote compositions (As (80-200 ppm), Sb (10-150 ppm), Pb (20-100 ppm), Mn (6000-2000 ppm), Zn (5-30 ppm), Cu (<0.2-8 ppm), Sn (1-10 ppm)), suggests that these vein types are coeval. The primary difference between V3 and V6 classifications relates to the relative proportions of epidote and quartz (V3 epidote-rich, V6 ~equal epidote/quartz), thus they could quite easily be variants derived from the same kind of fluid.

Sample RCS074, located approximately 3.5 km southwest of RCS078 (Figure 8.28), contains a V6 vein with epidote that has a very similar composition to the V6 epidote in RCS078. Furthermore, the replacement epidote in the A3 assemblage in the wallrock of the V6 vein in RCS074 also shows comparable, anomalous As and Sb concentrations. This can be interpreted to assume that V6 and A3 are contemporaneous; it is consistent with the apatite age of 68.3 ± 7.2 Ma obtained for the A3 assemblage in RCS075, ~750 m northeast of RCS074.

The breccia-hosted epidote sample RCS023, located in section 1 on the IFS (Figure 8.28) has a fairly precise zircon date of 67.6 ± 2.7 Ma. This, combined with the nearby V2 date of 69.9 ± 6.5 Ma (RCS018) and the comparable chemistry of V2 epidote in RCS017 and A3 alteration in RCS018, suggests that a Late Cretaceous event was widespread in the western part of the area. Furthermore, it links V2 vein assemblages with A3 alteration, which is perhaps unsurprising given its high temperature, actinolite assemblages. RCS016 and RCS014 in the same area did not provide adequate dates for comparison, but the different compositional features of the A6 epidote present in these samples does not rule out a

contemporaneous origin if this could be explained by a lower temperature of formation (chlorite-calcite assemblage) at a greater distance from a high temperature IFS fault conduit.

The A4 assemblage is distinctive in the presence of albite. Notably, the three dated A4 assemblages are the youngest determined, at 64.2 ± 6.5 Ma (RCS033) and 57.4 ± 2.9 Ma (RCS003) to the east of the district, and 44.9 ± 3.5 Ma (RCS104) in its centre. This suggests that the A4 assemblage is of a different, later origin. RCS003 is located ~5 km north of the Toquepala porphyry deposit and the A4 age is consistent with this assemblage forming in the distal part of the Toquepala porphyry halo.

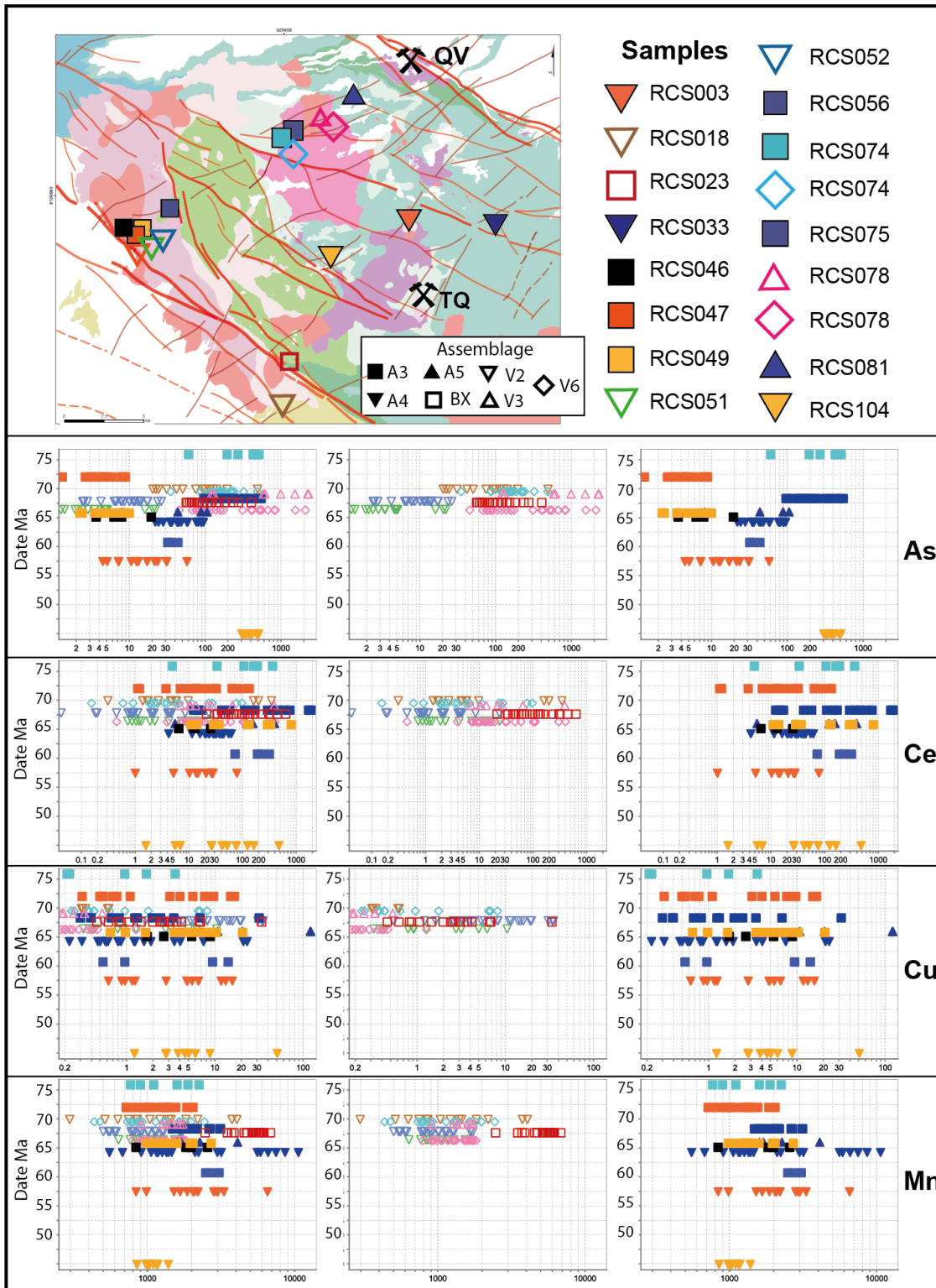


Figure 8.27. Epidote trace element chemistry for temporally constrained samples applying the dates acquired in Chapter 7. Data are attributed on epidote alteration assemblage

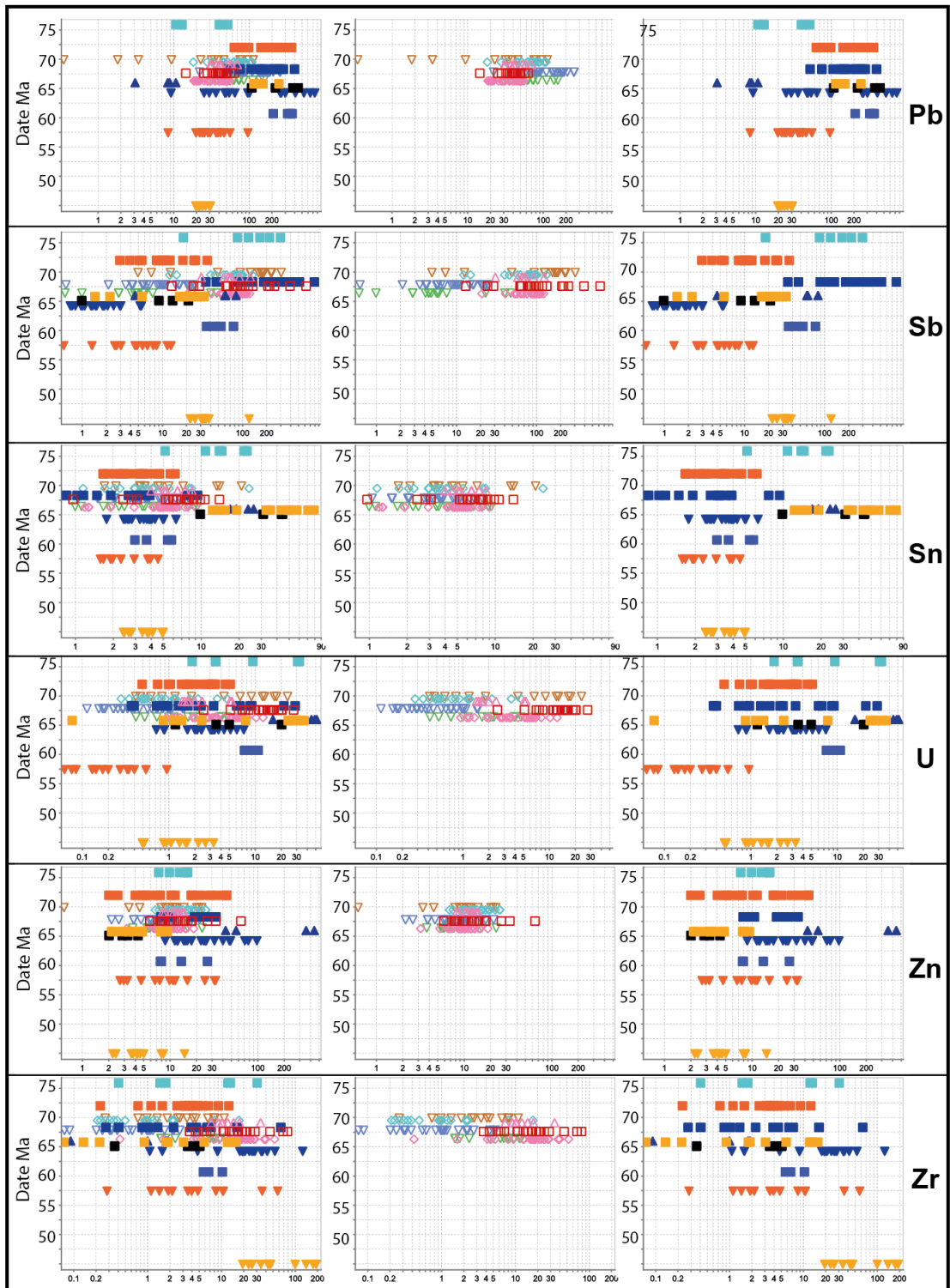


Figure 8.28. A continuation of epidote trace element chemistry for temporally constrained samples. Data are attributed on epidote alteration assemblage. Sample information and location are shown on Figure 8.28

8.5.7 Interpretation of epidote chemistry using discriminant projection analysis

A brief summary of discriminant projection analysis (DPA) is given in Section 8.4.7. The parameters and fields for the discriminant plot used in this study (Figure 8.20) were determined by J.J. Wilkinson (PersComm. 2021) using the data acquired from numerous porphyry systems and several metamorphic terranes worldwide as part of a series of AMIRA projects. The x and y parameters ($x = DP1$, $y = DP2$) are linear sums of scaled log concentrations of 11 discriminant trace elements: Ce, Bi, As, Mg, Sb, Th, U, Y, Yb, Zn and Mn. The fields defined by the training process are: high sulphidation epithermal (HS), intermediate sulphidation epithermal (IS), low sulphidation epithermal (LS), porphyry Cu-Mo and metamorphic. As with the chlorite discriminant diagram, the field in which the data plot is indicative of epidote is typically associated with that type of system, but cannot be a definitive classification given the amount of overlap between the fields. This is unsurprising as there are natural transitions in pressure, temperature and fluid compositional parameters between deep, high sulphidation and porphyry, between porphyry and laterally equivalent intermediate sulphidation, and between intermediate and low sulphidation environments (e.g. Sillitoe, 2010). One key point is that propylitic alteration in the halo of porphyry systems is essentially an IS-LS environment so that data from a broad propylitic halo around a porphyry deposit will tend to spread from the porphyry into the IS and perhaps LS fields. Data from samples within a porphyry-HS system will tend to spread between these fields with the HS-classifying data expected to represent samples at shallower depths, or perhaps a later, telescoped overprint of the porphyry itself.

Each area (Figure 8.29) is discussed in order with a summary of the discriminant analysis and other key findings:

- a) The summary plot with all of the epidote data highlights the lack of data plotting in the metamorphic field, and few within the LS epithermal field. Retrospectively looking at the As vs Sb comparison between Quellaveco and metamorphic data (Figure 8.29) the discriminant analysis suggests that the overlap of Quellaveco data with the upper range of metamorphic epidotes is likely to indicate samples that may be relatively proximal to

a potential porphyry centre, or samples that are very distal – beyond the distal enrichment halo (>5 km).

- b)** This area contains five samples (RCS003, RCS006, RCS007, RCS008 and RCS009) containing four different assemblages: A3, A4, A5 and V3. The data spread between the IS epithermal, porphyry, and HS epithermal fields, and there is a clear separation of the assemblages between the fields. The A5 and V3 assemblages (both from RCS008) span the border between HS and the porphyry, whilst the A3 and A4 cluster together on the LS epithermal and porphyry fields. Given the proximity to the Toquepala deposit and the date from RCS003 that overlaps with the age of the Toquepala system, these data can be explained by the sampling of part of a true porphyry-propylitic halo, with RCS008 being influenced by a localised HS system
- c)** The data from this area (RCS023-RCS014) is divided approximately 60-40 between the porphyry Cu-Mo field and the HS epithermal fields, respectively. Interestingly, the data within the HS epithermal field are predominantly from the breccia- and V2 vein epidotes proximal to the IFS, plus the few analyses of A3 epidote in RCS018. Conversely, the data from the A6 epidote wallrock replacement in RCS014 and RCS016 plot solely within the porphyry field. This distinction tends to support the concept of two groupings here, rather than a simple zonation away from the IFS, with a possible porphyry target located in the vicinity of RCS014 and RCS016. It also provides further support for a link between V2 and BX, formed at ~67-69 Ma (see above).
- d)** The epidote within these three samples (RCS031, RCS032, and RCS033) is all classified within A4 assemblages, with RCS031 also hosting a V3 vein. The data plot within the porphyry and IS epithermal fields, with the vein data plotting on the porphyry-HS boundary.
- e)** The ten most IFS-proximal samples (RCS037-RCS052) on section 2, comprising mostly A3 and A4 assemblages with a V3 vein in RCS038, show characteristics of IS to LS epithermal formation conditions. The data mostly plot across the porphyry to IS fields with the data in the

former being typically from A3 assemblages whereas nearly all the V2 vein data plot in the IS field. There is a variation in dates for the assemblage in this group, from predominant older ages such as 69.0 ± 2.8 (RCS053), to younger ages such as 60.7 ± 1.4 Ma (RCS056). This implies multiple phases of alteration throughout a ~10 My period in this area.

- f)** The two samples (RCS056 and RCS059) within area (f) contain A3 assemblages and plot comfortably in the HS field, suggesting a relatively strong HS signal. RCS056 has an A3 date of 66.7 ± 1.4 Ma, consistent with other dates in this area.
- g)** Areas (g) and (h) combine on the discriminant plot in order to remain consistent with chlorite analysis. Data spreads from the porphyry field into both HS and IS domains on the discriminant plot.
- h)** The data show a relatively strong HS epithermal signal in the high As-Sb A3, V3 and V6 samples located along section 2 towards QV. There are several temporal constraints for this time.
- i)** The limited data in this sample is on the borderline of the porphyry-IS classification.
- j)** This is a very young A4 sample (44.9 ± 3.5 Ma) with a relatively strong HS discriminant signature.

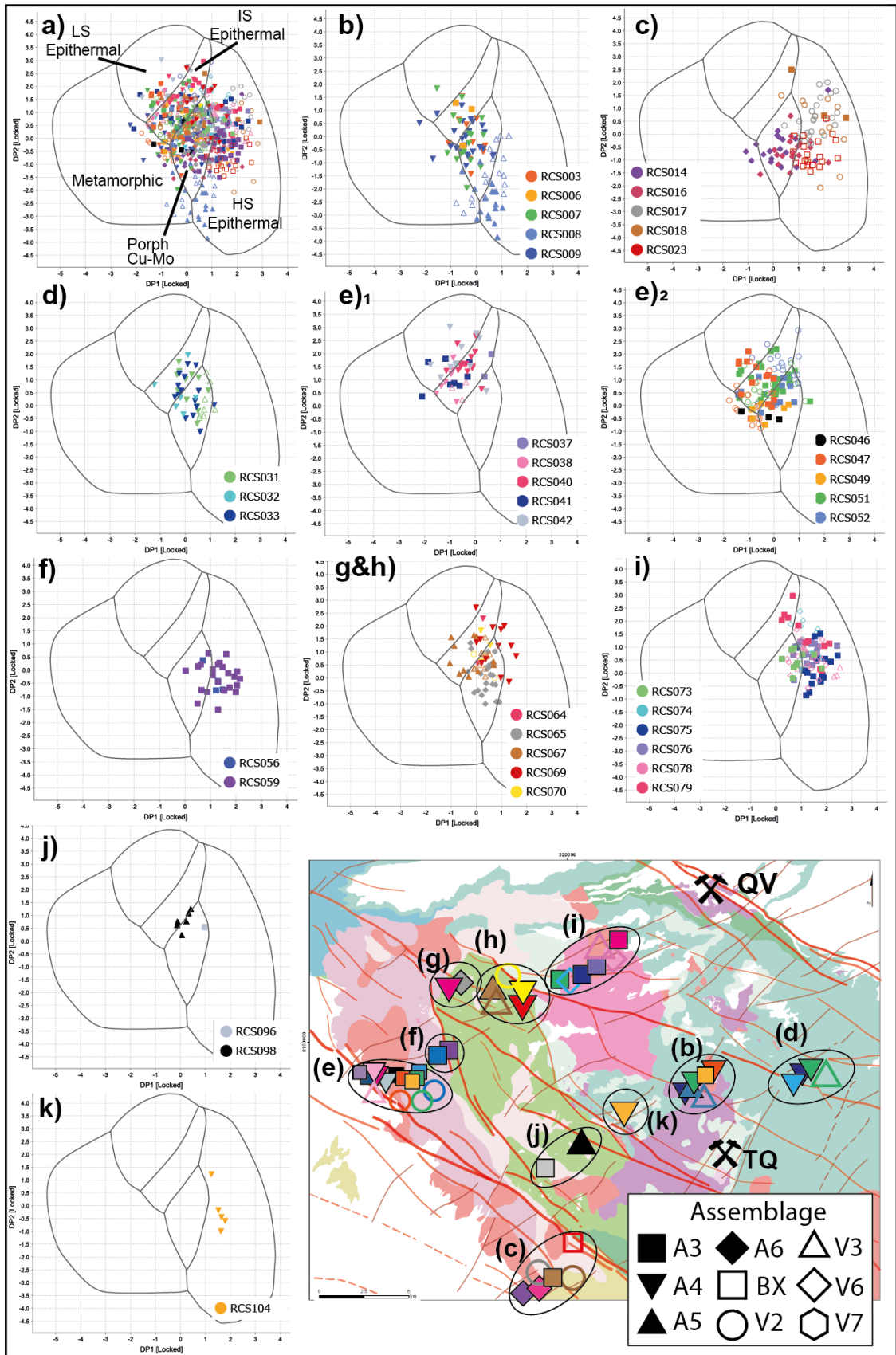


Figure 8.29. Discriminant plots for epidote trace element data: **a)** all data plotted with geochemical fields highlighted; **b-k)** geographically grouped samples, the alteration assemblage is attributed by shape. Area **(e)** is split and **(g)** and **(h)** are combined to show the extent of the data while correlated to the areas for the chlorite plots (discriminant diagram formulated by J.J Wilkinson (PersComm, 2021).

8.6 Comparative summary of chlorite and epidote

The initial metamorphic assessment of both datasets showed a clear distinction between the Quellaveco dataset and known metamorphic characteristics (e.g. Wilkinson *et al.*, 2015; 2020; Baker *et al.* 2020). Elevations in elements such as Ca and Sr in chlorite and Sb and As in epidote were indicative of an area associated with porphyry centres. Where there was overlap with the metamorphic dataset, for example in the Ca-Sr chlorite plot, those data could have represented either proximal porphyry or ultra-distal propylitic.

A consistent area of significance for both epidote and chlorite is the samples in area (g) (see (Figure 8.20 and Figure 8.29) located the MF and CF (RCS064-RCS065). Discriminant analysis of both epidote and chlorite in area (g), plot within the porphyry Cu-Mo and IS epithermal fields. Specifically, RCS064 and RCS065 have the closest compositions to porphyry Cu-Mo signals, and therefore suggest the most proximal sample. Further corresponding evidence is the widespread variations in Mn and Zn, with the peak maxima coinciding with samples RCS064 and RCS065. Structurally, this area lies on the Micalaco Fault confluence of the PPF and close to the CF.

Areas (h) and (i) in both minerals reiterated the possibility of the presence of fertile fluids in the area of (g) because of very distinct gradients leading away from this area (h). In epidote, this can be observed as an increase in As and Sb with distance from (g), and a rapid increase to 1.5 km with a gentle decrease away in Mn and Zn. This is indicative of porphyry-distal propylitic alteration. The discriminant analysis shows data fell within the porphyry Cu-Mo and IS epithermal field, whilst chlorite highlighted porphyry Cu Mo characteristics. Although temporal constraint for the immediate area near (g) is absent, genetic connections made between A3, V6 and V3 in epidote and chlorite samples have allowed the age of the gradients in area (i) to be constrained to between 70-67 Ma.

8.7 Conclusions

- When compared with data from known metamorphic terranes, the Quellaveco trace element chemistry of epidote and chlorite did not show any of the typical signatures associated with background metamorphism.

- An area on the intersection of the Puca-Porquene Fault and Micalaco Fault (area g) showed a strong chemical signal of a distal propylitic halo of a fertile porphyry. Because of the low abundance in titanium and vanadium, the target is hypothesised to be at depth.
- Significant geochemical gradients were detected in both the epidote and chlorite chemistry, up to 6 km from the potential porphyry source (area g). This substantiates the significance of area (g) as the gradient indicates a transition from proximal to distal propylitic halo.
- The presence of high temperature fluids and subsequent propylitic alteration was detected by decreasing titanium and changes in mineral alteration assemblage with distance from the faults. The high temperatures signatures were not consistently observed along the IFS, and therefore highlighted the potential significance of the PPF as a fluid conduit during the early phases of alteration.

9 Timing and Origins of Propylitic Alteration in the Quellaveco District

At the beginning of this study, a working hypothesis was developed which involved faults facilitating the district-scale dispersion of propylitic alteration fluids away from a porphyry centre. This hypothesis has, in part, been disproved. The project's multi-dimensional approach has revealed that the reality is much more complex; although district-scale, fault focused propylitic alteration clearly developed, this occurred over a much longer time frame than expected and, for the most part, had no direct connection with the eventual economic porphyry mineralisation.

In order to account for the spatial and temporal patterns defined in the study, this discussion can best be summarized through three conceptual block models, each representing a different time slice covering ~15 My prior to mineralisation at Quellaveco, Toquepala and Cuajone (72 – 57 Ma) (see Figure 9.1-Figure 9.3). To enable direct comparison of the models with the geochemical results, area references, for example Area (b), correlate with the epidote and chlorite discriminant projection analysis (see 8.4.5 and 8.5.7).

9.1 Regional metamorphic or metasomatic propylitic alteration

From the metamorphic comparison and discriminant projection analysis (see 8.4.5 and 8.5.7), the geochemical signals from chlorite and epidote in the Quellaveco district are largely distinct from the metamorphic chlorite and epidote characteristics defined in previous work (e.g. Wilkinson *et al.*, 2015, 2020; Baker *et al.*, 2020; Cooke *et al.*, 2020). Elevated As and Sb in the chlorite and epidote data (see 8.4.2, 8.5.2), and distinctively high Ca, Sr, Si and Zn concentrations in the Quellaveco chlorite data are in keeping with differentiations made by previous authors. Relative depletion of Al and Ti in the Quellaveco chlorites was also noted as indicative of non-metamorphic terranes (see 8.4.2). In the multivariate analysis, the 11-element discriminant projection diagram for chlorite only classified 3/753 (0.4%) and for the epidote only 26/1069 (2.4%) of analyses in the metamorphic field. No individual sample or alteration assemblage had a predominantly metamorphic classification. Thus, there is little evidence for a

typical regional metamorphic signature at any stage of development of the district.

This conclusion begs the question as to what type of system or systems did control the widespread propylitic alteration in the district. Given that more than ~95% of the samples collected in this study are located outside of the realm (>5 km) of the propylitic haloes known to be associated with porphyry centres (Sillitoe & Mortensen, 2010; Simmons *et al.*, 2013a), it is unlikely that the known systems of Quellaveco, Toquepala and Cuajone contributed directly (and are essentially excluded based on temporal constraints; see below). Other possibilities include unknown porphyry centres, various types of epithermal systems, or potential large-scale, metasomatic alteration that creates the specific features observed in the mineral chemistry but which is characteristic of porphyry-fertile arc settings and are distinct from isochemical metamorphic products.

9.2 Model 1 (72- 67 Ma)

9.2.1 The onset of plutonism

The oldest events documented in this study relate to the emplacement of the composite Yarabamba Batholith into mid to late Cretaceous precursor Toquepala Group volcanics (~91 – 69 Ma; Simmons, 2013). This is thought to have incrementally occurred between ~71 – 59 Ma (Mukasa, 1986; Simmons *et al.*, 2013a), with the initiation of magmatism occurring during a transcurrent fault regime, related to oblique plate convergence between the Farallon and South American plates (Pitcher & Bussell, 1977; Pardo-Casas & Molnar, 1987; Jaillard & Soler, 1996). The oldest dated intrusive phases in this study, diorite and monzodiorite, yielded representative igneous ages of 69.2 ± 2.3 Ma and 69.0 ± 6.7 Ma (see 7.6), consistent with the previous data. The Toquepala volcanics host the Yarabamba Batholith, and were dated between 77.4 ± 2.7 Ma and 65.2 ± 2.3 Ma (see 7.6).

9.2.2 Early high temperature fluids and alteration

The earliest indication of propylitic alteration recorded in the Quellaveco region is mostly seen to the southwest of the IFS (area c) and PPF (area f) (see 7.8). U-Pb dating of apatite, titanite and zircon minerals yielded

alteration ages between ~71-67 Ma in V2 and A2 and A3 (actinolite-bearing) assemblages. Based on overlapping dates, geochemical characteristics and location along the same structural trends, these assemblages are considered to be part of the same broad event. Given the apparent age range for this alteration, it is thought to be related to fluids associated with the earliest intrusive magmatic pulses, at the start of batholith construction.

Ti, and to a lesser extent V, in chlorite proximal to the south-western section of the IFS and north-western area of the PPF decrease with distance from the faults. Titanium-in-biotite is an established geothermometer (Douce, 1993; Henry & Guidotti, 2002) but, more recently, it has also been shown to have a thermal dependence in chlorite (Wilkinson *et al.*, 2015, 2020). The zonation observed in these areas can therefore be interpreted to reflect focusing of elevated temperature fluids along the major faults and dissipation of these fluids into the surrounding rocks to produce the observed propylitic assemblages. This is consistent with the presence of actinolite-bearing A2 and A3 assemblages near the faults, which are typically observed in higher temperature propylitic domains (Cooke *et al.*, 2014) and the disappearance of epidote in the most proximal A2 assemblages because of its upper stability limit of ~400°C (Dilles, 2010; Cooke *et al.*, 2014b;).

Fault kinematics during this inferred stage of activity on the IFS and PPF are difficult to isolate from successive events. However, given the known tectonic regime of σ_1 orientated NNE and σ_3 orientated ~ESE (Pardo-Casas & Molnar, 1987) there are two possibilities for movement sense on the IFS: dextral strike-slip; or sinistral movement, in which the IFS would act as an antithetic Reidel fault in a dextral regime (Fossen, 2016). As a splay of the IFS, with distance the strike of the PPF moves from NW-SE to NNW-SSE. Therefore, dextral transtension along the PPF is most likely, during this tectonic regime.

There is no evidence for thermally anomalous samples further along the IFS (area e) beyond the point of divergence of the PPF splay. This suggests that the PPF is the primary conduit for fluid migration at this time.

One question remains: why is the presence of high temperature chlorite seemingly not reflected on the north-eastern side of both the IFS and PPF (area (j) and area (g))? There are two possible reasons for this: the lateral dispersion of fluids on the north-eastern throw is transected by subsequent fault movement; or the lack of analysed chlorite in the samples to the north-east of the IFS would mean that any high temperature propylitic alteration potentially present is not represented. The first theory is the most favoured in this study because of ensuing upthrow on the south-eastern side of the PPF (see Model 2).

9.2.3 *Porphyry-like signals (area g-h)*

From all of the chlorite and epidote data analysed in this study, Area g-h (see 8.4.5) is the most significant with respect to the presence of strong porphyry-like signals in an apparently unexplored area (see 8.4 and 8.5). Discriminant projection analysis shows the propylitic alteration has multivariate characteristics in both minerals that are typical of porphyry Cu-Mo systems. The limited spread of data into the high sulphidation and intermediate sulphidation epithermal fields can reflect slightly more distal propylitic alteration conditions. Based on the chlorite Mn:Zn fertility assessment (see 8.4.5) samples 061 and 065 both have elevated concentrations, consistent with their location within in the halo (typically ~1.5 km) of a fertile porphyry centre. Further compelling evidence of the area's significance is seen by distinctive geochemical gradients in the epidote and chlorite data reaching up to 5-6 km (possibly further) from area (g) (see 8.4.3 and 8.5.5). This gradation connects samples RCS068 as far as RCS079 (areas h and i). In the chlorite chemistry, the gradients are defined as an increase in Ca, Li and As with distance, and Ti and V decrease with distance from area (g). Mn increases to approximately 1.5 km from area (g) (between RCS070 and RCS074) before decreasing rapidly, which is indicative of a 'marked shoulder' in the propylitic alteration. These trends are suggestive of a change from porphyry proximal to distal propylitic alteration (Wilkinson et al., 2015; 2017; 2020). However, the Ti and V concentrations within the area of interest are comparatively low (relative to comparison studies), which would indicate distance from the source.

Structurally, this area is of interest. In the field, where the PPF and MF intersect, there is an extensively argillically altered fault core. Structural mapping and specific drone model analysis of area (g) to the north-east highlight an abundance of high-angle, parallel, NE-SW-trending faults (see 6.4). Interestingly, the junction between the PPF and MF is also characterised by relatively low-magnetic results (AA internal report, 2018), suggestive of magnetite breakdown – typically observed in phyllically altered domains.

Temporally constraining this putative porphyry centre is hindered by the absence of precise alteration ages within the most proximal samples (in area g). However, A3 alteration (in RCS075) and V3 and V6 alteration (in RCS078) are geochemically linked to the aforementioned gradients, and have yielded precise ages of 68.3 ± 7.2 Ma (A3), 68.3 ± 6.8 (V6) and 69.2 ± 2.6 Ma (V3) (see 7.6). Closer to area (g), but not necessarily geochemically correlated, is RCS061 which yields an age of 70.3 ± 5.2 . This sample is part of the high temperature, A2 assemblage located along the PPF.

In conclusion, the signals in area (g) are consistent with the presence of a fertile porphyry system, localised at a major fault intersection. This study suggests this occurred at approximately 69 Ma. The relatively low temperature chlorite signals, combined with the knowledge that no near-surface porphyry has been explored, imply that any such system is buried at some unknown depth.

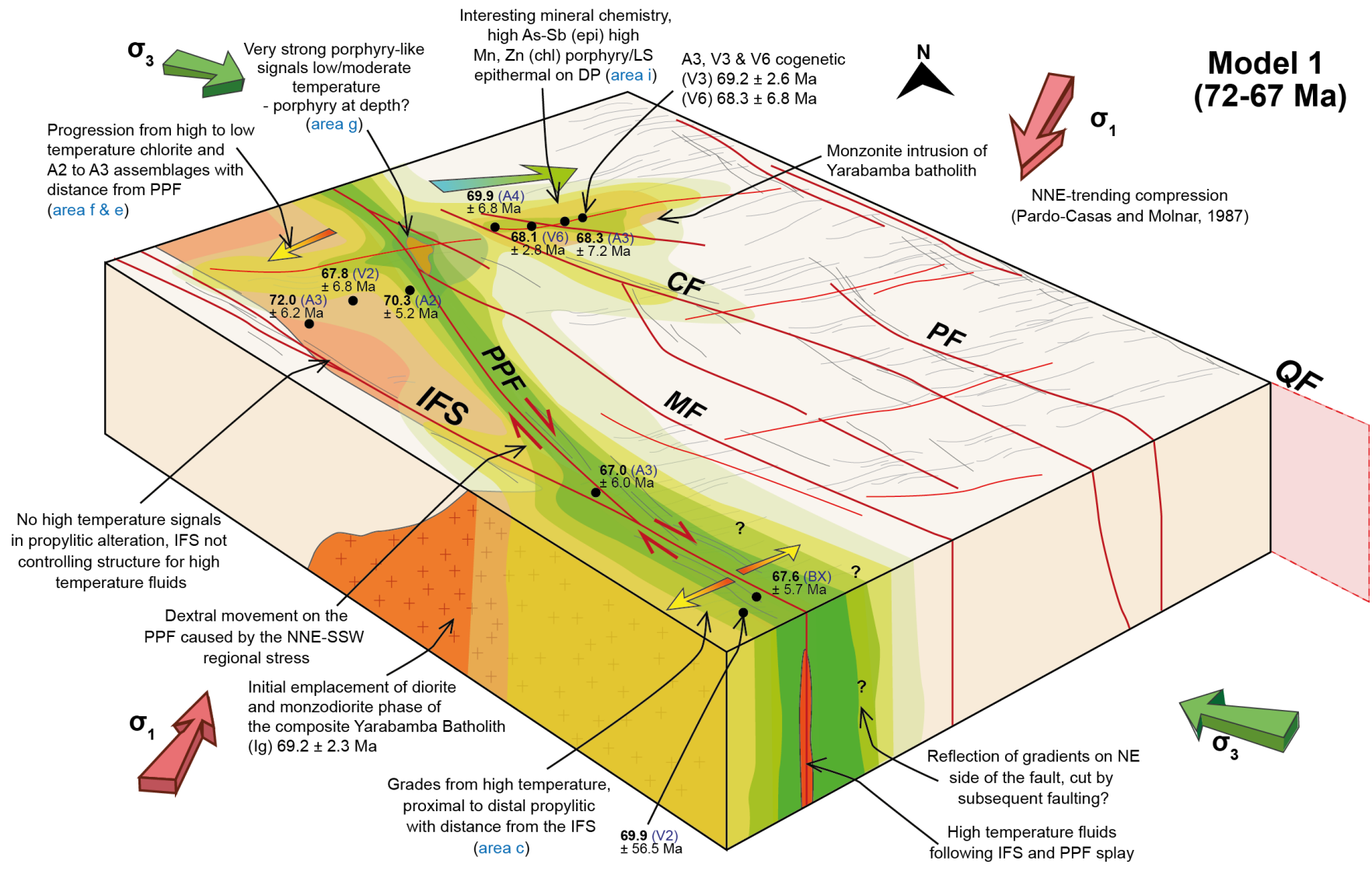


Figure 9.1. Model 1 (72-67 Ma) – a summary model of the findings and interpretations from this study

9.3 Model 2 (66 – 64 Ma).

9.3.1 *Pacay high-sulphidation epithermal system*

Field mapping highlighted an area of anomalously intense, pervasive propylitic alteration in the area (d) (Figure 9.2). This area is bounded by the sericitically altered Capulline Fault to the southwest, and the potassically altered Pacay Fault to the northeast. Along transect ~2 km from this zone there is no other apparent alteration. The propylitic alteration is defined by epidote-chlorite-albite (A4) and epidote-titanite (A5), with an abundance of V3 epidote-quartz veins with dominantly NE-SW orientation. From field observations alone, the propylitic alteration appears to be confined to between the Capulline and Pacay faults.

High Mn and Zn concentrations in chlorite are comparable to those discussed in parts of area (h) above. Discriminant analysis of epidote and chlorite both imply that multivariate geochemical signatures are more consistent with an intermediate (to high) sulphidation epithermal environment. Epidote-chlorite-albite (A4) alteration yielded a date of 64.2 ± 6.5 Ma (see 7.6, 8.4.5 and 8.5.7).

This area is particularly interesting structurally as it is located ~4-5 km along-strike of the Pacay Fault, to the southeast of a potential Anglo American target (AA internal report, 2018). The 'Pacay – Tumba Cactus' area has been flagged for anomalous results including increased Mo concentrations in whole rock and magnetic lows. This prospect is located on an intersection between the Pacay fault and a NE-SW trending 'Yarito-Pacay' Fault. This NE-SW trending structure also shows a clear low-magnetic corridor toward the intersection with the Pacay Fault (AA internal report, 2018). N-S and NE-SW-trending D-veins and quartz-tourmaline epithermal veins, are abundant in the area. An area of advanced argillic alteration is present to the SE.

The potential genetic similarities between the Pacay-Tumba Cactus prospect and the propylitic alteration observed further to the southeast suggests the localisation of intermediate to high sulphidation epithermal fluids along NE-structures in the area, potentially 5-6 My prior to the onset of porphyry mineralisation at Toquepala and Quellaveco. Additional magnetic resistivity anomalies highlight several areas along strike of the CF to the northwest, at intersection points with NE-SW

structures. Not only does this provide further evidence for fluid localisation by NE-SW and NW-SE faults, but highlights the importance of the CF.

9.4 Model 3 (62 – 57 Ma)

9.4.1 A change in far-field stress axis

In the Paleocene (~59 Ma), the convergence direction of the subducting Farallon plate (subsequently known as the Nazca plate) shifted from NNE to NE/ENE (Pardo-Casas & Molnar, 1987; Jaillard & Soler, 1996). Rotation of the plate coincided with an increase in velocity of both the overriding (South American plate) and subducting plates (Sdrolias & Müller, 2006; Horton, 2018). The velocity profile by Horton (2018) records trench-normal absolute velocities of 25 mm/yr for 19°S (southern Peru). This sudden increase in velocity is at odds with the middle and southern parts of south America, which experienced plate deceleration; for example, at 40°S the velocity dropped from 10 mm/yr to 4 mm/yr (Horton, 2018)

The effects of these changes in plate motion were wide-reaching, producing accelerated uplift and erosion and a deepening locus of differentiation of mantle-derived magmas. In the Quellaveco region, the realigned stress axes resulted in increased dilation of NE-SW and ENE-WSW structures. Ultimately, these processes led to the emplacement of fertile magmas in the upper crust and the formation of economic porphyry deposits (Nathwani *et al.*, 2021).

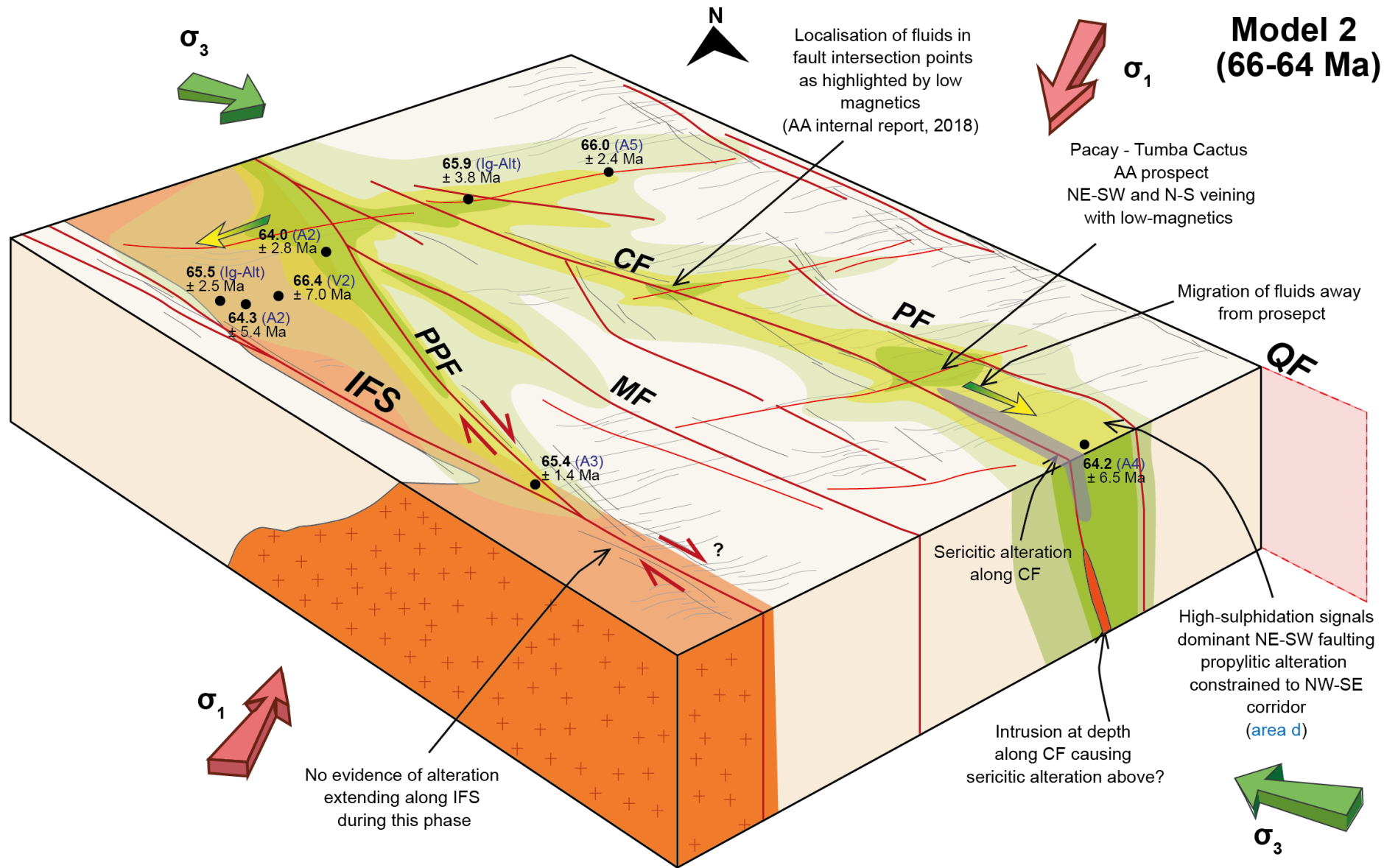


Figure 9.2. Model 2 (66-64 Ma) – a summary model of the findings and interpretations from this study

9.4.2 Evidence of transpression and thrusting

As a result of the plate rotation at 59 Ma, it is probable that the stress regime along the major NW-SE structures changed from dextral transtension to sinistral transtension.

The oldest phases of the Yarabamba Batholith, diorite and monzodiorite, crop out in the southwestern part of the district and display an apparent NW-SE trend, largely bound between the IFS to the southwest and the PPF to the northeast. The northeastern contact with volcanics of the Toquepala Group is sharp implying a fault control by the PPF. An increase in the frequency of NW-SE-trending, high-angle faults was recorded in this area (see 6.3), often containing fault-fill palygorskite clay and with reverse kinematic indicators. Thus, the exposure of these older Yarabamba units is interpreted to be due to thrusting along the PPF (Sanchez, 2017). The recently activated sinistral motion on the PPF could have caused local transpression in the NNW-SSE-trending northern segment of the PPF where the strike change acted as a restraining bend (Pardo-Casas & Molnar, 1987; Jaillard & Soler, 1996; Fossen, 2016).

Other occurrences of positive flower structures and features of sinistral transpression have been noted throughout the region along the IFS. Characteristically, these contain steep to moderately ($>35^\circ$) SW-dipping reverse faults (Jacay *et al.*, 2002), such as those recorded in areas e and f (Figure 9.3).

9.4.3 Magmatism and associated porphyry formation

Regional granodiorite (GRD)

The emplacement of the regional granodiorites is documented to be the last phase of the Yarabamba Batholith. Published U-Pb zircon ages by Simmons *et al.* (2013) give an emplacement age of between 60.3 ± 1.6 Ma to 61.5 ± 1.5 Ma at Toquepala, and 60 ± 0.9 Ma at Quellaveco. Nathwani *et al.* (2021) obtained dates of $61.64 +0.26/-1.26$ and $60.96 +0.66/-1.39$ Ma for the Toquepala Granodiorite and $58.99 +0.23/-1.20$ Ma for the Quellaveco granodiorite. Apatite U-Pb dating in this study of the Quellaveco

Granodiorite yielded a slightly younger age of 56.3 ± 2.1 Ma (see 7.6), but it is possible that the sampled phase was part of the 'earliest porphyry' date by Simmons et al. (2013) at 58.5-57.5 Ma. This magmatic pulse marks the point at which porphyry-fertile magmatic conditions are first recorded in whole rock Eu/Eu* and Sr/Y, and zircon Eu/Eu*, reflecting deep, hydrous fractionation and oxidizing conditions (Nathwani et al., 2021).

This increase in magma fertility occurred $\sim 3.5 \pm 1.7$ My prior to the major mineralizing event at Quellaveco (~ 55 Ma, Sillitoe and Mortensen, 2010). This interval is suggested to have provided sufficient time for the accumulation of hydrous magma in a shallow crustal reservoir, prior to porphyry emplacement and hydrothermal fluid release (Nathwani et al., 2021). Crustal-scale fault systems are envisaged to have been the primary conduits for magma transport from a deep crustal 'hot zone', with secondary structures playing a role in localization magmas and fluids during their emplacement into the brittle, shallow crust.

Toquepala

On a map-scale, the pre-porphyry emplacement of the granodiorite intrusions appears to be structurally influenced. At Toquepala, where there is the largest body of granodiorite, the intrusion follows a distinct NE-SW orientation. This is interspersed with a minor area of branching along NW-SE structures. These branches coincide with the location of major NW-SE lineaments and faults, such as the MF. This suggests that the localisation of magmatism at this time was influenced by dilation of NE-SW structures, particularly at intersections between these and the NW-SE faults.

Early porphyries at Toquepala are reported to follow NE-SW trends. The deposit itself formed at the convergence of the Micalaco and a substantial NE-trending fault (AA internal report, 2018). Porphyry emplacement at Toquepala occurred between 57-54 Ma (Sillitoe and Mortensen, 2010; Simmons et al., 2013). A4 propylitic

alteration approximately 4.5-5 km north of Toquepala yielded an age of 57.4 ± 2.9 Ma (see 7.6), consistent with the outer parts of the porphyry-related halo. The collection of samples (RCS003-RCS009) in area (b) showed signals of intermediate to low sulphidation epithermal character in the discriminant projection analysis (see 8.4.5 and 8.5.7) which is a characteristic feature of intermediate to distal samples within porphyry-related propylitic alteration.

Quellaveco porphyry

Vein stockwork associated with the Quellaveco porphyry is shown to follow predominantly NE-SW and NW-SE orientations (AA internal report, 2018, see 6.5). The dominant orientation of veining in the porphyry proximal (<3 km) area is NE-SW. Minor N-S oriented veins, recorded to the south of the deposits (Sanchez, 2017), suggest a potential radial distribution of the veining.

The similarity in formation age for three deposits (~57-54 Ma) is a little unusual given the distance between Cuajone and Toquepala (~30 km). As a typical upper crustal batholith rarely exceeds 15 km in length, a single magma body is unlikely. Therefore, Simmons et al. (2013) suggested that almost coeval emplacement of porphyries was a result of contemporaneous, but spatially distinct late stage magmatism around the margins of the Yarabamba batholith.

Evidence that the NE-SW structures influenced fluid migration during the waning of the Quellaveco system is provided by the late-stage quartz-pyrite (V9) veins, classified as 'D-type' veins (e.g. Gustafson and Hunt, 1975; Sillitoe and Mortensen, 2010; Simmons, 2014). Field observations in the region of 1.5-3 km from the deposit recorded V9 veins with a clear NE-SW influence (see 6.5); proximal to Quellaveco (<1 km) the D-type veins are observed as parallel, NW-SE-trending veins, following the Quellaveco Fault (AA internal report, 2018). A distinct NW- to WNW corridor of advanced argillic and sericitic alteration also follows the Quellaveco fault,

propagating along strike from the deposit itself (AA internal report, 2018).

9.4.4 *Post mineralisation fault activity and alteration*

One isolated sample (RCS104), located ~5 km WNW of Toquepala, and directly adjacent to the MF, is briefly mentioned here because of its structural and geochronological significance. The A4 alteration in this sample yielded a much younger age (44.9 ± 3.5 Ma) than any other sample and showed anomalous geochemical signatures that also contrast with other samples, for example exceptionally low Zn ppm (see 8.4.5). Discriminant projection analysis of the epidote data classified the alteration as having an intermediate to low sulphidation affinity.

The sample is located in the Yarito area, which occurs along the intersection between the Micalaco Fault and the NE-SW Yarito-Pacay lineament and which is thought to be responsible for the 'Pacay – Tumba Cactus' prospect discussed in Model 2. Low magnetic anomalies highlight this NE-SW corridor (AA internal report, 2018). The MF is also believed to be the feeder structure for the Toquepala deposit (Zweng P. & Clark, 1996; Richards, 2003; Simmons *et al.*, 2013; Sanchez, 2017). Therefore, if the geochronology is to be trusted, this would provide evidence for continued fault activation, and much later propylitic alteration potentially related to an epithermal system.

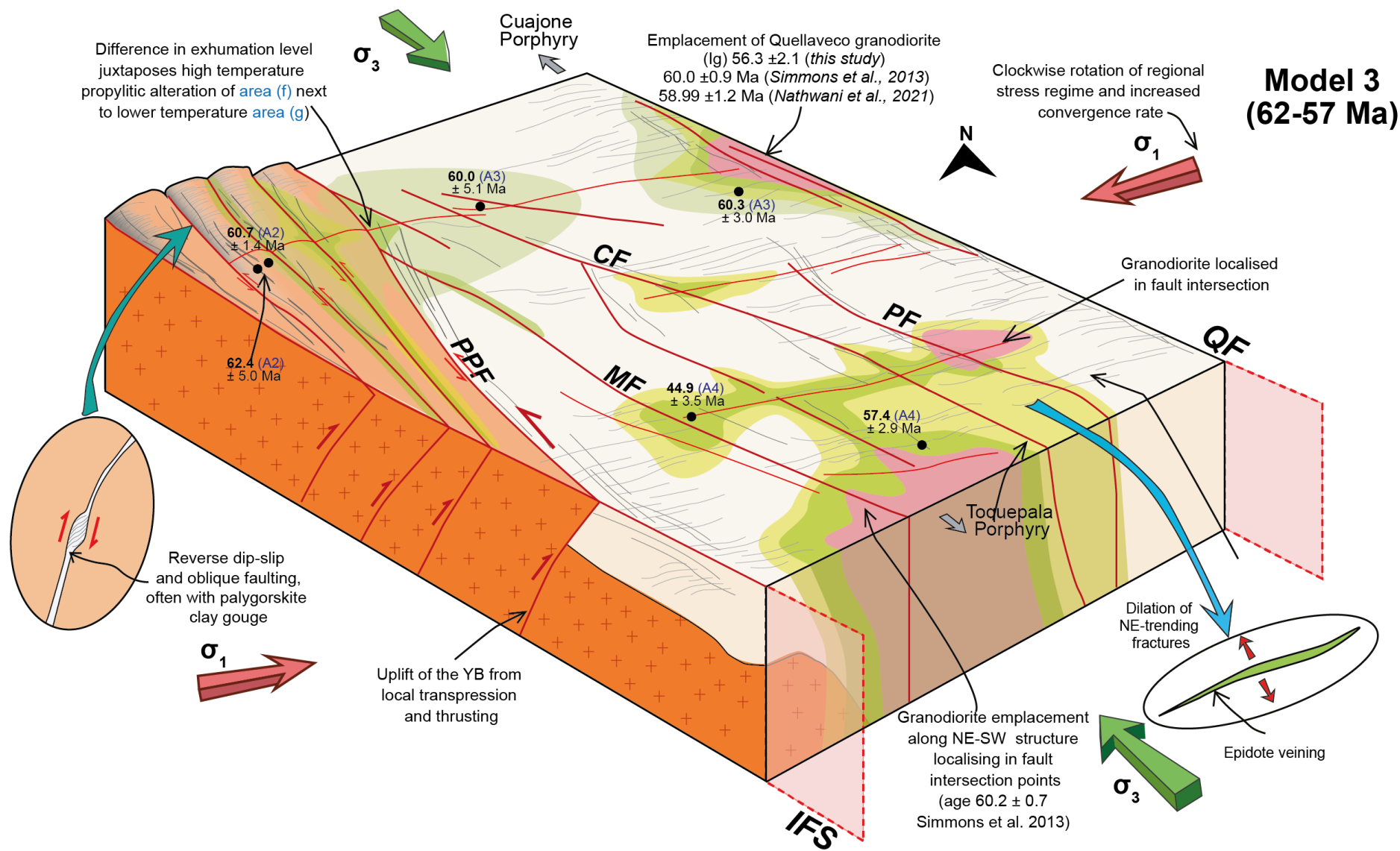


Figure 9.3. Model 3 (62-57 Ma) – a summary model of the findings and interpretations from this study

10 Conclusions

- Comparisons made between known metamorphic terranes and the Quellaveco dataset highlighted distinct differences in the mineral chemistry of the Quellaveco-district propylitic alteration. The characteristics of its dataset showed a closer affinity to propylitic alteration associated with distal areas of porphyry centres.
- U-Pb dating of propylitic apatite, titanite, epidote and zircon revealed an extensive period of propylitic alteration between 72-60 Ma, with an alteration maximum concentrating at 65-69 Ma. This peak in propylitic alteration occurred ~8-12 My prior to the onset of mineralisation at the known porphyry centres in the Quellaveco region. It is concluded that the propylitic alteration developed over a much longer time frame than previously thought.
- The mineral chemistry of epidote and chlorite identified an unexplored area (area g) displaying strong porphyry-like signals and high Mn and Zn fertility. Geochemical gradients recorded a lateral transition from porphyry-proximal to distal porphyry propylitic alteration. These trends are detected up to 6 km from the suggested porphyry zone (area g). Dating of alteration assemblages exhibiting these gradients has constrained the approximate timing of this event to 68-70 Ma.
- Chlorite vectoring and geothermometry provided evidence for high temperature fluids utilizing the PPF and parts of the IFS. Distinct changes in chlorite titanium concentrations and propylitic actinolite assemblages recorded the dispersion of high temperature alteration away from the NW-SE structures.
- A shift in the regional stress field at 59 Ma caused sinistral transpression along the IFS. It is believed that this led to thrusting and a positive flower structure between the IFS and PPF, resulting in the exhumation of the oldest units of the Yarabamba Batholith and high temperature propylitic alteration.
- Fracture mapping and modelling have highlighted the importance of the NE-SW structures, in particular the intersections between NE-SW and

NW-SE major faults in the localisation fluids and concentration of alteration.

11 References

- Abdi, H. & Williams, L.J. (2010), 'Principal component analysis', *Interdisciplinary Reviews: Computational Statistics* **2** (4), 433–459.
- Acocella, V. & Funiciello, F. (2010), 'Kinematic setting and structural control of arc volcanism', *Earth and Planetary Science Letters* **289**(1-2), 43–53.
- Albarède, F. (2009), *Geochemistry: an introduction.*, 2nd edn, Cambridge University Press, Cambridge.
- Allaby, M. (2008) *Oxford Dictionary of Earth Sciences*. Oxford University Press Inc
- Allmendinger, R.W., Smalley, R., Bevis, M., Caprio, H. & Brooks, B. (2005), 'Bending the Bolivian orocline in real time.' *Geology*. **33** (11), 905–908.
- Andersen, T. (2002), 'Correction of common lead in U-Pb analyses that do not report 204Pb', *Chemical Geology* **192**(1-2), 59–79.
- Arancibia G; Matthews, S. & de Arce, C. (2006), 'K-Ar and 40Ar/39Ar geochronology of supergene processes in the Atacama Desert, Northern Chile: tectonic and climatic relations', *Journal of the Geological Society* **163**, 107– 118.
- Arevalo, R., Ni, Z. & Danell, R. M. (2020), 'Mass spectrometry and planetary exploration: A brief review and future projection', *Journal of Mass Spectrometry* **55**(1).
- Arriagada, C., Roperch, P., Mpodozis, C. & Cobbold, P.R. (2008), 'Paleogene building of the Bolivian Orocline: Tectonic restoration of the central Andes in 2-D map view', *Tectonics* **27** (6), 1–14.
- Audin, L., David, C., Hall, S., Farber, D. & H´erail, G. (2006), 'Geomorphic evidences of recent tectonic activity in the forearc, southern Peru', *Revista de la Asociacion Geologica Argentina* **61**(4), 545–554.
- Audin, L., Lacan, P., Tavera, H. & Bondoux, F. (2008), 'Upper plate deformation and seismic barrier in front of Nazca subduction zone: The Chololo Fault

- System and active tectonics along the Coastal Cordillera, southern Peru', *Tectonophysics* **459** (1–4), 174–185.
- Bailey, S.W. (1980), 'Summary of recommendations of AIPEA Nomenclature Committee on clay minerals', *American Mineralogist* **65** (1–2), 1–7.
- Baker, M., Cooke, D., Hollings, P. & Piquer, J. (2017) Identification of hydrothermal alteration related to mineralisation using epidote mineral chemistry'. In: *Proceedings of the 14th SGA Biennial Meeting: Mineral Resources to Discover*, 1069–1071.
- Baker, M. J., Crawford, A. J. & Withnall, I. W. (2010), 'Geochemical, Sm-Nd isotopic characteristics and petrogenesis of Paleoproterozoic mafic rocks from the Georgetown Inlier, north Queensland: Implications for relationship with the Broken Hill and Mount Isa Eastern Succession', *Precambrian Research* **177**(1-2), 39–54.
- Baker, M.J., Wilkinson, J.J., Wilkinson, C.C., Cooke, D.R. & Ireland, T. (2020), 'Epidote Trace Element Chemistry as an Exploration Tool in the Collahuasi District, Northern Chile', *Economic Geology* **115**(4), 749–770.
- Balberg, I., Anderson, C. H., Alexander, S. & Wagner, N. (1984), 'Excluded volume and its relation to the onset of percolation', *Physical Review B* **30**(7), 3933–3943.
- Ballantyne, G. H. (1981), 'Chemical and mineralogical variations in propylitic zones surrounding porphyry copper deposits', MPhil Thesis, University of Utah.
- Bartholomew, D.J. (2010) 'Principal Components Analysis'. In: *International Encyclopedia of Education*. pp. 374–377.
- Barton, C.C., Hsieh, P.A., Angelier, J., Bergerat, F., Bouroz, c., Dettinger, M. & Weeks E. (1989), 'Physical and Hydrologic-Flow Properties of Fractures Las Vegas, Nevada—Zion Canyon, Utah—Grand Canyon, Arizona—Yucca Mountain, Nevada July 20–24, 1989,' *American Geophysical Union*.
- Battles, D. A. & Barton, M. D. (1995), 'Arc-related sodic hydrothermal alteration in the western US', *Geology* **23**(10), 913–916.

- Bellido, E. (1979), 'Geología del cuadrángulo de Moquegua (hoja: 35-u): Lima, Peru', *Geológico Minero y Metalurgico* **15**, 78.
- Belousova, E. A., Walters, S., Griffin, W. L. & O'Reilly, S. Y. (2001), 'Trace element signatures of apatites in granitoids from the Mt Isa Inlier, Northwestern Queensland', *Australian Journal of Earth Sciences* **48**(4), 603–619.
- Belov, N.V. & Rumanova, J.W. (1953), 'The crystal structure of epidote $\text{Ca}_2\text{Al}_2\text{FeSi}_3\text{O}_{12}(\text{OH})$ ' *Doklady Akademii Nauk SSSR*. **89** (853–6).
- Berger, B. R., Ayuso, R. A., Wynn, J. C., Seal, R. R. (2008), 'Preliminary model of porphyry copper deposits', *Open File Report - U.S. Geological Survey* p. 55.
- Berger B.R. & Drew, L. J. (2002), *Mineral-Deposit models*, Vol. 80, Springer, Dordrecht.
- Berkowitz, B. (2002), 'Characterizing flow and transport in fractured geological media: A review', *Advances in Water Resources* **25**(8-12), 861–884.
- Bernet, M. & Garver, J. (2005), 'Fission-track analysis of detrital zircon', *Reviews in Mineralogy and Geochemistry* **58**, 205–238.
- Bernini, D., Audetat, A., Dolejs, D. & Keppler, H. (2013), 'Zircon solubility in aqueous fluids at high temperatures and pressures', *Geochimica et Cosmochimica Acta* **119**, 178–187.
- Bonazzi, P. & Menchetti, S. (1995), 'Monoclinic members of the epidote group: effects of the Al - Fe³⁺- Fe²⁺ substitution and of the entry of REE³⁺', *Mineralogy and Petrology* **53**, 133–153.
- Bonnier, F. & Byrne, H.J. (2012), 'Understanding the molecular information contained in principal component analysis of vibrational spectra of biological systems', *The Analyst*, **137** (2), 322–332.
- Boutelier, D.A. & Oncken, O. (2010), 'Role of the plate margin curvature in the plateau buildup: Consequences for the central Andes', *Journal of Geophysical Research: Solid Earth* **115** (4), 1–18.

- Bouzari, F., Hart, C.J.R., Bissig, T. & Barker, S. (2016), 'Hydrothermal Alteration Revealed by Apatite Luminescence and Chemistry: A Potential Indicator Mineral for Exploring Covered Porphyry Copper Deposits', *Economic Geology* **111** (6), 1397–1410.
- Bravo, E. B. (1979), 'Geología del Cuadrángulo de Moquegua', *Instituto geológico minero y metalúrgico* **20**, 85.
- Brugge, E. R. (2020), 'Apatite in Porphyry Systems and its Applications in Mineral Exploration', PhD Thesis, Imperial College London, 298.
- Buick, I.S., Frei, R. & Cartwright, I. (1999), 'The timing of high-temperature retrogression in the Reynolds Range, central Australia: constraints from garnet and epidote Pb-Pb dating', *Contributions to Mineralogy and Petrology* **135** (2), 244–254.
- Burnham, A. D. & Berry, A. J. (2012), 'An experimental study of trace element partitioning between zircon and melt as a function of oxygen fugacity', *Geochimica et Cosmochimica Acta* **95**, 196–212.
- Caine, J. S., Evans, J. P. & Forster, C. B. (1996), 'Fault zone architecture and permeability structure', *Geology* **24**(11), 1025–1028.
- Camus, F. & Dilles, J. H. (2001), 'A special issue devoted to porphyry copper deposits of northern Chile preface', *Economic Geology* **96**(2), 233–237.
- Celik, M., Karakaya, N. & Temel, A. (1999), 'Clay Minerals in Hydrothermally Altered Volcanic Rocks, Eastern Pontides, Turkey', *Clays and Clay Minerals* **47**(6), 708–717.
- Celis, A. (2015), Titanite as an indicator mineral for alkalic Cu-Au porphyry deposits in south central British Columbia, Thesis.
- Cembrano, J. (2014) Fondecyt 'National Research Funding Competition' *National Commission for Scientific & Technological Research Official Version 2014*.
- Cembrano, J., González, G., Arancibia, G., Ahumada, I., Olivares, V. & Herrera, V. (2005), 'Fault zone development and strain partitioning in an extensional

strike-slip duplex: A case study from the Mesozoic Atacama fault system, Northern Chile', *Tectonophysics* **400**(1-4), 105–125.

Cembrano, J. & Lara, L. (2009) The link between volcanism and tectonics in the southern volcanic zone of the Chilean Andes: A review. *Tectonophysics*. [Online] 471 (1–2), 96–113.

Černý, P. (1970), 'Compositional variations in cookeite', *The Canadian Mineralogist* (10), 636–647.

Chang, Z., Hedenquist, J. W., White, N. C., Cooke, D. R., Roach, M., Deyell, C. L., Garcia, J., Gemmell, J. B., McKnight, S. & Cuisson, A. L. (2011), 'Exploration tools for linked porphyry and epithermal deposits: Example from the mankayan intrusion-centered Cu-Au district, Luzon, Philippines', *Economic Geology* **106**(8), 1365–1398.

Charrier, R., Baeza, O., Elgueta, S., Flynn, J. J., Gans, P., Kay, S. M., Munoz, N., Wyss, A. R. & Zurita, E. (2002), 'Evidence for Cenozoic extensional basin development and tectonic inversion south of the flat-slab segment, southern Central Andes, Chile (33 -36 S.L.)', *Journal of South American Earth Sciences* **15**(1), 117–139.

Charrier, R., Hérail, G., Pinto, L., García, M., Riquelme, R., Farías, M & Muñoz, N. (2013), 'Cenozoic tectonic evolution in the Central Andes in northern Chile and west central Bolivia: Implications for paleogeographic, magmatic and mountain building evolution', *International Journal of Earth Sciences* **102** (1), 235–264.

Chen, Y. W., Wu, J. & Suppe, J. (2019), 'Southward propagation of Nazca subduction along the Andes', *Nature* **565**(7740), 441–447.

Chew, D.M., Petrus, J.A. & Kamber, B.S. (2014) U-Pb LA-ICPMS dating using accessory mineral standards with variable common Pb. *Chemical Geology*. [Online] 363, 185–199.

Chew, D. M., Sylvester, P. J. & Tubrett, M. N. (2011), 'U-Pb and Th-Pb dating of apatite by LA-ICPMS', *Chemical Geology* **280**(1-2), 200–216.

- Clark, A. H., Tosdal, R. M., Farrar, E. & Plazolles V., A. (1990), 'Geomorphologic environment and age of supergene enrichment of the Cuajone, Quellaveco, and Toquepala porphyry copper deposits, southeastern Peru', *Economic Geology* **85**(7), 1604–1628.
- Coira, B., Davidson, J., Mpodozis, C. & Ramos, V. (1982), 'Tectonic and magmatic evolution of the Andes of northern Argentina and Chile', *Earth Science Reviews* **18**(3-4), 303–332.
- Condie, K. (2015), 'Changing tectonic settings through time: Indiscriminate use of geochemical discriminant diagrams', *Precambrian Research* **266**, 587–591.
- Cooke, D. R., Agnew, P., Hollings, P., Baker, M., Chang, Z., Wilkinson, J. J., Ahmed, A., White, N. C., Zhang, L., Thompson, J., Gemmell, J. B., Danyushevsky, L. & Chen, H. (2020), 'Recent advances in the application of mineral chemistry to exploration for porphyry copper–gold–molybdenum deposits: detecting the geochemical fingerprints and footprints of hypogene mineralization and alteration', *Geochemistry: Exploration, Environment, Analysis* **20**(2), 176–188.
- Cooke, D. R., Agnew, P., Hollings, P., Baker, M., Chang, Z., Wilkinson, J. J., White, N., Zhang, L., Thompson, J., Gemmell, J. B., Fox, N., Chen, H. & Wilkinson, C. C. (2017), Porphyry indicator minerals (PIMS) and porphyry vectoring and fertility tools (PVFTS) – indicators of mineralization styles and recorders of Hypogene geochemical dispersion halos, *in* P. o. E. 17, ed., 'Exploration 17: Sixth Decennial International Conference on Mineral Exploration', pp. 457–470.
- Cooke, D.R., Baker, M., Hollings, P., Sweet, G., Chang, Z., Danyushevsky, L., Gilbert, S., Zhou, T., White, N., Gemmell, B. & Inglis, S. (2014a), New advances in detecting the distal geochemical footprints of porphyry systems – epidote mineral chemistry as a tool for vectoring and fertility assessments. In: Karen Kelley & Howard Golden (eds.). *Building Exploration Capability for the 21st Century*. Boulder, CO, USA, Society of Economic Geologists. pp. 127–152.

- Cooke, D. R., Heithersay, P. S., Wolfe, R. & Calderon, A. L. (1998), 'Australian and western Pacific porphyry Cu-Au deposits', *AGSO Journal of Australian Geology and Geophysics* **17**(4), 97–104.
- Cooke, D. R., Hollings, P. & Walshe, J. L. (2005), 'Giant porphyry deposits: Characteristics, distribution, and tectonic controls', *Economic Geology* **100**(5), 801–818.
- Cooke, D. R., Hollings, P., Wilkinson, J. J. & Tosdal, R. M. (2014b), 'Geochemistry of Porphyry Deposits', in: Holland, H. D. & Turekian, K. K. (eds), 'Treatise on Geochemistry', 2nd edn. Elsevier, Oxford **13**, 357–381.
- Cooke, D. R., Wilkinson, J. J., Baker, M., Agnew, P., Wilkinson, C. C., Martin, H., Chang, Z., Chen, H., Gemmell, J. B., Inglis, S., Danyushevsky, L., Gilbert, S., Hollings, P. (2015), 'Using mineral chemistry to detect the location of concealed porphyry deposits – an example from Resolution, Arizona', *International Applied Geochemistry Symposium*, (April), 1–6.
- Corfu, F. & Stone, D. (1998), 'The significance of titanite and apatite U-Pb ages: Constraints for the post-magmatic thermal-hydrothermal evolution of a batholithic complex, Berens River area, northwestern Superior Province, Canada', *Geochimica et Cosmochimica Acta* **62**(17), 2979–2995.
- Cox, S.F., Knackstedt, M.A. & Braun, J. (2001) Principles of Structural Control on Permeability and Fluid Flow in Hydrothermal Systems. In: J P Richards & R Tosdal (eds.). 'Structural Controls on Ore Genesis', *Society of Economic Geologist Reviews*. p. 1–24.
- Cunningham, W. D. & Mann, P. (2007), 'Tectonics of strike-slip restraining and releasing bends', *Geological Society Special Publication* **290**, 1–12.
- Davidson, C., Schmid, S. & Hollister, L. (1994), 'Role of melt during deformation in the deep crust', *Terra Nova* **6** (2), 133–142.
- Davis, D. W., Williams, I. S. & Krogh, T. E. (2018), 'Historical development of zircon geochronology', *Zircon* pp. 145–181.
- Deer, W. A., Howie, R. A. & Zussman., J. (2013), *An Introduction to the Rock Forming Minerals*, 3rd edn, The Mineralogical Society.

- Deer, W.A., Howie, R.A. & Zussman., J. (2009) *Rock Forming Minerals 3B: Layered Silicates Excluding Micas and Clay Minerals*. 2nd edn. Geological Society of London.
- Demouy, S., Paquette, J. L., de Saint Blanquat, M., Benoit, M., Belousova, E. A., O'Reilly, S. Y., Garcia, F., Tejada, L. C., Gallegos, R. & Sempere, T. (2012), 'Spatial and temporal evolution of Liassic to Paleocene arc activity in southern Peru unravelled by zircon U-Pb and Hf in-situ data on plutonic rocks', *Lithos* **155**, 183–200.
- Dickin, A. P. (2018), *Radiogenic Isotope Geology*, 3 edn, Cambridge University Press.
- Dilles, J.H. (2010) 'Hydrothermal Alteration'. In: D A John (ed.). 'Porphyry copper deposit model: Chapter B of Mineral deposit models for resource assessment', *US Geological Survey Scientific Investigations Report*, 57–62
- Dilles, J. H., Farmer, G. I. & Field, C. W. (1995), 'Sodium-Calcium Alteration by Non-Magmatic Saline Fluids in Porphyry Copper Deposits: Results from Yerington, Nevada', *Mineralogical Association of Canada Short Course Series* **23**, 309–338.
- Dilles, J. H., Kent, A., Wooden, J. L., Tosdal, R. M., Koleszar, A., Lee, R. G. & Farmer, L. (2015), 'Zircon compositional evidence for sulfur-degassing from ore-forming arc magmas', *Economic Geology* **110**, 241–251.
- Djouka-Fonkwé, M. L., Kyser, K., Clark, A. H., Urqueta, E., Oates, C. J. & Ihlenfeld, C. (2012), 'Recognizing propylitic alteration associated with porphyry Cu-Mo deposits in lower greenschist facies metamorphic terrain of the Collahuasi district, northern Chile-implications of petrographic and carbon isotope relationships', *Economic Geology* **107**(7), 1457–1478.
- Douce, A.E.P. (1993), 'Titanium substitution in biotite: an empirical model with applications to thermometry, O₂ and H₂O barometries, and consequences for biotite stability', *Chemical Geology* **108** (1–4), 133–162.
- Duncan, R.J. & Maas, R. (2014), 'Assessing the origin of old apparent ages derived by Pb stepwise leaching of vein - hosted epidote from Mount Isa , northwest.'

- Dupuis, C. & Beaudoin, G. (2011), 'Discriminant diagrams for iron oxide trace element fingerprinting of mineral deposit types', *Mineralium Deposita* **46**, 319–335.
- Eisenbeiss, H. (2009) 'UAV Photogrammetry'. PhD thesis, ETH Swiss Federal Institute of Technology in Zürich.
- Elderry, S. M., Diaz, G. C., Prior, D. J. & Flint, S. S. (1996), 'Structural Styles in the Domeyko Range', pp. 17–19
- Fallourd, S., Poujol, M., Boulvais, P., Paquette, J. L., de Saint Blanquat, M. & Rémy, P. (2014), 'In situ LA-ICP-MS U-Pb titanite dating of Na-Ca metasomatism in orogenic belts: The North Pyrenean example', *International Journal of Earth Sciences* **103**(3), 667–682.
- Faulkner, D. R., Lewis, A. C. & Rutter, E. H. (2003), 'On the internal structure and mechanics of large strike-slip fault zones: Field observations of the Carboneras fault in southeastern Spain', *Tectonophysics* **367**(3-4), 235–251.
- Febbo, G.E., Kennedy, L.A., Nelson, J.A.L., Savell, M.J., Campbell, M.E., Creaser, R.A., Friedman, R.M., van Straaten, B.I. & Stein, H.J. (2019), 'The evolution and structural modification of the supergiant Mitchell Au-Cu porphyry, Northwestern British Columbia', *Economic Geology* **114** (2), 303–324.
- Feng, R., Machado, N. & Ludden, J. (1993), 'Lead geochronology of zircon by Laser Probe-inductively coupled plasma mass spectrometry (LP-ICPMS)', *Geochimica et Cosmochimica Acta* **57**(14), 3479–3486.
- Fossen, H. (2010), *Structural Geology*, 2nd edition, Cambridge University Press, University Printing House, Cambridge, UK.
- Fossen, H. & Tikoff, B. (1993), 'The deformation matrix for simultaneous simple shearing, pure shearing and volume change, and its application to transpression-transension tectonics', *Journal of Structural Geology* **15**(35), 413–422.

- Fossen, H. & Tikoff, B. (1998), 'Extended models of transpression and transtension, and application to tectonic settings', *Geological Society Special Publication* **135**, 15–33.
- Foster, M.D. (1962) Interpretation of the composition and a classification of the chlorites, *Professional Paper*
- Franz, G. & Liebscher, A. (2004) 'Physical and Chemical Properties of the Epidote Minerals-An Introduction', *Reviews in Mineralogy and Geochemistry* **56** (1), 1–81.
- Frei, D., Liebscher, A., Franz, G. & Dulski, P. (2004), 'Trace element geochemistry of epidote minerals', *Reviews in Mineralogy and Geochemistry* **56** (January), 553–605.
- Frei, R. & Kamber, B.S. (1995) 'Single mineral Pb-Pb dating', *Earth and Planetary Science Letters* **129** (1–4), 261–268.
- Frost, B. R., Chamberlain, K. R. & Schumacher, J. C. (2001), 'Sphene (titanite): Phase relations and role as a geochronometer', *Chemical Geology* **172**(1-2), 131–148.
- Fryer, B. J., Jackson, S. E. & Longerich, H. P. (1993), 'The application of laser ablation microprobe-inductively coupled plasma-mass spectrometry (LAMICP-MS) to in situ (U)Pb geochronology', *Chemical Geology* **109**(1-4), 1–8.
- Galbraith, R.F. (1988), 'Graphical Display of Estimates Having Differing Standard Errors', *Technometrics* **30** (3), 271–281.
- Galbraith, R. F. (1990), 'The radial plot: Graphical assessment of spread in ages', *International Journal of Radiation Applications and Instrumentation. Part* **17**(3), 207–214.
- Garwin, S. (2002), 'The geologic setting of intrusion-related hydrothermal systems near the Batu Hijau porphyry copper-gold deposit, Sumbawa, Indonesia': In Goldfarb, R. & Nielsen, R (eds) 'Integrated Methods for Discovery: Global Exploration in the Twenty-First Century', *Special Publications of the society of Economic Geologists* **9**.

- Geisler, T., Pidgeon, R.T., Kurtz, R., van Bronswijk, W. & Schleicher, H. (2003), 'Experimental hydrothermal alteration of partially metamict zircon', *American Mineralogist* **88** (10), 1496–1513.
- Geisler, T., Schaltegger, U. & Tomaschek, F. (2007), 'Re-equilibration of zircon in aqueous fluids and melts', *Elements* **3** (1), 43–50.
- Giambiagi, L. B., Ramos, V. A., Godoy, E., Alvarez, P. P. & Orts, S. (2003), 'Cenozoic deformation and tectonic style of the Andes, between 33 and 34 south latitude', *Tectonics* **22**(4)
- Grapes, R.H. & Hoskin, P.W. (2004) 'Epidote group minerals in low–medium pressure metamorphic terranes', *Reviews in Mineralogy and Geochemistry* **56** (1), 301–345.
- Grebennikov, A. V. & Khanchuk, A. I. (2021), 'Pacific-type transform and convergent margins: igneous rocks, geochemical contrasts and discriminant diagrams', *International Geology Review* **63**(5), 601–629.
- Gustafson, L. B. & Hunt, J. P. (1975), 'The porphyry copper deposit at El Salvador, Chile', *Economic Geology* **70** (5), 857–912.
- Haederle, M. & Atherton, M. P. (2002), 'Shape and intrusion style of the Coastal Batholith, Peru', *Tectonophysics* **345**(1-4), 17–28.
- Halley, S. (2016), 'Pathfinder element patterns in porphyry copper systems', *Course notes* p. 3.
- Halley S., Dilles. J. H. & Tosdal, R. M. (2015), 'Footprints: Hydrothermal Alteration and Geochemical Dispersion Around Porphyry Copper Deposits', *SEG Newsletter* **100**(100), 12–17.
- Harrison, T.M. & McDougall, I. (1980), 'Investigations of an intrusive contact, northwest Nelson, New Zealand—II. Diffusion of radiogenic and excess ^{40}Ar in hornblende revealed by $^{40}\text{Ar}/^{39}\text{Ar}$ age spectrum analysis', *Geochimica et Cosmochimica Acta* **44** (12), 2005–2020.
- Hart-Madigan, L. (2019), 'Mineral Transformations and Element Fluxes during Propylitic Alteration in Porphyry Ore Systems', PhD thesis, Imperial College London.

- Hart-Madigan, L., Wilkinson, J. J., Lasalle, S. & Armstrong, R. N. (2020), 'U-pb dating of hydrothermal titanite resolves multiple phases of propylitic alteration in the Oyu Tolgoi Porphyry District, Mongolia', *Economic Geology* **115**(8), 1605–1618.
- Hart, L., Wilkinson, J., Armstrong, R. & Araujo, D. (2016), 'Element mobility during propylitic alteration in porphyry ore systems: a case study of the Oyu Tolgoi deposits, Mongolia', *Applied Earth Science* **125**(2), 84.
- Healy, D., Rizzo, R. E., Cornwell, D. G., Farrell, N. J. C., Watkins, H., Timms, N. E., Gomez-Rivas, E. & Smith, M. (2017), 'FracPaQ: A MATLAB toolbox for the quantification of fracture patterns', *Journal of Structural Geology* **95**, 1–16.
- Heaman, L. M. (2009), 'The application of U–Pb geochronology to mafic, ultramafic and alkaline rocks: An evaluation of three mineral standards', *Chemical Geology* **261** (1), 43–52.
- Hedenquist, J. W., Arribas, A. & Reynolds, T. J. (1998), 'Evolution of an intrusion-centered hydrothermal system; Far Southeast-Lepanto porphyry and epithermal Cu-Au deposits, Philippines', *Economic geology and the bulletin of the Society of Economic Geologists* **93**(4), 373–404.
- Hedenquist, J. & Lowenstern, J. (1994a), 'The role of magmas in the formation of hydrothermal ore deposits', *Nature* **370**(6490), 519–527.
- Henry, D. J. & Guidotti, C. V. (2002), 'Titanium in biotite from metapelitic rocks: Temperature effects, crystal-chemical controls, and petrologic applications', *American Mineralogist* **87** (4), 375–382.
- Hervé, F., Pankhurst, R. J., Drake, R., Beck, M. E. & Mpodozis, C. (1993), 'Granite generation and rapid unroofing related to strike-slip faulting, Aysén, Chile', *Earth and Planetary Science Letters* **120**(3-4), 375–386.
- Hirata, T. & Nesbitt, R. W. (1995), 'U-Pb isotope geochronology of zircon: evaluation of the laser probe-inductively coupled plasma mass spectrometry technique', *Geochimica et Cosmochimica Acta* **59**(12), 2491–2500.

- Hodges, K. V. (2013), *Thermochronology in Orogenic Systems*, Vol. 4, 2 edn, Elsevier Ltd.
- Holliday, J.R. & Cooke, D.R. (2007), 'Advances in Geological Models and Exploration Methods for Copper ± Gold Porphyry Deposits,' *Proceedings of Exploration 07: Fifth Decennial International Conference on Mineral Exploration*, 791–809.
- Horn, I., Rudnick, R. L. & McDonough, W. F. (2000), 'Precise elemental and isotope ratio determination by simultaneous solution nebulization and laser ablation-ICP-MS: Application to U-Pb geochronology', *Chemical Geology* **164**(3-4), 281–301.
- Horstwood, M. S. A., Kořsler, J., Gehrels, G., Jackson, S. E., McLean, N. M., Paton, C., Pearson, N. J., Sircombe, K., Sylvester, P., Vermeesch, P., Bowring, J. F., Condon, D. J. & Schoene, B. (2016), 'Community-Derived Standards for LA-ICP-MS U-(Th)-Pb Geochronology – Uncertainty Propagation, Age Interpretation and Data Reporting', *Geostandards and Geoanalytical Research* **40**(3), 311–332.
- Horton, B. K. (2018), 'Tectonic Regimes of the Central and Southern Andes: Responses to Variations in Plate Coupling During Subduction', *Tectonics* **37**(2), 402–429.
- Hoyt, J. W. (1965), Regional Geology and Tectonic Setting for Mineral Deposits of Southwestern Peru, Thesis.
- Ito, T., Morimoto, N. & Sadanga, R. (1954), 'On the structure of Epidote', *Acta Crystallographica Section 7* (53–9).
- Jacay, J. & Sempere, T. (2005), 'Emplacement levels of the Coastal Batholith in Central Peru', *6th International Symposium on Andean Geodynamics (ISAG 2005, Barcelona)* (1), 397–399.
- Jacay, J., Sempere, T., Husson, L. & Pino, A. (2002), 'Structural Characteristics of the Incapuquio Fault System, Southern Peru', *International Symposium on Andean Geodynamics* (1), 319–321.

- Jackson, S.E., Longerich, H.P., Horn, I., Dunning, R. (1996), 'The application of laser ablation microprobe (LAM)-ICP-MS to in situ U-Pb zircon geochronology,' *Journal of Conference Abstracts* **1** (283).
- Jaillard, E., Hérail, G., Monfret, T. & Diaz-Martinez, E. (2000), 'Tectonic evolution of the Andes of Ecuador, Peru, Bolivia and Northernmost Chile'. In: *Tectonic evolution of South America* (Cordani, U.; Milani, E.; Thomaz Filho, A.; Campos; D.; editors). *International Geological Congress* : Río de Janeiro. 31 (January), 481–559.
- Jaillard, E. & Soler, P. (1996), 'Cretaceous to Early Paleogene tectonic evolution of the Northern Central Andes (0-18°S) and its relations to geodynamics' *Tectonophysics* 259.
- Jenner, F. E. & Arevalo, R. D. (2016), 'Major and Trace Element Analysis of Natural and Experimental Igneous Systems using LA-ICP-MS', *Elements* **12**, 311–316.
- Jochum, K.P., Weis, U., Stoll, B., Kuzmin, D., Yang, Q., Raczek, I., Jacob, D., Stracke, J.A., Birbaum, K., Frick, D., Günther, D. & Enzweiler, J. (2011), 'Determination of Reference Values for NIST SRM 610–617 Glasses Following ISO Guidelines', *Geostandards and Geoanalytical Research* **35** (4), 397–429.
- John, D. A., Ayuso, R. A., Barton, M. D., Blakely, R. J., Bodnar, R. J., Dilles, J. H., Gray, F., Graybeal, F. T., Mars, J. C., McPhee, D. K., Seal, R. R., Taylor, R. D. & Vikre, P. G. (2010), Porphyry Copper Deposit Model, *in* D. A. John, ed., 'Mineral Deposit Models for Resource Assessment', U. S. Geological Survey, Reston, Virginia, p. 186.
- Kelley, S. (2002), 'K-Ar and Ar-Ar dating', *Reviews in Mineralogy and Geochemistry* 47.
- Kielman, R., Whitehouse, M., Nemchin, A. & Kemp, A. (2018), 'A tonalitic analogue to ancient detrital zircon', *Chemical Geology* **499**(September), 43– 57.

- Kihien, A. (1995), 'Geologia, genesis de la mineralizacion-alteracion y evolucion de los fluidos hidrotermales en el partido de cobre de Quellaveco', *Sociedad Geologica del Peru Jubilar AI*, 159–178.
- Kirkland, C. L., Yakymchuk, C., Szilas, K., Evans, N., Hollis, J., McDonald, B. & Gardiner, N. J. (2018), 'Apatite: a U-Pb thermochronometer or geochronometer?', *Lithos* **318-319**, 143–157.
- Klein, C. & Philpotts, A. (2017), 'Earth materials: introduction to mineralogy and petrology', *Cambridge University Press*, 2nd edn, p. 616.
- Kley, J. (1999), 'Geologic and geometric constraints on a kinematic model of the Bolivian orocline', *Journal of South American Earth Sciences* **12** (2), 221–235.
- Kohn, M. J. & Corrie, S. L. (2011), 'Preserved Zr-temperatures and U-Pb ages in high-grade metamorphic titanite: Evidence for a static hot channel in the Himalayan orogen', *Earth and Planetary Science Letters* **311**(1-2), 136–143.
- Korenius, T., Laurikkala, J. & Juhola, M. (2007), 'On principal component analysis, cosine and Euclidean measures in information retrieval', *Information Sciences* **177** (22), 4893–4905.
- Lacy, W. C. (1991), 'Discovery and Development of the Toquepala and Cuajone deposits, Peru', Society for Mining, Metallurgy, and Exploration, Littleton, Colorado, pp. 53–61.
- Lang, J. R., Lueck, B., Mortensen, J. K., Russell, J. K., Stanley, C. R. & Thompson, J. F. H. (1995), 'Triassic-Jurassic silica-undersaturated and silica-saturated alkalic intrusions in the Cordillera of British Columbia: Implications for arc magmatism', *Geology* **23**, 451–454.
- Lauf, R.J. (2010), 'Collector's Guide to the Chlorite Group', *Rocks & minerals* **85** (4), 318–325.
- Lee, R. G., Byrne, K. & Lesage, G. (2020), 'Distal alteration facies of Late Triassic to Early Jurassic porphyry copper deposits, British Columbia , Canada : A green rock perspective', pp. 1–20.

- Li, X. C., Zhou, M. F., Chen, W. T., Zhao, X. F. & Tran, M. D. (2018), 'Uranium-lead dating of hydrothermal zircon and monazite from the Sin Quyen Fe-Cu-REE-Au-(U) deposit, northwestern Vietnam', *Mineralium Deposita* **53**(3), 399–416.
- Li, X. H., Liang, X. R., Sun, M., Guan, H. & Malpas, J. G. (2001), 'Precise $^{206}\text{Pb}/^{238}\text{U}$ age determination on zircons by laser ablation microprobe inductively coupled plasma-mass spectrometry using continuous linear ablation', *Chemical Geology* **175**(3-4), 209–219.
- Li, Y. & Vermeesch, P. (2021), 'Inverse isochron regression for Re–Os, K–Ca and other chronometers', *Geochronology Discussions* 1–8.
- Lindsay, D.D., Zentilli, M. & Rivera, J.R.D. La (1995), 'Evolution of an Active Ductile to Brittle Shear System Controlling Mineralization at the Chuquicamata Porphyry Copper Deposit, Northern Chile', *International Geology Review* **37** (11), 945–958.
- Lloyd, N.S., Sadekov, A.Y. & Misra, S. (2018), 'Application of 10 13 ohm Faraday cup current amplifiers for boron isotopic analyses by solution mode and laser ablation multicollector inductively coupled plasma mass spectrometry', *Rapid Communications in Mass Spectrometry* **32** (1), 9–18.
- Loader, M. A., Wilkinson, J. J. & Armstrong, R. N. (2017), 'The effect of titanite crystallisation on Eu and Ce anomalies in zircon and its implications for the assessment of porphyry Cu deposit fertility', *Earth and Planetary Science Letters* **472**, 107–119.
- Lowell, J. D. & Guilbert, J. M. (1970), 'Lateral and vertical alteration mineralization zoning in porphyry ore deposits', *Economic Geology* **65**(4), 373–408.
- Ludwig, K. R. (1991), 'Isoplot - a plotting and regression program for radiogenic isotope data', *Open-File Report - U. S. Geological Survey* pp. 91–445.
- Ludwig, K. R. (1998), 'On the treatment of concordant uranium-lead ages', *Geochimica et Cosmochimica Acta* **62**(4), 665–676.

- Maitre, R. W., Streckeisen, A., Le Zanettin, B., Le Bas, M. J., Bonin, B. & Bateman, P. (2002), *Igneous Rocks: A Classification and Glossary of Terms*, 2nd edn, Cambridge University Press, Cambridge, New York.
- Mamani, M., Tassara, A. & Worner, G. (2008), 'Composition and structural control of crustal domains in the central Andes', *Geochemistry, Geophysics, Geosystems* **9** (3).
- Manzocchi, T. (2002), 'The connectivity of two-dimensional networks of spatially correlated fractures', *Water Resources Research* **38** (9), 1-1-1–20.
- Mao, M., Rukhlov, A.S., Rowins, S.M., Spence, J. & Coogan, L. (2016), 'Apatite trace element compositions: A robust new tool for mineral exploration', *Economic Geology* **111** (5), 1187–1222.
- Martínez-Valladares, W., Marchena-Campos, A., Otero-Aguílar, J., Cervantes-Gárate, J., León-Lecaros, W. (2017), 'Geología y controles Tectonomagmáticos de los Sistemas Porfíricos en el Arco Magmático Occidental Sur de Perú', *INSTITUTO GEOLÓGICO MINERO Y METALÚRGICO - INGEMMET Dirección de Recursos Minerales y Energéticos - DRME Programa*. 113.
- Martinez, W. & Zuloaga, A. (2000), 'Memoria explicativa de la geología del cuadrángulo de Moquegua (35-u)', *Instituto Geológico, Minero y Metalurgico*, INGEMMET. 12.
- Martinod, J., Husson, L., Roperch, P., Guillaume, B. & Espurt, N. (2010), 'Horizontal subduction zones, convergence velocity and the building of the Andes', *Earth and Planetary Science Letters* **299** 299–309.
- Masterman, G. J. (2003), 'Structural and geochemical evolution of the Rosario copper-molybdenum porphyry deposit and related copper-silver veins, Collahuasi District', *PhD thesis, University of Tasmania* p. 253.
- Mauldon, M., Dunne, W. M. & Rohrbaugh, M.B. (2001), 'Circular scanlines and circular windows: new tools for characterizing the geometry of fracture traces', *Journal of Structural Geology* **23** (2), 247–258.

- McCaffrey, R. (1992), 'Oblique Plate Convergence, Slip Vectors, and Forearc Deformation', *Journal of Geophysical Research* **97**(B6), 8905–8915.
- McDowell, F. W., McIntosh, W. C. & Farley, K. A. (2005), 'A precise ^{40}Ar - ^{39}Ar reference age for the Durango apatite (U-Th)/He and fission-track dating standard', *Chemical Geology* **214**(3-4), 249–263
- McIntyre, G. A., Brooks, C., Compston, W. & Turek, A. (1966), 'The Statistical Assessment of Rb-Sr Isochrons', **71**(22), 5459–5468.
- MéGard, F. (1987), 'Cordilleran Andes and Marginal Andes: a Review of Andean Geology North of the Arica Elbow', *American Geophysical Union* 71–95.
- Mezger, K. & Krogstad, E. J. (1997), 'Interpretation of discordant U-Pb zircon ages: An evaluation', *Journal of Metamorphic Geology* **15**(1), 127–140.
- Mitchell, T. M. & Faulkner, D. R. (2009), 'The nature and origin of off-fault damage surrounding strike-slip fault zones with a wide range of displacements: A field study from the Atacama fault system, northern Chile', *Journal of Structural Geology* **31**(8), 802–816.
- Mpodozis, C., Arriagada, C., Basso, M., Roperch, P., Cobbold, P. & Reich, M. (2005), 'Late Mesozoic to Paleogene stratigraphy of the Salar de Atacama Basin, Antofagasta, Northern Chile: Implications for the tectonic evolution of the Central Andes', *Tectonophysics* **399**(1-4 SPEC. ISS.), 125–154.
- Mpodozis, C. & Ramos, V. (1989), 'The Andes of Chile and Argentina, in: Geology of the Andes and its Relation to Hydrocarbon and Mineral Resources', *Earth Sciences Series* **11**, 59–90.
- Mukasa, S.B. (1986), 'Zircon U – Pb ages of super-units in the Coastal Batholith, Peru. Implications for magmatic and tectonic processes', *in:* 'Zircon U-Pb ages of super-units in the Coastal batholith, Peru', *Geological Society of America Bulletin* **7606**.
- Mungall, J. (2002), 'Roasting the mantle: Slab melting and the genesis of major Au and Au-rich Cu deposits', *Geology* **30**(10), 915–918.

- Murray, H. H. (2007), 'Applied Clay Mineralogy - Occurrences, Processing and Application of Kaolins, Benoitites, Palygorskite-Sepiolite, and Common Clays', 1st edn, Elsevier, The Netherlands.
- Nathwani, C. L., Loader, M. A., Wilkinson, J. J., Buret, Y., Sievwright, R. H. & Hollings, P. (2020), 'Multi-stage arc magma evolution recorded by apatite in volcanic rocks', *Geology* **48**(4), 323–327.
- Nathwani, C. L., Simmons, A. T., Large, S. J. E., Wilkinson, J. J., Buret, Y. & Ihlenfeld, C. (2021), 'From long-lived batholith construction to giant porphyry copper deposit formation: petrological and zircon chemical evolution of the Quellaveco District, Southern Peru', *Contributions to Mineralogy and Petrology* **176**(2), 1–21.
- Neal, L. C., Wilkinson, J. J., Mason, P. J. & Chang, Z. (2018), 'Spectral characteristics of propylitic alteration minerals as a vectoring tool for porphyry copper deposits', *Journal of Geochemical Exploration* **184**(October 2017), 179–198.
- Noble, D. C., S'ebrier, M., Megard, F. & McKee, E. H. (1985), 'Demonstration of two pulses of Paleogene deformation in the Andes of Peru', *Earth and Planetary Science Letters* **73**(2-4), 345–349.
- Nozik, Y.K., Kanepit, V.N., Fykin, L.Y. & Makarov, Y.S. (1978), 'A neutron diffraction study of the structure of epidote' *Geochem. Int* **15** (66–69).
- Ossandón C., G., Fréaut C., R., Gustafson, L. B., Lindsay, D. D., Zentilli, M. (2001), 'Geology of the Chuquicamata mine: A progress report', *Economic Geology* **96**(2), 249–270.
- Pacey, A. (2017), The characteristics, geochemistry and origin of propylitic alteration in the Northparkes porphyry Cu-Au system., Thesis.
- Pacey, A., Wilkinson, J. J. & Cooke, D. R. (2020), 'Chlorite and epidote mineral chemistry in porphyry ore systems: A case study of the Northparkes district, New South Wales, Australia', *Economic Geology* **115**(4), 701–727.

- Pardo-Casas, F. & Molnar, P. (1987), 'Relative motion of the Nazca (Farallon) and South American Plates since Late Cretaceous time', *Tectonics* **6**(3), 233–248.
- Pawłowsky-Glahn, V., Egozcue, J.J. & Tolosana-Delgado, R. (2007), 'Lecture Notes on Compositional Data Analysis'
- Peacor, D., Rouse, R. & Bailey, S. (1988), 'Crystal structure of franklinfurnaceite: a tri-dioctahedral zincosilicate intermediate between chlorite and mica', *The American mineralogist* **73** (7), 876–887.
- Pelleter, E., Cheilletz, A., Gasquet, D., Mouttaqi, A., Annich, M., El Hakour, A., Deloule, E. & F'eraud, G. (2007), 'Hydrothermal zircons: A tool for ion microprobe U-Pb dating of gold mineralization (Tamlalt-Menhouhou gold deposit - Morocco)', *Chemical Geology* **245**(3-4), 135–161.
- Pfiffner, O. A. & Gonzalez, L. (2013), 'Mesozoic-cenozoic evolution of the western margin of South America: Case study of the peruvian andes', *Geosciences (Switzerland)* **3**(2), 262–310.
- Phillips, J. (2019), Geologic and geochemical vectors to mineralisation at the Resolution porphyry Cu-Mo deposit, Arizona, Phd thesis, University of Tazmania.
- Piquer, J., Berry, R. F., Scott, R. J. & Cooke, D. R. (2016), 'Arc-oblique fault systems: Their role in the Cenozoic structural evolution and metallogenesis of the Andes of central Chile', *Journal of Structural Geology* **89**, 101–117.
- Piquer, J., Skarmeta, J. & Cooke, D. R. (2015), 'Structural Evolution of the Rio Blanco-Los Bronces District, Andes of Central Chile: Controls on Stratigraphy, Magmatism, and Mineralization', *Economic Geology* **110**(8), 1995–2023.
- Pitcher, W.S. & Bussell, M.A. (1977), 'Structural control of batholithic emplacement in Peru: a review', *Journal of the Geological Society* **133** (3), 249–255.

- Quang, C.X. (2003), A thesis submitted to the Department of Geological Sciences and Geological Engineering in conformity with the requirements for the degree of Master of Science.
- Quang, C. X., Clark, A. H., W. Lee, J. K. & Hawkes, N. (2005), 'Response of Supergene Processes to Episodic Cenozoic Uplift, Pediment Erosion, and Ignimbrite Eruption in the Porphyry Copper Province of Southern Peru', *Economic Geology* **100**(1), 87–114.
- Ramos, V. A. (2010), 'The tectonic regime along the Andes: Present-day and Mesozoic regimes', *Geological Journal* **45**(1), 2–25.
- Ramos, V. A. & Folguera, A. (2009), 'Andean flat-slab subduction through time', *Geological Society Special Publication* **327**, 31–54.
- Reiners, P.W., Carlson, R.W., Renne, P.R., Cooper, K.M., Granger, D., McLean, N & Schoene, B. (2018), *Geochronology and thermochronology*, Wiley-Blackwell.
- Richards, J. P. (2003), 'Tectono-magmatic precursors for porphyry Cu-(Mo-Au) deposit formation', *Economic Geology* **98**(8), 1515–1533.
- Richards, J. P. (2015), 'The oxidation state, and sulfur and Cu contents of arc magmas: implications for metallogeny', *Lithos* **233**, 27–45.
- Richards, J. P., Boyce, A. J. & Pringle, M. S. (2001), 'Geologic evolution of the Escondida area, northern Chile: A model for spatial and temporal localization of porphyry Cu mineralization', *Economic Geology* **96**(2), 271–305.
- Robb, L. J. (2009), *Introduction to Ore-Forming Processes*, Wiley Blackwell.
- Roperch, P., Carlotto, V., Ruffet, G. & Fornari, M. (2011), 'Tectonic rotations and transcurrent deformation south of the Abancay deflection in the Andes of southern Peru', *Tectonics* **30**(2).
- Roperch, P., Sempere, T., Macedo, O., Arriagada, C., Fornari, M., Tapia, C., García, M. & Laj, C. (2006) 'Counter-clockwise rotation of late Eocene-Oligocene fore-arc deposits in southern Peru and its significance for oroclinal bending in the central Andes,' *Tectonics* **25** (3), 1–29.

- Rosenbaum, G., Giles, D., Saxon, M., Betts, P. G., Weinberg, R. F. & Duboz, C. (2005), 'Subduction of the Nazca Ridge and the Inca Plateau: Insights into the formation of ore deposits in Peru', *Earth and Planetary Science Letters* **239**(1), 18–32.
- Rukhlov, A.S., Plouffe, A., Ferbey, T., Mao, M. & Spence, J. (2016), 'Application of trace-element compositions of detrital apatite to explore for porphyry deposits in central British Columbia', *Geological Fieldwork* **2015** 145–179.
- Sanchez, M. (2017) 'Structure of the Quellaveco District - Technical Report and Recommendations'.
- Sandeman H., C. A. & Farrar, E. (1995), 'An Integrated Tectono-Magmatic Model for the Evolution of the Southern Peruvian Andes (13-20 S) since 55 Ma', *International Geology Review* **37**, 1039–1073.
- Sanderson, D. J. & Nixon, C. W. (2015), 'The use of topology in fracture network characterization', *Journal of Structural Geology* **72**, 55–66.
- Schaltegger, U., Schmitt, A. K. & Horstwood, M. S. A. (2015), 'U-Th-Pb zircon geochronology by ID-TIMS, SIMS, and laser ablation ICP-MS: Recipes, interpretations, and opportunities', *Chemical Geology* **402**, 89–110.
- Schepers, G., Van Hinsbergen, D. J. J., Spakman, W., Kosters, M. E., Boschman, L. M. & McQuarrie, N. (2017), 'South-American plate advance and forced Andean trench retreat as drivers for transient flat subduction episodes', *Nature Communications* **8**(0316), 1–9.
- Schneider, S., Hammerschmidt, K., Rosenberg, C. L., Gerdes, A., Frei, D. & Bertrand, A. (2015), 'U-Pb ages of apatite in the western Tauern Window (Eastern Alps): Tracing the onset of collision-related exhumation in the European plate', *Earth and Planetary Science Letters* **418**, 53–65.
- Schoene, B. (2014). 'U-Th-Pb Geochronology', *in*: Holland H., & Turekian, K., 'Treatise on Geochemistry', *Elsevier*, 341-378.
- Schoene, B., Condon, D. J., Morgan, L. & McLean, N. (2013), 'Precision and accuracy in geochronology', *Elements* **9**(1), 19–24.

- Sdrolias, M. & Müller, R.D. (2006), 'Controls on back-arc basin formation', *Geochemistry, Geophysics, Geosystems* **7** (4).
- Seedorff, E., Dilles, J. H., Proffett Jr., J. M., Einaudi, M. T., Zurcher, L., Stavast, W. J. A., Johnson, D. A. & Barton, M. D. (2005), 'Porphyry Deposits: Characteristics and Origin of Hypogene Features'.
- Sempere, T., Carlier, G., Soler, P., Fornari, M., Carlotto, V., Jacay, J., Arispe, O., Néraudeau, D., Cárdenas, J., Rosas, S. & Jiménez, N. (2002), 'Late Permian–Middle Jurassic lithospheric thinning in Peru and Bolivia, and its bearing on Andean-age tectonics', *Tectonophysics* **345**(1), 153–181.
- Sibson, R. H. (1986), 'Brecciation processes in fault zones: Inferences from earthquake rupturing', *Pure and Applied Geophysics PAGEOPH* **124**(12), 159–175.
- Sibson, R. H. (1987), 'Earthquake rupturing as a mineralizing agent in hydrothermal systems', *Geology* **15**(8), 701.
- Sibson, R. H. (2001), Seismogenic Framework for Hydrothermal Transport and Ore Deposition, in 'Structural Control of Mineral Deposits', pp. 25–50.
- Sibson, R. H., Robert, F. & Poulsen, K.H. (1988), 'High-angle reverse faults, fluid-pressure cycling, and mesothermal gold-quartz deposits', *Geology* **16** (6), 551–555.
- Siewwright, R. (2017), 'Developing magnetite chemistry as an exploration tool for porphyry copper deposits'. PhD thesis. Imperial College London.
- Sillitoe, R. H. (1972), 'A plate tectonic model for the origin of porphyry copper deposits', *Economic Geology* **67**(2), 184–197.
- Sillitoe, R.H. (1973) The tops and bottoms of porphyry copper deposits. *Economic Geology* **68** (6), 799–815.
- Sillitoe, R. H. (1993), *Gold-rich porphyry copper deposits: Geological model and exploration implications*, Vol. 40, pp. 465–478.
- Sillitoe, R. H. (1997), 'Characteristics and Controls of the Largest Porphyry Copper-Gold and Epithermal Gold Deposits in the Circum-Pacific Region', *Australian Journal of Earth Sciences* **44**, 373–388

- Sillitoe, R. H. (2008), 'Special paper: Major Gold Deposits and belts of the North and South American Cordillera: Distribution, tectonomagmatic settings, and metallogenic considerations', *Economic Geology* **103**(4), 663–687.
- Sillitoe, R. H. (2010), 'Porphyry copper systems', *Economic Geology* **105**(1), 3–41.
- Sillitoe, R. H. (2015), 'Epithermal paleosurfaces', *Mineralium Deposita* **50**(7), 767–793.
- Sillitoe, R. H. & Gappe, I. M. (1984), *Philippine porphyry copper deposits: geologic setting and characteristics*, Vol. 14, United Nations ESCAP, Bangkok, Thailand.
- Sillitoe, R. H. & McKee, E. H. (1996), 'Age of supergene oxidation and enrichment in the Chilean porphyry copper province', *Economic Geology* **91**(1), 164–179.
- Sillitoe, R. H. & Mortensen, J. K. (2010), 'Longevity of Porphyry copper formation at Quellaveco, Peru', *Economic Geology* **105**(6), 1157–1162.
- Sillitoe, R. H. & Perello, J. (2005), 'Andean copper province: Tectonomagmatic settings, deposit types, metallogeny, exploration, and discovery', *Economic Geology 100th Anni*, 845–890.
- Simmons, A. (2010), 'Report of Zircon U-Pb SHEIMP-RG Geochronology Results from the Toquepala and Cujone Mines', Internal report, Southern Peru Copper Corporation Anglo American Exploration Peru Minera Quellaveco.
- Simmons, A. (2013), 'Magmatic and Hydrothermal Stratigraphy of Paleocene and Eocene Porphyry Cu-Mo Deposits in Southern Peru', PhD Thesis, University of British Columbia, Vancouver.
- Simmons, A. T., Tosdal, R. M., Wooden, J. L., Mattos, R., Concha, O., McCracken, S. & Beale, T. (2013), 'Punctuated magmatism associated with porphyry Cu-Mo formation in the paleocene to Eocene of southern Peru', *Economic Geology* **108**(4), 625–639.
- Smilde, A.K., Jansen, J.J., Hoefsloot, H.C.J., Lamers, R.J.A., Van Der Greef, J.

- & Timmerman, M. (2005) ANOVA-simultaneous component analysis (ASCA): a new tool for analyzing designed metabolomics data. *Bioinformatics*. **21** (13), 3043–3048.
- Snow, D. T. (1968), 'Rock Fracture Spacings, Openings, and Porosities', *Journal of the Soil Mechanics and Foundations Divisions* **94**, 73–92.
- Soler, P. & Bonhomme, M. G. (1990), 'Relation of magmatic activity to plate dynamics in central Peru from Late Cretaceous to present', *Geological Society of America Bulletin* **241**, 173–192.
- Spencer, E. T., Wilkinson, J. J., Creaser, R. A. & Seguel, J. (2015), 'The distribution and timing of molybdenite mineralization at the El Teniente Cu-Mo porphyry deposit, Chile', *Economic Geology* **110**(2), 387–421.
- Spencer, K. J., Hacker, B. R., Kylander-Clark, A. R. C., Andersen, T. B., Cottle, J. M., Stearns, M. A., Poletti, J. E. & Seward, G. G. E. (2013), 'Campaign style titanite U-Pb dating by laser-ablation ICP: Implications for crustal flow, phase transformations and titanite closure', *Chemical Geology* **341**, 84–101.
- Stacey, J. S. & Kramers, J. D. (1975), 'Approximation of terrestrial lead isotope evolution by a two-stage model', *Earth and Planetary Science Letters* **26**(2), 207–221.
- Steiger, R. H. & Jäger, E. (1977), 'Subcommission on geochronology: Convention on the use of decay constants in geo- and cosmochemistry', *Earth and Planetary Science Letters* **36**(3), 359–362.
- Storey, C. D., Smith, M. P. & Jeffries, T. E. (2007), 'In situ LA-ICP-MS U-Pb dating of metavolcanics of Norrbotten, Sweden: Records of extended geological histories in complex titanite grains', *Chemical Geology* **240**(1-2), 163–181.
- Streckeisen, A. (1974), 'Classification and Nomenclature of Plutonic Rocks', *Geologische Rundschau* **63**(2), 773–786.

- Sylvester, P. J. & Jackson, S. E. (2016), 'A Brief History of Laser Ablation Inductively Coupled Plasma Mass Spectrometry (LA-ICP-MS)', *Elements* **12**, 307–310.
- Thomson, S. N., Gehrels, G. E., Ruiz, J. & Buchwaldt, R. (2012), 'Routine low-damage apatite U-Pb dating using laser ablation-multicollector-ICPMS', *Geochemistry, Geophysics, Geosystems* **13**(1), 1–23.
- Tibaldi, A. (2005), 'Volcanism in compressional tectonic settings: Is it possible?', *Geophysical Research Letters* **32**(6), 1–4.
- Tiepolo, M. (2003), 'In situ Pb geochronology of zircon with laser ablation inductively coupled plasma-sector field mass spectrometry', *Chemical Geology* **199**(1-2), 159–177.
- Tikoff, B. & Teyssier, C. (1994), 'Strain modelling of displacement-field partitioning in transpressional orogens', *Journal of Structural Geology* **16**(11), 1575–1588.
- Titley, S. R. (1993), 'Porphyry copper occurrence in the American southwest' [abs], *in*: Thorman, C.H. & Lane, D.E. (eds), 'U.S Geological Survey research on mineral resources – 1994, Part B Guidebook for field trips', *U.S. Geological Survey Circular* 1103, 15-23.
- Tombe, S.P., Richards, J.P., Greig, C.J., Board, W.S., Creaser, R.A., Muehlenbachs, K.A., Larson, P.B., DuFrane, S.A. & Spell, T. (2018), 'Origin of the high-grade Early Jurassic Brucejack epithermal Au-Ag deposits, Sulphurets Mining Camp, northwestern British Columbia', *Ore Geology Reviews* **95**, 480–517.
- Tosdal, R. M. (2005), Overview of the geologic setting and porphyry Cu-Mo deposits of southern Peru, *in* 'IV International Congress of the Prospectors and Explorers', Lima, Peru, pp. 1–22.
- Tosdal, R. M. & Richards, J. P. (2001), *Magmatic and Structural Controls on the Development of Porphyry Cu + Mo + Au Deposits*, Vol. 14, Society of Economic Geologist Reviews, book section 6, pp. 157–181.

- Vermeesch, P. (2012), 'On the visualisation of detrital age distributions', *Chemical Geology* **312-313**, 190–194.
- Vermeesch, P. (2018), 'IsoplotR: A free and open toolbox for geochronology', *Geoscience Frontiers* **9**, 1479–1493.
- Vermeesch, P. (2020), 'Unifying the U–Pb and Th–Pb methods: joint isochron regression and common Pb correction', *Geochronology* **2**(1), 119–131.
- Vermeesch, P. (2021), 'On the treatment of discordant detrital zircon U–Pb data', *Geochronology Discussions* pp. 1–19.
- Watson, E.B. & Harrison, T.M. (1983), 'Zircon saturation revisited: temperature and composition effects in a variety of crustal magma types', *Earth and Planetary Science Letters* **64** (2), 295–304.
- Watson, E.B., Wark, D.A. & Thomas, J.B. (2006), 'Crystallization thermometers for zircon and rutile', *Contributions to Mineralogy and Petrology* **151** (4), 413–433.
- Wendt, I. & Carl, C. (1991), 'The statistical distribution of the mean squared weighted deviation', *Chemical Geology: Isotope Geoscience Section* **86**(4), 275–285.
- White, W. M. (2015), 'Isotope Geochemistry', first edn, *Wiley-Blackwell*.
- Wibberley, C. A. J. & Shimamoto, T. (2003a), 'Internal structure and permeability of major strike-slip fault zones', *Journal of Structural Geology* **25**, 59– 78.
- Wiedenbeck, M., Allé, P., Corfu, F., Griffin, W.L., Meier, M., Oberli, F., Von Quadt, A., Roddick, J. & Spiegel, W. (1995), 'Three natural zircon standards for U-Th-Pb, Lu-Hf, trace element and REE analyses', *Geostandards Newsletter*. **19** (1), 1–23.
- Wilkinson, J. J. (2013), 'Triggers for the formation of porphyry ore deposits in magmatic arcs', *Nature Geoscience* **6** (11), 917–925.
- Wilkinson, J.J., Baker, M.J., Cooke, D.R. & Wilkinson, C.C. (2020), 'Exploration targeting in porphyry cu systems using propylitic mineral chemistry: A case

study of the El Teniente deposit, Chile', *Economic Geology*. **115** (4), 771–791.

Wilkinson, J. J., Chang, Z., Cooke, D. R., Baker, M. J., Wilkinson, C. C., Inglis, S., Chen, H. & Bruce Gemmell, J. (2015), 'The chlorite proximitor: A new tool for detecting porphyry ore deposits', *Journal of Geochemical Exploration* **152**, 10–26.

Wilkinson, J.J., Cooke, D.R., Baker, M.J., Chang, Z., Wilkinson, C. C., Chen, H., Fox, N., Hollings, P., White, N., Gemmell, J., Loader, M., Pacey, A., Sievwright, R., Hart, L. & Brugge, E. (2017), 'Porphyry indicator minerals and their mineral chemistry as vectoring and fertility tools', *in*: Mc Clenaghan, M. B. & Layton-Matthews, D, 'Application of indicator mineral methods to bedrock and sediments', *Geological Survey of Canada open file 8345*, 67–77.

Wotzlaw, J. F., Schaltegger, U., Frick, D.A., Dungan, M.A., Gerdes, A. & Günther, D. (2013), 'Tracking the evolution of large-volume silicic magma reservoirs from assembly to supereruption', *Geology*. **41**(8), 867–870.

York, D. (1968), 'Least squares fitting of a straight line with correlated errors', *Earth and Planetary Science Letters* **5** (C), 320–324.

Zimmermann, J. (1983), 'Détermination par la Méthode K/Ar de l'âge des Intrusions et des Minéralisations Associées dans le Porphyre Cuprifère de Quellaveco (Sud Ouest du Pérou)', *Mineralium Deposita* **18**, 207–213.

Zweng, P. L. & Clark, A. H. (1995), 'Hypogene evolution of the Toquepala porphyry copper-molybdenum deposit, Moquegua, southeastern Peru, in Pierce, F.W., and Bolm, J.G., eds', *Porphyry copper deposits of the American Cordillera: Arizona Geological Society Digest* **20**, 566–612.

Appendix A

Sample Information

Appendix A1: Tables with sample information: section number, geographical positioning, lithology/unit (TG: Toquepala Group, YB: Yarabamba Batholith), whether or not there has been whole rock geochemical analysis carried out on particular samples. Also present is the fracture intensity and density calculate using FracPaQ software (see Chapter 6 for more details). The abbreviations for the alteration classifications (outlined in Chapter 5) within each sample are as follows;

- Replacement alteration types: A1 potassic, A2 epidote-actinolite, A3 epidote-quartz, A4 albite-epidote, A5 epidote-titanite, A6 chlorite-calcite, A7 sericitic, A8 advanced argillic
- Vein types: V1 K-felspar, V2 epidote-actinolite, V3 epidote-quartz, V4 albite-epidote, V5 quartz, V6 quartz-albite-epidote, V7 calcite-epidote-chlorite, V8 sericite-dickite, V9 quartz-pyrite (no samples collected), BX breccia.

Identity		Position			Lithology/Unit				Whole Rock	Alteration Classification	Fractures	
Sample	Section	EAST_X	NORTH_Y	Elevation	Lithology	AA Map	Code	Unit			Intensity	Density
RCS001	1	333933	8098403	3966	Andesite?	Rhyolite	Q-SAM	TG	Y	A4, V4	0.073299	0.013937
RCS002	1	333918	8098392	3970	Granodiorite	Rhyolite	Q-SAM	TG	Y	/	0.073322	0.013902
RCS003	1	327486	8098122	3617	Andesite?	Granodiorite	P-GRD	TG	Y	A4	0.065867	0.011879
RCS004	1	327486	8098122	3617	Fault Material	Granodiorite	/	TG		/	0.065867	0.011879
RCS005	1	327487	8098117	3616	Fault Material	Granodiorite	/	TG		/	0.065844	0.011875
RCS006	1	327173	8097815	3597	Diorite	Granodiorite	P-GRD	TG	Y	A1, A3	0.063153	0.011542
RCS007	1	326876	8097584	3565	Rhyolite	Granodiorite	P-GRD	TG	Y	A4	0.060877	0.011270
RCS008	1	326826	8097426	3569	Rhyolite	Granodiorite		TG		A5, V3	0.059877	0.011118
RCS009	1	326840	8097385	3555	Rhyolite	Granodiorite	P-GRD	TG	Y	A4	0.059731	0.011089
RCS010	1	324204	8097696	3493	Rhyolite	Rhyolite	Q-SAM	TG	Y	/	0.051179	0.010570
RCS011	1	323967	8097403	3606	Rhyolite	Rhyolite	Q-SAM	TG	Y	/	0.050356	0.010431
RCS012	1	323711	8096614	3525	Rhyolite	Rhyolite	Q-SAM	TG	Y	A7	0.049410	0.010779
RCS013	1	323012	8096093	3448	Fault Material	/	/	/		/	0.047239	0.011567
RCS014	1	318331	8086042	2296	Andesite	Andesite	HUARA	TG	Y	A6	0.081553	0.016618
RCS015	1	318331	8086042	2296	Fault Material	/	/	/		/	0.081553	0.016618
RCS016	1	318610	8086214	2282	Andesite	Andesite	HUARA	TG	Y	A6	0.080510	0.016175
RCS017	1	318975	8086688	2277	Monzodiorite	Monzodiorite	P-MZD	YB	Y	A3, V2	0.078436	0.015682
RCS018	1	319006	8086784	2285	Monzodiorite	Monzodiorite		YB		A3, V2	0.078136	0.015666
RCS019	1	318978	8087411	2327	Monzodiorite	Monzodiorite	P-DRT	YB	Y	A2	0.075135	0.015648
RCS020	1	318978	8087411	2327	Fault Material	/	/	/		/	0.075135	0.015648
RCS021	1	319793	8088248	2428	Monzodiorite	Monzodiorite	P-MZD	YB	Y	/	0.065599	0.014980
RCS022	1	320101	8088633	2463	Monzodiorite	Monzodiorite	P-MZD	YB	Y	A2	0.061628	0.015160
RCS023	1	320306	8088971	2480	Monzodiorite	Monzodiorite	P-MZD	YB	Y	A1, BX	0.058436	0.015497
RCS024	1	335465	8102268	4235	Andesite	Rhyolite	Q-SAM	TG	Y	UA	0.077029	0.019113
RCS025	1	336024	8101160	4191	Andesite	Rhyolite	Q-SAM	TG	Y	A5	0.079837	0.020006
RCS026	1	335257	8099757	4028	Andesite	Rhyolite	Q-SAM	TG	Y	UA	0.074400	0.017553
RCS027	1	334807	8099506	4000	Andesite	Rhyolite	Q-SAM	TG	Y	UA	0.072645	0.016448
RCS028	1	334724	8099048	3974	Andesite	Rhyolite	Q-SAM	TG	Y	UA	0.073229	0.016000
RCS029	1	334468	8098825	3944	Rhyolite	Rhyolite	Q-SAM	TG	Y	A1	0.073014	0.015323
RCS030	1	333373	8098457	3958	Andesite	Rhyolite	Q-SAM	TG	Y	A5	0.072200	0.012922
RCS031	1	333133	8098221	3978	Rhyolite	Rhyolite	Q-SAM	TG	Y	A4, V3	0.073161	0.012426

Identity		Position			Lithology/Unit				Whole Rock	Alteration Classification	Fractures	
Sample	Section	EAST_X	NORTH_Y	Elevation	Lithology	AA Map	Code	Unit			Intensity	Density
RCS032	1	333020	8098020	3991	Andesite	Rhyolite	Q-SAM	TG	Y	A4	0.074128	0.012111
RCS033	1	333053	8098079	3988	Andesite	Rhyolite	Q-SAM	TG	Y	A4	0.073841	0.012204
RCS034	1	332652	8097796	4011	Rhyolite	Rhyolite	Q-SAM	TG	Y	A7	0.075002	0.011565
RCS035	1	332283	8097846	4052	Rhyolite	Rhyolite	Q-SAM	TG	Y	/	0.074152	0.011403
RCS036	1	332071	8097749	4041	Rhyolite	Rhyolite	Q-SAM	TG	Y	A1, A7	0.074188	0.011338
RCS037	2	309039	8098201	2623	Diorite	Diorite	P-DRT	YB	Y	A3	0.054093	0.016186
RCS038	2	309092	8098048	2624	Diorite	Diorite		YB		A4	0.052842	0.016078
RCS039	2	309094	8098144	2633	Diorite	Diorite	P-DRT	YB	Y	A3	0.053512	0.016143
RCS040	2	309255	8098068	2644	Diorite	Diorite		YB		A4	0.052436	0.016090
RCS041	2	309255	8098068	2644	Diorite	Diorite	P-DRT	YB	Y	A3	0.052436	0.016090
RCS042	2	309368	8098034	2647	Diorite	Diorite	P-DRT	YB	Y	A4	0.051810	0.016072
RCS043	2	309464	8098030	2671	Fault Material	/	/	/		/	0.051455	0.016071
RCS044	2	309671	8098052	2670	Diorite	Diorite	P-DRT	YB	Y	A2	0.050920	0.016081
RCS045	2	309865	8098031	2680	Fault Material	/	/	/		/	0.050105	0.016077
RCS046	2	310256	8098095	2730	Diorite	Diorite	P-DRT	YB	Y	A3	0.049295	0.016074
RCS047	2	310659	8097900	2749	Diorite	Diorite		YB		A3, V2	0.046360	0.016115
RCS048	2	310755	8097977	2759	Diorite	Diorite		YB		/	0.046681	0.016083
RCS049	2	310936	8098053	2774	Diorite	Diorite	P-DRT	YB	Y	A3	0.046834	0.015964
RCS050	2	310954	8098051	2776	Fault Material	/	/	/		/	0.046770	0.015957
RCS051	2	311239	8097639	2795	Diorite	Diorite Monz		YB		A3, V2, V4, V6	0.042456	0.016172
RCS052	2	311586	8097667	2831	Diorite	Diorite Monz	PDRTM	YB	Y	A3, V2	0.042229	0.015872
RCS053	2	311962	8098331	2931	Diorite	Diorite Monz	PDRTM	YB	Y	A1, A2	0.046597	0.014897
RCS054	2	312332	8098767	2942	Diorite	Diorite Monz	PDRTM	YB	Y	A1, A2	0.048400	0.014051
RCS055	2	312349	8098799	2959	Fault Material	/	/	/		/	0.048533	0.014002
RCS056	2	312635	8099146	3008	Diorite	Diorite Monz	PDRTM	YB	Y	A2, V1	0.049327	0.013308
RCS057	2	312843	8099427	3038	Diorite	Diorite Monz	PDRTM	YB	Y	A2	0.049670	0.012771
RCS058	2	312975	8099463	3052	Fault Material	/	/	/		BX	0.049134	0.012549
RCS059	2	313084	8099435	3056	Diorite	Diorite Monz	PDRTM	YB	Y	A3	0.048455	0.012416
RCS060	2	313282	8099504	3064	Rhyolite	Rhyolite	Q-YAR	TG	Y	/	0.047647	0.012070
RCS061	2	313262	8099430	3063	Diorite	Diorite Monz	PDRTM	YB	Y	A2	0.047515	0.012162
RCS062	2	312878	8101583	3016	Rhyolite	Rhyolite	Q-YAR	TG	Y	/	0.058918	0.010963

Identity		Position			Lithology/Unit				Whole Rock	Alteration Classification	Fractures	
Sample	Section	EAST_X	NORTH_Y	Elevation	Lithology	AA Map	Code	Unit			Intensity	Density
RCS063	2	312913	8102391	3006	Rhyolite	Rhyolite	Q-YAR	TG	Y	A8, V8	0.062410	0.010785
RCS064	2	313314	8103122	3051	Rhyolite	Rhyolite	Q-YAR	TG	Y	A4	0.061874	0.010692
RCS065	2	313946	8103328	3071	Rhyolite?	Rhyolite	Q-YAR	TG	Y	A6	0.056474	0.010325
RCS066	2	314786	8103733	3154	Rhyolite?	Rhyolite	Q-YAR	TG	Y	A3	0.051398	0.010328
RCS067	2	315528	8103261	3215	Andesite?	Rhyolite	Q-YAR	TG	Y	A5, V3	0.039032	0.008807
RCS068	2	316526	8102844	3244	Rhyolite	Rhyolite	Q-YAR	TG	Y	A6	0.024340	0.006906
RCS069	2	317558	8102200	3177	Rhyolite	Rhyolite	Q-YAR	TG	Y	A4	0.017220	0.006038
RCS070	2	317511	8102862	3082	Rhyolite	Rhyolite	Q-YAR	TG	Y	A4, V7	0.023389	0.007128
RCS071	2	318068	8102904	3041	Granodiorite	Monzodiorite	P-MZT	YB	Y	A3	0.025593	0.007595
RCS072	2	317788	8103570	3085	Rhyolite	Rhyolite	Q-CAR	TG	Y	A4, V7	0.033653	0.008834
RCS073	2	319697	8103557	3219	Granodiorite	Monzodiorite	P-MZT	YB	Y	A3	0.038720	0.009147
RCS074	2	320100	8103564	3234	Granodiorite	Monzodiorite		YB		A3, V5, V6	0.039930	0.009224
RCS075	2	320740	8103917	3280	Granodiorite	Monzodiorite	P-MZT	YB	Y	A3	0.046976	0.009434
RCS076	2	321732	8104324	3411	Diorite	Diorite	P-DRT	YB	Y	A3	0.056390	0.009400
RCS077	2	322032	8104843	3488	Granodiorite	Diorite	P-DRT	YB	Y	A3	0.065002	0.009230
RCS078	2	322734	8105674	3559	Fault Material	/	/	/	Y	V3, V4, V6	0.077932	0.008822
RCS079	2	322739	8105681	3560	Granodiorite	Monzodiorite	P-MZT	YB	Y	A3	0.078024	0.008819
RCS080	2	323952	8106353	3856	Rhyolite	Rhyolite	Q-SAM	TG	Y	/	0.083856	0.008973
RCS081	2	324357	8106351	3901	Rhyolite	Rhyolite	Q-SAM	TG	Y	A5	0.082790	0.009204
RCS082	2	324819	8107037	3917	Rhyolite	Rhyolite	Q-SAM	TG	Y	/	0.083885	0.009130
RCS083	2	325083	8107222	3931	Rhyolite	Rhyolite	Q-SAM	TG	Y	A7	0.083076	0.009256
RCS084	2	326283	8106997	3913	Rhyolite?	Rhyolite	Q-CAR	TG	Y	A3	0.077807	0.009800
RCS085	2	326283	8106997	3913	Fault Material	/	/	/		/	0.077807	0.009800
RCS086	2	327743	8106481	3963	Andesite?	Rhyolite	Q-CAR	TG	Y	A2	0.075822	0.010874
RCS087	2	327949	8106779	3979	Rhyolite	Rhyolite	Q-ASA	TG	Y	A6	0.075214	0.010627
RCS088	2	327949	8106779	3979	Rhyolite	Rhyolite		TG		A7	0.075214	0.010627
RCS089	2	328094	8107074	3992	Rhyolite	Granodiorite	P-GRD	QP	Y	A6	0.075289	0.010513
RCS090	2	328114	8107383	3865	Rhyolite	Granodiorite	P-GRD	YB	Y	A1	0.075113	0.010425
RCS091	2	328253	8107645	3853	Rhyolite?	Granodiorite	P-GRD	YB	Y	A7	0.076711	0.010823
RCS092	1	317413	8091544	2545	Monzodiorite	Monzodiorite	P-MZD	YB	Y	A3	0.046861	0.008466
RCS093	1	317574	8091857	2581	Rhyolite	Rhyolite	Q-YAR	TG	Y	A6	0.045726	0.008810

Identity		Position			Lithology/Unit				Whole Rock	Alteration Classification	Fractures	
Sample	Section	EAST_X	NORTH_Y	Elevation	Lithology	AA Map	Code	Unit			Intensity	Density
RCS094	1	317949	8092193	2637	Rhyolite?	Rhyolite	Q-YAR	TG	Y	A8	0.044514	0.009855
RCS095	1	318466	8092255	2718	Rhyolite	Rhyolite	Q-YAR	TG	Y	/	0.043744	0.011399
RCS096	1	318853	8092814	2857	Monzodiorite	Monzodiorite	P-MZD	YB	Y	A3	0.043086	0.012189
RCS097	1	322234	8095023	3401	Rhyolite	Rhyolite	Q-YAR	TG	Y	A5	0.043814	0.014107
RCS098	1	321007	8094745	3519	Rhyolite	Rhyolite	Q-YAR	TG	Y	A5	0.042906	0.014001
RCS099	1	320874	8094307	3478	Rhyolite	Rhyolite	Q-YAR	TG	Y	A5	0.042271	0.014656
RCS100	1	320637	8093924	3353	Rhyolite	Rhyolite	Q-YAR	TG	Y	/	0.041900	0.014937
RCS101	1	320437	8093441	3259	Rhyolite	Rhyolite	Q-YAR	TG	Y	/	0.041399	0.015343
RCS102	1	319887	8093304	3203	Rhyolite	Rhyolite	Q-YAR	TG	Y	A4	0.041998	0.014291
RCS103	1	322513	8095266	3328	Rhyolite	Rhyolite	Q-SAM	TG	Y	/	0.044666	0.013534
RCS104	1	323197	8096126	3506	Andesite	Rhyolite	Q-CAR	TG	Y	A4	0.047733	0.011456
RCS105	1	322755	8095774	3404	Rhyolite	Rhyolite	Q-CAR	TG	Y	V7	0.046050	0.012338
RCS106	1	320765	8089634	2550	Rhyolite	Rhyolite	Q-YAR	TG	Y	IFS	0.052169	0.016667
RCS107	1	320477	8089253	2507	Rhyolite	Rhyolite	Q-ASA	TG	Y	IFS	0.055815	0.015893

Appendix A1

Appendix B

Structure

Appendix B1 – A compilation table of all structural measurements (2345) recorded in the field. These are primarily recorded as fractures, but notes are made where kinematic indicators and other fault-indicative features are present.

Appendix B2 – Table showing all lineation data recorded in the field.

No.	X(East)	Y(North)	Z	Dip	Az	Strike	Type	Time Stamp	Remarks
1	317802.8	8092088.1	2611	73	4	274	Fracture	1540824656	
2	317792.52	8092084.9	2610	86	116	26	Fracture	1540824642	
3	317783.17	8092073.9	2607	88	318	228	Fracture	1540824407	Ne fractures (pic)
4	317782.35	8092080.6	2610	89	312	222	Fracture	1540824357	
5	317771.44	8092070.1	2606	80	289	199	Fracture	1540824315	
6	317771.44	8092070.1	2606	66	49	319	Fracture	1540824306	
7	317641.96	8091920.1	2575	72	135	45	Fracture	1540823724	
8	317638.34	8091924.4	2575	74	64	334	Fracture	1540823716	
9	317638.34	8091924.4	2575	67	139	49	Fracture	1540823706	(Pic)
10	317638.34	8091924.4	2575	58	151	61	Fracture	1540823687	
11	317608.3	8091919.8	2581	80	130	40	Fracture	1540823578	
12	317580.55	8091843.4	2565	68	324	234	Fracture	1540823244	
13	317576.9	8091851.2	2566	69	318	228	Fracture	1540823234	
14	317576.9	8091851.2	2566	73	61	331	Fracture	1540823227	
15	317565.06	8091833.9	2563	73	50	320	Fracture	1540822766	Large Fe-oxide fault zone (pic)
16	317567.19	8091837.5	2564	78	39	309	Fracture	1540822631	
17	317541.49	8091804.5	2560	87	60	330	Fracture	1540822112	
18	317538.19	8091799.1	2559	21	112	22	Fracture	1540822042	R16.1
19	317538.19	8091799.1	2559	76	351	261	Fracture	1540822024	
20	317534.96	8091796.6	2560	83	236	146	Fracture	1540821846	R16.1
21	317536.66	8091798.1	2560	65	66	336	Fracture	1540821809	
22	317526.82	8091799.8	2563	66	47	317	Fracture	1540821741	
23	317526.88	8091793.6	2561	78	61	331	Fracture	1540821728	
24	317528.77	8091782.1	2558	72	342	252	Fracture	1540821647	
25	317528.77	8091782.1	2558	82	76	346	Fracture	1540821635	
26	317516	8091763.4	2557	58	306	216	Fracture	1540821505	
27	317516	8091763.4	2557	72	29	299	Fracture	1540821498	
28	317514.29	8091754.5	2555	75	30	300	Fracture	1540821486	
29	317457.51	8091648.8	2542	60	127	37	Fracture	1540821229	
30	317457.51	8091648.8	2542	60	131	41	Fracture	1540821221	
31	317457.51	8091648.8	2542	61	29	299	Fracture	1540821187	
32	317454.4	8091643.1	2541	67	31	301	Fracture	1540821170	
33	317454.4	8091643.1	2541	71	29	299	Fracture	1540821160	
34	317454.4	8091643.1	2541	59	356	266	Fracture	1540821139	
35	317415.75	8091513.4	2533	66	153	63	Fracture	1540819659	
36	317415.75	8091513.4	2533	83	63	333	Fracture	1540819647	
37	317329.65	8091378.3	2512	78	352	262	Fracture	1540819325	
38	317318.4	8091365	2511	62	347	257	Fracture	1540819316	
39	317293.46	8091327.1	2507	57	255	165	Fracture	1540819208	
40	317288.45	8091322	2507	49	20	290	Fracture	1540819191	
41	317288.45	8091322	2507	72	134	44	Fracture	1540819183	
42	317288.45	8091322	2507	62	253	163	Fracture	1540819170	
43	317291.76	8091305.7	2505	58	343	253	Fracture	1540819084	
44	317282.41	8091291.2	2505	47	270	180	Fracture	1540819045	La parallel
45	317276.54	8091289.9	2507	73	53	323	Fracture	1540818960	
46	317276.54	8091289.9	2507	61	312	222	Fracture	1540818937	
47	317281	8091284.9	2505	48	327	237	Fracture	1540818867	
48	317271.28	8091272.2	2506	79	58	328	Fracture	1540818764	
49	317271.28	8091272.2	2506	47	6	276	Fracture	1540818756	
50	317245.36	8091250.9	2498	74	67	337	Fracture	1540818670	
51	317230.85	8091231.3	2496	87	128	38	Fracture	1540818650	
52	317230.85	8091231.3	2496	52	275	185	Fracture	1540818641	
53	317230.85	8091231.3	2496	80	50	320	Fracture	1540818617	
54	317214.84	8091232.8	2495	82	65	335	Fracture	1540818607	
55	317213	8091221.4	2495	46	147	57	Fracture	1540818515	Lots of epi on low angle fault (pic)
56	317187.02	8091209.8	2497	63	182	92	Fracture	1540818360	
57	317187.02	8091209.8	2497	74	75	345	Fracture	1540818332	
58	317203.19	8091226.2	2496	68	328	238	Fracture	1540818312	
59	317203	8091226.2	2496	86	79	349	Fracture	1540818299	Epi
60	313966.91	8103331.1	3081	58	249	159	Fracture	1540393360	RCS065
61	313961.03	8103333.1	3080	71	240	150	Fracture	1540393179	
62	313960.58	8103327	3085	59	217	127	Fracture	1540393140	Lots of parallel fractures
63	313953.12	8103329.4	3082	76	152	62	Fracture	1540393110	Fe-oxide on plane
64	313952.08	8103325	3085	50	258	168	Fracture	1540393070	
65	313952.08	8103325	3085	70	34	304	Fracture	1540393054	
66	313929.6	8103299.5	3090	27	14	284	Fracture	1540392832	R12.4
67	313929.6	8103299.5	3090	63	235	145	Fracture	1540392790	R12.4
68	313932.68	8103281.1	3093	23	143	53	Fracture	1540392530	La
69	313930.96	8103285.7	3092	83	235	145	Fracture	1540392360	Second contact between conglomerate and diorite
70	313933.99	8103282.6	3094	49	185	95	Fracture	1540392172	
71	313931.03	8103276.3	3092	50	181	91	Fracture	1540392157	
72	313931.03	8103276.3	3092	70	234	144	Fracture	1540392146	Back in diorite
73	313923.31	8103259	3087	57	53	323	Fracture	1540392085	
74	313910.95	8103230.7	3078	64	221	131	Fracture	1540392051	Lith contact?
75	313912.55	8103216.7	3078	72	44	314	Fracture	1540391757	Red staining
76	313903.07	8103191.5	3068	77	158	68	Fracture	1540391691	
77	313898.23	8103204	3066	49	7	277	Fracture	1540391673	
78	313874.66	8103194.4	3054	72	234	144	Fracture	1540391649	
79	313879.49	8103194.4	3057	83	168	78	Fracture	1540391639	

No.	X(East)	Y(North)	Z	Dip	Az	Strike	Type	Time Stamp	Remarks
80	313879.49	8103194.4	3057	74	219	129	Fracture	1540391597	
81	313797.98	8103168.6	3075	86	94	4	Fracture	1540391464	white clay
82	313780.54	8103179.4	3077	62	103	13	Fracture	1540391396	
83	313767.82	8103191.9	3072	66	111	21	Fracture	1540391376	white clay
84	313767.82	8103191.9	3072	83	91	1	Fracture	1540391358	white clay
85	313743.77	8103197.9	3076	84	105	15	Fracture	1540391298	
86	313743.77	8103197.9	3076	67	230	140	Fracture	1540391267	
87	313743.77	8103197.9	3076	51	233	143	Fracture	1540391250	
88	313724.81	8103202.5	3083	61	228	138	Fracture	1540391231	
89	313737.36	8103210.4	3071	59	214	124	Fracture	1540391207	
90	313421.13	8103190.1	3057	51	117	27	Fracture	1540390910	Parallel fractures
91	313421.13	8103190.1	3057	60	357	267	Fracture	1540390880	
92	313389.68	8103188.1	3050	55	80	350	Fracture	1540390863	
93	313389.68	8103188.1	3050	57	205	115	Fracture	1540390852	White gouge
94	313354.73	8103151.3	3052	52	117	27	Fracture	1540390780	
95	313356.75	8103160.4	3053	49	115	25	Fracture	1540390771	
96	313356.75	8103160.4	3053	77	212	122	Fracture	1540390766	
97	313343.48	8103112.2	3041	73	200	110	Fracture	1540390205	
98	313343	8103149.2	3043	84	215	125	Fracture	1540389977	Large fault and gouge with pink alteration (pic)
99	313337.83	8103119.2	3039	71	36	306	Fracture	1540389929	white clay and some Fe-oxide
100	313331.13	8103100	3027	45	123	33	Fracture	1540389894	
101	313332.43	8103108.2	3031	46	119	29	Fracture	1540389886	
102	313324.11	8103117.7	3028	34	250	160	Fracture	1540389869	
103	313333.64	8103121.8	3035	30	249	159	Fracture	1540389860	
104	313205.58	8103002	3043	87	33	303	Fracture	1540389616	
105	313223.29	8103015.8	3034	52	120	30	Fracture	1540389515	
106	313203.94	8103012.8	3035	42	139	49	Fracture	1540389496	
107	313225.74	8103032.1	3024	80	76	346	Fracture	1540389471	
108	313225.74	8103032.1	3024	49	127	37	Fracture	1540389460	Parallel fractures
109	313242.13	8103041.8	3022	85	31	301	Fracture	1540389424	Minor gouge
110	313244.81	8103048.6	3019	42	119	29	Fracture	1540389391	
111	312937.88	8102968.8	3039	35	175	85	Fracture	1540387428	
112	312940.39	8102974.8	3040	84	355	265	Fracture	1540387395	Fe-oxide staining
113	312940.39	8102974.8	3040	52	307	217	Fracture	1540387364	
114	312936.08	8102979	3041	56	307	217	Fracture	1540387355	
115	312923.05	8103016.2	3046	27	287	197	Fracture	1540387191	La white alteration
116	312923.82	8103024.7	3046	79	170	80	Fracture	1540387081	
117	312920.92	8103035.8	3049	61	59	329	Fracture	1540386973	Lots of white mineral on
118	312919.95	8103045	3049	84	192	102	Fracture	1540386877	
119	312919.95	8103045	3049	32	274	184	Fracture	1540386865	
120	312916.59	8103046.7	3050	84	186	96	Fracture	1540386850	
121	312917.6	8103052.7	3048	87	23	293	Fracture	1540386639	Large Fracture with gouge and feix
122	312934.56	8103063.8	3038	25	66	336	Fracture	1540386549	
123	312934.56	8103063.8	3038	23	78	348	Fracture	1540386536	Parallel la
124	312950.46	8103077.6	3028	76	183	93	Fracture	1540386111	
125	312938.87	8103088.9	3032	25	6	276	Fracture	1540386081	
126	312938.87	8103088.9	3032	29	13	283	Fracture	1540386075	
127	312938.87	8103088.9	3032	85	358	268	Fracture	1540386047	
128	312937.36	8103097.5	3032	71	354	264	Fracture	1540386029	
129	312937.36	8103097.5	3032	79	1	271	Fracture	1540386014	
130	312910.16	8103089.6	3051	74	193	103	Fracture	1540385877	
131	313005.06	8102416.1	3006	76	202	112	Fracture	1540384563	
132	313005.06	8102416.1	3006	69	116	26	Fracture	1540384555	
133	313009.92	8102421.4	3006	89	216	126	Fracture	1540384537	
134	313007.12	8102420	3005	80	223	133	Fracture	1540384524	
135	312996.07	8102406.3	3008	44	21	291	Fracture	1540384201	
136	312996.07	8102406.3	3008	50	16	286	Fracture	1540384173	
137	312996.07	8102406.3	3008	84	207	117	Fracture	1540384162	
138	312989.06	8102405.9	3007	71	205	115	Fracture	1540384156	
139	312989.06	8102405.9	3007	66	119	29	Fracture	1540384150	
140	312973.31	8102393.9	3012	80	29	299	Fracture	1540383981	
141	312970.51	8102393.5	3011	69	40	310	Fracture	1540383961	
142	312970.51	8102393.5	3011	63	118	28	Fracture	1540383944	
143	312966.31	8102392.4	3011	79	98	8	Fracture	1540383898	
144	312965.59	8102395.2	3010	75	99	9	Fracture	1540383884	
145	312948.15	8102384.9	3013	59	206	116	Fracture	1540383826	
146	312948.15	8102384.9	3013	61	42	312	Fracture	1540383816	
147	312944.3	8102384.6	3013	69	49	319	Fracture	1540383795	
148	312933.08	8102378.2	3014	58	49	319	Fracture	1540383700	
149	312933.08	8102378.2	3014	70	30	300	Fracture	1540383694	
150	312923.62	8102377.5	3014	74	118	28	Fracture	1540383668	
151	312923.62	8102377.5	3014	69	31	301	Fracture	1540383661	
152	312923.62	8102377.5	3014	66	36	306	Fracture	1540383657	
153	312928.86	8102378.9	3014	72	32	302	Fracture	1540383652	
154	312895.45	8102369.9	3018	58	117	27	Fracture	1540382076	
155	312895.45	8102369.9	3018	66	241	151	Fracture	1540382061	
156	312902.45	8102372.1	3018	68	69	339	Fracture	1540382049	Large with Fe-oxide
157	312915.18	8102376.6	3014	51	235	145	Fracture	1540381652	Large cutting through other parallel
158	312915.18	8102376.6	3014	65	25	295	Fracture	1540381622	

No.	X(East)	Y(North)	Z	Dip	Az	Strike	Type	Time Stamp	Remarks
159	312915.18	8102376.6	3014	60	46	316	Fracture	1540381603	
160	312915.18	8102376.6	3014	70	35	305	Fracture	1540381596	
161	312912.74	8102375.6	3015	67	33	303	Fracture	1540381587	Parallel fractures
162	312869.2	8102369.2	3012	79	125	35	Fracture	1540381402	
163	312869.2	8102369.2	3012	77	136	46	Fracture	1540381394	
164	312879.06	8102367.9	3017	62	223	133	Fracture	1540381360	
165	312907.12	8102377.9	3014	71	234	144	Fracture	1540381348	
166	312897.34	8102370.9	3018	58	239	149	Fracture	1540381336	White clay along fracture
167	312881.29	8101578	3022	53	71	341	Fracture	1540327158	
168	312881.29	8101578	3022	69	207	117	Fracture	1540327122	
169	312881.29	8101578	3022	53	91	1	Fracture	1540327113	
170	312888.73	8101590.1	3019	38	238	148	Fracture	1540326233	RCS062
171	312888.09	8101589.6	3019	59	101	11	Fracture	1540326185	RCS062
172	312883.77	8101580.5	3022	61	90	360	Fracture	1540325922	
173	312888.29	8101585	3020	74	208	118	Fracture	1540325900	
174	312885.18	8101585.4	3020	81	108	18	Fracture	1540325867	
175	312892.22	8101591.4	3018	48	92	2	Fracture	1540325806	
176	312892.22	8101591.4	3018	69	209	119	Fracture	1540325744	R11.7
177	312884.69	8101604.6	3016	70	212	122	Fracture	1540325084	
178	312884.69	8101604.6	3016	59	87	357	Fracture	1540325052	
179	312881.11	8101601.4	3017	63	213	123	Fracture	1540325006	
180	312881.11	8101601.4	3017	40	76	346	Fracture	1540324943	
181	312879.65	8101599.1	3018	46	64	334	Fracture	1540324907	R11.7
182	312914.48	8101264	3037	39	98	8	Fracture	1540323932	
183	312914.48	8101264	3037	68	294	204	Fracture	1540323901	
184	312914.48	8101264	3037	66	289	199	Fracture	1540323890	
185	312913.03	8101264.5	3037	60	304	214	Fracture	1540323879	
186	312913.03	8101264.5	3037	79	213	123	Fracture	1540323867	
187	312913.03	8101264.5	3037	83	205	115	Fracture	1540323841	
188	312913.03	8101264.5	3037	89	33	303	Fracture	1540323832	R11.6 Parallel fractures
189	312978.15	8100969.1	3057	71	253	163	Fracture	1540323608	
190	312980.31	8100951.2	3058	82	226	136	Fracture	1540323549	
191	312982.57	8100936	3057	87	52	322	Fracture	1540323529	
192	312982.57	8100936	3057	79	227	137	Fracture	1540323524	
193	312982.57	8100936	3057	69	207	117	Fracture	1540323513	
194	312980.24	8100917.4	3060	88	55	325	Fracture	1540323435	
195	312987.5	8100901.9	3059	86	223	133	Fracture	1540323409	
196	312987.5	8100901.9	3059	75	233	143	Fracture	1540323398	
197	312990.44	8100892	3061	62	329	239	Fracture	1540323367	
198	312990.44	8100892	3061	64	304	214	Fracture	1540323360	
199	313004.62	8100883.6	3058	71	245	155	Fracture	1540323322	Very Fe-oxide
200	312993.27	8100879.2	3063	80	246	156	Fracture	1540323308	
201	313017.28	8100770	3057	57	23	293	Fracture	1540322925	
202	313018.37	8100745.9	3063	80	253	163	Fracture	1540322798	Fe-oxide staining particularly on this Fracture type
203	313015.47	8100748.8	3063	46	248	158	Fracture	1540322750	
204	313033.51	8100763.1	3056	54	234	144	Fracture	1540322602	
205	313034.6	8100731.9	3060	35	258	168	Fracture	1540322569	
206	313017.68	8100716.7	3064	79	164	74	Fracture	1540322555	
207	313021.82	8100681.6	3068	79	163	73	Fracture	1540322371	
208	313023.19	8100688.6	3067	70	153	63	Fracture	1540322359	
209	313017.7	8100713.7	3065	85	255	165	Fracture	1540322311	
210	313262.11	8099941.8	3093	74	155	65	Fracture	1540321847	
211	313262.11	8099941.8	3093	57	63	333	Fracture	1540321820	
212	313262.26	8099925.4	3094	62	69	339	Fracture	1540321807	
213	313286.11	8099900.5	3104	89	332	242	Fracture	1540321735	
214	313282.11	8099906.8	3103	87	336	246	Fracture	1540321710	
215	313282.11	8099906.8	3103	51	61	331	Fracture	1540321699	
216	313276.06	8099900.5	3098	52	60	330	Fracture	1540321688	
217	313274.37	8099916.3	3101	51	63	333	Fracture	1540321584	
218	313291.3	8099468.5	3059	56	241	151	Fracture	1540316693	Major NW FZ
219	313293.61	8099476.1	3061	38	347	257	Fracture	1540316670	Major NW FZ
220	313293.61	8099476.1	3061	64	39	309	Fracture	1540316655	Major NW FZ
221	313291.8	8099469.8	3060	75	16	286	Fracture	1540316205	Major NW FZ
222	313279	8099429.6	3056	86	124	34	Fracture	1540315872	Major NW FZ
223	313271.43	8099413.2	3057	72	5	275	Fracture	1540315814	Major NW FZ
224	313271.43	8099413.2	3057	66	100	10	Fracture	1540315805	Major NW FZ
225	313271.64	8099411.9	3058	18	248	158	Fracture	1540315737	Another Ia with Fe-oxide and black mineral
226	313264.88	8099406.4	3060	86	301	211	Fracture	1540315686	Major NW FZ
227	313253.13	8099400	3060	70	127	37	Fracture	1540315637	Major NW FZ
228	313257.67	8099400.5	3061	83	128	38	Fracture	1540315623	Major NW FZ
229	313246.79	8099398.6	3060	78	40	310	Fracture	1540315585	Major NW FZ
230	313246.37	8099395	3061	63	24	294	Fracture	1540315570	Major NW FZ
231	313237.73	8099396.3	3061	72	237	147	Fracture	1540315553	Major NW FZ
232	313236.38	8099394.9	3062	72	244	154	Fracture	1540315544	Major NW FZ
233	313232.34	8099389.9	3064	26	271	181	Fracture	1540315456	Major NW FZ
234	313233.53	8099390.4	3064	79	183	93	Fracture	1540315397	Major NW FZ
235	313226.26	8099390.8	3063	26	240	150	Fracture	1540315363	Major NW FZ
236	313218.48	8099393.7	3062	65	244	154	Fracture	1540315277	Major NW FZ
237	313214.33	8099396.4	3061	57	255	165	Fracture	1540315234	Major NW FZ

No.	X(East)	Y(North)	Z	Dip	Az	Strike	Type	Time Stamp	Remarks
238	313205.18	8099395.6	3060	58	136	46	Fracture	1540315208	Major NW FZ
239	313205.18	8099395.6	3060	39	244	154	Fracture	1540315172	Major NW FZ
240	313199.3	8099394.3	3059	44	249	159	Fracture	1540315139	Major NW FZ
241	313199.3	8099394.3	3059	57	232	142	Fracture	1540315110	
242	313195	8099392.9	3060	71	186	96	Fracture	1540315076	Epi
243	313189	8099398.9	3059	73	194	104	Fracture	1540315053	Epi
244	313179.98	8099401.5	3059	38	234	144	Fracture	1540314993	Gouge with black mineral too
245	313164.18	8099398.9	3060	54	353	263	Fracture	1540314926	
246	313164.18	8099398.9	3060	73	197	107	Fracture	1540314922	
247	313164.18	8099398.9	3060	71	5	275	Fracture	1540314886	
248	313161.3	8099404.5	3058	30	251	161	Fracture	1540313618	
249	313158.24	8099407	3057	45	216	126	Fracture	1540313475	White and punk
250	313147.04	8099410.4	3052	44	264	174	Fracture	1540313179	R1q.5
251	313150.89	8099412	3052	79	277	187	Fracture	1540313149	R11.5
252	313145.75	8099412.9	3051	75	271	181	Fracture	1540313036	Gouge zone 10cm with Fe-oxide
253	313140.65	8099416.9	3050	75	153	63	Fracture	1540312987	
254	313140.65	8099416.9	3050	50	254	164	Fracture	1540312978	
255	313136.87	8099416.7	3049	55	250	160	Fracture	1540312964	
256	313132.56	8099418.3	3049	52	248	158	Fracture	1540312956	
257	313100.16	8099433.1	3049	69	142	52	Fracture	1540312753	
258	313100.16	8099433.1	3049	32	267	177	Fracture	1540312737	
259	313097.02	8099433.6	3049	37	268	178	Fracture	1540312723	
260	313097.02	8099433.6	3049	41	249	159	Fracture	1540312711	
261	313091.34	8099435.8	3049	39	244	154	Fracture	1540312688	Parallel fractures
262	313047.19	8099451.5	3043	82	219	129	Fracture	1540312562	
263	313043.81	8099451.7	3043	75	221	131	Fracture	1540312547	
264	313043.81	8099451.7	3043	89	124	34	Fracture	1540312540	white clay
265	313038.86	8099452.6	3044	78	256	166	Fracture	1540312473	
266	313039	8099452.6	3044	73	214	124	Fracture	1540312427	Lots of epi ant punk mineral on plane
267	313017.56	8099458.2	3039	70	340	250	Fracture	1540312341	
268	313016.73	8099459.1	3039	80	211	121	Fracture	1540312317	
269	313014.27	8099457.8	3039	57	281	191	Fracture	1540312288	
270	313008.03	8099459	3039	34	249	159	Fracture	1540311203	Black mineral as vein in fractured zone RCS058
271	313006.11	8099461.4	3038	71	221	131	Fracture	1540311118	
272	312998.98	8099459.4	3038	78	215	125	Fracture	1540311106	
273	312988.48	8099457.9	3038	87	71	341	Fracture	1540310974	Qtz with pink mineral
274	312980.4	8099456.8	3038	65	17	287	Fracture	1540310848	
275	312974.64	8099454.9	3039	76	26	296	Fracture	1540310825	White mineral
276	312959.86	8099448.1	3040	40	226	136	Fracture	1540310613	
277	312957.51	8099445.3	3041	80	231	141	Fracture	1540310594	
278	312964	8099446.8	3041	85	60	330	Fracture	1540310397	White mineral with Fe-oxide, with epi and pink mineral in the middle Fe-oxide along* Fracture
279	312952.2	8099448.3	3041	83	191	101	Fracture	1540310245	
280	312905.6	8099463.8	3029	86	221	131	Fracture	1540310158	
281	312905.6	8099463.8	3029	82	82	352	Fracture	1540310103	
282	312898.01	8099462.9	3028	78	94	4	Fracture	1540310049	
283	312879	8099458.3	3024	88	149	59	Fracture	1540309520	Epi
284	312864	8099459.5	3020	85	23	293	Fracture	1540309447	Epi
285	312864.13	8099459.5	3020	70	79	349	Fracture	1540309435	
286	312858.98	8099443.3	3027	70	98	8	Fracture	1540309395	
287	312847.01	8099440.6	3025	68	92	2	Fracture	1540309335	
288	312834.15	8099433.4	3024	75	176	86	Fracture	1540309167	
289	312834.15	8099433.4	3024	83	322	232	Fracture	1540309159	
290	312820.44	8099435.4	3020	30	284	194	Fracture	1540309128	
291	312796.35	8099425.2	3019	65	137	47	Fracture	1540309085	
292	312767.51	8099411.2	3019	76	130	40	Fracture	1540309002	
293	312753.09	8099404.9	3018	85	5	275	Fracture	1540308996	
294	312753.09	8099404.9	3018	74	118	28	Fracture	1540308984	
295	312714.62	8099383.9	3025	79	135	45	Fracture	1540308959	
296	312696.28	8099376.8	3025	12	277	187	Fracture	1540308846	Very la zone (pic)
297	312701.33	8099381.6	3022	70	92	2	Fracture	1540308807	
298	312663.02	8099350.1	3029	72	201	111	Fracture	1540308698	
299	312640.58	8099333.2	3024	67	184	94	Fracture	1540308588	Lots of white mineral in pulverised parallel fractures
300	312629.24	8099324.5	3022	67	147	57	Fracture	1540308504	
301	312626.03	8099319.1	3021	52	157	67	Fracture	1540308491	
302	312616.15	8099307.6	3018	75	158	68	Fracture	1540308289	R11.4
303	312616.15	8099307.6	3018	71	201	111	Fracture	1540308266	R11.4
304	312604	8099280	3018	75	166	76	Fracture	1540308021	Epi
305	312599.59	8099271.8	3018	56	191	101	Fracture	1540307997	
306	312599.59	8099271.8	3018	62	166	76	Fracture	1540307965	
307	312650.14	8099135	2998	79	328	238	Fracture	1540307495	R1q.3
308	312654.48	8099133.3	2998	79	339	249	Fracture	1540306911	R11.3
309	312654.48	8099133.3	2998	61	110	20	Fracture	1540306887	R11.3
310	312603.91	8099031.6	2988	42	268	178	Fracture	1540306583	La parallel
311	312523.05	8099054.9	2991	79	112	22	Fracture	1540306105	White mineral ne smokey qtz
312	312508.56	8099066.3	2988	73	129	39	Fracture	1540305941	White mineral
313	312496.19	8099071.1	2986	79	134	44	Fracture	1540305901	
314	312474.06	8099066	2986	79	137	47	Fracture	1540305893	

No.	X(East)	Y(North)	Z	Dip	Az	Strike	Type	Time Stamp	Remarks
315	312432.91	8099072.4	2978	82	118	28	Fracture	1540305770	Thick white clay
316	312412.11	8099078	2974	84	160	70	Fracture	1540305688	
317	312422.26	8099073.3	2978	83	129	39	Fracture	1540305680	
318	312422.26	8099073.3	2978	81	1	271	Fracture	1540305660	White clay
319	312353.43	8099065.8	2973	65	86	356	Fracture	1540305435	
320	312350	8099058.4	2974	78	108	18	Fracture	1540305392	Parallel with epi
321	312343.88	8099054.8	2973	86	103	13	Fracture	1540305327	
322	312338.14	8099044.6	2972	58	165	75	Fracture	1540305257	
323	312332.32	8099043.1	2972	71	179	89	Fracture	1540305246	
324	312332.36	8099038	2973	55	186	96	Fracture	1540305237	Lots of parallel
325	312324.36	8099019.1	2973	80	6	276	Fracture	1540305147	Zone 10cm with white clay on either side
326	312327	8099004.6	2976	89	199	109	Fracture	1540305057	Epi and white clay
327	312324	8099000.2	2975	82	98	8	Fracture	1540304967	Lots of epi along planes
328	312331.02	8098989	2977	87	116	26	Fracture	1540304932	
329	312331.02	8098989	2977	74	286	196	Fracture	1540304915	
330	312336.33	8098955.7	2974	80	35	305	Fracture	1540304904	
331	312336.33	8098955.7	2974	87	139	49	Fracture	1540304883	
332	312357	8098929.3	2972	89	98	8	Fracture	1540304685	Epi
333	312368	8098913.6	2967	85	293	203	Fracture	1540304648	Epi on fracture
334	312368.38	8098913.6	2967	80	7	277	Fracture	1540304625	
335	312357.37	8098818.3	2952	54	221	131	Fracture	1540303719	
336	312348.28	8098802.9	2953	79	171	81	Fracture	1540303223	Purple clay with slicken l8nes and slicken sides
337	312354	8098778.1	2959	84	181	91	Fracture	1540303107	Epi
338	312353.47	8098768.4	2961	67	172	82	Fracture	1540303048	
339	312348.99	8098763.1	2961	61	190	100	Fracture	1540302638	white clay
340	312348.99	8098763.1	2961	72	156	66	Fracture	1540302612	
341	312345.3	8098762.2	2960	88	196	106	Fracture	1540302600	White mineral
342	312338	8098748.2	2962	84	267	177	Fracture	1540302540	Epi near RCS054
343	312317	8098741.8	2961	84	132	42	Fracture	1540302416	Epi on most planes
344	312307.25	8098729.3	2963	78	142	52	Fracture	1540302389	
345	312323	8098711.5	2964	83	139	49	Fracture	1540302109	Epi and white
346	312225.27	8098588.5	2934	51	227	137	Fracture	1540301865	Lots of same black mineral
347	312208.98	8098572.8	2941	84	302	212	Fracture	1540301717	
348	312198	8098562.6	2940	86	303	213	Fracture	1540301707	Minor epi on plane
349	312184.58	8098546.2	2929	85	162	72	Fracture	1540301546	
350	312191	8098548.6	2930	83	150	60	Fracture	1540301509	Minor epi on planes
351	312191.39	8098548.6	2930	86	180	90	Fracture	1540301483	In rhyolite
352	312162.85	8098485.3	2919	74	347	257	Fracture	1540300990	
353	312161.35	8098479	2921	88	8	278	Fracture	1540300960	
354	312161.35	8098479	2921	89	17	287	Fracture	1540300952	
355	312162.26	8098388	2916	43	211	121	Fracture	1540300435	
356	312162.26	8098388	2916	58	165	75	Fracture	1540300418	
357	312146.36	8098360	2918	75	145	55	Fracture	1540300310	
358	312146.36	8098360	2918	58	164	74	Fracture	1540300300	Parallel fractures
359	312086.58	8098341.9	2919	42	269	179	Fracture	1540299910	Lots of dark/black mineral
360	312070.87	8098338.3	2919	35	96	6	Fracture	1540299800	
361	312067.83	8098335.7	2917	49	252	162	Fracture	1540299736	Dark pink clay
362	312064.74	8098335.2	2917	78	275	185	Fracture	1540299600	
363	312057.86	8098336.8	2918	72	235	145	Fracture	1540299513	Large zone with 0cm gouge
364	312051.31	8098333.7	2915	86	315	225	Fracture	1540299403	
365	312045.61	8098335	2914	89	317	227	Fracture	1540299381	
366	312041.23	8098335.4	2915	62	333	243	Fracture	1540299321	
367	312036.01	8098332.7	2914	64	320	230	Fracture	1540299311	
368	312007.56	8098329.8	2923	53	333	243	Fracture	1540298709	
369	312000.78	8098330.8	2924	73	46	316	Fracture	1540298621	Large zone with 20cm of lilac clay
370	311988.27	8098327.3	2923	70	51	321	Fracture	1540298524	
371	311982.59	8098325	2921	51	264	174	Fracture	1540298509	Thin white parallel fractures
372	311917.33	8098311.8	2913	77	157	67	Fracture	1540298254	
373	311917.33	8098311.8	2913	86	153	63	Fracture	1540298243	
374	311924	8098302.7	2906	80	157	67	Fracture	1540298227	Epi
375	311920	8098290.1	2899	76	217	127	Fracture	1540298102	Large Fracture with white mineral and clay alt of WR with epi prominent in zone
376	311904.96	8098272.8	2902	52	235	145	Fracture	1540297932	White mineral
377	311906	8098272.8	2902	89	138	48	Fracture	1540297913	Epi
378	311918	8098268.4	2897	80	319	229	Fracture	1540297890	Lots of epi
379	311907.45	8098251.2	2900	57	238	148	Fracture	1540297785	
380	311907.45	8098251.2	2900	82	327	237	Fracture	1540297770	
381	311907.19	8098236.3	2904	83	350	260	Fracture	1540297652	Purple clay
382	311935.21	8098186.3	2895	89	315	225	Fracture	1540297478	Same purple and quartz
383	311943.41	8098169.2	2893	84	130	40	Fracture	1540297355	Gouge with plates mineral
384	311956.11	8098162.5	2892	85	358	268	Fracture	1540297254	
385	311985.05	8098138.8	2886	84	344	254	Fracture	1540297055	With lilac clays with some quartz
386	311980.78	8098122.8	2890	88	121	31	Fracture	1540296822	
387	312002.73	8098103.5	2888	65	301	211	Fracture	1540296692	Large zone with gouge and quartz along main shear (pic)
388	312009.76	8098088.8	2894	81	122	32	Fracture	1540296521	
389	312009.76	8098088.8	2894	87	201	111	Fracture	1540296507	
390	312014.47	8098077	2894	82	135	45	Fracture	1540296144	R11.1
391	312014	8098077	2894	77	321	231	Fracture	1540296110	R11.1 Epi

No.	X(East)	Y(North)	Z	Dip	Az	Strike	Type	Time Stamp	Remarks
392	312016.81	8098072.4	2893	74	164	74	Fracture	1540296076	R11.1
393	312016.81	8098072.4	2893	65	329	239	Fracture	1540296030	R11.1 gouge 20cm
394	312020.51	8098074.5	2893	55	202	112	Fracture	1540295756	Parallel fracture zone 1m
395	312017	8098054.2	2892	80	340	250	Fracture	1540295642	Epi
396	312017	8098054.2	2892	83	84	354	Fracture	1540295630	Green pink white
397	312017	8098046.7	2890	51	336	246	Fracture	1540295471	Epi
398	312018.87	8098033.8	2886	59	325	235	Fracture	1540295457	
399	311953.68	8098035.1	2877	62	230	140	Fracture	1540295219	
400	311953.68	8098035.1	2877	77	319	229	Fracture	1540295209	
401	311942.51	8098035	2873	79	324	234	Fracture	1540295199	
402	311925.49	8098036.7	2870	84	311	221	Fracture	1540295187	White and pink
403	311864.27	8098027.1	2873	68	221	131	Fracture	1540295054	
404	311864.27	8098027.1	2873	84	326	236	Fracture	1540295035	
405	311824.73	8098018.2	2874	75	56	326	Fracture	1540241309	Purple red mineral
406	311821.88	8098016.6	2873	89	263	173	Fracture	1540241269	
407	311816.36	8098012.9	2871	89	46	316	Fracture	1540241175	
408	311811.97	8098008.5	2868	66	106	16	Fracture	1540241130	
409	311781.99	8097979.6	2865	71	155	65	Fracture	1540241087	
410	311783.21	8097992.1	2868	73	162	72	Fracture	1540241077	
411	311778	8097975.9	2866	87	337	247	Fracture	1540241012	Lots of pink green and white
412	311775	8097959.7	2866	83	332	242	Fracture	1540240904	Lots of epi on plane
413	311766	8097956.7	2869	70	233	143	Fracture	1540240865	epi
414	311765.37	8097945	2871	89	145	55	Fracture	1540240654	R10.9
415	311765	8097945	2871	73	234	144	Fracture	1540240604	10.9 epi
416	311764.71	8097936.2	2871	82	130	40	Fracture	1540240547	
417	311770	8097937.7	2869	86	298	208	Fracture	1540240524	Epi on fracture
418	311772.74	8097923.8	2868	82	130	40	Fracture	1540240481	
419	311772.74	8097923.8	2868	74	220	130	Fracture	1540240454	Pink and white mineral
420	311773.56	8097915	2868	62	204	114	Fracture	1540240431	Gouge Fracture
421	311775.86	8097905.5	2867	68	211	121	Fracture	1540240381	
422	311773.08	8097886.4	2872	55	231	141	Fracture	1540240315	
423	311773.08	8097886.4	2872	77	323	233	Fracture	1540240302	Covered in lot# of green white and pink (pic)
424	311778.57	8097874.7	2872	43	190	100	Fracture	1540240230	
425	311796.19	8097837.5	2861	80	224	134	Fracture	1540239881	
426	311796.19	8097837.5	2861	84	174	84	Fracture	1540239873	
427	311792.09	8097802.2	2860	31	65	335	Fracture	1540239793	La plane with white mineral near other nw parallel white fractures - cross cut them?
428	311793.66	8097805.2	2860	87	29	299	Fracture	1540239633	Lots of roughly parallel white mineral fractures
429	311797.39	8097800.8	2857	86	219	129	Fracture	1540239515	Large zone of parallel anastomosing fractures
430	311805.76	8097789.2	2850	84	313	223	Fracture	1540239397	
431	311805.76	8097789.2	2850	85	226	136	Fracture	1540239390	
432	311800.01	8097785.4	2854	82	228	138	Fracture	1540239337	White lilac mineral
433	311813.88	8097756.5	2843	80	254	164	Fracture	1540239207	
434	311796.75	8097759.6	2850	67	53	323	Fracture	1540239099	
435	311773.35	8097738.1	2855	88	294	204	Fracture	1540239050	
436	311773.35	8097738.1	2855	82	25	295	Fracture	1540239044	
437	311758.35	8097730.5	2854	33	106	16	Fracture	1540238810	R10.8
438	311719.53	8097738.6	2849	85	319	229	Fracture	1540238549	
439	311703.51	8097731	2840	88	153	63	Fracture	1540238542	
440	311703.51	8097731	2840	76	223	133	Fracture	1540238511	
441	311697.3	8097729.9	2838	80	224	134	Fracture	1540238504	
442	311614.55	8097702.8	2838	83	302	212	Fracture	1540238318	
443	311620.13	8097701	2836	81	310	220	Fracture	1540238276	White and pink
444	311609.07	8097693.5	2838	57	14	284	Fracture	1540238256	Lots of white mineral
445	311604.77	8097690.4	2839	89	254	164	Fracture	1540238158	
446	311601.13	8097682.4	2835	87	44	314	Fracture	1540238068	
447	311603.61	8097681.8	2834	77	298	208	Fracture	1540238059	
448	311596	8097679.9	2836	80	309	219	Fracture	1540237057	Lots of epi on plane RCS051
449	311579	8097657.2	2837	88	298	208	Fracture	1540236936	White pink and green minerals on plane
450	311566.44	8097646.4	2837	82	295	205	Fracture	1540236867	
451	311564	8097637.6	2833	57	33	303	Fracture	1540236800	white clay - lots of epi alt in WR now
452	311546	8097624.8	2830	86	116	26	Fracture	1540236641	WTH epi
453	311455.17	8097559.6	2821	83	289	199	Fracture	1540236409	
454	311505.19	8097576.6	2825	62	329	239	Fracture	1540236356	
455	311489.6	8097564.8	2823	63	128	38	Fracture	1540236241	
456	311489.6	8097564.8	2823	85	64	334	Fracture	1540236202	White mineral
457	311473.91	8097564.6	2823	67	45	315	Fracture	1540236003	
458	311424.04	8097565.2	2820	78	320	230	Fracture	1540235740	
459	311408	8097576.9	2821	86	102	12	Fracture	1540235131	RCS050 epidote very clear
460	311389.21	8097592.5	2819	75	107	17	Fracture	1540234957	
461	311373	8097589.4	2815	77	110	20	Fracture	1540234948	Pink green white minerals
462	311344.03	8097593.5	2810	89	51	321	Fracture	1540234893	Plane next to previous but only white clay
463	311341	8097603.6	2810	75	110	20	Fracture	1540234686	Covered in white green and pink minerals - slickenlines
464	311244.39	8097656.3	2819	89	141	51	Fracture	1540234589	
465	311226.86	8097661.9	2813	61	34	304	Fracture	1540234547	
466	311157.8	8097712.1	2802	54	12	282	Fracture	1540234252	With white clay and Fe-oxide

No.	X(East)	Y(North)	Z	Dip	Az	Strike	Type	Time Stamp	Remarks
467	311134.33	8097729.2	2799	63	54	324	Fracture	1540234121	
468	311134.33	8097729.2	2799	63	57	327	Fracture	1540234111	
469	311125.72	8097729.1	2798	70	4	274	Fracture	1540234024	With white clay and red (pic)
470	311105.3	8097731.8	2793	60	321	231	Fracture	1540233945	With white clay and red ox
471	311081.9	8097755.7	2792	72	100	10	Fracture	1540233839	
472	311081.9	8097755.7	2792	73	102	12	Fracture	1540233818	
473	311081.9	8097755.7	2792	67	7	277	Fracture	1540233791	
474	311013.41	8097803.1	2791	70	28	298	Fracture	1540230283	
475	311009.95	8097806.8	2791	89	25	295	Fracture	1540230252	
476	311010.24	8097816.7	2791	85	113	23	Fracture	1540230215	
477	311010.24	8097816.7	2791	69	41	311	Fracture	1540230187	
478	311008.29	8097821.9	2792	83	113	23	Fracture	1540230169	
479	311002.19	8097822.6	2789	67	32	302	Fracture	1540230137	
480	311002.13	8097829.5	2791	43	52	322	Fracture	1540230100	
481	311003.95	8097838.6	2792	52	31	301	Fracture	1540230051	
482	311005.8	8097844.6	2793	63	212	122	Fracture	1540229990	
483	311005.8	8097844.6	2793	84	95	5	Fracture	1540229979	
484	311005.8	8097844.6	2793	49	204	114	Fracture	1540229934	
485	311008.94	8097854.2	2794	33	228	138	Fracture	1540229371	Large Fracture with crystalline pinkish mineral along it
486	311012.28	8097861.7	2795	47	235	145	Fracture	1540229225	
487	311009.39	8097867.4	2794	79	148	58	Fracture	1540229135	
488	311013.8	8097872	2794	75	167	77	Fracture	1540229105	
489	311013.8	8097872	2794	56	22	292	Fracture	1540229064	
490	311020.42	8097883.2	2796	77	21	291	Fracture	1540228987	
491	311020.42	8097883.2	2796	50	186	96	Fracture	1540228973	
492	311024.71	8097885.4	2798	71	26	296	Fracture	1540228881	Lots of white mineral
493	311028.24	8097895.4	2799	58	16	286	Fracture	1540228662	
494	311030.32	8097913.2	2794	67	51	321	Fracture	1540228585	
495	311032.69	8097925.2	2792	51	24	294	Fracture	1540228532	Lots of parallel gouge Fractures
496	311032.69	8097925.2	2792	53	216	126	Fracture	1540228498	
497	311032.69	8097925.2	2792	57	34	304	Fracture	1540228487	
498	311044.22	8097927.2	2796	81	160	70	Fracture	1540228349	White clay conjugates?
499	311044.22	8097927.2	2796	89	34	304	Fracture	1540228310	White mineral
500	311036	8098002.8	2774	76	323	233	Fracture	1540228136	
501	311039.75	8098020.3	2780	66	42	312	Fracture	1540228072	
502	311034.01	8098006.7	2774	75	42	312	Fracture	1540228060	
503	311034.01	8098006.7	2774	71	356	266	Fracture	1540228030	
504	311014.21	8098035.6	2778	89	151	61	Fracture	1540227976	
505	311014.21	8098035.6	2778	83	339	249	Fracture	1540227943	
506	310967.34	8098052.2	2772	47	348	258	Fracture	1540226306	Larger zone RCS049
507	310967.34	8098052.2	2772	55	330	240	Fracture	1540226100	
508	310963.73	8098063.6	2778	61	341	251	Fracture	1540226068	
509	310936.43	8098061.4	2774	48	69	339	Fracture	1540226040	
510	310938.5	8098061.5	2774	89	331	241	Fracture	1540225992	
511	310938.5	8098061.5	2774	86	146	56	Fracture	1540225956	white clay large with some gouge
512	310813.37	8098047.1	2762	69	41	311	Fracture	1540224633	
513	310812.34	8098045.7	2762	60	357	267	Fracture	1540224164	R10.6
514	310798.2	8098024.4	2760	89	47	317	Fracture	1540223374	Parallel sets
515	310792.51	8098019.4	2761	61	226	136	Fracture	1540223256	
516	310768.15	8097990.1	2765	66	229	139	Fracture	1540223135	
517	310748.61	8097960.6	2761	88	23	293	Fracture	1540223032	
518	310748.61	8097960.6	2761	87	21	291	Fracture	1540223019	Pulverised zone
519	310733	8097951	2761	81	8	278	Fracture	1540222931	Epi along plane
520	310672	8097894.1	2751	61	157	67	Fracture	1540222247	RCS047 Covered in dust but lots of epi on plane
521	310665.18	8097895.4	2751	84	336	246	Fracture	1540222194	
522	310655.99	8097895.9	2750	70	355	265	Fracture	1540222160	
523	310609.65	8097911.9	2745	65	29	299	Fracture	1540222106	
524	310602.75	8097915.5	2743	72	118	28	Fracture	1540222089	
525	310602.75	8097915.5	2743	76	18	288	Fracture	1540222074	
526	310543.56	8097926.8	2743	82	319	229	Fracture	1540221836	
527	310536.22	8097927.7	2743	87	229	139	Fracture	1540221782	
528	310534.26	8097924.5	2741	64	52	322	Fracture	1540221721	white clay in filling fractures
529	310510.91	8097922	2740	79	111	21	Fracture	1540221654	
530	310510.91	8097922	2740	78	80	350	Fracture	1540221583	
531	310504.94	8097923.8	2742	76	106	16	Fracture	1540221541	
532	310501.74	8097923.3	2741	77	42	312	Fracture	1540221515	
533	310474.13	8097932.2	2742	67	30	300	Fracture	1540221315	
534	310475.08	8097928.1	2740	70	30	300	Fracture	1540221305	
535	310452.93	8097945.6	2742	64	37	307	Fracture	1540221137	
536	310452.93	8097945.6	2742	79	116	26	Fracture	1540221115	
537	310452.93	8097945.6	2742	73	4	274	Fracture	1540221108	
538	310447.58	8097953.7	2742	73	342	252	Fracture	1540220991	white clay
539	310445.89	8097957.6	2741	79	357	267	Fracture	1540220980	With white clay
540	310437.84	8097967	2739	86	348	258	Fracture	1540220859	Parallel fractures white clay
541	310304.32	8097942.3	2721	65	10	280	Fracture	1540220532	
542	310297.14	8097943.8	2722	71	351	261	Fracture	1540220449	Very large pulverised zone 4m+
543	310298.06	8097955.2	2727	63	32	302	Fracture	1540220111	
544	310287.18	8097951.8	2722	84	317	227	Fracture	1540220041	

No.	X(East)	Y(North)	Z	Dip	Az	Strike	Type	Time Stamp	Remarks
545	310287.18	8097951.8	2722	70	36	306	Fracture	1540220027	
546	310281.19	8097963.4	2725	87	123	33	Fracture	1540219980	
547	310281.19	8097963.4	2725	84	206	116	Fracture	1540219973	
548	310281.19	8097963.4	2725	85	122	32	Fracture	1540219961	
549	310281.96	8097971	2729	86	220	130	Fracture	1540219904	
550	310276.96	8097979.3	2730	87	327	237	Fracture	1540219872	
551	310276.96	8097979.3	2730	89	223	133	Fracture	1540219864	
552	310273.48	8097992.6	2733	78	42	312	Fracture	1540219832	
553	310273.48	8097992.6	2733	81	42	312	Fracture	1540219818	
554	310271.69	8098005.1	2734	71	44	314	Fracture	1540219761	
555	310265.41	8098025.1	2728	77	49	319	Fracture	1540219320	Another large Fracture zone 60cm gouge
556	310269.17	8098039	2727	67	21	291	Fracture	1540218986	
557	310268.17	8098042.6	2726	77	49	319	Fracture	1540218883	Large Fracture zone with lots of red staining Fe-oxide
558	310269.87	8098054.6	2726	79	134	44	Fracture	1540218805	
559	310270.93	8098058.4	2726	65	37	307	Fracture	1540218737	
560	310270.93	8098058.4	2726	64	54	324	Fracture	1540218727	
561	310275.11	8098071.8	2728	82	150	60	Fracture	1540218248	R10.4
562	310273	8098070.7	2727	68	45	315	Fracture	1540218217	R10.4 Large nW Fracture with alt and epi/white mineral along plane RCS046 larger Fracture
563	310268.71	8098093.8	2723	55	47	317	Fracture	1540217051	
564	310227.4	8098146.5	2711	88	329	239	Fracture	1540216450	
565	310216.71	8098146.4	2711	84	153	63	Fracture	1540216370	
566	310208.88	8098152.1	2714	68	40	310	Fracture	1540216300	
567	310208.88	8098152.1	2714	83	148	58	Fracture	1540216293	
568	310180	8098151.8	2714	89	147	57	Fracture	1540216177	Epi and white clay - slickenside suggesting dextral?
569	310165	8098150.7	2713	87	326	236	Fracture	1540216063	Epi and white clay
570	310165	8098150.7	2713	63	51	321	Fracture	1540216046	With epi and white clay
571	310150.64	8098158.3	2716	64	53	323	Fracture	1540215936	
572	310143.93	8098156.4	2714	55	56	326	Fracture	1540215820	Large Fracture altered with 15+ cm gouge
573	310136.09	8098163.1	2715	87	158	68	Fracture	1540215666	
574	310104.88	8098155.1	2703	70	310	220	Fracture	1540215532	Fe-oxide alt Fracture with minor white clay
575	310104.88	8098155.1	2703	73	324	234	Fracture	1540215378	Fe-oxide alt Fracture with minor white clay
576	310093.12	8098157.8	2703	50	89	359	Fracture	1540215127	Inside Fracture zone
577	310093.12	8098157.8	2703	77	56	326	Fracture	1540215018	Large Fracture zone
578	310067	8098157.6	2707	83	51	321	Fracture	1540214837	Large Fracture with epi and white clay
579	310054	8098150.7	2704	85	50	320	Fracture	1540214773	Lots of epi on pkane
580	310042.86	8098149.6	2704	80	56	326	Fracture	1540214745	
581	310042.86	8098149.6	2704	80	299	209	Fracture	1540214735	white clay
582	310012.69	8098153.2	2710	81	53	323	Fracture	1540214564	White mineral next to other fracture
583	310013	8098153.2	2710	84	140	50	Fracture	1540214493	Slicken lines with epi
584	309982	8098151.1	2707	80	131	41	Fracture	1540214087	R10.3 two sets of slicken lines? white clay epi
585	309982.33	8098151.1	2707	75	244	154	Fracture	1540213999	
586	309982	8098151.1	2707	87	130	40	Fracture	1540213992	Epi white clay
587	309916.46	8098108.7	2684	77	231	141	Fracture	1540213590	Alt colours (pic)
588	309900	8098087	2687	87	310	220	Fracture	1540213368	Lots of epi on plane
589	309900	8098076.6	2683	87	319	229	Fracture	1540213290	Lots of epi on plane
590	309896.49	8098073.4	2684	74	209	119	Fracture	1540213243	
591	309888.78	8098060.5	2686	82	42	312	Fracture	1540213069	Large Fracture with Fe-oxide with and quartz (similar to rcs045) white mineral and gouge
592	309886	8098046.1	2686	79	322	232	Fracture	1540212294	R10.2 - white clay and minor epi
593	309886.29	8098046.1	2686	20	211	121	Fracture	1540212258	R10.2
594	309886.29	8098046.1	2686	59	240	150	Fracture	1540212239	R10.2 - white clay and Quartz
595	309880	8098049.5	2689	82	128	38	Fracture	1540212032	Epi on plane - pic and minor white clay
596	309873	8098019.8	2684	61	126	36	Fracture	1540211972	R10.1 with epi on plane
597	309876.27	8098030.9	2685	38	233	143	Fracture	1540211883	R10.1
598	309876.27	8098030.9	2685	33	91	1	Fracture	1540211812	R10.1
599	309858	8098031.7	2689	69	121	31	Fracture	1540209402	Epi on planes
600	309858	8098031.7	2689	76	117	27	Fracture	1540209385	Epi on planes
601	309844.92	8098024.2	2688	89	247	157	Fracture	1540209167	Parallel fractures
602	309830.29	8098018.6	2682	72	56	326	Fracture	1540209063	
603	309821.03	8098020.4	2680	87	345	255	Fracture	1540209036	
604	309821	8098020.4	2680	77	67	337	Fracture	1540208948	Epi on plane
605	309806	8098016.5	2679	78	165	75	Fracture	1540208820	Epi on plane - slicken sides showing dextral movement?
606	309789	8098023.7	2681	89	338	248	Fracture	1540208648	Epi on plane
607	309789.37	8098023.7	2681	75	235	145	Fracture	1540208594	
608	309784.24	8098010.8	2672	36	285	195	Fracture	1540208578	Parallel LA fractures
609	309760.24	8098018	2681	89	342	252	Fracture	1540208461	
610	309760.24	8098018	2681	79	108	18	Fracture	1540208419	Parallel fractures
611	309760.24	8098018	2681	69	228	138	Fracture	1540208313	white clay
612	309711.88	8098028.5	2679	62	62	332	Fracture	1540206877	
613	309702.62	8098032.2	2674	38	221	131	Fracture	1540206792	La
614	309702.62	8098032.2	2674	51	293	203	Fracture	1540206764	White mineral on plane
615	309693.51	8098032	2668	59	58	328	Fracture	1540206718	
616	309693.51	8098032	2668	71	116	26	Fracture	1540206709	
617	309564.08	8098065.3	2676	68	49	319	Fracture	1539980888	R9.7 with white mineral

No.	X(East)	Y(North)	Z	Dip	Az	Strike	Type	Time Stamp	Remarks
618	309563.93	8098066.5	2676	33	233	143	Fracture	1539980846	R9.7
619	309592.84	8098069.3	2678	33	219	129	Fracture	1539980597	
620	309587.37	8098075.3	2682	88	55	325	Fracture	1539980577	
621	309591.46	8098079.2	2683	89	42	312	Fracture	1539980554	
622	309592	8098075.5	2682	88	121	31	Fracture	1539980544	Epi and white on plane
623	309544.1	8098052.3	2668	71	87	357	Fracture	1539979505	White mineral
624	309535.05	8098049.3	2666	43	243	153	Fracture	1539979062	La shear zone with lots of white mineral
625	309540.38	8098041.2	2664	86	238	148	Fracture	1539978928	
626	309535.07	8098047.6	2665	67	65	335	Fracture	1539978870	
627	309538.41	8098047.6	2665	85	120	30	Fracture	1539978858	
628	309542.23	8098048.6	2666	80	59	329	Fracture	1539978853	
629	309537.01	8098044.8	2665	86	53	323	Fracture	1539978846	
630	309533.16	8098047.5	2665	83	54	324	Fracture	1539978782	Lots parallel fractures
631	309440.04	8098041.2	2659	81	344	254	Fracture	1539978388	Leading off from main ne Fracture where RCS043 was taken
632	309454	8098050.5	2663	81	129	39	Fracture	1539978139	Lots of white mineral with epi RCS043
633	309447	8098038.4	2658	74	71	341	Fracture	1539977905	Epi and white mineral along plane
634	309504.56	8098039.9	2666	81	306	216	Fracture	1539977515	
635	309496.82	8098049.9	2670	42	321	231	Fracture	1539977495	
636	309493.48	8098049.9	2669	45	349	259	Fracture	1539977249	
637	309496.88	8098043.5	2667	43	294	204	Fracture	1539977229	
638	309381.68	8098047.9	2658	26	271	181	Fracture	1539977091	
639	309375.96	8098046.1	2657	61	46	316	Fracture	1539976950	
640	309377.21	8098011.3	2646	68	52	322	Fracture	1539976876	Other side of road parallel Fractures
641	309371.65	8098047	2657	79	59	329	Fracture	1539976493	Clear slicken lines
642	309376.89	8098048.8	2658	85	69	339	Fracture	1539976397	R9.6
643	309378.83	8098046.1	2657	64	53	323	Fracture	1539976113	R9.6 potentially controlling alt?
644	309292	8098066.4	2644	66	317	227	Fracture	1539968683	Epi inside Fracture gouge? (pic)
645	309316.12	8098058.4	2646	62	112	22	Fracture	1539967440	R9.5
646	309313.2	8098063.8	2647	54	307	217	Fracture	1539967419	R9.5 Conjugate larger one
647	309238.58	8098072.2	2637	74	85	355	Fracture	1539966940	R9.4
648	309232.8	8098077.8	2640	81	38	308	Fracture	1539966876	R9.4
649	309226.65	8098070.3	2636	43	313	223	Fracture	1539966507	
650	309213.74	8098072	2638	67	335	245	Fracture	1539966448	Large fractured parallel zones
651	309225.69	8098079.4	2642	73	337	247	Fracture	1539966348	
652	309192.3	8098092.9	2649	74	327	237	Fracture	1539965896	R9.3 white clay
653	309194.84	8098095.8	2651	79	53	323	Fracture	1539965876	R9.3
654	309189.26	8098096.6	2650	31	177	87	Fracture	1539965850	Low angle
655	309142	8098104.4	2649	82	324	234	Fracture	1539965663	Epi covered fracture
656	309082.9	8098121.8	2640	84	75	345	Fracture	1539953465	RCS039
657	309092.71	8098138	2634	81	243	153	Fracture	1539952928	
658	309092.71	8098138	2634	59	11	281	Fracture	1539952912	
659	309017	8098108.7	2637	73	72	342	Fracture	1539952599	Particularly epi rich vein
660	309017.48	8098108.7	2637	71	118	28	Fracture	1539952413	
661	309017.48	8098108.7	2637	81	15	285	Fracture	1539952406	
662	309017.48	8098108.7	2637	65	359	269	Fracture	1539952393	
663	308973.44	8098102	2633	77	321	231	Fracture	1539951554	Mineral lineation's? Slicken lines
664	308973.44	8098102	2633	81	8	278	Fracture	1539951275	With mineral liberations (white clay)
665	308977.69	8098104.1	2633	79	229	139	Fracture	1539951131	Parallel fractures by main Fracture
666	308969.43	8098089.4	2637	82	321	231	Fracture	1539951053	From parallel fractures (along main fault? Pic)
667	308931.72	8098082.8	2636	80	74	344	Fracture	1539950420	
668	308925.23	8098091.2	2632	82	109	19	Fracture	1539950398	
669	308937.93	8098080.8	2638	82	108	18	Fracture	1539950185	
670	308937.86	8098089.2	2634	87	103	13	Fracture	1539950175	
671	308925.54	8098078.6	2636	87	110	20	Fracture	1539950144	White clay
672	308929.32	8098082.8	2636	86	94	4	Fracture	1539950100	White mineral
673	308933.58	8098087	2635	83	117	27	Fracture	1539949870	white clay
674	308933.86	8098080.7	2637	81	102	12	Fracture	1539949825	Lots of white mineral
675	308929	8098076.5	2638	87	49	319	Fracture	1539949282	R9.2 epi and white mineral
676	308916.87	8098078.5	2634	75	114	24	Fracture	1539948918	R9.1 white clay conjugate
677	308902.25	8098078.4	2633	79	327	237	Fracture	1539948393	White mineral
678	308897.46	8098065.9	2636	65	336	246	Fracture	1539948365	White mineral
679	308919.13	8098078.5	2634	87	53	323	Fracture	1539948348	
680	308891.75	8098078.2	2631	76	69	339	Fracture	1539948335	
681	308895.82	8098072	2633	85	46	316	Fracture	1539948177	White mineral along plane
682	319093	8087629.7	2331	79	231	141	Fracture	1539719333	
683	319087.1	8087613.8	2329	72	227	137	Fracture	1539719316	
684	319023	8087546.1	2326	87	355	265	Fracture	1539719176	Epi on fracture
685	319023.41	8087546.1	2326	43	19	289	Fracture	1539719138	
686	319017.04	8087539.7	2326	42	57	327	Fracture	1539719095	
687	319017.04	8087539.7	2326	72	39	309	Fracture	1539719079	
688	319008	8087469.2	2310	84	210	120	Fracture	1539718240	R7.8 Epidote in gouge, white gouge
689	319007.71	8087469.2	2310	84	338	248	Fracture	1539717881	
690	319004.5	8087485.2	2313	87	113	23	Fracture	1539717653	
691	318890.94	8087203	2299	45	348	258	Fracture	1539717198	
692	318897.59	8087187.1	2295	48	1	271	Fracture	1539717071	Slightly larger, more prominent fracture
693	318894.66	8087155.1	2295	38	181	91	Fracture	1539717011	
694	318894.66	8087155.1	2295	73	64	334	Fracture	1539716997	
695	318894.66	8087155.1	2295	77	57	327	Fracture	1539716991	

No.	X(East)	Y(North)	Z	Dip	Az	Strike	Type	Time Stamp	Remarks
696	318894.66	8087155.1	2295	39	171	81	Fracture	1539716984	
697	318926.31	8086978.7	2279	54	54	324	Fracture	1539716325	
698	318941.68	8086919.8	2277	47	61	331	Fracture	1539716219	
699	318934	8086919.7	2282	83	205	115	Fracture	1539715645	R7.7 Epi vein RCS017
700	318942.16	8086893.9	2276	51	78	348	Fracture	1539715410	
701	318965.01	8086820.4	2264	77	341	251	Fracture	1539715263	
702	318965.01	8086820.4	2264	62	57	327	Fracture	1539715254	
703	318954	8086801.8	2277	82	332	242	Fracture	1539714421	RCS017 Epidote on plane
704	318971.36	8086744.8	2269	88	165	75	Fracture	1539712644	Fe-oxide fractures
705	318965.07	8086697.6	2264	75	19	289	Fracture	1539712533	With Fe-oxide
706	318962.04	8086657.3	2261	73	28	298	Fracture	1539712492	Parallel fractures
707	318962.04	8086657.3	2261	84	143	53	Fracture	1539712470	
708	318962.04	8086657.3	2261	87	1	271	Fracture	1539712461	
709	318933.26	8086468.6	2247	29	337	247	Fracture	1539711927	R7.6 horsetail?
710	318940.26	8086458.6	2239	65	340	250	Fracture	1539711886	
711	318940.5	8086383.8	2235	25	219	129	Fracture	1539711764	
712	318928.02	8086327.4	2242	84	6	276	Fracture	1539711681	Fe ox along fracture
713	318922.4	8086314.4	2245	40	58	328	Fracture	1539711602	Parallel fractures
714	318928.01	8086285.9	2242	87	342	252	Fracture	1539711388	
715	318929.95	8086276.7	2242	60	325	235	Fracture	1539711334	
716	318928.17	8086267.5	2244	73	126	36	Fracture	1539711264	
717	318934.87	8086243.6	2241	21	219	129	Fracture	1539711183	La
718	318934.05	8086232.5	2244	75	122	32	Fracture	1539711126	Red Fe-oxide staining
719	318939.65	8086228	2241	86	319	229	Fracture	1539711078	
720	318950.26	8086181.1	2245	41	21	291	Fracture	1539710923	
721	318950.33	8086173.7	2247	84	128	38	Fracture	1539710886	
722	318953.21	8086156.2	2246	84	126	36	Fracture	1539710749	
723	318953.21	8086156.2	2246	52	14	284	Fracture	1539710724	
724	318897.15	8086140.6	2251	86	131	41	Fracture	1539710406	Fe-oxide alteration
725	318867.69	8086160.5	2257	45	9	279	Fracture	1539709908	R7.5 main
726	318867.69	8086160.5	2257	28	134	44	Fracture	1539709848	R7.5 la ne Fracture with veining
727	318848.85	8086147.9	2248	45	12	282	Fracture	1539709672	Lots of gouge
728	318812.39	8086181.3	2250	57	324	234	Fracture	1539709133	R7.4 white clay with lots of Fe-oxide
729	318789.01	8086216.7	2256	49	85	355	Fracture	1539708676	Parallel fractures
730	318789.01	8086216.7	2256	49	13	283	Fracture	1539708653	
731	318498.04	8086267.8	2272	82	208	118	Fracture	1539702004	R7.3b minor plane synchronous
732	318487.1	8086261	2271	51	50	320	Fracture	1539701269	R7.3 third Fe-oxide Fracture
733	318490.58	8086260.1	2271	70	72	342	Fracture	1539701178	R7.3 conjugate
734	318489.77	8086259.4	2271	42	52	322	Fracture	1539701095	R7.3
735	318471.31	8086240.7	2273	18	173	83	Fracture	1539701049	R7.3 shear structure
736	318472.29	8086248.3	2273	41	39	309	Fracture	1539700355	Second large Fracture with gouge and veining along plane, Fe-oxide alt
737	318459.37	8086232	2275	52	39	309	Fracture	1539698988	Large Fe-oxide altered gouge - big fault?
738	318452.09	8086226.4	2274	81	225	135	Fracture	1539698699	Shear fabrics
739	318432.24	8086200.8	2276	64	72	342	Fracture	1539698340	Parallel fractures
740	318417.55	8086190.1	2280	40	218	128	Fracture	1539697811	R7.2 second gouge
741	318414.51	8086193.9	2282	50	48	318	Fracture	1539697715	Conjugate?
742	318412.12	8086184	2284	43	64	334	Fracture	1539697651	Gouge
743	318412.12	8086184	2284	38	54	324	Fracture	1539697635	Parallel fractures
744	318363.91	8086050.6	2284	19	221	131	Fracture	1539697174	Low angle veining along plane - calcite
745	318349.12	8086043.1	2286	56	26	296	Fracture	1539696980	R7.1 white clay
746	318319.49	8086018.2	2286	59	26	296	Fracture	1539696822	R7.1 white clay
747	318317.07	8086018.2	2286	29	188	98	Fracture	1539696168	R7.1 low angle
748	318334.03	8086028.2	2286	64	46	316	Fracture	1539695653	R7.1 large Fracture with gouge and veining within white clay
759	317761.48	8092044.1	2603	83	28	298	Veining	1540824102	
760	317761.48	8092044.1	2603	42	78	348	Veining	1540824094	
761	317766.62	8092057	2606	73	81	351	Veining	1540824066	
762	318789.01	8086216.7	2256	18	213	123	Bedding	1539708583	Andesite
763	318561.89	8086349.2	2291	15	196	106	Bedding	1539705533	Diorite rhyolite contact
764	320502.49	8089343.4	2511	38	205	115	Fracture	1541012915	IFS Fracture - highly Fe-oxide altered and brecciated
765	320476.94	8089315.6	2517	70	64	334	Fracture	1541012734	IFS Fracture - highly Fe-oxide altered and brecciated
766	320532.43	8089336.3	2494	88	343	253	Fracture	1541012507	IFS Fracture - highly Fe-oxide altered and brecciated
767	320532.43	8089336.3	2494	86	245	155	Fracture	1541012495	IFS Fracture - highly Fe-oxide altered and brecciated
768	322489.51	8095330.5	3322	74	97	7	Fracture	1540999946	
769	322503.72	8095331.5	3324	68	12	282	Fracture	1540999921	
770	322498.31	8095341.2	3325	64	91	1	Fracture	1540999896	
771	322498.31	8095341.2	3325	87	210	120	Fracture	1540999872	
772	322494.04	8095337.7	3323	89	89	359	Fracture	1540999860	
773	322494.04	8095337.7	3323	84	205	115	Fracture	1540999849	
774	322493.03	8095351.8	3326	73	193	103	Fracture	1540999803	Lots of parallel
775	322491.09	8095353.5	3325	79	185	95	Fracture	1540999777	
776	322490.43	8095359.7	3326	59	36	306	Fracture	1540999702	
777	322481.61	8095386.7	3329	63	155	65	Fracture	1540999577	(Pic)
778	322481.61	8095386.7	3329	72	50	320	Fracture	1540999570	

No.	X(East)	Y(North)	Z	Dip	Az	Strike	Type	Time Stamp	Remarks
779	322483.38	8095395	3329	49	29	299	Fracture	1540999529	
780	322478.65	8095409.6	3328	78	200	110	Fracture	1540999495	
781	322478.65	8095409.6	3328	86	60	330	Fracture	1540999477	
782	322476.78	8095413.2	3328	73	198	108	Fracture	1540999445	
783	322481.38	8095412.3	3329	82	145	55	Fracture	1540999403	
784	322484.05	8095423.3	3328	38	45	315	Fracture	1540999395	
785	322481.33	8095418.7	3328	68	125	35	Fracture	1540999374	
786	322481.33	8095418.7	3328	35	60	330	Fracture	1540999364	
787	322510.01	8095434.5	3330	83	310	220	Fracture	1540999262	Gouge (pic)
788	322537.56	8095442	3332	83	23	293	Fracture	1540999240	
789	322550.35	8095453.1	3328	18	202	112	Fracture	1540999145	
790	322545.57	8095447.7	3331	62	121	31	Fracture	1540999131	
791	322545.57	8095447.7	3331	76	27	297	Fracture	1540999125	
792	322552.85	8095456.9	3327	86	32	302	Fracture	1540999089	
793	322552.85	8095456.9	3327	81	307	217	Fracture	1540999075	
794	322590.4	8095479.2	3328	68	354	264	Fracture	1540999017	
795	322590.4	8095479.2	3328	77	110	20	Fracture	1540999003	
796	322608.66	8095492.9	3331	64	96	6	Fracture	1540998941	
797	322616.83	8095506.7	3328	82	193	103	Fracture	1540998896	
798	322616.83	8095506.7	3328	71	278	188	Fracture	1540998883	
799	322646.95	8095541.2	3328	71	127	37	Fracture	1540998763	
800	322643.85	8095547.3	3326	76	112	22	Fracture	1540998730	
801	322646.6	8095555.9	3328	62	111	21	Fracture	1540998533	Now parallel purple ne Fractures (pic)
802	322649.6	8095556.9	3330	60	112	22	Fracture	1540998485	
803	322652.87	8095573.9	3331	81	45	315	Fracture	1540998427	
804	322652.87	8095573.9	3331	57	76	346	Fracture	1540998420	With Fe-oxide and gouge
805	322662	8095587.5	3333	63	76	346	Fracture	1540998344	
806	322667.77	8095591	3335	66	76	346	Fracture	1540998330	
807	322667.77	8095591	3335	60	76	346	Fracture	1540998321	
808	322670.99	8095601.1	3335	59	70	340	Fracture	1540998243	Parallel purple Fractures (pic)
809	322678.56	8095613.9	3337	81	58	328	Fracture	1540998189	
810	322680.2	8095621.6	3335	56	328	238	Fracture	1540998134	
811	322680.2	8095621.6	3335	82	46	316	Fracture	1540998113	
812	322680.2	8095621.6	3335	85	187	97	Fracture	1540998100	
813	322675.64	8095655.4	3339	87	305	215	Fracture	1540998010	
814	322669.72	8095656.3	3337	82	27	297	Fracture	1540997985	
815	322730.45	8095738.2	3360	58	131	41	Fracture	1540997729	
816	322748.18	8095759.6	3365	87	186	96	Fracture	1540997638	
817	322748.18	8095759.6	3365	84	96	6	Fracture	1540997625	
818	322766.85	8095771.6	3369	88	139	49	Fracture	1540997271	
819	322654.06	8095692.5	3344	80	223	133	Fracture	1540996527	
820	322654.06	8095692.5	3344	64	132	42	Fracture	1540996474	
821	322654.06	8095692.5	3344	76	121	31	Fracture	1540996371	
822	322641.34	8095684	3343	80	122	32	Fracture	1540996311	
823	322630.64	8095678	3344	89	293	203	Fracture	1540996092	Fe-oxide Fracture with breccia (pic)
824	322610.86	8095676.9	3350	89	202	112	Fracture	1540995864	Large Fracture zone with gouge (pic)
825	322603.18	8095676.9	3351	80	122	32	Fracture	1540995842	
826	322608.31	8095675.2	3349	75	124	34	Fracture	1540995760	
827	322597.34	8095661.5	3349	58	3	273	Fracture	1540995711	
828	322587.04	8095661.5	3351	65	65	335	Fracture	1540995655	Fracture xo e with Fe-oxide (pic)
829	322579.3	8095668.3	3355	59	352	262	Fracture	1540995600	
830	322565.71	8095661.4	3353	79	21	291	Fracture	1540995590	
831	322565.71	8095661.4	3353	76	34	304	Fracture	1540995563	
832	322565.71	8095661.4	3353	48	354	264	Fracture	1540995552	
833	322553.73	8095669.7	3355	87	37	307	Fracture	1540995436	Fracture zone with Fe-oxide (pic)
834	322541.61	8095689.9	3359	85	25	295	Fracture	1540995373	
835	322544.2	8095678.9	3355	85	112	22	Fracture	1540995354	
836	322544.2	8095678.9	3355	79	36	306	Fracture	1540995338	
837	322498.67	8095715	3360	56	18	288	Fracture	1540995263	
838	322498.67	8095715	3360	69	341	251	Fracture	1540995239	
839	322487.83	8095717.5	3361	81	341	251	Fracture	1540995211	
840	322487.83	8095717.5	3361	23	254	164	Fracture	1540995185	
841	322481.45	8095717.4	3362	80	41	311	Fracture	1540995118	With gouge (pic)
842	322454.06	8095739.2	3368	43	270	180	Fracture	1540995034	
843	322454.06	8095739.2	3368	70	35	305	Fracture	1540995025	
844	322451.45	8095731.5	3364	60	15	285	Fracture	1540995009	
845	322433.41	8095756.3	3365	33	302	212	Fracture	1540994954	
846	322433.41	8095756.3	3365	86	279	189	Fracture	1540994945	
847	322436.01	8095754.1	3366	43	324	234	Fracture	1540994928	
848	322436	8095754.1	3366	88	277	187	Fracture	1540994918	Minor epi
849	322407.35	8095785	3370	65	337	247	Fracture	1540994809	
850	322404.12	8095786.2	3370	46	158	68	Fracture	1540994796	
851	322405.63	8095781.8	3368	44	153	63	Fracture	1540994790	
852	322393.69	8095790.5	3369	60	348	258	Fracture	1540994692	R18.3
853	322393.79	8095788.9	3369	77	336	246	Fracture	1540994483	R18.3
854	322377.2	8095803.6	3371	89	117	27	Fracture	1540994136	R18.2
855	322377.2	8095803.6	3371	77	58	328	Fracture	1540994110	R18.2
856	322376.04	8095809.6	3372	72	59	329	Fracture	1540994102	
857	322380.45	8095811.9	3373	77	62	332	Fracture	1540994094	
858	322381.48	8095822.3	3374	71	10	280	Fracture	1540993957	

No.	X(East)	Y(North)	Z	Dip	Az	Strike	Type	Time Stamp	Remarks
859	322381.48	8095822.3	3374	21	242	152	Fracture	1540993949	
860	322378.66	8095829.5	3374	17	234	144	Fracture	1540993941	Lots of low angle nw Fractures (pic) Minor gouge
861	322379.13	8095838.8	3375	58	67	337	Fracture	1540993885	
862	322379.13	8095838.8	3375	83	95	5	Fracture	1540993862	
863	322383.55	8095840	3376	83	94	4	Fracture	1540993850	
864	322380.6	8095847.1	3375	43	91	1	Fracture	1540993713	Large Fracture with gouge (pic)
865	322383.95	8095864.6	3376	37	263	173	Fracture	1540993564	
866	322383.95	8095864.6	3376	64	51	321	Fracture	1540993544	
867	322388.06	8095870	3378	83	111	21	Fracture	1540993513	
868	322388.06	8095870	3378	63	41	311	Fracture	1540993499	
869	322433.41	8095972.1	3390	86	57	327	Fracture	1540993279	Parallel fractures (pic)
870	322444.95	8095980.6	3394	89	232	142	Fracture	1540993227	
871	322455.2	8096018.9	3392	77	199	109	Fracture	1540993121	R18.1
872	322457.35	8096016.8	3394	77	163	73	Fracture	1540992863	R18.1 altered breccia fill?
873	322500.92	8096031.9	3405	89	36	306	Fracture	1540992625	Fracture with breccia fill? (Pic)
874	322536.62	8095267.4	3322	59	45	315	Fracture	1540928340	
875	319902.36	8093241.1	3181	79	303	213	Fracture	1540915556	
876	319902.36	8093241.1	3181	71	3	273	Fracture	1540915552	
877	319872.6	8093251.6	3193	72	358	268	Fracture	1540915483	
878	319874.63	8093273.1	3185	71	1	271	Fracture	1540915018	
879	320487.07	8093473.6	3264	72	55	325	Fracture	1540913810	
880	320487.16	8093463.2	3264	65	42	312	Fracture	1540913794	
881	320498.14	8093477.2	3265	78	43	313	Fracture	1540913143	(Pic)
882	320510.36	8093492.7	3266	70	42	312	Fracture	1540913006	
883	320526.11	8093541	3275	63	41	311	Fracture	1540912856	
884	320532.62	8093556.8	3280	40	59	329	Fracture	1540912846	
885	320532.62	8093556.8	3280	62	56	326	Fracture	1540912837	
886	320670.71	8093936	3347	61	16	286	Fracture	1540911669	
887	320670.71	8093936	3347	63	2	272	Fracture	1540911608	
888	320654.86	8093920.1	3351	71	2	272	Fracture	1540911578	
889	320836.14	8094212.3	3428	80	208	118	Fracture	1540910237	
890	320899.05	8094297.2	3461	72	38	308	Fracture	1540910124	
891	320899	8094297.2	3461	23	271	181	Fracture	1540910115	Epi
892	320921.49	8094310.4	3465	35	260	170	Fracture	1540909476	
893	321017.97	8094477	3449	86	248	158	Fracture	1540908928	
894	321002.89	8094541.8	3442	73	62	332	Fracture	1540908851	
895	320971.96	8094707.2	3489	75	67	337	Fracture	1540908466	
896	321007.4	8094707.5	3482	70	71	341	Fracture	1540908456	(Pic)
897	321008.7	8094730.7	3495	58	2	272	Fracture	1540907894	
898	321226.2	8094840.5	3499	70	233	143	Fracture	1540907372	
899	321262.99	8094834.7	3500	23	39	309	Fracture	1540907363	
900	321262.99	8094834.7	3500	27	38	308	Fracture	1540907357	
901	321262.99	8094834.7	3500	74	243	153	Fracture	1540907349	
902	321336.7	8094841.4	3520	77	243	153	Fracture	1540907273	
903	321281.51	8094831.8	3505	67	237	147	Fracture	1540907199	
904	321312.18	8094826	3507	68	233	143	Fracture	1540907192	
905	322338.55	8094918.3	3421	82	248	158	Fracture	1540905723	
906	321952.63	8094786	3467	21	167	77	Fracture	1540905703	
907	321962.06	8094758.7	3483	29	164	74	Fracture	1540905696	
908	321962.06	8094758.7	3483	52	238	148	Fracture	1540905681	
909	321962.06	8094758.7	3483	67	240	150	Fracture	1540905669	
910	322162.96	8094856.5	3457	80	336	246	Fracture	1540905415	
911	322162.96	8094856.5	3457	82	182	92	Fracture	1540905398	
912	322159.37	8094861.7	3454	77	164	74	Fracture	1540905389	
913	322235.87	8095029.6	3404	76	157	67	Fracture	1540904941	
914	322244	8095032.2	3401	62	228	138	Fracture	1540904327	
915	322226.76	8095023.6	3409	69	242	152	Fracture	1540904314	
916	318831.83	8092817.6	2815	82	313	223	Fracture	1540834689	
917	318831.83	8092817.6	2815	75	38	308	Fracture	1540834681	
918	318853.68	8092827.8	2828	81	31	301	Fracture	1540834615	
919	318604.81	8092558.2	2744	87	301	211	Fracture	1540833144	
920	318610.53	8092559.2	2744	73	216	126	Fracture	1540832946	
921	318598.13	8092557.2	2745	89	311	221	Fracture	1540832932	
922	318593.3	8092563.8	2749	42	182	92	Fracture	1540832905	
923	318593.3	8092563.8	2749	83	138	48	Fracture	1540832899	
924	318593.3	8092563.8	2749	89	209	119	Fracture	1540832886	
925	318584.74	8092559.1	2748	81	218	128	Fracture	1540832851	
926	318591.46	8092447.1	2743	88	95	5	Fracture	1540832490	
927	318602.92	8092447.2	2751	85	103	13	Fracture	1540832471	
928	318601.1	8092436.8	2754	85	12	282	Fracture	1540832461	
929	318610.22	8092444.4	2756	76	6	276	Fracture	1540832336	
930	318480.43	8092254.7	2699	55	296	206	Fracture	1540831442	
931	318480.43	8092254.7	2699	52	135	45	Fracture	1540831389	R16.4
932	318490.93	8092249	2701	74	135	45	Fracture	1540830260	R16.4 Quartz Vuggy vein
933	318486.19	8092252	2700	49	145	55	Fracture	1540829229	Very vuggy quartz
934	318481.89	8092251.4	2700	48	138	48	Fracture	1540829202	Very vuggy quartz
935	318342.63	8092226.3	2693	85	91	1	Fracture	1540827844	
936	318354.84	8092225	2694	72	185	95	Fracture	1540827805	
937	318354.84	8092225	2694	89	92	2	Fracture	1540827796	
938	318349.71	8092225	2693	85	82	352	Fracture	1540827783	

No.	X(East)	Y(North)	Z	Dip	Az	Strike	Type	Time Stamp	Remarks
939	318351.45	8092200.7	2684	33	91	1	Fracture	1540827573	R16.3 Fe-oxide la fault
940	318351.45	8092200.7	2684	80	6	276	Fracture	1540827547	R16.3 Breccia
941	318344.86	8092200.6	2685	74	192	102	Fracture	1540827241	Breccia (pic)
942	318346.77	8092192.7	2682	88	345	255	Fracture	1540827158	
943	318329.26	8092192.5	2682	87	329	239	Fracture	1540827139	
944	318332.13	8092181.7	2679	82	325	235	Fracture	1540826941	R16.2
945	318332.13	8092181.7	2679	31	110	20	Fracture	1540826922	R16.2 min Fracture Fe-oxide
946	318321.66	8092180.9	2680	31	207	117	Fracture	1540826865	
947	318308.04	8092175.9	2680	89	207	117	Fracture	1540826851	
948	318308.04	8092175.9	2680	79	103	13	Fracture	1540826842	
949	318316.8	8092168.6	2678	73	91	1	Fracture	1540826836	
950	318279.91	8092159	2674	57	354	264	Fracture	1540826681	
951	318279.91	8092159	2674	43	236	146	Fracture	1540826672	
952	318279.91	8092159	2674	81	315	225	Fracture	1540826618	
953	318205.74	8092160.9	2664	66	94	4	Fracture	1540826487	
954	318190.69	8092158.2	2666	84	344	254	Fracture	1540826430	
955	318153.17	8092148.8	2656	66	311	221	Fracture	1540826264	
956	318140.58	8092152.6	2656	63	326	236	Fracture	1540826199	
957	318145.36	8092150.3	2656	85	56	326	Fracture	1540826190	
958	318145.36	8092150.3	2656	62	331	241	Fracture	1540826179	
959	318135.81	8092155	2655	69	323	233	Fracture	1540826168	
960	318135.81	8092155	2655	65	327	237	Fracture	1540826160	
961	317977.25	8092185.8	2643	78	328	238	Fracture	1540825938	
962	317970.08	8092185.7	2642	73	328	238	Fracture	1540825925	
963	317974.05	8092183.4	2645	70	69	339	Fracture	1540825891	
964	317966.09	8092186.5	2641	72	68	338	Fracture	1540825876	
965	317954.98	8092188	2636	66	27	297	Fracture	1540825816	
966	317964.48	8092189.6	2638	67	26	296	Fracture	1540825801	
967	317964.48	8092189.6	2638	85	86	356	Fracture	1540825687	
968	324346.77	8106303.3	3887	87	159	69	Fracture	1540587983	
969	324360.05	8106315.4	3890	54	158	68	Fracture	1540587969	
970	324375.95	8106334.1	3890	61	155	65	Fracture	1540587957	
971	324375.95	8106334.1	3890	87	257	167	Fracture	1540587951	
972	324402.17	8106387.5	3884	66	151	61	Fracture	1540587589	
973	324395.7	8106372.9	3886	31	279	189	Fracture	1540587577	
974	324395.7	8106372.9	3886	62	160	70	Fracture	1540587562	
975	324397.11	8106364.9	3889	62	166	76	Fracture	1540587554	Parallel fractures
976	328256.98	8107643.3	3843	80	10	280	Fracture	1540585984	
977	328256.98	8107643.3	3843	88	116	26	Fracture	1540585977	
978	328261.53	8107638.7	3846	80	219	129	Fracture	1540585712	
979	328004.67	8107054.2	3979	46	123	33	Fracture	1540582144	BT veins (pic)
980	328000.87	8107051.6	3979	60	99	9	Fracture	1540582026	Highly alt fractures and area (pic)
981	327933.81	8106928.4	3964	86	18	288	Fracture	1540581694	
982	327931.14	8106878.9	3958	83	228	138	Fracture	1540581592	
983	327931.14	8106878.9	3958	78	119	29	Fracture	1540581587	
984	327931.14	8106878.9	3958	81	119	29	Fracture	1540581579	
985	327922.06	8106827.8	3957	37	215	125	Fracture	1540581324	Bright touquise mineral on plane! (Pic)
986	327922.06	8106827.8	3957	87	108	18	Fracture	1540581250	
987	327930.99	8106777.5	3966	65	123	33	Fracture	1540580944	
988	327974.24	8106681.6	3978	86	116	26	Fracture	1540579500	
989	328069.18	8106591.7	3975	63	115	25	Fracture	1540579122	Veining
990	328070.95	8106590.2	3974	73	109	19	Fracture	1540579112	Py (Fe-oxide)
991	328071.93	8106587.9	3973	80	111	21	Fracture	1540578914	Parallel alt veins with py in wr (pic) Fe-oxide
992	328083.64	8106571.8	3971	35	209	119	Fracture	1540578491	Very faint trace of coy??
993	328083.64	8106571.8	3971	86	239	149	Fracture	1540578404	
994	328083.64	8106571.8	3971	89	109	19	Fracture	1540578392	
995	328084.83	8106559.9	3965	81	231	141	Fracture	1540578330	R14.6
996	328084.83	8106559.9	3965	45	41	311	Fracture	1540578283	R14.6 la
997	328079.78	8106562.9	3964	77	285	195	Fracture	1540578171	
998	328079.78	8106562.9	3964	86	280	190	Fracture	1540578159	R14.6 large linear rock with Fe-oxide - solidified d veins
999	327824.9	8106450.3	3956	71	104	14	Fracture	1540575132	R14.5 Parallel d veins Fe-oxide
1000	327794.11	8106401.1	3978	65	105	15	Fracture	1540574981	Fe-oxide
1001	327778.54	8106383.8	3978	70	115	25	Fracture	1540574946	Fe-oxide
1002	327770.01	8106376.9	3975	87	3	273	Fracture	1540574866	
1003	327770.01	8106376.9	3975	84	103	13	Fracture	1540574861	
1004	327768.39	8106363.1	3975	58	8	278	Fracture	1540574834	
1005	327768.39	8106363.1	3975	76	114	24	Fracture	1540574825	
1006	327757.44	8106362	3969	83	109	19	Fracture	1540574799	
1007	327747.01	8106348.4	3967	70	109	19	Fracture	1540574420	
1008	327733.61	8106331.9	3958	78	106	16	Fracture	1540574401	
1009	327733.61	8106331.9	3958	77	192	102	Fracture	1540574365	
1010	327722.33	8106339.7	3955	84	98	8	Fracture	1540574353	
1011	327722.33	8106339.7	3955	85	103	13	Fracture	1540574335	Multiple parallel tight fracture sets
1012	327215.29	8106573	3912	74	322	232	Fracture	1540573903	
1013	327215.29	8106573	3912	61	220	130	Fracture	1540573894	
1014	327196.21	8106570.8	3922	89	332	242	Fracture	1540573549	R14.3Very large Fe-oxide Fracture
1015	327176.91	8106602.2	3916	87	140	50	Fracture	1540573331	
1016	327084.86	8106864.4	3836	89	152	62	Fracture	1540573269	Fe-oxide

No.	X(East)	Y(North)	Z	Dip	Az	Strike	Type	Time Stamp	Remarks
1017	327058.81	8106875.5	3829	60	128	38	Fracture	1540572864	Parallel fractures (pic)
1018	327050	8106871.8	3832	36	359	269	Fracture	1540572764	Epi
1019	327039	8106872.9	3830	86	89	359	Fracture	1540572702	
1020	327039	8106872.9	3830	65	132	42	Fracture	1540572695	
1021	327020.68	8106874.4	3826	78	132	42	Fracture	1540572568	D vein?(pic)
1022	327010.31	8106874.5	3834	63	213	123	Fracture	1540572425	
1023	327010.31	8106874.5	3834	79	117	27	Fracture	1540572407	
1024	327010.31	8106874.5	3834	79	127	37	Fracture	1540572403	
1025	327010.31	8106874.5	3834	21	17	287	Fracture	1540572385	
1026	326649.94	8107096.9	3791	65	135	45	Fracture	1540571877	
1027	326565.82	8107146.1	3826	57	138	48	Fracture	1540571870	
1028	326624.66	8107117.5	3794	58	132	42	Fracture	1540571856	
1029	326624.66	8107117.5	3794	84	240	150	Fracture	1540571847	
1030	326624.66	8107117.5	3794	53	158	68	Fracture	1540571837	
1031	326586.73	8107121.3	3811	58	144	54	Fracture	1540571314	RCS085
1032	326416.4	8107211.3	3866	60	138	48	Fracture	1540570508	Quartz vein along fracture with black mineral in the middle (Pic)
1033	326389.33	8107224.5	3865	63	150	60	Fracture	1540570405	Qtz vein
1034	326353.68	8107188.5	3878	62	152	62	Fracture	1540570267	R14.2 lots of tight parallel fractures
1035	326324.44	8107200.1	3868	55	132	42	Fracture	1540570128	
1036	326281.34	8107216.8	3850	69	289	199	Fracture	1540570120	
1037	326293.04	8107188.5	3864	32	312	222	Fracture	1540569976	
1038	326281.02	8107212.9	3852	53	134	44	Fracture	1540569924	
1039	326281.02	8107212.9	3852	72	235	145	Fracture	1540569915	
1040	326281.02	8107212.9	3852	48	105	15	Fracture	1540569910	Parallel fractures
1041	326281.02	8107212.9	3852	50	129	39	Fracture	1540569893	
1042	325892	8107238.1	3883	66	110	20	Fracture	1540569489	
1043	325865.6	8107240.2	3886	49	156	66	Fracture	1540569234	
1044	325865.6	8107240.2	3886	56	153	63	Fracture	1540569222	
1045	325865.6	8107240.2	3886	37	334	244	Fracture	1540569215	
1046	325823.78	8107231.6	3891	30	317	227	Fracture	1540568687	
1047	325811.68	8107249.7	3877	39	325	235	Fracture	1540568673	
1048	325823.9	8107257.8	3870	41	321	231	Fracture	1540568488	
1049	325825.61	8107241.7	3883	85	89	359	Fracture	1540568470	
1050	325779.27	8107292.1	3880	66	143	53	Fracture	1540568341	
1051	325753.06	8107286.3	3912	88	234	144	Fracture	1540568324	
1052	325753.06	8107286.3	3912	28	331	241	Fracture	1540568301	
1053	325753.06	8107286.3	3912	51	148	58	Fracture	1540568294	
1054	325751.57	8107293.1	3910	57	150	60	Fracture	1540568223	
1055	325751.57	8107293.1	3910	31	322	232	Fracture	1540568209	
1056	325360.89	8107220.8	3960	45	89	359	Fracture	1540567858	
1057	325342.1	8107221.9	3950	48	291	201	Fracture	1540567845	Lots of parallel fractures
1058	325342.01	8107233.9	3941	50	301	211	Fracture	1540567826	
1059	325342.01	8107233.9	3941	44	87	357	Fracture	1540567819	
1060	325342.01	8107233.9	3941	52	309	219	Fracture	1540567810	
1061	325265.48	8107214.6	3936	46	315	225	Fracture	1540567712	
1062	325265.48	8107214.6	3936	74	60	330	Fracture	1540567704	
1063	325254.28	8107207.1	3940	67	307	217	Fracture	1540567422	
1064	325216.86	8107194.7	3942	48	336	246	Fracture	1540567177	
1065	325216.86	8107194.7	3942	54	139	49	Fracture	1540567161	
1066	325209.66	8107205.3	3934	35	336	246	Fracture	1540566981	
1067	325209.66	8107205.3	3934	84	230	140	Fracture	1540566954	
1068	325159.75	8107190.7	3940	27	327	237	Fracture	1540566920	Parallel fractures
1069	325039.92	8107196.6	3940	39	311	221	Fracture	1540566822	
1070	325018.13	8107208.8	3934	78	75	345	Fracture	1540566747	
1071	325033.64	8107208.9	3932	75	72	342	Fracture	1540566740	
1072	324987.09	8107210.1	3933	37	330	240	Fracture	1540566630	
1073	324987.09	8107210.1	3933	35	325	235	Fracture	1540566625	
1074	324978.06	8107211.6	3929	31	165	75	Fracture	1540566577	
1075	324964.04	8107219.2	3921	34	154	64	Fracture	1540566567	
1076	324941.08	8107182	3916	49	139	49	Fracture	1540566529	
1077	324930.26	8107177.3	3909	78	220	130	Fracture	1540566499	
1078	324930.26	8107177.3	3909	47	141	51	Fracture	1540566490	
1079	324930.26	8107177.3	3909	57	153	63	Fracture	1540566479	
1080	324920.93	8107180.3	3906	58	158	68	Fracture	1540566469	
1081	324812.05	8107037.3	3908	40	48	318	Fracture	1540566107	
1082	324815.2	8107041.3	3908	46	113	23	Fracture	1540566094	
1083	324815.2	8107041.3	3908	33	238	148	Fracture	1540566083	
1084	324810.28	8107033.5	3909	81	43	313	Fracture	1540565644	
1085	324447.87	8106738.1	3898	80	228	138	Fracture	1540561424	
1086	324397.77	8106695.8	3895	86	100	10	Fracture	1540560968	
1087	324387.77	8106683.1	3894	72	74	344	Fracture	1540560915	
1088	324387.77	8106683.1	3894	66	121	31	Fracture	1540560904	
1089	324392.96	8106672.2	3893	82	93	3	Fracture	1540560882	White clay
1090	324389.5	8106670.4	3893	88	184	94	Fracture	1540560831	With gouge (pic)
1091	324350.11	8106625.2	3893	88	83	353	Fracture	1540560740	
1092	324346.29	8106617.5	3893	89	343	253	Fracture	1540560723	
1093	324338.33	8106601.9	3896	89	272	182	Fracture	1540560676	
1094	324324.88	8106584.5	3897	87	197	107	Fracture	1540560633	
1095	324324.88	8106584.5	3897	84	255	165	Fracture	1540560619	

No.	X(East)	Y(North)	Z	Dip	Az	Strike	Type	Time Stamp	Remarks
1096	324324.88	8106584.5	3897	84	259	169	Fracture	1540560611	
1097	324324.88	8106584.5	3897	85	332	242	Fracture	1540560602	
1098	324365.02	8106660.1	3893	77	56	326	Fracture	1540560395	
1099	324369.24	8106627.4	3888	87	65	335	Fracture	1540560378	
1100	324430.47	8106728.3	3894	82	93	3	Fracture	1540560045	
1101	324003.39	8106348.3	3868	61	73	343	Fracture	1540499432	
1102	324003.39	8106348.3	3868	89	153	63	Fracture	1540499418	
1103	324003.39	8106348.3	3868	26	185	95	Fracture	1540499411	
1104	323988.21	8106353.9	3869	87	154	64	Fracture	1540499296	
1105	323988.21	8106353.9	3869	89	336	246	Fracture	1540499286	
1106	323987.97	8106361.8	3872	31	169	79	Fracture	1540499062	
1107	323987.97	8106361.8	3872	27	161	71	Fracture	1540499059	
1108	322923.65	8105787.9	3550	78	121	31	Fracture	1540497042	
1109	322937	8105796.2	3551	79	114	24	Fracture	1540497035	Epi - whole area fractured etc difficult to tell plane
1110	322749	8105679.6	3549	77	239	149	Fracture	1540495663	Green channel with white clay either side
1111	322712	8105645.4	3551	77	247	157	Fracture	1540495452	Epi and white clay
1112	322683.95	8105627.2	3558	20	108	18	Fracture	1540495286	R13.5 quartz
1113	322683.95	8105627.2	3558	56	260	170	Fracture	1540495272	R13.5
1114	322644.14	8105625.2	3554	78	237	147	Fracture	1540495140	Vein direction altered fractures
1115	322596.43	8105616.6	3552	76	51	321	Fracture	1540495081	
1116	322581.68	8105606.7	3554	83	73	343	Fracture	1540495031	
1117	322491.39	8105566.6	3544	81	189	99	Fracture	1540494865	
1118	322447.37	8105530.2	3542	88	246	156	Fracture	1540494686	R13.4 qtz
1119	322447.49	8105522	3546	55	210	120	Fracture	1540494631	With quartz
1120	322436.01	8105515.4	3544	40	238	148	Fracture	1540494590	
1121	321988.9	8105334.4	3520	78	44	314	Fracture	1540494213	
1122	321991.07	8105322.6	3524	89	194	104	Fracture	1540493977	
1123	321983.97	8105317	3521	83	201	111	Fracture	1540493941	
1124	321980.38	8105294	3522	84	44	314	Fracture	1540493839	Large Fracture with 30cm gouge (pic)
1125	321980.49	8105276.7	3523	81	191	101	Fracture	1540493695	Large Fracture with quartz and minor Fe-oxide (pic)
1126	321974.82	8105272.6	3521	86	201	111	Fracture	1540493635	More quartz
1127	321977.34	8105256.9	3523	84	129	39	Fracture	1540493594	
1128	321973.29	8105265.5	3520	75	127	37	Fracture	1540493586	
1129	321968.97	8105249.8	3518	79	195	105	Fracture	1540493532	Quartz vein (pic)
1130	321961.93	8105237.9	3516	82	43	313	Fracture	1540493492	
1131	321961.93	8105237.9	3516	84	163	73	Fracture	1540493485	
1132	321897.15	8104930.7	3501	38	226	136	Fracture	1540493158	
1133	321920.42	8104905.3	3504	66	26	296	Fracture	1540493145	
1134	321920.42	8104905.3	3504	68	330	240	Fracture	1540493127	
1135	321931.29	8104902.7	3508	87	48	318	Fracture	1540493097	
1136	321933.62	8104900	3508	78	342	252	Fracture	1540493085	
1137	321937.88	8104877.2	3503	38	224	134	Fracture	1540493051	
1138	321942.03	8104901.5	3509	74	149	59	Fracture	1540492960	
1139	321940.85	8104881.2	3504	76	54	324	Fracture	1540492952	
1140	321974.76	8104880.2	3504	71	50	320	Fracture	1540492894	
1141	321968.05	8104872	3502	81	50	320	Fracture	1540492874	
1142	321983.62	8104861.4	3499	79	6	276	Fracture	1540492825	
1143	321993.19	8104854.4	3493	70	3	273	Fracture	1540492816	
1144	321993.19	8104854.4	3493	73	15	285	Fracture	1540492809	
1145	322001.08	8104858.4	3496	73	48	318	Fracture	1540492752	
1146	322028.1	8104850.7	3494	77	49	319	Fracture	1540492716	
1147	322015.39	8104854.6	3495	42	282	192	Fracture	1540492703	
1148	322015.39	8104854.6	3495	77	51	321	Fracture	1540492695	
1149	322031.72	8104846.6	3491	45	298	208	Fracture	1540492479	
1150	322178.7	8104498.7	3447	86	224	134	Fracture	1540491862	
1151	322155.79	8104486.4	3447	38	223	133	Fracture	1540491855	
1152	322155.79	8104486.4	3447	85	59	329	Fracture	1540491794	
1153	322144.59	8104481.7	3448	74	65	335	Fracture	1540491673	
1154	322129.49	8104484.3	3443	89	344	254	Fracture	1540491663	
1155	322129.49	8104484.3	3443	76	67	337	Fracture	1540491651	
1156	322108.97	8104474.6	3445	80	280	190	Fracture	1540491536	Black halo
1157	322091.11	8104478.5	3439	71	64	334	Fracture	1540491501	R13.3
1158	322091.32	8104468.9	3445	35	50	320	Fracture	1540491448	
1159	322081.97	8104466.1	3445	49	242	152	Fracture	1540491303	R13.3
1160	322081.97	8104466.1	3445	36	49	319	Fracture	1540491286	R13.3 conjugate
1161	322075.13	8104463.3	3445	75	119	29	Fracture	1540491232	
1162	322075.13	8104463.3	3445	43	263	173	Fracture	1540491226	
1163	322057.44	8104448.2	3451	74	280	190	Fracture	1540491190	Dark halos
1164	322045.16	8104441.3	3451	71	256	166	Fracture	1540491167	
1165	322024.36	8104435.6	3450	67	77	347	Fracture	1540491083	With dark halo? Houdini)
1166	322001.92	8104413.7	3455	77	88	358	Fracture	1540491058	
1167	322001.92	8104413.7	3455	83	16	286	Fracture	1540491028	
1168	321949.49	8104399	3450	89	102	12	Fracture	1540491023	
1169	321949.49	8104399	3450	89	161	71	Fracture	1540490987	
1170	321920.05	8104404.3	3441	28	249	159	Fracture	1540490920	
1171	321769.45	8104347.6	3415	23	269	179	Fracture	1540490676	
1172	321757.34	8104343.2	3412	22	253	163	Fracture	1540490664	
1173	321748.81	8104338.9	3409	75	70	340	Fracture	1540490656	

No.	X(East)	Y(North)	Z	Dip	Az	Strike	Type	Time Stamp	Remarks
1174	321739.26	8104321.4	3407	77	54	324	Fracture	1540487062	
1175	321745.76	8104325.8	3410	78	157	67	Fracture	1540487056	
1176	321745.76	8104325.8	3410	87	62	332	Fracture	1540487010	
1177	321388.44	8103959.9	3332	75	59	329	Fracture	1540486345	
1178	321383	8103958.9	3333	89	162	72	Fracture	1540486334	Epi
1179	321382.58	8103958.9	3333	76	50	320	Fracture	1540486324	
1180	321383.58	8103965.8	3330	75	307	217	Fracture	1540486275	Larger Fracture with white clay (pic)
1181	321362.98	8103969.5	3330	66	50	320	Fracture	1540486207	
1182	321336.3	8103983	3321	66	48	318	Fracture	1540485988	White mineral with striations (pic)
1183	321315	8103992.5	3317	78	179	89	Fracture	1540485921	Epi and white clay
1184	321314.67	8103992.5	3317	62	46	316	Fracture	1540485905	
1185	321295.05	8103995.3	3318	67	111	21	Fracture	1540485894	
1186	321295.05	8103995.3	3318	58	38	308	Fracture	1540485883	
1187	321283.33	8103992.2	3321	60	46	316	Fracture	1540485868	
1188	321273	8103998	3319	60	47	317	Fracture	1540485846	Epi
1189	321254.92	8104000.7	3319	18	245	155	Fracture	1540485792	Parallel la fractures
1190	321234.13	8104000.8	3319	84	178	88	Fracture	1540485752	White clay
1191	321234.13	8104000.8	3319	86	223	133	Fracture	1540485736	
1192	321226.44	8103999.4	3322	89	144	54	Fracture	1540485714	
1193	321226.44	8103999.4	3322	65	215	125	Fracture	1540485705	
1194	321218.97	8104003.9	3319	52	71	341	Fracture	1540485687	
1195	321214.97	8104003.3	3319	67	227	137	Fracture	1540485679	
1196	321214.97	8104003.3	3319	58	51	321	Fracture	1540485669	
1197	321209.83	8104002.7	3318	75	64	334	Fracture	1540485656	
1198	321194.98	8104001.4	3315	68	55	325	Fracture	1540485634	
1199	321204.12	8104001.5	3317	62	67	337	Fracture	1540485626	
1200	321204.12	8104001.5	3317	74	161	71	Fracture	1540485621	
1201	321204.12	8104001.5	3317	74	144	54	Fracture	1540485614	
1202	321180.48	8103994.4	3314	65	83	353	Fracture	1540485545	
1203	321180.48	8103994.4	3314	51	356	266	Fracture	1540485538	
1204	321167.88	8103981.4	3316	38	337	247	Fracture	1540485492	(Pic)
1205	321168	8103981.4	3316	81	158	68	Fracture	1540485480	(Pic) wit(b epi
1206	321157	8103969.8	3313	84	148	58	Fracture	1540485423	Major Epi on plane
1207	321155	8103958.1	3312	83	154	64	Fracture	1540485374	Epi in olane
1208	321155	8103958.1	3312	76	56	326	Fracture	1540485369	Epi on plane
1209	321154.97	8103952	3313	70	62	332	Fracture	1540485345	
1210	321154.97	8103952	3313	88	325	235	Fracture	1540485332	
1211	321137	8103944.6	3304	88	5	275	Fracture	1540485245	Fracture with white mineral and epi in mineral (pic)
1212	321013.7	8103916.7	3291	68	68	338	Fracture	1540485131	
1213	321020.04	8103914.5	3290	74	149	59	Fracture	1540485114	
1214	321025.9	8103902.9	3292	69	45	315	Fracture	1540485100	
1215	321023.93	8103930.4	3286	84	243	153	Fracture	1540485063	
1216	320994.53	8103928.3	3291	54	97	7	Fracture	1540485044	
1217	320995	8103928.3	3291	78	344	254	Fracture	1540485034	Lots of epi
1218	320994.53	8103928.3	3291	74	39	309	Fracture	1540485007	
1219	320975.55	8103926.4	3292	75	46	316	Fracture	1540484999	
1220	320949.62	8103929.6	3294	71	43	313	Fracture	1540484958	
1221	320921.9	8103939.7	3293	68	97	7	Fracture	1540484949	White clay
1222	320921.9	8103939.7	3293	58	59	329	Fracture	1540484932	
1223	320892.57	8103936	3295	69	49	319	Fracture	1540484903	
1224	320892.57	8103936	3295	80	12	282	Fracture	1540484894	
1225	320789.08	8103921.4	3273	84	202	112	Fracture	1540484822	
1226	320789.08	8103921.4	3273	62	50	320	Fracture	1540484814	
1227	320747.71	8103913.7	3269	89	196	106	Fracture	1540483336	
1228	320408.71	8103668.1	3265	81	143	53	Fracture	1540482699	
1229	320499.28	8103750.6	3250	68	125	35	Fracture	1540482547	Large Fracture with gouge and white mineral
1230	320499.28	8103750.6	3250	56	33	303	Fracture	1540482520	
1231	320497.55	8103732.6	3254	66	54	324	Fracture	1540482436	Large Fracture with fractures and gouge (pic)
1232	320490.96	8103713.5	3259	74	53	323	Fracture	1540482338	White clay
1233	320479.53	8103719.1	3257	50	47	317	Fracture	1540482322	
1234	320468	8103711.1	3258	69	126	36	Fracture	1540482296	Epi
1235	320468.34	8103711.1	3258	69	128	38	Fracture	1540482275	
1236	320453.78	8103700.9	3258	70	121	31	Fracture	1540482268	Lots of white (gouge?)
1237	320453.78	8103700.9	3258	83	170	80	Fracture	1540482236	
1238	320453.78	8103700.9	3258	82	162	72	Fracture	1540482230	
1239	320379.91	8103647.7	3266	80	201	111	Fracture	1540482098	
1240	320357.45	8103639.7	3262	76	307	217	Fracture	1540482023	
1241	320357.45	8103639.7	3262	79	45	315	Fracture	1540482013	
1242	320325	8103631.5	3255	71	135	45	Fracture	1540481975	Epi
1243	320311.39	8103625.8	3254	64	121	31	Fracture	1540481962	
1244	320311.39	8103625.8	3254	87	21	291	Fracture	1540481944	
1245	320297.89	8103624.6	3249	79	45	315	Fracture	1540481932	
1246	320260.87	8103607.5	3246	89	224	134	Fracture	1540481883	White clay
1247	320261	8103607.5	3246	82	126	36	Fracture	1540481870	Epi
1248	320233	8103591.2	3247	78	132	42	Fracture	1540480984	Another with epi going into wr from plane (pic)
1249	320180.81	8103565.8	3250	77	134	44	Fracture	1540480844	Lots of gorge (pic)

No.	X(East)	Y(North)	Z	Dip	Az	Strike	Type	Time Stamp	Remarks
1250	320144.65	8103565.5	3248	77	33	303	Fracture	1540480782	
1251	320130.96	8103565.3	3247	83	61	331	Fracture	1540480720	
1252	320040.98	8103564.6	3242	28	2	272	Fracture	1540480626	
1253	320040.98	8103564.6	3242	68	141	51	Fracture	1540480618	
1254	320040.98	8103564.6	3242	76	47	317	Fracture	1540480613	
1255	320040.98	8103564.6	3242	63	113	23	Fracture	1540480606	Gougea d Fe-oxide
1256	319998	8103550.8	3244	78	149	59	Fracture	1540480421	White clay and epi (pic)
1257	319982.66	8103552.9	3239	44	207	117	Fracture	1540480389	
1258	319982.66	8103552.9	3239	44	220	130	Fracture	1540480382	
1259	319957.97	8103546	3240	70	48	318	Fracture	1540480280	
1260	319957.97	8103546	3240	78	213	123	Fracture	1540480267	
1261	319957.97	8103546	3240	77	156	66	Fracture	1540480262	White clay
1262	319837.22	8103526.8	3216	88	33	303	Fracture	1540480156	
1263	319813.68	8103525.2	3218	83	25	295	Fracture	1540480145	
1264	319819.29	8103532.1	3215	79	145	55	Fracture	1540480087	Lots of White clay (pic)
1265	319812	8103536.2	3215	78	143	53	Fracture	1540480051	White clay and epi
1266	319787.5	8103523.5	3228	85	48	318	Fracture	1540480012	
1267	319788	8103523.5	3228	85	323	233	Fracture	1540480005	Epi
1268	319775.06	8103520.7	3232	79	135	45	Fracture	1540479991	
1269	319775.06	8103520.7	3232	83	64	334	Fracture	1540479986	
1270	319766.73	8103522	3233	84	49	319	Fracture	1540479964	
1271	319745	8103528.7	3229	64	173	83	Fracture	1540479880	Lots of epi on plane
1272	319668.25	8103520.1	3212	89	23	293	Fracture	1540479180	White mineral and lineations?
1273	319668	8103520.1	3212	78	146	56	Fracture	1540479152	Epi and pink mineral on plane
1274	318576.76	8103767.8	3129	86	113	23	Fracture	1540478273	
1275	318563.32	8103771.6	3125	75	112	22	Fracture	1540478250	
1276	318532.27	8103767.2	3127	69	110	20	Fracture	1540478150	
1277	318532.27	8103767.2	3127	42	251	161	Fracture	1540478142	
1278	318520.12	8103772.5	3123	34	240	150	Fracture	1540478130	
1279	318485.28	8103770.8	3125	76	57	327	Fracture	1540478088	
1280	318485.28	8103770.8	3125	70	29	299	Fracture	1540478075	
1281	318477.1	8103786.8	3117	51	327	237	Fracture	1540478048	
1282	318477.1	8103786.8	3117	69	33	303	Fracture	1540478043	
1283	318424.78	8103790.3	3115	70	36	306	Fracture	1540477986	
1284	318390.08	8103794	3109	82	124	34	Fracture	1540477889	
1285	318398.15	8103791.4	3113	85	136	46	Fracture	1540477883	
1286	318398.15	8103791.4	3113	81	57	327	Fracture	1540477869	
1287	318410.22	8103790.2	3113	81	77	347	Fracture	1540477863	
1288	318299.1	8103798.6	3108	59	80	350	Fracture	1540477731	
1289	318291.56	8103796.2	3109	65	64	334	Fracture	1540477647	
1290	318286.3	8103796.2	3108	65	67	337	Fracture	1540477634	Parallel fractures
1291	318277.04	8103798.7	3106	79	357	267	Fracture	1540477583	
1292	318277	8103798.7	3106	73	85	355	Fracture	1540477568	Epi
1293	318209.34	8103794.2	3112	81	72	342	Fracture	1540477327	
1294	318209.34	8103794.2	3112	79	42	312	Fracture	1540477309	
1295	318194.54	8103793	3124	82	44	314	Fracture	1540477300	
1296	318194.54	8103793	3124	70	143	53	Fracture	1540477288	
1297	318162.87	8103785.4	3127	27	347	257	Fracture	1540477249	
1298	318162.87	8103785.4	3127	75	149	59	Fracture	1540477237	
1299	318093.17	8103756.4	3125	40	252	162	Fracture	1540476970	R13.2
1300	318093.17	8103756.4	3125	36	100	10	Fracture	1540476955	R13.2
1301	318090	8103756.3	3124	28	101	11	Fracture	1540476931	R13.2 two parallel
1302	318072.23	8103732	3128	44	135	45	Fracture	1540476845	
1303	318065.88	8103731.9	3128	42	135	45	Fracture	1540476837	
1304	318065.88	8103731.9	3128	73	51	321	Fracture	1540476829	
1305	318032.21	8103711.7	3129	65	354	264	Fracture	1540476759	
1306	318036	8103721.2	3130	72	88	358	Fracture	1540476704	Epi and white clay
1307	318023.7	8103708.5	3125	84	11	281	Fracture	1540476627	Gouge and Fe-oxide (pic)
1308	318002	8103694.6	3118	69	118	28	Fracture	1540476560	Lots of epi and chlorite (pic)
1309	317989	8103687.2	3120	82	354	264	Fracture	1540476533	Epi
1310	317989	8103687.2	3120	79	133	43	Fracture	1540476466	Epi
1311	317972.19	8103673.3	3120	32	19	289	Fracture	1540476453	
1312	317972	8103673.3	3120	75	113	23	Fracture	1540476440	Parallel fractures with epi
1313	317967	8103672.2	3117	64	168	78	Fracture	1540476282	Minor gouge much more epi along planes
1314	317914.46	8103632.8	3100	89	51	321	Fracture	1540476159	
1315	317914	8103632.8	3100	51	131	41	Fracture	1540476143	Epi
1316	317888.14	8103617.9	3107	51	129	39	Fracture	1540476042	
1317	317888.14	8103617.9	3107	82	51	321	Fracture	1540476036	
1318	317875.58	8103603	3107	75	135	45	Fracture	1540475995	
1319	317862.89	8103602.9	3101	74	126	36	Fracture	1540475989	White gouge
1320	317821.78	8103585.7	3102	82	7	277	Fracture	1540475975	
1321	317821.78	8103585.7	3102	85	346	256	Fracture	1540475835	
1322	317821.78	8103585.7	3102	75	33	303	Fracture	1540475828	
1323	317793.19	8103588.6	3109	85	46	316	Fracture	1540475752	
1324	317779.44	8103588.5	3111	80	141	51	Fracture	1540475745	
1325	317779.44	8103588.5	3111	81	58	328	Fracture	1540475717	
1326	317790.99	8103598.1	3104	86	45	315	Fracture	1540475710	
1327	317742.26	8103612	3096	77	130	40	Fracture	1540475634	
1328	317746.88	8103607.4	3098	79	161	71	Fracture	1540475069	
1329	317325.85	8103612.3	3105	86	289	199	Fracture	1540474508	White clay

No.	X(East)	Y(North)	Z	Dip	Az	Strike	Type	Time Stamp	Remarks
1330	317295.93	8103599.2	3108	79	55	325	Fracture	1540474425	
1331	317295.93	8103599.2	3108	69	129	39	Fracture	1540474419	
1332	317300.8	8103609.1	3107	73	133	43	Fracture	1540474412	
1333	317286.99	8103608	3102	39	29	299	Fracture	1540474328	More low angle round here?
1334	317280.22	8103588.2	3104	83	311	221	Fracture	1540474296	
1335	317370.53	8103469.7	3105	73	358	268	Fracture	1540474115	Fe-oxide and gouge
1336	317383.65	8103444.2	3095	81	2	272	Fracture	1540473995	Parallel ew with white clay
1337	317391	8103443.3	3098	86	289	199	Fracture	1540473930	Parallel (pic) epi
1338	317402.85	8103422.8	3099	83	95	5	Fracture	1540473889	
1339	317408.83	8103419.9	3100	84	90	360	Fracture	1540473853	
1340	317419.87	8103412.1	3101	81	329	239	Fracture	1540473765	Gouge Fracture (pic)
1341	317433.85	8103401.4	3099	89	101	11	Fracture	1540473733	
1342	317424.97	8103396.4	3095	87	101	11	Fracture	1540473726	
1343	317433.97	8103387.6	3091	88	285	195	Fracture	1540473698	
1344	317442.98	8103378.8	3089	79	359	269	Fracture	1540473686	
1345	317442.98	8103378.8	3089	89	286	196	Fracture	1540473681	
1346	317442.8	8103374.8	3087	81	342	252	Fracture	1540473644	
1347	317445.82	8103369.9	3084	78	336	246	Fracture	1540473632	
1348	317486.66	8103334.7	3087	87	140	50	Fracture	1540473501	Fracture with pink clay (pic)
1349	317499.5	8103339.8	3092	89	93	3	Fracture	1540473437	
1350	317499.69	8103324	3092	82	172	82	Fracture	1540473424	
1351	317507	8103322.1	3092	85	77	347	Fracture	1540473403	Epi and pink alt
1352	317520.88	8103312.4	3094	87	347	257	Fracture	1540473365	
1353	317505.12	8103300.5	3081	71	354	264	Fracture	1540473356	
1354	317523.15	8103288.8	3083	72	353	263	Fracture	1540473281	Large gouge Fracture again with pink alt
1355	317543.14	8103271.2	3082	80	175	85	Fracture	1540473226	
1356	317543.14	8103271.2	3082	76	102	12	Fracture	1540473218	
1357	317543.14	8103271.2	3082	73	100	10	Fracture	1540473208	
1358	317550.1	8103269.3	3084	72	100	10	Fracture	1540473201	
1359	317558.37	8103258.8	3081	89	93	3	Fracture	1540473157	Parallel fractures
1360	317576	8103258.9	3088	48	17	287	Fracture	1540473063	(Pic) gouge with epi parallel
1361	317594.82	8103260.8	3092	87	348	258	Fracture	1540472946	
1362	317600.8	8103256.6	3091	85	344	254	Fracture	1540472912	
1363	317602.58	8103248.2	3084	87	349	259	Fracture	1540472898	
1364	317622.08	8103250.9	3083	87	78	348	Fracture	1540472847	
1365	317633.12	8103251	3082	83	69	339	Fracture	1540472831	
1366	317633.12	8103251	3082	88	157	67	Fracture	1540472821	
1367	317650.93	8103254.5	3081	89	98	8	Fracture	1540472813	
1368	317670.86	8103256.4	3082	75	348	258	Fracture	1540472631	More large Fracture with gouge
1369	317676	8103251.3	3077	88	265	175	Fracture	1540472567	
1370	317718	8103245	3084	48	343	253	Fracture	1540472472	More large Epi gouge Fractures
1371	317726.3	8103240.1	3080	83	66	336	Fracture	1540472409	
1372	317734.8	8103239.3	3081	89	260	170	Fracture	1540472400	Large
1373	317744	8103231.8	3078	86	348	258	Fracture	1540472369	Epi
1374	317759.66	8103231.8	3077	90	344	254	Fracture	1540472292	R13.1
1375	317758.83	8103230.2	3076	58	334	244	Fracture	1540471976	R13.1 Large Fracture wit(gouge - several parallel
1376	317780.07	8103229.6	3071	87	73	343	Fracture	1540471887	
1377	317786.01	8103229.6	3068	80	338	248	Fracture	1540471872	Gouge and pink mineral
1378	317802.05	8103231.5	3059	72	146	56	Fracture	1540471756	
1379	317815.18	8103229.8	3055	74	169	79	Fracture	1540471740	
1380	317838	8103216.9	3055	87	244	154	Fracture	1540471688	White mineral and epi
1381	317837.79	8103216.9	3055	56	96	6	Fracture	1540471632	With gouge
1382	317849.06	8103215.2	3056	86	85	355	Fracture	1540471601	
1383	317864.1	8103209.7	3053	77	110	20	Fracture	1540471562	
1384	317862	8103217.2	3056	83	78	348	Fracture	1540471522	Epi
1385	317909	8103206.4	3048	70	184	94	Fracture	1540471449	Epi
1386	317909	8103206.4	3048	79	359	269	Fracture	1540471429	Epi
1387	317909	8103206.4	3048	77	96	6	Fracture	1540471403	Epi
1388	317975	8103164.2	3061	53	111	21	Fracture	1540471271	Epi and gouge (pic)
1389	317930	8103193.6	3045	88	101	11	Fracture	1540471170	Epi covering plane
1390	318157	8102877.8	3030	87	318	228	Fracture	1540415237	Epi
1391	318144	8102878.5	3031	88	147	57	Fracture	1540415213	Epi
1392	318128.44	8102875.1	3037	36	187	97	Fracture	1540415185	
1393	318115.87	8102884.9	3037	88	156	66	Fracture	1540415155	Pink
1394	318102.55	8102885.6	3039	65	80	350	Fracture	1540415077	
1395	318102.55	8102885.6	3039	86	179	89	Fracture	1540415072	
1396	318090	8102891.3	3040	81	354	264	Fracture	1540414649	Epi RCS071
1397	318008.68	8102915.4	3050	20	252	162	Fracture	1540412372	
1398	318009	8102915.4	3050	86	354	264	Fracture	1540412355	Epi
1399	317979.44	8102929.2	3055	71	92	2	Fracture	1540412321	
1400	317979	8102929.2	3055	87	168	78	Fracture	1540412317	Epi
1401	317969.47	8102927.5	3062	88	263	173	Fracture	1540412271	
1402	317961.13	8102929.9	3063	62	167	77	Fracture	1540412255	
1403	317961.13	8102929.9	3063	76	92	2	Fracture	1540412250	
1404	317948.52	8102944.6	3058	69	84	354	Fracture	1540412150	
1405	317927.57	8102961	3050	68	57	327	Fracture	1540412119	
1406	317927.57	8102961	3050	60	86	356	Fracture	1540412109	
1407	317927.57	8102961	3050	89	358	268	Fracture	1540412091	Pink

No.	X(East)	Y(North)	Z	Dip	Az	Strike	Type	Time Stamp	Remarks
1408	317906	8102965.7	3056	89	161	71	Fracture	1540412007	Large Fracture with gouge and pink and green alt (pic)
1409	317880.34	8102973.8	3069	70	88	358	Fracture	1540411942	
1410	317880.34	8102973.8	3069	87	328	238	Fracture	1540411928	Pink alt
1411	317867.05	8102971.2	3077	88	167	77	Fracture	1540411889	Pink alt
1412	317867.05	8102971.2	3077	23	92	2	Fracture	1540411859	La with 10 cm gouge
1413	317852.59	8102975.2	3077	66	260	170	Fracture	1540411549	R12.9 conjugate pink alt
1414	317852.59	8102975.2	3077	71	108	18	Fracture	1540411522	R12.9 conjugate pink alt
1415	317820	8102970	3074	85	324	234	Fracture	1540411427	Pink alt with minor epi
1416	317818.33	8102970.4	3074	87	191	101	Fracture	1540411349	
1417	317792.28	8102946.2	3081	67	144	54	Fracture	1540411337	Pink alt
1418	317792.28	8102946.2	3081	72	68	338	Fracture	1540411305	
1419	317765.86	8102938.7	3073	70	162	72	Fracture	1540411246	Also pink alt
1420	317763.54	8102940.6	3072	87	146	56	Fracture	1540411226	Pink alt
1421	317754.46	8102936	3069	71	134	44	Fracture	1540411170	Very pink alt
1422	317750.43	8102934.7	3069	75	86	356	Fracture	1540410864	12.7 very pink alt
1423	317750.43	8102934.7	3069	26	257	167	Fracture	1540410812	
1424	317727	8102920.3	3077	64	308	218	Fracture	1540410590	Epi
1425	317719.69	8102916.3	3079	77	316	226	Fracture	1540410575	
1426	317701.54	8102905.8	3080	22	246	156	Fracture	1540410524	La parallel
1427	317697.6	8102908.4	3079	69	166	76	Fracture	1540410476	
1428	317687.26	8102899.2	3082	60	41	311	Fracture	1540410431	
1429	317687.26	8102899.2	3082	70	98	8	Fracture	1540410406	
1430	317678.83	8102894	3085	88	134	44	Fracture	1540410381	
1431	317657.42	8102884.1	3097	79	328	238	Fracture	1540410353	
1432	317657.42	8102884.1	3097	64	67	337	Fracture	1540410342	
1433	317648.3	8102883.3	3097	57	46	316	Fracture	1540410314	
1434	317637.95	8102875.5	3100	66	28	298	Fracture	1540410293	
1435	317631.46	8102872.2	3100	62	56	326	Fracture	1540410280	
1436	317631.46	8102872.2	3100	86	97	7	Fracture	1540410270	
1437	317622.18	8102869.4	3097	72	46	316	Fracture	1540410192	Conjugate
1438	317620.89	8102868.2	3097	76	112	22	Fracture	1540410175	
1439	317615.88	8102869.4	3093	64	51	321	Fracture	1540410141	
1440	317609.42	8102863.5	3092	64	41	311	Fracture	1540410123	
1441	317600.31	8102862.1	3089	32	285	195	Fracture	1540410108	La parallel
1442	317589.26	8102858.1	3084	71	41	311	Fracture	1540410085	
1443	317589.26	8102858.1	3084	82	112	22	Fracture	1540410073	
1444	317596.42	8102859.5	3088	81	112	22	Fracture	1540410064	
1445	317586.19	8102863.2	3081	48	178	88	Fracture	1540409967	Gouge lilac? (Pic)
1446	317573.27	8102853.2	3075	49	163	73	Fracture	1540409922	
1447	317587.24	8102857.3	3083	89	174	84	Fracture	1540409912	
1448	317532.28	8102851.8	3082	61	78	348	Fracture	1540409849	
1449	317525.31	8102848.8	3086	89	29	299	Fracture	1540409812	
1450	317506.38	8102840.6	3095	85	30	300	Fracture	1540409795	
1451	317514.32	8102847.7	3089	86	29	299	Fracture	1540409790	
1452	317475.07	8102810.7	3091	72	169	79	Fracture	1540409127	
1453	317475.07	8102810.7	3091	72	29	299	Fracture	1540409105	
1454	317474.98	8102821.5	3088	71	39	309	Fracture	1540409091	
1455	317485.83	8102828.4	3092	83	72	342	Fracture	1540409083	
1456	317559.41	8102849.3	3071	88	276	186	Fracture	1540408486	
1457	317544.16	8102852	3075	86	102	12	Fracture	1540408473	
1458	317535.87	8102864.1	3072	88	72	342	Fracture	1540408422	
1459	317796.83	8102088.6	3155	81	163	73	Fracture	1540407732	
1460	317798.61	8102097.9	3151	73	168	78	Fracture	1540407714	
1461	317759.71	8102058.6	3152	70	61	331	Fracture	1540407651	
1462	317761.57	8102058.6	3152	82	356	266	Fracture	1540407631	
1463	317744.08	8102069.6	3153	54	39	309	Fracture	1540407564	
1464	317744.08	8102069.6	3153	62	27	297	Fracture	1540407560	
1465	317731.69	8102066.4	3157	72	36	306	Fracture	1540407536	
1466	317731.69	8102066.4	3157	72	25	295	Fracture	1540407528	
1467	317646.1	8102001.5	3198	83	99	9	Fracture	1540407508	
1468	317722.64	8102066.4	3159	82	64	334	Fracture	1540407496	
1469	317672.25	8102081.9	3162	53	126	36	Fracture	1540407399	Fe-oxide (pic)
1470	317655.39	8102092.8	3158	79	109	19	Fracture	1540407343	
1471	317634.85	8102098.8	3165	61	135	45	Fracture	1540407329	
1472	317634.85	8102098.8	3165	71	107	17	Fracture	1540407253	White clay
1473	317631.09	8102101.9	3167	27	273	183	Fracture	1540407242	
1474	317624.82	8102109.2	3167	62	112	22	Fracture	1540407228	
1475	317607.96	8102120.2	3166	48	250	160	Fracture	1540407183	
1476	317607.96	8102120.2	3166	83	110	20	Fracture	1540407166	White clay
1477	317596.73	8102126.3	3166	72	98	8	Fracture	1540407133	
1478	317596.73	8102126.3	3166	72	139	49	Fracture	1540407097	
1479	317510.54	8102252.2	3169	15	257	167	Fracture	1540405978	
1480	317499.87	8102258.8	3178	56	246	156	Fracture	1540405962	
1481	317499.87	8102258.8	3178	80	186	96	Fracture	1540405946	
1482	317493.15	8102264.2	3182	72	166	76	Fracture	1540405918	White clay (pic)
1483	317485	8102272.5	3184	88	173	83	Fracture	1540405860	Epi
1484	317475.99	8102274.1	3186	61	42	312	Fracture	1540405804	
1485	317466.42	8102286.7	3181	68	107	17	Fracture	1540405759	White clay
1486	317458.59	8102291.1	3180	88	327	237	Fracture	1540405680	White clay

No.	X(East)	Y(North)	Z	Dip	Az	Strike	Type	Time Stamp	Remarks
1487	317459	8102291.1	3180	85	25	295	Fracture	1540405657	Epi
1488	317444.32	8102296.3	3176	56	88	358	Fracture	1540405527	
1489	317444	8102296.3	3176	87	193	103	Fracture	1540405502	Epi on plane
1490	317431.11	8102300.8	3176	65	85	355	Fracture	1540405484	
1491	317425	8102303.2	3177	86	5	275	Fracture	1540405388	Epi on plane
1492	317424.82	8102303.2	3177	80	13	283	Fracture	1540405365	
1493	317424.82	8102303.2	3177	39	96	6	Fracture	1540405342	
1494	317416.34	8102306.2	3177	84	125	35	Fracture	1540405287	
1495	317416.34	8102306.2	3177	66	118	28	Fracture	1540405273	
1496	317396.28	8102317.9	3179	69	62	332	Fracture	1540405189	
1497	317388.43	8102317.9	3183	83	183	93	Fracture	1540405109	
1498	317374.32	8102333.7	3182	58	73	343	Fracture	1540405103	
1499	317344.24	8102345.2	3189	55	71	341	Fracture	1540405044	
1500	317344.24	8102345.2	3189	72	176	86	Fracture	1540405033	
1501	317312.26	8102343	3201	46	157	67	Fracture	1540405007	
1502	317308	8102355.6	3195	70	188	98	Fracture	1540404981	Epi and white clay
1503	317294.7	8102358.5	3198	61	73	343	Fracture	1540404945	
1504	317285.27	8102368.6	3196	70	211	121	Fracture	1540404923	
1505	317282.06	8102382.9	3189	49	99	9	Fracture	1540404907	
1506	317266.64	8102385.8	3194	42	148	58	Fracture	1540404894	
1507	317273.88	8102383.8	3192	56	81	351	Fracture	1540404878	
1508	317262.52	8102390.9	3193	73	266	176	Fracture	1540404861	
1509	317254.34	8102394.9	3193	82	180	90	Fracture	1540404806	
1510	317246.93	8102402	3192	73	5	275	Fracture	1540404776	
1511	317233.56	8102411.1	3193	37	115	25	Fracture	1540404714	With Fe-oxide
1512	317206.89	8102424.8	3195	28	325	235	Fracture	1540404519	R12.7
1513	317206.89	8102424.8	3195	83	169	79	Fracture	1540404494	R12.7
1514	317152.31	8102449	3206	28	351	261	Fracture	1540404384	
1515	317091.7	8102483.1	3201	85	86	356	Fracture	1540404323	
1516	317085.29	8102491.1	3198	40	2	272	Fracture	1540404310	
1517	317085.29	8102491.1	3198	80	98	8	Fracture	1540404296	
1518	317008.13	8102572.5	3234	43	104	14	Fracture	1540403959	
1519	317008.13	8102572.5	3234	81	203	113	Fracture	1540403929	
1520	317008.18	8102577	3234	71	205	115	Fracture	1540403871	
1521	317031.45	8102531.8	3211	39	106	16	Fracture	1540403834	
1522	317031.45	8102531.8	3211	89	21	291	Fracture	1540403828	
1523	317030.05	8102551.5	3216	37	125	35	Fracture	1540403731	La
1524	317030.05	8102551.5	3216	82	211	121	Fracture	1540403719	
1525	316530.49	8102824	3254	85	152	62	Fracture	1540402135	
1526	316535.47	8102822.7	3255	50	51	321	Fracture	1540402126	
1527	316523.95	8102821.7	3255	57	60	330	Fracture	1540402104	
1528	316574.61	8102821.3	3248	54	77	347	Fracture	1540402077	
1529	316566.77	8102818.5	3253	33	72	342	Fracture	1540401992	
1530	316546.12	8102827.2	3250	78	318	228	Fracture	1540401389	With slicken lines near RCS068
1531	316501.97	8102822.3	3252	40	46	316	Fracture	1540401324	
1532	316511.45	8102827.8	3249	72	309	219	Fracture	1540401314	
1533	316474.55	8102846.4	3235	57	68	338	Fracture	1540401249	
1534	316446.72	8103105.6	3268	31	62	332	Fracture	1540400805	
1535	316436.68	8103108	3270	81	133	43	Fracture	1540400763	
1536	316443.02	8103109.2	3267	38	206	116	Fracture	1540400743	
1537	316416.4	8103114	3270	82	128	38	Fracture	1540400685	Fe-oxide
1538	316403.91	8103113.1	3273	86	311	221	Fracture	1540400621	Altered with minor gouge and Fe-oxide
1539	316390.02	8103115.4	3271	77	137	47	Fracture	1540400570	
1540	316379.36	8103117.6	3268	33	29	299	Fracture	1540400563	
1541	316379.36	8103117.6	3268	76	141	51	Fracture	1540400558	
1542	316366.28	8103125.7	3262	9	353	263	Fracture	1540400522	La (pic)
1543	316366.28	8103125.7	3262	81	315	225	Fracture	1540400483	
1544	316301.17	8103124	3268	82	313	223	Fracture	1540400377	
1545	316297.5	8103136.9	3261	83	123	33	Fracture	1540400357	
1546	316287.87	8103155.6	3259	89	324	234	Fracture	1540400332	
1547	316287.87	8103155.6	3259	33	251	161	Fracture	1540400323	Fractured low angle
1548	316258.96	8103215.3	3265	88	25	295	Fracture	1540400283	Fractured
1549	316250.54	8103230.5	3262	83	312	222	Fracture	1540400232	
1550	316236.21	8103243.3	3264	89	131	41	Fracture	1540400170	
1551	316236	8103233.8	3267	89	134	44	Fracture	1540400151	
1552	316224.02	8103250.2	3269	19	250	160	Fracture	1540400123	La
1553	316215.66	8103259.5	3269	89	301	211	Fracture	1540400108	
1554	316204.16	8103257.1	3276	86	306	216	Fracture	1540400064	
1555	316207.53	8103272.4	3270	82	310	220	Fracture	1540400050	
1556	316217.07	8103264.3	3267	58	27	297	Fracture	1540400035	
1557	315613.6	8103299.8	3254	81	303	213	Fracture	1540399815	
1558	315597.77	8103289.5	3254	89	29	299	Fracture	1540399801	
1559	315603.43	8103293	3254	87	200	110	Fracture	1540399793	
1560	315618.91	8103300.8	3255	85	299	209	Fracture	1540399708	
1561	315611.29	8103294.3	3256	87	214	124	Fracture	1540399696	
1562	315601.14	8103284.1	3260	15	353	263	Fracture	1540399688	La fractures
1563	315599.51	8103292.9	3253	87	297	207	Fracture	1540399632	
1564	315590.64	8103282.7	3254	85	298	208	Fracture	1540399623	
1565	315579.06	8103286.3	3245	89	209	119	Fracture	1540399613	
1566	315579.48	8103273.7	3252	85	190	100	Fracture	1540399580	

No.	X(East)	Y(North)	Z	Dip	Az	Strike	Type	Time Stamp	Remarks
1567	315562.94	8103263.4	3246	86	307	217	Fracture	1540399565	
1568	315547.63	8103258.2	3240	89	299	209	Fracture	1540399530	
1569	315561	8103264.6	3245	44	4	274	Fracture	1540399517	Epi like sample
1570	315530.19	8103255.4	3229	87	309	219	Fracture	1540398723	RCS067
1571	315511	8103247.4	3224	46	16	286	Fracture	1540398634	La with epi on RCS067
1572	315487.91	8103258	3217	89	117	27	Fracture	1540398446	
1573	315482.49	8103259.7	3219	88	296	206	Fracture	1540398417	
1574	315448.29	8103261.2	3240	89	129	39	Fracture	1540398401	
1575	315441.02	8103268.3	3240	89	127	37	Fracture	1540398349	
1576	315433.85	8103282.4	3237	77	267	177	Fracture	1540398273	Minor gouge and Fe-oxide
1577	315422.93	8103296.7	3239	88	130	40	Fracture	1540398227	
1578	315419.12	8103319.9	3234	89	124	34	Fracture	1540398192	
1579	315420.81	8103332.4	3227	89	315	225	Fracture	1540398172	
1580	315415.44	8103353.9	3223	89	127	37	Fracture	1540398126	
1581	315420.67	8103373.6	3215	88	123	33	Fracture	1540398106	
1582	315416.91	8103379	3217	86	123	33	Fracture	1540398088	
1583	315409.5	8103402.1	3220	89	125	35	Fracture	1540398044	
1584	315413.28	8103382.5	3219	89	310	220	Fracture	1540398016	Multiple parallel structures
1585	315314.28	8103578.8	3202	87	130	40	Fracture	1540397815	
1586	315301.07	8103574	3204	85	12	282	Fracture	1540397801	
1587	315301.07	8103574	3204	89	125	35	Fracture	1540397796	
1588	315283.43	8103570.6	3203	88	14	284	Fracture	1540397776	
1589	315264.07	8103578.4	3197	28	56	326	Fracture	1540397761	
1590	315264	8103578.4	3197	87	125	35	Fracture	1540397747	Minor epi
1591	315235.43	8103567	3211	87	124	34	Fracture	1540397668	
1592	315230.63	8103576.5	3204	89	307	217	Fracture	1540397650	
1593	315208.08	8103582.7	3196	83	318	228	Fracture	1540397615	
1594	315175.58	8103595.2	3183	84	132	42	Fracture	1540397579	
1595	315175.58	8103595.2	3183	75	212	122	Fracture	1540397572	
1596	315198.1	8103592.3	3188	77	212	122	Fracture	1540397562	
1597	314794.82	8103730.4	3157	72	112	22	Fracture	1540397315	
1598	314787.01	8103732.9	3153	82	121	31	Fracture	1540397301	
1599	314716.66	8103738.3	3163	79	108	18	Fracture	1540396502	
1600	314693.98	8103738.1	3170	78	108	18	Fracture	1540396450	
1601	314679.79	8103732.7	3166	77	93	3	Fracture	1540396404	
1602	314686.35	8103728.8	3171	73	332	242	Fracture	1540396391	white clay
1603	314662.27	8103736.5	3157	84	88	358	Fracture	1540396333	
1604	314657.13	8103713.9	3166	82	180	90	Fracture	1540396318	
1605	314646.52	8103707.2	3166	89	88	358	Fracture	1540396301	
1606	314655.73	8103721.9	3161	34	175	85	Fracture	1540396289	
1607	314655.73	8103721.9	3161	84	91	1	Fracture	1540396282	
1608	314588.51	8103699.7	3155	86	196	106	Fracture	1540396117	
1609	314588.51	8103699.7	3155	83	91	1	Fracture	1540396110	
1610	314606.83	8103676.7	3176	87	203	113	Fracture	1540396035	Fe-oxide and pink coloured gouge
1611	314591.35	8103670.1	3172	89	93	3	Fracture	1540396003	
1612	314591.35	8103670.1	3172	83	12	282	Fracture	1540395995	
1613	314571	8103653.1	3176	59	358	268	Fracture	1540395915	Epi on fracture
1614	314561	8103658.2	3169	84	92	2	Fracture	1540395894	Epi on fracture
1615	314549.79	8103651.7	3170	88	16	286	Fracture	1540395849	
1616	314504.99	8103641.1	3163	56	189	99	Fracture	1540395580	R12.5
1617	314501.11	8103635.9	3165	89	261	171	Fracture	1540395502	R12.5Close parallel fractures
1618	314469	8103642	3159	76	197	107	Fracture	1540395396	White pink and green mineral
1619	314425.97	8103646.8	3156	84	206	116	Fracture	1540395248	Thick white min (pic)
1620	314420.38	8103649.3	3156	84	87	357	Fracture	1540395197	
1621	314400.79	8103667.2	3151	72	217	127	Fracture	1540395162	
1622	314386.45	8103677.4	3151	85	86	356	Fracture	1540395152	
1623	314386.45	8103677.4	3151	86	89	359	Fracture	1540395110	
1624	314390.37	8103676.1	3150	72	235	145	Fracture	1540395090	
1625	314382.68	8103667	3158	85	94	4	Fracture	1540395069	
1626	314380	8103677.3	3154	74	241	151	Fracture	1540395054	
1627	314361.65	8103701.6	3144	80	99	9	Fracture	1540395026	
1628	314351.16	8103715.6	3139	87	90	360	Fracture	1540395003	Block ck fracturing
1629	314351.16	8103715.6	3139	82	256	166	Fracture	1540394973	
1630	314334.34	8103719.2	3140	87	96	6	Fracture	1540394904	
1631	314328.23	8103299.3	3111	88	35	305	Fracture	1540394546	
1632	314285.17	8103295.6	3121	77	26	296	Fracture	1540394502	
1633	314253.6	8103303.6	3116	78	206	116	Fracture	1540394463	white clay and Fe-oxide
1634	314227.02	8103309.9	3115	56	255	165	Fracture	1540394443	
1635	314207.14	8103309.8	3111	70	268	178	Fracture	1540394346	
1636	314205.84	8103301.5	3118	51	223	133	Fracture	1540394324	
1637	314197.46	8103311.4	3106	62	282	192	Fracture	1540394316	
1638	314177.63	8103306.2	3108	67	215	125	Fracture	1540394264	Parallel fractures (like in pic)
1639	314167.74	8103304.5	3106	70	203	113	Fracture	1540394219	
1640	314136.23	8103305.9	3102	73	211	121	Fracture	1540394200	
1641	314116.86	8103315.4	3099	80	114	24	Fracture	1540394091	
1642	314116.86	8103315.4	3099	58	244	154	Fracture	1540394082	
1643	314101.03	8103318.7	3101	70	243	153	Fracture	1540394061	
1644	314066.92	8103321.9	3105	72	127	37	Fracture	1540393999	
1645	314074.68	8103330.7	3100	64	243	153	Fracture	1540393986	
1646	314067.24	8103327.2	3101	68	252	162	Fracture	1540393970	

No.	X(East)	Y(North)	Z	Dip	Az	Strike	Type	Time Stamp	Remarks
1647	314044.51	8103333.9	3092	70	243	153	Fracture	1540393960	Lots of tight parallel fractures
1648	335131.12	8099744.5	3999	85	9	279	Fracture	1539889207	Dextral slickensides
1649	335131.12	8099744.5	3999	71	39	309	Fracture	1539889147	Cuts ne Fracture
1650	335131.12	8099744.5	3999	85	308	218	Fracture	1539889129	
1651	335991.93	8101143.1	4176	89	330	240	Fracture	1539887976	Only main fractures seen here
1652	335486.16	8102280.5	4213	79	30	300	Fracture	1539881787	
1653	335486.16	8102280.5	4213	85	247	157	Fracture	1539881772	
1654	335486.16	8102280.5	4213	19	203	113	Fracture	1539881750	R8.7
1655	335485.26	8102276.8	4213	63	29	299	Fracture	1539881716	R8.7 main Fracture
1656	335468.59	8102290.6	4221	65	47	317	Fracture	1539881304	
1657	335466.27	8102284.7	4219	85	46	316	Fracture	1539881148	
1658	335466.27	8102284.7	4219	87	124	34	Fracture	1539881139	
1659	335448.79	8102266.8	4214	82	49	319	Fracture	1539880901	
1660	335448.79	8102266.8	4214	89	297	207	Fracture	1539880892	
1661	335448.79	8102266.8	4214	87	316	226	Fracture	1539880847	
1662	335432.45	8102246.3	4215	33	229	139	Fracture	1539880706	R8.6
1663	335432.45	8102246.3	4215	83	48	318	Fracture	1539880671	R8.6
1664	335421.13	8102228.8	4214	86	121	31	Fracture	1539880508	
1665	335403.56	8102214.1	4211	87	287	197	Fracture	1539880497	
1666	335388.93	8102222.7	4216	74	188	98	Fracture	1539880320	
1667	335388.93	8102222.7	4216	71	186	96	Fracture	1539880309	
1668	335348.14	8102205	4218	89	48	318	Fracture	1539880245	
1669	335371.59	8102208.1	4216	85	62	332	Fracture	1539880220	
1670	335309.89	8102204.6	4222	53	187	97	Fracture	1539879758	
1671	335309.89	8102204.6	4222	85	61	331	Fracture	1539879743	
1672	334772.75	8103686.5	4222	79	248	158	Fracture	1539878199	
1673	334776.51	8103727.9	4218	88	324	234	Fracture	1539877595	
1674	334781.28	8103800.6	4213	87	302	212	Fracture	1539876410	
1675	334782.58	8103806.6	4213	89	124	34	Fracture	1539876396	
1676	333625.51	8104403.6	4216	82	115	25	Fracture	1539874926	
1677	333616.31	8104410.1	4216	84	58	328	Fracture	1539874896	
1678	333616.31	8104410.1	4216	84	52	322	Fracture	1539874888	
1679	333616.31	8104410.1	4216	86	350	260	Fracture	1539874863	
1680	333565.24	8104418.7	4218	82	39	309	Fracture	1539874696	
1681	333539	8104428.9	4218	80	40	310	Fracture	1539874642	
1682	333527.22	8104430.1	4219	85	30	300	Fracture	1539874627	
1683	333500.78	8104440.3	4221	86	179	89	Fracture	1539874202	R8.2
1684	333500.78	8104440.3	4221	79	267	177	Fracture	1539874187	R8.2
1685	333492.78	8104440.2	4222	74	274	184	Fracture	1539874019	R8.2 black mineral in vein (Fe-oxide)
1686	333455.17	8104459	4219	89	159	69	Fracture	1539873777	
1687	333455.17	8104459	4219	36	333	243	Fracture	1539873741	
1688	333441.89	8104459.3	4219	54	155	65	Fracture	1539873503	R8.1
1689	333441.89	8104459.3	4219	86	11	281	Fracture	1539873484	
1690	333441.89	8104459.3	4219	80	48	318	Fracture	1539873476	
1691	333441.89	8104459.3	4219	85	44	314	Fracture	1539873462	
1692	333382.59	8104459.2	4221	65	302	212	Fracture	1539872955	In heavily Fractured zone ne Fractures slickenside showing oblique dextral
1693	333382.58	8104460.2	4220	76	44	314	Fracture	1539872806	
1694	333356.56	8104469.7	4218	81	222	132	Fracture	1539872626	
1695	333356.62	8104462.2	4220	81	38	308	Fracture	1539872588	Fe-oxide parallel fractures in altered zone (pic)
1696	333327.72	8104461.5	4219	53	327	237	Fracture	1539872405	Plumose structures
1697	333327.72	8104461.5	4219	86	43	313	Fracture	1539872374	
1698	333317.63	8104459.8	4220	82	49	319	Fracture	1539872266	More sinistral movement
1699	333305.78	8104456.3	4223	74	57	327	Fracture	1539872226	
1700	333293.87	8104454.5	4223	88	237	147	Fracture	1539872136	Fracture with gouge and Fe-oxide (pic)
1701	333276.23	8104446	4223	81	13	283	Fracture	1539871795	Slicken sides showing sinistral movement
1702	333276.23	8104446	4223	76	31	301	Fracture	1539871725	
1703	320305.72	8088995	2473	39	245	155	Fracture	1539724802	Gouge and white mineral
1704	320314.14	8088992.2	2465	70	170	80	Fracture	1539724778	
1705	320314.14	8088992.2	2465	74	11	281	Fracture	1539724763	
1706	320300.25	8088986.6	2471	20	291	201	Fracture	1539724717	LA planes with gouge (?) and white plates mineral
1707	320217.69	8088825.9	2450	68	348	258	Fracture	1539723625	
1708	320209.41	8088813.3	2458	34	60	330	Fracture	1539723559	
1709	320206.56	8088803.6	2459	47	230	140	Fracture	1539723357	R7.1p
1710	320199.74	8088795.2	2459	46	49	319	Fracture	1539723160	R7.10
1711	320199.74	8088795.2	2459	80	52	322	Fracture	1539723133	R7.10
1712	320182.13	8088747.6	2436	65	189	99	Fracture	1539722545	
1713	320182.13	8088747.6	2436	55	40	310	Fracture	1539722537	
1714	320154.7	8088711.5	2433	49	211	121	Fracture	1539722370	
1715	320154.7	8088711.5	2433	71	64	334	Fracture	1539722322	White mineral on plane
1716	320154.7	8088711.5	2433	42	58	328	Fracture	1539722291	
1717	320154.7	8088711.5	2433	88	299	209	Fracture	1539722255	
1718	319882.89	8088441.9	2422	53	255	165	Fracture	1539721483	
1719	319851.14	8088396.9	2417	38	224	134	Fracture	1539721327	Thin white veins
1720	319864.44	8088371.4	2409	45	262	172	Fracture	1539721278	Thin white veins on some
1721	319854.79	8088365	2411	45	244	154	Fracture	1539721179	
1722	319816.59	8088355	2433	58	1	271	Fracture	1539720978	
1723	319816.64	8088358.2	2435	48	348	258	Fracture	1539720859	

No.	X(East)	Y(North)	Z	Dip	Az	Strike	Type	Time Stamp	Remarks
1724	319823.54	8088303.9	2404	57	247	157	Fracture	1539720746	Parallel fractures
1725	319823.54	8088303.9	2404	78	330	240	Fracture	1539720727	
1726	319797.63	8088290.9	2420	64	359	269	Fracture	1539720682	Foliations gouge 3cm
1727	319797.63	8088290.9	2420	37	87	357	Fracture	1539720572	
1728	319823	8088268.7	2396	79	199	109	Fracture	1539720518	Epi on plane
1729	319785.05	8088252.4	2414	37	312	222	Fracture	1539720472	
1730	319785.05	8088252.4	2414	42	30	300	Fracture	1539720463	
1731	319785.05	8088252.4	2414	61	6	276	Fracture	1539720433	
1732	322397.52	8095860.8	3383	69	101	11	Fracture	1539634984	
1733	322412.32	8095886.1	3385	67	110	20	Fracture	1539634841	Causing normal displacement
1734	322424.24	8095944	3387	66	120	30	Fracture	1539634256	R6.7 displaced bedding
1735	322424.89	8095965.3	3386	89	132	42	Fracture	1539633936	
1736	322471.7	8096005.9	3402	73	142	52	Fracture	1539633850	Lots parallel oxidised
1737	322488.27	8096043	3397	76	273	183	Fracture	1539633764	R6.6
1738	322488.27	8096043	3397	65	108	18	Fracture	1539633717	R6.6
1739	322528.71	8096073.6	3406	73	61	331	Fracture	1539633125	Quartz vein in fracture 4cm - vuggy
1740	322595.64	8096124.6	3416	77	297	207	Fracture	1539632930	Fracture gouge oxidised
1741	322605.65	8096124.7	3419	88	100	10	Fracture	1539632855	Oxidised
1742	322616.23	8096114.6	3425	58	327	237	Fracture	1539632815	Parallel fractures
1743	322656.18	8096118.3	3434	79	167	77	Fracture	1539631363	Large Fracture and gouge 1m
1744	322693.42	8096128.7	3434	74	334	244	Fracture	1539631144	Large Fracture with gouge
1745	322691.07	8096111.6	3443	54	127	37	Fracture	1539630990	
1746	322709.49	8096122.3	3434	55	110	20	Fracture	1539630913	Parallel fractures
1747	322750.12	8096104.7	3440	43	257	167	Fracture	1539630758	Fabrics
1748	322863.56	8096101.1	3449	64	107	17	Fracture	1539630623	R6.4 horsetail
1749	322865.1	8096115	3447	58	101	11	Fracture	1539630281	R6.4 vein along plane
1750	322924.09	8096097.5	3459	76	99	9	Fracture	1539629929	
1751	323194.87	8096109.3	3490	82	216	126	Sin fault	1539629285	Sinistral nw Fracture
1752	323263.03	8096178.3	3496	62	89	359	Fracture	1539628732	R6.2
1753	323263.03	8096178.3	3496	45	106	16	Fracture	1539628707	R6.2
1754	323263.03	8096178.3	3496	86	204	114	Fracture	1539628653	R6.2 main Fracture contains calcite
1755	323350.79	8096200.8	3509	83	323	233	Fracture	1539628238	
1756	323447.67	8096214	3503	86	126	36	Fracture	1539627377	Conjugate?
1757	323447.67	8096214	3503	81	74	344	Fracture	1539627331	Conjugate?
1758	323475.39	8096242.2	3509	84	194	104	Fracture	1539627216	White mineral in fracture
1759	323490.66	8096295.2	3511	85	74	344	Fracture	1539627077	
1760	323502.74	8096345	3518	81	223	133	Fracture	1539626876	
1761	323505.81	8096351.3	3519	73	102	12	Fracture	1539626766	
1762	323527.76	8096345.2	3523	65	50	320	Fracture	1539626645	
1763	323515	8096357.6	3520	77	131	41	Fracture	1539624897	Another ne Fracture with gouge rock contains green minerals 3/4 alt
1764	323549.59	8096367.2	3529	89	322	232	Fracture	1539624481	Fracture with 10cm gouge
1765	323577.57	8096386.1	3538	89	87	357	Fracture	1539624231	
1766	323577.57	8096386.1	3538	82	141	51	Fracture	1539624208	
1767	323577.57	8096386.1	3538	89	86	356	Fracture	1539624192	
1768	323577.57	8096386.1	3538	89	88	358	Fracture	1539624175	
1769	323660.86	8096483.2	3530	87	71	341	Fracture	1539623811	
1770	323664.26	8096486.3	3532	74	78	348	Fracture	1539623733	
1771	323664.64	8096386.1	3546	76	67	337	Fracture	1539623356	
1772	323732.63	8096508.7	3541	75	74	344	Fracture	1539622644	
1773	323645.41	8096632	3515	86	159	69	Fracture	1539622151	
1774	323793.87	8096624.6	3563	72	88	358	Fracture	1539621569	
1775	323820.02	8096632.6	3563	81	190	100	Fracture	1539621347	
1776	323820.02	8096632.6	3563	69	82	352	Fracture	1539621336	
1777	323829.79	8096647.1	3559	85	261	171	Fracture	1539621204	
1778	323851.91	8096659.9	3562	89	262	172	Fracture	1539621127	
1779	323874.12	8096663.3	3568	86	197	107	Fracture	1539621100	
1780	323874.12	8096663.3	3568	82	256	166	Fracture	1539621084	
1781	323911.62	8096736.2	3555	70	82	352	Fracture	1539620720	
1782	323911.62	8096736.2	3555	80	91	1	Fracture	1539620676	
1783	324013.64	8096737.1	3573	71	77	347	Fracture	1539620202	
1784	323809.64	8097349.7	3588	72	22	292	Fracture	1539619116	
1785	323809.64	8097349.7	3588	70	321	231	Fracture	1539619107	
1786	323809.64	8097349.7	3588	63	320	230	Fracture	1539619090	
1787	323810.3	8097359.2	3594	69	102	12	Fracture	1539618491	R6.q1 With orangey matrix and quartz inside
1788	323810.3	8097359.2	3594	63	27	297	Fracture	1539618446	R6.1 With red matrix inside
1789	323824.79	8097366.7	3599	74	28	298	Fracture	1539618272	
1790	323824.79	8097366.7	3599	73	23	293	Fracture	1539618264	
1791	323950.22	8097393.4	3593	87	243	153	Fracture	1539617438	
1792	323950.22	8097393.4	3593	66	345	255	Fracture	1539617401	
1793	324045.38	8097429.5	3600	75	207	117	Fracture	1539613249	
1794	324065.98	8097436.5	3603	54	205	115	Fracture	1539613229	Parallel fractures
1795	324174.74	8097605.2	3574	81	70	340	Fracture	1539613045	
1796	324184.87	8097629.2	3572	78	177	87	Fracture	1539613016	
1797	324205.15	8097673.9	3570	59	268	178	Fracture	1539612877	
1798	324211.66	8097718.4	3559	73	141	51	Fracture	1539612789	
1799	324287.12	8097773.9	3525	88	76	346	Fracture	1539612456	Fracture
1800	324156.57	8097440.1	3607	79	63	333	Fracture	1539611090	
1801	324110.19	8097459.4	3610	63	144	54	Fracture	1539610931	Fractures

No.	X(East)	Y(North)	Z	Dip	Az	Strike	Type	Time Stamp	Remarks
1802	326653	8097202	3534	81	96	6	Fracture	1539374932	With some epi
1803	326653.28	8097202	3534	70	347	257	Fracture	1539374901	
1804	326665.48	8097247.3	3533	73	7	277	Fracture	1539373750	
1805	326660	8097254.6	3532	87	116	26	Fracture	1539373580	Dark green epi on planes RCS009
1806	326684	8097311.1	3534	60	243	153	Fracture	1539373395	Strong epi on planes
1807	326624.7	8097378.4	3528	74	139	49	Fracture	1539372811	
1808	326622.79	8097382	3528	77	191	101	Fracture	1539371465	R55 Fracture within Fracture
1809	326623	8097382	3528	74	144	54	Fracture	1539371421	R5.5 Fracture with white mineral and green?
1810	326652.22	8097345.2	3535	71	197	107	Fracture	1539371052	White mineral
1811	326831.61	8097388	3542	82	114	24	Fracture	1539370201	R5.4
1812	326831.61	8097388	3542	72	71	341	Fracture	1539370186	R5.4 with white mineral
1813	326828.91	8097396.2	3541	87	264	174	Fracture	1539369608	White mineral vein in Fracture with Fe-oxide around edge
1814	326830.02	8097400.8	3542	88	50	320	Fracture	1539369140	Fe-oxide fracture
1815	326830	8097400.8	3542	77	70	340	Fracture	1539367948	Altered powered granite with plane with epi
1816	326832.44	8097420.7	3548	72	255	165	Fracture	1539367578	Highly ox Fracture
1817	326816.08	8097488.7	3552	71	108	18	Fracture	1539366190	
1818	326816	8097488.7	3552	88	345	255	Fracture	1539366159	Epi fracture
1819	326815.77	8097527.7	3550	89	90	360	Fracture	1539365770	White mineral
1820	326837.68	8097579.8	3552	83	162	72	Fracture	1539365639	
1821	326870.47	8097635.9	3555	79	81	351	Fracture	1539365455	Large Fracture with gouge - orange suture
1822	326897.71	8097671.3	3558	85	303	213	Fracture	1539365228	Fracture or joint?
1823	326894	8097673.5	3556	80	7	277	Fracture	1539365110	Epidote and white mineral
1824	326952.48	8097699.9	3564	80	78	348	Fracture	1539364820	
1825	326985.39	8097729.8	3561	82	19	289	Fracture	1539364653	
1826	327009.88	8097730.1	3566	85	97	7	Fracture	1539364555	
1827	327190.93	8097857.1	3575	87	106	16	Fracture	1539363222	Parallel fractures
1828	327239.14	8097911	3579	15	215	125	Fracture	1539362898	
1829	327313.19	8097960.8	3583	76	194	104	Fracture	1539362566	
1830	327336.1	8097981	3584	20	232	142	Fracture	1539362420	
1831	327336.1	8097981	3584	80	3	273	Fracture	1539362392	
1832	327332.16	8097975.5	3585	79	286	196	Fracture	1539362360	R5.3 Fracture gouge
1833	327360.52	8098002.4	3588	83	105	15	Fracture	1539361556	
1834	327365.61	8098009.7	3588	83	117	27	Fracture	1539361495	
1835	327373.76	8098019.3	3588	67	93	3	Fracture	1539361414	
1836	327381	8098028.3	3587	64	3	273	Fracture	1539361170	Minor epi on plane granodiorite
1837	327497.56	8098136.8	3599	86	89	359	Fracture	1539360082	Oxidised fracture
1838	327474.73	8098159.4	3600	53	169	79	Fracture	1539359852	Fracture containing white mineral
1839	327474	8098158.9	3600	84	307	217	Fracture	1539359461	Veining within fracture - dark green in white different to last RCS005
1840	327483.69	8098154.7	3601	86	133	43	Fracture	1539356879	Lots of white plates mineral calcite?
1841	327484	8098154.7	3601	87	234	144	Fracture	1539356825	Epidote and minor white clay on fracture
1842	327442	8098202	3591	56	89	359	Fracture	1539356355	Faint epidote in fracture
1843	327447.4	8098207.2	3593	81	182	92	Fracture	1539356306	
1844	327451.46	8098223.4	3594	65	125	35	Fracture	1539356012	R5.1 dextral
1845	327452.29	8098222.7	3595	24	156	66	Fracture	1539355888	R5.1
1846	327454.09	8098224.2	3595	20	172	82	Fracture	1539355845	R5.1
1847	327452.73	8098245.6	3594	56	164	74	Fracture	1539355676	
1848	327452.64	8098256.8	3595	86	159	69	Fracture	1539355646	Fractured
1849	327475.75	8098315.2	3599	85	98	8	Fracture	1539355534	
1850	327470.47	8098292.1	3594	59	162	72	Fracture	1539355397	
1851	327441.9	8098184.3	3591	52	105	15	Fracture	1539355075	
1852	327441.9	8098184.3	3591	72	351	261	Fracture	1539355055	
1853	329645.44	8096719.5	3799	84	331	241	Fracture	1539287113	With orangey rusty mineral on plane - slickensides suggest sinistral
1854	329695.07	8096698.9	3815	79	66	336	Fracture	1539287047	
1855	329682.11	8096658.8	3827	71	329	239	Fracture	1539287017	
1856	329682.11	8096658.8	3827	74	329	239	Fracture	1539287005	
1857	329696.53	8096714.9	3812	85	337	247	Fracture	1539286605	Dextral
1858	329672.41	8096759.2	3794	72	122	32	Fracture	1539286524	
1859	329664.73	8096765.6	3793	87	287	197	Fracture	1539286496	
1860	329835.8	8096745.1	3832	76	352	262	Fracture	1539286366	
1861	329829.35	8096774.9	3822	73	349	259	Fracture	1539286273	
1862	330026.21	8096679.1	3840	77	351	261	Fracture	1539286124	
1863	330028.59	8096669.9	3843	88	358	268	Fracture	1539286115	
1864	329896.53	8096711.8	3853	31	221	131	Fracture	1539285978	R4.q1 Low angle in conglomerate
1865	329918.6	8096765.3	3831	78	353	263	Fracture	1539285644	
1866	329890.57	8096767.8	3831	83	349	259	Fracture	1539285560	
1867	329919.52	8096739.8	3841	77	327	237	Fracture	1539285538	
1868	329938.72	8096732.6	3842	71	348	258	Fracture	1539285509	
1869	329956.64	8096710.5	3844	77	123	33	Fracture	1539285483	
1870	330019.94	8096687.4	3839	73	99	9	Fracture	1539285328	
1871	329991.12	8096656.1	3849	75	10	280	Fracture	1539285285	
1872	330063.6	8096638.1	3854	82	104	14	Fracture	1539285179	
1873	330053.21	8096629.9	3853	85	156	66	Fracture	1539284981	Slickensides implying sinistral moment
1874	330068.18	8096619.7	3858	85	114	24	Fracture	1539284923	
1875	330112.14	8096663.2	3857	83	13	283	Fracture	1539284866	
1876	330110.24	8096679.6	3854	80	336	246	Fracture	1539284838	

No.	X(East)	Y(North)	Z	Dip	Az	Strike	Type	Time Stamp	Remarks
1877	330111.97	8096684.6	3853	75	97	7	Fracture	1539284823	
1878	330112.14	8096685.4	3853	83	158	68	Fracture	1539284815	
1879	330116.37	8096688.2	3854	82	95	5	Fracture	1539284787	
1880	330149.32	8096690.8	3863	77	111	21	Fracture	1539284729	
1881	330207.41	8096676.2	3883	78	115	25	Fracture	1539284706	
1882	330082.1	8096608.6	3863	81	116	26	Fracture	1539284692	
1883	330052.93	8096621.1	3855	83	333	243	Fracture	1539284637	
1884	330054.71	8096619.4	3856	82	119	29	Fracture	1539284623	
1885	330649.83	8097029.2	3889	68	336	246	Fracture	1539284354	
1886	330656.1	8097042.3	3892	55	335	245	Fracture	1539284320	
1887	330656.22	8097049.2	3893	56	338	248	Fracture	1539284278	
1888	330655.15	8097050.6	3893	54	342	252	Fracture	1539284261	
1889	330667.44	8097065.5	3891	69	332	242	Fracture	1539284091	White mineral in fracture
1890	330661.05	8097065.8	3893	64	328	238	Fracture	1539284013	
1891	330660.51	8097066.9	3893	70	312	222	Fracture	1539284008	
1892	330658.14	8097074.6	3896	56	11	281	Fracture	1539283990	
1893	330659.57	8097095.5	3898	57	337	247	Fracture	1539283943	
1894	330652.33	8097112.6	3904	73	354	264	Fracture	1539283884	
1895	330676.12	8097130.5	3899	84	324	234	Fracture	1539283693	Sinistral slickensides?
1896	330668.36	8097125.6	3901	88	138	48	Fracture	1539283609	
1897	330673.76	8097137.5	3900	40	199	109	Fracture	1539283537	Low angle fracture zone
1898	330669	8097134.5	3902	77	317	227	Fracture	1539283489	
1899	330668.49	8097152.9	3904	75	341	251	Fracture	1539283449	
1900	330686.27	8097190.1	3906	53	331	241	Fracture	1539283017	R4.10 Lithology much coarser
1901	330689.44	8097192	3906	58	254	164	Fracture	1539282976	R4.10
1902	330683.59	8097170.9	3903	64	257	167	Fracture	1539282922	
1903	330700.08	8097170.1	3897	33	8	278	Fracture	1539282866	
1904	330693.14	8097195.5	3905	57	357	267	Fracture	1539282796	Large fracture set
1905	330683.95	8097213.5	3911	74	88	358	Fracture	1539282673	
1906	330703.87	8097227.2	3911	80	89	359	Fracture	1539282613	
1907	330702.39	8097234.5	3914	27	171	81	Fracture	1539282556	
1908	330705.83	8097247.3	3917	21	179	89	Fracture	1539282427	
1909	330717.48	8097274.3	3922	78	2	272	Fracture	1539282294	
1910	330724.85	8097262.9	3917	76	299	209	Fracture	1539282144	
1911	330724.85	8097262.9	3917	88	114	24	Fracture	1539282123	
1912	330726.26	8097263.3	3917	84	297	207	Fracture	1539282075	
1913	330726.26	8097263.3	3917	74	13	283	Fracture	1539282067	
1914	331251.94	8097475.3	3959	86	178	88	Fracture	1539281732	
1915	331265.14	8097486.7	3960	62	138	48	Fracture	1539281681	
1916	331271.99	8097494.7	3962	84	114	24	Fracture	1539281532	4.9 Inside strike slip shear
1917	331271.87	8097487.7	3961	86	140	50	Fracture	1539281213	R4.9 Fracture set
1918	331277.01	8097487.3	3961	85	259	169	Fracture	1539281130	
1919	331287.78	8097493	3963	84	116	26	Fracture	1539281087	
1920	331295.01	8097498.4	3963	86	115	25	Fracture	1539281030	Slicken lines but no orientation
1921	331295.01	8097498.4	3963	89	226	136	Fracture	1539280991	
1922	331300.28	8097503.6	3964	89	115	25	Fracture	1539280973	
1923	331308.76	8097507.7	3965	89	296	206	Fracture	1539280960	
1924	331319.74	8097509.1	3966	88	158	68	Fracture	1539280944	
1925	331323.29	8097508.7	3966	87	111	21	Fracture	1539280889	
1926	331347.87	8097516.3	3968	87	355	265	Fracture	1539280764	
1927	331358.78	8097525.6	3969	76	112	22	Fracture	1539280664	
1928	331343.08	8097516.8	3968	84	124	34	Fracture	1539279523	
1929	331343.08	8097516.8	3968	81	119	29	Fracture	1539279503	
1930	331736.32	8097578.7	4000	82	101	11	Fracture	1539279009	
1931	331740.08	8097574.3	4000	67	47	317	Fracture	1539278867	
1932	331745.36	8097556.5	3999	81	63	333	Fracture	1539278808	
1933	331800.4	8097524.5	4000	89	156	66	Fracture	1539278342	
1934	331803.24	8097524.3	4000	80	139	49	Fracture	1539278326	
1935	331836.86	8097532.9	4004	67	103	13	Fracture	1539278242	
1936	331836.15	8097532.7	4003	83	113	23	Fracture	1539278234	
1937	331845.48	8097539.9	4005	79	55	325	Fracture	1539278152	
1938	331856.56	8097550.9	4006	84	125	35	Fracture	1539278109	
1939	331862	8097558.3	4005	85	338	248	Fracture	1539278093	
1940	331871.31	8097568.6	4007	81	41	311	Fracture	1539278051	
1941	331876.42	8097572.3	4008	86	117	27	Fracture	1539278036	
1942	331877.81	8097576.5	4007	87	131	41	Fracture	1539278020	
1943	331882.39	8097579.3	4007	82	327	237	Fracture	1539278004	
1944	331887.83	8097586.8	4008	74	151	61	Fracture	1539277966	
1945	331947.4	8097629.1	4013	84	110	20	Fracture	1539277821	Large Fracture NS/nne
1946	331949	8097632.8	4013	82	334	244	Fracture	1539277736	Very faint poss epi in plane?
1947	331968.02	8097644.4	4016	84	278	188	Fracture	1539277417	Conjugate
1948	331966.79	8097643.5	4016	80	341	251	Fracture	1539277390	Conjugate
1949	331979.46	8097654.5	4018	78	340	250	Fracture	1539277333	
1950	331979.64	8097654.1	4018	67	104	14	Fracture	1539277322	
1951	331981.05	8097655.2	4019	73	97	7	Fracture	1539277303	
1952	331980.68	8097657.8	4018	69	100	10	Fracture	1539277284	
1953	331996.95	8097684.3	4018	89	328	238	Fracture	1539277131	
1954	331999.77	8097686.7	4018	72	94	4	Fracture	1539277103	
1955	332010.47	8097700.3	4021	80	88	358	Fracture	1539277021	

No.	X(East)	Y(North)	Z	Dip	Az	Strike	Type	Time Stamp	Remarks
1956	332012	8097704.2	4021	70	83	353	Fracture	1539276757	Containing gouge and pale green mineral (smectite?)
1957	332021.72	8097712	4023	63	98	8	Fracture	1539276580	Large Fracture
1958	332022.43	8097711.8	4023	80	66	336	Fracture	1539276563	
1959	332026.09	8097719.8	4022	87	150	60	Fracture	1539276467	
1960	332029.95	8097724.1	4023	79	100	10	Fracture	1539276437	
1961	332035.2	8097733	4024	63	135	45	Fracture	1539276350	R4.8 inside of shear
1962	332036.09	8097732.8	4024	66	116	26	Fracture	1539276194	R4.8 outside of dextral Fracture
1963	332045.15	8097730.5	4028	65	103	13	Fracture	1539275993	
1964	332042.82	8097732.8	4027	68	126	36	Fracture	1539275967	
1965	332050.98	8097733.3	4028	24	205	115	Fracture	1539275890	Low angle
1966	332051.16	8097732	4028	66	119	29	Fracture	1539275875	
1967	332054.81	8097741.4	4028	77	287	197	Fracture	1539275780	
1968	332058.89	8097740.5	4028	64	65	335	Fracture	1539275758	
1969	332058.89	8097740.7	4028	60	72	342	Fracture	1539275739	
1970	332083.25	8097754.6	4028	89	135	45	Fracture	1539275660	Slicken sides sinistral
1971	332091.54	8097758.9	4029	72	314	224	Fracture	1539275152	R4.7 outside of shear slickensides suggest sinistral
1972	332091.9	8097758.9	4029	88	102	12	Fracture	1539275088	R4.7 With slicken lines within shear
1973	332097.91	8097760.9	4030	69	99	9	Fracture	1539274844	
1974	332096.3	8097762.6	4030	86	89	359	Fracture	1539274808	
1975	332103.04	8097761.9	4031	87	147	57	Fracture	1539274742	
1976	332105.7	8097762.3	4031	78	96	6	Fracture	1539274717	
1977	332108.17	8097763.2	4031	74	124	34	Fracture	1539274250	R4.6 In shear fabric
1978	332108.18	8097762.3	4031	88	105	15	Fracture	1539274223	R4.6
1979	332240.54	8097836.1	4033	79	81	351	Fracture	1539273817	Fracture with slicken lines
1980	332245.29	8097840.7	4034	89	16	286	Fracture	1539273698	
1981	332295.52	8097855.1	4030	87	355	265	Fracture	1539273617	
1982	332310.51	8097864.7	4030	84	168	78	Fracture	1539273583	
1983	332442.33	8097874.8	4023	87	280	190	Fracture	1539271679	
1984	332446.97	8097871	4023	76	275	185	Fracture	1539271651	
1985	332446.99	8097868.4	4022	84	279	189	Fracture	1539271632	
1986	332484.63	8097840.6	4020	87	268	178	Fracture	1539271502	
1987	332520.81	8097817.3	4016	80	269	179	Fracture	1539271417	
1988	332521.69	8097818.1	4016	89	174	84	Fracture	1539271402	
1989	332541.23	8097813.2	4015	85	226	136	Fracture	1539270842	Some parallel fractures
1990	332540.87	8097813.4	4015	78	120	30	Fracture	1539270785	Inside Fracture zone
1991	332540.52	8097813.1	4015	75	328	238	Fracture	1539270645	Other side of Fracture
1992	332540.34	8097813.1	4015	78	315	225	Fracture	1539270619	Fracture zone 1m wide
1993	332645.59	8097797.9	4005	71	131	41	Fracture	1539270054	R4.4 high angle
1994	332645.24	8097797.9	4005	21	313	223	Fracture	1539270000	R4.4 low angle
1995	332662.28	8097795.6	4005	89	218	128	Fracture	1539269590	R4.3
1996	332660	8097797.6	4005	83	119	29	Fracture	1539269422	Epi/ chlorite covering frailty with slickenlines dextral movement
1997	332665.83	8097794.5	4004	42	337	247	Fracture	1539268854	R4.3 Large Fracture zone
1998	332671.69	8097794.2	4003	71	316	226	Fracture	1539268795	Rubbly Fracture
1999	332679.45	8097798.5	4002	44	164	74	Fracture	1539268732	
2000	332679.64	8097797.6	4002	53	166	76	Fracture	1539268702	With plumose structure to east
2001	332682.05	8097805.7	4004	34	316	226	Fracture	1539268332	R4.2 Low angle imbricate?
2002	332702.87	8097818.6	4003	75	110	20	Fracture	1539268090	Minor white mineral
2003	332702	8097818.2	4003	86	157	67	Fracture	1539268010	Epi covered plane
2004	332790.51	8097876.5	3996	75	189	99	Fracture	1539266784	White plate mineral covering fracture
2005	332997.51	8097994.2	3975	57	318	228	Fracture	1539203333	Foliations
2006	333004.68	8098006.3	3976	68	70	340	Fracture	1539203171	
2007	333014.15	8098018.5	3974	80	82	352	Fracture	1539203113	
2008	333019.8	8098021.7	3972	75	76	346	Fracture	1539203101	
2009	333018.38	8098022.6	3972	29	170	80	Fracture	1539203022	
2010	333016.21	8098026.8	3974	80	64	334	Fracture	1539202999	
2011	333017.81	8098026.6	3974	80	65	335	Fracture	1539202918	Large Fracture nw
2012	333037.25	8098056.3	3973	76	98	8	Fracture	1539202675	
2013	333039.13	8098064.6	3974	31	299	209	Fracture	1539202629	
2014	333042.46	8098070.2	3973	78	72	342	Fracture	1539202540	Very fractured fracture
2015	333048.45	8098074.1	3971	89	39	309	Fracture	1539202450	White veining
2016	333052	8098076.7	3970	86	292	202	Fracture	1539202348	Strong epi along fracture
2017	333047.81	8098087.6	3976	81	236	146	Fracture	1539202273	White veining along fracture
2018	333065.71	8098110.8	3972	73	57	327	Fracture	1539201947	
2019	333066.48	8098103.2	3970	23	195	105	Fracture	1539201756	Parallel low angle fractures
2020	333078.59	8098117.7	3967	54	267	177	Fracture	1539201646	
2021	333088.64	8098124.8	3964	34	232	142	Fracture	1539201255	R3.6. Bands controlling prop?
2022	333089.79	8098135.9	3966	70	78	348	Fracture	1539200777	Parallel fractures
2023	333091.52	8098132.8	3964	29	212	122	Fracture	1539200694	Parallel fractures
2024	333095.03	8098145.1	3965	75	64	334	Fracture	1539200622	Albite(?) in Fracture
2025	333101.41	8098146.5	3962	83	74	344	Fracture	1539200379	Also with white mineral
2026	333099.97	8098148.7	3963	78	58	328	Fracture	1539199725	R3.5 Large nw Fracture with white sheeted mineral inside
2027	333108	8098157	3961	86	82	352	Fracture	1539199480	Few parallel fractures in very green rock
2028	333104.14	8098159	3963	46	268	178	Fracture	1539199051	
2029	333107.87	8098157.8	3961	41	273	183	Fracture	1539199015	Lith/colour change boundary
2030	333122.77	8098201.4	3962	62	15	285	Fracture	1539198597	Very crumbly
2031	333136.21	8098204.9	3957	34	215	125	Fracture	1539198512	Flow banding?

No.	X(East)	Y(North)	Z	Dip	Az	Strike	Type	Time Stamp	Remarks
2032	333135	8098206	3958	56	252	162	Fracture	1539198126	Fractures and green alt following direction
2033	333122	8098218.4	3965	83	124	34	Fracture	1539198032	Epi covered
2034	333130	8098221.8	3961	83	117	27	Fracture	1539197958	Epi covered
2035	333124	8098221.9	3964	86	80	350	Fracture	1539197891	Epi covering plane
2036	333126.85	8098223.2	3963	83	47	317	Fracture	1539197753	
2037	333127	8098222.3	3963	35	188	98	Fracture	1539197703	Main Fracture near epi patches
2038	333136.94	8098246.4	3959	43	274	184	Fracture	1539196961	Fractures
2039	333130.44	8098239.3	3963	76	260	170	Fracture	1539195214	R3.4 Fracture drag
2040	333127.48	8098232.6	3963	78	326	236	Fracture	1539195139	R3.4 main Fracture NE
2041	333130.42	8098241.2	3963	50	294	204	Fracture	1539195031	
2042	333131.14	8098240.6	3963	65	310	220	Fracture	1539194998	R3.4
2043	333131.48	8098241.5	3963	59	288	198	Fracture	1539194977	R3.4 fracture
2044	333135.57	8098283.8	3959	49	194	104	Fracture	1539193591	
2045	333140.95	8098299.2	3958	37	229	139	Fracture	1539193499	
2046	333140	8098311.9	3960	36	228	138	Fracture	1539193194	Fracture orientation around epi patch
2047	333143.35	8098330.2	3959	70	225	135	Fracture	1539192827	R3.3
2048	333143.35	8098330.2	3959	84	74	344	Fracture	1539192782	R3.3
2049	333143.35	8098330.3	3959	73	244	154	Fracture	1539192752	R3.3
2050	333145	8098330	3958	87	101	11	Fracture	1539192196	Minor epi on plane
2051	333145	8098330.4	3958	83	359	269	Fracture	1539191993	Epi covered
2052	333143.35	8098330.9	3959	87	236	146	Fracture	1539191965	
2053	333144.74	8098333.7	3958	89	347	257	Fracture	1539191926	
2054	333144.75	8098333.5	3958	76	352	262	Fracture	1539191479	R3.2
2055	333144.75	8098333.5	3958	68	250	160	Fracture	1539191467	R3.2
2056	333148.59	8098340.5	3957	63	260	170	Fracture	1539191139	
2057	333147.89	8098339.8	3957	57	255	165	Fracture	1539191096	Main Fracture?
2058	333144.35	8098338.8	3958	73	255	165	Fracture	1539190542	
2059	333146.48	8098338.7	3957	35	165	75	Fracture	1539189846	
2060	333146.65	8098339	3957	42	239	149	Fracture	1539189825	
2061	333146.45	8098341.8	3958	53	253	163	Fracture	1539189807	
2062	333146.63	8098341.8	3958	74	263	173	Fracture	1539189798	
2063	333146.8	8098342.7	3958	49	251	161	Fracture	1539189589	R3.1 parallel lineations in granodiorite
2064	333208.11	8098434	3953	51	64	334	Fracture	1539115884	
2065	333209.54	8098433.1	3953	51	63	333	Fracture	1539115876	
2066	333343.47	8098445.6	3951	53	244	154	Fracture	1539115337	
2067	333375.55	8098446.2	3951	20	147	57	Fracture	1539115191	
2068	333382.44	8098449.8	3952	22	137	47	Fracture	1539115162	
2069	333382.09	8098470.6	3952	72	229	139	Fracture	1539115049	Large broken Fracture with gouge
2070	333371.66	8098467.4	3954	51	59	329	Fracture	1539114076	R2.9 Very fractured Fracture - disp.
2071	333359.37	8098451.8	3951	63	197	107	Fracture	1539113984	R2.9
2072	333338.56	8098437.8	3950	23	148	58	Fracture	1539113755	
2073	333338.56	8098437.8	3950	86	338	248	Fracture	1539113745	
2074	333338.21	8098437.4	3950	82	345	255	Fracture	1539113691	
2075	333696.59	8098669.4	3934	78	324	234	Fracture	1539113361	
2076	333699.43	8098669.2	3934	87	302	212	Fracture	1539113198	
2077	333700.84	8098670	3934	89	306	216	Fracture	1539113185	
2078	333700.66	8098670.4	3934	87	94	4	Fracture	1539113179	
2079	333706.49	8098673.2	3934	76	183	93	Fracture	1539113130	
2080	333909.59	8098418.4	3956	77	340	250	Fracture	1539112411	
2081	333909.59	8098419	3956	76	342	252	Fracture	1539112389	Back in granodiorite
2082	333915.11	8098393.8	3957	88	52	322	Fracture	1539112111	
2083	333917.66	8098385.8	3956	83	48	318	Fracture	1539111109	R2.8
2084	333917.66	8098385.7	3956	78	49	319	Fracture	1539111072	R2.8 main fracture with malachite
2085	333917.66	8098385.5	3956	82	285	195	Fracture	1539110978	R2.8
2086	333920.6	8098394.7	3956	89	54	324	Fracture	1539110089	Directly next to RCS001 malachite vein
2087	333920.78	8098394.7	3956	87	125	35	Fracture	1539110024	Malachite plane RCS002
2088	333923.62	8098394.4	3955	84	124	34	Fracture	1539106085	Fractures in different lith surrounded by malachite
2089	333932.3	8098394.3	3954	87	292	202	Fracture	1539105619	
2090	333931.57	8098396.8	3954	82	307	217	Fracture	1539105496	
2091	333932.98	8098398.3	3953	78	309	219	Fracture	1539105461	
2092	334458.1	8098775.1	3933	84	133	43	Fracture	1539104191	
2093	334557.07	8098835.5	3935	89	291	201	Fracture	1539103998	
2094	334557.07	8098835.7	3935	85	343	253	Fracture	1539103988	
2095	334564.35	8098878.7	3937	89	326	236	Fracture	1539103597	Striations showing oblique movement
2096	334554.66	8098871.5	3937	78	308	218	Fracture	1539103055	
2097	334580.06	8098931.1	3939	76	12	282	Fracture	1539102787	Larger Fracture
2098	334580.57	8098934.4	3939	69	50	320	Fracture	1539102728	
2099	334583.21	8098936.6	3939	84	4	274	Fracture	1539102704	
2100	334586.54	8098941.1	3939	78	316	226	Fracture	1539102693	Vertical slickensides (reverse movement ?)
2101	334598.36	8098948.5	3940	89	157	67	Fracture	1539102362	
2102	334598.36	8098948.7	3940	89	121	31	Fracture	1539102270	
2103	334607.9	8098952.7	3940	80	301	211	Fracture	1539102223	
2104	334607.55	8098952.5	3940	69	129	39	Fracture	1539101880	R2.6 in fracture zone
2105	334606.83	8098954.1	3939	77	61	331	Fracture	1539101759	R2.6
2106	334612.32	8098953.8	3940	38	231	141	Fracture	1539101672	R2.6 low angle Fracture
2107	334615.87	8098953.7	3940	67	3	273	Fracture	1539100717	R2.5
2108	334616.4	8098953.8	3941	72	14	284	Fracture	1539100680	R2.5
2109	334619.04	8098956.4	3941	88	44	314	Fracture	1539100324	F2.5 - Large NW Fracture? Potential drag?

No.	X(East)	Y(North)	Z	Dip	Az	Strike	Type	Time Stamp	Remarks
2110	334619.58	8098955.5	3941	73	54	324	Fracture	1539100106	Sinistral movement?
2111	334619.58	8098955	3941	67	60	330	Fracture	1539100087	
2112	334620.27	8098957.6	3941	79	154	64	Fracture	1539100033	
2113	334626.09	8098961.7	3941	43	144	54	Fracture	1539099972	Fractures R2.4
2114	334625.55	8098962.8	3940	87	122	32	Fracture	1539099911	R2.4
2115	334627.71	8098958.4	3942	69	118	28	Fracture	1539099481	R2.4
2116	334626.82	8098959.6	3942	79	121	31	Fracture	1539099450	R2.4 Fracture zone approx 1m
2117	334633.17	8098963.4	3941	72	2	272	Fracture	1539099156	With plumose
2118	334640.62	8098962.5	3942	78	1	271	Fracture	1539099095	Large flat plane along road side -plumose.
2119	334644.67	8098966.2	3942	75	59	329	Fracture	1539098981	
2120	334646.63	8098964.8	3943	77	64	334	Fracture	1539098830	In highly fractured zone with NE structures
2121	334646.81	8098964.8	3943	62	288	198	Fracture	1539098782	Plumose structures
2122	334646.99	8098964.8	3943	78	126	36	Fracture	1539098679	
2123	334655.33	8098963.8	3945	72	269	179	Fracture	1539098525	R2.3
2124	334657.95	8098967.6	3944	84	129	39	Fracture	1539098385	R2.3
2125	334661.5	8098968.2	3943	82	301	211	Fracture	1539097780	
2126	334662.2	8098968.4	3943	71	159	69	Fracture	1539097754	
2127	334660.08	8098967.7	3944	82	301	211	Fracture	1539097654	
2128	334661.32	8098968	3943	77	312	222	Fracture	1539097609	
2129	334664.86	8098969.4	3943	89	129	39	Fracture	1539097586	
2130	334688.67	8098962.4	3947	89	164	74	Fracture	1539097287	Dextral
2131	334685.65	8098962.5	3947	83	167	77	Fracture	1539097215	
2132	334686.19	8098962.3	3947	84	253	163	Fracture	1539097197	
2133	334680.71	8098959.3	3947	76	68	338	Fracture	1539097149	
2134	334680.18	8098960.1	3947	75	2	272	Fracture	1539097063	
2135	334742.97	8098977.7	3952	67	112	22	Fracture	1539096744	Approx difficult to reach
2136	334756.49	8099017.1	3960	84	191	101	Fracture	1539096310	R2.2 sinistral?
2137	334757.21	8099015.1	3960	83	214	124	Fracture	1539096161	R2.2
2138	334757.39	8099015.1	3960	88	0	270	Fracture	1539096055	R2.2
2139	334721.14	8099025.7	3951	46	15	285	Fracture	1539094703	R2.1
2140	334720.65	8099020.3	3950	72	15	285	Fracture	1539094508	R2.1
2141	334718.15	8099022	3950	81	158	68	Fracture	1539094486	R2.1
2142	334714.1	8099040.6	3951	89	323	233	Fracture	1539093671	
2143	334739.33	8099032.4	3957	67	47	317	Fracture	1539048074	R1.3
2144	334738.82	8099032.5	3957	81	8	278	Fracture	1539029211	R1.3
2145	334738.82	8099032.5	3957	84	350	260	Fracture	1539029149	
2146	334727.24	8099038.3	3953	84	176	86	Fracture	1539029060	R1.3
2147	334737.15	8099062.5	3955	78	359	269	Fracture	1539028408	
2148	334737.15	8099062.5	3955	72	359	269	Fracture	1539028392	
2149	334737.15	8099062.5	3955	87	295	205	Fracture	1539028384	
2150	334737.15	8099062.5	3955	70	358	268	Fracture	1539028364	
2151	334737.15	8099062.3	3955	67	12	282	Fracture	1539028356	
2152	334734.7	8099059	3955	81	346	256	Fracture	1539028339	
2153	334744.73	8099068.5	3957	59	44	314	Fracture	1539027793	Fracture complex
2154	334744.73	8099068.5	3957	84	358	268	Fracture	1539027740	Fracture complex
2155	334744.73	8099068.5	3957	72	6	276	Fracture	1539027680	Fracture complex (with sketch)
2156	334743.61	8099074.8	3955	82	356	266	Fracture	1539027316	
2157	334746.96	8099077.4	3955	77	1	271	Fracture	1539026898	EW Fracture with slickenlines indicating normal movement to north
2158	334750.67	8099079.2	3956	79	1	271	Fracture	1539026696	
2159	334754.92	8099080.6	3957	81	3	273	Fracture	1539026656	
2160	334758.77	8099085.8	3957	87	111	21	Fracture	1539026628	
2161	334756.63	8099087.6	3956	73	7	277	Fracture	1539026607	
2162	334757.83	8099092.6	3955	71	357	267	Fracture	1539026583	
2163	334760.98	8099098	3956	85	347	257	Fracture	1539026233	Being cut by NW Fracture?
2164	334762.24	8099095.2	3956	73	41	311	Fracture	1539026178	Fractures nw x intersecting and cutting EW
2165	334769.21	8099111.1	3958	86	173	83	Fracture	1539025959	
2166	334768.65	8099114.1	3958	81	168	78	Fracture	1539025878	
2167	334766.96	8099126	3957	67	154	64	Fracture	1539025448	Dextral NE conjugate set
2168	334765.18	8099126.9	3956	84	106	16	Fracture	1539025408	Sinistral NE-SW/NS fault - Conjugate Fracture with NE
2169	334774.61	8099123.5	3961	71	75	345	Fracture	1539024478	
2170	334776.01	8099125.6	3961	85	112	22	Fracture	1539024448	
2171	334775.47	8099126.5	3961	81	110	20	Fracture	1539024426	
2172	334774.89	8099132.4	3960	65	22	292	Fracture	1539024246	Minor fracture with Fracture zone
2173	334775.07	8099131.6	3960	88	18	288	Fracture	1539023581	
2174	334775.07	8099132	3960	73	352	262	Fracture	1539023572	
2175	334775	8099130.9	3960	87	13	283	Fracture	1539023562	EW/NW large Fracture with 1.5 m of parallel fractures - slight pale green staining along plane?
2176	334780.69	8099138.7	3962	86	2	272	Fracture	1539023374	Lots of small EW fractures next to NW Fracture
2177	334781.01	8099143.1	3962	71	63	333	Fracture	1539023179	NW
2178	334783.1	8099147.6	3962	89	290	200	Fracture	1539022932	Parallel fractures
2179	334788.28	8099164.4	3962	80	108	18	Fracture	1539022517	
2180	334788.28	8099164.4	3962	84	108	18	Fracture	1539022354	Sinistral movement
2181	334739.08	8099219.9	3966	87	107	17	Fracture	1539021748	
2182	334743.19	8099238.4	3966	86	301	211	Fracture	1539021427	Smaller fracture cutting NS - conjugate?
2183	334773.81	8099245.2	3966	82	83	353	Fracture	1539021380	Larger fracture

No.	X(East)	Y(North)	Z	Dip	Az	Strike	Type	Time Stamp	Remarks
2184	334745.81	8099220.9	3967	80	343	253	Fracture	1539021132	
2185	334750.42	8099217.6	3966	77	93	3	Fracture	1539020974	Small
2186	334746.6	8099217.5	3966	72	79	349	Fracture	1539020955	
2187	334795.06	8099292.3	3971	81	62	332	Fracture	1539020539	
2188	334795.06	8099292.3	3971	83	109	19	Fracture	1539020490	
2189	334795.06	8099292.3	3971	87	103	13	Sin fault	1539020239	Parallel fractures
2190	334795.06	8099292.3	3971	78	5	275	Fracture	1539019825	Large fracture
2191	334795.18	8099299.5	3973	68	22	292	Fracture	1539019688	
2192	334791.98	8099300.7	3972	65	22	292	Fracture	1539019610	Clear Fracture with parallel fractures
2193	334783.96	8099306.2	3973	87	106	16	Fracture	1539017478	
2194	334783.96	8099306.2	3973	83	292	202	Fracture	1539017377	Parallel fractures just off larger NS Fracture
2195	334783.96	8099306.2	3973	86	72	342	Fracture	1539017274	
2196	334786.08	8099306.4	3974	89	301	211	Fracture	1539017185	
2197	334786.45	8099304.9	3973	80	352	262	Fracture	1539017165	
2198	334777.88	8099312.2	3973	84	337	247	Fracture	1539016232	Slickenlines showing horizontal movement
2199	334776.1	8099312.8	3973	83	107	17	Fracture	1539016107	
2200	334784.65	8099308.6	3974	88	266	176	Fracture	1539016066	Fracture
2201	334787.15	8099306	3974	77	110	20	Fracture	1539016009	Fracture with gouge
2202	334780.36	8099312.2	3974	70	353	263	Fracture	1539015789	Quite a large Fracture
2203	334770.03	8099318.1	3974	89	192	102	Fracture	1539015637	
2204	334768.61	8099319	3974	88	7	277	Fracture	1539015619	
2205	334767.18	8099320.3	3974	88	16	286	Fracture	1539015603	
2206	334709.45	8099355.8	3977	83	1	271	Fracture	1539014916	
2207	334708.37	8099357.8	3978	78	354	264	Fracture	1539014894	
2208	334701.55	8099367.5	3979	79	22	292	Fracture	1539014835	
2209	334701.38	8099367.5	3979	83	31	301	Fracture	1539014808	NW fractures
2210	334686.84	8099411.7	3974	76	68	338	Fracture	1539014443	
2211	334845.35	8099543.9	3980	68	43	313	Fracture	1539013407	
2212	334845.35	8099544.1	3980	73	43	313	Fracture	1539013383	NW intersection with NE
2213	334843.05	8099542.6	3980	85	119	29	Fracture	1539013214	
2214	334843.23	8099542.6	3980	89	302	212	Fracture	1539013183	
2215	334844.65	8099542	3980	84	301	211	Fracture	1539013173	
2216	334866.96	8099567.7	3982	87	355	265	Fracture	1539013064	
2217	334866.79	8099566.7	3982	81	359	269	Fracture	1539013019	
2218	334879.85	8099574.6	3983	76	11	281	Fracture	1539012891	Fracture sets
2219	334880.03	8099574.6	3983	71	159	69	Fracture	1539012839	
2220	334904.9	8099613.2	3985	85	128	38	Fracture	1539012466	NE structures
2221	334904.9	8099613.2	3985	88	355	265	Fracture	1539012329	
2222	334912.76	8099627.2	3986	88	173	83	Fracture	1539012096	
2223	334940.83	8099642.8	3988	89	179	89	Fracture	1539011995	EW Fracture in valley of NE STRUCTURE
2224	334934.45	8099531.9	3996	73	82	352	Fracture	1539011461	
2225	334929.66	8099532.2	3995	81	356	266	Fracture	1539011402	
2226	334910.58	8099523.9	3993	89	175	85	Dex fault Fracture	1539011250	Dextral fault plane
2227	334905.64	8099520.2	3993	73	10	280	Fracture	1539011146	
2228	334904.59	8099518.7	3993	77	313	223	Fracture	1539011118	
2229	334852.99	8099497.3	3996	85	342	252	Fracture	1539010819	
2230	334852.99	8099497.3	3996	89	154	64	Fracture	1539010795	
2231	334852.99	8099497.3	3996	78	57	327	Fracture	1539010715	
2232	334852.99	8099497.3	3996	70	68	338	Fracture	1539010668	
2233	334852.99	8099497.3	3996	74	49	319	Sin fault	1539010508	
2234	334854.33	8099506.7	3992	64	45	315	Fracture	1539010113	Sinistral movement
2235	334838.36	8099530.4	3981	82	346	256	Fracture	1539009776	Dextral movement?
2236	334842	8099496.8	3995	84	60	330	Fracture	1539009382	Larger looking Fracture 104 with smaller splay fractures
2237	334840.81	8099512.5	3989	70	48	318	Fracture	1539009044	
2238	334816.21	8099507.3	3986	86	358	268	Dex fault Fracture	1539008888	Slickensides showing dextral movement (272.10)
2239	334818.18	8099504.7	3988	86	351	261	Fracture	1539008502	
2240	334818.17	8099505.3	3988	86	131	41	Fracture	1539008487	
2241	334817.99	8099506	3987	87	122	32	Fracture	1539008471	
2242	334817	8099507.5	3986	87	128	38	Fracture	1539008251	Separate fracture sets - orthogonal ?
2243	334814.21	8099490.9	3991	85	349	259	Fracture	1539008173	
2244	334780.52	8099475.8	3987	85	350	260	Fracture	1539008147	
2245	334780.52	8099475.8	3987	87	353	263	Dex fault Fracture	1539007669	Slickenside show dextral movement
2246	334775.72	8099493.7	3984	84	169	79	Fracture	1539007592	
2247	334774.13	8099492.2	3983	89	349	259	Fracture	1539007577	
2248	334775.72	8099493.3	3984	84	356	266	Dex fault Fracture	1539007369	
2249	334760	8099483.8	3982	88	233	143	Dex fault Fracture	1539006816	Subvertical stepping appears dextral
2250	334752.3	8099473.8	3982	82	316	226	Fracture	1539006443	Subvertical fractures - kinematics?
2251	334731.8	8099465.3	3978	81	62	332	Fracture	1539006237	
2252	334734.41	8099449.1	3982	77	104	14	Fracture	1539005867	Lots of parallel fractures
2253	320752.71	8089615.8	2514	42	254	164	Fracture	1541011196	
2254	320752.71	8089615.8	2514	83	128	38	Fracture	1541011180	
2255	334749.71	8099331.4	3974	6	75	345	Bedding	1539015469	Bedding??
2285	328108.65	8107393.4	3858	24	2	272	Veining	1540584649	

No.	X(East)	Y(North)	Z	Dip	Az	Strike	Type	Time Stamp	Remarks
2286	328108.65	8107393.4	3858	79	144	54	Veining	1540584638	
2287	328108.65	8107393.4	3858	80	35	305	Veining	1540584630	
2288	328070.66	8107077.1	3981	70	106	16	Veining	1540583606	BT malachite vein close to RCS089
2289	328064.23	8107073.8	3982	69	110	20	Veining	1540583564	
2290	328037.2	8107072.4	3980	57	133	43	Veining	1540583424	More BT veining
2291	328029.78	8107069.2	3980	68	205	115	Veining	1540582486	
2292	327982.6	8106677.2	3980	58	117	27	Veining	1540579692	
2293	327982.6	8106677.2	3980	78	128	38	Veining	1540579683	
2294	327982.6	8106677.2	3980	57	115	25	Veining	1540579624	Main veining direction (pic)
2295	335283.53	8102210.2	4226	14	187	97	Bedding	1539879809	Bedding in andesite?
2296	334765.83	8103668.2	4224	87	198	108	Veining	1539878667	
2297	334766.4	8103668.1	4224	76	122	32	Veining	1539878377	
2298	334766.4	8103668.1	4224	73	92	2	Veining	1539878371	
2299	334766.4	8103668.1	4224	72	90	360	Veining	1539878365	R8.5
2300	334772.75	8103686.5	4222	89	207	117	Veining	1539878179	
2301	334769.11	8103692.1	4221	89	16	286	Veining	1539878159	
2302	334771.32	8103693.3	4221	89	196	106	Veining	1539878044	Most in this orientation
2303	334777.76	8103744.3	4216	82	335	245	Veining	1539877520	
2304	334777.76	8103744.3	4216	80	320	230	Veining	1539877513	
2305	334777.71	8103750.7	4216	64	242	152	Veining	1539877424	
2306	334777.71	8103750.7	4216	82	182	92	Veining	1539877371	
2307	334777.71	8103750.7	4216	89	9	279	Veining	1539877360	
2308	334778.12	8103756.2	4216	63	242	152	Veining	1539877339	
2309	334778.12	8103756.2	4216	59	271	181	Veining	1539877331	
2310	334777.96	8103765.4	4215	86	291	201	Veining	1539877196	R8.4
2311	334777.57	8103765.8	4215	86	141	51	Veining	1539877110	R8.4 being slight6 offset?
2312	334777.57	8103765.8	4215	61	6	276	Veining	1539877081	R8.4
2313	334777.57	8103765.8	4215	49	52	322	Veining	1539877062	R8.4 showing slight offset?
2314	334780.93	8103793.7	4214	75	18	288	Veining	1539876572	
2315	334780.93	8103793.7	4214	63	197	107	Veining	1539876559	
2316	334780.93	8103793.7	4214	86	54	324	Veining	1539876543	
2317	334785.39	8103812.7	4213	83	0	270	Veining	1539876354	
2318	334785.39	8103812.7	4213	48	165	75	Veining	1539876345	
2319	334785.39	8103812.7	4213	43	158	68	Veining	1539876338	
2320	334785.76	8103816.8	4213	71	312	222	Veining	1539876227	
2321	334785.76	8103816.8	4213	17	258	168	Veining	1539876117	R8.3
2322	334785.76	8103816.8	4213	74	315	225	Veining	1539876090	R8.3
2323	334786.16	8103816.3	4213	77	351	261	Veining	1539876010	R8.3
2324	333512.46	8104441.7	4218	67	275	185	Veining	1539874580	
2325	333510	8104437.7	4219	37	159	69	Veining	1539874517	
2326	333510	8104437.7	4219	77	122	32	Veining	1539874507	
2327	333510	8104437.7	4219	69	270	180	Veining	1539874497	R8.2 detail
2328	333455.17	8104459	4219	89	231	141	Veining	1539873719	
2329	333455.17	8104459	4219	82	120	30	Veining	1539873700	
2330	320182.13	8088747.6	2436	59	108	18	Dyke	1539722611	Pink felsic dyke?
2331	322424.24	8095944	3387	14	228	138	Bedding	1539634299	Bedding that is displaced R6.7
2332	322924.09	8096097.5	3459	11	199	109	Bedding	1539629904	Bedding? Darker continuous layer
2333	326816	8097451.8	3548	72	111	21	Dyke	1539366618	Small dyke not very continuous- contains minor epidote
2334	327282.68	8097934.4	3584	58	100	10	Dyke	1539362713	
2335	327291.59	8097942.3	3584	82	111	21	Dyke	1539362666	
2336	327343.62	8097986.8	3586	74	110	20	Dyke	1539361679	R5.3
2337	327458.49	8098167.3	3596	65	95	5	Dyke	1539359064	Dyke contact
2338	329907.07	8096744.4	3840	17	234	144	Bedding	1539285759	Bedding with conglomerates
2339	329965.27	8096717	3840	18	218	128	Bedding	1539285405	Bedding? Low angle and layered
2340	331322.93	8097508.7	3966	63	168	78	Joint	1539280922	Plumose fracture
2341	332684.53	8097805.9	4003	12	42	312	Joint	1539268385	R4.2 Within imbricate
2342	332762	8097859.1	3997	68	287	197	Veining	1539267740	Epi
2343	332763.17	8097858.6	3997	71	284	194	Veining	1539267659	
2344	332767	8097861	3997	72	113	23	Veining	1539267110	Veining with lots of white mineral and some epi. Darker halo in host rock
2345	332797	8097874.2	3992	86	146	56	Veining	1539266150	Veining ne direction contains white and green mineral

Appendix B1

No.	X(East)	Y(North)	Z	Plunge	Plunge azimuth	Type	Time Stamp	Remarks
749	312347	8098802	2953	13	259	Slickenside	1540303334	Sinistral movement
750	311342	8097605	2810	48	178	Slickenside	1540234820	
751	310193	8098149	2713	5	238	Slickenside	1540216249	Dextral on ne Fault
752	310013	8098153	2710	9	228	Slickenside	1540214526	
753	309982	8098151	2707	68	189	Slickenside	1540214131	R10.3
754	309982	8098151	2707	27	215	Slickenside	1540214109	R10.3
755	309806	8098016	2679	14	250	Slickenside	1540208853	Dextral movement in NE EnE Fault with epi
756	309373	8098053	2657	81	18	Slickenside	1539976627	Slickensides on ne Fault white mineral
757	308973	8098102	2633	65	261	Lineation	1539951589	NE fault lineations
758	308973	8098102	2633	85	80	Lineation	1539951315	Ew lineations
2256	321336	8103983	3321	36	127	Slickenside	1540486024	White mineral on nw Fault
2257	319668	8103520	3212	26	293	Lineation	1540479192	
2258	317669	8103258	3084	71	18	Lineation	1540472710	? On ne gouge
2259	316546	8102827	3250	45	29	Slickenside	1540401416	
2260	333384	8104461	4220	35	243	Slickenside	1539873019	
2261	333276	8104449	4223	9	304	Slickenside	1539871886	Sinistral nw Fault
2262	326832	8097388	3542	4	327	Lineation	1539370597	
2263	329645	8096720	3799	15	237	Slickenside	1539287186	
2264	330068	8096614	3860	6	239	Slickenside	1539285054	Sinistral
2265	330671	8097138	3901	3	232	Slickenside	1539283709	Sinistral
2266	331291	8097499	3963	12	206	Slickenside	1539281052	
2267	332083	8097754	4029	15	226	Slickenside	1539275679	Sinistral
2268	332092	8097759	4029	10	189	Slickenside	1539275107	R4.7
2269	332241	8097839	4034	15	172	Slickenside	1539273869	NNW Fault slicken lines
2270	332661	8097797	4005	17	209	Slickenside	1539269435	
2271	334551	8098876	3937	53	237	Lineation	1539103676	Oblique striations on NW fault
2272	334554	8098880	3937	19	217	Slickenside	1539103313	Ne Fault sinistral?
2273	334608	8098953	3940	9	337	Slickenside	1539102143	R2.6 dextral on nw Fault
2274	334752	8099021	3959	18	274	Slickenside	1539096460	R2.2 sinistral
2275	334731	8099079	3953	80	11	Slickenside	1539027184	Normal movement on fault
2276	334778	8099122	3963	12	21	Slickenside	1539025629	On sinistral NS/NE fault
2277	334775	8099121	3961	7	256	Slickenside	1539025597	On dextral NE fault
2278	334788	8099165	3962	1	17	Slickenside	1539022444	For 018 fracture
2279	334795	8099292	3971	16	198	Slickenside	1539020314	013 SV fault
2280	334911	8099524	3993	8	273	Slickenside	1539011316	For 085 fault
2281	334853	8099493	3996	3	135	Slickenside	1539010466	NW fracture slicken line
2282	334846	8099512	3989	10	258	Slickenside	1539009844	
2283	334781	8099476	3987	12	267	Slickenside	1539007683	
2284	334776	8099491	3984	2	266	Slickenside	1539007525	Slickenside dextral movement

Appendix B2

Appendix C

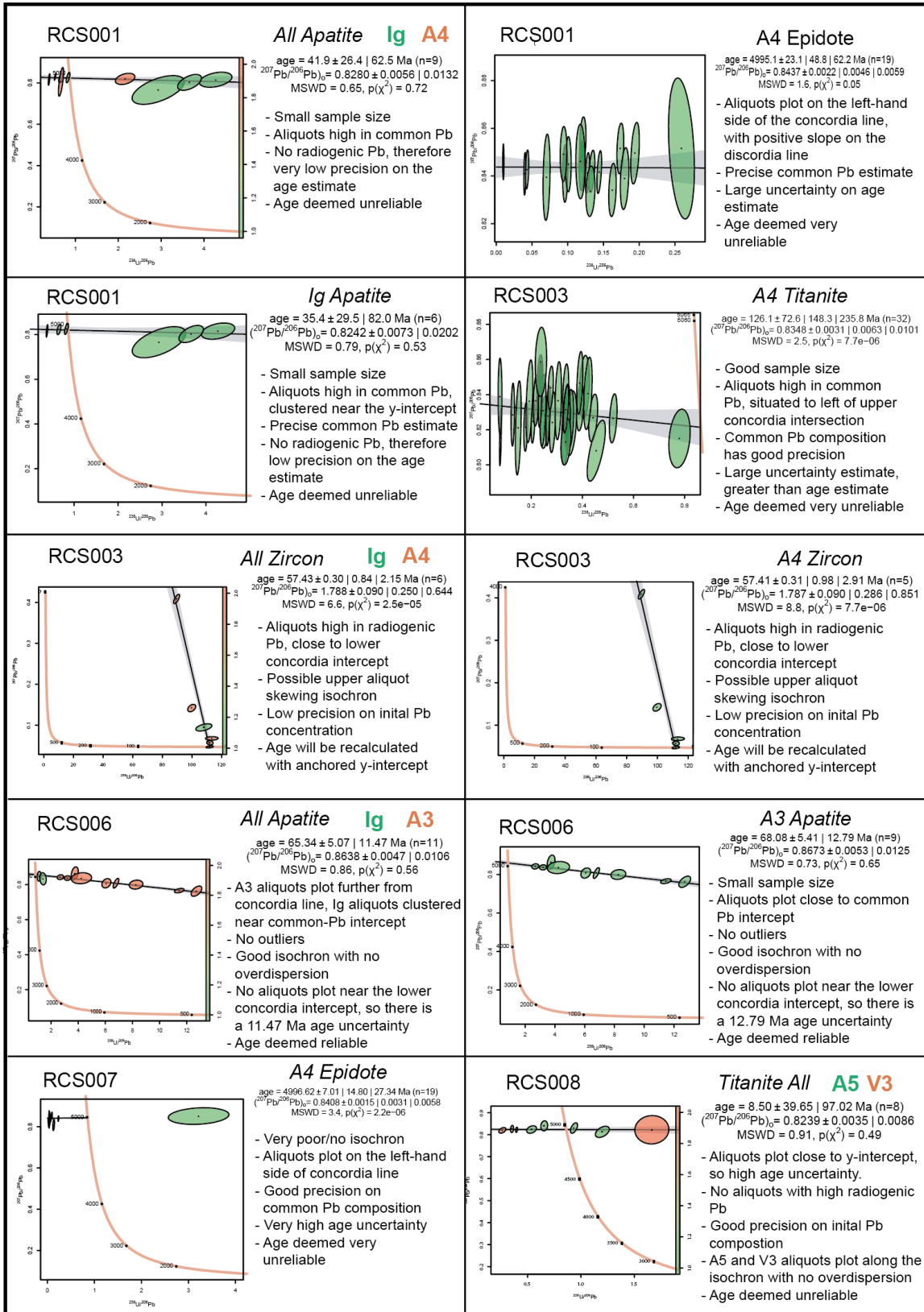
Geochronology

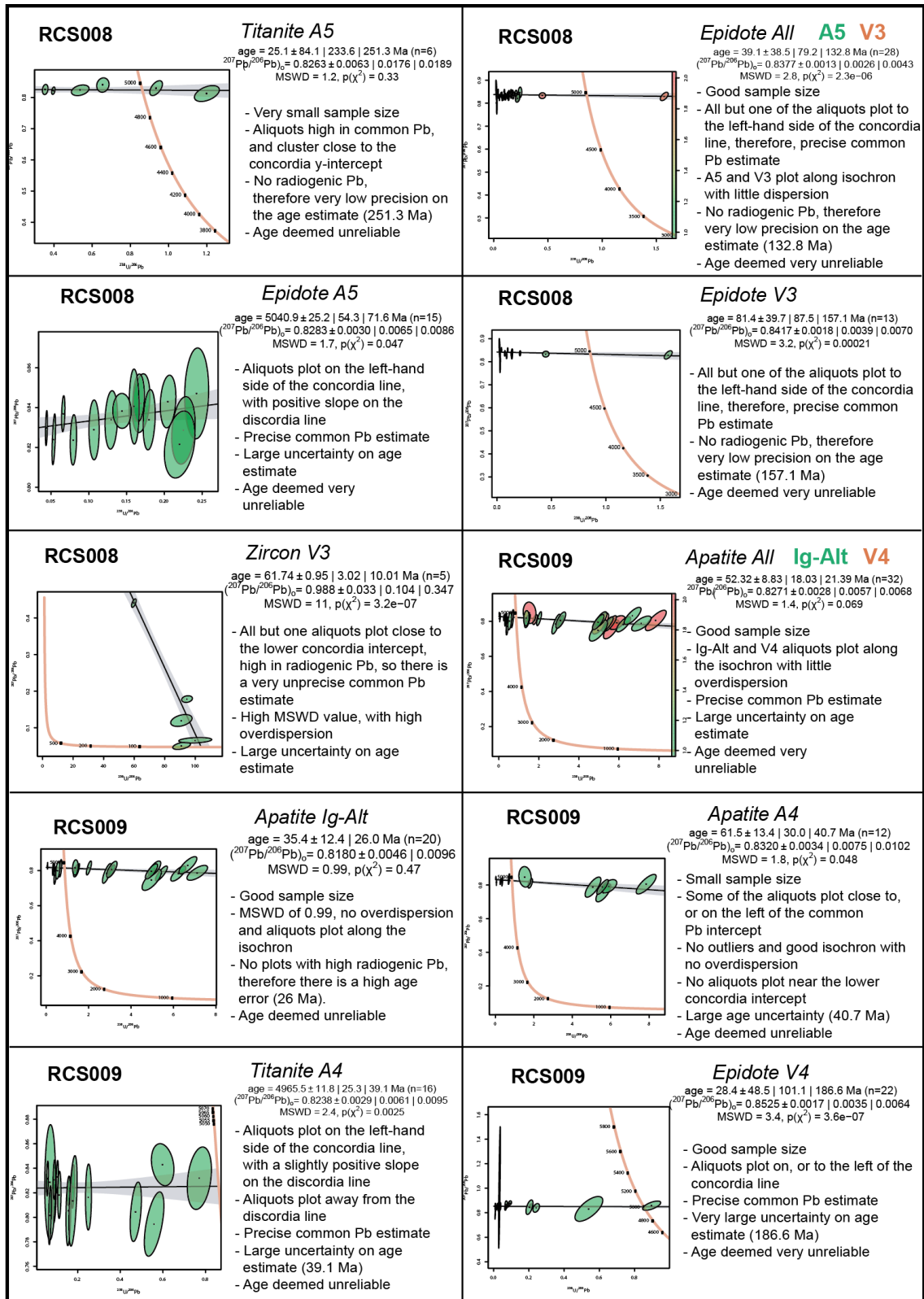
Appendix C1 – Tables showing all of the Tera-Wasserburg concordia plots for each combination of dates calculated where sufficient data is available for that sample. These plots are also separated based on the dated mineral. Where there are multiple textural classifications, and sufficient data present, these textures are separate (with individual T-W plots) and also combined into one plot, but distinguished by colour. Notes are provided for each calculation.

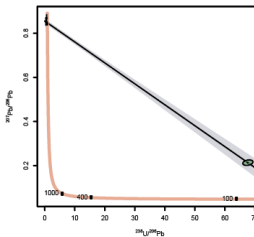
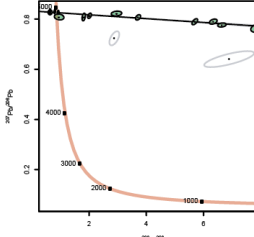
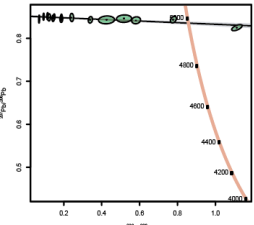
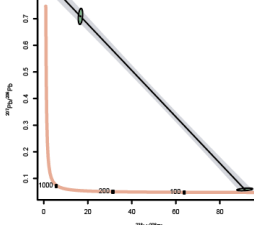
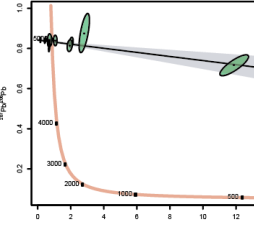
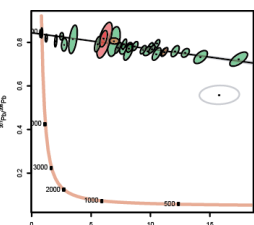
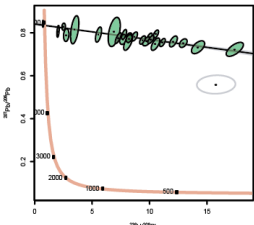
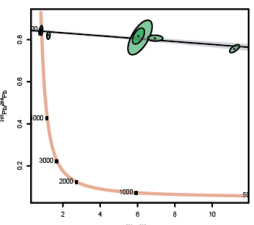
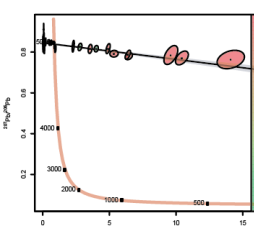
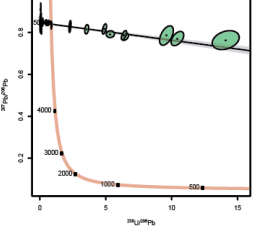
Appendix C2 – Tables of all of the raw (un-anchored) and anchored ages calculated, with the common Pb intercept values. These include those that were omitted. In some samples or textures, there was sufficient data to calculate the age, however the presence of these data are acknowledged in this table. Column abbreviations are:

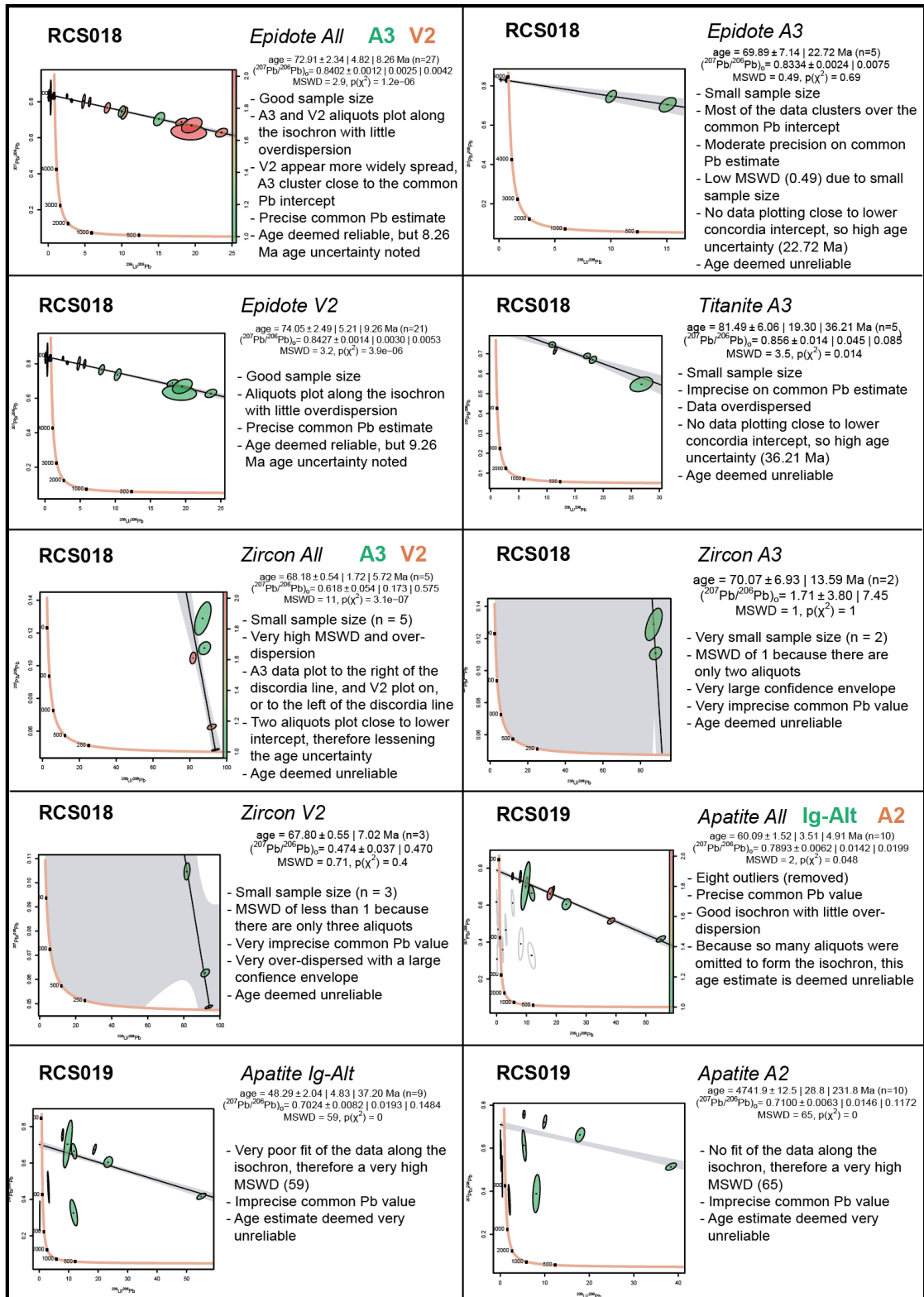
- +/-: the analytical uncertainty (σ) of t
- 2nd error: the studentised 100(1- σ)% confidence interval for t using the appropriate number of degrees of freedom
- 3rd error: the approximate 100(1- σ)% confidence interval for t with overdispersion, calculated as = 2nd error $\sqrt{\text{MSWD}}$
- Uncertainty: the calculated percentage uncertainty of the ages using the 3rd error

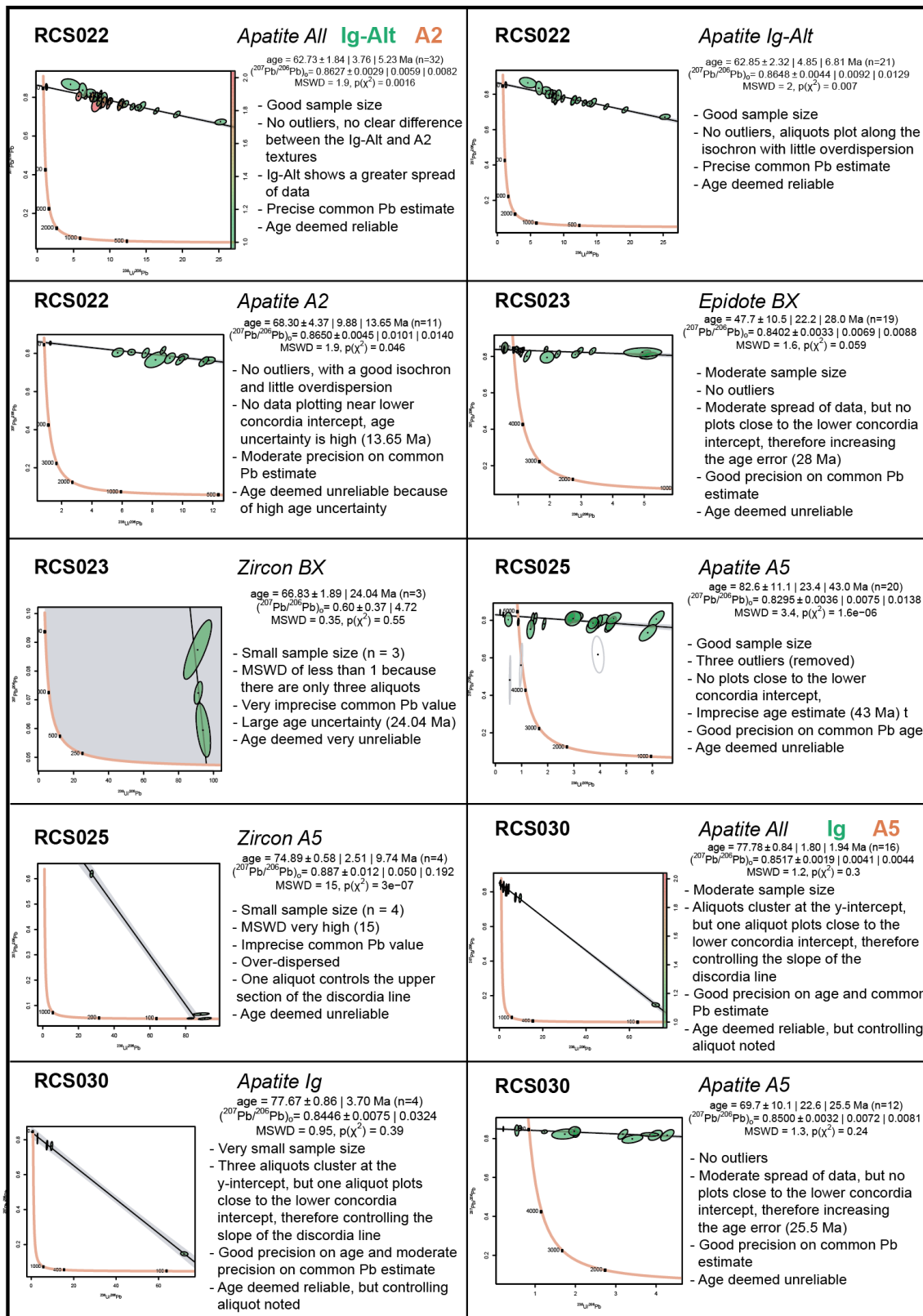
Appendix C3 – Tables containing only 'precise' ages (<10% uncertainty) which were deemed acceptable for use in the analysis in Chapters 7, 8 and discussion in 9. A 'Y' located in the 'replaced' column indicates those age categories which has both raw and anchored ages with high enough precision to be accepted. In these cases, only one of the ages were selected (in order to minimise duplication). Comments on the why the raw or anchored ages were selected for particular categories are highlighted.

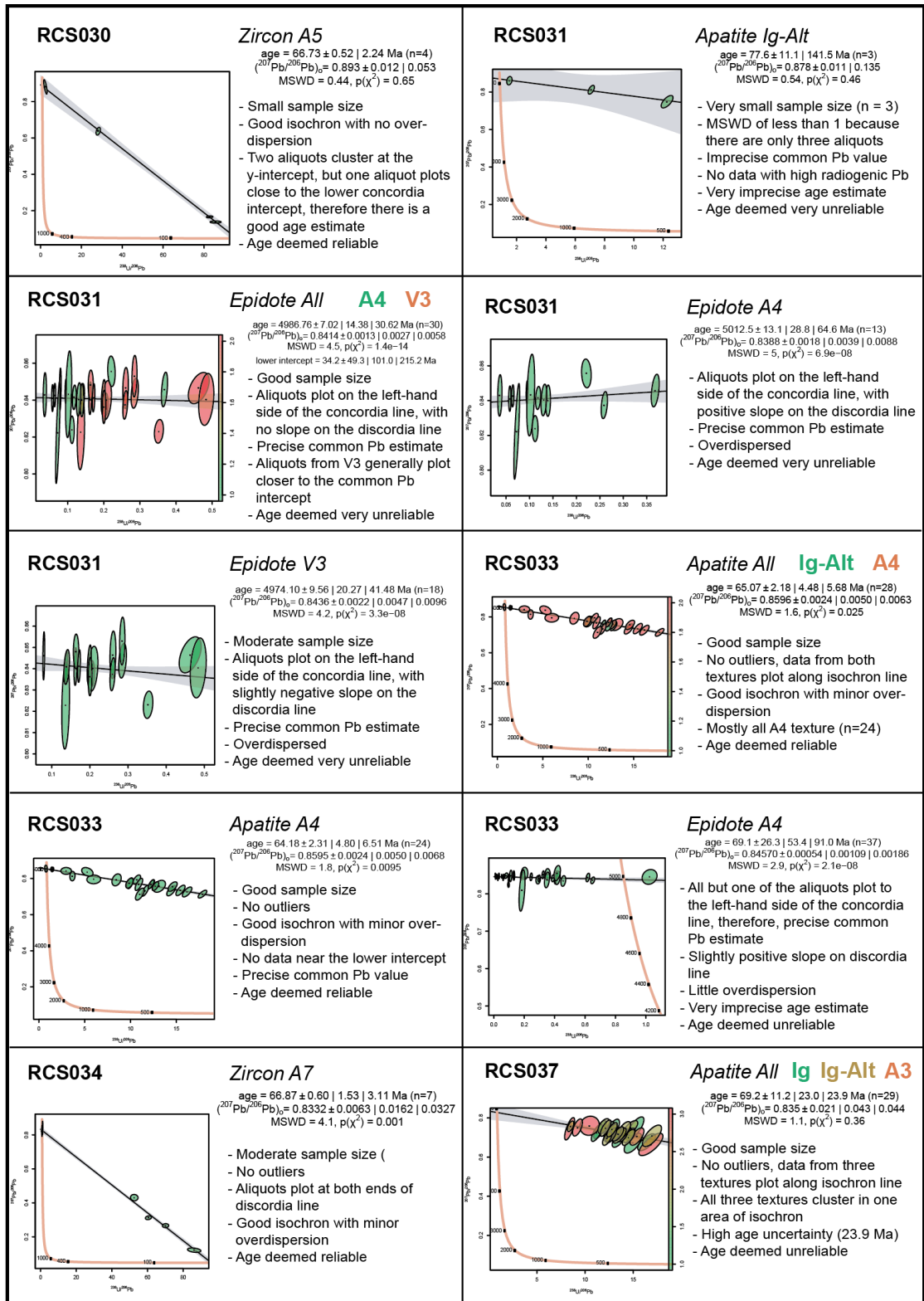


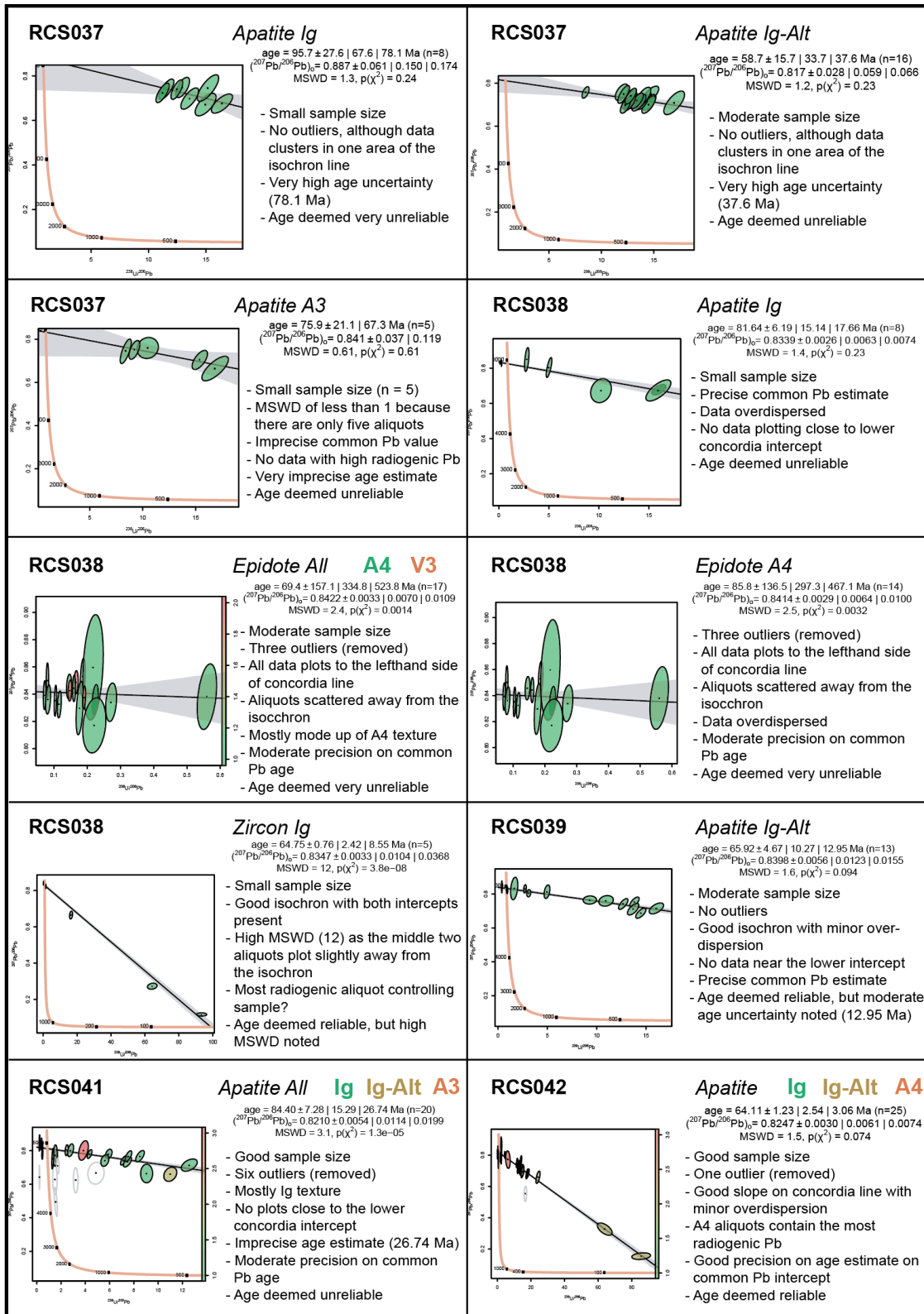


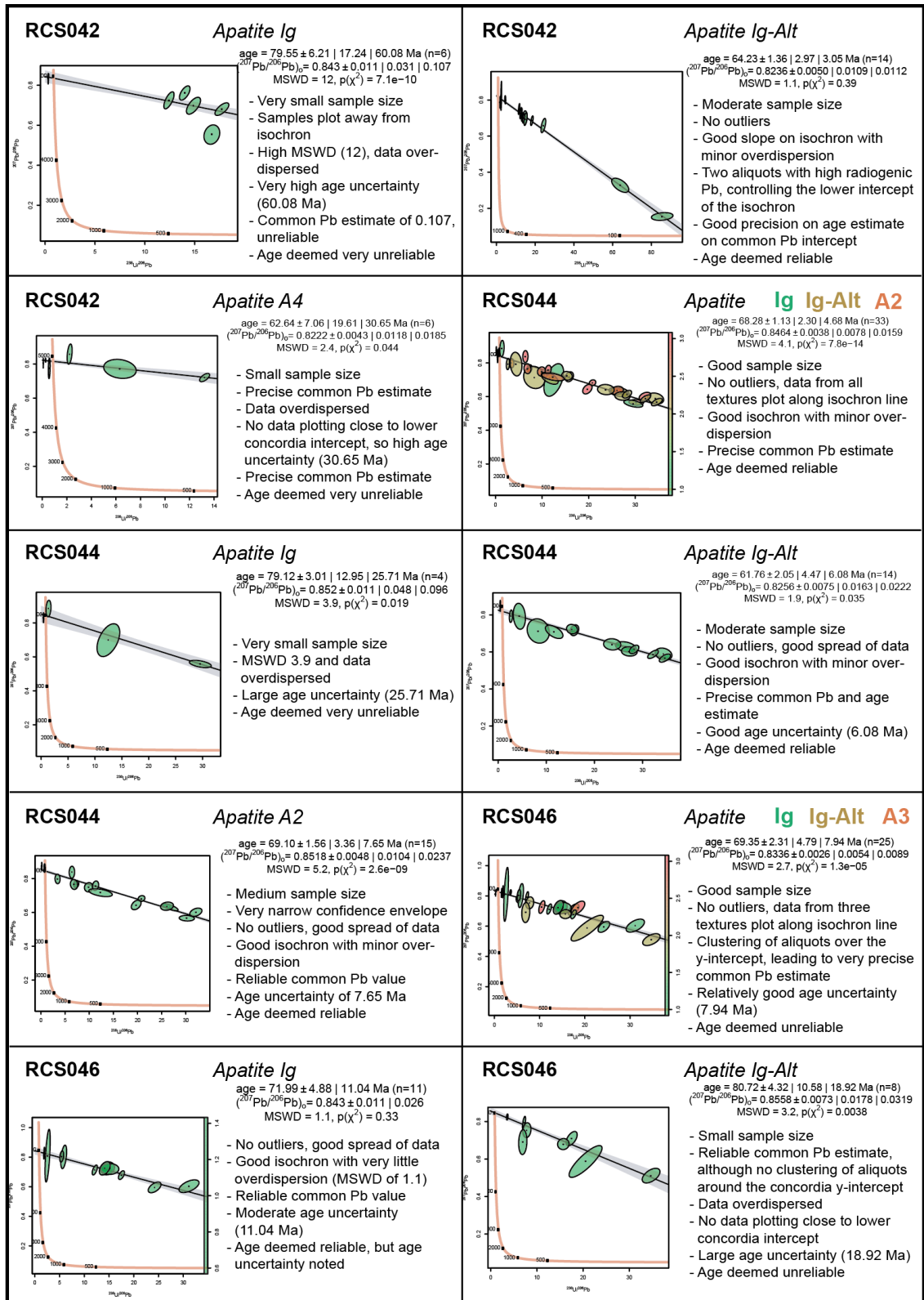
<p>RCS010</p> 	<p>Apatite ?</p> <p>age = 75.27 ± 1.08 4.66 10.19 Ma (n=4) $(^{207}\text{Pb}/^{206}\text{Pb})_c = 0.8553 \pm 0.0024$ 0.0102 0.0223 MSWD = 4.8, $p(\chi^2) = 0.0084$</p> <ul style="list-style-type: none"> - Small sample size - One aliquot plots close to the lower concordia intercept, therefore this plot controls the age estimate - Age deemed reliable, but small sample size noted 	<p>RCS014</p> 	<p>Titanite A6</p> <p>age = 62.42 ± 3.85 8.48 14.61 Ma (n=13) $(^{207}\text{Pb}/^{206}\text{Pb})_c = 0.8325 \pm 0.0018$ 0.0040 0.0068 MSWD = 3, $p(\chi^2) = 0.0059$</p> <ul style="list-style-type: none"> - Two outliers (rejected), the remaining plots form a good isochron - Precise common Pb estimate - No aliquots plot close to lower concordia intercept, therefore there is a moderate age uncertainty (14.61 Ma) - Age deemed unreliable because of age uncertainty
<p>RCS014</p> 	<p>Epidote A6</p> <p>age = 149.7 ± 21.9 47.2 50.4 Ma (n=15) $(^{207}\text{Pb}/^{206}\text{Pb})_c = 0.8516 \pm 0.0012$ 0.0027 0.0029 MSWD = 1.1, $p(\chi^2) = 0.32$</p> <ul style="list-style-type: none"> - All but one of the aliquots plot to the left-hand side of the concordia line, therefore, precise common Pb estimate - No radiogenic Pb, therefore very low precision on the age estimate (50.4 Ma) - Relatively good isochron with little dispersion - Age deemed unreliable 	<p>RCS014</p> 	<p>Zircon Ig</p> <p>age = 69.23 ± 1.19 2.33 Ma (n=2) $(^{207}\text{Pb}/^{206}\text{Pb})_c = 0.854 \pm 0.017$ 0.033 MSWD = 1, $p(\chi^2) = 1$</p> <ul style="list-style-type: none"> - Small sample size (n = 2) - MSWD of 1 because there are only two aliquots - One aliquot plots on the lower concordia intercept, therefore high age precision - Age deemed reliable, but small sample size noted
<p>RCS016</p> 	<p>Apatite A6</p> <p>age = 82.4 ± 15.7 35.5 45.5 Ma (n=11) $(^{207}\text{Pb}/^{206}\text{Pb})_c = 0.8416 \pm 0.0026$ 0.0059 0.0075 MSWD = 1.6, $p(\chi^2) = 0.096$</p> <ul style="list-style-type: none"> - Small sample size - Most of the data clusters over the common Pb intercept - Good precision on common Pb estimate - One aliquot appears to control the slope of the discordia line - Good isochron with minor over-dispersion - Age deemed unreliable 	<p>RCS017</p> 	<p>Apatite All Ig-AIt A3</p> <p>age = 59.92 ± 2.34 4.77 6.30 Ma (n=35) $(^{207}\text{Pb}/^{206}\text{Pb})_c = 0.8440 \pm 0.0021$ 0.0044 0.0058 MSWD = 1.7, $p(\chi^2) = 0.0051$</p> <ul style="list-style-type: none"> - Good sample size - One outlier (from Ig-AIt texture), remaining data from both textures plot along isochron line - Good isochron with minor over-dispersion - Age deemed reliable
<p>RCS017</p> 	<p>Apatite Ig-AIt</p> <p>age = 58.37 ± 2.97 6.12 7.90 Ma (n=27) $(^{207}\text{Pb}/^{206}\text{Pb})_c = 0.8406 \pm 0.0032$ 0.0065 0.0084 MSWD = 1.7, $p(\chi^2) = 0.019$</p> <ul style="list-style-type: none"> - Good sample size - One outlier (rejected), other aliquots plot along discordia line - Moderate spread of data, but no plots close to the lower concordia intercept, therefore increasing the age error - Good precision on common Pb age - Age deemed reliable 	<p>RCS017</p> 	<p>Apatite A3</p> <p>age = 55.22 ± 5.37 13.13 18.08 Ma (n=8) $(^{207}\text{Pb}/^{206}\text{Pb})_c = 0.8459 \pm 0.0030$ 0.0073 0.0100 MSWD = 1.9, $p(\chi^2) = 0.078$</p> <ul style="list-style-type: none"> - Small sample size - No outliers, data plots along isochron line - Good isochron with minor over-dispersion - Large age uncertainty (18.08 Ma) - Age deemed unreliable
<p>RCS017</p> 	<p>Epidote All A3 V2</p> <p>age = 65.56 ± 4.32 8.81 12.88 Ma (n=32) $(^{207}\text{Pb}/^{206}\text{Pb})_c = 0.8457 \pm 0.0012$ 0.0024 0.0035 MSWD = 2.1, $p(\chi^2) = 0.00029$</p> <ul style="list-style-type: none"> - Good sample size - A3 and V2 aliquots plot along the isochron with little overdispersion - V2 appear more widely spread, A3 cluster close to the common Pb intercept - Precise common Pb estimate - Age deemed reliable, but 12.88 Ma age uncertainty noted 	<p>RCS017</p> 	<p>Epidote V2</p> <p>age = 67.29 ± 4.55 9.36 13.26 Ma (n=28) $(^{207}\text{Pb}/^{206}\text{Pb})_c = 0.8469 \pm 0.0013$ 0.0026 0.0037 MSWD = 2, $p(\chi^2) = 0.0017$</p> <ul style="list-style-type: none"> - Good sample size - No outliers - Moderate spread of data, but no plots close to the lower concordia intercept, therefore increasing the age error (13.26 Ma) - Very good precision on common Pb age - Age deemed reliable, but age uncertainty noted



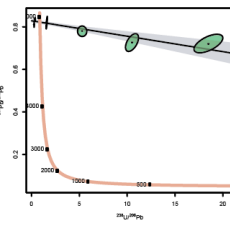
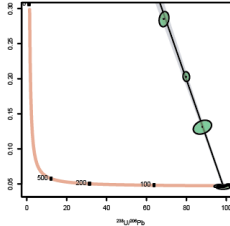
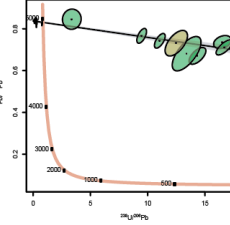
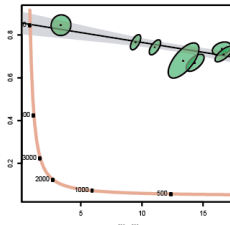
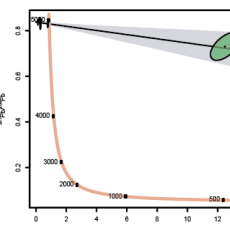
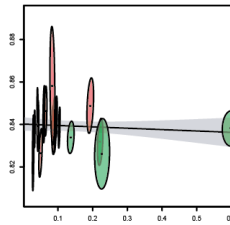
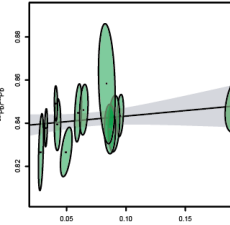
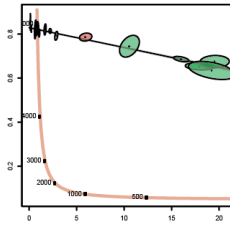
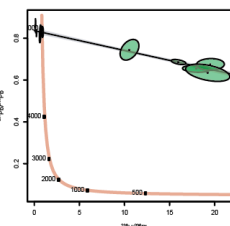
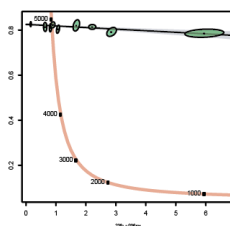


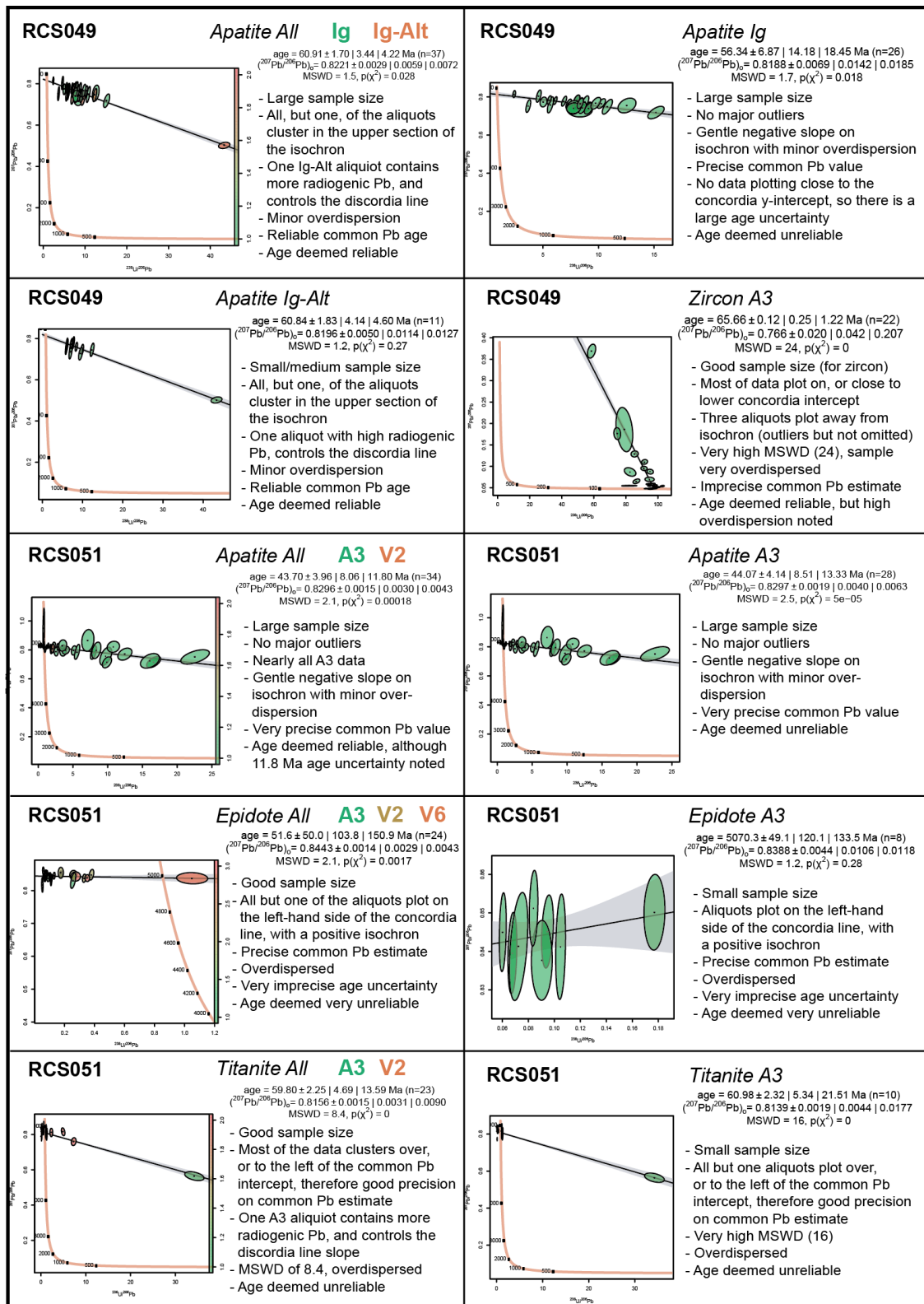


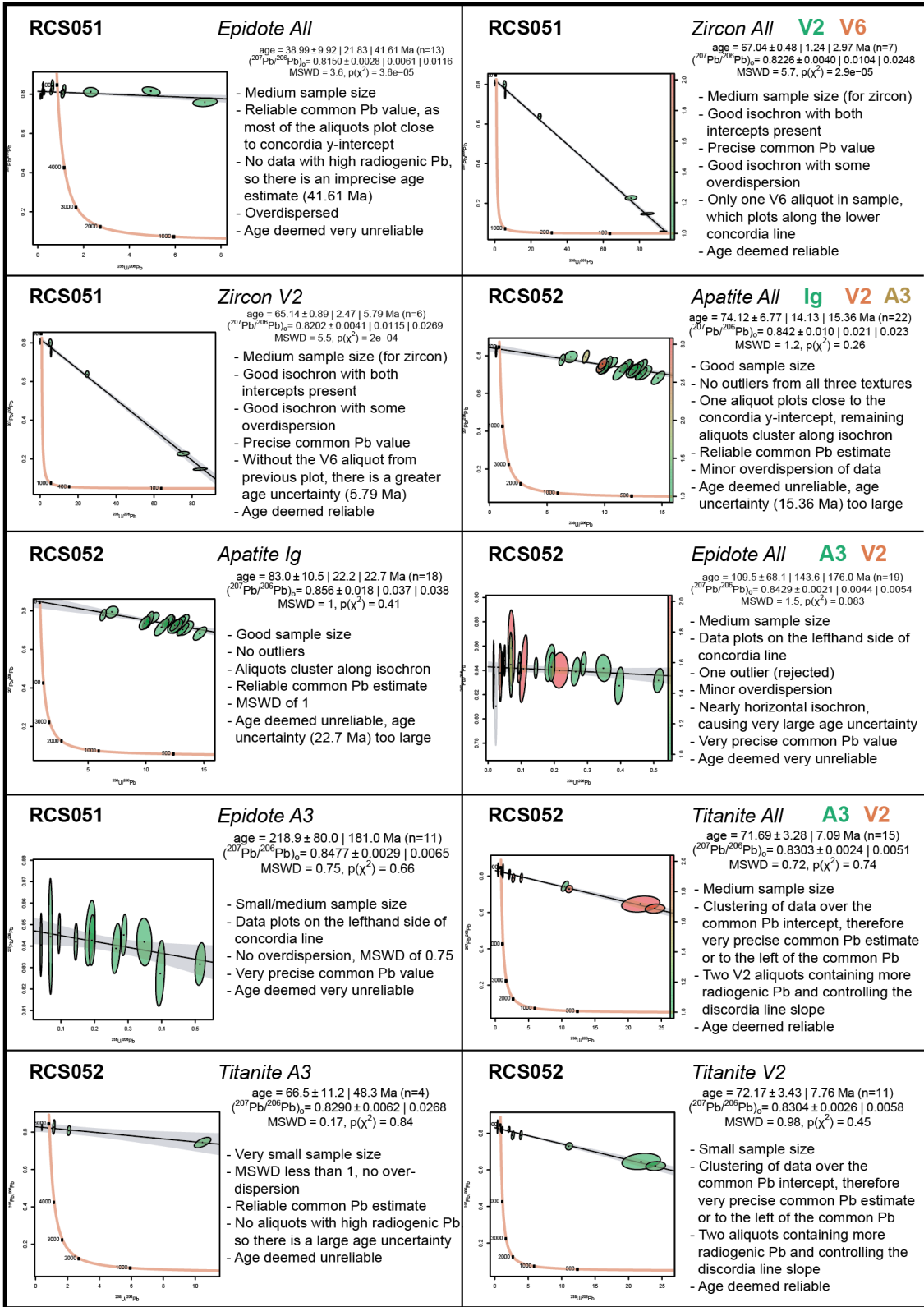


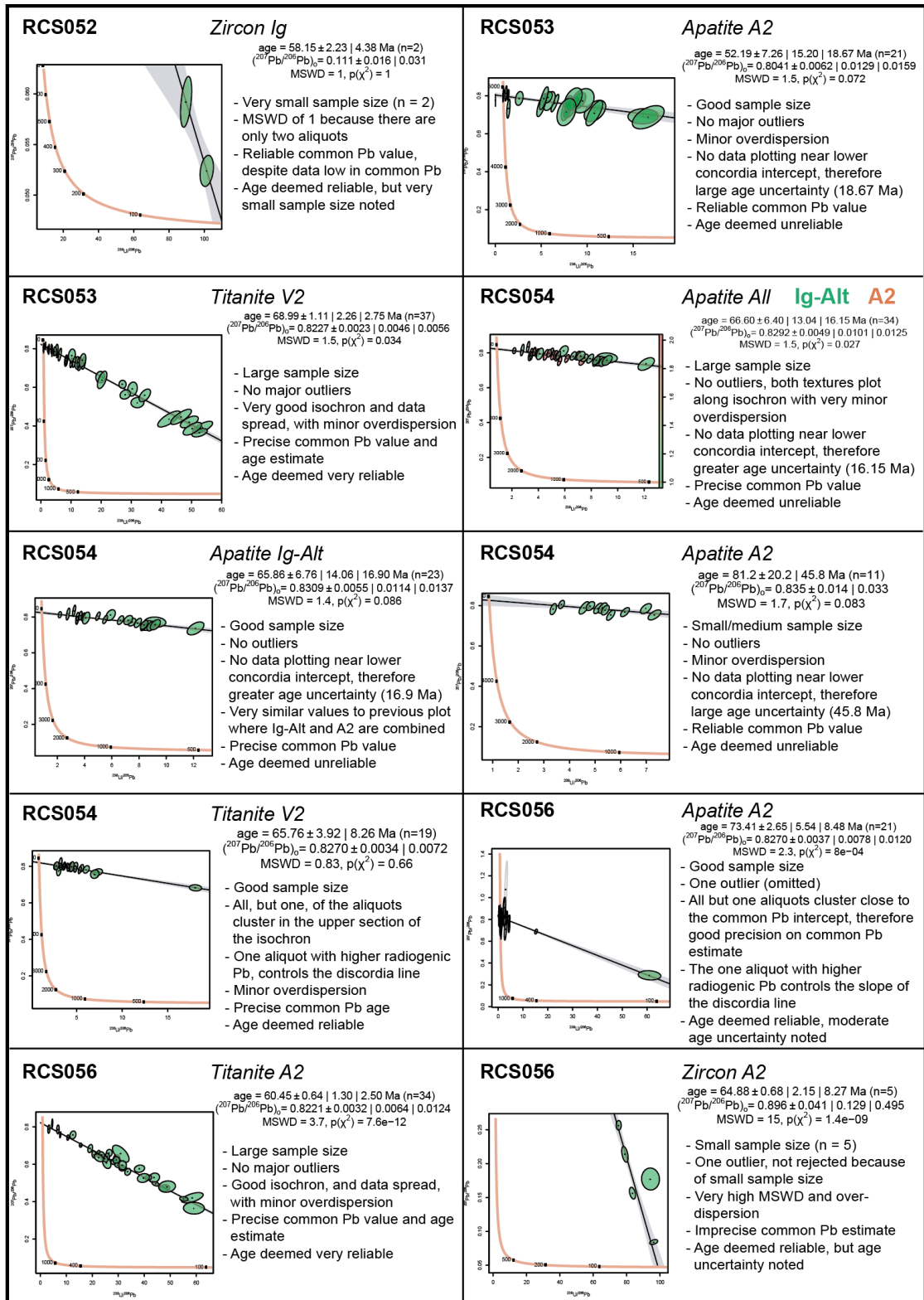


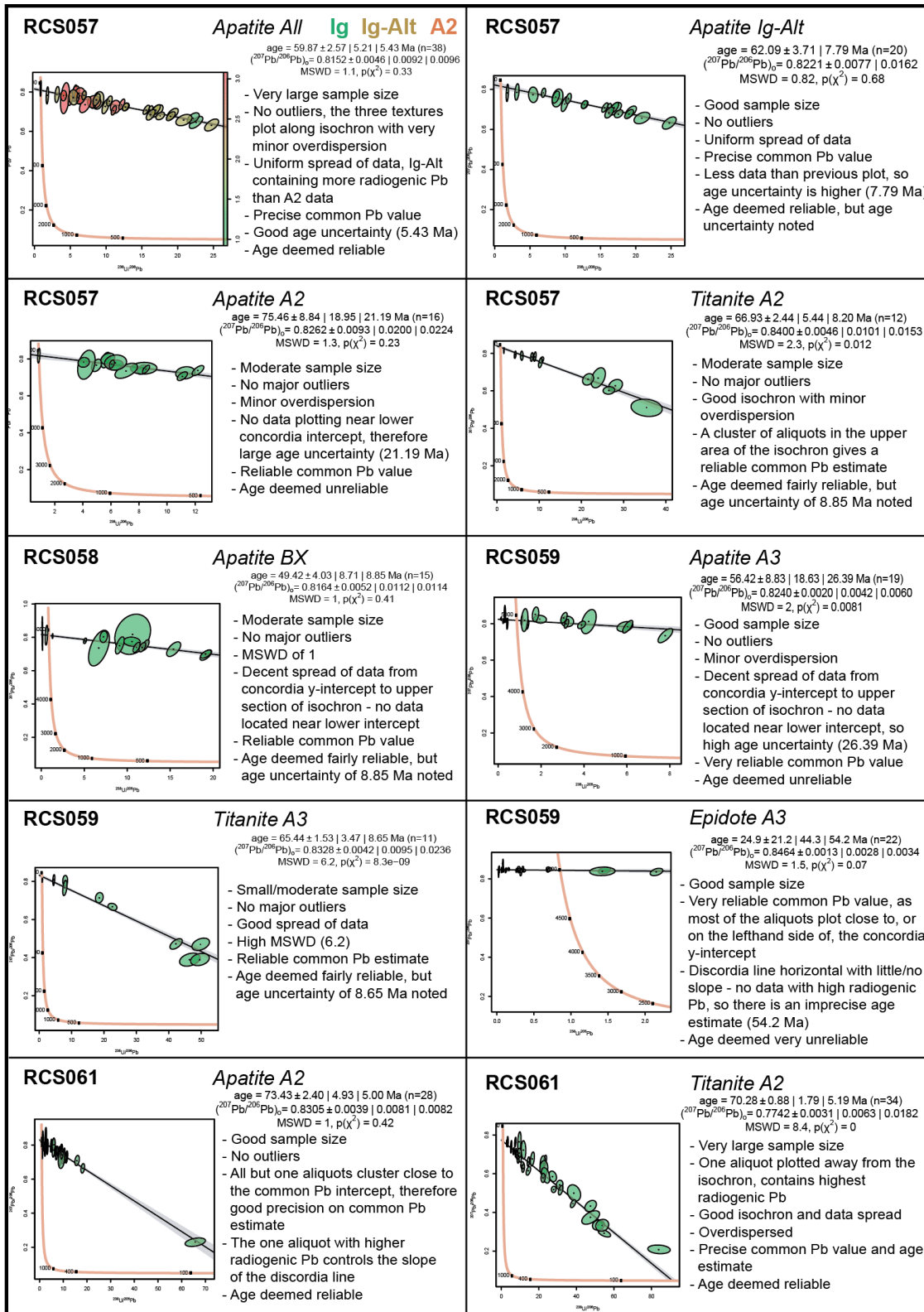
Appendix C1

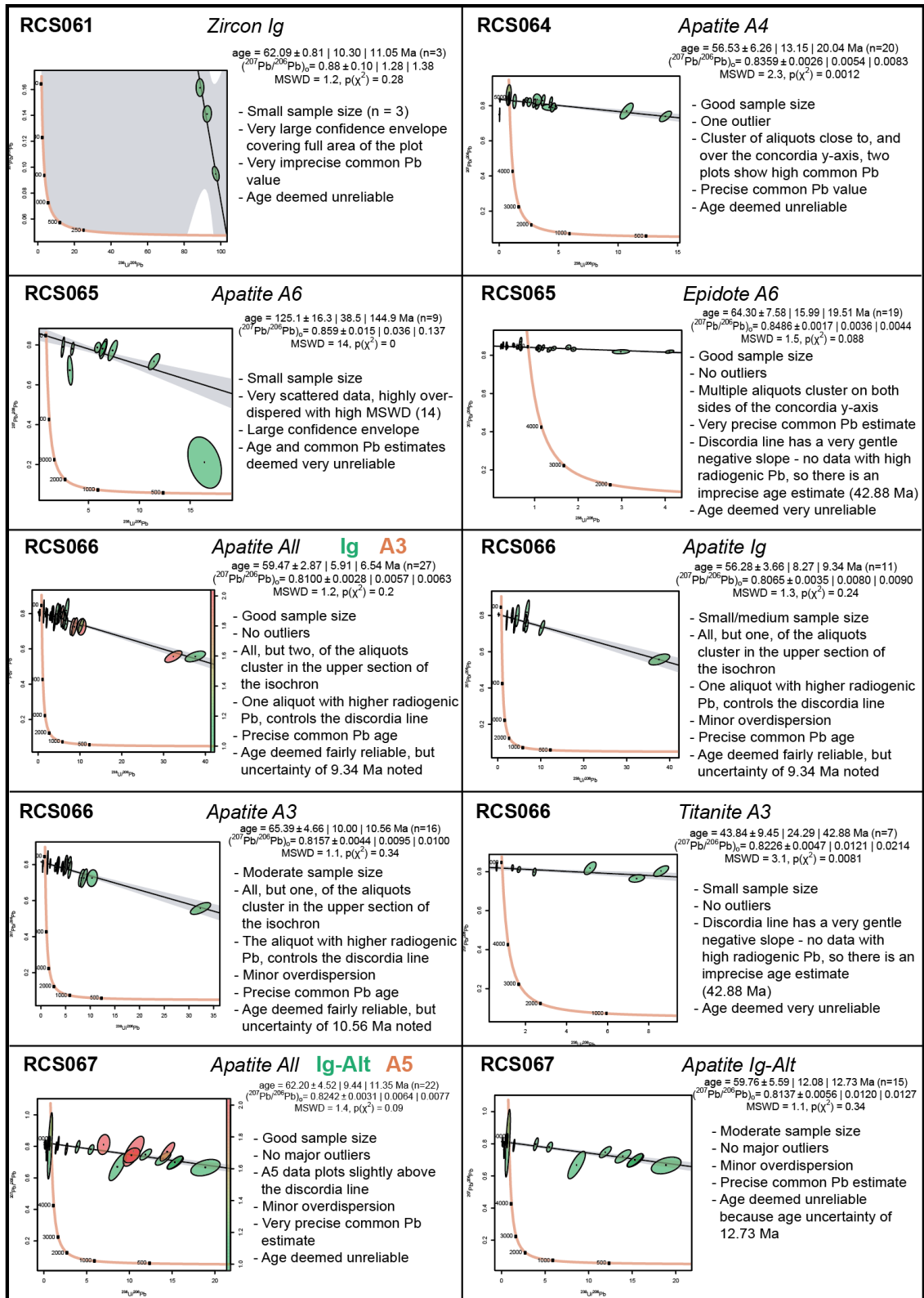
<p>RCS046</p> <p>Apatite A3</p> <p>age = 59.63 ± 7.27 20.20 44.40 Ma (n=6) $(^{207}\text{Pb}/^{206}\text{Pb})_c = 0.8287 \pm 0.0029$ 0.0082 0.0179 MSWD = 4.8, $p(\chi^2) = 0.00068$</p>  <ul style="list-style-type: none"> - Small sample size (n = 6) - Overdispersed - Reliable common Pb value, as two aliquots plot over the y-intercept - No data with high radiogenic Pb, so there is an imprecise age estimate - Age deemed very unreliable 	<p>RCS046</p> <p>Zircon Ig</p> <p>age = 85.17 ± 0.17 0.41 1.15 Ma (n=9) $(^{207}\text{Pb}/^{206}\text{Pb})_c = 0.857 \pm 0.024$ 0.056 0.158 MSWD = 7.9, $p(\chi^2) = 1.5e-09$</p>  <ul style="list-style-type: none"> - Good sample size (for zircon) - MSWD 7.9, sample overdispersed - Six aliquots plot on the lower concordia intercept, therefore there is a good age estimate (1.15 Ma) - Imprecise common Pb estimate - Age deemed reliable
<p>RCS047</p> <p>Apatite All Ig-Alt V2 A3</p> <p>age = 63.68 ± 4.07 8.87 12.33 Ma (n=14) $(^{207}\text{Pb}/^{206}\text{Pb})_c = 0.8372 \pm 0.0023$ 0.0049 0.0068 MSWD = 1.9, $p(\chi^2) = 0.026$</p>  <ul style="list-style-type: none"> - Medium sample size - Reliable common Pb estimate, A3 and V2 aliquots plot on, or to the left of concordia line - Minor overdispersion - No data plotting close to lower concordia intercept - Moderate age uncertainty - Age deemed reliable, but age uncertainty noted 	<p>RCS047</p> <p>Apatite Ig-Alt</p> <p>age = 73.0 ± 10.5 27.1 50.8 Ma (n=7) $(^{207}\text{Pb}/^{206}\text{Pb})_c = 0.858 \pm 0.021$ 0.053 0.100 MSWD = 3.5, $p(\chi^2) = 0.0035$</p>  <ul style="list-style-type: none"> - Small sample size - Unreliable common Pb estimate, no aliquots near the concordia y-intercept - Data overdispersed - No data plotting close to lower concordia intercept - Large age uncertainty (50.8 Ma) - Age deemed unreliable
<p>RCS047</p> <p>Apatite A3</p> <p>age = 74.2 ± 17.4 48.4 49.5 Ma (n=6) $(^{207}\text{Pb}/^{206}\text{Pb})_c = 0.8375 \pm 0.0026$ 0.0071 0.0073 MSWD = 1, $p(\chi^2) = 0.38$</p>  <ul style="list-style-type: none"> - Small sample size - Most of the data clusters over, or to the left of the common Pb intercept - Very good precision on common Pb estimate - MSWD of 1, all but one sample cluster. One sample controlling the slope of isochron - Age deemed very unreliable 	<p>RCS047</p> <p>Epidote A3 V2</p> <p>age = 52.5 ± 54.0 115.2 181.7 Ma (n=17) $(^{207}\text{Pb}/^{206}\text{Pb})_c = 0.8402 \pm 0.0015$ 0.0031 0.0050 MSWD = 2.5, $p(\chi^2) = 0.0011$</p>  <ul style="list-style-type: none"> - Medium sample size - Lots of data scatter away from isochron, large confidence envelope around isochron - Majority of data V2 texture - One aliquot with minor radiogenic Pb controlling isochron - Very imprecise age estimate - Precise common Pb estimate - Age deemed very unreliable
<p>RCS047</p> <p>Epidote V2</p> <p>age = 5058.1 ± 41.5 92.5 141.7 Ma (n=12) $(^{207}\text{Pb}/^{206}\text{Pb})_c = 0.8382 \pm 0.0027$ 0.0061 0.0093 MSWD = 2.3, $p(\chi^2) = 0.0091$</p>  <ul style="list-style-type: none"> - Medium sample size - Lots of data scatter away from isochron, large confidence envelope around isochron - Positive slope on isochron - Very imprecise age estimate - Precise common Pb estimate - Age deemed very unreliable 	<p>RCS047</p> <p>Titanite A3 V2</p> <p>age = 73.75 ± 1.90 4.02 5.24 Ma (n=19) $(^{207}\text{Pb}/^{206}\text{Pb})_c = 0.8286 \pm 0.0019$ 0.0040 0.0052 MSWD = 1.7, $p(\chi^2) = 0.035$</p>  <ul style="list-style-type: none"> - Good sample size - No outliers, A3 and V2 plot along isochron, A3 is more spread - Good isochron with minor overdispersion - Cluster of data over concordia y-intercept, giving a good precision on common Pb estimate - Age deemed reliable
<p>RCS047</p> <p>Titanite A3</p> <p>age = 76.95 ± 2.62 6.19 8.71 Ma (n=9) $(^{207}\text{Pb}/^{206}\text{Pb})_c = 0.8360 \pm 0.0051$ 0.0122 0.0171 MSWD = 2, $p(\chi^2) = 0.054$</p>  <ul style="list-style-type: none"> - Small/moderate sample size - No outliers - Moderate spread of data, but no plots close to the lower concordia intercept, therefore increasing the age error - Cluster of data over concordia y-intercept, there is good precision on common Pb estimate - Age deemed reliable 	<p>RCS047</p> <p>Titanite V2</p> <p>age = 58.1 ± 10.5 24.3 27.9 Ma (n=10) $(^{207}\text{Pb}/^{206}\text{Pb})_c = 0.8254 \pm 0.0025$ 0.0057 0.0065 MSWD = 1.3, $p(\chi^2) = 0.23$</p>  <ul style="list-style-type: none"> - Moderate sample size - No outliers - Moderate spread of data, but no plots close to the lower concordia intercept, therefore increasing the age error (27.9 Ma) - Good spread of data, with reliable common Pb estimate - Age deemed unreliable

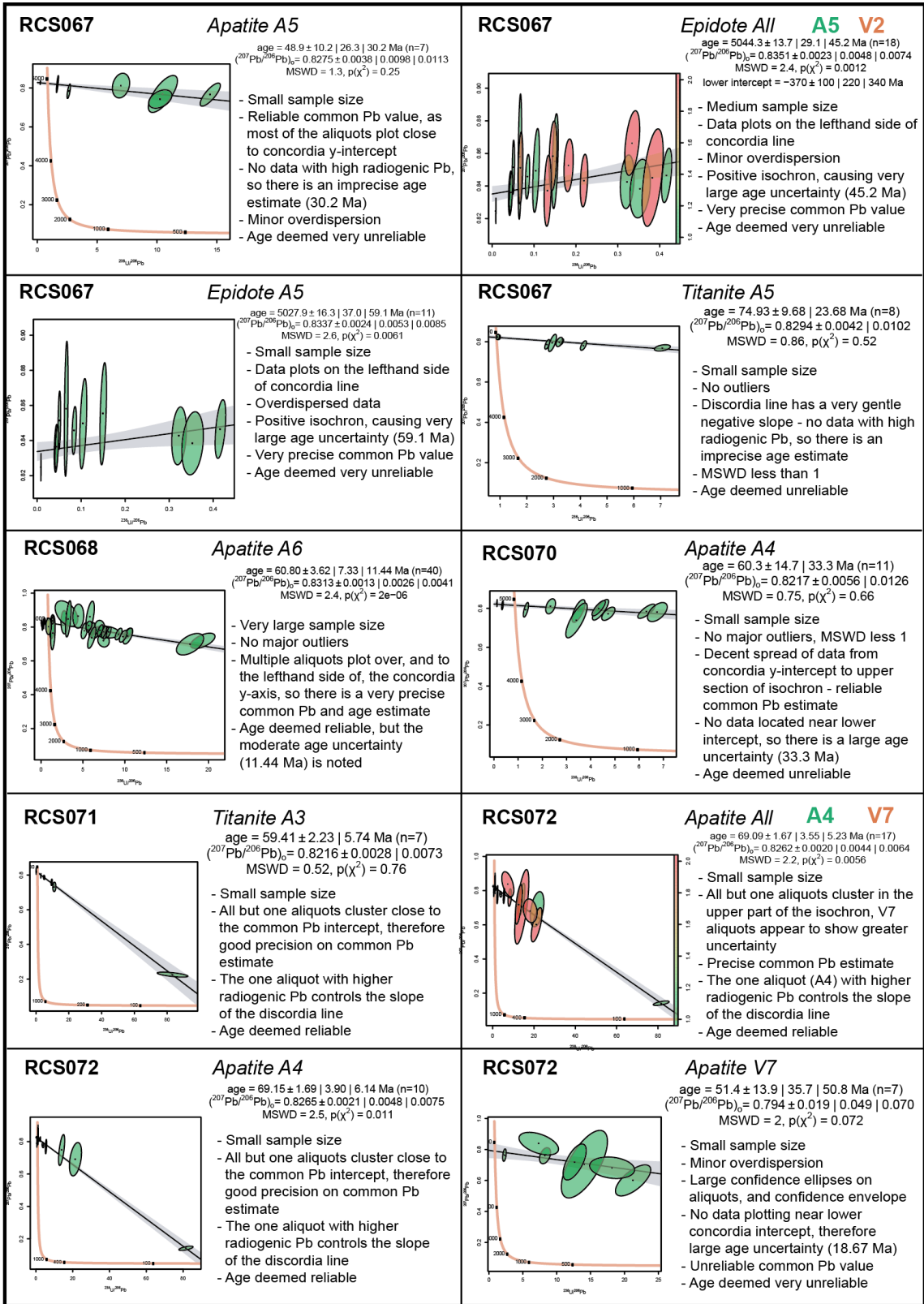


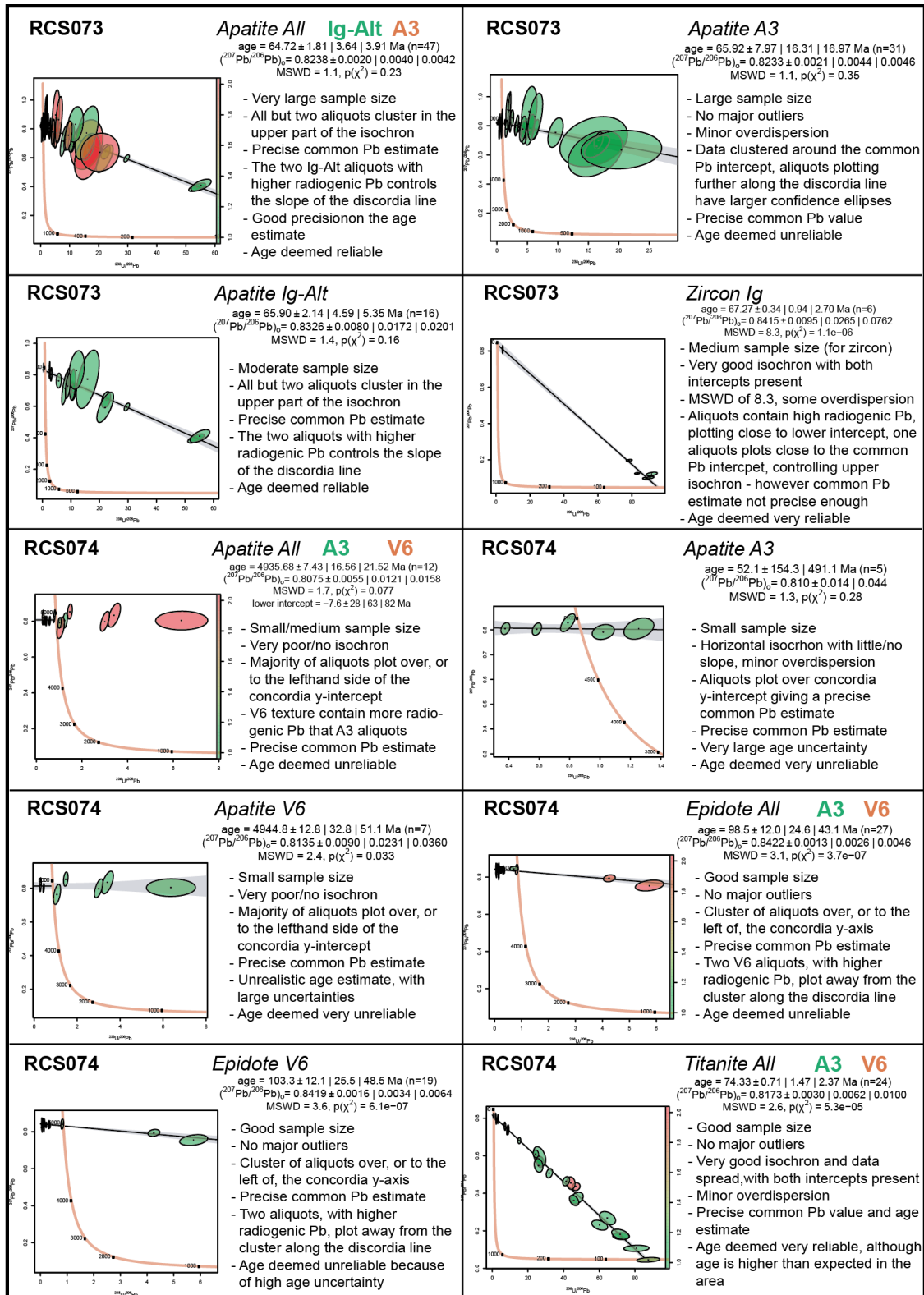


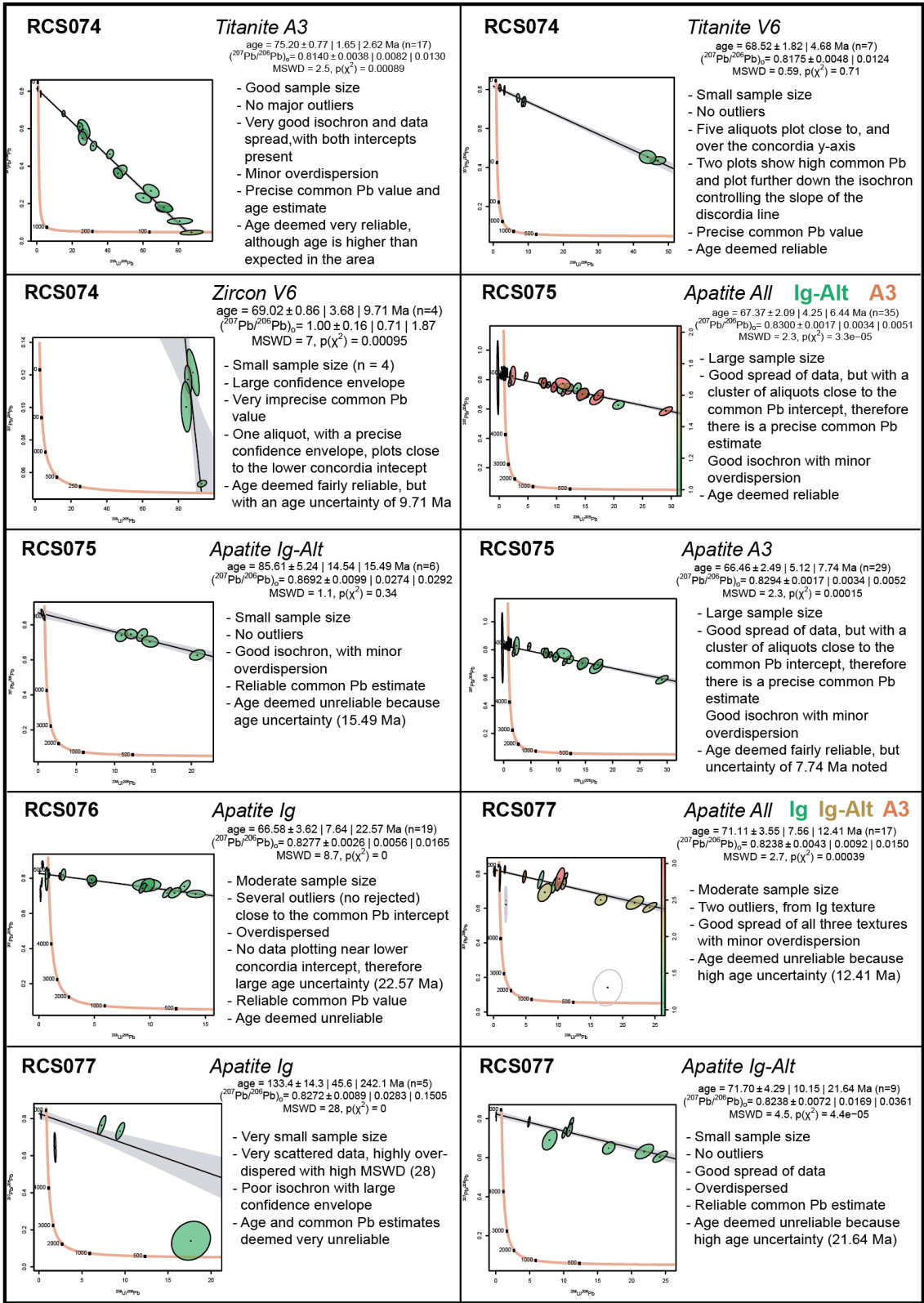


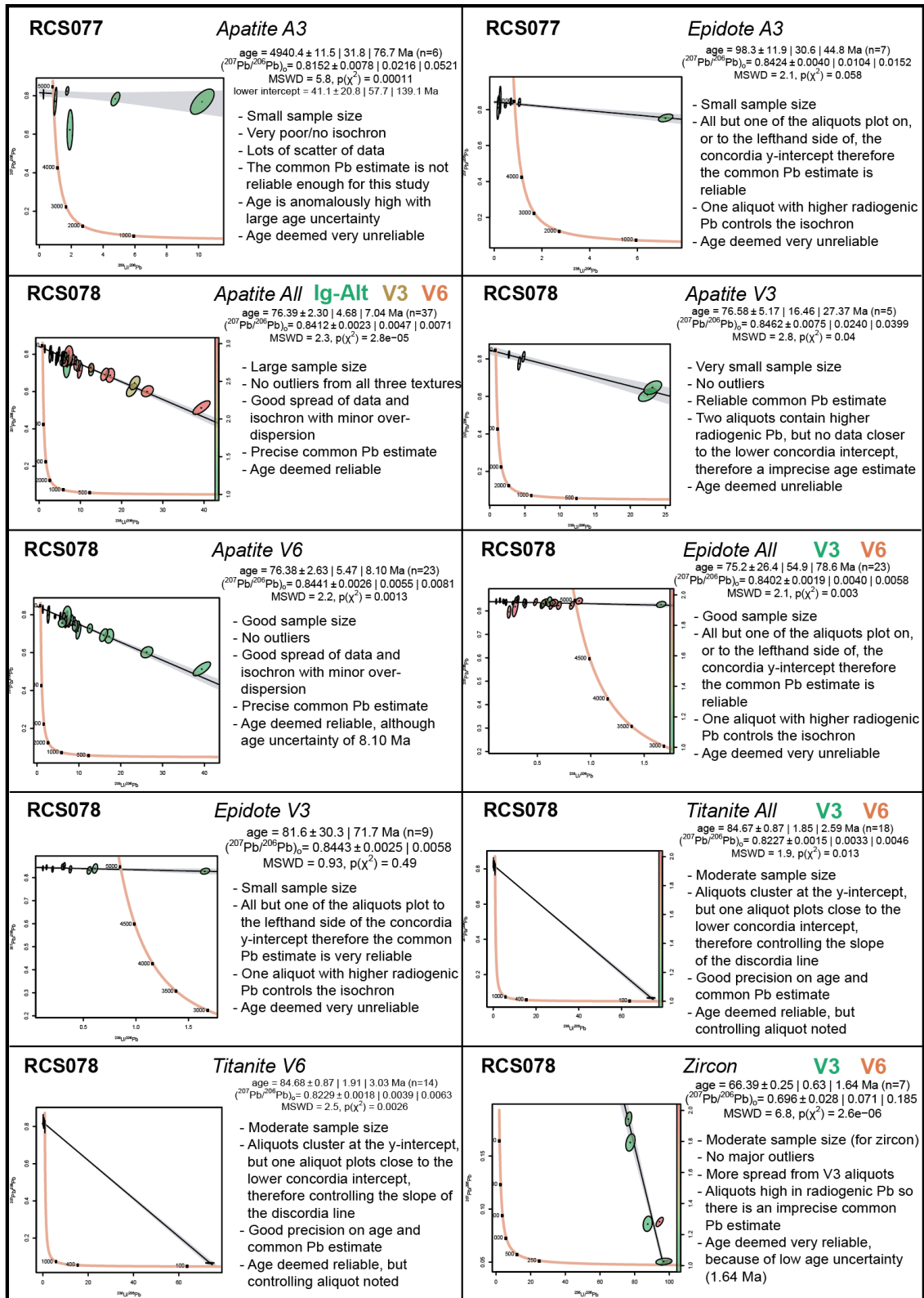


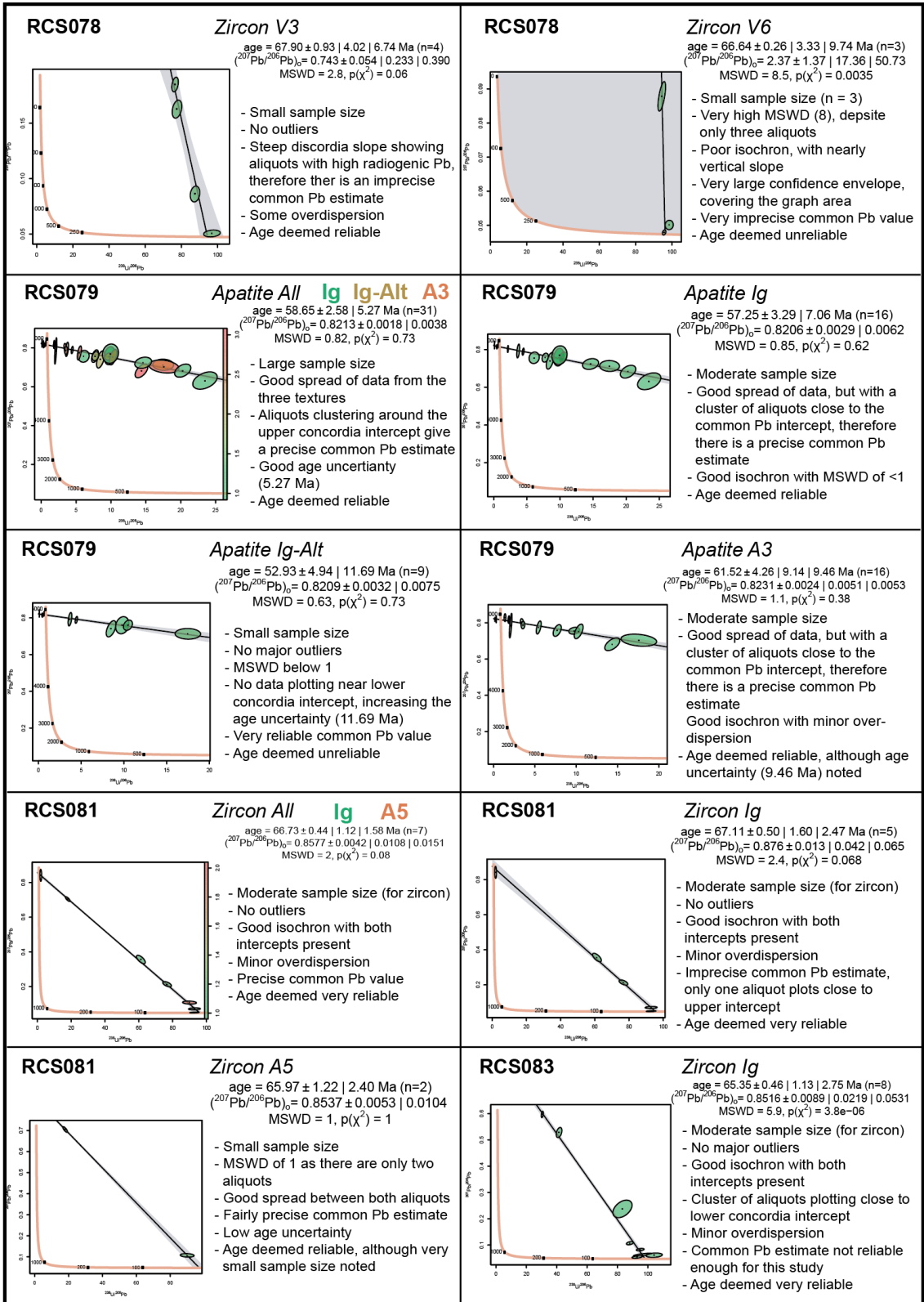


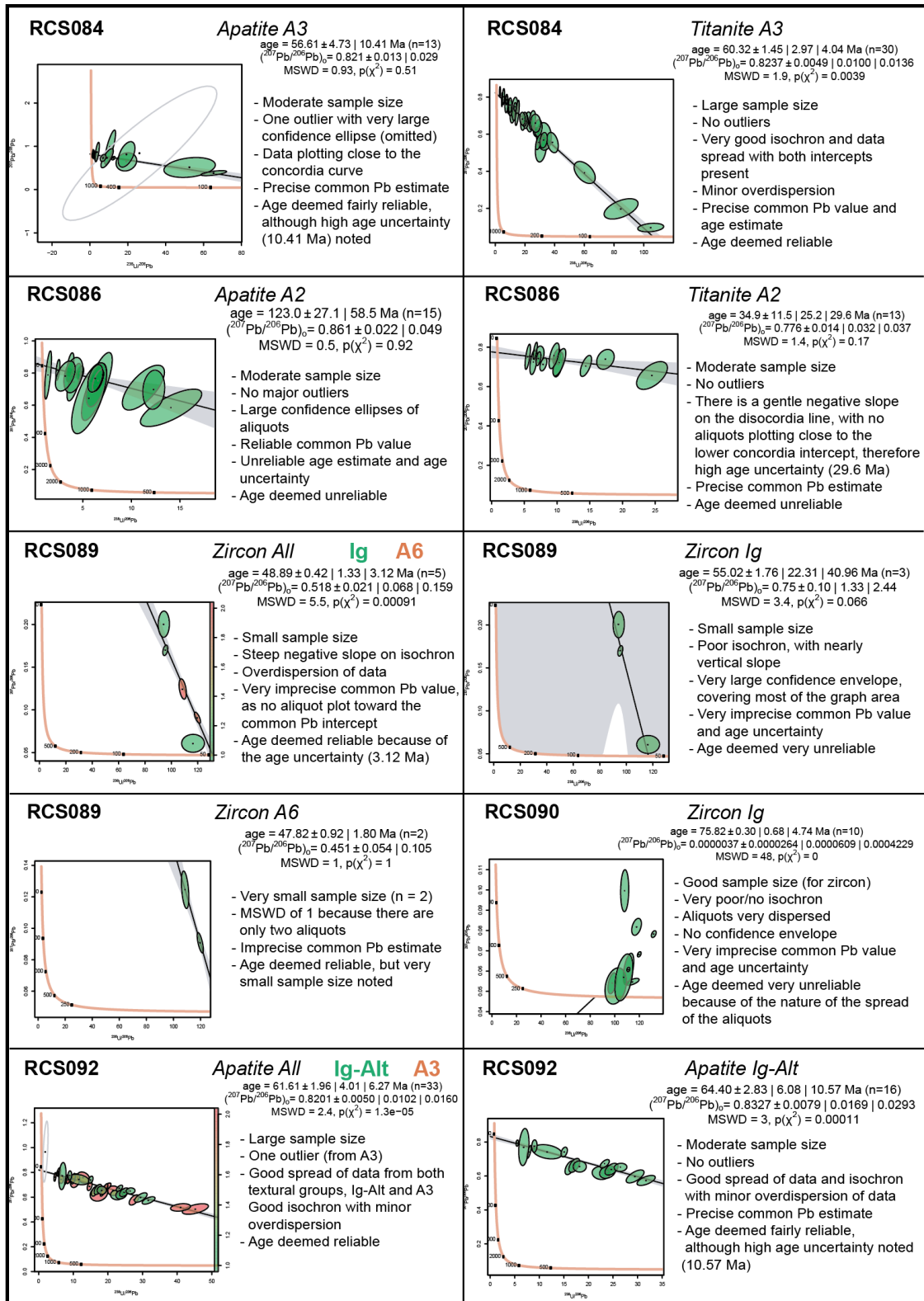


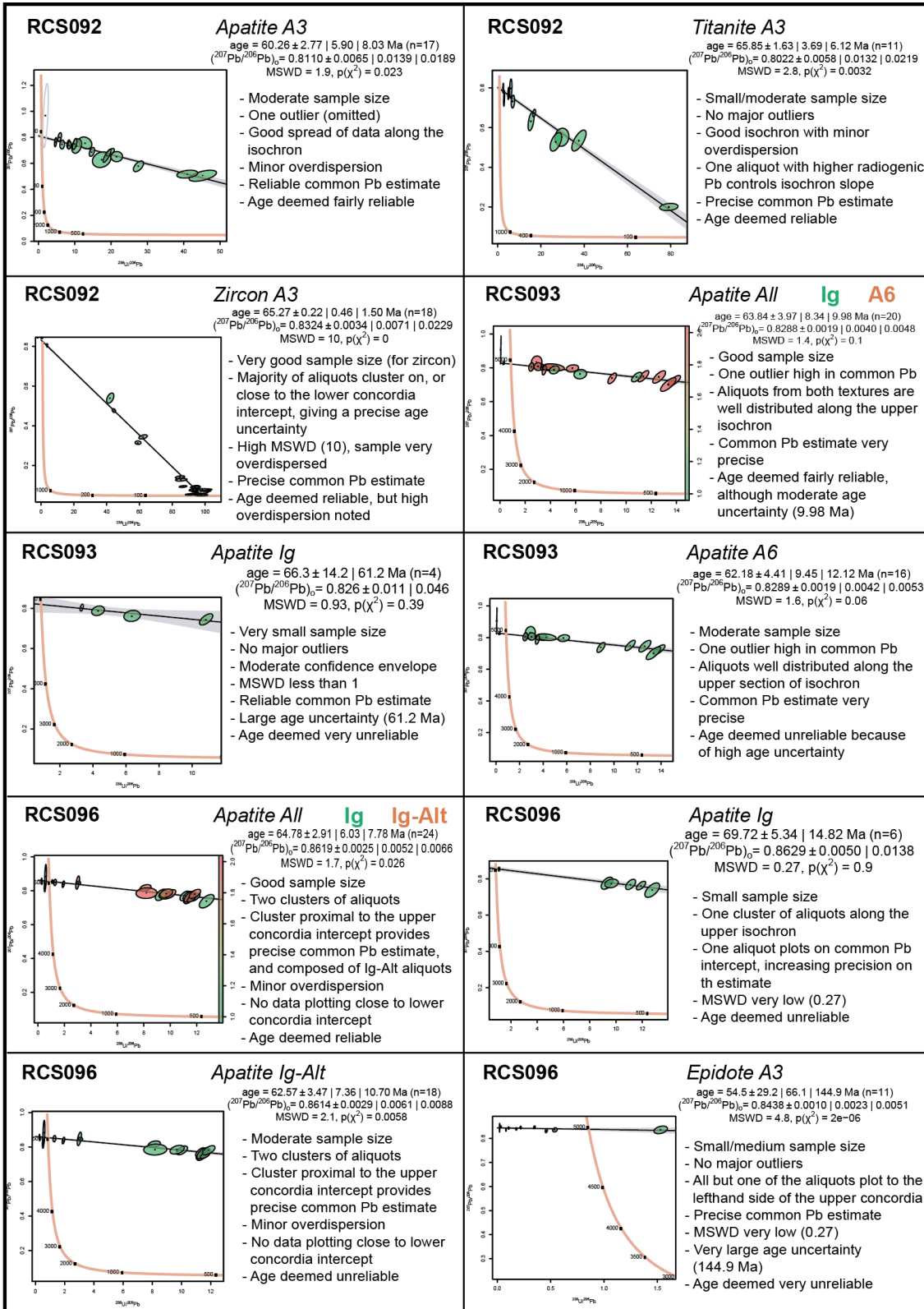


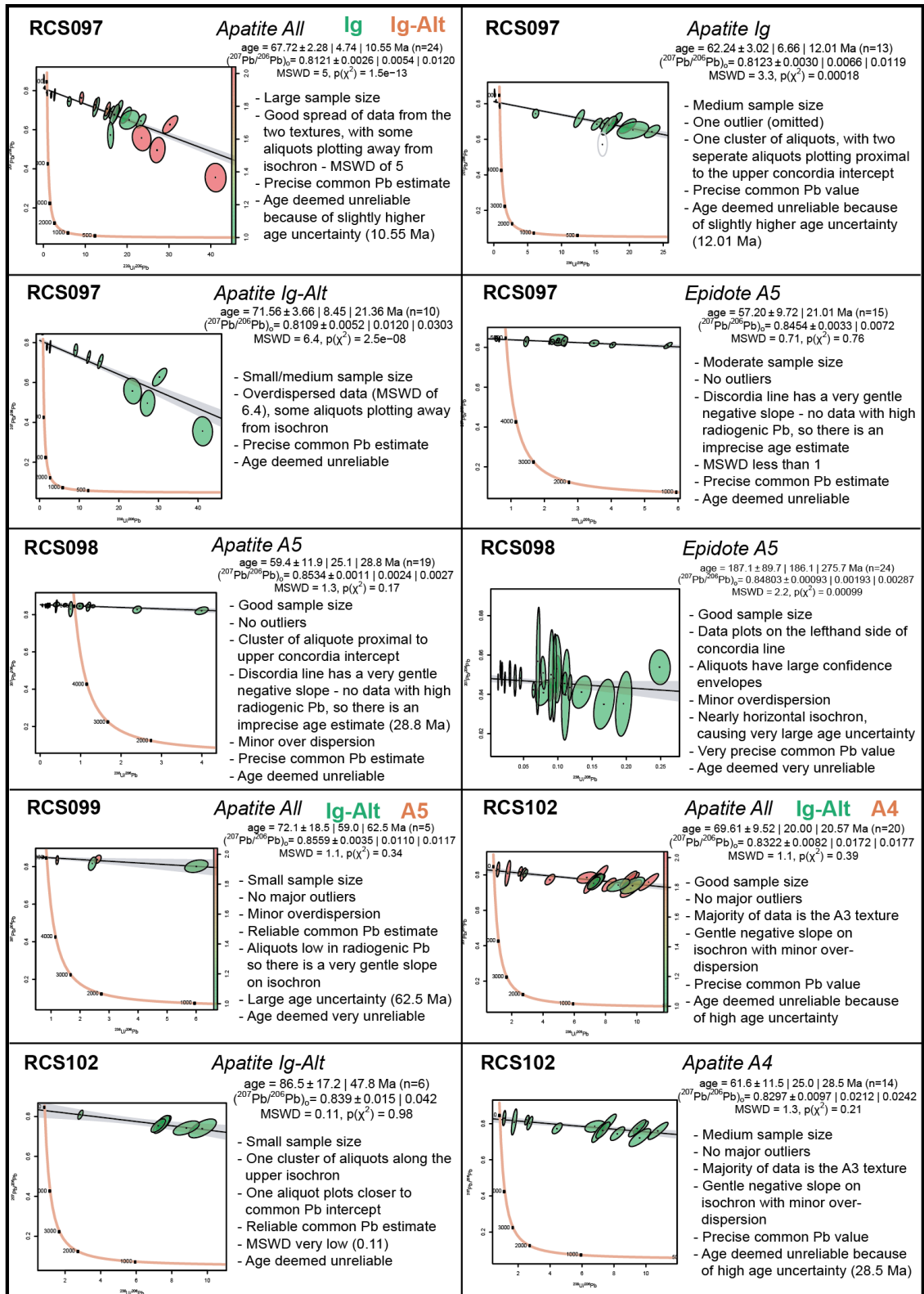


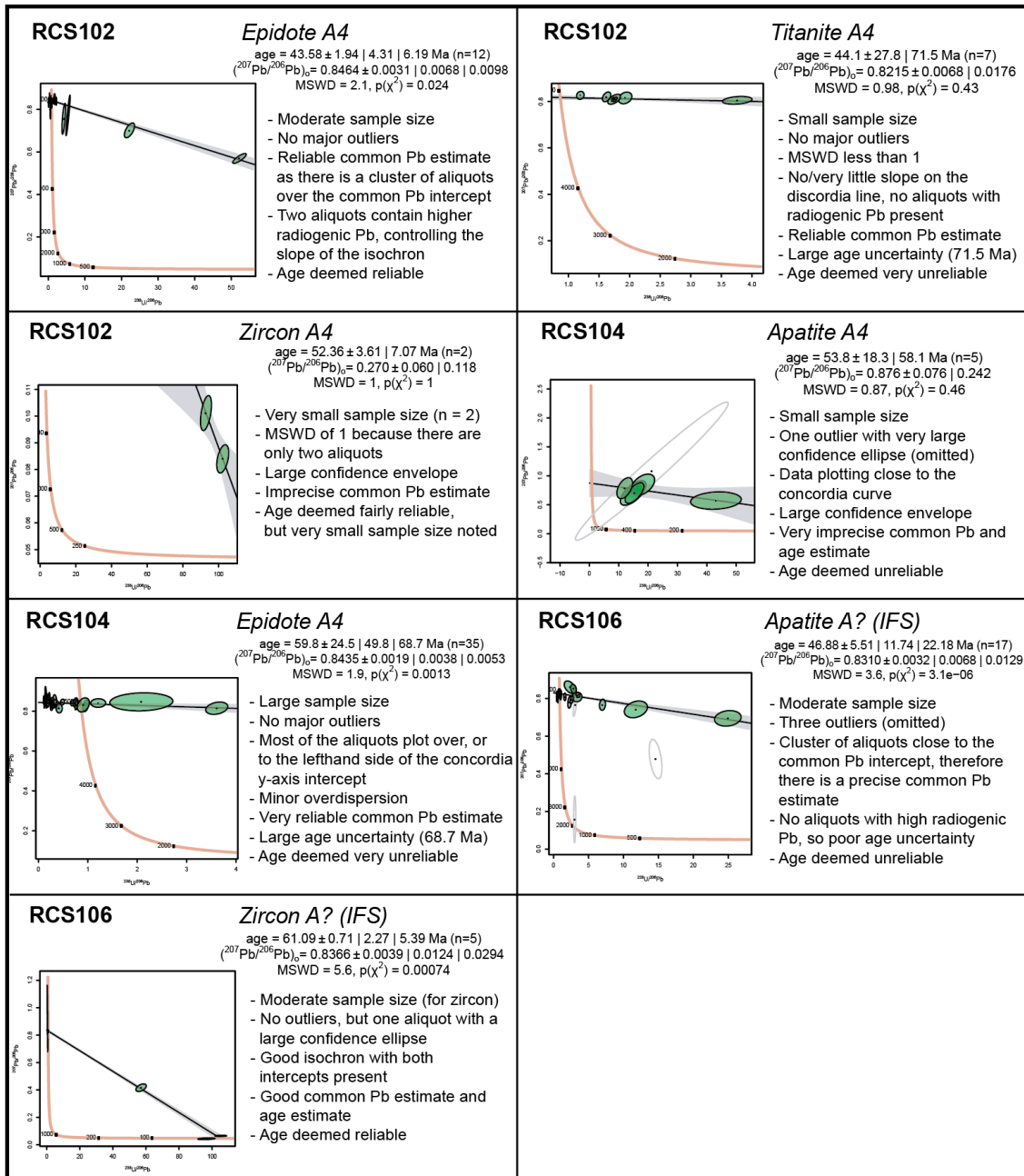












Appendix C1

Sample	Mineral	Alt	Points	Raw Age and Error						Common Pb Intercept			Anchored Age and Error					
				Age (Ma)	±	2nd Err	3rd Err	Uncertainty	MSWD	Pb0	CI for Pb0	± CI for Pb0	Age (Ma)	±	2nd Err	3rd Err	Uncertainty	MSWD
RCS001	Ap	A4	3	\	\	\	\	\	\	\	\	\	\	\	\	\	\	
RCS001	Ap	Ig	6	35.4	29.5	82		2.32	0.79	0.8242	0.0202		59.2	20.9	53.7		0.91	0.9
RCS001	Ap	All	3	41.9	26.4	62.5		1.49	0.65	0.828	0.0132		57.2	18.4	42.5		0.74	0.65
RCS001	Ttn	A4	14	\	\	\	\	\	\	\	\	\	\	\	\	\	\	\
RCS001	Ep	A4	19	4995.1	23.1	48.8	62.2	0.01	1.6	0.8437	0.0046	0.0059	11.8	11.8	24.7		2.09	1.5
RCS003	Ttn	A4	32	126.1	72.6		235.8	1.87	2.5	0.8348	0.0063	0.0101	4984.31	5	10.19	17.32	0.00	2.9
RCS003	Ep	A4	9	240.4	66.9	158.1	334.1	1.39	4.5	0.85	0.0069	0.0146	79.7	57.5	136	291.1	3.65	4.6
RCS003	Zrn	A4	5	57.41	0.31		2.91	0.05	8.8	1.787	0.286	0.851	54.07	0.28	0.77	8.57	0.16	120
RCS003	Zrn	Ig	1	\	\	\	\	\	\	\	\	\	\	\	\	\	\	\
RCS003	Zrn	All	6	57.32	0.3	0.84	2.15	0.04	6.6	1.788	0.25	0.644	54.15	0.27	0.7	6.95	0.13	100
RCS006	Ap	A3	9	68.08	5.41	12.79		0.19	0.73	0.8673	0.0125		37.34	3.04	7	17.74	0.48	6.4
RCS006	Ap	Ig	2	\	\	\	\	\	\	\	\	\	\	\	\	\	\	\
RCS006	Ap	All	11	65.34	5.07	11.47		0.18	0.86	0.8638	0.0106		37.09	3.03	6.75	15.8	0.43	55
RCS006	Ep	A3	6	\	\	\	\	\	\	\	\	\	361	167	429	1912	5.30	20
RCS007	Ttn	A4	19	\	\	\	\	\	\	\	\	\	4992	12	25	50.4	0.01	4
RCS007	Ep	A4	19	4996.62	7.01	14.8	27.34	0.01	3.4	0.8408	0.0031	0.0058	4997.07	7.02	14.75	26.93	0.01	3.3
RCS008	Ap	V3	3	\	\	\	\	\	\	\	\	\	\	\	\	\	\	\
RCS008	Ttn	A5	6	25.1	84.1	233.6	251.3	10.01	1.2	0.8263	0.0176	0.0189	4964.27	7.15	18.38		0.00	0.95
RCS008	Ttn	V3	2	\	\	\	\	\	\	\	\	\	\	\	\	\	\	\
RCS008	Ttn	All	8	8.5	39.65	97.02		11.41	0.91	0.8239	0.0086		4962.76	6.68	15.79		0.00	0.77
RCS008	Ep	A5	15	5040.9	25.3	54.3	71.6	0.01	1.7	0.8283	0.0065	0.0086	356.5	76.2	163.5	294	0.82	3.2
RCS008	Ep	V3	13	81.4	39.7	87.5	157.1	1.93	3.2	0.8417	0.0039	0.007	96.3	33	72	124.5	1.29	3
RCS008	Ep	All	15	39.1	38.5	79.2	132.8	3.40	2.8	0.8377	0.0026	0.0043	136.2	30.3	62.2	114.1	0.84	3.4
RCS008	Zrn	V3	5	61.74	0.95	3.02	10.01	0.16	11	0.988	0.104	0.347	58.04	0.63	1.76	6.83	0.12	15
RCS009	Ap	A4	12	61.5	13.4	30	40.7	0.66	1.8	0.832	0.0075	0.0102	62.5	12.2	26.8		0.43	0.83
RCS009	Ap	Ig-Alt	20	35.5	12.4	26		0.73	0.99	0.818	0.0096		61.66	9.1	19.04		0.31	1.5
RCS009	Ap	All	32	52.32	8.83	18.03	21.39	0.41	1.4	0.8271	0.0057	0.0068	61.97	7.28	14.86	18.11	0.29	1.5

Sample	Mineral	Alt	Points	Raw Age and Error						Common Pb Intercept			Anchored Age and Error						
RCS009	Ttn	A4	16	4965.5	11.8	25.3	39.1	0.01	2.4	0.8238	0.0061	0.0095	23.6	33.2	7.8	106.8	4.53	2.3	
RCS009	Ep	A4	22	28.4	48.5	101.1	186.6	6.57	3.4	0.8525	0.0035	0.0064	5066.7	16.9	35.1	70.7	0.01	4.1	
RCS010	Ap	Ig?	4	75.27	1.08	4.66	10.19	0.14	4.8	0.8553	0.0102	0.0223	74.25	1.09	3.46	20.15	0.27	34	
RCS014	Ttn	A6	13	62.42	3.85	8.48	14.61	0.23	3	0.8325	0.004	0.0068	47.59	2.56	5.59	12.39	0.26	4.9	
RCS014	Ep	A6	15	149.7	21.9	47.2	50.4	0.34	1.1	0.8516	0.0012	0.0029	35.4	14.7	31.6	67.2	1.90	4.5	
RCS014	Zrn	Ig	2	69.23	1.19	2.33		0.03	1	0.854	0.033		69.07	1.17	14.83		0.21	0.46	
RCS016	Ap	A6	11	82.4	15.7	35.5	45.5	0.55	1.6	0.8416	0.0059	0.0075	53.6	13.5	30	49.3	0.92	2.7	
RCS017	Ap	A3	8	55.222	5.37	13.13	18.08	0.33	1.9	0.8459	0.0073	0.01	40.29	4.27	10.1	21.4	0.53	4.5	
RCS017	Ap	Ig-Alt	27	58.37	2.97	6.12	7.9	0.14	1.7	0.8406	0.0065	0.0084	52.15	1.7	3.49	4.75	0.09	1.9	
RCS017	Ap	All	35	59.92	2.34	4.77	6.3	0.11	1.7	0.844	0.0044	0.0058	50.52	1.58	3.21	5.11	0.10	2.5	
RCS017	Ep	V2	28	67.29	4.55	9.36	13.26	0.20	9.36	0.8469	0.0026	0.0037	61.71	4.2	8.61	13.03	0.21	2.3	
RCS017	Ep	A3	4	\	\	\	\	\	\	\	\	\	\	\	\	\	\	\	\
RCS017	Ep	All	32	65.56	4.32	8.81	12.88	0.20	2.1	0.8457	0.0024	0.0035	61.28	3.91	7.98	11.95	0.20	2.2	
RCS018	Ttn	A3	5	81.49	6.06	19.3	36.21	0.44	3.5	0.856	0.045	0.085	67.91	1.9	5.27	10.57	0.16	4	
RCS018	Ep	V2	21	74.05	2.49	5.21	9.26	0.13	3.2	0.8427	0.003	0.0053	74.18	2.33	4.86	8.43	0.11	3	
RCS018	Ep	A3	5	69.89	7.14	22.72		0.33	0.49	0.8334	0.0075		79.44	6.7	17.23	32.9	0.41	3.6	
RCS018	Ep	All	27	72.91	2.34	4.82	8.26	0.11	2.9	0.8402	0.0025	0.0042	74.75	2.2	4.53	7.88	0.11	3	
RCS018	Zrn	V2	3	67.8	0.55	7.02		0.10	0.71	0.474	0.47		69.89	0.38	1.65	6.53	0.09	16	
RCS018	Zrn	A3	2	70.07	6.93	13.59		0.19	1	1.71	7.45		66.78	0.88	11.18		0.17	0.22	
RCS018	Zrn	All	5	68.18	0.54	1.72	5.72	0.08	11	0.618	0.173	0.575	69.39	0.35	0.98	3.17	0.05	10	
RCS019	Ap	A2	10(4)	4741.9	12.5	28.8	231.8	0.05	65	0.71	0.0146	0.1172	70.18	1.9	6.04	15.3	0.22		
RCS019	Ap	Ig-Alt	9	48.29	2.04	4.83	37.2	0.77	59	0.7024	0.0193	0.1484	64.71	1.43	3.67	10.02	0.15	7.4	
RCS019	Ap	All	10	60.09	1.52	3.51	4.91	0.08	2	0.7893	0.0142	0.0199	66.69	1.14	2.58	6.76	0.10	6.9	
RCS022	Ap	A2	11	68.3	4.37	9.88	13.65	0.20	1.9	0.865	0.0101	0.014	41.11	2.52	5.61	14.93	0.36	7.1	
RCS022	Ap	Ig-Alt	21	62.85	2.32	4.85	6.81	0.11	2	0.8648	0.0092	0.0129	47.59	1.17	2.44	5.21	0.11	4.6	
RCS022	Ap	All	32	62.73	1.84	3.76	5.23	0.08	1.9	0.8627	0.0059	0.0082	46.44	1.06	2.16	5.03	0.11	5.4	
RCS023	Ep	BX	19	47.7	10.5	22.2	28	0.59	1.6	0.8402	0.0069	0.0088	54.81	6.14	12.9		0.24	1.5	
RCS023	Zrn	BX/Ig?	3	66.83	1.89	24.04		0.36	0.35	0.6	4.72		67.64	0.62	2.66		0.04	0.28	

Sample	Mineral	Alt	Points	Raw Age and Error						Common Pb Intercept			Anchored Age and Error					
RCS025	Ap	A5	20	82.6	11.1	23.4	43	0.52	3.4	0.8295	0.0075	0.0138	89.44	7.9	16.54	29.72	0.33	3.2
RCS025	Zrn	A5	4	74.89	0.58	2.51	9.74	0.13	15	0.887	0.05	0.192	74.22	0.56	1.79	7.09	0.10	16
RCS030	Ap	A5	12	69.7	10.1	22.6	25.5	0.37	1.3	0.85	0.0072	0.0081	24.43	6.13	13.49	26.6	1.09	3.9
RCS030	Ap	Ig	4	77.67	0.86	3.7		0.05	0.95	0.8446	0.0324		77.36	0.84	2.68		0.03	1.5
RCS030	Ap	All	16	77.78	0.84	1.8	1.94	0.02	1.2	0.8517	0.0041	0.0044	76.37	0.83	1.78	5.04	0.07	8.1
RCS030	Ep	A5	9	\	\	\	\	\	\				167	31.7	73.1		0.44	1.8
RCS030	Zrn	A5	4	66.73	0.52	2.24		0.03	0.44	0.893	0.053		65.85	0.48	1.52	3.3	0.05	4.7
RCS031	Ep	V3	18	4974	9.56	20.2	41.48	0.01	4.2	0.8436	0.0047	0.0096	104.7	26.5	56	111.2	1.06	3.9
RCS031	Ep	A4	13	5012.5	13.1	28.8	64.6	0.01	5	0.8388	0.0039	0.0088	6.78	34.77	76.53	175.98	25.96	5.3
RCS031	Ep	All	30	4986.76	7.02	14.38	30.62	0.01	4.5	0.8414	0.0027	0.0058	83.9	23.9	48.8	102.7	1.22	4.4
RCS031	Ap	Ig-Alt	3	77.6	11.1	141.5		1.82	0.54	0.878	0.135		37.82	7.19	30.92	100.41	2.65	11
RCS033	Ap	A4	24	64.18	2.31	4.8	6.51	0.10	1.8	0.8595	0.005	0.0068	47.2	1.8	3.72	9.98	0.21	7.2
RCS033	Ap	Ig	4	78	39.8	171.4		2.20	0.037	0.875	0.306		52.8	3.86	12.27		0.23	0.15
RCS033	Ap	All	28	65.07	2.18	4.48	5.68	0.09	1.6	0.8596	0.005	0.0063	48.2	1.63	3.34	8.33	0.17	6.2
RCS033	Ep	A4	37	69.1	26.3	53.4	91	1.32	2.9	0.8457	0.00109	0.00186	0.026	2.348	4.762	8.971	345.04	3.5
RCS034	Zrn	A7	7	66.87	0.6	1.53	3.11	0.05	4.1	0.8332	0.0162	0.0327	67.19	0.55	1.35	2.62	0.04	3.8
RCS037	Ap	A3	5	75.9	21.1	67.3		0.89	0.61	0.841	0.119		71.27	6.41	17.81		0.25	0.47
RCS037	Ap	Ig	8	95.7	27.6	67.6	78.1	0.82	1.3	0.887	0.15	0.174	69.88	4.47	10.57		0.15	1.3
RCS037	Ap	Ig-Alt	16	58.7	15.7	33.7	37.6	0.64	1.2	0.817	0.0059	0.066	67.05	2.61	5.56		0.08	1.2
RCS037	Ap	All	28	69.2	11.2	23	23.9	0.35	1.1	0.8596	0.005	0.0063	68.15	2.13	4.36		0.06	0.83
RCS038	Ap	Ig	8	81.64	6.19	15.14	17.66	0.22	1.4	0.8339	0.0063	0.0074	80.86	6.01	14.2		0.18	1.2
RCS038	Ep	A4	14	85.8	136.5	287.3	467.1	5.44	2.5	0.8414	0.0064	0.01	150.9	63.8	137.8	209	1.39	2.3
RCS038	Ep	V3	3	\	\	\	\	\	\	\	\	\	\	\	\	\	\	\
RCS038	Ep	All	16	98.1	134.4	288.4	456.7	4.66	2.5	0.8426	0.0062	0.0097	105.3	52.6	111.5	168.9	1.60	2.3
RCS038	Zrn	Ig	5	64.75	0.76	2.42	8.55	0.13	12	0.8347	0.0104	0.0368	64.96	0.76	2.1	6.87	0.11	11
RCS039	Ap	Ig-Alt	13	65.92	4.67	10.27	12.95	0.20	1.6	0.8398	0.0123	0.0155	61.35	3.07	6.7		0.11	1.6
RCS041	Ap	A3	2	\	\	\	\	\	\	\	\	\	\	\	\	\	\	\
RCS041	Ap	Ig	18	88.98	7.49	15.87	27.6	0.31	3	0.8254	0.0124	0.0215	96.13	4.64	9.78	16.75	0.17	2.9

Sample	Mineral	Alt	Points	Raw Age and Error						Common Pb Intercept			Anchored Age and Error					
RCS041	Ap	All	20	84.4	7.28	15.29	26.74	0.32	3.1	8.21	0.0114	0.0199	96.15	4.62	9.66	17.1	0.18	3.1
RCS042	Ap	A4	6	62.64	7.06	19.61	30.65	0.49	2.4	0.8222	0.0118	0.0185	69.46	6.44	16.54	29.3	0.42	3.1
RCS042	Ap	Ig	6	79.55	6.21	17.24	60.08	0.76	12	0.843	0.031	0.107	74.84	4.06	10.44	32.87	0.44	9.9
RCS042	Ap	Ig-Alt	14	64.23	1.36	2.97	3.05	0.05	1.1	0.8236	0.0109	0.0112	65.49	1.16	2.51		0.04	1.2
RCS042	Ap	All	25	64.11	1.23	2.54	3.06	0.05	1.5	0.8247	0.0061	0.0074	65.5	1.11	2.28	2.97	0.05	1.7
RCS044	Ap	A2	15	69.1	1.56	3.36	7.65	0.11	5.2	0.8518	0.0104	0.0237	64.3	1.04	2.24	5.44	0.08	5.9
RCS044	Ap	Ig	4	79.12	3.01	12.95	25.71	0.32	3.9	0.852	0.048	0.096	75.65	2.26	7.2	13.67	0.18	3.6
RCS044	Ap	Ig-Alt	14	61.76	2.05	4.47	6.08	0.10	1.9	0.8256	0.0163	0.0222	63.33	1.16	2.51	3.34	0.05	1.8
RCS044	Ap	All	33	68.28	1.13	2.3	4.68	0.07	4.1	0.8464	0.0078	0.0159	65.1	0.73	1.49	3.14	0.05	4.4
RCS046	Ap	Ig	11	71.99	4.88	11.04		0.15	1.1	0.843	0.026		68.11	2.79	6.23		0.09	1.1
RCS046	Ap	Ig-Alt	8	80.72	4.32	10.58	18.92	0.23	3.2	0.8558	0.0178	0.0319	71.31	3.27	7.73	15.93	0.22	4.3
RCS046	Ap	A3	6	59.63	7.27	20.2	44.4	0.74	4.8	0.8287	0.0082	0.0179	63.24	6.74	17.33	35.6	0.56	4.2
RCS046	Ap	All	25	69.35	2.31	4.79	7.94	0.11	2.7	0.8336	0.0054	0.0089	68.9	2.03	4.18	6.8	0.10	2.6
RCS046	Zrn	A3	9	65.17	0.17	0.41	1.15	0.02	7.9	0.857	0.056	0.158	65.13	0.16	0.38	1	0.02	6.9
RCS047	Ap	A3	6	74.2	17.4	48.4	49.5	0.67	1	0.8375	0.0071	0.0073	61.8	16.3	41.8		0.68	1.6
RCS047	Ap	V2	1	\	\	\	\	\	\	\	\	\	\	\	\	\	\	\
RCS047	Ap	Ig-Alt	7	73	10.5	27.1	50.8	0.70	3.5	0.858	0.053	0.1	60.81	3.94	9.65	17.19	0.28	3.2
RCS047	Ap	All	14	63.68	4.07	8.87	12.33	0.19	1.9	0.8372	0.0049	0.0068	60.81	3.83	8.28	11.99	0.20	2.1
RCS047	Ttn	A3	9	76.95	2.62	6.19	8.71	0.11	2	0.836	0.0122	0.0171	71.97	1.7	3.92	6.2	0.09	2.5
RCS047	Ttn	V2	10	58.1	10.5	24.3	27.9	0.48	1.3	8.254	0.0057	0.0065	52.53	8.04	18.18		0.35	1.2
RCS047	Ttn	All	19	73.75	1.9	4.02	5.24	0.07	1.7	0.8286	0.004	0.0052	71.13	1.66	3.5	5	0.07	2
RCS047	Ep	A3	5	4988.3	9.07	28.87	30.97	0.01	1.2	0.8335	0.0093	0.01	130.6	41.4	115.1	211.9	1.62	3.4
RCS047	Ep	V2	12	5058.1	41.5	92.5	141.7	0.03	2.3	0.8382	0.0061	0.0093	4995.2	25.1	55.2	85.6	0.02	2.4
RCS047	Ep	All	17	52.5	54	115.2	181.7	3.46	2.5	0.8402	0.0031	0.005	120.1	39.8	84.3	134.7	1.12	2.6
RCS049	Ap	Ig	26	56.34	6.87	14.18	18.45	0.33	1.7	0.8188	0.0142	0.0185	68.96	2.45	5.04	6.72	0.10	1.8
RCS049	Ap	Ig-Alt	11	60.84	1.83	4.14	4.6	0.08	1.2	0.8196	0.0114	0.0127	63.73	1.43	3.18		0.05	1.8
RCS049	Ap	All	37	60.91	1.7	3.44	4.22	0.07	1.5	0.8221	0.0059	0.0072	65.06	1.23	2.5	3.38	0.05	1.8
RCS049	Zrn	A3?	22	65.66	0.12	0.25	1.22	0.02	24	0.766	0.042	0.207	65.82	0.11	0.23	1.11	0.02	24

Sample	Mineral	Alt	Points	Raw Age and Error						Common Pb Intercept			Anchored Age and Error					
RCS051	Ap	A3	28	44.07	4.14	8.51	13.33	0.30	2.5	0.8297	0.004	0.0063	47.06	3.62	7.45	11.43	0.24	2.4
RCS051	Ap	V2	6	\	\	\	\	\	\	\	\	\	\	\	\	\	\	\
RCS051	Ap	All	33	43.66	3.96	8.07	11.56	0.26	2.1	0.8295	0.003	0.0042	47.14	3.6	7.33	10.69	0.23	2.1
RCS051	Ttn	A3	10	60.98	2.32	25.34	21.51	0.35	16	0.8139	0.0044	0.0177	62.95	2.27	5.13	21.21	0.34	17
RCS051	Ttn	V2	13	38.99	9.92	21.83	41.61	1.07	3.6	0.815	0.0061	0.0116	55.7	8.13	17.72	35.8	0.64	4.1
RCS051	Ttn	All	23	59.8	2.25	4.69	13.59	0.23	8.4	0.8156	0.0031	0.009	62.43	2.18	4.53	13.78	0.22	9.3
RCS051	Ep	A3	10	5070.3	49.1	120.1	133.5	0.03	1.2	0.8388	0.0106	0.0118	64.7	70	158.4	224.9	3.48	2
RCS051	Ep	V2	9	\	\	\	\	\	\	\	\	\	5005.8	13.2	30.4	55	0.01	3.3
RCS051	Ep	V6	5	\	\	\	\	\	\	\	\	\	\	\	\	\	\	\
RCS051	Ep	All	24	51.6	50	103.8	150.9	2.92	2.1	0.8443	0.0029	0.0043	18.8	35.8	74.1	106.4	5.66	2.1
RCS051	Zrn	V2	6	65.14	0.89	2.47	5.79	0.09	5.5	0.8202	0.0115	0.0269	66.41	0.86	2.2	6.94	0.10	10
RCS051	Zrn	V6	1	\	\	\	\	\	\	\	\	\	\	\	\	\	\	\
RCS051	Zrn	All	7	67.04	0.48	1.24	2.97	0.04	5.7	0.8226	0.004	0.0104	67.41	0.48	1.17	3.43	0.05	8.6
RCS052	Ap	Ig	18	83	10.5	22.2	22.7	0.27	1	0.856	0.037	0.38	68.77	2.43	5.14		0.07	1.1
RCS052	Ap	V2	2	\	\	\	\	\	\	\	\	\	\	\	\	\	\	\
RCS052	Ap	A3	2	\	\	\	\	\	\	\	\	\	\	\	\	\	\	\
RCS052	Ap	All	21(22)	87.03	9.86	20.63	21.46	0.25	1.1	0.864	0.034	0.036	67.91	2.28	4.75		0.07	1.2
RCS052	Ttn	A3	4	66.5	11.2	48.3		0.73	0.17	0.829	0.0268		61.04	9.43	30.03		0.49	0.39
RCS052	Ttn	V2	11	72.17	3.43	7.76		0.11	0.98	0.8304	0.0058		67.76	3.05	6.79		0.10	1.7
RCS052	Ttn	All	15	71.69	3.28	7.09		0.10	0.72	0.8303	0.0051		67.13	2.9	6.22		0.09	1.3
RCS052	Ep	A3	11	218.9	80	181		0.83	0.75	0.8477	0.0065		104.2	40.5	90.3		0.87	0.95
RCS052	Ep	V2	9	\	\	\	\	\	\	\	\	\	\	\	\	\	\	\
RCS052	Ep	All	19	109.5	68.1	143.6	176	1.61	1.5	0.842	0.0044	0.0054	110.8	39.4	82.4	105.3	0.95	1.6
RCS052	Zrn	Ig	2	58.15	2.23	4.38		0.08	1	0.111	0.031		66.32	0.71	9.04	47.99	0.72	28
RCS053	Ap	A2	21	52.19	7.26	15.2	18.67	0.36	1.5	0.8041	0.0129	0.0159	75.49	4.94	10.3	15.93	0.21	2.4
RCS053	Ttn	A2	37	68.99	1.11	2.26	2.75	0.04	1.5	0.8227	0.0046	0.0056	69.17	0.96	1.94	2.33	0.03	1.4
RCS054	Ap	A2	11	81.2	20.2	45.8		0.56	1.7	0.835	0.033		78.49	4.7	10.48		0.13	1.5
RCS054	Ap	Ig-Alt	23	65.86	6.76	14.06	16.9	0.26	1.4	0.8309	0.0114	0.0137	65.75	2.89	6		0.09	1.4

Sample	Mineral	Alt	Points	Raw Age and Error						Common Pb Intercept			Anchored Age and Error					
RCS054	Ap	All	34	66.6	6.4	13.4	16.15	0.24	1.5	0.8292	0.0101	0.0125	70.69	2.46	5.01	6.14	0.09	1.5
RCS054	Ttn	A2	19	65.76	3.92	8.26		0.13	0.83	0.827	0.0072		62.43	2.39	5.02		0.08	0.64
RCS056	Ap	A2	21	73.41	2.65	5.54	8.48	0.12	2.3	0.827	0.0078	0.012	74.46	2.55	5.31	8.12	0.11	2.3
RCS056	Ttn	A2	34	60.45	0.64	1.3	2.5	0.04	3.7	0.8221	0.0064	0.0124	60.65	0.37	0.75	1.43	0.02	3.6
RCS056	Zrn	A2?	5	64.88	0.68	2.15	8.27	0.13	15	0.896	0.129	0.495	64.02	0.3	0.82	2.8	0.04	12
RCS057	Ap	A2	16	75.46	8.84	18.95	21.19	0.28	1.3	0.8262	0.02	0.0224	81.03	3.32	7.08		0.09	1.2
RCS057	Ap	Ig-Alt	20	62.09	3.71	7.79		0.13	0.82	0.8221	0.0162		66.65	1.45	3.03		0.05	0.87
RCS057	Ap	All	38	59.87	2.57	5.21	5.43	0.09	1.1	0.8152	0.0092	0.0096	68.27	1.24	2.51	3.01	0.04	1.4
RCS057	Ttn	A2	12	66.93	2.44	5.44	8.2	0.12	2.3	0.84	0.0101	0.0153	60.52	1.74	3.82	6.94	0.11	3.3
RCS058	Ap	BX	15	49.42	4.03	8.71	8.85	0.18	1	0.8164	0.0112	0.0114	58.88	2.57	5.52		0.09	1.6
RCS059	Ap	A3	19	56.42	8.83	18.63	26.39	0.47	2	0.824	0.0042	0.006	76.97	7.36	15.45	26.39	0.34	2.9
RCS059	Ttn	A3	11	65.44	1.53	3.47	8.65	0.13	6.2	0.8328	0.0095	0.0236	63.62	1.31	2.92	7.23	0.11	6.1
RCS059	Ep	A3	22	24.9	21.2	44.3	54.2	2.18	1.5	0.8464	0.0028	0.0034	3.11	7.02	14.6	19.46	6.26	1.8
RCS061	Ap	A2	28	73.43	2.4	4.93	5	0.07	1	0.8305	0.0081	0.0082	74.28	1.81	3.71		0.05	1
RCS061	Ttn	A2	34	70.28	0.88	1.79	5.19	0.07	8.4	0.7742	0.0063	0.0182	78.26	0.7	1.42	5.53	0.07	15
RCS061	Zrn	Ig?	3	62.09	0.81	10.3	11.05	0.18	1.2	0.88	1.28	1.38	61.79	0.32	1.38		0.02	0.66
RCS064	Ap	A4	20	56.53	6.26	13.15	20.04	0.35	2.3	0.8359	0.0054	0.0083	51.01	4.58	9.58	14.49	0.28	2.3
RCS065	Ap	A6	9	125.1	16.3	38.5	144.9	1.16	14	0.859	0.036	0.137	98.95	7.27	16.77	59.96	0.61	13
RCS065	Ep	A6	19	64.3	7.58	15.99	19.51	0.30	1.5	0.8486	0.0036	0.0044	45.09	4.94	10.39	14.78	0.33	2
RCS066	Ap	A3	16	65.39	4.66	10	10.56	0.16	1.1	0.8157	0.0095	0.01	74.34	3.99	8.49	11.89	0.16	2
RCS066	Ap	Ig	11	56.28	3.66	8.27	9.34	0.17	1.3	0.8065	0.008	0.009	64.38	3.46	7.71	18.07	0.28	5.5
RCS066	Ap	All	27	59.47	2.87	5.91	6.54	0.11	1	0.81	0.0057	0.0063	68.66	2.61	5.37	9.87	0.14	3.4
RCS066	Ttn	A3	7	43.84	9.45	24.29	42.88	0.98	3.1	0.8226	0.0121	0.0214	45.02	6.28	15.36	24.77	0.55	2.6
RCS067	Ap	A5	7	48.9	10.2	26.3	30.2	0.62	1.3	0.8275	0.0098	0.0113	53.85	9.47	23.18		0.43	1.4
RCS067	Ap	Ig-Alt	15	59.76	5.59	12.08	12.73	0.21	1.1	0.8137	0.012	0.0127	70.72	4.47	9.58	12.82	0.18	1.8
RCS067	Ap	All	22	62.2	4.52	9.44	11.35	0.18	1.4	0.8242	0.0064	0.0077	67.64	4.04	8.4	11	0.16	1.7
RCS067	Ttn	A5	8	74.93	9.68	23.68		0.32	0.86	0.8294	0.012		63.98	6.05	14.32		0.22	1
RCS067	Ep	A5	11	5027.9	16.3	37	59.1	0.01	2.6	0.8337	0.0053	0.0085	4996.4	15.1	33.7	65.6	0.01	3.8

Sample	Mineral	Alt	Points	Raw Age and Error						Common Pb Intercept			Anchored Age and Error					
RCS067	Ep	V3	7	\	\	\	\	\	\	\	\	\	\	\	\	\	\	\
RCS067	Ep	All	18	5044.3	13.7	29.1	45.2	0.01	2.4	0.8351	0.0048	0.0074	5016.1	11.7	24.7	42.6	0.01	3
RCS068	Ap	A6	40	60.8	3.62	7.33	11.44	0.19	2.4	0.8313	0.0026	0.0041	62.14	3.37	6.82	10.55	0.17	2.4
RCS070	Ap	A4	11	60.3	14.7	33.3		0.55	0.75	0.8217	0.0126		78.6	11.2	24.8		0.32	1
RCS071	Ttn	A3	7	59.41	2.23	5.41		0.09	0.52	0.8216	0.0073		59.94	2.08	5.09		0.08	0.51
RCS071	Ep	A3	20	\	\	\	\	\	\				5025.63	9.51	19.85	37.16	0.01	3.5
RCS071	Zrn	Ig	1	\	\	\	\	\	\	\	\	\	\	\	\	\	\	\
RCS072	Ap	A4	10	69.15	1.69	3.9	6.14	0.09	2.5	0.8265	0.0048	0.0075	69.82	1.68	3.79	6.72	0.10	3.1
RCS072	Ap	V7	7	51.4	13.9	35.7	50.8	0.99	2	0.794	0.049	0.07	71.63	8.62	21.1	31.9	0.45	2.3
RCS072	Ap	All	17	69.09	1.67	3.55	5.23	0.08	2.2	0.8262	0.0044	0.0064	69.88	1.64	3.49	5.65	0.08	2.6
RCS073	Ap	A3	31	65.92	7.97	16.31	16.97	0.26	1.1	0.8233	0.0044	0.0046	78.64	7.34	14.99	19.29	0.25	1.7
RCS073	Ap	Ig-Alt	16	65.9	2.14	4.59	5.35	0.08	1.4	0.8326	0.0172	0.0201	65.89	1.8	3.84		0.06	1.3
RCS073	Ap	All	47	64.72	1.81	3.64	3.91	0.06	1.1	0.8238	0.004	0.0042	66.62	1.75	3.52	4.4	0.07	1.6
RCS073	Zrn	Ig	6	67.27	0.34	0.94	2.7	0.04	8.3	0.8415	0.0265	0.0762	67.28	0.32	0.83	2.14	0.03	6.6
RCS074	Ap	A3	5	52.1	154.3	491.1		9.43	1.3	0.81	0.014	0.044	277.9	57.7	160.1		0.58	1.6
RCS074	Ap	V6	7	4944.8	12.8	32.8	51.1	0.01	2.4	0.8135	0.0231	0.036	41.9	22.5	55	91.2	2.18	2.8
RCS074	Ap	All	12	4935.68	7.43	16.56	21.52	0.00	1.7	0.8075	0.0121	0.0158	72.1	20.9	46.1	84.8	1.18	3.4
RCS074	Ttn	A3	17	75.2	0.77	1.65	2.62	0.03	2.5	0.814	0.0082	0.013	75.94	0.71	1.5	2.49	0.03	2.7
RCS074	Ttn	V6	7	68.52	1.82	4.68		0.07	0.59	0.8175	0.0124		69.54	1.61	3.94		0.06	0.73
RCS074	Ttn	All	24	74.33	0.71	1.47	2.37	0.03	2.6	0.8173	0.0062	0.01	74.9	0.65	1.34	2.2	0.03	2.7
RCS074	Ep	A3	8	\	\	\	\	\	\	\	\	\	\	\	\	\	\	\
RCS074	Ep	V6	19	103.3	12.1	25.5	48.5	0.47	3.6	0.8419	0.0034	0.0064	106	11.4	23.9	44.3	0.42	3.4
RCS074	Ep	All	27	98.5	12	24.6	43.1	0.44	3.1	0.8422	0.0026	0.0046	101.4	11	22.7	39	0.38	3
RCS074	Zrn	V6?	4	69.02	0.86	3.68	9.71	0.14	7	1	0.71	1.87	68.13	0.38	1.22	2.75	0.04	5.1
RCS075	Ap	A3	29	66.46	2.49	5.12	7.74	0.12	2.3	0.8294	0.0034	0.0052	68.33	2.29	4.68	7.16	0.10	2.3
RCS075	Ap	Ig-Alt	6	85.61	5.24	14.54	15.49	0.18	1.1	0.8692	0.0274	0.0292	69.81	3.31	8.51	13.53	0.19	2.5
RCS075	Ap	All	35	67.37	2.09	4.25	6.44	0.10	2.3	0.83	0.0034	0.0051	68.81	1.88	3.82	5.8	0.08	2.3
RCS076	Ap	Ig	19	66.58	3.62	7.64	22.57	0.34	8.7	0.8277	0.0056	0.0165	70.2	3.03	6.36	18.47	0.26	8.4

Sample	Mineral	Alt	Points	Raw Age and Error						Common Pb Intercept			Anchored Age and Error					
RCS077	Ap	A3	6	4940.4	11.5	31.8	76.7	0.02	5.8	0.8152	0.0216	0.0521	71	15.5	39.8	94.3	1.33	5.6
RCS077	Ap	Ig-Alt	9	71.7	4.29	10.15	21.64	0.30	4.5	0.8238	0.0169	0.0361	75.51	2.92	6.74	13.75	0.18	4.2
RCS077	Ap	Ig	5	133.4	14.3	45.6	242.1	1.81	28	0.8272	0.0233	0.1505	137.6	124	34.5	159.2	1.16	21
RCS077	Ap	All	17	71.11	3.55	7.56	12.41	0.17	2.7	0.8238	0.0092	0.015	75.47	2.81	5.96	9.96	0.13	2.8
RCS077	Ep	A3	7	98.3	11.9	30.6	44.8	0.46	2.1	0.8424	0.0104	0.0152	99.1	10.3	25.3		0.26	1.8
RCS078	Ap	V6	23	76.38	2.63	5.47	8.1	0.11	2.2	0.8441	0.0055	0.0081	68.25	1.89	3.92	6.76	0.10	3
RCS078	Ap	V3	5	76.58	5.17	16.46	27.37	0.36	2.8	0.8462	0.024	0.0399	70.79	4.12	11.44	19.5	0.28	2.9
RCS078	Ap	Ig-Alt	9	68.4	12.7	30.1		0.44	1.1	0.821	0.024		81.82	4.72	10.89		0.13	1.1
RCS078	Ap	All	37	76.39	2.3	4.68	7.04	0.09	2	0.8412	0.0047	0.0071	70.22	1.62	3.28	5.27	0.08	2.6
RCS078	Ttn	V6	14	84.68	0.87	1.91	3.03	0.04	2.5	0.8229	0.0039	0.0063	84.68	0.87	1.89	2.89	0.03	2.3
RCS078	Ttn	V3	4	\	\	\	\	\	\	\	\	\	\	\	\	\	\	\
RCS078	Ttn	All	18	84.67	0.87	1.85	2.59	0.03	1.9	0.8227	0.0033	0.0046	84.69	0.87	1.84	2.5	0.03	1.8
RCS078	Ep	V3	9	81.6	30.3	71.3		0.87	0.93	0.8443	0.0058		70.4	22.5	51.9		0.74	0.85
RCS078	Ep	V6	14	\	\	\	\	\	\				138.8	22	47.5	76.4	0.55	2.6
RCS078	Ep	All	23	75.2	26.4	54.9	78.6	1.05	2.1	0.8402	0.004	0.0058	105.2	15.7	32.6	46.7	0.44	2.1
RCS078	Zrn	V6	3	66.64	0.26	3.33	9.74	0.15	8.5	2.37	17.36	50.73	66.3	0.24	1.04	3.11	0.05	8.9
RCS078	Zrn	V3	4	67.9	0.93	4.02	6.74	0.10	2.8	0.743	0.233	0.39	69.17	0.5	1.58	2.62	0.04	2.8
RCS078	Zrn	All	7	66.39	0.25	0.063	1.64	0.02	6.8	0.696	0.072	0.185	66.86	0.22	0.53	1.58	0.02	8.8
RCS079	Ap	Ig	16	57.25	3.29	7.06		0.12	0.85	0.8206	0.0062		67.64	3.36	7.59	11.67	0.17	2.4
RCS079	Ap	Ig-Alt	9	52.93	4.94	11.69		0.22	0.63	0.8209	0.0075		59.16	4.65	11.95		0.20	1.1
RCS079	Ap	A3	16	61.52	4.26	9.14	9.46	0.15	1.1	0.8231	0.0051	0.0053	71	3.55	7.62	11.1	0.16	2.1
RCS079	Ap	All	31	58.65	2.58	5.27		0.09	0.82	0.8213	0.0038		67.04	2.16	4.41	6.26	0.09	2
RCS079	Ep	A3	5	\	\	\	\	\	\	\	\	\	\	\	\	\	\	\
RCS079	Zrn	A3	1	\	\	\	\	\	\	\	\	\	\	\	\	\	\	\
RCS081	Zrn	A5	2	65.97	1.22	2.4		0.04	1	0.8537	0.0104		64.28	0.93	11.8	25.15	0.39	4.5
RCS081	Zrn	Ig	5	67.11	0.5	1.6	2.47	0.04	2.4	0.876	0.042	0.065	66.48	0.44	1.23	2.32	0.03	3.6
RCS081	Zrn	All	7	66.3	0.44	1.12	1.58	0.02	2	0.8577	0.0108	0.0151	66.07	0.4	0.98	1.93	0.03	3.9
RCS083	Zrn	Ig	8	65.35	0.46	1.13	2.75	0.04	5.9	0.8516	0.0219	0.0531	65.16	0.43	1.01	2.3	0.04	5.2

Sample	Mineral	Alt	Points	Raw Age and Error						Common Pb Intercept			Anchored Age and Error					
RCS084	Ap	A3	13	56.61	4.73	10.41		0.18	0.93	0.821	0.029		58.4	4.21	9.17		0.16	0.91
RCS084	Ttn	A3	30	60.32	1.45	2.97	4.04	0.07	1.9	0.8237	0.01	0.0136	60.27	1.1	2.26	3.02	0.05	1.8
RCS086	Ap	A2	15	123	27.1	58.5		0.48	0.5	0.861	0.049		92.2	13.8	29.5		0.32	0.59
RCS086	Ttn	A2	13	34.9	11.5	25.2	29.6	0.85	1.4	0.776	0.032	0.037	67.05	4.62	10.06	14.61	0.22	2.1
RCS089	Zrn	Ig?	3	55.02	1.76	22.31	40.96	0.74	3.4	0.75	1.33	2.44	56.31	0.49	2.12		0.04	2
RCS089	Zrn	A6?	2	47.82	0.92	1.8		0.04	1	0.451	0.105		51.34	0.26	3.28	14.84	0.29	20
RCS089	Zrn	All	5	48.89	0.42	1.33	3.12	0.06	5.5	0.518	0.068	0.159	52.41	0.23	0.63	3.24	0.06	26
RCS090	Zrn	Ig?	10	75.82	0.3	0.68	4.74	0.06	48	3.7E-06	6.1E-05	0.00042	52.84	0.15	0.35	3.26	0.06	88
RCS092	Ap	A3	17	60.26	2.77	5.9	8.03	0.13	1.9	0.811	0.0139	0.0189	67	1.82	3.85	5.96	0.09	2.4
RCS092	Ap	Ig-Alt	16	64.4	2.83	6.08	10.57	0.16	3	0.8327	0.0169	0.0293	64.36	1.54	3.29	5.52	0.09	2.8
RCS092	Ap	All	33	61.61	1.96	4.01	6.27	0.10	2.4	0.8201	0.0102	0.016	65.47	1.18	2.39	3.83	0.06	2.6
RCS092	Ttn	A3	11	65.85	1.63	3.69	6.12	0.09	2.8	0.8022	0.0132	0.0219	68.3	1.47	3.28	6.36	0.09	3.8
RCS092	Zrn	A3?	18	65.27	0.22	0.46	1.5	0.02	10	0.8324	0.0071	0.0229	65.43	0.21	0.45	1.44	0.02	10
RCS093	Ap	Ig	4	66.3	14.2	61.2		0.92	0.93	0.826	0.046		73.65	6.72	21.39		0.29	0.74
RCS093	Ap	A6	16	62.18	4.41	9.45	12.12	0.19	1.6	0.8289	0.0042	0.0053	66.22	3.83	8.17	10.87	0.16	1.8
RCS093	Ap	All	20	63.84	3.97	8.34	9.98	0.16	1.4	0.8288	0.004	0.0048	68.05	3.33	6.97		0.10	1.6
RCS096	Ep	A3	11	54.5	29.2	66.1	144.9	2.66	4.8	0.8438	0.0023	0.0051	37.4	20.2	44.9	94.1	2.52	4.4
RCS096	Ap	Ig	6	69.72	5.34	14.82		0.21	0.27	0.8629	0.0138		46.9	3.99	10.25	28.59	0.61	7.8
RCS096	Ap	Ig-Alt	18	62.57	3.47	7.36	10.7	0.17	2.1	0.8614	0.0061	0.0088	38.08	2.57	5.43	15.4	0.40	8
RCS096	Ap	All	23	64.68	3.03	6.31	8.32	0.13	1.7	0.8619	0.0052	0.0068	40.67	2.16	4.47	12.48	0.31	7.8
RCS097	Ap	Ig	13	62.24	3.02	6.66	12.01	0.19	3.3	0.8123	0.0066	0.0119	73.37	2.63	5.69	15.66	0.21	7.6
RCS097	Ap	Ig-Alt	10	71.56	3.66	8.45	21.36	0.30	6.4	0.8109	0.012	0.0303	80.06	2.95	6.68	18.32	0.23	7.5
RCS097	Ap	All	24	67.72	2.28	4.74	10.55	0.16	5	0.8121	0.0054	0.012	76.33	1.96	4.06	11.02	0.14	7.4
RCS097	Ep	A5	15	57.2	9.72	21.02		0.37	0.71	0.8454	0.0072		50.83	4.68	10.04		0.20	0.7
RCS098	Ap	A5	19	59.4	11.9	25.1	28.8	0.48	1.3	0.8534	0.0024	0.0027	4992.28	1.66	3.48	15.5	0.00	20
RCS098	Ep	A5	24	187.1	89.7	186.1	275.7	1.47	2.2	0.84803	0.00193	0.00287	5030.46	9.78	20.24	37.31	0.01	3.4
RCS099	Ap	A5	2	\	\	\	\	\	\	\	\	\	\	\	\	\	\	\
RCS099	Ap	Ig-Alt	3	\	\	\	\	\	\	\	\	\	\	\	\	\	\	\

Sample	Mineral	Alt	Points	Raw Age and Error						Common Pb Intercept			Anchored Age and Error					
RCS099	Ap	All	5	72.1	18.5	59	62.5	0.87	1.1	0.8559	0.011	0.0117	11.3	6.36	17.67	67.79	6.00	15
RCS099	Ep	A5	41	\	\	\	\	\	\				0.1	1.826	3.688	4.847	48.47	1.7
RCS102	Ap	A4	14	61.6	11.5	25	28.5	0.46	1.3	0.8297	0.0212	0.0242	64.53	5.61	12.11		0.19	1.2
RCS102	Ap	Ig-Alt	6	86.5	17.2	47.8		0.55	0.11	0.839	0.042		79.94	7.54	19.39		0.24	0.12
RCS102	Ap	All	20	69.61	9.52	20	20.57	0.30	1.1	0.8322	0.0172	0.0177	70.01	4.5	9.42		0.13	1
RCS102	Ttn	A4	7	44.1	27.8	71.5	0.0176	0.00	0.98	0.8215	0.0176		51.58	9.03	22.09		0.43	0.83
RCS102	Ep	A4	12	43.58	1.94	4.31	6.19	0.14	2.1	0.8464	0.0068	0.0098	42.98	1.86	4.1	5.79	0.13	2
RCS102	Zrn	A4	2	52.36	3.61	7.07		0.14	1	0.27	0.118		61.79	0.66	8.37	28.71	0.46	12
RCS104	Ap	A4	5	53.8	18.3	58.1		1.08	0.87	0.876	0.242		44.9	11	3.5		0.08	0.73
RCS104	Ep	A4	35	59.8	24.5	49.8	68.7	1.15	1.9	0.8435	0.0038	0.0053	54.7	16.8	34.2	46.5	0.85	1.9
RCS106	Ap	A?	17	46.88	5.51	11.74	22.18	0.47	3.6	0.831	0.0068	0.0129	49.08	4.34	9.16	16.77	0.34	3.4
RCS106	Zrn	A?	5	61.09	0.71	2.27	5.39	0.09	5.6	0.8366	0.0124	0.0294	61.16	0.71	1.98	4.32	0.07	4.8

Appendix C2

Sample	Type	EAST_X	NORTH_Y	Elevation	Class	Mineral	Age (Ma)	±	2nd Err	3rd Err	Uncertainty	MSWD	Replaced	Comments
RCS003	RAW	327486	8098122	3617	A4	Zrn	57.41	0.31	0.98	2.91	0.05	8.8		
RCS003	RAW	327486	8098122	3617	All	Zrn	57.32	0.3	0.84	2.15	0.04	6.6		
RCS014	RAW	318331	8086042	2296	lg	Zrn	69.23	1.19	2.33		0.03	1		
RCS017	ANCH	318975	8086688	2277	lg-Alt	Ap	52.15	1.7	3.49	4.75	0.09	1.9		
RCS017	ANCH	318975	8086688	2277	All	Ap	50.52	1.58	3.21	5.11	0.10	2.5		
RCS018	ANCH	319006	8086784	2285	V2	Zrn	69.89	0.38	1.65	6.53	0.09	16	Y	
RCS018	ANCH	319006	8086784	2285	All	Zrn	69.39	0.35	0.98	3.17	0.05	10	Y	
RCS022	RAW	320101	8088633	2463	All	Ap	62.73	1.84	3.76	5.23	0.08	1.9		
RCS023	ANCH	320306	8088971	2480	BX	Zrn	67.64	0.62	2.66		0.04	0.28		
RCS025	ANCH	336024	8101160	4191	A5	Zrn	74.22	0.56	1.79	7.09	0.10	16		
RCS030	RAW	333373	8098457	3958	All	Ap	77.78	0.84	1.8	1.94	0.02	1.2	Y	Good common Pb
RCS030	RAW	333373	8098457	3958	A5	Zrn	66.73	0.52	2.24		0.03	0.44	Y	Aliquot with good common Pb
RCS030	ANCH	333373	8098457	3958	lg	Ap	77.36	0.84	2.68		0.03	1.5	Y	Better precision and isochron
RCS033	RAW	333053	8098079	3988	A4	Ap	64.18	2.31	4.8	6.51	0.10	1.8		
RCS033	RAW	333053	8098079	3988	All	Ap	65.07	2.18	4.48	5.68	0.09	1.6		
RCS034	ANCH	332652	8097796	4011	A7	Zrn	67.19	0.55	1.35	2.62	0.04	3.8	Y	Better precision and isochron
RCS037	ANCH	309039	8098201	2623	lg-Alt	Ap	67.05	2.61	5.56		0.08	1.2		
RCS037	ANCH	309039	8098201	2623	All	Ap	68.15	2.13	4.36		0.06	0.83		
RCS042	ANCH	309368	8098034	2647	lg-Alt	Ap	65.49	1.16	2.51		0.04	1.2	Y	Better precision and isochron
RCS042	ANCH	309368	8098034	2647	All	Ap	65.50	1.11	2.28	2.97	0.05	1.7	Y	Better precision and isochron
RCS044	RAW	309671	8098052	2670	All	Ap	68.28	1.13	2.3	4.68	0.07	4.1	Y	Good common Pb, precise age
RCS044	ANCH	309671	8098052	2670	A2	Ap	64.30	1.04	2.24	5.44	0.08	5.9		
RCS044	ANCH	309671	8098052	2670	lg-Alt	Ap	63.33	1.16	2.51	3.34	0.05	1.8	Y	Better precision and isochron
RCS046	ANCH	310256	8098095	2730	lg	Ap	68.11	2.79	6.23		0.09	1.1		
RCS046	ANCH	310256	8098095	2730	All	Ap	68.90	2.03	4.18	6.8	0.10	2.6		
RCS046	ANCH	310256	8098095	2730	A3	Zrn	65.13	0.16	0.38	1	0.02	6.9	Y	Very similar, slightly better precision

Sample	Type	EAST_X	NORTH_Y	Elevation	Class	Mineral	Age (Ma)	±	2nd Err	3rd Err	Uncertainty	MSWD	Replaced	Comments
RCS047	RAW	310659	8097900	2749	All	Ttn	73.75	1.9	4.02	5.24	0.07	1.7	Y	Good common Pb
RCS047	ANCH	310659	8097900	2749	A3	Ttn	71.97	1.7	3.92	6.2	0.09	2.5		
RCS049	ANCH	310936	8098053	2774	Ig	Ap	68.96	2.45	5.04	6.72	0.10	1.8		
RCS049	ANCH	310936	8098053	2774	Ig-Alt	Ap	63.73	1.43	3.18		0.05	1.8	Y	Better precision and isochron, one point controlling
RCS049	ANCH	310936	8098053	2774	All	Ap	65.06	1.23	2.5	3.38	0.05	1.8	Y	
RCS049	ANCH	310936	8098053	2774	A3	Zrn	65.82	0.11	0.23	1.11	0.02	24	Y	Very similar, slightly better precision
RCS051	ANCH	311239	8097639	2795	V2	Zrn	66.41	0.86	2.2	6.94	0.10	10	Y	Fits with radiogenic Pb
RCS051	ANCH	311239	8097639	2795	All	Zrn	67.41	0.48	1.17	3.43	0.05	8.6	Y	Fits with radiogenic Pb
RCS052	ANCH	311586	8097667	2831	Ig	Ap	68.77	2.43	5.14		0.07	1.1		
RCS052	ANCH	311586	8097667	2831	All	Ap	67.91	2.28	4.75		0.07	1.2		
RCS052	ANCH	311586	8097667	2831	V2	Ttn	67.76	3.05	6.79		0.10	1.7		
RCS052	ANCH	311586	8097667	2831	All	Ttn	67.13	2.9	6.22		0.09	1.3	Y	Better precision and isochron
RCS053	RAW	311962	8098331	2931	A2	Ttn	68.99	1.11	2.26	2.75	0.04	1.5	Y	Very similar to anchored, trusting common Pb in raw
RCS054	ANCH	312332	8098767	2942	Ig-Alt	Ap	65.75	2.89	6		0.09	1.4		
RCS054	ANCH	312332	8098767	2942	All	Ap	70.69	2.46	5.01	6.14	0.09	1.5		
RCS054	ANCH	312332	8098767	2942	A2	Ttn	62.43	2.39	5.02		0.08	0.64		
RCS056	ANCH	312635	8099146	3008	A2	Ttn	60.65	0.37	0.75	1.43	0.02	3.6	Y	
RCS056	ANCH	312635	8099146	3008	A2	Zrn	64.02	0.3	0.82	2.8	0.04	12		
RCS057	ANCH	312843	8099427	3038	A2	Ap	81.03	3.32	7.08		0.09	1.2		
RCS057	ANCH	312843	8099427	3038	Ig-Alt	Ap	66.65	1.45	3.03		0.05	0.87		
RCS057	ANCH	312843	8099427	3038	All	Ap	68.27	1.24	2.51	3.01	0.04	1.4	Y	Better precision and isochron
RCS058	ANCH	312975	8099463	3052	BX	Ap	58.88	2.57	5.52		0.09	1.6		
RCS061	RAW	313262	8099430	3063	A2	Ttn	70.28	0.88	1.79	5.19	0.07	8.4	Y	Slightly better precision, and isochron - age more reliable too
RCS061	ANCH	313262	8099430	3063	A2	Ap	74.28	1.81	3.71		0.05	1	Y	Better precision and isochron

Sample	Type	EAST_X	NORTH_Y	Elevation	Class	Mineral	Age (Ma)	±	2nd Err	3rd Err	Uncertainty	MSWD	Replaced	Comments
RCS061	ANCH	313262	8099430	3063	Ig	Zrn	61.79	0.32	1.38		0.02	0.66		
RCS071	ANCH	318068	8102904	3041	A3	Ttn	59.94	2.08	5.09		0.08	0.51	Y	
RCS072	ANCH	317788	8103570	3085	A4	Ap	69.82	1.68	3.79	6.72	0.10	3.1	Y	Very similar, slightly better precision
RCS072	ANCH	317788	8103570	3085	All	Ap	69.88	1.64	3.49	5.65	0.08	2.6	Y	Very similar to raw
RCS073	RAW	319697	8103557	3219	All	Ap	64.72	1.81	3.64	3.91	0.06	1.1	Y	Very similar, slightly better precision
RCS073	ANCH	319697	8103557	3219	Ig-Alt	Ap	65.89	1.8	3.84		0.06	1.3	Y	
RCS073	ANCH	319697	8103557	3219	Ig	Zrn	67.28	0.32	0.83	2.14	0.03	6.6	Y	One common pb aliquot so anchored age better
RCS074	ANCH	320100	8103564	3234	A3	Ttn	75.94	0.71	1.5	2.49	0.03	2.7	Y	Very similar to raw, slightly better precision
RCS074	ANCH	320100	8103564	3234	V6	Ttn	69.54	1.61	3.94		0.06	0.73	Y	Very similar to raw, slightly better precision
RCS074	ANCH	320100	8103564	3234	All	Ttn	74.90	0.65	1.34	2.2	0.03	2.7	Y	Very similar to raw, slightly better precision
RCS074	ANCH	320100	8103564	3234	V6	Zrn	68.13	0.38	1.22	2.75	0.04	5.1		
RCS075	ANCH	320740	8103917	3280	A3	Ap	68.33	2.29	4.68	7.16	0.10	2.3		
RCS075	ANCH	320740	8103917	3280	All	Ap	68.81	1.88	3.82	5.8	0.08	2.3	Y	Better precision and isochron
RCS078	ANCH	322734	8105674	3559	V6	Ap	68.25	1.89	3.92	6.76	0.10	3		
RCS078	ANCH	322734	8105674	3559	All	Ap	70.22	1.62	3.28	5.27	0.08	2.6		
RCS078	ANCH	322734	8105674	3559	V6	Ttn	84.68	0.87	1.89	2.89	0.03	2.3	Y	Very similar to raw, one controlling radiogenic Pb
RCS078	ANCH	322734	8105674	3559	All	Ttn	84.69	0.87	1.84	2.5	0.03	1.8	Y	Very similar to raw, one controlling radiogenic Pb
RCS078	ANCH	322734	8105674	3559	V6	Zrn	66.30	0.24	1.04	3.11	0.05	8.9		
RCS078	ANCH	322734	8105674	3559	V3	Zrn	69.17	0.5	1.58	2.62	0.04	2.8	Y	Very similar to raw
RCS078	ANCH	322734	8105674	3559	All	Zrn	66.86	0.22	0.53	1.58	0.02	8.8	Y	Very similar to raw
RCS079	RAW	322739	8105681	3560	All	Ap	58.65	2.58	5.27		0.09	0.82	Y	
RCS081	RAW	324357	8106351	3901	A5	Zrn	65.97	1.22	2.4		0.04	1		

Sample	Type	EAST_X	NORTH_Y	Elevation	Class	Mineral	Age (Ma)	±	2nd Err	3rd Err	Uncertainty	MSWD	Replaced	Comments
RCS081	RAW	324357	8106351	3901	All	Zrn	66.3	0.44	1.12	1.58	0.02	2	Y	Very similar to anchored, slightly better fit of isochron
RCS081	ANCH	324357	8106351	3901	lg	Zrn	66.48	0.44	1.23	2.32	0.03	3.6	Y	
RCS083	ANCH	325083	8107222	3931	lg	Zrn	65.16	0.43	1.01	2.3	0.04	5.2	Y	Very similar to raw, good isochron
RCS084	ANCH	326283	8106997	3913	A3	Ttn	60.27	1.1	2.26	3.02	0.05	1.8	Y	Very similar to raw, good isochron
RCS089	RAW	328094	8107074	3992	A6	Zrn	47.82	0.92	1.8		0.04	1		Only two points
RCS089	ANCH	328094	8107074	3992	lg	Zrn	56.31	0.49	2.12		0.04	2		Only 3 points
RCS089	ANCH	328094	8107074	3992	All	Zrn	52.41	0.23	0.63	3.24	0.06	26	Y	
RCS092	RAW	317413	8091544	2545	A3	Ttn	65.85	1.63	3.69	6.12	0.09	2.8	Y	Better isochron fit
RCS092	ANCH	317413	8091544	2545	A3	Ap	67.00	1.82	3.85	5.96	0.09	2.4		
RCS092	ANCH	317413	8091544	2545	lg-Alt	Ap	64.36	1.54	3.29	5.52	0.09	2.8		
RCS092	ANCH	317413	8091544	2545	All	Ap	65.47	1.18	2.39	3.83	0.06	2.6	Y	Slightly better precision
RCS092	ANCH	317413	8091544	2545	A3	Zrn	65.43	0.21	0.45	1.44	0.02	10	Y	Good isochron
RCS093	ANCH	317574	8091857	2581	All	Ap	68.05	3.33	6.97		0.10	1.6		
RCS104	ANCH	323197	8096126	3506	A4	Ap	44.90	11	3.5		0.08	0.73		
RCS106	ANCH	320765	8089634	2550	Fault	Zrn	61.16	0.71	1.98	4.32	0.07	4.8	Y	Good isochron

Appendix C3

Appendix D

Geochemistry

Appendix D1 – Whole rock data tables

Appendix D2 – Tables containing the SEM-EDS major element chemistry for chlorite

Appendix D3 – Tables containing the SEM-EDS major element chemistry for epidote

Appendix D4 – Statistical summary tables of the chlorite LA-ICP-MS trace element analysis. The column abbreviations are:

- A: alteration classification
- M: mean of the data within that element
- Md: median of the data within that element
- R: range of the data within that element
- 25%: 25th percentile
- 75%: 75th percentile

Appendix D5 – Statistical summary tables of the epidote LA-ICP-MS trace element data. The column abbreviations are the same as those stated for the chlorite chemistry above.

Sample	Ag_P PB	Al2O3 pct	As_P PM	Au_PP B	B_PP M	Ba_PP M	Be_PP M	Bi_PP M	CaO_p ct	Cd_PP M	Ce_PP M	Co_PP M	Cr_PP M	Cr2O3 _pct	Cs_PP M	Cu_PP M	Dy_PP M	Er_PP M	Eu_PP M	Fe2O3 _pct	Ga_PP M	Gd_PP M	Ge_PP M	Hf_PP M
RCS001	20 3911	16.15	7.1	0.9	5	919	1.2	0.03	2.52	0.16	65.7	3.9	4.3	<0.002	1.5	3.55 >10000	5.58	3.37	1.69	4.9	17.6	6.14	0.3	5.7
RCS002	2	16.75	4.2	0.3	<1	431	0.2	0.02	0.7	0.41	62.3	5.4	1.2	<0.002	1.5	.00	4.87	3.33	1.52	4.44	17.5	5.61	<0.1	6
RCS003	197	17.29	2.6	1.3	3	674	0.4	0.16	5.27	0.05	40.2	20	16.2	0.002	1.8	56.38	2.43	1.33	1.1	7.09	18.8	3.3	<0.1	3.1
RCS006	94	17.07	2.9	1.4	2	634	0.1	<0.02	3.36	0.03	38.9	12.4	2.6	<0.002	2.8	77.52	2.25	1.21	1.01	5.55	19.5	3.06	<0.1	3.3
RCS007	133	17.4	4.7	<0.2	3	451	<0.1	0.13	4.08	0.12	38	15.4	5.2	<0.002	6.1	274.87	2.34	1.31	1.06	5.92	19.3	3.13	<0.1	2.9
RCS009	32	17.38	4.2	2.9	2	719	0.3	<0.02	4.21	0.09	44.4	20.4	31.6	0.004	3.4	72.65	2.57	1.38	1.14	6.6	19.2	3.45	<0.1	3.2
RCS010	14	13.09	10.1	1.8	2	1244	0.5	0.02	0.47	0.03	49.1	1.2	4.3	<0.002	4.7	9.6	2.91	1.91	0.68	1.62	11.7	3.27	<0.1	2.8
RCS011	66	12.48	5.1	0.6	5	1065	0.2	0.06	0.17	0.04	49.5	0.7	5.2	<0.002	5.3	31.85	2.26	1.35	0.53	1.18	9.2	2.61	<0.1	3.2
RCS012	363	11.75	16.8	3.3	18	512	<0.1	0.35	0.11	0.04	20.5	0.4	5.8	<0.002	11	15.32	1.4	1.15	0.2	1.57	12.6	0.96	<0.1	2.6
RCS014	18	15.27	10.2	<0.2	6	739	0.3	0.03	2.54	0.02	42.9	6.9	4.7	<0.002	5.4	6.44	2.13	1.47	0.75	3.56	16	2.48	<0.1	4.3
RCS016	51	16.69	15.6	0.9	12	507	0.8	0.37	3.1	0.12	36.1	17.5	4.2	<0.002	13.6	20.88	3.07	1.63	1.15	6.8	18.2	3.68	<0.1	3.1
RCS017	32	15.33	11	0.4	5	611	0.4	0.03	4.52	0.02	66.4	10.2	10.7	<0.002	4.9	59.07	5.43	3.2	1.47	7.39	17.9	6.31	0.1	6.1
RCS019	34	15.22	1.2	1.5	3	685	0.2	<0.02	3.6	0.01	46.6	6.6	14.9	<0.002	7.3	33.5	3.49	2.29	0.84	4.67	15.9	3.78	<0.1	5.9
RCS021	34	15.31	7.6	<0.2	3	601	0.2	0.04	4.15	0.04	64.9	8.8	18.8	0.002	10.7	92.86	4.79	2.95	1.03	6.25	16.8	5.41	0.1	8.5
RCS022	25	15.96	6.2	0.5	5	741	0.2	0.03	4.07	0.12	56.4	20.4	19	0.003	13.5	53.09	4.8	2.91	1.05	6.32	17.1	5.28	0.1	7.3
RCS023	42	15.13	13	<0.2	3	822	<0.1	0.2	1.55	0.15	45.3	6.7	8.2	<0.002	2.2	11.53	2.28	1.51	0.86	3.73	16.1	2.82	0.2	3.8
RCS024	11	15.82	1.3	0.4	2	621	0.9	0.07	1.55	0.11	42.8	7	3.7	<0.002	9.4	2.44	2.44	1.63	0.92	3.67	15.4	2.83	<0.1	4.3
RCS025	5	14.82	12.5	<0.2	1	743	0.7	<0.02	3.99	0.08	38.4	5.1	2.5	<0.002	4.6	6.64	1.9	1.19	0.73	3.18	13.6	2.25	<0.1	3.8
RCS026	39	11.73	0.5	<0.2	1	136	0.2	0.09	0.18	0.02	8.6	0.1	7.5	<0.002	6.8	7.43	2.1	1.58	0.04	0.53	11.7	1.43	<0.1	2.1
RCS027	6	12.79	8.8	<0.2	2	43	0.5	0.03	0.22	<0.01	12.7	<0.1	6.4	<0.002	4.8	2.41	3.08	2.07	0.05	0.78	15.2	2.02	<0.1	2.5
RCS028	7	12.66	2.2	0.7	2	138	0.4	0.04	0.19	0.02	12.2	0.2	4.2	<0.002	3.6	4.49	2.3	1.68	0.06	0.77	14.5	1.57	<0.1	2.6
RCS029	10	12.37	0.6	0.2	2	288	0.2	0.06	0.14	<0.01	20.3	<0.1	2.6	<0.002	2.8	2.65	2.25	1.57	0.11	0.7	11.7	1.87	<0.1	2.7
RCS030	36	13.51	3.7	<0.2	2	848	0.9	0.06	0.51	0.09	43.4	1.3	3.8	<0.002	5.9	5.41	2.92	2.13	0.53	1.48	12.1	3.05	<0.1	3.1
RCS031	12	15.91	15.7	0.6	4	616	0.7	<0.02	5.18	0.04	53.8	15.9	26.2	0.006	3	11.15	3.61	2.17	1.01	5.6	17.2	3.99	0.2	5.9
RCS032	29	17.83	13.3	1.4	4	1122	0.7	0.08	3.14	0.05	52.6	33	61.1	0.011	2.5	16.65	4.24	2.48	1.32	8.25	15.5	5.08	0.3	5.2
RCS033	18	17.72	17.8	2.3	3	134	0.7	0.05	8.05	0.04	51.5	25.7	44.6	0.011	1.9	27.44	3.98	2.3	1.24	7.67	18.3	4.62	0.2	5.5
RCS034	23	13.58	1	0.5	4	220	0.6	0.06	0.16	0.02	64.4	0.4	2.3	<0.002	11.8	5.34	3.18	2.21	0.51	1.69	14.7	3.49	<0.1	5.4
RCS035	7	13.56	1.5	0.4	1	611	0.2	<0.02	0.21	0.05	52.4	1.6	4.1	<0.002	3.8	1.81	3.11	2.17	0.48	1.65	15.4	3.14	<0.1	5.1
RCS036	10	13.87	1.3	<0.2	<1	620	0.3	0.04	0.13	0.03	65.3	2.6	2.4	<0.002	3.8	2.25	3.68	2.34	0.65	2.17	15.3	3.96	<0.1	5.3
RCS037	22	16.11	0.8	1.4	3	560	0.2	<0.02	5.1	0.02	55	13.1	25.8	0.005	7.4	67.16	4.2	2.56	1.03	6.46	18.1	4.59	<0.1	7.1
RCS039	29	15.77	2.2	2	1	578	0.5	<0.02	3.86	<0.01	58.8	13.6	22.9	0.004	10.8	58.42	4.27	2.64	0.97	6.22	17.4	4.95	<0.1	8.3
RCS041	22	15.96	1.3	1.1	3	571	0.4	<0.02	4.57	0.01	55.8	12.3	23	0.004	8.3	69.82	4.55	2.76	0.96	6.3	17.6	4.88	<0.1	7.6
RCS042	9	15.48	1.8	0.7	<1	612	0.7	<0.02	3.35	0.02	69.4	11.1	14.8	0.003	7.6	48.94	4.37	2.68	1.02	5.62	16.8	5	<0.1	8.5
RCS044	69	16.39	2.5	1.2	3	507	0.1	<0.02	5.84	0.07	52.5	7.5	22	0.004	9.7	88.87	4.3	2.62	1.08	7.11	17.3	4.65	<0.1	6.7
RCS046	27	16.23	2.6	3.7	2	498	0.4	<0.02	5.43	0.03	49.9	14.2	28.3	0.006	12.9	74.6	3.9	2.57	1	6.86	16.5	4.47	0.2	7.4
RCS049	26	16	0.8	1.5	1	534	0.2	<0.02	5.85	0.03	49	13	30.9	0.006	10.6	80.63	4.01	2.52	1.04	7.54	16.4	4.54	0.1	6.3
RCS052	27	16.23	2	0.3	3	546	0.3	<0.02	5.46	0.02	49.8	10.9	28.2	0.007	6.7	65.95	4.01	2.54	1.03	6.98	15.8	4.45	0.1	5.2

Sample	Ag_P PB	Al2O3 pct	As_P PM	Au_PP B	B_PP M	Ba_PP M	Be_PP M	Bi_PP M	CaO_p ct	Cd_PP M	Ce_PP M	Co_PP M	Cr_PP M	Cr2O3 _pct	Cs_PP M	Cu_PP M	Dy_PP M	Er_PP M	Eu_PP M	Fe2O3 _pct	Ga_PP M	Gd_PP M	Ge_PP M	Hf_PP M	
RCS053	17	15.91	2.8	2.1	2	650	0.7	<0.02	4.37	0.02	60.4	10.1	16.1	0.002	5	36.37	4.86	2.92	1.05	6.29	16.5	5.19	0.1	8.6	
RCS054	35	17.11	0.9	0.9	<1	568	0.2	<0.02	5.84	0.03	52.5	14.4	28.1	0.005	6.4	81.03	4.59	2.77	1.16	7.64	17.3	4.98	<0.1	6.6	
RCS056	20	15.19	4.4	0.3	3	674	0.8	<0.02	3.33	0.04	70.4	8.3	12.6	0.004	5.4	34.4	5.31	3.28	1.14	5.53	16.3	5.64	0.1	9.4	
RCS057	68	16.13	3.8	1.2	<1	577	<0.1	<0.02	5.97	0.01	58.2	15.4	38.2	0.008	9.7	126.44	4.85	3	1.13	7.58	16.3	5.25	<0.1	7.6	
RCS059	30	16.8	8.5	2.1	3	438	0.3	<0.02	5.99	0.04	40.4	14.9	42.9	0.01	11.6	39.43	4.09	2.53	1	8.63	18.5	4.35	<0.1	5	
RCS060	23	15.9	8.2	1	3	661	0.7	0.16	0.58	0.05	98.2	1	1.2	<0.002	9.2	5.08	6.13	4.01	1.51	2.04	16.2	6.7	<0.1	11	
RCS061	40	15.9	7.3	0.5	2	589	0.3	<0.02	5.05	<0.01	60.8	11.4	29.1	0.006	14.3	54.32	5.14	3.29	1.16	7.21	15.6	5.62	<0.1	8.1	
RCS062	27	13.9	5.1	<0.2	2	1250	<0.1	<0.02	0.12	<0.01	53.2	0.2	0.8	<0.002	9.6	3.16	2.98	2.54	0.61	0.7	16.4	2.84	<0.1	14.4	
RCS063	29	15.58	14.4	1.5	5	842	0.3	0.09	0.27	0.36	143.7	9.1	1.8	<0.002	12.1	10.8	4.97	3.31	0.93	2.27	15.8	5.33	<0.1	11.9	
RCS064	23	14.78	9.2	1.5	4	832	0.9	0.02	1.14	0.05	81.1	2.7	5.7	0.002	8.1	20.76	6.29	3.93	1.15	3.22	16	6.48	0.1	11.7	
RCS065	52	15.05	4.4	0.8	4	839	0.6	0.04	1.79	0.08	81.8	3.4	6.8	0.002	11	24.16	6.15	3.83	1.23	3.4	16.4	6.5	<0.1	11.4	
RCS066	26	15.02	9.4	1.1	6	880	0.4	<0.02	1.76	0.04	84.4	2.8	6.5	<0.002	11	14.58	5.91	3.81	1.3	3.45	16.7	6.51	0.1	11.5	
RCS067	54	14.81	7.4	1.7	4	827	0.7	<0.02	1.57	0.02	79.5	3	6.8	<0.002	9.1	22.16	5.27	3.34	1.19	3.4	16.3	5.93	0.1	11.5	
RCS068	108	16.28	31	6.5	8	166	0.2	0.27	0.88	0.21	35.5	14.6	14.4	0.003	23.3	8.38	2.7	1.54	0.95	6.5	17.9	3.12	<0.1	3.8	
RCS069	51	16.95	26.1	1.4	6	762	0.4	0.14	3.54	0.05	66.6	12.7	14.8	0.004	4.7	38.62	4.89	2.9	1.42	6.19	17.2	5.67	<0.1	6.9	
RCS070	28	16.4	32.6	1.8	5	599	0.6	0.06	4.87	0.2	60.4	12.7	4.9	<0.002	2.7	29.58	4.77	2.81	1.48	6.63	19.3	5.61	<0.1	5.5	
RCS071	27	15.36	51	0.6	5	814	0.6	<0.02	3.45	0.05	91.2	6.9	9.1	0.003	9.2	43.47	7.15	4.42	1.53	6.34	16.6	7.77	0.3	8.9	
RCS072	35	15.03	13.4	2.3	4	976	0.3	0.05	1.47	0.09	82.4	4.2	5.4	0.002	4.1	11.82	5.8	3.79	1.38	3.8	16.3	6.42	0.2	9.9	
RCS073	20	15.47	40.8	1	16	741	0.7	<0.02	3.77	0.02	85.3	8.3	11.5	0.002	8.4	41.12	6.47	4.18	1.52	6.71	17	7.25	0.2	9.8	
RCS075	45	14.82	25.6	3	4	592	0.6	0.07	3.43	0.05	71.4	9	18	0.004	12.2	87.13	5.19	3.14	1.05	5.78	15.5	5.76	<0.1	8.4	
RCS076	50	16.17	17.5	2.1	7	618	0.9	<0.02	3.2	0.06	66.8	11.3	12.6	<0.002	9.2	42.19	4.91	3.16	1.13	5.93	17	5.33	0.1	9	
RCS077	47	15.93	11.2	<0.2	6	575	0.6	<0.02	4.09	0.02	61.7	9	11	0.003	8.3	61.6	5.05	3.1	1.01	6.1	16.1	5.1	<0.1	7.3	
RCS078	14	16.73	42.1	1.3	9	32	0.7	0.07	16.06	0.01	75.5	4.4	7.4	<0.002	0.4	4.86	6.01	3.79	1.26	9.41	42.7	6.53	0.2	8	
RCS079	25	15.3	18.4	0.6	5	674	1	<0.02	3.65	0.04	78.6	8	10.2	0.004	7.5	52.08	6.47	4.02	1.36	6.36	18.8	7.38	<0.1	8	
RCS080	22	12.94	2.3	1.6	6	909	0.5	0.04	0.46	0.35	44.8	1.3	4.5	<0.002	6.5	4.5	2.96	1.93	0.71	1.64	13.7	3.46	<0.1	2.9	
RCS081	332	12.97	2.7	1.2	4	1045	0.9	0.19	0.35	0.22	34.6	0.5	4.3	<0.002	6.1	25.12	5.37	3.8	0.89	1.66	13.2	4.92	<0.1	3.4	
RCS082	32	12.73	0.9	<0.2	2	1106	0.7	0.04	0.49	0.41	38.2	1.4	7.1	<0.002	3.4	6.15	3.72	2.31	0.82	1.47	11.7	4.16	<0.1	2.9	
RCS083	8	12.89	0.3	<0.2	3	1005	0.3	0.03	0.53	0.04	35.5	1.2	5.8	<0.002	3.4	4.08	2.03	1.48	0.46	1.6	12.4	2.12	<0.1	2.7	
RCS084	128	17.7	14.7	3.3	3	112	0.1	0.04	6.7	0.17	37.8	2.3	4.1	<0.002	2.8	2.8	4.34	2.72	1.83	5.99	18.5	5.44	0.1	4.4	
RCS086	455	19.57	5.7	<0.2	1	420	<0.1	<0.02	8.56	0.05	48.5	6.2	1.8	<0.002	6.6	126.45	4.07	2.36	1.58	8.11	19.8	4.9	<0.1	3.3	
RCS087	231	16.48	0.6	0.8	4	517	0.6	0.06	3.04	4.22	31.4	5.6	7.5	<0.002	8.2	45.13	1.24	0.66	0.76	3.05	17.8	1.79	<0.1	3.1	
RCS089	1656	17.56	1	7.4	3	814	0.1	1.04	1.14	0.08	29.8	3.4	2.8	<0.002	3.8	7927.6	9	1.74	0.9	0.83	1.62	17.2	2.1	<0.1	2.7
RCS090	163	17.84	3.1	3.1	3	708	0.3	0.27	0.89	0.03	14.8	0.8	1.3	<0.002	1.3	318.02	0.85	0.5	0.34	2.61	17.6	0.97	<0.1	3.2	
RCS091	590	16.57	2.3	0.9	3	2249	<0.1	3.4	0.29	0.14	21.1	0.8	1.6	<0.002	1.6	410.84	0.45	0.29	0.23	3.09	15.6	0.48	<0.1	2.8	
RCS092	25	16.07	5.7	<0.2	2	613	0.5	0.03	4.03	0.02	48.4	15	21.8	0.003	10.5	91.46	3.8	2.21	0.96	6.17	15.3	4.15	<0.1	6.4	
RCS093	24	15.1	9.8	0.7	6	774	0.4	0.07	0.38	0.01	29.2	4	2.6	<0.002	10.4	24.42	3.55	2.93	0.39	3.15	16	2.6	<0.1	11.5	
RCS094	11	19.53	2.4	0.9	2	977	<0.1	0.51	0.03	<0.01	72.3	0.2	1.4	<0.002	3.6	6.3	6.29	4.03	0.88	1.11	18.6	7.19	<0.1	8.5	

Sample	Ag_P PB	Al2O3 pct	As_P PM	Au_PP B	B_PP M	Ba_PP M	Be_PP M	Bi_PP M	CaO_p ct	Cd_PP M	Ce_PP M	Co_PP M	Cr_PP M	Cr2O3 _pct	Cs_PP M	Cu_PP M	Dy_PP M	Er_PP M	Eu_PP M	Fe2O3 _pct	Ga_PP M	Gd_PP M	Ge_PP M	Hf_PP M
RCS095	54	15.06	22.4	1.2	8	515	0.2	0.87	0.17	<0.01	27.8	5.6	2.8	0.003	9.9	27.97	2.93	1.87	0.79	2.68	26.2	3.1	<0.1	3
RCS096	22	15.77	4.7	<0.2	5	794	0.1	0.02	3.22	0.11	67.1	4.6	5.9	<0.002	9.5	36.8	5.35	3.31	1.29	4.97	17	5.92	<0.1	9
RCS097	4	14.89	19.9	0.7	5	849	0.5	<0.02	1.18	0.04	76.7	3	2.1	<0.002	5.9	30.7	5.75	3.54	1.13	3.07	15.7	6.32	<0.1	11.4
RCS098	25	14.64	4.7	0.6	3	911	0.1	<0.02	0.82	0.04	69.5	1.9	4.8	<0.002	6.6	21.35	3.58	2.4	0.7	3	16.3	3.83	<0.1	11.9
RCS099	20	14.6	8.7	1.1	2	956	0.8	<0.02	1.03	0.1	76.5	2.8	5.7	<0.002	10.5	26.03	5.52	3.55	1.11	3	16.5	6.06	0.2	12.1
RCS100	23	14.78	8	0.4	3	976	0.6	0.05	1.29	0.06	74.9	2	5.1	<0.002	12.5	22.26	5.56	3.59	1.02	3.09	16.2	5.88	0.2	12.2
RCS101	24	14.73	10.9	0.8	6	901	0.6	0.04	1.32	0.17	76.4	2.4	6.4	<0.002	6.7	23.01	5.78	3.63	1.11	3.17	16.5	6.31	0.2	12.1
RCS102	19	14.64	7.4	<0.2	6	867	0.4	0.03	1.45	0.1	80.9	2.9	8.1	<0.002	8	19.16	6.51	4.13	1.12	3.17	16.6	6.88	0.2	11.9
RCS103	97	14.07	10	1.4	8	316	0.1	0.26	0.19	0.04	9.2	0.2	3	<0.002	9.7	51.86	0.94	0.83	0.19	4.23	14.7	0.91	<0.1	6.2
RCS104	12	16.88	73.6	<0.2	8	237	0.6	0.03	4.92	<0.01	45.3	11.7	26.3	0.005	0.8	39.58	4.3	2.59	1.23	6.89	18.8	4.71	0.2	4.8
RCS105	48	11.55	23.6	1.2	3	1112	0.1	0.04	0.27	0.1	35.1	1.3	3.9	<0.002	3.9	7.46	1.83	1.23	0.42	1.18	5	2.1	<0.1	2.6
RCS106	22	14.18	17	0.4	2	1505	0.3	0.37	0.38	0.09	60.5	6.3	7.6	<0.002	8.4	63.56	5.08	3.67	0.87	3.03	14.4	4.98	<0.1	12.3
RCS107	87	14.91	36.9	0.8	5	1650	<0.1	0.3	0.57	<0.01	31.1	0.8	9	<0.002	10.5	61.4	1.79	1.6	0.33	3.31	14.9	1.77	<0.1	6.5

Appendix D1

Sample	Hg	PPbHo	PPMIn	PPMK2O	pctLa	PPMLi	PPMLu	PPMMgO	pctMn	PPMMnO	pctMo	pctMo	PPMNa2O	pctNb	PPMNd	PPMNI	PPMNI	PPMP2O5	pctPb	pctPb	PPMPd	PPBPr	PPMPt	PPB
RCS001	<5	1.15	0.03	3.81	33.4	13.6	0.52	1.03	732	0.12	<0.001	1.11	4.79	11	33.6	<10	0.3	0.29	<0.02	9.96	<10	8.56	<2	
RCS002	<5	1.09	<0.02	1.91	32.6	23.9	0.55	1.14	984	0.13	<0.001	0.44	5.93	11.3	36.7	<10	0.2	0.3	<0.02	21.73	<10	9.14	<2	
RCS003	<5	0.47	0.02	2.03	21.2	22.9	0.19	3.68	2293	0.32	<0.001	0.13	3.35	5.9	19.8	27	28.1	0.27	<0.02	5.13	<10	4.96	<2	
RCS006	14	0.48	<0.02	2.24	20	14.4	0.21	2.22	685	0.13	<0.001	0.44	5.04	4.4	18.9	<10	4.1	0.24	<0.02	8.15	<10	4.81	<2	
RCS007	<5	0.5	<0.02	1.66	18.7	15.2	0.2	2.64	657	0.12	<0.001	0.17	4.08	4.2	18.9	<10	7.2	0.25	<0.02	7.45	<10	4.7	<2	
RCS009	<5	0.51	<0.02	2.24	21.9	16.8	0.21	3.22	613	0.11	<0.001	0.32	4.1	5.7	22.7	24	24	0.28	<0.02	3.9	<10	5.47	<2	
RCS010	<5	0.59	<0.02	4.04	32.8	3.2	0.32	0.23	173	0.02	<0.001	0.3	3.93	6.3	20.2	<10	1.2	0.08	<0.02	3.49	<10	5.84	<2	
RCS011	16	0.46	<0.02	5.67	30.8	0.6	0.26	0.33	37	<0.01	<0.001	0.28	1.96	5.8	19.1	<10	1.6	0.05	<0.02	3.15	<10	5.67	<2	
RCS012	11	0.34	<0.02	3.35	13.9	0.6	0.22	0.24	40	0.04	0.002	24.01	0.05	5.5	7	<10	0.7	0.05	<0.02	35.03	<10	2.09	<2	
RCS014	<5	0.48	<0.02	3.08	24.8	17.3	0.25	1.64	262	0.06	<0.001	0.38	3.61	5.9	16.2	<10	3.1	0.13	<0.02	3.74	<10	4.6	<2	
RCS016	35	0.62	0.04	2.19	19.4	24.7	0.25	2.99	866	0.12	<0.001	0.21	3.7	4.2	20.5	<10	6.1	0.23	<0.02	11.48	<10	4.89	<2	
RCS017	<5	1.09	<0.02	2.82	33.2	18.5	0.47	2.64	222	0.11	<0.001	0.75	3.69	8	34.7	<10	6.4	0.47	<0.02	4.75	<10	8.46	<2	
RCS019	7	0.72	<0.02	3.63	23.8	10.8	0.37	1.8	130	0.08	<0.001	0.77	3.55	6.6	21.5	<10	6.2	0.15	<0.02	8.98	<10	5.6	<2	
RCS021	<5	1	<0.02	3.84	32.5	6.5	0.42	2.49	173	0.1	<0.001	0.93	3.43	11	32.1	<10	6.3	0.24	<0.02	8.39	<10	8.06	<2	
RCS022	10	1.01	<0.02	3.63	27.2	14.1	0.42	2.43	816	0.2	<0.001	1.73	3.43	9.7	28.3	18	13.4	0.23	<0.02	7.39	<10	6.99	<2	
RCS023	5	0.5	<0.02	3.74	24.8	6.7	0.26	0.8	382	0.1	<0.001	0.41	4.37	6.8	18.3	<10	4.9	0.14	<0.02	11.73	<10	4.95	<2	
RCS024	<5	0.53	<0.02	3.33	25.7	19	0.29	1.26	1747	0.22	<0.001	0.41	3.27	5.9	18.2	<10	2.5	0.15	<0.02	28.02	<10	4.96	<2	
RCS025	<5	0.42	0.02	3.15	22.5	28.9	0.22	1.87	943	0.13	<0.001	0.27	4.5	5.6	15.4	<10	1.6	0.13	<0.02	10.09	<10	4.15	<2	
RCS026	<5	0.52	<0.02	5.54	4.7	0.4	0.28	0.06	56	0.02	<0.001	0.19	2.51	9.6	3.9	<10	0.6	0.03	<0.02	14.6	<10	1.15	<2	
RCS027	<5	0.67	<0.02	5.21	5.5	0.7	0.34	0.19	417	0.09	<0.001	0.26	3.26	11.2	5.2	<10	0.4	0.04	<0.02	7.61	<10	1.58	<2	
RCS028	<5	0.52	<0.02	4.85	5.2	0.9	0.28	0.19	164	0.03	<0.001	0.27	3	9.7	4.7	<10	0.6	0.02	<0.02	13.02	<10	1.31	<2	
RCS029	<5	0.5	<0.02	4.45	9.9	0.3	0.26	0.14	124	0.02	<0.001	0.03	2.87	8.3	7.8	<10	0.3	0.02	<0.02	3.49	<10	2.32	<2	
RCS030	<5	0.66	<0.02	4.14	30.2	0.8	0.36	0.38	999	0.13	<0.001	0.3	3.15	6.5	17.9	<10	2.3	0.05	<0.02	15.06	<10	5.22	2	
RCS031	<5	0.76	<0.02	3.24	26.4	38.3	0.35	1.98	805	0.17	<0.001	0.29	3.25	8.8	24.6	18	19.8	0.21	<0.02	14.65	<10	6.4	3	
RCS032	<5	0.9	0.03	3.32	25.5	60.1	0.37	4.55	1907	0.26	<0.001	0.45	4.05	7.8	27.7	39	42	0.29	<0.02	18.72	<10	6.75	4	
RCS033	<5	0.8	<0.02	0.52	25.6	73.8	0.34	5.19	1112	0.2	<0.001	0.43	3.03	8.1	25.5	34	35.8	0.27	<0.02	14.94	<10	6.36	<2	
RCS034	<5	0.66	<0.02	3.95	35.2	0.7	0.38	0.42	38	0.02	<0.001	0.21	1.7	11.1	25.5	<10	0.6	0.03	<0.02	22.85	<10	7.29	<2	
RCS035	<5	0.65	<0.02	5.33	31.5	2.3	0.36	0.19	308	0.05	<0.001	0.47	3.59	12.1	21.3	<10	1.2	0.04	<0.02	11.25	<10	6.19	<2	
RCS036	<5	0.76	<0.02	5.07	36.1	1.7	0.41	0.14	431	0.06	<0.001	0.27	3.95	11.4	25.7	<10	1	0.03	<0.02	13.6	<10	7.35	<2	
RCS037	<5	0.89	<0.02	3.3	25.3	10	0.36	2.84	254	0.11	<0.001	1.48	3.18	8.6	25.7	15	12.7	0.21	<0.02	3.02	<10	6.67	<2	
RCS039	5	0.87	<0.02	3.69	28.8	10.8	0.4	2.46	269	0.1	<0.001	0.82	3.36	9.2	27.2	14	13.6	0.21	<0.02	4.63	<10	7.06	<2	
RCS041	7	0.96	<0.02	3.43	26.8	9.2	0.41	2.71	234	0.1	<0.001	0.72	3.28	8.5	27.3	17	13.7	0.2	<0.02	4.51	<10	6.87	<2	
RCS042	<5	0.9	<0.02	3.91	32.6	9	0.42	2.01	198	0.09	<0.001	0.44	3.42	9.9	31	<10	9.1	0.21	<0.02	4.11	<10	8.24	2	
RCS044	<5	0.87	<0.02	2.99	24.9	5.9	0.39	3.19	73	0.12	<0.001	1.7	3.26	7.6	25.8	15	8.3	0.21	<0.02	4.03	<10	6.47	4	
RCS046	14	0.86	0.02	2.63	23.3	16.1	0.37	2.94	213	0.11	<0.001	0.46	3.12	7.5	23.7	20	16.3	0.22	<0.02	3.36	<10	5.93	3	
RCS049	10	0.83	<0.02	2.64	22.9	15.7	0.4	3.33	125	0.12	<0.001	0.52	3.02	7.1	23.5	23	16.9	0.22	<0.02	2.42	<10	5.89	<2	
RCS052	10	0.86	<0.02	3.41	24	9	0.38	3.01	153	0.11	<0.001	0.44	3.09	6.9	24.3	18	12.5	0.22	<0.02	2.86	<10	6.18	<2	
RCS053	<5	1.02	<0.02	3.76	28.3	3.7	0.45	2.24	230	0.1	<0.001	0.43	3.15	8.7	29.3	<10	8.4	0.23	<0.02	2.52	<10	7.52	<2	

Sample	Hg	PPBHo	PPMIn	PPMK2O	pctLa	PPMLi	PPMLu	PPMMgO	pctMn	PPMMnO	pctMo	pctMo	PPMNa2O	pctNb	PPMNd	PPMNI	PPMNI	PPMP2O5	pctPb	pctPb	PPMPd	PPBPr	PPMPt	PPB
RCS054	12	0.96	<0.02	3.35	24.7	7.8	0.41	3.36	223	0.11	<0.001	0.19	3.7	7.2	26.8	17	13.2	0.25	<0.02	3.29	<10	6.52	<2	
RCS056	27	1.13	<0.02	4.07	33.1	6.2	0.51	1.44	232	0.07	<0.001	0.27	3.38	9.9	32.9	<10	8.1	0.24	<0.02	3.96	<10	8.52	<2	
RCS057	12	1.04	<0.02	2.95	25.6	9.3	0.43	3.67	282	0.12	<0.001	0.22	3.17	8.1	28.3	32	25	0.26	<0.02	3.07	<10	7.02	<2	
RCS059	6	0.84	<0.02	2.45	19.7	11	0.34	3.58	270	0.13	<0.001	0.5	3.65	5.6	21.4	27	17.4	0.2	<0.02	7.05	<10	5.2	3	
RCS060	<5	1.31	<0.02	3.61	47.8	0.9	0.63	0.33	141	0.02	<0.001	0.87	4.1	15	43.2	<10	0.6	0.1	<0.02	7.7	<10	11.8	<2	
RCS061	<5	1.08	0.02	3.78	29.2	8.1	0.48	2.59	240	0.12	<0.001	0.37	3.37	8.9	31.6	18	13.6	0.28	<0.02	4.97	<10	7.67	<2	
RCS062	<5	0.7	<0.02	6.16	30.6	1.4	0.53	0.19	12	<0.01	<0.001	1.14	0.26	16.9	22	<10	0.4	0.06	<0.02	3.07	<10	5.98	<2	
RCS063	267	1.1	0.04	5.68	34	2.6	0.55	0.12	506	0.07	<0.001	2.71	2.34	13.6	29.7	<10	1.3	0.12	<0.02	11.54	<10	7.95	2	
RCS064	<5	1.29	0.04	4.99	38.5	3.7	0.63	0.5	264	0.08	<0.001	1.29	4.38	14.2	37.2	<10	1	0.1	<0.02	15.09	<10	9.77	3	
RCS065	40	1.22	<0.02	4.77	38.7	7.3	0.6	0.73	315	0.07	<0.001	3	3.96	13.8	36.8	<10	1.3	0.11	<0.02	10.64	<10	9.87	3	
RCS066	<5	1.29	<0.02	4.81	39.1	7.6	0.61	0.66	195	0.08	<0.001	1.16	4.19	14.2	37.9	<10	1.5	0.11	<0.02	12.29	<10	10.01	2	
RCS067	<5	1.11	<0.02	4.82	33.6	4.9	0.56	0.41	210	0.07	<0.001	1.61	4.1	14.1	33.1	<10	0.9	0.12	<0.02	16.3	<10	8.9	<2	
RCS068	82	0.53	0.03	2.15	18	25.8	0.22	2.84	404	0.06	<0.001	0.3	2.78	4.5	18.9	14	14	0.24	<0.02	17.99	<10	4.61	<2	
RCS069	<5	0.98	<0.02	3.12	30.2	24.6	0.43	2.33	959	0.16	<0.001	0.42	3.73	8.8	31.7	<10	9.5	0.35	<0.02	8.23	<10	7.92	<2	
RCS070	7	1	0.03	2.3	28	17	0.43	1.84	1287	0.21	<0.001	0.54	5.39	7.6	30	<10	3.3	0.42	<0.02	9.48	<10	7.59	<2	
RCS071	<5	1.53	<0.02	3.86	45.3	18.6	0.67	1.44	318	0.17	<0.001	0.7	4.53	11.9	42.7	<10	2.8	0.34	<0.02	14.06	<10	10.88	<2	
RCS072	<5	1.22	0.04	4.77	40.3	8.9	0.58	0.82	344	0.05	<0.001	0.7	4.48	13	37.8	<10	1.4	0.15	<0.02	1.83	<10	9.98	<2	
RCS073	<5	1.36	<0.02	3.82	39.9	5.3	0.63	1.82	275	0.13	<0.001	1.88	4.06	12.1	40.2	<10	3.6	0.34	<0.02	9.16	<10	10.28	2	
RCS075	<5	1.11	<0.02	4.01	34.7	7.5	0.52	1.84	226	0.11	<0.001	0.7	3.77	12.8	33	<10	7.7	0.23	<0.02	10.75	<10	8.65	2	
RCS076	<5	1.08	<0.02	3.53	32.7	19.9	0.51	1.98	282	0.12	<0.001	0.91	4.1	10.6	29.8	<10	7.4	0.22	<0.02	13.68	<10	8.02	3	
RCS077	<5	1.06	0.02	3.5	28.1	11.1	0.5	2.3	216	0.11	<0.001	0.99	3.52	9.6	28.1	<10	8.3	0.21	<0.02	12.11	<10	7.32	<2	
RCS078	5	1.26	<0.02	0.18	36.7	0.9	0.59	0.18	118	0.12	<0.001	1.6	0.3	10	35.1	<10	1.7	0.28	<0.02	11.51	<10	9.24	3	
RCS079	<5	1.42	<0.02	4.15	39	10	0.61	1.9	203	0.12	<0.001	2.47	3.78	13	39.2	<10	4.6	0.31	<0.02	12.87	<10	10.17	<2	
RCS080	<5	0.62	<0.02	4.08	33.7	1.5	0.36	0.3	400	0.06	<0.001	0.43	2.92	7.2	21.7	<10	1.1	0.03	<0.02	8.85	<10	6.22	<2	
RCS081	<5	1.25	<0.02	4.6	21	0.6	0.65	0.37	56	0.02	<0.001	0.88	1.86	7	18.6	<10	0.8	0.04	<0.02	6.2	<10	4.74	<2	
RCS082	6	0.75	<0.02	5.03	40.8	0.8	0.39	0.26	371	0.06	<0.001	0.14	2.44	6.4	26	<10	1	0.04	<0.02	4.36	<10	7.18	2	
RCS083	<5	0.46	<0.02	4.56	28	1.3	0.28	0.3	142	0.02	<0.001	0.2	2.85	6.5	16.5	<10	0.6	0.03	<0.02	5.27	<10	4.87	<2	
RCS084	<5	0.93	<0.02	0.84	13.4	3.1	0.43	3.25	73	0.03	<0.001	0.06	4.83	7.8	26	<10	2.3	0.36	<0.02	6.95	<10	5.82	<2	
RCS086	<5	0.85	<0.02	1	24.8	3.6	0.33	2.71	110	0.05	<0.001	0.2	3.56	5.1	27.1	<10	1.8	0.32	<0.02	1.49	<10	6.45	<2	
RCS087	<5	0.23	0.03	2.27	18.9	15.6	0.09	1.26	505	0.07	<0.001	0.12	4.26	3.8	15	<10	4.5	0.15	<0.02	15.42	<10	4.03	<2	
RCS089	15	0.34	0.19	3.16	17.3	1.4	0.12	0.86	198	0.04	<0.001	1.34	3.03	3.8	14.5	<10	1.9	0.13	<0.02	134.51	<10	3.76	<2	
RCS090	7	0.16	0.03	2.8	8.3	0.7	0.08	0.28	30	<0.01	<0.001	1.62	2.87	3.5	6.8	<10	0.9	0.07	<0.02	12.47	<10	1.89	<2	
RCS091	18	0.13	0.43	7.42	12.7	0.8	0.07	0.64	136	0.1	<0.001	0.9	1.54	3.3	4.1	<10	0.5	0.06	<0.02	36.46	<10	1.74	<2	
RCS092	<5	0.78	<0.02	3.65	24	14.3	0.35	2.08	245	0.1	<0.001	0.54	3.66	7.7	23.6	13	10.1	0.2	<0.02	7.18	<10	5.95	4	
RCS093	<5	0.91	<0.02	5.63	12.7	1.7	0.53	0.19	35	<0.01	<0.001	1.98	3.68	13.4	12.6	<10	1.8	0.1	<0.02	9.63	<10	3.32	<2	
RCS094	<5	1.34	<0.02	1.07	37.5	1.4	0.73	0.03	4	<0.01	<0.001	4.94	0.3	10.4	29	<10	0.2	0.08	<0.02	1.79	<10	8.11	<2	
RCS095	34	0.61	<0.02	3.55	14.3	0.3	0.27	0.85	34	0.01	<0.001	1.88	0.23	3.9	15.6	<10	3.4	0.1	<0.02	9.36	<10	3.72	2	
RCS096	<5	1.09	<0.02	3.91	33.8	7	0.51	1.29	147	0.1	<0.001	1.03	3.95	10.3	33.3	<10	2.8	0.24	<0.02	6.64	<10	8.56	3	

Sample	Hg	PPBHo	PPMin	PPMK2O	pctLa	PPMLi	PPMLu	PPMMgO	pctMn	PPMMnO	pctMo	pctMo	PPMNa2O	pctNb	PPMNd	PPMNI	PPMNI	PPMP2O5	pctPb	pctPb	PPMPd	PPBPr	PPMPt	PPB
RCS097	<5	1.18	<0.02	5.24	38.6	6.6	0.55	0.49	390	0.09	<0.001	0.45	3.68	13.6	36	<10	0.7	0.11	<0.02	4.15	<10	9.55	<2	
RCS098	<5	0.77	0.04	5.26	24	1.9	0.39	0.33	137	0.03	<0.001	0.43	3.82	13.4	24.1	<10	0.8	0.13	<0.02	22.35	<10	6.43	<2	
RCS099	<5	1.16	0.03	5.27	35.6	8.2	0.58	0.51	328	0.07	<0.001	1.22	3.83	14.3	34.9	<10	1.4	0.1	<0.02	16.26	<10	9.37	<2	
RCS100	13	1.15	0.02	5.26	35.8	9.4	0.54	0.48	187	0.06	<0.001	1.72	3.88	13.7	36.3	<10	1.1	0.1	<0.02	21.11	<10	9.5	<2	
RCS101	10	1.17	0.03	5.05	38.5	6.4	0.56	0.53	249	0.07	<0.001	2.44	3.91	13.8	36.9	<10	0.9	0.1	<0.02	26.34	<10	9.66	<2	
RCS102	7	1.35	0.04	4.97	41.1	8.3	0.61	0.54	298	0.08	<0.001	1.76	3.99	13.5	38.3	<10	1.4	0.09	<0.02	20.06	<10	9.99	<2	
RCS103	<5	0.25	<0.02	3.62	5.5	1.1	0.17	0.75	15	0.03	<0.001	1.28	0.23	6.5	6.3	<10	0.5	0.11	<0.02	2.03	<10	1.24	<2	
RCS104	6	0.87	<0.02	1.27	23.3	50.6	0.38	3.54	320	0.07	<0.001	0.08	4.54	6.2	26.2	19	21.1	0.18	<0.02	1.09	<10	6.18	<2	
RCS105	10	0.38	<0.02	4.08	23.4	1.6	0.22	0.24	77	0.03	<0.001	0.25	2.85	5.3	15.1	<10	1.4	0.07	<0.02	133.99	<10	4.38	<2	
RCS106	19	1.15	<0.02	5.8	28.2	5.4	0.61	0.42	98	0.01	<0.001	1.97	3.22	14	28.9	<10	1.9	0.08	<0.02	3.28	<10	7.6	2	
RCS107	16	0.46	0.03	6.8	18	10.2	0.39	1.22	94	0.02	<0.001	0.7	1.1	7.7	12.4	<10	5.9	0.06	<0.02	14.79	<10	3.45	6	

Appendix D1 continued

Sample	Rb	PPMRe	PPBSb	PPMSc	PPMSe	PPMSiO2	pctSm	PPMSn	PPMSr	PPMSum	pctTa	PPMTb	PPMTe	PPMTh	PPMTiO2	pctTI	PPMTm	PPMTOT	C	pctTOT	S	pct U	PPM
RCS001	96.3	<1	0.22	12	<0.1	63.39	6.78	2	396.6	99.83	0.7	0.95	<0.02	9.2	0.72	<0.02	0.5	0.11	0.02	2.4			
RCS002	53.3	<1	0.05	13	0.2	61.92	6.74	2	115.7	97.5	0.7	0.85	0.67	9.8	0.76	<0.02	0.5	0.03	0.01	2.7			
RCS003	70.4	<1	0.43	16	<0.1	54.48	3.65	1	376.5	99.83	0.4	0.45	<0.02	5.1	0.81	0.03	0.19	0.23	<0.01	0.9			
RCS006	58.3	<1	0.3	11	<0.1	60.72	3.71	1	553.8	99.83	0.3	0.41	<0.02	4.4	0.67	<0.02	0.18	0.08	<0.01	0.9			
RCS007	50	<1	0.26	14	<0.1	59.5	3.69	1	461.7	99.81	0.3	0.43	<0.02	4	0.75	0.03	0.2	0.03	0.01	1.2			
RCS009	66.6	<1	0.16	17	<0.1	57.35	4.03	1	602.9	99.81	0.3	0.48	<0.02	5.8	0.84	<0.02	0.21	0.01	<0.01	1.5			
RCS010	122.8	<1	0.81	3	<0.1	74.82	3.48	1	139	99.89	0.5	0.48	<0.02	14.7	0.17	0.09	0.28	0.04	0.05	2.7			
RCS011	209.9	<1	0.35	3	<0.1	76.59	2.96	<1	174.2	99.89	0.5	0.38	0.07	14	0.16	0.11	0.22	0.03	0.02	3			
RCS012	126.2	<1	0.81	3	1.5	80.09	0.99	1	49.7	99.91	0.5	0.2	0.1	14	0.16	0.08	0.18	0.03	0.03	2.7			
RCS014	108.1	<1	0.29	8	<0.1	66.67	2.76	<1	288	99.86	0.5	0.38	0.03	13.4	0.42	<0.02	0.22	0.02	<0.01	3			
RCS016	106.6	<1	3.43	15	<0.1	57.71	4.12	1	167.8	99.88	0.3	0.54	0.02	4.2	0.72	0.06	0.27	0.46	<0.01	2.9			
RCS017	114.9	<1	0.71	20	<0.1	59.34	6.98	2	318.5	99.82	0.5	0.93	0.03	13.4	1.14	<0.02	0.46	0.02	<0.01	3.4			
RCS019	144.3	1	0.11	13	<0.1	65.33	4.07	2	267.7	99.84	0.5	0.58	0.02	17	0.62	0.04	0.34	<0.01	<0.01	4.3			
RCS021	165.4	1	0.36	18	<0.1	61.38	6.01	2	266.2	99.81	0.7	0.85	<0.02	19.3	0.97	<0.02	0.41	0.01	<0.01	5			
RCS022	171.4	<1	0.53	18	<0.1	60.69	5.54	2	313.7	99.81	0.7	0.81	<0.02	17.4	0.91	0.1	0.43	0.02	0.01	3.7			
RCS023	108.3	<1	1.12	6	1.1	68.1	3.14	<1	286.4	99.86	0.4	0.41	0.09	14.8	0.42	0.03	0.23	<0.01	<0.01	2.9			
RCS024	122.7	<1	0.23	7	<0.1	66.68	3.08	<1	191.1	99.86	0.4	0.43	<0.02	13.4	0.45	0.04	0.25	0.23	<0.01	3			
RCS025	114.2	<1	0.41	6	0.1	63.18	2.56	<1	245.2	99.88	0.4	0.33	<0.02	12	0.41	0.02	0.18	0.67	<0.01	1.6			
RCS026	158.1	<1	0.08	5	<0.1	78.2	1.26	1	47.2	99.92	0.8	0.31	<0.02	9.1	0.07	0.05	0.27	0.02	0.01	3.5			
RCS027	165.5	<1	0.22	5	<0.1	76.48	1.81	2	22.6	99.92	0.8	0.45	<0.02	9.9	0.08	0.05	0.33	0.02	<0.01	2.9			
RCS028	133.6	<1	0.74	5	<0.1	76.74	1.35	1	26.8	99.93	0.7	0.33	<0.02	9.9	0.09	0.05	0.25	0.02	<0.01	3			
RCS029	109.6	<1	0.21	4	<0.1	77.67	1.9	1	52.6	99.92	0.6	0.35	<0.02	9.4	0.1	0.05	0.24	0.02	0.01	1.4			
RCS030	141.2	<1	0.41	3	<0.1	74.44	3.17	1	115.2	99.9	0.6	0.48	<0.02	17.3	0.15	0.04	0.31	0.02	0.01	3.4			
RCS031	113.6	<1	0.31	16	<0.1	60.81	4.82	2	448.4	99.81	0.6	0.63	<0.02	16.4	0.74	<0.02	0.34	0.02	<0.01	4.7			
RCS032	79.2	<1	0.51	24	<0.1	53.14	5.47	1	324.2	99.8	0.5	0.72	<0.02	10.9	1	<0.02	0.37	0.02	<0.01	3.1			
RCS033	16.4	<1	0.39	23	<0.1	51.67	4.88	2	399.6	99.8	0.6	0.65	0.03	10.9	0.98	<0.02	0.33	0.14	0.01	2.5			
RCS034	227.6	<1	0.27	4	<0.1	75.99	4.39	2	96.4	99.88	1	0.53	0.02	33.9	0.21	0.14	0.33	<0.01	<0.01	8			
RCS035	222	<1	0.41	3	<0.1	74.05	3.74	1	71.6	99.89	0.9	0.5	<0.02	29.7	0.23	<0.02	0.34	0.01	<0.01	5			
RCS036	205.2	<1	0.68	6	<0.1	73.24	4.25	2	73.1	99.88	0.9	0.61	<0.02	30.6	0.29	0.03	0.37	0.01	<0.01	5.5			
RCS037	158.1	<1	0.14	19	<0.1	59.71	5.32	2	291.4	99.82	0.5	0.72	<0.02	18.4	0.86	<0.02	0.37	<0.01	<0.01	4.7			
RCS039	166.2	<1	0.21	17	<0.1	61.06	5.22	4	289.1	99.82	0.6	0.76	<0.02	22.7	0.84	<0.02	0.39	0.01	<0.01	7			
RCS041	158.6	<1	0.2	18	<0.1	60.27	5.4	2	301	99.82	0.5	0.76	<0.02	19.7	0.84	<0.02	0.41	0.01	<0.01	4.7			
RCS042	185.4	<1	0.11	16	<0.1	61.99	5.87	2	269.2	99.82	0.7	0.74	<0.02	23.5	0.87	<0.02	0.4	<0.01	<0.01	5.1			
RCS044	145.3	1	0.14	21	<0.1	59.16	5.26	2	333.1	99.81	0.5	0.74	<0.02	17.8	0.88	0.08	0.38	0.02	<0.01	4.9			
RCS046	124.3	<1	0.14	21	<0.1	58.6	4.69	2	337.4	99.81	0.5	0.69	<0.02	15.4	0.89	0.08	0.37	0.01	<0.01	3.6			
RCS049	117.3	1	0.13	22	<0.1	58.05	4.83	2	387.3	99.81	0.5	0.72	<0.02	15.8	0.94	0.1	0.38	0.02	<0.01	3.5			
RCS052	163.3	<1	0.16	20	<0.1	58.53	5.01	2	361.4	99.82	0.5	0.72	0.03	16.4	0.88	0.03	0.36	<0.01	<0.01	3.6			
RCS053	158.9	<1	0.22	18	<0.1	60.63	5.91	2	446.9	99.8	0.5	0.85	<0.02	21.6	0.9	<0.02	0.43	0.01	<0.01	4.9			

Sample	Rb	PPMRe	PPBSb	PPMSc	PPMSe	PPMSiO2	pctSm	PPMSn	PPMSr	PPMSum	pctTa	PPMTb	PPMTe	PPMTh	PPMTiO2	pctTI	PPMTm	PPMTOT	C	pctTOT	S	pct U	PPM
RCS054	141.2	1	0.24	23	<0.1	55.64	5.32	2	404.4	99.8	0.4	0.77	<0.02	15.6	0.99	0.04	0.4	<0.01	<0.01	4			
RCS056	192	<1	0.59	15	<0.1	63.68	6.38	2	257.9	99.82	0.7	0.93	<0.02	27.1	0.83	<0.02	0.48	0.01	<0.01	6.6			
RCS057	121.2	<1	0.31	22	<0.1	57.47	5.81	2	325	99.8	0.5	0.85	<0.02	17.7	1.01	0.16	0.44	0.01	<0.01	4.7			
RCS059	128.7	<1	0.55	25	<0.1	55.16	4.52	2	385.2	99.82	0.4	0.7	0.02	14.1	0.94	0.02	0.37	<0.01	<0.01	3.9			
RCS060	179.8	2	0.36	8	<0.1	70.52	8.13	3	174	99.82	1	1.04	0.08	26	0.46	0.05	0.63	0.05	<0.01	6.4			
RCS061	157.1	<1	0.56	20	<0.1	59.06	6.25	2	291.8	99.82	0.5	0.88	0.03	20.6	1.02	0.1	0.46	0.01	<0.01	5.1			
RCS062	264.1	<1	0.62	9	0.9	74.52	3.82	4	180.7	99.83	1	0.44	0.04	22.6	0.64	0.03	0.43	0.02	0.04	9.7			
RCS063	282.1	<1	0.84	9	<0.1	70.25	5.94	4	145.5	99.81	1	0.88	0.05	31.5	0.55	0.06	0.54	0.02	<0.01	4.6			
RCS064	239.4	<1	0.85	10	<0.1	69.09	7.37	4	152.7	99.83	0.8	1.04	0.06	29.6	0.53	<0.02	0.58	0.01	<0.01	7.4			
RCS065	224.2	<1	0.8	9	<0.1	67.91	7.47	3	176.3	99.83	0.9	1.03	<0.02	29.2	0.54	<0.02	0.57	0.06	<0.01	8.4			
RCS066	221.3	<1	0.56	10	<0.1	68.39	7.43	4	197.4	99.82	0.8	1.04	<0.02	29.2	0.55	<0.02	0.58	0.03	<0.01	6.4			
RCS067	222.9	2	0.7	10	<0.1	68.57	6.3	3	180.7	99.83	0.9	0.92	0.02	29.3	0.57	<0.02	0.52	0.01	<0.01	5.3			
RCS068	138.8	<1	1.12	15	0.4	63.29	3.78	1	131.9	99.87	0.3	0.45	0.57	9.3	0.76	0.05	0.23	0.06	<0.01	3.1			
RCS069	112.9	<1	1.38	17	<0.1	59.41	6.33	2	343.9	99.81	0.5	0.85	0.1	14.1	0.99	0.05	0.45	0.03	<0.01	4.1			
RCS070	79	1	2.73	18	0.1	57.83	6.21	2	353.8	99.83	0.4	0.85	0.03	9.9	1.12	<0.02	0.41	0.2	<0.01	3			
RCS071	175.4	<1	0.77	19	<0.1	61.74	8.42	2	317	99.79	0.8	1.24	<0.02	24.1	0.98	<0.02	0.64	0.01	<0.01	5.8			
RCS072	198.7	<1	0.77	11	0.3	66.78	7.37	2	207.3	99.83	0.8	1.02	0.03	20.5	0.63	0.04	0.56	0.17	<0.01	5			
RCS073	180.3	<1	0.78	18	<0.1	61.07	8.15	3	261.9	99.81	0.7	1.14	0.03	22.5	0.99	0.02	0.61	0.06	<0.01	5.2			
RCS075	216.9	<1	0.85	16	<0.1	63.04	6.53	3	242.8	99.81	0.9	0.91	0.04	28	0.87	<0.02	0.49	0.01	<0.01	5.9			
RCS076	193.2	2	0.71	18	<0.1	61.23	5.99	3	317.2	99.81	0.7	0.84	<0.02	25.1	0.83	<0.02	0.49	<0.01	<0.01	5.2			
RCS077	188.8	<1	0.37	18	<0.1	61.17	5.68	3	300.3	99.81	0.7	0.84	<0.02	23.5	0.8	<0.02	0.48	0.02	<0.01	5			
RCS078	8.9	2	2.59	17	<0.1	53.35	7.26	3	1736.5	99.65	0.7	1.03	0.66	22.8	0.81	<0.02	0.58	0.03	<0.01	5.7			
RCS079	194.9	<1	1.14	17	<0.1	61.83	7.82	3	261.1	99.82	0.9	1.12	0.03	23.2	0.95	<0.02	0.6	<0.01	<0.01	5.6			
RCS080	137.9	2	0.44	2	<0.1	75.67	4.02	1	161	99.89	0.6	0.49	<0.02	16.2	0.17	0.08	0.32	<0.01	<0.01	3.4			
RCS081	157.7	<1	0.32	3	0.2	75.65	4.18	1	207.8	99.87	0.6	0.83	0.13	15.9	0.17	0.06	0.59	<0.01	0.01	4			
RCS082	151.5	<1	0.24	3	<0.1	75.88	4.37	1	263.7	99.88	0.6	0.6	0.03	16.3	0.16	0.1	0.34	<0.01	<0.01	3.7			
RCS083	138.5	<1	0.26	2	<0.1	75.53	2.71	<1	171.3	99.91	0.6	0.32	0.02	16.7	0.16	0.05	0.24	<0.01	<0.01	3.3			
RCS084	34.7	<1	0.34	19	<0.1	57.3	5.7	3	422.5	99.84	0.5	0.77	0.02	5.9	1.06	0.04	0.4	<0.01	<0.01	1.6			
RCS086	47.6	<1	0.07	21	<0.1	53.68	5.31	1	708.4	99.79	0.3	0.7	<0.02	2.1	1.02	0.18	0.33	<0.01	<0.01	0.7			
RCS087	66.8	<1	0.05	5	<0.1	64.28	2.53	<1	427.5	99.83	0.2	0.24	0.04	2.8	0.36	0.06	0.1	0.53	0.01	0.8			
RCS089	87.4	<1	0.07	6	0.3	67.23	2.77	4	399.5	98.87	0.2	0.3	0.1	3.4	0.41	0.07	0.13	<0.01	0.08	3.6			
RCS090	71.6	1	0.1	5	0.1	68.33	1.3	2	338.8	99.84	0.3	0.15	0.07	2.2	0.35	0.06	0.07	0.02	0.02	1.2			
RCS091	156.2	1	0.23	4	1.1	66.65	0.61	<1	552.9	99.78	0.2	0.07	0.18	2.7	0.33	0.09	0.06	<0.01	0.15	2.3			
RCS092	139	<1	0.22	16	<0.1	60.88	4.65	2	342.1	99.83	0.5	0.63	<0.02	14.8	0.82	0.04	0.35	<0.01	<0.01	3.1			
RCS093	237.1	3	5.45	9	0.2	69.6	2.58	4	91.7	99.86	0.9	0.51	0.04	29.7	0.52	0.03	0.49	<0.01	<0.01	4.3			
RCS094	54.2	<1	0.37	8	0.8	73.91	6.33	3	265.3	99.86	0.9	1.08	0.31	45.1	0.29	0.03	0.68	<0.01	0.04	10.9			
RCS095	275.9	<1	0.29	22	0.1	73.7	3.07	11	315.7	99.85	0.2	0.48	0.77	7.1	0.82	0.13	0.27	<0.01	0.05	3.5			
RCS096	176.5	<1	0.39	14	<0.1	64.18	6.64	3	280.8	99.83	0.7	0.91	0.02	22.1	0.8	<0.02	0.47	0.04	<0.01	5			

Sample	Rb	PPMRe	PPBSb	PPMSc	PPMSe	PPMSiO2	pctSm	PPMSn	PPMSr	PPMSum	pctTa	PPMTb	PPMTe	PPMTh	PPMTiO2	pctTI	PPMTm	PPMTOT	C	pctTOT	S	pct U	PPM
RCS097	222.5	<1	3.28	9	<0.1	69.1	7.09	2	202.9	99.83	0.9	0.96	0.05	30	0.52	<0.02	0.54	<0.01	<0.01	<0.01	<0.01	<0.01	7.2
RCS098	254.8	<1	1.14	8	<0.1	69.67	4.52	1	126.3	99.85	0.9	0.6	0.02	29.8	0.49	<0.02	0.34	0.07	<0.01	<0.01	<0.01	<0.01	5.9
RCS099	248.5	<1	0.97	8	<0.1	69.15	6.79	3	159.6	99.83	0.9	0.94	<0.02	30.3	0.5	0.04	0.54	0.01	<0.01	<0.01	<0.01	<0.01	5
RCS100	247.6	<1	0.74	9	<0.1	69.07	6.89	3	140.4	99.83	1	0.96	<0.02	31.8	0.51	0.06	0.54	0.03	<0.01	<0.01	<0.01	<0.01	8.3
RCS101	239.1	<1	0.83	9	<0.1	69.38	7.15	4	146.6	99.83	0.9	0.97	<0.02	30.8	0.51	0.04	0.54	0.04	<0.01	<0.01	<0.01	<0.01	6.9
RCS102	232	1	0.75	9	<0.1	69.31	7.33	4	147.3	99.84	0.9	1.05	<0.02	30.3	0.5	<0.02	0.62	<0.01	<0.01	<0.01	<0.01	<0.01	4.7
RCS103	186.8	<1	1.8	12	5.4	71.78	1.31	6	58.7	99.88	0.4	0.14	0.15	7	0.64	0.06	0.14	0.21	0.37	0.37	0.37	0.37	3.3
RCS104	47	<1	1.98	23	<0.1	57.86	5.04	2	418.5	99.84	0.4	0.7	0.16	8.5	0.93	<0.02	0.36	<0.01	<0.01	<0.01	<0.01	<0.01	2.4
RCS105	177.3	<1	0.55	3	<0.1	78	2.43	<1	102.9	99.86	0.5	0.3	0.11	13.5	0.15	0.11	0.2	0.01	0.01	0.01	0.01	0.01	2.1
RCS106	235	<1	0.85	9	5.9	70.59	5.79	4	170.5	99.84	1	0.82	0.71	31.4	0.47	0.07	0.56	<0.01	0.02	0.02	0.02	0.02	10.6
RCS107	327.8	1	2.05	12	3.4	66.86	2.07	3	301.6	99.83	0.5	0.28	1.75	19.1	0.61	0.05	0.27	<0.01	0.41	0.41	0.41	0.41	9.9

Appendix D1 continued

Sample	V_PPM	W_PPM	Y_PPM	Yb_PPM	Zn_pct	Zn_PPM	Zr_PPM
RCS001	53	1.2	30.3	3.19	<0.01	78.8	215.2
RCS002	57	0.8	27.9	3.28	<0.01	89.2	220.8
RCS003	156	0.8	13	1.24	0.02	228.3	115.6
RCS006	106	0.6	13.3	1.26	<0.01	86.6	123.5
RCS007	134	0.9	12.8	1.16	<0.01	92.6	109.7
RCS009	158	0.8	13.5	1.3	<0.01	89.8	120.9
RCS010	16	2.4	18.8	1.86	<0.01	31.4	95.6
RCS011	28	1.3	14	1.51	<0.01	27.2	101
RCS012	27	<0.5	10.3	1.29	<0.01	13.8	89.4
RCS014	102	1.3	13.4	1.54	<0.01	44	165.9
RCS016	107	2	17.1	1.63	<0.01	83.1	111.6
RCS017	163	2.1	30.5	2.92	<0.01	50.8	234.8
RCS019	92	1.3	20.8	2.36	<0.01	34.7	221.5
RCS021	135	1.7	27.7	2.81	<0.01	32.1	334.6
RCS022	149	1.9	26.9	2.67	0.01	69.1	274.8
RCS023	63	1.4	13.9	1.44	<0.01	52.8	146.1
RCS024	88	1.8	16.2	1.67	0.02	189.9	169.9
RCS025	40	0.7	11.7	1.3	<0.01	50.7	144.7
RCS026	<8	1.4	13.7	1.76	<0.01	20.9	51.3
RCS027	<8	0.8	19.5	2.19	<0.01	10.2	58
RCS028	<8	1.4	15	1.87	<0.01	12.3	68.8
RCS029	<8	0.6	15.6	1.69	<0.01	5.6	75.2
RCS030	<8	1.5	23.7	2.18	<0.01	45	98.9
RCS031	124	1.9	21	2.17	0.01	141.8	219.7
RCS032	180	1.8	24	2.27	0.03	319.1	206.4
RCS033	166	0.9	22	2.17	0.03	248.7	210.6
RCS034	17	2	19.7	2.59	<0.01	25.7	179.6
RCS035	15	2.2	19.6	2.34	<0.01	52.4	162.1
RCS036	24	1.6	23.2	2.44	<0.01	33.7	169.2
RCS037	134	2	23.6	2.47	<0.01	44.5	262
RCS039	129	1.6	24.7	2.66	<0.01	47.4	308.2
RCS041	129	1.4	26.2	2.68	<0.01	49.2	294.1
RCS042	106	2.8	24.5	2.64	<0.01	49.3	323.5
RCS044	160	1.6	24.6	2.45	<0.01	21.7	245.2
RCS046	145	1.6	24	2.49	<0.01	43.7	269.9
RCS049	172	1.4	23.4	2.42	<0.01	35.1	235.6
RCS052	153	1.1	23.8	2.31	<0.01	33.6	197.5
RCS053	129	1	26.7	2.98	<0.01	41.3	325.9
RCS054	187	1.1	25.5	2.74	<0.01	52.8	241.1
RCS056	97	1.1	31.1	3.23	<0.01	31.7	344.5
RCS057	169	0.9	27.2	2.84	<0.01	46.8	271.7
RCS059	191	3.1	22.2	2.43	<0.01	35	182
RCS060	25	1.9	36.8	4.06	<0.01	25.9	417.5
RCS061	150	0.9	29.8	2.99	<0.01	42.4	302.8
RCS062	16	2.4	18.1	3.03	<0.01	3.6	529
RCS063	21	1.7	26.9	3.42	0.01	135.9	434.6
RCS064	20	2.1	34.4	3.85	<0.01	51.2	427.2
RCS065	21	2.3	35	3.81	<0.01	56.6	418.2
RCS066	21	2.1	35.4	3.89	<0.01	34.9	423.3
RCS067	22	2.2	30.5	3.52	<0.01	41.5	421.6
RCS068	119	1	13.8	1.48	0.01	84.5	143.1
RCS069	130	2.1	26.5	2.95	0.01	134.2	260.2
RCS070	128	3.8	27.5	2.65	<0.01	96.5	214.9
RCS071	90	19	40.9	4.36	<0.01	57.9	329.7
RCS072	32	3	33.7	3.82	<0.01	32.2	370.5
RCS073	93	2.3	37.7	3.92	<0.01	41.3	374.2
RCS075	102	3.5	30.5	3.2	<0.01	41.8	330.3
RCS076	122	2.5	28.5	3.39	<0.01	44.8	360.4

Sample	V_PPM	W_PPM	Y_PPM	Yb_PPM	Zn_pct	Zn_PPM	Zr_PPM
RCS077	131	2.3	28.1	3.16	<0.01	40	278.9
RCS078	166	2.3	34.7	3.77	<0.01	7.9	293.7
RCS079	96	2.4	36	3.99	<0.01	44.5	296.8
RCS080	23	1.8	18.2	2.35	<0.01	66.4	93.5
RCS081	21	1	37.7	3.98	0.01	110.2	111.9
RCS082	20	1.1	21.7	2.36	<0.01	43.3	100.6
RCS083	15	1.6	12.5	1.61	<0.01	20.6	87.3
RCS084	147	2.1	24.7	2.69	<0.01	23.9	166.2
RCS086	181	0.8	21.9	2.2	<0.01	24	121.1
RCS087	48	0.7	6.4	0.61	0.03	281.7	106.3
RCS089	55	15.4	10.3	0.83	0.02	89.7	101.1
RCS090	54	8.4	4.2	0.52	<0.01	10.5	109.9
RCS091	57	5.4	3.3	0.44	<0.01	42.1	99.6
RCS092	130	1.2	21.3	2.13	<0.01	42.2	235.9
RCS093	15	2.1	21.8	3.26	<0.01	35.8	414.1
RCS094	18	5.7	36.4	4.77	<0.01	3.7	278.7
RCS095	166	10	18	1.75	<0.01	11	109.8
RCS096	69	1.6	30.4	3.02	<0.01	39.2	313.9
RCS097	17	1.8	32.5	3.56	<0.01	49.6	415.8
RCS098	17	1.2	18.6	2.43	<0.01	53.2	430.6
RCS099	14	1.3	32	3.7	<0.01	49.2	446.6
RCS100	16	1	31.9	3.57	<0.01	47.1	432.8
RCS101	14	1.3	33.1	3.67	<0.01	61.6	437.4
RCS102	20	1.2	37.5	3.93	<0.01	43.4	419.6
RCS103	93	1.9	5.9	1.08	<0.01	5.9	219.2
RCS104	164	0.5	23.1	2.38	<0.01	38.2	171.5
RCS105	21	1.9	11.5	1.25	0.03	259.2	90.3
RCS106	23	1.5	29.8	3.76	<0.01	24.8	435.2
RCS107	256	3	13.2	2.07	<0.01	17.4	242.7

Appendix D1 continued

Sample	Reference	Lithology	Structure	Type	Alt	Texture	Na_pct	Mg_pct	Al_pct	Si_pct	K_pct	Ca_pct	Ti_pct	V_pct	Cr_pct	Mn_pct	Fe_pct	Co_pct	O_pct	Total
RCS031	RCS031_5_7	Andesite	033SE82	Fracture	A4	VH	<0.1	11.3	9.1	17.3	0.2	1.3	<0.1	<0.1	<0.1	0.3	8.3	<0.2	38.4	86.2
RCS031	RCS031_5_11	Andesite	033SE82	Fracture	A4	VH	<0.1	13.7	9.6	17.4	0.1	1.0	<0.1	<0.1	<0.1	0.5	7.3	<0.2	40.1	89.7
RCS031	RCS031_7_1	Andesite	033SE82	Fracture	A4	VH	<0.1	12.9	9.3	14.8	<0.1	0.4	<0.1	<0.1	<0.1	0.6	9.2	<0.2	36.7	83.8
RCS031	RCS031_7_2	Andesite	033SE82	Fracture	A4	VH	<0.1	13.5	9.0	15.5	<0.1	0.5	<0.1	<0.1	<0.1	0.6	8.3	<0.2	37.4	84.7
RCS031	RCS031_7_3	Andesite	033SE82	Fracture	A4	VH	<0.1	14.1	9.0	16.7	<0.1	0.6	<0.1	<0.1	<0.1	0.5	7.5	<0.2	39.0	87.6
RCS031	RCS031_7_4	Andesite	033SE82	Fracture	A4	VH	<0.1	13.2	9.7	14.9	<0.1	0.4	<0.1	<0.1	<0.1	0.7	9.1	<0.2	37.3	85.2
RCS031	RCS031_7_5	Andesite	033SE82	Fracture	A4	VH	<0.1	13.8	10.0	15.4	<0.1	0.4	<0.1	<0.1	<0.1	0.6	9.5	<0.2	38.6	88.2
RCS031	RCS031_7_6	Andesite	033SE82	Fracture	A4	VH	<0.1	13.9	9.0	15.7	<0.1	0.6	<0.1	<0.1	<0.1	0.5	8.0	<0.2	37.8	85.4
RCS031	RCS031_7_7	Andesite	033SE82	Fracture	A4	VH	<0.1	13.3	9.1	16.2	<0.1	0.7	<0.1	<0.1	<0.1	0.5	8.2	<0.2	38.1	86.0
RCS031	RCS031_7_9	Andesite	033SE82	Fracture	A4	VH	<0.1	13.0	9.2	14.6	<0.1	0.4	<0.1	<0.1	<0.1	0.6	9.0	<0.2	36.2	82.9
RCS031	RCS031_8_2	Andesite	033SE82	Fracture	A4	VH	<0.1	13.0	9.4	16.5	<0.1	0.8	<0.1	<0.1	<0.1	0.6	8.2	<0.2	38.6	87.0
RCS031	RCS031_8_3	Andesite	033SE82	Fracture	A4	VH	<0.1	12.7	9.3	16.4	<0.1	0.7	<0.1	<0.1	<0.1	0.6	8.4	<0.2	38.2	86.2
RCS031	RCS031_8_5	Andesite	033SE82	Fracture	A4	VH	<0.1	12.2	9.2	15.8	<0.1	0.8	<0.1	<0.1	<0.1	0.7	8.6	<0.2	37.4	84.7
RCS031	RCS031_8_6	Andesite	033SE82	Fracture	A4	VH	0.1	13.1	10.0	17.0	<0.1	0.7	<0.1	<0.1	0.1	0.5	8.7	<0.2	39.9	90.0
RCS031	RCS031_8_7	Andesite	033SE82	Fracture	A4	VH	<0.1	11.6	9.0	15.4	<0.1	0.9	<0.1	<0.1	<0.1	0.7	8.3	<0.2	36.3	82.2
RCS031	RCS031_8_8	Andesite	033SE82	Fracture	A4	VH	<0.1	12.7	9.1	16.0	<0.1	0.8	<0.1	<0.1	<0.1	0.6	8.0	<0.2	37.5	84.6
RCS031	RCS031_10_1	Andesite	033SE82	Fracture	A4	Replacement	<0.1	14.0	9.7	17.7	<0.1	1.3	<0.1	<0.1	<0.1	0.5	7.6	<0.2	41.0	91.8
RCS031	RCS031_10_2	Andesite	033SE82	Fracture	A4	Replacement	0.1	11.9	8.5	15.5	<0.1	1.1	<0.1	<0.1	<0.1	0.5	7.6	<0.2	35.8	80.9
RCS031	RCS031_12_4	Andesite	033SE82	Fracture	A4	Replacement	<0.1	12.3	8.9	15.7	<0.1	1.1	<0.1	<0.1	<0.1	0.5	8.2	<0.2	36.8	83.5
RCS031	RCS031_12_7	Andesite	033SE82	Fracture	A4	Replacement	0.1	13.1	9.4	17.1	<0.1	1.1	<0.1	<0.1	<0.1	0.4	7.5	<0.2	39.3	88.1
RCS031	RCS031_16_2	Andesite	033SE82	Fracture	A4	VH	<0.1	13.0	9.3	15.6	<0.1	0.5	<0.1	<0.1	<0.1	0.5	8.7	<0.2	37.5	85.1
RCS031	RCS031_20_1	Andesite	033SE82	Fracture	A4	Replacement	<0.1	11.9	9.2	16.8	<0.1	1.3	<0.1	<0.1	<0.1	0.5	7.7	<0.2	38.1	85.4
RCS031	RCS031_20_2	Andesite	033SE82	Fracture	A4	Replacement	<0.1	12.9	9.4	16.9	<0.1	1.1	<0.1	<0.1	<0.1	0.4	8.8	<0.2	39.3	88.9
RCS031	RCS031_20_3	Andesite	033SE82	Fracture	A4	Replacement	0.1	12.7	9.5	16.7	<0.1	1.2	<0.1	<0.1	<0.1	0.4	8.2	<0.2	38.9	87.9
RCS031	RCS031_20_5	Andesite	033SE82	Fracture	A4	Replacement	0.1	13.0	9.7	17.9	<0.1	1.1	<0.1	<0.1	<0.1	0.5	8.0	<0.2	40.6	90.8
RCS033	RCS033_6_7	Andesite	NA	NA	A4	Replacement	<0.1	13.9	9.7	14.7	<0.1	0.3	<0.1	<0.1	<0.1	0.5	8.3	<0.2	37.2	84.6
RCS033	RCS033_6_8	Andesite	NA	NA	A4	Replacement	<0.1	13.8	9.9	14.2	<0.1	0.3	<0.1	<0.1	<0.1	0.4	9.2	<0.2	37.0	84.8
RCS033	RCS033_6_9	Andesite	NA	NA	A4	Replacement	<0.1	14.3	10.2	15.4	<0.1	0.4	<0.1	<0.1	<0.1	0.5	8.4	<0.2	38.8	87.8
RCS033	RCS033_6_10	Andesite	NA	NA	A4	Replacement	<0.1	13.8	10.6	14.6	<0.1	0.3	<0.1	<0.1	0.1	0.5	9.3	<0.2	38.2	87.4

Sample	Reference	Lithology	Structure	Type	Alt	Texture	Na_pct	Mg_pct	Al_pct	Si_pct	K_pct	Ca_pct	Ti_pct	V_pct	Cr_pct	Mn_pct	Fe_pct	Co_pct	O_pct	Total
RCS033	RCS033_9_3	Andesite	NA	NA	A4	L Patches	<0.1	13.9	11.0	14.7	<0.1	0.2	<0.1	<0.1	<0.1	0.4	9.1	<0.2	38.5	87.8
RCS033	RCS033_9_4	Andesite	NA	NA	A4	L Patches	<0.1	13.3	9.4	14.2	<0.1	0.3	<0.1	<0.1	0.1	0.5	8.6	<0.2	36.0	82.4
RCS033	RCS033_11_1	Andesite	NA	NA	A4	L Patches	<0.1	14.0	10.3	14.2	<0.1	0.2	<0.1	<0.1	0.2	0.4	9.2	<0.2	37.5	86.0
RCS033	RCS033_11_2	Andesite	NA	NA	A4	L Patches	<0.1	14.1	10.5	14.8	<0.1	0.3	<0.1	<0.1	0.2	0.4	9.3	<0.2	38.5	88.2
RCS033	RCS033_11_4	Andesite	NA	NA	A4	L Patches	<0.1	13.8	9.6	14.5	<0.1	0.3	<0.1	<0.1	0.6	0.4	9.3	<0.2	37.5	86.2
RCS033	RCS033_11_6	Andesite	NA	NA	A4	L Patches	<0.1	14.1	10.0	14.7	<0.1	0.4	<0.1	<0.1	0.6	0.4	9.2	<0.2	38.1	87.3
RCS033	RCS033_11_7	Andesite	NA	NA	A4	L Patches	<0.1	14.0	10.7	13.8	<0.1	0.2	<0.1	<0.1	0.7	0.4	9.5	<0.2	37.7	86.8
RCS033	RCS033_12_7	Andesite	NA	NA	A4	L Patches	<0.1	13.2	9.4	13.9	<0.1	0.3	<0.1	<0.1	0.8	0.4	9.0	<0.2	36.0	82.9
RCS033	RCS033_12_9	Andesite	NA	NA	A4	L Patches	<0.1	13.8	10.3	14.4	<0.1	0.4	<0.1	<0.1	0.8	0.3	9.0	<0.2	37.9	86.9
RCS033	RCS033_12_10	Andesite	NA	NA	A4	L Patches	<0.1	14.4	9.8	14.9	<0.1	0.3	<0.1	<0.1	0.3	0.4	8.7	<0.2	38.0	86.7
RCS033	RCS033_12_11	Andesite	NA	NA	A4	L Patches	<0.1	13.6	9.7	15.2	<0.1	0.4	<0.1	<0.1	0.2	0.5	9.2	<0.2	38.0	86.9
RCS033	RCS033_12_12	Andesite	NA	NA	A4	L Patches	<0.1	14.1	9.7	14.7	<0.1	0.4	<0.1	<0.1	0.3	0.5	9.0	<0.2	37.6	86.2
RCS033	RCS033_15_1	Andesite	NA	NA	A4	Replacement	<0.1	14.4	9.8	14.6	<0.1	0.3	<0.1	<0.1	<0.1	0.5	8.4	<0.2	37.5	85.4
RCS033	RCS033_15_2	Andesite	NA	NA	A4	Replacement	<0.1	14.2	10.1	14.9	<0.1	0.3	<0.1	<0.1	<0.1	0.4	8.2	<0.2	38.0	86.2
RCS033	RCS033_15_4	Andesite	NA	NA	A4	Replacement	<0.1	14.0	9.5	14.6	<0.1	0.3	<0.1	<0.1	<0.1	0.5	8.2	<0.2	36.8	83.9
RCS033	RCS033_17_1	Andesite	NA	NA	A4	L Patches	<0.1	15.1	10.4	15.4	<0.1	0.2	<0.1	<0.1	<0.1	0.5	8.8	<0.2	39.6	90.1
RCS033	RCS033_17_2	Andesite	NA	NA	A4	L Patches	<0.1	14.8	10.0	15.1	<0.1	0.2	<0.1	<0.1	<0.1	0.4	8.6	<0.2	38.6	87.7
RCS033	RCS033_17_3	Andesite	NA	NA	A4	L Patches	<0.1	14.7	10.2	15.4	<0.1	0.3	<0.1	<0.1	<0.1	0.5	8.8	<0.2	39.0	88.8
RCS033	RCS033_17_4	Andesite	NA	NA	A4	L Patches	<0.1	13.8	9.6	14.8	<0.1	0.3	<0.1	<0.1	<0.1	0.4	8.7	<0.2	37.3	84.9
RCS033	RCS033_17_5	Andesite	NA	NA	A4	L Patches	<0.1	14.2	9.6	14.8	<0.1	0.3	<0.1	<0.1	<0.1	0.4	8.5	<0.2	37.5	85.4
RCS033	RCS033_17_7	Andesite	NA	NA	A4	L Patches	<0.1	13.8	9.6	14.1	<0.1	0.2	<0.1	<0.1	<0.1	0.5	9.0	<0.2	36.5	83.7
RCS033	RCS033_17_8	Andesite	NA	NA	A4	L Patches	<0.1	13.6	10.0	14.8	<0.1	0.3	<0.1	<0.1	<0.1	0.4	8.7	<0.2	37.6	85.4
RCS033	RCS033_18_7	Andesite	NA	NA	A4	L Patches	<0.1	13.5	10.0	14.3	<0.1	0.3	<0.1	<0.1	<0.1	0.5	8.5	<0.2	36.8	83.9
RCS033	RCS033_18_8	Andesite	NA	NA	A4	L Patches	<0.1	13.5	9.4	14.2	<0.1	0.2	<0.1	<0.1	<0.1	0.5	8.6	<0.2	36.1	82.4
RCS033	RCS033_18_9	Andesite	NA	NA	A4	L Patches	<0.1	13.5	9.3	14.3	<0.1	0.2	<0.1	<0.1	<0.1	0.5	8.5	<0.2	36.2	82.5
RCS033	RCS033_18_10	Andesite	NA	NA	A4	L Patches	<0.1	14.5	10.1	14.8	<0.1	0.2	<0.1	<0.1	<0.1	0.5	8.5	<0.2	38.1	86.6
RCS104	RCS104_6_3	Andesite	NA	NA	A4	Replacement	<0.1	13.0	9.1	14.2	<0.1	0.3	<0.1	0.1	<0.1	0.1	12.2	<0.2	36.6	85.6
RCS104	RCS104_6_6	Andesite	NA	NA	A4	Replacement	<0.1	12.9	8.9	13.8	<0.1	0.2	<0.1	<0.1	<0.1	<0.1	11.6	<0.2	35.7	83.1
RCS104	RCS104_6_7	Andesite	NA	NA	A4	Replacement	<0.1	13.9	9.1	14.3	<0.1	0.3	<0.1	<0.1	<0.1	<0.1	11.4	<0.2	36.9	85.8

Sample	Reference	Lithology	Structure	Type	Alt	Texture	Na_pct	Mg_pct	Al_pct	Si_pct	K_pct	Ca_pct	Ti_pct	V_pct	Cr_pct	Mn_pct	Fe_pct	Co_pct	O_pct	Total
RCS104	RCS104_6_8	Andesite	NA	NA	A4	Replacement	<0.1	13.9	9.3	14.8	<0.1	0.2	<0.1	<0.1	<0.1	0.1	12.1	<0.2	37.9	88.2
RCS104	RCS104_6_9	Andesite	NA	NA	A4	Replacement	<0.1	13.4	9.6	14.1	<0.1	0.2	<0.1	<0.1	<0.1	0.1	12.1	<0.2	37.0	86.5
RCS104	RCS104_6_10	Andesite	NA	NA	A4	Replacement	<0.1	13.3	9.0	13.8	<0.1	0.1	<0.1	<0.1	<0.1	<0.1	11.8	<0.2	35.9	83.8
RCS104	RCS104_6_11	Andesite	NA	NA	A4	Replacement	<0.1	13.7	9.5	14.7	<0.1	0.1	<0.1	<0.1	<0.1	0.1	11.9	<0.2	37.7	87.7
RCS104	RCS104_8_3	Andesite	NA	NA	A4	Replacement	<0.1	12.4	9.4	13.9	<0.1	0.2	<0.1	<0.1	<0.1	0.1	13.3	<0.2	36.3	85.7
RCS104	RCS104_11_8	Andesite	NA	NA	A4	Replacement	<0.1	12.6	9.1	14.6	<0.1	0.2	<0.1	<0.1	<0.1	0.2	12.0	<0.2	36.7	85.5
RCS104	RCS104_11_9	Andesite	NA	NA	A4	Replacement	<0.1	12.6	9.2	13.6	<0.1	<0.1	<0.1	<0.1	<0.1	0.2	12.0	<0.2	35.4	82.9
RCS104	RCS104_11_11	Andesite	NA	NA	A4	Replacement	<0.1	11.8	9.0	13.2	<0.1	0.1	<0.1	<0.1	<0.1	0.2	12.4	<0.2	34.5	81.2
RCS104	RCS104_13_11	Andesite	NA	NA	A4	Replacement	<0.1	12.6	8.6	14.9	<0.1	0.4	<0.1	<0.1	<0.1	0.3	11.2	<0.2	36.4	84.4
RCS104	RCS104_13_15	Andesite	NA	NA	A4	Replacement	<0.1	13.2	8.9	13.9	<0.1	<0.1	<0.1	<0.1	<0.1	0.2	11.4	<0.2	35.8	83.3
RCS104	RCS104_13_16	Andesite	NA	NA	A4	Replacement	<0.1	12.9	9.1	14.3	<0.1	0.2	<0.1	<0.1	<0.1	0.2	12.2	<0.2	36.6	85.6
RCS104	RCS104_13_17	Andesite	NA	NA	A4	Replacement	<0.1	12.9	9.4	13.8	<0.1	0.1	<0.1	<0.1	<0.1	0.3	11.8	<0.2	36.2	84.5
RCS104	RCS104_13_18	Andesite	NA	NA	A4	Replacement	<0.1	12.4	9.3	13.6	<0.1	<0.1	<0.1	<0.1	<0.1	0.3	11.9	<0.2	35.6	83.1
RCS104	RCS104_15_7	Andesite	NA	NA	A4	Replacement	<0.1	12.4	8.7	14.5	<0.1	0.2	<0.1	<0.1	<0.1	0.1	11.3	<0.2	35.9	83.3
RCS104	RCS104_15_16	Andesite	NA	NA	A4	Replacement	<0.1	12.7	8.6	15.2	<0.1	0.4	<0.1	<0.1	<0.1	0.2	10.8	<0.2	36.6	84.5
RCS104	RCS104_19_3	Andesite	NA	NA	A4	Replacement	<0.1	12.7	9.2	13.6	<0.1	0.2	<0.1	<0.1	<0.1	0.3	12.3	<0.2	35.7	83.9
RCS104	RCS104_19_4	Andesite	NA	NA	A4	Replacement	<0.1	13.4	9.5	14.0	<0.1	0.2	<0.1	<0.1	<0.1	0.4	12.2	<0.2	37.0	86.7
RCS104	RCS104_19_5	Andesite	NA	NA	A4	Replacement	<0.1	12.8	9.6	15.0	<0.1	0.2	<0.1	<0.1	<0.1	0.2	12.8	<0.2	37.9	88.5
RCS104	RCS104_19_6	Andesite	NA	NA	A4	Replacement	<0.1	12.8	9.6	14.4	<0.1	0.3	<0.1	<0.1	<0.1	0.2	11.8	<0.2	36.8	86.0
RCS104	RCS104_19_7	Andesite	NA	NA	A4	Replacement	<0.1	12.8	8.8	14.8	<0.1	0.3	<0.1	<0.1	<0.1	0.2	11.5	<0.2	36.6	85.0
RCS104	RCS104_19_8	Andesite	NA	NA	A4	Replacement	<0.1	13.2	8.8	15.0	<0.1	0.2	<0.1	<0.1	<0.1	0.2	11.2	<0.2	37.0	85.7
RCS104	RCS104_19_13	Andesite	NA	NA	A4	Replacement	<0.1	13.5	9.3	13.9	<0.1	0.1	<0.1	<0.1	<0.1	<0.1	11.8	<0.2	36.5	85.1
RCS104	RCS104_19_18	Andesite	NA	NA	A4	Replacement	<0.1	12.6	8.9	14.0	<0.1	0.2	<0.1	<0.1	<0.1	0.3	12.0	<0.2	35.7	83.6
RCS104	RCS104_19_19	Andesite	NA	NA	A4	Replacement	<0.1	13.1	9.6	14.1	<0.1	0.1	<0.1	<0.1	<0.1	<0.1	11.0	<0.2	36.5	84.4
RCS104	RCS104_20_8	Andesite	NA	NA	A4	Replacement	<0.1	13.0	9.0	14.2	<0.1	0.2	<0.1	<0.1	<0.1	0.3	11.9	<0.2	36.4	85.0
RCS104	RCS104_20_11	Andesite	NA	NA	A4	Replacement	<0.1	13.4	9.0	14.0	<0.1	<0.1	<0.1	<0.1	<0.1	0.1	11.6	<0.2	36.2	84.3
RCS104	RCS104_20_13	Andesite	NA	NA	A4	Replacement	<0.1	13.0	9.1	14.7	<0.1	0.3	<0.1	<0.1	<0.1	0.2	11.5	<0.2	36.9	85.7
RCS003	RCS003_6_2	Monzodiorite	144SW87	Fracture	A4	Replacement	<0.1	10.9	9.2	16.0	<0.1	0.7	<0.1	<0.1	<0.1	0.4	14.0	<0.2	38.0	89.0
RCS003	RCS003_6_3	Monzodiorite	144SW87	Fracture	A4	Replacement	<0.1	10.5	9.4	15.7	0.1	0.7	<0.1	<0.1	<0.1	0.5	14.7	<0.2	37.9	89.5

Sample	Reference	Lithology	Structure	Type	Alt	Texture	Na_pct	Mg_pct	Al_pct	Si_pct	K_pct	Ca_pct	Ti_pct	V_pct	Cr_pct	Mn_pct	Fe_pct	Co_pct	O_pct	Total
RCS003	RCS003_6_4	Monzodiorite	144SW87	Fracture	A4	Replacement	<0.1	11.2	8.9	15.2	<0.1	0.6	<0.1	<0.1	<0.1	0.4	14.0	<0.2	36.9	87.2
RCS003	RCS003_6_5	Monzodiorite	144SW87	Fracture	A4	Replacement	<0.1	10.7	8.8	15.1	<0.1	0.7	<0.1	<0.1	<0.1	0.4	14.0	<0.2	36.5	86.1
RCS003	RCS003_6_7	Monzodiorite	144SW87	Fracture	A4	Replacement	<0.1	10.0	8.2	14.9	<0.1	0.8	<0.1	<0.1	<0.1	0.3	13.2	<0.2	35.1	82.5
RCS003	RCS003_6_10	Monzodiorite	144SW87	Fracture	A4	Replacement	<0.1	10.2	9.1	15.3	<0.1	0.6	<0.1	<0.1	<0.1	0.4	14.5	<0.2	36.8	87.0
RCS003	RCS003_8_2	Monzodiorite	144SW87	Fracture	A4	Replacement	<0.1	9.0	10.1	13.5	0.1	0.3	<0.1	<0.1	<0.1	0.6	17.7	<0.2	35.8	87.1
RCS003	RCS003_8_3	Monzodiorite	144SW87	Fracture	A4	Replacement	<0.1	10.9	8.9	15.6	0.1	0.7	<0.1	<0.1	<0.1	0.4	13.8	<0.2	37.4	87.8
RCS003	RCS003_8_5	Monzodiorite	144SW87	Fracture	A4	Replacement	<0.1	10.4	8.1	14.8	<0.1	0.7	<0.1	<0.1	<0.1	0.4	12.9	<0.2	35.0	82.3
RCS003	RCS003_8_6	Monzodiorite	144SW87	Fracture	A4	Replacement	<0.1	10.9	8.7	15.5	<0.1	0.9	0.2	<0.1	<0.1	0.4	13.3	<0.2	37.1	86.9
RCS003	RCS003_8_10	Monzodiorite	144SW87	Fracture	A4	Replacement	0.1	10.2	9.0	14.8	<0.1	0.6	<0.1	<0.1	<0.1	0.5	14.8	<0.2	36.3	86.2
RCS003	RCS003_8_11	Monzodiorite	144SW87	Fracture	A4	Replacement	0.1	10.7	8.8	15.5	<0.1	0.7	<0.1	<0.1	<0.1	0.3	14.1	<0.2	37.1	87.4
RCS003	RCS003_8_12	Monzodiorite	144SW87	Fracture	A4	Replacement	<0.1	9.6	8.2	15.3	0.1	0.7	<0.1	<0.1	<0.1	0.3	14.4	<0.2	35.6	84.2
RCS003	RCS003_8_13	Monzodiorite	144SW87	Fracture	A4	Replacement	<0.1	11.5	9.3	16.3	<0.1	0.7	<0.1	<0.1	<0.1	0.3	13.5	<0.2	38.7	90.3
RCS003	RCS003_8_15	Monzodiorite	144SW87	Fracture	A4	Replacement	0.1	10.3	9.6	14.8	<0.1	0.5	<0.1	<0.1	<0.1	0.5	14.8	<0.2	36.9	87.6
RCS003	RCS003_10_11	Monzodiorite	144SW87	Fracture	A4	Replacement	<0.1	10.6	8.5	15.6	<0.1	0.8	<0.1	<0.1	<0.1	0.5	13.5	<0.2	36.6	86.1
RCS003	RCS003_10_13	Monzodiorite	144SW87	Fracture	A4	Replacement	0.1	11.3	9.1	16.5	<0.1	0.7	<0.1	<0.1	<0.1	0.3	13.3	<0.2	38.6	90.0
RCS003	RCS003_10_14	Monzodiorite	144SW87	Fracture	A4	Replacement	<0.1	10.8	9.0	15.9	<0.1	0.8	<0.1	<0.1	<0.1	0.3	13.6	<0.2	37.5	87.8
RCS003	RCS003_10_17	Monzodiorite	144SW87	Fracture	A4	Replacement	<0.1	10.8	9.0	15.7	<0.1	0.8	<0.1	<0.1	<0.1	0.4	13.6	<0.2	37.3	87.5
RCS003	RCS003_10_18	Monzodiorite	144SW87	Fracture	A4	Replacement	<0.1	11.0	8.6	15.7	<0.1	0.8	<0.1	<0.1	<0.1	0.2	13.1	<0.2	37.0	86.4
RCS003	RCS003_10_19	Monzodiorite	144SW87	Fracture	A4	Replacement	<0.1	10.8	9.1	15.6	<0.1	0.7	<0.1	<0.1	<0.1	0.4	14.2	<0.2	37.4	88.3
RCS003	RCS003_12_4	Monzodiorite	144SW87	Fracture	A4	Replacement	<0.1	11.0	8.8	16.3	0.1	0.8	<0.1	<0.1	<0.1	0.4	13.8	<0.2	38.1	89.2
RCS003	RCS003_14_2	Monzodiorite	144SW87	Fracture	A4	Replacement	<0.1	10.5	8.9	13.9	0.1	0.3	<0.1	<0.1	<0.1	0.4	14.9	0.2	35.2	84.2
RCS003	RCS003_14_3	Monzodiorite	144SW87	Fracture	A4	Replacement	<0.1	11.9	9.5	14.8	<0.1	0.3	<0.1	<0.1	<0.1	0.3	15.4	<0.2	37.8	89.9
RCS003	RCS003_14_4	Monzodiorite	144SW87	Fracture	A4	Replacement	<0.1	11.0	8.8	13.5	<0.1	0.2	<0.1	<0.1	<0.1	0.5	15.8	<0.2	35.2	85.0
RCS003	RCS003_14_5	Monzodiorite	144SW87	Fracture	A4	Replacement	<0.1	10.4	8.8	14.9	<0.1	0.6	<0.1	<0.1	<0.1	0.4	14.4	<0.2	36.2	85.6
RCS003	RCS003_14_6	Monzodiorite	144SW87	Fracture	A4	Replacement	<0.1	10.9	8.6	15.5	<0.1	0.6	<0.1	<0.1	<0.1	0.4	13.6	<0.2	36.7	86.1
RCS003	RCS003_14_7	Monzodiorite	144SW87	Fracture	A4	Replacement	<0.1	11.2	9.2	13.9	<0.1	0.3	<0.1	<0.1	<0.1	0.3	14.9	<0.2	35.9	85.6

Sample	Reference	Lithology	Structure	Type	Alt	Texture	Na_pct	Mg_pct	Al_pct	Si_pct	K_pct	Ca_pct	Ti_pct	V_pct	Cr_pct	Mn_pct	Fe_pct	Co_pct	O_pct	Total
RCS003	RCS003_14_8	Monzodiorite	144SW87	Fracture	A4	Replacement	<0.1	10.6	8.5	14.5	<0.1	0.5	<0.1	<0.1	<0.1	0.4	13.9	<0.2	35.6	84.0
RCS003	RCS003_15_5	Monzodiorite	144SW87	Fracture	A4	Replacement	<0.1	9.4	8.7	13.8	0.1	0.6	<0.1	<0.1	<0.1	0.4	14.3	<0.2	34.1	81.4
RCS009	RCS009_6_1	Monzonite	026SE87	Fracture vein	A4	Replacement	<0.1	12.1	8.7	14.7	<0.1	0.7	<0.1	0.1	<0.1	0.2	11.1	<0.2	35.9	83.3
RCS009	RCS009_6_2	Monzonite	026SE87	Fracture vein	A4	Replacement	<0.1	12.0	9.4	14.7	<0.1	0.5	<0.1	<0.1	<0.1	0.2	12.6	<0.2	36.9	86.2
RCS009	RCS009_6_3	Monzonite	026SE87	Fracture vein	A4	Replacement	<0.1	12.1	8.5	15.1	<0.1	0.6	<0.1	<0.1	<0.1	0.2	11.1	<0.2	36.1	83.8
RCS009	RCS009_6_4	Monzonite	026SE87	Fracture vein	A4	Replacement	<0.1	12.0	8.2	14.7	<0.1	0.7	<0.1	<0.1	<0.1	0.3	11.1	<0.2	35.6	82.6
RCS009	RCS009_6_5	Monzonite	026SE87	Fracture vein	A4	Replacement	<0.1	11.9	9.4	14.8	<0.1	0.5	<0.1	<0.1	<0.1	0.2	11.8	<0.2	36.6	85.2
RCS009	RCS009_7_19	Monzonite	026SE87	Fracture vein	A4	Replacement	<0.1	12.3	9.7	14.5	<0.1	0.4	<0.1	<0.1	<0.1	0.3	12.7	<0.2	37.3	87.1
RCS009	RCS009_9_5	Monzonite	026SE87	Fracture vein	A4	Replacement	<0.1	11.0	8.8	14.7	<0.1	0.8	<0.1	<0.1	<0.1	<0.1	12.0	<0.2	35.7	83.1
RCS009	RCS009_9_6	Monzonite	026SE87	Fracture vein	A4	Replacement	<0.1	10.3	8.2	14.0	<0.1	0.8	<0.1	0.1	<0.1	0.3	11.9	<0.2	33.8	79.2
RCS009	RCS009_9_12	Monzonite	026SE87	Fracture vein	A4	Replacement	0.1	12.5	9.3	15.0	<0.1	0.5	<0.1	<0.1	<0.1	0.3	11.5	<0.2	37.3	86.5
RCS009	RCS009_12_1	Monzonite	026SE87	Fracture vein	A4	Replacement	<0.1	11.6	8.1	15.4	<0.1	0.9	<0.1	<0.1	<0.1	0.2	8.0	<0.2	35.1	79.3
RCS009	RCS009_14_1	Monzonite	026SE87	Fracture vein	A4	L Patches	<0.1	11.4	8.8	14.9	<0.1	0.7	<0.1	<0.1	<0.1	0.2	10.7	<0.2	35.8	82.5
RCS009	RCS009_14_3	Monzonite	026SE87	Fracture vein	A4	L Patches	<0.1	11.5	10.3	14.1	0.1	0.3	<0.1	<0.1	<0.1	0.2	12.9	<0.2	36.7	86.0
RCS009	RCS009_14_4	Monzonite	026SE87	Fracture vein	A4	L Patches	<0.1	11.3	8.7	14.7	<0.1	0.8	<0.1	<0.1	<0.1	0.2	11.1	<0.2	35.6	82.3
RCS009	RCS009_14_5	Monzonite	026SE87	Fracture vein	A4	L Patches	<0.1	11.5	10.0	13.8	<0.1	0.4	<0.1	<0.1	<0.1	0.2	12.9	<0.2	36.3	85.1
RCS009	RCS009_14_7	Monzonite	026SE87	Fracture vein	A4	L Patches	<0.1	10.5	9.6	13.1	<0.1	0.3	<0.1	<0.1	<0.1	0.2	13.0	<0.2	34.4	81.1
RCS009	RCS009_14_8	Monzonite	026SE87	Fracture vein	A4	L Patches	<0.1	11.7	9.2	14.0	<0.1	0.5	<0.1	<0.1	<0.1	0.2	12.3	0.2	35.8	84.0
RCS009	RCS009_14_9	Monzonite	026SE87	Fracture vein	A4	L Patches	<0.1	9.7	9.7	14.5	0.1	0.6	<0.1	<0.1	<0.1	0.3	13.5	<0.2	35.9	84.2
RCS009	RCS009_14_10	Monzonite	026SE87	Fracture vein	A4	L Patches	<0.1	10.9	9.9	15.3	0.3	0.6	<0.1	<0.1	<0.1	0.2	11.8	<0.2	37.3	86.4
RCS009	RCS009_14_11	Monzonite	026SE87	Fracture vein	A4	L Patches	<0.1	9.1	10.1	14.5	0.4	0.5	<0.1	<0.1	<0.1	0.2	13.4	<0.2	35.6	83.6
RCS009	RCS009_14_12	Monzonite	026SE87	Fracture vein	A4	L Patches	<0.1	12.0	9.2	15.2	<0.1	0.8	<0.1	<0.1	<0.1	0.3	11.8	<0.2	37.3	86.6
RCS009	RCS009_17_3	Monzonite	026SE87	Fracture vein	A4	Replacement	<0.1	11.6	10.0	14.6	<0.1	0.5	<0.1	<0.1	<0.1	0.2	12.2	<0.2	37.0	86.1
RCS009	RCS009_17_6	Monzonite	026SE87	Fracture vein	A4	Replacement	<0.1	11.4	8.1	15.4	<0.1	1.1	<0.1	<0.1	<0.1	0.2	10.7	<0.2	35.9	82.7
RCS009	RCS009_19_1	Monzonite	026SE87	Fracture vein	A4	Replacement	<0.1	12.5	8.8	15.1	<0.1	0.6	<0.1	<0.1	<0.1	0.3	10.9	<0.2	36.7	84.8
RCS009	RCS009_19_2	Monzonite	026SE87	Fracture vein	A4	Replacement	<0.1	12.1	8.7	14.4	<0.1	0.6	<0.1	<0.1	<0.1	0.3	11.1	<0.2	35.7	82.9

Sample	Reference	Lithology	Structure	Type	Alt	Texture	Na_pct	Mg_pct	Al_pct	Si_pct	K_pct	Ca_pct	Ti_pct	V_pct	Cr_pct	Mn_pct	Fe_pct	Co_pct	O_pct	Total
RCS009	RCS009_19_4	Monzonite	026SE87	Fracture vein	A4	Replacement	0.1	12.0	8.7	15.3	<0.1	0.9	<0.1	<0.1	<0.1	0.3	11.2	<0.2	36.8	85.3
RCS006	RCS006_8_4	Monzonite	NA	NA	A3	Replacement	<0.1	13.1	8.6	15.3	<0.1	0.6	<0.1	<0.1	<0.1	0.4	13.4	0.2	37.8	89.2
RCS006	RCS006_8_5	Monzonite	NA	NA	A3	Replacement	<0.1	12.3	7.6	16.7	<0.1	0.7	<0.1	<0.1	<0.1	0.3	12.2	<0.2	37.8	87.6
RCS006	RCS006_9_7	Monzonite	NA	NA	A3	Replacement	<0.1	13.8	9.1	14.6	<0.1	0.1	<0.1	<0.1	<0.1	0.3	13.5	<0.2	37.8	89.3
RCS006	RCS006_11_3	Monzonite	NA	NA	A3	Replacement	<0.1	10.9	8.4	17.2	<0.1	0.8	0.1	<0.1	<0.1	0.2	12.1	<0.2	38.1	87.7
RCS006	RCS006_13_1	Monzonite	NA	NA	A3	L Patches	<0.1	12.7	8.7	14.4	<0.1	0.2	<0.1	<0.1	<0.1	0.3	12.8	<0.2	36.4	85.5
RCS006	RCS006_13_2	Monzonite	NA	NA	A3	L Patches	<0.1	13.5	9.0	15.3	<0.1	0.2	<0.1	<0.1	<0.1	0.4	12.7	<0.2	38.1	89.2
RCS006	RCS006_13_3	Monzonite	NA	NA	A3	L Patches	<0.1	13.0	8.9	15.2	<0.1	0.2	<0.1	<0.1	<0.1	0.4	13.0	<0.2	37.8	88.5
RCS006	RCS006_13_4	Monzonite	NA	NA	A3	L Patches	<0.1	11.1	8.0	14.4	<0.1	0.3	<0.1	<0.1	<0.1	0.4	12.7	<0.2	34.7	81.6
RCS006	RCS006_13_5	Monzonite	NA	NA	A3	L Patches	<0.1	12.2	8.7	14.4	<0.1	0.2	<0.1	<0.1	<0.1	0.5	13.2	<0.2	36.3	85.5
RCS006	RCS006_13_6	Monzonite	NA	NA	A3	L Patches	<0.1	12.7	8.7	14.4	<0.1	0.2	<0.1	<0.1	<0.1	0.3	13.0	<0.2	36.5	85.7
RCS006	RCS006_13_9	Monzonite	NA	NA	A3	L Patches	<0.1	12.3	8.6	14.8	<0.1	0.2	<0.1	<0.1	<0.1	0.4	12.8	<0.2	36.5	85.7
RCS006	RCS006_13_10	Monzonite	NA	NA	A3	L Patches	<0.1	13.8	9.3	14.9	<0.1	0.2	<0.1	<0.1	<0.1	0.4	13.2	<0.2	38.3	90.1
RCS006	RCS006_13_11	Monzonite	NA	NA	A3	L Patches	<0.1	11.2	8.5	15.7	<0.1	0.4	<0.1	<0.1	<0.1	0.4	13.1	<0.2	36.9	86.2
RCS006	RCS006_13_12	Monzonite	NA	NA	A3	L Patches	<0.1	12.7	8.9	14.5	<0.1	0.2	<0.1	<0.1	<0.1	0.5	13.1	<0.2	36.7	86.6
RCS006	RCS006_13_15	Monzonite	NA	NA	A3	L Patches	<0.1	10.9	8.5	17.8	<0.1	0.5	<0.1	<0.1	<0.1	0.3	11.9	<0.2	38.8	88.7
RCS016	RCS016_15_16	Andesite	NA	NA	A6	Patches	<0.1	12.4	10.8	13.7	<0.1	<0.1	<0.1	<0.1	<0.1	0.5	12.0	0.2	37.1	86.7
RCS016	RCS016_15_18	Andesite	NA	NA	A6	Patches	<0.1	11.7	10.2	13.4	<0.1	0.2	<0.1	<0.1	<0.1	0.5	11.1	<0.2	35.5	82.7
RCS016	RCS016_15_20	Andesite	NA	NA	A6	Patches	<0.1	11.2	11.0	13.7	<0.1	<0.1	<0.1	<0.1	<0.1	0.5	12.1	<0.2	36.4	85.0
RCS016	RCS016_15_21	Andesite	NA	NA	A6	Patches	<0.1	13.2	9.8	13.6	<0.1	0.1	<0.1	<0.1	<0.1	0.4	10.8	<0.2	36.3	84.2
RCS016	RCS016_15_24	Andesite	NA	NA	A6	Patches	<0.1	13.4	10.5	13.2	<0.1	<0.1	<0.1	<0.1	<0.1	0.5	11.5	<0.2	36.7	85.7
RCS016	RCS016_17_6	Andesite	NA	NA	A6	Patches	<0.1	13.1	10.1	13.2	<0.1	0.2	<0.1	<0.1	<0.1	0.5	11.2	<0.2	36.1	84.4
RCS016	RCS016_17_10	Andesite	NA	NA	A6	Patches	<0.1	11.2	9.7	14.1	0.1	0.2	<0.1	<0.1	<0.1	0.4	10.8	<0.2	35.4	82.0
RCS016	RCS016_19_4	Andesite	NA	NA	A6	Patches	<0.1	11.9	10.4	13.7	<0.1	0.2	<0.1	<0.1	<0.1	0.4	11.0	<0.2	36.1	83.7
RCS016	RCS016_19_5	Andesite	NA	NA	A6	Patches	<0.1	12.2	10.0	13.8	<0.1	0.2	<0.1	<0.1	<0.1	0.4	11.0	<0.2	36.1	83.7
RCS017	RCS017_9_1	Monzonite	242NW8 2	Fracture vein	A3	Replacement	<0.1	13.5	9.8	13.5	<0.1	<0.1	<0.1	<0.1	<0.1	0.3	12.9	<0.2	36.7	86.6
RCS017	RCS017_9_4	Monzonite	242NW8 2	Fracture vein	A3	Replacement	<0.1	12.8	9.5	13.4	<0.1	<0.1	<0.1	<0.1	<0.1	0.3	13.7	<0.2	36.3	86.1
RCS017	RCS017_9_5	Monzonite	242NW8 2	Fracture vein	A3	Replacement	<0.1	13.2	10.0	13.6	<0.1	<0.1	<0.1	<0.1	<0.1	0.3	13.3	<0.2	37.0	87.2
RCS017	RCS017_9_6	Monzonite	242NW8 2	Fracture vein	A3	Replacement	<0.1	12.9	9.9	13.3	<0.1	<0.1	<0.1	<0.1	<0.1	0.3	13.8	<0.2	36.5	86.5

Sample	Reference	Lithology	Structure	Type	Alt	Texture	Na_pct	Mg_pct	Al_pct	Si_pct	K_pct	Ca_pct	Ti_pct	V_pct	Cr_pct	Mn_pct	Fe_pct	Co_pct	O_pct	Total
RCS017	RCS017_9_8	Monzonite	242NW8 2	Fracture vein	A3	Replacement	<0.1	12.5	9.2	13.6	<0.1	<0.1	<0.1	<0.1	<0.1	0.3	14.7	<0.2	36.3	86.5
RCS019	RCS019_7_13	Granodiorite	NA	NA	A2	Replacement	<0.1	10.3	8.9	13.4	<0.1	0.1	<0.1	<0.1	<0.1	0.2	18.6	<0.2	35.5	87.0
RCS019	RCS019_9_1	Granodiorite	NA	NA	A2	Replacement	<0.1	11.4	8.0	14.5	0.3	0.2	<0.1	<0.1	<0.1	0.1	16.0	<0.2	36.0	86.5
RCS019	RCS019_9_3	Granodiorite	NA	NA	A2	Replacement	<0.1	11.8	8.1	14.1	<0.1	0.2	<0.1	<0.1	<0.1	0.1	15.5	<0.2	35.6	85.3
RCS019	RCS019_9_4	Granodiorite	NA	NA	A2	Replacement	<0.1	11.8	8.3	14.8	<0.1	0.3	<0.1	<0.1	<0.1	0.1	15.7	<0.2	36.7	87.6
RCS019	RCS019_9_6	Granodiorite	NA	NA	A2	Replacement	<0.1	11.5	7.8	14.0	<0.1	0.2	<0.1	<0.1	<0.1	0.1	15.6	<0.2	35.2	84.5
RCS019	RCS019_9_9	Granodiorite	NA	NA	A2	Replacement	<0.1	11.6	8.1	14.0	<0.1	0.2	<0.1	<0.1	<0.1	<0.1	16.0	0.2	35.6	85.9
RCS019	RCS019_15_9	Granodiorite	NA	NA	A2	Replacement	<0.1	9.7	7.9	14.1	<0.1	1.0	<0.1	<0.1	<0.1	0.2	17.9	<0.2	35.1	85.8
RCS019	RCS019_15_10	Granodiorite	NA	NA	A2	Replacement	<0.1	10.2	8.8	13.1	<0.1	0.1	<0.1	<0.1	<0.1	0.2	18.6	<0.2	34.8	85.7
RCS019	RCS019_17_3	Granodiorite	NA	NA	A2	Replacement	<0.1	10.2	7.1	15.7	<0.1	1.8	<0.1	<0.1	<0.1	0.2	16.5	<0.2	36.5	88.1
RCS019	RCS019_17_6	Granodiorite	NA	NA	A2	Replacement	<0.1	9.6	8.7	13.5	<0.1	0.2	<0.1	<0.1	<0.1	0.1	18.5	<0.2	34.9	85.5
RCS019	RCS019_17_11	Granodiorite	NA	NA	A2	Replacement	<0.1	10.4	9.0	13.1	<0.1	0.3	0.2	<0.1	<0.1	0.2	18.4	<0.2	35.4	86.9
RCS019	RCS019_17_17	Granodiorite	NA	NA	A2	Replacement	<0.1	9.9	9.0	13.4	<0.1	0.1	<0.1	<0.1	<0.1	0.2	19.2	<0.2	35.4	87.2
RCS019	RCS019_19_10	Granodiorite	NA	NA	A2	Replacement	<0.1	8.1	8.2	12.9	<0.1	0.2	<0.1	<0.1	<0.1	0.2	18.7	<0.2	32.8	80.9
RCS019	RCS019_19_13	Granodiorite	NA	NA	A2	Replacement	<0.1	9.8	8.5	13.1	<0.1	0.2	<0.1	<0.1	<0.1	0.2	19.2	<0.2	34.5	85.4
RCS019	RCS019_19_14	Granodiorite	NA	NA	A2	Replacement	<0.1	10.9	9.3	13.0	<0.1	0.1	<0.1	<0.1	<0.1	0.2	17.1	<0.2	35.4	86.1
RCS019	RCS019_19_16	Granodiorite	NA	NA	A2	Replacement	<0.1	10.8	9.1	13.5	<0.1	<0.1	<0.1	<0.1	<0.1	0.2	17.8	0.2	35.9	87.5
RCS019	RCS019_19_17	Granodiorite	NA	NA	A2	Replacement	<0.1	10.4	9.1	13.4	<0.1	0.1	<0.1	0.1	<0.1	0.3	19.1	0.3	35.8	88.4
RCS019	RCS019_19_18	Granodiorite	NA	NA	A2	Replacement	<0.1	10.5	8.7	13.5	<0.1	0.1	<0.1	<0.1	<0.1	0.2	18.0	<0.2	35.3	86.2
RCS019	RCS019_19_19	Granodiorite	NA	NA	A2	Replacement	<0.1	10.1	9.0	13.7	<0.1	0.2	<0.1	<0.1	<0.1	0.2	18.1	<0.2	35.6	86.8
RCS019	RCS019_22_4	Granodiorite	NA	NA	A2	Replacement	<0.1	11.3	8.6	13.3	<0.1	<0.1	<0.1	<0.1	<0.1	0.1	16.1	<0.2	35.0	84.3
RCS019	RCS019_22_6	Granodiorite	NA	NA	A2	Replacement	<0.1	11.4	8.2	14.0	<0.1	0.3	<0.1	<0.1	<0.1	0.1	15.1	<0.2	35.3	84.4
RCS019	RCS019_22_7	Granodiorite	NA	NA	A2	Replacement	<0.1	10.9	6.7	15.9	<0.1	1.2	<0.1	<0.1	<0.1	0.4	15.0	<0.2	36.3	86.4
RCS019	RCS019_24_1	Granodiorite	NA	NA	A2	Replacement	<0.1	10.8	9.1	13.3	<0.1	<0.1	<0.1	<0.1	<0.1	0.2	17.3	<0.2	35.5	86.3
RCS019	RCS019_24_2	Granodiorite	NA	NA	A2	Replacement	<0.1	10.1	7.8	14.5	0.6	0.9	0.9	<0.1	<0.1	0.2	16.3	<0.2	35.9	87.2
RCS022	RCS022_12_9	Monzonite	NA	NA	A2	L Patches	<0.1	10.4	9.0	14.1	0.2	0.4	<0.1	<0.1	<0.1	0.2	15.9	<0.2	35.8	86.0
RCS022	RCS022_12_12	Monzonite	NA	NA	A2	L Patches	<0.1	10.9	9.5	13.9	0.4	0.3	<0.1	<0.1	<0.1	0.3	15.5	<0.2	36.3	87.1
RCS022	RCS022_12_13	Monzonite	NA	NA	A2	L Patches	0.1	10.2	9.1	13.1	0.4	0.4	<0.1	<0.1	<0.1	<0.1	15.4	<0.2	34.5	83.3
RCS022	RCS022_12_14	Monzonite	NA	NA	A2	L Patches	<0.1	9.9	8.5	15.1	1.0	0.6	<0.1	<0.1	<0.1	<0.1	15.7	0.2	36.4	87.5

Sample	Reference	Lithology	Structure	Type	Alt	Texture	Na_pct	Mg_pct	Al_pct	Si_pct	K_pct	Ca_pct	Ti_pct	V_pct	Cr_pct	Mn_pct	Fe_pct	Co_pct	O_pct	Total
RCS022	RCS022_12_15	Monzonite	NA	NA	A2	L Patches	0.1	10.4	9.3	14.4	0.5	0.4	<0.1	<0.1	<0.1	0.2	15.8	<0.2	36.4	87.4
RCS022	RCS022_14_1	Monzonite	NA	NA	A2	L Patches	0.2	8.9	9.4	15.9	0.2	0.5	0.2	<0.1	<0.1	<0.1	16.8	<0.2	37.7	89.7
RCS022	RCS022_14_2	Monzonite	NA	NA	A2	L Patches	<0.1	11.0	8.8	13.4	<0.1	0.2	<0.1	<0.1	<0.1	0.1	17.8	<0.2	35.7	87.1
RCS022	RCS022_14_3	Monzonite	NA	NA	A2	L Patches	<0.1	11.8	10.6	13.3	<0.1	<0.1	<0.1	<0.1	<0.1	0.2	16.7	<0.2	37.3	89.9
RCS022	RCS022_14_5	Monzonite	NA	NA	A2	L Patches	<0.1	10.5	8.7	13.5	<0.1	0.1	<0.1	<0.1	<0.1	0.2	18.4	<0.2	35.4	86.8
RCS022	RCS022_14_6	Monzonite	NA	NA	A2	L Patches	<0.1	11.2	9.7	13.1	<0.1	<0.1	<0.1	<0.1	<0.1	<0.1	17.6	<0.2	36.2	87.8
RCS022	RCS022_14_8	Monzonite	NA	NA	A2	L Patches	<0.1	10.6	9.2	13.7	<0.1	0.2	<0.1	<0.1	<0.1	0.2	18.1	0.2	36.2	88.3
RCS022	RCS022_14_9	Monzonite	NA	NA	A2	L Patches	<0.1	11.7	10.5	13.0	<0.1	<0.1	<0.1	<0.1	<0.1	0.2	16.0	<0.2	36.6	87.9
RCS022	RCS022_14_10	Monzonite	NA	NA	A2	L Patches	<0.1	11.3	9.4	14.1	<0.1	0.2	<0.1	<0.1	<0.1	0.2	17.5	0.2	37.0	89.9
RCS022	RCS022_14_12	Monzonite	NA	NA	A2	L Patches	<0.1	11.0	10.0	13.3	<0.1	<0.1	<0.1	<0.1	<0.1	0.2	16.2	<0.2	36.1	86.7
RCS022	RCS022_14_13	Monzonite	NA	NA	A2	L Patches	<0.1	12.0	10.0	13.4	<0.1	<0.1	<0.1	<0.1	<0.1	0.2	16.1	0.2	36.9	88.8
RCS022	RCS022_14_14	Monzonite	NA	NA	A2	L Patches	<0.1	11.9	10.7	13.0	<0.1	<0.1	<0.1	<0.1	<0.1	0.3	16.2	<0.2	36.9	89.0
RCS022	RCS022_14_16	Monzonite	NA	NA	A2	L Patches	0.1	11.2	9.8	13.8	<0.1	0.2	<0.1	<0.1	<0.1	0.2	16.9	<0.2	36.9	88.9
RCS022	RCS022_14_17	Monzonite	NA	NA	A2	L Patches	<0.1	11.3	10.0	12.8	<0.1	<0.1	<0.1	<0.1	<0.1	0.2	16.0	<0.2	35.7	85.9
RCS022	RCS022_14_18	Monzonite	NA	NA	A2	L Patches	<0.1	11.0	9.6	13.3	<0.1	<0.1	<0.1	<0.1	<0.1	0.1	17.6	<0.2	36.1	87.7
RCS032	RCS032_6_3	Andesite	NA	NA	A4	Replacement	<0.1	11.2	9.5	14.1	<0.1	0.8	<0.1	<0.1	<0.1	0.4	10.4	<0.2	35.3	81.6
RCS032	RCS032_6_4	Andesite	NA	NA	A4	Replacement	<0.1	12.5	9.6	16.4	<0.1	0.8	<0.1	<0.1	<0.1	0.4	9.3	<0.2	38.7	87.7
RCS032	RCS032_6_6	Andesite	NA	NA	A4	Replacement	<0.1	10.4	9.7	14.7	<0.1	0.6	<0.1	<0.1	<0.1	0.6	9.9	<0.2	35.6	81.5
RCS032	RCS032_6_9	Andesite	NA	NA	A4	Replacement	<0.1	11.9	8.4	14.7	<0.1	0.6	<0.1	<0.1	<0.1	0.4	10.0	<0.2	35.4	81.5
RCS032	RCS032_6_10	Andesite	NA	NA	A4	Replacement	<0.1	12.8	9.4	15.8	<0.1	0.7	<0.1	<0.1	<0.1	0.5	10.2	<0.2	38.2	87.6
RCS032	RCS032_6_11	Andesite	NA	NA	A4	Replacement	0.1	12.2	9.4	15.5	<0.1	0.6	<0.1	<0.1	<0.1	0.5	10.2	<0.2	37.5	86.0
RCS032	RCS032_8_3	Andesite	NA	NA	A4	Replacement	<0.1	12.2	9.2	15.6	<0.1	0.7	<0.1	<0.1	<0.1	0.6	9.9	<0.2	37.3	85.4
RCS032	RCS032_8_4	Andesite	NA	NA	A4	Replacement	<0.1	12.5	9.7	15.4	<0.1	0.7	<0.1	<0.1	<0.1	0.5	10.0	<0.2	37.7	86.5
RCS032	RCS032_8_5	Andesite	NA	NA	A4	Replacement	0.1	12.6	9.5	16.2	<0.1	0.8	<0.1	<0.1	<0.1	0.5	10.3	<0.2	38.7	88.6
RCS032	RCS032_8_6	Andesite	NA	NA	A4	Replacement	<0.1	11.3	8.7	14.9	<0.1	0.8	<0.1	<0.1	<0.1	0.5	9.6	<0.2	35.4	81.3
RCS032	RCS032_8_7	Andesite	NA	NA	A4	Replacement	<0.1	12.5	9.2	15.7	<0.1	0.8	<0.1	<0.1	<0.1	0.5	9.9	<0.2	37.8	86.6
RCS032	RCS032_8_8	Andesite	NA	NA	A4	Replacement	<0.1	11.6	9.2	14.7	<0.1	0.8	<0.1	<0.1	<0.1	0.5	9.7	<0.2	35.8	82.2
RCS032	RCS032_8_9	Andesite	NA	NA	A4	Replacement	0.1	13.4	9.9	16.6	<0.1	0.8	<0.1	<0.1	<0.1	0.5	9.9	<0.2	39.8	90.9
RCS032	RCS032_8_10	Andesite	NA	NA	A4	Replacement	<0.1	12.6	9.6	15.7	<0.1	0.8	<0.1	<0.1	<0.1	0.5	9.5	<0.2	37.9	86.5

Sample	Reference	Lithology	Structure	Type	Alt	Texture	Na_pct	Mg_pct	Al_pct	Si_pct	K_pct	Ca_pct	Ti_pct	V_pct	Cr_pct	Mn_pct	Fe_pct	Co_pct	O_pct	Total
RCS032	RCS032_10_2	Andesite	NA	NA	A4	Replacement	<0.1	12.0	9.5	14.9	<0.1	0.7	<0.1	<0.1	<0.1	0.6	9.2	<0.2	36.5	83.3
RCS032	RCS032_10_3	Andesite	NA	NA	A4	Replacement	<0.1	12.1	9.5	15.1	<0.1	0.7	<0.1	<0.1	<0.1	0.6	9.6	<0.2	36.9	84.5
RCS032	RCS032_10_12	Andesite	NA	NA	A4	Replacement	<0.1	11.8	9.5	14.6	<0.1	0.8	<0.1	<0.1	<0.1	0.6	9.5	0.2	36.1	83.0
RCS032	RCS032_12_1	Andesite	NA	NA	A4	L Patches	<0.1	12.9	9.5	15.9	<0.1	0.7	<0.1	<0.1	<0.1	0.6	9.9	<0.2	38.3	87.7
RCS032	RCS032_12_2	Andesite	NA	NA	A4	L Patches	<0.1	12.5	9.1	15.4	<0.1	0.7	<0.1	<0.1	<0.1	0.5	10.1	<0.2	37.2	85.5
RCS032	RCS032_12_3	Andesite	NA	NA	A4	L Patches	<0.1	11.7	8.7	15.1	<0.1	0.7	<0.1	<0.1	<0.1	0.5	10.1	<0.2	36.0	82.9
RCS032	RCS032_12_4	Andesite	NA	NA	A4	L Patches	<0.1	12.0	9.0	14.7	<0.1	0.7	<0.1	<0.1	<0.1	0.6	9.5	<0.2	35.9	82.3
RCS032	RCS032_12_5	Andesite	NA	NA	A4	L Patches	<0.1	13.0	10.0	14.6	<0.1	0.4	<0.1	<0.1	<0.1	0.5	11.0	<0.2	37.6	87.1
RCS032	RCS032_12_6	Andesite	NA	NA	A4	L Patches	<0.1	12.6	9.6	16.1	<0.1	0.8	<0.1	<0.1	<0.1	0.6	9.9	<0.2	38.6	88.3
RCS032	RCS032_12_7	Andesite	NA	NA	A4	L Patches	<0.1	12.1	8.9	15.6	<0.1	0.8	<0.1	<0.1	<0.1	0.5	10.0	<0.2	37.0	84.8
RCS032	RCS032_12_8	Andesite	NA	NA	A4	L Patches	<0.1	11.9	9.4	14.7	<0.1	0.6	<0.1	<0.1	<0.1	0.6	9.9	<0.2	36.2	83.3
RCS032	RCS032_12_9	Andesite	NA	NA	A4	L Patches	<0.1	12.4	9.1	15.2	<0.1	0.7	<0.1	<0.1	<0.1	0.5	10.0	<0.2	36.9	84.7
RCS032	RCS032_13_1	Andesite	NA	NA	A4	Replacement	<0.1	12.0	8.8	15.2	<0.1	0.8	<0.1	<0.1	<0.1	0.4	9.4	<0.2	36.3	83.0
RCS032	RCS032_13_2	Andesite	NA	NA	A4	Replacement	<0.1	12.1	9.5	15.5	0.2	0.7	<0.1	<0.1	<0.1	0.5	9.8	<0.2	37.5	85.8
RCS096	RCS096_9_6	Granodiorite	NA	NA	A3	Replacement	<0.1	9.8	9.4	14.1	0.6	0.1	<0.1	<0.1	<0.1	0.3	17.4	0.3	36.3	88.2
RCS096	RCS096_11_1	Granodiorite	NA	NA	A3	Replacement	<0.1	10.9	9.5	13.2	<0.1	0.1	<0.1	<0.1	<0.1	0.3	17.2	<0.2	35.7	86.9
RCS096	RCS096_11_2	Granodiorite	NA	NA	A3	Replacement	<0.1	11.1	9.6	13.1	<0.1	<0.1	<0.1	<0.1	<0.1	0.3	16.9	<0.2	35.6	86.4
RCS096	RCS096_11_3	Granodiorite	NA	NA	A3	Replacement	<0.1	11.0	9.5	13.1	<0.1	<0.1	<0.1	<0.1	<0.1	0.3	16.9	<0.2	35.6	86.4
RCS096	RCS096_11_4	Granodiorite	NA	NA	A3	Replacement	<0.1	10.6	9.8	13.0	<0.1	<0.1	<0.1	<0.1	<0.1	0.4	17.6	<0.2	35.8	87.2
RCS096	RCS096_11_6	Granodiorite	NA	NA	A3	Replacement	<0.1	10.7	9.2	14.1	0.4	0.1	<0.1	<0.1	<0.1	0.3	16.1	<0.2	36.1	86.9
RCS096	RCS096_16_5	Granodiorite	NA	NA	A3	Replacement	<0.1	10.2	8.7	13.7	0.2	0.3	<0.1	<0.1	<0.1	0.2	15.2	<0.2	34.7	83.1
RCS096	RCS096_16_6	Granodiorite	NA	NA	A3	Replacement	<0.1	10.6	9.0	13.3	0.1	0.1	<0.1	<0.1	<0.1	0.2	15.9	0.3	34.9	84.4
RCS096	RCS096_18_2	Granodiorite	NA	NA	A3	Replacement	<0.1	8.9	9.2	15.3	0.7	1.1	<0.1	<0.1	<0.1	0.3	17.2	0.2	37.2	90.2
RCS096	RCS096_18_3	Granodiorite	NA	NA	A3	Replacement	<0.1	10.3	9.9	13.1	0.2	<0.1	<0.1	<0.1	<0.1	0.3	17.3	<0.2	35.6	86.6
RCS096	RCS096_23_14	Granodiorite	NA	NA	A3	Replacement	<0.1	10.5	9.3	14.1	0.8	0.2	<0.1	<0.1	<0.1	0.2	16.0	<0.2	36.2	87.3
RCS007	RCS007_3_6	Diorite	NA	NA	A4	Patches	<0.1	10.4	8.5	15.1	<0.1	0.6	<0.1	<0.1	<0.1	0.3	13.1	<0.2	35.8	83.8
RCS007	RCS007_5_4	Diorite	NA	NA	A4	Patches	<0.1	10.7	8.7	15.0	<0.1	0.5	<0.1	<0.1	<0.1	0.4	14.2	<0.2	36.4	86.0
RCS007	RCS007_5_6	Diorite	NA	NA	A4	Patches	<0.1	10.9	8.6	15.8	<0.1	0.6	<0.1	<0.1	<0.1	0.3	13.4	<0.2	37.1	86.6
RCS007	RCS007_6_8	Diorite	NA	NA	A4	Patches	<0.1	9.8	9.1	15.0	<0.1	0.6	<0.1	<0.1	<0.1	0.3	14.8	<0.2	36.3	85.9

Sample	Reference	Lithology	Structure	Type	Alt	Texture	Na_pct	Mg_pct	Al_pct	Si_pct	K_pct	Ca_pct	Ti_pct	V_pct	Cr_pct	Mn_pct	Fe_pct	Co_pct	O_pct	Total
RCS007	RCS007_6_9	Diorite	NA	NA	A4	Patches	<0.1	10.1	8.5	14.9	<0.1	0.7	<0.1	<0.1	<0.1	0.3	13.9	<0.2	35.6	84.0
RCS007	RCS007_8_10	Diorite	NA	NA	A4	Patches	<0.1	11.4	8.6	15.9	<0.1	0.4	<0.1	<0.1	<0.1	0.4	13.1	<0.2	37.3	87.0
RCS007	RCS007_8_11	Diorite	NA	NA	A4	Patches	<0.1	10.9	8.4	15.8	<0.1	0.7	<0.1	<0.1	<0.1	0.4	12.2	<0.2	36.6	85.0
RCS007	RCS007_9_1	Diorite	NA	NA	A4	Patches	<0.1	10.3	9.0	15.5	<0.1	0.7	<0.1	<0.1	<0.1	0.3	14.1	<0.2	36.8	86.6
RCS007	RCS007_9_4	Diorite	NA	NA	A4	Patches	<0.1	10.3	8.8	15.0	<0.1	0.6	<0.1	<0.1	<0.1	0.4	14.2	<0.2	36.2	85.5
RCS007	RCS007_9_5	Diorite	NA	NA	A4	Patches	<0.1	10.9	8.6	15.3	<0.1	0.5	<0.1	<0.1	<0.1	0.3	13.6	<0.2	36.5	85.7
RCS007	RCS007_9_6	Diorite	NA	NA	A4	Patches	<0.1	10.7	8.9	15.6	<0.1	0.7	<0.1	<0.1	<0.1	0.3	14.0	<0.2	37.1	87.1
RCS007	RCS007_9_7	Diorite	NA	NA	A4	Patches	<0.1	10.3	8.9	15.7	<0.1	0.6	<0.1	<0.1	<0.1	0.4	14.1	<0.2	37.1	87.1
RCS007	RCS007_9_10	Diorite	NA	NA	A4	Patches	<0.1	10.8	8.7	15.8	<0.1	0.7	<0.1	<0.1	<0.1	0.3	13.5	<0.2	37.1	86.9
RCS007	RCS007_9_11	Diorite	NA	NA	A4	Patches	<0.1	10.1	8.8	15.5	<0.1	0.6	<0.1	<0.1	<0.1	0.4	14.3	<0.2	36.6	86.2
RCS007	RCS007_9_12	Diorite	NA	NA	A4	Patches	<0.1	10.3	9.1	15.0	<0.1	0.5	<0.1	<0.1	<0.1	0.4	14.6	<0.2	36.5	86.3
RCS007	RCS007_9_13	Diorite	NA	NA	A4	Patches	<0.1	10.5	8.6	16.0	<0.1	0.7	<0.1	<0.1	<0.1	0.3	13.7	<0.2	37.1	86.9
RCS007	RCS007_11_14	Diorite	NA	NA	A4	Patches	<0.1	10.7	9.1	15.3	<0.1	0.5	<0.1	<0.1	<0.1	0.4	13.8	0.2	37.0	87.1
RCS007	RCS007_11_16	Diorite	NA	NA	A4	Patches	<0.1	10.8	8.6	15.6	<0.1	0.4	<0.1	<0.1	<0.1	0.3	12.6	<0.2	36.6	85.0
RCS007	RCS007_11_17	Diorite	NA	NA	A4	Patches	<0.1	9.3	8.4	14.1	<0.1	0.4	<0.1	<0.1	<0.1	0.4	14.2	<0.2	34.1	81.0
RCS007	RCS007_12_7	Diorite	NA	NA	A4	Patches	<0.1	11.2	8.4	15.8	<0.1	0.5	<0.1	<0.1	<0.1	0.4	12.7	<0.2	36.8	85.8
RCS007	RCS007_12_8	Diorite	NA	NA	A4	Patches	<0.1	11.1	9.0	15.7	<0.1	0.6	<0.1	<0.1	<0.1	0.2	13.1	<0.2	37.1	86.7
RCS007	RCS007_14_5	Diorite	NA	NA	A4	Patches	<0.1	10.9	8.8	15.9	<0.1	0.5	<0.1	<0.1	<0.1	0.3	12.7	<0.2	37.1	86.3
RCS007	RCS007_14_6	Diorite	NA	NA	A4	Patches	<0.1	10.2	9.2	14.6	<0.1	0.4	<0.1	<0.1	<0.1	0.5	14.3	<0.2	36.0	85.1
RCS007	RCS007_14_9	Diorite	NA	NA	A4	Patches	<0.1	9.5	9.5	14.0	<0.1	0.3	<0.1	<0.1	<0.1	0.4	15.8	<0.2	35.6	85.2
RCS007	RCS007_16_1	Diorite	NA	NA	A4	L Patches	<0.1	10.7	9.2	15.2	<0.1	0.5	<0.1	<0.1	<0.1	0.4	13.9	<0.2	36.8	86.6
RCS007	RCS007_16_2	Diorite	NA	NA	A4	L Patches	<0.1	10.5	8.2	15.7	<0.1	0.6	<0.1	<0.1	<0.1	0.4	13.2	<0.2	36.2	84.7
RCS007	RCS007_16_3	Diorite	NA	NA	A4	L Patches	<0.1	10.9	8.6	16.2	<0.1	0.6	<0.1	<0.1	<0.1	0.4	13.5	<0.2	37.5	87.7
RCS007	RCS007_16_5	Diorite	NA	NA	A4	L Patches	<0.1	10.7	8.5	15.4	<0.1	0.6	<0.1	<0.1	<0.1	0.3	12.6	<0.2	36.1	84.2
RCS007	RCS007_16_6	Diorite	NA	NA	A4	L Patches	<0.1	10.2	10.0	14.0	<0.1	0.3	<0.1	<0.1	<0.1	0.4	15.9	0.3	36.5	87.6
RCS007	RCS007_16_7	Diorite	NA	NA	A4	L Patches	<0.1	10.4	9.6	14.3	<0.1	0.3	<0.1	<0.1	<0.1	0.5	15.0	0.3	36.5	87.0
RCS007	RCS007_16_8	Diorite	NA	NA	A4	L Patches	<0.1	10.2	9.3	14.7	<0.1	0.4	<0.1	<0.1	<0.1	0.4	15.5	<0.2	36.5	87.1
RCS007	RCS007_17_4	Diorite	NA	NA	A4	L Patches	<0.1	10.5	8.8	15.3	<0.1	0.5	<0.1	<0.1	<0.1	0.3	12.9	<0.2	36.1	84.4
RCS007	RCS007_19_11	Diorite	NA	NA	A4	Patches	<0.1	9.6	8.2	13.6	<0.1	0.3	<0.1	<0.1	<0.1	0.4	15.4	<0.2	33.9	81.5

Sample	Reference	Lithology	Structure	Type	Alt	Texture	Na_pct	Mg_pct	Al_pct	Si_pct	K_pct	Ca_pct	Ti_pct	V_pct	Cr_pct	Mn_pct	Fe_pct	Co_pct	O_pct	Total
RCS007	RCS007_19_13	Diorite	NA	NA	A4	Patches	<0.1	10.1	8.8	16.2	<0.1	0.6	<0.1	<0.1	<0.1	0.2	13.6	<0.2	37.1	86.5
RCS007	RCS007_23_7	Diorite	NA	NA	A4	Patches	<0.1	10.1	9.2	15.2	<0.1	0.6	<0.1	<0.1	<0.1	0.4	14.6	0.2	36.8	87.1
RCS007	RCS007_23_9	Diorite	NA	NA	A4	Patches	<0.1	10.1	9.4	14.6	<0.1	1.0	<0.1	<0.1	<0.1	0.4	15.2	<0.2	36.4	86.9
RCS041	RCS041_8_8	Monzonite	NA	NA	A3	Replacement	0.1	11.3	8.0	14.5	<0.1	0.5	<0.1	<0.1	<0.1	<0.1	13.9	<0.2	35.2	83.4
RCS041	RCS041_8_9	Monzonite	NA	NA	A3	Replacement	<0.1	9.9	7.1	16.3	<0.1	1.9	<0.1	<0.1	<0.1	0.3	14.4	<0.2	36.3	86.2
RCS041	RCS041_14_11	Monzonite	NA	NA	A3	Patches	0.1	10.4	8.1	14.8	<0.1	0.8	<0.1	<0.1	<0.1	0.2	13.9	0.2	35.5	84.2
RCS041	RCS041_14_13	Monzonite	NA	NA	A3	Patches	0.1	9.5	9.5	16.3	<0.1	0.8	<0.1	0.1	<0.1	0.1	12.5	<0.2	37.3	86.1
RCS041	RCS041_14_22	Monzonite	NA	NA	A3	Patches	0.1	9.9	8.0	15.9	<0.1	1.8	<0.1	<0.1	<0.1	0.2	13.6	<0.2	36.4	85.9
RCS041	RCS041_17_1	Monzonite	NA	NA	A3	Replacement	<0.1	10.6	7.7	16.1	<0.1	0.9	<0.1	<0.1	<0.1	0.2	12.7	<0.2	36.2	84.4
RCS041	RCS041_17_3	Monzonite	NA	NA	A3	Replacement	0.1	9.9	7.7	16.4	<0.1	1.1	<0.1	<0.1	<0.1	<0.1	12.8	<0.2	36.2	84.1
RCS041	RCS041_17_4	Monzonite	NA	NA	A3	Replacement	0.1	8.4	9.0	16.6	<0.1	0.4	<0.1	<0.1	<0.1	0.1	12.1	<0.2	36.2	82.9
RCS041	RCS041_17_6	Monzonite	NA	NA	A3	Replacement	<0.1	11.0	7.9	15.3	<0.1	0.8	<0.1	<0.1	<0.1	0.3	13.6	<0.2	36.1	85.0
RCS041	RCS041_17_7	Monzonite	NA	NA	A3	Replacement	<0.1	10.9	8.2	15.1	<0.1	0.7	<0.1	<0.1	<0.1	0.2	14.4	<0.2	36.2	85.6
RCS041	RCS041_17_9	Monzonite	NA	NA	A3	Replacement	<0.1	10.7	7.5	15.7	<0.1	1.2	<0.1	<0.1	<0.1	0.2	13.9	<0.2	36.0	85.2
RCS041	RCS041_19_2	Monzonite	NA	NA	A3	Replacement	<0.1	10.3	7.6	16.7	<0.1	1.5	<0.1	<0.1	<0.1	0.2	13.1	<0.2	37.0	86.4
RCS041	RCS041_19_24	Monzonite	NA	NA	A3	Replacement	0.1	10.2	7.9	16.6	<0.1	1.4	<0.1	<0.1	<0.1	0.2	13.4	<0.2	37.3	87.0
RCS041	RCS041_19_25	Monzonite	NA	NA	A3	Replacement	<0.1	10.8	9.0	14.9	<0.1	0.8	<0.1	<0.1	<0.1	0.2	14.4	<0.2	36.5	86.6
RCS041	RCS041_21_14	Monzonite	NA	NA	A3	Replacement	<0.1	10.3	8.0	15.3	<0.1	1.1	<0.1	<0.1	<0.1	0.2	12.6	<0.2	35.5	82.9
RCS041	RCS041_21_15	Monzonite	NA	NA	A3	Replacement	0.1	10.4	8.0	15.6	0.1	1.6	<0.1	<0.1	<0.1	0.2	15.2	0.2	36.8	88.2
RCS041	RCS041_21_17	Monzonite	NA	NA	A3	Replacement	0.2	10.4	7.4	16.1	<0.1	1.2	<0.1	<0.1	<0.1	0.2	12.9	<0.2	36.1	84.5
RCS041	RCS041_21_19	Monzonite	NA	NA	A3	Replacement	0.2	9.9	9.6	17.1	<0.1	0.6	<0.1	<0.1	<0.1	0.2	11.9	<0.2	38.3	87.7
RCS052	RCS052_16_14	Monzonite	219NW80	Fracture vein	A6	Patches	<0.1	11.4	8.5	14.0	<0.1	0.3	<0.1	<0.1	<0.1	0.2	15.4	<0.2	35.6	85.3
RCS052	RCS052_16_18	Monzonite	219NW80	Fracture vein	A6	Patches	<0.1	12.0	9.2	14.0	<0.1	0.3	<0.1	<0.1	<0.1	0.2	13.7	<0.2	36.2	85.5
RCS052	RCS052_17_11	Monzonite	219NW80	Fracture vein	A6	Patches	<0.1	13.5	8.4	17.3	<0.1	0.6	<0.1	<0.1	<0.1	<0.1	10.3	<0.2	39.3	89.4
RCS052	RCS052_19_1	Monzonite	219NW80	Fracture vein	A6	Replacement	<0.1	9.9	8.1	16.8	<0.1	1.3	<0.1	<0.1	<0.1	<0.1	11.6	<0.2	36.8	84.5
RCS052	RCS052_19_3	Monzonite	219NW80	Fracture vein	A6	Replacement	<0.1	9.0	7.9	17.1	0.1	1.1	<0.1	<0.1	<0.1	0.2	11.2	<0.2	36.1	82.6
RCS052	RCS052_19_4	Monzonite	219NW80	Fracture vein	A6	Replacement	0.1	10.3	8.1	17.1	<0.1	1.5	<0.1	<0.1	<0.1	0.2	10.7	<0.2	37.4	85.4
RCS052	RCS052_19_5	Monzonite	219NW80	Fracture vein	A6	Replacement	<0.1	9.0	7.7	15.4	<0.1	1.3	<0.1	<0.1	<0.1	0.1	11.3	<0.2	34.2	79.0

Sample	Reference	Lithology	Structure	Type	Alt	Texture	Na_pct	Mg_pct	Al_pct	Si_pct	K_pct	Ca_pct	Ti_pct	V_pct	Cr_pct	Mn_pct	Fe_pct	Co_pct	O_pct	Total
RCS052	RCS052_19_6	Monzonite	219NW80	Fracture vein	A6	Replacement	<0.1	9.3	8.2	16.2	<0.1	1.4	<0.1	<0.1	<0.1	0.2	10.9	<0.2	35.6	81.8
RCS052	RCS052_19_7	Monzonite	219NW80	Fracture vein	A6	Replacement	<0.1	11.1	8.6	14.4	0.1	0.9	<0.1	<0.1	<0.1	0.2	11.5	0.3	35.2	82.3
RCS052	RCS052_19_10	Monzonite	219NW80	Fracture vein	A6	Replacement	<0.1	9.7	6.8	16.3	0.2	0.8	<0.1	<0.1	<0.1	<0.1	13.8	<0.2	35.5	83.2
RCS052	RCS052_25_2	Monzonite	219NW80	Fracture vein	A6	Replacement	<0.1	13.4	8.8	17.8	<0.1	0.6	<0.1	<0.1	<0.1	0.2	9.8	<0.2	40.1	90.7
RCS052	RCS052_25_15	Monzonite	219NW80	Fracture vein	A6	Replacement	<0.1	11.3	7.4	15.0	<0.1	0.7	<0.1	<0.1	<0.1	<0.1	10.0	<0.2	34.4	78.8
RCS068	RCS068_2_5	Dacite	228NW78	Fracture	A6	Replacement	<0.1	9.9	10.3	13.1	<0.1	<0.1	<0.1	<0.1	<0.1	0.3	17.6	<0.2	35.7	86.9
RCS068	RCS068_2_7	Dacite	228NW78	Fracture	A6	Replacement	<0.1	9.8	10.0	13.1	<0.1	<0.1	<0.1	<0.1	<0.1	0.3	17.6	<0.2	35.5	86.3
RCS068	RCS068_2_8	Dacite	228NW78	Fracture	A6	Replacement	0.1	8.5	11.7	14.0	0.5	0.2	<0.1	<0.1	<0.1	0.2	16.0	<0.2	36.8	88.1
RCS068	RCS068_11_12	Dacite	228NW78	Fracture	A6	Replacement	<0.1	9.6	11.0	13.1	0.1	0.2	<0.1	<0.1	<0.1	0.2	16.4	<0.2	36.0	86.8
RCS068	RCS068_11_13	Dacite	228NW78	Fracture	A6	Replacement	<0.1	9.5	10.5	13.0	<0.1	0.2	<0.1	<0.1	<0.1	0.3	17.2	<0.2	35.6	86.3
RCS068	RCS068_11_16	Dacite	228NW78	Fracture	A6	Replacement	<0.1	9.8	10.9	13.1	<0.1	0.1	<0.1	0.1	<0.1	0.3	16.0	0.2	35.9	86.4
RCS068	RCS068_13_3	Dacite	228NW78	Fracture	A6	Replacement	<0.1	10.4	9.9	13.0	<0.1	0.1	<0.1	<0.1	<0.1	0.3	17.4	<0.2	35.6	86.7
RCS068	RCS068_13_4	Dacite	228NW78	Fracture	A6	Replacement	<0.1	9.5	10.3	13.0	<0.1	0.1	<0.1	<0.1	<0.1	0.4	18.4	0.3	35.8	87.7
RCS068	RCS068_13_5	Dacite	228NW78	Fracture	A6	Replacement	<0.1	9.8	11.0	13.5	0.2	0.1	<0.1	<0.1	<0.1	0.3	16.8	0.3	36.7	88.7
RCS068	RCS068_13_6	Dacite	228NW78	Fracture	A6	Replacement	<0.1	10.3	10.2	13.3	0.1	0.2	<0.1	<0.1	<0.1	0.3	17.0	<0.2	36.1	87.6
RCS068	RCS068_13_7	Dacite	228NW78	Fracture	A6	Replacement	<0.1	9.4	10.5	13.2	0.4	0.2	<0.1	<0.1	<0.1	0.3	16.4	<0.2	35.5	85.7
RCS068	RCS068_14_8	Dacite	228NW78	Fracture	A6	Replacement	<0.1	10.3	10.2	13.7	<0.1	0.2	<0.1	<0.1	<0.1	0.2	17.2	<0.2	36.6	88.5
RCS068	RCS068_14_10	Dacite	228NW78	Fracture	A6	Replacement	<0.1	8.5	10.6	12.9	0.2	0.2	<0.1	<0.1	<0.1	0.2	17.4	0.3	35.0	85.2
RCS068	RCS068_14_11	Dacite	228NW78	Fracture	A6	Replacement	<0.1	8.8	11.4	13.4	0.2	0.2	<0.1	<0.1	<0.1	0.3	17.4	<0.2	36.5	88.2
RCS068	RCS068_14_12	Dacite	228NW78	Fracture	A6	Replacement	<0.1	10.2	10.1	13.6	<0.1	0.2	<0.1	<0.1	<0.1	0.2	17.6	<0.2	36.4	88.3
RCS068	RCS068_17_1	Dacite	228NW78	Fracture	A6	Replacement	<0.1	9.3	10.9	13.3	0.1	0.2	<0.1	<0.1	<0.1	0.3	17.1	0.3	36.2	87.5
RCS068	RCS068_17_2	Dacite	228NW78	Fracture	A6	Replacement	<0.1	11.1	10.9	12.9	<0.1	0.1	<0.1	<0.1	<0.1	0.4	15.5	<0.2	36.3	87.3
RCS068	RCS068_17_3	Dacite	228NW78	Fracture	A6	Replacement	<0.1	9.3	11.1	13.0	<0.1	0.1	<0.1	<0.1	<0.1	0.3	17.5	<0.2	35.9	87.1
RCS068	RCS068_17_4	Dacite	228NW78	Fracture	A6	Replacement	<0.1	11.6	11.0	12.7	<0.1	<0.1	<0.1	<0.1	<0.1	0.4	15.2	0.2	36.4	87.4
RCS068	RCS068_17_5	Dacite	228NW78	Fracture	A6	Replacement	<0.1	10.0	10.7	13.4	<0.1	0.2	<0.1	<0.1	<0.1	0.4	17.3	<0.2	36.5	88.4
RCS068	RCS068_17_6	Dacite	228NW78	Fracture	A6	Replacement	<0.1	9.6	11.2	14.2	0.3	0.2	<0.1	<0.1	<0.1	0.3	16.6	<0.2	37.5	89.9

Sample	Reference	Lithology	Structure	Type	Alt	Texture	Na_pct	Mg_pct	Al_pct	Si_pct	K_pct	Ca_pct	Ti_pct	V_pct	Cr_pct	Mn_pct	Fe_pct	Co_pct	O_pct	Total
RCS068	RCS068_17_8	Dacite	228NW78	Fracture	A6	Replacement	<0.1	9.1	11.3	13.6	<0.1	0.2	<0.1	<0.1	<0.1	0.3	16.3	0.2	36.4	87.4
RCS068	RCS068_17_9	Dacite	228NW78	Fracture	A6	Replacement	<0.1	9.6	10.7	13.5	0.1	0.2	<0.1	<0.1	<0.1	0.3	16.6	<0.2	36.2	87.1
RCS068	RCS068_17_10	Dacite	228NW78	Fracture	A6	Replacement	<0.1	9.8	10.8	14.1	<0.1	0.2	<0.1	<0.1	<0.1	0.2	17.0	<0.2	37.2	89.3
RCS068	RCS068_19_1	Dacite	228NW78	Fracture	A6	Replacement	0.1	10.2	10.8	13.3	<0.1	0.1	<0.1	<0.1	<0.1	0.2	16.2	<0.2	36.3	87.1
RCS068	RCS068_19_2	Dacite	228NW78	Fracture	A6	Replacement	<0.1	9.4	11.1	13.3	0.2	0.2	<0.1	<0.1	<0.1	0.3	16.1	0.3	36.1	87.0
RCS068	RCS068_19_3	Dacite	228NW78	Fracture	A6	Replacement	<0.1	11.0	10.8	13.4	<0.1	0.1	<0.1	<0.1	<0.1	0.2	15.9	<0.2	36.8	88.3
RCS068	RCS068_19_4	Dacite	228NW78	Fracture	A6	Replacement	<0.1	9.8	10.5	13.1	<0.1	0.1	<0.1	<0.1	<0.1	0.3	16.5	<0.2	35.5	85.8
RCS068	RCS068_19_5	Dacite	228NW78	Fracture	A6	Replacement	<0.1	10.4	10.4	13.1	<0.1	0.2	<0.1	0.1	<0.1	0.3	16.3	<0.2	35.9	86.5
RCS068	RCS068_19_6	Dacite	228NW78	Fracture	A6	Replacement	<0.1	10.6	10.7	13.4	<0.1	0.2	<0.1	<0.1	<0.1	0.3	15.9	<0.2	36.6	87.7
RCS068	RCS068_19_8	Dacite	228NW78	Fracture	A6	Replacement	<0.1	10.3	10.1	13.3	<0.1	0.2	<0.1	<0.1	<0.1	0.2	16.2	<0.2	35.7	86.0
RCS068	RCS068_19_9	Dacite	228NW78	Fracture	A6	Replacement	<0.1	9.6	10.9	13.6	0.1	0.3	<0.1	<0.1	<0.1	0.3	16.5	<0.2	36.5	87.7
RCS068	RCS068_19_10	Dacite	228NW78	Fracture	A6	Replacement	<0.1	10.9	10.9	13.1	<0.1	0.1	<0.1	<0.1	<0.1	0.4	16.4	<0.2	36.6	88.3
RCS068	RCS068_19_11	Dacite	228NW78	Fracture	A6	Replacement	<0.1	9.6	10.8	13.3	<0.1	0.2	<0.1	<0.1	<0.1	0.3	16.5	<0.2	36.1	86.7
RCS068	RCS068_22_6	Dacite	228NW78	Fracture	A6	Replacement	<0.1	9.8	10.1	13.6	0.1	0.2	<0.1	<0.1	<0.1	0.3	16.8	<0.2	36.0	86.9
RCS068	RCS068_22_7	Dacite	228NW78	Fracture	A6	Replacement	<0.1	8.7	11.2	13.6	0.2	0.2	<0.1	<0.1	<0.1	0.2	17.3	<0.2	36.2	87.6
RCS068	RCS068_22_8	Dacite	228NW78	Fracture	A6	Replacement	<0.1	9.4	10.0	13.0	0.1	0.4	<0.1	<0.1	<0.1	0.4	16.9	<0.2	35.0	85.1
RCS070	RCS070_2_4	Andesite	NA	NA	A4	Patches	<0.1	11.9	9.4	14.1	<0.1	0.3	<0.1	<0.1	0.1	0.8	12.7	<0.2	36.3	85.6
RCS070	RCS070_2_7	Andesite	NA	NA	A4	Patches	<0.1	12.2	9.8	13.8	<0.1	0.2	<0.1	<0.1	<0.1	0.9	13.4	<0.2	36.8	87.2
RCS070	RCS070_4_6	Andesite	NA	NA	A4	Patches	0.2	12.4	9.6	13.2	<0.1	0.2	<0.1	<0.1	<0.1	0.9	11.5	<0.2	35.5	83.5
RCS070	RCS070_6_12	Andesite	NA	NA	A4	VH	<0.1	11.5	9.7	14.9	<0.1	0.5	0.2	<0.1	<0.1	1.1	13.7	<0.2	37.8	89.3
RCS070	RCS070_6_16	Andesite	NA	NA	A4	VH	<0.1	11.3	9.3	14.0	<0.1	0.3	<0.1	<0.1	<0.1	1.1	13.5	<0.2	36.0	85.4
RCS070	RCS070_6_17	Andesite	NA	NA	A4	VH	0.1	11.6	9.4	14.4	<0.1	0.3	<0.1	<0.1	<0.1	1.0	13.5	<0.2	36.7	86.9
RCS070	RCS070_6_18	Andesite	NA	NA	A4	VH	0.1	11.5	10.0	13.9	<0.1	0.3	<0.1	<0.1	<0.1	1.2	14.1	<0.2	36.9	88.0
RCS070	RCS070_6_19	Andesite	NA	NA	A4	VH	0.1	11.4	9.4	13.6	<0.1	0.3	<0.1	<0.1	<0.1	1.1	14.0	<0.2	35.9	85.7
RCS070	RCS070_7_10	Andesite	NA	NA	A4	VH	0.1	10.5	9.8	13.9	<0.1	0.3	<0.1	<0.1	<0.1	1.1	15.0	0.2	36.3	87.2
RCS070	RCS070_12_3	Andesite	NA	NA	A4	VH	0.1	10.9	9.6	14.5	0.2	0.2	<0.1	<0.1	<0.1	1.0	13.2	<0.2	36.5	86.2
RCS070	RCS070_13_9	Andesite	NA	NA	A4	Patches	<0.1	11.8	9.9	14.0	<0.1	0.3	<0.1	<0.1	<0.1	1.0	14.6	<0.2	37.1	88.7

Sample	Reference	Lithology	Structure	Type	Alt	Texture	Na_pct	Mg_pct	Al_pct	Si_pct	K_pct	Ca_pct	Ti_pct	V_pct	Cr_pct	Mn_pct	Fe_pct	Co_pct	O_pct	Total
RCS070	RCS070_15_4	Andesite	NA	NA	A4	Patches	<0.1	11.8	9.8	14.4	<0.1	0.3	<0.1	<0.1	<0.1	1.1	13.7	<0.2	37.2	88.2
RCS070	RCS070_15_5	Andesite	NA	NA	A4	Patches	<0.1	11.2	9.8	13.7	<0.1	0.2	<0.1	<0.1	<0.1	1.1	14.5	0.2	36.4	87.1
RCS070	RCS070_15_7	Andesite	NA	NA	A4	Patches	<0.1	11.5	9.4	14.1	<0.1	0.3	<0.1	<0.1	<0.1	1.1	13.2	<0.2	36.3	85.9
RCS070	RCS070_16_11	Andesite	NA	NA	A4	VH	<0.1	13.3	9.9	14.5	<0.1	0.4	0.1	<0.1	<0.1	0.8	11.0	<0.2	37.8	87.8
RCS070	RCS070_16_12	Andesite	NA	NA	A4	VH	0.1	11.5	9.7	14.1	<0.1	0.5	0.2	<0.1	<0.1	1.0	13.8	<0.2	36.9	87.8
RCS070	RCS070_16_14	Andesite	NA	NA	A4	VH	<0.1	13.1	9.7	14.2	<0.1	0.2	0.2	<0.1	<0.1	0.7	11.5	<0.2	37.3	86.9
RCS070	RCS070_16_15	Andesite	NA	NA	A4	VH	<0.1	8.0	10.6	14.1	<0.1	0.3	0.1	<0.1	<0.1	1.2	17.3	<0.2	36.4	87.9
RCS070	RCS070_16_24	Andesite	NA	NA	A4	VH	0.3	8.9	10.4	15.3	<0.1	0.5	<0.1	<0.1	<0.1	1.1	15.6	<0.2	37.7	89.8
RCS070	RCS070_21_2	Andesite	NA	NA	A4	Patches	<0.1	11.7	10.2	14.3	<0.1	0.3	<0.1	<0.1	<0.1	1.0	13.5	<0.2	37.4	88.4
RCS070	RCS070_21_3	Andesite	NA	NA	A4	Patches	0.1	10.6	10.4	14.1	<0.1	0.2	<0.1	<0.1	<0.1	1.1	16.5	0.2	37.6	90.9
RCS070	RCS070_21_5	Andesite	NA	NA	A4	Patches	<0.1	14.6	9.8	14.4	<0.1	0.2	<0.1	<0.1	<0.1	0.6	9.5	<0.2	37.7	86.8
RCS070	RCS070_23_5	Andesite	NA	NA	A4	VH	<0.1	13.5	10.6	14.6	<0.1	0.2	<0.1	<0.1	<0.1	0.6	11.2	<0.2	38.4	89.1
RCS070	RCS070_23_11	Andesite	NA	NA	A4	VH	<0.1	13.1	10.0	14.6	<0.1	0.2	<0.1	<0.1	<0.1	0.7	11.7	<0.2	37.8	88.1
RCS070	RCS070_24_5	Andesite	NA	NA	A4	VH	0.1	12.5	10.4	14.1	<0.1	0.2	<0.1	<0.1	<0.1	1.0	13.2	<0.2	37.7	89.3
RCS070	RCS070_24_6	Andesite	NA	NA	A4	VH	<0.1	13.2	10.2	14.1	<0.1	0.2	<0.1	<0.1	<0.1	0.7	11.9	<0.2	37.6	87.9
RCS070	RCS070_24_7	Andesite	NA	NA	A4	VH	<0.1	13.1	10.3	14.3	<0.1	0.2	<0.1	<0.1	<0.1	0.7	11.5	<0.2	37.7	87.8
RCS070	RCS070_24_8	Andesite	NA	NA	A4	VH	<0.1	11.3	9.3	13.8	<0.1	0.3	<0.1	<0.1	<0.1	1.0	13.5	<0.2	35.9	85.1
RCS070	RCS070_24_10	Andesite	NA	NA	A4	VH	<0.1	13.2	10.7	14.0	<0.1	0.2	<0.1	<0.1	<0.1	1.1	11.6	<0.2	38.0	88.7
RCS074	RCS074_9_8	Monzonite	042SE78	Fracture vein	V6	Vein	0.2	11.1	8.3	16.4	<0.1	0.5	<0.1	<0.1	<0.1	0.2	12.7	<0.2	37.3	86.7
RCS074	RCS074_15_12	Monzonite	042SE78	Fracture vein	V6	Vein	<0.1	11.6	8.8	16.1	<0.1	0.5	<0.1	<0.1	<0.1	0.2	12.8	<0.2	37.8	87.8
RCS074	RCS074_15_14	Monzonite	042SE78	Fracture vein	V6	Vein	<0.1	12.0	10.1	14.2	<0.1	0.3	<0.1	0.1	<0.1	0.2	15.2	0.2	37.7	89.9
RCS074	RCS074_16_8	Monzonite	042SE78	Fracture vein	V6	Vein	<0.1	10.4	9.1	17.6	<0.1	0.4	0.1	<0.1	<0.1	0.2	15.0	<0.2	39.7	92.5
RCS074	RCS074_18_3	Monzonite	042SE78	Fracture vein	V6	Vein	<0.1	11.6	9.6	14.0	<0.1	0.2	<0.1	<0.1	<0.1	0.2	15.6	<0.2	36.9	88.2
RCS074	RCS074_25_12	Monzonite	042SE78	Fracture vein	A3	VH	0.1	9.9	9.6	17.8	0.1	0.9	<0.1	<0.1	<0.1	0.2	15.1	<0.2	40.3	94.0
RCS074	RCS074_25_13	Monzonite	042SE78	Fracture vein	A3	VH	<0.1	10.0	9.1	15.2	<0.1	0.6	<0.1	<0.1	<0.1	0.2	15.0	<0.2	36.6	86.6
RCS076	RCS076_2_3	Monzonite	NA	NA	A3	L Patches	<0.1	11.5	8.8	14.8	<0.1	0.4	<0.1	<0.1	<0.1	0.2	15.3	<0.2	36.8	87.8
RCS076	RCS076_4_8	Monzonite	NA	NA	A3	L Patches	0.1	9.1	8.9	15.9	<0.1	0.6	<0.1	<0.1	<0.1	0.2	15.9	<0.2	37.0	87.7
RCS076	RCS076_4_9	Monzonite	NA	NA	A3	L Patches	<0.1	8.7	9.4	16.7	<0.1	0.7	<0.1	<0.1	<0.1	0.2	16.0	<0.2	38.1	89.7

Sample	Reference	Lithology	Structure	Type	Alt	Texture	Na_pct	Mg_pct	Al_pct	Si_pct	K_pct	Ca_pct	Ti_pct	V_pct	Cr_pct	Mn_pct	Fe_pct	Co_pct	O_pct	Total
RCS076	RCS076_5_1	Monzonite	NA	NA	A3	Replacement	<0.1	10.2	9.5	15.0	<0.1	0.5	<0.1	<0.1	<0.1	0.2	16.8	<0.2	37.4	89.6
RCS076	RCS076_5_2	Monzonite	NA	NA	A3	Replacement	0.1	10.3	9.4	14.9	<0.1	0.4	<0.1	<0.1	<0.1	0.2	16.3	<0.2	37.1	88.7
RCS076	RCS076_5_5	Monzonite	NA	NA	A3	Replacement	<0.1	9.4	8.1	15.6	<0.1	0.9	<0.1	<0.1	<0.1	0.2	14.3	<0.2	35.8	84.3
RCS076	RCS076_5_6	Monzonite	NA	NA	A3	Replacement	<0.1	10.2	8.7	15.2	<0.1	0.7	<0.1	<0.1	<0.1	0.3	15.1	<0.2	36.6	86.8
RCS076	RCS076_5_7	Monzonite	NA	NA	A3	Replacement	<0.1	6.4	8.7	16.8	<0.1	1.0	<0.1	<0.1	<0.1	0.4	16.1	<0.2	36.2	85.6
RCS076	RCS076_5_9	Monzonite	NA	NA	A3	Replacement	<0.1	8.5	9.3	15.3	<0.1	0.5	<0.1	<0.1	<0.1	0.2	17.5	<0.2	36.7	88.0
RCS076	RCS076_5_10	Monzonite	NA	NA	A3	Replacement	0.2	8.8	8.0	15.4	<0.1	0.6	<0.1	<0.1	<0.1	0.2	14.5	<0.2	35.1	82.9
RCS076	RCS076_5_12	Monzonite	NA	NA	A3	Replacement	<0.1	10.9	8.9	15.1	<0.1	0.4	<0.1	<0.1	<0.1	0.3	15.9	<0.2	37.1	88.5
RCS076	RCS076_5_14	Monzonite	NA	NA	A3	Replacement	<0.1	11.1	8.8	14.4	<0.1	0.4	<0.1	<0.1	<0.1	0.2	15.2	<0.2	36.1	86.2
RCS076	RCS076_7_2	Monzonite	NA	NA	A3	Replacement	<0.1	10.9	9.4	15.5	<0.1	0.4	<0.1	<0.1	<0.1	0.2	14.3	<0.2	37.5	88.2
RCS076	RCS076_7_3	Monzonite	NA	NA	A3	Replacement	<0.1	8.3	8.7	17.8	<0.1	0.9	<0.1	<0.1	<0.1	0.1	13.2	<0.2	37.8	86.8
RCS076	RCS076_7_4	Monzonite	NA	NA	A3	Replacement	<0.1	10.5	8.5	14.8	<0.1	0.4	<0.1	<0.1	<0.1	<0.1	14.9	0.2	35.9	85.2
RCS076	RCS076_7_5	Monzonite	NA	NA	A3	Replacement	<0.1	6.7	8.2	16.9	<0.1	0.9	<0.1	0.2	<0.1	0.3	14.8	<0.2	35.9	83.8
RCS076	RCS076_7_6	Monzonite	NA	NA	A3	Replacement	0.1	10.0	9.3	16.1	<0.1	0.5	<0.1	<0.1	<0.1	0.2	14.9	<0.2	37.9	89.0
RCS076	RCS076_8_1	Monzonite	NA	NA	A3	Replacement	<0.1	7.8	9.5	15.6	<0.1	0.6	<0.1	<0.1	<0.1	0.4	18.1	<0.2	37.0	89.0
RCS076	RCS076_8_4	Monzonite	NA	NA	A3	Replacement	<0.1	7.3	9.1	15.9	<0.1	0.6	<0.1	<0.1	<0.1	0.3	15.9	<0.2	35.8	84.8
RCS076	RCS076_10_4	Monzonite	NA	NA	A3	Replacement	<0.1	10.2	9.0	15.8	<0.1	0.6	<0.1	<0.1	<0.1	0.3	14.9	<0.2	37.4	88.1
RCS076	RCS076_10_5	Monzonite	NA	NA	A3	Replacement	<0.1	8.5	8.5	16.5	<0.1	0.8	<0.1	<0.1	<0.1	0.2	16.6	<0.2	37.1	88.2
RCS076	RCS076_10_6	Monzonite	NA	NA	A3	Replacement	<0.1	8.3	9.0	16.6	<0.1	0.7	<0.1	<0.1	<0.1	0.2	15.6	<0.2	37.2	87.5
RCS076	RCS076_10_7	Monzonite	NA	NA	A3	Replacement	0.1	9.7	8.7	15.7	<0.1	0.6	<0.1	<0.1	<0.1	<0.1	14.7	<0.2	36.6	86.1
RCS076	RCS076_10_8	Monzonite	NA	NA	A3	Replacement	<0.1	11.9	9.7	15.9	<0.1	0.5	<0.1	<0.1	<0.1	0.2	14.3	<0.2	39.0	91.4
RCS076	RCS076_10_9	Monzonite	NA	NA	A3	Replacement	<0.1	8.4	9.4	17.1	<0.1	0.7	<0.1	<0.1	<0.1	0.3	16.2	<0.2	38.5	90.6
RCS076	RCS076_10_10	Monzonite	NA	NA	A3	Replacement	<0.1	8.4	8.7	15.9	<0.1	0.7	<0.1	<0.1	<0.1	0.2	16.7	<0.2	36.5	87.1
RCS076	RCS076_10_11	Monzonite	NA	NA	A3	Replacement	<0.1	8.3	8.2	15.0	<0.1	0.7	<0.1	<0.1	<0.1	0.2	18.9	<0.2	35.6	86.9
RCS076	RCS076_10_13	Monzonite	NA	NA	A3	Replacement	<0.1	9.5	8.7	15.8	<0.1	0.7	<0.1	<0.1	<0.1	0.2	14.9	<0.2	36.8	86.7
RCS076	RCS076_12_13	Monzonite	NA	NA	A3	Replacement	<0.1	12.1	9.7	14.3	<0.1	0.1	<0.1	<0.1	<0.1	0.1	14.4	<0.2	37.0	87.7
RCS076	RCS076_12_15	Monzonite	NA	NA	A3	Replacement	<0.1	9.8	8.6	15.1	<0.1	0.5	<0.1	<0.1	<0.1	0.2	14.6	<0.2	35.9	84.7
RCS076	RCS076_12_16	Monzonite	NA	NA	A3	Replacement	<0.1	9.6	8.8	16.8	<0.1	0.8	<0.1	<0.1	<0.1	0.2	13.8	0.2	37.8	88.0
RCS076	RCS076_12_17	Monzonite	NA	NA	A3	Replacement	<0.1	11.2	9.4	14.5	<0.1	0.3	<0.1	<0.1	<0.1	0.1	14.5	<0.2	36.6	86.6

Sample	Reference	Lithology	Structure	Type	Alt	Texture	Na_pct	Mg_pct	Al_pct	Si_pct	K_pct	Ca_pct	Ti_pct	V_pct	Cr_pct	Mn_pct	Fe_pct	Co_pct	O_pct	Total
RCS076	RCS076_12_20	Monzonite	NA	NA	A3	Replacement	0.1	9.0	9.4	15.5	<0.1	0.5	<0.1	<0.1	<0.1	0.3	15.8	<0.2	36.7	87.3
RCS076	RCS076_12_21	Monzonite	NA	NA	A3	Replacement	<0.1	11.2	8.7	15.2	<0.1	0.4	<0.1	<0.1	<0.1	<0.1	13.8	<0.2	36.6	85.8
RCS076	RCS076_14_21	Monzonite	NA	NA	A3	Replacement	<0.1	11.4	8.9	15.0	<0.1	0.5	<0.1	<0.1	<0.1	0.2	16.0	<0.2	37.3	89.2
RCS076	RCS076_16_5	Monzonite	NA	NA	A3	L Patches	<0.1	7.1	8.8	15.3	<0.1	0.6	<0.1	<0.1	<0.1	0.2	18.4	<0.2	35.6	86.1
RCS076	RCS076_16_6	Monzonite	NA	NA	A3	L Patches	<0.1	8.6	8.7	16.7	<0.1	0.8	<0.1	<0.1	<0.1	0.3	14.3	<0.2	37.0	86.5
RCS076	RCS076_16_10	Monzonite	NA	NA	A3	L Patches	<0.1	9.8	8.5	15.3	<0.1	0.6	<0.1	<0.1	<0.1	0.3	14.6	0.3	36.0	85.2
RCS076	RCS076_16_11	Monzonite	NA	NA	A3	L Patches	<0.1	11.3	9.1	14.7	<0.1	0.3	<0.1	<0.1	<0.1	0.2	15.4	<0.2	36.8	87.7
RCS047	RCS047_22_18	Diorite	067SW6 1	Fracture vein	A3	Replacement	0.2	11.3	7.1	17.3	<0.1	0.6	<0.1	<0.1	<0.1	0.2	8.9	<0.2	36.3	81.8
RCS047	RCS047_22_21	Diorite	067SW6 1	Fracture vein	A3	Replacement	0.1	12.3	7.9	17.0	<0.1	0.6	<0.1	<0.1	<0.1	0.2	8.8	<0.2	37.4	84.2
RCS047	RCS047_22_22	Diorite	067SW6 1	Fracture vein	A3	Replacement	<0.1	12.7	7.7	17.3	<0.1	0.4	<0.1	<0.1	<0.1	0.1	8.5	<0.2	37.7	84.5
RCS047	RCS047_24_2	Diorite	067SW6 1	Fracture vein	A3	Replacement	0.2	12.1	7.4	16.8	<0.1	0.8	<0.1	<0.1	<0.1	0.1	8.3	<0.2	36.6	82.3
RCS047	RCS047_24_3	Diorite	067SW6 1	Fracture vein	A3	Replacement	0.2	11.7	7.6	16.5	<0.1	0.7	<0.1	<0.1	<0.1	0.2	8.8	<0.2	36.3	81.9
RCS047	RCS047_24_4	Diorite	067SW6 1	Fracture vein	A3	Replacement	0.2	10.6	7.0	18.0	<0.1	0.6	<0.1	<0.1	<0.1	0.1	10.3	<0.2	37.0	83.7
RCS047	RCS047_24_7	Diorite	067SW6 1	Fracture vein	A3	Replacement	0.1	10.3	6.8	17.1	0.2	1.0	<0.1	<0.1	<0.1	0.2	10.4	<0.2	35.8	81.8
RCS047	RCS047_25_5	Diorite	067SW6 1	Fracture vein	A3	Replacement	0.1	12.1	7.7	17.2	<0.1	1.3	<0.1	<0.1	<0.1	0.2	8.8	<0.2	37.6	85.0
RCS047	RCS047_25_6	Diorite	067SW6 1	Fracture vein	A3	Replacement	0.1	13.1	8.5	17.5	<0.1	1.0	<0.1	<0.1	<0.1	0.1	9.3	<0.2	39.3	88.9
RCS047	RCS047_25_7	Diorite	067SW6 1	Fracture vein	A3	Replacement	0.1	11.7	7.8	16.7	<0.1	1.1	<0.1	<0.1	<0.1	<0.1	8.8	<0.2	36.7	82.9
RCS047	RCS047_25_8	Diorite	067SW6 1	Fracture vein	A3	Replacement	<0.1	12.4	8.1	16.5	<0.1	1.0	<0.1	<0.1	<0.1	<0.1	8.7	<0.2	37.2	83.9
RCS047	RCS047_25_9	Diorite	067SW6 1	Fracture vein	A3	Replacement	0.1	12.0	7.4	16.6	<0.1	0.8	<0.1	<0.1	<0.1	0.2	9.2	<0.2	36.5	82.8
RCS047	RCS047_25_10	Diorite	067SW6 1	Fracture vein	A3	Replacement	<0.1	12.3	8.2	16.8	<0.1	0.9	<0.1	<0.1	<0.1	0.1	8.3	<0.2	37.4	84.0
RCS047	RCS047_25_11	Diorite	067SW6 1	Fracture vein	A3	Replacement	0.2	12.1	8.0	17.2	<0.1	0.8	<0.1	<0.1	<0.1	0.1	8.8	0.2	37.7	85.1
RCS047	RCS047_25_12	Diorite	067SW6 1	Fracture vein	A3	Replacement	<0.1	12.2	7.9	16.9	<0.1	0.9	<0.1	<0.1	<0.1	0.3	9.0	0.2	37.3	84.6
RCS047	RCS047_25_13	Diorite	067SW6 1	Fracture vein	A3	Replacement	0.2	12.5	8.1	16.4	<0.1	0.7	<0.1	<0.1	<0.1	0.2	9.2	<0.2	37.2	84.6
RCS047	RCS047_27_13	Diorite	067SW6 1	Fracture vein	A3	Replacement	<0.1	11.9	8.3	16.4	<0.1	0.8	<0.1	<0.1	<0.1	0.2	9.0	<0.2	36.9	83.4
RCS047	RCS047_27_14	Diorite	067SW6 1	Fracture vein	A3	Replacement	0.2	12.6	8.2	16.8	<0.1	0.8	<0.1	<0.1	<0.1	0.1	8.2	<0.2	37.5	84.4
RCS047	RCS047_29_17	Diorite	067SW6 1	Fracture vein	A3	Replacement	<0.1	12.3	8.2	17.0	<0.1	1.0	<0.1	<0.1	<0.1	0.2	8.9	<0.2	37.7	85.2

Sample	Reference	Lithology	Structure	Type	Alt	Texture	Na_pct	Mg_pct	Al_pct	Si_pct	K_pct	Ca_pct	Ti_pct	V_pct	Cr_pct	Mn_pct	Fe_pct	Co_pct	O_pct	Total
RCS047	RCS047_29_18	Diorite	067SW6 1	Fracture vein	A3	Replacement	<0.1	12.4	7.9	16.8	<0.1	0.9	<0.1	<0.1	0.1	0.3	9.3	<0.2	37.5	85.2
RCS047	RCS047_29_19	Diorite	067SW6 1	Fracture vein	A3	Replacement	<0.1	12.5	8.0	16.5	<0.1	0.8	<0.1	<0.1	<0.1	0.1	9.1	<0.2	37.1	84.1
RCS047	RCS047_29_20	Diorite	067SW6 1	Fracture vein	A3	Replacement	<0.1	12.3	8.3	17.3	<0.1	0.7	<0.1	<0.1	<0.1	0.2	9.9	<0.2	38.3	86.9
RCS047	RCS047_29_22	Diorite	067SW6 1	Fracture vein	A3	Replacement	0.1	12.1	8.0	17.0	<0.1	0.8	<0.1	<0.1	<0.1	0.1	9.0	<0.2	37.4	84.6
RCS047	RCS047_29_23	Diorite	067SW6 1	Fracture vein	A3	Replacement	<0.1	12.0	7.6	17.8	<0.1	1.2	<0.1	<0.1	<0.1	0.2	9.1	<0.2	38.1	86.0
RCS047	RCS047_29_24	Diorite	067SW6 1	Fracture vein	A3	Replacement	0.2	11.8	8.3	16.8	<0.1	0.9	<0.1	<0.1	<0.1	0.2	8.9	<0.2	37.3	84.4
RCS061	RCS061_8_12	Monzonite	NA	NA	A2	Replacement	0.1	12.9	10.0	14.1	<0.1	0.2	<0.1	<0.1	<0.1	0.6	12.3	<0.2	37.4	87.6
RCS061	RCS061_11_5	Monzonite	NA	NA	A2	Replacement	<0.1	13.2	10.2	14.0	<0.1	<0.1	<0.1	<0.1	<0.1	0.7	13.1	<0.2	37.8	89.0
RCS061	RCS061_11_9	Monzonite	NA	NA	A2	Replacement	<0.1	13.5	9.9	14.2	<0.1	0.2	<0.1	<0.1	<0.1	0.5	11.7	<0.2	37.5	87.6
RCS061	RCS061_11_10	Monzonite	NA	NA	A2	Replacement	<0.1	13.2	9.9	15.7	0.5	0.6	0.1	<0.1	<0.1	0.5	11.0	<0.2	39.1	90.6
RCS061	RCS061_11_13	Monzonite	NA	NA	A2	Replacement	<0.1	14.0	10.2	14.1	0.1	0.2	<0.1	<0.1	<0.1	0.5	12.3	<0.2	38.2	89.5
RCS061	RCS061_11_15	Monzonite	NA	NA	A2	Replacement	<0.1	13.3	10.1	14.8	0.2	0.3	0.1	0.1	<0.1	0.5	12.0	<0.2	38.5	89.9
RCS061	RCS061_11_16	Monzonite	NA	NA	A2	Replacement	<0.1	13.7	9.8	13.9	0.2	0.2	0.2	<0.1	<0.1	0.5	11.7	<0.2	37.4	87.6
RCS061	RCS061_11_18	Monzonite	NA	NA	A2	Replacement	<0.1	13.5	10.0	14.1	0.2	0.1	<0.1	<0.1	<0.1	0.5	12.2	<0.2	37.7	88.3
RCS061	RCS061_11_19	Monzonite	NA	NA	A2	Replacement	<0.1	13.7	10.0	14.2	<0.1	0.3	<0.1	<0.1	<0.1	0.5	11.7	<0.2	37.7	88.1
RCS061	RCS061_11_20	Monzonite	NA	NA	A2	Replacement	<0.1	12.8	9.0	14.4	0.4	<0.1	<0.1	<0.1	<0.1	0.5	14.2	<0.2	37.2	88.5
RCS061	RCS061_13_1	Monzonite	NA	NA	A2	Replacement	<0.1	13.8	9.9	13.9	<0.1	<0.1	<0.1	<0.1	<0.1	0.6	12.5	<0.2	37.6	88.3
RCS061	RCS061_13_2	Monzonite	NA	NA	A2	Replacement	<0.1	13.2	9.6	13.9	0.1	0.1	<0.1	<0.1	<0.1	0.7	12.7	<0.2	36.9	87.2
RCS061	RCS061_13_3	Monzonite	NA	NA	A2	Replacement	<0.1	13.4	10.1	13.7	<0.1	0.1	<0.1	<0.1	<0.1	0.4	12.3	<0.2	37.1	87.0
RCS061	RCS061_13_4	Monzonite	NA	NA	A2	Replacement	<0.1	13.7	10.0	13.6	<0.1	<0.1	<0.1	<0.1	<0.1	0.6	11.9	<0.2	37.2	87.1
RCS064	RCS064_6_1	Rhyolite	NA	NA	A4	Replacement	0.1	6.9	8.8	12.1	<0.1	0.1	<0.1	<0.1	<0.1	0.4	24.0	0.2	33.4	86.0
RCS064	RCS064_6_2	Rhyolite	NA	NA	A4	Replacement	<0.1	7.2	8.7	13.2	0.1	0.2	<0.1	<0.1	<0.1	0.5	23.7	<0.2	34.6	88.1
RCS064	RCS064_6_4	Rhyolite	NA	NA	A4	Replacement	<0.1	7.2	8.9	12.6	<0.1	0.1	<0.1	<0.1	<0.1	0.4	24.4	<0.2	34.2	87.8
RCS064	RCS064_6_5	Rhyolite	NA	NA	A4	Replacement	<0.1	7.6	9.1	12.6	<0.1	<0.1	<0.1	<0.1	<0.1	0.4	24.2	<0.2	34.6	88.5
RCS064	RCS064_6_8	Rhyolite	NA	NA	A4	Replacement	<0.1	7.7	9.2	12.8	<0.1	<0.1	<0.1	<0.1	<0.1	0.3	23.9	<0.2	34.8	88.7
RCS064	RCS064_6_9	Rhyolite	NA	NA	A4	Replacement	<0.1	6.9	9.8	12.1	<0.1	<0.1	<0.1	<0.1	<0.1	0.5	24.1	<0.2	34.2	87.6
RCS064	RCS064_6_10	Rhyolite	NA	NA	A4	Replacement	<0.1	6.9	8.4	13.3	0.1	0.2	<0.1	<0.1	<0.1	0.4	22.5	0.3	33.9	86.1
RCS064	RCS064_8_1	Rhyolite	NA	NA	A4	Replacement	<0.1	7.4	9.2	12.3	<0.1	<0.1	<0.1	<0.1	<0.1	0.4	24.1	<0.2	34.1	87.5
RCS064	RCS064_8_3	Rhyolite	NA	NA	A4	Replacement	<0.1	7.3	8.6	12.5	<0.1	<0.1	<0.1	<0.1	<0.1	0.5	24.1	<0.2	33.8	86.6

Sample	Reference	Lithology	Structure	Type	Alt	Texture	Na_pct	Mg_pct	Al_pct	Si_pct	K_pct	Ca_pct	Ti_pct	V_pct	Cr_pct	Mn_pct	Fe_pct	Co_pct	O_pct	Total
RCS064	RCS064_8_5	Rhyolite	NA	NA	A4	Replacement	<0.1	7.1	9.4	12.4	<0.1	0.1	<0.1	<0.1	<0.1	0.4	23.9	<0.2	34.3	87.6
RCS064	RCS064_8_7	Rhyolite	NA	NA	A4	Replacement	<0.1	6.7	8.6	13.8	0.2	0.3	<0.1	<0.1	<0.1	0.5	22.1	<0.2	34.4	86.4
RCS064	RCS064_9_3	Rhyolite	NA	NA	A4	Replacement	<0.1	7.0	9.1	12.3	<0.1	0.2	0.4	<0.1	<0.1	0.4	23.7	<0.2	34.0	87.0
RCS064	RCS064_9_18	Rhyolite	NA	NA	A4	Replacement	0.1	8.0	9.0	12.6	<0.1	<0.1	<0.1	<0.1	<0.1	0.4	22.6	0.3	34.3	87.3
RCS064	RCS064_9_19	Rhyolite	NA	NA	A4	Replacement	0.1	7.5	8.4	13.7	<0.1	0.4	<0.1	<0.1	<0.1	0.4	21.7	<0.2	34.5	86.7
RCS064	RCS064_9_20	Rhyolite	NA	NA	A4	Replacement	<0.1	7.1	8.9	13.3	<0.1	0.3	<0.1	<0.1	<0.1	0.3	22.4	<0.2	34.4	86.7
RCS064	RCS064_11_4	Rhyolite	NA	NA	A4	Replacement	<0.1	6.4	10.0	11.8	<0.1	<0.1	<0.1	<0.1	<0.1	0.5	24.7	<0.2	34.0	87.5
RCS064	RCS064_11_5	Rhyolite	NA	NA	A4	Replacement	<0.1	6.9	8.8	12.6	<0.1	<0.1	<0.1	<0.1	<0.1	0.5	24.6	<0.2	34.0	87.3
RCS064	RCS064_11_6	Rhyolite	NA	NA	A4	Replacement	<0.1	7.3	8.5	12.4	<0.1	<0.1	<0.1	<0.1	<0.1	0.5	24.4	<0.2	33.7	86.7
RCS064	RCS064_11_7	Rhyolite	NA	NA	A4	Replacement	<0.1	7.0	8.7	12.4	<0.1	<0.1	<0.1	<0.1	<0.1	0.6	24.7	<0.2	33.8	87.3
RCS064	RCS064_11_8	Rhyolite	NA	NA	A4	Replacement	<0.1	7.0	8.6	12.4	<0.1	<0.1	<0.1	<0.1	<0.1	0.5	25.2	0.2	34.0	87.9
RCS064	RCS064_13_1	Rhyolite	NA	NA	A4	Replacement	<0.1	7.4	8.9	12.3	<0.1	<0.1	<0.1	<0.1	<0.1	0.4	23.6	<0.2	33.7	86.3
RCS064	RCS064_13_2	Rhyolite	NA	NA	A4	Replacement	<0.1	8.2	9.2	12.8	<0.1	0.1	<0.1	<0.1	<0.1	0.5	22.9	<0.2	34.8	88.5
RCS064	RCS064_13_3	Rhyolite	NA	NA	A4	Replacement	<0.1	7.2	8.8	13.2	<0.1	0.3	<0.1	<0.1	<0.1	0.4	23.0	<0.2	34.5	87.3
RCS064	RCS064_13_4	Rhyolite	NA	NA	A4	Replacement	<0.1	7.7	8.9	12.6	<0.1	0.1	<0.1	<0.1	<0.1	0.4	23.4	<0.2	34.2	87.4
RCS064	RCS064_13_5	Rhyolite	NA	NA	A4	Replacement	0.1	7.9	8.9	12.8	<0.1	<0.1	<0.1	<0.1	<0.1	0.3	23.3	0.2	34.5	88.1
RCS064	RCS064_13_6	Rhyolite	NA	NA	A4	Replacement	<0.1	8.0	9.3	12.5	<0.1	<0.1	<0.1	0.1	<0.1	0.2	23.0	<0.2	34.6	87.8
RCS064	RCS064_13_7	Rhyolite	NA	NA	A4	Replacement	<0.1	7.7	9.0	12.7	<0.1	<0.1	<0.1	<0.1	<0.1	0.4	23.7	0.2	34.5	88.2
RCS064	RCS064_13_8	Rhyolite	NA	NA	A4	Replacement	<0.1	8.5	8.9	12.7	0.1	<0.1	<0.1	<0.1	<0.1	0.3	23.0	<0.2	34.8	88.3
RCS064	RCS064_13_9	Rhyolite	NA	NA	A4	Replacement	0.1	8.2	9.3	12.7	<0.1	<0.1	<0.1	<0.1	<0.1	0.3	23.3	<0.2	34.9	88.7
RCS064	RCS064_15_1	Rhyolite	NA	NA	A4	Replacement	<0.1	7.7	9.3	12.5	<0.1	<0.1	<0.1	<0.1	<0.1	0.3	23.4	<0.2	34.4	87.5
RCS064	RCS064_15_3	Rhyolite	NA	NA	A4	Replacement	0.1	7.7	8.9	12.4	<0.1	<0.1	<0.1	<0.1	<0.1	0.3	23.1	<0.2	33.9	86.4
RCS064	RCS064_16_12	Rhyolite	NA	NA	A4	L Patches	<0.1	7.4	9.1	12.3	<0.1	0.2	<0.1	<0.1	<0.1	0.4	24.0	0.4	34.1	87.8
RCS064	RCS064_16_13	Rhyolite	NA	NA	A4	L Patches	<0.1	7.7	10.0	12.0	<0.1	<0.1	<0.1	<0.1	<0.1	0.5	23.5	<0.2	34.6	88.3
RCS064	RCS064_16_15	Rhyolite	NA	NA	A4	L Patches	<0.1	7.1	9.7	12.0	<0.1	<0.1	<0.1	<0.1	<0.1	0.5	23.0	<0.2	33.7	85.9
RCS075	RCS075_4_7	Monzonite	NA	NA	A3	Patches	0.1	10.6	9.5	15.5	<0.1	1.0	<0.1	<0.1	<0.1	0.2	10.2	<0.2	36.5	83.4
RCS075	RCS075_6_1	Monzonite	NA	NA	A3	Patches	<0.1	11.0	8.9	15.7	<0.1	0.6	<0.1	<0.1	<0.1	0.2	12.4	<0.2	36.9	85.8
RCS075	RCS075_9_17	Monzonite	NA	NA	A3	Patches	<0.1	9.9	8.6	15.5	<0.1	1.0	<0.1	<0.1	<0.1	0.2	11.6	<0.2	35.7	82.6
RCS075	RCS075_16_4	Monzonite	NA	NA	A3	Patches	<0.1	10.1	8.1	17.2	<0.1	1.9	<0.1	<0.1	<0.1	0.4	12.2	<0.2	37.8	87.6

Sample	Reference	Lithology	Structure	Type	Alt	Texture	Na_pct	Mg_pct	Al_pct	Si_pct	K_pct	Ca_pct	Ti_pct	V_pct	Cr_pct	Mn_pct	Fe_pct	Co_pct	O_pct	Total
RCS075	RCS075_18_6	Monzonite	NA	NA	A3	Patches	<0.1	11.4	8.9	16.5	<0.1	0.6	<0.1	<0.1	<0.1	0.2	12.9	<0.2	38.2	88.8
RCS075	RCS075_29_2	Monzonite	NA	NA	A3	Replacement	<0.1	10.7	10.0	15.7	<0.1	0.7	<0.1	<0.1	<0.1	0.3	14.6	<0.2	38.3	90.2
RCS075	RCS075_29_3	Monzonite	NA	NA	A3	Replacement	0.1	10.7	8.9	16.3	<0.1	0.9	<0.1	<0.1	<0.1	0.2	10.5	<0.2	36.9	84.5
RCS075	RCS075_29_4	Monzonite	NA	NA	A3	Replacement	<0.1	12.4	9.4	16.4	<0.1	1.0	<0.1	<0.1	<0.1	0.2	11.5	<0.2	39.0	89.8
RCS075	RCS075_29_7	Monzonite	NA	NA	A3	Replacement	<0.1	11.1	8.6	16.1	<0.1	0.9	<0.1	<0.1	<0.1	0.2	11.0	<0.2	36.9	84.8
RCS075	RCS075_29_9	Monzonite	NA	NA	A3	Replacement	<0.1	11.5	9.0	16.3	<0.1	0.9	<0.1	<0.1	<0.1	0.2	10.9	<0.2	37.6	86.3
RCS075	RCS075_29_10	Monzonite	NA	NA	A3	Replacement	<0.1	10.4	9.6	17.4	<0.1	0.9	<0.1	<0.1	<0.1	0.2	11.1	<0.2	38.9	88.5
RCS075	RCS075_29_11	Monzonite	NA	NA	A3	Replacement	<0.1	8.8	8.2	15.2	0.1	0.9	<0.1	<0.1	<0.1	0.3	13.8	<0.2	34.9	82.2
RCS075	RCS075_29_12	Monzonite	NA	NA	A3	Replacement	<0.1	10.5	8.8	16.8	<0.1	1.1	<0.1	<0.1	<0.1	0.1	11.6	<0.2	37.7	86.5
RCS075	RCS075_29_15	Monzonite	NA	NA	A3	Replacement	<0.1	11.1	8.5	16.2	<0.1	1.2	<0.1	<0.1	<0.1	0.2	11.6	<0.2	37.2	86.0
RCS075	RCS075_29_16	Monzonite	NA	NA	A3	Replacement	<0.1	10.0	8.9	16.8	<0.1	0.9	<0.1	<0.1	<0.1	0.3	13.0	<0.2	37.8	87.7
RCS075	RCS075_29_17	Monzonite	NA	NA	A3	Replacement	<0.1	8.5	9.7	17.4	0.1	0.9	<0.1	<0.1	<0.1	0.2	13.2	<0.2	38.2	88.1
RCS075	RCS075_29_18	Monzonite	NA	NA	A3	Replacement	<0.1	9.2	9.9	17.0	<0.1	1.1	<0.1	<0.1	<0.1	0.2	11.4	<0.2	37.9	86.6
RCS075	RCS075_29_19	Monzonite	NA	NA	A3	Replacement	<0.1	10.2	9.1	16.5	<0.1	1.1	<0.1	<0.1	<0.1	<0.1	9.3	<0.2	36.8	83.0
RCS075	RCS075_29_20	Monzonite	NA	NA	A3	Replacement	<0.1	9.9	9.4	17.4	<0.1	1.2	<0.1	<0.1	<0.1	0.1	11.4	<0.2	38.5	87.8
RCS075	RCS075_29_21	Monzonite	NA	NA	A3	Replacement	<0.1	9.0	9.4	17.3	<0.1	1.0	<0.1	<0.1	<0.1	0.2	10.2	<0.2	37.4	84.6
RCS075	RCS075_29_22	Monzonite	NA	NA	A3	Replacement	<0.1	11.3	8.9	16.3	<0.1	0.9	<0.1	<0.1	<0.1	0.3	12.6	<0.2	38.0	88.2
RCS075	RCS075_29_23	Monzonite	NA	NA	A3	Replacement	<0.1	11.6	8.8	16.3	<0.1	1.0	<0.1	<0.1	<0.1	0.2	11.5	<0.2	37.8	87.2
RCS079	RCS079_9_1	Monzonite	NA	NA	A3	Replacement	<0.1	8.3	9.5	12.9	<0.1	0.1	<0.1	<0.1	<0.1	0.2	22.8	<0.2	35.4	89.3
RCS079	RCS079_9_2	Monzonite	NA	NA	A3	Replacement	<0.1	7.3	9.3	13.4	<0.1	0.3	<0.1	<0.1	<0.1	0.2	24.2	0.2	35.4	90.3
RCS079	RCS079_9_3	Monzonite	NA	NA	A3	Replacement	<0.1	8.6	8.6	13.8	<0.1	0.2	<0.1	<0.1	<0.1	0.3	22.0	<0.2	35.5	89.0
RCS079	RCS079_9_4	Monzonite	NA	NA	A3	Replacement	<0.1	8.4	10.0	13.1	<0.1	0.2	<0.1	<0.1	<0.1	0.3	22.9	0.3	36.0	91.1
RCS079	RCS079_9_5	Monzonite	NA	NA	A3	Replacement	<0.1	8.5	9.3	12.8	<0.1	<0.1	<0.1	<0.1	<0.1	0.3	22.7	<0.2	35.1	88.6
RCS079	RCS079_9_6	Monzonite	NA	NA	A3	Replacement	<0.1	9.0	9.3	13.3	<0.1	0.2	<0.1	<0.1	<0.1	0.4	22.2	0.2	35.9	90.5
RCS079	RCS079_9_7	Monzonite	NA	NA	A3	Replacement	<0.1	8.6	9.2	13.7	<0.1	0.2	<0.1	<0.1	<0.1	0.3	23.1	0.3	36.4	91.7
RCS079	RCS079_9_8	Monzonite	NA	NA	A3	Replacement	<0.1	8.9	8.2	14.2	<0.1	0.2	<0.1	<0.1	<0.1	0.2	22.5	<0.2	36.0	90.2
RCS079	RCS079_9_9	Monzonite	NA	NA	A3	Replacement	<0.1	8.8	8.6	14.1	<0.1	0.3	<0.1	<0.1	<0.1	0.2	22.1	<0.2	36.0	90.1
RCS079	RCS079_9_10	Monzonite	NA	NA	A3	Replacement	<0.1	8.6	8.7	13.5	<0.1	0.3	<0.1	<0.1	<0.1	0.3	21.8	<0.2	35.2	88.3
RCS079	RCS079_9_11	Monzonite	NA	NA	A3	Replacement	<0.1	8.1	9.7	13.2	<0.1	<0.1	<0.1	<0.1	<0.1	0.3	22.5	<0.2	35.6	89.3

Sample	Reference	Lithology	Structure	Type	Alt	Texture	Na_pct	Mg_pct	Al_pct	Si_pct	K_pct	Ca_pct	Ti_pct	V_pct	Cr_pct	Mn_pct	Fe_pct	Co_pct	O_pct	Total
RCS079	RCS079_9_12	Monzonite	NA	NA	A3	Replacement	<0.1	8.7	8.0	14.0	<0.1	0.3	<0.1	<0.1	<0.1	0.2	21.5	<0.2	35.2	87.9
RCS079	RCS079_11_6	Monzonite	NA	NA	A3	Replacement	<0.1	8.7	9.5	13.1	<0.1	0.1	<0.1	<0.1	<0.1	0.2	22.5	<0.2	35.6	89.7
RCS079	RCS079_13_1	Monzonite	NA	NA	A3	Replacement	<0.1	8.5	8.3	13.7	<0.1	0.4	<0.1	<0.1	<0.1	0.2	22.0	<0.2	35.1	88.1
RCS079	RCS079_13_2	Monzonite	NA	NA	A3	Replacement	<0.1	8.6	8.2	13.5	<0.1	0.2	<0.1	<0.1	0.1	0.3	22.9	<0.2	35.3	89.2
RCS079	RCS079_13_4	Monzonite	NA	NA	A3	Replacement	<0.1	7.9	7.7	14.2	<0.1	0.5	<0.1	<0.1	<0.1	0.3	22.3	<0.2	35.0	87.9
RCS079	RCS079_13_5	Monzonite	NA	NA	A3	Replacement	0.2	8.4	8.6	13.9	<0.1	0.2	<0.1	<0.1	<0.1	0.2	22.8	<0.2	35.8	90.0
RCS079	RCS079_13_9	Monzonite	NA	NA	A3	Replacement	<0.1	8.5	8.7	13.1	<0.1	0.2	<0.1	<0.1	<0.1	0.2	22.3	<0.2	34.9	87.8
RCS079	RCS079_14_2	Monzonite	NA	NA	A3	Replacement	<0.1	8.7	8.3	13.7	<0.1	0.1	<0.1	<0.1	<0.1	0.3	22.9	<0.2	35.4	89.4
RCS079	RCS079_20_6	Monzonite	NA	NA	A3	Replacement	0.1	8.3	9.1	12.7	<0.1	<0.1	<0.1	<0.1	<0.1	0.2	22.4	0.2	34.7	87.9
RCS079	RCS079_20_7	Monzonite	NA	NA	A3	Replacement	<0.1	7.8	8.8	12.8	0.1	0.1	<0.1	<0.1	<0.1	0.2	22.1	0.2	34.1	86.3
RCS079	RCS079_21_10	Monzonite	NA	NA	A3	Replacement	<0.1	8.3	9.4	13.3	<0.1	<0.1	<0.1	<0.1	<0.1	0.2	22.8	0.3	35.8	90.1
RCS079	RCS079_21_11	Monzonite	NA	NA	A3	Replacement	<0.1	8.2	9.1	12.6	<0.1	<0.1	<0.1	<0.1	<0.1	0.2	22.7	<0.2	34.5	87.3
RCS087	RCS087_9_4	Dacite	NA	NA	A6	Replacement	0.1	10.1	9.6	14.8	0.1	0.4	<0.1	<0.1	<0.1	0.4	16.2	<0.2	37.0	88.7
RCS087	RCS087_9_9	Dacite	NA	NA	A6	Replacement	<0.1	9.9	10.0	14.9	0.4	0.2	<0.1	<0.1	<0.1	0.2	15.3	<0.2	37.0	87.9
RCS087	RCS087_9_10	Dacite	NA	NA	A6	Replacement	0.1	10.2	9.3	14.6	<0.1	0.3	<0.1	<0.1	<0.1	0.1	16.3	0.3	36.5	87.8
RCS087	RCS087_9_11	Dacite	NA	NA	A6	Replacement	<0.1	9.7	9.8	15.1	0.7	0.3	<0.1	<0.1	<0.1	0.2	14.6	0.2	37.0	87.6
RCS087	RCS087_9_12	Dacite	NA	NA	A6	Replacement	0.1	8.7	10.4	13.7	0.3	0.6	<0.1	<0.1	<0.1	0.1	15.6	<0.2	35.4	84.9
RCS087	RCS087_9_14	Dacite	NA	NA	A6	Replacement	<0.1	10.1	9.7	14.7	0.4	0.3	<0.1	<0.1	<0.1	0.1	14.9	<0.2	36.4	86.5
RCS087	RCS087_9_18	Dacite	NA	NA	A6	Replacement	0.1	10.5	9.7	14.5	<0.1	0.3	<0.1	<0.1	<0.1	0.3	16.0	<0.2	36.9	88.2
RCS087	RCS087_10_3	Dacite	NA	NA	A6	Replacement	0.1	9.9	11.0	14.9	0.4	0.2	<0.1	<0.1	<0.1	0.2	15.1	<0.2	37.9	89.8
RCS087	RCS087_10_6	Dacite	NA	NA	A6	Replacement	<0.1	10.1	9.7	14.5	0.2	0.4	<0.1	<0.1	<0.1	0.1	15.8	<0.2	36.5	87.2
RCS087	RCS087_10_7	Dacite	NA	NA	A6	Replacement	<0.1	10.9	9.4	14.7	<0.1	0.2	<0.1	<0.1	<0.1	0.5	16.1	<0.2	37.2	88.9
RCS087	RCS087_10_8	Dacite	NA	NA	A6	Replacement	<0.1	11.2	9.9	15.3	<0.1	0.3	<0.1	<0.1	<0.1	0.2	15.8	<0.2	38.3	90.9
RCS087	RCS087_10_12	Dacite	NA	NA	A6	Replacement	<0.1	11.2	9.2	14.4	<0.1	0.2	0.1	<0.1	<0.1	0.2	16.1	<0.2	36.9	88.4
RCS087	RCS087_10_13	Dacite	NA	NA	A6	Replacement	0.1	9.5	10.4	15.3	0.8	0.3	<0.1	<0.1	<0.1	0.2	14.9	<0.2	37.7	89.3
RCS087	RCS087_10_14	Dacite	NA	NA	A6	Replacement	0.1	10.9	9.2	14.6	<0.1	0.2	<0.1	<0.1	<0.1	0.2	15.7	<0.2	36.7	87.6
RCS087	RCS087_10_15	Dacite	NA	NA	A6	Replacement	0.1	11.2	9.2	14.6	<0.1	0.1	<0.1	<0.1	<0.1	0.3	14.6	<0.2	36.6	86.6
RCS087	RCS087_12_7	Dacite	NA	NA	A6	Replacement	<0.1	12.1	9.2	14.5	<0.1	0.2	<0.1	<0.1	<0.1	<0.1	14.0	<0.2	36.9	86.9
RCS087	RCS087_12_8	Dacite	NA	NA	A6	Replacement	0.1	10.1	9.2	14.6	<0.1	0.2	<0.1	<0.1	<0.1	0.2	16.2	<0.2	36.3	86.8

Sample	Reference	Lithology	Structure	Type	Alt	Texture	Na_pct	Mg_pct	Al_pct	Si_pct	K_pct	Ca_pct	Ti_pct	V_pct	Cr_pct	Mn_pct	Fe_pct	Co_pct	O_pct	Total
RCS087	RCS087_13_6	Dacite	NA	NA	A6	Replacement	0.1	9.6	10.1	14.4	0.6	0.1	0.1	<0.1	<0.1	0.3	16.3	<0.2	36.8	88.6
RCS087	RCS087_15_3	Dacite	NA	NA	A6	Replacement	0.1	9.9	10.1	13.7	<0.1	0.2	<0.1	<0.1	<0.1	0.2	16.3	<0.2	36.0	86.5
RCS087	RCS087_17_3	Dacite	NA	NA	A6	Patches	<0.1	9.8	10.6	14.3	0.3	0.2	<0.1	<0.1	<0.1	0.1	15.6	<0.2	36.9	87.8
RCS087	RCS087_17_4	Dacite	NA	NA	A6	Patches	<0.1	10.3	9.8	14.5	<0.1	0.2	<0.1	<0.1	<0.1	0.1	15.8	<0.2	36.8	87.6
RCS087	RCS087_17_5	Dacite	NA	NA	A6	Patches	0.2	10.6	10.2	14.7	0.1	0.2	<0.1	<0.1	<0.1	<0.1	15.7	<0.2	37.5	89.1
RCS087	RCS087_17_12	Dacite	NA	NA	A6	Patches	<0.1	10.9	9.8	15.1	0.2	0.3	<0.1	<0.1	<0.1	0.2	15.2	<0.2	37.7	89.4
RCS087	RCS087_19_3	Dacite	NA	NA	A6	Replacement	0.2	11.0	8.8	14.1	<0.1	0.2	<0.1	<0.1	<0.1	<0.1	15.4	<0.2	35.7	85.4
RCS087	RCS087_19_4	Dacite	NA	NA	A6	Replacement	<0.1	11.3	9.3	14.8	<0.1	0.2	<0.1	<0.1	<0.1	0.1	15.2	<0.2	37.1	88.1
RCS087	RCS087_19_5	Dacite	NA	NA	A6	Replacement	<0.1	10.6	8.6	14.6	<0.1	0.2	<0.1	<0.1	<0.1	0.2	15.7	<0.2	36.0	85.8
RCS087	RCS087_19_7	Dacite	NA	NA	A6	Replacement	<0.1	10.9	9.8	14.7	0.3	0.3	<0.1	<0.1	<0.1	<0.1	15.6	<0.2	37.4	88.8
RCS087	RCS087_19_8	Dacite	NA	NA	A6	Replacement	0.1	11.3	9.1	14.6	<0.1	0.2	<0.1	<0.1	<0.1	0.2	15.7	<0.2	36.9	88.1
RCS038	RCS038_2_4	Monzonite	31NE87	Fault Zone	A4	Patches	<0.1	9.7	7.9	16.4	<0.1	1.3	<0.1	<0.1	<0.1	0.1	14.4	<0.2	36.8	86.5
RCS038	RCS038_4_8	Monzonite	31NE87	Fault Zone	A4	Patches	<0.1	9.6	7.7	17.4	<0.1	1.0	<0.1	<0.1	<0.1	0.1	13.2	<0.2	37.2	86.2
RCS038	RCS038_6_2	Monzonite	31NE87	Fault Zone	A4	Patches	<0.1	9.9	7.8	16.5	0.1	1.0	<0.1	<0.1	<0.1	0.1	14.4	<0.2	37.0	86.9
RCS038	RCS038_7_14	Monzonite	31NE87	Fault Zone	A4	Replacement	<0.1	10.1	8.3	15.8	<0.1	0.6	<0.1	<0.1	<0.1	0.2	15.1	<0.2	36.8	86.9
RCS038	RCS038_7_15	Monzonite	31NE87	Fault Zone	A4	Replacement	<0.1	9.9	8.6	15.1	<0.1	0.7	<0.1	<0.1	<0.1	0.1	14.9	<0.2	36.1	85.4
RCS038	RCS038_7_16	Monzonite	31NE87	Fault Zone	A4	Replacement	0.1	9.9	8.5	15.1	<0.1	0.7	<0.1	<0.1	<0.1	0.2	15.7	<0.2	36.1	86.2
RCS038	RCS038_7_17	Monzonite	31NE87	Fault Zone	A4	Replacement	<0.1	10.0	8.6	15.1	<0.1	0.7	<0.1	<0.1	<0.1	0.2	15.3	<0.2	36.2	86.1
RCS038	RCS038_7_18	Monzonite	31NE87	Fault Zone	A4	Replacement	<0.1	9.9	8.9	14.9	<0.1	0.7	<0.1	<0.1	<0.1	0.2	16.5	0.2	36.5	87.8
RCS038	RCS038_7_19	Monzonite	31NE87	Fault Zone	A4	Replacement	<0.1	9.3	8.4	16.0	0.1	0.8	<0.1	<0.1	<0.1	0.2	14.5	<0.2	36.4	85.7
RCS038	RCS038_7_20	Monzonite	31NE87	Fault Zone	A4	Replacement	<0.1	10.1	7.9	15.9	<0.1	1.0	<0.1	<0.1	<0.1	0.1	13.6	<0.2	36.2	84.8
RCS038	RCS038_7_21	Monzonite	31NE87	Fault Zone	A4	Replacement	<0.1	10.1	8.0	16.3	<0.1	0.9	<0.1	<0.1	<0.1	0.2	14.0	<0.2	36.7	86.2
RCS038	RCS038_7_22	Monzonite	31NE87	Fault Zone	A4	Replacement	<0.1	9.4	8.4	15.2	<0.1	0.9	<0.1	<0.1	<0.1	0.2	15.3	<0.2	35.8	85.2
RCS038	RCS038_7_23	Monzonite	31NE87	Fault Zone	A4	Replacement	<0.1	10.0	9.0	15.3	<0.1	0.8	<0.1	<0.1	<0.1	0.2	15.4	<0.2	36.8	87.4
RCS038	RCS038_7_24	Monzonite	31NE87	Fault Zone	A4	Replacement	<0.1	9.4	8.1	15.9	<0.1	1.0	<0.1	<0.1	<0.1	0.2	13.6	<0.2	35.8	83.8
RCS038	RCS038_7_25	Monzonite	31NE87	Fault Zone	A4	Replacement	<0.1	10.3	8.1	15.9	<0.1	0.7	<0.1	<0.1	<0.1	0.2	14.0	<0.2	36.5	85.6
RCS038	RCS038_9_8	Monzonite	31NE87	Fault Zone	A4	Patches	<0.1	9.7	7.9	17.1	0.1	1.1	<0.1	<0.1	<0.1	0.2	14.0	<0.2	37.4	87.6
RCS038	RCS038_9_10	Monzonite	31NE87	Fault Zone	A4	Patches	0.1	9.2	7.7	17.3	0.1	1.2	<0.1	<0.1	<0.1	<0.1	13.9	<0.2	37.2	86.7
RCS038	RCS038_11_17	Monzonite	31NE87	Fault Zone	A4	VH	<0.1	10.6	6.7	16.7	<0.1	1.3	<0.1	<0.1	<0.1	0.1	12.7	0.2	36.2	84.5

Sample	Reference	Lithology	Structure	Type	Alt	Texture	Na_pct	Mg_pct	Al_pct	Si_pct	K_pct	Ca_pct	Ti_pct	V_pct	Cr_pct	Mn_pct	Fe_pct	Co_pct	O_pct	Total
RCS038	RCS038_11_18	Monzonite	31NE87	Fault Zone	A4	VH	<0.1	9.5	7.5	17.4	<0.1	1.2	<0.1	<0.1	0.1	<0.1	13.5	<0.2	37.2	86.4
RCS038	RCS038_13_14	Monzonite	31NE87	Fault Zone	A4	Patches	<0.1	9.6	8.1	17.5	0.1	1.2	<0.1	<0.1	<0.1	0.1	13.2	<0.2	37.8	87.6
RCS038	RCS038_13_15	Monzonite	31NE87	Fault Zone	A4	Patches	<0.1	9.2	7.2	17.9	0.2	1.1	<0.1	<0.1	<0.1	<0.1	13.3	<0.2	37.3	86.2
RCS038	RCS038_13_16	Monzonite	31NE87	Fault Zone	A4	Patches	<0.1	9.7	7.7	16.8	0.1	1.0	<0.1	<0.1	<0.1	0.2	13.7	<0.2	36.8	86.0
RCS038	RCS038_17_2	Monzonite	31NE87	Fault Zone	A4	Replacement	<0.1	9.5	6.9	17.9	0.3	1.4	<0.1	<0.1	<0.1	0.2	13.4	<0.2	37.3	86.7
RCS038	RCS038_17_4	Monzonite	31NE87	Fault Zone	A4	Replacement	<0.1	10.0	8.1	16.4	<0.1	0.9	<0.1	<0.1	<0.1	0.1	13.5	<0.2	36.7	85.6
RCS038	RCS038_17_6	Monzonite	31NE87	Fault Zone	A4	Replacement	<0.1	9.3	8.3	15.3	<0.1	1.0	<0.1	<0.1	<0.1	0.1	13.8	<0.2	35.4	83.2
RCS040	RCS040_2_6	Monzonite	227NW6 6	Fracture	A4	Patches	0.1	11.4	7.7	17.2	0.1	1.8	<0.1	<0.1	<0.1	0.1	12.7	<0.2	38.4	89.4
RCS040	RCS040_7_3	Monzonite	227NW6 6	Fracture	A4	Replacement	<0.1	11.4	9.1	16.7	<0.1	1.1	<0.1	<0.1	<0.1	0.2	12.0	0.3	38.7	89.4
RCS040	RCS040_7_25	Monzonite	227NW6 6	Fracture	A4	Replacement	0.1	8.8	9.1	16.6	<0.1	1.1	<0.1	<0.1	<0.1	0.2	10.7	<0.2	36.4	83.0
RCS040	RCS040_7_26	Monzonite	227NW6 6	Fracture	A4	Replacement	0.1	10.9	8.7	17.0	<0.1	1.0	<0.1	<0.1	<0.1	0.1	11.9	<0.2	38.3	88.1
RCS040	RCS040_10_3	Monzonite	227NW6 6	Fracture	A4	Replacement	0.1	11.6	8.4	17.5	<0.1	1.3	<0.1	<0.1	<0.1	0.1	11.8	<0.2	39.1	90.0
RCS040	RCS040_13_3	Monzonite	227NW6 6	Fracture	A4	Replacement	0.1	10.8	7.8	16.8	<0.1	1.6	<0.1	<0.1	<0.1	0.2	12.7	<0.2	37.7	87.7
RCS040	RCS040_15_2	Monzonite	227NW6 6	Fracture	A4	Patches	0.2	11.3	8.2	17.4	<0.1	1.5	<0.1	<0.1	<0.1	0.1	12.2	<0.2	38.8	89.7
RCS040	RCS040_15_5	Monzonite	227NW6 6	Fracture	A4	Patches	<0.1	10.2	8.6	16.9	<0.1	1.3	<0.1	<0.1	<0.1	<0.1	12.3	<0.2	37.7	86.9
RCS040	RCS040_16_1	Monzonite	227NW6 6	Fracture	A4	Patches	0.2	11.0	7.6	17.3	<0.1	1.5	<0.1	<0.1	<0.1	<0.1	11.6	<0.2	37.7	86.9
RCS040	RCS040_18_3	Monzonite	227NW6 6	Fracture	A4	Patches	<0.1	12.0	8.7	15.9	<0.1	0.8	<0.1	<0.1	<0.1	0.2	13.6	0.2	38.2	89.6
RCS040	RCS040_18_5	Monzonite	227NW6 6	Fracture	A4	Patches	0.2	10.7	7.9	17.3	0.2	1.4	<0.1	<0.1	<0.1	<0.1	13.5	<0.2	38.3	89.4
RCS040	RCS040_18_6	Monzonite	227NW6 6	Fracture	A4	Patches	0.1	10.8	7.7	17.1	0.1	1.9	<0.1	<0.1	<0.1	0.2	13.6	<0.2	38.3	89.8
RCS040	RCS040_19_3	Monzonite	227NW6 6	Fracture	A4	Patches	0.1	10.0	7.0	15.5	0.2	1.5	<0.1	<0.1	<0.1	0.2	12.1	<0.2	34.8	81.4
RCS040	RCS040_19_4	Monzonite	227NW6 6	Fracture	A4	Patches	0.2	10.9	7.8	17.8	<0.1	1.8	<0.1	<0.1	<0.1	0.2	12.3	<0.2	38.9	89.9
RCS040	RCS040_19_5	Monzonite	227NW6 6	Fracture	A4	Patches	0.2	11.1	8.0	17.6	<0.1	1.3	<0.1	<0.1	<0.1	0.2	11.9	<0.2	38.6	88.8
RCS040	RCS040_19_6	Monzonite	227NW6 6	Fracture	A4	Patches	<0.1	11.9	8.0	16.8	<0.1	1.1	<0.1	<0.1	<0.1	0.1	12.6	<0.2	38.3	88.9
RCS040	RCS040_19_7	Monzonite	227NW6 6	Fracture	A4	Patches	0.1	11.0	8.0	16.8	<0.1	1.3	<0.1	<0.1	<0.1	0.2	12.8	<0.2	37.8	88.0
RCS040	RCS040_21_2	Monzonite	227NW6 6	Fracture	A4	Patches	<0.1	11.7	8.1	17.7	<0.1	1.3	<0.1	<0.1	<0.1	0.2	9.8	<0.2	38.5	87.4
RCS040	RCS040_21_3	Monzonite	227NW6 6	Fracture	A4	Patches	0.1	12.5	8.2	17.1	<0.1	1.5	<0.1	<0.1	<0.1	0.2	10.0	<0.2	38.6	88.3

Sample	Reference	Lithology	Structure	Type	Alt	Texture	Na_pct	Mg_pct	Al_pct	Si_pct	K_pct	Ca_pct	Ti_pct	V_pct	Cr_pct	Mn_pct	Fe_pct	Co_pct	O_pct	Total
RCS040	RCS040_21_4	Monzonite	227NW6 6	Fracture	A4	Patches	0.2	9.9	7.6	17.6	0.1	1.7	<0.1	<0.1	<0.1	<0.1	10.8	<0.2	37.3	85.2
RCS059	RCS059_2_4	Monzodiorite	NA	NA	A3	Replacement	0.1	7.9	8.3	17.6	0.2	1.4	<0.1	<0.1	<0.1	0.1	9.8	<0.2	36.2	81.7
RCS059	RCS059_2_7	Monzodiorite	NA	NA	A3	Replacement	0.1	10.2	8.3	16.5	<0.1	1.1	<0.1	<0.1	<0.1	0.3	10.7	<0.2	36.6	83.8
RCS059	RCS059_4_4	Monzodiorite	NA	NA	A3	Replacement	0.2	10.2	8.7	16.6	0.4	1.0	<0.1	<0.1	<0.1	0.3	11.6	<0.2	37.3	86.2
RCS059	RCS059_6_1	Monzodiorite	NA	NA	A3	Replacement	<0.1	11.5	9.7	16.6	0.2	0.9	<0.1	<0.1	<0.1	0.3	11.1	<0.2	38.8	89.2
RCS059	RCS059_6_2	Monzodiorite	NA	NA	A3	Replacement	0.1	11.5	8.8	16.7	0.8	0.7	<0.1	<0.1	<0.1	0.3	12.5	<0.2	38.6	90.0
RCS059	RCS059_6_3	Monzodiorite	NA	NA	A3	Replacement	<0.1	11.5	9.8	16.6	0.2	0.6	<0.1	<0.1	<0.1	0.3	12.2	<0.2	39.1	90.2
RCS059	RCS059_6_4	Monzodiorite	NA	NA	A3	Replacement	<0.1	12.4	9.6	16.1	<0.1	0.5	<0.1	<0.1	<0.1	0.4	12.3	<0.2	39.0	90.3
RCS059	RCS059_6_5	Monzodiorite	NA	NA	A3	Replacement	<0.1	11.8	10.0	16.5	<0.1	0.7	<0.1	<0.1	<0.1	0.3	11.9	<0.2	39.4	90.6
RCS059	RCS059_6_6	Monzodiorite	NA	NA	A3	Replacement	<0.1	10.6	10.3	16.6	0.2	0.7	<0.1	<0.1	<0.1	0.3	12.1	<0.2	38.9	89.6
RCS059	RCS059_6_7	Monzodiorite	NA	NA	A3	Replacement	<0.1	8.7	10.7	17.2	0.6	0.6	<0.1	<0.1	<0.1	0.4	13.2	<0.2	39.1	90.4
RCS059	RCS059_6_10	Monzodiorite	NA	NA	A3	Replacement	<0.1	13.0	9.9	15.3	<0.1	0.4	<0.1	<0.1	<0.1	0.4	12.4	<0.2	38.7	90.1
RCS059	RCS059_12_5	Monzodiorite	NA	NA	A3	Replacement	0.1	11.0	8.6	16.8	0.4	1.2	<0.1	<0.1	<0.1	0.3	11.2	<0.2	38.0	87.5
RCS059	RCS059_15_3	Monzodiorite	NA	NA	A3	Replacement	0.1	11.2	9.2	17.4	<0.1	1.0	<0.1	<0.1	<0.1	0.3	11.1	<0.2	39.2	89.4
RCS059	RCS059_15_5	Monzodiorite	NA	NA	A3	Replacement	0.2	8.7	9.0	17.3	<0.1	1.0	<0.1	<0.1	<0.1	0.3	10.3	<0.2	37.0	83.7
RCS059	RCS059_20_8	Monzodiorite	NA	NA	A3	Replacement	0.1	11.1	8.0	16.8	0.2	1.6	<0.1	<0.1	<0.1	0.3	9.8	<0.2	37.2	85.0
RCS059	RCS059_20_9	Monzodiorite	NA	NA	A3	Replacement	0.1	10.8	8.1	16.1	0.4	1.2	<0.1	<0.1	<0.1	0.3	10.2	<0.2	36.4	83.6
RCS014	RCS014_6_11	Dacite	NA	NA	A6	Replacement	<0.1	16.23	9.98	16	<0.1	0.28	<0.1	<0.1	<0.1	0.24	5.69	<0.2	39.65	88.07
RCS014	RCS014_6_12	Dacite	NA	NA	A6	Replacement	<0.1	15.4	9.84	16.27	0.1	0.36	<0.1	<0.1	<0.1	0.36	6.45	<0.2	39.57	88.35
RCS014	RCS014_7_8	Dacite	NA	NA	A6	Replacement	<0.1	15.09	10.09	16.34	0.38	0.35	<0.1	<0.1	<0.1	0.33	5.1	<0.2	39.34	87.02
RCS014	RCS014_7_9	Dacite	NA	NA	A6	Replacement	<0.1	15.22	9.59	16.07	<0.1	0.37	<0.1	<0.1	<0.1	0.31	5.27	<0.2	38.64	85.47
RCS014	RCS014_9_3	Dacite	NA	NA	A6	Replacement	<0.1	15.07	9.5	15.66	<0.1	0.42	<0.1	<0.1	<0.1	0.32	5.11	<0.2	38	84.08
RCS014	RCS014_9_4	Dacite	NA	NA	A6	Replacement	<0.1	15.54	10.34	15.88	0.23	0.29	<0.1	<0.1	<0.1	0.34	5.18	<0.2	39.27	87.07
RCS014	RCS014_9_5	Dacite	NA	NA	A6	Replacement	<0.1	13.04	9.96	17.56	<0.1	0.52	<0.1	<0.1	<0.1	0.28	5.03	<0.2	39.25	85.64
RCS014	RCS014_9_6	Dacite	NA	NA	A6	Replacement	<0.1	16.15	9.86	15.85	<0.1	0.34	<0.1	<0.1	<0.1	0.32	5.08	<0.2	39.22	86.82
RCS014	RCS014_9_7	Dacite	NA	NA	A6	Replacement	<0.1	15.69	9.45	15.74	<0.1	0.37	<0.1	<0.1	<0.1	0.31	5.28	<0.2	38.47	85.31
RCS014	RCS014_9_8	Dacite	NA	NA	A6	Replacement	<0.1	15.01	9.83	16.41	0.17	0.42	<0.1	<0.1	<0.1	0.36	5.2	<0.2	39.17	86.57
RCS014	RCS014_9_9	Dacite	NA	NA	A6	Replacement	<0.1	16.02	10.02	16.15	0.19	0.34	<0.1	<0.1	<0.1	0.35	5.41	<0.2	39.77	88.25
RCS014	RCS014_9_10	Dacite	NA	NA	A6	Replacement	<0.1	15.91	9.97	16.12	<0.1	0.37	<0.1	<0.1	<0.1	0.27	5.27	<0.2	39.51	87.42

Sample	Reference	Lithology	Structure	Type	Alt	Texture	Na_pct	Mg_pct	Al_pct	Si_pct	K_pct	Ca_pct	Ti_pct	V_pct	Cr_pct	Mn_pct	Fe_pct	Co_pct	O_pct	Total
RCS014	RCS014_11_8	Dacite	NA	NA	A6	Replacement	<0.1	15.57	10	16.54	0.19	0.37	<0.1	<0.1	<0.1	0.38	6.36	<0.2	40.17	89.58
RCS014	RCS014_11_9	Dacite	NA	NA	A6	Replacement	<0.1	15.25	9.88	16.83	0.19	0.39	<0.1	<0.1	<0.1	0.36	6.6	<0.2	40.26	89.76
RCS014	RCS014_11_10	Dacite	NA	NA	A6	Replacement	<0.1	14.95	9.66	16.01	<0.1	0.36	<0.1	<0.1	<0.1	0.38	6.89	<0.2	38.95	87.2
RCS014	RCS014_13_13	Dacite	NA	NA	A6	Replacement	0.24	13.77	10.02	17.54	0.21	0.55	<0.1	<0.1	<0.1	0.32	6.24	<0.2	40.22	89.11
RCS014	RCS014_13_15	Dacite	NA	NA	A6	Replacement	<0.1	14.08	8.6	15.17	<0.1	0.45	<0.1	<0.1	<0.1	0.42	7.29	<0.2	36.62	82.63
RCS014	RCS014_18_2	Dacite	NA	NA	A6	Replacement	<0.1	14.33	9.64	15.69	<0.1	0.41	<0.1	<0.1	<0.1	0.29	5.86	<0.2	37.88	84.1
RCS014	RCS014_18_3	Dacite	NA	NA	A6	Replacement	<0.1	15.94	10.1	16.39	0.1	0.35	<0.1	<0.1	<0.1	0.33	5.45	<0.2	40.05	88.71
RCS014	RCS014_18_5	Dacite	NA	NA	A6	Replacement	<0.1	16.05	10.2	15.99	<0.1	0.32	<0.1	<0.1	<0.1	0.37	5.72	<0.2	39.79	88.44
RCS014	RCS014_19_11	Dacite	NA	NA	A6	Replacement	<0.1	16.01	10.62	16.55	0.19	0.33	<0.1	<0.1	<0.1	0.34	5.2	<0.2	40.65	89.89
RCS014	RCS014_19_14	Dacite	NA	NA	A6	Replacement	<0.1	14	9.79	17.14	<0.1	0.51	<0.1	<0.1	<0.1	0.25	5.19	<0.2	39.22	86.1
RCS037	RCS037_8_18	Monzonite	NA	NA	A3	Replacement	<0.1	10.6	8.05	13.92	<0.1	0.17	<0.1	<0.1	<0.1	0.23	18.02	0.22	35.42	86.63
RCS037	RCS037_8_20	Monzonite	NA	NA	A3	Replacement	<0.1	9.66	7.5	14.98	0.13	0.88	<0.1	<0.1	<0.1	0.26	16.97	<0.2	35.42	85.8
RCS037	RCS037_8_23	Monzonite	NA	NA	A3	Replacement	<0.1	10.44	7.96	13.93	<0.1	0.12	<0.1	<0.1	<0.1	0.25	17.92	0.21	35.17	86
RCS037	RCS037_8_24	Monzonite	NA	NA	A3	Replacement	<0.1	10.4	7.85	14.53	<0.1	1.21	<0.1	<0.1	<0.1	0.2	17.1	<0.2	35.82	87.11
RCS037	RCS037_8_25	Monzonite	NA	NA	A3	Replacement	<0.1	10.46	8.32	13.92	<0.1	0.59	<0.1	<0.1	<0.1	0.2	17.64	<0.2	35.58	86.71
RCS037	RCS037_10_8	Monzonite	NA	NA	A3	Replacement	<0.1	9.94	8.67	13.87	<0.1	0.3	<0.1	<0.1	<0.1	0.19	16.97	<0.2	35.16	85.1
RCS037	RCS037_11_1	Monzonite	NA	NA	A3	Patches	<0.1	10.33	9.02	13.94	<0.1	0.25	<0.1	<0.1	<0.1	0.19	16.76	0.25	35.73	86.47
RCS037	RCS037_11_5	Monzonite	NA	NA	A3	Patches	<0.1	9.34	7.54	15.29	0.33	1.09	<0.1	<0.1	<0.1	0.14	15.89	<0.2	35.44	85.06
RCS037	RCS037_13_16	Monzonite	NA	NA	A3	Patches	0.38	9.53	8.63	14.29	<0.1	0.43	<0.1	<0.1	<0.1	0.19	16.68	<0.2	35.37	85.5
RCS037	RCS037_13_17	Monzonite	NA	NA	A3	Patches	<0.1	10.47	9.06	13.7	<0.1	0.15	<0.1	<0.1	<0.1	0.21	17.35	0.23	35.7	86.87
RCS037	RCS037_13_18	Monzonite	NA	NA	A3	Patches	<0.1	10.25	9.26	13.81	<0.1	0.16	<0.1	<0.1	<0.1	0.24	17.19	<0.2	35.88	86.79
RCS037	RCS037_13_19	Monzonite	NA	NA	A3	Patches	<0.1	10.48	9.39	13.3	<0.1	0.13	<0.1	<0.1	<0.1	0.25	17.9	<0.2	35.73	87.18
RCS037	RCS037_13_20	Monzonite	NA	NA	A3	Patches	<0.1	10.6	9.33	13.1	<0.1	<0.1	<0.1	<0.1	<0.1	0.19	17.98	<0.2	35.55	86.75
RCS037	RCS037_13_21	Monzonite	NA	NA	A3	Patches	<0.1	10.38	9.3	13.12	<0.1	<0.1	<0.1	<0.1	<0.1	0.18	17.78	<0.2	35.28	86.04
RCS037	RCS037_13_22	Monzonite	NA	NA	A3	Patches	<0.1	10.31	9.14	13.51	<0.1	0.14	<0.1	<0.1	<0.1	0.16	17.54	0.2	35.49	86.49
RCS037	RCS037_13_23	Monzonite	NA	NA	A3	Patches	0.17	10.33	9.07	14	<0.1	0.16	<0.1	<0.1	<0.1	0.22	17.51	0.29	36.1	87.85
RCS037	RCS037_13_24	Monzonite	NA	NA	A3	Patches	<0.1	9.7	8.2	13.57	<0.1	0.1	<0.1	<0.1	<0.1	0.32	17.61	<0.2	34.31	83.81
RCS037	RCS037_15_4	Monzonite	NA	NA	A3	Replacement	<0.1	10.02	9.69	13.01	<0.1	0.11	<0.1	<0.1	<0.1	0.19	18.06	<0.2	35.39	86.47
RCS037	RCS037_15_6	Monzonite	NA	NA	A3	Replacement	<0.1	10.27	9.5	13.2	<0.1	<0.1	<0.1	<0.1	<0.1	0.19	17.57	<0.2	35.4	86.13

Sample	Reference	Lithology	Structure	Type	Alt	Texture	Na_pct	Mg_pct	Al_pct	Si_pct	K_pct	Ca_pct	Ti_pct	V_pct	Cr_pct	Mn_pct	Fe_pct	Co_pct	O_pct	Total
RCS037	RCS037_18_13	Monzonite	NA	NA	A3	Patches	<0.1	10.53	8.56	14.24	<0.1	0.17	<0.1	<0.1	<0.1	0.25	17.07	0.23	35.89	86.94
RCS037	RCS037_18_19	Monzonite	NA	NA	A3	Patches	<0.1	9.19	8.04	15.07	<0.1	1.26	<0.1	<0.1	<0.1	0.26	16.72	<0.2	35.8	86.34
RCS037	RCS037_20_2	Monzonite	NA	NA	A3	Replacement	<0.1	10.39	8.4	14.25	<0.1	0.72	<0.1	<0.1	<0.1	0.2	16.63	<0.2	35.73	86.32
RCS037	RCS037_22_6	Monzonite	NA	NA	A3	Replacement	<0.1	10.42	8.84	13.83	<0.1	0.38	<0.1	<0.1	<0.1	0.24	17.39	0.23	35.87	87.2
RCS037	RCS037_22_9	Monzonite	NA	NA	A3	Replacement	<0.1	10.66	8.71	13.6	<0.1	0.14	<0.1	<0.1	<0.1	0.23	17.32	<0.2	35.42	86.08
RCS042	RCS042_2_6	Monzonite	NA	NA	A4	Patches	<0.1	9.88	7.65	16.46	<0.1	1.01	<0.1	<0.1	<0.1	0.11	13.08	<0.2	36.28	84.47
RCS042	RCS042_7_5	Monzonite	NA	NA	A4	Patches	<0.1	9.8	9.36	13.65	<0.1	0.29	<0.1	<0.1	<0.1	0.15	16.33	<0.2	35.25	84.83
RCS042	RCS042_9_1	Monzonite	NA	NA	A4	Patches	<0.1	10.5	7.2	15.62	<0.1	1.09	<0.1	<0.1	<0.1	0.12	12.23	<0.2	35.12	81.88
RCS042	RCS042_9_3	Monzonite	NA	NA	A4	Patches	<0.1	11.47	7.28	15.93	<0.1	0.63	<0.1	<0.1	<0.1	0.19	12.46	<0.2	36.09	84.05
RCS042	RCS042_9_4	Monzonite	NA	NA	A4	Patches	<0.1	10.65	6.73	16.88	<0.1	1.05	<0.1	<0.1	<0.1	0.11	11.06	<0.2	35.9	82.38
RCS042	RCS042_9_6	Monzonite	NA	NA	A4	Patches	<0.1	10.55	8.88	14.22	<0.1	0.38	<0.1	<0.1	<0.1	<0.1	14.37	<0.2	35.37	83.77
RCS042	RCS042_11_1	Monzonite	NA	NA	A4	Replacement	<0.1	10.27	9.76	13.86	<0.1	0.25	<0.1	<0.1	<0.1	0.12	15.2	<0.2	35.79	85.25
RCS042	RCS042_11_2	Monzonite	NA	NA	A4	Replacement	<0.1	10.53	9.65	14.03	<0.1	0.35	<0.1	<0.1	<0.1	0.23	15.57	<0.2	36.2	86.56
RCS042	RCS042_11_3	Monzonite	NA	NA	A4	Replacement	<0.1	10.31	9.13	15.16	<0.1	0.97	<0.1	<0.1	<0.1	0.14	15.67	<0.2	37.17	88.55
RCS042	RCS042_11_4	Monzonite	NA	NA	A4	Replacement	<0.1	10.48	9.43	14.85	<0.1	0.44	<0.1	<0.1	<0.1	<0.1	14.76	<0.2	36.65	86.61
RCS042	RCS042_11_5	Monzonite	NA	NA	A4	Replacement	<0.1	10.36	9.39	13.75	<0.1	0.24	<0.1	<0.1	<0.1	0.23	15.83	<0.2	35.59	85.39
RCS042	RCS042_11_6	Monzonite	NA	NA	A4	Replacement	<0.1	10.29	9.79	14.05	<0.1	0.29	<0.1	<0.1	<0.1	0.21	15.37	<0.2	36.14	86.14
RCS042	RCS042_11_7	Monzonite	NA	NA	A4	Replacement	<0.1	10.81	9.8	13.37	<0.1	0.2	<0.1	<0.1	<0.1	0.12	16.19	<0.2	35.89	86.38
RCS042	RCS042_13_3	Monzonite	NA	NA	A4	Replacement	<0.1	11.46	8.22	15.92	<0.1	0.74	<0.1	<0.1	<0.1	0.13	12.16	<0.2	36.88	85.51
RCS042	RCS042_13_4	Monzonite	NA	NA	A4	Replacement	<0.1	10.45	8.67	15.78	<0.1	0.66	<0.1	<0.1	<0.1	0.1	12.88	0.2	36.64	85.38
RCS042	RCS042_13_5	Monzonite	NA	NA	A4	Replacement	<0.1	11	8.39	16.04	<0.1	0.82	<0.1	<0.1	<0.1	0.15	12.32	<0.2	36.95	85.67
RCS042	RCS042_13_6	Monzonite	NA	NA	A4	Replacement	<0.1	10.61	7.63	15.58	<0.1	0.95	<0.1	<0.1	<0.1	0.2	12.79	<0.2	35.63	83.39
RCS042	RCS042_13_7	Monzonite	NA	NA	A4	Replacement	<0.1	10.25	8.34	15.76	<0.1	0.84	<0.1	<0.1	<0.1	0.16	12.89	<0.2	36.27	84.51
RCS042	RCS042_13_8	Monzonite	NA	NA	A4	Replacement	<0.1	11.04	8.75	15.85	<0.1	0.73	<0.1	<0.1	<0.1	0.17	12.72	<0.2	37.14	86.4
RCS042	RCS042_13_9	Monzonite	NA	NA	A4	Replacement	<0.1	11.17	8.34	16.12	<0.1	0.74	<0.1	<0.1	<0.1	0.15	12.63	<0.2	37.17	86.32
RCS042	RCS042_13_10	Monzonite	NA	NA	A4	Replacement	<0.1	9.3	8.03	17.34	<0.1	1	<0.1	<0.1	<0.1	<0.1	12.14	<0.2	36.95	84.76
RCS042	RCS042_13_11	Monzonite	NA	NA	A4	Replacement	<0.1	11.17	8.64	16.64	<0.1	0.72	<0.1	<0.1	<0.1	0.14	12.49	<0.2	38	87.8
RCS042	RCS042_17_1	Monzonite	NA	NA	A4	Patches	<0.1	11.63	9	14.81	<0.1	0.24	<0.1	<0.1	<0.1	0.25	13.87	<0.2	36.66	86.46
RCS042	RCS042_19_2	Monzonite	NA	NA	A4	Patches	<0.1	10.18	7.18	15.86	<0.1	1.13	<0.1	<0.1	<0.1	0.12	13.03	<0.2	35.46	82.96

Sample	Reference	Lithology	Structure	Type	Alt	Texture	Na_pct	Mg_pct	Al_pct	Si_pct	K_pct	Ca_pct	Ti_pct	V_pct	Cr_pct	Mn_pct	Fe_pct	Co_pct	O_pct	Total
RCS042	RCS042_19_3	Monzonite	NA	NA	A4	Patches	<0.1	11.35	8.37	14.75	<0.1	0.56	<0.1	<0.1	<0.1	0.17	13.33	<0.2	35.85	84.38
RCS042	RCS042_19_5	Monzonite	NA	NA	A4	Patches	<0.1	10.42	7.75	15.88	<0.1	0.9	<0.1	<0.1	<0.1	<0.1	12.73	<0.2	35.92	83.6
RCS042	RCS042_19_7	Monzonite	NA	NA	A4	Patches	<0.1	10.36	8.08	15.8	<0.1	0.92	<0.1	<0.1	<0.1	0.17	13.48	<0.2	36.36	85.17
RCS042	RCS042_19_8	Monzonite	NA	NA	A4	Patches	<0.1	10.58	7.54	15.51	<0.1	1.04	<0.1	<0.1	<0.1	0.16	12.74	<0.2	35.52	83.09
RCS042	RCS042_23_5	Monzonite	NA	NA	A4	Replacement	<0.1	11.67	8.1	14.87	<0.1	0.31	<0.1	<0.1	<0.1	0.23	14.01	<0.2	36.07	85.26
RCS065	RCS065_2_5	Trachyte	159SW5 8	Fracture	A6	Replacement	<0.1	9.74	9.94	12.64	<0.1	0.11	<0.1	<0.1	<0.1	0.78	18.2	<0.2	35.21	86.62
RCS065	RCS065_2_6	Trachyte	159SW5 9	Fracture	A6	Replacement	0.1	9.7	9.91	12.93	<0.1	0.13	<0.1	<0.1	<0.1	0.76	18.17	<0.2	35.55	87.25
RCS065	RCS065_2_7	Trachyte	159SW6 0	Fracture	A6	Replacement	<0.1	9.86	10.07	12.61	<0.1	<0.1	<0.1	<0.1	<0.1	0.69	18.2	<0.2	35.32	86.75
RCS065	RCS065_2_8	Trachyte	159SW6 1	Fracture	A6	Replacement	<0.1	10.37	9.53	13.15	<0.1	<0.1	<0.1	<0.1	<0.1	0.67	16.83	<0.2	35.45	86
RCS065	RCS065_2_9	Trachyte	159SW6 2	Fracture	A6	Replacement	0.12	9.86	9.8	12.68	<0.1	<0.1	<0.1	<0.1	<0.1	0.67	17.57	0.21	35	85.91
RCS065	RCS065_2_10	Trachyte	159SW6 3	Fracture	A6	Replacement	<0.1	8.75	10.14	12.16	<0.1	<0.1	<0.1	<0.1	<0.1	0.77	19.71	0.22	34.67	86.42
RCS065	RCS065_2_11	Trachyte	159SW6 4	Fracture	A6	Replacement	<0.1	9.74	9.6	12.34	<0.1	<0.1	<0.1	<0.1	<0.1	0.76	17.66	<0.2	34.36	84.46
RCS065	RCS065_7_1	Trachyte	159SW6 5	Fracture	A6	Patches	<0.1	10.59	9.55	13.7	<0.1	0.27	<0.1	<0.1	<0.1	0.56	15.78	<0.2	35.99	86.44
RCS065	RCS065_7_3	Trachyte	159SW6 7	Fracture	A6	Patches	<0.1	10.23	9.57	13.43	<0.1	0.19	<0.1	<0.1	<0.1	0.65	16.12	<0.2	35.48	85.67
RCS065	RCS065_12_23	Trachyte	159SW7 0	Fracture	A6	Replacement	<0.1	10.43	9.55	13.16	<0.1	0.17	<0.1	<0.1	<0.1	0.6	15.66	<0.2	35.15	84.72
RCS065	RCS065_13_1	Trachyte	159SW7 2	Fracture	A6	Replacement	<0.1	11.07	9.88	13.67	<0.1	0.17	<0.1	<0.1	<0.1	0.53	15.19	<0.2	36.23	86.74
RCS065	RCS065_13_2	Trachyte	159SW7 3	Fracture	A6	Replacement	<0.1	9.7	8.95	12.54	<0.1	0.27	<0.1	<0.1	<0.1	0.57	15.78	<0.2	33.5	81.31
RCS065	RCS065_13_3	Trachyte	159SW7 4	Fracture	A6	Replacement	<0.1	11.29	9.9	13.74	<0.1	0.25	<0.1	<0.1	<0.1	0.52	14.71	<0.2	36.4	86.81
RCS065	RCS065_13_4	Trachyte	159SW7 5	Fracture	A6	Replacement	<0.1	11.29	9.33	13.57	<0.1	0.27	<0.1	<0.1	<0.1	0.5	14.28	<0.2	35.52	84.76
RCS065	RCS065_15_9	Trachyte	159SW8 0	Fracture	A6	Replacement	<0.1	10.4	9.9	13.34	<0.1	0.13	<0.1	<0.1	<0.1	0.66	16.78	<0.2	35.96	87.17
RCS065	RCS065_15_10	Trachyte	159SW8 1	Fracture	A6	Replacement	<0.1	10.23	9.54	13.9	<0.1	0.24	<0.1	<0.1	<0.1	0.57	16.31	<0.2	36.04	86.83
RCS065	RCS065_15_11	Trachyte	159SW8 2	Fracture	A6	Replacement	<0.1	10.28	10.03	13.42	<0.1	0.11	<0.1	<0.1	<0.1	0.69	16.78	<0.2	36.11	87.42
RCS069	RCS069_2_9	Andesite	NA	NA	A4	Replacement	<0.1	8.76	10.55	13.36	<0.1	0.28	<0.1	<0.1	<0.1	0.59	17.94	0.21	35.95	87.64
RCS069	RCS069_2_10	Andesite	NA	NA	A4	Replacement	<0.1	9.3	10.99	13.93	<0.1	0.22	<0.1	<0.1	<0.1	0.61	17.05	<0.2	37.01	89.11
RCS069	RCS069_2_11	Andesite	NA	NA	A4	Replacement	<0.1	9.07	10.88	13.23	<0.1	0.16	<0.1	<0.1	<0.1	0.62	18.35	<0.2	36.27	88.58
RCS069	RCS069_4_5	Andesite	NA	NA	A4	Patches	0.12	8.73	11.36	13.78	0.1	0.19	<0.1	<0.1	<0.1	0.67	17.98	0.25	37.13	90.31
RCS069	RCS069_6_6	Andesite	NA	NA	A4	Replacement	<0.1	7.57	10.88	13.72	0.29	0.21	<0.1	<0.1	<0.1	0.64	17.11	<0.2	35.59	86.01

Sample	Reference	Lithology	Structure	Type	Alt	Texture	Na_pct	Mg_pct	Al_pct	Si_pct	K_pct	Ca_pct	Ti_pct	V_pct	Cr_pct	Mn_pct	Fe_pct	Co_pct	O_pct	Total
RCS069	RCS069_6_8	Andesite	NA	NA	A4	Replacement	0.11	9.67	11.26	13.77	<0.1	0.14	<0.1	<0.1	<0.1	0.62	17.04	<0.2	37.26	89.87
RCS069	RCS069_6_9	Andesite	NA	NA	A4	Replacement	<0.1	9.26	11.42	13.66	<0.1	0.2	<0.1	<0.1	<0.1	0.58	17.11	0.2	37.11	89.54
RCS069	RCS069_6_12	Andesite	NA	NA	A4	Replacement	<0.1	8.27	10.55	13.04	0.2	0.19	<0.1	<0.1	<0.1	0.62	18.5	<0.2	35.39	86.76
RCS069	RCS069_6_13	Andesite	NA	NA	A4	Replacement	0.14	8.27	10.05	12.63	<0.1	0.43	0.31	<0.1	<0.1	0.63	17.49	<0.2	34.45	84.4
RCS069	RCS069_6_14	Andesite	NA	NA	A4	Replacement	0.12	6.91	10.48	14.06	0.26	0.38	<0.1	<0.1	<0.1	0.62	17.76	<0.2	35.47	86.06
RCS069	RCS069_8_8	Andesite	NA	NA	A4	Replacement	0.14	10.46	11.51	13.38	<0.1	0.15	<0.1	<0.1	<0.1	0.62	16.17	<0.2	37.31	89.74
RCS069	RCS069_8_10	Andesite	NA	NA	A4	Replacement	0.1	10.47	10.96	14.04	<0.1	0.21	<0.1	<0.1	<0.1	0.48	15.27	<0.2	37.3	88.83
RCS069	RCS069_8_11	Andesite	NA	NA	A4	Replacement	0.31	8.65	11.32	14.6	0.24	0.26	<0.1	<0.1	<0.1	0.53	17.08	<0.2	37.76	90.75
RCS069	RCS069_8_12	Andesite	NA	NA	A4	Replacement	<0.1	9.71	11.04	12.88	<0.1	0.12	<0.1	<0.1	<0.1	0.6	16.34	<0.2	35.88	86.57
RCS069	RCS069_8_13	Andesite	NA	NA	A4	Replacement	<0.1	7.7	10.43	14.08	<0.1	0.41	0.14	<0.1	<0.1	0.54	17.66	<0.2	35.98	86.94
RCS069	RCS069_8_14	Andesite	NA	NA	A4	Replacement	<0.1	8.65	10.73	13.57	<0.1	0.25	<0.1	<0.1	<0.1	0.52	17.48	<0.2	36.05	87.25
RCS069	RCS069_10_10	Andesite	NA	NA	A4	Replacement	<0.1	9.25	10.47	13.4	<0.1	0.16	<0.1	0.1	<0.1	0.55	17.57	<0.2	36.09	87.59
RCS069	RCS069_10_12	Andesite	NA	NA	A4	Replacement	0.14	8.83	10.41	13.68	<0.1	0.24	<0.1	<0.1	<0.1	0.49	17.02	<0.2	35.9	86.71
RCS069	RCS069_12_4	Andesite	NA	NA	A4	Replacement	0.1	8.68	10.96	12.98	<0.1	0.18	<0.1	<0.1	<0.1	0.59	17.29	<0.2	35.52	86.3
RCS069	RCS069_12_5	Andesite	NA	NA	A4	Replacement	<0.1	8.82	10.96	12.99	<0.1	0.21	<0.1	<0.1	<0.1	0.57	18.08	<0.2	35.83	87.46
RCS069	RCS069_12_6	Andesite	NA	NA	A4	Replacement	0.12	9.06	10.58	12.99	<0.1	0.15	<0.1	<0.1	<0.1	0.59	17.56	<0.2	35.47	86.52
RCS069	RCS069_12_7	Andesite	NA	NA	A4	Replacement	<0.1	11.24	10.9	14.16	<0.1	0.16	<0.1	<0.1	<0.1	0.48	14.86	<0.2	37.74	89.54
RCS069	RCS069_14_6	Andesite	NA	NA	A4	L Patches	0.14	8.2	10.38	13.59	<0.1	0.24	<0.1	<0.1	<0.1	0.61	17.98	<0.2	35.67	86.81
RCS069	RCS069_14_7	Andesite	NA	NA	A4	L Patches	0.11	9.28	10.98	13.06	<0.1	0.16	<0.1	<0.1	<0.1	0.6	18.04	<0.2	36.23	88.46
RCS069	RCS069_18_5	Andesite	NA	NA	A4	Replacement	<0.1	8.68	10.9	13.15	<0.1	0.15	<0.1	<0.1	<0.1	0.62	18.62	0.26	36.14	88.52

Sample	Reference	Lithology	Structure	Type	Alt	Texture	Na_pct	Mg_pct	Al_pct	Si_pct	K_pct	Ca_pct	Ti_pct	V_pct	Cr_pct	Mn_pct	Fe_pct	Co_pct	O_pct	Total_pct
RCS030	RCS030_6_13	Rhyolite	NA	NA	A5	Replacement	<0.1	<0.2	13.0	17.0	<0.1	15.2	<0.1	<0.1	<0.1	1.5	6.8	<0.2	39.3	92.8
RCS030	RCS030_6_17	Rhyolite	NA	NA	A5	Replacement	<0.1	<0.2	12.7	16.9	<0.1	15.0	<0.1	<0.1	<0.1	2.1	7.3	<0.2	39.3	93.2
RCS030	RCS030_6_20	Rhyolite	NA	NA	A5	Replacement	<0.1	<0.2	12.2	16.7	<0.1	15.6	0.2	<0.1	<0.1	1.2	8.9	<0.2	39.1	93.7
RCS030	RCS030_9_9	Rhyolite	NA	NA	A5	Replacement	<0.1	<0.2	13.0	17.0	<0.1	15.4	<0.1	<0.1	<0.1	1.4	7.1	<0.2	39.5	93.4
RCS030	RCS030_23_15	Rhyolite	NA	NA	A5	Replacement	<0.1	<0.2	13.2	17.0	<0.1	15.2	<0.1	<0.1	<0.1	2.0	6.8	<0.2	39.6	93.8
RCS030	RCS030_23_16	Rhyolite	NA	NA	A5	Replacement	<0.1	<0.2	12.4	17.1	<0.1	15.8	<0.1	<0.1	<0.1	1.1	8.3	<0.2	39.6	94.3
RCS030	RCS030_23_17	Rhyolite	NA	NA	A5	Replacement	<0.1	<0.2	12.2	17.1	<0.1	15.9	0.1	<0.1	<0.1	1.1	8.2	<0.2	39.4	94.0
RCS030	RCS030_25_3	Rhyolite	NA	NA	A5	Replacement	<0.1	<0.2	13.5	16.7	<0.1	15.1	<0.1	<0.1	<0.1	1.3	6.9	<0.2	39.4	92.9
RCS030	RCS030_33_1	Rhyolite	NA	NA	A5	Replacement	<0.1	<0.2	13.1	17.3	<0.1	16.1	<0.1	<0.1	<0.1	0.9	7.1	<0.2	40.1	94.6
RCS031	RCS031_2_1	Andesite	033SE82	Fracture	V3	Vein	0.1	<0.2	12.1	17.6	<0.1	16.9	<0.1	<0.1	<0.1	0.3	10.3	<0.2	40.6	98.0
RCS031	RCS031_2_2	Andesite	033SE82	Fracture	V3	Vein	<0.1	<0.2	14.0	17.5	<0.1	16.9	<0.1	<0.1	<0.1	0.2	6.3	<0.2	41.1	96.0
RCS031	RCS031_2_3	Andesite	033SE82	Fracture	V3	Vein	<0.1	<0.2	13.7	17.3	<0.1	16.7	<0.1	<0.1	<0.1	0.4	6.9	<0.2	40.6	95.4
RCS031	RCS031_2_4	Andesite	033SE82	Fracture	V3	Vein	<0.1	<0.2	13.0	17.6	<0.1	16.3	<0.1	<0.1	<0.1	1.1	8.4	<0.2	41.0	97.5
RCS031	RCS031_2_5	Andesite	033SE82	Fracture	V3	Vein	<0.1	<0.2	13.1	17.6	<0.1	16.0	<0.1	<0.1	<0.1	1.4	8.3	<0.2	40.9	97.2
RCS031	RCS031_2_6	Andesite	033SE82	Fracture	V3	Vein	<0.1	<0.2	12.3	17.3	<0.1	16.1	<0.1	<0.1	<0.1	0.8	9.5	<0.2	40.0	95.9
RCS031	RCS031_3_1	Andesite	033SE82	Fracture	V3	Vein	<0.1	<0.2	12.9	17.3	<0.1	16.6	<0.1	<0.1	<0.1	0.7	8.5	<0.2	40.5	96.5
RCS031	RCS031_3_2	Andesite	033SE82	Fracture	V3	Vein	<0.1	<0.2	11.7	17.3	<0.1	15.5	<0.1	<0.1	<0.1	1.6	10.6	<0.2	39.9	96.5
RCS031	RCS031_3_3	Andesite	033SE82	Fracture	V3	Vein	<0.1	<0.2	13.1	17.6	<0.1	16.4	<0.1	<0.1	<0.1	1.1	7.6	<0.2	40.8	96.6
RCS031	RCS031_3_4	Andesite	033SE82	Fracture	V3	Vein	<0.1	<0.2	13.5	17.2	<0.1	16.7	<0.1	<0.1	<0.1	0.5	7.3	<0.2	40.6	95.8
RCS031	RCS031_3_5	Andesite	033SE82	Fracture	V3	Vein	<0.1	<0.2	13.6	17.7	<0.1	17.4	<0.1	<0.1	<0.1	0.3	7.8	<0.2	41.7	98.5
RCS031	RCS031_3_6	Andesite	033SE82	Fracture	V3	Vein	<0.1	<0.2	12.5	17.3	<0.1	16.6	<0.1	<0.1	<0.1	0.5	8.8	<0.2	40.1	95.9
RCS031	RCS031_5_1	Andesite	033SE82	Fracture	V3	Vein	0.1	<0.2	12.9	17.4	<0.1	17.1	<0.1	<0.1	<0.1	<0.1	8.3	<0.2	40.7	96.5
RCS031	RCS031_5_2	Andesite	033SE82	Fracture	V3	Vein	<0.1	<0.2	12.0	17.4	<0.1	17.0	0.1	<0.1	<0.1	0.1	9.8	<0.2	40.3	96.6
RCS031	RCS031_5_4	Andesite	033SE82	Fracture	V3	Vein	<0.1	<0.2	12.3	17.4	<0.1	17.0	<0.1	<0.1	<0.1	<0.1	9.3	<0.2	40.3	96.3
RCS031	RCS031_5_5	Andesite	033SE82	Fracture	A4	VH	<0.1	<0.2	13.5	17.2	<0.1	17.1	<0.1	<0.1	<0.1	0.2	6.7	<0.2	40.5	95.3
RCS031	RCS031_5_8	Andesite	033SE82	Fracture	V3	Vein	<0.1	<0.2	13.6	17.5	<0.1	17.4	<0.1	<0.1	<0.1	<0.1	7.0	<0.2	41.0	96.5
RCS031	RCS031_7_10	Andesite	033SE82	Fracture	A4	Replacement	0.2	<0.2	12.3	17.3	<0.1	16.8	<0.1	<0.1	<0.1	0.2	9.0	<0.2	40.1	96.0
RCS031	RCS031_7_11	Andesite	033SE82	Fracture	A4	Replacement	<0.1	<0.2	12.1	17.2	<0.1	16.9	<0.1	<0.1	<0.1	0.2	10.0	<0.2	40.1	96.5
RCS031	RCS031_7_12	Andesite	033SE82	Fracture	A4	Replacement	<0.1	<0.2	11.4	17.3	<0.1	16.3	<0.1	<0.1	<0.1	0.6	11.0	<0.2	39.7	96.2
RCS031	RCS031_7_13	Andesite	033SE82	Fracture	A4	Replacement	<0.1	<0.2	11.2	17.2	<0.1	16.9	<0.1	<0.1	<0.1	0.1	11.5	<0.2	39.7	96.6
RCS031	RCS031_8_9	Andesite	033SE82	Fracture	A4	Replacement	0.1	<0.2	11.7	17.1	<0.1	16.7	<0.1	<0.1	<0.1	0.1	10.0	<0.2	39.6	95.4
RCS031	RCS031_8_10	Andesite	033SE82	Fracture	A4	Replacement	<0.1	<0.2	12.5	17.1	<0.1	16.5	<0.1	<0.1	<0.1	0.2	8.8	<0.2	39.8	94.9
RCS031	RCS031_8_11	Andesite	033SE82	Fracture	A4	Replacement	<0.1	<0.2	11.2	16.9	<0.1	16.7	<0.1	<0.1	<0.1	0.2	10.4	<0.2	38.9	94.4
RCS031	RCS031_10_4	Andesite	033SE82	Fracture	A4	L Patches	<0.1	<0.2	12.8	17.6	<0.1	17.3	<0.1	<0.1	0.1	<0.1	8.6	<0.2	40.9	97.2
RCS031	RCS031_10_5	Andesite	033SE82	Fracture	A4	L Patches	<0.1	<0.2	11.7	17.6	<0.1	16.7	<0.1	<0.1	<0.1	0.2	10.0	<0.2	40.1	96.3

Sample	Reference	Lithology	Structure	Type	Alt	Texture	Na_pct	Mg_pct	Al_pct	Si_pct	K_pct	Ca_pct	Ti_pct	V_pct	Cr_pct	Mn_pct	Fe_pct	Co_pct	O_pct	Total_pct
RCS031	RCS031_10_6	Andesite	033SE82	Fracture	A4	L Patches	<0.1	<0.2	12.7	17.6	<0.1	16.9	<0.1	<0.1	<0.1	<0.1	8.7	<0.2	40.5	96.3
RCS031	RCS031_12_1	Andesite	033SE82	Fracture	A4	L Patches	<0.1	<0.2	12.3	17.1	<0.1	16.7	<0.1	<0.1	<0.1	<0.1	9.1	<0.2	39.8	95.1
RCS031	RCS031_12_2	Andesite	033SE82	Fracture	A4	L Patches	<0.1	<0.2	13.3	17.6	<0.1	17.2	<0.1	<0.1	<0.1	0.1	7.7	<0.2	41.1	97.0
RCS031	RCS031_12_5	Andesite	033SE82	Fracture	A4	L Patches	<0.1	<0.2	12.2	17.2	<0.1	16.9	0.1	<0.1	<0.1	0.1	9.3	<0.2	39.9	95.6
RCS031	RCS031_16_6	Andesite	033SE82	Fracture	V3	Vein	<0.1	<0.2	13.7	17.7	<0.1	16.9	<0.1	<0.1	<0.1	0.3	7.5	<0.2	41.4	97.4
RCS031	RCS031_16_7	Andesite	033SE82	Fracture	V3	Vein	<0.1	<0.2	12.8	17.4	<0.1	17.2	0.1	<0.1	<0.1	0.1	8.7	<0.2	40.7	97.0
RCS033	RCS033_6_2	Andesite	NA	NA	A4	L Patches	<0.1	<0.2	13.4	17.6	<0.1	17.2	<0.1	<0.1	<0.1	0.2	8.4	<0.2	41.3	98.1
RCS033	RCS033_6_4	Andesite	NA	NA	A4	L Patches	<0.1	<0.2	14.4	17.9	<0.1	17.6	<0.1	<0.1	0.1	<0.1	6.1	<0.2	42.1	98.2
RCS033	RCS033_9_10	Andesite	NA	NA	A4	L Patches	<0.1	<0.2	13.8	17.7	<0.1	17.0	<0.1	<0.1	0.1	0.5	7.7	<0.2	41.6	98.4
RCS033	RCS033_11_8	Andesite	NA	NA	A4	L Patches	<0.1	<0.2	12.1	17.5	<0.1	16.9	<0.1	<0.1	0.1	0.4	10.2	<0.2	40.5	97.7
RCS033	RCS033_11_10	Andesite	NA	NA	A4	L Patches	<0.1	<0.2	12.5	17.6	<0.1	17.1	<0.1	<0.1	<0.1	<0.1	8.6	<0.2	40.6	96.4
RCS033	RCS033_11_11	Andesite	NA	NA	A4	L Patches	<0.1	<0.2	14.2	17.8	<0.1	16.9	<0.1	<0.1	0.2	0.5	6.3	<0.2	41.7	97.6
RCS033	RCS033_11_12	Andesite	NA	NA	A4	L Patches	<0.1	<0.2	12.6	17.5	<0.1	16.4	<0.1	<0.1	0.1	1.2	9.5	<0.2	40.9	98.3
RCS033	RCS033_12_2	Andesite	NA	NA	A4	L Patches	<0.1	<0.2	12.9	17.6	<0.1	16.3	<0.1	<0.1	0.1	1.3	8.7	<0.2	40.9	97.8
RCS033	RCS033_12_4	Andesite	NA	NA	A4	L Patches	<0.1	<0.2	12.0	17.4	<0.1	17.1	0.1	<0.1	0.2	0.2	10.1	<0.2	40.4	97.4
RCS033	RCS033_12_5	Andesite	NA	NA	A4	L Patches	<0.1	<0.2	12.1	17.4	<0.1	16.7	<0.1	<0.1	<0.1	0.6	9.8	<0.2	40.3	96.8
RCS033	RCS033_12_6	Andesite	NA	NA	A4	L Patches	<0.1	<0.2	12.9	17.6	<0.1	17.4	<0.1	<0.1	<0.1	<0.1	8.5	<0.2	41.1	97.5
RCS033	RCS033_12_15	Andesite	NA	NA	A4	L Patches	<0.1	<0.2	13.6	17.5	<0.1	16.9	0.1	<0.1	0.4	0.4	8.1	<0.2	41.4	98.3
RCS033	RCS033_14_4	Andesite	NA	NA	A4	L Patches	<0.1	<0.2	13.3	17.9	<0.1	17.3	<0.1	<0.1	<0.1	0.2	8.7	<0.2	41.7	99.1
RCS033	RCS033_14_5	Andesite	NA	NA	A4	L Patches	<0.1	<0.2	14.2	17.6	<0.1	17.4	<0.1	<0.1	<0.1	<0.1	6.9	<0.2	41.6	97.7
RCS033	RCS033_15_8	Andesite	NA	NA	A4	L Patches	<0.1	<0.2	12.7	17.6	<0.1	17.1	<0.1	<0.1	<0.1	0.2	9.1	<0.2	40.9	97.7
RCS033	RCS033_15_11	Andesite	NA	NA	A4	L Patches	<0.1	<0.2	12.9	17.9	<0.1	17.6	<0.1	<0.1	<0.1	0.2	9.6	<0.2	41.6	99.7
RCS033	RCS033_15_12	Andesite	NA	NA	A4	L Patches	<0.1	<0.2	12.3	17.5	<0.1	17.5	<0.1	<0.1	<0.1	<0.1	10.1	<0.2	40.8	98.2
RCS033	RCS033_15_14	Andesite	NA	NA	A4	L Patches	<0.1	<0.2	12.0	17.3	<0.1	17.1	<0.1	<0.1	<0.1	<0.1	10.0	<0.2	40.2	96.5
RCS033	RCS033_17_10	Andesite	NA	NA	A4	L Patches	<0.1	<0.2	11.9	17.5	<0.1	17.2	<0.1	<0.1	<0.1	<0.1	10.2	<0.2	40.3	97.1
RCS033	RCS033_18_1	Andesite	NA	NA	A4	L Patches	<0.1	<0.2	13.4	17.7	<0.1	17.2	<0.1	<0.1	0.1	0.1	8.2	<0.2	41.3	98.1
RCS033	RCS033_18_2	Andesite	NA	NA	A4	L Patches	<0.1	<0.2	13.6	17.7	<0.1	17.5	0.1	<0.1	<0.1	<0.1	7.5	<0.2	41.5	98.0
RCS033	RCS033_18_3	Andesite	NA	NA	A4	L Patches	<0.1	<0.2	13.5	17.6	<0.1	17.0	<0.1	<0.1	<0.1	<0.1	7.3	<0.2	41.0	96.3
RCS033	RCS033_18_4	Andesite	NA	NA	A4	L Patches	0.2	<0.2	13.0	18.0	<0.1	16.2	<0.1	<0.1	<0.1	0.1	8.0	<0.2	41.0	96.6
RCS033	RCS033_18_11	Andesite	NA	NA	A4	L Patches	<0.1	<0.2	14.1	17.8	<0.1	17.2	<0.1	<0.1	<0.1	0.1	6.8	<0.2	41.6	97.5
RCS099	RCS099_6_3	Rhyolite	NA	NA	A5	Replacement	<0.1	<0.2	11.6	16.8	<0.1	16.5	<0.1	<0.1	<0.1	0.2	10.2	<0.2	39.0	94.2
RCS099	RCS099_6_4	Rhyolite	NA	NA	A5	Replacement	0.2	<0.2	11.6	16.7	<0.1	16.1	<0.1	<0.1	<0.1	0.3	8.8	<0.2	38.3	92.0
RCS099	RCS099_6_5	Rhyolite	NA	NA	A5	Replacement	<0.1	<0.2	11.7	17.0	<0.1	16.1	<0.1	<0.1	<0.1	0.6	9.5	<0.2	39.1	93.9
RCS099	RCS099_6_6	Rhyolite	NA	NA	A5	Replacement	<0.1	<0.2	11.3	17.0	<0.1	16.6	<0.1	<0.1	<0.1	0.1	10.6	<0.2	39.1	94.7
RCS099	RCS099_6_7	Rhyolite	NA	NA	A5	Replacement	<0.1	<0.2	12.3	16.8	<0.1	16.4	<0.1	<0.1	<0.1	0.3	8.1	<0.2	39.1	93.0

Sample	Reference	Lithology	Structure	Type	Alt	Texture	Na_pct	Mg_pct	Al_pct	Si_pct	K_pct	Ca_pct	Ti_pct	V_pct	Cr_pct	Mn_pct	Fe_pct	Co_pct	O_pct	Total_pct
RCS099	RCS099_6_8	Rhyolite	NA	NA	A5	Replacement	<0.1	<0.2	12.8	17.0	<0.1	16.5	<0.1	<0.1	0.1	0.2	7.5	<0.2	39.6	93.7
RCS099	RCS099_6_9	Rhyolite	NA	NA	A5	Replacement	<0.1	<0.2	12.3	17.1	<0.1	16.7	<0.1	<0.1	<0.1	0.2	8.2	<0.2	39.6	94.1
RCS099	RCS099_6_10	Rhyolite	NA	NA	A5	Replacement	<0.1	<0.2	12.9	17.1	<0.1	16.9	<0.1	<0.1	<0.1	0.1	7.6	<0.2	39.8	94.3
RCS099	RCS099_6_11	Rhyolite	NA	NA	A5	Replacement	<0.1	<0.2	13.1	17.0	<0.1	16.6	<0.1	<0.1	<0.1	0.4	7.4	<0.2	39.9	94.3
RCS099	RCS099_6_13	Rhyolite	NA	NA	A5	Replacement	<0.1	<0.2	11.3	17.1	<0.1	16.4	<0.1	<0.1	<0.1	<0.1	10.7	<0.2	39.2	94.5
RCS099	RCS099_6_14	Rhyolite	NA	NA	A5	Replacement	<0.1	<0.2	13.1	17.1	<0.1	16.8	<0.1	<0.1	<0.1	0.2	7.3	<0.2	40.1	94.6
RCS099	RCS099_6_15	Rhyolite	NA	NA	A5	Replacement	<0.1	<0.2	13.9	17.0	<0.1	16.4	<0.1	<0.1	<0.1	0.6	6.0	<0.2	40.3	94.3
RCS099	RCS099_6_16	Rhyolite	NA	NA	A5	Replacement	<0.1	<0.2	13.1	17.2	<0.1	16.3	<0.1	<0.1	<0.1	0.5	7.3	<0.2	40.0	94.4
RCS099	RCS099_6_17	Rhyolite	NA	NA	A5	Replacement	<0.1	<0.2	11.4	16.8	<0.1	16.3	<0.1	<0.1	<0.1	0.2	9.9	<0.2	38.7	93.3
RCS099	RCS099_6_18	Rhyolite	NA	NA	A5	Replacement	<0.1	<0.2	12.4	16.9	<0.1	16.3	<0.1	<0.1	0.1	0.6	8.7	<0.2	39.4	94.2
RCS099	RCS099_6_19	Rhyolite	NA	NA	A5	Replacement	<0.1	<0.2	12.2	17.2	<0.1	16.2	<0.1	<0.1	<0.1	0.5	9.8	<0.2	39.8	95.6
RCS099	RCS099_7_12	Rhyolite	NA	NA	A5	Replacement	<0.1	<0.2	12.4	17.4	<0.1	16.6	<0.1	<0.1	<0.1	0.3	9.4	<0.2	40.3	96.2
RCS099	RCS099_7_13	Rhyolite	NA	NA	A5	Replacement	<0.1	<0.2	11.8	17.0	<0.1	16.6	<0.1	<0.1	<0.1	<0.1	9.8	<0.2	39.4	94.5
RCS099	RCS099_7_15	Rhyolite	NA	NA	A5	Replacement	<0.1	<0.2	12.9	17.2	<0.1	16.8	<0.1	<0.1	<0.1	<0.1	7.6	<0.2	40.0	94.6
RCS099	RCS099_7_16	Rhyolite	NA	NA	A5	Replacement	0.9	<0.2	12.0	17.9	<0.1	15.4	<0.1	<0.1	<0.1	0.2	8.2	<0.2	39.9	94.4
RCS099	RCS099_7_17	Rhyolite	NA	NA	A5	Replacement	<0.1	<0.2	9.8	16.6	<0.1	16.4	<0.1	<0.1	<0.1	0.2	13.7	<0.2	38.2	94.9
RCS099	RCS099_7_18	Rhyolite	NA	NA	A5	Replacement	<0.1	<0.2	11.5	17.0	<0.1	16.6	<0.1	<0.1	<0.1	0.2	10.3	<0.2	39.3	95.0
RCS099	RCS099_7_19	Rhyolite	NA	NA	A5	Replacement	0.3	<0.2	13.0	17.9	<0.1	16.5	0.1	<0.1	<0.1	0.3	7.0	<0.2	40.8	95.8
RCS099	RCS099_7_20	Rhyolite	NA	NA	A5	Replacement	<0.1	<0.2	11.8	17.1	<0.1	16.7	<0.1	<0.1	<0.1	0.2	10.4	<0.2	39.7	95.8
RCS099	RCS099_7_21	Rhyolite	NA	NA	A5	Replacement	<0.1	<0.2	13.4	17.3	<0.1	17.1	<0.1	<0.1	<0.1	0.1	6.9	<0.2	40.5	95.3
RCS099	RCS099_7_22	Rhyolite	NA	NA	A5	Replacement	<0.1	<0.2	13.6	17.1	<0.1	16.1	<0.1	<0.1	<0.1	0.8	7.1	<0.2	40.4	95.1
RCS099	RCS099_7_23	Rhyolite	NA	NA	A5	Replacement	<0.1	<0.2	12.0	17.2	<0.1	16.5	<0.1	<0.1	<0.1	0.3	9.3	<0.2	39.6	94.9
RCS099	RCS099_7_24	Rhyolite	NA	NA	A5	Replacement	<0.1	<0.2	12.8	17.1	<0.1	16.4	<0.1	<0.1	<0.1	0.5	7.7	<0.2	39.8	94.3
RCS099	RCS099_7_25	Rhyolite	NA	NA	A5	Replacement	<0.1	<0.2	12.0	17.0	<0.1	16.3	<0.1	<0.1	<0.1	0.5	9.5	<0.2	39.5	94.8
RCS099	RCS099_7_26	Rhyolite	NA	NA	A5	Replacement	<0.1	<0.2	12.9	17.0	<0.1	16.3	<0.1	<0.1	<0.1	0.8	7.9	<0.2	39.8	94.8
RCS099	RCS099_7_27	Rhyolite	NA	NA	A5	Replacement	<0.1	<0.2	12.0	17.2	<0.1	16.9	<0.1	<0.1	<0.1	<0.1	9.8	<0.2	39.8	95.7
RCS099	RCS099_11_1	Rhyolite	NA	NA	A5	Replacement	<0.1	<0.2	12.3	17.4	<0.1	16.8	0.2	<0.1	<0.1	0.1	9.0	<0.2	40.3	96.0
RCS099	RCS099_11_2	Rhyolite	NA	NA	A5	Replacement	<0.1	<0.2	12.0	17.2	<0.1	16.4	<0.1	<0.1	<0.1	0.4	9.6	<0.2	39.7	95.2
RCS099	RCS099_11_3	Rhyolite	NA	NA	A5	Replacement	<0.1	<0.2	12.1	17.4	<0.1	16.9	<0.1	<0.1	<0.1	0.3	9.5	<0.2	40.2	96.4
RCS099	RCS099_11_4	Rhyolite	NA	NA	A5	Replacement	<0.1	<0.2	13.1	17.3	<0.1	16.7	<0.1	0.1	<0.1	0.6	7.7	<0.2	40.5	95.9
RCS099	RCS099_18_1	Rhyolite	NA	NA	A5	Replacement	<0.1	<0.2	12.2	17.3	<0.1	16.7	<0.1	<0.1	<0.1	0.3	9.1	<0.2	40.0	95.6
RCS104	RCS104_9_3	Andesite	NA	NA	A4	Replacement	<0.1	<0.2	13.0	17.2	<0.1	16.8	<0.1	<0.1	0.1	<0.1	8.0	<0.2	40.3	95.4
RCS104	RCS104_9_5	Andesite	NA	NA	A4	Replacement	<0.1	<0.2	13.9	17.7	<0.1	17.2	<0.1	<0.1	<0.1	<0.1	6.9	<0.2	41.5	97.1
RCS104	RCS104_9_8	Andesite	NA	NA	A4	Replacement	<0.1	<0.2	13.0	17.4	<0.1	17.0	<0.1	<0.1	0.1	<0.1	8.3	<0.2	40.7	96.6
RCS104	RCS104_9_11	Andesite	NA	NA	A4	Replacement	<0.1	<0.2	12.9	17.4	<0.1	17.0	<0.1	0.1	<0.1	<0.1	8.7	<0.2	40.7	96.9

Sample	Reference	Lithology	Structure	Type	Alt	Texture	Na_pct	Mg_pct	Al_pct	Si_pct	K_pct	Ca_pct	Ti_pct	V_pct	Cr_pct	Mn_pct	Fe_pct	Co_pct	O_pct	Total_pct
RCS104	RCS104_9_12	Andesite	NA	NA	A4	Replacement	<0.1	<0.2	14.6	17.5	<0.1	17.3	<0.1	<0.1	<0.1	<0.1	5.6	<0.2	41.5	96.4
RCS104	RCS104_9_13	Andesite	NA	NA	A4	Replacement	<0.1	<0.2	12.9	17.1	<0.1	16.9	<0.1	<0.1	<0.1	0.2	8.2	<0.2	40.2	95.5
RCS104	RCS104_9_14	Andesite	NA	NA	A4	Replacement	<0.1	<0.2	13.2	17.2	<0.1	17.0	<0.1	0.1	<0.1	<0.1	7.6	<0.2	40.5	95.6
RCS104	RCS104_11_1	Andesite	NA	NA	A4	Replacement	<0.1	<0.2	14.1	17.3	<0.1	16.6	<0.1	<0.1	<0.1	0.2	6.9	<0.2	41.0	96.0
RCS104	RCS104_11_3	Andesite	NA	NA	A4	Replacement	<0.1	<0.2	13.3	17.5	<0.1	17.0	<0.1	<0.1	<0.1	<0.1	7.2	<0.2	40.8	95.8
RCS104	RCS104_11_4	Andesite	NA	NA	A4	Replacement	<0.1	<0.2	12.6	17.6	<0.1	16.9	<0.1	0.1	<0.1	0.2	9.1	<0.2	40.9	97.4
RCS104	RCS104_11_6	Andesite	NA	NA	A4	Replacement	<0.1	<0.2	12.1	17.3	<0.1	16.5	<0.1	<0.1	0.1	0.2	10.1	<0.2	40.1	96.3
RCS104	RCS104_13_1	Andesite	NA	NA	A4	Replacement	<0.1	<0.2	13.0	17.0	<0.1	16.7	<0.1	<0.1	<0.1	0.1	7.7	<0.2	40.0	94.5
RCS104	RCS104_13_2	Andesite	NA	NA	A4	Replacement	<0.1	<0.2	12.7	17.1	<0.1	16.9	<0.1	<0.1	<0.1	<0.1	8.0	<0.2	39.9	94.6
RCS104	RCS104_13_3	Andesite	NA	NA	A4	Replacement	<0.1	<0.2	13.3	16.8	<0.1	16.7	<0.1	<0.1	<0.1	0.2	7.2	<0.2	39.9	94.1
RCS104	RCS104_13_4	Andesite	NA	NA	A4	Replacement	<0.1	<0.2	12.6	17.3	<0.1	17.0	<0.1	<0.1	<0.1	<0.1	8.6	<0.2	40.2	95.6
RCS104	RCS104_13_5	Andesite	NA	NA	A4	Replacement	<0.1	<0.2	12.7	17.4	<0.1	17.0	<0.1	<0.1	0.1	0.1	8.7	<0.2	40.6	96.7
RCS104	RCS104_13_6	Andesite	NA	NA	A4	Replacement	<0.1	<0.2	12.8	17.3	<0.1	17.1	0.4	<0.1	<0.1	0.1	8.7	<0.2	40.8	97.1
RCS104	RCS104_13_7	Andesite	NA	NA	A4	Replacement	<0.1	<0.2	12.0	17.0	<0.1	16.5	<0.1	<0.1	<0.1	0.3	9.2	<0.2	39.5	94.5
RCS104	RCS104_13_8	Andesite	NA	NA	A4	Replacement	<0.1	<0.2	12.9	16.9	<0.1	16.8	<0.1	<0.1	<0.1	0.1	8.0	<0.2	40.0	94.8
RCS104	RCS104_13_10	Andesite	NA	NA	A4	Replacement	<0.1	<0.2	13.0	17.2	<0.1	17.0	<0.1	<0.1	<0.1	0.1	8.1	<0.2	40.5	96.0
RCS104	RCS104_15_13	Andesite	NA	NA	A4	Replacement	<0.1	<0.2	12.4	17.4	<0.1	17.1	<0.1	<0.1	<0.1	<0.1	9.3	<0.2	40.3	96.4
RCS104	RCS104_17_2	Andesite	NA	NA	A4	Replacement	<0.1	<0.2	13.2	17.1	<0.1	17.0	<0.1	<0.1	<0.1	0.1	7.3	<0.2	40.3	95.0
RCS104	RCS104_20_2	Andesite	NA	NA	A4	Replacement	<0.1	<0.2	13.3	17.4	<0.1	16.9	<0.1	<0.1	<0.1	0.1	7.3	<0.2	40.6	95.6
RCS003	RCS003_6_13	Monzodiorite	144SW87	Fracture	A4	Replacement	<0.1	<0.2	10.5	17.1	<0.1	16.8	<0.1	<0.1	<0.1	0.1	12.8	<0.2	39.4	96.7
RCS003	RCS003_6_14	Monzodiorite	144SW87	Fracture	A4	Replacement	<0.1	<0.2	10.3	16.9	<0.1	16.7	<0.1	<0.1	0.1	<0.1	13.1	<0.2	38.9	95.9
RCS003	RCS003_6_17	Monzodiorite	144SW87	Fracture	A4	Replacement	<0.1	<0.2	11.3	17.2	<0.1	15.7	<0.1	<0.1	<0.1	1.2	11.2	<0.2	39.6	96.3
RCS003	RCS003_6_20	Monzodiorite	144SW87	Fracture	A4	Replacement	<0.1	<0.2	14.5	17.6	<0.1	17.2	<0.1	<0.1	<0.1	0.1	5.5	<0.2	41.5	96.5
RCS003	RCS003_6_21	Monzodiorite	144SW87	Fracture	A4	Replacement	<0.1	<0.2	11.9	17.6	<0.1	17.5	<0.1	<0.1	<0.1	<0.1	10.5	<0.2	40.6	98.1
RCS003	RCS003_6_23	Monzodiorite	144SW87	Fracture	A4	Replacement	<0.1	<0.2	13.7	17.9	<0.1	17.3	<0.1	<0.1	<0.1	0.1	7.8	<0.2	41.8	98.6
RCS003	RCS003_10_4	Monzodiorite	144SW87	Fracture	A4	Replacement	<0.1	<0.2	12.1	17.5	<0.1	17.3	<0.1	<0.1	0.1	<0.1	10.0	<0.2	40.5	97.3
RCS003	RCS003_10_6	Monzodiorite	144SW87	Fracture	A4	Replacement	<0.1	<0.2	13.0	17.6	<0.1	16.9	<0.1	<0.1	<0.1	0.2	8.1	<0.2	40.8	96.6
RCS003	RCS003_10_7	Monzodiorite	144SW87	Fracture	A4	Replacement	<0.1	<0.2	14.3	17.4	<0.1	16.6	<0.1	<0.1	<0.1	0.6	6.1	<0.2	41.2	96.3
RCS003	RCS003_10_8	Monzodiorite	144SW87	Fracture	A4	Replacement	<0.1	<0.2	13.3	17.6	<0.1	16.7	<0.1	<0.1	<0.1	0.5	7.9	<0.2	41.0	97.0
RCS003	RCS003_10_20	Monzodiorite	144SW87	Fracture	A4	Replacement	<0.1	<0.2	14.4	17.7	<0.1	16.9	<0.1	<0.1	<0.1	0.5	6.3	<0.2	41.7	97.4
RCS003	RCS003_12_7	Monzodiorite	144SW87	Fracture	A4	Replacement	<0.1	<0.2	14.0	17.7	<0.1	17.0	<0.1	<0.1	<0.1	0.1	6.5	<0.2	41.4	96.8
RCS003	RCS003_12_8	Monzodiorite	144SW87	Fracture	A4	Replacement	<0.1	<0.2	12.3	17.3	<0.1	17.0	<0.1	<0.1	<0.1	0.1	9.1	<0.2	40.1	95.9
RCS003	RCS003_12_11	Monzodiorite	144SW87	Fracture	A4	Replacement	<0.1	<0.2	13.8	17.8	<0.1	17.0	<0.1	0.1	<0.1	0.3	7.6	<0.2	41.8	98.4
RCS003	RCS003_12_13	Monzodiorite	144SW87	Fracture	A4	Replacement	<0.1	<0.2	13.7	17.9	<0.1	17.3	<0.1	<0.1	<0.1	0.2	7.6	<0.2	41.8	98.5
RCS003	RCS003_12_14	Monzodiorite	144SW87	Fracture	A4	Replacement	<0.1	<0.2	14.4	17.8	<0.1	16.8	<0.1	<0.1	<0.1	0.5	6.3	<0.2	41.8	97.6

Sample	Reference	Lithology	Structure	Type	Alt	Texture	Na_pct	Mg_pct	Al_pct	Si_pct	K_pct	Ca_pct	Ti_pct	V_pct	Cr_pct	Mn_pct	Fe_pct	Co_pct	O_pct	Total_pct
RCS003	RCS003_14_10	Monzodiorite	144SW87	Fracture	A4	Replacement	<0.1	<0.2	10.7	17.1	<0.1	16.6	<0.1	0.1	<0.1	0.4	12.6	<0.2	39.4	96.9
RCS003	RCS003_14_12	Monzodiorite	144SW87	Fracture	A4	Replacement	<0.1	<0.2	9.2	17.0	<0.1	16.8	<0.1	<0.1	<0.1	<0.1	15.1	<0.2	38.5	96.6
RCS003	RCS003_14_13	Monzodiorite	144SW87	Fracture	A4	Replacement	<0.1	<0.2	10.2	17.1	<0.1	16.6	<0.1	<0.1	<0.1	0.4	13.0	<0.2	39.0	96.2
RCS003	RCS003_17_2	Monzodiorite	144SW87	Fracture	A4	Replacement	<0.1	<0.2	10.5	17.3	<0.1	16.1	<0.1	<0.1	<0.1	0.5	12.3	<0.2	39.2	95.9
RCS009	RCS009_6_10	Monzonite	026SE87	Fracture vein	A4	Replacement	<0.1	<0.2	12.0	17.1	<0.1	16.7	<0.1	<0.1	<0.1	0.2	9.3	<0.2	39.6	94.8
RCS009	RCS009_6_13	Monzonite	026SE87	Fracture vein	A4	Replacement	0.3	<0.2	12.7	17.9	<0.1	16.5	<0.1	<0.1	<0.1	0.2	8.7	<0.2	41.0	97.3
RCS009	RCS009_6_14	Monzonite	026SE87	Fracture vein	A4	Replacement	<0.1	<0.2	12.5	17.0	<0.1	16.3	<0.1	<0.1	<0.1	0.2	8.5	<0.2	39.5	94.0
RCS009	RCS009_7_1	Monzonite	026SE87	Fracture vein	A4	L Patches	<0.1	<0.2	12.3	17.3	<0.1	16.7	<0.1	<0.1	0.1	0.2	9.3	<0.2	40.1	95.9
RCS009	RCS009_7_4	Monzonite	026SE87	Fracture vein	A4	L Patches	<0.1	<0.2	11.3	17.0	<0.1	16.7	<0.1	<0.1	<0.1	<0.1	10.5	<0.2	39.2	94.7
RCS009	RCS009_7_5	Monzonite	026SE87	Fracture vein	A4	L Patches	0.1	<0.2	12.5	17.1	<0.1	16.9	<0.1	<0.1	<0.1	<0.1	8.9	<0.2	40.1	95.6
RCS009	RCS009_7_7	Monzonite	026SE87	Fracture vein	A4	L Patches	<0.1	<0.2	12.4	17.3	<0.1	17.0	0.1	0.1	<0.1	<0.1	9.0	<0.2	40.4	96.4
RCS009	RCS009_7_8	Monzonite	026SE87	Fracture vein	A4	L Patches	<0.1	<0.2	12.4	17.4	<0.1	17.0	<0.1	<0.1	<0.1	<0.1	9.0	<0.2	40.3	96.2
RCS009	RCS009_7_9	Monzonite	026SE87	Fracture vein	A4	L Patches	<0.1	<0.2	11.9	17.2	<0.1	16.9	<0.1	<0.1	<0.1	0.1	10.2	<0.2	39.9	96.3
RCS009	RCS009_7_10	Monzonite	026SE87	Fracture vein	A4	L Patches	<0.1	<0.2	12.8	17.1	<0.1	16.9	<0.1	<0.1	0.1	0.2	8.0	<0.2	40.0	95.1
RCS009	RCS009_7_12	Monzonite	026SE87	Fracture vein	A4	L Patches	<0.1	<0.2	12.9	17.2	<0.1	16.6	<0.1	<0.1	<0.1	0.4	8.2	<0.2	40.2	95.5
RCS009	RCS009_7_13	Monzonite	026SE87	Fracture vein	A4	L Patches	0.2	<0.2	12.4	17.4	<0.1	16.8	<0.1	<0.1	<0.1	0.1	9.0	<0.2	40.2	96.0
RCS009	RCS009_7_15	Monzonite	026SE87	Fracture vein	A4	L Patches	<0.1	0.5	11.7	17.9	<0.1	16.2	<0.1	<0.1	<0.1	0.5	9.3	<0.2	40.5	96.6
RCS009	RCS009_9_2	Monzonite	026SE87	Fracture vein	A4	Replacement	<0.1	<0.2	11.8	17.2	<0.1	17.0	<0.1	0.1	<0.1	0.2	9.7	<0.2	39.8	95.7
RCS009	RCS009_9_10	Monzonite	026SE87	Fracture vein	A4	Replacement	<0.1	<0.2	13.7	17.4	<0.1	16.9	<0.1	<0.1	0.2	0.2	7.1	<0.2	40.9	96.3
RCS009	RCS009_9_11	Monzonite	026SE87	Fracture vein	A4	Replacement	<0.1	<0.2	12.9	17.4	<0.1	16.8	<0.1	0.1	<0.1	0.2	7.9	<0.2	40.4	95.6
RCS009	RCS009_11_1	Monzonite	026SE87	Fracture vein	A4	Replacement	<0.1	<0.2	11.7	16.8	<0.1	15.7	<0.1	<0.1	<0.1	<0.1	8.5	<0.2	38.3	90.9
RCS009	RCS009_11_2	Monzonite	026SE87	Fracture vein	A4	Replacement	<0.1	<0.2	12.0	16.7	<0.1	15.7	<0.1	<0.1	0.1	<0.1	8.1	<0.2	38.4	91.0
RCS009	RCS009_11_3	Monzonite	026SE87	Fracture vein	A4	Replacement	<0.1	<0.2	12.5	16.8	<0.1	15.7	<0.1	<0.1	<0.1	<0.1	7.8	<0.2	38.8	91.6
RCS009	RCS009_11_4	Monzonite	026SE87	Fracture vein	A4	Replacement	<0.1	<0.2	12.9	16.9	<0.1	15.2	<0.1	<0.1	<0.1	0.4	6.8	<0.2	38.8	90.9
RCS009	RCS009_11_5	Monzonite	026SE87	Fracture vein	A4	Replacement	0.1	<0.2	13.0	16.8	<0.1	15.7	<0.1	<0.1	<0.1	0.2	6.7	<0.2	39.0	91.5
RCS009	RCS009_12_5	Monzonite	026SE87	Fracture vein	A4	Replacement	<0.1	<0.2	12.7	16.7	<0.1	15.3	<0.1	<0.1	<0.1	0.3	6.9	<0.2	38.5	90.4
RCS009	RCS009_12_6	Monzonite	026SE87	Fracture vein	A4	Replacement	<0.1	<0.2	11.4	16.8	<0.1	16.0	<0.1	<0.1	<0.1	0.1	9.2	<0.2	38.4	92.0
RCS009	RCS009_12_7	Monzonite	026SE87	Fracture vein	A4	Replacement	<0.1	<0.2	12.6	16.8	<0.1	16.0	<0.1	<0.1	<0.1	0.3	7.2	<0.2	38.9	91.8
RCS009	RCS009_12_9	Monzonite	026SE87	Fracture vein	A4	Replacement	<0.1	<0.2	12.0	16.8	<0.1	15.1	<0.1	<0.1	<0.1	0.3	7.9	<0.2	38.3	90.4
RCS009	RCS009_14_15	Monzonite	026SE87	Fracture vein	A4	Replacement	<0.1	<0.2	11.0	17.0	<0.1	16.0	<0.1	<0.1	<0.1	0.2	11.1	<0.2	39.0	94.3
RCS009	RCS009_17_8	Monzonite	026SE87	Fracture vein	A4	Replacement	<0.1	<0.2	12.7	17.2	<0.1	17.0	<0.1	<0.1	<0.1	0.1	8.4	<0.2	40.2	95.6
RCS009	RCS009_17_9	Monzonite	026SE87	Fracture vein	A4	Replacement	<0.1	<0.2	12.7	17.4	<0.1	16.9	<0.1	<0.1	<0.1	0.1	8.7	<0.2	40.5	96.3
RCS009	RCS009_19_5	Monzonite	026SE87	Fracture vein	A4	Replacement	<0.1	<0.2	12.8	17.4	<0.1	17.0	<0.1	<0.1	<0.1	0.1	8.1	<0.2	40.5	95.9
RCS009	RCS009_19_6	Monzonite	026SE87	Fracture vein	A4	Replacement	<0.1	<0.2	13.1	17.4	<0.1	17.1	<0.1	<0.1	<0.1	<0.1	7.4	<0.2	40.6	95.6
RCS009	RCS009_19_9	Monzonite	026SE87	Fracture vein	A4	Replacement	<0.1	<0.2	12.4	16.9	<0.1	16.5	<0.1	<0.1	<0.1	0.1	8.8	<0.2	39.5	94.1

Sample	Reference	Lithology	Structure	Type	Alt	Texture	Na_pct	Mg_pct	Al_pct	Si_pct	K_pct	Ca_pct	Ti_pct	V_pct	Cr_pct	Mn_pct	Fe_pct	Co_pct	O_pct	Total_pct
RCS018	RCS018_6_3	\	115SW83	Vein	V2	Vein	<0.1	<0.2	13.1	17.2	<0.1	16.8	<0.1	<0.1	<0.1	0.2	7.4	<0.2	40.2	95.0
RCS018	RCS018_6_4	\	115SW83	Vein	V2	Vein	<0.1	<0.2	13.4	17.1	<0.1	16.0	<0.1	<0.1	<0.1	0.8	7.2	<0.2	40.0	94.5
RCS018	RCS018_7_1	\	115SW83	Vein	V2	Vein	<0.1	<0.2	11.8	17.2	<0.1	16.9	<0.1	<0.1	0.1	<0.1	9.8	<0.2	39.8	95.6
RCS018	RCS018_7_2	\	115SW83	Vein	V2	Vein	<0.1	<0.2	11.5	17.0	<0.1	16.8	<0.1	<0.1	<0.1	0.1	10.5	<0.2	39.3	95.1
RCS018	RCS018_7_4	\	115SW83	Vein	V2	Vein	<0.1	<0.2	11.4	16.9	<0.1	16.6	<0.1	<0.1	<0.1	<0.1	10.5	<0.2	39.1	94.5
RCS018	RCS018_9_5	\	115SW83	Vein	V2	Vein	<0.1	<0.2	13.4	17.0	<0.1	16.7	<0.1	<0.1	<0.1	0.1	6.6	<0.2	39.9	93.7
RCS018	RCS018_9_6	\	115SW83	Vein	V2	Vein	<0.1	<0.2	11.2	16.7	<0.1	15.9	<0.1	<0.1	<0.1	0.5	10.8	<0.2	38.6	93.7
RCS018	RCS018_10_1	\	115SW83	Vein	V2	Vein	<0.1	<0.2	10.5	16.3	<0.1	16.0	<0.1	<0.1	<0.1	<0.1	10.8	<0.2	37.2	90.8
RCS018	RCS018_10_3	\	115SW83	Vein	V2	Vein	<0.1	<0.2	11.2	16.7	<0.1	16.6	<0.1	0.1	<0.1	<0.1	10.5	<0.2	38.7	93.9
RCS018	RCS018_10_5	\	115SW83	Vein	V2	Vein	<0.1	<0.2	11.9	16.8	<0.1	16.6	<0.1	<0.1	<0.1	<0.1	9.4	<0.2	39.1	93.7
RCS018	RCS018_10_10	\	115SW83	Vein	V2	Vein	<0.1	<0.2	11.8	17.0	<0.1	16.7	<0.1	<0.1	<0.1	0.1	10.0	<0.2	39.5	95.2
RCS018	RCS018_12_3	\	115SW83	Vein	A3	VH	<0.1	<0.2	11.1	16.8	<0.1	16.6	0.1	<0.1	0.1	<0.1	10.4	<0.2	38.8	93.9
RCS018	RCS018_15_4	\	115SW83	Vein	V2	Vein	<0.1	<0.2	12.5	17.5	<0.1	16.9	<0.1	<0.1	0.1	0.2	9.4	<0.2	40.7	97.3
RCS018	RCS018_16_9	\	115SW83	Vein	V2	Vein	<0.1	<0.2	11.5	17.0	<0.1	16.4	<0.1	<0.1	<0.1	0.3	10.5	<0.2	39.2	94.8
RCS018	RCS018_16_10	\	115SW83	Vein	V2	Vein	<0.1	<0.2	13.2	17.5	<0.1	16.3	<0.1	<0.1	<0.1	0.6	8.8	<0.2	41.0	97.3
RCS018	RCS018_21_4	\	115SW83	Vein	V2	Vein	<0.1	<0.2	14.3	17.8	<0.1	17.1	<0.1	<0.1	<0.1	0.6	6.7	<0.2	42.0	98.3
RCS018	RCS018_22_2	\	115SW83	Vein	A3	VH	<0.1	<0.2	10.8	17.0	<0.1	16.8	<0.1	0.2	<0.1	<0.1	12.1	<0.2	39.2	96.0
RCS018	RCS018_22_3	\	115SW83	Vein	A3	VH	<0.1	<0.2	11.6	17.4	<0.1	16.9	0.1	<0.1	<0.1	<0.1	10.8	<0.2	40.2	97.1
RCS018	RCS018_22_4	\	115SW83	Vein	A3	VH	<0.1	<0.2	14.1	17.6	<0.1	17.1	<0.1	<0.1	0.1	<0.1	6.5	<0.2	41.3	96.7
RCS018	RCS018_22_6	\	115SW83	Vein	A3	VH	<0.1	<0.2	12.7	17.4	<0.1	16.8	<0.1	<0.1	0.1	<0.1	8.1	<0.2	40.3	95.5
RCS006	RCS006_13_14	Monzonite	NA	NA	A3	Patches	<0.1	<0.2	11.5	17.6	<0.1	17.0	<0.1	<0.1	<0.1	0.2	11.6	<0.2	40.6	98.5
RCS006	RCS006_13_18	Monzonite	NA	NA	A3	Patches	<0.1	<0.2	9.9	17.5	<0.1	17.3	<0.1	<0.1	<0.1	<0.1	14.9	<0.2	40.0	99.6
RCS006	RCS006_13_19	Monzonite	NA	NA	A3	Patches	<0.1	<0.2	11.7	17.7	<0.1	17.2	<0.1	<0.1	<0.1	0.1	11.4	<0.2	40.8	99.0
RCS006	RCS006_13_20	Monzonite	NA	NA	A3	Patches	<0.1	<0.2	10.7	17.3	<0.1	16.9	<0.1	<0.1	<0.1	0.1	12.5	<0.2	39.7	97.2
RCS006	RCS006_13_21	Monzonite	NA	NA	A3	Patches	<0.1	<0.2	10.4	17.7	<0.1	17.3	<0.1	<0.1	<0.1	<0.1	13.8	<0.2	40.4	99.6
RCS006	RCS006_18_5	Monzonite	NA	NA	A3	Patches	<0.1	<0.2	11.9	17.8	<0.1	17.2	<0.1	<0.1	<0.1	0.1	11.2	<0.2	41.1	99.4
RCS006	RCS006_18_6	Monzonite	NA	NA	A3	Patches	<0.1	<0.2	12.2	17.7	<0.1	17.5	<0.1	<0.1	<0.1	<0.1	10.3	<0.2	41.1	98.8
RCS006	RCS006_18_7	Monzonite	NA	NA	A3	Patches	<0.1	<0.2	12.8	17.8	<0.1	17.3	<0.1	<0.1	<0.1	0.2	9.5	<0.2	41.5	99.1
RCS006	RCS006_18_8	Monzonite	NA	NA	A3	Patches	<0.1	<0.2	12.4	17.8	<0.1	17.3	<0.1	<0.1	<0.1	0.2	10.1	<0.2	41.2	99.0
RCS006	RCS006_18_9	Monzonite	NA	NA	A3	Patches	<0.1	<0.2	11.2	17.6	<0.1	17.1	<0.1	<0.1	<0.1	0.2	11.6	<0.2	40.4	98.1
RCS006	RCS006_18_10	Monzonite	NA	NA	A3	Patches	<0.1	<0.2	12.7	17.7	<0.1	17.0	<0.1	<0.1	0.1	0.2	9.1	<0.2	41.0	97.9
RCS006	RCS006_18_11	Monzonite	NA	NA	A3	Patches	0.1	<0.2	11.3	17.8	<0.1	16.8	<0.1	<0.1	<0.1	0.4	12.3	<0.2	40.7	99.3
RCS006	RCS006_18_12	Monzonite	NA	NA	A3	Patches	<0.1	<0.2	11.5	17.7	<0.1	17.4	<0.1	<0.1	<0.1	0.2	11.5	<0.2	40.9	99.3
RCS006	RCS006_18_13	Monzonite	NA	NA	A3	Patches	<0.1	<0.2	12.4	17.9	<0.1	17.4	<0.1	<0.1	<0.1	<0.1	10.0	<0.2	41.2	98.9
RCS016	RCS016_6_3	Andesite	NA	NA	A6	Replacement	<0.1	<0.2	13.1	17.3	<0.1	16.8	<0.1	<0.1	<0.1	0.4	8.1	<0.2	40.6	96.3

Sample	Reference	Lithology	Structure	Type	Alt	Texture	Na_pct	Mg_pct	Al_pct	Si_pct	K_pct	Ca_pct	Ti_pct	V_pct	Cr_pct	Mn_pct	Fe_pct	Co_pct	O_pct	Total_pct
RCS016	RCS016_6_4	Andesite	NA	NA	A6	Replacement	<0.1	<0.2	12.5	17.6	0.1	16.8	<0.1	<0.1	<0.1	0.2	9.4	<0.2	40.7	97.3
RCS016	RCS016_6_5	Andesite	NA	NA	A6	Replacement	<0.1	<0.2	11.6	17.3	<0.1	16.8	<0.1	<0.1	0.1	<0.1	11.0	<0.2	39.9	96.7
RCS016	RCS016_6_6	Andesite	NA	NA	A6	Replacement	<0.1	<0.2	11.0	17.1	<0.1	17.0	<0.1	<0.1	<0.1	0.1	11.8	<0.2	39.5	96.5
RCS016	RCS016_6_7	Andesite	NA	NA	A6	Replacement	<0.1	<0.2	11.4	17.4	<0.1	17.1	<0.1	<0.1	<0.1	<0.1	10.8	<0.2	39.9	96.5
RCS016	RCS016_6_8	Andesite	NA	NA	A6	Replacement	<0.1	<0.2	12.8	17.4	<0.1	17.0	<0.1	0.1	<0.1	0.1	8.8	<0.2	40.7	96.8
RCS016	RCS016_6_10	Andesite	NA	NA	A6	Replacement	<0.1	<0.2	10.7	17.1	<0.1	16.6	<0.1	<0.1	<0.1	<0.1	11.8	<0.2	39.1	95.3
RCS016	RCS016_6_12	Andesite	NA	NA	A6	Replacement	<0.1	<0.2	11.7	17.3	<0.1	16.5	<0.1	<0.1	<0.1	0.1	10.0	<0.2	39.7	95.4
RCS016	RCS016_6_13	Andesite	NA	NA	A6	Replacement	<0.1	<0.2	10.8	16.9	<0.1	16.8	<0.1	<0.1	<0.1	<0.1	11.7	<0.2	38.9	95.1
RCS016	RCS016_6_14	Andesite	NA	NA	A6	Replacement	<0.1	<0.2	11.3	16.9	<0.1	16.3	<0.1	<0.1	<0.1	0.2	10.8	<0.2	39.1	94.6
RCS016	RCS016_9_2	Andesite	NA	NA	A6	Replacement	0.1	<0.2	12.9	17.1	<0.1	16.4	0.1	<0.1	<0.1	0.2	8.2	<0.2	40.2	95.3
RCS016	RCS016_9_4	Andesite	NA	NA	A6	Replacement	<0.1	<0.2	12.7	17.0	<0.1	16.8	<0.1	<0.1	<0.1	0.1	8.3	0.2	40.0	95.1
RCS016	RCS016_9_5	Andesite	NA	NA	A6	Replacement	<0.1	<0.2	12.6	17.0	<0.1	16.7	<0.1	<0.1	<0.1	0.2	8.2	<0.2	39.6	94.2
RCS016	RCS016_9_6	Andesite	NA	NA	A6	Replacement	<0.1	<0.2	12.1	17.3	<0.1	16.7	0.3	<0.1	<0.1	0.1	8.8	<0.2	40.0	95.2
RCS016	RCS016_11_6	Andesite	NA	NA	A6	Replacement	<0.1	<0.2	11.2	17.1	<0.1	16.7	<0.1	<0.1	<0.1	0.2	11.3	<0.2	39.3	95.8
RCS016	RCS016_13_1	Andesite	NA	NA	A6	Replacement	<0.1	<0.2	9.9	16.7	<0.1	16.4	<0.1	<0.1	<0.1	<0.1	12.9	<0.2	38.1	94.1
RCS016	RCS016_13_2	Andesite	NA	NA	A6	Replacement	<0.1	<0.2	12.6	17.0	<0.1	16.7	<0.1	0.1	<0.1	<0.1	8.7	<0.2	39.8	94.9
RCS016	RCS016_13_6	Andesite	NA	NA	A6	Replacement	<0.1	<0.2	11.1	17.2	<0.1	15.5	<0.1	<0.1	<0.1	0.3	10.1	<0.2	38.8	93.0
RCS016	RCS016_15_2	Andesite	NA	NA	A6	Replacement	<0.1	<0.2	11.4	17.0	<0.1	16.7	<0.1	<0.1	<0.1	0.1	10.1	<0.2	39.2	94.6
RCS016	RCS016_15_5	Andesite	NA	NA	A6	Replacement	<0.1	<0.2	10.6	16.9	<0.1	16.5	<0.1	0.1	<0.1	<0.1	11.5	<0.2	38.7	94.3
RCS016	RCS016_15_7	Andesite	NA	NA	A6	Replacement	<0.1	<0.2	11.4	17.1	<0.1	15.9	<0.1	<0.1	0.1	0.7	10.8	<0.2	39.3	95.3
RCS016	RCS016_15_8	Andesite	NA	NA	A6	Replacement	<0.1	<0.2	12.7	17.3	<0.1	17.0	0.3	<0.1	<0.1	<0.1	8.1	<0.2	40.4	95.8
RCS017	RCS017_11_1	Monzonite	242NW82	Fracture vein	V2	Vein	<0.1	<0.2	13.1	17.3	<0.1	17.2	<0.1	<0.1	<0.1	0.1	7.8	<0.2	40.7	96.3
RCS017	RCS017_11_3	Monzonite	242NW82	Fracture vein	V2	Vein	<0.1	<0.2	12.3	17.7	<0.1	16.9	<0.1	<0.1	<0.1	0.3	10.6	<0.2	41.0	98.6
RCS017	RCS017_11_4	Monzonite	242NW82	Fracture vein	V2	Vein	<0.1	<0.2	13.3	17.9	<0.1	17.5	<0.1	<0.1	<0.1	0.2	8.7	<0.2	41.7	99.2
RCS017	RCS017_11_5	Monzonite	242NW82	Fracture vein	V2	Vein	<0.1	<0.2	13.1	17.8	<0.1	17.6	<0.1	<0.1	<0.1	<0.1	9.2	<0.2	41.6	99.3
RCS017	RCS017_11_6	Monzonite	242NW82	Fracture vein	V2	Vein	<0.1	<0.2	12.4	17.8	<0.1	17.5	<0.1	<0.1	<0.1	<0.1	10.2	<0.2	41.2	99.1
RCS017	RCS017_11_8	Monzonite	242NW82	Fracture vein	V2	Vein	<0.1	<0.2	13.6	18.0	<0.1	17.6	<0.1	<0.1	<0.1	<0.1	8.0	<0.2	42.0	99.2
RCS017	RCS017_11_10	Monzonite	242NW82	Fracture vein	V2	Vein	<0.1	<0.2	12.5	17.7	<0.1	17.2	<0.1	<0.1	<0.1	<0.1	9.8	<0.2	41.0	98.1
RCS017	RCS017_11_11	Monzonite	242NW82	Fracture vein	V2	Vein	<0.1	<0.2	12.9	17.7	<0.1	17.4	<0.1	<0.1	<0.1	<0.1	9.0	<0.2	41.2	98.2
RCS017	RCS017_12_1	Monzonite	242NW82	Fracture vein	V2	Vein	<0.1	<0.2	11.8	17.7	<0.1	17.1	0.1	<0.1	<0.1	0.1	10.6	<0.2	40.7	98.2
RCS017	RCS017_12_2	Monzonite	242NW82	Fracture vein	V2	Vein	<0.1	<0.2	12.3	17.4	<0.1	16.4	<0.1	<0.1	<0.1	0.5	10.0	<0.2	40.5	97.1
RCS017	RCS017_12_3	Monzonite	242NW82	Fracture vein	V2	Vein	<0.1	<0.2	11.9	17.4	<0.1	17.1	<0.1	<0.1	<0.1	<0.1	10.2	<0.2	40.3	96.9
RCS017	RCS017_12_4	Monzonite	242NW82	Fracture vein	V2	Vein	<0.1	<0.2	12.6	17.6	<0.1	17.1	<0.1	<0.1	<0.1	<0.1	9.2	<0.2	40.8	97.4
RCS017	RCS017_12_5	Monzonite	242NW82	Fracture vein	V2	Vein	<0.1	<0.2	12.0	17.8	<0.1	17.2	<0.1	<0.1	0.1	<0.1	10.3	<0.2	40.8	98.1
RCS017	RCS017_12_6	Monzonite	242NW82	Fracture vein	V2	Vein	<0.1	<0.2	12.3	17.6	<0.1	16.7	<0.1	<0.1	0.1	0.6	10.2	<0.2	40.7	98.1

Sample	Reference	Lithology	Structure	Type	Alt	Texture	Na_pct	Mg_pct	Al_pct	Si_pct	K_pct	Ca_pct	Ti_pct	V_pct	Cr_pct	Mn_pct	Fe_pct	Co_pct	O_pct	Total_pct
RCS017	RCS017_12_7	Monzonite	242NW82	Fracture vein	V2	Vein	<0.1	<0.2	12.3	17.5	<0.1	17.3	<0.1	<0.1	<0.1	<0.1	10.0	<0.2	40.7	97.7
RCS017	RCS017_12_10	Monzonite	242NW82	Fracture vein	V2	Vein	<0.1	<0.2	12.9	17.5	<0.1	17.5	<0.1	<0.1	0.1	<0.1	8.5	<0.2	41.0	97.5
RCS017	RCS017_14_1	Monzonite	242NW82	Fracture vein	V2	Vein	<0.1	<0.2	12.0	17.5	<0.1	17.1	<0.1	<0.1	<0.1	<0.1	10.4	<0.2	40.5	97.5
RCS017	RCS017_14_2	Monzonite	242NW82	Fracture vein	V2	Vein	<0.1	<0.2	12.1	17.4	<0.1	16.9	<0.1	<0.1	<0.1	0.2	9.9	<0.2	40.3	96.8
RCS017	RCS017_14_3	Monzonite	242NW82	Fracture vein	V2	Vein	<0.1	<0.2	12.1	17.4	<0.1	17.2	<0.1	<0.1	<0.1	<0.1	10.0	<0.2	40.4	97.1
RCS017	RCS017_14_4	Monzonite	242NW82	Fracture vein	V2	Vein	<0.1	<0.2	12.7	17.6	<0.1	16.6	<0.1	<0.1	<0.1	0.5	9.5	<0.2	41.0	97.8
RCS017	RCS017_14_5	Monzonite	242NW82	Fracture vein	V2	Vein	<0.1	<0.2	12.2	17.4	<0.1	16.5	<0.1	<0.1	<0.1	0.3	9.4	<0.2	40.1	95.9
RCS017	RCS017_14_6	Monzonite	242NW82	Fracture vein	V2	Vein	<0.1	<0.2	12.5	17.6	<0.1	17.1	<0.1	<0.1	<0.1	0.3	9.9	<0.2	41.0	98.4
RCS017	RCS017_14_7	Monzonite	242NW82	Fracture vein	V2	Vein	<0.1	<0.2	12.6	17.6	<0.1	17.2	<0.1	<0.1	<0.1	<0.1	9.5	<0.2	40.8	97.6
RCS017	RCS017_14_8	Monzonite	242NW82	Fracture vein	V2	Vein	<0.1	<0.2	12.4	17.7	<0.1	17.0	<0.1	<0.1	<0.1	0.4	10.3	<0.2	41.0	98.8
RCS017	RCS017_14_11	Monzonite	242NW82	Fracture vein	V2	Vein	<0.1	<0.2	12.6	17.7	<0.1	17.1	<0.1	<0.1	<0.1	0.2	10.0	<0.2	41.2	98.6
RCS017	RCS017_14_12	Monzonite	242NW82	Fracture vein	V2	Vein	<0.1	<0.2	12.2	17.5	<0.1	16.4	<0.1	<0.1	<0.1	0.5	10.6	<0.2	40.6	97.7
RCS017	RCS017_14_13	Monzonite	242NW82	Fracture vein	V2	Vein	<0.1	<0.2	12.1	17.5	<0.1	17.2	<0.1	<0.1	0.1	<0.1	10.2	<0.2	40.6	97.7
RCS017	RCS017_18_3	Monzonite	242NW82	Fracture vein	A3	Replacement	<0.1	<0.2	12.2	17.4	<0.1	16.5	<0.1	<0.1	<0.1	0.1	9.1	<0.2	40.1	95.4
RCS032	RCS032_6_1	Andesite	NA	NA	A4	Replacement	<0.1	<0.2	11.5	17.3	<0.1	16.8	<0.1	<0.1	<0.1	0.1	11.3	<0.2	39.9	96.8
RCS032	RCS032_6_13	Andesite	NA	NA	A4	Replacement	<0.1	<0.2	10.6	17.1	<0.1	16.8	<0.1	<0.1	<0.1	<0.1	12.5	<0.2	39.2	96.1
RCS032	RCS032_6_14	Andesite	NA	NA	A4	Replacement	0.2	<0.2	12.3	17.2	<0.1	16.9	<0.1	<0.1	<0.1	0.2	9.7	<0.2	40.3	96.7
RCS032	RCS032_6_16	Andesite	NA	NA	A4	Replacement	<0.1	<0.2	11.2	17.2	<0.1	16.9	<0.1	<0.1	<0.1	0.1	11.2	<0.2	39.5	96.0
RCS032	RCS032_6_18	Andesite	NA	NA	A4	Replacement	<0.1	<0.2	12.4	17.1	<0.1	16.9	<0.1	<0.1	<0.1	0.1	9.3	<0.2	40.0	95.8
RCS032	RCS032_6_19	Andesite	NA	NA	A4	Replacement	<0.1	<0.2	11.9	17.2	<0.1	16.5	<0.1	<0.1	<0.1	0.5	9.8	<0.2	39.8	95.6
RCS032	RCS032_6_20	Andesite	NA	NA	A4	Replacement	<0.1	<0.2	12.7	17.4	<0.1	17.0	<0.1	0.1	<0.1	<0.1	7.8	<0.2	40.2	95.2
RCS032	RCS032_6_21	Andesite	NA	NA	A4	Replacement	<0.1	<0.2	11.6	17.2	<0.1	16.7	<0.1	<0.1	<0.1	0.3	10.5	<0.2	39.7	95.9
RCS032	RCS032_6_24	Andesite	NA	NA	A4	Replacement	<0.1	<0.2	12.6	17.5	<0.1	16.4	<0.1	<0.1	<0.1	0.5	9.2	<0.2	40.5	96.7
RCS032	RCS032_8_13	Andesite	NA	NA	A4	Replacement	<0.1	<0.2	11.7	17.3	<0.1	16.6	<0.1	<0.1	<0.1	0.4	10.6	<0.2	39.9	96.4
RCS032	RCS032_8_14	Andesite	NA	NA	A4	Replacement	<0.1	<0.2	13.2	17.5	<0.1	16.9	<0.1	<0.1	0.1	0.4	8.3	<0.2	41.0	97.3
RCS032	RCS032_8_15	Andesite	NA	NA	A4	Replacement	<0.1	<0.2	12.6	17.5	<0.1	16.9	<0.1	<0.1	<0.1	0.2	9.1	<0.2	40.8	97.2
RCS032	RCS032_8_16	Andesite	NA	NA	A4	Replacement	<0.1	<0.2	13.6	17.1	<0.1	16.5	<0.1	<0.1	0.1	0.6	7.0	<0.2	40.4	95.2
RCS032	RCS032_8_17	Andesite	NA	NA	A4	Replacement	<0.1	<0.2	13.3	17.1	<0.1	16.5	<0.1	<0.1	<0.1	0.2	7.6	<0.2	40.2	94.9
RCS032	RCS032_8_18	Andesite	NA	NA	A4	Replacement	<0.1	<0.2	11.2	17.2	<0.1	16.6	<0.1	<0.1	<0.1	<0.1	10.3	<0.2	39.2	94.5
RCS032	RCS032_12_10	Andesite	NA	NA	A4	Replacement	<0.1	<0.2	11.9	17.4	<0.1	16.7	<0.1	<0.1	<0.1	0.2	9.5	<0.2	40.0	95.7
RCS032	RCS032_15_1	Andesite	NA	NA	A4	Replacement	0.2	<0.2	12.1	17.4	<0.1	16.6	<0.1	<0.1	<0.1	0.1	8.8	<0.2	39.9	95.0
RCS032	RCS032_15_2	Andesite	NA	NA	A4	Replacement	<0.1	<0.2	11.5	17.2	<0.1	16.8	<0.1	<0.1	<0.1	0.1	10.4	<0.2	39.6	95.6
RCS032	RCS032_15_3	Andesite	NA	NA	A4	Replacement	<0.1	0.3	11.7	17.0	<0.1	16.2	<0.1	<0.1	<0.1	<0.1	9.7	<0.2	39.4	94.4
RCS032	RCS032_15_4	Andesite	NA	NA	A4	Replacement	0.2	<0.2	12.5	17.6	<0.1	16.6	<0.1	<0.1	0.1	0.3	9.1	<0.2	40.7	97.1
RCS032	RCS032_15_5	Andesite	NA	NA	A4	Replacement	<0.1	<0.2	12.3	17.0	<0.1	16.1	<0.1	<0.1	<0.1	0.6	8.7	<0.2	39.5	94.3

Sample	Reference	Lithology	Structure	Type	Alt	Texture	Na_pct	Mg_pct	Al_pct	Si_pct	K_pct	Ca_pct	Ti_pct	V_pct	Cr_pct	Mn_pct	Fe_pct	Co_pct	O_pct	Total_pct
RCS032	RCS032_15_6	Andesite	NA	NA	A4	Replacement	<0.1	<0.2	11.7	16.9	<0.1	16.5	<0.1	<0.1	0.2	0.2	9.8	<0.2	39.3	94.7
RCS096	RCS096_22_8	Granodiorite	NA	NA	A3	Replacement	<0.1	<0.2	12.2	17.4	<0.1	16.1	<0.1	<0.1	<0.1	0.6	9.6	<0.2	40.1	96.0
RCS096	RCS096_22_13	Granodiorite	NA	NA	A3	Replacement	<0.1	<0.2	13.3	17.4	<0.1	17.0	<0.1	<0.1	<0.1	0.3	7.7	<0.2	40.8	96.4
RCS096	RCS096_23_4	Granodiorite	NA	NA	A3	Replacement	<0.1	<0.2	12.6	17.3	<0.1	16.8	<0.1	0.1	<0.1	<0.1	9.4	<0.2	40.5	96.6
RCS098	RCS098_4_4	Rhyolite	NA	NA	A5	Replacement	<0.1	<0.2	10.0	16.9	<0.1	16.4	<0.1	<0.1	0.1	0.3	12.9	<0.2	38.4	94.9
RCS098	RCS098_4_5	Rhyolite	NA	NA	A5	Replacement	<0.1	<0.2	12.4	17.1	<0.1	17.1	<0.1	<0.1	<0.1	0.2	9.4	<0.2	40.1	96.2
RCS098	RCS098_4_6	Rhyolite	NA	NA	A5	Replacement	<0.1	<0.2	12.2	17.3	<0.1	16.7	<0.1	<0.1	<0.1	0.3	9.1	<0.2	39.8	95.3
RCS098	RCS098_4_7	Rhyolite	NA	NA	A5	Replacement	<0.1	<0.2	11.6	17.1	<0.1	16.6	<0.1	<0.1	<0.1	0.3	10.6	<0.2	39.5	95.7
RCS098	RCS098_4_8	Rhyolite	NA	NA	A5	Replacement	<0.1	<0.2	11.5	17.6	<0.1	17.0	<0.1	<0.1	<0.1	<0.1	10.7	<0.2	40.1	96.7
RCS098	RCS098_4_9	Rhyolite	NA	NA	A5	Replacement	<0.1	<0.2	11.5	17.1	<0.1	16.7	<0.1	<0.1	0.1	<0.1	10.3	<0.2	39.4	95.0
RCS098	RCS098_4_11	Rhyolite	NA	NA	A5	Replacement	<0.1	<0.2	13.1	17.3	<0.1	15.4	<0.1	<0.1	<0.1	1.7	8.0	<0.2	40.2	95.6
RCS098	RCS098_4_12	Rhyolite	NA	NA	A5	Replacement	<0.1	<0.2	10.5	17.0	<0.1	16.5	<0.1	<0.1	<0.1	0.2	12.1	<0.2	38.9	95.2
RCS098	RCS098_4_13	Rhyolite	NA	NA	A5	Replacement	<0.1	<0.2	12.4	17.3	<0.1	16.8	<0.1	<0.1	<0.1	0.5	8.9	<0.2	40.1	95.9
RCS098	RCS098_6_1	Rhyolite	NA	NA	A5	Replacement	<0.1	<0.2	12.8	17.6	<0.1	16.7	<0.1	<0.1	<0.1	0.3	9.0	<0.2	40.9	97.3
RCS098	RCS098_6_2	Rhyolite	NA	NA	A5	Replacement	<0.1	<0.2	12.2	17.5	<0.1	16.8	<0.1	<0.1	<0.1	0.3	9.8	<0.2	40.5	97.0
RCS098	RCS098_6_3	Rhyolite	NA	NA	A5	Replacement	<0.1	<0.2	11.5	17.4	<0.1	16.8	<0.1	<0.1	<0.1	0.1	10.9	<0.2	40.0	96.6
RCS098	RCS098_6_4	Rhyolite	NA	NA	A5	Replacement	<0.1	<0.2	12.7	17.5	<0.1	16.5	0.1	<0.1	<0.1	0.5	9.0	<0.2	40.8	97.2
RCS098	RCS098_6_5	Rhyolite	NA	NA	A5	Replacement	<0.1	<0.2	11.2	17.1	<0.1	16.5	<0.1	<0.1	<0.1	0.2	10.8	<0.2	39.2	95.0
RCS098	RCS098_6_6	Rhyolite	NA	NA	A5	Replacement	<0.1	<0.2	11.7	18.1	<0.1	16.4	<0.1	<0.1	0.1	0.2	10.1	<0.2	40.7	97.3
RCS098	RCS098_6_7	Rhyolite	NA	NA	A5	Replacement	<0.1	<0.2	10.9	17.0	<0.1	16.6	0.1	<0.1	<0.1	<0.1	11.2	<0.2	39.0	94.8
RCS098	RCS098_6_10	Rhyolite	NA	NA	A5	Replacement	<0.1	<0.2	11.2	17.0	<0.1	16.9	0.1	<0.1	<0.1	<0.1	10.4	<0.2	39.1	94.7
RCS098	RCS098_6_11	Rhyolite	NA	NA	A5	Replacement	<0.1	<0.2	11.9	17.1	<0.1	16.8	0.2	<0.1	<0.1	0.2	9.7	<0.2	39.7	95.4
RCS098	RCS098_6_12	Rhyolite	NA	NA	A5	Replacement	<0.1	<0.2	12.3	17.1	<0.1	16.7	<0.1	<0.1	<0.1	0.1	9.0	<0.2	39.8	95.0
RCS098	RCS098_7_1	Rhyolite	NA	NA	A5	Replacement	<0.1	<0.2	10.7	17.1	<0.1	16.7	<0.1	<0.1	0.1	<0.1	12.6	<0.2	39.3	96.5
RCS098	RCS098_7_2	Rhyolite	NA	NA	A5	Replacement	<0.1	<0.2	11.0	17.4	<0.1	16.8	0.1	<0.1	0.1	<0.1	11.3	<0.2	39.8	96.5
RCS098	RCS098_7_4	Rhyolite	NA	NA	A5	Replacement	<0.1	<0.2	13.4	17.7	<0.1	17.1	<0.1	<0.1	0.1	<0.1	7.9	<0.2	41.2	97.4
RCS098	RCS098_7_5	Rhyolite	NA	NA	A5	Replacement	<0.1	<0.2	12.1	18.5	<0.1	15.7	<0.1	<0.1	<0.1	0.2	8.0	<0.2	40.5	95.0
RCS098	RCS098_8_9	Rhyolite	NA	NA	A5	Replacement	<0.1	<0.2	10.4	17.8	<0.1	15.4	<0.1	<0.1	<0.1	0.2	10.4	<0.2	38.7	92.8
RCS098	RCS098_15_1	Rhyolite	NA	NA	A5	Replacement	<0.1	<0.2	9.8	17.3	<0.1	15.4	<0.1	<0.1	<0.1	0.2	12.6	<0.2	38.3	93.6
RCS007	RCS007_2_4	Diorite	NA	NA	A4	Replacement	<0.1	<0.2	12.5	17.4	<0.1	17.0	<0.1	<0.1	<0.1	<0.1	9.1	<0.2	40.3	96.2
RCS007	RCS007_2_8	Diorite	NA	NA	A4	Replacement	0.5	<0.2	10.7	17.5	<0.1	16.4	<0.1	<0.1	<0.1	<0.1	12.0	<0.2	39.7	96.7
RCS007	RCS007_3_3	Diorite	NA	NA	A4	Replacement	<0.1	<0.2	15.0	17.8	<0.1	17.2	<0.1	<0.1	<0.1	0.2	5.3	<0.2	42.2	97.6
RCS007	RCS007_6_2	Diorite	NA	NA	A4	Replacement	<0.1	<0.2	10.8	17.2	<0.1	16.6	<0.1	<0.1	<0.1	0.2	12.2	<0.2	39.4	96.4
RCS007	RCS007_6_3	Diorite	NA	NA	A4	Replacement	<0.1	<0.2	12.3	17.5	<0.1	16.5	<0.1	<0.1	<0.1	0.6	9.5	<0.2	40.3	96.6
RCS007	RCS007_6_4	Diorite	NA	NA	A4	Replacement	<0.1	<0.2	10.0	17.3	<0.1	16.5	<0.1	<0.1	<0.1	<0.1	13.6	<0.2	39.1	96.5

Sample	Reference	Lithology	Structure	Type	Alt	Texture	Na_pct	Mg_pct	Al_pct	Si_pct	K_pct	Ca_pct	Ti_pct	V_pct	Cr_pct	Mn_pct	Fe_pct	Co_pct	O_pct	Total_pct
RCS007	RCS007_6_5	Diorite	NA	NA	A4	Replacement	<0.1	<0.2	10.1	17.0	<0.1	16.2	<0.1	<0.1	<0.1	0.4	12.7	<0.2	38.6	95.0
RCS007	RCS007_6_6	Diorite	NA	NA	A4	Replacement	<0.1	<0.2	10.6	16.2	<0.1	16.5	<0.1	<0.1	<0.1	0.1	11.0	<0.2	37.7	92.0
RCS007	RCS007_6_12	Diorite	NA	NA	A4	Replacement	<0.1	<0.2	14.6	17.6	<0.1	16.3	<0.1	<0.1	<0.1	0.8	6.1	<0.2	41.6	96.9
RCS007	RCS007_8_6	Diorite	NA	NA	A4	Replacement	<0.1	<0.2	14.2	17.7	<0.1	17.0	<0.1	<0.1	<0.1	0.4	6.4	<0.2	41.7	97.4
RCS007	RCS007_8_7	Diorite	NA	NA	A4	Replacement	<0.1	<0.2	14.8	17.8	<0.1	16.7	<0.1	<0.1	<0.1	0.6	5.4	<0.2	41.9	97.1
RCS007	RCS007_8_8	Diorite	NA	NA	A4	Replacement	<0.1	<0.2	14.4	17.7	<0.1	17.0	<0.1	0.1	<0.1	0.2	5.7	<0.2	41.6	96.6
RCS007	RCS007_8_9	Diorite	NA	NA	A4	Replacement	<0.1	<0.2	11.5	17.6	<0.1	15.9	<0.1	<0.1	<0.1	1.1	11.6	<0.2	40.3	97.9
RCS007	RCS007_9_14	Diorite	NA	NA	A4	Replacement	0.2	<0.2	10.6	17.6	<0.1	16.8	<0.1	<0.1	<0.1	<0.1	12.6	<0.2	39.9	97.6
RCS007	RCS007_9_15	Diorite	NA	NA	A4	Replacement	<0.1	<0.2	10.1	17.3	<0.1	16.6	<0.1	<0.1	<0.1	0.1	13.4	<0.2	39.2	96.7
RCS007	RCS007_9_17	Diorite	NA	NA	A4	Replacement	0.2	<0.2	11.2	17.9	<0.1	16.1	<0.1	<0.1	<0.1	0.2	10.9	<0.2	40.1	96.6
RCS007	RCS007_9_19	Diorite	NA	NA	A4	Replacement	<0.1	<0.2	12.5	17.6	<0.1	17.0	<0.1	<0.1	<0.1	0.3	9.5	<0.2	40.8	97.6
RCS007	RCS007_9_21	Diorite	NA	NA	A4	Replacement	<0.1	<0.2	10.4	17.2	<0.1	16.7	<0.1	<0.1	<0.1	0.2	13.2	<0.2	39.3	97.0
RCS007	RCS007_9_23	Diorite	NA	NA	A4	Replacement	0.1	<0.2	11.7	17.8	<0.1	16.2	<0.1	<0.1	<0.1	0.9	11.0	<0.2	40.6	98.2
RCS007	RCS007_9_26	Diorite	NA	NA	A4	Replacement	<0.1	<0.2	9.6	16.8	<0.1	16.4	<0.1	<0.1	<0.1	<0.1	13.5	<0.2	38.2	94.6
RCS007	RCS007_11_1	Diorite	NA	NA	A4	Replacement	<0.1	<0.2	9.6	17.2	<0.1	16.5	<0.1	<0.1	<0.1	<0.1	14.5	<0.2	39.0	96.9
RCS007	RCS007_11_2	Diorite	NA	NA	A4	Replacement	<0.1	<0.2	10.5	17.2	<0.1	16.8	<0.1	<0.1	<0.1	0.2	12.6	<0.2	39.4	96.6
RCS007	RCS007_11_3	Diorite	NA	NA	A4	Replacement	<0.1	<0.2	10.6	17.2	<0.1	16.8	<0.1	<0.1	<0.1	0.1	12.5	<0.2	39.4	96.6
RCS007	RCS007_11_6	Diorite	NA	NA	A4	Replacement	<0.1	<0.2	10.4	17.1	<0.1	16.3	<0.1	<0.1	<0.1	0.1	11.7	<0.2	38.7	94.3
RCS007	RCS007_16_12	Diorite	NA	NA	A4	Replacement	<0.1	<0.2	13.4	17.7	<0.1	16.9	<0.1	0.2	<0.1	0.3	7.5	<0.2	41.1	97.0
RCS007	RCS007_16_13	Diorite	NA	NA	A4	Replacement	<0.1	<0.2	11.6	17.4	<0.1	16.6	<0.1	<0.1	<0.1	0.2	10.7	<0.2	39.9	96.4
RCS007	RCS007_16_16	Diorite	NA	NA	A4	Replacement	<0.1	<0.2	13.5	17.6	<0.1	16.7	<0.1	<0.1	<0.1	0.8	7.7	<0.2	41.1	97.3
RCS007	RCS007_16_17	Diorite	NA	NA	A4	Replacement	0.1	<0.2	12.1	18.0	<0.1	17.1	<0.1	<0.1	<0.1	<0.1	10.1	<0.2	40.9	98.3
RCS007	RCS007_19_7	Diorite	NA	NA	A4	Replacement	<0.1	<0.2	11.9	17.2	<0.1	16.0	<0.1	<0.1	<0.1	0.9	10.6	<0.2	39.9	96.4
RCS007	RCS007_21_4	Diorite	NA	NA	A4	Replacement	<0.1	<0.2	9.8	17.2	<0.1	16.9	<0.1	<0.1	<0.1	<0.1	13.7	<0.2	39.0	96.5
RCS007	RCS007_21_5	Diorite	NA	NA	A4	Replacement	<0.1	<0.2	9.4	17.2	<0.1	16.5	<0.1	<0.1	<0.1	0.2	15.0	<0.2	39.0	97.3
RCS007	RCS007_21_6	Diorite	NA	NA	A4	Replacement	<0.1	<0.2	13.8	17.5	<0.1	17.1	<0.1	<0.1	<0.1	0.2	6.9	<0.2	41.1	96.6
RCS041	RCS041_8_5	Monzonite	NA	NA	A3	Patches	<0.1	<0.2	13.7	17.8	<0.1	17.0	<0.1	<0.1	<0.1	0.2	7.5	<0.2	41.6	97.8
RCS041	RCS041_8_6	Monzonite	NA	NA	A3	Patches	<0.1	<0.2	12.9	17.6	<0.1	16.3	0.1	<0.1	<0.1	0.5	9.0	<0.2	40.9	97.3
RCS041	RCS041_9_5	Monzonite	NA	NA	A3	Patches	<0.1	<0.2	12.1	17.6	<0.1	17.2	<0.1	<0.1	<0.1	<0.1	9.6	<0.2	40.4	96.9
RCS041	RCS041_9_6	Monzonite	NA	NA	A3	Patches	0.3	<0.2	12.5	17.7	<0.1	16.6	0.1	<0.1	<0.1	<0.1	9.1	<0.2	40.7	96.9
RCS041	RCS041_9_7	Monzonite	NA	NA	A3	Patches	<0.1	<0.2	14.4	17.6	<0.1	16.8	<0.1	<0.1	<0.1	0.1	5.8	<0.2	41.3	96.0
RCS041	RCS041_11_8	Monzonite	NA	NA	A3	Replacement	<0.1	<0.2	12.9	17.4	<0.1	17.1	<0.1	<0.1	<0.1	<0.1	8.8	<0.2	40.7	96.9
RCS041	RCS041_11_9	Monzonite	NA	NA	A3	Replacement	<0.1	<0.2	13.5	17.5	<0.1	16.7	0.1	<0.1	<0.1	0.2	7.5	<0.2	41.0	96.4
RCS041	RCS041_11_10	Monzonite	NA	NA	A3	Replacement	<0.1	<0.2	13.3	17.6	<0.1	17.1	<0.1	<0.1	<0.1	<0.1	7.2	<0.2	40.7	95.9
RCS041	RCS041_11_11	Monzonite	NA	NA	A3	Replacement	<0.1	<0.2	12.9	17.3	<0.1	17.0	<0.1	<0.1	<0.1	<0.1	8.6	<0.2	40.4	96.1

Sample	Reference	Lithology	Structure	Type	Alt	Texture	Na_pct	Mg_pct	Al_pct	Si_pct	K_pct	Ca_pct	Ti_pct	V_pct	Cr_pct	Mn_pct	Fe_pct	Co_pct	O_pct	Total_pct
RCS041	RCS041_11_12	Monzonite	NA	NA	A3	Replacement	<0.1	<0.2	12.3	17.5	<0.1	17.2	<0.1	0.1	<0.1	<0.1	9.6	<0.2	40.6	97.4
RCS041	RCS041_12_4	Monzonite	NA	NA	A3	Replacement	<0.1	<0.2	12.9	17.6	<0.1	16.9	<0.1	0.1	<0.1	0.2	8.5	<0.2	40.9	97.1
RCS041	RCS041_12_13	Monzonite	NA	NA	A3	Replacement	<0.1	<0.2	11.1	17.2	<0.1	16.6	<0.1	<0.1	<0.1	<0.1	11.1	<0.2	39.3	95.3
RCS041	RCS041_14_15	Monzonite	NA	NA	A3	Replacement	<0.1	<0.2	12.9	17.6	<0.1	17.0	<0.1	<0.1	<0.1	<0.1	8.6	<0.2	40.9	97.1
RCS041	RCS041_14_16	Monzonite	NA	NA	A3	Replacement	<0.1	<0.2	12.8	17.6	<0.1	17.1	0.1	<0.1	<0.1	<0.1	8.2	<0.2	40.7	96.5
RCS041	RCS041_14_17	Monzonite	NA	NA	A3	Replacement	<0.1	<0.2	11.4	17.7	<0.1	17.1	0.3	<0.1	<0.1	<0.1	10.8	<0.2	40.5	97.8
RCS041	RCS041_14_18	Monzonite	NA	NA	A3	Replacement	<0.1	<0.2	12.7	17.9	<0.1	17.2	<0.1	<0.1	<0.1	<0.1	8.9	<0.2	41.3	98.0
RCS041	RCS041_14_19	Monzonite	NA	NA	A3	Replacement	<0.1	<0.2	11.3	17.6	<0.1	17.2	0.3	0.3	<0.1	0.1	10.6	<0.2	40.4	97.7
RCS041	RCS041_14_20	Monzonite	NA	NA	A3	Replacement	<0.1	<0.2	11.4	17.4	<0.1	16.9	0.2	0.2	<0.1	<0.1	11.0	<0.2	40.2	97.2
RCS041	RCS041_14_21	Monzonite	NA	NA	A3	Replacement	<0.1	<0.2	13.1	17.9	<0.1	17.2	<0.1	<0.1	<0.1	<0.1	8.0	<0.2	41.4	97.6
RCS041	RCS041_15_3	Monzonite	NA	NA	A3	Replacement	<0.1	<0.2	11.2	17.5	<0.1	16.7	<0.1	<0.1	<0.1	<0.1	10.9	<0.2	39.8	96.0
RCS041	RCS041_15_4	Monzonite	NA	NA	A3	Replacement	<0.1	<0.2	11.0	17.1	<0.1	16.8	0.1	<0.1	<0.1	<0.1	11.4	<0.2	39.4	95.9
RCS041	RCS041_15_5	Monzonite	NA	NA	A3	Replacement	<0.1	<0.2	12.3	17.6	<0.1	16.3	<0.1	<0.1	<0.1	0.2	9.5	<0.2	40.5	96.4
RCS041	RCS041_17_10	Monzonite	NA	NA	A3	Replacement	<0.1	<0.2	12.3	17.1	<0.1	16.1	<0.1	<0.1	<0.1	0.4	9.7	<0.2	39.8	95.3
RCS041	RCS041_19_13	Monzonite	NA	NA	A3	Replacement	<0.1	<0.2	11.8	17.5	<0.1	17.0	0.1	0.2	<0.1	<0.1	9.9	<0.2	40.3	96.7
RCS041	RCS041_19_15	Monzonite	NA	NA	A3	Replacement	<0.1	<0.2	13.1	17.5	<0.1	17.0	<0.1	<0.1	<0.1	0.3	8.1	<0.2	40.8	96.8
RCS041	RCS041_19_16	Monzonite	NA	NA	A3	Replacement	0.1	<0.2	12.9	17.6	<0.1	16.6	<0.1	<0.1	<0.1	0.3	8.7	<0.2	40.8	97.0
RCS041	RCS041_19_18	Monzonite	NA	NA	A3	Replacement	<0.1	<0.2	12.9	17.4	<0.1	17.0	<0.1	0.1	<0.1	0.1	8.8	<0.2	40.7	97.0
RCS041	RCS041_19_19	Monzonite	NA	NA	A3	Replacement	<0.1	<0.2	13.8	17.8	<0.1	17.1	0.1	<0.1	<0.1	<0.1	6.9	<0.2	41.4	97.1
RCS041	RCS041_19_21	Monzonite	NA	NA	A3	Replacement	<0.1	<0.2	12.7	17.6	<0.1	17.2	<0.1	<0.1	<0.1	<0.1	9.1	0.2	40.9	97.7
RCS051	RCS051_4_5	Monzonite	012E 86	Fracture vein	A3	VH	<0.1	<0.2	12.5	17.7	<0.1	17.2	<0.1	<0.1	<0.1	<0.1	9.8	<0.2	41.0	98.2
RCS051	RCS051_4_6	Monzonite	012E 86	Fracture vein	A3	VH	<0.1	<0.2	12.5	17.8	<0.1	17.0	0.1	<0.1	<0.1	0.2	9.3	<0.2	41.0	98.0
RCS051	RCS051_4_7	Monzonite	012E 86	Fracture vein	A3	VH	<0.1	<0.2	12.4	17.7	<0.1	16.8	0.2	<0.1	<0.1	0.3	9.5	<0.2	40.8	97.6
RCS051	RCS051_4_9	Monzonite	012E 86	Fracture vein	A3	VH	<0.1	<0.2	12.9	17.6	<0.1	16.7	<0.1	<0.1	0.1	0.2	8.7	<0.2	40.9	97.1
RCS051	RCS051_6_4	Monzonite	012E 86	Fracture vein	A3	VH	<0.1	<0.2	12.3	17.4	<0.1	16.8	<0.1	<0.1	<0.1	<0.1	9.8	<0.2	40.2	96.6
RCS051	RCS051_6_8	Monzonite	012E 86	Fracture vein	A3	VH	<0.1	<0.2	11.6	17.4	<0.1	16.8	<0.1	<0.1	<0.1	<0.1	10.4	<0.2	39.9	96.0
RCS051	RCS051_6_12	Monzonite	012E 86	Fracture vein	A3	VH	0.2	<0.2	12.1	17.7	<0.1	16.9	<0.1	0.2	0.1	0.2	10.1	<0.2	41.0	98.4
RCS051	RCS051_6_13	Monzonite	012E 86	Fracture vein	A3	VH	<0.1	<0.2	11.5	17.5	<0.1	16.7	<0.1	<0.1	0.1	<0.1	11.0	<0.2	40.2	97.1
RCS051	RCS051_6_14	Monzonite	012E 86	Fracture vein	A3	VH	<0.1	<0.2	12.7	17.7	<0.1	16.4	<0.1	<0.1	<0.1	0.4	9.8	<0.2	41.1	98.1
RCS051	RCS051_6_15	Monzonite	012E 86	Fracture vein	A3	VH	<0.1	<0.2	12.7	17.7	<0.1	16.8	<0.1	<0.1	<0.1	<0.1	9.4	<0.2	40.9	97.4
RCS051	RCS051_6_16	Monzonite	012E 86	Fracture vein	A3	VH	<0.1	<0.2	11.8	17.5	<0.1	16.6	<0.1	<0.1	<0.1	<0.1	10.5	<0.2	40.1	96.5
RCS051	RCS051_6_22	Monzonite	012E 86	Fracture vein	A3	VH	<0.1	<0.2	12.8	17.9	<0.1	17.1	0.2	0.1	<0.1	<0.1	9.0	<0.2	41.4	98.5
RCS051	RCS051_6_23	Monzonite	012E 86	Fracture vein	A3	VH	<0.1	<0.2	13.0	17.8	<0.1	17.4	<0.1	<0.1	<0.1	0.1	8.7	<0.2	41.3	98.3
RCS051	RCS051_7_3	Monzonite	012E 86	Fracture vein	A3	VH	<0.1	<0.2	11.7	17.5	<0.1	17.2	0.2	<0.1	<0.1	0.2	10.4	<0.2	40.5	97.6
RCS051	RCS051_7_4	Monzonite	012E 86	Fracture vein	A3	VH	<0.1	<0.2	13.2	17.8	<0.1	17.1	0.1	<0.1	<0.1	<0.1	8.3	<0.2	41.3	97.8

Sample	Reference	Lithology	Structure	Type	Alt	Texture	Na_pct	Mg_pct	Al_pct	Si_pct	K_pct	Ca_pct	Ti_pct	V_pct	Cr_pct	Mn_pct	Fe_pct	Co_pct	O_pct	Total_pct
RCS051	RCS051_7_5	Monzonite	012E 86	Fracture vein	A3	VH	<0.1	<0.2	12.3	17.6	<0.1	17.1	0.2	0.1	<0.1	0.2	10.1	<0.2	40.9	98.3
RCS051	RCS051_7_6	Monzonite	012E 86	Fracture vein	A3	VH	0.1	<0.2	12.8	17.8	<0.1	17.2	<0.1	0.1	0.1	<0.1	8.8	<0.2	41.3	98.3
RCS051	RCS051_7_8	Monzonite	012E 86	Fracture vein	A3	VH	<0.1	<0.2	12.3	17.7	<0.1	17.1	<0.1	<0.1	<0.1	<0.1	9.9	<0.2	40.9	98.0
RCS051	RCS051_7_9	Monzonite	012E 86	Fracture vein	A3	VH	<0.1	<0.2	12.8	18.0	<0.1	17.3	<0.1	<0.1	<0.1	<0.1	9.7	<0.2	41.6	99.3
RCS051	RCS051_7_10	Monzonite	012E 86	Fracture vein	A3	VH	<0.1	<0.2	12.0	17.3	<0.1	16.5	0.2	0.1	0.1	0.2	10.0	0.3	40.2	96.8
RCS051	RCS051_7_11	Monzonite	012E 86	Fracture vein	A3	VH	<0.1	<0.2	11.7	17.6	<0.1	16.8	0.1	<0.1	0.1	<0.1	10.0	<0.2	40.1	96.3
RCS051	RCS051_9_10	Monzonite	012E 86	Fracture vein	A3	VH	<0.1	<0.2	13.2	17.7	<0.1	16.7	0.1	<0.1	<0.1	0.5	7.9	<0.2	41.1	97.2
RCS051	RCS051_9_12	Monzonite	012E 86	Fracture vein	A3	VH	<0.1	<0.2	12.4	18.2	<0.1	17.0	<0.1	<0.1	<0.1	<0.1	8.8	<0.2	41.2	97.5
RCS051	RCS051_9_15	Monzonite	012E 86	Fracture vein	A3	VH	<0.1	<0.2	12.0	17.6	<0.1	17.3	0.1	<0.1	<0.1	<0.1	10.2	<0.2	40.8	98.0
RCS051	RCS051_9_16	Monzonite	012E 86	Fracture vein	A3	VH	<0.1	<0.2	11.8	17.3	<0.1	16.7	<0.1	0.1	<0.1	0.1	10.8	<0.2	40.1	96.9
RCS051	RCS051_11_11	Monzonite	012E 86	Fracture vein	A3	VH	<0.1	0.9	10.8	18.2	<0.1	15.9	<0.1	<0.1	<0.1	0.1	10.5	<0.2	40.3	96.7
RCS051	RCS051_11_12	Monzonite	012E 86	Fracture vein	A3	VH	<0.1	<0.2	12.1	17.5	<0.1	16.7	<0.1	<0.1	<0.1	<0.1	10.9	<0.2	40.6	97.7
RCS051	RCS051_11_13	Monzonite	012E 86	Fracture vein	A3	VH	<0.1	<0.2	12.4	17.8	<0.1	16.8	<0.1	0.1	<0.1	0.1	9.8	<0.2	41.0	98.0
RCS051	RCS051_11_14	Monzonite	012E 86	Fracture vein	A3	VH	<0.1	0.2	12.4	18.0	<0.1	17.0	0.1	<0.1	<0.1	0.2	9.6	<0.2	41.4	98.9
RCS051	RCS051_11_15	Monzonite	012E 86	Fracture vein	A3	VH	<0.1	<0.2	12.5	17.8	<0.1	17.2	0.1	<0.1	<0.1	<0.1	9.9	<0.2	41.0	98.5
RCS051	RCS051_13_7	Monzonite	012E 86	Fracture vein	V2	Vein	0.1	<0.2	11.5	16.8	<0.1	16.4	<0.1	<0.1	<0.1	0.1	10.3	<0.2	39.0	94.2
RCS051	RCS051_13_8	Monzonite	012E 86	Fracture vein	V2	Vein	<0.1	<0.2	12.5	18.1	<0.1	17.3	0.1	<0.1	<0.1	0.2	10.1	<0.2	41.5	99.7
RCS051	RCS051_13_9	Monzonite	012E 86	Fracture vein	V2	Vein	<0.1	<0.2	12.6	17.3	<0.1	16.5	<0.1	<0.1	<0.1	0.2	8.1	<0.2	40.0	94.7
RCS051	RCS051_13_10	Monzonite	012E 86	Fracture vein	V2	Vein	<0.1	<0.2	12.8	17.8	<0.1	16.8	0.1	<0.1	<0.1	0.1	8.6	<0.2	40.9	97.1
RCS051	RCS051_13_11	Monzonite	012E 86	Fracture vein	V2	Vein	0.3	<0.2	12.6	17.4	<0.1	16.6	<0.1	<0.1	<0.1	0.2	8.6	<0.2	40.4	96.2
RCS051	RCS051_13_12	Monzonite	012E 86	Fracture vein	V2	Vein	<0.1	<0.2	12.1	17.4	<0.1	16.8	<0.1	<0.1	<0.1	0.1	10.1	<0.2	40.3	96.7
RCS051	RCS051_13_13	Monzonite	012E 86	Fracture vein	V2	Vein	0.1	<0.2	11.5	17.2	<0.1	16.6	<0.1	0.1	<0.1	<0.1	10.9	<0.2	39.7	96.1
RCS051	RCS051_13_14	Monzonite	012E 86	Fracture vein	V2	Vein	<0.1	<0.2	11.8	17.5	<0.1	17.2	0.2	<0.1	<0.1	<0.1	10.1	<0.2	40.2	96.9
RCS051	RCS051_14_5	Monzonite	012E 86	Fracture vein	V2	Vein	<0.1	<0.2	12.7	17.6	<0.1	16.8	<0.1	<0.1	<0.1	<0.1	8.6	<0.2	40.6	96.3
RCS051	RCS051_14_7	Monzonite	012E 86	Fracture vein	V2	Vein	<0.1	<0.2	11.3	17.4	<0.1	16.7	0.2	<0.1	<0.1	<0.1	11.4	<0.2	39.9	96.8
RCS051	RCS051_14_9	Monzonite	012E 86	Fracture vein	V2	Vein	<0.1	<0.2	12.9	17.6	<0.1	17.4	<0.1	<0.1	<0.1	0.1	8.8	<0.2	41.2	97.9
RCS051	RCS051_16_15	Monzonite	012E 86	Fracture vein	V2	VH	0.3	<0.2	13.1	18.2	<0.1	16.8	<0.1	<0.1	<0.1	<0.1	8.9	<0.2	42.0	99.3
RCS051	RCS051_16_16	Monzonite	012E 86	Fracture vein	V2	VH	<0.1	<0.2	13.4	17.9	<0.1	17.3	<0.1	<0.1	<0.1	<0.1	8.3	<0.2	41.6	98.4
RCS051	RCS051_17_2	Monzonite	012E 86	Fracture vein	V2	VH	<0.1	0.3	12.0	17.8	<0.1	16.8	<0.1	<0.1	<0.1	<0.1	9.7	<0.2	40.6	97.1
RCS051	RCS051_17_3	Monzonite	012E 86	Fracture vein	V2	VH	<0.1	<0.2	11.0	17.4	<0.1	17.0	0.2	<0.1	0.1	<0.1	11.3	<0.2	39.9	96.8
RCS051	RCS051_19_11	Monzonite	012E 86	Fracture vein	V2	Vein	<0.1	<0.2	12.8	17.4	<0.1	16.8	<0.1	0.1	<0.1	0.1	8.8	<0.2	40.5	96.6
RCS051	RCS051_19_13	Monzonite	012E 86	Fracture vein	V2	Vein	<0.1	<0.2	13.0	17.7	<0.1	16.9	<0.1	<0.1	<0.1	0.3	8.6	<0.2	41.2	97.7
RCS051	RCS051_21_4	Monzonite	012E 86	Fracture vein	V2	Vein	<0.1	<0.2	11.9	17.4	<0.1	17.2	0.1	<0.1	<0.1	<0.1	10.0	<0.2	40.4	97.0
RCS051	RCS051_21_10	Monzonite	012E 86	Fracture vein	V2	Vein	<0.1	<0.2	10.6	16.5	<0.1	16.5	0.2	0.1	<0.1	<0.1	10.8	<0.2	38.3	93.0
RCS052	RCS052_2_5	Monzonite	219NW80	Fracture vein	A3	VH	0.1	<0.2	12.8	17.6	<0.1	17.2	<0.1	<0.1	<0.1	0.2	9.1	<0.2	41.0	97.8

Sample	Reference	Lithology	Structure	Type	Alt	Texture	Na_pct	Mg_pct	Al_pct	Si_pct	K_pct	Ca_pct	Ti_pct	V_pct	Cr_pct	Mn_pct	Fe_pct	Co_pct	O_pct	Total_pct
RCS052	RCS052_4_7	Monzonite	219NW80	Fracture vein	A3	Patches	<0.1	<0.2	11.4	17.3	<0.1	17.0	<0.1	<0.1	0.1	<0.1	11.3	<0.2	39.9	97.1
RCS052	RCS052_6_3	Monzonite	219NW80	Fracture vein	A3	Replacement	<0.1	<0.2	11.8	17.2	<0.1	16.8	<0.1	0.1	<0.1	0.2	10.6	<0.2	39.8	96.4
RCS052	RCS052_6_19	Monzonite	219NW80	Fracture vein	A3	Replacement	<0.1	<0.2	11.5	17.2	<0.1	16.9	0.1	0.1	<0.1	<0.1	11.2	<0.2	40.2	97.3
RCS052	RCS052_6_20	Monzonite	219NW80	Fracture vein	A3	Replacement	<0.1	<0.2	10.8	17.1	<0.1	16.9	0.2	<0.1	<0.1	<0.1	11.4	<0.2	39.2	95.6
RCS052	RCS052_8_2	Monzonite	219NW80	Fracture vein	V2	Vein	<0.1	<0.2	12.7	17.7	<0.1	16.8	<0.1	<0.1	<0.1	0.2	9.2	<0.2	40.8	97.3
RCS052	RCS052_8_5	Monzonite	219NW80	Fracture vein	V2	Vein	<0.1	<0.2	13.4	17.7	<0.1	17.2	0.1	0.1	<0.1	<0.1	7.5	<0.2	41.3	97.2
RCS052	RCS052_8_7	Monzonite	219NW80	Fracture vein	V2	Vein	<0.1	<0.2	12.6	17.7	<0.1	17.4	<0.1	<0.1	<0.1	<0.1	9.0	<0.2	40.9	97.7
RCS052	RCS052_8_8	Monzonite	219NW80	Fracture vein	V2	Vein	<0.1	<0.2	13.6	17.9	<0.1	17.2	<0.1	<0.1	<0.1	<0.1	7.5	<0.2	41.6	97.8
RCS052	RCS052_8_9	Monzonite	219NW80	Fracture vein	V2	Vein	<0.1	0.2	12.4	18.1	<0.1	15.8	<0.1	<0.1	<0.1	0.2	8.7	<0.2	40.7	96.1
RCS052	RCS052_8_10	Monzonite	219NW80	Fracture vein	V2	Vein	<0.1	<0.2	12.7	17.8	<0.1	17.1	<0.1	<0.1	0.1	<0.1	9.6	<0.2	41.2	98.5
RCS052	RCS052_8_11	Monzonite	219NW80	Fracture vein	V2	Vein	<0.1	<0.2	13.5	17.9	<0.1	17.5	<0.1	<0.1	<0.1	0.1	8.2	<0.2	41.8	99.0
RCS052	RCS052_8_13	Monzonite	219NW80	Fracture vein	V2	Vein	<0.1	<0.2	9.8	17.4	<0.1	17.1	0.1	<0.1	<0.1	<0.1	14.2	<0.2	39.6	98.2
RCS052	RCS052_8_16	Monzonite	219NW80	Fracture vein	V2	Vein	<0.1	<0.2	11.8	17.6	<0.1	17.0	<0.1	<0.1	<0.1	<0.1	10.5	<0.2	40.4	97.3
RCS052	RCS052_9_10	Monzonite	219NW80	Fracture vein	V2	Vein	<0.1	<0.2	12.4	17.8	<0.1	16.7	<0.1	<0.1	<0.1	0.1	9.6	<0.2	40.8	97.4
RCS052	RCS052_9_12	Monzonite	219NW80	Fracture vein	V2	Vein	<0.1	<0.2	10.4	17.5	<0.1	17.0	0.1	0.2	<0.1	0.1	12.5	<0.2	39.9	97.7
RCS052	RCS052_9_13	Monzonite	219NW80	Fracture vein	V2	Vein	<0.1	<0.2	12.4	17.6	<0.1	17.3	<0.1	<0.1	<0.1	<0.1	9.9	<0.2	40.8	97.9
RCS052	RCS052_9_15	Monzonite	219NW80	Fracture vein	V2	Vein	<0.1	<0.2	10.7	17.4	<0.1	17.0	0.3	<0.1	<0.1	0.1	12.0	<0.2	39.8	97.1
RCS052	RCS052_9_16	Monzonite	219NW80	Fracture vein	V2	Vein	<0.1	<0.2	10.8	17.5	<0.1	17.1	0.3	0.1	<0.1	<0.1	12.1	<0.2	40.2	98.2
RCS052	RCS052_9_18	Monzonite	219NW80	Fracture vein	V2	Vein	<0.1	<0.2	13.0	17.9	<0.1	17.1	0.1	<0.1	0.2	<0.1	8.8	<0.2	41.4	98.5
RCS052	RCS052_9_21	Monzonite	219NW80	Fracture vein	V2	Vein	<0.1	<0.2	12.9	17.6	<0.1	17.2	<0.1	0.1	<0.1	<0.1	8.8	<0.2	41.0	97.6
RCS052	RCS052_9_23	Monzonite	219NW80	Fracture vein	V2	Vein	<0.1	<0.2	11.2	17.5	<0.1	16.9	<0.1	<0.1	<0.1	<0.1	11.0	<0.2	39.9	96.5
RCS052	RCS052_11_10	Monzonite	219NW80	Fracture vein	V2	Vein	<0.1	<0.2	13.4	17.9	<0.1	17.4	0.1	<0.1	0.1	<0.1	7.5	<0.2	41.6	98.0
RCS052	RCS052_11_12	Monzonite	219NW80	Fracture vein	V2	Vein	<0.1	<0.2	10.9	17.3	<0.1	16.5	<0.1	<0.1	<0.1	0.1	12.1	<0.2	39.6	96.6
RCS052	RCS052_11_14	Monzonite	219NW80	Fracture vein	V2	Vein	<0.1	<0.2	10.4	17.4	<0.1	16.6	<0.1	0.1	<0.1	<0.1	12.3	<0.2	39.5	96.3
RCS052	RCS052_11_16	Monzonite	219NW80	Fracture vein	V2	Vein	<0.1	<0.2	11.9	17.5	<0.1	16.9	<0.1	<0.1	<0.1	<0.1	10.4	<0.2	40.3	97.0
RCS052	RCS052_12_12	Monzonite	219NW80	Fracture vein	V2	Vein	<0.1	<0.2	12.4	17.7	<0.1	17.1	<0.1	<0.1	<0.1	<0.1	10.1	<0.2	40.9	98.2
RCS052	RCS052_14_2	Monzonite	219NW80	Fracture vein	V2	Vein	<0.1	<0.2	11.8	17.6	<0.1	17.0	<0.1	<0.1	<0.1	<0.1	11.0	<0.2	40.6	98.1
RCS052	RCS052_14_4	Monzonite	219NW80	Fracture vein	V2	Vein	<0.1	<0.2	11.3	17.2	<0.1	16.7	<0.1	<0.1	<0.1	<0.1	11.2	<0.2	39.5	95.9
RCS052	RCS052_16_2	Monzonite	219NW80	Fracture vein	A3	Replacement	<0.1	<0.2	12.9	17.7	<0.1	17.3	<0.1	<0.1	<0.1	<0.1	8.9	<0.2	41.1	97.8
RCS052	RCS052_16_6	Monzonite	219NW80	Fracture vein	A3	Replacement	<0.1	<0.2	12.0	17.2	<0.1	17.1	<0.1	<0.1	<0.1	0.2	9.9	<0.2	40.1	96.5
RCS052	RCS052_16_7	Monzonite	219NW80	Fracture vein	A3	Replacement	<0.1	<0.2	12.4	17.1	<0.1	17.1	<0.1	<0.1	<0.1	<0.1	10.0	<0.2	40.3	96.8
RCS052	RCS052_16_9	Monzonite	219NW80	Fracture vein	A3	Replacement	<0.1	<0.2	11.6	17.2	<0.1	16.7	<0.1	<0.1	<0.1	0.2	10.7	<0.2	39.8	96.2
RCS052	RCS052_16_11	Monzonite	219NW80	Fracture vein	A3	Replacement	<0.1	<0.2	13.4	17.0	<0.1	16.8	<0.1	<0.1	<0.1	<0.1	7.8	<0.2	40.5	95.4
RCS052	RCS052_16_12	Monzonite	219NW80	Fracture vein	A3	Replacement	<0.1	<0.2	11.6	17.2	<0.1	17.0	<0.1	<0.1	<0.1	<0.1	10.2	<0.2	39.7	95.6
RCS052	RCS052_19_24	Monzonite	219NW80	Fracture vein	A3	Replacement	<0.1	<0.2	12.5	18.0	<0.1	16.9	0.1	0.1	<0.1	0.2	9.8	<0.2	41.5	99.2

Sample	Reference	Lithology	Structure	Type	Alt	Texture	Na_pct	Mg_pct	Al_pct	Si_pct	K_pct	Ca_pct	Ti_pct	V_pct	Cr_pct	Mn_pct	Fe_pct	Co_pct	O_pct	Total_pct
RCS052	RCS052_20_1	Monzonite	219NW80	Fracture vein	A3	Replacement	<0.1	<0.2	12.0	17.8	<0.1	16.7	<0.1	<0.1	<0.1	0.3	10.0	<0.2	40.6	97.2
RCS052	RCS052_22_11	Monzonite	219NW80	Fracture vein	V2	Vein	<0.1	<0.2	11.6	17.4	<0.1	16.7	0.1	<0.1	<0.1	0.1	10.5	<0.2	40.1	96.7
RCS052	RCS052_22_14	Monzonite	219NW80	Fracture vein	V2	Vein	<0.1	0.3	11.9	18.0	<0.1	16.6	0.2	<0.1	<0.1	0.2	10.4	<0.2	41.0	98.4
RCS052	RCS052_24_2	Monzonite	219NW80	Fracture vein	A3	Replacement	<0.1	<0.2	11.5	17.5	<0.1	17.2	<0.1	<0.1	<0.1	<0.1	11.0	<0.2	40.3	97.5
RCS052	RCS052_24_3	Monzonite	219NW80	Fracture vein	A3	Replacement	<0.1	<0.2	12.6	17.7	<0.1	17.3	<0.1	<0.1	<0.1	0.2	9.5	0.2	41.1	98.6
RCS052	RCS052_25_8	Monzonite	219NW80	Fracture vein	A3	Replacement	<0.1	<0.2	12.4	17.5	<0.1	17.1	<0.1	<0.1	<0.1	0.1	9.7	<0.2	40.6	97.4
RCS052	RCS052_25_9	Monzonite	219NW80	Fracture vein	A3	Replacement	<0.1	<0.2	12.8	17.5	<0.1	17.4	<0.1	<0.1	<0.1	<0.1	8.9	<0.2	40.8	97.4
RCS070	RCS070_2_3	Andesite	NA	NA	A4	Patches	<0.1	<0.2	11.2	17.3	<0.1	17.0	<0.1	<0.1	<0.1	0.2	11.8	<0.2	39.9	97.4
RCS070	RCS070_6_1	Andesite	NA	NA	A4	Patches	<0.1	<0.2	11.9	17.7	<0.1	17.0	<0.1	<0.1	<0.1	0.2	10.5	<0.2	40.8	98.1
RCS070	RCS070_6_2	Andesite	NA	NA	A4	Patches	<0.1	<0.2	11.4	17.5	<0.1	17.5	<0.1	<0.1	<0.1	<0.1	12.1	<0.2	40.5	99.0
RCS070	RCS070_6_3	Andesite	NA	NA	A4	Patches	0.2	<0.2	11.5	18.0	<0.1	16.7	<0.1	<0.1	<0.1	0.2	11.7	<0.2	41.1	99.5
RCS070	RCS070_6_5	Andesite	NA	NA	A4	Patches	0.1	<0.2	11.1	17.7	<0.1	16.9	<0.1	<0.1	<0.1	0.2	12.9	<0.2	40.6	99.5
RCS070	RCS070_6_6	Andesite	NA	NA	A4	Patches	<0.1	<0.2	11.5	17.5	<0.1	16.7	<0.1	<0.1	<0.1	0.6	12.4	<0.2	40.4	99.0
RCS070	RCS070_7_1	Andesite	NA	NA	V7	Vein	<0.1	<0.2	11.8	17.6	<0.1	17.0	<0.1	<0.1	<0.1	0.3	11.0	<0.2	40.5	98.1
RCS070	RCS070_7_2	Andesite	NA	NA	V7	Vein	<0.1	<0.2	10.7	17.7	<0.1	17.1	<0.1	<0.1	<0.1	0.1	12.9	<0.2	40.3	98.7
RCS070	RCS070_7_3	Andesite	NA	NA	V7	Vein	<0.1	<0.2	12.5	17.8	<0.1	17.4	<0.1	<0.1	<0.1	0.2	9.6	<0.2	41.1	98.6
RCS070	RCS070_7_4	Andesite	NA	NA	V7	Vein	<0.1	<0.2	11.2	17.6	<0.1	16.9	<0.1	<0.1	<0.1	0.1	12.1	<0.2	40.4	98.3
RCS070	RCS070_7_5	Andesite	NA	NA	V7	Vein	<0.1	<0.2	12.1	18.1	<0.1	17.0	<0.1	<0.1	<0.1	0.6	10.5	<0.2	41.4	99.6
RCS070	RCS070_7_6	Andesite	NA	NA	V7	Vein	<0.1	<0.2	10.7	17.4	<0.1	17.0	<0.1	<0.1	<0.1	0.5	13.0	<0.2	40.1	98.7
RCS070	RCS070_9_4	Andesite	NA	NA	V7	Vein	<0.1	<0.2	10.7	17.3	<0.1	16.9	<0.1	<0.1	<0.1	0.1	12.0	<0.2	39.5	96.5
RCS070	RCS070_9_5	Andesite	NA	NA	V7	Vein	0.2	<0.2	13.0	17.5	<0.1	16.6	<0.1	<0.1	<0.1	0.9	8.9	<0.2	41.1	98.2
RCS070	RCS070_9_6	Andesite	NA	NA	V7	Vein	<0.1	<0.2	9.9	17.5	<0.1	16.8	<0.1	<0.1	<0.1	0.3	13.9	0.2	39.7	98.4
RCS070	RCS070_10_1	Andesite	NA	NA	V7	Vein	<0.1	<0.2	11.1	17.8	<0.1	17.3	<0.1	<0.1	<0.1	<0.1	11.9	0.2	40.4	98.8
RCS070	RCS070_10_2	Andesite	NA	NA	V7	Vein	<0.1	<0.2	11.6	17.5	<0.1	17.2	<0.1	<0.1	<0.1	0.2	11.3	<0.2	40.5	98.3
RCS070	RCS070_10_3	Andesite	NA	NA	V7	Vein	<0.1	0.3	10.7	17.9	<0.1	16.9	<0.1	<0.1	<0.1	0.3	12.3	<0.2	40.5	98.9
RCS070	RCS070_10_4	Andesite	NA	NA	V7	Vein	0.1	<0.2	10.8	17.9	<0.1	17.0	<0.1	<0.1	<0.1	<0.1	12.1	<0.2	40.3	98.2
RCS070	RCS070_10_5	Andesite	NA	NA	V7	Vein	<0.1	<0.2	9.9	17.5	<0.1	16.7	<0.1	<0.1	<0.1	0.1	13.8	<0.2	39.5	97.5
RCS070	RCS070_12_13	Andesite	NA	NA	A4	Patches	<0.1	<0.2	12.6	17.8	<0.1	16.6	0.1	<0.1	<0.1	0.8	9.7	<0.2	41.3	98.9
RCS070	RCS070_15_18	Andesite	NA	NA	A4	Patches	<0.1	<0.2	11.0	17.6	<0.1	17.2	<0.1	<0.1	<0.1	0.2	11.9	<0.2	40.2	98.1
RCS070	RCS070_15_19	Andesite	NA	NA	A4	Patches	<0.1	<0.2	10.8	17.5	<0.1	16.9	<0.1	<0.1	<0.1	0.2	12.9	<0.2	40.0	98.3
RCS070	RCS070_15_21	Andesite	NA	NA	A4	Patches	<0.1	<0.2	11.8	17.6	<0.1	17.2	<0.1	<0.1	<0.1	0.1	10.4	<0.2	40.6	97.7
RCS070	RCS070_15_26	Andesite	NA	NA	A4	Patches	<0.1	<0.2	12.1	17.7	<0.1	16.8	<0.1	<0.1	<0.1	0.7	10.5	<0.2	40.9	98.6
RCS070	RCS070_16_3	Andesite	NA	NA	A4	Patches	<0.1	<0.2	11.9	17.3	<0.1	16.4	<0.1	<0.1	<0.1	0.4	10.4	<0.2	40.0	96.3
RCS070	RCS070_16_6	Andesite	NA	NA	A4	Patches	<0.1	<0.2	11.9	17.6	<0.1	16.9	0.1	<0.1	<0.1	0.6	11.2	<0.2	40.9	99.1
RCS070	RCS070_18_1	Andesite	NA	NA	V7	Vein	0.1	<0.2	11.8	17.6	<0.1	17.2	<0.1	<0.1	<0.1	0.3	11.1	<0.2	40.7	98.7

Sample	Reference	Lithology	Structure	Type	Alt	Texture	Na_pct	Mg_pct	Al_pct	Si_pct	K_pct	Ca_pct	Ti_pct	V_pct	Cr_pct	Mn_pct	Fe_pct	Co_pct	O_pct	Total_pct
RCS070	RCS070_18_7	Andesite	NA	NA	V7	Vein	0.1	<0.2	9.5	17.3	<0.1	17.0	<0.1	<0.1	<0.1	<0.1	14.6	<0.2	39.2	97.8
RCS070	RCS070_19_2	Andesite	NA	NA	V7	Vein	<0.1	<0.2	11.4	17.6	<0.1	16.7	<0.1	<0.1	<0.1	0.9	11.9	<0.2	40.5	98.9
RCS070	RCS070_19_4	Andesite	NA	NA	V7	Vein	<0.1	<0.2	12.4	17.8	<0.1	16.7	<0.1	<0.1	<0.1	0.4	9.4	<0.2	40.8	97.5
RCS070	RCS070_19_6	Andesite	NA	NA	V7	Vein	<0.1	<0.2	10.8	17.6	<0.1	17.0	<0.1	<0.1	<0.1	<0.1	12.6	<0.2	40.1	98.1
RCS070	RCS070_19_8	Andesite	NA	NA	V7	Vein	0.1	<0.2	10.6	17.5	<0.1	16.8	<0.1	<0.1	<0.1	0.2	12.5	<0.2	39.8	97.4
RCS070	RCS070_21_1	Andesite	NA	NA	A4	Patches	<0.1	<0.2	9.4	17.4	<0.1	17.1	0.3	0.1	<0.1	<0.1	14.6	<0.2	39.5	98.3
RCS074	RCS074_6_3	\	042SE78	Fracture vein	V6	Vein	<0.1	<0.2	13.1	18.1	<0.1	17.6	<0.1	<0.1	<0.1	<0.1	8.5	<0.2	41.8	99.1
RCS074	RCS074_6_4	\	042SE78	Fracture vein	V6	Vein	<0.1	<0.2	12.5	18.0	<0.1	17.4	<0.1	<0.1	<0.1	0.1	9.8	<0.2	41.4	99.2
RCS074	RCS074_6_5	\	042SE78	Fracture vein	V6	Vein	0.3	<0.2	12.6	18.1	<0.1	17.0	<0.1	<0.1	<0.1	0.1	9.3	<0.2	41.4	98.8
RCS074	RCS074_6_6	\	042SE78	Fracture vein	V6	Vein	<0.1	<0.2	13.5	17.9	<0.1	17.7	<0.1	<0.1	<0.1	<0.1	7.4	<0.2	41.7	98.2
RCS074	RCS074_6_7	\	042SE78	Fracture vein	V6	Vein	<0.1	<0.2	13.2	18.0	<0.1	17.5	<0.1	0.1	<0.1	0.1	8.6	<0.2	41.7	99.3
RCS074	RCS074_6_9	\	042SE78	Fracture vein	V6	Vein	<0.1	<0.2	12.8	18.0	<0.1	17.3	<0.1	<0.1	0.1	0.2	9.8	<0.2	41.6	99.7
RCS074	RCS074_6_11	\	042SE78	Fracture vein	V6	Vein	<0.1	<0.2	13.0	17.9	<0.1	17.5	<0.1	<0.1	<0.1	<0.1	9.1	<0.2	41.7	99.1
RCS074	RCS074_6_12	\	042SE78	Fracture vein	V6	Vein	<0.1	<0.2	13.7	17.9	<0.1	17.6	<0.1	<0.1	<0.1	<0.1	8.1	<0.2	41.9	99.1
RCS074	RCS074_6_13	\	042SE78	Fracture vein	V6	Vein	<0.1	<0.2	13.3	17.4	<0.1	17.3	<0.1	<0.1	<0.1	<0.1	8.6	<0.2	41.1	97.8
RCS074	RCS074_6_14	\	042SE78	Fracture vein	V6	Vein	<0.1	<0.2	14.0	17.9	<0.1	17.5	<0.1	<0.1	<0.1	0.1	7.1	<0.2	41.9	98.4
RCS074	RCS074_7_6	\	042SE78	Fracture vein	V6	Vein	<0.1	<0.2	12.6	17.8	<0.1	17.2	<0.1	0.1	<0.1	<0.1	9.6	<0.2	41.2	98.6
RCS074	RCS074_7_8	\	042SE78	Fracture vein	V6	Vein	<0.1	<0.2	13.1	18.0	<0.1	17.3	<0.1	<0.1	<0.1	0.4	9.1	<0.2	41.8	99.8
RCS074	RCS074_7_11	\	042SE78	Fracture vein	V6	Vein	<0.1	<0.2	12.8	18.0	<0.1	17.3	<0.1	<0.1	<0.1	0.2	9.2	<0.2	41.6	99.0
RCS074	RCS074_7_12	\	042SE78	Fracture vein	V6	Vein	<0.1	<0.2	12.6	17.6	<0.1	17.2	<0.1	<0.1	<0.1	0.1	8.9	<0.2	40.8	97.1
RCS074	RCS074_10_9	\	042SE78	Fracture vein	V6	Vein	<0.1	<0.2	12.2	18.0	<0.1	17.3	<0.1	<0.1	<0.1	<0.1	10.1	<0.2	41.1	98.7
RCS074	RCS074_10_12	\	042SE78	Fracture vein	V6	Vein	<0.1	<0.2	13.4	18.0	<0.1	16.9	<0.1	<0.1	<0.1	0.4	8.4	<0.2	41.6	98.7
RCS074	RCS074_12_9	\	042SE78	Fracture vein	V6	Vein	<0.1	<0.2	14.0	17.9	<0.1	17.5	<0.1	<0.1	0.1	0.1	7.4	<0.2	42.1	99.1
RCS074	RCS074_15_6	\	042SE78	Fracture vein	V6	Vein	<0.1	<0.2	13.8	18.1	<0.1	17.7	<0.1	<0.1	<0.1	<0.1	7.9	<0.2	42.3	99.7
RCS074	RCS074_15_9	\	042SE78	Fracture vein	V6	Vein	<0.1	<0.2	13.8	17.9	<0.1	17.1	<0.1	<0.1	<0.1	0.3	7.7	<0.2	41.7	98.4
RCS074	RCS074_18_4	\	042SE78	Fracture vein	V6	VH	<0.1	<0.2	13.0	18.0	<0.1	16.8	<0.1	0.1	<0.1	0.4	9.6	<0.2	41.7	99.6
RCS074	RCS074_20_5	\	042SE78	Fracture vein	A3	Replacement	<0.1	<0.2	13.6	18.1	<0.1	17.6	<0.1	<0.1	<0.1	<0.1	7.7	<0.2	42.0	99.0
RCS074	RCS074_20_6	\	042SE78	Fracture vein	A3	Replacement	<0.1	<0.2	13.6	17.8	<0.1	17.6	<0.1	<0.1	<0.1	<0.1	7.9	<0.2	41.7	98.6
RCS074	RCS074_20_8	\	042SE78	Fracture vein	A3	Replacement	<0.1	<0.2	12.3	17.8	<0.1	17.4	<0.1	<0.1	<0.1	0.1	10.1	<0.2	41.2	98.9
RCS074	RCS074_20_9	\	042SE78	Fracture vein	A3	Replacement	<0.1	<0.2	12.9	17.9	<0.1	17.4	<0.1	0.1	<0.1	<0.1	9.4	<0.2	41.7	99.4
RCS074	RCS074_24_1	\	042SE78	Fracture vein	A3	Replacement	<0.1	<0.2	12.1	17.8	<0.1	17.6	0.2	0.1	<0.1	<0.1	10.8	<0.2	41.2	99.7
RCS074	RCS074_24_4	\	042SE78	Fracture vein	A3	Replacement	<0.1	<0.2	14.0	17.8	<0.1	17.1	<0.1	<0.1	<0.1	0.2	7.2	<0.2	41.6	97.8
RCS074	RCS074_24_11	\	042SE78	Fracture vein	A3	Replacement	<0.1	<0.2	12.0	17.7	<0.1	17.1	0.2	0.1	<0.1	<0.1	10.8	<0.2	40.9	98.7
RCS074	RCS074_24_12	\	042SE78	Fracture vein	A3	Replacement	<0.1	<0.2	12.0	17.9	<0.1	17.2	0.2	<0.1	0.1	<0.1	10.1	<0.2	41.0	98.4
RCS074	RCS074_25_2	\	042SE78	Fracture vein	A3	Replacement	<0.1	<0.2	11.8	17.5	<0.1	17.3	<0.1	<0.1	<0.1	<0.1	10.5	<0.2	40.4	97.5

Sample	Reference	Lithology	Structure	Type	Alt	Texture	Na_pct	Mg_pct	Al_pct	Si_pct	K_pct	Ca_pct	Ti_pct	V_pct	Cr_pct	Mn_pct	Fe_pct	Co_pct	O_pct	Total_pct
RCS074	RCS074_25_3	\	042SE78	Fracture vein	A3	Replacement	<0.1	<0.2	11.8	17.7	<0.1	17.2	<0.1	<0.1	0.1	<0.1	10.9	<0.2	40.7	98.3
RCS074	RCS074_25_6	\	042SE78	Fracture vein	A3	Replacement	0.1	<0.2	12.5	17.6	<0.1	17.4	<0.1	<0.1	<0.1	<0.1	10.0	<0.2	41.1	98.7
RCS074	RCS074_25_7	\	042SE78	Fracture vein	A3	Replacement	<0.1	<0.2	12.4	17.8	<0.1	17.2	<0.1	<0.1	<0.1	0.2	10.0	<0.2	41.1	98.6
RCS076	RCS076_2_6	Monzonite	NA	NA	A3	Replacement	<0.1	<0.2	12.3	17.7	<0.1	17.0	<0.1	<0.1	<0.1	0.1	10.3	<0.2	41.1	98.5
RCS076	RCS076_2_8	Monzonite	NA	NA	A3	Replacement	<0.1	<0.2	12.9	18.1	<0.1	17.3	<0.1	<0.1	<0.1	0.1	9.1	<0.2	41.8	99.3
RCS076	RCS076_10_15	Monzonite	NA	NA	A3	Replacement	<0.1	<0.2	12.7	17.8	<0.1	17.3	<0.1	<0.1	<0.1	<0.1	9.0	<0.2	41.1	97.9
RCS076	RCS076_12_1	Monzonite	NA	NA	A3	Replacement	<0.1	<0.2	12.4	17.4	<0.1	16.7	<0.1	<0.1	<0.1	0.3	9.3	<0.2	40.3	96.5
RCS076	RCS076_12_3	Monzonite	NA	NA	A3	Replacement	<0.1	<0.2	13.5	17.6	<0.1	17.1	<0.1	<0.1	<0.1	<0.1	8.0	<0.2	41.2	97.5
RCS076	RCS076_12_4	Monzonite	NA	NA	A3	Replacement	<0.1	<0.2	11.9	17.5	<0.1	17.0	<0.1	<0.1	<0.1	<0.1	10.4	<0.2	40.5	97.2
RCS076	RCS076_12_5	Monzonite	NA	NA	A3	Replacement	<0.1	<0.2	12.6	17.8	<0.1	17.3	<0.1	<0.1	<0.1	0.2	9.7	<0.2	41.2	98.7
RCS076	RCS076_12_6	Monzonite	NA	NA	A3	Replacement	<0.1	<0.2	13.0	17.9	<0.1	17.3	<0.1	<0.1	0.1	0.1	8.8	0.2	41.6	99.1
RCS076	RCS076_12_7	Monzonite	NA	NA	A3	Replacement	0.1	<0.2	11.0	17.4	<0.1	16.3	<0.1	<0.1	<0.1	0.1	11.7	<0.2	39.5	96.1
RCS076	RCS076_14_1	Monzonite	NA	NA	A3	Replacement	<0.1	<0.2	11.9	18.0	<0.1	17.3	<0.1	<0.1	<0.1	<0.1	11.4	<0.2	41.2	99.8
RCS076	RCS076_14_2	Monzonite	NA	NA	A3	Replacement	<0.1	<0.2	11.5	17.7	<0.1	17.2	<0.1	<0.1	<0.1	0.1	10.9	<0.2	40.6	98.1
RCS076	RCS076_14_3	Monzonite	NA	NA	A3	Replacement	0.1	<0.2	11.4	17.6	<0.1	17.3	<0.1	<0.1	<0.1	<0.1	11.5	<0.2	40.6	98.5
RCS076	RCS076_14_4	Monzonite	NA	NA	A3	Replacement	<0.1	<0.2	11.8	17.8	<0.1	17.2	<0.1	<0.1	<0.1	<0.1	11.3	<0.2	40.9	99.0
RCS076	RCS076_14_5	Monzonite	NA	NA	A3	Replacement	<0.1	<0.2	11.7	17.8	<0.1	17.4	<0.1	<0.1	<0.1	0.1	10.9	<0.2	40.7	98.4
RCS076	RCS076_14_6	Monzonite	NA	NA	A3	Replacement	<0.1	<0.2	12.6	17.7	<0.1	17.3	0.1	<0.1	<0.1	<0.1	9.0	<0.2	41.0	97.8
RCS076	RCS076_14_7	Monzonite	NA	NA	A3	Replacement	<0.1	<0.2	11.9	17.5	<0.1	17.1	<0.1	<0.1	<0.1	<0.1	10.9	<0.2	40.6	98.0
RCS076	RCS076_14_8	Monzonite	NA	NA	A3	Replacement	<0.1	<0.2	12.6	17.7	<0.1	17.4	0.1	<0.1	<0.1	0.1	9.3	<0.2	41.0	98.3
RCS076	RCS076_14_9	Monzonite	NA	NA	A3	Replacement	<0.1	<0.2	11.7	17.5	<0.1	16.9	0.1	<0.1	<0.1	0.2	10.7	<0.2	40.3	97.4
RCS076	RCS076_14_10	Monzonite	NA	NA	A3	Replacement	<0.1	<0.2	13.1	17.5	<0.1	17.1	<0.1	<0.1	<0.1	<0.1	8.6	<0.2	40.9	97.2
RCS076	RCS076_14_12	Monzonite	NA	NA	A3	Replacement	<0.1	<0.2	11.8	17.4	<0.1	16.9	<0.1	<0.1	<0.1	<0.1	10.5	<0.2	40.2	96.8
RCS076	RCS076_14_13	Monzonite	NA	NA	A3	Replacement	0.2	<0.2	12.1	17.8	<0.1	17.2	<0.1	<0.1	<0.1	<0.1	10.3	<0.2	41.0	98.5
RCS076	RCS076_16_1	Monzonite	NA	NA	A3	Replacement	<0.1	<0.2	11.3	18.0	<0.1	17.3	<0.1	<0.1	<0.1	<0.1	10.8	<0.2	40.7	98.1
RCS076	RCS076_16_2	Monzonite	NA	NA	A3	Replacement	<0.1	<0.2	10.5	17.3	<0.1	17.2	<0.1	0.1	<0.1	<0.1	12.5	<0.2	39.7	97.2
RCS076	RCS076_18_1	Monzonite	NA	NA	A3	Replacement	<0.1	<0.2	12.0	17.5	<0.1	16.9	<0.1	<0.1	<0.1	0.3	11.0	<0.2	40.7	98.4
RCS076	RCS076_18_3	Monzonite	NA	NA	A3	Replacement	<0.1	<0.2	11.9	17.7	<0.1	17.1	<0.1	<0.1	<0.1	0.2	9.9	<0.2	40.6	97.5
RCS076	RCS076_18_4	Monzonite	NA	NA	A3	Replacement	<0.1	<0.2	12.2	18.0	<0.1	16.9	<0.1	<0.1	<0.1	<0.1	9.4	<0.2	41.0	97.4
RCS076	RCS076_18_5	Monzonite	NA	NA	A3	Replacement	<0.1	<0.2	12.1	17.8	<0.1	17.2	0.2	<0.1	<0.1	0.1	10.1	<0.2	41.1	98.4
RCS076	RCS076_18_6	Monzonite	NA	NA	A3	Replacement	<0.1	<0.2	13.4	17.9	<0.1	17.6	<0.1	<0.1	<0.1	0.2	8.5	<0.2	41.8	99.3
RCS076	RCS076_18_7	Monzonite	NA	NA	A3	Replacement	<0.1	<0.2	13.3	17.9	<0.1	17.3	<0.1	<0.1	<0.1	<0.1	8.7	<0.2	41.6	98.7
RCS047	RCS047_6_7	Diorite	067SW61	Fracture vein	A3	Replacement	<0.1	0.9	11.0	17.9	<0.1	16.0	0.1	0.1	<0.1	<0.1	9.5	<0.2	40.1	95.6
RCS047	RCS047_6_8	Diorite	067SW61	Fracture vein	A3	Replacement	<0.1	0.3	11.3	17.4	<0.1	16.1	<0.1	<0.1	<0.1	0.1	10.1	<0.2	39.6	95.0
RCS047	RCS047_7_3	Diorite	067SW61	Fracture vein	A3	Replacement	0.1	<0.2	12.6	17.2	<0.1	16.9	<0.1	<0.1	0.1	<0.1	8.5	<0.2	40.2	95.7

Sample	Reference	Lithology	Structure	Type	Alt	Texture	Na_pct	Mg_pct	Al_pct	Si_pct	K_pct	Ca_pct	Ti_pct	V_pct	Cr_pct	Mn_pct	Fe_pct	Co_pct	O_pct	Total_pct
RCS047	RCS047_9_2	Diorite	067SW61	Fracture vein	A3	Replacement	<0.1	<0.2	11.7	17.6	<0.1	17.2	0.1	<0.1	<0.1	<0.1	10.2	<0.2	40.4	97.2
RCS047	RCS047_9_3	Diorite	067SW61	Fracture vein	A3	Replacement	<0.1	<0.2	12.2	17.5	<0.1	16.9	<0.1	<0.1	<0.1	<0.1	9.7	<0.2	40.3	96.6
RCS047	RCS047_9_5	Diorite	067SW61	Fracture vein	A3	Replacement	0.3	<0.2	13.1	17.5	<0.1	16.7	<0.1	<0.1	<0.1	0.3	8.6	<0.2	40.9	97.1
RCS047	RCS047_9_6	Diorite	067SW61	Fracture vein	A3	Replacement	<0.1	<0.2	11.8	17.5	<0.1	16.9	<0.1	<0.1	<0.1	0.1	10.0	<0.2	40.1	96.5
RCS047	RCS047_9_7	Diorite	067SW61	Fracture vein	A3	Replacement	<0.1	<0.2	11.1	17.3	<0.1	16.5	<0.1	<0.1	<0.1	<0.1	10.7	<0.2	39.4	95.0
RCS047	RCS047_9_9	Diorite	067SW61	Fracture vein	A3	Replacement	<0.1	<0.2	11.8	17.3	<0.1	16.8	<0.1	<0.1	<0.1	<0.1	9.5	<0.2	39.7	95.1
RCS047	RCS047_12_9	Diorite	067SW61	Fracture vein	A3	Replacement	<0.1	<0.2	11.5	17.0	<0.1	16.6	0.1	<0.1	<0.1	0.2	10.5	<0.2	39.3	95.1
RCS047	RCS047_14_3	Diorite	067SW61	Fracture vein	V2	Vein	<0.1	<0.2	12.6	17.4	<0.1	16.9	<0.1	0.1	<0.1	0.1	8.5	<0.2	40.4	95.9
RCS047	RCS047_14_4	Diorite	067SW61	Fracture vein	V2	Vein	<0.1	<0.2	11.2	17.3	<0.1	16.6	<0.1	<0.1	<0.1	0.1	11.2	<0.2	39.6	96.0
RCS047	RCS047_14_6	Diorite	067SW61	Fracture vein	V2	Vein	<0.1	<0.2	12.2	17.2	<0.1	16.8	<0.1	<0.1	<0.1	0.2	9.1	<0.2	39.9	95.5
RCS047	RCS047_14_10	Diorite	067SW61	Fracture vein	V2	Vein	<0.1	<0.2	10.6	17.3	<0.1	16.7	0.2	<0.1	<0.1	<0.1	11.7	<0.2	39.4	95.8
RCS047	RCS047_14_12	Diorite	067SW61	Fracture vein	V2	Vein	<0.1	<0.2	11.2	17.4	<0.1	16.9	0.2	0.2	<0.1	<0.1	10.9	<0.2	39.9	96.4
RCS047	RCS047_15_7	Diorite	067SW61	Fracture vein	V2	Vein	<0.1	<0.2	13.2	17.6	<0.1	16.9	0.1	<0.1	<0.1	0.4	8.2	<0.2	41.1	97.5
RCS047	RCS047_15_10	Diorite	067SW61	Fracture vein	V2	Vein	<0.1	<0.2	11.7	17.5	<0.1	17.0	<0.1	<0.1	<0.1	<0.1	10.6	<0.2	40.3	97.2
RCS047	RCS047_15_13	Diorite	067SW61	Fracture vein	V2	Vein	0.1	<0.2	11.9	17.5	<0.1	17.0	<0.1	0.1	<0.1	0.1	10.4	<0.2	40.5	97.6
RCS047	RCS047_15_15	Diorite	067SW61	Fracture vein	V2	Vein	<0.1	<0.2	13.0	17.4	<0.1	16.8	<0.1	<0.1	<0.1	0.2	9.0	<0.2	40.8	97.2
RCS047	RCS047_15_16	Diorite	067SW61	Fracture vein	V2	Vein	<0.1	<0.2	11.7	17.4	<0.1	17.0	<0.1	<0.1	<0.1	<0.1	10.2	<0.2	40.1	96.4
RCS047	RCS047_17_9	Diorite	067SW61	Fracture vein	V2	Vein	<0.1	<0.2	10.7	16.7	<0.1	16.5	0.3	<0.1	<0.1	0.2	11.4	<0.2	38.7	94.5
RCS047	RCS047_17_11	Diorite	067SW61	Fracture vein	V2	Vein	<0.1	<0.2	11.9	17.6	<0.1	16.8	0.1	<0.1	<0.1	<0.1	10.6	<0.2	40.5	97.5
RCS047	RCS047_17_12	Diorite	067SW61	Fracture vein	V2	Vein	<0.1	<0.2	11.5	17.1	<0.1	16.5	<0.1	<0.1	<0.1	<0.1	10.3	<0.2	39.3	94.6
RCS047	RCS047_17_14	Diorite	067SW61	Fracture vein	V2	Vein	<0.1	<0.2	12.0	17.5	<0.1	17.1	<0.1	<0.1	<0.1	<0.1	10.2	<0.2	40.6	97.4
RCS047	RCS047_17_18	Diorite	067SW61	Fracture vein	V2	Vein	<0.1	<0.2	12.2	17.5	<0.1	16.6	<0.1	<0.1	<0.1	0.2	9.3	<0.2	40.1	95.9
RCS047	RCS047_17_19	Diorite	067SW61	Fracture vein	V2	Vein	<0.1	<0.2	11.7	17.0	<0.1	16.7	<0.1	<0.1	<0.1	0.1	10.4	<0.2	39.4	95.1
RCS047	RCS047_18_6	Diorite	067SW61	Fracture vein	V2	Vein	<0.1	<0.2	12.0	17.2	<0.1	16.6	0.1	<0.1	<0.1	0.3	9.8	<0.2	39.9	96.1
RCS047	RCS047_18_9	Diorite	067SW61	Fracture vein	V2	Vein	<0.1	<0.2	12.0	17.5	<0.1	16.8	<0.1	<0.1	<0.1	0.3	10.1	<0.2	40.3	97.1
RCS047	RCS047_18_10	Diorite	067SW61	Fracture vein	V2	Vein	<0.1	<0.2	12.2	17.4	<0.1	16.7	<0.1	0.1	<0.1	0.2	9.3	<0.2	40.1	96.0
RCS047	RCS047_20_7	Diorite	067SW61	Fracture vein	V2	Vein	<0.1	<0.2	11.6	17.4	<0.1	17.2	<0.1	<0.1	<0.1	0.1	10.7	<0.2	40.2	97.1
RCS047	RCS047_20_10	Diorite	067SW61	Fracture vein	V2	Vein	<0.1	<0.2	11.6	17.4	<0.1	16.6	<0.1	<0.1	<0.1	0.2	10.7	<0.2	39.8	96.3
RCS047	RCS047_22_3	Diorite	067SW61	Fracture vein	A3	L Patches	<0.1	<0.2	12.1	17.5	<0.1	17.2	<0.1	<0.1	<0.1	0.1	10.0	<0.2	40.5	97.4
RCS047	RCS047_22_5	Diorite	067SW61	Fracture vein	A3	L Patches	<0.1	<0.2	11.8	17.4	<0.1	17.3	<0.1	<0.1	<0.1	0.2	10.2	<0.2	40.3	97.3
RCS047	RCS047_22_6	Diorite	067SW61	Fracture vein	A3	L Patches	<0.1	<0.2	11.8	17.7	<0.1	17.1	<0.1	<0.1	<0.1	<0.1	10.3	<0.2	40.4	97.3
RCS047	RCS047_22_8	Diorite	067SW61	Fracture vein	A3	L Patches	<0.1	<0.2	11.9	17.3	<0.1	16.7	<0.1	<0.1	<0.1	<0.1	9.9	<0.2	39.8	95.6
RCS047	RCS047_22_10	Diorite	067SW61	Fracture vein	A3	L Patches	<0.1	<0.2	12.2	16.9	<0.1	16.7	<0.1	<0.1	<0.1	0.2	9.1	<0.2	39.4	94.5
RCS047	RCS047_24_9	Diorite	067SW61	Fracture vein	A3	L Patches	<0.1	<0.2	12.3	17.5	<0.1	16.7	0.2	<0.1	<0.1	0.2	9.3	<0.2	40.4	96.5
RCS047	RCS047_24_11	Diorite	067SW61	Fracture vein	A3	L Patches	<0.1	<0.2	10.2	16.9	<0.1	16.7	0.2	<0.1	<0.1	<0.1	12.5	<0.2	38.7	95.2

Sample	Reference	Lithology	Structure	Type	Alt	Texture	Na_pct	Mg_pct	Al_pct	Si_pct	K_pct	Ca_pct	Ti_pct	V_pct	Cr_pct	Mn_pct	Fe_pct	Co_pct	O_pct	Total_pct
RCS047	RCS047_24_14	Diorite	067SW61	Fracture vein	A3	L Patches	0.1	0.3	12.3	17.7	<0.1	16.9	0.2	<0.1	<0.1	0.1	8.3	<0.2	40.7	96.6
RCS047	RCS047_24_15	Diorite	067SW61	Fracture vein	A3	L Patches	0.1	<0.2	11.7	17.4	<0.1	16.6	<0.1	<0.1	<0.1	0.2	10.4	<0.2	40.0	96.3
RCS047	RCS047_25_2	Diorite	067SW61	Fracture vein	A3	L Patches	<0.1	<0.2	12.3	17.6	<0.1	17.0	<0.1	<0.1	<0.1	0.1	9.4	<0.2	40.4	96.8
RCS047	RCS047_29_4	Diorite	067SW61	Fracture vein	A3	L Patches	<0.1	<0.2	11.2	16.7	<0.1	15.9	<0.1	<0.1	<0.1	0.1	10.5	<0.2	38.3	92.7
RCS064	RCS064_6_6	Rhyolite	NA	NA	A4	Replacement	<0.1	<0.2	12.3	17.4	<0.1	16.9	0.2	<0.1	<0.1	0.1	9.3	<0.2	40.4	96.6
RCS064	RCS064_9_9	Rhyolite	NA	NA	A4	Replacement	<0.1	<0.2	12.1	17.5	<0.1	16.4	<0.1	<0.1	<0.1	0.4	10.1	<0.2	40.4	96.9
RCS064	RCS064_9_10	Rhyolite	NA	NA	A4	Replacement	<0.1	<0.2	12.1	17.2	<0.1	16.6	<0.1	<0.1	<0.1	0.1	10.2	<0.2	40.2	96.4
RCS064	RCS064_9_11	Rhyolite	NA	NA	A4	Replacement	0.1	<0.2	11.9	17.2	<0.1	16.6	0.1	<0.1	<0.1	0.1	10.3	<0.2	40.0	96.4
RCS064	RCS064_9_12	Rhyolite	NA	NA	A4	Replacement	<0.1	<0.2	11.7	17.4	<0.1	16.8	<0.1	<0.1	<0.1	<0.1	10.5	<0.2	39.9	96.2
RCS064	RCS064_9_14	Rhyolite	NA	NA	A4	Replacement	<0.1	<0.2	11.8	17.5	<0.1	17.0	<0.1	<0.1	0.1	<0.1	10.5	<0.2	40.3	97.1
RCS064	RCS064_9_16	Rhyolite	NA	NA	A4	Replacement	<0.1	<0.2	12.9	17.6	<0.1	16.3	<0.1	<0.1	<0.1	0.7	9.2	<0.2	40.9	97.5
RCS064	RCS064_9_17	Rhyolite	NA	NA	A4	Replacement	<0.1	<0.2	12.7	17.3	<0.1	16.2	<0.1	<0.1	<0.1	0.8	9.7	<0.2	40.5	97.0
RCS064	RCS064_11_9	Rhyolite	NA	NA	A4	Replacement	<0.1	<0.2	11.9	17.4	<0.1	17.0	<0.1	<0.1	<0.1	0.2	9.8	<0.2	40.2	96.6
RCS064	RCS064_13_13	Rhyolite	NA	NA	A4	Replacement	<0.1	<0.2	10.4	17.1	0.2	16.3	0.1	<0.1	<0.1	0.1	12.9	<0.2	39.2	96.2
RCS064	RCS064_15_9	Rhyolite	NA	NA	A4	Replacement	<0.1	<0.2	12.0	17.6	<0.1	16.5	<0.1	<0.1	<0.1	0.2	10.4	<0.2	40.4	97.1
RCS064	RCS064_15_11	Rhyolite	NA	NA	A4	Replacement	0.1	<0.2	11.7	17.2	<0.1	16.6	0.1	<0.1	0.1	<0.1	10.1	<0.2	39.7	95.6
RCS064	RCS064_15_12	Rhyolite	NA	NA	A4	Replacement	<0.1	<0.2	13.0	17.4	<0.1	16.9	<0.1	<0.1	<0.1	0.2	7.9	<0.2	40.5	95.9
RCS075	RCS075_4_8	Qtz-Monzonite	NA	NA	A3	Replacement	<0.1	<0.2	13.3	17.9	<0.1	17.1	<0.1	<0.1	<0.1	0.3	7.9	<0.2	41.3	97.6
RCS075	RCS075_6_18	Qtz-Monzonite	NA	NA	A3	Replacement	<0.1	<0.2	13.0	17.8	<0.1	17.0	<0.1	<0.1	<0.1	0.3	9.2	<0.2	41.4	98.7
RCS075	RCS075_9_1	Qtz-Monzonite	NA	NA	A3	Replacement	<0.1	<0.2	12.6	17.5	<0.1	17.2	<0.1	<0.1	<0.1	0.2	9.4	<0.2	40.7	97.6
RCS075	RCS075_9_3	Qtz-Monzonite	NA	NA	A3	Replacement	<0.1	<0.2	13.8	17.9	<0.1	17.1	<0.1	<0.1	<0.1	0.4	7.6	<0.2	41.8	98.6
RCS075	RCS075_9_4	Qtz-Monzonite	NA	NA	A3	Replacement	<0.1	<0.2	12.1	17.4	<0.1	16.7	<0.1	<0.1	<0.1	0.2	10.4	<0.2	40.3	97.0
RCS075	RCS075_9_8	Qtz-Monzonite	NA	NA	A3	Replacement	0.1	<0.2	13.6	17.9	<0.1	17.2	<0.1	<0.1	<0.1	0.4	8.2	<0.2	41.8	99.1
RCS075	RCS075_9_9	Qtz-Monzonite	NA	NA	A3	Replacement	<0.1	<0.2	12.5	18.2	<0.1	17.2	<0.1	<0.1	<0.1	0.3	9.5	<0.2	41.5	99.1
RCS075	RCS075_9_10	Qtz-Monzonite	NA	NA	A3	Replacement	<0.1	<0.2	12.2	17.5	<0.1	17.0	<0.1	<0.1	<0.1	0.1	10.3	<0.2	40.6	97.7
RCS075	RCS075_9_11	Qtz-Monzonite	NA	NA	A3	Replacement	<0.1	<0.2	12.2	17.8	<0.1	17.3	<0.1	<0.1	<0.1	0.1	9.9	<0.2	40.9	98.2
RCS075	RCS075_9_12	Qtz-Monzonite	NA	NA	A3	Replacement	<0.1	<0.2	12.5	17.7	<0.1	17.1	0.1	<0.1	<0.1	0.1	10.1	<0.2	41.0	98.6
RCS075	RCS075_11_8	Qtz-Monzonite	NA	NA	A3	Replacement	<0.1	<0.2	11.5	17.7	<0.1	17.2	<0.1	<0.1	<0.1	<0.1	11.3	<0.2	40.4	98.0
RCS075	RCS075_13_2	Qtz-Monzonite	NA	NA	A3	Replacement	<0.1	<0.2	12.1	17.4	<0.1	16.4	<0.1	<0.1	<0.1	0.2	9.7	<0.2	39.9	95.7
RCS075	RCS075_15_6	Qtz-Monzonite	NA	NA	A3	Replacement	<0.1	<0.2	11.8	17.7	<0.1	16.8	<0.1	<0.1	<0.1	0.2	10.4	<0.2	40.5	97.4
RCS075	RCS075_15_7	Qtz-Monzonite	NA	NA	A3	Replacement	<0.1	<0.2	13.0	18.1	<0.1	17.4	<0.1	<0.1	<0.1	0.4	8.9	<0.2	41.9	99.8
RCS075	RCS075_16_2	Qtz-Monzonite	NA	NA	A3	Replacement	<0.1	<0.2	13.3	17.8	<0.1	17.4	<0.1	<0.1	<0.1	0.2	8.1	<0.2	41.4	98.2
RCS075	RCS075_16_3	Qtz-Monzonite	NA	NA	A3	Replacement	<0.1	<0.2	15.1	18.2	<0.1	17.7	<0.1	0.1	<0.1	0.1	4.9	<0.2	42.9	99.0
RCS075	RCS075_18_1	Qtz-Monzonite	NA	NA	A3	Replacement	<0.1	<0.2	12.4	17.8	<0.1	17.2	<0.1	<0.1	<0.1	0.2	9.5	<0.2	40.9	98.0
RCS075	RCS075_25_2	Qtz-Monzonite	NA	NA	A3	Replacement	<0.1	<0.2	13.3	18.2	<0.1	17.7	<0.1	<0.1	<0.1	<0.1	8.6	<0.2	42.1	99.9

Sample	Reference	Lithology	Structure	Type	Alt	Texture	Na_pct	Mg_pct	Al_pct	Si_pct	K_pct	Ca_pct	Ti_pct	V_pct	Cr_pct	Mn_pct	Fe_pct	Co_pct	O_pct	Total_pct
RCS075	RCS075_25_3	Qtz-Monzonite	NA	NA	A3	Replacement	0.1	<0.2	13.6	17.9	<0.1	17.4	<0.1	<0.1	<0.1	0.1	7.6	<0.2	41.7	98.5
RCS075	RCS075_25_4	Qtz-Monzonite	NA	NA	A3	Replacement	<0.1	<0.2	12.3	17.7	<0.1	17.3	<0.1	<0.1	<0.1	0.1	9.9	<0.2	40.9	98.3
RCS075	RCS075_25_5	Qtz-Monzonite	NA	NA	A3	Replacement	<0.1	<0.2	13.7	17.9	<0.1	17.1	<0.1	<0.1	<0.1	0.1	7.8	<0.2	41.8	98.5
RCS075	RCS075_25_6	Qtz-Monzonite	NA	NA	A3	Replacement	0.1	<0.2	12.3	18.0	<0.1	17.2	<0.1	<0.1	<0.1	<0.1	9.7	<0.2	41.2	98.5
RCS075	RCS075_25_7	Qtz-Monzonite	NA	NA	A3	Replacement	<0.1	<0.2	12.7	17.6	<0.1	17.2	<0.1	<0.1	<0.1	<0.1	9.2	<0.2	41.0	97.7
RCS075	RCS075_25_8	Qtz-Monzonite	NA	NA	A3	Replacement	<0.1	<0.2	13.0	17.9	<0.1	17.4	<0.1	<0.1	<0.1	0.1	8.6	<0.2	41.3	98.3
RCS075	RCS075_25_9	Qtz-Monzonite	NA	NA	A3	Replacement	<0.1	<0.2	13.6	18.2	<0.1	17.6	0.1	<0.1	<0.1	<0.1	7.9	<0.2	42.2	99.6
RCS075	RCS075_25_10	Qtz-Monzonite	NA	NA	A3	Replacement	<0.1	<0.2	12.9	18.1	<0.1	17.4	<0.1	<0.1	<0.1	0.1	8.8	<0.2	41.6	98.8
RCS078	RCS078_2_6	Vein	149SW77	Fault Zone	V6	Vein	<0.1	<0.2	13.0	18.1	<0.1	17.6	<0.1	0.1	<0.1	<0.1	8.7	<0.2	41.8	99.4
RCS078	RCS078_2_7	Vein	149SW77	Fault Zone	V6	Vein	<0.1	<0.2	12.5	17.7	<0.1	17.4	0.1	<0.1	<0.1	<0.1	9.4	<0.2	41.2	98.4
RCS078	RCS078_4_5	Vein	149SW77	Fault Zone	V6	Vein	<0.1	<0.2	13.7	18.0	<0.1	16.9	<0.1	<0.1	<0.1	0.5	8.4	<0.2	42.0	99.4
RCS078	RCS078_6_15	Vein	149SW77	Fault Zone	V6	Vein	<0.1	<0.2	12.6	18.0	<0.1	16.9	<0.1	<0.1	0.1	0.2	9.6	<0.2	41.4	98.9
RCS078	RCS078_6_16	Vein	149SW77	Fault Zone	V6	Vein	<0.1	<0.2	12.8	17.8	<0.1	17.7	<0.1	<0.1	<0.1	<0.1	9.6	<0.2	41.5	99.4
RCS078	RCS078_6_19	Vein	149SW77	Fault Zone	V6	Vein	<0.1	<0.2	12.6	18.0	<0.1	17.6	<0.1	<0.1	<0.1	<0.1	9.4	<0.2	41.5	99.1
RCS078	RCS078_6_20	Vein	149SW77	Fault Zone	V6	Vein	<0.1	<0.2	13.4	18.1	<0.1	17.5	<0.1	<0.1	<0.1	<0.1	8.3	<0.2	41.8	99.1
RCS078	RCS078_6_21	Vein	149SW77	Fault Zone	V6	Vein	<0.1	<0.2	13.0	18.1	<0.1	17.5	<0.1	<0.1	<0.1	<0.1	8.6	<0.2	41.6	98.7
RCS078	RCS078_6_22	Vein	149SW77	Fault Zone	V6	Vein	<0.1	<0.2	12.4	17.8	<0.1	16.9	<0.1	<0.1	<0.1	0.3	10.2	<0.2	41.0	98.6
RCS078	RCS078_8_6	Vein	149SW77	Fault Zone	V6	Vein	<0.1	<0.2	12.0	17.9	<0.1	17.5	<0.1	<0.1	<0.1	<0.1	10.7	<0.2	41.3	99.5
RCS078	RCS078_8_7	Vein	149SW77	Fault Zone	V6	Vein	<0.1	<0.2	12.6	17.6	<0.1	17.3	<0.1	<0.1	<0.1	0.1	10.1	<0.2	41.2	98.9
RCS078	RCS078_11_5	Vein	149SW77	Fault Zone	V6	Vein	<0.1	0.2	12.4	17.8	<0.1	16.7	<0.1	<0.1	<0.1	0.1	10.2	<0.2	41.1	98.5
RCS078	RCS078_11_6	Vein	149SW77	Fault Zone	V6	Vein	<0.1	<0.2	12.7	17.9	<0.1	17.6	<0.1	<0.1	<0.1	0.1	9.6	<0.2	41.6	99.4
RCS078	RCS078_11_8	Vein	149SW77	Fault Zone	V6	Vein	<0.1	<0.2	13.5	18.0	<0.1	17.1	<0.1	0.2	0.1	0.2	8.4	<0.2	42.0	99.5
RCS078	RCS078_11_9	Vein	149SW77	Fault Zone	V6	Vein	<0.1	0.6	10.7	16.4	<0.1	15.2	<0.1	<0.1	<0.1	0.2	9.7	<0.2	37.5	90.3
RCS078	RCS078_16_8	Vein	149SW77	Fault Zone	V6	Vein	0.1	<0.2	12.8	17.7	<0.1	16.8	<0.1	<0.1	<0.1	0.5	9.0	<0.2	40.9	97.7
RCS078	RCS078_16_9	Vein	149SW77	Fault Zone	V6	Vein	<0.1	<0.2	10.9	17.7	<0.1	17.2	0.4	<0.1	0.1	<0.1	12.2	<0.2	40.6	99.0
RCS078	RCS078_16_10	Vein	149SW77	Fault Zone	V6	Vein	<0.1	<0.2	10.9	17.6	<0.1	16.9	<0.1	<0.1	<0.1	<0.1	12.0	0.2	40.1	97.7
RCS078	RCS078_18_4	Vein	149SW77	Fault Zone	V3	Vein	<0.1	<0.2	11.7	17.4	<0.1	17.1	<0.1	<0.1	<0.1	<0.1	11.1	<0.2	40.4	97.7
RCS078	RCS078_18_5	Vein	149SW77	Fault Zone	V3	Vein	<0.1	<0.2	13.5	17.9	<0.1	17.4	<0.1	<0.1	<0.1	<0.1	7.9	<0.2	41.5	98.2
RCS078	RCS078_18_7	Vein	149SW77	Fault Zone	V3	Vein	<0.1	<0.2	12.9	17.9	<0.1	17.1	<0.1	<0.1	<0.1	0.1	9.1	<0.2	41.3	98.4
RCS078	RCS078_20_5	Vein	149SW77	Fault Zone	V6	Vein	<0.1	<0.2	11.5	16.9	<0.1	16.8	<0.1	<0.1	<0.1	<0.1	10.6	<0.2	39.2	94.9
RCS078	RCS078_20_6	Vein	149SW77	Fault Zone	V6	Vein	<0.1	<0.2	12.1	17.7	<0.1	17.4	<0.1	<0.1	<0.1	<0.1	10.7	<0.2	41.1	99.0
RCS078	RCS078_20_7	Vein	149SW77	Fault Zone	V6	Vein	<0.1	<0.2	12.9	17.6	<0.1	17.5	<0.1	<0.1	<0.1	<0.1	9.2	<0.2	41.3	98.5
RCS078	RCS078_20_8	Vein	149SW77	Fault Zone	V6	Vein	<0.1	<0.2	12.9	17.8	<0.1	17.5	0.1	<0.1	<0.1	0.1	9.2	<0.2	41.6	99.2
RCS078	RCS078_20_9	Vein	149SW77	Fault Zone	V6	Vein	<0.1	<0.2	11.6	17.7	<0.1	16.8	<0.1	<0.1	<0.1	0.2	10.7	<0.2	40.3	97.2
RCS078	RCS078_22_5	Vein	149SW77	Fault Zone	V3	Vein	<0.1	<0.2	12.6	17.8	<0.1	17.6	<0.1	<0.1	<0.1	0.2	9.7	<0.2	41.4	99.3

Sample	Reference	Lithology	Structure	Type	Alt	Texture	Na_pct	Mg_pct	Al_pct	Si_pct	K_pct	Ca_pct	Ti_pct	V_pct	Cr_pct	Mn_pct	Fe_pct	Co_pct	O_pct	Total_pct
RCS078	RCS078_22_8	Vein	149SW77	Fault Zone	V3	Vein	<0.1	<0.2	12.7	17.2	<0.1	17.3	0.2	<0.1	<0.1	0.1	9.9	<0.2	40.9	98.2
RCS078	RCS078_23_6	Vein	149SW77	Fault Zone	V3	Vein	<0.1	<0.2	12.5	17.9	<0.1	17.4	0.1	<0.1	<0.1	0.2	10.2	<0.2	41.6	99.8
RCS078	RCS078_25_5	Vein	149SW77	Fault Zone	V3	Vein	<0.1	<0.2	12.5	18.0	<0.1	17.4	<0.1	<0.1	0.1	<0.1	10.1	<0.2	41.6	99.7
RCS078	RCS078_25_8	Vein	149SW77	Fault Zone	V3	Vein	<0.1	<0.2	13.1	17.8	<0.1	17.5	<0.1	<0.1	<0.1	<0.1	9.3	<0.2	41.8	99.5
RCS078	RCS078_27_9	Vein	149SW77	Fault Zone	V6	Vein	<0.1	<0.2	12.2	17.5	<0.1	17.1	0.1	<0.1	<0.1	<0.1	9.9	<0.2	40.8	97.6
RCS078	RCS078_29_2	Vein	149SW77	Fault Zone	V6	Vein	<0.1	<0.2	12.0	17.9	<0.1	17.1	<0.1	<0.1	<0.1	0.1	10.8	<0.2	41.0	98.8
RCS078	RCS078_29_3	Vein	149SW77	Fault Zone	V6	Vein	<0.1	<0.2	12.5	17.8	<0.1	17.0	<0.1	<0.1	<0.1	0.1	9.8	<0.2	41.1	98.3
RCS079	RCS079_4_11	Qtz-Monzonite	NA	NA	A3	Replacement	<0.1	<0.2	12.4	17.8	<0.1	17.4	<0.1	<0.1	<0.1	<0.1	10.0	<0.2	41.3	98.9
RCS079	RCS079_14_8	Qtz-Monzonite	NA	NA	A3	Replacement	<0.1	<0.2	10.43	17.43	<0.1	17.05	0.3	<0.1	<0.1	<0.1	12.7	<0.2	39.9	97.81
RCS079	RCS079_14_9	Qtz-Monzonite	NA	NA	A3	Replacement	<0.1	<0.2	12.65	17.83	<0.1	17.29	<0.1	<0.1	0.14	<0.1	9.34	<0.2	41.19	98.44
RCS079	RCS079_14_15	Qtz-Monzonite	NA	NA	A3	Replacement	0.28	<0.2	11.51	17.72	<0.1	17.13	0.1	<0.1	<0.1	<0.1	10.48	<0.2	40.57	97.79
RCS079	RCS079_14_16	Qtz-Monzonite	NA	NA	A3	Replacement	<0.1	<0.2	12	17.77	<0.1	17.35	0.1	<0.1	<0.1	0.11	9.93	<0.2	40.86	98.12
RCS079	RCS079_14_17	Qtz-Monzonite	NA	NA	A3	Replacement	<0.1	<0.2	13	17.71	<0.1	17.27	<0.1	<0.1	<0.1	<0.1	8.42	<0.2	41.13	97.53
RCS079	RCS079_14_18	Qtz-Monzonite	NA	NA	A3	Replacement	<0.1	<0.2	12.4	17.5	<0.1	17.21	<0.1	<0.1	<0.1	0.15	9.49	<0.2	40.65	97.4
RCS079	RCS079_14_22	Qtz-Monzonite	NA	NA	A3	Replacement	<0.1	<0.2	10.08	17.38	<0.1	16.8	0.11	<0.1	<0.1	<0.1	13.24	<0.2	39.36	96.97
RCS079	RCS079_24_1	Qtz-Monzonite	NA	NA	A3	Replacement	<0.1	<0.2	13.4	17.85	<0.1	17.13	<0.1	<0.1	<0.1	0.18	8.12	<0.2	41.62	98.3
RCS079	RCS079_24_2	Qtz-Monzonite	NA	NA	A3	Replacement	<0.1	<0.2	12.9	18.08	<0.1	17.64	<0.1	<0.1	<0.1	<0.1	8.95	<0.2	41.73	99.3
RCS079	RCS079_24_3	Qtz-Monzonite	NA	NA	A3	Replacement	<0.1	<0.2	13.32	17.88	<0.1	17.51	<0.1	<0.1	<0.1	<0.1	8.32	<0.2	41.74	98.77
RCS079	RCS079_24_4	Qtz-Monzonite	NA	NA	A3	Replacement	<0.1	<0.2	11.95	17.81	<0.1	17.27	<0.1	<0.1	<0.1	<0.1	10.3	<0.2	40.89	98.22
RCS079	RCS079_24_6	Qtz-Monzonite	NA	NA	A3	Replacement	<0.1	0.33	11.6	18.32	<0.1	16.52	0.11	<0.1	<0.1	0.14	10.08	<0.2	41.02	98.12
RCS079	RCS079_24_10	Qtz-Monzonite	NA	NA	A3	Replacement	0.11	<0.2	13.56	17.97	<0.1	17.4	<0.1	<0.1	<0.1	0.22	8.18	<0.2	41.96	99.4
RCS081	RCS081_10_3	Rhyolite	NA	NA	A5	Replacement	<0.1	<0.2	12.03	17.68	<0.1	17.18	<0.1	<0.1	<0.1	0.17	10.88	<0.2	40.89	98.83
RCS081	RCS081_10_4	Rhyolite	NA	NA	A5	Replacement	<0.1	<0.2	13.01	17.85	<0.1	16.54	<0.1	<0.1	<0.1	0.41	8.56	<0.2	41.23	97.6
RCS081	RCS081_14_1	Rhyolite	NA	NA	A5	Replacement	<0.1	<0.2	12.26	17.67	<0.1	16.79	<0.1	<0.1	<0.1	0.45	10.16	<0.2	40.78	98.11
RCS081	RCS081_14_3	Rhyolite	NA	NA	A5	Replacement	<0.1	<0.2	12.04	18	<0.1	17.23	<0.1	<0.1	<0.1	<0.1	10.63	<0.2	41.18	99.08
RCS081	RCS081_14_4	Rhyolite	NA	NA	A5	Replacement	<0.1	<0.2	12.37	17.59	<0.1	17.08	<0.1	<0.1	<0.1	0.17	8.99	<0.2	40.56	96.76
RCS008	RCS008_2_4	Granodiorite	054SE74	Vein	A5	Replacement	<0.1	<0.2	13.4	17.1	<0.1	15.9	<0.1	<0.1	0.1	0.8	7.3	<0.2	40.2	94.8
RCS008	RCS008_2_5	Granodiorite	054SE74	Vein	A5	Replacement	<0.1	<0.2	13.5	17.5	<0.1	16.3	<0.1	<0.1	<0.1	0.7	7.1	<0.2	40.7	95.7
RCS008	RCS008_2_6	Granodiorite	054SE74	Vein	A5	Replacement	<0.1	<0.2	13.3	17.6	<0.1	16.6	<0.1	<0.1	<0.1	0.3	8.1	<0.2	40.9	96.7
RCS008	RCS008_4_5	Granodiorite	054SE74	Vein	V3	VH	<0.1	<0.2	12.2	17.5	<0.1	16.7	<0.1	<0.1	0.1	0.1	9.7	<0.2	40.2	96.5
RCS008	RCS008_4_6	Granodiorite	054SE74	Vein	V3	VH	<0.1	<0.2	14.0	17.5	<0.1	16.9	<0.1	<0.1	<0.1	0.1	6.0	<0.2	40.9	95.4
RCS008	RCS008_5_3	Granodiorite	054SE74	Vein	A5	VH	<0.1	<0.2	12.9	17.5	<0.1	16.4	<0.1	<0.1	<0.1	0.4	8.1	<0.2	40.4	95.8
RCS008	RCS008_5_5	Granodiorite	054SE74	Vein	A5	VH	<0.1	<0.2	13.9	17.8	<0.1	17.0	0.1	<0.1	<0.1	0.1	6.8	<0.2	41.4	97.1
RCS008	RCS008_5_7	Granodiorite	054SE74	Vein	A5	VH	<0.1	<0.2	12.8	17.6	<0.1	16.7	0.1	<0.1	<0.1	0.1	7.8	<0.2	40.4	95.6
RCS008	RCS008_5_8	Granodiorite	054SE74	Vein	A5	VH	<0.1	<0.2	13.0	17.5	<0.1	16.8	0.2	<0.1	<0.1	<0.1	7.9	<0.2	40.7	96.1

Sample	Reference	Lithology	Structure	Type	Alt	Texture	Na_pct	Mg_pct	Al_pct	Si_pct	K_pct	Ca_pct	Ti_pct	V_pct	Cr_pct	Mn_pct	Fe_pct	Co_pct	O_pct	Total_pct
RCS008	RCS008_7_7	Granodiorite	054SE74	Vein	A5	L Patches	<0.1	<0.2	14.3	17.8	<0.1	17.0	<0.1	<0.1	<0.1	0.1	5.7	<0.2	41.5	96.4
RCS008	RCS008_7_8	Granodiorite	054SE74	Vein	A5	L Patches	<0.1	<0.2	13.9	17.7	<0.1	16.2	<0.1	<0.1	<0.1	0.6	6.8	<0.2	41.1	96.3
RCS008	RCS008_7_10	Granodiorite	054SE74	Vein	A5	L Patches	<0.1	<0.2	13.2	17.6	<0.1	16.3	<0.1	<0.1	<0.1	0.7	7.7	<0.2	40.8	96.4
RCS008	RCS008_7_13	Granodiorite	054SE74	Vein	A5	L Patches	<0.1	<0.2	13.7	17.6	<0.1	16.8	<0.1	<0.1	<0.1	0.4	6.9	<0.2	41.1	96.5
RCS008	RCS008_7_15	Granodiorite	054SE74	Vein	A5	L Patches	<0.1	<0.2	13.5	17.7	<0.1	17.0	<0.1	<0.1	<0.1	<0.1	7.5	<0.2	41.1	96.7
RCS008	RCS008_7_17	Granodiorite	054SE74	Vein	A5	L Patches	<0.1	<0.2	13.4	17.7	<0.1	16.7	<0.1	<0.1	<0.1	0.2	7.6	<0.2	40.9	96.5
RCS008	RCS008_7_18	Granodiorite	054SE74	Vein	A5	L Patches	<0.1	<0.2	13.2	17.8	<0.1	16.9	<0.1	<0.1	<0.1	0.3	8.0	<0.2	41.2	97.4
RCS008	RCS008_7_20	Granodiorite	054SE74	Vein	A5	L Patches	<0.1	<0.2	13.2	17.1	<0.1	16.7	<0.1	<0.1	<0.1	0.2	7.7	<0.2	40.2	95.1
RCS008	RCS008_9_4	Granodiorite	054SE74	Vein	A5	Replacement	<0.1	<0.2	12.9	17.3	<0.1	16.5	<0.1	<0.1	<0.1	0.1	8.0	<0.2	40.1	94.9
RCS008	RCS008_9_8	Granodiorite	054SE74	Vein	A5	Replacement	<0.1	<0.2	13.1	17.8	<0.1	16.9	<0.1	<0.1	0.1	<0.1	8.2	<0.2	41.0	97.0
RCS008	RCS008_9_10	Granodiorite	054SE74	Vein	A5	Replacement	<0.1	<0.2	13.0	17.6	<0.1	16.7	0.1	<0.1	0.1	0.2	8.3	<0.2	40.8	96.7
RCS008	RCS008_9_12	Granodiorite	054SE74	Vein	A5	Replacement	<0.1	<0.2	13.2	17.8	<0.1	17.0	<0.1	<0.1	0.1	0.2	7.9	<0.2	41.3	97.4
RCS008	RCS008_11_4	Granodiorite	054SE74	Vein	A5	Replacement	<0.1	<0.2	13.5	18.0	<0.1	16.4	<0.1	<0.1	<0.1	0.6	7.8	<0.2	41.6	98.0
RCS008	RCS008_13_1	Granodiorite	054SE74	Vein	V3	Vein	<0.1	<0.2	13.0	17.5	<0.1	17.1	<0.1	<0.1	0.2	<0.1	8.5	<0.2	40.8	97.1
RCS008	RCS008_13_3	Granodiorite	054SE74	Vein	V3	Vein	<0.1	<0.2	12.6	17.4	<0.1	17.0	0.2	<0.1	0.1	<0.1	8.4	<0.2	40.5	96.2
RCS008	RCS008_13_4	Granodiorite	054SE74	Vein	V3	Vein	<0.1	<0.2	13.0	17.2	<0.1	16.0	<0.1	<0.1	<0.1	0.7	7.9	<0.2	40.1	94.9
RCS008	RCS008_13_6	Granodiorite	054SE74	Vein	V3	Vein	<0.1	<0.2	13.5	17.6	<0.1	16.1	<0.1	<0.1	<0.1	0.9	7.5	<0.2	40.9	96.4
RCS008	RCS008_13_9	Granodiorite	054SE74	Vein	V3	Vein	<0.1	<0.2	13.6	17.7	<0.1	16.4	<0.1	<0.1	0.1	0.8	7.2	<0.2	41.1	96.9
RCS008	RCS008_13_11	Granodiorite	054SE74	Vein	V3	Vein	<0.1	<0.2	14.2	17.7	<0.1	16.9	<0.1	<0.1	<0.1	0.2	6.1	<0.2	41.4	96.5
RCS008	RCS008_15_5	Granodiorite	054SE74	Vein	V3	Vein	<0.1	<0.2	13.2	17.7	<0.1	16.4	<0.1	<0.1	0.1	0.7	8.0	<0.2	41.0	97.1
RCS008	RCS008_15_6	Granodiorite	054SE74	Vein	V3	Vein	<0.1	<0.2	14.4	17.9	<0.1	17.0	<0.1	<0.1	<0.1	0.2	5.9	<0.2	41.8	97.2
RCS008	RCS008_15_7	Granodiorite	054SE74	Vein	V3	Vein	<0.1	<0.2	13.3	17.6	<0.1	16.2	<0.1	<0.1	0.1	0.8	8.2	<0.2	41.0	97.1
RCS008	RCS008_15_13	Granodiorite	054SE74	Vein	V3	Vein	<0.1	<0.2	13.6	17.8	<0.1	16.9	<0.1	<0.1	<0.1	0.1	7.2	<0.2	41.3	96.9
RCS008	RCS008_15_14	Granodiorite	054SE74	Vein	V3	Vein	<0.1	<0.2	13.8	17.8	<0.1	16.8	<0.1	<0.1	0.1	0.2	7.2	<0.2	41.4	97.2
RCS008	RCS008_17_3	Granodiorite	054SE74	Vein	V3	Vein	<0.1	<0.2	11.0	17.4	<0.1	16.7	<0.1	<0.1	0.1	<0.1	11.6	0.2	39.8	96.9
RCS008	RCS008_17_6	Granodiorite	054SE74	Vein	V3	Vein	<0.1	<0.2	12.2	17.6	<0.1	16.9	<0.1	<0.1	<0.1	0.2	9.6	<0.2	40.5	96.9
RCS008	RCS008_17_8	Granodiorite	054SE74	Vein	V3	Vein	<0.1	<0.2	14.6	17.7	<0.1	16.7	<0.1	<0.1	0.1	0.5	5.4	<0.2	41.6	96.6
RCS008	RCS008_17_10	Granodiorite	054SE74	Vein	V3	Vein	<0.1	<0.2	13.3	17.5	<0.1	16.8	<0.1	<0.1	<0.1	0.2	7.3	<0.2	40.7	95.9
RCS008	RCS008_21_10	Granodiorite	054SE74	Vein	V3	Vein	<0.1	<0.2	13.6	17.6	<0.1	17.1	<0.1	<0.1	<0.1	<0.1	7.1	<0.2	41.1	96.4
RCS008	RCS008_21_11	Granodiorite	054SE74	Vein	V3	Vein	<0.1	<0.2	13.0	17.5	<0.1	16.8	<0.1	<0.1	<0.1	<0.1	7.8	<0.2	40.5	95.5
RCS038	RCS038_2_3	Monzonite	31NE87	Fault Zone	A4	Replacement	<0.1	<0.2	12.6	18.0	<0.1	17.6	0.1	<0.1	<0.1	<0.1	9.6	<0.2	41.6	99.5
RCS038	RCS038_2_7	Monzonite	31NE87	Fault Zone	A4	Replacement	<0.1	<0.2	13.5	17.8	<0.1	17.2	0.2	<0.1	0.1	0.1	8.4	<0.2	41.7	98.8
RCS038	RCS038_4_3	Monzonite	31NE87	Fault Zone	A4	Replacement	<0.1	<0.2	13.3	18.0	<0.1	17.3	<0.1	<0.1	<0.1	<0.1	8.3	<0.2	41.8	98.8
RCS038	RCS038_6_5	Monzonite	31NE87	Fault Zone	A4	Replacement	<0.1	<0.2	14.2	18.1	<0.1	16.9	<0.1	<0.1	<0.1	0.4	7.3	<0.2	42.3	99.2
RCS038	RCS038_6_8	Monzonite	31NE87	Fault Zone	A4	Replacement	<0.1	<0.2	12.7	18.0	<0.1	17.4	0.1	<0.1	0.1	<0.1	9.5	<0.2	41.7	99.5

Sample	Reference	Lithology	Structure	Type	Alt	Texture	Na_pct	Mg_pct	Al_pct	Si_pct	K_pct	Ca_pct	Ti_pct	V_pct	Cr_pct	Mn_pct	Fe_pct	Co_pct	O_pct	Total_pct
RCS038	RCS038_6_10	Monzonite	31NE87	Fault Zone	A4	Replacement	<0.1	<0.2	14.2	18.0	<0.1	17.2	<0.1	<0.1	<0.1	0.4	6.9	<0.2	42.3	99.0
RCS038	RCS038_6_11	Monzonite	31NE87	Fault Zone	A4	Replacement	<0.1	<0.2	14.7	18.2	<0.1	17.8	<0.1	<0.1	0.1	<0.1	5.7	<0.2	42.6	99.2
RCS038	RCS038_6_14	Monzonite	31NE87	Fault Zone	A4	Replacement	<0.1	<0.2	14.3	18.1	<0.1	17.1	<0.1	<0.1	0.2	0.3	7.0	<0.2	42.3	99.2
RCS038	RCS038_6_17	Monzonite	31NE87	Fault Zone	A4	Replacement	<0.1	<0.2	12.4	16.9	<0.1	16.7	<0.1	<0.1	<0.1	<0.1	8.2	<0.2	39.4	93.6
RCS038	RCS038_6_18	Monzonite	31NE87	Fault Zone	A4	Replacement	<0.1	<0.2	13.9	17.9	<0.1	16.8	<0.1	<0.1	<0.1	0.5	7.6	<0.2	41.8	98.4
RCS038	RCS038_6_19	Monzonite	31NE87	Fault Zone	A4	Replacement	<0.1	<0.2	14.3	18.2	<0.1	17.7	<0.1	<0.1	<0.1	<0.1	6.3	<0.2	42.3	98.8
RCS038	RCS038_6_25	Monzonite	31NE87	Fault Zone	A4	Replacement	<0.1	<0.2	13.1	17.9	<0.1	17.5	<0.1	<0.1	<0.1	<0.1	8.4	<0.2	41.6	98.5
RCS038	RCS038_7_7	Monzonite	31NE87	Fault Zone	A4	Replacement	<0.1	<0.2	10.3	17.7	<0.1	16.9	0.2	<0.1	<0.1	<0.1	13.5	<0.2	40.1	98.7
RCS038	RCS038_7_8	Monzonite	31NE87	Fault Zone	A4	Replacement	<0.1	<0.2	14.0	18.2	<0.1	17.6	<0.1	<0.1	0.1	<0.1	7.0	<0.2	42.3	99.1
RCS038	RCS038_7_9	Monzonite	31NE87	Fault Zone	A4	Replacement	<0.1	<0.2	13.5	18.0	<0.1	17.2	<0.1	<0.1	<0.1	0.1	8.3	<0.2	41.8	99.1
RCS038	RCS038_7_10	Monzonite	31NE87	Fault Zone	A4	Replacement	<0.1	<0.2	13.7	18.1	<0.1	17.3	0.1	<0.1	<0.1	<0.1	7.6	<0.2	42.1	98.9
RCS038	RCS038_7_11	Monzonite	31NE87	Fault Zone	A4	Replacement	<0.1	<0.2	12.5	18.1	<0.1	17.5	0.1	<0.1	<0.1	<0.1	9.6	<0.2	41.6	99.5
RCS038	RCS038_9_7	Monzonite	31NE87	Fault Zone	A4	Replacement	<0.1	<0.2	13.0	17.8	<0.1	17.2	<0.1	<0.1	0.1	<0.1	8.9	<0.2	41.4	98.5
RCS038	RCS038_11_1	Monzonite	31NE87	Fault Zone	V3	Vein	<0.1	<0.2	14.2	17.9	<0.1	16.8	<0.1	<0.1	<0.1	0.5	6.9	<0.2	41.9	98.2
RCS038	RCS038_11_2	Monzonite	31NE87	Fault Zone	V3	Vein	<0.1	<0.2	13.9	18.2	<0.1	17.0	<0.1	<0.1	0.1	0.4	7.4	<0.2	42.2	99.0
RCS038	RCS038_11_4	Monzonite	31NE87	Fault Zone	V3	Vein	<0.1	<0.2	13.8	18.0	<0.1	17.4	<0.1	<0.1	<0.1	0.2	7.5	<0.2	42.0	99.0
RCS038	RCS038_11_7	Monzonite	31NE87	Fault Zone	V3	Vein	<0.1	<0.2	12.8	18.1	<0.1	17.3	<0.1	0.1	<0.1	<0.1	9.3	<0.2	41.7	99.3
RCS038	RCS038_13_18	Monzonite	31NE87	Fault Zone	A4	Replacement	<0.1	<0.2	13.0	17.7	<0.1	17.0	<0.1	<0.1	<0.1	0.2	8.3	<0.2	41.0	97.2
RCS038	RCS038_13_19	Monzonite	31NE87	Fault Zone	A4	Replacement	<0.1	<0.2	13.0	17.9	<0.1	17.4	0.1	0.1	<0.1	<0.1	8.6	<0.2	41.6	98.7
RCS038	RCS038_15_13	Monzonite	31NE87	Fault Zone	A4	Replacement	<0.1	<0.2	13.7	18.2	<0.1	17.6	<0.1	<0.1	<0.1	<0.1	7.8	<0.2	42.3	99.5
RCS038	RCS038_17_13	Monzonite	31NE87	Fault Zone	A4	Replacement	<0.1	<0.2	14.0	17.9	<0.1	17.2	<0.1	<0.1	<0.1	0.1	6.6	<0.2	41.6	97.5
RCS038	RCS038_17_14	Monzonite	31NE87	Fault Zone	A4	Replacement	<0.1	<0.2	13.1	18.0	<0.1	17.5	<0.1	<0.1	<0.1	0.1	8.8	<0.2	41.8	99.4
RCS038	RCS038_17_15	Monzonite	31NE87	Fault Zone	A4	Replacement	<0.1	<0.2	12.3	17.7	<0.1	17.2	0.1	0.1	<0.1	<0.1	10.0	<0.2	41.2	98.6
RCS038	RCS038_17_18	Monzonite	31NE87	Fault Zone	A4	Replacement	<0.1	<0.2	14.7	18.3	<0.1	17.7	<0.1	<0.1	<0.1	<0.1	6.1	<0.2	42.8	99.6
RCS040	RCS040_4_5	Monzonite	227NW66	Fracture	A4	Replacement	<0.1	<0.2	13.2	18.2	<0.1	17.6	<0.1	<0.1	<0.1	0.2	8.8	<0.2	42.1	100.1
RCS040	RCS040_4_7	Monzonite	227NW66	Fracture	A4	Replacement	0.1	<0.2	13.2	18.6	<0.1	17.8	<0.1	<0.1	<0.1	0.2	8.8	<0.2	42.6	101.2
RCS040	RCS040_4_8	Monzonite	227NW66	Fracture	A4	Replacement	<0.1	<0.2	13.9	18.5	<0.1	17.5	0.1	<0.1	<0.1	0.3	7.8	<0.2	42.8	101.0
RCS040	RCS040_4_13	Monzonite	227NW66	Fracture	A4	Replacement	<0.1	<0.2	12.0	18.3	<0.1	17.3	<0.1	0.1	<0.1	<0.1	11.1	<0.2	41.9	100.6
RCS040	RCS040_4_14	Monzonite	227NW66	Fracture	A4	Replacement	<0.1	<0.2	12.2	18.3	<0.1	17.6	<0.1	<0.1	0.1	<0.1	10.9	<0.2	42.0	101.1
RCS040	RCS040_4_15	Monzonite	227NW66	Fracture	A4	Replacement	<0.1	<0.2	13.0	18.4	<0.1	17.0	<0.1	<0.1	<0.1	0.2	9.2	<0.2	42.1	100.0
RCS040	RCS040_4_16	Monzonite	227NW66	Fracture	A4	Replacement	<0.1	<0.2	13.3	18.5	<0.1	17.7	<0.1	<0.1	<0.1	0.2	8.8	<0.2	42.5	101.0
RCS040	RCS040_5_4	Monzonite	227NW66	Fracture	A4	Replacement	<0.1	<0.2	12.7	18.4	<0.1	17.7	<0.1	<0.1	<0.1	<0.1	9.6	<0.2	42.2	100.6
RCS040	RCS040_5_13	Monzonite	227NW66	Fracture	A4	Replacement	<0.1	<0.2	11.9	18.0	<0.1	17.4	0.4	<0.1	<0.1	<0.1	10.6	<0.2	41.5	99.8
RCS040	RCS040_5_14	Monzonite	227NW66	Fracture	A4	Replacement	<0.1	<0.2	13.9	18.4	<0.1	17.7	<0.1	<0.1	<0.1	<0.1	7.9	<0.2	42.7	100.6
RCS040	RCS040_7_6	Monzonite	227NW66	Fracture	A4	Replacement	<0.1	<0.2	13.7	18.4	<0.1	17.9	<0.1	<0.1	<0.1	0.1	8.6	<0.2	43.0	101.6

Sample	Reference	Lithology	Structure	Type	Alt	Texture	Na_pct	Mg_pct	Al_pct	Si_pct	K_pct	Ca_pct	Ti_pct	V_pct	Cr_pct	Mn_pct	Fe_pct	Co_pct	O_pct	Total_pct
RCS040	RCS040_7_7	Monzonite	227NW66	Fracture	A4	Replacement	<0.1	<0.2	12.9	18.5	<0.1	17.8	0.2	<0.1	<0.1	<0.1	10.0	<0.2	42.7	102.0
RCS040	RCS040_7_8	Monzonite	227NW66	Fracture	A4	Replacement	<0.1	<0.2	11.8	18.3	<0.1	17.7	0.1	0.1	<0.1	<0.1	11.5	<0.2	41.9	101.5
RCS040	RCS040_7_11	Monzonite	227NW66	Fracture	A4	Replacement	<0.1	<0.2	13.5	18.5	<0.1	17.8	<0.1	<0.1	<0.1	0.2	8.6	<0.2	42.7	101.2
RCS040	RCS040_7_12	Monzonite	227NW66	Fracture	A4	Replacement	<0.1	<0.2	13.1	18.4	<0.1	17.9	<0.1	<0.1	0.1	<0.1	9.6	<0.2	42.6	101.8
RCS040	RCS040_7_14	Monzonite	227NW66	Fracture	A4	Replacement	<0.1	<0.2	12.6	18.4	<0.1	17.5	<0.1	<0.1	<0.1	0.1	10.5	<0.2	42.2	101.2
RCS040	RCS040_7_15	Monzonite	227NW66	Fracture	A4	Replacement	0.2	<0.2	13.5	18.5	<0.1	17.6	<0.1	<0.1	<0.1	<0.1	8.6	<0.2	42.7	101.0
RCS040	RCS040_7_16	Monzonite	227NW66	Fracture	A4	Replacement	<0.1	<0.2	12.3	18.1	<0.1	17.5	<0.1	0.1	<0.1	<0.1	10.4	<0.2	41.7	100.1
RCS040	RCS040_7_17	Monzonite	227NW66	Fracture	A4	Replacement	<0.1	<0.2	11.1	18.1	<0.1	17.3	0.2	<0.1	<0.1	<0.1	11.8	<0.2	41.0	99.5
RCS040	RCS040_7_18	Monzonite	227NW66	Fracture	A4	Replacement	<0.1	<0.2	12.8	18.2	<0.1	17.0	0.2	<0.1	<0.1	0.5	10.0	<0.2	42.1	100.7
RCS040	RCS040_8_4	Monzonite	227NW66	Fracture	A4	Replacement	<0.1	<0.2	13.0	18.2	<0.1	17.8	<0.1	<0.1	<0.1	<0.1	9.8	<0.2	42.3	101.2
RCS040	RCS040_8_5	Monzonite	227NW66	Fracture	A4	Replacement	<0.1	<0.2	13.1	18.3	<0.1	17.9	<0.1	0.1	<0.1	0.1	8.9	<0.2	42.4	100.7
RCS040	RCS040_8_6	Monzonite	227NW66	Fracture	A4	Replacement	<0.1	<0.2	13.2	18.2	<0.1	17.6	<0.1	<0.1	<0.1	0.1	9.3	<0.2	42.3	100.7
RCS040	RCS040_8_7	Monzonite	227NW66	Fracture	A4	Replacement	<0.1	<0.2	13.9	18.3	<0.1	17.6	<0.1	<0.1	<0.1	0.1	8.2	<0.2	42.6	100.7
RCS040	RCS040_8_8	Monzonite	227NW66	Fracture	A4	Replacement	<0.1	<0.2	11.8	18.2	<0.1	17.4	<0.1	<0.1	<0.1	<0.1	11.1	<0.2	41.5	100.0
RCS040	RCS040_8_9	Monzonite	227NW66	Fracture	A4	Replacement	<0.1	<0.2	13.1	18.4	<0.1	17.6	<0.1	<0.1	0.1	<0.1	9.6	<0.2	42.4	101.1
RCS040	RCS040_8_10	Monzonite	227NW66	Fracture	A4	Replacement	<0.1	<0.2	12.5	18.4	<0.1	17.8	0.2	0.1	<0.1	<0.1	10.7	<0.2	42.6	102.3
RCS040	RCS040_12_3	Monzonite	227NW66	Fracture	A4	Replacement	<0.1	<0.2	13.6	18.4	<0.1	17.6	<0.1	<0.1	0.2	0.3	8.6	<0.2	42.8	101.5
RCS040	RCS040_12_4	Monzonite	227NW66	Fracture	A4	Replacement	<0.1	<0.2	12.9	18.5	<0.1	17.9	<0.1	<0.1	0.1	<0.1	9.7	<0.2	42.6	101.7
RCS046	RCS046_4_8	Diorite	317NE55	Fracture	A3	Replacement	<0.1	<0.2	12.3	18.5	<0.1	17.6	<0.1	<0.1	<0.1	0.1	11.2	<0.2	42.3	101.9
RCS046	RCS046_5_6	Diorite	317NE55	Fracture	A3	Replacement	<0.1	<0.2	12.8	18.2	<0.1	16.9	<0.1	<0.1	<0.1	0.3	9.8	<0.2	41.8	99.7
RCS046	RCS046_7_1	Diorite	317NE55	Fracture	A3	Replacement	<0.1	<0.2	12.2	18.1	<0.1	17.3	<0.1	<0.1	<0.1	0.2	10.6	<0.2	41.7	100.1
RCS046	RCS046_7_2	Diorite	317NE55	Fracture	A3	Replacement	0.1	<0.2	12.0	18.0	<0.1	17.5	<0.1	<0.1	<0.1	<0.1	10.8	<0.2	41.5	99.9
RCS046	RCS046_7_5	Diorite	317NE55	Fracture	A3	Replacement	<0.1	<0.2	12.6	18.3	<0.1	16.9	<0.1	<0.1	<0.1	0.4	10.5	<0.2	41.9	100.6
RCS046	RCS046_16_1	Diorite	317NE55	Fracture	A3	Replacement	<0.1	<0.2	12.5	18.5	<0.1	17.8	<0.1	<0.1	<0.1	0.1	10.6	<0.2	42.4	101.8
RCS046	RCS046_16_2	Diorite	317NE55	Fracture	A3	Replacement	0.1	<0.2	13.0	18.5	<0.1	17.4	<0.1	<0.1	0.1	0.1	9.3	<0.2	42.5	101.1
RCS046	RCS046_16_3	Diorite	317NE55	Fracture	A3	Replacement	<0.1	<0.2	12.4	18.4	<0.1	17.1	<0.1	<0.1	<0.1	0.3	11.0	<0.2	42.1	101.3
RCS046	RCS046_16_4	Diorite	317NE55	Fracture	A3	Replacement	<0.1	<0.2	12.2	18.3	<0.1	17.7	<0.1	<0.1	<0.1	0.2	10.9	<0.2	42.1	101.3
RCS046	RCS046_21_2	Diorite	317NE55	Fracture	A3	Replacement	<0.1	<0.2	11.8	18.3	<0.1	17.2	<0.1	<0.1	<0.1	0.1	11.5	<0.2	41.7	100.6
RCS046	RCS046_21_4	Diorite	317NE55	Fracture	A3	Replacement	<0.1	<0.2	11.4	18.1	<0.1	17.3	0.2	<0.1	<0.1	<0.1	12.0	<0.2	41.4	100.3
RCS046	RCS046_25_1	Diorite	317NE55	Fracture	A3	Replacement	<0.1	<0.2	12.9	18.5	<0.1	17.6	<0.1	<0.1	<0.1	0.2	9.8	<0.2	42.5	101.5
RCS046	RCS046_25_3	Diorite	317NE55	Fracture	A3	Replacement	<0.1	<0.2	10.7	17.3	<0.1	15.4	<0.1	<0.1	<0.1	0.1	11.3	<0.2	38.2	93.1
RCS049	RCS049_2_9	Diorite	NA	NA	A3	Patches	<0.1	0.4	12.2	17.9	<0.1	16.1	0.2	<0.1	0.1	0.5	9.3	<0.2	41.0	97.5
RCS049	RCS049_2_10	Diorite	NA	NA	A3	Patches	<0.1	<0.2	12.1	17.5	<0.1	16.7	<0.1	<0.1	<0.1	0.1	10.3	<0.2	40.4	97.1
RCS049	RCS049_7_1	Diorite	NA	NA	A3	Patches	0.1	<0.2	12.5	17.9	<0.1	17.0	<0.1	<0.1	<0.1	0.2	9.6	<0.2	41.2	98.5
RCS049	RCS049_7_2	Diorite	NA	NA	A3	Patches	0.1	<0.2	12.9	17.8	<0.1	17.2	<0.1	<0.1	<0.1	0.1	9.1	<0.2	41.4	98.6

Sample	Reference	Lithology	Structure	Type	Alt	Texture	Na_pct	Mg_pct	Al_pct	Si_pct	K_pct	Ca_pct	Ti_pct	V_pct	Cr_pct	Mn_pct	Fe_pct	Co_pct	O_pct	Total_pct
RCS049	RCS049_7_3	Diorite	NA	NA	A3	Patches	<0.1	<0.2	12.1	17.7	<0.1	17.0	<0.1	<0.1	<0.1	<0.1	10.1	<0.2	40.8	97.6
RCS049	RCS049_10_6	Diorite	NA	NA	A3	Patches	<0.1	<0.2	11.8	17.9	<0.1	17.0	0.1	<0.1	<0.1	<0.1	10.8	<0.2	40.9	98.5
RCS049	RCS049_10_7	Diorite	NA	NA	A3	Patches	<0.1	0.3	10.5	17.6	0.1	16.3	0.1	<0.1	0.1	<0.1	12.7	<0.2	39.8	97.5
RCS049	RCS049_15_5	Diorite	NA	NA	A3	Patches	<0.1	<0.2	12.7	18.0	<0.1	17.1	<0.1	<0.1	<0.1	0.2	9.9	<0.2	41.6	99.5
RCS049	RCS049_15_6	Diorite	NA	NA	A3	Patches	<0.1	<0.2	12.1	17.6	<0.1	17.3	<0.1	<0.1	0.1	<0.1	10.3	<0.2	40.8	98.2
RCS049	RCS049_15_7	Diorite	NA	NA	A3	Patches	<0.1	<0.2	11.8	18.0	<0.1	17.1	<0.1	<0.1	0.1	0.1	11.4	0.2	41.2	99.8
RCS049	RCS049_15_8	Diorite	NA	NA	A3	Patches	0.1	<0.2	11.4	17.7	<0.1	16.6	0.2	<0.1	<0.1	<0.1	10.9	<0.2	40.3	97.3
RCS049	RCS049_17_1	Diorite	NA	NA	A3	Replacement	0.1	<0.2	12.6	18.0	<0.1	17.3	<0.1	<0.1	<0.1	0.1	10.0	<0.2	41.7	99.8
RCS049	RCS049_17_2	Diorite	NA	NA	A3	Replacement	<0.1	<0.2	12.7	18.2	<0.1	17.1	<0.1	<0.1	<0.1	0.2	9.7	<0.2	41.8	99.7
RCS049	RCS049_17_3	Diorite	NA	NA	A3	Replacement	<0.1	<0.2	12.5	18.0	<0.1	17.6	<0.1	0.1	<0.1	<0.1	9.3	<0.2	41.5	98.9
RCS049	RCS049_17_5	Diorite	NA	NA	A3	Replacement	<0.1	<0.2	12.8	18.1	<0.1	17.4	<0.1	<0.1	<0.1	<0.1	9.6	<0.2	41.7	99.5
RCS056	RCS056_8_1	Qtz-Monzonite	NA	NA	A3	Patches	<0.1	<0.2	10.9	17.5	<0.1	16.8	0.2	<0.1	<0.1	<0.1	11.7	<0.2	40.0	97.1
RCS056	RCS056_8_2	Qtz-Monzonite	NA	NA	A3	Patches	<0.1	<0.2	11.9	17.7	<0.1	17.0	<0.1	0.2	<0.1	0.3	10.5	<0.2	40.8	98.3
RCS056	RCS056_8_3	Qtz-Monzonite	NA	NA	A3	Patches	<0.1	<0.2	11.9	17.8	<0.1	16.8	<0.1	0.1	<0.1	0.2	10.1	<0.2	40.8	97.8
RCS056	RCS056_8_4	Qtz-Monzonite	NA	NA	A3	Patches	<0.1	<0.2	11.8	17.8	<0.1	17.1	<0.1	0.1	<0.1	0.2	10.3	<0.2	40.8	98.1
RCS056	RCS056_8_6	Qtz-Monzonite	NA	NA	A3	Patches	<0.1	<0.2	12.1	17.7	<0.1	17.0	<0.1	<0.1	<0.1	0.1	10.1	<0.2	40.7	97.8
RCS056	RCS056_8_7	Qtz-Monzonite	NA	NA	A3	Patches	<0.1	<0.2	12.4	17.8	<0.1	16.9	<0.1	0.1	<0.1	0.3	9.6	<0.2	41.0	98.2
RCS056	RCS056_8_15	Qtz-Monzonite	NA	NA	A3	Patches	<0.1	0.3	11.7	17.6	0.3	15.8	<0.1	<0.1	<0.1	0.3	9.8	<0.2	39.9	95.6
RCS056	RCS056_10_8	Qtz-Monzonite	NA	NA	A3	Patches	<0.1	<0.2	12.4	18.0	<0.1	16.7	0.1	<0.1	<0.1	0.3	9.3	<0.2	41.0	97.8
RCS056	RCS056_13_3	Qtz-Monzonite	NA	NA	A3	Patches	<0.1	<0.2	13.4	17.8	<0.1	16.3	<0.1	0.1	<0.1	0.8	8.2	<0.2	41.4	98.0
RCS056	RCS056_15_4	Qtz-Monzonite	NA	NA	A3	Patches	<0.1	<0.2	11.6	17.5	<0.1	16.8	0.2	<0.1	<0.1	0.3	10.6	<0.2	40.3	97.2
RCS056	RCS056_19_3	Qtz-Monzonite	NA	NA	A3	Patches	<0.1	<0.2	12.1	17.6	<0.1	16.9	<0.1	0.1	<0.1	0.1	9.7	<0.2	40.5	97.0
RCS056	RCS056_22_5	Qtz-Monzonite	NA	NA	A3	Patches	<0.1	<0.2	14.8	18.4	<0.1	17.6	<0.1	<0.1	0.1	0.1	5.3	<0.2	42.8	99.2
RCS059	RCS059_2_6	Monzodiorite	NA	NA	A3	Replacement	<0.1	<0.2	12.6	18.6	<0.1	17.5	0.2	<0.1	0.1	0.2	10.2	<0.2	42.7	102.2
RCS059	RCS059_9_1	Monzodiorite	NA	NA	A3	Replacement	<0.1	<0.2	12.8	18.3	<0.1	17.7	<0.1	<0.1	<0.1	0.1	10.3	<0.2	42.4	101.6
RCS059	RCS059_9_2	Monzodiorite	NA	NA	A3	Replacement	<0.1	<0.2	12.3	18.3	<0.1	17.8	<0.1	<0.1	<0.1	0.1	10.8	<0.2	42.0	101.3
RCS059	RCS059_9_3	Monzodiorite	NA	NA	A3	Replacement	<0.1	<0.2	12.6	18.5	<0.1	17.7	<0.1	<0.1	<0.1	<0.1	10.8	<0.2	42.5	102.2
RCS059	RCS059_9_5	Monzodiorite	NA	NA	A3	Replacement	<0.1	<0.2	13.3	18.5	<0.1	17.6	0.1	<0.1	<0.1	0.2	9.1	<0.2	42.8	101.6
RCS059	RCS059_9_6	Monzodiorite	NA	NA	A3	Replacement	<0.1	<0.2	13.0	18.4	<0.1	17.9	<0.1	<0.1	0.1	0.1	9.6	<0.2	42.5	101.6
RCS059	RCS059_9_7	Monzodiorite	NA	NA	A3	Replacement	0.1	<0.2	12.6	18.5	<0.1	17.5	0.1	<0.1	<0.1	0.2	10.4	<0.2	42.6	102.1
RCS059	RCS059_9_9	Monzodiorite	NA	NA	A3	Replacement	<0.1	<0.2	12.1	18.4	<0.1	17.7	0.2	<0.1	0.1	0.2	11.3	<0.2	42.2	102.1
RCS059	RCS059_9_10	Monzodiorite	NA	NA	A3	Replacement	<0.1	<0.2	12.6	18.3	<0.1	17.4	0.1	0.2	<0.1	0.3	10.2	<0.2	42.4	101.4
RCS059	RCS059_9_11	Monzodiorite	NA	NA	A3	Replacement	<0.1	<0.2	12.6	18.4	<0.1	17.4	<0.1	<0.1	<0.1	0.3	10.4	<0.2	42.4	101.5
RCS059	RCS059_9_16	Monzodiorite	NA	NA	A3	Replacement	<0.1	<0.2	12.9	18.5	<0.1	18.0	<0.1	<0.1	<0.1	<0.1	10.0	<0.2	42.7	102.1
RCS059	RCS059_10_3	Monzodiorite	NA	NA	A3	Replacement	<0.1	<0.2	12.2	18.2	<0.1	17.7	<0.1	0.2	<0.1	0.2	11.0	<0.2	42.0	101.5

Sample	Reference	Lithology	Structure	Type	Alt	Texture	Na_pct	Mg_pct	Al_pct	Si_pct	K_pct	Ca_pct	Ti_pct	V_pct	Cr_pct	Mn_pct	Fe_pct	Co_pct	O_pct	Total_pct
RCS059	RCS059_10_5	Monzodiorite	NA	NA	A3	Replacement	<0.1	<0.2	13.8	18.5	<0.1	17.5	<0.1	<0.1	0.1	0.3	8.5	<0.2	42.9	101.5
RCS059	RCS059_10_6	Monzodiorite	NA	NA	A3	Replacement	<0.1	<0.2	13.0	18.6	<0.1	17.9	<0.1	<0.1	<0.1	0.1	9.9	<0.2	42.9	102.3
RCS059	RCS059_12_9	Monzodiorite	NA	NA	A3	Replacement	<0.1	<0.2	12.0	18.1	<0.1	17.5	<0.1	0.1	<0.1	<0.1	11.3	<0.2	41.7	100.7
RCS059	RCS059_13_11	Monzodiorite	NA	NA	A3	Replacement	<0.1	<0.2	12.8	18.2	<0.1	17.4	<0.1	<0.1	<0.1	0.2	9.8	<0.2	42.1	100.4
RCS059	RCS059_13_12	Monzodiorite	NA	NA	A3	Replacement	<0.1	<0.2	12.7	18.2	<0.1	17.7	0.1	0.1	<0.1	<0.1	9.8	<0.2	42.2	100.8
RCS059	RCS059_13_13	Monzodiorite	NA	NA	A3	Replacement	<0.1	<0.2	11.9	18.2	<0.1	17.5	0.2	<0.1	0.1	0.2	10.7	<0.2	41.7	100.4
RCS059	RCS059_13_14	Monzodiorite	NA	NA	A3	Replacement	<0.1	<0.2	12.5	18.2	<0.1	17.5	<0.1	<0.1	<0.1	0.2	10.3	<0.2	42.0	100.7
RCS059	RCS059_13_15	Monzodiorite	NA	NA	A3	Replacement	<0.1	<0.2	12.3	18.2	<0.1	17.2	<0.1	0.1	<0.1	0.2	10.5	<0.2	41.8	100.3
RCS059	RCS059_13_19	Monzodiorite	NA	NA	A3	Replacement	<0.1	<0.2	13.0	18.3	<0.1	17.0	<0.1	<0.1	<0.1	0.8	9.5	<0.2	42.2	100.8
RCS059	RCS059_13_20	Monzodiorite	NA	NA	A3	Replacement	<0.1	<0.2	12.3	18.2	<0.1	17.4	<0.1	<0.1	<0.1	0.2	10.5	<0.2	41.8	100.4
RCS059	RCS059_15_11	Monzodiorite	NA	NA	A3	Replacement	<0.1	<0.2	12.5	18.3	<0.1	17.5	<0.1	0.1	0.1	0.4	10.8	<0.2	42.3	102.0
RCS059	RCS059_15_12	Monzodiorite	NA	NA	A3	Replacement	<0.1	<0.2	13.1	18.6	<0.1	17.9	<0.1	0.1	<0.1	0.2	9.8	<0.2	42.9	102.5
RCS059	RCS059_15_13	Monzodiorite	NA	NA	A3	Replacement	<0.1	<0.2	13.3	18.4	<0.1	17.6	<0.1	<0.1	0.1	0.2	8.8	0.2	42.6	101.2
RCS059	RCS059_15_14	Monzodiorite	NA	NA	A3	Replacement	<0.1	<0.2	13.5	18.5	<0.1	17.8	<0.1	<0.1	<0.1	0.2	8.7	<0.2	42.9	101.6
RCS059	RCS059_15_17	Monzodiorite	NA	NA	A3	Replacement	<0.1	<0.2	13.0	18.4	<0.1	17.0	<0.1	0.2	<0.1	0.7	9.7	<0.2	42.4	101.3
RCS059	RCS059_15_19	Monzodiorite	NA	NA	A3	Replacement	<0.1	<0.2	13.2	18.5	<0.1	18.0	0.2	<0.1	<0.1	0.2	9.3	<0.2	42.9	102.2
RCS059	RCS059_15_21	Monzodiorite	NA	NA	A3	Replacement	<0.1	<0.2	13.0	18.4	<0.1	17.8	<0.1	<0.1	<0.1	0.1	9.9	<0.2	42.4	101.5
RCS059	RCS059_15_23	Monzodiorite	NA	NA	A3	Replacement	<0.1	<0.2	12.8	18.3	<0.1	17.5	0.1	<0.1	<0.1	0.3	9.9	<0.2	42.3	101.2
RCS059	RCS059_16_6	Monzodiorite	NA	NA	A3	Replacement	<0.1	<0.2	12.6	18.2	<0.1	17.3	<0.1	<0.1	<0.1	0.1	10.3	<0.2	41.8	100.2
RCS059	RCS059_16_9	Monzodiorite	NA	NA	A3	Replacement	0.2	<0.2	12.3	18.2	<0.1	17.3	<0.1	0.1	<0.1	0.1	10.8	<0.2	41.8	100.8
RCS059	RCS059_18_6	Monzodiorite	NA	NA	A3	Replacement	<0.1	<0.2	13.1	18.6	<0.1	17.7	<0.1	<0.1	<0.1	0.2	9.3	<0.2	42.7	101.5
RCS059	RCS059_18_9	Monzodiorite	NA	NA	A3	Replacement	<0.1	<0.2	13.0	18.5	<0.1	17.0	<0.1	<0.1	<0.1	0.9	9.9	<0.2	42.6	101.8
RCS059	RCS059_20_3	Monzodiorite	NA	NA	A3	Replacement	<0.1	<0.2	13.3	18.4	<0.1	17.7	<0.1	<0.1	<0.1	0.1	9.0	<0.2	42.5	101.1
RCS073	RCS073_6_14	Monzonite	NA	NA	A3	Patches	<0.1	<0.2	12.4	18.0	<0.1	17.3	<0.1	<0.1	<0.1	<0.1	9.8	<0.2	41.4	98.9
RCS073	RCS073_6_20	Monzonite	NA	NA	A3	Patches	<0.1	<0.2	12.0	17.9	<0.1	17.1	<0.1	<0.1	<0.1	<0.1	10.6	<0.2	41.1	98.7
RCS073	RCS073_9_2	Monzonite	NA	NA	A3	Replacement	<0.1	<0.2	12.2	17.7	<0.1	17.0	<0.1	<0.1	<0.1	0.1	9.7	<0.2	40.6	97.3
RCS073	RCS073_9_3	Monzonite	NA	NA	A3	Replacement	<0.1	<0.2	12.7	17.8	<0.1	17.2	<0.1	<0.1	<0.1	0.2	9.3	<0.2	41.3	98.5
RCS073	RCS073_9_4	Monzonite	NA	NA	A3	Replacement	<0.1	<0.2	12.0	17.7	<0.1	17.1	<0.1	<0.1	0.2	0.2	10.5	<0.2	40.8	98.3
RCS073	RCS073_9_5	Monzonite	NA	NA	A3	Replacement	<0.1	<0.2	11.4	17.6	<0.1	17.1	<0.1	<0.1	<0.1	<0.1	11.5	<0.2	40.3	97.9
RCS073	RCS073_9_6	Monzonite	NA	NA	A3	Replacement	<0.1	<0.2	12.1	17.7	<0.1	17.0	<0.1	<0.1	<0.1	0.1	10.3	<0.2	40.8	98.1
RCS073	RCS073_9_7	Monzonite	NA	NA	A3	Replacement	<0.1	<0.2	11.6	17.8	<0.1	17.0	<0.1	<0.1	0.1	0.1	11.1	<0.2	40.6	98.2
RCS073	RCS073_9_8	Monzonite	NA	NA	A3	Replacement	<0.1	<0.2	12.2	17.7	<0.1	17.2	<0.1	<0.1	<0.1	0.2	9.7	<0.2	40.7	97.6
RCS073	RCS073_9_9	Monzonite	NA	NA	A3	Replacement	<0.1	<0.2	12.2	17.7	<0.1	16.8	<0.1	<0.1	<0.1	0.3	10.1	<0.2	40.7	97.7
RCS073	RCS073_9_10	Monzonite	NA	NA	A3	Replacement	<0.1	<0.2	11.0	17.6	<0.1	16.9	<0.1	<0.1	<0.1	<0.1	11.5	<0.2	39.9	96.9
RCS073	RCS073_9_11	Monzonite	NA	NA	A3	Replacement	<0.1	<0.2	11.5	17.8	<0.1	17.0	<0.1	<0.1	0.1	<0.1	11.5	<0.2	40.7	98.5

Sample	Reference	Lithology	Structure	Type	Alt	Texture	Na_pct	Mg_pct	Al_pct	Si_pct	K_pct	Ca_pct	Ti_pct	V_pct	Cr_pct	Mn_pct	Fe_pct	Co_pct	O_pct	Total_pct
RCS073	RCS073_11_20	Monzonite	NA	NA	A3	Replacement	<0.1	<0.2	13.7	18.1	<0.1	17.4	0.1	<0.1	<0.1	0.2	7.9	<0.2	42.3	99.7
RCS073	RCS073_11_22	Monzonite	NA	NA	A3	Replacement	<0.1	<0.2	13.3	18.0	<0.1	17.4	<0.1	<0.1	<0.1	0.3	8.7	<0.2	41.9	99.5
RCS073	RCS073_14_3	Monzonite	NA	NA	A3	Patches	<0.1	<0.2	15.3	18.3	<0.1	17.4	<0.1	<0.1	0.1	0.1	5.1	<0.2	43.0	99.4
RCS073	RCS073_17_1	Monzonite	NA	NA	A3	Patches	<0.1	<0.2	12.5	17.7	0.3	16.6	<0.1	<0.1	<0.1	<0.1	10.3	<0.2	40.9	98.3
RCS073	RCS073_17_3	Monzonite	NA	NA	A3	Patches	<0.1	<0.2	12.2	17.7	<0.1	17.3	<0.1	<0.1	0.2	0.2	10.0	<0.2	40.9	98.4
RCS073	RCS073_17_4	Monzonite	NA	NA	A3	Patches	<0.1	<0.2	12.4	17.9	<0.1	17.3	<0.1	<0.1	0.1	0.2	9.2	<0.2	41.1	98.1
RCS073	RCS073_17_6	Monzonite	NA	NA	A3	Patches	<0.1	<0.2	12.1	18.0	<0.1	17.0	<0.1	<0.1	<0.1	<0.1	10.5	<0.2	41.3	98.9
RCS073	RCS073_17_7	Monzonite	NA	NA	A3	Patches	<0.1	<0.2	12.0	17.7	<0.1	17.2	<0.1	<0.1	0.1	<0.1	10.5	<0.2	40.8	98.3
RCS014	RCS014_6_1	Dacite	NA	NA	A6	Replacement	<0.1	<0.2	12.4	17.9	<0.1	16.4	<0.1	<0.1	<0.1	1.2	10.3	<0.2	41.3	99.4
RCS014	RCS014_6_2	Dacite	NA	NA	A6	Replacement	<0.1	<0.2	13.1	18.0	<0.1	16.6	<0.1	0.1	<0.1	1.0	8.5	<0.2	41.7	99.0
RCS014	RCS014_6_3	Dacite	NA	NA	A6	Replacement	<0.1	<0.2	12.3	18.0	<0.1	17.0	0.1	0.2	<0.1	0.7	9.3	<0.2	41.4	98.9
RCS014	RCS014_6_5	Dacite	NA	NA	A6	Replacement	<0.1	<0.2	12.3	18.1	<0.1	17.3	0.2	<0.1	0.1	0.4	10.2	<0.2	41.7	100.2
RCS014	RCS014_6_7	Dacite	NA	NA	A6	Replacement	<0.1	<0.2	11.7	17.3	<0.1	16.4	0.1	<0.1	<0.1	0.5	9.9	<0.2	39.7	95.6
RCS014	RCS014_6_8	Dacite	NA	NA	A6	Replacement	<0.1	<0.2	11.7	17.7	<0.1	16.6	<0.1	0.1	<0.1	0.6	10.3	<0.2	40.5	97.5
RCS014	RCS014_6_9	Dacite	NA	NA	A6	Replacement	<0.1	<0.2	11.1	16.9	<0.1	15.9	0.2	<0.1	<0.1	0.4	12.2	<0.2	39.2	95.8
RCS014	RCS014_7_4	Dacite	NA	NA	A6	Replacement	<0.1	<0.2	12.8	17.9	<0.1	16.5	0.2	<0.1	<0.1	0.9	8.4	<0.2	41.2	97.7
RCS014	RCS014_7_5	Dacite	NA	NA	A6	Replacement	<0.1	<0.2	12.4	17.8	<0.1	16.8	<0.1	<0.1	<0.1	0.7	9.2	<0.2	41.0	97.8
RCS014	RCS014_9_13	Dacite	NA	NA	A6	Replacement	<0.1	<0.2	12.5	17.9	<0.1	17.1	0.2	0.2	<0.1	0.4	10.1	<0.2	41.6	100.0
RCS014	RCS014_9_14	Dacite	NA	NA	A6	Replacement	<0.1	<0.2	13.5	18.2	<0.1	16.6	0.1	<0.1	<0.1	0.4	7.2	<0.2	41.6	97.5
RCS014	RCS014_9_15	Dacite	NA	NA	A6	Replacement	<0.1	<0.2	12.6	17.8	<0.1	17.0	<0.1	0.1	<0.1	0.4	9.3	<0.2	41.2	98.4
RCS014	RCS014_9_16	Dacite	NA	NA	A6	Replacement	<0.1	<0.2	12.9	17.9	<0.1	17.2	<0.1	<0.1	<0.1	0.5	9.3	<0.2	41.6	99.3
RCS014	RCS014_9_17	Dacite	NA	NA	A6	Replacement	<0.1	<0.2	12.4	17.7	<0.1	16.5	0.1	<0.1	<0.1	0.8	9.3	<0.2	40.8	97.5
RCS014	RCS014_9_18	Dacite	NA	NA	A6	Replacement	<0.1	<0.2	12.2	17.7	<0.1	16.5	<0.1	<0.1	<0.1	0.7	9.3	<0.2	40.6	97.0
RCS014	RCS014_9_19	Dacite	NA	NA	A6	Replacement	<0.1	<0.2	12.9	17.9	<0.1	15.5	<0.1	<0.1	0.1	2.4	8.9	<0.2	41.4	99.0
RCS014	RCS014_9_20	Dacite	NA	NA	A6	Replacement	<0.1	<0.2	12.0	18.0	<0.1	17.2	0.1	0.1	<0.1	0.3	10.2	<0.2	41.3	99.3
RCS014	RCS014_9_21	Dacite	NA	NA	A6	Replacement	<0.1	<0.2	12.8	18.1	<0.1	17.0	0.1	0.1	<0.1	0.5	9.2	<0.2	41.8	99.6
RCS014	RCS014_9_22	Dacite	NA	NA	A6	Replacement	<0.1	<0.2	13.4	17.9	<0.1	16.1	<0.1	<0.1	<0.1	1.5	7.7	<0.2	41.5	98.0
RCS014	RCS014_13_3	Dacite	NA	NA	A6	Replacement	<0.1	<0.2	12.2	18.1	<0.1	17.2	<0.1	0.2	<0.1	0.4	9.9	<0.2	41.6	99.5
RCS014	RCS014_13_5	Dacite	NA	NA	A6	Replacement	<0.1	<0.2	13.2	18.2	<0.1	16.9	0.1	<0.1	<0.1	0.5	8.6	<0.2	42.0	99.5
RCS014	RCS014_13_6	Dacite	NA	NA	A6	Replacement	<0.1	<0.2	13.0	18.1	<0.1	17.1	<0.1	<0.1	<0.1	0.3	9.1	<0.2	41.7	99.2
RCS014	RCS014_13_7	Dacite	NA	NA	A6	Replacement	<0.1	<0.2	13.5	17.9	<0.1	16.9	<0.1	<0.1	<0.1	0.6	7.8	<0.2	41.6	98.3
RCS014	RCS014_13_8	Dacite	NA	NA	A6	Replacement	<0.1	<0.2	12.5	17.9	<0.1	17.2	<0.1	0.1	<0.1	0.1	10.0	<0.2	41.4	99.2
RCS014	RCS014_13_9	Dacite	NA	NA	A6	Replacement	<0.1	<0.2	12.8	18.0	<0.1	16.8	<0.1	0.1	0.1	0.2	8.7	<0.2	41.4	98.2
RCS014	RCS014_13_10	Dacite	NA	NA	A6	Replacement	<0.1	<0.2	13.2	17.9	<0.1	17.2	<0.1	<0.1	0.1	0.2	8.3	<0.2	41.6	98.6
RCS014	RCS014_16_1	Dacite	NA	NA	A6	Replacement	<0.1	<0.2	10.5	17.6	<0.1	16.8	0.3	0.1	<0.1	0.1	12.6	<0.2	40.1	98.1

Sample	Reference	Lithology	Structure	Type	Alt	Texture	Na_pct	Mg_pct	Al_pct	Si_pct	K_pct	Ca_pct	Ti_pct	V_pct	Cr_pct	Mn_pct	Fe_pct	Co_pct	O_pct	Total_pct
RCS014	RCS014_19_6	Dacite	NA	NA	A6	Replacement	<0.1	<0.2	11.4	17.9	<0.1	17.1	0.2	<0.1	<0.1	0.3	11.3	<0.2	41.0	99.2
RCS014	RCS014_19_8	Dacite	NA	NA	A6	Replacement	<0.1	<0.2	13.1	17.9	<0.1	15.5	<0.1	<0.1	<0.1	2.4	8.5	<0.2	41.4	98.8
RCS023	RCS023_5_1	Qtz-Monzonite	NA	NA	BX	Patches	<0.1	<0.2	12.4	17.3	<0.1	16.1	<0.1	<0.1	0.1	1.1	8.9	<0.2	40.1	96.0
RCS023	RCS023_5_2	Qtz-Monzonite	NA	NA	BX	Patches	<0.1	<0.2	12.3	17.5	<0.1	16.5	<0.1	<0.1	<0.1	0.4	9.6	<0.2	40.3	96.7
RCS023	RCS023_7_2	Qtz-Monzonite	NA	NA	BX	Patches	<0.1	<0.2	12.1	17.3	<0.1	16.8	<0.1	<0.1	<0.1	0.2	9.0	<0.2	39.9	95.3
RCS023	RCS023_7_3	Qtz-Monzonite	NA	NA	BX	Patches	<0.1	<0.2	12.0	17.2	<0.1	16.5	<0.1	<0.1	<0.1	0.2	8.7	<0.2	39.4	93.8
RCS023	RCS023_7_4	Qtz-Monzonite	NA	NA	BX	Patches	<0.1	<0.2	11.8	16.7	<0.1	16.4	<0.1	<0.1	0.1	0.3	8.9	<0.2	39.0	93.2
RCS023	RCS023_10_1	Qtz-Monzonite	NA	NA	BX	Patches	<0.1	<0.2	12.4	16.8	<0.1	15.1	0.1	<0.1	0.1	1.0	8.1	<0.2	38.9	92.5
RCS023	RCS023_10_2	Qtz-Monzonite	NA	NA	BX	Patches	<0.1	<0.2	12.3	17.6	<0.1	16.4	<0.1	<0.1	0.1	0.3	9.3	<0.2	40.5	96.6
RCS023	RCS023_10_5	Qtz-Monzonite	NA	NA	BX	Patches	<0.1	<0.2	13.8	17.6	<0.1	16.9	<0.1	<0.1	<0.1	0.2	6.7	<0.2	41.1	96.3
RCS023	RCS023_12_2	Qtz-Monzonite	NA	NA	BX	Patches	<0.1	<0.2	12.6	17.5	<0.1	16.6	<0.1	<0.1	<0.1	0.3	8.9	<0.2	40.6	96.5
RCS023	RCS023_13_2	Qtz-Monzonite	NA	NA	BX	Patches	<0.1	<0.2	13.0	17.5	<0.1	16.8	<0.1	<0.1	<0.1	0.3	8.1	<0.2	40.7	96.3
RCS023	RCS023_15_1	Qtz-Monzonite	NA	NA	BX	Patches	<0.1	<0.2	13.2	17.5	<0.1	16.8	<0.1	<0.1	<0.1	0.3	7.6	<0.2	40.9	96.3
RCS023	RCS023_15_2	Qtz-Monzonite	NA	NA	BX	Patches	0.2	<0.2	12.3	17.9	<0.1	16.2	<0.1	<0.1	<0.1	0.3	9.1	<0.2	40.6	96.6
RCS023	RCS023_15_3	Qtz-Monzonite	NA	NA	BX	Patches	0.1	<0.2	11.9	17.4	<0.1	16.4	<0.1	<0.1	<0.1	0.4	9.0	<0.2	39.7	94.9
RCS023	RCS023_15_4	Qtz-Monzonite	NA	NA	BX	Patches	<0.1	<0.2	13.1	17.6	<0.1	16.5	<0.1	<0.1	0.1	0.6	7.9	<0.2	40.9	96.7
RCS023	RCS023_15_5	Qtz-Monzonite	NA	NA	BX	Patches	0.1	<0.2	12.3	17.4	<0.1	15.9	<0.1	<0.1	0.1	0.6	9.0	<0.2	40.0	95.5
RCS023	RCS023_15_6	Qtz-Monzonite	NA	NA	BX	Patches	<0.1	<0.2	13.9	17.7	<0.1	16.9	<0.1	<0.1	0.1	0.5	6.8	<0.2	41.4	97.1
RCS023	RCS023_15_7	Qtz-Monzonite	NA	NA	BX	Patches	<0.1	<0.2	12.1	17.6	<0.1	16.6	<0.1	<0.1	<0.1	0.5	9.5	<0.2	40.5	96.8
RCS023	RCS023_15_8	Qtz-Monzonite	NA	NA	BX	Patches	<0.1	<0.2	13.0	17.4	<0.1	16.5	<0.1	0.1	<0.1	0.6	8.0	<0.2	40.6	96.2
RCS023	RCS023_15_9	Qtz-Monzonite	NA	NA	BX	Patches	<0.1	<0.2	12.4	17.5	<0.1	16.3	<0.1	<0.1	<0.1	0.7	9.1	<0.2	40.3	96.2
RCS023	RCS023_15_10	Qtz-Monzonite	NA	NA	BX	Patches	<0.1	<0.2	12.3	17.5	<0.1	16.2	<0.1	<0.1	<0.1	0.6	9.3	<0.2	40.3	96.3
RCS023	RCS023_15_12	Qtz-Monzonite	NA	NA	BX	Patches	<0.1	<0.2	13.4	17.8	<0.1	16.3	<0.1	<0.1	<0.1	0.6	8.3	<0.2	41.2	97.6
RCS023	RCS023_17_1	Qtz-Monzonite	NA	NA	BX	Patches	<0.1	<0.2	12.8	17.4	<0.1	16.0	<0.1	0.1	<0.1	0.8	9.0	<0.2	40.6	96.8
RCS023	RCS023_17_2	Qtz-Monzonite	NA	NA	BX	Patches	<0.1	<0.2	12.2	17.4	<0.1	16.5	<0.1	<0.1	<0.1	0.5	9.5	<0.2	40.1	96.1
RCS023	RCS023_23_2	Qtz-Monzonite	NA	NA	BX	Patches	<0.1	<0.2	12.5	17.5	<0.1	16.7	<0.1	<0.1	<0.1	0.3	8.8	<0.2	40.3	96.1
RCS023	RCS023_24_8	Qtz-Monzonite	NA	NA	BX	Patches	<0.1	<0.2	13.3	17.5	<0.1	16.4	<0.1	<0.1	0.1	0.4	7.6	<0.2	40.8	96.0
RCS037	RCS037_10_5	Monzonite	NA	NA	A3	Replacement	0.2	<0.2	10.6	17.4	<0.1	16.1	0.3	<0.1	<0.1	<0.1	11.4	<0.2	39.4	95.2
RCS037	RCS037_10_6	Monzonite	NA	NA	A3	Replacement	<0.1	0.7	11.0	17.7	0.2	15.1	0.2	<0.1	<0.1	<0.1	11.2	<0.2	39.8	95.9
RCS037	RCS037_13_1	Monzonite	NA	NA	A3	Replacement	<0.1	<0.2	12.9	17.5	<0.1	17.1	<0.1	0.1	<0.1	<0.1	8.0	<0.2	40.8	96.6
RCS037	RCS037_13_2	Monzonite	NA	NA	A3	Replacement	<0.1	<0.2	12.8	17.6	<0.1	16.8	<0.1	<0.1	<0.1	<0.1	8.6	<0.2	40.7	96.5
RCS037	RCS037_13_3	Monzonite	NA	NA	A3	Replacement	<0.1	<0.2	12.4	17.8	<0.1	16.4	<0.1	<0.1	<0.1	<0.1	8.3	<0.2	40.3	95.2
RCS037	RCS037_13_4	Monzonite	NA	NA	A3	Replacement	<0.1	<0.2	13.9	17.7	<0.1	16.8	<0.1	<0.1	<0.1	0.2	7.0	<0.2	41.3	96.9
RCS037	RCS037_13_5	Monzonite	NA	NA	A3	Replacement	<0.1	<0.2	12.8	17.5	<0.1	16.8	<0.1	0.1	0.1	<0.1	8.3	<0.2	40.6	96.2
RCS037	RCS037_13_6	Monzonite	NA	NA	A3	Replacement	<0.1	<0.2	13.7	17.5	<0.1	17.1	<0.1	<0.1	<0.1	0.1	7.2	<0.2	41.2	96.8

Sample	Reference	Lithology	Structure	Type	Alt	Texture	Na_pct	Mg_pct	Al_pct	Si_pct	K_pct	Ca_pct	Ti_pct	V_pct	Cr_pct	Mn_pct	Fe_pct	Co_pct	O_pct	Total_pct
RCS037	RCS037_13_7	Monzonite	NA	NA	A3	Replacement	<0.1	<0.2	13.0	17.4	<0.1	17.0	<0.1	<0.1	<0.1	0.1	8.0	<0.2	40.5	95.9
RCS037	RCS037_13_8	Monzonite	NA	NA	A3	Replacement	<0.1	<0.2	13.4	17.7	<0.1	16.9	<0.1	<0.1	0.1	<0.1	7.4	<0.2	41.1	96.6
RCS037	RCS037_13_9	Monzonite	NA	NA	A3	Replacement	<0.1	<0.2	13.1	17.6	<0.1	16.8	0.1	<0.1	0.1	<0.1	7.6	<0.2	40.7	96.0
RCS037	RCS037_13_11	Monzonite	NA	NA	A3	Replacement	<0.1	<0.2	12.5	17.5	<0.1	16.1	<0.1	<0.1	0.1	0.3	9.3	<0.2	40.4	96.2
RCS037	RCS037_13_12	Monzonite	NA	NA	A3	Replacement	<0.1	<0.2	11.8	17.6	<0.1	17.0	<0.1	0.1	0.1	<0.1	10.4	<0.2	40.4	97.4
RCS037	RCS037_13_13	Monzonite	NA	NA	A3	Replacement	<0.1	<0.2	13.6	17.6	<0.1	17.1	<0.1	<0.1	<0.1	0.1	7.3	<0.2	41.3	97.0
RCS037	RCS037_13_14	Monzonite	NA	NA	A3	Replacement	<0.1	<0.2	13.4	17.5	<0.1	16.7	<0.1	<0.1	<0.1	<0.1	7.1	<0.2	40.7	95.4
RCS037	RCS037_17_7	Monzonite	NA	NA	A3	Replacement	<0.1	<0.2	13.4	17.7	<0.1	16.9	<0.1	<0.1	<0.1	0.1	7.5	<0.2	41.2	96.9
RCS037	RCS037_18_18	Monzonite	NA	NA	A3	Replacement	<0.1	<0.2	12.6	17.4	<0.1	16.7	0.1	<0.1	<0.1	<0.1	8.5	<0.2	40.4	95.7
RCS037	RCS037_22_3	Monzonite	NA	NA	A3	Replacement	<0.1	<0.2	11.2	17.4	<0.1	16.5	0.2	0.1	<0.1	<0.1	10.5	<0.2	39.7	95.5
RCS042	RCS042_5_1	Monzonite	NA	NA	A4	L Patches	<0.1	<0.2	13.0	17.5	<0.1	17.1	<0.1	0.2	<0.1	<0.1	7.7	<0.2	40.7	96.1
RCS042	RCS042_5_2	Monzonite	NA	NA	A4	L Patches	<0.1	<0.2	11.8	17.4	<0.1	16.9	0.1	<0.1	<0.1	<0.1	10.0	<0.2	40.1	96.2
RCS042	RCS042_5_3	Monzonite	NA	NA	A4	L Patches	<0.1	<0.2	10.8	17.3	<0.1	16.6	0.4	<0.1	<0.1	<0.1	11.6	<0.2	39.6	96.3
RCS042	RCS042_5_4	Monzonite	NA	NA	A4	L Patches	<0.1	<0.2	12.0	17.3	<0.1	16.8	0.1	<0.1	<0.1	<0.1	9.7	<0.2	40.0	96.0
RCS042	RCS042_5_5	Monzonite	NA	NA	A4	L Patches	<0.1	<0.2	12.5	17.4	<0.1	16.8	0.2	0.1	<0.1	<0.1	9.0	<0.2	40.5	96.5
RCS042	RCS042_5_6	Monzonite	NA	NA	A4	L Patches	<0.1	<0.2	11.8	17.5	<0.1	16.8	0.2	0.1	<0.1	<0.1	9.9	<0.2	40.3	96.5
RCS042	RCS042_5_7	Monzonite	NA	NA	A4	L Patches	<0.1	<0.2	12.7	17.6	<0.1	17.2	<0.1	<0.1	<0.1	<0.1	8.9	<0.2	40.8	97.2
RCS042	RCS042_5_8	Monzonite	NA	NA	A4	L Patches	<0.1	<0.2	12.9	17.7	<0.1	16.6	0.1	<0.1	<0.1	0.3	8.2	<0.2	40.8	96.7
RCS042	RCS042_5_9	Monzonite	NA	NA	A4	L Patches	<0.1	<0.2	10.8	17.5	<0.1	16.7	0.3	<0.1	<0.1	<0.1	11.3	<0.2	39.7	96.1
RCS042	RCS042_5_10	Monzonite	NA	NA	A4	L Patches	<0.1	<0.2	11.8	17.3	<0.1	16.6	<0.1	<0.1	<0.1	0.1	9.7	<0.2	39.8	95.3
RCS042	RCS042_5_11	Monzonite	NA	NA	A4	L Patches	<0.1	<0.2	11.6	17.2	<0.1	16.6	<0.1	<0.1	<0.1	<0.1	10.0	<0.2	39.6	95.0
RCS042	RCS042_5_12	Monzonite	NA	NA	A4	L Patches	<0.1	<0.2	13.7	17.6	<0.1	17.1	<0.1	<0.1	<0.1	<0.1	6.5	<0.2	40.9	95.7
RCS042	RCS042_5_13	Monzonite	NA	NA	A4	L Patches	<0.1	<0.2	12.2	17.2	<0.1	16.7	<0.1	<0.1	0.1	<0.1	9.2	<0.2	39.9	95.3
RCS042	RCS042_5_14	Monzonite	NA	NA	A4	L Patches	<0.1	<0.2	12.7	17.4	<0.1	16.8	<0.1	<0.1	0.1	<0.1	8.1	<0.2	40.1	95.2
RCS042	RCS042_5_15	Monzonite	NA	NA	A4	L Patches	<0.1	<0.2	14.4	18.0	<0.1	17.5	<0.1	<0.1	0.1	<0.1	5.9	<0.2	42.1	98.0
RCS042	RCS042_5_16	Monzonite	NA	NA	A4	L Patches	<0.1	<0.2	13.9	18.0	<0.1	17.3	<0.1	<0.1	<0.1	<0.1	6.5	<0.2	41.7	97.4
RCS042	RCS042_5_17	Monzonite	NA	NA	A4	L Patches	<0.1	<0.2	12.8	17.9	<0.1	17.2	<0.1	<0.1	<0.1	0.1	8.7	<0.2	41.3	98.1
RCS042	RCS042_5_18	Monzonite	NA	NA	A4	L Patches	<0.1	<0.2	13.8	17.8	<0.1	17.1	<0.1	<0.1	<0.1	<0.1	6.7	<0.2	41.4	96.9
RCS042	RCS042_9_14	Monzonite	NA	NA	A4	Replacement	<0.1	<0.2	12.9	17.6	<0.1	16.9	<0.1	<0.1	<0.1	0.2	8.5	<0.2	40.8	96.7
RCS042	RCS042_9_15	Monzonite	NA	NA	A4	Replacement	<0.1	<0.2	12.9	17.6	<0.1	17.0	0.1	<0.1	<0.1	<0.1	8.3	<0.2	40.8	96.6
RCS042	RCS042_9_16	Monzonite	NA	NA	A4	Replacement	<0.1	<0.2	13.0	17.5	<0.1	17.1	<0.1	<0.1	<0.1	0.1	7.7	<0.2	40.8	96.3
RCS042	RCS042_9_17	Monzonite	NA	NA	A4	Replacement	<0.1	<0.2	13.6	17.7	<0.1	16.9	<0.1	<0.1	0.1	0.2	7.3	<0.2	41.3	97.1
RCS042	RCS042_9_18	Monzonite	NA	NA	A4	Replacement	<0.1	<0.2	13.4	17.4	<0.1	16.4	0.1	<0.1	<0.1	0.4	7.6	<0.2	40.7	96.1
RCS042	RCS042_11_13	Monzonite	NA	NA	A4	Replacement	<0.1	<0.2	13.3	17.6	<0.1	16.8	0.1	<0.1	<0.1	<0.1	7.6	<0.2	41.0	96.5
RCS042	RCS042_11_14	Monzonite	NA	NA	A4	Replacement	<0.1	<0.2	12.7	17.4	<0.1	17.0	<0.1	<0.1	0.1	<0.1	8.5	<0.2	40.3	95.9

Sample	Reference	Lithology	Structure	Type	Alt	Texture	Na_pct	Mg_pct	Al_pct	Si_pct	K_pct	Ca_pct	Ti_pct	V_pct	Cr_pct	Mn_pct	Fe_pct	Co_pct	O_pct	Total_pct
RCS042	RCS042_13_12	Monzonite	NA	NA	A4	Replacement	<0.1	<0.2	13.1	17.7	<0.1	16.9	<0.1	<0.1	<0.1	<0.1	8.1	<0.2	41.0	96.7
RCS042	RCS042_13_14	Monzonite	NA	NA	A4	Replacement	<0.1	<0.2	11.1	17.3	<0.1	16.6	0.2	<0.1	<0.1	<0.1	10.8	<0.2	39.4	95.4
RCS042	RCS042_13_16	Monzonite	NA	NA	A4	Replacement	<0.1	<0.2	11.0	17.2	<0.1	16.3	<0.1	<0.1	<0.1	<0.1	10.9	<0.2	39.1	94.5
RCS042	RCS042_17_9	Monzonite	NA	NA	A4	Replacement	<0.1	<0.2	14.5	17.8	<0.1	17.0	<0.1	<0.1	<0.1	<0.1	5.3	<0.2	41.5	96.1
RCS042	RCS042_17_10	Monzonite	NA	NA	A4	Replacement	<0.1	<0.2	12.3	17.6	<0.1	16.8	<0.1	<0.1	<0.1	0.2	9.4	<0.2	40.6	96.8
RCS042	RCS042_21_7	Monzonite	NA	NA	A4	Replacement	<0.1	<0.2	12.6	17.7	<0.1	17.1	<0.1	<0.1	<0.1	<0.1	8.6	<0.2	40.8	96.8
RCS042	RCS042_21_14	Monzonite	NA	NA	A4	Replacement	<0.1	<0.2	12.6	17.5	<0.1	17.0	<0.1	<0.1	<0.1	<0.1	8.5	<0.2	40.5	96.1
RCS065	RCS065_6_1	Trachyte	159SW58	Fracture	A6	Replacement	<0.1	<0.2	10.9	17.6	<0.1	17.2	0.2	<0.1	<0.1	0.2	11.9	<0.2	40.3	98.2
RCS065	RCS065_6_3	Trachyte	159SW58	Fracture	A6	Replacement	<0.1	<0.2	12.3	17.7	<0.1	17.0	<0.1	<0.1	0.1	0.3	9.6	<0.2	41.0	98.0
RCS065	RCS065_6_4	Trachyte	159SW58	Fracture	A6	Replacement	<0.1	<0.2	11.5	17.7	<0.1	16.8	0.1	<0.1	<0.1	0.3	11.5	<0.2	40.5	98.3
RCS065	RCS065_6_5	Trachyte	159SW58	Fracture	A6	Replacement	<0.1	<0.2	11.5	17.5	<0.1	17.2	0.4	<0.1	<0.1	0.2	10.6	<0.2	40.6	98.1
RCS065	RCS065_6_6	Trachyte	159SW58	Fracture	A6	Replacement	<0.1	<0.2	10.9	17.5	<0.1	16.8	<0.1	<0.1	<0.1	0.2	11.7	<0.2	39.9	97.1
RCS065	RCS065_6_7	Trachyte	159SW58	Fracture	A6	Replacement	<0.1	<0.2	12.3	17.5	<0.1	17.0	<0.1	0.1	<0.1	0.2	9.6	<0.2	40.7	97.3
RCS065	RCS065_6_8	Trachyte	159SW58	Fracture	A6	Replacement	<0.1	<0.2	11.4	17.6	<0.1	16.7	<0.1	<0.1	<0.1	0.2	11.1	<0.2	40.2	97.0
RCS065	RCS065_6_11	Trachyte	159SW58	Fracture	A6	Replacement	<0.1	<0.2	12.1	17.7	0.2	16.4	<0.1	<0.1	<0.1	0.3	9.7	<0.2	40.6	97.0
RCS065	RCS065_6_12	Trachyte	159SW58	Fracture	A6	Replacement	<0.1	<0.2	11.7	17.6	<0.1	16.8	<0.1	<0.1	<0.1	0.3	10.5	0.2	40.4	97.4
RCS065	RCS065_6_13	Trachyte	159SW58	Fracture	A6	Replacement	<0.1	<0.2	11.9	17.6	<0.1	16.5	<0.1	<0.1	<0.1	0.8	10.2	<0.2	40.3	97.2
RCS065	RCS065_9_1	Trachyte	159SW58	Fracture	A6	Replacement	<0.1	<0.2	11.4	17.8	<0.1	16.9	<0.1	<0.1	<0.1	0.2	11.8	<0.2	40.7	98.9
RCS065	RCS065_10_2	Trachyte	159SW58	Fracture	A6	Replacement	<0.1	<0.2	12.2	17.6	<0.1	16.8	<0.1	<0.1	0.1	0.1	10.0	<0.2	40.7	97.6
RCS065	RCS065_10_5	Trachyte	159SW58	Fracture	A6	Replacement	<0.1	<0.2	12.2	17.9	<0.1	17.0	0.1	<0.1	<0.1	0.4	10.3	<0.2	41.2	99.1
RCS065	RCS065_12_2	Trachyte	159SW58	Fracture	A6	Replacement	<0.1	<0.2	12.9	17.9	<0.1	17.2	<0.1	<0.1	0.1	0.4	8.9	<0.2	41.4	98.8
RCS065	RCS065_12_4	Trachyte	159SW58	Fracture	A6	Replacement	<0.1	<0.2	12.9	17.8	<0.1	17.2	<0.1	<0.1	<0.1	0.2	9.3	<0.2	41.4	98.7
RCS065	RCS065_12_6	Trachyte	159SW58	Fracture	A6	Replacement	<0.1	<0.2	13.1	17.9	<0.1	17.3	<0.1	<0.1	<0.1	0.2	8.5	<0.2	41.5	98.6
RCS065	RCS065_12_7	Trachyte	159SW58	Fracture	A6	Replacement	<0.1	0.5	10.6	17.9	0.3	16.1	<0.1	<0.1	<0.1	0.3	12.2	<0.2	40.3	98.1
RCS065	RCS065_12_15	Trachyte	159SW58	Fracture	A6	Replacement	<0.1	<0.2	12.6	17.5	<0.1	16.5	<0.1	<0.1	<0.1	0.6	9.0	<0.2	40.6	96.8
RCS065	RCS065_12_16	Trachyte	159SW58	Fracture	A6	Replacement	<0.1	<0.2	12.2	17.5	<0.1	17.1	<0.1	<0.1	0.1	0.2	9.8	<0.2	40.6	97.5
RCS065	RCS065_12_19	Trachyte	159SW58	Fracture	A6	Replacement	0.6	<0.2	12.7	18.8	<0.1	15.8	<0.1	<0.1	<0.1	0.3	8.4	<0.2	41.8	98.4
RCS065	RCS065_12_20	Trachyte	159SW58	Fracture	A6	Replacement	<0.1	<0.2	11.7	16.9	<0.1	16.2	<0.1	<0.1	<0.1	0.3	9.3	<0.2	38.9	93.2
RCS065	RCS065_13_6	Trachyte	159SW58	Fracture	A6	Replacement	<0.1	<0.2	11.7	17.3	<0.1	16.6	<0.1	<0.1	<0.1	0.2	10.3	<0.2	39.9	95.9
RCS065	RCS065_13_7	Trachyte	159SW58	Fracture	A6	Replacement	<0.1	<0.2	11.0	17.4	<0.1	16.9	<0.1	<0.1	<0.1	0.2	12.2	<0.2	39.9	97.6
RCS065	RCS065_13_9	Trachyte	159SW58	Fracture	A6	Replacement	<0.1	<0.2	11.2	17.6	<0.1	16.8	<0.1	<0.1	<0.1	0.3	11.6	<0.2	40.2	97.7
RCS065	RCS065_13_10	Trachyte	159SW58	Fracture	A6	Replacement	<0.1	<0.2	13.4	17.9	<0.1	16.7	<0.1	<0.1	<0.1	0.7	8.3	<0.2	41.5	98.5
RCS065	RCS065_15_5	Trachyte	159SW58	Fracture	A6	Replacement	<0.1	<0.2	12.3	17.7	<0.1	16.6	<0.1	<0.1	<0.1	0.3	9.9	<0.2	40.7	97.4
RCS065	RCS065_15_6	Trachyte	159SW58	Fracture	A6	Replacement	<0.1	<0.2	12.3	17.6	<0.1	16.9	<0.1	<0.1	<0.1	0.2	10.0	<0.2	40.7	97.6
RCS067	RCS067_2_5	Trachyte	286NE46	Fracture vein	A5	Replacement	<0.1	<0.2	12.9	18.0	<0.1	16.2	<0.1	<0.1	<0.1	0.8	9.5	<0.2	41.4	98.8

Sample	Reference	Lithology	Structure	Type	Alt	Texture	Na_pct	Mg_pct	Al_pct	Si_pct	K_pct	Ca_pct	Ti_pct	V_pct	Cr_pct	Mn_pct	Fe_pct	Co_pct	O_pct	Total_pct
RCS067	RCS067_2_6	Trachyte	286NE46	Fracture vein	A5	Replacement	<0.1	<0.2	13.0	17.9	<0.1	17.4	<0.1	<0.1	<0.1	0.2	8.7	<0.2	41.5	98.6
RCS067	RCS067_2_7	Trachyte	286NE46	Fracture vein	A5	Replacement	<0.1	<0.2	13.3	18.0	<0.1	17.2	<0.1	<0.1	0.1	0.2	8.3	<0.2	41.8	98.9
RCS067	RCS067_2_8	Trachyte	286NE46	Fracture vein	A5	Replacement	<0.1	<0.2	12.1	17.6	<0.1	17.1	<0.1	<0.1	<0.1	0.4	10.1	<0.2	40.7	98.0
RCS067	RCS067_2_9	Trachyte	286NE46	Fracture vein	A5	Replacement	<0.1	<0.2	13.4	17.8	<0.1	16.7	<0.1	<0.1	<0.1	0.3	7.7	<0.2	41.1	97.0
RCS067	RCS067_6_3	Trachyte	286NE46	Fracture vein	A5	Replacement	<0.1	<0.2	10.6	17.8	<0.1	17.2	0.1	<0.1	<0.1	0.1	12.6	<0.2	40.4	98.9
RCS067	RCS067_7_4	Trachyte	286NE46	Fracture vein	A5	Replacement	<0.1	<0.2	12.2	17.9	<0.1	16.8	<0.1	<0.1	<0.1	0.3	10.2	<0.2	41.0	98.4
RCS067	RCS067_7_6	Trachyte	286NE46	Fracture vein	A5	Replacement	<0.1	<0.2	12.0	17.8	<0.1	16.7	<0.1	<0.1	<0.1	0.2	10.7	<0.2	41.0	98.4
RCS067	RCS067_11_14	Trachyte	286NE46	Fracture vein	A5	L Patches	<0.1	<0.2	12.4	18.1	<0.1	17.0	<0.1	<0.1	0.1	0.2	9.6	<0.2	41.3	98.7
RCS067	RCS067_11_15	Trachyte	286NE46	Fracture vein	A5	L Patches	<0.1	<0.2	12.6	17.6	<0.1	17.1	<0.1	<0.1	<0.1	0.3	9.2	<0.2	40.9	97.7
RCS067	RCS067_11_20	Trachyte	286NE46	Fracture vein	A5	L Patches	<0.1	<0.2	12.0	17.7	<0.1	17.0	<0.1	<0.1	<0.1	0.2	10.2	<0.2	40.7	97.8
RCS067	RCS067_12_7	Trachyte	286NE46	Fracture vein	A5	L Patches	<0.1	<0.2	12.1	17.5	<0.1	16.9	<0.1	<0.1	<0.1	0.3	10.0	<0.2	40.5	97.4
RCS067	RCS067_12_8	Trachyte	286NE46	Fracture vein	A5	L Patches	<0.1	<0.2	12.5	18.1	<0.1	17.1	<0.1	<0.1	<0.1	<0.1	9.1	<0.2	41.3	98.1
RCS067	RCS067_12_10	Trachyte	286NE46	Fracture vein	A5	L Patches	<0.1	<0.2	12.8	18.1	<0.1	17.3	<0.1	<0.1	<0.1	0.1	9.5	<0.2	41.8	99.7
RCS067	RCS067_12_12	Trachyte	286NE46	Fracture vein	A5	L Patches	<0.1	<0.2	12.4	17.9	<0.1	16.6	<0.1	<0.1	<0.1	0.6	10.0	<0.2	41.1	98.5
RCS067	RCS067_12_13	Trachyte	286NE46	Fracture vein	A5	L Patches	<0.1	<0.2	11.9	17.9	<0.1	17.0	<0.1	<0.1	<0.1	<0.1	10.7	<0.2	40.9	98.4
RCS067	RCS067_16_3	Trachyte	286NE46	Fracture vein	V3	Vein	<0.1	<0.2	12.2	17.9	<0.1	17.4	0.2	<0.1	<0.1	0.1	9.9	<0.2	41.2	98.7
RCS067	RCS067_16_4	Trachyte	286NE46	Fracture vein	V3	Vein	<0.1	<0.2	12.9	17.9	<0.1	17.3	<0.1	<0.1	0.1	0.1	9.2	<0.2	41.5	99.0
RCS067	RCS067_16_5	Trachyte	286NE46	Fracture vein	V3	Vein	0.1	<0.2	12.7	18.0	<0.1	17.4	0.1	<0.1	<0.1	0.2	8.9	<0.2	41.6	99.0
RCS067	RCS067_16_6	Trachyte	286NE46	Fracture vein	V3	Vein	<0.1	<0.2	13.5	18.2	<0.1	17.5	<0.1	<0.1	0.2	0.1	7.8	<0.2	42.1	99.3
RCS067	RCS067_16_7	Trachyte	286NE46	Fracture vein	V3	Vein	<0.1	<0.2	11.8	17.6	<0.1	17.0	<0.1	<0.1	<0.1	0.4	9.9	<0.2	40.4	97.1
RCS067	RCS067_17_3	Trachyte	286NE46	Fracture vein	V3	Vein	<0.1	<0.2	12.4	18.1	<0.1	17.1	<0.1	<0.1	<0.1	0.1	9.6	<0.2	41.4	98.7
RCS067	RCS067_17_4	Trachyte	286NE46	Fracture vein	V3	Vein	<0.1	<0.2	12.7	18.0	<0.1	17.3	0.1	<0.1	0.1	0.1	9.2	<0.2	41.5	98.9
RCS067	RCS067_17_6	Trachyte	286NE46	Fracture vein	V3	Vein	<0.1	<0.2	13.5	18.2	<0.1	17.4	0.1	<0.1	<0.1	0.2	7.8	<0.2	42.2	99.4
RCS067	RCS067_17_8	Trachyte	286NE46	Fracture vein	V3	Vein	<0.1	<0.2	12.7	17.5	<0.1	16.9	<0.1	<0.1	<0.1	0.4	8.0	<0.2	40.6	96.1
RCS067	RCS067_19_1	Trachyte	286NE46	Fracture vein	V3	Vein	<0.1	<0.2	13.2	17.7	<0.1	17.1	<0.1	<0.1	<0.1	0.2	8.3	<0.2	41.2	97.7
RCS067	RCS067_19_2	Trachyte	286NE46	Fracture vein	V3	Vein	<0.1	<0.2	12.8	17.8	<0.1	17.1	<0.1	<0.1	<0.1	0.3	8.7	<0.2	41.2	97.8
RCS067	RCS067_19_4	Trachyte	286NE46	Fracture vein	V3	Vein	<0.1	<0.2	11.5	17.8	<0.1	17.0	<0.1	<0.1	<0.1	0.2	10.4	<0.2	40.4	97.2
RCS067	RCS067_19_7	Trachyte	286NE46	Fracture vein	V3	Vein	<0.1	<0.2	13.5	18.1	<0.1	17.4	0.1	<0.1	<0.1	0.2	8.2	<0.2	42.1	99.6
RCS067	RCS067_19_8	Trachyte	286NE46	Fracture vein	V3	Vein	<0.1	<0.2	13.1	18.1	<0.1	17.0	<0.1	<0.1	<0.1	0.5	9.2	<0.2	41.9	99.7
RCS069	RCS069_4_3	Andesite	NA	NA	A4	Patches	<0.1	<0.2	12.3	17.8	<0.1	17.1	<0.1	<0.1	<0.1	0.3	9.7	<0.2	41.0	98.3
RCS069	RCS069_4_4	Andesite	NA	NA	A4	Patches	<0.1	<0.2	12.9	17.5	<0.1	16.1	<0.1	<0.1	<0.1	0.8	8.8	<0.2	40.7	96.8
RCS069	RCS069_4_8	Andesite	NA	NA	A4	Patches	<0.1	<0.2	12.4	17.7	<0.1	17.1	0.1	<0.1	<0.1	0.4	9.7	<0.2	41.1	98.5
RCS069	RCS069_6_1	Andesite	NA	NA	A4	Patches	<0.1	<0.2	13.7	18.1	<0.1	17.0	<0.1	<0.1	<0.1	0.6	7.9	<0.2	42.1	99.5
RCS069	RCS069_6_2	Andesite	NA	NA	A4	Patches	0.1	<0.2	10.2	17.7	<0.1	16.9	<0.1	<0.1	<0.1	0.2	13.1	<0.2	40.0	98.2
RCS069	RCS069_6_3	Andesite	NA	NA	A4	Patches	<0.1	<0.2	12.5	17.9	<0.1	16.9	<0.1	<0.1	<0.1	0.5	9.7	<0.2	41.3	98.7

Sample	Reference	Lithology	Structure	Type	Alt	Texture	Na_pct	Mg_pct	Al_pct	Si_pct	K_pct	Ca_pct	Ti_pct	V_pct	Cr_pct	Mn_pct	Fe_pct	Co_pct	O_pct	Total_pct
RCS069	RCS069_6_4	Andesite	NA	NA	A4	Patches	<0.1	<0.2	13.0	17.8	<0.1	16.4	<0.1	<0.1	0.1	0.7	9.1	<0.2	41.4	98.5
RCS069	RCS069_10_2	Andesite	NA	NA	A4	Patches	<0.1	<0.2	12.6	17.9	<0.1	17.3	0.1	0.1	0.1	0.1	9.4	<0.2	41.3	98.9
RCS069	RCS069_10_4	Andesite	NA	NA	A4	Patches	<0.1	<0.2	13.1	17.9	<0.1	16.5	<0.1	<0.1	0.1	0.7	8.3	<0.2	41.2	97.8
RCS069	RCS069_10_5	Andesite	NA	NA	A4	Patches	<0.1	<0.2	12.9	17.7	<0.1	16.7	<0.1	<0.1	<0.1	0.4	8.6	<0.2	40.9	97.2
RCS069	RCS069_10_8	Andesite	NA	NA	A4	Patches	<0.1	<0.2	13.9	17.9	<0.1	16.0	<0.1	<0.1	<0.1	1.2	7.7	<0.2	41.7	98.4
RCS069	RCS069_12_1	Andesite	NA	NA	A4	Replacement	<0.1	<0.2	13.9	17.9	<0.1	16.8	<0.1	<0.1	0.1	0.6	7.3	<0.2	41.8	98.4
RCS069	RCS069_12_2	Andesite	NA	NA	A4	Replacement	<0.1	<0.2	13.3	17.9	<0.1	16.4	<0.1	0.2	<0.1	0.6	8.5	<0.2	41.6	98.3
RCS069	RCS069_12_3	Andesite	NA	NA	A4	Replacement	<0.1	<0.2	13.4	17.7	<0.1	16.4	<0.1	<0.1	<0.1	0.8	8.1	<0.2	41.4	97.8
RCS069	RCS069_14_1	Andesite	NA	NA	A4	Replacement	<0.1	<0.2	10.7	18.0	<0.1	15.2	0.2	0.1	<0.1	0.1	11.1	<0.2	39.7	95.1
RCS069	RCS069_14_2	Andesite	NA	NA	A4	Replacement	<0.1	<0.2	12.1	17.8	<0.1	17.1	0.1	0.1	<0.1	0.1	10.0	<0.2	40.9	98.2
RCS069	RCS069_16_1	Andesite	NA	NA	A4	Replacement	<0.1	<0.2	13.4	18.0	<0.1	17.1	<0.1	<0.1	<0.1	0.2	7.8	<0.2	41.5	98.0
RCS069	RCS069_16_2	Andesite	NA	NA	A4	Replacement	<0.1	<0.2	11.3	17.2	<0.1	16.5	<0.1	<0.1	<0.1	0.3	11.0	<0.2	39.6	95.8
RCS069	RCS069_16_3	Andesite	NA	NA	A4	Replacement	<0.1	<0.2	11.1	17.7	<0.1	16.9	<0.1	<0.1	<0.1	0.3	12.1	<0.2	40.5	98.5
RCS069	RCS069_16_4	Andesite	NA	NA	A4	Replacement	<0.1	<0.2	10.3	17.7	<0.1	16.7	<0.1	<0.1	<0.1	0.2	12.9	<0.2	39.7	97.5
RCS069	RCS069_18_2	Andesite	NA	NA	A4	Replacement	<0.1	<0.2	11.5	16.7	<0.1	16.7	<0.1	<0.1	0.1	<0.1	10.0	<0.2	39.0	94.0

Appendix D2

Sample	A	Li ppm					B ppm					Na ppm					Mg ppm					Al ppm				
		M	Md	R	25%	75%	M	Md	R	25%	75%	M	Md	R	25%	75%	M	Md	R	25%	75%	M	Md	R	25%	75%
RCS003	A4	122	126	68	102	136	4.9	5.4	2.9	4.1	5.7	204	178	292	132	220	103754	103354	23186	98538	107422	89157	88350	18300	86225	90900
RCS006	A3	111	116	35	107	118	5.8	5.9	5.8	4.5	6.6	192	88	683	66	272	116536	119940	36790	111099	124772	87389	87200	12900	86100	89500
RCS007	A4	123	126	60	117	136	3.8	3.4	3.9	3.1	4.6	204	186	523	156	196	103657	103753	24456	100811	107101	88295	87550	18000	86300	91100
RCS009	A4	98	98	35	90	106	7.7	6.5	11.3	6.0	8.0	170	177	151	134	197	116243	117342	30458	111847	119912	92092	92300	20900	86550	96600
RCS014	A6	276	279	41	266	284	13.9	12.9	9.0	12.5	15.3	139	99	391	86	113	148109	149194	23814	142106	152084	98211	98300	8900	95450	100400
RCS016	A6	136	138	10	130	140	19.2	21.9	14.6	10.6	25.2	58	63	20	46	66	88618	85493	23378	78492	101870	103367	101900	11600	98300	109900
RCS017	A3	202	206	45	180	220	3.4	3.4	0.0	3.4	3.4	514	518	234	402	622	126501	125984	12986	121786	131733	97850	98200	4200	95950	99400
RCS019	A2	185	185	154	162	197	3.8	4.1	2.5	2.8	4.5	142	139	197	81	186	106771	110020	30962	97079	115907	83408	81750	26300	78725	91000
RCS022	A2	185	186	99	171	190	6.9	6.2	5.2	5.7	8.1	263	278	565	81	385	114064	112761	27256	106279	121732	99600	99800	18400	96200	105350
RCS031	A4	521	519	256	472	547	7.0	6.4	7.3	5.3	8.3	161	170	159	120	181	130114	130695	24662	125299	135536	93458	93400	15400	90300	97100
RCS032	A4	354	367	180	349	385	5.8	5.7	7.6	4.8	6.4	187	186	231	158	199	119138	119496	24295	115396	122622	92742	93750	15500	89775	95100
RCS033	A4	451	462	257	354	548	8.4	7.9	8.9	6.7	9.8	36	34	54	31	39	138675	137654	17861	134213	142287	98984	98100	17000	96250	101500
RCS037	A3	107	104	28	99	116	3.5	3.5	0.1	3.5	3.6	1333	421	2864	248	2876	101417	102190	5502	99154	103295	92240	93000	10200	88700	95400
RCS038	A4	102	105	48	83	120	3.2	2.9	2.6	2.6	3.8	214	178	254	140	309	97680	98215	13376	94223	101268	81679	80500	17500	78650	85825
RCS040	A4	87	89	16	83	91	7.6	6.3	5.7	6.1	10.4	2676	2390	3268	1243	4259	103939	104307	17312	98202	110686	81143	78500	14900	76800	86900
RCS041	A3	86	86	32	77	94	5.1	4.7	5.6	3.1	7.3	1456	958	3034	640	2439	107611	105475	17742	102227	113795	80056	80100	24800	75500	81600
RCS042	A4	79	82	41	70	86	3.3	3.4	3.6	2.1	4.2	166	143	271	103	234	102730	101652	30095	97794	106386	84165	83400	26200	76500	91300
RCS047	A3	142	145	55	127	153	3.1	2.9	2.9	2.3	3.8	1739	1722	1266	1431	2090	120378	121394	24564	117242	124224	78268	78800	17300	76400	81700
RCS052	A6	143	137	94	120	170	6.3	5.8	5.7	4.2	8.9	562	576	269	426	692	108283	101218	62418	92088	128011	80860	81400	13500	76850	84600
RCS059	A3	124	119	53	109	144	4.7	4.2	5.3	2.9	7.0	769	837	738	463	1035	106636	109131	36644	104284	114070	90013	86900	21100	83000	99100
RCS061	A2	164	164	53	147	176	2.7	2.8	0.6	2.4	2.9	1074	238	3139	116	2279	134338	132648	13313	129044	137979	99586	100000	6400	99100	100500
RCS064	A4	89	89	36	82	96	2.6	2.3	1.9	1.9	3.4	35	36	28	30	39	73532	73587	18973	68088	78191	90132	89200	16200	87725	92425
RCS065	A6	191	190	117	138	243	-	-	-	-	-	187	89	1154	83	112	103547	104861	14254	97935	108027	97355	98800	11900	95400	100300
RCS068	A6	229	231	168	194	262	26.4	21.3	34.0	16.7	33.7	53	50	49	43	57	96743	96170	17916	94183	98033	108105	109200	13800	107600	110800
RCS069	A4	184	186	31	176	191	7.5	7.4	8.9	5.2	9.9	987	442	2449	350	1572	89889	91244	15036	86440	93379	108850	109600	10400	105525	110950
RCS070	A4	209	211	37	197	221	9.6	10.0	10.7	6.2	12.7	512	351	919	222	858	125689	125291	18868	120918	131877	101278	102100	12900	97100	104900
RCS074	A3	248	248	0	248	248	7.6	7.6	0.0	7.6	7.6	379	379	0	379	379	91058	91058	0	91058	91058	96400	96400	0	96400	96400
RCS074	V6	268	284	77	229	290	4.9	4.6	3.5	3.5	6.6	162	164	181	92	230	104956	104243	24944	95477	115149	94075	93750	13200	88675	99800
RCS075	A3	146	144	36	142	157	5.6	5.6	0.0	5.6	5.6	268	222	295	202	353	101439	104084	24362	93652	111042	93014	93700	15200	88700	98900
RCS076	A3	218	221	97	214	228	8.6	7.8	14.4	6.4	10.7	432	419	411	359	507	91001	88885	49469	80981	101611	89297	88550	16800	86875	93475
RCS079	A3	115	117	30	111	118	4.0	3.7	3.1	3.3	4.6	117	107	146	86	153	81150	81051	12244	80064	82983	86607	86100	18000	82400	92700
RCS087	A6	259	248	51	241	287	20.5	21.3	11.9	16.9	23.6	155	77	335	62	291	87323	85413	31134	82168	88670	94714	91500	17500	87700	101900
RCS096	A3	207	216	50	185	223	5.0	4.9	2.0	4.4	5.9	86	67	132	60	150	103679	109295	25016	95470	110413	95429	95100	6400	93900	98000
RCS104	A4	317	327	102	305	342	19.4	18.5	25.2	13.7	24.2	749	152	3758	70	1335	123322	125161	23301	117561	129955	90973	90900	9400	89300	93100

Si ppm	K ppm	Ca ppm	Ti ppm	V ppm
--------	-------	--------	--------	-------

M	Md	R	25%	75%	M	Md	R	25%	75%	M	Md	R	25%	75%	M	Md	R	25%	75%	M	Md	R	25%	75%
152003	148575	40141	142252	163433	912	780	1300	650	1153	5450	5343	4984	3758	7050	43	40	59	27	54	173	165	116	141	203
153238	151495	48716	144323	162478	300	251	627	208	290	3544	3241	4073	2775	4298	75	74	111	32	115	68	64	35	61	71
150366	148024	66173	145801	153180	276	237	452	186	328	4881	4802	4525	4317	5743	48	38	97	32	53	165	157	104	139	186
150334	149652	37951	145124	159078	628	427	1578	361	716	6016	5972	3392	5166	6644	47	42	80	20	65	91	87	61	74	102
157515	157141	15938	152770	162870	1554	1147	2428	1112	1888	4305	4225	1325	4002	4694	183	93	369	53	368	94	101	35	78	105
146433	141315	59536	119224	178760	1626	1523	2294	531	2825	1738	1714	662	1419	2081	63	68	25	49	74	88	83	32	75	107
128055	128648	10865	123208	132309	276	236	237	202	391	913	930	774	603	1206	35	36	32	19	50	187	183	91	149	228
133957	134955	31399	132804	142312	461	424	961	187	679	3434	2860	7042	1821	4218	917	184	3162	65	2069	161	155	115	130	190
158734	156407	58121	139627	173535	3375	3048	8116	1445	4648	6791	6108	14812	2057	10535	964	596	2116	451	1497	370	384	150	333	402
162918	158663	54469	151577	172967	283	290	274	204	347	8161	7393	9402	5923	11130	65	48	194	29	70	58	58	23	53	66
153718	152955	42662	149197	161292	395	347	549	312	448	7003	7061	4531	6384	7991	27	25	20	24	28	133	134	41	129	140
146220	146637	28145	141002	150824	136	129	185	117	153	2904	2712	3077	2333	3069	32	32	27	28	34	71	70	26	66	76
135311	132983	18693	130058	141729	1262	356	3522	239	2738	2214	2029	4780	767	3754	37	32	27	30	46	96	91	63	79	115
160545	159787	36514	148672	173584	990	704	1613	498	1655	10013	10000	7007	8066	11632	58	58	83	34	71	73	69	52	56	86
166606	164518	29658	158368	176940	662	462	919	379	1174	15335	15720	9778	11829	18909	46	52	48	25	69	70	71	36	58	79
173078	161406	68128	154678	200456	697	618	765	422	1007	17981	18293	23401	12717	23499	96	115	117	65	129	89	91	41	76	96
148488	150465	33837	141573	155360	233	197	629	124	281	7784	7882	9275	7060	8485	71	66	172	43	81	97	86	103	66	131
165152	164312	67103	152800	170872	332	300	593	205	411	7840	7972	7654	7021	8291	101	86	140	63	139	100	100	58	92	105
171372	160686	76849	153353	194736	643	584	248	549	768	11502	12783	10768	7819	14546	72	51	125	41	112	142	128	122	107	184
162387	156848	52396	151696	166676	2268	1807	3930	1065	3377	9436	10919	10935	4386	12905	123	103	174	95	140	193	191	122	161	237
135545	136483	26005	127680	142112	1339	875	2192	710	2447	2645	2335	4193	1538	4376	1327	1182	1797	884	2002	213	212	37	205	228
115639	114480	20409	112598	119401	89	80	195	46	127	551	523	697	403	599	41	27	87	22	61	93	94	38	84	101
124677	125508	14391	119333	127298	199	180	363	79	310	1757	2223	2581	517	2641	41	30	58	26	65	63	65	37	49	72
136688	132655	54600	126795	145590	1876	1627	4358	906	2554	1588	1603	1299	1340	1850	112	118	75	94	131	166	165	25	161	170
132375	131746	20342	127290	136583	722	668	1535	313	1131	3006	2296	5825	1663	3640	151	143	133	132	162	170	172	59	160	180
137974	135089	22519	132386	141879	183	182	193	141	250	2870	2447	2845	2264	3482	87	61	159	53	115	149	153	38	135	160
191545	191545	0	191545	191545	399	399	0	399	399	14794	14794	0	14794	14794	65	65	0	65	65	83	83	0	83	83
149362	141777	56241	130265	176045	168	133	284	62	309	5485	5422	6866	2639	8393	18	20	20	10	25	82	62	96	55	128
164344	162174	36240	157349	168915	461	203	1959	129	308	10642	10141	5004	9282	11638	47	41	75	36	56	73	71	28	68	76
158120	156801	38693	149720	167196	181	171	306	131	219	6136	5988	5481	5447	7076	89	88	208	64	108	129	130	127	102	147
125594	123600	25299	119686	130429	248	223	441	170	281	1920	1587	4662	1193	2124	21	20	20	17	23	48	48	12	46	50
128858	126610	31158	120814	129299	5901	5958	5273	4019	8230	2153	2250	1590	1681	2666	248	203	384	151	315	166	155	107	144	178
141498	136456	26535	131584	157000	5043	643	11397	447	10999	1878	420	5828	341	3392	45	34	38	29	66	94	95	14	87	100
142537	140173	24523	135948	150663	161	165	248	85	204	2080	1896	2136	1427	2703	35	32	36	30	47	143	125	103	109	189

Appendix D2

Cr ppm					Mn ppm					Fe ppm					Co ppm					Ni ppm				
M	Md	R	25%	75%	M	Md	R	25%	75%	M	Md	R	25%	75%	M	Md	R	25%	75%	M	Md	R	25%	75%
19.6	15.	44.8	12.	19.2	355	342	125	330	389	14592	14265	3520	14017	15036	96	96	22	91	99	51	51	21	46	56

7.1	7.7	8.0	5.0	8.6	363	366	169	352	406	12533	12744	2875	12105	13245	14	14	36	135	146	48	49	17	46	51
16.7	13.	44.6	7.0	23.2	335	327	171	309	349	13810	13624	3397	13244	14269	88	88	25	85	90	54	52	24	49	62
65.4	61.	140.	19.	100.	226	230	572	216	239	11749	11838	3392	10769	12278	11	11	28	111	120	13	14	59	121	149
7.3	4.7	25.0	4.3	5.1	277	279	519	269	289	52091	52887	1029	49921	54285	99	10	15	97	103	42	42	9	41	44
1.9	1.9	2.5	0.7	3.2	343	346	978	292	390	88172	89913	2271	75944	98659	10	10	37	81	118	36	37	11	30	41
2.5	1.6	5.1	1.0	4.9	244	244	139	239	250	16319	16245	1913	15574	17139	16	16	11	156	166	97	96	11	93	102
16.0	12.	29.7	6.8	29.1	169	176	835	138	195	17002	17003	7919	15379	19701	13	14	52	128	146	11	11	52	102	126
19.0	18.	13.2	16.	21.7	199	195	701	179	229	18846	18408	5972	17637	19924	16	17	50	160	174	18	17	71	161	204
228	135	634	107	241	523	524	220	480	545	85513	86105	2175	82112	90206	15	15	57	149	166	24	24	10	228	260
43.7	36.	76.9	29.	53.0	489	487	203	473	506	10126	10134	1770	97843	10575	12	12	33	121	132	20	20	82	198	218
1765	341	7774	37	2949	419	424	142	384	451	90119	90280	1544	87323	92375	14	14	27	136	146	19	19	47	190	204
11.4	4.1	23.1	2.8	23.5	204	205	74	202	206	17837	17974	1417	17351	18255	12	12	7	119	125	11	10	22	103	118
50.5	17.	215.	14.	83.7	155	154	485	142	171	14907	14828	2214	14245	15761	10	10	35	93	114	14	14	32	133	148
5.0	3.7	10.9	2.3	8.3	149	149	663	126	165	12624	12807	2871	11325	13907	10	10	41	93	123	12	11	23	116	128
20.5	12.	60.1	6.5	30.7	204	204	560	196	213	14555	14181	3267	14009	15366	11	11	32	106	123	12	11	49	109	141
27.3	2.8	155.	1.9	46.4	160	156	834	140	177	13908	13486	4620	12788	15119	10	11	44	97	116	89	83	81	74	109
30.6	15.	250.	4.1	31.9	162	161	408	157	172	89713	89638	2633	86167	91998	15	15	41	155	165	26	27	14	246	287
16.0	4.0	51.6	3.3	34.8	114	116	268	106	122	10733	10756	1632	10155	11300	16	14	10	131	213	31	24	22	227	437
69.4	68.	162.	43.	82.6	287	290	183	262	323	11484	11693	4356	99432	12354	16	15	77	147	183	26	27	15	213	325
44.8	40.	77.1	21.	72.2	595	592	830	567	614	12017	11922	1437	11684	12382	20	19	36	198	212	23	23	37	217	249
3.2	3.2	7.3	1.6	4.2	380	356	187	339	412	22802	22781	3953	21781	23649	58	58	19	52	61	10	11	6	8	12
6.6	3.4	19.9	2.7	11.2	597	575	221	541	678	16076	16426	5443	14572	17423	60	61	13	59	62	14	13	5	13	15
42.9	39.	68.5	20.	68.0	287	287	561	279	291	16185	16134	3476	15638	16709	71	72	12	68	75	89	91	28	83	96
3.4	2.1	12.2	1.4	3.4	583	585	841	559	607	17344	17484	2044	16680	17780	81	82	9	79	83	60	60	10	57	63
44.2	44.	87.5	0.5	88.0	878	880	213	798	946	12709	12873	2061	11963	13389	12	12	15	119	125	35	36	19	33	38
80.8	80.	0.0	80.	80.8	200	200	0	200	200	16751	16751	0	16751	16751	79	79	0	79	79	82	82	0	82	82
37.1	7.9	119.	6.9	96.6	197	208	829	159	224	15472	16092	4651	13160	17164	17	17	45	154	189	22	21	79	197	263
4.7	4.4	3.6	3.4	6.3	201	192	134	167	218	12257	11751	3803	11453	12744	14	15	42	138	157	10	10	36	102	119
21.2	13.	77.8	7.5	30.5	208	205	125	181	232	14927	15046	4227	14364	15529	74	74	39	68	80	62	64	43	51	70
2.4	2.0	5.0	0.8	3.5	235	232	589	223	249	21603	21601	3591	21384	22088	46	46	13	44	48	33	32	6	31	34
74.0	11.	367.	4.4	102.	148	144	614	128	164	13353	12922	3598	12829	13430	88	86	23	83	94	70	59	72	46	108
3.3	3.5	7.6	0.6	5.8	265	274	487	258	278	17207	17559	1643	16701	17688	11	11	7	115	119	47	33	55	32	57
115.	93.	277.	58.	184.	170	181	108	149	198	11945	12117	1610	11613	12190	59	59	11	57	61	13	13	42	129	147

Appendix D3

Cu ppm					Zn ppm					As ppm					Sr ppm					Y ppm				
M	Md	R	25%	75%	M	Md	R	25%	75%	M	Md	R	25%	75%	M	Md	R	25%	75%	M	Md	R	25%	75%
287	284	243	230	328	898	877	285	848	946	1.67	1.18	4.98	0.97	2.15	34	34	35	29	40	0.17	0.16	0.34	0.06	0.26
565	551	173	520	627	990	1013	357	959	1057	1.27	1.02	3.01	0.76	1.33	30	28	26	26	33	5.36	5.63	4.22	4.05	6.11
303	319	303	241	362	917	918	238	868	953	1.01	0.76	2.48	0.55	1.09	40	38	34	36	47	0.18	0.10	0.86	0.03	0.27
210	205	79	189	234	518	511	137	503	536	0.76	0.56	1.79	0.39	1.05	29	30	10	29	31	0.57	0.26	2.85	0.14	0.75
34	33	13	30	36	903	900	129	858	958	9.21	2.62	21.47	2.09	22.35	25	25	7	22	28	0.38	0.25	0.75	0.22	0.53
47	50	9	41	50	520	528	102	465	567	2.91	3.21	1.47	2.03	3.50	7	7	1	6	7	0.76	0.50	1.04	0.37	1.41
103	110	46	82	118	1293	1282	228	1209	1388	2.06	1.90	1.42	1.59	2.68	11	11	6	8	13	0.42	0.40	0.28	0.30	0.55
495	495	369	365	633	762	751	242	710	803	0.72	0.70	0.62	0.54	0.94	15	13	16	10	22	2.71	1.65	8.03	0.74	4.73
249	173	676	123	300	1342	1350	537	1207	1535	12.54	10.60	16.28	7.71	19.15	11	10	22	6	16	4.19	3.25	13.87	0.91	5.72
95	91	49	80	110	1788	1744	713	1626	1963	2.48	1.86	4.35	1.41	3.35	39	40	46	30	44	0.76	0.74	1.27	0.51	0.98
94	97	64	90	106	1480	1488	483	1408	1554	0.49	0.42	1.19	0.34	0.54	31	30	25	28	38	0.61	0.57	0.83	0.50	0.70
82	77	58	68	98	1249	1221	663	1082	1383	0.81	0.72	1.04	0.64	0.98	13	10	38	8	13	0.14	0.11	0.39	0.09	0.20
262	271	214	199	321	543	528	93	508	587	1.76	1.76	0.00	1.76	1.76	29	21	40	14	48	0.93	0.22	3.67	0.13	2.10
508	507	483	355	673	615	616	96	591	639	1.21	0.58	3.61	0.29	2.77	67	62	90	47	79	0.59	0.49	1.88	0.20	0.79
627	474	681	441	957	699	671	256	620	755	2.50	2.33	4.05	0.81	4.37	94	99	34	80	103	1.18	0.96	4.32	0.17	1.03
386	411	424	240	480	675	670	175	637	699	1.08	1.19	1.09	0.59	1.46	47	43	57	33	55	3.30	3.57	6.26	1.32	4.90
203	216	295	99	255	655	652	268	605	705	9.88	5.49	24.54	3.06	17.50	48	49	72	40	53	0.72	0.70	1.89	0.33	0.97
371	373	166	334	405	877	873	202	838	922	0.45	0.45	0.09	0.41	0.50	43	41	49	39	55	0.22	0.15	0.54	0.10	0.32
691	579	689	536	903	819	780	523	675	982	0.84	0.84	0.00	0.84	0.84	81	89	45	64	94	0.11	0.08	0.10	0.07	0.15
130	112	134	94	174	601	601	189	562	660	1.92	1.62	3.51	1.13	3.26	82	90	70	51	103	0.70	0.20	2.76	0.16	1.24
104	94	133	59	169	1316	1273	448	1212	1376	2.91	2.24	3.18	1.81	4.52	16	14	17	10	18	1.02	0.98	1.23	0.67	1.51
60	54	62	50	62	1109	1109	341	1047	1159	3.11	2.87	4.16	2.37	3.54	15	15	14	13	17	3.45	3.50	3.32	2.94	3.85
66	74	88	38	94	1474	1545	405	1379	1570	1.29	1.05	2.19	0.88	1.19	8	9	9	6	10	0.80	0.70	1.94	0.56	0.87
6	6	5	5	7	662	680	197	616	712	1.64	1.52	2.71	1.40	1.81	9	10	4	8	10	0.48	0.43	0.50	0.37	0.55
207	212	104	197	232	1092	1096	145	1070	1124	8.52	7.88	16.89	5.10	9.79	26	13	67	10	41	0.68	0.30	2.32	0.23	1.06
43	43	18	38	46	1210	1223	245	1167	1258	12.66	14.30	17.21	8.88	16.70	17	11	39	9	24	0.41	0.24	0.70	0.20	0.67
412	412	0	412	412	878	878	0	878	878	2.74	2.74	0.00	2.74	2.74	77	77	0	77	77	0.60	0.60	0.00	0.60	0.60
266	200	456	103	494	1026	970	342	913	1194	5.87	5.21	9.73	2.06	10.34	67	65	69	38	97	0.29	0.30	0.44	0.10	0.45
608	607	264	567	682	1074	1095	284	998	1143	3.86	3.01	7.52	2.38	5.75	66	61	29	55	77	1.32	0.62	4.29	0.28	2.22
407	402	290	370	462	534	536	216	511	562	13.52	9.75	32.09	5.52	20.28	46	46	37	40	51	2.97	2.42	6.07	1.86	3.47
154	157	147	106	186	574	578	90	557	599	4.49	4.18	4.87	2.90	6.22	10	10	9	8	12	2.48	2.08	6.91	1.14	2.79
357	338	203	284	398	2424	2483	838	2073	2639	0.68	0.66	0.46	0.57	0.85	23	24	11	22	25	0.83	0.86	0.63	0.52	1.09
142	123	132	109	174	1036	1032	71	1015	1047	2.60	2.48	1.47	2.03	3.16	20	10	41	9	28	0.69	0.48	0.88	0.43	1.06
303	307	447	212	353	223	248	226	161	273	5.97	3.83	16.15	2.37	9.12	15	11	28	8	26	0.85	0.80	0.90	0.60	1.23

Appendix D3

Zr ppm					Ag ppm					Cd ppm					Sn ppm					Sb ppm				
M	Md	R	25%	75%	M	Md	R	25%	75%	M	Md	R	25%	75%	M	Md	R	25%	75%	M	Md	R	25%	75%
5.85	5.89	5.44	4.37	7.34	0.13	0.13	0.00	0.13	0.13	0.28	0.27	0.07	0.26	0.30	1.55	1.55	1.12	1.41	1.63	0.17	0.18	0.19	0.10	0.22
2.64	2.10	6.63	1.55	2.86	0.06	0.06	0.00	0.06	0.06	0.25	0.25	0.06	0.23	0.28	1.26	1.20	1.01	1.07	1.33	0.21	0.19	0.28	0.13	0.30
6.28	6.41	7.35	4.20	7.81	0.02	0.02	0.00	0.02	0.02	0.22	0.22	0.25	0.16	0.24	0.60	0.56	0.54	0.50	0.68	0.14	0.14	0.15	0.10	0.15
4.02	3.61	3.77	3.19	4.78	-	-	-	-	-	0.26	0.26	0.07	0.24	0.29	1.32	1.30	1.18	1.18	1.56	0.22	0.22	0.00	0.22	0.22
12.16	11.10	16.66	8.68	13.25	-	-	-	-	-	0.41	0.41	0.27	0.27	0.54	0.83	0.86	0.35	0.68	0.93	0.54	0.49	0.53	0.37	0.74
6.01	2.58	13.16	1.14	14.30	0.13	0.13	0.00	0.13	0.13	-	-	-	-	-	1.22	1.33	0.52	0.90	1.42	0.88	0.87	0.54	0.62	1.16
0.08	0.08	0.09	0.03	0.13	-	-	-	-	-	-	-	-	-	-	1.00	0.99	0.04	0.98	1.02	0.31	0.32	0.09	0.27	0.34
0.53	0.36	1.94	0.09	0.83	-	-	-	-	-	0.33	0.26	0.23	0.25	0.48	1.65	1.31	1.82	1.22	2.22	0.44	0.40	0.80	0.22	0.54
6.98	2.91	33.83	0.79	7.25	-	-	-	-	-	0.38	0.37	0.16	0.33	0.46	1.91	2.02	0.97	1.57	2.22	0.99	0.95	1.26	0.54	1.38
4.67	3.73	5.63	3.13	6.14	-	-	-	-	-	0.29	0.25	0.29	0.23	0.37	1.40	1.33	0.98	1.21	1.70	0.16	0.16	0.12	0.13	0.19
1.49	1.54	0.74	1.36	1.60	0.05	0.05	0.02	0.04	0.06	0.30	0.27	0.32	0.23	0.35	1.39	1.37	0.73	1.28	1.47	0.41	0.40	0.85	0.28	0.47
1.15	1.09	1.38	0.84	1.32	-	-	-	-	-	0.28	0.26	0.09	0.25	0.32	1.34	1.33	0.94	1.25	1.40	0.16	0.15	0.09	0.13	0.19
0.32	0.20	0.79	0.06	0.64	-	-	-	-	-	-	-	-	-	-	0.56	0.57	0.22	0.47	0.64	-	-	-	-	-
2.19	1.38	9.90	0.46	2.73	0.61	0.40	1.57	0.27	0.86	0.15	0.14	0.07	0.12	0.18	0.79	0.68	0.88	0.61	0.93	0.22	0.20	0.24	0.15	0.31
1.68	1.46	2.65	0.99	2.70	0.34	0.09	1.01	0.06	0.74	0.14	0.14	0.00	0.14	0.14	0.83	0.71	0.99	0.49	1.28	0.59	0.63	0.41	0.37	0.78
2.90	3.33	4.99	1.98	3.92	0.07	0.06	0.12	0.05	0.08	-	-	-	-	-	1.42	1.07	3.28	0.93	1.69	0.95	1.07	1.16	0.63	1.17
8.14	8.06	16.28	3.75	11.60	0.17	0.10	0.56	0.05	0.23	0.31	0.33	0.24	0.19	0.40	0.50	0.48	0.62	0.41	0.61	0.69	0.45	1.30	0.28	1.25
2.53	1.78	10.45	1.36	2.81	-	-	-	-	-	0.16	0.16	0.02	0.16	0.17	0.93	0.75	3.35	0.61	0.91	0.15	0.12	0.23	0.10	0.22
0.77	0.44	1.82	0.25	1.46	-	-	-	-	-	-	-	-	-	-	0.79	0.88	0.54	0.52	0.97	0.42	0.42	0.00	0.42	0.42
0.34	0.11	1.10	0.06	0.79	0.08	0.08	0.12	0.02	0.14	0.15	0.15	0.03	0.13	0.16	0.65	0.53	0.96	0.44	0.85	0.66	0.37	1.75	0.23	1.15
0.54	0.30	0.97	0.27	1.03	0.05	0.05	0.05	0.03	0.07	-	-	-	-	-	0.67	0.67	0.70	0.49	0.68	1.24	1.01	3.01	0.80	1.13
0.54	0.40	1.23	0.33	0.68	-	-	-	-	-	0.20	0.18	0.20	0.17	0.24	0.78	0.78	0.36	0.68	0.88	0.20	0.19	0.24	0.17	0.25
0.32	0.09	1.59	0.07	0.43	-	-	-	-	-	0.30	0.28	0.11	0.25	0.36	0.94	0.83	0.91	0.70	1.17	0.42	0.41	0.51	0.17	0.68
1.72	1.62	1.59	1.44	1.88	0.05	0.03	0.09	0.03	0.08	0.24	0.23	0.25	0.16	0.26	0.78	0.79	0.64	0.58	0.90	0.38	0.30	0.62	0.28	0.46
5.01	4.52	7.20	3.68	5.79	0.05	0.04	0.09	0.04	0.08	0.26	0.23	0.09	0.23	0.32	0.68	0.63	0.78	0.50	0.81	1.73	0.84	6.58	0.51	2.37
2.10	2.44	4.59	0.45	3.10	-	-	-	-	-	0.14	0.14	0.00	0.14	0.14	0.53	0.52	0.35	0.42	0.64	0.85	0.54	2.10	0.36	1.40
7.22	7.22	0.00	7.22	7.22	-	-	-	-	-	-	-	-	-	-	4.04	4.04	0.00	4.04	4.04	-	-	-	-	-
0.68	0.36	1.94	0.10	1.57	-	-	-	-	-	-	-	-	-	-	0.46	0.44	0.40	0.27	0.67	1.04	0.88	1.72	0.26	1.98
0.49	0.15	2.01	0.11	0.81	-	-	-	-	-	-	-	-	-	-	0.99	0.77	1.34	0.73	1.04	0.53	0.40	0.65	0.34	0.84
9.76	9.80	25.48	4.20	13.17	0.02	0.02	0.02	0.01	0.03	0.15	0.15	0.09	0.13	0.19	1.15	1.10	1.64	0.87	1.41	0.91	0.61	2.24	0.42	1.34
0.28	0.17	1.09	0.08	0.39	0.03	0.03	0.00	0.03	0.03	-	-	-	-	-	0.64	0.60	0.50	0.56	0.71	0.67	0.33	2.18	0.15	0.98
2.91	2.84	1.62	2.39	3.60	0.09	0.09	0.00	0.09	0.09	2.28	2.11	3.26	1.71	3.00	2.04	1.90	2.48	1.49	2.22	0.22	0.22	0.23	0.14	0.30
0.41	0.07	1.75	0.04	0.52	-	-	-	-	-	0.42	0.42	0.00	0.42	0.42	1.32	1.38	0.70	1.20	1.53	0.37	0.37	0.31	0.21	0.52
1.45	1.37	1.98	0.87	2.11	-	-	-	-	-	0.21	0.21	0.00	0.21	0.21	1.16	1.28	0.78	0.94	1.34	0.51	0.22	1.95	0.16	0.67

Appendix D3

Zr ppm					Ag ppb					Cd ppm					Sn ppm					Sb ppm					Ba ppm	
M	Md	R	25%	75%	M	Md	R	25%	75%	M	Md	R	25%	75%	M	Md	R	25%	75%	M	Md	R	25%	75%	M	Md
5.85	5.89	5.44	4.37	7.34	0.13	0.13	0.00	0.13	0.13	0.28	0.27	0.07	0.26	0.30	1.55	1.55	1.12	1.41	1.63	0.17	0.18	0.19	0.10	0.22	26.5	22.4
2.64	2.10	6.63	1.55	2.86	0.06	0.06	0.00	0.06	0.06	0.25	0.25	0.06	0.23	0.28	1.26	1.20	1.01	1.07	1.33	0.21	0.19	0.28	0.13	0.30	68.6	74.9
6.28	6.41	7.35	4.20	7.81	0.02	0.02	0.00	0.02	0.02	0.22	0.22	0.25	0.16	0.24	0.60	0.56	0.54	0.50	0.68	0.14	0.14	0.15	0.10	0.15	24.6	22.7
4.02	3.61	3.77	3.19	4.78	-	-	-	-	-	0.26	0.26	0.07	0.24	0.29	1.32	1.30	1.18	1.18	1.56	0.22	0.22	0.00	0.22	0.22	21.2	16.6
12.16	11.10	16.66	8.68	13.25	-	-	-	-	-	0.41	0.41	0.27	0.27	0.54	0.83	0.86	0.35	0.68	0.93	0.54	0.49	0.53	0.37	0.74	9.9	9.8
6.01	2.58	13.16	1.14	14.30	0.13	0.13	0.00	0.13	0.13	-	-	-	-	-	1.22	1.33	0.52	0.90	1.42	0.88	0.87	0.54	0.62	1.16	22.4	16.5
0.08	0.08	0.09	0.03	0.13	-	-	-	-	-	-	-	-	-	-	1.00	0.99	0.04	0.98	1.02	0.31	0.32	0.09	0.27	0.34	15.2	12.1
0.53	0.36	1.94	0.09	0.83	-	-	-	-	-	0.33	0.26	0.23	0.25	0.48	1.65	1.31	1.82	1.22	2.22	0.44	0.40	0.80	0.22	0.54	10.1	7.0
6.98	2.91	33.83	0.79	7.25	-	-	-	-	-	0.38	0.37	0.16	0.33	0.46	1.91	2.02	0.97	1.57	2.22	0.99	0.95	1.26	0.54	1.38	13.9	12.8
4.67	3.73	5.63	3.13	6.14	-	-	-	-	-	0.29	0.25	0.29	0.23	0.37	1.40	1.33	0.98	1.21	1.70	0.16	0.16	0.12	0.13	0.19	25.8	25.5
1.49	1.54	0.74	1.36	1.60	0.05	0.05	0.02	0.04	0.06	0.30	0.27	0.32	0.23	0.35	1.39	1.37	0.73	1.28	1.47	0.41	0.40	0.85	0.28	0.47	68.4	58.9
1.15	1.09	1.38	0.84	1.32	-	-	-	-	-	0.28	0.26	0.09	0.25	0.32	1.34	1.33	0.94	1.25	1.40	0.16	0.15	0.09	0.13	0.19	17.5	17.3
0.32	0.20	0.79	0.06	0.64	-	-	-	-	-	-	-	-	-	-	0.56	0.57	0.22	0.47	0.64	-	-	-	-	-	17.6	9.9
2.19	1.38	9.90	0.46	2.73	0.61	0.40	1.57	0.27	0.86	0.15	0.14	0.07	0.12	0.18	0.79	0.68	0.88	0.61	0.93	0.22	0.20	0.24	0.15	0.31	1.9	2.0
1.68	1.46	2.65	0.99	2.70	0.34	0.09	1.01	0.06	0.74	0.14	0.14	0.00	0.14	0.14	0.83	0.71	0.99	0.49	1.28	0.59	0.63	0.41	0.37	0.78	2.4	2.5
2.90	3.33	4.99	1.98	3.92	0.07	0.06	0.12	0.05	0.08	-	-	-	-	-	1.42	1.07	3.28	0.93	1.69	0.95	1.07	1.16	0.63	1.17	3.7	2.6
8.14	8.06	16.28	3.75	11.60	0.17	0.10	0.56	0.05	0.23	0.31	0.33	0.24	0.19	0.40	0.50	0.48	0.62	0.41	0.61	0.69	0.45	1.30	0.28	1.25	0.5	0.4
2.53	1.78	10.45	1.36	2.81	-	-	-	-	-	0.16	0.16	0.02	0.16	0.17	0.93	0.75	3.35	0.61	0.91	0.15	0.12	0.23	0.10	0.22	1.6	0.7
0.77	0.44	1.82	0.25	1.46	-	-	-	-	-	-	-	-	-	-	0.79	0.88	0.54	0.52	0.97	0.42	0.42	0.00	0.42	0.42	11.5	12.1
0.34	0.11	1.10	0.06	0.79	0.08	0.08	0.12	0.02	0.14	0.15	0.15	0.03	0.13	0.16	0.65	0.53	0.96	0.44	0.85	0.66	0.37	1.75	0.23	1.15	4.5	3.0
0.54	0.30	0.97	0.27	1.03	0.05	0.05	0.05	0.03	0.07	-	-	-	-	-	0.67	0.67	0.70	0.49	0.68	1.24	1.01	3.01	0.80	1.13	18.7	16.8
0.54	0.40	1.23	0.33	0.68	-	-	-	-	-	0.20	0.18	0.20	0.17	0.24	0.78	0.78	0.36	0.68	0.88	0.20	0.19	0.24	0.17	0.25	2.6	2.7
0.32	0.09	1.59	0.07	0.43	-	-	-	-	-	0.30	0.28	0.11	0.25	0.36	0.94	0.83	0.91	0.70	1.17	0.42	0.41	0.51	0.17	0.68	11.4	9.9
1.72	1.62	1.59	1.44	1.88	0.05	0.03	0.09	0.03	0.08	0.24	0.23	0.25	0.16	0.26	0.78	0.79	0.64	0.58	0.90	0.38	0.30	0.62	0.28	0.46	29.7	27.0
5.01	4.52	7.20	3.68	5.79	0.05	0.04	0.09	0.04	0.08	0.26	0.23	0.09	0.23	0.32	0.68	0.63	0.78	0.50	0.81	1.73	0.84	6.58	0.51	2.37	4.5	4.1
2.10	2.44	4.59	0.45	3.10	-	-	-	-	-	0.14	0.14	0.00	0.14	0.14	0.53	0.52	0.35	0.42	0.64	0.85	0.54	2.10	0.36	1.40	5.6	5.4
7.22	7.22	0.00	7.22	7.22	-	-	-	-	-	-	-	-	-	-	4.04	4.04	0.00	4.04	4.04	-	-	-	-	-	8.9	8.9
0.68	0.36	1.94	0.10	1.57	-	-	-	-	-	-	-	-	-	-	0.46	0.44	0.40	0.27	0.67	1.04	0.88	1.72	0.26	1.98	4.7	4.6
0.49	0.15	2.01	0.11	0.81	-	-	-	-	-	-	-	-	-	-	0.99	0.77	1.34	0.73	1.04	0.53	0.40	0.65	0.34	0.84	13.1	9.6
9.76	9.80	25.48	4.20	13.17	0.02	0.02	0.02	0.01	0.03	0.15	0.15	0.09	0.13	0.19	1.15	1.10	1.64	0.87	1.41	0.91	0.61	2.24	0.42	1.34	7.7	7.6
0.28	0.17	1.09	0.08	0.39	0.03	0.03	0.00	0.03	0.03	-	-	-	-	-	0.64	0.60	0.50	0.56	0.71	0.67	0.33	2.18	0.15	0.98	25.4	25.9
2.91	2.84	1.62	2.39	3.60	0.09	0.09	0.00	0.09	0.09	2.28	2.11	3.26	1.71	3.00	2.04	1.90	2.48	1.49	2.22	0.22	0.22	0.23	0.14	0.30	222.1	214.0
0.41	0.07	1.75	0.04	0.52	-	-	-	-	-	0.42	0.42	0.00	0.42	0.42	1.32	1.38	0.70	1.20	1.53	0.37	0.37	0.31	0.21	0.52	11.3	9.6
1.45	1.37	1.98	0.87	2.11	-	-	-	-	-	0.21	0.21	0.00	0.21	0.21	1.16	1.28	0.78	0.94	1.34	0.51	0.22	1.95	0.16	0.67	11.6	12.1

Appendix D3

Ba ppm			La ppm					Ce ppm					Pb ppm					Bi ppm					U ppm				
R	0.3	75%	M	Md	R	25%	75%	M	Md	R	25%	75%	M	Md	R	25%	75%	M	Md	R	25%	75%	M	Md	R	25%	75%
39.1	17.1	31.7	0.09	0.07	0.26	0.03	0.12	0.20	0.16	0.50	0.07	0.32	4.6	4.6	9.4	2.3	5.6	0.03	0.03	0.00	0.03	0.03	0.04	0.04	0.05	0.02	0.04
43.6	54.6	79.5	2.17	2.05	3.88	1.16	2.72	3.13	2.62	8.38	1.42	4.09	6.9	7.0	5.9	6.1	8.3	-	-	-	-	-	0.04	0.04	0.04	0.03	0.05
22.1	19.6	27.7	0.08	0.04	0.39	0.01	0.09	0.20	0.03	1.34	0.01	0.27	2.1	1.9	2.7	1.5	2.5	0.02	0.02	0.00	0.01	0.02	0.02	0.02	0.08	0.01	0.03
28.8	13.1	29.2	0.64	0.28	3.43	0.15	0.65	1.56	0.68	8.36	0.32	1.63	0.7	0.6	0.9	0.5	0.7	0.12	0.12	0.05	0.09	0.14	0.04	0.03	0.05	0.02	0.05
4.0	8.9	11.0	0.12	0.02	0.58	0.02	0.19	0.25	0.02	1.24	0.01	0.46	2.8	2.9	3.2	2.0	3.7	-	-	-	-	-	0.20	0.16	0.35	0.10	0.31
24.0	13.3	37.3	0.44	0.19	0.86	0.14	1.00	0.56	0.14	1.33	0.10	1.43	0.5	0.5	0.0	0.5	0.5	-	-	-	-	-	0.10	0.06	0.17	0.05	0.21
15.1	11.0	22.6	0.15	0.15	0.10	0.10	0.19	0.16	0.17	0.11	0.11	0.20	3.6	3.0	2.9	2.8	5.1	0.05	0.05	0.00	0.05	0.05	0.21	0.23	0.18	0.13	0.29
15.0	5.9	15.4	0.58	0.19	2.50	0.11	0.86	1.59	0.50	6.57	0.20	2.31	38.2	37.1	59.5	26.3	55.7	0.07	0.06	0.06	0.05	0.11	0.43	0.16	1.94	0.11	0.53
31.5	7.3	16.3	0.64	0.62	1.26	0.19	1.04	2.37	2.36	5.30	0.66	3.96	10.6	8.6	27.3	6.3	11.4	-	-	-	-	-	0.34	0.35	0.59	0.16	0.54
29.6	18.7	32.5	1.64	1.63	2.57	1.10	2.25	1.44	1.04	3.56	0.65	1.81	8.7	5.7	23.5	2.7	12.1	0.05	0.05	0.00	0.05	0.05	0.08	0.06	0.15	0.04	0.12
84.6	44.5	95.0	0.20	0.14	0.75	0.10	0.22	0.32	0.14	2.26	0.06	0.35	1.5	1.4	1.4	1.3	1.6	-	-	-	-	-	0.03	0.03	0.04	0.02	0.03
28.2	12.4	21.1	0.08	0.06	0.17	0.03	0.11	0.15	0.11	0.42	0.06	0.23	2.7	2.2	4.9	2.0	2.8	-	-	-	-	-	0.03	0.03	0.06	0.02	0.04
50.2	5.1	33.9	0.41	0.21	1.12	0.14	0.79	0.94	0.78	2.16	0.38	1.59	5.4	4.4	8.3	2.7	8.5	-	-	-	-	-	0.17	0.19	0.18	0.11	0.23
3.8	0.7	2.7	0.12	0.03	0.85	0.02	0.17	0.25	0.07	1.04	0.05	0.44	0.8	0.7	1.3	0.4	1.0	-	-	-	-	-	0.17	0.14	0.32	0.06	0.31
1.5	2.1	2.6	0.09	0.09	0.18	0.02	0.15	0.49	0.30	1.53	0.10	0.97	4.3	0.9	20.1	0.4	4.5	-	-	-	-	-	0.11	0.10	0.15	0.08	0.17
7.7	2.0	5.1	0.19	0.17	0.56	0.07	0.21	0.55	0.58	0.85	0.21	0.84	3.5	2.7	7.1	2.0	4.3	-	-	-	-	-	0.23	0.22	0.38	0.10	0.34
1.8	0.3	0.5	0.35	0.24	1.47	0.11	0.42	0.37	0.22	1.83	0.08	0.43	2.3	2.0	4.3	1.1	3.2	-	-	-	-	-	0.16	0.12	0.37	0.08	0.26
7.9	0.5	1.9	0.09	0.03	0.47	0.01	0.14	0.16	0.04	1.06	0.01	0.23	1.4	1.4	1.7	1.1	1.6	0.22	0.09	0.64	0.06	0.37	0.10	0.07	0.27	0.06	0.12
10.1	7.0	15.7	0.03	0.03	0.06	0.01	0.06	0.07	0.03	0.21	0.02	0.14	1.5	0.7	3.2	0.6	2.7	-	-	-	-	-	0.12	0.06	0.27	0.04	0.23
10.5	2.1	6.9	0.12	0.09	0.20	0.05	0.21	0.32	0.16	0.99	0.06	0.68	8.4	7.9	16.0	5.7	10.0	-	-	-	-	-	0.12	0.11	0.16	0.06	0.18
19.5	13.5	21.7	0.26	0.15	0.74	0.07	0.43	0.88	0.49	2.36	0.38	1.49	31.0	27.2	77.1	5.6	51.1	-	-	-	-	-	0.16	0.17	0.19	0.13	0.21
1.9	2.2	3.0	2.30	2.17	2.77	1.87	2.67	1.15	0.80	5.82	0.55	1.17	247	245	244	200	300	0.04	0.04	0.06	0.03	0.06	0.13	0.13	0.14	0.11	0.16
19.4	8.4	13.9	0.45	0.24	1.70	0.08	0.60	0.73	0.20	3.15	0.07	0.79	5.9	0.9	23.6	0.7	13.3	-	-	-	-	-	0.48	0.32	1.38	0.09	0.80
38.1	18.8	33.4	0.05	0.03	0.23	0.02	0.06	0.10	0.04	0.65	0.01	0.11	1.6	1.6	1.2	1.3	1.8	-	-	-	-	-	0.02	0.02	0.03	0.02	0.02
8.2	2.5	6.7	0.54	0.18	2.09	0.05	0.88	0.72	0.11	3.03	0.02	1.07	3.2	2.4	3.4	2.2	4.7	0.03	0.03	0.05	0.02	0.04	0.08	0.05	0.29	0.03	0.10
5.3	4.4	6.5	0.27	0.03	1.13	0.02	0.52	0.50	0.06	2.47	0.02	0.83	1.8	1.5	2.8	1.3	2.2	-	-	-	-	-	0.07	0.05	0.11	0.04	0.10
0.0	8.9	8.9	0.04	0.04	0.00	0.04	0.04	0.21	0.21	0.00	0.21	0.21	2.4	2.4	0.0	2.4	2.4	-	-	-	-	-	0.21	0.21	0.00	0.21	0.21
0.7	4.4	5.0	0.22	0.12	0.60	0.04	0.49	0.19	0.09	0.56	0.03	0.46	3.4	3.3	3.6	1.8	4.9	-	-	-	-	-	0.22	0.19	0.21	0.15	0.31
25.1	9.5	11.5	0.04	0.03	0.06	0.02	0.06	0.03	0.03	0.05	0.02	0.05	15.0	9.0	48.6	5.4	21.4	0.07	0.07	0.01	0.07	0.07	0.29	0.26	0.43	0.19	0.37
9.1	6.6	8.0	0.21	0.17	0.61	0.08	0.28	0.35	0.33	1.02	0.14	0.50	10.6	8.6	22.7	5.8	13.2	0.02	0.02	0.01	0.02	0.02	0.42	0.34	0.62	0.29	0.59
23.5	16.0	30.4	0.32	0.20	0.94	0.08	0.43	0.56	0.30	1.98	0.12	0.73	70.1	82.8	166.6	13.4	105.0	0.03	0.03	0.02	0.02	0.04	0.19	0.19	0.18	0.13	0.25
122.0	201.0	273.0	0.65	0.64	1.33	0.24	0.92	1.54	0.24	8.34	0.13	1.08	18.9	16.2	18.7	14.0	25.1	0.04	0.03	0.02	0.03	0.05	0.03	0.02	0.02	0.02	0.03
7.7	9.2	15.0	0.56	0.37	1.37	0.24	0.70	1.31	0.89	3.52	0.59	1.44	69.7	89.5	89.0	34.6	99.1	-	-	-	-	-	0.67	0.20	1.97	0.16	1.51
13.4	9.0	14.7	0.50	0.14	2.74	0.02	0.63	0.68	0.08	3.18	0.02	1.62	0.2	0.1	0.7	0.1	0.4	-	-	-	-	-	0.04	0.03	0.03	0.03	0.05

Appendix D3

Appendix D4

Sample	A	Li ppm					Be ppm					B ppm					Na ppm					Mg ppm				
		M	Md	R	0.25	75%	M	Md	R	0.25	75%	M	Md	R	0.25	75%	M	Md	R	0.25	75%	M	Md	R	0.25	75%
RCS003	A4	2.16	2.30	2.42	1.28	2.89	2.05	2.01	2.70	1.21	2.97	60	64	89	34	85	2194	1779	5210	684	3859	944	503	2677	318	1700
RCS006	A3	1.88	1.56	2.07	1.21	2.88	-	-	-	-	-	22	21	15	17	27	2167	572	7076	460	4446	858	448	3174	235	1248
RCS007	A4	2.39	2.52	4.34	1.13	3.79	1.45	1.45	1.47	1.08	1.79	64	60	128	39	81	640	398	2408	189	1042	904	457	3253	228	1005
RCS008	A5	2.53	2.53	0.00	2.53	2.53	1.61	1.44	2.63	1.01	1.91	57	42	136	25	75	109	78	329	26	141	90	92	133	60	112
RCS008	V3	2.64	2.64	0.00	2.64	2.64	1.48	1.34	2.14	0.68	2.10	39	26	109	12	62	19	18	21	14	25	104	79	187	67	183
RCS009	A4	2.43	1.69	6.88	1.13	2.98	1.66	1.40	4.14	0.84	1.96	66	65	115	38	77	1350	926	4149	498	1908	827	391	4988	246	710
RCS014	A6	6.16	4.72	13.17	2.54	8.75	4.11	3.70	7.73	2.48	5.36	82	70	134	50	100	80	50	202	29	123	2201	1428	6355	906	3387
RCS016	A6	11.00	9.35	30.77	4.10	15.17	3.33	3.13	5.24	2.01	4.35	31	26	104	16	36	75	67	172	43	96	1401	1344	2613	837	1852
RCS017	V2	3.49	1.56	14.17	1.17	4.10	1.36	1.15	3.45	0.76	1.89	58	48	125	34	79	507	192	2831	104	641	964	390	4870	289	874
RCS018	A3	1.17	1.17	0.00	1.17	1.17	3.23	3.19	2.98	1.99	4.52	32	21	56	15	60	41	41	37	23	60	208	204	55	187	234
RCS018	V2	1.33	1.37	0.53	1.04	1.57	4.01	2.88	14.51	1.69	4.78	31	28	106	16	34	54	23	135	16	104	203	228	224	169	237
RCS023	BX	2.57	2.57	0.31	2.41	2.73	2.74	2.14	5.75	1.99	3.23	304	102	1222	64	614	549	431	1820	241	696	797	429	2170	254	1279
RCS031	A4	5.62	3.63	15.47	1.71	9.21	3.30	2.67	8.40	1.70	4.15	114	122	215	42	164	275	147	816	94	445	1350	699	3994	364	2506
RCS031	V3	3.07	2.40	4.72	1.04	5.76	2.61	1.93	5.06	1.49	3.79	115	116	252	55	148	14	11	22	8	20	168	67	825	52	257
RCS032	A4	6.13	2.57	15.47	1.55	11.74	2.81	2.55	6.22	1.41	4.07	131	128	245	92	167	846	286	4600	105	1149	1319	477	5721	340	1339
RCS033	A4	6.74	4.74	20.06	2.28	10.27	2.30	2.44	6.34	1.29	2.63	105	78	242	55	167	258	100	1135	26	390	2114	1331	5606	803	3506
RCS037	A3	4.69	4.69	0.00	4.69	4.69	-	-	-	-	-	13	14	11	7	18	116	131	57	87	137	1876	648	6319	499	3866
RCS038	A4	3.95	3.61	4.74	2.24	5.83	4.38	4.05	6.62	2.42	5.84	6	6	5	5	7	138	83	524	34	141	1500	697	5629	467	1778
RCS038	V3	-	-	-	-	-	3.40	3.60	2.35	2.36	4.23	5	5	1	5	6	22	22	0	22	22	281	298	162	201	343
RCS040	A4	4.52	4.52	2.02	3.51	5.53	3.27	2.95	3.81	1.84	4.76	14	13	26	10	16	2034	1290	6275	88	4443	737	591	1732	462	880
RCS041	A3	3.08	2.29	10.54	1.41	3.21	3.39	2.44	7.40	1.68	5.45	8	8	10	6	10	2258	2020	6674	246	3349	542	470	890	347	768
RCS042	A4	2.84	1.98	5.16	1.18	4.82	1.70	1.57	3.42	0.94	2.54	7	7	12	5	8	723	100	4833	21	814	1043	459	6264	296	740
RCS046	A3	-	-	-	-	-	1.54	1.54	0.31	1.38	1.69	10	10	0	10	10	231	190	397	85	417	259	223	211	196	359
RCS047	A3	3.83	3.62	4.23	1.82	5.95	2.10	2.08	2.06	1.33	2.66	7	7	6	5	9	366	169	1677	85	394	1878	475	5394	250	4394
RCS047	V2	0.99	0.99	0.00	0.99	0.99	1.23	1.22	1.84	0.91	1.49	4	4	2	3	4	196	114	773	54	187	311	211	1868	153	312
RCS049	A3	-	-	-	-	-	-	-	-	-	-	5	5	0	5	5	852	352	3451	196	1295	646	449	1664	203	1151
RCS051	A3	1.83	1.00	5.89	0.80	1.87	3.00	2.61	6.34	1.70	4.31	8	7	16	3	13	735	448	3286	89	958	1486	555	5405	300	1840
RCS051	V2	1.21	0.97	1.02	0.83	1.85	2.81	1.67	12.92	0.67	3.34	6	4	18	3	7	205	112	926	42	320	598	241	3998	187	625
RCS052	A3	2.21	2.21	0.96	1.73	2.69	0.75	0.70	0.85	0.46	1.08	4	4	9	3	5	240	96	1001	43	455	450	414	840	205	606
RCS052	V2	1.20	1.15	1.14	1.10	1.50	1.76	1.69	3.40	1.01	2.34	6	6	9	4	8	69	43	289	15	114	735	474	3056	358	747
RCS056	A2	-	-	-	-	-	5.92	4.89	4.62	4.13	8.75	19	19	0	19	19	71	71	0	71	71	1050	881	1341	589	1680
RCS059	A3	-	-	-	-	-	2.42	2.25	2.82	1.56	3.11	27	20	52	13	46	956	226	5032	70	1529	490	403	1476	229	650
RCS064	A4	5.04	3.54	6.76	3.20	7.63	3.26	3.69	2.92	1.96	4.31	40	36	52	28	49	68	68	80	28	108	2457	1839	5625	769	4295
RCS065	A6	4.82	4.68	12.62	2.65	5.74	3.31	2.68	4.57	2.35	4.40	71	65	121	39	91	295	121	1719	53	364	1815	1040	7284	623	2836
RCS067	A5	3.88	4.01	4.08	2.56	4.77	4.62	3.24	10.78	1.22	8.40	123	128	215	77	176	276	58	2290	19	238	1803	1030	7201	427	1633
RCS067	V3	2.36	2.09	2.04	1.93	2.76	4.61	4.78	4.96	3.47	6.12	65	56	99	46	84	25	22	27	14	41	438	386	805	211	651
RCS069	A4	6.60	5.37	13.80	3.46	8.44	4.99	4.96	6.57	3.91	6.42	130	121	229	84	153	441	355	1451	63	552	2704	1485	6617	708	5820
RCS070	A4	3.67	3.60	3.29	2.30	5.11	3.13	2.62	4.75	1.88	4.26	30	22	46	12	53	386	198	1556	38	534	815	645	1895	159	1245
RCS070	V7	2.51	1.82	3.93	1.26	4.44	2.50	1.66	4.71	0.87	4.05	35	38	39	22	48	251	128	717	56	453	887	759	1779	427	1159
RCS073	A3	4.33	4.33	0.00	4.33	4.33	5.70	4.95	6.30	4.47	7.63	106	77	188	68	102	1324	66	4862	34	3280	138	122	200	81	185
RCS074	A3	2.33	2.05	1.53	1.71	3.24	2.85	2.65	5.18	1.13	4.28	104	106	109	60	152	345	79	1286	62	761	340	366	282	265	421
RCS074	V6	2.31	2.08	3.94	1.36	3.20	3.12	2.54	5.85	2.01	4.19	138	104	335	76	164	455	54	1949	32	805	420	227	1055	183	605
RCS075	A3	2.59	2.55	1.04	2.09	3.13	5.05	3.88	9.81	2.42	7.60	113	114	174	65	168	273	172	772	43	505	410	253	1017	198	552
RCS076	A3	1.99	1.71	4.20	0.99	2.66	1.25	1.35	2.03	0.82	1.51	159	117	409	84	220	88	51	358	26	116	587	518	1284	302	816
RCS078	V3	1.97	1.99	1.31	1.41	2.52	11.28	11.05	7.93	9.78	13.17	241	263	438	87	369	99	63	289	31	139	418	354	612	315	527
RCS078	V6	2.10	1.92	1.52	1.61	2.78	8.78	7.79	14.10	6.38	11.20	105	83	359	61	113	187	64	764	31	340	376	288	1458	194	411
RCS079	A3	2.28	2.28	1.33	1.98	2.75	3.61	3.85	6.72	1.78	4.62	239	221	235	189	274	1116	1291	2512	54	1874	761	539	1664	425	1126
RCS081	A5	11.16	11.16	9.29	6.51	15.80	2.53	2.53	0.00	2.53	2.53	63	62	85	25	103	-	-	-	-	-	1938	1944	3166	402	3468
RCS096	A3	3.44	3.44	0.00	3.44	3.44	5.68	5.68	0.00	5.68	5.68	258	258	0	258	258	79	79	0	79	79	3015	3015	0	3015	3015
RCS098	A5	1.93	1.77	2.23	1.33	2.35	5.22	4.91	7.11	3.71	6.80	44	40	67	28	61	114	62	479	41	156	255	128	1511	107	246
RCS099	A5	1.99	1.65	4.37	1.21	2.19	6.96	6.95	11.54	5.30	7.98	99	97	97	79	115	1178	398	6647	235	733	324	196	1121	161	404
RCS104	A4	4.63	4.67	5.54	3.43	5.97	4.15	3.30	3.26	3.15	5.44	278	276	203	253	332	2704	2754	7259	641	3252	1550	1326	2647	805	2058

Al ppm					Si ppm					P ppm					K ppm					Ca ppm				
M	Md	R	0.25	75%	M	Md	R	0.25	75%	M	Md	R	0.25	75%	M	Md	R	0.25	75%	M	Md	R	0.25	75%
129775	133750	49202	114263	142670	192609	193070	31423	184183	202709	198	138	361	120	304	267	110	1171	60	381	168023	168900	15700	166250	171200
120164	118050	22265	114528	126578	207743	206370	33241	198486	217370	-	-	-	-	-	45	36	110	27	45	171767	172500	6200	169650	173650
119080	113220	42031	110732	124426	183846	184653	35645	177113	190012	192	109	860	61	265	54	22	430	13	49	166074	166300	12300	164300	168500
133447	133992	10305	130817	136467	179487	181419	25898	172525	185097	511	477	968	262	662	154	45	394	12	406	165994	166800	10700	163500	168500
132974	132732	20180	129842	136447	183878	184217	8833	180485	186604	302	217	1026	81	487	5	5	1	5	6	167089	168400	10800	163900	169000
128456	130498	28207	123238	133106	188218	190810	60928	178544	196805	187	160	327	131	241	174	126	718	71	252	164243	167000	19900	157850	169375
125310	126197	25212	122750	130408	179614	180463	30125	172951	186722	153	96	968	77	123	115	93	338	39	186	167111	169200	18100	164300	171500
111954	116406	51693	99695	122639	173128	174081	92363	148185	201442	425	150	1948	138	443	568	441	2203	321	635	165632	166700	15400	164400	167800
129675	130421	17800	126029	132832	191869	191026	41743	184276	198200	247	217	633	113	343	103	35	1038	15	114	170885	171300	12200	169000	173100
122728	126969	22246	111643	129572	196930	197493	3862	195192	198106	432	368	285	321	606	9	9	0	9	9	169175	168900	2700	168175	170450
124983	124975	22344	115983	133621	187704	190430	20727	180949	194466	111	84	206	72	116	8	8	8	4	11	165336	166000	11400	162550	167700
127352	126142	29429	123024	129435	183986	182389	65735	168860	194533	137	113	470	94	136	51	39	165	16	65	164355	164350	10400	162450	166600
129297	129073	17911	124894	133921	192141	190499	30676	183383	201533	103	101	123	84	114	20	18	51	9	20	168321	168350	10400	167100	169575
130394	133881	24347	124232	136798	193926	193072	25142	189171	199216	71	76	59	44	93	19	19	24	7	31	166606	167000	19000	163450	170175
124320	123872	17996	118290	130241	193217	194207	44506	186140	198877	134	115	251	92	168	150	111	308	43	279	166395	166300	8800	164850	168550
132249	132004	30951	127826	134168	190157	190633	29184	182490	195161	159	124	377	84	197	419	118	2184	25	592	170395	171150	14500	168575	173250
125498	127330	14770	118761	131319	184827	183384	22667	177038	193337	124	124	0	124	124	480	633	725	42	767	167440	167500	10000	164050	170800
136062	134693	15962	131760	139844	183255	183656	26536	176055	187932	73	66	79	56	85	101	89	226	40	178	172494	172200	11000	170700	175250
130822	130674	7832	127879	133913	176543	176793	13930	170727	182109	71	73	13	64	77	8	8	4	7	10	171275	171700	6300	168275	173850
131570	131862	27652	128374	136017	189379	186613	45106	180983	193194	114	80	331	55	124	181	51	1134	17	200	176100	176500	9000	175150	178400
134186	132834	35788	130498	139417	190152	187065	44637	184427	196598	181	100	596	61	249	112	62	522	29	173	169300	169900	11400	168575	170975
126181	127876	34005	118273	132840	181272	179604	37704	175665	184796	100	61	594	44	95	118	55	468	32	124	168886	168500	10400	166750	170700
123331	125023	11808	117831	127139	186061	187007	16628	178679	192497	78	77	52	53	105	436	31	1228	25	1253	174625	175050	6800	171625	177200
123221	122441	20911	119302	125357	183271	184623	24541	177546	188781	193	131	287	119	278	182	47	811	21	287	167759	168300	12400	166100	170450
123410	124749	22542	119841	127440	181598	182527	25053	177969	186738	173	147	491	70	211	15	15	10	10	19	167900	167700	7200	166350	169350
125910	126213	27064	123095	128157	183257	182640	35672	172730	189423	181	155	193	118	223	371	248	1156	43	736	170600	171050	15300	169750	173125
124779	125815	21928	122227	127976	183925	184998	37544	178071	189294	116	103	267	78	126	78	46	355	18	72	169004	169150	15100	167200	171450
122541	122958	13343	119556	126222	188584	189284	15544	183322	193311	145	143	217	76	195	40	12	198	7	64	168213	167700	9900	166300	169200
122224	122235	15821	120755	124564	187205	189017	23621	179964	190475	101	90	112	76	142	119	53	621	22	117	170023	170600	6900	167650	171750
121995	122389	34173	117542	127240	184422	185894	24927	180926	188076	77	59	229	40	112	92	35	827	9	118	169772	170400	16800	167550	171750
117269	116512	6321	114998	120297	173854	174770	6967	170436	176355	97	97	0	97	97	358	111	1123	56	905	169375	169000	2900	168325	170800
127375	127037	20875	124567	131084	192570	191883	63117	183363	198771	112	110	176	66	147	180	35	2032	22	204	176070	176500	10200	174700	177600
123743	123339	18920	120169	125596	180770	182400	19906	177629	185346	303	129	604	88	692	61	28	241	12	90	165238	165250	8000	162550	167450
119729	119073	17517	116158	123595	177251	179380	23821	171641	183446	230	69	886	50	330	274	97	1225	27	460	167568	168600	15400	165075	170350
123848	122870	18626	120906	126620	191768	188245	73501	180495	195129	77	58	129	49	101	240	77	1180	30	204	169575	170000	11400	167600	171575
132759	133936	11841	130731	135162	192330	188301	57599	185167	196440	60	45	118	38	69	29	11	183	5	23	171993	172150	5300	170200	173650
127564	127364	36828	120825	130278	186716	185684	71357	172334	193741	108	91	153	78	125	275	109	1285	47	399	166347	167200	20700	164300	170500
116319	115090	10798	112673	121544	190603	187349	23955	184227	197058	271	212	456	72	528	391	123	2084	33	242	168729	169400	8000	168100	169900
111953	110164	36377	101124	124040	183959	182467	87721	164860	192831	281	153	972	87	415	335	322	796	152	422	170333	169900	5600	169300	171400
124950	120162	31873	118684	132095	193896	192439	63707	176854	203754	111	110	47	89	135	73	38	159	28	137	171845	171700	4600	170400	174000
128182	127690	10563	124364	131575	185428	183216	16320	180826	192576	586	519	274	483	757	11	11	5	9	14	173350	173200	4400	171850	174525
129982	129417	16830	127947	132149	191525	191192	58636	185569	193450	58	58	65	38	75	47	39	197	10	59	173156	173150	8400	171650	175125
131364	131322	20387	128471	134074	183607	183663	23939	180834	188944	125	134	150	68	168	287	25	1974	12	129	172459	172000	8900	171350	173700
123818	123135	14641	120122	128216	186859	186214	31665	182106	192766	64	62	72	43	78	70	43	325	19	104	171709	172000	8300	169900	173100
127566	127300	10759	125092	131270	183698	182879	8364	180803	187286	78	71	85	57	93	197	148	627	6	332	173350	173700	4900	171425	174550
125640	128267	20925	118491	131066	176935	177599	25281	173890	181141	56	56	4	54	58	65	24	465	16	46	171348	171800	25400	168750	175050
129288	129670	14752	125123	134267	182754	185649	15932	177200	187683	504	56	2648	50	763	50	14	292	12	28	172518	172700	8400	171300	174000
138465	140184	13237	132132	143079	225332	233779	70638	190118	252100	399	399	423	187	610	254	226	455	55	482	170075	171300	6900	166750	172175
117853	117853	0	117853	117853	169587	169587	0	169587	169587	-	-	-	-	-	290	290	0	290	290	168000	168000	0	168000	168000
125657	124930	30558	121462	130623	202738	199464	77032	193688	210828	236	272	323	127	326	111	41	611	19	161	165040	166500	17600	164300	167950
123131	122985	15573	121248	125291																				

Sc ppm					Ti ppm					V ppm					Cr ppm					Mn ppm					Fe ppm									
M	Md	R	0.25	75%	M	Md	R	0.25	75%	M	Md	R	0.25	75%	M	Md	R	0.25	75%	M	Md	R	0.25	75%	M	Md	R	0.25	75%	M	Md	R	0.25	75%
12.6	8.8	39.2	1.3	23.9	254	235	572	151	313	248	246	387	150	351	9.7	4.5	21.4	1.6	23.0	2449	2091	5711	1593	2973	100396	102510	87486	78866	124778					
1.2	0.9	2.0	0.8	2.2	172	119	505	100	169	110	55	300	21	232	-	-	-	-	-	1653	1485	2452	1308	2016	132508	134894	33617	123777	139692					
5.0	3.0	16.4	1.8	5.5	183	168	343	135	197	243	109	916	32	369	1.4	0.9	1.6	0.9	2.5	2897	2638	6581	1700	3025	112914	117972	78089	103780	128927					
6.0	4.0	17.6	2.0	11.4	278	265	555	177	352	262	239	784	212	266	11.9	4.1	109.6	2.3	7.2	3743	3348	5268	2498	4527	78179	79298	23629	72201	82422					
1.7	1.7	3.5	1.1	2.2	253	249	409	141	328	246	216	243	184	306	1.0	0.9	0.3	0.8	1.1	3686	2389	6516	1922	5565	81601	80615	38664	77220	85571					
23.4	6.7	204.5	1.1	26.2	362	346	413	267	439	275	272	427	170	347	11.8	5.3	79.5	1.9	10.3	1974	2037	2293	1588	2291	91628	93469	32800	87220	97329					
80.6	71.5	196.0	47.9	95.2	1146	778	4390	594	1371	545	489	606	402	635	1.6	1.7	1.0	1.2	2.0	6954	7388	6776	5594	8191	99220	97635	49278	92973	103864					
24.1	19.5	66.8	11.4	28.7	322	247	976	165	416	329	330	360	231	409	5.0	5.0	1.2	4.4	5.6	2025	1804	2599	1386	2705	91122	86661	67955	78140	98014					
1.5	0.8	6.0	0.5	1.5	324	251	793	183	396	204	199	339	124	275	-	-	-	-	-	2019	1660	4143	1369	2614	105234	106008	30010	100571	110108					
0.6	0.6	0.2	0.5	0.7	360	365	436	180	534	142	105	174	91	229	-	-	-	-	-	2637	3023	3943	754	4135	103871	103877	9694	99338	108400					
0.8	0.5	2.9	0.4	0.9	463	371	905	271	805	227	208	439	144	307	-	-	-	-	-	1488	1128	3758	716	1919	96741	95503	39363	84877	105215					
11.5	10.3	21.1	7.2	15.3	428	375	1057	265	537	422	426	637	304	586	12.5	12.5	22.8	5.3	17.1	5127	5394	4384	4590	5822	98196	96461	40591	93721	102590					
17.2	2.2	136.3	1.3	11.4	365	273	1030	185	526	213	191	207	171	282	33.4	8.7	135.3	3.7	71.2	2281	2157	3447	1652	2692	101898	104316	37069	94079	106890					
1.3	0.5	7.3	0.4	1.1	156	66	595	32	281	227	238	209	157	297	5.4	5.5	8.6	1.1	9.8	5753	6074	9273	2199	8662	96136	97414	36317	89280	104851					
10.7	2.1	77.7	0.6	5.9	80	78	132	44	122	223	219	258	190	268	3.3	2.9	4.9	1.8	4.5	1992	1936	3759	1129	2629	111177	108919	37616	101016	120661					
12.7	11.9	29.0	3.7	16.8	393	261	1499	175	520	227	226	192	187	278	387.8	46.9	1137.1	7.2	947.8	3314	1784	10064	1161	5802	98529	97119	35345	92614	109106					
9.5	2.2	37.4	1.4	21.3	1219	609	3558	267	2477	421	463	223	319	502	27.8	27.8	0.0	27.8	27.8	1238	888	1865	747	1904	99879	96216	18218	93632	107958					
47.7	34.2	107.4	20.5	75.6	517	438	962	338	641	247	261	259	199	293	4.0	3.8	7.0	1.8	5.5	1454	1195	2043	974	2094	85989	86680	16140	81507	90781					
10.7	11.1	10.9	5.7	15.3	348	394	232	235	414	212	201	99	174	260	-	-	-	-	-	1187	1233	817	855	1472	79888	79015	13796	75148	85501					
2.5	1.4	14.0	1.0	2.5	513	347	1770	281	596	385	346	336	320	431	5.6	3.1	15.4	1.5	10.1	1000	954	1435	643	1252	99992	98585	37740	94389	105410					
6.2	5.0	18.0	2.8	5.7	750	656	1343	364	1029	454	464	560	320	563	9.5	9.5	16.4	1.3	17.7	1765	1316	4220	856	2742	89821	91420	43283	86226	95423					
6.8	5.0	37.7	1.8	9.0	791	571	2641	334	944	470	367	2010	263	521	4.0	3.6	6.8	1.3	7.0	987	944	2284	555	1159	93778	91129	47507	82086	106249					
1.5	1.4	1.5	1.0	2.2	500	512	154	426	562	193	163	158	148	268	-	-	-	-	-	1804	1907	1727	1086	2420	108175	108774	10101	103999	111753					
7.3	2.3	25.7	1.5	10.9	678	590	1102	401	1029	305	298	327	241	414	13.7	11.3	29.8	4.9	21.7	1203	1158	1325	896	1422	105500	104054	34235	97557	112245					
2.6	1.5	7.1	1.0	4.1	526	469	1314	338	628	358	342	587	270	402	3.0	1.6	8.2	1.0	5.1	1354	1194	3101	909	1606	101358	103192	37242	95405	106798					
15.1	1.0	43.0	0.5	40.7	417	324	993	216	669	264	204	498	96	447	4.5	4.5	0.0	4.5	4.5	1577	1374	1727	1246	2000	104027	105406	22417	99241	109635					
4.9	3.8	15.1	2.6	5.4	795	668	2725	616	870	528	483	882	410	569	13.2	5.1	42.3	2.3	23.9	1280	1116	1931	1053	1474	99929	99117	25791	95312	103328					
5.4	2.5	27.1	2.4	8.5	671	663	1235	468	738	303	272	503	235	396	4.7	3.2	14.5	2.5	5.8	1055	1045	1021	833	1192	104332	104367	27098	96737	112307					
1.9	1.5	2.3	1.3	2.4	548	506	1173	277	824	337	343	413	254	410	-	-	-	-	-	996	995	1121	751	1239	105722	105776	21121	100028	109457					
1.8	1.4	7.0	1.3	1.8	716	695	1377	517	828	394	363	541	314	500	-	-	-	-	-	954	901	1223	607	1138	107007	105686	39621	101883	111176					
68.2	64.4	20.8	62.0	78.2	400	381	127	357	461	892	873	163	833	969	2.4	2.4	1.1	1.9	3.0	2810	2842	574	2531	3058	104468	103667	4275	103235	106501					
16.7	12.2	74.3	3.6	30.5	437	405	952	298	522	582	532	1098	216	887	4.6	3.1	10.0	2.3	7.0	2827	2713	3018	1915	3523	103715	104016	24363	100815	107607					
23.3	13.1	67.5	9.7	32.6	462	490	242	377	534	181	177	135	154	199	4.3	4.5	3.6	2.6	5.8	1872	1795	948	1667	2206	113623	112508	27320	106000	123493					
131.0	90.8	563.5	45.1	168.1	619	447	1843	301	746	235	159	678	108	302	8.0	6.0	21.1	2.5	12.5	3411	3291	2787	2794	4001	110622	112111	46884	99520	118261					
29.5	16.5	106.9	10.1	31.3	631	590	1532	237	906	115	108	269	61	163	1.5	1.6	1.3	0.9	2.1	2887	2308	4795	2052	3615	109069	109655	30009	102623	115269					
7.0	6.3	16.1	4.6	7.6	374	341	487	249	499	82	79	92	70	86	-	-	-	-	-	2892	2854	2186	2385	3358	89420	89116	15880	86883	93466					
62.6	31.0	225.3	12.0	76.5	876	461	3837	186	720	373	347	665	203	506	3.6	3.5	2.3	2.7	4.8	3558	3470	3310	3281	3844	102870	98904	46863	92603	111257					
65.7	38.4	282.9	18.5	40.6	546	634	669	305	695	338	362	453	148	442	3.5	3.5	1.9	2.5	4.4	3321	3240	3648	2355	4178	116829	118939	26307	110953	125737					
19.7	19.1	40.2	7.5	29.2	461	444	1148	194	626	328	361	446	177	448	1.0	1.0	0.0	1.0	1.0	3361	3033	4609	2157	4519	114499	109490	41836	106042	121894					
4.1	1.4	18.0	0.6	6.9	167	85	476	60	280	281	303	330	208	365	1.0	1.0	0.1	0.9	1.1	1700	1546	2356	1173	2214	99597	103233	49850	86342	106983					
29.3	15.5	82.9	7.9	56.8	232	236	342	116	326	327	286	413	193	466	15.7	8.3	53.2	4.5	24.6	1415	1349	1477	866	1974	102863	102193	16758	97996	109656					
7.9	2.1	100.9	1.5	3.0	172	181	300	91	218	218	198	598	168	259	6.2	4.8	12.0	2.4	9.3	1230	1213	2002	794	1661	98550	101122	38462	91146	104677					
4.2	1.4	24.5	1.1	4.2	277	309	541	103	417	170	123	313	94	251	11.8	11.8	0.0	11.8	11.8	2163	2049	1658	1726	2637	94709	97619	36177	85855	101164					
3.9	2.2	13.8	1.4	5.4	311	313	565	147	450	221	183	442	144	311	2.9	2.9	1.5	2.1	3.7	1563	1510	1391	1336	1684	107449	107643	24409	102934	112732					
26.4	18.8	79.0	10.1	31.7	451	390	476	322	616	322	312	231	260	373	6.8	5.9	9.2	4.3	10.3	1421	1407	834	1291	1655	103120	101782	11666	99728	107874					
51.5	28.6	243.3	9.6	84.2	382	349	502	275	485	337	320	417	290	379	26.8	3.5	248.0	1.8	7.6	1291	1268	1026	964	1569										

Co ppm					Ni ppm					Cu ppm					Zn ppm					Ga ppm					Ge ppm									
M	Md	R	0.25	75%	M	Md	R	0.25	75%	M	Md	R	0.25	75%	M	Md	R	0.25	75%	M	Md	R	0.25	75%	M	Md	R	0.25	75%	M	Md	R	0.25	75%
1.23	0.82	2.78	0.38	2.26	1.07	0.92	0.75	0.80	1.46	5.4	4.8	15.2	1.1	9.2	12.7	10	30	4	20	55	46	65	35	73	3.9	4.0	6.3	2.3	4.9					
1.47	0.87	5.27	0.41	2.05	1.32	1.26	1.63	0.53	2.16	8.9	5.8	22.9	2.8	16.5	16.9	11	39	8	28	80	88	49	70	91	7.8	8.2	10.1	4.6	10.3					
1.41	0.71	9.94	0.49	1.53	0.72	0.50	2.16	0.34	0.89	5.3	2.1	27.2	1.3	7.5	14.3	9	49	5	20	48	42	65	35	58	3.9	2.8	13.1	1.9	4.6					
0.15	0.14	0.30	0.08	0.19	0.86	0.86	1.30	0.21	1.51	0.5	0.5	0.8	0.2	0.9	2.5	2	5	1	3	67	67	25	60	75	5.2	5.4	5.0	4.1	6.0					
0.20	0.15	0.50	0.12	0.31	0.30	0.26	0.21	0.22	0.40	0.7	0.3	1.7	0.2	1.5	2.8	2	6	1	5	74	78	40	61	84	6.1	5.2	10.3	4.1	8.4					
1.17	0.50	5.90	0.40	1.25	1.45	0.63	6.14	0.43	2.16	2.6	1.1	10.8	0.7	4.3	9.0	7	35	4	10	55	54	33	48	60	4.0	4.2	3.1	3.3	4.6					
1.98	1.35	6.35	0.88	2.34	1.01	0.45	2.73	0.35	1.69	1.3	1.1	3.9	0.5	1.7	33.4	28	85	17	48	107	109	31	98	113	14.3	13.5	17.4	12.3	15.9					
0.54	0.51	1.22	0.30	0.61	0.63	0.64	0.70	0.41	0.90	8.7	8.0	14.6	6.0	9.9	5.1	5	8	3	6	53	55	43	40	63	3.8	3.4	5.2	2.3	5.1					
1.03	0.60	3.13	0.45	1.15	0.89	0.65	2.03	0.44	1.19	5.9	1.1	39.8	0.9	6.0	11.8	8	43	6	10	88	85	124	60	101	5.4	5.0	9.5	3.0	7.4					
0.74	0.72	0.39	0.59	0.91	1.06	0.91	1.46	0.49	1.77	1.4	0.6	3.7	0.3	3.2	10.4	9	10	7	15	76	68	51	60	101	7.3	5.8	7.7	5.0	11.0					
0.92	0.89	1.44	0.73	1.12	1.60	1.52	3.00	0.67	2.42	0.4	0.3	0.3	0.3	0.6	11.2	10	22	7	16	90	93	64	77	104	6.9	7.5	8.9	3.4	9.6					
0.36	0.23	2.10	0.15	0.35	1.06	0.65	3.37	0.48	1.33	4.6	2.5	33.4	0.9	4.1	15.3	10	58	8	17	97	101	87	82	109	21.022	8.372	14.3	26.3						
2.33	1.06	9.25	0.63	3.13	2.63	1.96	7.02	0.69	3.70	1.3	0.6	3.0	0.6	1.9	29.9	16	93	11	47	53	53	15	49	57	3.9	3.6	4.4	3.1	4.0					
0.91	0.18	8.84	0.16	0.55	0.84	0.33	3.97	0.21	0.88	0.8	0.6	2.0	0.2	1.5	14.0	14	18	13	16	57	57	22	52	64	6.1	4.5	9.4	4.2	6.2					
1.66	0.70	6.22	0.48	1.44	2.81	0.97	9.56	0.67	4.09	1.9	0.9	12.6	0.6	2.0	17.5	7	64	4	22	52	53	43	43	61	2.8	2.4	2.8	2.1	3.0					
2.44	1.60	5.63	1.07	3.46	3.07	1.85	8.77	1.17	4.92	3.7	0.9	23.0	0.6	3.5	33.4	25	89	14	48	34	27	62	24	32	4.5	3.9	10.6	2.1	6.5					
3.09	2.60	7.20	1.02	5.40	4.45	1.06	11.08	0.61	11.68	7.4	4.7	18.4	1.1	16.4	18.7	12	35	9	31	78	78	3	77	79	6.2	6.9	7.8	3.0	9.1					
1.86	0.96	6.52	0.58	2.31	2.27	0.99	9.11	0.56	2.63	6.5	3.3	26.7	1.6	8.5	16.0	11	48	8	16	62	62	22	58	66	6.7	6.5	5.0	5.8	7.5					
0.50	0.50	0.15	0.43	0.57	0.31	0.31	0.08	0.26	0.35	0.4	0.4	0.6	0.2	0.7	6.7	6	4	5	9	60	57	13	57	67	7.0	6.3	4.2	5.7	9.1					
0.89	0.84	1.08	0.72	1.07	0.52	0.47	0.76	0.36	0.70	28.2	4.0	308.6	1.5	8.9	14.2	13	19	11	18	69	69	27	65	73	6.6	6.0	5.6	5.0	8.6					
1.06	0.98	1.24	0.81	1.18	0.82	0.81	1.03	0.57	1.10	3.7	1.4	29.0	0.5	3.5	11.6	11	16	10	14	66	67	31	62	71	5.5	5.2	7.5	4.8	5.9					
1.41	0.97	8.26	0.66	1.29	1.10	0.58	4.74	0.27	1.54	5.8	1.6	17.8	0.3	14.5	16.1	12	73	6	16	78	81	55	65	93	6.5	6.2	13.2	3.7	8.0					
0.37	0.33	0.27	0.28	0.49	0.74	0.74	0.00	0.74	0.74	4.7	4.1	7.2	1.9	8.0	3.1	3	2	2	4	63	63	7	60	66	10.311	1.7	6.7	13.1						
2.38	0.87	7.27	0.57	4.58	2.96	0.79	10.99	0.47	4.95	4.7	2.1	16.4	0.5	8.2	15.8	10	42	5	25	72	72	33	64	81	8.2	8.0	4.7	7.0	9.5					
0.76	0.62	2.64	0.44	0.89	0.84	0.75	2.50	0.44	1.00	0.6	0.4	1.8	0.2	0.8	5.5	5	12	4	7	57	55	59	47	70	9.2	9.4	6.4	7.3	10.8					
0.91	0.71	1.86	0.31	1.59	1.95	1.97	2.91	1.08	2.72	6.5	5.3	20.0	1.6	9.6	4.8	4	7	3	8	64	66	30	52	73	10.710	7.4	6.6	10.1	11.9					
2.02	1.24	5.81	0.87	2.70	3.40	2.20	18.56	1.62	3.38	5.3	2.2	67.1	0.7	4.0	12.4	9	35	7	14	83	78	45	71	94	8.2	8.1	8.4	7.3	8.7					
2.35	0.88	16.96	0.53	0.98	1.06	0.67	3.73	0.50	0.86	2.6	0.9	10.2	0.4	4.1	8.4	7	19	6	9	59	64	93	42	69	7.8	8.0	6.0	6.2	8.9					
0.84	0.82	1.17	0.58	1.02	0.79	0.64	1.60	0.36	1.09	7.9	2.9	38.4	0.6	10.4	6.1	7	7	4	8	66	70	37	55	73	6.0	6.5	7.1	4.3	7.2					
1.30	1.15	3.24	0.83	1.50	0.96	0.80	2.76	0.54	1.32	10.6	7.4	34.7	3.0	15.5	9.1	9	20	6	11	72	74	46	68	79	7.2	7.1	7.4	5.9	9.4					
1.50	0.93	2.65	0.77	2.82	1.42	1.35	1.46	0.91	2.01	6.3	5.2	13.7	0.6	13.0	13.9	11	19	8	23	165	168	29	152	174	16.717	1.6	6.6	13.9	19.1					
0.98	0.74	3.11	0.51	1.10	1.50	1.12	4.92	0.73	1.58	4.2	1.7	18.1	0.8	6.0	8.2	7	19	6	10	98	106	88	69	115	6.3	6.8	10.0	3.9	8.2					
5.34	4.05	12.61	1.97	9.75	0.58	0.50	0.92	0.32	0.75	10.5	6.0	28.7	2.9	17.6	57.7	45	131	19	105	97	102	36	90	106	8.0	7.8	7.7	5.2	10.7					
1.41	1.11	3.48	0.58	2.12	0.56	0.53	1.24	0.30	0.69	2.9	1.8	10.9	0.9	3.1	41.4	31	142	22	48	80	82	53	65	93	9.5	9.0	13.5	6.8	11.9					
0.99	0.78	2.86	0.39	1.17	0.46	0.34	0.52	0.29	0.68	6.5	3.1	44.1	0.8	7.1	21.2	17	46	11	28	102	112	96	83	122	7.6	5.6	16.2	3.2	12.4					
0.36	0.33	0.38	0.28	0.43	0.24	0.24	0.10	0.20	0.28	0.9	0.5	3.9	0.3	0.9	9.6	10	7	8	11	82	83	27	77	89	8.0	7.2	12.4	5.7	9.7					
1.94	1.23	5.54	0.88	2.63	1.93	1.34	4.12	0.93	2.66	11.0	6.2	36.6	1.9	16.6	38.6	27	99	18	47	66	66	63	49	77	4.5	4.3	6.5	2.5	5.8					
1.18	1.17	2.43	0.43	1.85	0.33	0.33	0.28	0.22	0.45	1.4	1.6	1.6	0.9	1.9	20.4	20	36	8	33	72	81	51	51	94	6.0	4.6	13.7	3.4	6.8					
0.90	0.83	1.67	0.54	1.08	0.54	0.52	0.92	0.34	0.73	1.6	1.4	4.2	0.6	2.0	15.8	11	29	10	21	65	62	61	48	87	6.0	6.4	7.8	3.0	8.7					
0.88	0.75	1.09	0.65	1.15	0.39	0.39	0.06	0.36	0.42	527.5	544.0	1725.6	51.6	682.0	31.1	31	35	26	37	120	118	82	112	137	7.6	7.6	8.1	6.3	9.2					
0.98	0.92	1.18	0.62	1.31	0.70	0.76	0.52	0.44	0.93	1.3	1.0	3.3	0.2	2.6	12.8	14	9	9	16	141	142	144	71	210	18.217	8.19	5.12	4.25	1.1					
1.08	0.75	3.64	0.56	1.44	1.32	0.66	5.07	0.57	1.36	2.1	0.4	7.9	0.4	4.1	14.9	13	19	10	19	74	72	63	58	77	9.6	9.5	10.4	9.1	10.7					
0.96	0.88	2.31	0.62	1.12	0.54	0.49	1.29	0.35	0.59	4.3	1.3	31.6	0.5	3.2	22.1	25	26	15	29	100	97	90	80	120	9.3	8.1	14.5	6.3	11.4					
0.64	0.39	4.33	0.28	0.63	0.58	0.57	0.90	0.30	0.77	2.9	1.1	14.3	0.6	3.9	9.4	9	13	6	13	87	86	31	78	95	12.011	0.17	9.10	0.12	9.9					
0.27	0.25	0.27	0.19	0.39	0.50	0.52	0.46	0.41	0.61	0.3	0.3	0.3	0.2	0.4	11.3	12	6	9	13	97	98	19	94	102	15.314	1.7	0.13	6.17	1.1					
0.43	0.35	1.11	0.24	0.51	0.59	0.39	1.85	0.33	0.62	0.4	0.3	1.1	0.2	0.4	10.4	10	15	9	13	81	82	30	76	87	13.012	9.14	7.10	2.15	4.4					
0.53	0.48	0.69	0.37	0.76	0.39	0.36	0.33	0.30	0.48	1.9	1.0	7.9	0.7	2.0	17.7	15	23	12	24	82	82	37	79	90	11.311	0.6	0.10	0.12	5.5					
0.30	0.29	0.36	0.14	0.48	1.43	1.43	1.18	0.84	2.02	68.6	70.8	111.2	13.2	121.8	223.6	206	397	46	419	216	211	38	203	235	13.814	2.8	1.0	4.16	9.9					
3.04	3.04	0.00	3.04	3.04	2.24</																													

As ppm					Rb ppm					Sr ppm					Y ppm					Zr ppm					Nb ppm				
M	Md	R	0.25	75%	M	Md	R	0.25	75%	M	Md	R	0.25	75%	M	Md	R	25%	75%	M	Md	R	0.25	75%	M	Md	R	25%	75%
18.6	13.1	53.3	7.2	27.2	1.13	0.47	5.52	0.25	1.09	2392	1617	3972	1455	3405	5.1	5.8	12.1	2.0	7.0	10.9	4.0	57.4	1.7	10.5	0.07	0.060	14.0	0.03	0.11
18.0	17.0	30.4	8.7	27.0	0.22	0.23	0.17	0.14	0.28	1351	1310	1478	1114	1694	4.1	2.5	10.4	1.7	6.5	1.9	1.0	6.4	0.8	2.6	0.13	0.110	25.0	0.06	0.15
17.3	13.0	50.0	10.2	25.4	0.23	0.14	1.59	0.10	0.20	1729	1527	2564	1112	2299	4.7	1.6	48.2	0.6	5.9	1.8	1.7	7.4	0.4	2.2	0.06	0.060	16.0	0.04	0.08
28.6	30.6	50.1	16.7	38.9	0.35	0.12	0.98	0.10	0.84	2699	2646	2972	2045	3240	12.4	13.2	19.1	7.3	17.0	7.9	6.6	23.5	3.5	8.7	0.13	0.051	37.0	0.02	0.06
33.9	22.7	90.8	15.1	46.6	0.09	0.07	0.08	0.05	0.13	2171	2329	4064	1771	2673	7.2	8.0	17.1	3.0	10.1	2.3	2.3	4.0	0.9	3.7	0.16	0.110	99.0	0.03	0.17
19.8	16.5	65.9	11.4	23.1	0.81	0.53	3.35	0.32	0.94	1878	1854	1033	1723	2065	21.5	14.0	102.8	6.5	27.6	23.4	12.7	113.4	3.8	35.2	0.19	0.140	59.0	0.06	0.27
54.8	31.2	332.3	19.6	60.3	0.94	0.77	2.47	0.36	1.40	1161	1150	530	1061	1227	87.5	76.3	161.2	41.3	124.6	24.9	7.8	127.4	3.9	35.9	1.88	0.798	62.0	0.40	3.32
79.4	52.7	279.5	37.3	102.0	6.08	4.79	25.01	3.31	7.59	900	735	1396	525	1377	28.6	27.3	48.2	19.8	34.6	25.5	16.7	153.0	9.0	23.1	0.15	0.061	26.0	0.05	0.10
160.3	123.0	275.0	84.0	237.0	0.61	0.24	4.14	0.12	0.64	1174	1043	2126	827	1398	20.4	7.2	138.9	2.2	28.6	0.8	0.4	2.3	0.3	1.2	0.12	0.051	36.0	0.03	0.07
120.0	118.5	218.9	35.6	206.0	0.11	0.11	0.14	0.05	0.18	1907	1868	803	1556	2296	6.1	6.0	8.9	2.7	9.5	2.1	1.7	2.9	1.2	3.3	0.22	0.190	30.0	0.11	0.37
109.3	84.0	471.6	29.4	131.5	0.11	0.10	0.08	0.07	0.14	1502	1533	2962	505	1964	15.3	5.4	81.4	1.9	15.8	4.0	3.1	10.6	1.3	6.9	1.08	0.963	83.0	0.24	1.58
125.8	91.9	350.3	67.1	149.6	0.45	0.35	1.14	0.26	0.59	1403	1399	1633	1240	1721	69.9	47.9	310.2	24.2	97.3	21.4	15.9	74.5	8.0	23.8	0.69	0.373	79.0	0.22	0.80
44.9	44.6	52.9	38.3	51.1	0.16	0.14	0.23	0.11	0.18	1817	1707	2996	1388	1939	12.7	8.3	43.3	2.6	21.6	19.3	5.0	114.5	1.3	26.5	0.35	0.152	24.0	0.07	0.42
59.9	58.8	87.3	30.7	88.2	0.15	0.09	0.32	0.06	0.31	2674	2645	2315	2223	3228	6.3	6.2	11.8	1.6	10.4	2.4	0.3	10.6	0.1	5.0	0.16	0.100	56.0	0.06	0.16
35.8	34.8	53.6	25.7	38.8	0.99	0.70	2.32	0.19	1.74	618	615	639	502	683	20.0	9.2	89.5	3.9	18.4	1.3	0.8	5.0	0.3	1.3	0.09	0.060	26.0	0.04	0.11
55.6	46.7	73.2	34.8	81.1	1.41	0.29	8.09	0.06	3.05	1541	1717	3562	537	2180	13.4	7.9	49.1	6.1	17.6	27.6	22.4	124.9	11.1	34.9	0.24	0.161	0.00	0.07	0.37
16.1	10.4	30.7	7.4	27.5	9.17	10.89	15.95	0.34	16.29	1134	1147	1157	673	1589	20.4	6.0	76.7	0.8	47.4	15.8	2.8	68.8	0.9	37.2	0.81	0.372	69.0	0.14	1.69
6.0	5.5	4.3	4.9	7.3	0.65	0.51	1.52	0.31	0.98	1636	1416	2604	1184	1838	38.9	31.4	74.5	22.0	58.3	46.7	41.7	91.2	25.5	65.6	0.41	0.192	48.0	0.12	0.37
4.8	5.1	3.7	3.3	6.1	0.09	0.09	0.06	0.06	0.12	1241	1242	457	1048	1433	8.1	7.2	7.5	5.7	11.4	34.6	35.9	23.8	24.6	43.3	0.20	0.200	33.0	0.05	0.35
15.0	12.3	35.8	6.6	21.3	0.70	0.25	3.32	0.11	0.92	1052	977	885	797	1287	24.8	11.0	177.0	4.6	33.5	5.4	4.4	23.6	2.2	5.4	0.20	0.120	72.0	0.09	0.24
9.1	6.8	23.9	4.5	14.3	0.62	0.33	2.13	0.11	0.92	1037	1004	1475	824	1120	29.9	12.0	164.0	3.2	32.4	5.7	4.4	15.1	2.4	8.0	0.14	0.080	56.0	0.04	0.19
5.5	4.8	12.8	2.5	7.8	0.58	0.37	1.60	0.12	0.84	996	873	1702	737	1182	15.3	4.6	129.4	2.3	10.5	27.8	23.0	118.7	10.8	34.5	0.27	0.150	99.0	0.06	0.29
9.3	7.1	15.9	4.3	16.6	2.21	0.20	6.11	0.16	6.27	1036	1124	962	579	1404	29.4	20.5	49.5	14.5	53.2	3.3	3.9	4.7	1.1	4.9	0.07	0.070	0.08	0.10	0.10
5.2	4.4	7.5	3.2	8.0	1.92	0.21	6.87	0.15	4.66	1120	1028	1096	886	1399	37.9	14.4	205.5	4.9	52.7	4.2	3.6	12.4	2.0	5.1	0.07	0.040	48.0	0.03	0.06
3.4	2.6	9.4	1.9	5.1	0.13	0.13	0.00	0.13	0.13	830	859	858	665	981	5.4	3.8	21.9	1.8	7.3	4.7	3.8	14.7	2.1	5.6	0.07	0.050	17.0	0.03	0.09
6.1	6.7	7.8	3.5	8.5	2.74	2.02	9.29	0.23	5.61	1699	1482	2409	1379	1698	82.7	18.3	282.6	1.4	176.0	5.0	1.9	15.6	0.2	12.1	0.13	0.100	35.0	0.04	0.19
7.9	4.1	30.1	2.8	10.3	0.67	0.30	3.31	0.13	0.83	1810	1763	2206	1447	1959	14.3	12.5	50.6	4.2	18.0	10.7	8.7	27.5	5.3	12.9	0.35	0.154	70.0	0.10	0.30
6.5	3.5	20.8	2.1	5.1	0.20	0.12	0.99	0.06	0.22	1419	1414	1540	1149	1657	7.2	5.5	25.1	1.8	9.4	6.9	7.0	15.3	2.4	9.6	0.16	0.110	47.0	0.05	0.19
7.0	6.8	12.5	3.8	10.3	0.78	0.44	5.00	0.10	0.76	994	1031	1516	690	1280	6.5	6.2	18.0	1.5	9.9	13.7	2.6	117.7	1.3	10.2	0.13	0.080	61.0	0.04	0.17
11.0	10.8	24.0	6.6	13.9	0.71	0.16	8.42	0.07	0.47	1332	1350	1940	973	1746	1.3	0.4	13.3	0.2	1.0	1.5	1.0	5.3	0.3	2.2	0.24	0.130	87.0	0.09	0.36
35.9	33.9	11.6	32.2	41.6	3.31	0.85	11.04	0.36	8.74	1676	1572	541	1520	1936	40.2	39.4	4.3	38.8	42.3	7.2	6.4	4.6	5.8	9.4	0.04	0.040	0.60	0.02	0.07
64.5	51.0	121.8	28.6	114.0	1.56	0.46	9.05	0.16	2.22	1487	1505	1858	954	2009	16.0	10.4	52.8	4.0	29.3	12.7	10.8	37.3	4.6	19.8	0.11	0.070	35.0	0.04	0.17
117.0	86.5	170.4	82.1	165.8	0.73	0.26	2.94	0.20	1.03	1391	1394	525	1234	1543	41.4	35.7	57.5	19.4	67.9	32.7	33.9	38.6	25.4	38.8	0.40	0.300	66.0	0.21	0.62
81.5	74.4	122.7	53.9	107.7	4.08	1.22	22.96	0.51	6.27	487	454	725	289	627	240.7	181.6	543.3	138.6	393.8	7.1	4.1	35.0	2.5	8.8	0.66	0.194	95.0	0.09	0.47
81.7	69.5	161.4	58.1	103.9	2.57	0.70	15.02	0.22	1.76	692	702	717	407	899	100.9	80.7	357.7	30.1	132.0	5.6	3.0	20.1	1.2	8.1	0.57	0.292	22.0	0.07	0.94
68.0	62.1	68.0	53.7	80.7	0.26	0.10	0.99	0.07	0.28	1199	1139	1110	971	1555	25.1	19.7	43.0	16.4	33.7	22.0	23.5	23.3	15.8	28.7	0.45	0.381	33.0	0.25	0.47
172.6	140.9	630.2	81.5	207.0	2.03	0.88	9.04	0.36	2.60	1557	1314	2288	1250	1898	32.9	28.0	73.4	17.6	48.9	47.8	35.3	166.9	11.7	58.8	0.77	0.193	86.0	0.15	0.90
48.3	36.9	121.5	12.7	62.1	2.13	0.41	11.47	0.15	1.68	1480	1520	2698	957	1693	19.0	23.2	27.2	8.0	27.8	21.0	14.6	64.5	6.2	36.9	0.32	0.230	80.0	0.13	0.41
49.8	43.2	86.9	31.6	72.9	2.22	1.90	6.05	0.76	3.08	1502	1639	1313	1074	1928	14.2	14.0	30.2	3.9	22.7	16.1	16.6	31.1	7.8	23.1	0.25	0.130	96.0	0.07	0.33
273.1	188.0	566.0	130.0	369.0	0.38	0.19	0.93	0.15	0.72	1494	1495	902	1160	1788	34.7	10.9	93.2	5.2	74.5	1.4	1.1	5.1	0.4	1.3	0.09	0.090	12.0	0.06	0.13
320.6	350.0	452.6	161.4	469.5	0.25	0.25	0.00	0.25	0.25	936	909	409	836	1007	129.1	70.4	330.8	40.0	263.0	9.9	7.0	30.1	1.2	17.5	0.08	0.040	14.0	0.03	0.16
177.6	157.0	453.8	121.8	219.3	0.55	0.17	2.86	0.12	0.86	971	973	1385	823	1138	6.9	4.7	19.7	2.8	9.8	2.3	1.0	17.1	0.3	2.2	0.08	0.070	14.0	0.05	0.13
247.4	206.0	451.6	140.5	352.0	3.24	0.25	32.18	0.16	0.80	974	973	1511	704	1145	116.8	20.4	721.9	3.0	124.9	8.3	3.9	63.4	0.9	7.2	0.12	0.090	50.0	0.05	0.15
233.9	223.0	582.4	117.0	323.0	0.55	0.42	2.31	0.18	0.67	1041	1051	1032	846	1188	74.8	62.0	261.9	30.3	105.0	3.6	1.6	20.6	0.9	6.0	0.28	0.202	21.0	0.08	0.31
1067.5	801.5	2190.0	243.5	2078.3	1.70	1.55	4.27	0.51	2.57	1830	1646	2914																	

Mo ppm					Cd ppm					Sn ppm					Sb ppm					Cs ppm					Ba ppm				
M	M	R	25	75	M	M	R	25	75	M	M	R	0.2	75	M	Md	R	0.2	75	M	M	R	0.2	75	M	Md	R	0.2	75
0.1	0.1	0.3	0.0	0.1	-	-	-	-	-	2.7	2.3	3.0	1.8	3.8	5.5	4.8	12.	2.6	8.1	0.3	0.2	1.2	0.1	0.3	16.	15.	25.3	11.	20.
0.3	0.2	0.4	0.2	0.5	-	-	-	-	-	3.6	2.9	4.9	2.2	5.5	2.9	2.6	5.5	1.8	4.0	0.1	0.1	0.3	0.0	0.3	9.5	6.7	26.8	4.6	10.
0.0	0.0	0.1	0.0	0.1	0.2	0.2	0.1	0.1	0.2	2.0	1.3	8.3	1.0	1.6	7.5	4.6	29.	2.5	9.4	0.1	0.1	0.4	0.0	0.2	13.	11.	27.7	8.6	16.
0.0	0.0	0.1	0.0	0.1	0.3	0.3	0.1	0.2	0.3	1.6	1.5	1.6	1.2	1.9	8.3	8.5	14.	3.2	13.	0.2	0.0	1.1	0.0	0.1	5.8	4.5	21.8	2.9	6.6
0.0	0.0	0.1	0.0	0.1	0.2	0.2	0.2	0.2	0.4	1.2	1.1	1.5	1.0	1.3	7.0	3.2	20.	2.0	11.	0.1	0.0	0.5	0.0	0.1	3.3	2.9	9.70	1.9	4.0
0.1	0.1	0.2	0.1	0.2	0.2	0.2	0.0	0.2	0.2	2.6	2.3	5.8	1.6	3.0	6.9	5.4	15.	3.7	9.3	0.3	0.3	0.8	0.2	0.4	11.	11.	21.5	5.6	16.
0.2	0.2	0.2	0.1	0.2	0.7	0.5	2.0	0.4	0.7	5.8	5.6	6.9	4.3	7.0	10.	7.0	37.	4.6	15.	0.5	0.3	1.2	0.2	0.6	2.4	2.0	7.63	1.3	2.7
0.1	0.1	0.2	0.0	0.1	1.0	1.1	1.0	0.8	1.2	3.0	2.8	3.6	2.1	3.6	17.	8.1	43.	3.5	31.	5.4	4.9	17.	2.4	6.4	13.	10.	58.1	6.7	15.
0.1	0.0	0.1	0.0	0.1	0.5	0.5	0.2	0.4	0.7	4.0	2.7	9.1	2.0	5.7	115	68.	543	41.	151	0.2	0.0	0.9	0.0	0.1	3.7	1.8	28.6	0.9	4.0
0.0	0.0	0.0	0.0	0.1	0.1	0.1	0.0	0.1	0.1	3.0	3.4	1.8	2.1	3.6	119	126	134	64.	167	0.1	0.0	0.3	0.0	0.3	0.9	0.9	1.50	0.3	1.6
0.0	0.1	0.0	0.0	0.1	-	-	-	-	-	6.5	4.1	19.	3.3	8.7	133	142	299	39.	195	0.1	0.1	0.1	0.0	0.1	0.6	0.5	1.26	0.2	1.0
0.2	0.1	1.1	0.1	0.1	0.7	0.7	0.0	0.6	0.7	6.7	6.7	13.	5.3	8.0	140	86.	608	64.	189	0.2	0.2	0.6	0.1	0.3	1.2	1.0	2.58	0.6	1.6
0.1	0.1	0.2	0.1	0.1	0.7	0.4	1.5	0.3	1.5	2.6	2.0	6.4	1.5	3.0	3.2	3.5	4.7	1.8	4.1	0.3	0.2	0.6	0.1	0.4	4.9	4.7	6.53	3.3	5.8
0.1	0.1	0.2	0.1	0.1	0.6	0.5	0.4	0.5	0.8	3.5	3.5	5.3	2.3	4.0	3.7	3.6	7.8	1.8	5.6	0.1	0.0	0.4	0.0	0.2	4.8	1.9	28.4	1.5	5.0
0.1	0.1	0.3	0.1	0.2	0.3	0.3	0.0	0.3	0.3	2.0	2.1	2.3	1.6	2.5	0.9	0.8	1.3	0.7	1.1	0.1	0.1	0.3	0.0	0.2	4.8	5.4	6.44	2.7	7.0
0.1	0.1	0.2	0.1	0.2	0.5	0.5	0.4	0.2	0.7	3.6	3.8	4.5	2.7	4.0	2.0	1.5	4.8	1.0	2.5	0.4	0.2	2.0	0.0	0.7	7.2	4.4	58.9	2.4	5.6
-	-	-	-	-	-	-	-	-	-	9.4	5.9	16.	3.6	17.	12.	9.8	29.	1.7	26.	1.1	0.2	3.8	0.1	3.0	7.5	3.8	17.2	3.0	13.
0.0	0.0	0.0	0.0	0.0	0.2	0.2	0.1	0.2	0.3	2.1	2.1	1.9	1.6	2.4	13.	12.	19.	9.5	18.	0.4	0.2	2.0	0.1	0.5	5.0	3.6	13.2	2.5	5.2
-	-	-	-	-	0.2	0.2	0.1	0.2	0.3	1.6	1.7	1.0	1.2	2.0	19.	20.	10.	15.	23.	0.1	0.1	0.2	0.0	0.2	1.6	1.5	0.64	1.4	1.9
0.1	0.1	0.1	0.0	0.1	0.4	0.5	0.5	0.3	0.5	6.0	6.1	9.2	3.8	8.4	23.	17.	114	7.0	31.	0.5	0.4	1.8	0.2	0.7	4.7	3.1	16.3	1.9	6.4
0.0	0.0	0.1	0.0	0.1	0.3	0.3	0.4	0.3	0.5	6.7	4.7	36.	2.5	8.8	19.	11.	87.	5.0	21.	0.2	0.2	0.8	0.1	0.4	7.5	6.0	15.3	4.6	8.9
0.0	0.0	0.0	0.0	0.0	0.4	0.4	0.6	0.3	0.4	5.1	3.5	22.	2.4	6.0	7.6	4.0	35.	1.2	12.	0.2	0.1	1.3	0.0	0.3	2.2	1.3	9.96	0.5	3.0
0.0	0.0	0.0	0.0	0.0	0.6	0.6	0.3	0.5	0.8	32.	37.	34.	15.	44.	11.	11.	20.	3.0	19.	0.0	0.0	0.0	0.0	0.1	14.	14.	14.8	8.1	21.
0.0	0.0	0.0	0.0	0.0	0.5	0.5	0.3	0.4	0.6	3.3	3.2	4.5	2.2	4.2	13.	10.	33.	7.0	21.	0.2	0.1	0.6	0.0	0.5	4.2	3.9	9.71	1.7	6.4
0.0	0.0	0.0	0.0	0.0	0.5	0.5	0.5	0.3	0.6	9.6	8.3	23.	3.7	15.	5.0	4.9	12.	2.4	7.2	0.0	0.0	0.1	0.0	0.1	4.8	4.6	11.3	1.9	7.6
0.0	0.0	0.0	0.0	0.0	0.4	0.4	0.2	0.4	0.5	39.	39.	66.	16.	55.	17.	18.	31.	8.3	24.	0.5	0.5	1.4	0.0	1.0	10.	10.	17.5	7.5	13.
0.1	0.0	0.8	0.0	0.1	0.3	0.3	0.5	0.2	0.4	3.7	2.5	8.8	1.8	4.6	21.	16.	81.	6.0	25.	0.2	0.1	1.3	0.0	0.2	2.3	1.3	16.5	0.7	3.0
0.1	0.1	0.5	0.0	0.1	0.4	0.4	0.5	0.3	0.5	4.5	3.6	8.3	1.9	7.9	10.	4.9	47.	2.9	7.5	0.1	0.0	0.5	0.0	0.2	4.6	4.1	8.20	3.4	5.4
0.0	0.0	0.0	0.0	0.0	0.3	0.3	0.5	0.2	0.6	3.6	3.1	6.1	1.9	5.5	9.0	8.4	19.	1.8	14.	0.1	0.1	0.4	0.0	0.2	2.1	1.9	6.01	1.3	2.7
0.0	0.0	0.2	0.0	0.1	0.3	0.3	0.3	0.2	0.4	3.8	3.7	6.9	2.4	5.1	12.	10.	24.	5.7	20.	0.2	0.1	1.8	0.0	0.3	1.9	1.5	6.12	0.6	1.9
0.1	0.0	0.0	0.0	0.1	1.3	1.4	0.6	1.0	1.5	4.5	4.5	2.8	3.1	5.7	52.	48.	41.	37.	71.	0.3	0.2	0.4	0.1	0.5	5.4	1.8	15.2	1.3	13.
0.1	0.0	0.3	0.0	0.1	0.4	0.4	0.4	0.3	0.6	2.8	2.6	5.7	2.1	3.8	93.	86.	234	30.	141	1.1	0.2	10.	0.1	0.7	8.0	1.6	102.	0.5	6.0
0.1	0.1	0.3	0.0	0.3	0.4	0.4	0.0	0.4	0.4	5.6	4.9	11.	3.1	6.0	16.	15.	26.	8.4	22.	1.4	1.0	3.6	0.6	1.5	2.5	2.8	2.53	1.6	3.3
0.7	0.1	5.0	0.0	0.5	0.3	0.3	0.4	0.2	0.3	15.	15.	19.	11.	20.	43.	39.	91.	28.	58.	1.1	0.6	2.9	0.3	1.8	6.6	5.2	14.7	3.5	9.3
0.1	0.0	0.2	0.0	0.1	-	-	-	-	-	11.	11.	16.	7.5	16.	32.	23.	67.	16.	45.	1.1	0.5	4.1	0.3	1.0	5.5	4.5	15.8	1.4	9.3
0.0	0.0	0.1	0.0	0.0	-	-	-	-	-	4.9	4.7	2.6	4.3	5.5	48.	40.	72.	32.	67.	0.1	0.1	0.3	0.0	0.2	2.0	1.3	5.87	0.9	2.8
0.1	0.1	0.1	0.0	0.2	0.5	0.5	0.0	0.5	0.5	3.9	3.3	5.5	2.5	5.0	71.	64.	135	37.	99.	0.5	0.4	1.3	0.1	0.7	2.6	2.0	5.81	1.2	3.9
0.0	0.0	0.0	0.0	0.0	-	-	-	-	-	1.4	1.5	1.3	0.8	1.9	55.	26.	184	19.	77.	0.4	0.3	1.4	0.1	0.7	6.7	4.6	20.7	2.8	5.1
0.1	0.1	0.1	0.0	0.2	0.5	0.2	0.6	0.2	0.9	1.5	1.3	1.9	1.0	1.9	45.	35.	72.	26.	69.	1.1	0.3	5.9	0.1	1.2	7.0	6.7	8.79	4.3	10.
0.3	0.2	0.7	0.1	0.4	0.2	0.2	0.0	0.2	0.2	2.2	1.7	3.6	1.3	3.0	69.	43.	159	36.	69.	0.3	0.3	0.4	0.2	0.3	4.3	3.4	8.83	2.7	5.5
0.1	0.1	0.1	0.0	0.2	-	-	-	-	-	14.	14.	17.	9.4	22.	150	142	279	69.	237	0.2	0.2	0.5	0.0	0.4	1.3	1.2	0.63	1.1	1.4
0.2	0.0	0.7	0.0	0.4	0.2	0.2	0.2	0.1	0.4	5.0	3.5	22.	2.8	5.0	72.	79.	120	55.	89.	0.8	0.5	2.0	0.3	1.3	1.2	0.9	3.89	0.7	1.5
0.1	0.1	0.2	0.1	0.1	0.3	0.3	0.0	0.3	0.3	3.2	3.1	8.5	1.2	3.8	245	198	753	112	317	0.5	0.3	3.3	0.2	0.5	3.3	0.8	23.1	0.6	2.1
0.0	0.0	0.1	0.0	0.1	0.1	0.1	0.1	0.0	0.1	6.8	6.0	11.	3.8	9.6	137	101	447	57.	176	0.9	0.6	2.7	0.2	1.2	4.2	3.2	17.3	1.7	4.6
0.5	0.2	2.9	0.0	0.3	-	-	-	-	-	6.0	5.9	4.4	4.7	7.2	72.	69.	94.	60.	87.	0.3	0.3	0.4	0.2	0.4	6.5	5.2	12.2	2.9	11.
0.1	0.0	0.5	0.0	0.1	0.3	0.3	0.2	0.2	0.3	4.7	4.8	7.8	3.5	6.0	79.	86.	102	56.	99.	0.3	0.2	0.5	0.2	0.4	6.8	3.9	29.6	2.4	9.7
0.0	0.0	0.0	0.0	0.0	-	-	-	-	-	4.9	4.5	6.4	3.8	6.3	259	261	317	189	302	0.2	0.2	0.5	0.1	0.5	2.3	1.3	9.14	0.9	2.7
-	-	-	-	-	-	-	-	-	-	21.	21.	9.1	17.	25.	52.	60.	78.	18.	77.	0.2	0.2	0.3	0.1	0.3	8.2	8.0	15.1	1.6	15.
0.1	0.1	0.0	0.1	0.1	-	-	-	-	-	11.	11.	0.0	11.	11.	5.9	5.9	0.0	5.9	5.9	3.6	3.6	0.0	3.6	3.6	3.3	3.3	0.00	3.3	3.3
0.0	0.0	0.0	0.0	0.1	1.3	0.9	2.6	0.6	1.9	3.6	3.5	4.0	2.4	4.9	66.	65.	142	31.	92.	0.2	0.2	0.6	0.2	0.3	13.	3.4	74.7	1.8	15.
0.1	0.1	0.2	0.0	0.1	0.2	0.2	0.2	0.1	0.3	2.1	2.1	2.5	1.6	2.4	52.	46.	123	21.	82.	0.2	0.2	0.4	0.1	0.4					

La ppm					Ce ppm					Pr ppm					Nd ppm					Sm ppm					Eu ppm				
M	Md	R	0.2	75	M	Md	R	0.2	75	M	M	R	0.	75	M	Md	R	0.2	75	M	M	R	0.	75	M	Md	R	0.2	75
14.	13.	43.	7.3	17.	23.	21.	77.5	12.	27.9	2.4	2.	8.0	1.4	2.9	9.1	8.1	29.8	4.7	11.	1.	1.	6.0	0.9	2.1	2.4	2.3	4.3	1.5	2.8
11.	10.	19.	6.1	14.	14.	12.	25.6	7.7	17.9	1.6	1.	3.0	0.7	2.1	5.8	4.9	10.7	3.6	7.8	1.	0.	1.4	0.5	1.7	4.8	3.3	15.	1.7	6.8
9.1	7.3	40.	4.0	10.	13.	10.	66.0	6.0	14.7	1.5	0.	8.5	0.6	1.6	5.9	3.6	36.6	1.8	5.4	1.	0.	10.	0.3	1.2	2.1	1.4	6.0	1.2	2.1
43.	35.	132	29.	48.	70.	54.	249.	34.	78.5	7.4	6.	26.	3.8	8.3	26.	21.	91.0	13.	28.	4.	4.	13.	2.3	5.1	3.5	3.2	4.2	2.9	4.4
16.	13.	39.	10.	23.	21.	19.	50.7	12.	30.6	2.2	2.	4.9	1.4	2.9	8.3	7.8	17.5	5.3	10.	1.	1.	3.3	0.9	2.2	2.5	2.5	5.7	1.7	3.1
19.	16.	43.	10.	27.	34.	27.	101.	15.	48.5	4.3	2.	13.	1.9	5.7	18.	12.	71.2	7.7	24.	4.	2.	23.	1.6	5.6	3.5	3.0	7.4	2.5	4.4
244	150	974	75.	223	567	253	294	158	474.	61.	25	324	18.	45.	221	97.	116	76.	169	33	22	139	14.	30.	9.4	8.0	18.	5.3	12.
51.	56.	85.	39.	65.	51.	52.	86.1	30.	72.7	10.	10	17.	7.8	14.	40.	38.	71.4	30.	53.	7.	8.	14.	6.2	10.	2.5	2.3	5.1	1.5	3.1
16.	7.2	176	3.0	11.	32.	9.6	363.	3.5	20.1	4.1	1.	43.	0.5	2.7	17.	4.1	168.	1.8	12.	4.	0.	28.	0.4	3.0	2.3	1.7	5.4	1.4	3.3
1.2	1.3	1.3	0.7	1.7	1.3	1.3	0.7	0.9	1.5	0.2	0.	0.1	0.1	0.3	1.0	1.1	0.5	0.7	1.1	0.	0.	0.2	0.2	0.4	0.1	0.1	0.0	0.1	0.1
29.	2.7	170	1.3	26.	53.	4.8	346.	1.7	47.6	5.8	0.	37.	0.3	5.0	22.	2.3	137.	1.2	19.	4.	0.	26.	0.4	5.5	1.2	0.2	7.6	0.1	1.4
92.	64.	313	25.	158	166	111	614.	47.	290.	17.	11	67.	5.6	29.	66.	41.	238.	19.	111	13	7.	51.	3.8	21.	6.5	4.0	19.	3.3	9.7
15.	12.	51.	8.3	15.	23.	16.	97.8	10.	22.1	3.0	2.	13.	1.2	2.5	12.	7.9	55.1	4.0	11.	2.	1.	12.	0.6	2.9	2.6	2.4	5.1	1.6	3.2
6.8	7.1	11.	2.9	9.7	8.4	8.6	16.0	2.4	13.4	1.0	1.	1.8	0.4	1.5	4.0	4.0	6.7	1.4	6.5	0.	0.	2.0	0.3	1.5	0.7	0.6	1.2	0.3	1.1
15.	7.1	76.	4.4	13.	31.	11.	179.	5.9	21.6	4.2	1.	25.	0.8	2.9	19.	5.9	117.	3.4	12.	5.	1.	29.	0.7	2.9	1.5	1.2	3.4	1.0	1.8
16.	15.	26.	10.	23.	31.	30.	57.7	21.	43.3	3.8	3.	7.2	2.7	4.9	14.	13.	29.0	8.4	20.	3.	2.	6.1	1.6	4.2	1.0	0.8	1.7	0.6	1.5
18.	3.5	52.	1.3	43.	32.	6.6	105.	1.9	76.0	3.7	0.	12.	0.2	8.8	14.	1.9	52.8	0.7	34.	3.	0.	11.	0.3	9.0	3.1	4.0	5.0	0.6	5.1
22.	19.	67.	11.	25.	38.	36.	109.	16.	44.3	4.9	4.	10.	2.2	5.6	19.	19.	36.1	9.5	25.	5.	4.	9.2	2.3	7.3	3.6	3.4	6.9	2.2	4.2
6.2	6.4	6.2	3.4	8.7	8.6	8.6	9.3	4.5	12.5	1.0	1.	0.8	0.6	1.3	3.6	3.7	2.3	2.6	4.6	0.	0.	0.5	0.5	0.8	1.6	1.5	1.5	1.0	2.3
11.	8.1	32.	3.6	15.	17.	10.	59.4	4.0	28.4	2.3	1.	7.7	0.7	3.3	8.8	5.4	30.7	2.3	12.	1.	0.	8.0	0.5	2.6	3.0	2.4	5.0	1.7	3.8
14.	11.	23.	7.8	20.	22.	17.	43.5	12.	29.4	2.7	2.	4.5	1.5	4.1	9.7	9.4	16.9	5.5	13.	2.	1.	5.8	0.7	3.1	3.4	2.9	7.1	1.9	5.0
37.	2.4	791	0.8	22.	80.	3.5	184	1.4	31.0	8.7	0.	197	0.2	2.9	31.	1.8	681.	0.9	9.6	5.	0.	95.	0.2	1.6	2.1	1.1	9.6	0.3	3.5
8.3	7.8	9.8	4.7	12.	14.	12.	19.1	8.0	22.5	1.7	1.	2.3	1.0	2.7	7.0	5.4	9.2	4.3	11.	1.	1.	2.5	0.9	2.8	2.9	2.9	1.4	2.3	3.6
18.	10.	62.	4.7	25.	37.	17.	132.	7.8	64.6	4.9	2.	16.	1.0	10.	21.	10.	72.7	4.0	44.	5.	2.	17.	0.8	9.5	2.3	2.1	7.5	0.8	3.3
6.8	4.7	47.	2.1	6.0	10.	6.5	76.6	2.7	10.6	1.3	0.	8.3	0.5	1.6	5.0	3.3	29.5	1.3	6.2	1.	0.	6.1	0.2	1.3	0.5	0.2	1.9	0.1	0.8
88.	45.	329	20.	156	181	80.	801.	29.	322.	21.	8.	101	2.5	37.	83.	25.	399.	6.6	141	16	3.	79.	0.7	27.	8.7	7.3	25.	1.8	14.
15.	8.0	64.	4.5	18.	30.	14.	153.	8.0	42.3	3.8	1.	18.	1.0	5.1	15.	7.1	69.8	3.4	20.	3.	1.	11.	0.7	4.4	1.0	0.6	6.4	0.2	1.4
4.6	3.8	9.4	1.2	7.9	7.2	4.2	23.2	1.2	12.6	1.1	0.	3.5	0.2	1.7	4.7	2.6	18.2	0.7	7.2	1.	0.	6.4	0.3	1.6	0.5	0.4	2.0	0.1	0.7
13.	9.5	50.	2.5	18.	20.	13.	94.1	2.4	25.1	2.2	1.	9.8	0.5	2.7	7.5	4.7	32.5	1.6	9.0	1.	1.	3.8	0.4	1.5	2.2	1.2	5.1	0.6	3.9
3.2	1.9	17.	1.3	4.8	2.9	1.1	23.8	0.8	4.1	0.5	0.	2.1	0.3	0.8	1.4	0.9	6.9	0.5	2.0	0.	0.	0.9	0.1	0.3	1.0	0.7	3.0	0.2	1.6
111	112	132	59.	162	202	210	244.	102	295.	22.	23	26.	11.	32.	86.	88.	99.1	46.	124	14	14	13.	8.7	19.	6.7	6.6	1.8	5.9	7.6
80.	80.	264	20.	105	143	132	539.	35.	185.	14.	12	52.	3.5	19.	52.	48.	184.	12.	66.	7.	8.	25.	1.5	10.	5.8	3.1	24.	1.5	8.6
30.	28.	39.	17.	47.	69.	69.	78.3	36.	104.	9.1	9.	10.	4.9	13.	35.	35.	45.7	19.	50.	7.	7.	10.	4.3	8.9	2.2	1.2	6.0	0.9	2.8
345	338	963	189	486	895	803	331	461	114	109	96	470	57.	130	410	357	184	231	474	74	64	310	40.	90.	7.8	7.1	20.	4.3	9.5
51.	49.	150	16.	70.	102	121	216.	29.	155.	12.	14	25.	4.0	19.	54.	59.	113.	17.	87.	13	12	31.	4.4	20.	5.7	3.5	22.	2.2	5.5
12.	8.5	43.	6.6	13.	38.	18.	201.	11.	38.9	3.5	2.	12.	1.5	4.3	15.	9.9	52.1	6.1	19.	3.	2.	12.	1.5	5.1	1.1	1.0	1.5	0.8	1.4
17.	15.	49.	8.5	22.	30.	26.	84.2	13.	37.0	4.3	3.	10.	2.3	5.5	18.	14.	47.0	7.6	22.	4.	3.	12.	2.0	6.5	2.5	2.4	7.3	1.1	3.7
9.2	6.5	21.	4.8	13.	20.	15.	45.6	12.	30.4	3.1	2.	6.3	1.6	4.6	13.	14.	28.8	6.9	19.	3.	4.	6.8	1.8	5.1	1.5	1.4	4.0	0.6	2.4
11.	7.5	25.	5.6	18.	22.	17.	53.8	9.0	33.6	3.2	2.	5.6	1.5	5.2	13.	12.	23.0	5.4	21.	2.	2.	5.4	0.9	4.4	1.4	1.0	3.4	0.5	2.2
24.	17.	71.	3.9	34.	45.	29.	138.	8.6	66.5	5.4	2.	17.	0.6	9.4	23.	8.5	77.8	2.2	47.	5.	1.	19.	0.7	15.	3.6	3.3	6.2	1.1	5.6
64.	62.	151	11.	108	143	134	358.	26.	233.	18.	14	45.	3.7	32.	81.	59.	203.	19.	153	21	13	51.	6.1	44.	5.2	6.5	7.8	1.8	7.4
11.	3.0	52.	1.5	18.	16.	4.8	97.3	1.9	24.5	1.7	0.	10.	0.2	2.1	6.1	2.1	40.0	1.0	7.1	1.	0.	5.6	0.3	1.3	0.5	0.2	2.2	0.2	0.4
211	126	760	19.	308	500	172	187	29.	675.	62.	18	233	2.9	81.	264	85.	104	9.9	336	52	14	254	1.1	66.	9.7	5.6	28.	3.2	16.
62.	32.	473	20.	60.	106	55.	815.	26.	134.	11.	5.	83.	2.7	17.	44.	22.	292.	10.	65.	9.	5.	52.	2.2	15.	12.	11.	31.	5.8	18.
32.	8.5	178	4.3	26.	68.	17.	385.	10.	55.9	7.9	2.	42.	1.6	6.2	30.	11.	149.	7.2	24.	6.	3.	27.	2.1	4.4	1.1	0.8	3.0	0.4	1.3
27.	7.6	191	3.9	27.	55.	15.	403.	9.3	53.5	6.9	2.	44.	1.3	6.6	30.	12.	174.	6.8	28.	8.	3.	38.	2.2	8.7	2.3	0.8	11.	0.3	3.7
57.	47.	140	10.	91.	91.	65.	205.	27.	143.	9.5	6.	20.	4.3	15.	35.	23.	90.9	15.	63.	7.	4.	21.	2.6	10.	5.7	4.3	7.1	3.7	7.4
93.	75.	215	17.	185	169	138	390.	34.	336.	18.	15	43.	4.0	37.	68.	54.	160.	13.	137	15	13	32.	3.5	28.	7.0	6.4	10.	3.2	11.
42.	42.	0.0	42.	42.	68.	68.	0.0	68.	68.6	6.9	6.	0.0	6.9	6.9	28.	28.	0.0	28.	28.	5.	5.	0.0	5.2	5.2	12.	12.	0.0	12.	12.
8.1	5.6	41.	3.5	8.8	16.	12.	83.8	7.2	16.6	2.2	1.	12.	1.0	2.1	9.5	7.1	54.9	4.3	8.8	2.	1.	15.	1.1	2.5	1.2	1.0	3.3	0.6	1.5
21.	13.	76.	7.8	27.	27.	15.	126.	7.2	35.8	3.9	2.	14.	1.5	4.9	13.	8.8	55.4	4.5	17.	2.	1.	9.7	0.9	3.2	3.1	1.5	17.	0.8	3.6
49.	20.	266	5.3	65.	91.	41.	476.	6.9	124.	9.9	4.	48.	1.2	13.	36.	16.	163.	6.7	49.	5.	2.	20.	1.3	8.5	1.3	0.8	4.3	0.3	2.0

Gd ppm					Tb ppm					Dy ppm					Ho ppm					Er ppm					Tm ppm				
M	Md	R	0.2	75	M	M	R	0.	75	M	Md	R	0.2	75	M	M	R	0.	75	M	Md	R	0.2	75	M	M	R	0.	75
1.3	1.2	4.20	0.6	1.6	0.	0.	0.5	0.0	0.2	1.0	0.9	2.66	0.3	1.1	0.	0.	0.5	0.0	0.2	0.5	0.5	1.1	0.2	0.6	0.	0.	0.	0.0	0.1
0.8	0.7	0.91	0.5	1.2	0.	0.	0.1	0.0	0.1	0.5	0.5	0.96	0.3	0.7	0.	0.	0.1	0.1	0.1	0.4	0.4	0.7	0.2	0.7	0.	0.	0.	0.0	0.1
1.1	0.4	11.0	0.2	1.3	0.	0.	1.3	0.0	0.1	0.8	0.3	7.86	0.1	1.0	0.	0.	1.6	0.0	0.2	0.4	0.2	4.2	0.0	0.5	0.	0.	0.	0.0	0.0
3.3	3.1	8.72	1.8	4.1	0.	0.	0.9	0.2	0.5	2.2	1.9	4.91	1.3	3.0	0.	0.	0.7	0.2	0.6	1.1	1.1	1.8	0.7	1.5	0.	0.	0.	0.1	0.2
1.6	1.6	3.04	0.9	2.0	0.	0.	0.4	0.1	0.2	1.2	1.3	2.84	0.4	1.6	0.	0.	0.5	0.1	0.3	0.7	0.7	1.8	0.3	1.0	0.	0.	0.	0.0	0.1
4.4	2.5	22.9	1.3	6.2	0.	0.	3.3	0.1	0.8	3.7	2.3	20.8	1.0	5.3	0.	0.	3.9	0.2	1.0	2.0	1.4	10.	0.5	2.8	0.	0.	1.	0.0	0.4
23.	17.	83.8	10.	27.	2.	2.	7.3	1.2	3.4	13.	10.	32.6	6.1	19.	2.	2.	6.0	1.1	3.7	6.9	6.4	16.	2.7	10.	0.	0.	1.	0.3	1.2
6.7	6.7	11.7	4.0	8.8	0.	0.	1.4	0.4	1.0	4.9	4.8	8.61	3.3	6.7	0.	0.	1.5	0.6	1.1	2.4	2.2	3.3	1.6	3.0	0.	0.	0.	0.1	0.3
3.6	1.0	28.4	0.3	3.7	0.	0.	4.0	0.0	0.6	3.3	1.0	26.2	0.3	3.9	0.	0.	5.2	0.0	1.0	2.3	0.8	14.	0.2	3.6	0.	0.	1.	0.0	0.5
0.4	0.4	0.48	0.3	0.6	0.	0.	0.1	0.0	0.1	0.8	0.7	1.35	0.3	1.3	0.	0.	0.3	0.0	0.3	0.6	0.6	1.0	0.2	1.0	0.	0.	0.	0.0	0.1
3.3	0.4	22.2	0.2	2.5	0.	0.	2.7	0.0	0.5	2.8	0.8	15.7	0.3	2.9	0.	0.	2.8	0.0	0.4	1.5	0.6	6.1	0.3	1.7	0.	0.	0.	0.0	0.2
14.	6.2	56.1	3.8	23.	2.	1.	9.5	0.6	3.4	12.	6.2	59.1	4.1	18.	2.	1.	10.	0.8	3.2	5.8	4.9	25.	2.0	7.2	0.	0.	2.	0.2	0.9
2.7	1.2	12.2	0.5	3.4	0.	0.	1.4	0.0	0.4	2.0	1.1	6.34	0.3	3.2	0.	0.	1.4	0.0	0.6	1.1	0.6	4.5	0.2	1.7	0.	0.	0.	0.0	0.2
1.1	1.1	2.43	0.2	2.0	0.	0.	0.4	0.0	0.3	1.1	1.0	2.59	0.1	1.9	0.	0.	0.3	0.0	0.3	0.4	0.4	0.9	0.1	0.7	0.	0.	0.	0.0	0.0
5.0	1.7	26.6	0.8	3.2	0.	0.	3.6	0.1	0.4	4.0	1.3	20.7	0.6	2.8	0.	0.	3.7	0.1	0.5	1.7	0.5	7.6	0.3	1.3	0.	0.	0.	0.0	0.1
3.1	2.5	6.54	1.7	4.4	0.	0.	1.1	0.2	0.5	2.7	2.0	7.82	1.4	4.1	0.	0.	1.7	0.2	0.6	1.2	0.7	4.9	0.6	1.3	0.	0.	0.	0.0	0.1
4.2	1.2	10.2	0.5	10.	0.	0.	1.2	0.1	1.3	3.1	1.0	10.1	0.3	8.0	0.	0.	2.6	0.0	2.0	4.3	1.4	10.	0.6	10.	0.	0.	1.	0.1	2.1
5.1	4.4	9.99	2.4	7.1	0.	0.	1.7	0.3	1.3	5.8	4.7	11.3	2.7	9.1	1.	1.	2.2	0.6	1.8	4.0	3.1	8.4	2.0	5.7	0.	0.	1.	0.3	0.9
0.6	0.7	0.34	0.5	0.7	0.	0.	0.0	0.0	0.1	0.7	0.7	0.56	0.5	1.0	0.	0.	0.1	0.1	0.2	0.7	0.6	0.7	0.4	1.0	0.	0.	0.	0.0	0.2
2.2	0.9	14.1	0.4	2.4	0.	0.	2.7	0.0	0.4	2.8	1.1	23.7	0.4	3.0	0.	0.	5.1	0.1	0.7	2.1	0.9	16.	0.3	2.7	0.	0.	2.	0.0	0.4
2.2	1.3	7.27	0.5	3.0	0.	0.	1.5	0.0	0.4	2.8	1.4	13.6	0.4	3.2	0.	0.	3.6	0.1	0.7	2.5	1.2	13.	0.3	3.0	0.	0.	2.	0.0	0.5
3.7	0.5	53.4	0.2	1.6	0.	0.	5.7	0.0	0.1	2.5	0.6	26.0	0.2	1.3	0.	0.	4.2	0.0	0.3	1.5	0.5	11.	0.2	1.1	0.	0.	1.	0.0	0.2
2.0	1.5	2.88	1.2	3.4	0.	0.	0.5	0.1	0.5	2.6	1.7	4.12	1.4	4.6	0.	0.	1.0	0.3	1.2	3.1	2.3	5.0	1.5	5.5	0.	0.	0.	0.3	1.0
5.6	2.5	22.9	0.6	9.3	0.	0.	4.2	0.0	1.3	5.8	2.4	31.5	0.6	7.6	1.	0.	6.9	0.1	1.6	3.8	1.5	20.	0.6	4.9	0.	0.	2.	0.0	0.6
1.1	0.6	5.29	0.4	1.0	0.	0.	0.7	0.0	0.1	0.9	0.6	4.20	0.3	1.2	0.	0.	0.7	0.0	0.2	0.5	0.5	2.1	0.1	0.7	0.	0.	0.	0.0	0.1
13.	2.8	61.9	0.3	25.	1.	0.	8.5	0.0	3.8	12.	2.5	56.6	0.2	23.	2.	0.	10.	0.0	5.2	9.5	1.9	32.	0.1	18.	1.	0.	4.	0.0	3.1
2.9	2.0	9.04	0.7	3.8	0.	0.	1.0	0.0	0.4	2.1	1.6	7.17	0.6	3.2	0.	0.	1.6	0.1	0.6	1.4	1.2	5.2	0.4	1.8	0.	0.	0.	0.0	0.2
1.3	0.7	7.36	0.2	1.5	0.	0.	0.9	0.0	0.2	1.1	0.8	5.86	0.3	1.5	0.	0.	1.1	0.0	0.2	0.7	0.6	2.6	0.2	0.8	0.	0.	0.	0.0	0.1
1.2	1.0	2.42	0.7	1.9	0.	0.	0.2	0.0	0.2	0.9	1.0	2.47	0.2	1.3	0.	0.	0.5	0.0	0.3	0.6	0.5	2.1	0.2	0.9	0.	0.	0.	0.0	0.1
0.2	0.1	0.78	0.0	0.2	0.	0.	0.1	0.0	0.0	0.2	0.0	1.27	0.0	0.1	0.	0.	0.3	0.0	0.0	0.1	0.0	1.9	0.0	0.1	0.	0.	0.	0.0	0.0
12.	12.	8.22	8.6	14.	1.	1.	0.8	0.8	1.5	6.4	6.8	2.59	5.2	7.3	1.	1.	0.2	1.1	1.3	3.1	3.0	0.8	2.9	3.5	0.	0.	0.	0.3	0.4
5.6	5.4	16.9	1.0	8.3	0.	0.	1.6	0.1	0.8	3.0	2.5	8.90	0.7	4.5	0.	0.	1.6	0.1	0.9	1.3	0.8	3.9	0.3	2.4	0.	0.	0.	0.0	0.2
6.8	6.1	10.5	3.5	10.	0.	0.	1.4	0.4	1.4	5.6	5.2	8.27	2.9	8.0	1.	1.	1.7	0.5	1.9	3.6	3.3	5.2	1.9	5.5	0.	0.	0.	0.2	0.7
58.	49.	224.	31.	80.	7.	6.	23.	4.1	11.	40.	32.	101.	25.	58.	7.	6.	19.	4.3	9.7	18.	15.	61.	10.	24.	2.	2.	8.	1.3	2.9
13.	12.	37.2	4.6	22.	2.	1.	6.1	0.6	3.3	14.	11.	43.5	4.2	19.	3.	2.	9.8	0.8	3.9	9.8	7.4	33.	2.3	12.	1.	1.	5.	0.4	1.8
3.5	2.3	9.64	1.6	4.7	0.	0.	1.4	0.2	0.6	3.3	2.2	7.65	1.6	4.8	0.	0.	1.3	0.3	0.9	2.1	1.7	4.3	1.2	2.7	0.	0.	0.	0.1	0.4
5.2	4.6	12.8	2.3	7.6	0.	0.	2.2	0.2	1.2	5.5	5.4	13.8	1.9	8.5	1.	1.	2.9	0.4	1.7	3.3	3.4	8.0	1.4	5.0	0.	0.	1.	0.2	0.6
4.8	5.5	4.84	3.2	5.9	0.	0.	0.8	0.3	0.8	4.2	4.4	4.94	3.1	5.5	0.	0.	1.2	0.2	0.9	2.0	2.0	2.7	1.5	2.5	0.	0.	0.	0.1	0.3
2.6	1.9	6.13	0.5	4.2	0.	0.	0.8	0.1	0.7	2.1	2.0	4.64	0.5	3.8	0.	0.	1.0	0.1	0.6	1.3	1.3	3.1	0.3	1.9	0.	0.	0.	0.0	0.3
6.6	1.4	21.3	0.5	17.	0.	0.	3.0	0.1	2.4	5.7	1.4	16.7	0.5	14.	1.	0.	3.1	0.1	2.7	3.1	0.9	8.2	0.3	6.4	0.	0.	1.	0.0	0.8
23.	13.	54.9	6.5	50.	3.	1.	8.1	0.8	7.4	21.	12.	53.2	6.0	45.	4.	2.	11.	1.2	9.2	12.	6.6	32.	3.2	26.	1.	0.	4.	0.5	3.3
1.1	0.5	5.40	0.2	1.2	0.	0.	0.5	0.0	0.2	1.0	0.5	3.54	0.3	1.3	0.	0.	0.7	0.0	0.2	0.7	0.4	2.0	0.3	1.0	0.	0.	0.	0.0	0.1
41.	9.7	224.	0.7	50.	4.	0.	27.	0.1	5.1	22.	3.9	142.	0.4	27.	4.	0.	25.	0.1	4.2	10.	1.8	62.	0.2	9.1	1.	0.	7.	0.0	1.0
9.6	6.1	43.7	2.5	14.	1.	1.	5.7	0.4	1.8	10.	8.5	39.0	3.0	13.	2.	2.	8.6	0.8	3.1	8.4	8.6	27.	3.4	11.	1.	1.	3.	0.5	1.7
5.7	3.8	19.6	2.6	5.2	0.	0.	2.6	0.3	0.9	5.1	3.7	14.1	2.2	6.1	1.	0.	2.4	0.4	1.2	3.0	2.4	6.1	1.5	3.9	0.	0.	0.	0.2	0.6
9.3	3.9	39.6	2.1	9.3	1.	0.	6.4	0.3	1.5	10.	4.5	44.1	2.3	10.	2.	0.	9.9	0.4	2.1	6.9	3.1	31.	1.8	6.4	1.	0.	5.	0.2	0.9
7.4	6.2	18.3	1.5	11.	1.	0.	3.2	0.1	1.8	8.1	6.3	26.1	1.2	12.	1.	1.	6.2	0.2	2.7	5.7	4.4	20.	0.7	8.7	0.	0.	2.	0.1	1.4
16.	18.	26.7	5.3	26.	2.	3.	3.9	0.9	4.1	21.	25.	27.4	8.0	30.	4.	5.	6.0	2.0	6.8	13.	15.	14.	5.9	18.	1.	1.	1.	0.7	2.2
6.2	6.2	0.00	6.2	6.2	0.	0.	0.0	0.8	0.8	5.5	5.5	0.00	5.5	5.5	1.	1.	0.0	1.5	1.5	4.7	4.7	0.0	4.7	4.7	0.	0.	0.	0.7	0.7
2.7	2.0	15.3	0.9	2.6	0.	0.	2.2	0.1	0.3	2.6	1.9	12.7	1.0	2.5	0.	0.	2.5	0.2	0.6	1.7	1.2	7.5	0.7	2.1	0.	0.	1.	0.1	0.3
2.0	1.4	6.92	0.7	3.3	0.	0.	0.9	0.0	0.5	1.7	1.4	6.52	0.5	3.2	0.	0.	1.2	0.1	0.5	1.0	0.9	3.4	0.4	1.6	0.	0.	0.	0.0	0.2
5.3	3.7	14.5	2.2	8.0	0.	0.	1.2	0.3	0.8	3.5	2.7	6.10	1.8	4.4	0.	0.	1.1	0.4	0.9	2.0	1.8	2.8	1.3	2.5	0.	0.	0.	0.1	0.3

Yb ppm					Lu ppm					Hf ppm					W ppm					Au ppm					Pb ppm				
M	Md	R	0.25	75%	M	Md	R	0.25	75%	M	Md	R	0.25	75%	M	Md	R	0.25	75%	M	Md	R	0.25	75%	M	Md	R	0.25	75%
0.50	0.51	1.02	0.20	0.76	0.08	0.09	0.11	0.03	0.11	0.60	0.26	2.33	0.14	0.93	0.53	0.45	1.16	0.19	0.62	-	-	-	-	-	36	30	88	23	44
0.39	0.37	0.54	0.17	0.62	0.08	0.07	0.16	0.05	0.12	0.16	0.14	0.17	0.11	0.21	1.23	0.32	4.37	0.22	2.69	-	-	-	-	-	166	155	359	45	289
0.51	0.21	3.42	0.08	0.55	0.08	0.04	0.40	0.01	0.09	0.08	0.08	0.14	0.04	0.11	0.45	0.38	1.59	0.12	0.57	-	-	-	-	-	32	27	92	19	39
1.00	1.14	1.51	0.66	1.31	0.13	0.14	0.20	0.10	0.17	0.41	0.32	1.40	0.14	0.50	0.05	0.04	0.14	0.03	0.05	-	-	-	-	-	45	45	102	31	57
0.59	0.63	1.69	0.23	0.82	0.09	0.08	0.22	0.03	0.12	0.09	0.07	0.29	0.05	0.14	0.08	0.06	0.16	0.03	0.13	0.01	0.01	0.00	0.01	0.01	66	45	155	34	99
1.93	1.21	9.35	0.50	2.52	0.31	0.16	1.41	0.07	0.40	0.75	0.47	3.58	0.13	0.95	0.17	0.17	0.25	0.12	0.23	-	-	-	-	-	75	72	138	55	97
6.70	6.40	13.90	3.78	8.29	1.02	0.88	2.11	0.53	1.25	0.90	0.30	3.54	0.12	1.56	0.98	0.67	2.67	0.51	1.31	0.01	0.01	0.00	0.01	0.01	244	246	198	230	269
1.95	1.71	2.84	1.30	2.50	0.27	0.24	0.41	0.18	0.31	0.70	0.63	2.97	0.35	0.73	0.23	0.15	0.33	0.14	0.37	-	-	-	-	-	90	71	191	40	150
2.25	0.90	10.67	0.28	3.58	0.33	0.14	1.21	0.04	0.54	0.06	0.05	0.09	0.03	0.08	0.13	0.10	0.34	0.08	0.16	0.03	0.03	0.01	0.02	0.03	66	43	285	14	93
0.71	0.71	1.17	0.22	1.20	0.10	0.10	0.13	0.04	0.15	0.09	0.09	0.04	0.07	0.10	0.31	0.25	0.53	0.08	0.61	-	-	-	-	-	48	49	47	28	66
1.34	1.04	4.05	0.42	1.62	0.18	0.14	0.54	0.04	0.24	0.24	0.22	0.56	0.08	0.32	0.29	0.15	0.93	0.10	0.58	-	-	-	-	-	45	37	113	8	77
3.97	3.46	11.67	1.84	5.56	0.53	0.54	0.82	0.26	0.80	0.95	0.60	3.35	0.33	1.07	0.22	0.15	0.64	0.10	0.31	-	-	-	-	-	41	41	49	37	48
1.12	0.61	4.29	0.20	1.29	0.18	0.11	0.76	0.03	0.21	0.53	0.14	2.54	0.08	0.77	0.62	0.49	1.08	0.35	0.98	-	-	-	-	-	138	83	875	75	96
0.31	0.31	0.48	0.25	0.42	0.05	0.04	0.09	0.03	0.06	0.17	0.19	0.32	0.04	0.26	0.38	0.34	0.75	0.19	0.55	-	-	-	-	-	135	128	348	91	163
1.20	0.55	5.01	0.20	1.07	0.17	0.06	0.55	0.04	0.27	0.15	0.13	0.26	0.08	0.21	0.82	0.85	1.35	0.44	1.12	-	-	-	-	-	30	30	37	23	36
0.80	0.48	3.77	0.30	0.86	0.11	0.06	0.46	0.04	0.14	1.38	1.13	5.80	0.59	1.64	0.19	0.14	0.82	0.07	0.24	-	-	-	-	-	224	180	728	48	301
4.37	2.10	16.27	0.30	9.58	0.65	0.27	2.21	0.11	1.37	1.16	1.16	2.01	0.15	2.17	0.75	0.71	0.95	0.30	1.25	-	-	-	-	-	103	98	85	67	140
5.52	4.07	11.29	2.60	8.30	0.89	0.71	1.90	0.46	1.33	1.73	1.21	4.73	0.56	2.67	0.12	0.12	0.22	0.08	0.16	0.01	0.01	0.00	0.01	0.01	73	73	41	63	84
1.61	1.36	2.01	0.90	2.59	0.31	0.30	0.37	0.15	0.49	1.21	1.32	0.80	0.82	1.48	0.10	0.09	0.14	0.06	0.16	-	-	-	-	-	63	62	18	56	71
2.48	1.60	14.96	0.72	2.70	0.32	0.18	1.68	0.07	0.36	0.18	0.14	0.66	0.06	0.29	1.14	0.80	4.69	0.33	1.57	-	-	-	-	-	108	104	109	83	135
3.91	2.03	22.32	0.45	5.71	0.58	0.46	3.04	0.07	0.80	0.18	0.17	0.37	0.07	0.26	0.65	0.44	2.06	0.28	0.93	0.02	0.02	0.00	0.02	0.02	97	94	107	70	118
2.06	0.75	13.86	0.38	2.10	0.33	0.11	2.02	0.05	0.32	0.81	0.68	3.88	0.35	1.02	0.63	0.38	3.08	0.19	0.72	-	-	-	-	-	92	79	183	63	121
5.16	3.90	7.36	2.90	8.68	0.75	0.58	1.04	0.43	1.23	0.10	0.10	0.06	0.07	0.13	0.28	0.29	0.40	0.11	0.44	-	-	-	-	-	288	301	335	137	427
3.52	1.54	17.21	0.53	4.12	0.50	0.25	2.13	0.09	0.55	0.15	0.15	0.33	0.07	0.18	0.10	0.07	0.28	0.05	0.11	0.01	0.01	0.00	0.01	0.01	157	143	301	81	224
0.63	0.53	2.11	0.19	1.00	0.10	0.08	0.29	0.02	0.15	0.16	0.11	0.71	0.07	0.20	0.07	0.07	0.16	0.04	0.09	-	-	-	-	-	85	70	166	54	110
11.45	1.87	33.97	0.17	26.33	2.17	1.76	5.20	0.04	4.45	0.26	0.15	0.59	0.04	0.56	0.27	0.24	0.49	0.10	0.40	-	-	-	-	-	143	133	132	122	151
1.38	1.37	3.44	0.49	1.89	0.20	0.20	0.55	0.08	0.32	0.41	0.23	1.67	0.18	0.50	0.45	0.27	1.91	0.15	0.56	0.01	0.01	0.01	0.01	0.02	128	122	119	98	151
0.73	0.62	2.10	0.23	1.10	0.10	0.07	0.29	0.03	0.15	0.22	0.20	0.71	0.07	0.28	0.43	0.13	2.50	0.05	0.48	0.02	0.02	0.00	0.02	0.02	72	62	124	44	85
0.69	0.52	2.31	0.16	1.13	0.11	0.06	0.31	0.03	0.13	0.65	0.13	5.02	0.05	0.45	0.28	0.18	0.97	0.12	0.36	-	-	-	-	-	80	82	182	37	122
0.22	0.08	2.37	0.05	0.14	0.04	0.02	0.34	0.01	0.02	0.05	0.05	0.15	0.01	0.07	0.49	0.27	1.50	0.16	0.76	-	-	-	-	-	134	137	235	81	182
2.61	2.46	1.04	2.29	3.07	0.45	0.42	0.16	0.41	0.53	0.37	0.39	0.16	0.30	0.42	0.27	0.14	0.40	0.14	0.54	-	-	-	-	-	313	337	162	237	365
1.04	0.66	3.29	0.35	1.65	0.17	0.11	0.70	0.06	0.24	0.66	0.54	2.29	0.26	0.91	0.15	0.11	0.41	0.09	0.19	0.02	0.02	0.01	0.01	0.03	143	135	271	69	174
3.44	3.29	4.50	1.74	4.96	0.57	0.53	0.71	0.32	0.79	0.95	0.92	1.64	0.64	1.09	0.60	0.70	0.61	0.36	0.81	-	-	-	-	-	62	54	93	48	67
15.30	13.08	62.80	7.97	19.44	2.33	1.93	9.42	1.18	3.12	0.35	0.19	1.10	0.14	0.41	1.06	0.70	4.46	0.62	1.30	0.00	0.00	0.00	0.00	0.00	69	62	113	51	89
11.76	8.43	41.46	5.76	14.09	1.74	1.41	6.90	0.46	2.27	0.42	0.28	1.18	0.18	0.56	0.73	0.53	1.55	0.33	1.14	-	-	-	-	-	52	45	107	41	53
2.49	2.24	3.15	1.82	3.06	0.40	0.37	0.49	0.27	0.52	0.57	0.62	0.66	0.40	0.73	0.53	0.25	2.90	0.19	0.50	-	-	-	-	-	36	37	21	28	43
2.90	3.15	6.58	1.17	4.21	0.44	0.43	0.98	0.15	0.66	1.66	1.07	6.22	0.36	2.55	0.63	0.43	1.67	0.35	1.10	-	-	-	-	-	83	57	346	43	87
1.59	1.68	3.44	0.70	2.29	0.31	0.30	0.55	0.14	0.45	0.87	0.54	2.01	0.20	1.75	0.28	0.15	0.67	0.07	0.43	0.02	0.02	0.00	0.02	0.02	46	36	66	24	79
1.30	1.18	2.41	0.66	1.93	0.17	0.15	0.46	0.07	0.23	0.51	0.41	1.09	0.20	0.79	0.19	0.17	0.19	0.13	0.24	0.03	0.03	0.01	0.02	0.03	48	50	65	35	61
3.05	2.42	8.47	0.80	4.93	0.58	0.68	1.54	0.12	0.87	0.08	0.03	0.20	0.03	0.16	0.77	0.71	1.12	0.50	1.15	0.01	0.01	0.00	0.01	0.01	80	75	74	61	96
11.95	6.15	31.82	3.53	23.92	2.01	1.03	5.28	0.66	3.91	0.56	0.55	1.38	0.12	1.01	0.60	0.33	1.43	0.17	1.17	-	-	-	-	-	29	27	41	12	46
0.73	0.57	2.03	0.32	1.02	0.13	0.10	0.43	0.05	0.19	0.15	0.07	0.77	0.04	0.08	1.00	0.66	3.00	0.33	1.61	0.01	0.01	0.00	0.01	0.01	67	72	91	46	87
8.86	1.18	49.13	0.41	7.74	1.04	0.15	6.03	0.05	1.06	0.32	0.21	1.67	0.10	0.38	0.54	0.56	0.94	0.17	0.94	0.04	0.04	0.00	0.04	0.04	188	189	345	121	248
9.33	6.24	26.86	4.48	12.60	1.28	0.98	3.59	0.63	1.71	0.16	0.12	0.81	0.05	0.22	1.24	1.10	3.86	0.39	1.60	-	-	-	-	-	47	46	104	31	56
3.54	2.72	7.35	1.76	4.60	0.61	0.47	1.26	0.31	0.80	0.60	0.46	1.39	0.35	0.60	0.76	0.77	1.02	0.50	0.87	-	-	-	-	-	45	41	39	33	57
8.26	3.67	41.82	2.01	7.87	1.26	0.67	6.97	0.38	1.21	0.89	0.72	2.45	0.36	1.25	0.62	0.54	1.63	0.38	0.83	0.02	0.02	0.00	0.02	0.02	36	35	37	24	49
6.62	4.03	18.20	0.91	11.90	0.93	0.53	2.50	0.10	1.84	0.28	0.19	0.96	0.12	0.29	1.81	1.60	3.76	1.14	2.17	-	-	-	-	-	49	41	72	35	66
7.68	7.62	9.50	4.09	11.35	1.01	0.92	1.26	0.54	1.55	0.11	0.11																		

Bi					Th					U				
M	Md	R	0.25	75%	M	Md	R	0.25	75%	M	Md	R	25%	75%
1.73	1.22	4.99	0.28	2.55	1.16	0.78	3.78	0.34	1.72	0.28	0.20	0.89	0.11	0.37
0.29	0.18	0.58	0.12	0.58	1.32	2.09	2.47	0.18	2.22	0.39	0.19	1.59	0.12	0.51
2.39	1.69	8.38	0.98	3.26	0.82	0.53	3.51	0.12	1.10	0.23	0.09	1.56	0.04	0.28
1.55	1.33	3.05	0.94	1.77	16.56	7.95	77.73	1.76	20.55	1.61	1.58	2.03	1.29	2.04
1.31	0.88	4.28	0.50	1.98	0.18	0.10	0.58	0.04	0.26	2.04	1.36	8.48	0.60	3.35
0.61	0.23	5.19	0.12	0.65	1.72	1.54	4.10	0.65	2.37	1.66	0.83	9.53	0.40	1.25
2.35	2.14	3.50	1.48	2.96	4.13	1.39	34.74	0.51	4.78	11.18	9.80	13.91	7.86	15.21
1.14	0.69	2.58	0.36	1.96	10.09	5.99	55.39	2.17	12.40	2.04	1.78	6.09	0.67	3.07
3.38	2.40	13.06	1.15	3.69	0.43	0.22	2.32	0.08	0.70	3.39	1.26	12.43	0.49	5.86
3.52	3.70	4.90	1.57	5.29	0.07	0.05	0.08	0.04	0.12	7.59	5.31	17.85	1.76	15.71
3.38	2.86	9.57	1.55	3.58	6.50	1.21	28.52	0.46	11.48	7.72	5.51	23.19	0.78	13.75
2.25	2.01	3.24	1.55	2.97	15.78	12.68	56.72	7.83	21.96	13.61	14.46	25.23	9.04	16.38
0.12	0.10	0.18	0.08	0.15	0.47	0.45	1.03	0.23	0.67	3.98	2.89	13.16	1.66	5.07
0.16	0.16	0.16	0.10	0.19	0.34	0.07	0.93	0.03	0.74	6.44	5.60	12.97	3.32	8.59
0.09	0.09	0.07	0.07	0.10	0.40	0.13	2.75	0.07	0.28	2.98	2.55	5.02	2.17	3.51
0.15	0.11	0.23	0.08	0.21	1.90	0.87	10.84	0.31	2.28	3.05	3.05	6.65	2.03	3.66
0.39	0.39	0.09	0.35	0.44	4.29	0.06	12.67	0.06	12.73	4.94	1.12	11.64	0.78	11.01
0.06	0.06	0.03	0.04	0.07	6.29	4.98	19.58	2.99	7.66	2.85	2.64	5.65	1.88	3.34
0.07	0.08	0.07	0.03	0.10	11.29	10.94	19.32	2.73	20.20	2.50	2.35	2.12	1.66	3.50
0.19	0.17	0.39	0.11	0.26	0.84	0.44	3.12	0.16	1.35	2.03	1.65	4.81	0.85	3.61
0.09	0.09	0.11	0.05	0.12	1.10	0.56	5.30	0.36	1.46	1.52	0.79	7.37	0.55	1.85
0.07	0.06	0.18	0.04	0.09	2.41	0.78	28.70	0.39	1.79	1.59	1.18	3.87	0.80	2.28
0.45	0.40	0.31	0.35	0.61	0.15	0.16	0.18	0.05	0.23	7.48	4.26	19.01	1.77	16.40
0.69	0.63	2.03	0.33	0.99	0.84	0.71	1.89	0.49	1.06	2.38	2.25	4.65	1.22	3.27
0.35	0.21	1.30	0.14	0.40	1.20	1.05	2.86	0.38	2.01	0.93	0.77	2.80	0.35	1.47
0.34	0.29	0.62	0.19	0.46	3.15	0.72	18.48	0.24	3.43	15.87	15.88	36.62	1.20	29.58
0.39	0.28	0.91	0.19	0.61	1.85	1.39	5.27	0.77	2.72	6.76	4.77	28.15	2.86	7.40
0.45	0.43	1.01	0.18	0.64	1.82	1.48	5.92	0.63	1.87	2.50	2.12	6.43	1.00	3.98
0.30	0.29	0.51	0.24	0.40	3.97	0.45	35.97	0.15	3.51	3.25	2.07	7.79	1.14	5.23
0.34	0.23	1.11	0.18	0.45	0.21	0.11	1.88	0.04	0.22	0.56	0.40	1.38	0.23	0.84
4.85	5.40	4.89	2.70	6.46	3.78	2.77	4.75	2.47	6.10	9.48	9.81	3.30	7.93	10.70
0.20	0.19	0.31	0.12	0.25	34.27	15.60	223.47	4.52	37.60	13.17	9.64	37.28	2.42	23.20
0.13	0.13	0.08	0.09	0.17	0.92	0.74	2.11	0.48	1.11	5.97	5.23	8.66	3.93	9.13
1.23	0.95	4.80	0.51	1.76	19.21	14.72	61.96	3.54	35.90	12.54	13.11	23.51	7.25	17.36
0.20	0.19	0.39	0.10	0.31	1.79	0.95	6.37	0.66	2.42	4.16	1.31	17.24	0.40	7.47
0.08	0.07	0.07	0.06	0.10	1.43	0.64	7.73	0.38	1.20	2.33	2.19	3.59	1.77	2.64
0.39	0.22	1.32	0.13	0.38	1.98	1.70	5.58	0.66	3.12	4.06	1.69	12.33	1.27	8.27
0.20	0.17	0.23	0.10	0.33	4.23	3.70	7.61	1.83	6.60	1.92	2.05	3.41	1.10	2.86
0.12	0.11	0.16	0.05	0.19	4.89	3.43	15.03	1.59	6.79	1.60	1.71	4.20	0.73	1.98
1.22	1.12	2.21	0.72	1.84	2.31	1.42	8.15	0.72	3.65	2.17	0.76	7.58	0.27	4.22
0.39	0.32	0.92	0.12	0.68	13.34	9.58	39.62	1.49	23.78	13.56	6.43	30.54	3.06	31.20
0.10	0.08	0.20	0.06	0.13	0.69	0.28	3.05	0.10	0.85	1.22	0.78	4.43	0.49	1.34
3.72	3.07	9.51	0.90	5.75	10.94	1.77	132.93	0.83	5.33	5.61	2.18	28.53	0.81	7.68
0.17	0.14	0.39	0.11	0.20	3.72	1.45	22.08	0.47	5.16	18.89	10.10	114.66	3.73	18.80
0.37	0.40	0.52	0.21	0.55	5.04	4.05	16.01	0.93	6.72	2.65	1.84	3.93	1.55	4.44
0.31	0.22	0.91	0.14	0.49	4.60	1.84	20.16	0.84	6.59	4.53	3.62	11.36	2.37	6.13
0.46	0.21	1.67	0.09	0.72	2.32	0.88	15.88	0.42	1.35	3.10	2.18	14.31	1.04	2.73
-	-	-	-	-	8.10	3.41	25.22	0.58	20.31	40.18	46.65	35.40	23.15	50.73
0.34	0.34	0.00	0.34	0.34	41.90	41.90	0.00	41.90	41.90	2.47	2.47	-	2.47	2.47
0.14	0.14	0.18	0.11	0.17	0.94	0.69	3.13	0.54	1.41	3.74	3.03	11.65	2.07	4.98
-	-	-	-	-	2.99	2.42	9.37	1.39	3.80	1.66	1.28	4.28	0.59	2.37
0.13	0.12	0.07	0.11	0.15	10.95	7.30	33.10	4.80	19.20	1.50	1.33	2.80	0.87	2.19

